

Lecture Notes in Civil Engineering

Erol Tutumluer
Soheil Nazarian
Imad Al-Qadi
Issam I. A. Qamhia *Editors*

Advances in Transportation Geotechnics IV

Proceedings of the 4th International
Conference on Transportation
Geotechnics Volume 1

 Springer

Lecture Notes in Civil Engineering

Volume 164

Series Editors

Marco di Prisco, Politecnico di Milano, Milano, Italy

Sheng-Hong Chen, School of Water Resources and Hydropower Engineering,
Wuhan University, Wuhan, China

Ioannis Vayas, Institute of Steel Structures, National Technical University of
Athens, Athens, Greece

Sanjay Kumar Shukla, School of Engineering, Edith Cowan University, Joondalup,
WA, Australia

Anuj Sharma, Iowa State University, Ames, IA, USA

Nagesh Kumar, Department of Civil Engineering, Indian Institute of Science
Bangalore, Bengaluru, Karnataka, India

Chien Ming Wang, School of Civil Engineering, The University of Queensland,
Brisbane, QLD, Australia

Lecture Notes in Civil Engineering (LNCE) publishes the latest developments in Civil Engineering - quickly, informally and in top quality. Though original research reported in proceedings and post-proceedings represents the core of LNCE, edited volumes of exceptionally high quality and interest may also be considered for publication. Volumes published in LNCE embrace all aspects and subfields of, as well as new challenges in, Civil Engineering. Topics in the series include:

- Construction and Structural Mechanics
- Building Materials
- Concrete, Steel and Timber Structures
- Geotechnical Engineering
- Earthquake Engineering
- Coastal Engineering
- Ocean and Offshore Engineering; Ships and Floating Structures
- Hydraulics, Hydrology and Water Resources Engineering
- Environmental Engineering and Sustainability
- Structural Health and Monitoring
- Surveying and Geographical Information Systems
- Indoor Environments
- Transportation and Traffic
- Risk Analysis
- Safety and Security

To submit a proposal or request further information, please contact the appropriate Springer Editor:

- Pierpaolo Riva at pierpaolo.riva@springer.com (Europe and Americas);
- Swati Meherishi at swati.meherishi@springer.com (Asia - except China, and Australia, New Zealand);
- Wayne Hu at wayne.hu@springer.com (China).

All books in the series now indexed by Scopus and EI Compendex database!

More information about this series at <http://www.springer.com/series/15087>

Erol Tutumluer · Soheil Nazarian · Imad Al-Qadi ·
Issam I. A. Qamhia
Editors

Advances in Transportation Geotechnics IV

Proceedings of the 4th International
Conference on Transportation Geotechnics
Volume 1

 Springer

Editors

Erol Tutumluer
Department of Civil and Environmental
Engineering
University of Illinois at Urbana-Champaign
Urbana, IL, USA

Soheil Nazarian
Department of Civil Engineering
The University of Texas at El Paso
El Paso, TX, USA

Imad Al-Qadi
Department of Civil and Environmental
Engineering
University of Illinois at Urbana-Champaign
Urbana, IL, USA

Issam I. A. Qamhia
Department of Civil and Environmental
Engineering
University of Illinois at Urbana-Champaign
Urbana, IL, USA

ISSN 2366-2557

ISSN 2366-2565 (electronic)

Lecture Notes in Civil Engineering

ISBN 978-3-030-77229-1

ISBN 978-3-030-77230-7 (eBook)

<https://doi.org/10.1007/978-3-030-77230-7>

© The Editor(s) (if applicable) and The Author(s), under exclusive license to Springer Nature Switzerland AG 2022

This work is subject to copyright. All rights are solely and exclusively licensed by the Publisher, whether the whole or part of the material is concerned, specifically the rights of translation, reprinting, reuse of illustrations, recitation, broadcasting, reproduction on microfilms or in any other physical way, and transmission or information storage and retrieval, electronic adaptation, computer software, or by similar or dissimilar methodology now known or hereafter developed.

The use of general descriptive names, registered names, trademarks, service marks, etc. in this publication does not imply, even in the absence of a specific statement, that such names are exempt from the relevant protective laws and regulations and therefore free for general use.

The publisher, the authors and the editors are safe to assume that the advice and information in this book are believed to be true and accurate at the date of publication. Neither the publisher nor the authors or the editors give a warranty, expressed or implied, with respect to the material contained herein or for any errors or omissions that may have been made. The publisher remains neutral with regard to jurisdictional claims in published maps and institutional affiliations.

This Springer imprint is published by the registered company Springer Nature Switzerland AG
The registered company address is: Gewerbestrasse 11, 6330 Cham, Switzerland

Contents

Mechanistic-Empirical Design (Roads, Railways, Airfields and Harbor Facilities)	
A Conceptual System Dynamics Framework to Evaluate Performance of Pavement Foundations Under Moisture Variations	3
Sayedmasoud Mousavi, Majid Ghayoomi, and Eshan V. Dave	
Dynamic Response of a Beam on a Layered Half-Space with a Poroelastic Interlayer Subjected to Moving Loads	17
Yicheng Li, Xiaolei Zhang, and Shijin Feng	
Modification of Japanese Pavement Fatigue Life Criteria by Considering Climatic Effects in Cold Regions	29
Tianshu Lin, Tatsuya Ishikawa, Tetsuya Tokoro, Kimio Maruyama, and Chigusa Ueno	
Influence of Vehicle Braking on Pavement Shakedown Limits	41
Yuchen Dai, Jiangu Qian, and Feifei Lei	
Physical Modeling of Stress Propagation in Railway Pavement with LWD	49
Artur Cortês da Rosa, Maria Esther Soares Marques, Antônio Carlos Rodrigues Guimarães, Gleyciane Almeida Serra, and Marcelino Aurélio Vieira da Silva	
Verification of the Structural Design Parameters for Unbound Layers of Finnish Road Structures	61
Antti Kalliainen and Pauli Kolisoja	
FreeHyTE: A Hybrid-Trefftz Finite Element Platform for Poroelastodynamic Problems	73
Natalia Climent, Ionut Moldovan, and António Gomes Correia	
A Mechanistic-Based Analysis Procedure for Designing Geosynthetic Reinforcement in Pavement Systems	87
Peter Becker	

Geotechnical Characterization of a Low Volume Traffic Road	101
Marina M. Cabette, Antonio M. V. Paula, Manuel J. C. Minhoto, and Ewerton C. A. Fonseca	
Development of Prediction Models for Mechanistic Parameters of Granular Roads Using Combined Non-destructive Tests	113
Sajjad Satvati, Bora Cetin, and Jeramy C. Ashlock	
Influence of Foundation Layer Properties in a Roller-Compacted Concrete Pavement System Subjected to Heavy Vehicle Loads	127
Nancy Aguirre, Abbasali Taghavighalesari, Richard Rogers, Cesar Carrasco, and Soheil Nazarian	
R-Value and Resilient Modulus Prediction Models Based on Soil Index Properties for Colorado Soils	141
Cara Fragomeni and Ahmadreza Hedayat	
Performance Evaluation of Flexible Pavements with Asphalt-Treated Base Courses	157
Jun Liu, Jenny Liu, Peng Li, and Stephan Saboundjian	
Investigation of Instantaneous Shear Failure in Pavement Subgrade Subjected to Superheavy Load Vehicle	169
Hadi Nabizadeh, Mohamed Nimeri, Elie Y. Hajj, Raj V. Siddharthan, and Sherif Elfass	
Evaluation of Flexible Pavement Performance Models in Mississippi: A Neural Network Approach	179
Patrick Duckworth, Hakan Yasarer, and Yacoub Najjar	
Field Monitoring of Flexible and Rigid Pavement Responses in Thailand	191
Auckpath Sawangsuriya, Apiniti Jotisankasa, and Suphawut Malaikrisanachalee	
Class Discriminatory Information for Unbound Granular Layers Using Statistical Pattern Recognition Techniques	207
Reza S. Ashtiani	
Deformation and Failure Parameters of Cement-Modified Loess: Application to the Calculation of the Safety Factor of a Road Structure	229
Thomas Lenoir, Thierry Dubreucq, Thibaut Lambert, and Denis Killinger	
Physical Modeling of the Washboard Effect on Unpaved Roads	243
Bernardo Caicedo and Gregoire Aguetant	

Finite Element Analysis of Nonlinear Elastic Behavior of Unbound Aggregate Materials Under Repeated Loading 253
Haohang Huang, Jiayi Luo, Issam I. A. Qamhia, Erol Tutumluer, Jeb S. Tingle, and Carlos R. Gonzalez

Optimized Geomaterial (Including Hydraulically Bound Materials and Asphalt Mixtures) Use, Reuse and Recycling in Road Embankments and Structural Layers

Feasibility of Using Selected and Mixed Recycled Aggregates from Construction and Demolition Waste in Unbound Pavement Layers 267
Castorina S. Vieira, Paulo M. Pereira, and Maria de Lurdes Lopes

Study of Deformation and Failure States of Reinforced Mesh Cushion in the Geosynthetics-Reinforced and Pile-Supported Structure of High-Speed Railway 281
Tai-Feng Li, Degou Cai, Zhi-Bo Cheng, Qian-Li Zhang, Yin Gao, Colin Basye, Jing-Yu Liu, and Xin-Gang Zhang

Structural Pavement Rehabilitation with Recycled Materials in a Circular Economy Approach 293
A. C. Freire, E. Correia, J. Neves, I. Martins, A. J. Roque, M. I. M. Pinto, C. Ferreira, and A. Martins

Crushed Rock Geopolymer as a Future Road Construction Material: An Evaluation of Compaction and Strength Characteristics 305
Peerapong Jitsangiam, Teewara Suwan, Korakod Nusit, Prinya Chindaprasirt, and Sararat Kwunjai

Considerations for Design of Aggregate Gradation in Pavement Drainage Layers 317
Shubham A. Kalore, G. L. Sivakumar Babu, and Ratnakar R. Mahajan

The Potential of Quartzitic Rock for Use as Coarse Aggregates in Asphaltic Concrete 333
Thomas D. Arthur, Samuel I. K. Ampadu, and Simon K. Y. Gawu

Introduction of Stone Matrix Asphalt for National Highways in Japan’s Cold, Snowy Regions 349
Shunsuke Tanaka, Kimio Maruyama, and Shuichi Kameyama

Effects of Using Recycled Aggregates and Large Stones for Base and Subbase Layers on Modulus Properties of Pavements 363
Haluk Sinan Coban, Bora Cetin, Halil Ceylan, William Likos, and Tuncer B. Edil

Analysis of the Applicability of USCS, TRB and MCT Classification Systems to the Tropical Soils of Pernambuco, Brazil, for Use in Road Paving	373
Roberto Quental Coutinho and Mayssa Alves da Silva Sousa	
Behavior of Compacted Collapsible Soil After Adding Calcium Chloride	387
Weijuan Geng, Weiyang Zhou, and Jiankun Liu	
Evaluation of the Performance of SMC Modified Asphalt Mixtures and Its Environmental Benefits Analysis	401
Haoyuan Luo, Yanjun Qiu, and Ting Su	
Discrete Element Simulation of the Internal Structures of Asphalt Mixtures with High Content of Tire Rubber	425
Xiaodong Zhou, Siyu Chen, Dongzhao Jin, and Zhanping You	
Beneficial Use of Dredged Material in Flowable Fill	441
Pranshoo Solanki, Juan David Lopez, Harshvardhan Jain, and Bhupesh Jain	
Effective Subgrade Remediation by Materials Improved with Blast Furnace Type B Cement	451
Atsuko Sato, Osamu Hatakeyama, and Naoyuki Kuji	
Particle Breakage of a Crushed Sandstone–Mudstone Particle Mixture	463
Zhenfeng Qiu, Shaobo Yang, Junjie Wang, and Ting Cao	
Field Evaluation of Using Slag as Aggregates for Otta Seal Surfacing ...	475
Bo Yang, Yang Zhang, Halil Ceylan, and Sunghwan Kim	
The Key Technology of High-Speed Railway Foamed Lightweight Soil Subgrade	489
Jianping Yao, Degou Cai, Guanzhi Cheng, Si Li, and Jiao Xie	
Field Scale Trial of Fibre-Reinforced Ballast	503
Geoff Watson, Edgar Ferro, Louis Le Pen, David Milne, Tristan Rees White, and William Powrie	
Mechanical Performance of Tire-Derived Aggregate Permeable Pavements Under Live Traffic Loads	515
Ramin Raeesi, Amin Soltani, Russell King, and Mahdi M. Disfani	
Alternative Materials for the Construction of Landfills and Embankments	529
Meghana Yeluri, E. C. Nirmala Peter, and Srinivas Allena	
Geotechnical Properties of Modified Railway Sidings Coal Discard	541
Felix Okonta and Carl Hien Rottcha	

Fit-for-Purpose Road Recycling? Triaxial Evaluation of Bitumen Stabilized RAP and Secondary Materials 551
K. J. Jenkins, C. E. Rudman, and N. A. Mazibuko

Sustainability in Transportation Geotechnics

A Mixture of Waste Materials as a Construction Fill in Transportation Infrastructure 565
Miriam Tawk, Buddhima Indraratna, Cholachat Rujikiatkamjorn, and Ana Heitor

Finite Element Simulations of Recycled Asphalt Pavement (RAP) Materials to Be Utilized in Unbound Pavement Layers 579
Andreas Loizos, Brad Cliatt, and Christina Plati

Effectiveness of Double-Layer HDPE Geocell System to Reinforce Reclaimed Asphalt Pavement (RAP)-Base Layer 593
Md. Ashrafuzzaman Khan, Nripojjyoti Biswas, Aritra Banerjee, Surya Sarat Chandra Congress, and Anand J. Puppala

Geotechnical and Geoenvironmental Characterization of Fine-Grained Construction and Demolition Recycled Materials Reinforced with Geogrids 605
Castorina S. Vieira and Paulo M. Pereira

Strength Assessment of Quarry Dust Treated Soil—Reclaimed Asphalt Pavement (Rap) Mixture 619
Mildred Cakuru, Rajab Katuntu Tenywa, Samuel Jjuuko, and Denis Kalumba

Reuse of Waste HDPE Bottle-Derived Geocells for Stabilization of Hilly Roadway Slopes 631
Punit Bhanwar, Sunil Ahirwar, and Trudeep Dave

Physico-Chemical and Mechanical Characterization of Ferrochrome Slag Aggregates for Utilization as a Road Material 645
Narala Gangadhara Reddy and B. Hanumantha Rao

Durability of Stabilized Quarry By-Products in Base and Subbase Applications 659
Issam I. A. Qamhia, Erol Tutumluer, Hasan Ozer, Heather Shoup, and Andrew Stolba

Stabilization and Reinforcement of Geomaterials and Its Implications in Pavement and Rail Track Design

Prediction of Durability, Resilient Modulus and Resistance Value of Cement Kiln Dust-Stabilized Expansive Clay for Flexible Pavement Application Using Artificial Neural Networks	675
Anigilaje B. Salahudeen, Mehdi Jalili, Danial R. Eidgahee, Kennedy C. Onyelowe, and Mohsen K. Kabiri	
Seepage Behavior Within Embankment Constructed of Mixed Soil with Steel Slag	689
Katsuyuki Kawai, Kaito Arinishi, Satsuki Kataoka, and Koji Nakashima	
The Water-Repellent Ability of Road Pavement Material Stabilized with Synthetic and Natural Polymers	701
Korakod Nusit, Peerapong Jitsangiam, and Prinya Chindaprasirt	
Behavior of Polymer-Reinforced Granular Mixtures for Railway Sub-Ballasts	713
Eivy Alvarez, Xiaobin Chen, and Francisco Grajales-Saavedra	
Construction and Monitoring of the Short-Term Strength Development of a Cement-Stabilized Lateritic Pavement Layer Under Tropical Climatic Conditions	727
Samuel I. K. Ampadu, Thomas D. Arthur, Priscilla Ackah, and Fred Boadu	
Experimental Study on Mass Stabilization of Soft Soil Foundation Based on MgO-CO₂ Carbonation Technology	743
Song-yu Liu, Guang-hua Cai, Guang-yin Du, Liang Wang, Jia-fu Chen, Chuan Qin, and Jing Ruan	
Analytical Solution for Plane Strain Consolidation of Soft Soil Stabilised by Stone Columns	753
Sam Doan, Behzad Fatahi, Hadi Khabbaz, and Haleh Rasekh	
Impact of Lime Stabilization on Swelling and Soil Water Retention Behavior of Expansive Subgrade	769
Asmaa Al-Taie, Mahdi M. Disfani, Robert Evans, Arul Arulrajah, and Ehsan Yaghoubi	
Evaluation of Strength and Microstructural Characteristics of Weak Lateritic Soil Stabilized with Calcined Clay and Iron Slag Dust	781
H. A. Quadri, O. S. Abiola, S. O. Odunfa, and J. O. Azeez	
A Case Study on the Efficacy of Cement Treated Base/subbase	795
Ashish Gharpure, Prashant Navalakha, and Asita Dalvi	
Comparative Evaluation of Lime and Biopolymer Amended Expansive Soil	807
G. Landlin, B. Sharmila, and S. Bhuvaneshwari	

Evaluation of Penetration Index of Untreated and Treated Soil Using Dynamic Cone Penetrometer	823
V. S. N. Pavan Kumar Pratapa	
Fundamental Study on Combination of Paper Sludge Ash and Cement for Dredged Clay Soil Stabilization	837
Nguyen Binh Phan, Kimitoshi Hayano, and Yoshitoshi Mochizuki	
Shrinkage Curve of Treated Sulfate-Bearing Soils with GGBS	851
Hussein Al-Dakheeli, Amir Javid, Mengting Chen, and Rifat Bulut	
A Study on Electrokinetic Dewatering of Saturated Soil	861
Abhishek A. Sutar and Veerabhadrapa M. Rotte	
Evaluation of Mineral Formation in Sulfate Bearing Soil Stabilized with Slag Cement Using XRD	875
Mengting Chen, Hussein Al-Dakheeli, Jim Puckette, and Rifat Bulut	
CBR Characteristics of Kaolin-Simulated Clay Type Subgrade Stabilised with Cement, Lime, Poly-Fibre and Ionic Compounds mix	885
Chee-Ming Chan, Abdul Rashid Ahmad Nasri, Poi-Cheong Tan, and Danny Ng	
Influence of Moisture Content on Strength of Stabilised Drilling Slurry	897
Mingwei Feng, Juan Wang, Shu Liu, and Yunfeng Hu	
Compaction and CBR Behaviour of Cement-Stabilised Sand-Black Cotton Soil Mixtures	907
Charles M. O. Nwaiwu, Baba Benjamin, and Obinna U. Ubani	
Improving Mechanical Properties of Two Mexican Soils by Utilizing Calcium Oxide	921
Natalia Perez, Paul Garnica, Francisco Javier Castañeda, and Mario Enrique Peña	
Harbor Geotechnics	
Particle Breakage Observed in Both Transitional and Non-transitional Carbonate Sands	935
Chenxi Tong, Sheng Zhang, and Daichao Sheng	
Investigation of Interaction of Piles at New Cargo Sea Transportation Route and LRT Projects with Problematic Soils of Kazakhstan	945
Askar Zhussupbekov, Victor Kaliakin, Der-Wen Chang, and Abdulla Omarov	

Analysis and Design of a Special Port Pavement for Heavy Steel Coils 959
Nicolas Echeverri Pinto

A Study on Suction Properties, Subgrade Modulus and Compressibility of Marine Soil Subgrade for Flexible Pavements 973
Ram Wanare, Pritam Sinha, and Kannan K. R. Iyer

About the Editors

Erol Tutumluer is Abel Bliss Professor in the Department of Civil and Environmental Engineering and the Director of International Programs at the University of Illinois at Urbana-Champaign, USA, where he is also the Paul F. Kent Endowed Faculty Scholar. He has research interests and expertise in characterization of pavement and railroad track geomaterials, i.e., subgrade soils and base/ballast unbound aggregates, soil/aggregate stabilization, geosynthetics, applications of artificial intelligence and deep learning techniques to transportation infrastructure, structural health monitoring of transportation facilities using sensors, modeling granular foundation systems using innovative techniques, sustainable use of foundation geomaterials and construction practices for transportation infrastructure, discrete element analysis of ballast, dynamic response measurement and analyses of track systems, and mechanistic analysis and design. Dr. Tutumluer has served as an investigator on over 100 research projects and graduated 21 Ph.D. and 44 MS students, and authored/co-authored over 350 peer reviewed publications from his research projects. Dr. Tutumluer is the current Chair of the ISSMGE Technical Committee 202 on Transportation Geotechnics.

Soheil Nazarian is a Professor in the Department of Civil Engineering at the University of Texas at El Paso, USA. He has over 35 years of industry and academic experience in the area of transportation infrastructure, with an emphasis on structures materials, such as that of highways and bridges. His academic experience includes research and teaching positions at the Universities of Texas at Austin and El Paso, as well as the Director at the Center for Transportation Infrastructure Systems at UTEP. He holds a patent for the Moveable Seismic Pavement Analyzer, which is a non-destructive testing device used in evaluation of transportation infrastructure. Professor Nazarian has been a contributor in over 100 research projects focused on non-destructive materials testing and materials applications, as well as the author of more than 300 industry related articles and publications.

Imad Al-Qadi is a Professor in the Department of Civil and Environmental Engineering and the Director of the Advanced Transportation Research and Engineering Laboratory (ATREL), the Illinois Center for Transportation (ICT), and the Smart

Transportation Infrastructure Initiative (STII) at the University of Illinois at Urbana-Champaign, USA. He is also the President of the Transportation Engineering Solutions and Technologies, Inc. Al-Qadi's scholarly record features 700+ authored/co-authored publications, more than 400 of which are fully refereed papers (+280 in periodic journals). His research resulted in the development of new tests, testing specifications, advanced modeling and simulation of pavement loading, pavement layer interface and crack development, and analysis of radar electromagnetic wave interactions with civil engineering materials, roads, and bridges.

Issam I. A. Qamhia is a Postdoctoral research associate at the University of Illinois at Urbana-Champaign (UIUC). Dr. Qamhia holds a Ph.D. degree in civil engineering with transportation geotechnics specialization from UIUC, and M.S. and B.S. degrees in civil engineering from the University of Wisconsin Milwaukee and Birzeit University, respectively. He has over nine years of experience in aggregate characterization. His areas of expertise include repeated load testing, morphological shape characterization, tomography scanning, freeze-thaw testing, aggregate packing studies, as well as field characterization of bound and unbound aggregates through non-destructive and accelerated full-scale pavement testing. Dr. Qamhia has authored/co-authored more than 45 peer reviewed publications in prestigious international journals and conferences of repute, and is a frequent reviewer of journals and international conferences.

Mechanistic-Empirical Design (Roads, Railways, Airfields and Harbor Facilities)

A Conceptual System Dynamics Framework to Evaluate Performance of Pavement Foundations Under Moisture Variations



Sayedmasoud Mousavi , Majid Ghayoomi , and Eshan V. Dave 

Abstract Excess moisture in base and subgrade soil has detrimental impacts on longevity and serviceability of pavements. Seasonal ground water level fluctuations, inundations due to storms and post-storm recess, frost penetrations and freeze-thaw effects, and uncertain climatic conditions lead to continuous moisture variation and change of stress states in pavement foundation. Reliance of current analysis and design procedures on approximate empirical approaches results in limited analysis abilities to incorporate moisture-dependency and to conduct real-time, climate-informed, forecasted pavement capacity and load restriction analyses. This paper discusses a new system dynamics framework to evaluate the pavement foundation performance by holistically incorporating pavement structure, climatic conditions, traffic loads, and moisture movement processes within a pavement system. This will include a simultaneous mechanical, hydraulic, and statistical analysis of such system in real time and potentially projecting the upcoming hydro-mechanical loading scenarios. More specifically, the framework would address the sensitivity of pavement foundation response to each contributing factor and how these factors would interact under different state conditions. In addition, results of statistical analyses could be further incorporated in load restriction decision protocols and models.

Keywords Flooded pavement · Unsaturated soils · System dynamics

1 Introduction

Pavements are dynamic structures where their performance is affected by several parameters such as climatic conditions, loading patterns, and material properties. Excess moisture in base and subgrade soils is one of the factors that directly or indirectly influence the structural capacity of pavement systems. The changes in ground-water level during winter frost and spring thaw as well as water inundations due to storms and post-storm recess have propensity to cause certain amount of distress

S. Mousavi · M. Ghayoomi (✉) · E. V. Dave
University of New Hampshire, Durham, NH 03824, USA
e-mail: majid.ghayoomi@unh.edu

and/or failures on pavement structures. Specifically, soils' resilient modulus (M_R) is highly affected by the variation of moisture content and soil suction [1–3], which, in turn, impacts the structural performance and capacity of pavements, especially after extreme climatic events such as flooding. For example, Elshaer et al. [4] discussed that a rise in ground water level can result in up to 70% reduction in pavement bearing capacity. Subgrade soils may experience different levels of water saturation while most of the equations used in conventional pavement design were developed based on optimum moisture content conditions. Further, to date, common approaches that include excess moisture conditions in pavement capacity assessment are empirical, sometimes incorporating soil index parameters or one representative moisture or suction value. Thus, a mechanistic framework that holistically incorporates all the influential factors is still needed. This paper discusses a system dynamics (SD) framework to evaluate the performance of pavement foundations during changes of soil moisture, specifically during flooding events.

2 System Dynamics Framework Development

System dynamics modeling is an approach to study and manage complex systems that change over time. System dynamics modeling has been used to model and understand complex dynamic systems in various fields; some examples include environmental science, management, economics, natural and social sciences, and healthcare systems [5–7]. The use of system-based approach is necessary to integrate impacts of various stressors (e.g., soil moisture state, vehicular loads and volume, and climatic conditions), current pavement conditions, subgrade properties, soil hydro-geology, and short-term climate forecast on overall pavement performance. The SD framework can provide engineers with an instructive basis to understand significant factors governing pavement response to moisture variation and also develop a mechanistic approach for load restriction (both in current time and for future forecasting) decision making.

Any SD framework for moisture-dependent pavement response analysis should include three general structures, (1) a hydrological structure, (2) a geotechnical structure, and (3) a pavement response structure. Each structure consists of several components including data variables and their interrelationships. The SD framework should be able to model the interaction between these three structures. The overall pavement response during moisture variation would depend on the concurrent interactions among the three structures and their components over time. Each of these structures is described in following subsections.

2.1 Hydrological Structure

The hydrological structure of the proposed SD framework simulates the moisture flux in and out of pavement due to precipitation, evapotranspiration, thaw cycles, or ground water level (GWL) fluctuation. This is governed by complex interaction of several components including precipitation duration and rate, evapotranspiration rate, surface water runoff, moisture-dependent hydraulic properties of soil layers, current moisture state of soil, and the current and equivalent annual subsurface GWL. The hydrological structure models the complex interaction between these components to capture variation of moisture content and soil suction profiles during a period of time for geotechnical characterization and pavement response assessment.

The proposed hydrological structure for a flooding event is presented in Fig. 1. The height of ponded water on soil surface due to flooding can be treated as an input or be estimated from precipitation rate and duration, evaporation rate, subsurface runoff, and infiltration rate through the subsurface. The short-term climate forecast can be utilized to estimate precipitation rate and duration in a given period of time. The past precipitation time series also could be used as an input to calibrate and validate the proposed framework. The surface water runoff depends on the location of pavement, and it can be assumed to be zero for “flat areas” and equals precipitation minus infiltration and evaporation for pavements with significant grades. The rate of

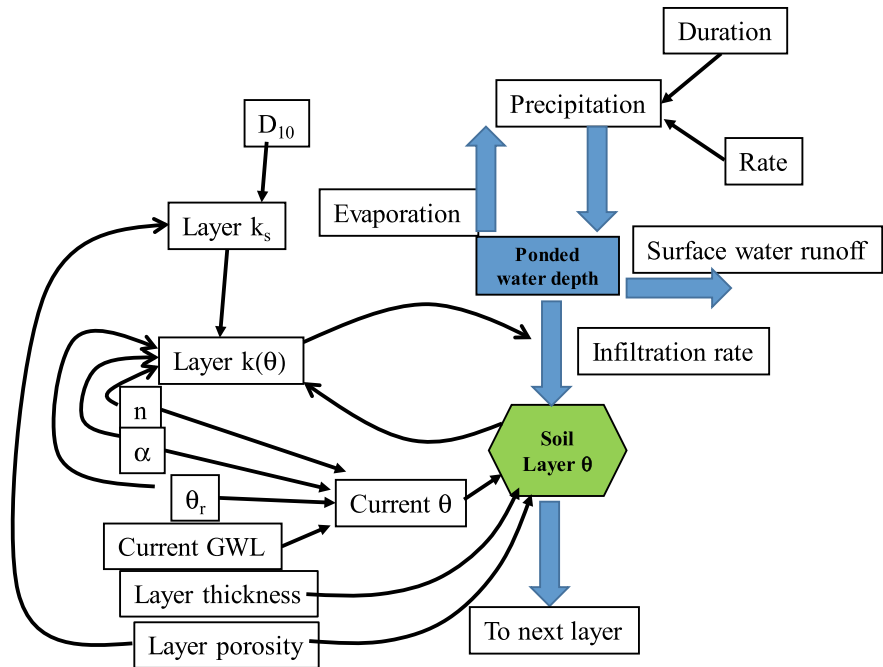


Fig. 1 Hydrological structure of proposed system dynamics framework

infiltration into the subsurface is dependent on the height of ponded water, hydraulic conductivity of the soil, and water content. The infiltration rate into unsaturated soil can be estimated by Richards' equation [8]. While Richards' equation is one of the most accurate methods to model the moisture infiltration into unsaturated soils, numerical solution of Richards' equation is usually required due to the challenges in setting the initial and boundary conditions. In this case, the transient moisture movement in the soil can be estimated, for example, by incorporating Green and Ampt [9] assumptions. Green-Ampt method assumes a piston-like advance of wetting front in soils under the combined effects of suction and gravity gradients. This assumption is specifically valid for a heavy rain event with ponded water on soil surface where an assumption of a sharp wetting front movement is fulfilled. The ponding infiltration rate according to Green-Ampt model can be expressed as follows:

$$q = k_0 \frac{(z - h_i) + h_0}{z} \quad (1)$$

where q is the infiltration rate, k_0 is the effective hydraulic conductivity of saturated layer, h_i is the effective suction head at wetting front, h_0 is the height of ponded water, and z is the depth of wetting front below the soil surface.

It is noteworthy that the effective hydraulic conductivity in Eq. 1 is less than hydraulic conductivity of a fully saturated soil (k_s) due to air entrapment during wetting process [10–12]. Hence, k_0 should be taken as the soil hydraulic conductivity at residual air saturation. Bouwer [13] suggested that the effective hydraulic conductivity can be assumed as $k_0 = 0.5 k_s$. The hydraulic conductivity of fully saturated soil layer can be obtained from field tests or be estimated by semi-empirical equations. Table 1 summarizes some empirical equations for estimation of hydraulic conductivity of soils in fully saturated state. The suction head at wetting front can also be determined by the method suggested by Bouwer [13] as follows:

$$h_i = \frac{h_a}{2} \quad (2)$$

where h_a is the air entry value of soil. Equation 1 can be used to estimate the real-time variation of soil water content at each layer. The real-time volumetric water content of each soil layer at each time step can be approximated by calculating the total inflow and outflow volume of water and initial volumetric water content. Initial water content of each layer can be estimated from soil water retention curve (SWRC) and having the current location of GWL according to van Genuchten [14] formula in Eq. 3:

$$\Theta = \frac{\theta - \theta_r}{\theta_s - \theta_r} = [1 + |\alpha h_m|^n]^m \quad (3)$$

Table 1 Empirical relations for estimation of hydraulic conductivity of fully saturated soils

Reference	Hydraulic conductivity (cm/s)	Notation	Remarks
Hazen [15]	$k_s = cD_{10}^2$	D_{10} = the diameter through which 10% of the total soil mass is finer (mm) c = constant	$c \approx 1$, applicable for fairly uniform sand
Chapius [16]	$k_s = 2.46 \left[D_{10}^2 \frac{e^3}{(1+e)} \right]^{0.78}$	e = void ratio of soil	Applicable for uniform gravel and sand and non-plastic silty sands
Mbonimpa et al. [17]	$k_s = C_p \frac{\gamma_w}{\mu_w} \frac{e^{3+x}}{(1+e)} \frac{1}{\rho_s^2 w_L^{2\chi}}$	γ_w = unit weight of water (kN/m ³) μ_w = Water dynamic viscosity (Pa s) ρ_s = Density (kg/m ³) of solids W_L = Liquid limit (%) $x = 7.7w_L^{-0.15} - 3$	Applicable for plastic soils, $\gamma_w \approx 9.8$, $\mu_w \approx 10^{-3}$, $\chi = 1.5$

where Θ is the soil relative volumetric water content, θ_s and θ_r are the saturated and residual soil water content, α and n are the shape parameters of the soil SWRC, $m = 1 - 1/n$, and h_m matric suction head of soil.

After infiltration of the ponded water into the soil, water is redistributed. The redistribution of water results in a reduction in soil's water content from top of the soil layers and movement of water toward GWL. Quantification of soil water content variation during the redistribution process in soil profile can be obtained using the partial differential equation (PDE) solution of Richard's equation:

$$\frac{\delta\theta}{\delta t} = \frac{\delta}{\delta z} \left[k(\theta) \left(\frac{\delta h_m}{\delta z} + 1 \right) \right] \quad (4)$$

where θ is the volumetric soil water content, z is the thickness of soil layer, and $k(\theta)$ is moisture-dependent hydraulic conductivity of the soil layer. The moisture-dependent hydraulic conductivity of soil in an unsaturated state can be defined according to Mualem [18]:

$$k(\theta) = k_s \Theta^{0.5} \left[1 - \left(1 - \Theta^{\frac{1}{m}} \right)^m \right]^2 \quad (5)$$

2.2 Geotechnical Structure

Excessive moisture in pavement systems especially in subgrade soils will reduce the pavement foundation capacity and result in surface deflection and cracking. This has been shown through numerical modeling (e.g., Elshaer et al. [4], Haider and Masud [19]), physical small-scale and full-scale modeling (e.g., Amiri [20], Saevarsdottir and Erlingsson [21]), and field performance assessment (e.g., Zhang et al. [22], Sultana et al. [23]). Geotechnical properties of soils play a key role in pavement response; thus, accurate assessment of these properties under various degrees of water saturation is crucial. Subgrade soil resilient modulus is probably the most influential factor that controls the overall stiffness of the pavement systems. Developing moisture-dependent resilient modulus has been in the forefront of transportation geotechnics research. Especially, with the advance of unsaturated soil mechanics, significant efforts have been made to correlate soil suction and state of stress to resilient modulus in a more mechanistic setting.

The geotechnical structure of the proposed SD framework incorporates the moisture/suction variation of soil layers obtained from the hydrological structure at each time step to estimate M_R of soils subjected to moisture variations. The proposed geotechnical structure for a given layer of pavement is presented in Fig. 2. Several analytical and empirical models have been proposed to estimate the resilient modulus of subgrade soil under various moisture and stress states; some being simple and applied and some being complex and mechanistic [1–3, 24–26]. To date, the most commonly used equation is the extended version of MEPDG equation for resilient

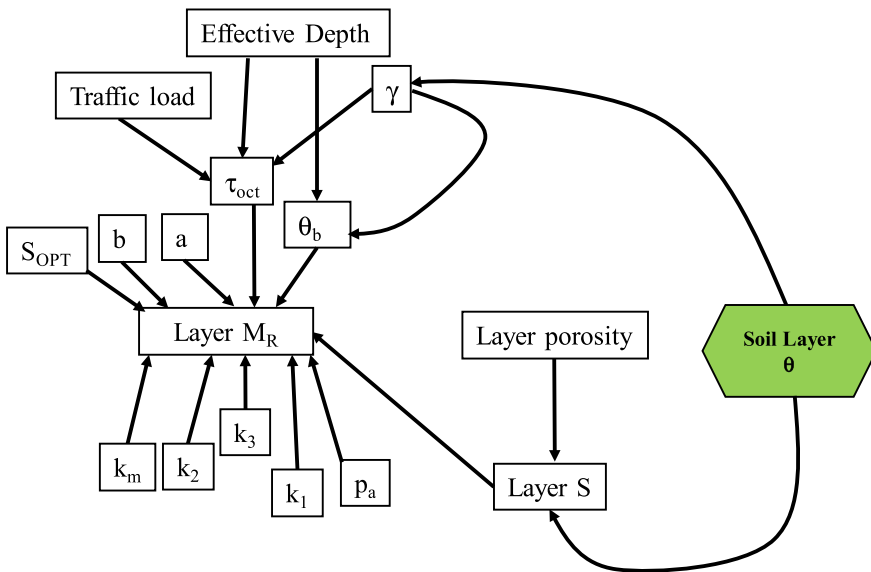


Fig. 2 Geotechnical structure of proposed system dynamics framework for given soil layer

modulus at optimum water content from the results of extensive experimental material evaluation [27]. In this method, the modulus obtained from Eq. 6 is used to adjust the estimated resilient modulus at optimum water content, based on the degree of water saturation.

$$\log\left(\frac{M_R}{M_{R-OPT}}\right) = a + \frac{b - a}{1 + \exp\left[\ln\left(-\frac{b}{a}\right) + k_m(S - S_{OPT})\right]} \quad (6)$$

where S = degree of saturation (expressed as fraction); S_{OPT} = degree of saturation at optimal water content (in decimals); a = minimum of $\log(M_R/M_{R-OPT})$; b = maximum of $\log(M_R/M_{R-OPT})$; and k_m = regression parameter. Parameter values $a = -0.5934$, $b = 0.4$, and $k_m = 6.1324$ are suggested for fine-grained soils, and parameter values $a = -0.3123$, $b = 0.3$, and $k_m = 6.8157$ are suggested for coarse-grained soils. The moisture-dependent modulus of each soil can be obtained depending on soil type, depth of soil layer and applied stress, and volumetric water content of soil as shown in Fig. 2.

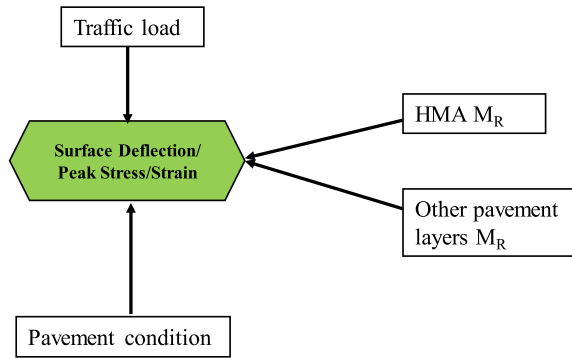
2.3 Pavement Response Structure

In the proposed framework, the pavement surface deflection will be considered as an indicator of the pavement capacity. Historically, different methods have been proposed to analyze the structural performance of pavement systems. The use of multilayer analysis, specifically layered elastic analysis, is current state of practice in the majority of flexible pavement analysis and design systems (such as, MnPAVE, PavementME, CalME etc.) [28–30]. For the pavement response structure, the use of two and three-layer solutions can be adopted in the SD framework. Studying pavement response in the context of SD framework enables real-time evaluation and sensitivity analysis of pavement response subjected to moisture variations.

The pavement response structure incorporates the real-time modulus values of pavement layers including hot mixed asphalt (HMA), base, subbase, and subgrade, traffic load, and pavement condition to estimate real-time surface deformation of pavement. There are two approaches to determine the expected loads on the given pavement over its entire design life. One approach is to convert all magnitudes of loading and repetitions of loading to an equivalent unit using approaches such as equivalent damage, a commonly used example for this is equivalent single axial load (ESAL). The other approach is to use a load spectrum, which characterizes loads directly by number of axles, configuration, and weight. This method is typically more complex since the structural analysis requires use of each vehicular combination to be evaluated to obtain relevant responses. Both methods follow typical equations and/or procedures that have been well laid out (such as, AASHTO [31] and FHWA [32]).

For the proposed SD framework, the use of ESAL approach is not appropriate, since the damage potential from each vehicle type needs to be evaluated. Thus, vehicle

Fig. 3 Pavement structure of proposed system dynamics framework



class-based traffic inputs can be more suitable. In this regard, the 13-category FHWA vehicle classification can be adopted (FHWA [33]). In this method, the induced stress on pavement surface from each category is obtained by considering the tire configuration, pressure, and wheel load using the superposition principle (Fig. 3).

2.4 Proposed System Dynamics Framework

The proposed SD framework for evaluation of the capacity of pavement foundations during excessive moisture event is presented in Fig. 4. Within the SD framework, the hydrological structure acquires climate and soil hydraulic variables and properties to model water flow in unsaturated and fully saturated pavement layers. The outcome of the hydrologic structure is time-dependent water content profile in depth of pavement layers. This is simultaneously used by geotechnical structure to estimate moisture-dependent mechanical properties of geomaterials (granular bases and subbases as well as subgrade) in pavement system. The pavement response structure incorporates the results geotechnical structures along with traffic load information to predict time-dependent, critical pavement response (e.g., surface deflection and peak vertical

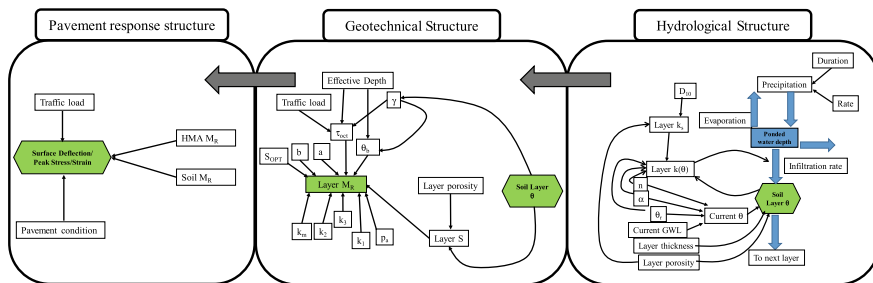


Fig. 4 Overall system dynamics framework

stress on top of the subgrade). Analysis of the pavement foundations subjected to moisture variation in the context of SD provides a basis to understand significance of factors governing the pavement response and develop a mechanistic approach for load restriction decision making.

3 A Simple Example of System Dynamics Simulation

The following sections are intended to provide a hypothetical one-dimensional (1D) flow example to describe the capabilities of SD modeling in simulating and understanding the system behavior. The example problem consists of a fully saturated column of soil subjected to inflow and outflow of water as shown in Fig. 5. A SD model was developed to simulate the ponded water height and outflow of water to the outflow container. Vensim PRO[®] was used, which utilizes levels (e.g., ponded water height, outflow volume) and associated inflows (e.g., precipitation) and outflows (e.g., infiltration, evaporation) to conduct a real-time dynamic characterization of the flow system.

Figure 5b presents the SD model developed in Vensim for the flow example. The model consists of a single hydrological structure. The inflow (q_{in}) and evaporation (q_E) rates were treated as constant variables. The ponded water height was calculated as an integral of water flux in and out of the soil surface (Eq. 7).

$$h_{0,t} = \int_0^t (q_{in} - q_E - q_{out})dt + h_{0,t=0} \tag{7}$$

where q_{out} is the infiltration rate of water through the soil, $h_{0,t}$ is the ponded water height at time t , and $h_{0,t=0}$ is the initial height of ponded water which is assumed to be zero in this hypothetical example. The infiltration rate is a variable which depends on hydraulic conductivity of the soil, height of ponded water, and soil thickness as

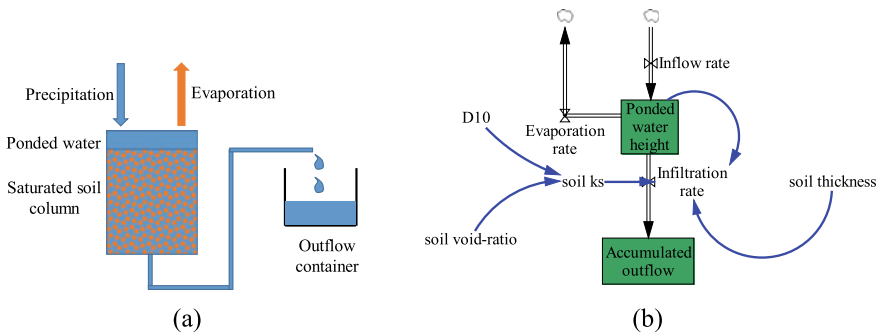


Fig. 5 a Schematic of the example problem, and b the system dynamic model of example problem

Table 2 Summary of variables and initial parameters for the hypothetical flow example

D_{10}	Soil thickness	Void ratio	Evaporation rate	Inflow rate
0.1 mm	5 m	0.5	0.02 m/h	0.1 m/h

it is shown in Fig. 5b. The hypothetical soil column is assumed to be a 5 m thick fine-grained sand with $D_{10} = 0.1$ and $e = 0.5$. The hydraulic conductivity of soil was calculated using Chapuis [12] empirical relation provided in Table 1. The accumulated water in outflow container was calculated as the integral of infiltration rate over time. Table 2 presents a summary of variables and initial parameters considered for the hypothetical model. It should be noted that all calculations are performed per unit area of the soil column.

3.1 Results of Simulation

Results of SD model simulation are presented in Fig. 6 in terms of ponded water height and accumulated outflow time series. The time period for simulation was 10 h. The SD model simulation indicated no ponded water and accumulated outflow at the initial time. This is in agreement with the system initial condition where the total head of water at the soil surface and end of the outflow tube are the same and the system is at equilibrium. Ponded water height time history showed an increasing trend with time, however, with decreasing rate with time. This is because the increase in ponded water height resulted in an increase in hydraulic gradient and subsequently infiltration rate. This is evident in accumulated outflow curve where the rate of water accumulation was increased with time. Overall, the results of simulation indicated a very well agreement between that SD model predictions and expected trends. This shows that SD can be a useful tool to model soil systems.

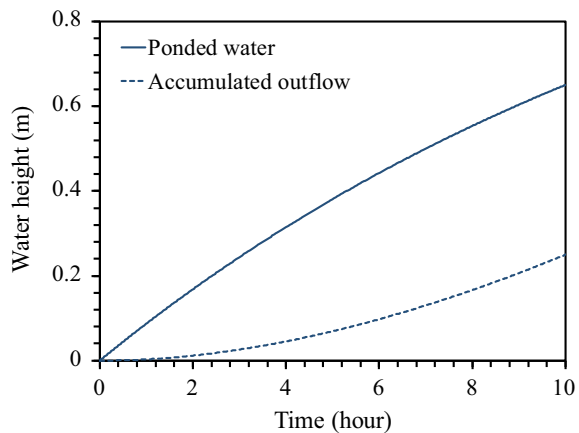
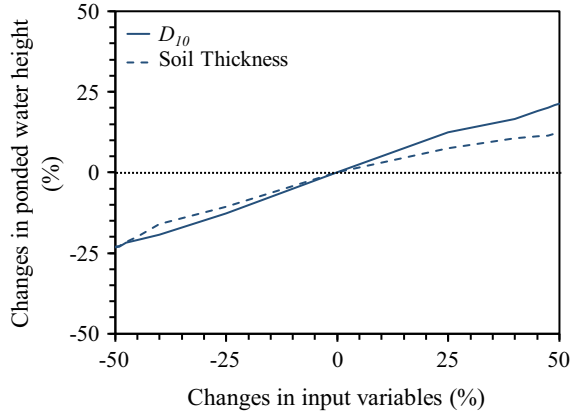
Fig. 6 Results of system dynamics model simulation

Fig. 7 Results of SD model sensitivity simulations



3.2 Sensitivity Simulation

One of the most important advantages of SD modeling using Vensim PRO[®] is the capability of running sensitivity simulations. This is specifically of great importance for complex systems such as flooded pavement systems where the existence of complex interdependent components increases the complications in understanding the influential factors governing the system behavior.

For the hypothetical flow example, the sensitivity of the ponded water height to variations of D_{10} and soil thickness was examined. The input variables were changed over a range of $\pm 50\%$, and the resulting influence of these changes on the ponded water height at 10 h was investigated. Figure 7 presents the results of ponded water height sensitivity to D_{10} and soil thickness variations. Regardless of the type of input variable, a significant change in model response in terms of ponded water height was observed by a change in input variables. The simulation results showed higher sensitivity of ponded water to D_{10} than soil thickness for positive changes in input variables. Overall, that sensitivity analysis of the SD model can provide a useful tool to understand the significance of the impact of uncertainty in input variables on model behavior.

4 Conclusion

This paper presented a conceptual framework of a system dynamics approach by which the real-time pavement capacity analysis with respect to foundation conditions with moisture variations can be evaluated. This new system dynamics framework was proposed to holistically incorporate pavement structure, climatic conditions, traffic loads, and moisture movement processes within a pavement system.

The proposed framework included simultaneous stochastic modeling of interactions between hydrological, geotechnical, and pavement response structures. The framework would address the sensitivity of pavement foundation response to each contributing factor and how these factors would interact under different state conditions. In addition, a simple flow example was provided to explain the performance and advantages of studying moisture variable pavement foundations in the context of system dynamics approach.

Acknowledgements The authors would like to acknowledge the support provided by the National Road Research Alliance through grant no. 1034192.

References

1. Yang RR, Huang WH, Tai YT (2005) Variation of resilient modulus with soil suction for compacted subgrade soils. *Transp Res Rec* 1913:99–106
2. Liang R, Rabab'ab S, Khasawneh M (2008) Predicting moisture dependent resilient modulus of cohesive soils using soil suction concept. *J Transp Eng* 134(1):34–40
3. Cary CE, Zapata CE (2010) Enhanced model for resilient response of soils resulting from seasonal changes as implemented in mechanistic–empirical pavement design guide. *Transp Res Rec* 2170:36–44
4. Elshaer M, Ghayoomi M, Daniel JS (2017) Bearing capacity analysis of pavement structures for short term flooding events. In: 10th International conference on the bearing capacity of roads, railways, and airfields, pp 2127–2133
5. Bixler TS, Houle J, Ballesterio T, Mo W (2019) A dynamic life cycle assessment of green infrastructures. *Sci Total Environ* 692:1146–1154
6. Forrester JW (1987) Lessons from system dynamics modeling. *Syst Dyn Rev* 3(2):136–149
7. Currie DJ, Smith C, Jagals P (2018) The application of system dynamics modelling to environmental health decision-making and policy—a scoping review. *BMC Public Health* 18(1):402
8. Richards LA (1931) Capillary conduction of liquids through porous mediums. *Physics* 1(5):318–333
9. Green WH, Ampt GA (1911) Studies on soil physics: I. Flow of air and water through soils. *J Agric Sci* 4:1–24
10. Bouwer H (1966) Rapid field measurement of air-entry value and hydraulic conductivity of soil as significant parameters in flow system analysis. *Water Resour Res* 2:729–738
11. Hammecker C, Antonino ACD, Maeght JL, Boivin P (2003) Experimental and numerical study of water flow in soil under irrigation in northern Senegal: evidence of air entrapment. *Eur J Soil Sci* 54:491–503
12. Khosravi A, Mousavi S, Serej AD (2016) Hydraulic behavior of infilled fractured rocks under unsaturated conditions. *Geotech Struct Eng Congr* 2016:1708–1718
13. Bouwer H (1969) Infiltration of water into nonuniform soil. *J Irrig Drainage Div* 95(IR4):451–462
14. van Genuchten MT (1980) A closed form equation for predicting the hydraulic conductivity of unsaturated soils. *Soil Sci Soc Am J* 44:892–898
15. Hazen A (1911) Dams on sand formations: discussion. *Trans ASCE* 73:199–203
16. Chapuis RP (2004) Predicting the saturated hydraulic conductivity of sand and gravel using effective diameter and void ratio. *Can Geotech J* 41(5):787–795
17. Mbonimpa M, Aubertin M, Chapuis RP, Bussière B (2002) Practical pedotransfer functions for estimating the saturated hydraulic conductivity. *Geotech Geol Eng* 20(3):235–259

18. Mualem Y (1976) A new model for predicting the hydraulic conductivity of unsaturated porous media. *Water Resour Res* 12:513–522
19. Haider SW, Masud MM (2018) Effect of moisture infiltration on flexible pavement using the AASHTOW are pavement-ME. In: *Advances in materials and pavement performance prediction*, pp 31–35
20. Amiri H (2004) Impact of moisture variation of stiffness response of pavements through small scale models. Master Thesis, University of Texas at El Paso
21. Saevarsdottir T, Erlingsson S (2013) Effect of moisture content on pavement behaviour in a heavy vehicle simulator test. *Road Mater Pavement Des* 14(S1):274–286
22. Zhang Z, Wu Z, Martinez M, Gaspard K (2008) Pavement structures damage caused by Hurricane Katrina flooding. *J Geotech Geoenvironmental Eng* 134(5):633–643
23. Sultana M, Chai G, Martin T, Chowdhury S (2016) Modeling the post-flood short-term behavior of flexible pavements. *J Transp Eng* 142(10):04016042
24. Seed HB, Mitry FG, Monismith CL, Chan CK (1967) Prediction of pavement deflection from laboratory repeated load tests. NCHRP Rep. No. 35, Washington, D.C.
25. Khoury NN, Zaman M (2004) Correlation among resilient modulus, moisture variation, and soil suction for subgrade soils. *Transp Res Rec* 1874:99–107
26. Khosravifar S, Afsharikia Z, Schwartz CW (2015) Evaluation of resilient modulus prediction models for cohesive and non cohesive soils. *Airfield Highway Pavements* 2015:778–788
27. Zapata CE, Andrei D, Witczak MW, Houston WN (2007) Incorporation of environmental effects in pavement design. *Road Mater Pavement Des* 8(4):667–693
28. Minnesota Department of Transportation (2012) MnPAVE user's guide
29. Ullidtz P, Harvey J, Basheer I, Jones D, Wu R, Lea J, Lu Q (2010) CalME, a mechanistic-empirical program to analyze and design flexible pavement rehabilitation. *Transp Res Rec* 2153(1):143–152
30. American Association of State Highway and Transportation Officials (AASHTO) (2008) *Mechanistic-empirical pavement design guide—a manual of practice*
31. AASHTO (1993) *Guide for design of pavement structures, vol Part III*. AASHTO, Washington, D.C.
32. FHWA 2014 (2019) *Traffic monitoring guide*. U.S. Department of Transportation/Federal Highway Administration. Accessed October 29
33. FHWA 2014 (2014) *Verification, refinement, and applicability of long-term pavement performance vehicle classification rules*, Report FHWA-HRT-13-091. Federal Highway Administration, McLean VA

Dynamic Response of a Beam on a Layered Half-Space with a Poroelastic Interlayer Subjected to Moving Loads



Yicheng Li, Xiaolei Zhang, and Shijin Feng

Abstract Vibration of a soil-structure system due to dynamic loads is a classical problem in transportation geotechnics. This paper investigates dynamic response of a practical stratified ground model coupled with a beam in the vicinity of moving loads. The ground consists of alternate distribution of different media: an elastic layer, a poroelastic interlayer and an elastic half-space from top to bottom, which considers soils of different properties and the existence of groundwater. Fourier transform and ‘adapted stiffness matrix method’ are applied to derive solutions to the system in the frequency-wavenumber domain. Inverse Fourier transform is applied through numerical integration to obtain results in the time-spatial domain. The method is then verified by comparing with existing research. Finally, influences of load characteristics, beam stiffness, groundwater existence on vibrations of the coupled system are comprehensively investigated. Main conclusions are drawn as follows: A ‘critical speed’ exists for vertical displacement of the beam, and it occurs due to the first wave propagation mode of the system. The existence of groundwater significantly influences vertical displacement of the beam. The influence substantially increases with load speed.

Keywords Dynamic response · Moving load · Beam · Stratified ground · Poroelastic interlayer

1 Introduction

Study on the dynamic response of a beam-foundation coupling system subjected to a moving load is important in the field of transportation geotechnics, because it helps with the understanding of the dynamic characteristics and the design of the track-ground system. Research studies in this field have been carried out in the past few decades.

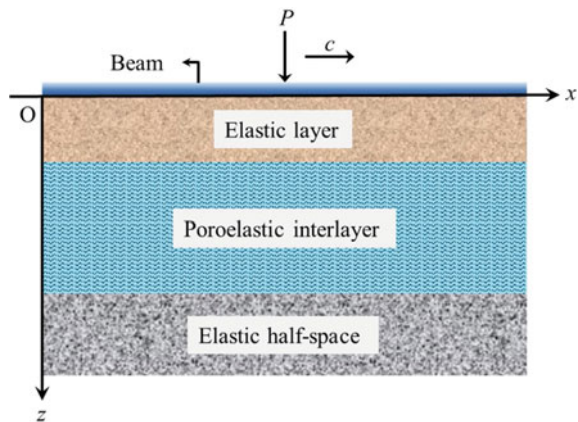
Y. Li (✉) · X. Zhang · S. Feng
Tongji University, Shanghai 200092, China
e-mail: liyichengtj@foxmail.com

According to the foundation model, existing researches on the vibration of a beam-ground system can be classified into the following categories. The first kind of works takes the ground as springs. Choros and Adams [1] derived close-form solutions to the dynamic response of a beam on a Winkler foundation. Results of the Timoshenko and Euler-Bernoulli beam on a Winkler foundation were compared by Ruge and Birk [2]. More recently, Yu et al. [3] used a beam-Winkler system to consider the vibration problem of a tunnel. To consider the shear action between the springs, a two-parameter spring model was also developed. For example, Uzzal et al. [4] investigated the problem of a moving mass on a beam supported by a Pasternak foundation.

The second type of foundation model is a continuum medium model such as elastic or poroelastic layers. Dieterman and Metrikine [5] investigated the dynamic problem of a beam overlying an elastic half-space with considering the critical speed. Dimitrovová [6] then also studied the critical speed effect of a finite or infinite beam supported by an elastic layer. To consider the existence of groundwater, the poroelastic medium was introduced to model saturated foundations according to Biot's theory [7]. For example, Xu et al. [8] took the ground as a layered poroelastic half-space. Lefeuvre-Mesgouez and Mesgouez [9] investigated the dynamic behavior of a beam on a two-layered poroelastic half-space. Shi and Selvadurai [10] derived solutions to a beam on a poroelastic half-space. More recently, Feng et al. [11] developed a ground model considering alternate distribution of different media, namely an elastic layer, a poroelastic interlayer and an elastic half-space from top to bottom. The existence of a groundwater table and substratum such as bedrock can be taken into account by this model.

This study investigates the dynamic responses of a beam-ground coupling system under a plane strain condition. The ground model is introduced from Feng et al. [11] (see Fig. 1) and coupled with the Euler-Bernoulli beam. A moving point load is applied to the beam. Dynamic responses of the coupled system in the frequency-wavenumber domain are derived by Fourier transform and 'adapted stiffness matrix

Fig. 1 Schematic diagram of the model in this study



method.' Results in the time-spatial domain are inverted by an integration method. The influence of the load and ground characteristics on the vibrations of the beam-ground system is comprehensively investigated.

2 Governing Equations and Solutions

2.1 General Solutions to the Layered Ground with a Poroelastic Interlayer

Governing equations of an elastic medium are

$$\mu^e u_{i,jj}^e + (\lambda^e + \mu^e) u_{j,ji}^e = \rho^e u_i^e \quad (1)$$

$$\sigma_{ij}^e = \lambda^e u_{k,k}^e \delta_{ij} + \mu^e (u_{i,j}^e + u_{j,i}^e) \quad (2)$$

where the superscript 'e' denotes 'elastic.' λ and μ are Lamé constants. u_i and σ_{ij} ($i, j = x, z$) denote displacement and stress. ρ is the material density. δ_{ij} is the Kronecker delta.

Governing equations of a poroelastic medium can be given as [7]

$$\mu u_{i,jj} + (\lambda + \beta^2 M + \mu) u_{j,ji} + \beta M w_{j,ji} = [(1 - n)\rho_s + n\rho_f] \ddot{u}_i + \rho_f \ddot{w}_i \quad (3)$$

$$\beta M u_{j,ji} + M w_{j,ji} = \rho_f \ddot{u}_i + \frac{a\rho_f}{n} \ddot{w}_i + \frac{1}{K} \dot{w}_i \quad (4)$$

$$\sigma_{ij} = [\lambda + M\beta^2] u_{k,k} \delta_{ij} + \mu (u_{i,j} + u_{j,i}) + \beta M w_{k,k} \delta_{ij} \quad (5)$$

$$p = -M\beta u_{k,k} - M w_{k,k} \quad (6)$$

The Lamé constants, displacements, and stresses are defined in the same way as those of the elastic medium (the subscript $i, j, k = x, z$). p is the pore pressure; n is the porosity; w_i is the relative displacement defined by $w_i = n(U_i - u_i)$, where U_i is the fluid displacement; ρ_s and ρ_f are the solid and fluid densities, respectively; K is the hydraulic permeability coefficient; a is the tortuosity factor; M and β are the Biot coefficients.

Equations (1–6) can be solved by introducing Fourier transform with respect to time, t , and space x .

$$\bar{f}(\omega) = \int_{-\infty}^{\infty} f(t) e^{-i\omega t} dt, \quad \bar{g}(k_x) = \int_{-\infty}^{\infty} g(x) e^{-ik_x x} dx \quad (7)$$

Thus, the element stiffness matrices of an arbitrary elastic layer or poroelastic layer can be derived as follows according to solutions to Eqs. (1–6).

$$\underbrace{\begin{bmatrix} \mathbf{S}_e^I & \mathbf{S}_e^R \mathbf{Z}_e^I \\ -\mathbf{S}_e^I \mathbf{Z}_e^I & -\mathbf{S}_e^R \end{bmatrix}}_{\mathbf{K}_{4 \times 4}^e} \underbrace{\begin{bmatrix} \mathbf{D}_e^I & \mathbf{D}_e^R \mathbf{Z}_e^I \\ \mathbf{D}_e^I \mathbf{Z}_e^I & \mathbf{D}_e^R \end{bmatrix}}^{-1} \begin{Bmatrix} \tilde{\mathbf{u}}_{|u}^e \\ \tilde{\mathbf{u}}_{|l}^e \end{Bmatrix} = \begin{Bmatrix} \tilde{\Sigma}_{|u}^e \\ -\tilde{\Sigma}_{|l}^e \end{Bmatrix} \quad (8)$$

$$\underbrace{\begin{bmatrix} \mathbf{S}^I & \mathbf{S}^R \mathbf{Z}^I \\ -\mathbf{S}^I \mathbf{Z}^I & -\mathbf{S}^R \end{bmatrix}}_{\mathbf{K}_{6 \times 6}} \underbrace{\begin{bmatrix} \mathbf{D}^I & \mathbf{D}^R \mathbf{Z}^I \\ \mathbf{D}^I \mathbf{Z}^I & \mathbf{D}^R \end{bmatrix}}^{-1} \begin{Bmatrix} \tilde{\mathbf{u}}_{|u} \\ \tilde{\mathbf{u}}_{|l} \end{Bmatrix} = \begin{Bmatrix} \tilde{\Sigma}_{|u} \\ -\tilde{\Sigma}_{|l} \end{Bmatrix} \quad (9)$$

Expressions of the matrices in Eqs. (8–9) can be found in Feng et al. [11].

After obtaining the element stiffness matrices in Eqs. (8–9), the next step is to assemble the global stiffness matrix. However, dimensions of element stiffness matrices of elastic and poroelastic layers disagree since fluid-related terms are not included in the element stiffness matrix of the elastic medium. Thus, the ‘adapted stiffness matrix method’ developed by Feng et al. [11] is adopted to solve this disagreement of dimensions. Finally, the global stiffness matrix of the layered system can be obtained as

$$\mathbf{K}_{\text{global}} \begin{Bmatrix} \tilde{\mathbf{u}}_1 \\ \tilde{\mathbf{u}}_2 \\ \tilde{\mathbf{u}}_3 \end{Bmatrix} = \begin{Bmatrix} \tilde{\Sigma}_1 \\ \mathbf{0} \\ \mathbf{0} \end{Bmatrix} \quad (10)$$

2.2 Solutions to the Beam-Ground Coupled System

Governing equation of the beam can be expressed as follow, a moving point load is applied on the beam

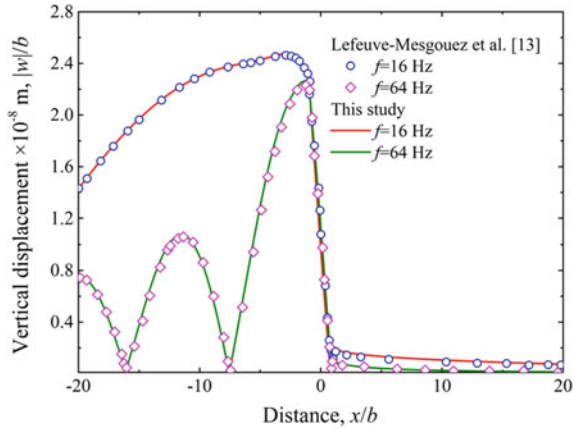
$$\rho_B \frac{\partial^2 w}{\partial t^2} + EI \frac{\partial^4 w}{\partial x^4} - F_s = P_0 \delta(x - ct) \quad (11)$$

where ρ_B and EI are density and bending stiffness of the beam. F_s denotes the contact force between the beam and ground per unit length. P_0 is the magnitude of the point load. δ is the Dirac delta function.

The continuity conditions at the beam-ground interface are

$$\sigma_{zz}(z = 0 \text{ m}) = -\frac{F_s}{L}, \quad \sigma_{zx}(z = 0 \text{ m}) = 0 \quad (12)$$

Fig. 2 Comparison with results reported by Lefeuvre-Mesgouez et al. [13]



where L is a geometrical parameter [12].

Fourier transforming Eqs. (11–12) with respect to t and x and substituting them into Eq. (10), solutions to the coupled system in the frequency-wavenumber domain can be obtained. Results in the time-spatial domain can be inverted by integration.

3 Comparison with Existing Research

In this section, the results of the model in this study are compared with those reported by Lefeuvre-Mesgouez et al. [13]. The parameters of the beam in Eq. (11) are set to be $\rho_B = 0 \text{ kg/m}^3$ and $EI = 0 \text{ N m}^2$. The thickness of the first elastic layer is 1000 m, and the parameters of it are the same as those in Lefeuvre-Mesgouez et al. [13]. A moving harmonic strip load is applied on the beam. Vertical displacements of the ground surface are presented in Fig. 2. It can be observed that the results in this study match well with those reported by Lefeuvre-Mesgouez et al. [13].

4 Numerical Results and Discussion

Dynamic responses of the beam-ground coupling system are investigated comprehensively based on the semi-analytical solutions in Sect. 2. Parameters of the system are presented in Table 1. A reference speed is given as the shear wave velocity of the first elastic layer $c_0 = 125 \text{ m/s}$.

Table 1 Parameters of the beam and ground

Parameter	Value
<i>Properties of the beam</i>	
EI/L (N m)	10^9
ρ_B/L (kg/m ²)	3×10^4
<i>Properties of the first layer</i>	
ρ (kg/m ³)	1900
E (Pa)	8×10^7
ν	0.35
h_1 (m)	0–30
<i>Properties of the second layer</i>	
λ	4.82×10^7
μ (Pa)	1.52×10^7
M (Pa)	5.08×10^9
β	0.9985
a	1.2
ρ_f (kg/m ³)	1000
ρ_s (kg/m ³)	2600
n	0.4
K (m ⁴ N ⁻¹ s ⁻¹)	10^{-10}
h_2 (m)	0–30
<i>Properties of half-space</i>	
ρ (kg/m ³)	2100
E (Pa)	4.54×10^9
ν	0.3

4.1 Influence of the Load Speed

The variation of maximum vertical displacement of the beam is presented in Fig. 3a. A peak of the curve can be observed, and the speed corresponding to it is called ‘critical speed.’ Time histories of four different load speeds including ‘critical speed’ ($c = 0.6c_0$) are given in Fig. 3b. Time history for $c = 0.3c_0$ is symmetric since the speed is lower than ‘critical speed’, and this state is defined as ‘quasi-static.’ When load speed further increases, time history fluctuates, and dynamic characteristics occur.

In order to further investigate the influence of load speed, the response spectra of u_z of the beam due to a unit vertical load are presented in $f - k_x$ plane in Fig. 4. According to Chahour et al. [14], the maxima of $|\tilde{u}_z|$ (i.e., the ridges in the contour plot) give the dispersion curves of wave propagation modes. Only one obvious dispersion curve occurs in Fig. 4. The load velocity line for $c = 0.6c_0$ is plotted based on the relationship $2\pi f = ck_x$, and it is almost tangent to the dispersion curve, making $0.6c_0$ to be the ‘critical speed.’

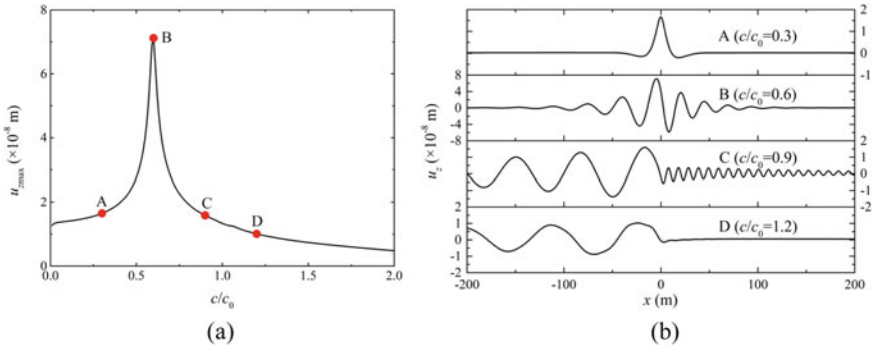


Fig. 3 Influence of the load speed on vertical displacement: **a** variation of maximum vertical displacement; **b** time history of vertical displacement

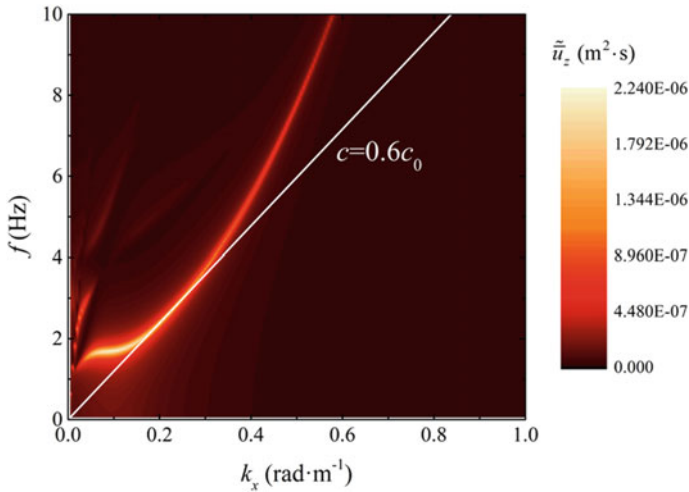


Fig. 4 Response spectrum of u_z of the beam due to a unit vertical load

The influence of load speed on pore pressure distribution in the poroelastic inter-layer is presented in Fig. 5. The x -axis is a spatial coordinate and the load is applied at the origin of the beam. The contour plot is almost symmetric when $c = 0.3c_0$. When the load speed is larger than ‘critical speed’ ($c = 0.9c_0$), the pore pressure mainly concentrates after the location of the load ($x < 0$ m). Moreover, positive and negative pore pressure alternately distributes for $x < 0$ m.

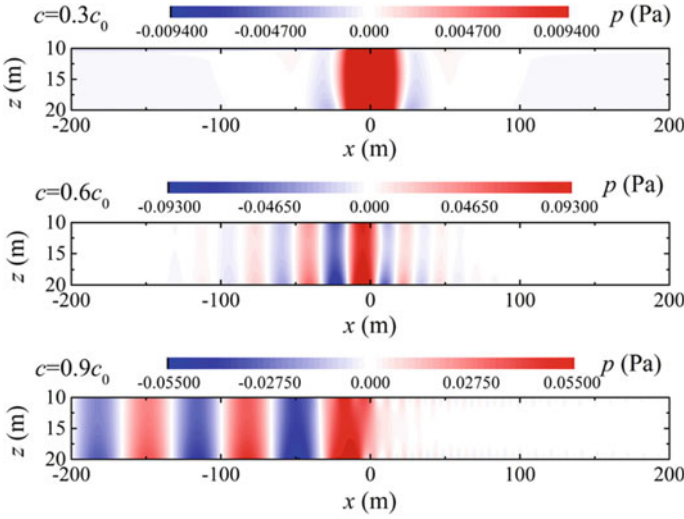


Fig. 5 Distribution of pore water pressure in the poroelastic interlayer under different load speed

4.2 Influence of the Existence of Groundwater

The existence of groundwater can be considered by the poroelastic interlayer in this study. This part investigates the influence of groundwater by comparing the results of the model in this study with those of an ‘equivalent’ layered elastic ground model. The ‘equivalent’ model is developed by replacing the poroelastic interlayer with an ‘equivalent’ elastic one. The Lamé constants of the ‘equivalent’ layer are the same as those of the poroelastic interlayer, and the density of it $\rho = n\rho_f + (1 - n)\rho_s$. The maximum vertical displacements of the beam are illustrated in Fig. 6. The subscript ‘ela’ and ‘poro’ are short for elastic and poroelastic, respectively. The parameter R_z is defined as

$$R_z = \left| \frac{u_z \max|_{\text{ela}} - u_z \max|_{\text{poro}}}{u_z \max|_{\text{poro}}} \right| \times 100\% \tag{13}$$

It can be observed that the existence of groundwater significantly influences the dynamic response of the system. R_z substantially increases with increasing load speed.

4.3 Influence of the Thickness of the Layers

Thicknesses of the layers are important parameters, since they define the geometrical characteristics of the ground. Influences of them are investigated in this section. A

contour plot of maximum vertical displacement of the beam is presented in Fig. 7a. The sum of the thicknesses of the first and second layers (i.e., h_1 and h_2) is 30 m. The highlighted area with warm color corresponds to ‘critical speed.’ The increase in h_1 leads to an increase in the critical speed when $h_1 < 17.1$ m, which may be due to the reason that the stiffness of the first elastic layer is higher than the second poroelastic one. When h_1 further increases to larger than 17.1 m, ‘critical speed’ remains unchanged, since the first elastic layer is thick enough and the second poroelastic interlayer has little influence on ‘critical speed.’

Variations of u_{zmax} with h_1 at different load speeds are presented in Fig. 7b by cutting the contour plot along lines perpendicular to the c/c_0 axis in Fig. 7a. Variations of u_{zmax} are different when the load speed is lower, equal to and higher than the critical speed (Fig. 7).

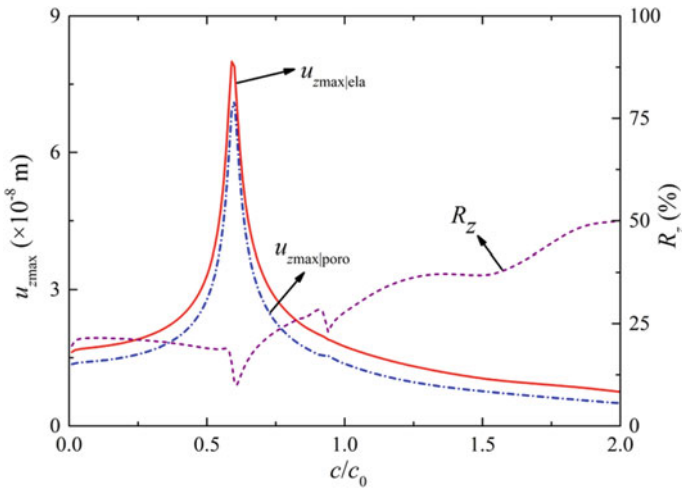


Fig. 6 Influence of the existence of groundwater

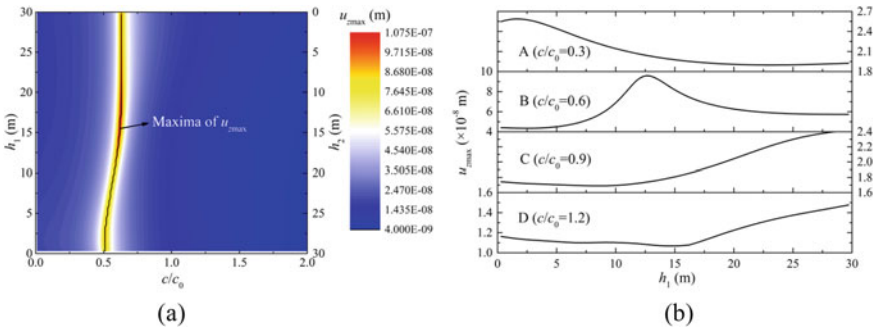


Fig. 7 Influence of the thickness of the layers on the vertical displacement of the beam

5 Conclusions

This study investigates the dynamic responses of a beam-ground coupling system. The ground is composed of an elastic layer, a poroelastic interlayer and an elastic half-space from top to bottom. The beam is modeled as the Euler-Bernoulli beam and a moving point load is applied on it. Solutions to the system in the frequency-wavenumber domain are derived adopting Fourier transform and an ‘adapted stiffness matrix method.’ The inverse Fourier transform is achieved by an integration method. Major conclusions of this study can be stated as follows:

1. A ‘critical speed’ exists for vertical displacement of the beam, and it occurs due to the first wave propagation mode of the system. The load speed affects the distribution characteristics of pore water pressure.
2. The existence of groundwater significantly influences the vertical displacement of the beam. The influence substantially increases with load speed.
3. The thickness of the first layer of the ground influences the value of the critical speed when it is smaller than 17.1 m in this study. The variation of vertical displacement of the beam is different for different load speeds.

References

1. Choros J, Adams GG (1979) A steadily moving load on an elastic beam resting on a tensionless Winkler foundation. *J Appl Mech* 46(1):175–180
2. Ruge P, Birk C (2007) A comparison of infinite Timoshenko and Euler-Bernoulli beam models on Winkler foundation in the frequency-and time-domain. *J Sound Vib* 304(3–5):932–947
3. Yu H, Cai C, Guan X, Yuan Y (2016) Analytical solution for long lined tunnels subjected to travelling loads. *Tunn Undergr Space Technol* 58:209–215
4. Uzzal RUA, Bhat RB, Ahmed W (2012) Dynamic response of a beam subjected to moving load and moving mass supported by Pasternak foundation. *Shock Vibr* 19(2):205–220
5. Dieterman HA, Metrikine A (1996) The equivalent stiffness of a half-space interacting with a beam. Critical velocities of a moving load along the beam. *Eur J Mech Ser A Solids* 15:67–90
6. Dimitrovová Z (2017) Analysis of the critical velocity of a load moving on a beam supported by a finite depth foundation. *Int J Solids Struct* 122:128–147
7. Biot MA (1956) Theory of propagation of elastic waves in a fluid-saturated porous solid. II. Higher frequency range. *J Acoust Soc Am* 28(2):179–191
8. Xu B, Lu JF, Wang JH (2007) Dynamic response of an infinite beam overlying a layered poroelastic half-space to moving loads. *J Sound Vib* 306(1–2):91–110
9. Lefeuvre-Mesgouez G, Mesgouez A (2012) Three-dimensional dynamic response of a porous multilayered ground under moving loads of various distributions. *Adv Eng Softw* 46(1):75–84
10. Shi L, Selvadurai APS (2016) Dynamic response of an infinite beam supported by a saturated poroelastic halfspace and subjected to a concentrated load moving at a constant velocity. *Int J Solids Struct* 88:35–55
11. Feng SJ, Li YC, Chen HX, Chen ZL (2019) Response of pavement and stratified ground due to vehicle loads considering rise of water table. *Int J Pavement Eng* 20(2):191–203
12. Metrikine AV, Vrouwenvelder A (2000) Surface ground vibration due to a moving train in a tunnel: two-dimensional model. *J Sound Vib* 234(1):43–66

13. Lefeuve-Mesgouez G, Le Houédec D, Peplow AT (2000) Ground vibration in the vicinity of a high-speed moving harmonic strip load. *J Sound Vib* 231(5):1289–1309
14. Chahour K, Lefeuve-Mesgouez G, Mesgouez A (2014) Spectral analysis of a railway track in contact with a multilayered poroviscoelastic soil subjected to a harmonic moving load. *Soil Dyn Earthq Eng* 64:24–37

Modification of Japanese Pavement Fatigue Life Criteria by Considering Climatic Effects in Cold Regions



Tianshu Lin, Tatsuya Ishikawa, Tetsuya Tokoro, Kimio Maruyama, and Chigusa Ueno

Abstract In Japanese pavement design method, fatigue life criteria for cracking and rutting come from the US Asphalt Institute model, which relates failure loading number to the tensile strain on the lower surface of the asphalt mixture layer and the compressive strain on the top layer of the subgrade, respectively. These strains closely relate to the moduli of each layer. Japanese pavement design method assumes the moduli of base and subgrade layers are constant throughout the whole year. However, as proven by numerous past studies, these moduli are strongly affected by variation of water content and freeze-thaw cycle. To be precise, rising water content, as a result of the inflow of water or the thawing of ice lenses, causes a temporary decrease in the stiffness of subgrade and base course material. Besides, ice formation tends to break some of the particle contacts and interlocking of soil particles, which also leads to a degradation of base course material. Basically, climatic effects (variation of water content and freeze-thaw cycle) on base and subgrade layers material are not fully captured in Japanese pavement design method now. This study calculates the fatigue life of eight local flexible pavement projects with variation of base layer moduli considering freeze-thaw action and seasonal fluctuation in water content to capture the effects of climate on the fatigue life of the pavement. Long-term measured performance data are used to calibrate the rutting model. Results proved that climate-related degradation of the granular base decreases the fatigue life against rutting of asphalt pavements in cold regions.

Keywords Climate effect · Freeze-thaw · Mechanical-empirical design method · Pavement design guide

T. Lin · T. Ishikawa (✉)
Hokkaido University, Sapporo 060-8628, Japan
e-mail: t-ishika@eng.hokudai.ac.jp

T. Tokoro
Hokkai-Gakuen University, Sapporo 064-0926, Japan

K. Maruyama · C. Ueno
Civil Engineering Research Institute for Cold Region, Sapporo 062-8602, Japan

1 Introduction

In Japanese pavement design method, fatigue life criteria for cracking and rutting come from the US Asphalt Institute model [1], which relates failure loading number to the tensile strain on the lower surface of the asphalt mixture layer and the compressive strain on the top layer of the subgrade, respectively. Consequently, the moduli of each layer strongly affect fatigue life prediction. Japanese pavement design method assumes the moduli of base and subgrade layers are constant throughout the whole year.

However, as proven by numerous past studies, no matter in laboratory tests or in situ measurements, these moduli are strongly affected by variation of water content [2–6] and freeze-thaw cycle [7–10]. To be precise, rising water content, as a result of the inflow of water during rainfall or the thawing of ice lenses, causes a temporary decrease in the stiffness of subgrade and base course material. Meanwhile, freeze-thaw action always decreases moduli of base and subgrade layer materials even with no excess water storage after thawing [11, 12], since ice formation tends to break some of the particle contacts and interlocking of soil particles and finally deteriorates the soil structure uniformity and stiffness.

Consequently, constant moduli of base and subgrade layers cannot give an accurate prediction of fatigue life. As a result, this study aims to modify present Japanese pavement design method by considering the effect of variation of water content and freeze-thaw cycle. Besides, a local calibration for fatigue rutting model for cold region is also performed based on measured pavement performance data as fatigue cracking model has been modified by previous research studies [13, 14].

2 Test Pavement

2.1 Pavement Structures

Test pavement locates in Bibi, south part of Hokkaido, Japan. Civil Engineering Research Institute for Cold Region (CERI) [13] designed and constructed them and Fig. 1 illustrates structures of each test pavement. All pavement structures consist of asphalt mixture, base layer, and subgrade layer with variation of materials and thickness.

Four types of asphalt mixtures are used in test pavement. Fine-graded asphalt mixture has a 0–13 mm gradation distribution. Middle-graded asphalt mixture has the same range of gradation distribution but more coarse aggregate. Coarse-graded and stabilized asphalt mixture have a 0–20 mm and 0–30 mm gradation distribution separately. Two types of base layer material are used as C-40, crusher-run with maximum 40 mm gradation distribution, and C-80, crusher-run with maximum 80 mm gradation distribution. Subgrade layer is composed of natural soil, which is classified as a gravel soil.

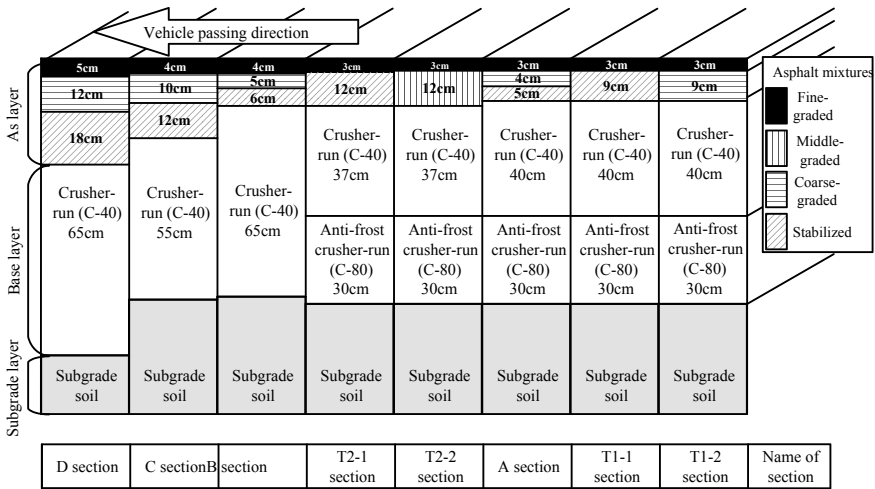


Fig. 1 Test road pavement structures

2.2 Traffic Volume Observation

CERI observed traffic volume of test pavement during the whole life (from 1990 to 2004). Total traffic volume that is average annual daily vehicle (car and truck) number in one lane, is 4974 per day per lane. Truck volume that is average annual daily truck number in one lane, is 1714 per day per lane. Wheel loads for all vehicles are in accordance with the normal distribution that ranges from 15 to 80 kN. As Japanese pavement design method calculates the allowable number of equivalent 49 kN wheel loads against rutting and fatigue cracking. CERI transferred the traffic volume to a 49 kN wheel loads number as 2398 per day per lane.

2.3 Rutting and Fatigue Crack Measurement

Figures 2 and 3 show the development of rutting depth and fatigue cracking with increasing loading number. The starting time is 1990 after the opening of test road. Serious rutting failure could be observed through Fig. 2 regardless of the pavement structures. All pavements have a rutting depth over 10 mm after first 1 million 49 kN wheel loads and final rutting depth are larger than 30 mm.

On the other hand, only A, B, T1-1, and T2-1 section suffered fatigue cracking and these cracking start after 9 million 49 kN wheel loads. It is reasonable to conclude that rutting is a more serious failure type for flexible pavement in cold region like Hokkaido.

Fig. 2 Rutting depth

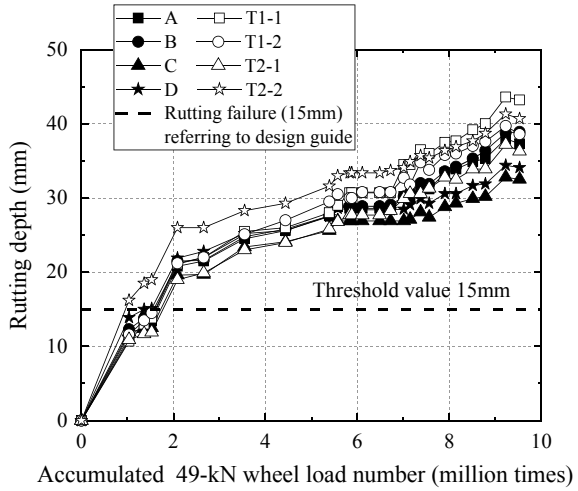
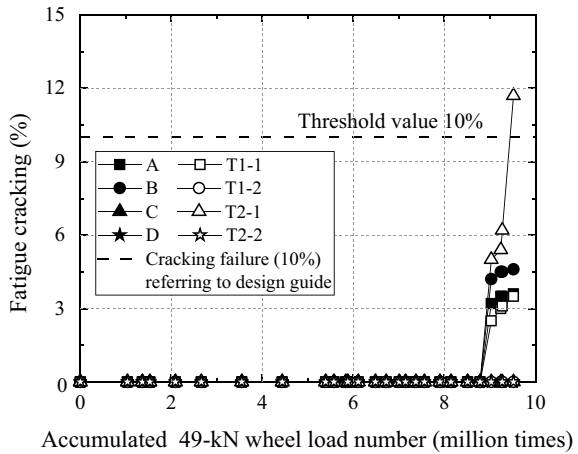


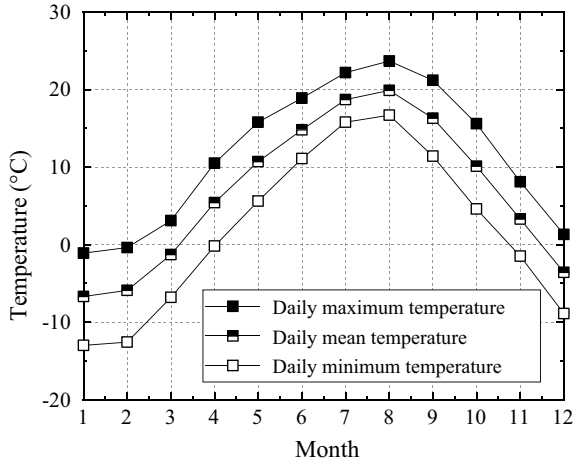
Fig. 3 Fatigue cracking



2.4 Climate Data

Climate data are collected from Automated Meteorological Data Acquisition System (AMeDAS). Figure 4 plots the monthly average value of daily temperatures during the whole life from 1990 to 2004. These climate data are used to determine the stiffness of the asphalt layer. Besides, the monthly representative temperature is also used to determine the frost-penetration depth, which highly relates to the stiffness of base and subgrade layer as frozen soil has a much larger stiffness. Determination of base layer stiffness will be introduced in next part.

Fig. 4 Monthly average value of daily temperatures



3 Modification of Design Guide

3.1 Current Predictive Models

Equations (1) and (2) are allowable number of equivalent 49 kN wheel loads against rutting (N_{fs}) and cracking (N_{fa}) [1]. Due to design method, N_{fs} is loading number when rutting depth reaches 15 mm, N_{fa} is loading number when fatigue cracking reaches 10%.

$$N_{fs} = \beta_{s1} \cdot \{1.365 \times 10^{-9} \cdot \epsilon_a^{-4.477 \cdot \beta_{s2}}\} \tag{1}$$

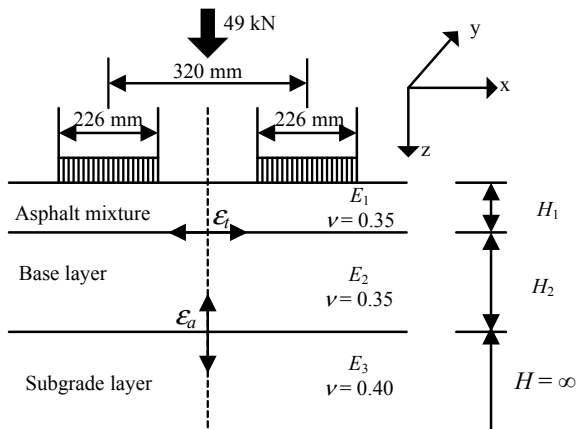
$$N_{fa} = \beta_{a1} \cdot C \cdot \{6.167 \times 10^{-5} \cdot \epsilon_t^{-3.291 \cdot \beta_{a2}} \cdot E_1^{-0.854 \cdot \beta_{a3}}\} \tag{2}$$

where β_{s1} , β_{s2} , β_{a1} , β_{a2} , and β_{a3} are the compensation rates for AI failure criteria based on the actual situation of Japanese pavement; E_1 is the moduli of asphalt layer; C is the material parameter. The tensile strain on the lower surface of the asphalt layer (ϵ_t) and the compressive strain on the top layer of the subgrade (ϵ_a) under a design wheel load of 49 kN (Fig. 5) were calculated using the General Analysis of Multi-layered Elastic Systems (GAMES) program [15]. Poisson’s ratio of asphalt mixture, base layer, and subgrade layer are set as 0.35, 0.35, and 0.4, respectively.

3.2 Determination of Stiffness

Stiffness of asphalt mixture. Stiffness of asphalt mixture (E_1) is determined through following equations [1, 14].

Fig. 5 Pavement structure models



$$E_1 = -278.4M_p + 10930 \quad (3)$$

$$M_p = M_a \left[1 + \frac{2.54}{z_1 + 10.16} \right] - \frac{25.4}{9(z_1 + 10.16)} + \frac{10}{3} \quad (4)$$

where M_p is the monthly mean temperature of asphalt mixture at depth of z_1 ; M_a is monthly mean air temperature; z_1 equals to one-third of the height of asphalt mixture (cm).

Stiffness of base layer. In general, the Japanese pavement design method assumes the elastic moduli of base and subgrade layers are constant throughout a whole year. However, in this study, to capture the seasonality of the elastic modulus for the base layer (E_2), the E_2 value varies considering freeze-thaw action and seasonal fluctuation in water content. The monthly representative elastic moduli were divided into three types of seasonal E_2 values (E_2 for freezing season, thawing season, and regular season except freezing and thawing seasons).

E2 for freezing season. The E_2 value for freezing season is set as 600 MPa, calculated from FWD test results during the freezing time [16]. This study assumes that when the average frost-penetration depth for the month reaches the base layer, the E_2 increases due to freezing. Here, the average frost-penetration depths (z) was calculated by substituting the freezing index obtained from the daily mean air temperatures measured at AMeDAS into the modified Berggren formula [17] shown below:

$$z = \alpha \sqrt{\frac{172800F}{(L/\lambda)_{\text{eff}}}} \quad (5)$$

where α is a correction coefficient; F is a freezing index which is the average air temperature during freezing season multiplied by its duration in days; $(L/\lambda)_{\text{eff}}$ is an effective ratio of L to λ ; L is latent heat of soil; and λ is a thermal conductivity of soil.

E_2 for regular season. The E_2 value for regular season is estimated through Liang model [2], which is modified by considering the effect of matric suction based on the AASHTO universal model [18], as shown in Eqs. (6) and (7), and previous resilient modulus test results on C-40 material with various water content [19].

$$M_R = k_1 p_a \left(\frac{\theta_b + \chi \psi}{p_a} \right)^{k_2} \left(\frac{\tau_{oct}}{p_a} + 1 \right)^{k_3} \tag{6}$$

$$\chi = \left[\frac{(u_a - u_w)_b}{(u_a - u_w)_f} \right]^{0.55} \tag{7}$$

where χ is Bishop’s effective stress parameter and $(u_a - u_w)_b$ is suction at AEV; ψ is matric suction; θ_b is bulk stress; τ_{oct} is octahedral shear stress; atmospheric pressure p_a is 101 kPa in this study.

Figure 6 shows the resilient modulus of C-40 under different water content. Table 1 lists the regression analysis results through Liang model. High R^2 value proves the validity of this model. With value of k_1 , k_2 , and k_3 , Eq. (6) could be written as the following equation.

$$M_R = 4.86091 \cdot p_a \left(\frac{\theta_b + \chi \psi}{p_a} \right)^{1.52515} \left(\frac{\tau_{oct}}{p_a} + 1 \right)^{-2.09233} \tag{8}$$

The matric suction in base layer is also necessary to estimate monthly representative resilient modulus of base layer through Eqs. (7) and (8). Ishikawa et al. [16] performed long-term field measurement of frost-penetration depth, daily precipitation, and degree of saturation in each layer of the pavement. Soil water characteristic curve (SWCC) of C-40 is also determined through laboratory water retentivity test

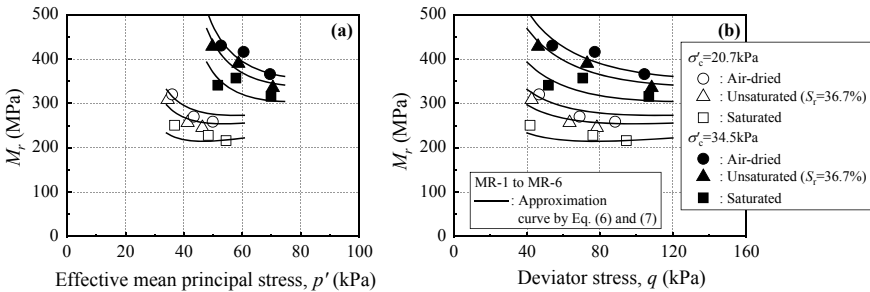


Fig. 6 Resilient modulus under different water content

Table 1 Results of regression analysis

k_1	k_2	k_3	R^2
4.86091	1.52515	-2.09233	0.95

[19]. By combining field-measured data of water content and SWCC of C-40, matric suction of base layer in each month could be determined. Consequently, resilient modulus of the base layer during regular season could be estimated.

E_2 for thawing season. By developing a freeze-thaw CBR test apparatus [19], Ishikawa investigated the effect of freeze-thaw on CBR and this effect is assumed to be expressed by a compensation function $f(N_f, \theta)$, which uses number of freeze-thaw process cycles (N_f) and volumetric water content (θ) for the sample as explanatory variables based on the test result. Effect of thaw weakening on resilient modulus is considered by adding $f(N_f, \theta)$ in the Eq. (8) as shown in the following:

$$M_R = f(N_f, \theta) \cdot 4.86091 \cdot p_a \left(\frac{\theta_b + \chi \psi}{p_a} \right)^{1.52515} \left(\frac{\tau_{\text{oct}}}{p_a} + 1 \right)^{-2.09233} \quad (9)$$

As a result, the E_2 value for thawing season is estimated in a similar method by combining Eqs. (7) and (9), field-measured data of water content, and SWCC of C-40.

4 Calibration

Figure 7 illustrates predicted fatigue life through original rutting model and modified one by considering variable base layer stiffness. Modified model predicts smaller allowable loading number as thaw weakening and sudden water content increasing greatly deteriorate base layer stiffness. Thus, it is important to consider the change in the stiffness of base layer caused by freeze-thaw and water content changing when developing a design method with high prediction accuracy for pavement structures in cold regions.

However, N_{fs} through modified model is still much larger than actual observed loading number when rutting depth reaches 15 mm (Fig. 2). Bias between predicted and actual pavement life are caused by large variability between designed and actual geography, climatic conditions, construction materials, construction practises, traffic compositions and volumes. It is desirable to calibrate the modified model at the local level by adjusting value of local calibration coefficient to make predicted and

Fig. 7 Allowable loading number against rutting

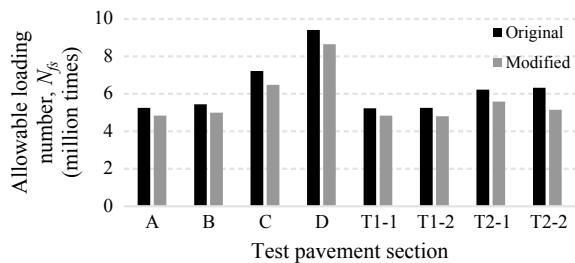
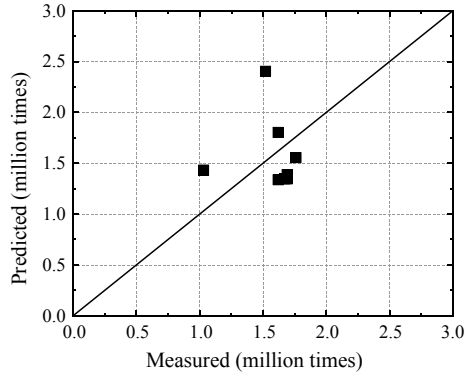


Fig. 8 Measured versus predicted allowable number with the locally calibrated coefficient



measured data satisfy the null hypothesis as shown in Eq. (10).

$$\sum (\text{Measured} - \text{Predicted}) = 0 \tag{10}$$

A local calibration coefficient equals 0.2777 makes modified model satisfy the null hypothesis that the sum of difference between predicted and measured failure loading number equals to zero. As shown in Fig. 8, measured versus predicted allowable loading number against rutting for local calibration factors wrapped nicely around the 45° line as expected.

5 Conclusions

In this study, the current Japanese pavement design method is modified by replacing constant layer modulus assumption with a variable that helps to adjust the modulus according to influences by water content and freeze-thaw history. Long-term measured performance data of eight test pavements are used to calibrate a modified rutting model. The following findings can be mainly listed:

- It is possible to estimate the resilient modulus of unsaturated granular base course materials subjected to repeated freeze-thaw actions by multiplying the compensation function for the evaluation of the freeze-thaw effects on a constitutive equation used in the AASHTO design standard.
- Freeze-thaw actions and the concurrent seasonal fluctuations in water content deteriorate the resilient deformation characteristics of granular base course materials and shorten the pavement fatigue life against rutting in cold regions.
- According to large variability between designed and actual situation, local calibration is a necessary and effective way to remove bias and give a more prediction accuracy on fatigue life.

These findings need further validation based on comprehensive future studies including more pavement structures, climate conditions, and granular materials. Besides, climate effect, namely freeze-thaw and fluctuating water content, on resilient deformation characteristics of the subgrade layer still need further study to develop a more comprehensive pavement design method.

Acknowledgements This research was supported in part by Grant-in-Aid for Scientific Research (B) (20360206) (C) (15K06214), and (A) (16H02360) from Japan Society for the Promotion of Science (JSPS) KA-KENHI. The authors also acknowledge the support by China Scholarship Council.

References

1. Japan Road Association (ed) (2006) Pavement design manual, 1st edn. Maruzen Print Co. Ltd., Tokyo (in Japanese)
2. Liang RY, Rabab'ah S, Khasawneh M (2008) Predicting moisture-dependent resilient modulus of cohesive soils using soil suction concept. *J Transp Eng* 134(1):34–40
3. Yang SR, Lin HD, Kung JHS, Huang WH (2008) Suction-controlled laboratory test on resilient modulus of unsaturated compacted subgrade soils. *J Geotechn Geoenvironmental Eng* 134(9):1375–1384
4. Cary CE, Zapata CE (2011) Resilient modulus for unsaturated unbound materials. *Road Mater Pavement Des* 12(3):615–638
5. Ng CWW, Zhou C, Yuan Q, Xu J (2013) Resilient modulus of unsaturated subgrade soil: experimental and theoretical investigations. *Can Geotech J* 50(2):223–232
6. Han Z, Vanapalli SK (2015) Model for predicting resilient modulus of unsaturated subgrade soil using soil-water characteristic curve. *Can Geotech J* 52(10):1605–1619
7. Johnson TC, Cole DM, Chamberlain EJ (1978) Influence of freezing and thawing on the resilient properties of a silt soil beneath an asphalt concrete pavement. Cold Regions Research and Engineering Laboratory, New Hampshire
8. Cole DM, Irwin LH, Johnson TC (1981) Effect of freezing and thawing on resilient modulus of a granular soil exhibiting nonlinear behavior. *Transp Res Rec* 809:19–26
9. Berg RL, Bigl SR, Stark JA, Durell GD (1996) Resilient modulus testing of materials from Mn/ROAD, Phase 1. Cold Regions Research and Engineering Laboratory, New Hampshire
10. Simonsen E, Janoo VC, Isacsson U (2002) Resilient properties of unbound road materials during seasonal frost conditions. *J Cold Reg Eng* 16(1):28–50
11. Lin T, Ishikawa T, Aoki R, Tokoro T (2019) Resilient properties of unbound granular materials subjected to freeze-thaw and wheel loads. In: 16th Asian regional conference on soil mechanics and geotechnical engineering, Taipei (in press)
12. Lin T, Ishikawa T, Tokoro T (2019) Testing method for resilient properties of unsaturated unbound granular materials subjected to freeze-thaw action. *Jpn Geotech Soc Spec Publ* 7(2):576–581
13. Maruyama K, Tako J, Kasahara A (2006) Long-term performance of asphalt pavements at Bibi new test road. *Jpn Soc Civ Eng Annu Meet E* 62(3):519–530 (in Japanese)
14. Maruyama K, Tako J, Kasahara A (2008) Fatigue failure life prediction method of asphalt pavement. *Jpn Soc Civ Eng Annu Meet E* 64(3):416–426 (in Japanese)
15. Maina JW, Matsui K (2004) Developing software for elastic analysis of pavement structure responses to vertical and horizontal surface loadings. *Transp Res Rec* 1896:107–118
16. Ishikawa T, Lin T, Kawabata S, Kameyama S, Tokoro T (2019) Effect evaluation of freeze-thaw on resilient modulus of unsaturated granular base course material in pavement. *Transp Geotech* (in press)

17. Aldrich HP Jr (1956) Frost penetration below highway and airfield pavements. Highw Res Board Bull 135:124–149
18. AASHTO (2008) Mechanistic-empirical pavement design guide: a manual of practice, 1st edn. AASHTO, Washington
19. Ishikawa T, Zhang Y, Tokoro T, Miura S (2014) Medium size triaxial apparatus for unsaturated granular subbase course materials. Soils Found 54(1):67–80

Influence of Vehicle Braking on Pavement Shakedown Limits



Yuchen Dai, Jiangu Qian, and Feifei Lei

Abstract Shakedown analysis has been regarded as a rational pavement design method in recent years. If the value of traffic load does not exceed the critical level (i.e., shakedown limit), pavement will not exhibit continuous accumulated plastic strains which eventually lead to failure within the pavement system. During the process of vehicle braking, the traffic moving speed is constantly changing with a relatively large friction coefficient between wheel and pavement surface. This study is aimed to investigate the dynamic effect of both vehicle speed and friction coefficient on pavement shakedown limits under braking condition. A finite element model is utilized to obtain the dynamic elastic stress field for the calculation of shakedown limit. The moving speed of the applied load using user subroutine is set to decrease continuously with a constant acceleration which is supervised by the horizontal frictional force. Results show that the shakedown limit of pavement decreases with the increasing of friction coefficient (corresponding to higher acceleration) and increases with the decreasing of load moving speed. The critical shakedown state occurs when the vehicle begins to decelerate. Dynamic shakedown analysis for both uniform and two-layered pavement systems is investigated.

Keywords Shakedown · Dynamic · Friction · Braking

1 Introduction

Since Sharp and Booker [1] first applied the shakedown theorem to the geotechnical materials of pavement structures, shakedown analysis has been proven to be a reasonable solution for pavement design. If the level of traffic load does not exceed a critical value (i.e., shakedown limit), the pavement structure will reach a stable state

Y. Dai · J. Qian (✉)

Department of Geotechnical Engineering, Tongji University, Shanghai 200092, China
e-mail: qianjiangu@tongji.edu.cn

F. Lei

Hangzhou CBD Construction Development Co., Ltd, Hangzhou 310020, China

after a certain number of load cycles with no further accumulating plastic deformation. Over the past decades, many lower-bound or upper-bound shakedown solutions have been proposed to estimate the shakedown limit of pavement materials [2–5]. However, most of the previous shakedown analyses were conducted assuming static responses of the pavement to vehicle loads. Qian et al. [6] further investigated the dynamic influence of vehicle moving speed on the shakedown limit while ignoring the effect of frictional contact. Actually, when the vehicle is driven normally on the pavement at a constant speed, the friction coefficient between tire and pavement surface is quite small and can even be negligible, but when considering the process of braking or accelerating, the tire-pavement frictional contact may significantly affect the pavement shakedown limit.

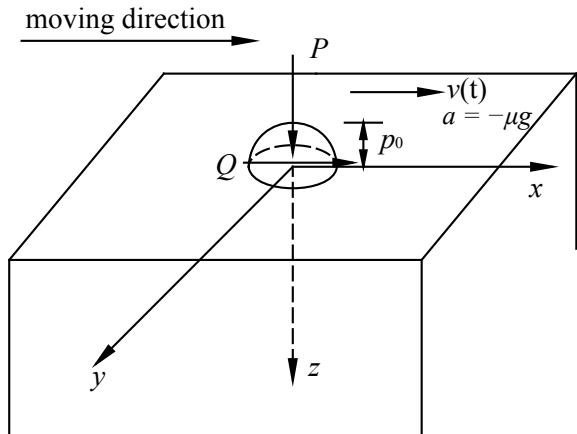
Hence, this work is intended to propose a dynamic shakedown analysis method to explore the combined influence of horizontal friction and load moving speed for the case of vehicle braking.

2 Problem Definition

In this work, the pavement system is considered as an infinite half-space subjected to a rolling and sliding point contact load moving with variable speed, as illustrated in Fig. 1. Pavement system under 3D moving Hertz load. The contact area is assumed to be a circular-shaped patch, and a 3D Hertz load is representative of the wheel load distribution, with both vertical and horizontal components defined as [7]:

$$p = \frac{3P}{2\pi r^3}(r^2 - x^2 - y^2)^{1/2} \tag{1}$$

Fig. 1 Pavement system under 3D moving Hertz load



$$q = \frac{3Q}{2\pi r^3} (r^2 - x'^2 - y'^2)^{1/2} \quad (2)$$

$$x'^2 + y'^2 < r^2 \quad (3)$$

where r is radius of the contact area, P and Q are total normal and tangential forces, respectively. $p_0 = 3P/2\pi r^2$ is the peak pressure at the center of the contact area. The normal and tangential loads are linked by the frictional coefficient μ as the following:

$$\mu = Q/P \quad (4)$$

To simulate the process of vehicle braking, the limit value of the braking force is considered to be equal to the horizontal friction force Q , so the traffic load is interested in movements with

$$v(t) = v_0 + at \quad (5)$$

$$a = -\mu g \quad (6)$$

where a is the acceleration of the moving load, g is the gravitational acceleration, $v = v(t)$ is velocity and $v_0 = \text{constant}$, the initial velocity at time $t = 0$ when the vehicle starts brake.

The Hertz load distribution then leads to an expression:

$$p = \frac{3P}{2\pi r^3} (r^2 - (x - v_0t - at^2/2)^2 - y^2)^{1/2} \quad (7)$$

$$q = \frac{3Q}{2\pi r^3} (r^2 - (x - v_0t - at^2/2)^2 - y^2)^{1/2} \quad (8)$$

$$(x - v_0t - at^2/2)^2 + y^2 < r^2 \quad (9)$$

where (x', y') is regarded as a local coordinate system and its origin $(x' = 0, y' = 0)$ is always the center of circular contact. They are correlated with the global Cartesian coordinate system (x, y, z) as $x = x' + v_0t + at^2/2$, $y = y'$, $z = 0$, and the x -axis is the moving direction.

3 Dynamic Shakedown Solution

Assuming that the pavement material is elastic and perfectly plastic with the Mohr-Coulomb criterion, a dynamic shakedown analysis method based on the lower-bound shakedown theorem [6] is proposed to determine the shakedown limit of pavement subjected to moving load with variable speed, which demands:

Maximize λ

$$\begin{cases} f(\lambda\sigma^e, \rho_{xx}(\lambda\sigma^e)) \leq 0 \\ \max_{z=j}(-M_i - \sqrt{-N_i}) \leq \rho_{xx} \leq \min_{z=j}(-M_i + \sqrt{-N_i}) \end{cases} \quad (10)$$

with

$$M = \lambda\sigma_{xx}^e - \lambda\sigma_{zz}^e + 2 \tan \phi (c - \lambda\sigma_{zz}^e \tan \phi) \quad (11)$$

$$N = 4(1 + \tan^2 \phi)[(\lambda\sigma_{xz}^e)^2 - (c - \lambda\sigma_{zz}^e \tan \phi)^2] \quad (12)$$

where σ_{ij}^e is the dynamic elastic stress field due to the applied load, ρ_{ij} is the time-independent, self-equilibrated residual stress field, f is the yield criterion for the material, c is the cohesion, and ϕ is the internal friction angle.

To obtain the realistic estimation of traffic-induced dynamic stresses in the pavement, a novel finite element model with infinite element artificial boundary (FE-IE) as mentioned in Qian et al. [6] has been established in ABAQUS. In this work, the dynamic stress analysis was carried out with Dynamic/Explicit in ABAQUS, and the user subroutine VDLOAD was utilized to simulate the moving load. Due to the defect that the horizontal moving force cannot be applied directly on the top boundary through the VDLOAD, a special method in which an equivalent “body force” is defined to mimic the moving load in any given direction is developed. Then, to apply the traffic load moving with variable speed on the top boundary, a thin-layer is built above the surface of the model [8], in which both equivalent vertical and horizontal moving body forces can be applied simultaneously. As a result, the friction coefficient which determines the acceleration of the moving load is conveniently controlled by changing the ratio of vertical and horizontal components of applied body forces. And then the corresponding variable speed of moving load is set to realize the simulation of the vehicle braking process.

Hence, according to the dynamic lower-bound shakedown solution (i.e., Eq. 10–12), once the dynamic stress fields induced by the applied moving load [defined as Eq. (7) and (9)] are determined by FEM and the pavement material properties are given as well, then the solution for the shakedown limit is required to find a possible residual stress field and load multiplier λ with satisfying Eq. (10) through an optimization procedure.

4 Results

4.1 Uniform Pavement System

In this paper, a pavement system of uniform cohesive-frictional material is for simplicity analyzed here with Young’s modulus $E = 20$ Mpa, Poisson’s ratio $\nu = 0.48$ and mass density $\rho = 1800$ kg/m³, and the normalized shakedown limit load is represented as $\lambda'p_0/c$

Firstly, Fig. 2 shows shakedown limits versus friction coefficient for various values of internal friction angle when the load moves on the pavement surface at a constant speed $v = 10$ m/s. It is clear that the shakedown limit decreases with increasing frictional coefficient, but increases with increasing friction angle, which is similar to previous static result [4]. Noted that the contact friction coefficient may reach to 0.5–1.0 during wheel locked braking [9], so the results of $\mu = 0.5$ which determines an acceleration $a = -5$ m/s² is chosen here for the following comparison with the case of braking.

To investigate the influence of vehicle braking on the shakedown limit load, Fig. 3 further demonstrates the curve of shakedown limit versus time during the process of vehicle braking. The initial velocity v_0 when the vehicle starts braking is 10 m/s. The friction coefficient set as $\mu = 0.5$ corresponds to the acceleration $a = -5$ m/s². As showed in Fig. 3, the vehicle braking significantly influences the shakedown limit of pavement. The shakedown limit rises with time as the vehicle speed decreases, and the minimum shakedown limit at the beginning is always smaller compared to the condition of the vehicle moving at a constant speed. When the internal friction angle $\phi = 30^\circ$, compared with the shakedown limit (about 6.55) of the special case where the traffic load moves at a constant speed $v = 10$ m/s with the same friction coefficient $\mu = 0.5$, the minimum shakedown limit (about 6.05) for the case of braking is about 7.6% lower. And the degree of reduction decreases with smaller internal friction

Fig. 2 Shakedown limits versus friction coefficient for various values of internal friction angle ($v = \text{constant} = 10$ m/s)

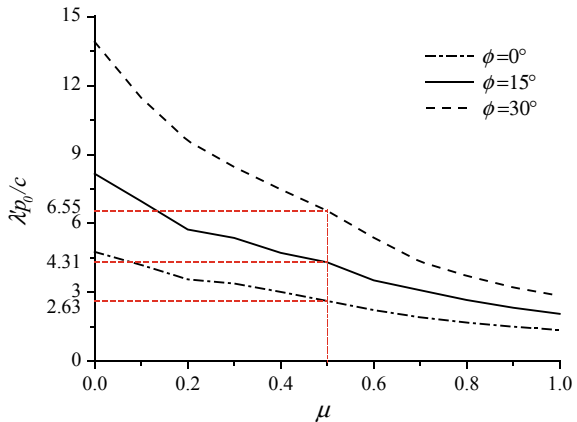
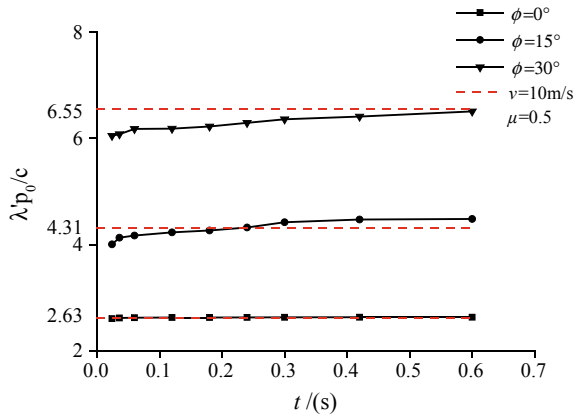


Fig. 3 Shakedown limits versus time for various values of internal friction angle ($v_0 = 10$ m/s, $a = -5$ m/s²)



angle, which is about 6.9% when $\phi = 15^\circ$ and 0.8% when $\phi = 0^\circ$. Then, if the load-pavement contact friction is not taken into account (i.e., $v = \text{constant} = 10$ m/s, $\mu = 0$) either, the reduction is about even 55.7%. The minimum shakedown limit during the braking process means that the highest dynamic response corresponds to the moment when the braking starts, which is expected to result in the critical state of pavement shakedown.

4.2 Two-Layered Pavement System

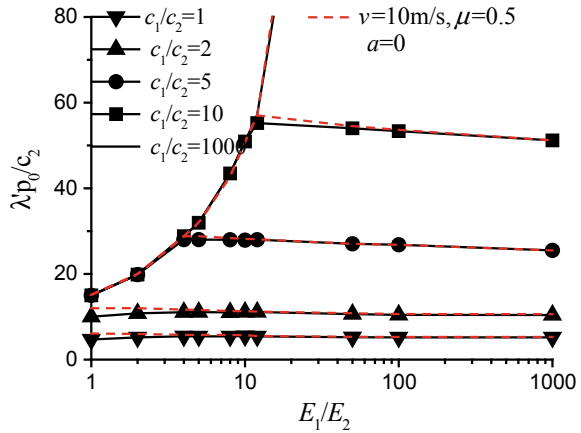
The proposed dynamic shakedown solution is then implemented at a two-layered pavement system. The parameters of the two-layered pavement system are given in Table 1. The material properties of the first layer (i.e., pavement surface) are varied to perform sensitivity studies of the shakedown limit, while the physical properties of the second layer (i.e., subgrade) remain unchanged. The thickness of the first layer is assumed to be $2r$ where r represents the radius of the load contact area.

Figure 4 shows the minimum shakedown limit (corresponding to the critical state of pavement shakedown which occurs at the moment when the braking starts) versus the stiffness ratio for a range of strength ratios when the initial velocity $v_0 = 10$ m/s and $a = -5$ m/s². For cases of $c_1/c_2 \geq 5$, the shakedown limit first increases to a peak and then turns to decrease with the rise of stiffness ratio E_1/E_2 . The peak point

Table 1 Material properties used in the two-layered pavement

Layer	Young's modulus (MPa)	Poisson's ratio	Density (kg/m ³)	Internal friction angle (°)
Pavement	20–20,000	0.25	2200	30
Subgrade	20	0.48	1800	0

Fig. 4 Minimum shakedown limits versus stiffness ratios for various values of strength ratio when $v_0 = 10$ m/s and $a = -5$ m/s²



indicates the change of critical point location from the second layer (increasing part) to the first layer (decreasing part). For cases of $c_1/c_2 \leq 2$, failure always occurs in the first layer. Compared with the results of the case when the vehicle moves at a constant speed $v = 10$ m/s with $\mu = 0.5$, it can be seen that vehicle braking will also reduce the shakedown limit to a certain extent. Nevertheless, it mainly has a significant impact when the failure occurs in the first layer and the stiffness ratio E_1/E_2 is relatively small.

5 Conclusions

This paper considered the problem of a pavement material subjected to repeated effects of braking or decelerating vehicles. A novel numerical way to modeling dynamic shakedown behavior of pavement subjected to repeated braking vehicles in movement is developed. The dynamic shakedown limits are discussed in both uniform and two-layered pavement system.

Results showed that the shakedown limit increases with decreasing load moving speed during vehicle braking. The critical state of pavement shakedown is the moment when the vehicle begins to decelerate. Compared with the condition of vehicle moving at a constant speed, the minimum shakedown limit at the beginning of braking is smaller, especially when the internal friction angle is larger. For the two-layered pavement system, vehicle braking mainly has a significant impact when the failure occurs in the first layer and the stiffness ratio E_1/E_2 is relatively small.

Acknowledgements This work was supported by the National Natural Science Foundation of China (Grant Nos. 51578413, 51238009).

References

1. Sharp RW, Booker JR (1984) Shakedown of pavements under moving surface loads. *J Transp Eng* 110:1–14
2. Collins IF, Wang AP, Saunders LR (1993) Shakedown in layered pavements under moving surface loads. *Int J Numer Anal Meth Geomech* 17(3):165–174
3. Wang J, Yu HS (2013) Shakedown analysis for design of flexible pavements under moving loads. *Road Mater Pavement Des* 14(3):703–722
4. Yu HS, Wang J (2012) Three-dimensional shakedown solutions for cohesive-frictional materials under moving surface loads. *Int J Solids Struct* 49(26):3797–3807
5. Zhuang Y, Wang KY (2018) Shakedown solutions for pavement structures with von Mises criterion subjected to Hertz loads. *Road Mater Pavement Des* 19(3):710–726
6. Qian JG, Wang YG, Wang J, Huang MS (2019) The influence of traffic moving speed on shakedown limits of flexible pavements. *Int J Pavement Eng* 20(2):233–244
7. Johnson KL (1985) Contact mechanics. *J Tribol* 108(4):464
8. Dai YC, Qian JG, Wang YG, Huang MS (2017) Dynamic shakedown analysis of flexible pavements under rolling and sliding contact considering moving speed. *Procedia Eng* 189:283–290
9. Goudie DW, Bowler JJ, Brown CA et al (2000) Tire friction during locked wheel braking. *Sae World Congress*

Physical Modeling of Stress Propagation in Railway Pavement with LWD



Artur Cortês da Rosa , Maria Esther Soares Marques ,
Antônio Carlos Rodrigues Guimarães , Gleyciane Almeida Serra ,
and Marcelino Aurélio Vieira da Silva 

Abstract This paper presents the study of the stress propagation of a large-scale model of railway pavement layers with the Light Weight Deflectometer (LWD). The large-scale physical model, where the test was carried out, is a test tank with 2 m depth and 4 m² area. The physical model simulating a railway pavement is composed of a set of layers: gravel bed, to allow the moisture capillary rise, subgrade, subballast and ballast. The stress variation was monitored by pressure cells, and displacements by LVDT sensors on settling plates. The aim of this study is to understand how the LWD test works in railway pavements, specifically when tested at the ballast layer, and verify how the strain–stress behavior really develops during LWD tests.

Keywords Light Weight Deflectometer · Railway · Pavement

1 Introduction

Among the geotechnical techniques of in situ tests for railways, the most commonly used is the Light Weight Deflectometer (LWD) test [1–6]. This test allows the evaluation of a track-bed, estimating the dynamic modulus of the soil at each construction stage of a track-bed and also used for quality control.

It is a known fact that soil stiffness and strength are related in the sense that soils with low resistance also tend to present low stiffness [7]. So, the LWD test can be used to obtain these properties in the field, such as deformation modulus.

The measured peak deflection can be used as a measure of soil stiffness or degree of compaction, and the peak force can be used to estimate the dynamic modulus [8].

Field and laboratory tests results conducted by [9] using LWD showed that the reliability of the LWD tests values depends on the stiffness of the material tested. Also, the subgrades with low bearing capacity have poor repeatability, on the other hand, rigid and well compacted layers presented better repeatability. Moreover, laboratory

A. C. da Rosa (✉) · M. E. S. Marques · A. C. R. Guimarães · G. A. Serra
Military Institute of Engineering, Rio de Janeiro, RJ 22290-270, Brazil

M. A. V. da Silva
Federal University of Rio de Janeiro, Rio de Janeiro, RJ 21941-901, Brazil

tests showed the influence of depth on LWD results, which ranged from 270 to 280 mm on that study, depending on the stiffness of the materials tested.

The depth of influence of the dynamic load of LWD test is about the same as the diameter of the loading plate [10, 11]. Between 1.2 and 1.4 times the plate diameter [12], and between 2.0–2.5 times the diameter of the LWD plate [13].

Mooney and Miller [14] tested three different soil layers under the LWD loading with pressure cells and LVDTs installed at different depths. They also tested with variable loads and plate size. The depth of influence was about 2 times the plate diameter, regardless of a peak load value, considering stress distribution measured by the pressure cells. However, the depth of influence based on strain measurements varied between 0.5 and 1.1 times the plate diameter.

Several studies were carried in soil layers representing roadway pavements. A few studies considered LWD tests to be used on railway pavement. Therefore, the aim of this study is to understand how the LWD test works in railway pavements, specifically when tested at the ballast layer, and verify how the stress–strain behavior really develops during LWD tests.

2 Materials and Methods

2.1 Materials

The materials of the experiment were Subgrade [15], Subballast [16] and Ballast [16]. The classification and properties of these materials are presented on Table 1. All the materials Resilient Modulus were obtained by cyclic triaxial tests, defined by a model in function of the applied confining and deviation stress.

2.2 Test Tank

The large-scale physical model used in this research, called “Test Tank of Pavements”, was developed by [17].

The Test Tank was used to simulate a pavement with dimensions close to the real ones in the field, mainly the thickness of the layers. The internal area of the tank is 4.0 m² and height 1.80 m and its internal volume is approximately 8.0 m³, with double walls of reinforced concrete with 0.20 m thickness. This tank is located at the COPPE / UFRJ Geotechnical Laboratory in Rio de Janeiro, Brazil.

Structure of the experimental pavement in the test tank. The large-scale physical model has a gravel bed on its bottom, which allows the rise of water through the subgrade, by capillarity. Over the gravel bed the materials were layered and the instrumentation installed along depth. The instrumentation wires were passed through outlets distributed along one of the walls of the structure, which allows the

Table 1 Soil and material classifications and properties

Classification/properties (standard)	Subgrade	Subballast	Ballast
USCS (ASTM D2487)	CH	–	–
AASHTO (ASTM D3282)	A-7-6	–	–
AREMA gradation range (AREMA/ASTM D6913)	–	–	AREMA 24
Resilient Modulus (ASTM D5311/D5311M-13)	$MR = 74,86 \cdot \sigma_3^{0,1637} \cdot \sigma_d^{-0,5844}$	$MR = 847,28 \cdot \sigma_3^{0,4228} \cdot \sigma_d^{-0,0763}$	$MR = 1465 \cdot \sigma_3^{0,489} \cdot \sigma_d^{-0,027}$
Los Angeles (ASTM C131/C131M-14)	–	–	16%
Treton (DNER-ME 399/99)	–	–	9%
Specific gravity (ASTM D891-18)	1.515 g/cm ³	2.125 g/cm ³	2.793 g/cm ³
Porosity (ASTM C830-00)	–	–	0.71%
Absorption (ASTM C642-13)	–	–	0.25%

Where MR is the Resilient Modulus in MPa, σ_3 is the applied confining stress in MPa, σ_d is the applied deviation stress in MPa.

connection to a acquisition system on the outside. Figure 1 shows the particle size distribution of the experimental pavement layers.

The subballast contains 44% of ½ in. gravel, 44% of ¾ in. gravel and 12% of CH soil (A-7-6) from the subgrade, meeting drainage criteria considered important by [18].

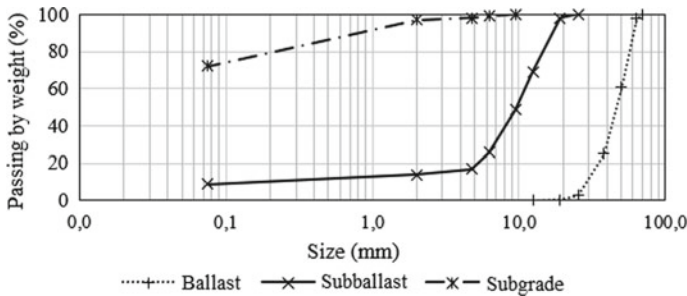


Fig. 1 Particle size distribution of the materials [16]

2.3 Instrumentation

The Geokon 3500 pressure cells were used to obtain pavement stress information at different depths. The pressure in the fluid is converted to electric potential difference (voltage), which were between 0 and 10 V. The maximum stress capacity is 1 MPa [19].

In the physical model, one pressure cell was positioned within the subgrade layer (CH05), one cell centered between the subgrade and the subballast (CH04), and another cell centered between the subballast and the ballast (CH07). Figure 2 shows each pressure cells placement, with their respective identifications.

The layer deflections were obtained using Instron LVDT displacement sensors. Settling plates attached to a rod and protected by a PVC pipe were positioned between the subgrade and the subballast and between the subballast and the ballast. The LVDT sensors were then positioned over the top of the settlement plate rod. All LVDT sensors were fixed to metal structures attached to the tank walls, which was not part of the tank reaction system, thus ensuring that the reference was undisplaced. Figure 2 shows the LVDT sensors used, with their respective identifications.

In Fig. 3 it is possible to observe how each LVDT was fixed, and the pressure cell CH07 (b and c) and LVDT sensor settling plate CH09 being allocated (a).

The pressure cells and LVDT sensors were connected to a Keysight 34902A multiplexer module acquisition unit. A total of, 3 pressure cells and 2 LVDT sensors were used.

2.4 LWD Equipment

The dynamic deflections obtained from LWD test were processed to estimate composite moduli of surface layer by considering Boussinesq's static linear-elastic half space theory, using the constitutive equation as shown in Eq. 1 [10, 20, 21].

$$E_0 = f'(1 - \nu^2) \frac{\sigma'_0 a}{d_n} \quad (1)$$

where:

- E_0 is the composite moduli of surface/subgrade layer;
- f' is the plate rigidity factor (2 is a standard value for a flexible plate);
- ν is Poisson's ratio, normally 0.35;
- σ'_0 is the maximum contact stress;
- a is the plate radius;
- d_0 is the maximum deflection.

The equipment used, Zorn ZFG 3000 LWD, has a 300 mm plate that, through dynamic load testing system applied by the 1150 mm drop of a 15 kg weight hammer

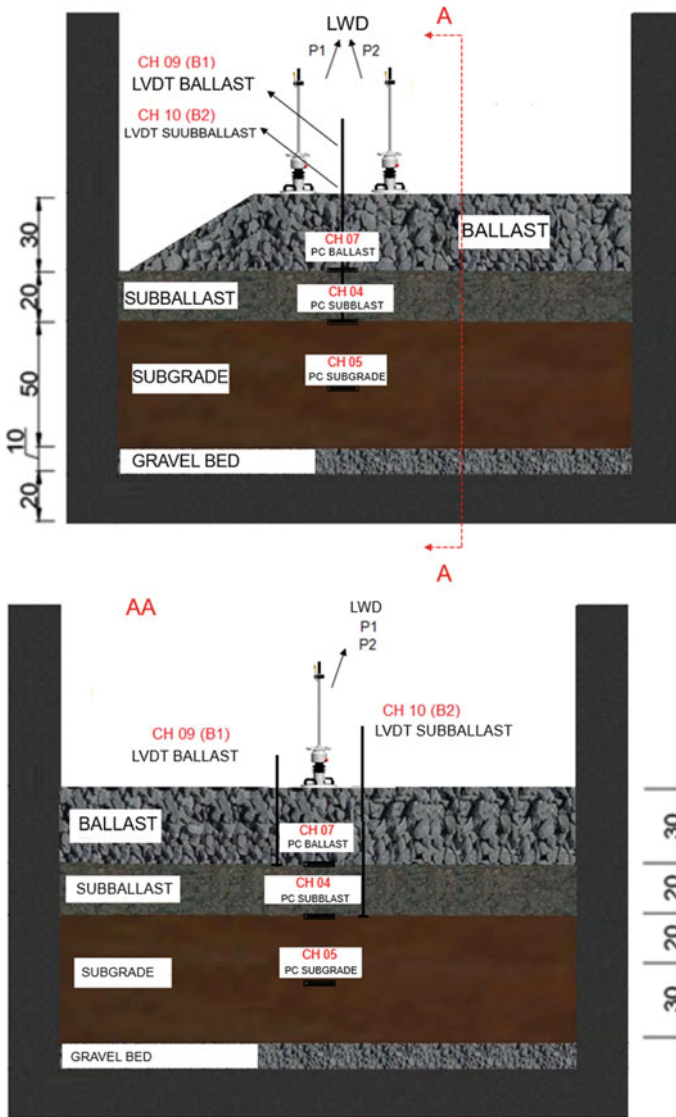


Fig. 2 Pressure cells, LVDT sensors and LWD test placement (P1 and P2)

allowing the measurement of the bearing capacity through the dynamic deformation module and sub-grid deflection unbound layers. The maximum drop force is 10,6 kN, pulse duration $17 \text{ ms} \pm 1,5 \text{ ms}$, and the maximum soil pressure 150 kPa [22].

It is a portable device and easily transported to a construction site. It provides a simple and cost effective response over other static plate load tests, which also

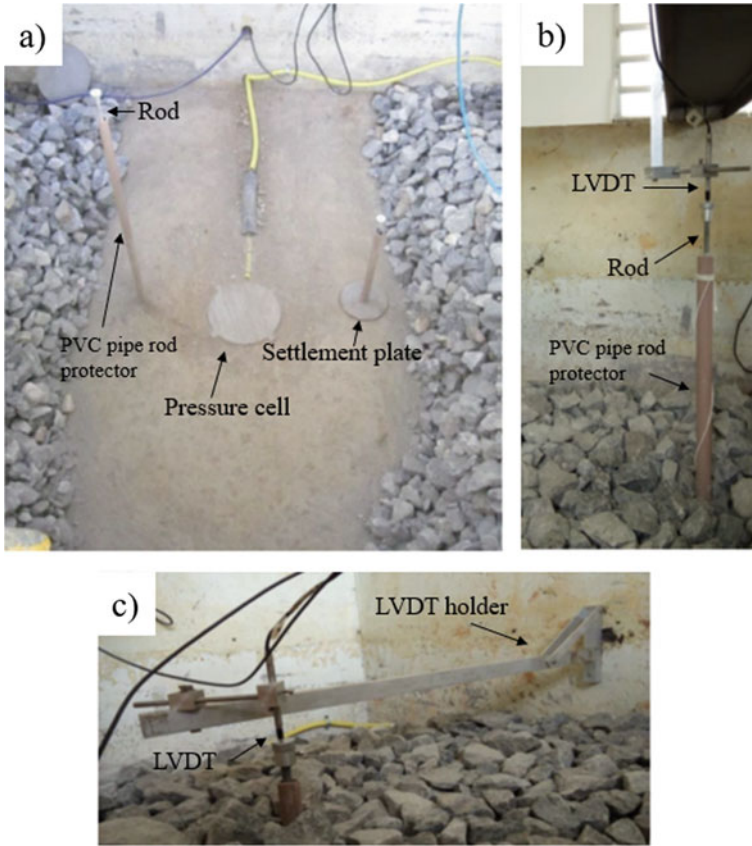


Fig. 3 Instrumentation detail. **a** Pressure cell and LVDT sensor settling plate. **b** and **c** LVDT support attachment

requires much longer response times. The main parameters provided by the equipment are the dynamic deformation modulus (E_{VD} or E_{LWD}) in MPa, the deflection (S_m) in mm and the compaction degree of the layer (s/v), in ms, which is the ratio of average deflection (s) and the average velocity for the last three impacts (v). All these properties are obtained through averaging three drop readings.

Testing three different brand LWD devices [23] showed a strong correlation between the modulus values measured in the static plate loading test with the values measured by the LWDs with R values of 0.88, 0.99, and 0.97 for Dynatest, Zorn, and Olson LWD, respectively. So, the LWD test come as a better solution, once PLT is expensive, time consuming, requires heavy equipment and in some cases it is very difficult to perform, particularly when the track to be characterized is part of a line in operation [24].

Fig. 4 LWD tests being performed on large scale model



2.5 Test Description

For evaluation of the LWD test on a railway pavement, 6 LWD tests were performed in the large scale physical model. The railway pavement was formed by a 50 cm subgrade layer of soil, 20 cm of subballast and 30 cm of ballast.

The LWD tests were performed on the ballast layer, as shown in Fig. 4. In order to obtain the layer deflections, the LVDT sensors monitored the subgrade and subballast layers, and the ballast layer through results of LWD equipment itself. The instrumentation and test positions (P1 and P2) are shown in Fig. 2, with 3 tests being performed in each position. The measuring procedure starts with three pre-loading drops for good contact with the ground, comprising a conditioning phase of the test. Then, three drops are executed for registration and calculation of the average value and dynamic deformation modulus E_{VD} and surface deflection.

3 Results and Discussion

The LWD tests results are show in Table 2. The average deflection of the surface of the ballast layer, indicated by the LWD device, was 0.558 mm. The average compaction degree measurement (s/v) was 2.64 ms and the average deformation modulus (E_{VD}) was 61.2 MPa.

Table 2 Light weight deflectometer test results

ID	E_{VD} (MPa)	s/v (ms)	S_m (mm)
P1 ballast test 1	58.45	2.881	0.602
P1 ballast test 2	60.86	2.554	0.553
P1 ballast test 3	62.87	2.352	0.535
P2 ballast test 1	60.85	2.785	0.552
P2 ballast test 2	62.43	2.869	0.548
P2 ballast test 3	61.67	2.384	0.562

Although the slight difference between s/v from P1 (2.596 average) and P2 (2.679 average), it can be seen that P1 tests near the shoulder indicated it was not as well compacted as P2. This can be compared with field behavior, when slopes are not as well compacted as the center of embankments, and verified with the dynamic deformation modulus with a higher value in average for P2 than P1. According to ZORN, 2011 for s/v lower than 3.5 ms, the layer is well compacted, for s/v higher than 3.5 ms, further compaction possible needed. The value of 3.5 ms is an empirical value, resulting from practical experience.

E_{VD} is the dynamic deformation modulus, and the most accurate means for judging deformation of a layer and, thus, a material's level of compaction. E_{VD} is used to measure bearing capacity and compaction quality of subgrade and granular layers.

Table 3 shows the average pressures from pressure cells. Table 4 shows the displacement results from LVDT sensors.

On average the pressure cells recorded a stress of 12.5 kPa for tests performed in position P1, showed in Fig. 5 and Table 3, and 10.3 kPa at P2, in between the ballast and the subballast (CH07). In between the subgrade and subgrade (CH 04) an average record of 2.2 kPa at P1 and 1.9 at P2. Within the subgrade layer (CH 05) it was recorded an average of 0.4 kPa at P1 and 0.3 kPa. The highest stresses values in the P1 position are explained by the confining lack effect, once it is closer from the shoulder of the simulated platform. Being P2 a more confined placement, the stress dissipation happens in more effectively way. Regarding the displacements, the same behavior can be noticed. A higher displacement at P1 position were to be expected,

Table 3 Average results of pressure cell instrumentation

ID	Stresses (kPa) P1	Stresses (kPa) P2
CH7	12.5	10.3
CH4	2.2	1.9
CH5	0.4	0.3

Table 4 LVDT sensors average displacements results

ID	Displacement (mm) P1	Displacement (mm) P2
CH9	0.0433	0.028
CH10	0.0144	0.009

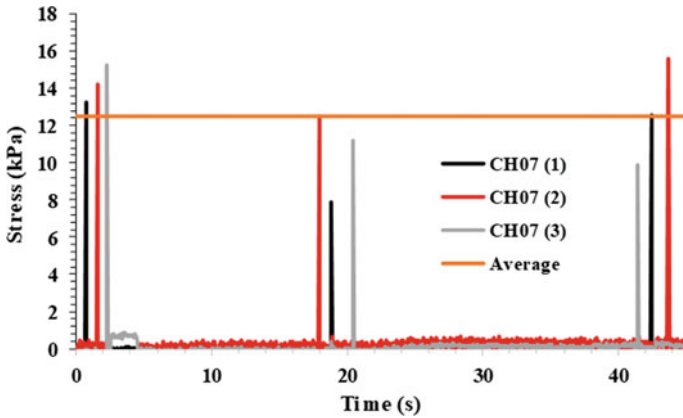


Fig. 5 Stresses during three drop loading of the LWD test at P1

since it is closer to the slope of the ballast shoulder, where confining stresses are lower. Thus the vertical stresses are to be also higher.

It was observed a stress dissipation at P1 of 92 and 93.13% at P2 through the 30 cm ballast layer, once the drop load of the LWD test induces a 150 kPa stress on the ballast surface.

Figure 5 shows the stress variation at the top of subballast layer (CH07) for the three drops of three LWD tests in P1. The black, red and silver curves show a set of three drops tests. At around 2.5 s in the test set 3 (silver), a noise at pressure reading can be seen, but nothing to consider or affect the results. The hammer drop works manually, and it was tried to perform the same interval of time between each drop, for the three tests, as seen in Fig. 5.

Figure 6 shows in detail the stress variation measured in each pressure cell of the pavement during a load application of the LWD test (zoomed view of the first drop of the black stress variation curve, from Fig. 5).

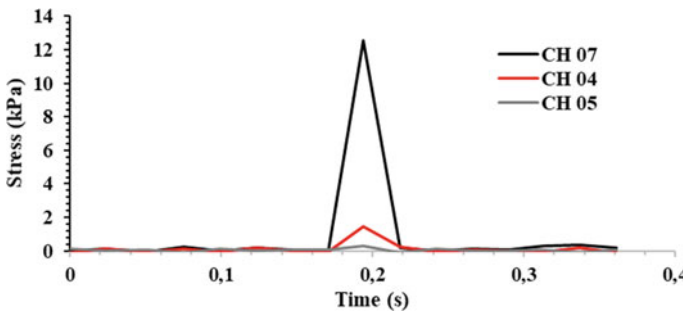


Fig. 6 Stresses during a drop loading of the LWD test at P1

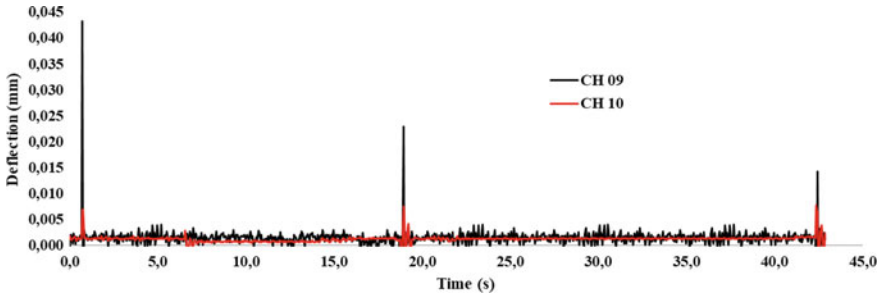


Fig. 7 Displacements during a three loadings of the LWD test at P1

During the first tests at each point, a non-elastic deflection was noticed, representing the special displacement of the ballast aggregates due to the applied load. It can be verified in the s/v values (measure of the degree of compaction of the layer), that it was higher for the first tests, meaning the last tests of each point had better compaction, due to the repetition of the test. It happens eventhough there are three drops of conditioning prior the test performance starts. Fleming et al. [20] discussed LWD tests on surfaces of granular material, such as ballast layers, that there may be an influence in stress dissipation due to the non-uniformity of plate contact with the surface. The fully elastic behavior, verified in the Fig. 7, indicates the deflection after the first test (three drops) causing the deflection measured by the settlement plate between ballast e subblast (CH09).

4 Conclusions

The stress caused by the load falling could be recorded significantly only in pressure cells CH 7 and CH 4, as shown in Fig. 6. The pressure cell CH 5, which is located within the subgrade layer and had an insignificant stress variation during the tests conducted. It represents that the influence depth of the LWD test on the ballast layer (30 cm), also was recorded in the subballast layer (20 cm), and ending close to the 20 cm of the subgrade layer, totaling approximately 650 to 700 mm from the top of the ballast, where the drop loads were performed. Therefore, the influence depth is approximately $2.3 \times$ plate diameter for that layer configuration and those materials, since the influence depth depends on the stiffness of the layers.

The pavement deflection on the top of ballast layer following the LWD device was 0.558 mm, on the top of subballast layer following the LVDT sensor CH09 data was in average 0.035 mm, and on the top of the subgrade layer following the LVDT sensor CH10 measurement was in average 0.012 mm. Those values represent the whole pavement deflection due to an applied LWD test load.

Acknowledgements The authors wish to thank COPPE/UFRJ for allowing and providing means for the use of the test tank in the Geotechnical/Pavements Laboratory. The authors also thank

Brazilian Federal Agency For Support And Evaluation of Graduate Education (CAPES) for the scholarship funding.

References

1. Lamas-Lopez, F, Cui YJ, Costa D'Aguiar S, Calon N (2016) Geotechnical auscultation of a french conventional railway track-bed for maintenance purposes. *Soils Found* 56(2):240–50
2. Elhakim AF, Elbaz K, Amer MI (2014) The use of light weight deflectometer for in situ evaluation of sand degree of compaction. *HBRC J* 10(3):298–307
3. Staatsministerium, Bayerischen (2016) Dynamic plate-load testing with the aid of the light drop-weight tester. TP BF-StB Part B 8.3
4. Shafiee M, Nassiri S, Khan RH, Bayat A (2011) Evaluation of new technologies for quality control/quality assurance of subgrade and unbound pavement layer moduli. Report for centre of transportation engineering and planning (C-TEP), University of Alberta
5. Tompai Z (2008) Conversion between static and dynamic load bearing capacity moduli and introduction of dynamic target values. *Period Polytech Civil Eng* 52:97–102
6. Woodward PK, Kennedy J, Laghrouche O, Connolly DP, Medero G (2014) Study of railway track stiffness modification by polyurethane reinforcement of the ballast. *Transp Geotech* 1:214–224
7. Selig ET, Waters JM (1994) Track geotechnology and substructure management. Thomas Telford Services Ltd.
8. Stamp DH, Mooney MA (2013) Influence of lightweight deflectometer characteristics on deflection measurement. *Geotech Test J* 36(2):216–226
9. Nazzal MD, Abu-Farsakh MY, Alshibli K, Mohammad L (2007) Evaluating the light falling weight deflectometer device for in situ measurement of elastic modulus of pavement layers. *Trans Res Rec* 1
10. Fleming PR, Frost MW, Rogers CDF (200) A comparison of devices for measuring stiffness in situ. In: *Proceedings of the unbound aggregates in road construction*, New York, NY, pp 193–200
11. Siekmeier JA, Young D, Beberg D (2000) Comparison of the dynamic cone penetrometer with other tests during subgrade and granular base characterization in minnesota. In: *Symposia nondestructive testing of pavements and backcalculation of moduli*, vol 3. Seattle, WA, pp 175–188
12. Nazzal M, Abu-Farsakh M, Alshibli K, Mohammad L (2004) Evaluating the potential use of a portable LFWD for characterizing pavement layers and subgrades. *Geotech Eng Trans Proj* 915–924
13. Tirado C, Mazari M, Carrasco C, Nazarian S (2015) Evaluating influence depth of light weight deflectometer through finite element modeling. In: *Airfield and highway pavements 2015*, ASCE, pp 789–800
14. Mooney MA, Miller PK (2009) Analysis of lightweight deflectometer test based on in situ stress and strain response. *J Geotech Geoenviron Eng Am Soc Civil Eng* 135(2):199–208
15. Silva CFSCE (2014) *Análise de Tensões em Pavimentos a Partir de Modelo Físico Instrumentado*. Masters Thesis, Federal University of Rio de Janeiro, RJ, Brazil
16. Rosa AF (2019) *Efeito Da Granulometria E Da Litologia No Comportamento De Lastros Ferroviários Em Laboratório E Por Análise Computacional*. Masters Thesis, Federal University of Rio de Janeiro, RJ, Brazil
17. Silva B-H, DE AE (2009) *Análise Mecânica de um Pavimento Rodoviário Submetido à Oscilação do Lençol Freático Simulada em Modelo Físico de Verdadeira Grandeza*. PhD Thesis, Federal University of Rio de Janeiro, RJ, Brazil
18. Indraratna B, Salim W, Rujikiatkamjorn C (2011) *Advanced rail geotechnology–ballasted track*. Taylor & Francis Group, p 413

19. GEOKON Instruction Manual (2017) Model 3500 series—earth pressure cells. Geokon
20. Fleming PR, Frost MW, Lambert JP (2007) Review of lightweight deflectometer for routine in situ assessment of pavement material stiffness
21. Livneh M, Goldberg Y (2001) Quality assessment during road formation and foundation construction: use of falling-weight deflectometer and light drop weight. *Trans Res Rec* 69–77
22. Zorn Instruments (2011) User manual for the light weight deflectometer (LWD). ZFG 3.0, Hansestadt Stendal, Germany
23. Khosravifar S (2015) Large-scale controlled-condition experiment to evaluate light weight deflectometers for modulus determination and compaction quality assurance of unbound pavement materials, PhD Thesis, University of Maryland, College Park
24. Fortunato E, Pinelo A, Fernandes MM (2009) In situ characterization of an old railway platform with DCP. In: *Proceedings of the 17th international conference on soil mechanics and geotechnical engineering*

Verification of the Structural Design Parameters for Unbound Layers of Finnish Road Structures



Antti Kalliainen and Pauli Kolisoja 

Abstract Approaches used for the structural design of road pavements are most often combinations of mechanistic and empirical elements, the latter ones of which take care of adaptation to the local ambient conditions and available construction materials. In Finland, the standard design approach is to use so called Oedemark's bearing capacity concept, in which the overall stiffness of a road structure is designed to meet a target value set based on the number of equivalent standard axle loads (ESALs) during an expected service life period. In the meantime, the stiffness value for each structural layer material is estimated based on its granularity and location in road structure, including, thus, at least to some extent indirectly also the stress conditions under which each material is exposed to during a heavy vehicle loading. However, when the design stiffness values are compared to those determined based on back-calculated response measurement values from two extensively instrumented road sections using a 3D finite element model, it is evident that the standard design stiffness values for unbound layer materials are far too low for describing the true mechanical responses of the instrumented road sections. Therefore, they cannot be applied as such in any purely mechanistic pavement performance analyses and related service life estimates. More realistic values for structural design parameters are suggested in this paper.

Keywords Stiffness value · Unbound material · Structural design

1 Introduction

Due to severe climate conditions prevailing in the Nordic countries like Finland, design against the action of seasonal frost is one of the most decisive aspects in the structural design of roads especially with regard to the overall thickness of road embankments [1]. Because the structural layers must be built fairly thick due to frost action in any case and good quality crushed rock aggregates are abundantly

A. Kalliainen · P. Kolisoja (✉)
Tampere University, P. O. Box 600, 33014 Tampere University Tampere, Finland
e-mail: pauli.kolisoja@tuni.fi

available almost all across the country, it is quite logical that unbound structural layers have an important role in providing the bearing capacity of road structures as well. Correspondingly, the thickness of bound layers is typically rather low, which further emphasizes the importance of unbound aggregate layers and, thus, the correctness of their material parameters in the mechanistic design of road structures.

In 2017, Finnish Transport Infrastructure Agency (FTIA) launched an open testing ecosystem of intelligent transport and infrastructure solutions, Aurora. The Aurora test area consists of about 10 km section of main highway E8 South from the village of Muonio in the Western part of Finnish Lapland. Regarding the road infrastructure, a key element of the testing ecosystem consists of two extensively instrumented road sections, one of which is located on stiff subgrade soil area and the other one on a somewhat softer subgrade soil. In this research, results obtained from the Aurora instrumentation sites are utilized in the verification of mechanical modelling parameters describing the true behaviour of these two main road sections under the loading effect of a nine-axle heavy truck weighing 740 kN. In the mechanical modelling of road structures, PLAXIS 3D finite element software tool was used.

2 Aurora Instrumentation Sites

2.1 Description of the Monitoring Sites

The installed structural monitoring systems utilized in this study include two road sections, Aurora 1 and 2, both located on the main road E8 about 4 km south from the municipality centre of Muonio.

On the Aurora 1 test site, the thickness of structural layers is about 1.1 m. The substructure of the Aurora 1 site is stiff, and it consists mainly of dense moraine with a number of stones and boulders. Before the structural instrumentations were installed, existing asphalt concrete (AC) layer was removed from the site. After the instrumentation, the site was overlain with about 120 mm of new AC material that was installed in two layers.

On the Aurora 2 test site, the overall thickness of unbound structural layers resting on top of a sandy embankment is about 1.5 m. Together with the sandy subgrade, it constitutes a substructure with markedly lower stiffness than that of the Aurora 1 test site. In terms of base curvature index, BCI, i.e. the difference in road surface deflections at the distances of 900 mm and 1200 mm from the centre of the falling weight deflectometer (FWD) loading plate, the determined values after the installation of measuring instruments were 19 for the Aurora 1 test site and 34 for the Aurora 2 test site, respectively (Table 1). In connection with the renovation works carried out on the Aurora 2 test site area in 2017, the old AC layer of about 70 mm thick was mix-milled with the existing unbound base course layer made of crushed rock. Finally, the road structure was overlain by 90 mm of new AC installed in two layers.

Table 1 Averaged FWD results on Aurora test sites after the installation of measurement instruments and the completion of rehabilitation works

D0	D200	D300	D450	D600	D900	D1200	SCI	BCI
<i>Aurora 1 test site</i>								
FWD averaged	378	265	210	149	111	65	46	113 19
<i>Aurora 2 test site</i>								
FWD averaged	543	418	355	279	229	158	124	125 34

2.2 Instrumentation for Structural Response Measurements

Both the Aurora 1 and 2 test sites are furnished with almost identical structural instrumentation systems, a schematic picture of which is shown in Fig. 1. The instrumentations consist of the following instrument types and the numbers of installed instruments given in parentheses for the Aurora 1 and Aurora 2 test sites, respectively, e.g. no displacement transducers were installed at Aurora 1 and three of them at Aurora 2:

- Displacement transducers monitoring the road surface deflection, RSDEF (0 + 3)
- Acceleration transducers monitoring the road surface deflection, RSACC (20 + 20)
- Horizontal strain transducers at the base of lower AC layer, ACSTR (5 + 6)
- Vertical pressure cells at two levels in unbound base course layer, BCPRE (8 + 8)
- Vertical strain transducers in the unbound base course layer, BCSTR (4 + 4)
- Percostation measurement probes monitoring dielectric value, electrical conductivity and temperature, PERCO (10 + 10).

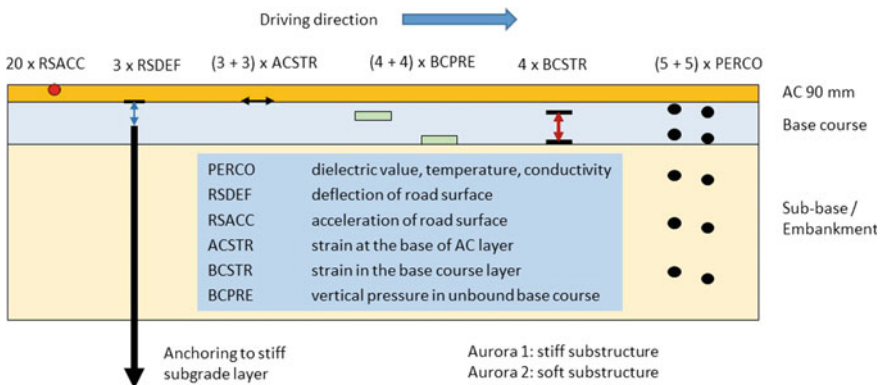


Fig. 1 Schematic picture of structural instrumentations at the Aurora 1 and 2 test sites

All the structural monitoring instruments on both sites have been installed under the outer wheel path of the lane from North to South. Parallel instruments are installed at a spacing of 150–200 mm in cross-sectional direction of road to enable a more complete picture of the 3D distribution of structural responses caused by vehicle overpasses to be obtained. The only exception is acceleration transducers that have been installed in two rows with an instrument to instrument spacing of only 100 mm.

2.3 Other Installed Instruments

In addition to the instrumentation for structural response measurements, both Aurora 1 and 2 sites have altogether 10 Percostation[®] probes monitoring changes in dielectric value, electrical conductivity and temperature at different depths varying from 0.15 to 1.10 m below the road surface. Meantime, on top of the road vehicle speed, dimensions and wheel path are monitored using a laser scanner, and at Aurora 2 site, the temperature of road surface is recorded using a thermal camera. A more detail description of these instrumentations as well as data acquisition systems used on the sites have been given earlier together with examples of the acquired monitoring results [2, 3].

3 Bearing Capacity Analysis

After the installation of measuring instruments and the completion of road rehabilitation works, the first step in the structural analysis of Aurora test sites was to perform a series of FWD measurements. The measurements were done on five parallel lines as follows:

- the outer wheel paths in both travel directions.
- the centerline of traffic lanes in both travel directions.
- the centerline of the road.

Altogether 75 FWD tests, 15 on each measurement line, were carried out on both Aurora test sites with a measurement point spacing of 2 m. The averaged results of all these measurements are summarized in Table 1.

The averaged deflection bowls of both Aurora test sites were used as a reference to back calculate the material parameters for unbound structural layers. The back calculation was performed with two different methods and software programs. The first software used in determining the stiffnesses of road structural layer materials was BISAR-PC provided by the oil company Shell [4]. BISAR uses a multi-layer linear elastic modelling approach. The program assumes the layers to be infinite in horizontal direction and to have a constant stiffness. In order to improve the analysis, the layer thicknesses were limited to a maximum of 0.3 m in the calculations performed in this study.

The size of loading plate (300 mm diameter) and loading intensity (707 kPa) of FWD measurements was replicated on top of the model. The stiffnesses of unbound structural layers were iterated to match the measured deflection bowls. In the last phase of analysis, the resilient moduli of unbound structural layers were calculated based on the simulated stress state in the middle of each unbound layer using the so called $k - \theta$ [5] and Uzan models [6] as shown in Eqs. 1 and 2, respectively.

$$M_r = K_1 \theta_0 \left(\frac{\theta}{\theta_0} \right)^{K_2} \tag{1}$$

where M_r is resilient modulus; K_1 is modulus number; K_2 is stress exponent; θ is sum of principal stresses and θ_0 is a reference stress, 100 kPa.

$$M_r = k_1 \theta_0 \left(\frac{\theta}{\theta_0} \right)^{k_2} \left(\frac{q}{\theta_0} \right)^{k_3} \tag{2}$$

where q is deviatoric stress; k_1 , k_2 and k_3 are model parameters.

Similar determination of unbound structural layer stiffnesses was also performed using finite element method and PLAXIS 3D software. FWD loading was applied on top of 3D structural model presented in Chap. 4. The results of parameter determination for the Aurora 1 test site are shown in Table 2. The k -values used in the analysis represent typical values obtained for Finnish unbound road construction materials, when they have been tested in large-scale repeated loading triaxial test facility as reported by Kolisoja [7].

Table 2 Resilient modulus values determined for the Aurora 1 test site

Layer	FEM analysis				BISAR analysis			
	<i>Kθ-model</i>							
	K_1	K_2	θ	M_r	K_1	K_2	θ	M_r
Base course	2500	0.5	296.1	430	2500	0.5	273.3	413
Subbase	2500	0.5	101.8	252	2500	0.5	103.1	254
Road structure	2500	0.5	66.3	204	2500	0.5	54.6	185
	<i>Uzan model</i>							
	k_1	k_2	k_3	M_r	k_1	k_2	k_3	M_r
Base course	2500	0.7	-0.2	545	2500	0.7	-0.2	504
Subbase	2500	0.7	-0.2	336	2500	0.7	-0.2	334
Road structure	2500	0.7	-0.2	272	2500	0.7	-0.2	228

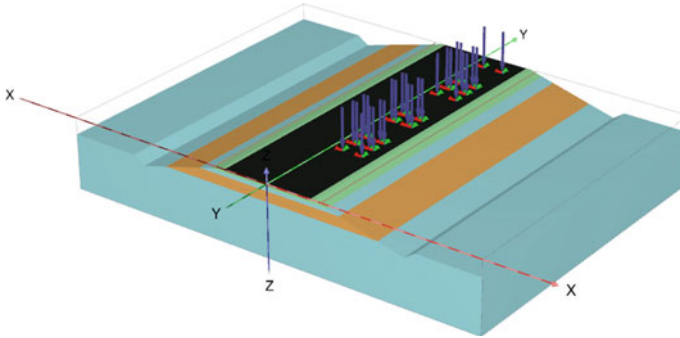


Fig. 2 Structural model used for 3D FEM simulations in this study

4 Structural Model

4.1 Finite Element Model Features

Figure 2 illustrates the basic idea of the finite element model used in this study. A 35 m long section with identical cross-section was used for both of the instrumented test sites. The tire contact areas of a nine axle, 740 kN vehicle were modelled as area loads having a constant intensity. The intensity of tire load was equal to the assumed tire inflation pressure (850 kPa), and the contact area for each tire was back calculated from the tire widths and measured axle loads. All single wheels of the loading vehicle were of the type 385/60 R22.5 and all the dual wheels of the type 315/80 R22.5.

PLAXIS 3D uses 10-node tetrahedral elements for volume elements (e.g. soil layers) and 6-node plate elements. User can define the refinement for elements and the program calculates a target element size based on outer model geometry dimensions. In addition, user can influence meshing procedure by defining a relative element size factor, polyline angle tolerance and surface angle tolerance [8]. In this project, the finest mesh of automatic meshing procedure was used, i.e. target element size was 0.5, polyline tolerance angle was 30° and surface angle tolerance 15° , respectively.

4.2 Material Models Used

Several different material models are included in PLAXIS 3D software. The material models used in this study are shortly described hereafter. The hardening soil model (HS) is an advanced model for the simulation of soil behaviour. Limiting states of stresses are described by means of the friction angle, φ , the cohesion, c , and the dilatancy angle, ψ . Soil stiffness is described by using three different input stiffnesses: the triaxial loading stiffness, E_{50} , the triaxial unloading stiffness, E_{ur} , and the

Table 3 HS-model parameters used in simulations

Structural layer	E_{50} (MPa)	E_{oed} (MPa)	E_{ur} (MPa)	m (-)	c (kPa)	ϕ (°)	ψ (°)	K_0 (-)	ν_{ur} (-)
Base course	500	500	1000	0.5	20	50	20	0.33	0.2
Subbase	350	350	700	0.5	10	45	15	0.33	0.2
Road structure	250	250	500	0.5	5	45	15	0.33	0.2

Table 4 LE-model parameters used in simulations

Layer	E (MPa)	ν (-)
AC layer, +40 °C	1500	0.35
AC layer, 0 °C	10,000	0.35
Subgrade, Aurora 1 test site	125	0.35
Subgrade, Aurora 2 test site	100	0.35

oedometer loading stiffness, E_{oed} . All these stiffnesses relate to a reference stress, 100 kPa in this study.

The HS model was chosen for unbound structural layers since the yield surface is not fixed but can expand due to plastic straining. The material parameters used in simulations are summarized in Table 3. They have been derived based on a number of laboratory tests carried out with similar materials and the back calculation of site specific FWD results obtained from Aurora test sites.

The hardening rules can be divided into two main types of hardening, namely shear and compression hardening. Shear hardening is used to model plastic strains due to primary deviatoric loading. Compression hardening is used to model irreversible strains in oedometric and isotropic loading. Therefore, the stiffnesses of aggregate layers are more appropriate on both sides of the yield surface, i.e. when subjected to deviatoric loading, the soil stiffness decreases simultaneously with the development of irreversible strains.

The linear elastic model (LE) was chosen for asphalt concrete (AC) and subgrade. Linear elasticity for subgrade was considered suitable since the modelled loading scheme is momentary, and the stiffness of subgrade determines the amount of deflection. The AC layer was also assumed to behave in linear range during a short-term loading. The moduli values used for LE layers are shown in Table 4.

5 Comparison of Modelled and Measured Responses

In order to obtain reliable data under heavy truck loading, two specific loading test series were performed at Aurora test sites. The first loading test was carried out in July (test I) when pavement temperature varied between +37 and +45 °C. During

the second loading test, pavement temperature was practically 0 °C (test II). Figure 3 indicates the measured and modelled values of road surface deflection at the Aurora 2 test site during loading test I. In all of the figures from Figs. 3, 4, 5, 6, 7 and 8 the charts have been arranged as follows:

- Modelled results are indicated using a blue or red dotted line
- Peak values measured with different parallel transducers are shown using separate dots with different transducer specific colours
- Upper left chart corresponds to a 85 kN single wheel axle
- Upper right chart corresponds to a 74 kN single wheel axle
- Lower left chart corresponds to a 113 kN dual wheel axle
- Lower right chart corresponds to a 78 kN dual wheel axle.

In general, the modelling results correspond well with the measured results under a dual wheel axle. In the case of single wheels, however, the measured peak values are somewhat higher. This might be due to the lack of exact tire inflation pressure information. Since the simulation series carried out in this study was a preliminary one, the effect of tire inflation pressure was not studied in detail.

Similar results were obtained when analysing the vertical pressures in the upper part of base course layer. During loading test I, the measured peak values under single wheel loads were again higher than the modelled ones at both Aurora test sites. The respective results of vertical pressures are illustrated in Figs. 4 and 5.

One more interesting example of modelling results is shown in Fig. 6. The only distinction in the FEM simulations between test I (Fig. 4) and test II (Fig. 6) was the

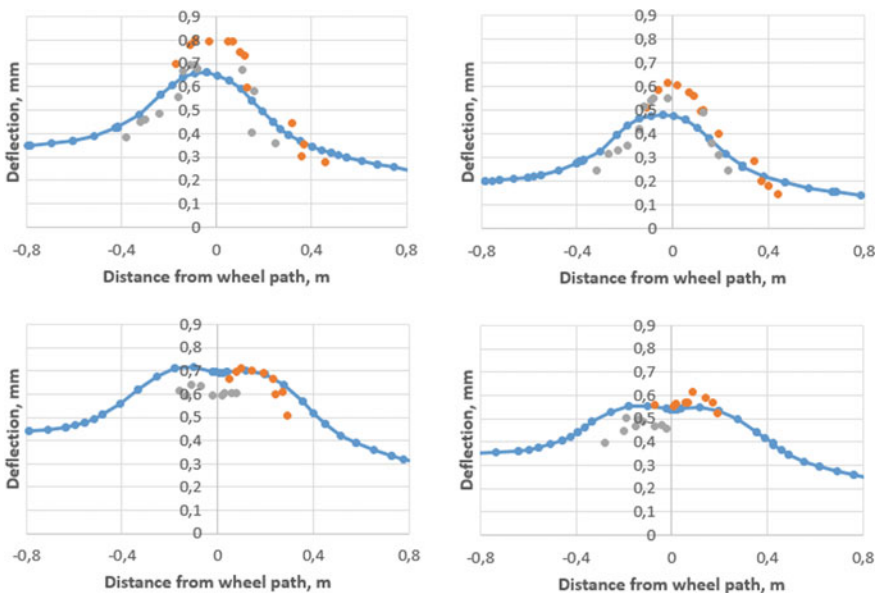


Fig. 3 Measured and modelled road surface deflections at the Aurora 2 test site in loading test I

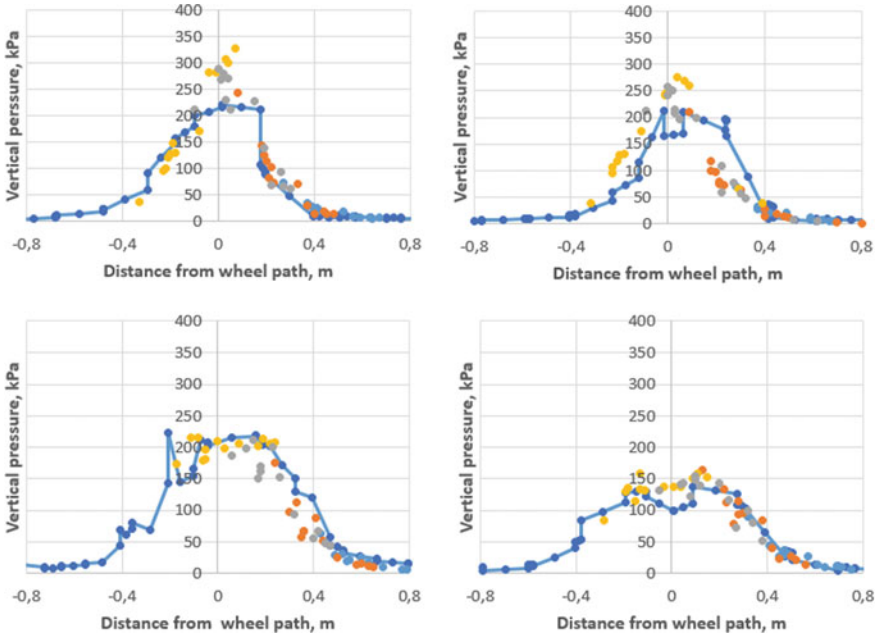


Fig. 4 Measured and modelled vertical pressures in the upper part of base course (180 mm depth) at the Aurora 1 test site in loading test I

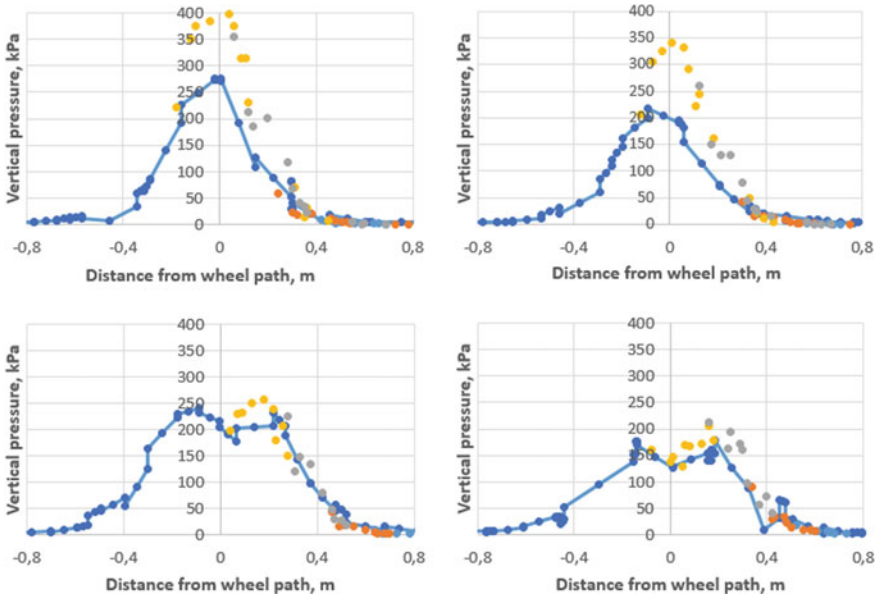


Fig. 5 Measured and modelled vertical pressures in the upper part of base course (220 mm depth) at the Aurora 2 test site in loading test I

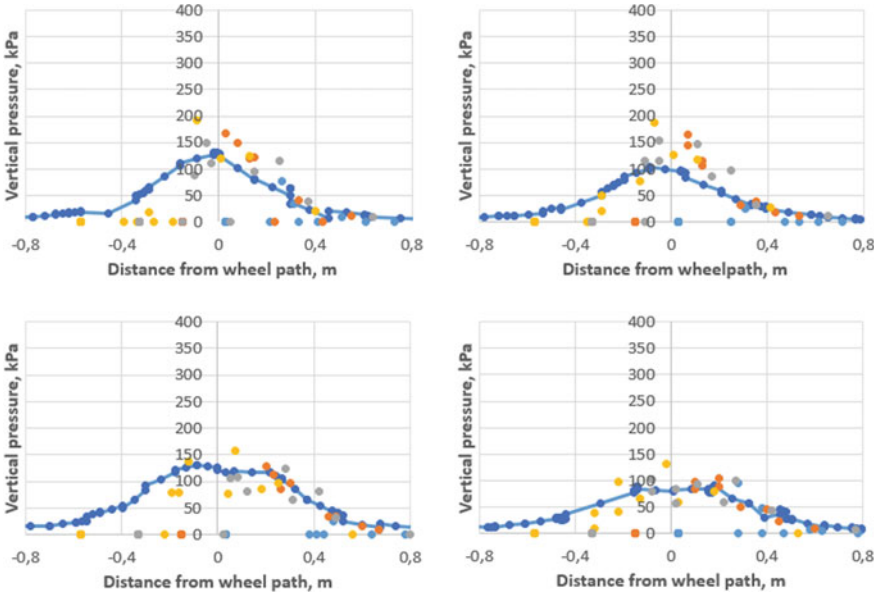


Fig. 6 Measured and modelled vertical pressures in the upper part of base course (180 mm depth) at the Aurora 1 test site in loading test II

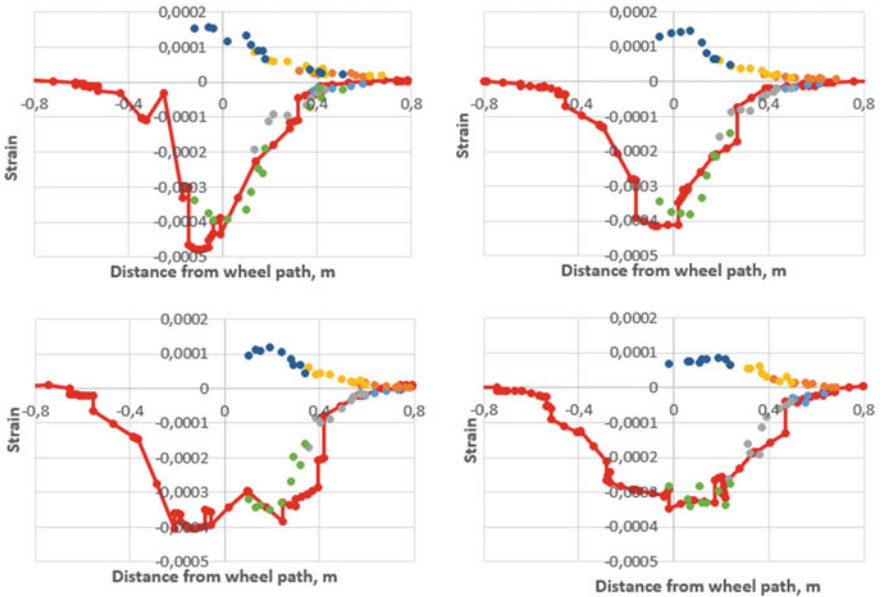


Fig. 7 Measured and modelled horizontal strains at the bottom of pavement layer in longitudinal direction at the Aurora 2 test site in loading test I

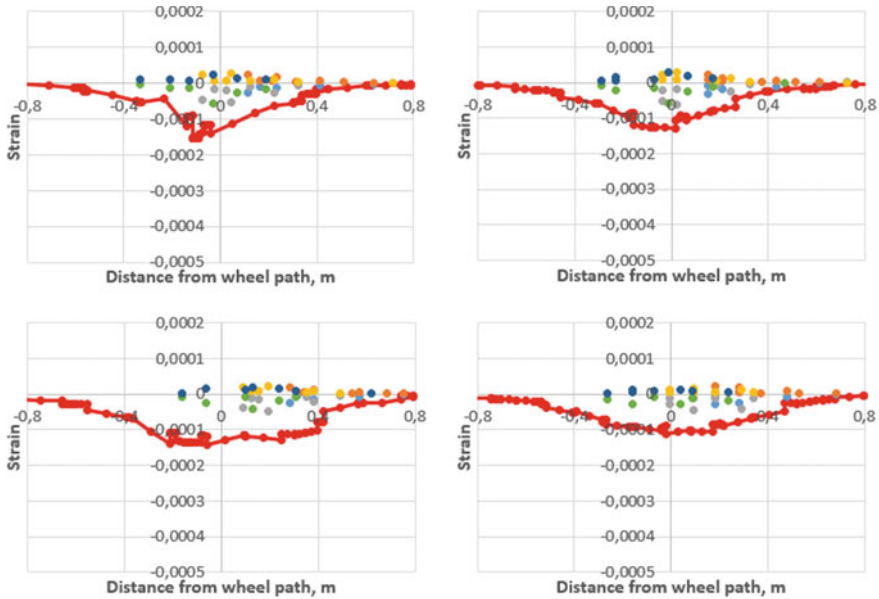


Fig. 8 Measured and modelled horizontal strains at the bottom of pavement layer in longitudinal direction at the Aurora 2 test site in loading test II

modulus value of AC layer. The temperature correction of AC layer stiffness appears to explain nicely the changes in the measured and modelled stress states.

Figures 7 and 8 illustrate the effect of pavement temperature on horizontal strains at the base of AC layer. The modelling results are somewhat scattered in comparison to the measured peak values, but the magnitude of modelled AC strains also appears to be correct, roughly from 300 to 500 microstrains, when AC temperature is close to +40 °C. During loading test II, temperature was so low that the measured responses may have been disturbed by partial freezing of the underlying base course layer (Fig. 8). In any case, the results indicate that more research would be needed to properly take into account the effects of pavement temperature and tire inflation pressure in the structural design of road structures. In Figs. 7 and 8, blue and yellow dots stand for the peak values of compressive AC strain preceding the approaching wheel load and are, therefore, not meaningful to compare with modelled strain values.

Altogether, the results obtained in this study strongly suggest that the design parameters for unbound structural layers in the current Finnish guidelines should be updated. Compared to the present design values, from 200 to 280 MPa depending on the base course aggregate grading [1], the modelling results suggest that the design stiffness values for unbound aggregates should be clearly higher.

6 Conclusions

The data obtained from the Aurora test sites is very valuable in enhancing the overall understanding on the load carrying capacity of road structures. Especially, this concerns road structures with relatively thin AC layer in which the role of unbound layers is pronounced.

The results obtained from these first modelling exercises clearly indicate that there is an obvious need to improve the current Finnish road dimensioning guidelines and to update respective design parameters. Two separate conclusions can be pointed out:

- The stiffness values of unbound layers should be increased in order to represent the actual responses under vehicle loading.
- The true behaviour of AC layer should be included into the dimensioning procedure. At a high temperature, both measured and modelled horizontal tensile strains at the bottom of AC layer clearly indicate that a life-cycle cost efficient design would require a more detailed dimensioning procedure for AC layers, especially in Finland, where AC layer thicknesses in general are rather thin.

Acknowledgements The authors gratefully thank the Finnish Transport Infrastructure Agency for funding this study and for providing the opportunity to gather exceptionally detailed data on the responses of road structures under heavy vehicle loading at the Aurora test sites.

References

1. Liikennevirasto (2018) Tierakenteen suunnittelu (Design of road structure) In Finnish. <https://www.doria.fi/handle/10024/164750>. Last accessed 11 Dec 2019
2. Kolisoja P, Vuorimies N, Kurki A, Saarenketo T (2019) Open structural monitoring data from two extensively instrumented road sections—case Aurora. In: Proceedings of the XVII ECSMGE, Reykjavik, p 8
3. Kolisoja P, Kurki A, Vuorimies N, Saarenketo T (2019) Integrated monitoring of seasonal variations and structural responses to enable intelligent asset management of road infrastructures. In: Proceedings of the 3rd ICITG Conference, Guimaraes, Portugal. Springer, pp 687–698
4. Shell (1995) BISAR-PC user manual. Version 1995, Release 2.0
5. Brown S, Pell P (1967) An experimental investigation of the stresses, strains and deflections in a layered pavement structure subjected to dynamic loads. In: Proceedings of 2nd international conference on structural design of asphalt pavements, Ann Arbor, USA, pp 487–504
6. Uzan J (1985) Characterization of Granular Materials. Transportation Research Record, No 1022, pp 52–59
7. Kolisoja P (1997) Resilient deformation characteristics of granular materials. Ph.D. Thesis, Laboratory of Foundations and Earth Structures, Tampere University of Technology, Tampere, Finland, p 188
8. Brinkreve R, Engin E, Swolfs W (2012) PLAXIS 3D 2012. User Manuals. Plaxis bv, The Netherlands

FreeHyTE: A Hybrid-Trefftz Finite Element Platform for Poroelastodynamic Problems



Natalia Climent, Ionut Moldovan, and António Gomes Correia

Abstract FreeHyTE is an open-source computational platform developed at the CERIS Research Centre, University of Lisbon. FreeHyTE employs hybrid-Trefftz finite elements, which are designed to avoid drawbacks of the conventional finite elements, such as the need of high mesh refinement under high frequency or short wavelength excitations. The key feature of the hybrid-Trefftz elements is that their approximation bases are problem-dependent and built using functions that satisfy exactly the homogeneous form of the differential equation governing the problem. FreeHyTE offers two modules for poroelastodynamic problems: The biphasic transient module and the triphasic transient module. In this paper, the theoretical background of the hybrid-Trefftz finite elements and their implementation in the FreeHyTE platform are presented, together with a simulation involving the propagation of a shock wave in a semi-infinite unsaturated medium to illustrate the different interfaces of the platform and some of its essential features.

Keywords Finite elements · Hybrid-Trefftz finite elements · Poroelastodynamics

1 Introduction

Numerical models open the possibility of better understanding the behavior of geomaterials under transient loading to improve the design of pavement and rail track infrastructures. However, the complex nature of geomaterials, the extremely small wavelength and the high frequency content of transient excitations hinder

N. Climent (✉) · I. Moldovan

CERIS, Instituto Superior Técnico, Universidade de Lisboa, Av. Rovisco Pais, 1049-001 Lisbon, Portugal

e-mail: natalia.climent@tecnico.ulisboa.pt

I. Moldovan

e-mail: dragos.moldovan@tecnico.ulisboa.pt

A. G. Correia

ISISE, Escola de Engenharia, Universidade do Minho, Azurem, 4800-058 Guimarães, Portugal

e-mail: agc@civil.uminho.pt

the solution of poroelastodynamic problems with conventional (conforming) finite elements.

Conversely, hybrid-Trefftz finite elements are designed to avoid these issues. The key feature of the hybrid-Trefftz elements is that their approximation bases are problem-dependent and built using functions that satisfy exactly the homogeneous form of the differential equation governing the problem. The physically meaningful information built into the finite element basis enhances its convergence and robustness as compared to conventional finite elements. For that reason, hybrid-Trefftz elements are less sensitive to gross mesh distortion and large wavelength variations [1].

Despite the advantages they offer over conventional elements, hybrid-Trefftz finite elements have only recently been included in public, user-friendly software. The computational platform FreeHyTE, presented at length in reference [2], offers hybrid-Trefftz finite elements for the solution of elliptic, parabolic, and hyperbolic boundary value problems, covering a wide range of physical problems. FreeHyTE is easy to use, as it features graphical user interfaces for the definition of the structure, as well as installation, user's and developer's manuals, and amenable to extension, as it includes a considerable breadth of standardized computational procedures and data structures, meaning that only formulation-specific coding needs to be performed.

The formulation and implementation of the hybrid-Trefftz finite elements included in two new FreeHyTE modules are presented in this paper. The elements are designed for the solution of poroelastodynamic problems defined on saturated (biphasic) and unsaturated (triphasic) porous media, with application to transportation infrastructure.

2 Hybrid-Trefftz Finite Elements for Poroelastodynamics

The concept that stands at the base of the Trefftz methods was suggested by Trefftz in 1926 [3] and the first application in the context of the finite element method was reported in 1973 [4]. In 1978, Jirousek presented four hybrid-Trefftz formulations generally applicable to solid mechanics problems [5]. Other significant contributions have been made after that by other authors, such as Herrera [6], Piltner [7], Qin [8] and Freitas [9], among many others.

The displacement model of the hybrid-Trefftz finite elements is used in this paper for the solution of transient problems involving wave propagation in saturated and unsaturated geomaterials. The model is based on the independent approximations of the (generalized) displacement fields in the domain of the element and traction and pore pressure fields on the boundaries where these quantities are unknown. The nodal values of the fields are not the main unknowns of the problem, as typical of conventional finite elements and the redefinition of the nodes does not call for any redefinition of the approximation functions.

The general expressions of the elastodynamic equations governing the elastic response of porous media are given in Sect. 2.1, followed by their adaptation to saturated and unsaturated materials in Sect. 2.2. The formulation of the Trefftz elements for each of these cases is given in Sect. 2.3.

2.1 Elastodynamic Problems

The porous material is considered (piecewise) homogeneous, and saturated by one or two immiscible fluids. It has a linearly elastic behavior, and displacements and deformations are considered small. Under these hypotheses, and after applying the weighted residual time discretization technique suggested in [10], the elastodynamic equations [11, 12] in a domain V can be expanded to a series of spectral Navier-type equations, defined by,

$$\mathcal{D}(\mathbf{k}\mathcal{D}^*\mathbf{u}(x, y)) + \omega^2\rho\mathbf{u}(x, y) = 0 \quad (1)$$

where $\mathbf{u}(x, y)$ is a vector listing the spectral components of the displacement in the solid and fluid phases, matrix ρ collects the material density and dissipation components, \mathbf{k} is the material stiffness matrix and ω is a generalized frequency, with complex values. \mathcal{D} and \mathcal{D}^* are the differential equilibrium operator and the differential compatibility operator, respectively, and they are adjoint in linear applications. The body forces are neglected because their presence does not change the wave propagation patterns. The initial conditions are considered null, which is probably true for most applications. It is noted that non-null body forces or initial conditions would render the Navier Eq (1) non-homogeneous. Constant body forces can be accounted for by the addition of an analytic particular solution to the Trefftz basis as, for instance, in reference [13]. However, no analytic particular solution can be found, in general, for non-null initial conditions. In this case, approximate particular solutions can be found as reported in references [14, 15].

The different types of boundaries that can be defined on a domain are: Dirichlet boundaries (Γ_u), where displacements are imposed, Neumann boundaries (Γ_σ), where tractions are imposed, absorbing boundaries (Γ_a), used to simulate semi-infinite domains by enforcing a non-reflection criterion [12], and Robin boundaries (Γ_R), which model flexible and impervious boundaries. The boundary conditions are described as

$$\mathbf{u}(x, y) = \mathbf{u}_\Gamma(x, y) \quad (\text{on } \Gamma_u) \quad (2)$$

$$\mathbf{N}\boldsymbol{\sigma}(x, y) = \mathbf{t}_\Gamma(x, y) \quad (\text{on } \Gamma_\sigma) \quad (3)$$

$$\mathbf{u}(x, y) = \mathbf{C}^{-1}\mathbf{t}(x, y) \quad (\text{on } \Gamma_a) \quad (4)$$

$$\mathbf{u}(x, y) + \mathbf{f}\mathbf{t}(x, y) = 0 \quad (\text{on } \Gamma_R) \quad (5)$$

where \mathbf{t}_Γ and \mathbf{u}_Γ represent the enforced boundary tractions and displacements, respectively, $\boldsymbol{\sigma}$ is a vector listing the independent components of the total stress and the pore pressures, \mathbf{t} are the tractions and the pore pressures on the boundaries and matrix \mathbf{N} collects the components of the outward normal to the Neumann boundary. Matrix \mathbf{f} collects the flexibility coefficients in the normal and tangential directions of the Robin boundary and \mathbf{C} is the absorbing boundary stiffness matrix. The quantities present in Eq (1)–(5) depend on the poroelastodynamic model adopted and are defined below.

2.2 Poroelastodynamic Models

The model adopted for biphasic (saturated) porous media is based on the Biot's theory [16]. The porous media is represented as an elastic solid phase fully permeated by a Darcy-compliant liquid phase. Both phases, solid and fluid, are assumed compressible. A solid displacement–fluid seepage ($\mathbf{u} - \mathbf{w}$) form is adopted for the Navier Eq (1). The stress vector $\boldsymbol{\sigma} = \{\sigma_{xx} \sigma_{yy} \sigma_{xy} \pi\}^T$ contains the components of the total stress tensor and the pore fluid pressure (π). The displacement vector $\mathbf{u} = \{u_x u_y w_x w_y\}^T$ collects the displacement components of the solid phase $\mathbf{u}^s = \{u_x u_y\}^T$ together with the fluid seepage components $\mathbf{w} = \{w_x w_y\}^T$. The generalized mass matrix $\boldsymbol{\rho}$ depends on the mass density of the mixture, the mass density of the fluid phase, and the dissipation. The stiffness matrix \mathbf{k} depends on the Lamé constants and the Biot coefficients. The exact expressions of those matrices and the differential operators \mathbf{D} and \mathbf{D}^* are further described in reference [12].

The absorbing boundary condition (4) relates the normal and tangential components of the displacement and traction fields

$$\begin{pmatrix} u_n \\ u_t \\ w_n \end{pmatrix} = \begin{pmatrix} C_{11} & 0 & C_{13} \\ 0 & C_{22} & 0 \\ C_{31} & 0 & C_{33} \end{pmatrix}^{-1} \begin{pmatrix} t_n \\ t_t \\ \pi \end{pmatrix} \quad (6)$$

where the components C_{ij} depend on the problem and are further described in [12].

Finally, boundary condition (5) relates the normal and tangential components of the displacement and traction fields

$$\begin{pmatrix} u_n \\ u_t \\ w_n \end{pmatrix} + \begin{pmatrix} f_n & 0 & 0 \\ 0 & f_t & 0 \\ 0 & 0 & 0 \end{pmatrix} \begin{pmatrix} t_n \\ t_t \\ \pi \end{pmatrix} = 0 \quad (7)$$

where f_n and f_t are the normal and the tangential flexibilities of the elastic boundary.

In triphasic (unsaturated) media, three immiscible phases are considered: the solid phase (S), the wetting fluid phase (W) and the non-wetting fluid phase (N) [17]. The mathematical model adopted for triphasic media is a linearized form of the theory of mixtures suggested in reference [18]. This theory includes the effect of the pore pressure gradients (macroscopic fluid flow) and neglects the effect of the capillary relaxation (microscopic fluid flow). The dynamic compatibility conditions on the interfaces between the three phases are taken into account.

The Navier Eq (1) also applies here. However, the vectors and matrices present in Eq (1)–(5) have different components than for the biphasic case. The stress vector lists the components of the total stress tensor and the pore pressure in each one of the two fluid phases, $\boldsymbol{\sigma} = \{\sigma_{xx} \sigma_{yy} \sigma_{xy} \pi^W \pi^N\}^T$. The displacement vector collects the displacement components in the solid phase and the fluid phases, $\mathbf{u} = \{u_x^S u_y^S u_x^W u_y^W u_x^N u_y^N\}^T$. The density matrix $\boldsymbol{\rho}$ and the stiffness matrix \mathbf{k} for triphasic media are fully described in reference [19].

Equation (4) relates the normal and tangential components of the displacement and traction fields on an absorbing boundary

$$\begin{pmatrix} u_n \\ u_t \\ w_n^W \\ w_n^N \end{pmatrix} = \begin{pmatrix} C_{11} & 0 & C_{13} & C_{14} \\ 0 & C_{22} & 0 & 0 \\ C_{31} & 0 & C_{33} & C_{34} \\ C_{41} & 0 & C_{43} & C_{44} \end{pmatrix}^{-1} \begin{pmatrix} t_n \\ t_t \\ \pi^W \\ \pi^N \end{pmatrix} \quad (8)$$

where the components C_{ij} of the absorbing boundary stiffness depend on the problem and are further described in reference [20].

Boundary condition (5) relates the normal and tangential components of the displacement and traction fields on a Robin boundary

$$\begin{pmatrix} u_n \\ u_t \\ w_n^W \\ w_n^N \end{pmatrix} + \begin{pmatrix} f_n & 0 & 0 & 0 \\ 0 & f_t & 0 & 0 \\ f_n & 0 & 0 & 0 \\ f_n & 0 & 0 & 0 \end{pmatrix} \begin{pmatrix} t_n \\ t_t \\ \pi^W \\ \pi^N \end{pmatrix} = 0 \quad (9)$$

where f_n and f_t are the normal and the tangential flexibility coefficients of the elastic boundary.

2.3 Hybrid-Trefftz Finite Element Model

Approximations of displacements and tractions

Equation (1) is solved using the displacement model of the hybrid-Trefftz finite element formulation. The domain is divided into finite elements and the (generalized) displacement field \mathbf{u} is approximated in each finite element. Considering one of

these elements V^e with boundary Γ^e , the generalized displacement field in V^e is approximated as

$$\mathbf{u} = \mathbf{U}\mathbf{X} \quad (10)$$

where matrix \mathbf{U} collects Trefftz-compliant approximation functions, as derived in the next section. The tractions in the solid phase and the pore pressures are approximated on all the boundaries of the element, except the Neumann boundaries where they are explicitly imposed. Interior boundaries (Γ_i^e) are defined as the boundaries of the element that are not exterior boundaries of the domain. Therefore, the tractions on the essential boundary $\Gamma_\varepsilon^e = \Gamma_u^e \cup \Gamma_a^e \cup \Gamma_R^e \cup \Gamma_i^e$ is approximated as

$$\mathbf{t} = \mathbf{Z}\mathbf{p} \quad (11)$$

where bases \mathbf{U} and \mathbf{Z} are independent of each other, constructed strictly hierarchically, and not linked to the nodes of the elements, and \mathbf{X} and \mathbf{p} are the weights of the approximation functions with no particular physical meaning.

Trefftz-compliant approximation functions

Shape functions in \mathbf{U} must satisfy the Navier Eq (1). After substituting Eq (10) in the Navier Eq (1), and writing the shape functions in \mathbf{U} as the sum of the irrotational and solenoidal components of some potentials functions ϕ_j [9], the Navier equation is reduced to a set of uncoupled Helmholtz equations,

$$\nabla^2 \phi_j + \beta_j^2 \phi_j = 0 \quad (12)$$

where ∇^2 is the Laplace operator. Wave numbers β_j , fully defined in reference [12] for biphasic media and in reference [21] for triphasic media, depend on the generalized frequency ω and material characteristics and $j = \{1, 2, 3\}$ for biphasic media or $j = \{1, 2, 3, 4\}$ for triphasic media. The solutions of the Helmholtz Eq. (12) in two dimensions using a polar referential (r, θ) , are of the type

$$\phi_j(r, \theta) = J_n(\beta_j r) \exp(\hat{i}n\theta) \quad (13)$$

where $J_n(\beta_j r)$ is the Bessel function of the first kind and integer order n . In biphasic media, the potential functions ϕ_j define two compression waves ($P1$ and $P2$) and one shear wave (S), and in triphasic media they define three compression waves ($P1$, $P2$ and $P3$) and one shear wave (S)

$$\mathbf{U}_{P,j}^S = \nabla \phi_{P,j} \quad (14)$$

$$\mathbf{U}_S^S = \tilde{\nabla} \phi_S \quad (15)$$

$$\mathbf{U}_{P,j}^{W,N} = \gamma_{P,j}^{W,N} \nabla \phi_{P,j} \quad (16)$$

$$\mathbf{U}_S^{W,N} = \gamma_S^{W,N} \tilde{\nabla} \phi_S \quad (17)$$

where $\mathbf{U}_{P,j}^S$ list the approximation functions of the displacements of the solid skeleton for the compression (P_j) waves; \mathbf{U}_S^S are the approximation functions of the displacements of the solid skeleton for the shear (S) wave; $\mathbf{U}_{P,j}^{W,N}$ corresponds to the displacements of the fluids (the unique fluid phase W in biphasic media, and the two fluid phases W and N in the triphasic media) for the compression (P_j) waves; and $\mathbf{U}_S^{W,N}$ corresponds to the displacements of the fluids for the shear wave. ∇ and $\tilde{\nabla}$ are the gradient and curl operators. The wave multipliers $\gamma_{P,j}^{W,N}$ and $\gamma_S^{W,N}$ are described in reference [12] for biphasic media and in reference [21] for triphasic media.

Hybrid-Trefftz finite element formulation

Enforcing weakly Eq (1) in the domain of the element and Eq (2) on its Dirichlet boundaries yields,

$$\int \hat{\mathbf{U}}^T (\mathcal{D}(k\mathcal{D}^* \mathbf{u}) + \omega^2 \rho \mathbf{u}) dV^e = 0 \quad (18)$$

$$\int \hat{\mathbf{Z}}^T (\mathbf{u} - \mathbf{u}_\Gamma) d\Gamma_u^e = 0 \quad (19)$$

where the $\hat{\mathbf{U}}^T$ and $\hat{\mathbf{Z}}^T$ are the transposed conjugates of \mathbf{U} and \mathbf{Z} . Finally, integrating by parts Eq (18) and substituting Eqs (10) and (11), the problem is reduced to solving the algebraic system [9, 12]

$$\begin{pmatrix} \mathbf{D} & -\mathbf{B} \\ -\hat{\mathbf{B}}^T & \mathbf{D}_a/\mathbf{D}_r \end{pmatrix} \begin{pmatrix} \mathbf{X} \\ \mathbf{p} \end{pmatrix} = \begin{pmatrix} \mathbf{f}_t \\ -\mathbf{q}_u \end{pmatrix} \quad (20)$$

$$\mathbf{D} = \int \hat{\mathbf{U}}^T \mathbf{N} \mathbf{S} d\Gamma^e \quad (21)$$

$$\mathbf{D}_a = \int \mathbf{Z}^T \mathbf{C}^{-1} \mathbf{Z} d\Gamma_a^e \quad (22)$$

$$\mathbf{D}_r = - \int \mathbf{Z}^T \mathbf{f} \mathbf{Z} d\Gamma_R^e \quad (23)$$

$$\mathbf{B} = \int \hat{\mathbf{U}}^T \mathbf{Z} d\Gamma_{u,a}^e \quad (24)$$

$$\mathbf{f}_t = \int \hat{\mathbf{U}}^T \mathbf{t}_\Gamma d\Gamma_\sigma^e \quad (25)$$

$$\mathbf{q}_u = \int \hat{\mathbf{Z}}^T \mathbf{u}_\Gamma d\Gamma_u^e \quad (26)$$

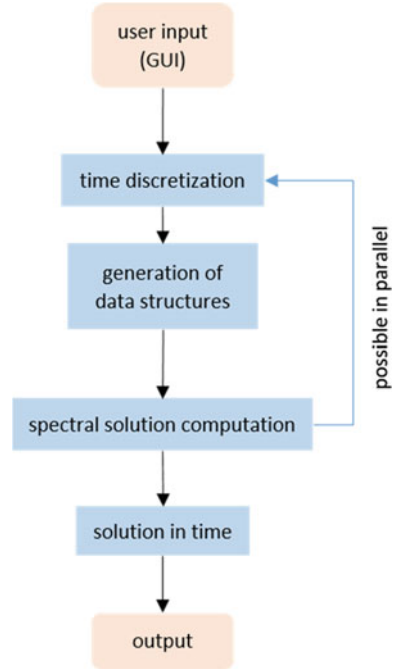
In-depth discussions of the formulation and implementation of hybrid-Trefftz finite elements for saturated and unsaturated porous media can be found in references [12, 21], respectively.

3 FreeHyTE: A Hybrid-Trefftz Finite Element Platform for Poroelastodynamic Problems

In this section, the FreeHyTE modules for the solution of poroelastodynamic problems are introduced. Further and more detailed information about the platform is available in reference [2].

The general structure of a FreeHyTE module is described in Fig. 1. The user input is the first step and consists in a sequence of graphical user interfaces (GUIs) where the problem and the solution parameters are defined. The most important steps of these sequences are presented below. After the user input, FreeHyTE performs the time discretization, reducing the original problem in time and space to a series of problems in space and generates the input data for each of those problems. Each spectral

Fig. 1 Structure of FreeHyTE



problem is independent of the others, supporting a parallel solution process. In the next step, each spectral problem is solved, and the resulting spectral displacement fields are computed according to approximation (10). The stress and pore pressure fields are computed by enforcing the compatibility and elasticity equations on the displacement approximation.

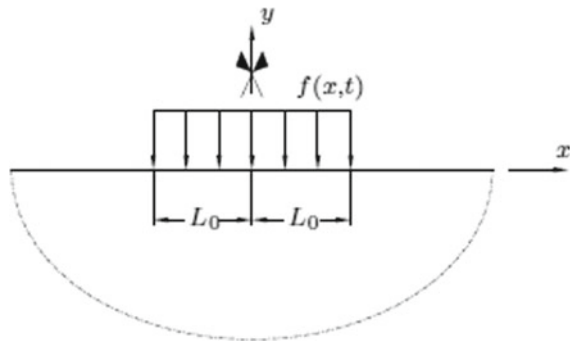
$$\sigma = \mathcal{D}(k\mathcal{D}^*U)X \quad (27)$$

The description of the GUI is given next, along with a numerical example involving a shock load applied to a semi-infinite triphasic medium. Dynamic loads, particularly shock pulses, applied to semi-infinite media are frequent in transportation infrastructures. For instance, the passage of high-speed trains over track imperfections may cause bumps that induce shock waves that travel through the track infrastructure and subsoil. Large stress gradients, high frequency excitations, and spurious reflections from the far-field artificial boundary are issues that hinder the solution when conventional elements are used to model such problems. All GUI data in Figs. 3, 4 and 5 correspond to the input of this simulation. The results are presented at the end of the section.

The physical model used as an example is presented in Fig. 2. It is a pulse perturbation test on a triphasic medium. The medium is subjected to a vertical pressure $\bar{f} = 1000$ Pa during 0.3 s applied on a $2L_0 = 16$ m region of its surface. The total time of the analysis is $t_{\max} = 10$ s. As a result of symmetry, boundary conditions are applied on a half-structure. The material parameters are listed in the first GUI (Fig. 3).

The FreeHyTE GUI consists of four main interfaces, complemented by the MATLAB pdetool interface for the definition of non-regular bodies and meshes. Figure 3 presents the first GUI of the triphasic transient module. The main data zones of the interface are identified with red frames. At the bottom of the first GUI are the 'Load' and 'Save' buttons. When the model is saved, FreeHyTE also stores the output data in output files. The output files are formatted for direct loading in the post-processing software Tecplot but can be used in other visualization software as well as, for example, in Paraview. The 'Algorithmic definitions' zone is where the

Fig. 2 Physical model of the example simulation



The screenshot shows the GUI for FreeHyTE, divided into several sections:

- Structure definition (except boundary conditions):** Contains introductory text and instructions for defining problem parameters, domain, mesh, and Gauss points.
- Geometry and meshing:** Includes fields for Structure dimension in x (1), Structure dimension in y (1), Number of elements in x (4), and Number of elements in y (4).
- Boundary and domain orders:** Includes fields for Edges order (3) and Loops order (3).
- Time integration:** Includes fields for Total time (10), Daubechies family (4), Daubechies refinement (6), and No of dyadic points (7).
- Algorithmic definitions:** Includes a dropdown for Mesh generation (non-regular mesh, triangular elements), Number of Gauss points (10), Order per element (0), Plotting points (10), and checkboxes for Parallel processing and Use least norm solvers.
- Material parameters:** A grid of input fields for various material properties such as Saturation, Viscosity of wetting fluid, Density of solid phase, Bulk modulus of non-wetting fluid, Permeability, Viscosity of non-wetting fluid, Density of wetting fluid, Density of non-wetting fluid, Pore size distribution index, Bulk modulus of wetting fluid, Air entry saturation, Air entry pressure, Intrinsic permeability, Brinley coefficient, and Bulk modulus of solid phase.
- Bottom section:** Includes a warning box, Save, Load, and Clear buttons, and a Run/Next button.

Fig. 3 Layout of GUI 1

user must choose between the two automatic mesh generators built in FreeHyTE. The regular mesh generator creates meshes of uniform rectangular elements and should be used to discretize rectangular domains. The non-regular mesh generator creates triangular elements and can be used for any geometry. Here, the non-regular mesh is chosen. Additionally, the user must specify the number of Gauss-Legendre quadrature points and the plotting points where the solution is stored in the output files. The checkbox ‘Parallel processing’ enables and disables the parallel solution. The checkbox ‘Use least norm solvers’ enables FreeHyTE to use least norm solvers on ill-conditioned solving systems. Finally, the user can request the solutions to be plotted at a certain number of (dyadic) time steps.

In ‘Geometry and meshing,’ the user can define a regular structure and mesh. For our example, this is disabled because the non-regular mesh generator is chosen. In ‘Boundary and domain orders,’ the user can set the orders of refinement in the domain of the elements (Loops order) and on their essential boundaries (Edges order).

The material parameters required for the execution of the analysis are set in ‘Material parameters.’ Here, the material parameters are the same as in reference [21]. In the ‘Time integration’ zone, the user specifies the total time of the analysis and the three calibration parameters that control the Daubechies wavelet basis. More information about the ‘Time integration’ parameters can be found in reference [2].

When the non-regular structure and mesh is chosen, the MATLAB pdeTool interface appears in the next step (Fig. 4). Here, the domain is a quarter of a 20 m circle. The left boundary is a Dirichlet boundary, the circumferential boundary is an absorbing boundary and the top boundary is a Neumann boundary. The second GUI is used to define the type of boundary (Dirichlet, Neumann, Robin or absorbing) for each exterior side of the domain, according to the boundary types in the third GUI (Fig. 5). The main data areas of the interface are identified with red frames. Three of the four

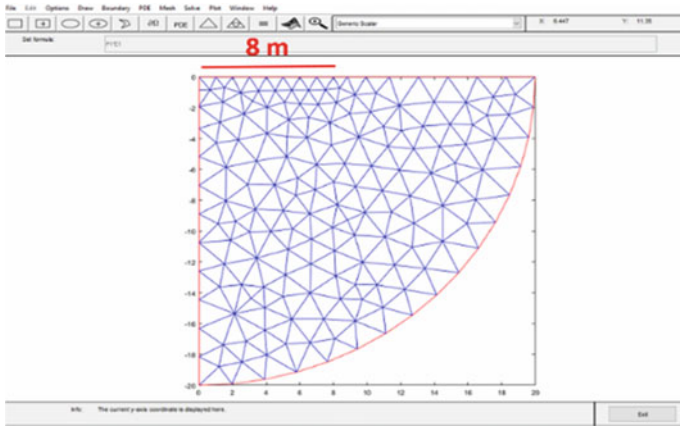


Fig. 4 MATLAB pde tool interface with the non-regular structure and mesh

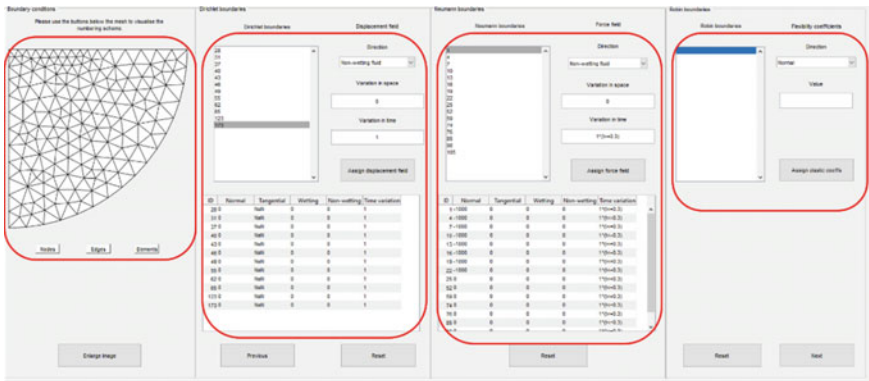


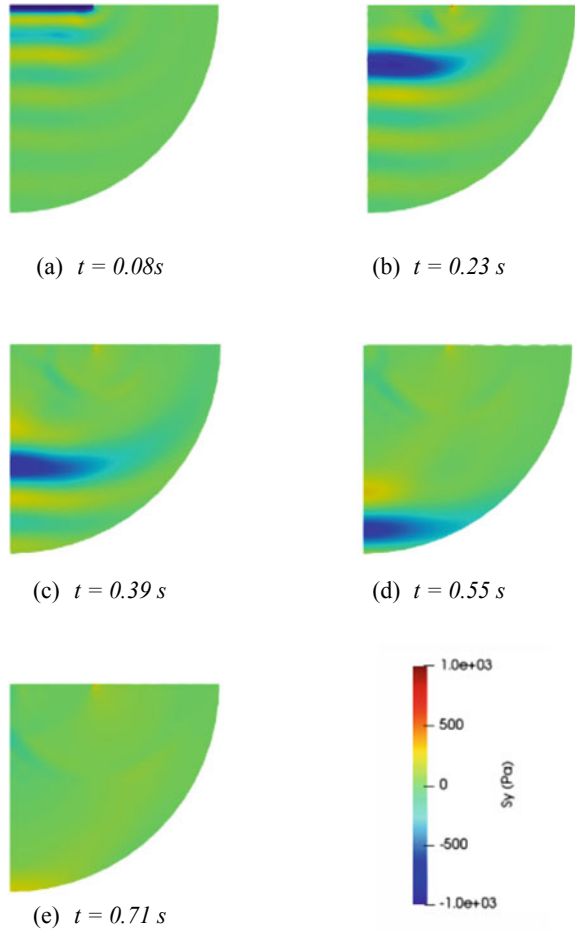
Fig. 5 Layout of GUI 3

input areas are used to define the Dirichlet, Neumann and Robin boundary conditions. Absorbing boundary conditions require no input from the user, as FreeHyTE automatically computes the stiffness coefficients. On the left, the user can visualize the mesh. For each boundary type (except absorbing), the exterior boundaries of that type are listed in each table. It can be observed in the second table that a 1000 Pa pulse is applied on the first 8 m of the Neumann boundary during the first 0.3 s of the simulation.

Finally, the last step before launching the execution of FreeHyTE is the verification GUI, where the user verifies the definitions of the structure and boundary conditions.

Figure 6 shows the total vertical stress in the domain for different time steps during the simulation. It can be observed how the first *P*-wave generated by the initial pulse moves to the bottom of the domain and it disappears when it reaches the boundary (it does not reflect on the boundary) due to the absorbing boundary condition. The

Fig. 6 Vertical stress for different time steps



solution is convergent and recovers correctly the boundary conditions applied to the medium. Moreover, the stress field is continuous between adjacent finite elements, which only happens upon convergence, as the stress continuity condition is not explicitly enforced in the formulation. No stress averaging is used in the results reported here. The Trefftz formulation dealing with saturated porous media was used to reproduce results obtained by other authors [12] and actual laboratory experiments [22], with very good results.

4 Conclusions

Hybrid-Trefftz finite elements have considerable advantages compared to the conventional finite elements when used to model poroelastodynamic problems: they are less sensitive to gross mesh distortion, large solution gradients and small wavelengths. These advantages make these models more convenient when highly transient excitations are expected and/or when the porous materials are modeled using mathematical theories that account for the presence of secondary compression waves of limiting low wavelengths. Hybrid-Trefftz finite elements for poroelastodynamics are implemented in the FreeHyTE platform. FreeHyTE is a user-friendly computational platform employing 2D hybrid-Trefftz finite elements developed at the CERIS Research Centre, Instituto Superior Técnico, University of Lisbon. The FreeHyTE modules for such problems have been presented in this paper from the theoretical background of the formulations to one example to illustrate how the platform and some of its features work.

Acknowledgements This research was supported by Fundação para a Ciência e a Tecnologia through grant PTDC/EAM-GTC/29923/2017.

References

1. Moldovan ID, Freitas JAT (2012) Hybrid-Trefftz displacement and stress elements for bounded poroelasticity problems. *Comput Geotech* 42:129–144
2. Moldovan ID, Cismasiu I FreeHyTE: theoretical bases and developer's manual. <https://drive.google.com/file/d/0BxuR3pKS2hNHTzB2N2Q4cXZKcGc/view>
3. Trefftz E (1926) Ein Gegenstück zum Ritzschen Verfahren. In: Proceedings of the 2nd international congress of applied mechanics, Orell Fussli Verlag, Zurich, pp 131–137
4. Tong P, Pian PH, Lasry SL (1973) A hybrid-element approach to crack problems in plane elasticity. *Int J Numer Meth Eng* 7:297–308
5. Jirousek J (1978) Basis for development of large finite elements locally satisfying all field equations. *Comput Methods Appl Mech Eng* 14:65–92
6. Herrera I (1984) Boundary methods—an algebraic theory. Pitman Advanced Publishing Program, Boston, London, Melbourne
7. Piltner R (1985) Special finite elements with holes and internal cracks. *Int J Numer Meth Eng* 21:1471–1485
8. Qin QH (1995) Postbuckling analysis of thin plates by a hybrid Trefftz finite element method. *Comput Methods Appl Math* 128:123–136
9. Freitas JAT, Moldovan ID, Cismasiu C (2011) Hybrid-Trefftz displacement element for bounded and unbounded poroelastic media. *Comput Mech* 48:659–673
10. Freitas JAT (2008) Mixed finite element solution of time-dependent problems. *Comput Methods Appl Mech Eng* 197:3657–3678
11. Timoshenko SP, Goodier JN (1999) Theory of elasticity, 3rd edn. McGraw-Hill Kogakusha Ltd, Singapore
12. Moldovan ID (2008) Hybrid-Trefftz finite elements for elastodynamic analysis of saturated porous media. Ph.D. Thesis. Universidade Técnica de Lisboa, Portugal
13. Moldovan ID, Radu L (2016) Trefftz-based dual reciprocity method for hyperbolic boundary value problems. *Int J Numer Meth Eng* 106(13):1043–1070

14. Moldovan ID (2015) A new particular solution strategy for hyperbolic boundary value problems using hybrid-Trefftz displacement elements. *Int J Numer Meth Eng* 102(6):1293–1315
15. Cismaşiu C (2000) The hybrid-Trefftz displacement element for static and dynamic structural analysis problems. Ph.D. Thesis. Instituto Superior Técnico, Portugal
16. Biot MA (1956) Theory of propagation of elastic waves in a fluid saturated porous solid. II. Higher frequency range. *J Acoust Soc Am* 28(2):179–191
17. Brooks H, Corey AT (1964) Hydraulic properties of porous media. Hydrology Paper No. 3, Colorado State University, Fort Collins
18. Wei C, Muraleetharan KK (2002) A continuum theory of porous media saturated by multiple immiscible fluids: I. linear poroelasticity. *Int J Eng Sci* 40:1087–1833
19. Moldovan ID, Cao DT, Freitas JAT (2014) Hybrid-Trefftz displacement finite elements for elastic unsaturated soils. *Int J Comput Methods* 11(2):1342005
20. Moldovan ID, Climent N, Bendea ED, Cismaşiu I, Correia AG (2020) A hybrid-Trefftz finite element platform for solid and porous elastodynamics. *Eng Anal Boundary Elem*
21. Cao DT (2013) Hybrid-Trefftz finite elements for elastostatic and elastodynamic problems in porous media. Ph.D. Thesis. Universidade Católica Portuguesa, Portugal
22. Moldovan ID, Gomes Correia A (2017) Fixed point automatic interpretation of bender based G0 measurements. *Comput Geotech* 89:128–142

A Mechanistic-Based Analysis Procedure for Designing Geosynthetic Reinforcement in Pavement Systems



Peter Becker 

Abstract Geosynthetics placed at the bottom of unbound aggregate base layers restrict base layer lateral spreading that consequently increases lateral confinement and stiffness (geosynthetic reinforcement). Although geosynthetic reinforcement is a well-established method for stabilizing unbound layers in pavement systems, many state transportation agencies seldom specify geosynthetic reinforcement in new pavement contracts because of the lack of a practical, mechanistic design procedure. Indeed, conventional design procedures first require conducting extensive local calibrations that still do not necessarily produce reliable design inputs. Therefore, this paper proposes a mechanistic-based analysis procedure for designing geosynthetic reinforcement that adapts Burmister's solution for the distribution of stresses and displacements in layered elastic mediums. A detailed derivation for the analysis procedure is provided, along with a brief study validating the proposed procedure. Applying continuity conditions representative of geosynthetic lateral spreading resistance caused unbound aggregate base bulk stress to increase by 129% in a typical county road pavement and by 30.3% in a typical interstate pavement, which is consistent with geosynthetic reinforcement mechanisms. Subgrade soil octahedral shear stress decreased by 65.4% in the county road pavement and by 33.8% in the interstate pavement, also consistent with geosynthetic reinforcement mechanisms. Limitations for the proposed analysis model are discussed, and recommendations are made for implementing the analysis procedure into pavement design practice.

Keywords Pavements · Geosynthetics · Design

1 Introduction

Geosynthetic reinforcement is a well-established and cost-effective method for stabilizing unbound layers in pavement systems. As described by Berg et al. [1], geosynthetics (geogrids typical) placed at the base-subgrade interface stiffen pavement

P. Becker (✉)

Division of Research and Development, Indiana Department of Transportation, West Lafayette, IN, USA

e-mail: pbecker1@indot.in.gov

systems by resisting base layer lateral spreading, which results in increased confinement of the base layer, reduced vertical stress transferred to the subgrade, and reduced shear strain distributed to the subgrade. Several past field studies have confirmed the existence of these geosynthetic-induced pavement system stiffening mechanisms [2–7]; however, current practice lacks any mechanistic approach for quantifying the increases in stiffness. Therefore, pavement designers must rely on empirical design procedures (e.g., traffic benefit ratio) that require foresight of pavement performance [1, 8–10]. However, in order to implement these geosynthetic reinforcement empirical design procedures, state transportation agencies must first conduct extensive local calibrations that still do not necessarily produce reliable design inputs. As a result, many state transportation agencies simply avoid specifying geosynthetic reinforcement in new pavement contracts altogether.

This paper aims to improve the geosynthetic reinforcement design process by proposing an analysis procedure for quantifying stiffness increases resulting from geosynthetic reinforcement derived from the theory of elasticity. The first part of this paper outlines the derivation for the analysis procedure, and the second part of this paper reports the results of a validation study for the analysis procedure. State transportation agencies interested in broadening their use of geosynthetic reinforcement practices in new pavement construction will find this paper of interest.

2 Geosynthetic Reinforcement Analysis Procedure Derivation

2.1 Geosynthetic Reinforcement of Pavement Systems

Conventional pavement systems generally comprise stiff layers (e.g., aggregate base) underlain by increasingly softer layers (e.g., subgrade soil). In accordance with Burmister's theoretical distribution of stresses in layered elastic mediums [11], a layered system comprising a stiff layer overlying a relatively softer layer exhibits a load-spreading effect that lessens the magnitude of vertical stress distributed to the underlying softer layer. For the layered elastic theory to be valid, layers must be in continuous contact with shearing resistance fully active between layers, so there is continuity in vertical stress, shear stress, vertical displacement, and radial displacement at layer interfaces. However, radial stress is not continuous at layer interfaces, rather radial stress tends to be tensile within the overlying stiff layer and compressive within the underlying soft layer. Tensile radial stresses in aggregate base layers induce lateral spreading and eventual permanent deformations. A planar geosynthetic reinforcement (geogrid typical) placed at a base-subgrade interface interlocks with base layer aggregates inducing shear stresses between the layers that are in turn transmitted to the geosynthetic as tensile stress. Because geosynthetic reinforcements tend to be considerably stiffer than compacted aggregates, the geosynthetic resists lateral

spreading, thereby inducing lateral confinement (compressive radial and tangential stresses) to base layer aggregates.

2.2 Modeling Distributions of Stresses in Geosynthetic Reinforced Pavements

The geosynthetic reinforcement analysis procedure proposed in this paper is based on Burmister’s layered elastic stress distribution theory; however, there is a modification in the continuity conditions to account for the lateral spreading resistance imposed by geosynthetic reinforcement. Elastic theory for the three-dimensional problem in cylindrical coordinates (z , r , and θ) must satisfy the elastic theory equations of equilibrium (Eq. 1–2) and compatibility (Eq. 3–4):

$$\frac{\partial \sigma_r}{\partial r} + \frac{\partial \tau_{rz}}{\partial z} + \frac{\sigma_r - \sigma_\theta}{r} = 0 \tag{1}$$

$$\frac{\partial \tau_{rz}}{\partial r} + \frac{\partial \sigma_z}{\partial z} + \frac{\tau_{rz}}{r} = 0 \tag{2}$$

$$\nabla^4 \phi = 0 \tag{3}$$

$$\nabla^2 = \frac{\partial^2}{\partial r^2} + \frac{1}{r} \left(\frac{\partial}{\partial r} \right) + \frac{\partial^2}{z^2} \tag{4}$$

where

- $\sigma_z, \sigma_r, \sigma_\theta$ normal stresses—vertical, radial, and tangential (respectively),
- τ_{rz} shear stress, and
- ϕ a stress function satisfying Eq. 3–4.

In his treatise [12], Love derived the elasticity equations of stress (Eq. 5–8) and displacement (Eq. 9–10) that satisfied Eq. 1–4.

$$\sigma_z = \frac{\partial}{\partial z} \left[(2 - \nu) \nabla^2 \phi - \frac{\partial^2 \phi}{\partial z^2} \right] \tag{5}$$

$$\sigma_r = \frac{\partial}{\partial z} \left[\nu \nabla^2 \phi - \frac{\partial^2 \phi}{\partial r^2} \right] \tag{6}$$

$$\sigma_\theta = \frac{\partial}{\partial z} \left[\nu \nabla^2 \phi - \frac{1}{r} \left(\frac{\partial \phi}{\partial r} \right) \right] \tag{7}$$

$$\tau_{rz} = \frac{\partial}{\partial r} \left[(1 - \nu) \nabla^2 \phi - \frac{\partial^2 \phi}{\partial z^2} \right] \tag{8}$$

$$\delta_z = \frac{1 + \nu}{E} \left[(1 - 2\nu) \nabla^2 \phi + \frac{\partial^2 \phi}{\partial r^2} + \frac{1}{r} \left(\frac{\partial \phi}{\partial r} \right) \right] \quad (9)$$

$$\delta_r = -\frac{1 + \nu}{E} \left[\frac{\partial^2 \phi}{\partial r^2} \right] \quad (10)$$

where

δ_z, δ_r displacements—vertical and radial (respectively),
 E modulus of elasticity, and
 ν Poisson's ratio.

Burmister recommended using the following stress function (Eq. 11):

$$\phi = J_0(mr) [A_i e^{mz} - B_i e^{-mz} + C_i z e^{mz} - D_i z e^{-mz}] \quad (11)$$

where

$J_0(\dots)$ Bessel function of the first kind and order zero,
 m a parameter,
 i layer number (from topmost), and
 A_i, B_i, C_i, D_i layer unique constants.

Combining Eq. 11 with Eqs. 5–10 yields the following equations for calculating stresses (Eq. 12–15) and displacements (Eq. 16–17):

$$\sigma_z = -m J_0(mr) \left\{ \frac{[A_i m^2 - C_i m(1 - 2\nu_i - mz)] e^{mz}}{+[B_i m^2 + D_i m(1 - 2\nu_i + mz)] e^{-mz}} \right\} \quad (12)$$

$$\sigma_r = \left(\begin{array}{l} m J_0(mr) \left\{ \frac{[A_i m^2 + C_i m(1 + 2\nu_i + mz)] e^{mz}}{+[B_i m^2 - D_i m(1 + 2\nu_i - mz)] e^{-mz}} \right\} \\ - \left(\frac{1}{r} \right) J_1(mr) \left\{ \frac{[A_i m^2 + C_i m(1 + mz)] e^{mz}}{+[B_i m^2 - D_i m(1 - mz)] e^{-mz}} \right\} \end{array} \right) \quad (13)$$

$$\sigma_\theta = \left(\begin{array}{l} 2m J_0(mr) [C_i m \nu_i e^{mz} - D_i m \nu_i e^{-mz}] \\ + \left(\frac{1}{r} \right) J_1(mr) \left\{ \frac{[A_i m^2 + C_i m(1 + mz)] e^{mz}}{+[B_i m^2 - D_i m(1 - mz)] e^{-mz}} \right\} \end{array} \right) \quad (14)$$

$$\tau_{rz} = m J_1(mr) \left\{ \frac{[A_i m^2 + C_i m(2\nu_i + mz)] e^{mz}}{-[B_i m^2 - D_i m(2\nu_i - mz)] e^{-mz}} \right\} \quad (15)$$

$$\delta_z = -\left(\frac{1 + \nu_i}{E_i} \right) J_0(mr) \left\{ \frac{[A_i m^2 - C_i m(2 - 4\nu_i - mz)] e^{mz}}{-[B_i m^2 + D_i m(2 - 4\nu_i + mz)] e^{-mz}} \right\} \quad (16)$$

$$\delta_r = \left(\frac{1 + \nu_i}{E_i} \right) J_1(mr) \left\{ \frac{[A_i m^2 + C_i m(1 + mz)] e^{mz}}{+[B_i m^2 - D_i m(1 - mz)] e^{-mz}} \right\} \quad (17)$$

where

$J_1(\dots)$ Bessel function of the first kind and order one.

Boundary and Continuity Conditions

Layer constants $A_i, B_i, C_i,$ and D_i for layers 1 to n are determined from boundary and continuity conditions. Equations 18–19 are boundary conditions at the surface of the layered system ($z = -H$):

$$\sigma_z = -mJ_0(mr) \left\{ \begin{aligned} & [A_i m^2 + C_i m(1 + mz)] e^{mz} \\ & + [B_i m^2 + D_i m(1 - 2\nu_1 - mH)] e^{mH} \end{aligned} \right\} = -mJ_0(mr) \quad (18)$$

$$\tau_{rz} = mJ_1(mr) \left\{ \begin{aligned} & [A_i m^2 + C_i m(2\nu_1 - mH)] e^{-mH} \\ & - [B_i m^2 - D_i m(1 - 2\nu_1 - mH)] e^{mH} \end{aligned} \right\} = 0 \quad (19)$$

where

$$H = \sum_{i=1}^{n-1} (h_i) \text{ and}$$

h_i i th layer thickness.

Continuity conditions at unreinforced layer interfaces (no geosynthetic) comprise continuities in δ_z (Eq. 20), δ_r (Eq. 21), σ_z (Eq. 22), and τ_{rz} (Eq. 23), which results in layers being in continuous contact with shearing resistance fully active between them.

$$\begin{aligned} & \left[\left(\frac{1 + \nu_i}{E_i} \right) \left(\begin{aligned} & \left\{ A_i m^2 - C_i m \left[2 - 4\nu_i + m \sum_{i=1}^{n-1} (h_{i+1}) \right] \right\} e^{-m \sum_{i=1}^{n-1} (h_{i+1})} \\ & - \left\{ B_i m^2 + D_i m \left[1 + m \sum_{i=1}^{n-1} (h_{i+1}) \right] \right\} e^{m \sum_{i=1}^{n-1} (h_{i+1})} \end{aligned} \right) \right] \\ & = \left[\left(\frac{1 + \nu_{i+1}}{E_{i+1}} \right) \left(\begin{aligned} & \left\{ A_{i+1} m^2 - C_{i+1} m \left[2 - 4\nu_i + m \sum_{i=1}^{n-1} (h_{i+1}) \right] \right\} e^{-m \sum_{i=1}^{n-1} (h_{i+1})} \\ & - \left\{ B_{i+1} m^2 + D_{i+1} m \left[1 + m \sum_{i=1}^{n-1} (h_{i+1}) \right] \right\} e^{m \sum_{i=1}^{n-1} (h_{i+1})} \end{aligned} \right) \right] \end{aligned} \quad (20)$$

$$\left[\left(\frac{1 + \nu_i}{E_i} \right) \left(\begin{aligned} & \left\{ A_i m^2 + C_i m \left[1 - m \sum_{i=1}^{n-1} (h_{i+1}) \right] \right\} e^{-m \sum_{i=1}^{n-1} (h_{i+1})} \\ & + \left\{ B_i m^2 - D_i m \left[1 + m \sum_{i=1}^{n-1} (h_{i+1}) \right] \right\} e^{m \sum_{i=1}^{n-1} (h_{i+1})} \end{aligned} \right) \right]$$

$$= \left[\left(\frac{1 + v_{i+1}}{E_{i+1}} \right) \left(\begin{aligned} & \left\{ A_{i+1}m^2 + C_{i+1}m \left[1 - m \sum_{i=1}^{n-1} (h_{i+1}) \right] \right\} e^{-m \sum_{i=1}^{n-1} (h_{i+1})} \\ & + \left\{ B_{i+1}m^2 - D_{i+1}m \left[1 + m \sum_{i=1}^{n-1} (h_{i+1}) \right] \right\} e^{m \sum_{i=1}^{n-1} (h_{i+1})} \end{aligned} \right) \right] \quad (21)$$

$$\begin{aligned} & \left(\begin{aligned} & \left\{ A_i m^2 - C_i m \left[1 - 2v_i + m \sum_{i=1}^{n-1} (h_{i+1}) \right] \right\} e^{-m \sum_{i=1}^{n-1} (h_{i+1})} \\ & + \left\{ B_i m^2 + D_i m \left[1 - 2v_i - m \sum_{i=1}^{n-1} (h_{i+1}) \right] \right\} e^{m \sum_{i=1}^{n-1} (h_{i+1})} \end{aligned} \right) \\ & = \left(\begin{aligned} & \left\{ A_{i+1}m^2 - C_{i+1}m \left[1 - 2v_i + m \sum_{i=1}^{n-1} (h_{i+1}) \right] \right\} e^{-m \sum_{i=1}^{n-1} (h_{i+1})} \\ & + \left\{ B_{i+1}m^2 + D_{i+1}m \left[1 - 2v_i - m \sum_{i=1}^{n-1} (h_{i+1}) \right] \right\} e^{m \sum_{i=1}^{n-1} (h_{i+1})} \end{aligned} \right) \end{aligned} \quad (22)$$

$$\begin{aligned} & \left(\begin{aligned} & \left\{ A_i m^2 + C_i m \left[2v_i - m \sum_{i=1}^{n-1} (h_{i+1}) \right] \right\} e^{-m \sum_{i=1}^{n-1} (h_{i+1})} \\ & - \left\{ B_i m^2 - D_i m \left[2v_i + m \sum_{i=1}^{n-1} (h_{i+1}) \right] \right\} e^{m \sum_{i=1}^{n-1} (h_{i+1})} \end{aligned} \right) \\ & = \left(\begin{aligned} & \left\{ A_{i+1}m^2 + C_{i+1}m \left[2v_i - m \sum_{i=1}^{n-1} (h_{i+1}) \right] \right\} e^{-m \sum_{i=1}^{n-1} (h_{i+1})} \\ & - \left\{ B_{i+1}m^2 - D_{i+1}m \left[2v_i + m \sum_{i=1}^{n-1} (h_{i+1}) \right] \right\} e^{m \sum_{i=1}^{n-1} (h_{i+1})} \end{aligned} \right) \end{aligned} \quad (23)$$

Continuity conditions at reinforced interfaces (with geosynthetic) comprise continuities in δ_z (Eq. 20) and σ_z (Eq. 22) (i.e., continuous contact). However, because geosynthetic reinforcements resist lateral spreading, δ_r equals zero at the geosynthetic reinforced interface resulting in alternative continuity equations for δ_r (Eq. 24–25).

$$\left(\frac{1 + v_i}{E_i} \right) \left(\begin{aligned} & \left\{ A_i m^2 + C_i m \left[1 - m \sum_{i=1}^{n-1} (h_{i+1}) \right] \right\} e^{-m \sum_{i=1}^{n-1} (h_{i+1})} \\ & + \left\{ B_i m^2 - D_i m \left[1 + m \sum_{i=1}^{n-1} (h_{i+1}) \right] \right\} e^{m \sum_{i=1}^{n-1} (h_{i+1})} \end{aligned} \right) = 0 \quad (24)$$

$$\left(\frac{1 + v_{i+1}}{E_{i+1}} \right) \left(\begin{aligned} & \left\{ A_{i+1}m^2 + C_{i+1}m \left[1 - m \sum_{i=1}^{n-1} (h_{i+1}) \right] \right\} e^{-m \sum_{i=1}^{n-1} (h_{i+1})} \\ & + \left\{ B_{i+1}m^2 - D_{i+1}m \left[1 + m \sum_{i=1}^{n-1} (h_{i+1}) \right] \right\} e^{m \sum_{i=1}^{n-1} (h_{i+1})} \end{aligned} \right) = 0 \quad (25)$$

Because stresses and displacements equal zero at infinite depth, n th layer constants A_n and C_n both equal zero to satisfy the boundary condition at z equaling infinity. Therefore, any n -layer system is determinate with $4n - 2$ unknowns and $4n - 2$ equations.

Loading Applied Uniformly over a Circular Area

Stresses and displacements calculated from Eqs. 12–17 are only general solutions resulting from a vertical load equal to $-mJ_0(mr)$. However, the Hankel transform method [13] can be used to find stresses and displacements due to a constant pressure (q) applied over a circular area of radius a (Eq. 26):

$$\bar{f}(m) = \int_0^a qr J_0(mr) dr = \frac{qa}{m} J_1(ma) \tag{26}$$

The Hankel inversion of Eq. 26 is:

$$q(r) = \int_0^\infty \bar{f}(m)m J_0(mr)dm = qa \int_0^\infty J_0(mr)J_1(ma)dm \tag{27}$$

So, a stress or displacement resulting from q applied over a circular area of radius a is calculated from Eq. 28:

$$R = qa \int_0^\infty \frac{R^*}{m} J_1(ma)dm \tag{28}$$

where

- R stress or displacement due to q applied over a circular area of radius a , and
- R^* stress or displacement due to loading $-mJ_0(mr)$ (i.e., Equation 12–17).

The mathematics required to integrate Eq. 28 is rather rigorous; however, integration may be approximated using Gaussian quadrature.

2.3 Stress-Strain Behavior of Unbound Materials

Unbound materials (i.e., soils and aggregates) do not tend to be linear-elastic, but rather they exhibit nonlinear stress-strain behavior. In general, stiffness (resilient modulus) tends to increase with increasing confinement and decrease with increasing shear strain. Confining effects tend to be more profound in cohesionless soils and aggregates, while cohesive soils tend to be more sensitive to shear strain. The mechanistic-empirical pavement design guide (MEPDG) that was an outcome of

NCHRP 1-37A [14] recommended Eqs. 29–31 as the generalized constitutive model for resilient modulus (M_r) of unbound materials:

$$M_r = k_1 p_a \left(\frac{\theta}{p_a} \right)^{k_2} \left(\frac{\tau_{\text{oct}}}{p_a} + 1 \right)^{k_3} \quad (29)$$

$$\theta = \sigma_1 + \sigma_2 + \sigma_3 \quad (30)$$

$$\tau_{\text{oct}} = \frac{1}{3} \sqrt{(\sigma_1 - \sigma_2)^2 + (\sigma_1 - \sigma_3)^2 + (\sigma_2 - \sigma_3)^2} \quad (31)$$

where

p_a	atmospheric pressure,
θ	bulk stress,
τ_{oct}	octahedral shear stress,
$\sigma_1, \sigma_2, \sigma_3$	principal stresses,
k_1, k_2, k_3	regression coefficients.

In situ principal stresses are the sum of at rest stresses—determined from layer unit weights, thicknesses, and at rest lateral earth pressures—and distributed stresses—determined from Eqs. 12–14.

The nonlinear constitutive model may be incorporated into the layered elastic distribution solution using trial and error. Assumed bulk stresses and octahedral stresses used to calculate resilient modulus values will eventually converge with theoretical bulk stresses and octahedral stresses after a finite amount of iterations.

3 Geosynthetic Reinforcement Analysis Procedure Validation

Two hypothetical pavement systems were generated to assess the proposed geosynthetic reinforcement analysis procedure—a low volume road (county road) pavement and a high volume road (interstate) pavement. The following sections provide structural and loading inputs for the assessment as well as the theoretical responses of the unreinforced and reinforced pavements.

3.1 Pavement Structure Inputs

Figure 1a shows the configuration of the county road pavement, and Fig. 1b shows the configuration of the interstate pavement. Both configurations consist of hot mix asphalt (HMA) layers ($E = 500$ ksi, $\nu = 0.3$, $\gamma = 140$ pcf); however, the county

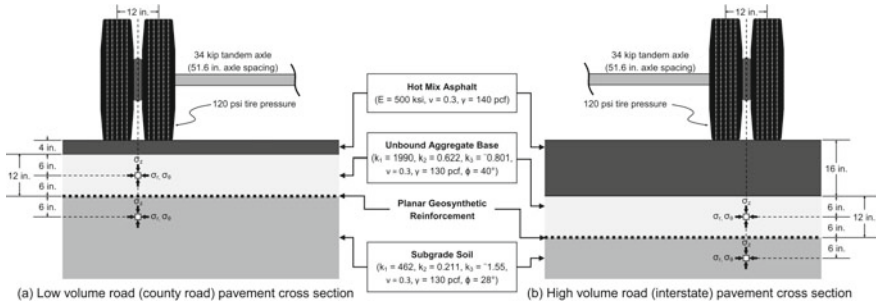


Fig. 1 a Low volume and b high volume road pavement cross sections used for assessing validity of geosynthetic reinforcement analysis procedure

road pavement HMA layer is 4 in. thick, while the interstate pavement HMA layer is 16 in. thick. HMA layers in both pavement configurations are underlain by 12 in. of unbound aggregate base and then by subgrade soil. Geosynthetic reinforcement is located at the base-subgrade interface.

Unbound Aggregate Base Properties

The unbound aggregate base used in the validation study is a No. 53 aggregate per Indiana Department of Transportation (INDOT) standard specifications. The No. 53 aggregate classified as well-graded gravel with silt and sand (GW-GM) per the United Soil Classification System (USCS) and as A-1-a per AASHTO. Minimum dry unit weight for the aggregate is 106.3 pcf (ASTM D 4254), and maximum dry unit weight for the aggregate is 128.5 pcf (ASTM D 4253). Resilient modulus testing (AASHTO T 307) was conducted on a sample of the aggregate compacted to 79.8% relative density (medium dense to dense). Resilient modulus test results (Table 1) were regressed to fit Eq. 29 ($adj. R^2 = 0.893$) that yielded $k_1 = 1990$, $k_2 = 0.622$, and $k_3 = -0.801$.

Subgrade Soil Material Properties

The soil used in the validation study was sourced from I-69 subgrade near Anderson, IN. The soil classified as sandy lean clay (CL) per USCS and as A-4(3) per AASHTO. Maximum dry unit weight for the soil per ASTM D 698 is 119.9 pcf with an optimum moisture content of 12.5%. Resilient modulus testing (AASHTO T 307)

Table 1 Resilient modulus (AASHTO T 307) test results for unbound aggregate base

Variable	Coefficient	Standard error	t-value	p-value
Intercept	3.30	0.0249	132	<0.001
$\log(\theta/p_a)$	0.622	0.0717	8.67	<0.001
$\log(\tau_{oct}/p_a + 1)$	-0.801	0.233	-3.43	0.005

Note $\log(M_r/p_a) = \log(k_1) + k_2 \log(\theta/p_a) + k_3 \log(\tau_{oct}/p_a + 1)$

Table 2 Resilient modulus (AASHTO T 307) test results for subgrade soil

Variable	Coefficient	Standard error	<i>t</i> -value	<i>p</i> -value
Intercept	2.66	0.0422	63.1	<0.001
$\log(\theta/p_a)$	0.211	0.119	1.78	0.100
$\log(\tau_{oct}/p_a + 1)$	-1.55	0.567	-2.74	0.0180

Note $\log(M_r/p_a) = \log(k_1) + k_2 \log(\theta/p_a) + k_3 \log(\tau_{oct}/p_a + 1)$

was conducted on a sample of the soil compacted to 96.1% relative compaction at 12.9% moisture content. Resilient modulus test results (Table 2) were regressed to fit Eq. 29 (adj. $R^2 = 0.290$) that yielded $k_1 = 462$, $k_2 = 0.211$, and $k_3 = -1.55$.

3.2 Loading Inputs

Loading in the model validation was applied using a 34-kip tandem axle (Fig. 1) that is the maximum tandem axle weight allowed by INDOT. As recommended by AASHTO [15], tandem axles were spaced at 51.6 in. on center, dual tires were spaced at 12 in., on center, and tire pressures were 120 psi. In situ stresses induced by the tandem axle loading were determined immediately below one of the axles in between the dual tires (Fig. 1).

3.3 Results of the Validation Study

Figure 2 summarizes results of the validation study in terms of theoretical in situ bulk stresses and octahedral shear stresses, as well as the calculated resilient moduli (Eq. 29), for aggregate base and subgrade soil layers comprising the county road and interstate pavements—both with and without geosynthetic reinforcement. In general, the incorporation of the geosynthetic reinforcement continuity equations (Eq. 20, 22, 24–25) into Burmister’s layer stress distribution model causes aggregate bulk stress to increase, subgrade octahedral shear stress to decrease, and subsequently resilient moduli for both layers to increase.

Unbound Aggregate Base Bulk Stress

Figure 2a shows the in situ bulk stresses within the aggregate base layers (with and without geosynthetic reinforcement) comprising the county road and interstate pavements. For the county road pavement, aggregate base bulk stress equaled 6.07 psi without geosynthetic reinforcement and 13.9 psi with geosynthetic reinforcement (129% increase). For the interstate pavement, aggregate base bulk stress equaled 3.63 psi without geosynthetic reinforcement and 4.73 psi with geosynthetic reinforcement (30.3% increase). Consistent with presumed geosynthetic reinforcement

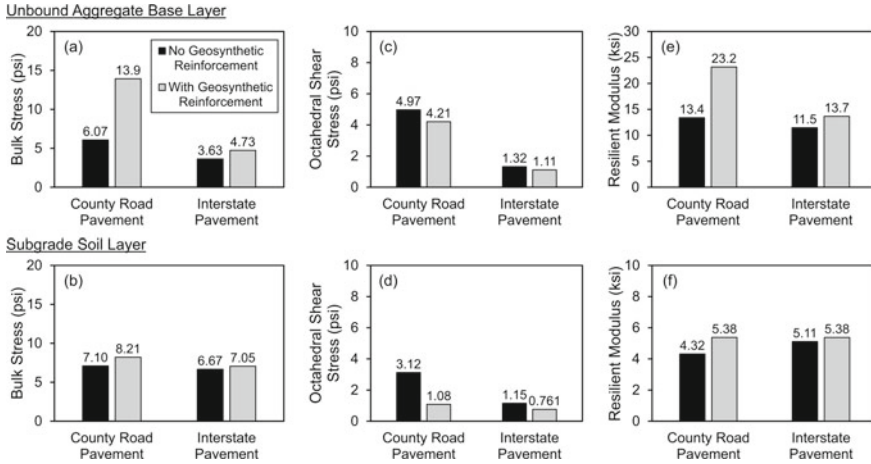


Fig. 2 Results of geosynthetic reinforcement analysis model validation study: **a** bulk stress in aggregate base layer, **b** bulk stress in subgrade layer, **c** octahedral shear stress in aggregate base layer, **d** octahedral shear stress in subgrade layer, **e** resilient modulus for aggregate base layer, and **f** resilient modulus for subgrade layer

mechanisms, lateral spreading resistance results in increased lateral confinement that increases bulk stress within the aggregate base layer. Additionally, bulk stress within the subgrade layer (Fig. 2b) increased from 7.10 to 8.21 psi (15.7% increase) for the county road pavement and from 6.67 to 7.05 psi (5.73% increase) for the interstate pavement.

Aggregate base layer bulk stresses are markedly higher in the county road pavement compared with the interstate pavement. Although the interstate pavement aggregate base has greater at rest bulk stress due to the greater HMA surcharge pressure, the county road pavement conveys greater bulk stress under loading since its aggregate base layer is closer to the pavement surface.

Subgrade Soil Octahedral Shear Stress

Figure 2d shows the in situ octahedral shear stresses within the subgrade soil layers (with and without geosynthetic reinforcement) comprising the county road and interstate pavements. For the county road pavement, subgrade octahedral shear stress equaled 3.12 psi without geosynthetic reinforcement and 1.08 psi with geosynthetic reinforcement (65.4% decrease). For the interstate pavement, subgrade octahedral stress equaled 1.15 psi without geosynthetic reinforcement and 0.761 psi with geosynthetic reinforcement (33.8% decrease). Because overlying aggregate base layers stiffen with increased confinement due to geosynthetic reinforcement, less vertical stress (and consequently shear strain) is distributed to the subgrade (i.e., increased load-spreading). Therefore, the decreases in octahedral shear stress agree with the presumed geosynthetic reinforcement mechanism. Additionally, octahedral shear stress within the aggregate base layer (Fig. 2c) decreased from 4.97 to 4.21

(15.3% decrease) for the county road pavement and from 1.32 to 1.11 psi (15.8% decrease) for the interstate pavement.

Subgrade soil within the county road pavement experiences a greater reduction in octahedral shear stress compared with the subgrade soil within the interstate pavement. Because octahedral shear stress is essentially the average principal stresses difference, octahedral shear stress increases with increasing major principal stress (i.e., vertical stress). Since the aggregate base in the county road pavement stiffens considerably more with geosynthetic reinforcement than the aggregate base in the interstate pavement, the county road pavement subgrade experiences a more effective vertical stress load-spreading effect than the subgrade within the interstate pavement.

Aggregate Base and Subgrade Resilient Moduli

Figure 2e shows calculated resilient moduli for the aggregate base layer (with and without geosynthetic reinforcement) comprising the county road and interstate pavements. Because resilient modulus for the base increases with increasing bulk stress as well as decreasing octahedral shear stress, aggregate base layer resilient modulus increased from 13.4 to 23.2 ksi (73.0% increase) for the county road pavement and from 11.5 to 13.7 ksi (19.1% increase) for the interstate pavement. Likewise, for the subgrade soil (Fig. 2f), resilient modulus increased from 4.32 to 5.38 ksi (24.6% increase) for the county road pavement and from 5.11 to 5.38 psi (5.17% increase).

The county road pavement structures appears to benefit greater from the inclusion of a geosynthetic reinforcement layer due to the relatively shallow depths of the base and subgrade layers below the pavement surface. Therefore, the benefit to cost ratio of geosynthetic reinforcement is likely to be higher for construction of lower volume road pavements (e.g., county roads, state routes, etc.) than for construction of higher volume roads (e.g., US highways, interstates, etc.). However, a detailed assessment of the benefits and costs of geosynthetic reinforcement is beyond the scope of this paper.

3.4 Limitations of the Geosynthetic Reinforcement Analysis Procedure

As previously demonstrated, the proposed geosynthetic reinforcement analysis procedure uses elastic theory to quantify improvements to aggregate base and subgrade soil resilient moduli; however, the model represents an idealized condition in which the geosynthetic is perfectly rigid (i.e., zero radial displacement) and no slippage occurs between the geosynthetic and adjoining pavement layers. In actuality, geosynthetics are not rigid, rather they experience tensile strain proportional to their respective stiffnesses. Furthermore, geosynthetic slippage depends on the soil/aggregate-geosynthetic interaction with the extent of slippage being a function of both soil/aggregate properties (e.g., particle size distribution, angle of internal friction, etc.) and geosynthetic properties (e.g., aperture area, junction strength, etc.).

Therefore, resilient modulus increases determined from the proposed geosynthetic reinforcement analysis procedure represent an upper boundary for geosynthetic stabilization. It is therefore recommended that an empirical study be performed to compare theoretical and actual resilient modulus increases before the proposed geosynthetic reinforcement model be implemented into practice. The goal of the empirical-theoretical comparison study would be to establish resilient modulus correction factors for different geosynthetic types (e.g., biaxial geogrid, woven geotextile, etc.).

4 Summary and Conclusions

This paper proposed a mechanistic-based analysis procedure for quantifying unbound aggregate base and subgrade soil resilient modulus increases due to planar geosynthetic reinforcement. By adapting Burmister's solution for stress and displacement distributions in layered elastic mediums to account for the lateral spreading resistance mechanism of geosynthetic reinforcements, engineers are able to predict relative increases in resilient modulus for different unbound material types and pavement configurations.

Results from the validation study for the proposed geosynthetic reinforcement analysis procedure demonstrated that the proposed model is consistent with presumed geosynthetic reinforcement mechanisms—increased confinement of the aggregate base, reduced vertical stress distributed to the subgrade soil, and reduced shear strain experienced by the subgrade soil. In addition, relative increases in resilient modulus for a typical county road pavement (73.0% for aggregate base, 24.6% increase for subgrade soil) were substantially higher than those for a typical interstate pavement (19.1% for aggregate base, 5.17% for subgrade soil), which suggests that geosynthetic reinforcement may be more beneficial for lower volume roads.

Despite the fact that the proposed geosynthetic reinforcement model is steeped in the theory of elasticity, the model represents an idealized case in which the geosynthetic is perfectly rigid and no slippage occurs between the geosynthetic and adjoining pavement layers. Since geosynthetics are stiff rather than rigid and slippage depends on the soil/aggregate-geosynthetic interaction, resilient modulus increases determined from the proposed analysis procedure correspond to an upper bound for stabilization by geosynthetic reinforcement. Future research will be required to establish correction factors for different geosynthetic types (e.g., biaxial geogrid, woven geotextile, etc.) before the model can be implemented into practice.





References

1. Berg R, Christopher B, Perkins S (2000) Geosynthetic reinforcement of the aggregate base/subbase courses of pavement structures. Geosynthetics Materials Association, Roseville, MN, USA

2. Al-Qadi I, Brandon T, Bhutta S (1996) Field evaluation of geosynthetically stabilized pavements. In: Proceedings of the fourth materials engineering conference. American Society of Civil Engineers, Washington, D.C., pp 10–14
3. Holder W, Andrese J (2004) Geogrid reinforcement to reduce pavement section thickness: a case study. In: Yegian M, Kavazanjian E (eds) Proceedings of geo-trans 2004, vol 1. American Society of Civil Engineers, Los Angeles, CA, pp 1006–1013
4. Al-Qadi, I., Tutumluer, E., Dessouky, S.: Construction and instrumentation of full-scale geogrid-reinforced flexible pavement test sections. In: Proceedings of the Airfield and Highway Pavement Specialty Conference, pp. 131–142. American Society of Civil Engineers, Atlanta, GA (2006)
5. Vischer W (2003) Low-volume road flexible pavement design with geogrid-reinforced base. *Transp Res Rec* 1819:247–254
6. Tang X, Chehab G, Palomino A (2008) Evaluation of geogrids for stabilizing weak pavement subgrade. *Int J Pavement Eng* 9(6):413–429
7. Ling H, Liu Z (2001) Performance of geosynthetic-reinforced asphalt pavements. *J Geotech Geoenvironmental Eng* 127(2):177–184
8. Holtz R, Christopher B, Berg R (2008) Geosynthetic design and construction guidelines (FHWA-NHI-07-092). Federal Highway Administration, Washington, D.C.
9. Perkins S, Edens M (2003) A design model for geosynthetic-reinforced pavements. *Int J Pavement Eng* 4(1):37–50
10. Kwon J, Tutumluer E, Kim M (2005) Development of a mechanistic model for geosynthetic-reinforced flexible pavements. *Geosynthetics Int* 12(6):310–320
11. Burmister D (1945) The general theory of stresses and displacements in layered systems I. *J Appl Phys* 16(89):89–94
12. Love A (1923) *Treatise on the mathematical theory of elasticity*. University Press, Cambridge, England
13. Huang Y (2004) *Pavement analysis and design*, 2nd edn. Pearson Prentice Hall, Upper Saddle River, NJ, USA
14. ARA Inc. (2004) *Guide for mechanistic-empirical design of new and rehabilitated pavement structures (NCHRP 1-37A)*. National Cooperative Highway Research Program, Washington, D.C.
15. AASHTO (2015) *Mechanistic-empirical pavement design guide: a manual of practice*. American Association of State Highway and Transportation Officials, Washington, D.C.

Geotechnical Characterization of a Low Volume Traffic Road



Marina M. Cabette , Antonio M. V. Paula , Manuel J. C. Minhoto ,
and Ewerton C. A. Fonseca 

Abstract This paper aims to study an unpaved low volume traffic road (LRV) in the Montesinho Natural Park, Portugal. Because it is a road that gives access to two dams that supply the localities of the region of Bragança, Portugal, in a nature reserve, it should be ensured the valorization of this natural park and also the safety and comfort of those who use it. The proper conservation of this road requires that its structural condition is periodically evaluated, involving a predominantly geotechnical characterization because it is unpaved. In order to evaluate whether structural tests are practical for the management and conservation models of unpaved roads are developed.

Keywords Unpaved road · Structural evaluation · Maintenance

1 Introduction

1.1 General Framework

Roads do not have a universal classification. Therefore, some countries have their own manuals, guides, norms regarding classification, as well as characterization, composition, construction techniques, and other elements related to paving in order to better comply with their own local needs. Low volume roads (LRV) are defined as

M. M. Cabette (✉)

University of Minho, Guimarães, Portugal

e-mail: marinacabette@gmail.com

A. M. V. Paula (✉) · M. J. C. Minhoto (✉)

Polytechnic Institute of Bragança, Bragança, Portugal

e-mail: mpaula@ipb.pt

M. J. C. Minhoto

e-mail: minhoto@ipb.pt

E. C. A. Fonseca (✉)

Federal University of Technology—Paraná, Campo Mourão, Brazil

e-mail: ewertonfonseca@utfpr.edu.br

roads through which circulate a low volume of annual average daily traffic (AADT); each country has values defined for this classification [1]. This type of road usually is part of the rural road network. Road standards use pavement sizing methods that consider the elastic-linear behavior of pavement materials, resulting in good results for bituminous pavements. These methods are not sufficient for unpaved roads, which mostly consist of soil or gravel [2].

Majority of the time, the approach to LRV is always based on the geotechnical characterization of pavements, performance evaluations, and guidelines/standards which have developed design methods, evaluation, implementation and maintenance and rehabilitation directed to roads low-traffic volume and unpaved roads such as Beckemeyer [3], Berkshire regional planning commission [4]; Alves [5], ERA [6], among others. Manuals such as MTPW [7] and SATCC [8] present LRV sizing methods, but refer to ERA [6] for unpaved roads, which presents a table-based method for sizing it. Thus, they present the unpaved LRV sizing method, called DCP-CBR method for the design of minor gravel roads.

According to Benevides [9], the functional and structural conditions of pavement should be evaluated by appropriate methodologies to ascertain the pathologies that appear on the pavement surface. Pavement performance can be affected by five main factors: the environment, traffic, structure, construction, and maintenance; these have directly influenced the quality of pavement over time [10]. One way to control the degradation of gravel roads is to conserve road performance and perform maintenance based on regular inspections to keep the road in good condition.

1.2 Objectives

This work studied an unpaved road, which is located in a Natural Park, in Northeast of Portugal. The geotechnical characteristics, namely sieve analysis test to determine the grain-size distribution of soil, Proctor density, light dynamic penetrometer (LDP), plate load test, and California bearing ratio (CBR) test in the laboratory, and the CBR, in situ were carried out in order to verify proper soil resistance to ensure more safety and comfort of those who use the road. In this work, several conservation management models are applied thorough structural evaluation. Therefore, the objective of the study is to contribute to the evaluation of the quality of unpaved roads.

2 Work Program

2.1 Study Area

Figure 1 shows the low-traffic unpaved road that lies in a mountainous region near the village of Montesinho, in northeastern Portugal, right next to the Spanish border. The



Fig. 1 LRV location, near the Portugal–Spain border

road is the main route to the two dams belonging to the municipality of Bragança, which make up the Albufeira de Veiguinhas and the Serra Serrada Albufeira (in red), located at 1200–1300 m in altitude.

The study LRV has its starting point at the coordinates (WGS84) 41°57'44" N and 6°48'28" W (ETRS89-TM06: $M = 109895.690$; $P = 255700.959$) (point A) and ends at coordinates 41°56'7" N and 6°48'50" W (ETRS89-TM06: $M = 109453.210$; $P = 253049.460$) (point B). The course selected for study is 3.06 km long.

2.2 Criteria for Selection of Soil Sampling Points

Due to the length of the road under study, the homogeneous subsections method, called the cumulative difference approach, indicated by AASHTO [11], was adopted.

With the delimitation of homogeneous sections, it is of great importance to determine the representative values of each delimited zone. For the current work, the 85% percentile is chosen. Equation 1 shows how to determine the characteristic value (K) [12].

$$K = m + 1.04 * s \tag{1}$$

where m is the arithmetic mean, and s is the standard deviation.

For each delimited subsection, the representative response of the pavement is determined. And therefore, one should select the location whose pavement response value approximates those obtained for the 85% percentile. To relate the values will be used the root mean square deviation (RMS), which is often used to measure the differences between the values predicted by a model or an estimator and the observed values (Eq. 2) [4].

Table 1 Geotechnical characterization tests

Tests	Standard	Parameter analyzed
Particle size analysis	LNEC E 239-1970	Unified soil classification system (USCS)—ASTM D 2487–85; HRB (highway research board) classification for roads
Standard proctor	ASTM D 698-07	Optimum moisture content; Dry density
CBR in laboratory	ASTM D 1883-07	Soil bearing capacity
CBR in situ	BS 1377:9-1990	Soil bearing capacity

$$\text{RMS} = \left[\frac{1}{n} * \sum_{i=1}^n \left(\frac{d_i^c - d_i^m}{d_i^m} \right)^2 \right] * 100 \quad (2)$$

where d_i^c is the value calculated at the point i ; d_i^m is the value measured at the point i and n is the number of points used.

The tests were performed every 100 m, and alternated on the right and left wheels (right from the other direction). Therefore, 31 spots were selected in the 3 km long road. For the case under study, the pavement response was measured by the light dynamic penetrometer (EN ISO 22476-2: 2005) and plate load (NF P 94-117-1: 2000) test.

2.3 Geotechnical Characterization and Structural Analysis

The structural analysis can be performed either in the laboratory or in situ. In laboratory tests, in situ extraction by drilling wells is necessary to determine the physical characteristics of the materials.

The tests presented are listed in Table 1 which indicates the representative points of each homogeneous section where tests were performed.

3 Results

3.1 Cumulative Difference Approach

This test was performed to a depth of 1.0 m (or until NEGA). However, soil sampling was only possible to collect soil to a depth of 0.4 m because the site belongs to a nature reserve, and it is not possible to use heavy equipment (backhoe type) to obtain soil at greater depth. Due to this limitation, Fig. 2a shows the homogeneous sections

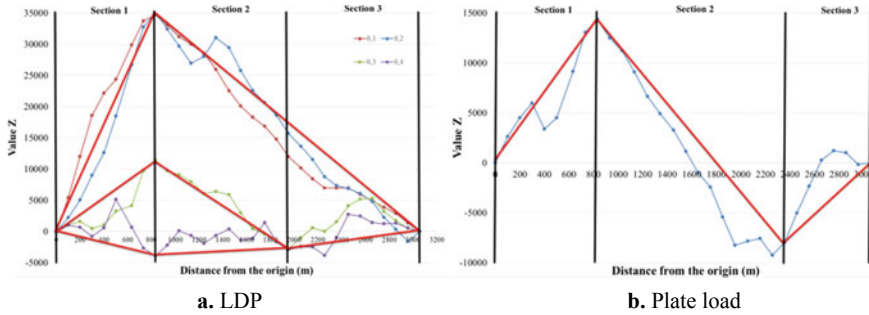


Fig. 2 Homogeneous sections were obtained

when considering only the results of the light dynamic penetrometer (LDP) test up to 0.4 m depth.

From the homogeneous sections obtained, the characteristic N10 values of each layer can be determined for each section, and by means of the RMS, determine the representative point of the section. Thus, taking into account the data obtained, the spots selected for sampling are 1 (0 m), 14 (1342 m), and 21 (2056 m) that obtained the lowest RMS values 23.7%, 27.6%, and 30.9%, respectively.

Figure 2b shows that three homogeneous sections were obtained through the results of the plate load test. The spots selected for sampling are 3 (300 m), 21 (2056 m), and 31 (3056 m) which obtained the RMS values of 0.3%, 12.6%, and 8.9%, respectively. The low error values should only have one comparison variable.

3.2 Geotechnical Characterization Tests

A total of five sampling spots representing the homogeneous sections were selected, namely 1 (0 m), 3 (300 m), 14 (1342 m), 21 (2056 m), and 31 (3056 m) (distance from the origin). At the five spots selected for sample collection, 35 kg of soil was obtained to a depth of 0.4 m for later laboratory testing. When excavating the subsoil, it was noted the existence of different layers of soil, so it was decided to separate the samples to perform the tests (layer (1) and layer (2)).

Particle size analysis and Normal Proctor

Figure 3a shows the particle size curves of all soil samples analyzed, and Fig. 3b shows the compaction curves obtained for each soil sample collected. Table 2 presents the results of the geotechnical characterization tests by 2 different nomination systems.

The soils of the different layers were subsequently sorted, first by unified soil classification system (USCS), regulated by ASTM D 2487-85, and then the HRB classification for road purposes.

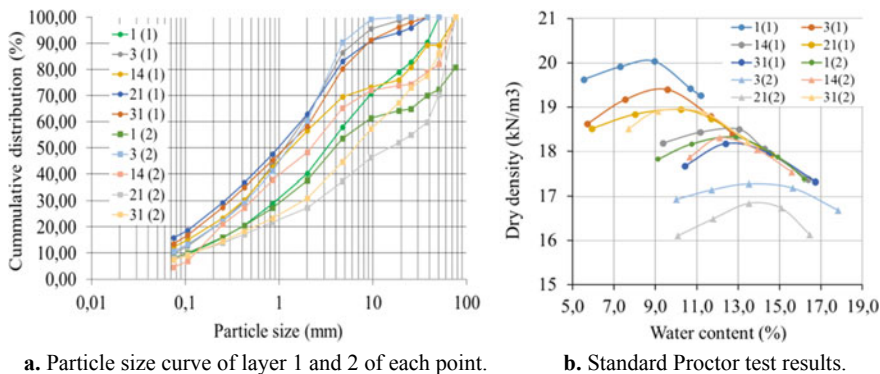


Fig. 3 Particle size analysis and standard proctor results

Table 2 Geotechnical characterization tests

Spot	Layer	Classification system	
		USCS	HRB
1	1.º	SW-SM a	A1a
3	2.º	GW-GM	A1a
14	1.º	SW-SM	A1b
	2.º	SP-SM	A1b
21	1.º	SM a	A1b
31	2.º	SP	A1a
	1.º	SM	A1b
	2.º	GW-GM	A1a
	1.º	SM	A1b
	2.º	GP-GM	A1a

It is emphasized that the soils collected at five sampling points has no plasticity index (PI). It follows that the soil found at all sampling points are suitable for use in the layers constituting pavement.

CBR (California Bearing Ratio) em laboratório e in situ

Table 3 presents the CBR values in situ and in the laboratory of the selected points. The laboratory CBR value obtained is for 95% of the maximum dry density.

It is observed that the laboratory CBR values at spots 1 and 3 are close and present high values of resistance. While at spot 14, in the first layer, the result obtained from CBR is the lowest presented. At spots 21 and 31, the results obtained from CBR in the first layer are also close and give good soil resistance.

As in the laboratory CBR test, it is observed that the in situ CBR values at spots 1 and 3 are identical and have high resistance values. While at point 14, the value obtained is the lowest of the 5 spots.

Table 3 CBR test results

Spots	CBR in situ (%)	Layer	CBR in laboratory (%)
1	37	1.º	39
		2.º	30
3	40	1.º	37
		2.º	23
14	24	1.º	18
		2.º	38
21	31	1.º	30
		2.º	21
31	28	1.º	30
		2.º	40

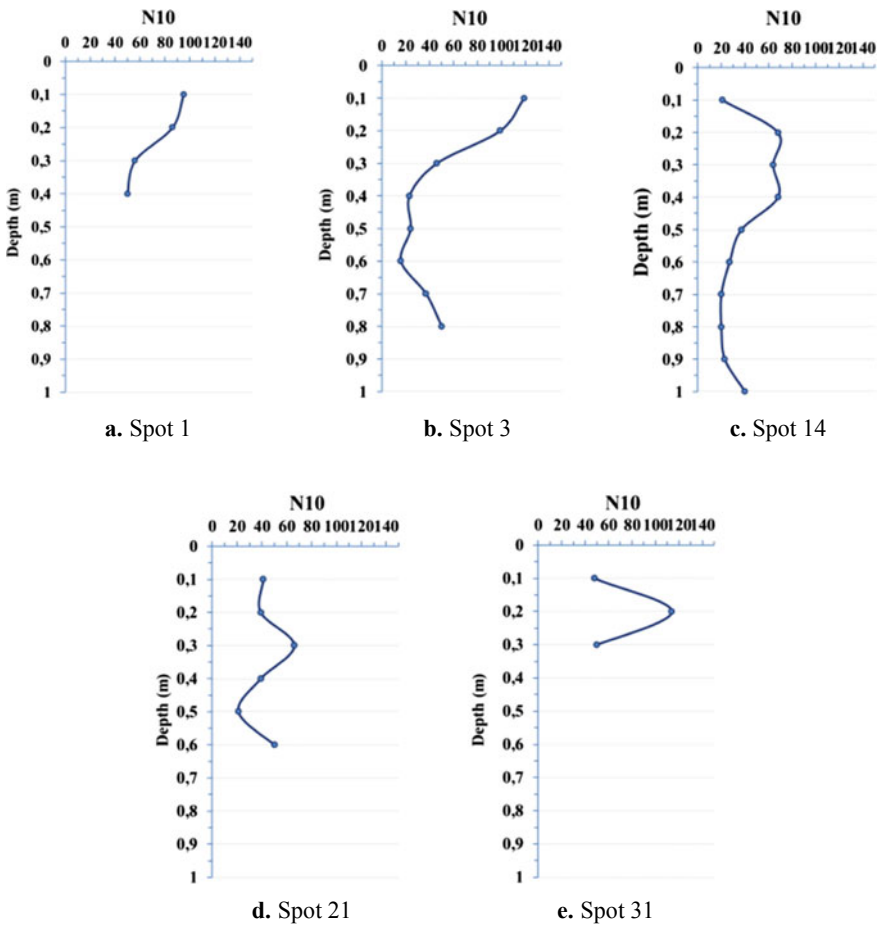


Fig. 4 LDP test results

Table 4 Plate load test results

Spots	EV1 (MPa)	EV2 (MPa)	EV2/EV1
1	108.6	157.2	1.448
3	124.9	142.6	1.142
14	37.9	63.0	1.663
21	124.5	101.8	0.818
31	67.1	99.6	1.485

Light dynamic penetrometer (LDP) and plate load test at representative spots

Figure 4 shows the LDP test result of the selected points. It is noted that at most spots such as 1, 3, 21, and 31, the ground is so strong that the test was completed before reaching 1 m when it had no cone penetration after 50 test strokes ($N_{10} = 50$).

However, point 14 shows that the number of strokes to reach 1 m depth is low, so it indicates low soil resistance. This is also observed in Table 4, where the results obtained from the soil deformability modulus from the plate load test.

Through the results, the road generally presented good compactness ($EV2/EV1 < 2$).

Correlations among test results

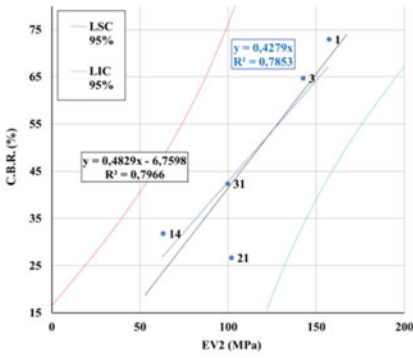
The most commonly used correlations among the test results are those developed from linear functions, as presented below, the lower and upper 95% confidence limits (LIC 95% and LSC 95%, respectively), represented by probability distribution T-Student. This distribution was used due to being suitable for limited samples, as is the case. The confidence interval is the 95% probability of occurring in the desired situation. The correlations between test results are shown in Fig. 5.

Figure 5a shows no correlation of CBR in the laboratory for the same degree of on-site compaction versus plate load test results (EV2 in MPa) using test data at the points selected by homogeneous analyses. The value of R^2 without passing through the origin is 0.7966. However, the correlation between the two parameters is not optimal as the curves define the 95% confidence limits from now on.

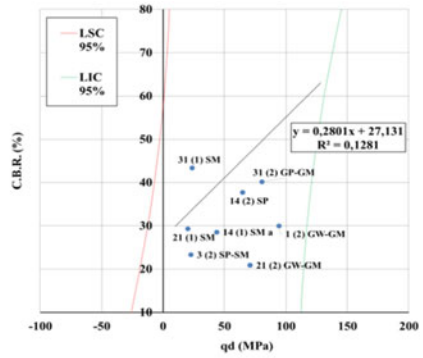
Figure 5b shows no correlation between laboratory CBR results for the same degree of in situ compactions versus q_d obtained using the selected assay data (for layers 1 and 2). As can be seen, there is no correlation between the results of the two types of tests. The linear correlation coefficient is very low (0.1281).

Figure 5c shows the correlation of EV2 versus q_d obtained using data from both test types for all points assessed. A linear correlation coefficient of 0.5038 was obtained, and the defining curves of the lower and upper 95% confidence limits are also well-defined.

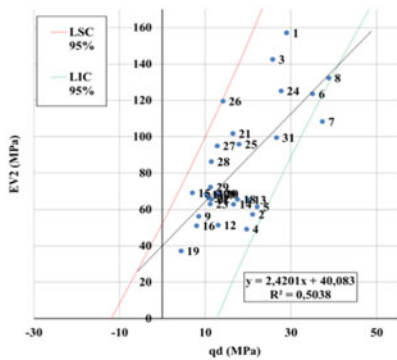
Figure 5d shows the correlation of soil carrying capacity values obtained by the in situ CBR test versus the EV2 values (in MPa) of the plate loading test at the representative points of the sections. A correlation coefficient of 0.9112 was obtained, and it was, therefore, possible to conclude the good linear correlation between these



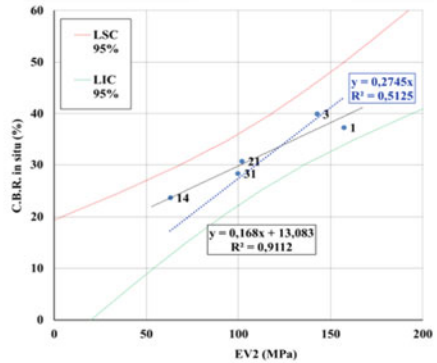
a. CBR laboratory vs EV2



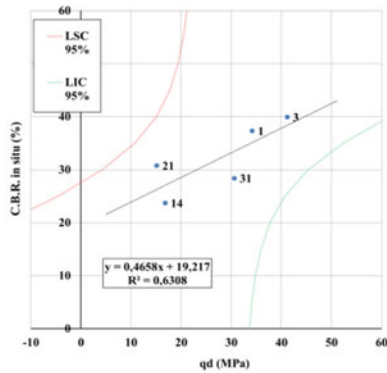
b. CBR laboratory vs q_d (LDP)



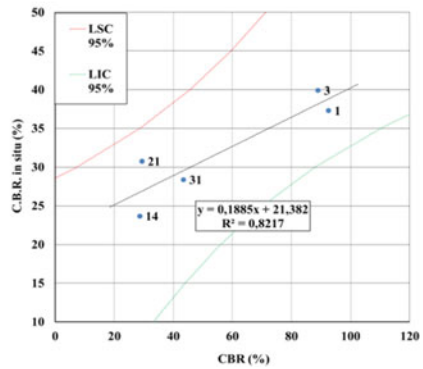
c. EV2 vs q_d



d. CBR in situ vs EV2



e. CBR in situ vs q_d



f. CBR in situ vs CBR laboratory

Fig. 5 Correlations among test results

two parameters. The curves corresponding to the lower and upper 95% confidence limits are also very close to the obtained points.

Figure 5e shows the correlation of CBR in situ versus q_d of the PDL assay obtained using the test results data at representative points of homogeneous sections. A correlation coefficient of 0.6308 was obtained; however, because of the way the correlation is presented, with little pronounced slope, and also because the defining curves of the 95% confidence upper and lower limit are quite far from the results. In the trials, the correlation between these two parameters is weak and unclear.

Figure 5f shows the correlation of the values obtained by the in situ CBR test versus the soil carrying capacity values of the laboratory CBR test for the same degree of in situ compactions at the representative points of the homogeneous sections. A linear correlation coefficient of 0.8217 was obtained. From the results obtained, it is possible to verify that there is a linear correlation between the two parameters obtained (in the laboratory and in the field). The lower and upper 95% confidence limits are also close to the results obtained.

4 Conclusion

In this case study, the unpaved road with low-traffic volume has good soil bearing capacity, and the highway research board (HRB) soil classification has an excellent sub-base function. Thus, with the geotechnical characterization, it can be concluded that the studied road does not need rehabilitation, as they present both good resistance and an adequate granulometric profile for a road.

It can also be concluded that commenting on a structural evaluation isn't possible to analyze the road as a whole, so one should always combine the geotechnical characterization with the functional evaluation so as to elaborate appropriate maintenance and/or rehabilitation plan for the road. This work is a small step toward the creation of a management model for the conservation of unpaved roads, showing the need for evaluation methods (without being structural) to better understand the needs of local maintenance.

This study was used to contribute to the enrichment of existing correlations [13] in the institution between various soil parameters, such as deformability modulus (for the first and second load cycles), peak resistance, soil carrying capacity in the laboratory, for the same degree of compaction in situ and directly in situ.

Acknowledgements The authors thank the Federal University of Technology (UTFPR) and the Polytechnic Institute of Bragança (IPB) for the Double Diplomation program between the entities, which provided the development of this research. They also thank the Bragança City council for providing the necessary resources for this research.

References

1. ACM Fernandes (2016) Low-volume roads pavements civil engineering supervisors : key words
2. Jorge LCDL (2014) Constituição, dimensionamento e conservação de pavimentos para baixos volumes de tráfego. Instituto Superior de Engenharia de Coimbra
3. Beckemeyer CA (1995) Rural road condition survey guide. No. SD95-16-G1
4. Berkshire Regional Planning Commission (2001) The Massachusetts unpaved roads BMP manual: a guidebook on how to improve water quality while addressing common problems. Prepared f
5. Alves MAN (2009) Características Geotécnicas de Estradas Não-pavimentadas do Município de Bauru/ SP. UNICAMP—Faculdade de Engenharia Civil, Dissertação de Mestrado
6. ERA (2011) Design manual for low volume roads, Part A, Part B and Part C. Ethiopia
7. Ministry of Transport and Public Works MTPW (2013) Design manual for low volume sealed roads using the DCP design method. República do Malawi
8. SATCC (2003) Guideline low-volume sealed roads. Botswana
9. SAS Benevides (2006) Modelos de desempenho de pavimentos asfálticos para um sistema de gestão de rodovias estaduais do Ceará. Universidade Federal do Rio de Janeiro, COPPE
10. Haas W, Ralph R, Norman H (2001) Reinventing the (pavement management) wheel
11. American Association of State Highway and Transportation Officials (1993) AASHTO guide for design of pavement structures
12. Alzubaidi H, Magnusson R (2011) Deterioration and rating of gravel roads deterioration and rating of gravel roads state of the art. 0629(2002). <https://doi.org/10.1080/14680629.2002.9689924>
13. Morais H, Minhoto M, Paula AM (2018) Relação entre módulo de deformabilidade e CBR para caracterização mecânica da fundação de pavimentos. In: 16º Congresso Nacional de Geotecnia. Ponta Delgada, Açores, Portugal

Development of Prediction Models for Mechanistic Parameters of Granular Roads Using Combined Non-destructive Tests



Sajjad Satvati, Bora Cetin, and Jeramy C. Ashlock

Abstract Characteristics of the surface aggregate materials are very important for the serviceability and performance of granular roads. Mechanical properties such as strength, abrasion resistance, and stiffness of these materials, along with the thickness of the aggregate surface layer are directly related to the performance of such roads. Therefore, the relationships between these various factors are important and may be used to predict the mechanical behavior of granular roadways. This study proposes statistical univariate and multivariate regression models to predict surface elastic modulus of granular road surfaces using data from falling weight deflectometer (FWD) and multichannel analysis of surface waves (MASW) tests. Stepwise regression analyses were performed to develop the models, and statistically significant independent variables were sought among the shear strength, density, thickness, moisture content, fines content, and gravel-to-sand ratio of the aggregate surface layer. Statistical analyses demonstrated that factorial multivariate models with inclusion of interaction between independent variables were useful for predicting the elastic modulus of granular road surfaces.

Keywords Granular roads · Elastic modulus · Shear strength · Multichannel analysis of surface waves · Falling weight deflectometer

1 Introduction

Typical long-term performance monitoring of roads includes field measurements of material quality and roadway structural stability, and how these parameters are affected by weather conditions and traffic volume [1–6]. Non-destructive field tests

S. Satvati
Terracon Consultants, Inc, Omaha, NE 68144, USA

B. Cetin (✉)
Michigan State University, East Lansing, MI 48824, USA
e-mail: cetinbor@msu.edu

J. C. Ashlock
Iowa State University, Ames, IA 50011, USA

are the most common methods used to measure the elastic modulus of granular roadways. Lightweight deflectometer (LWD) [7–9], falling weight deflectometer (FWD) [10–12], seismic cone penetration (SCPTs) [13, 14], multichannel analysis of surface waves (MASW) [15–20], and spectral analysis of surface waves (SASW) [21–23] tests are well-established methods for elastic modulus measurement of unbound materials at different stress and strain levels. Although these tests are common, various restrictions such as space, cost, and noise limit their universal utilization for performance evaluation. In addition, field tests have proven to be rather expensive and time-consuming. Because of the aforementioned drawbacks, it is useful to develop new approaches employing statistical methods to correlate surface elastic modulus to simpler geotechnical parameters such as index properties, and the structural and weather-related conditions of the road layers. Statistical approaches are powerful tools often used to find correlations between modulus and geotechnical parameters of unbound materials. Most studies have attempted to correlate modulus to stress, California bearing ratio (CBR), fines content, plasticity limit, and moisture content [24–28]. While such studies are plentiful for paved roads, research toward the development of performance prediction for granular roadways is comparatively limited.

To respond to this need, the present study is focused on development of a model to practically and easily predict in situ elastic modulus of surface aggregate layers of granular roadways using generalized regression analyses. Statistical modeling was used to correlate the following parameters: CBR, density, thickness, moisture content, fines content, and gravel-to-sand (G/S) ratio to the predicted surface elastic modulus, and validated via comparison to elastic modulus values obtained from FWD and MASW tests. The proposed model is based on previous field data measurements on several granular road test sections. The present study also investigated (1) the impact of different soil material properties on actual surface elastic modulus; (2) performance of univariate analysis to predict the surface elastic modulus from different factors; and (3) assessment of multivariate linear and factorial prediction models. The proposed models provide an approach for more accurate and simpler prediction of the elastic modulus of granular roadway surfaces.

2 Data Collection and Methods

Sieve analyses, DCP, nuclear gauge, FWD, and MASW tests were performed on 35 points of eight granular road test sections located on CR J22 Popcorn Road in Decatur County, Iowa. DCP tests were used to determine shear strength and thicknesses of the granular surface layer, nuclear gauge tests were used to determine the in situ moisture content and density of the surface aggregate materials, and MASW and FWD tests were performed to measure the surface elastic modulus of each point. Field tests and sample collection for sieve analyses were conducted on the same day.

2.1 FWD and MASW Test Results

FWD tests were conducted to measure the surface elastic modulus using a SN121 JILS model FWD device with a 300 mm diameter segmented loading plate. For each test location, a 5.3 kN seating load was applied followed by dynamic contact forces ranging from 17 to 22 kN. Boussinesq's solution was used to obtain stress, strain, and deformation at selected depths and radii in a homogeneous, linear-elastic half-space, and Odemark's theory was used to obtain an equivalent layer thickness and match the measured surface deflections to calculate deflections over the equivalent layer [17]. In accordance with the combined Boussinesq–Odemark theory, back-calculation was performed based on dynamic loads and peak deflections observed at the geophone locations on the two-layered system [29–34].

The MASW device used for this study had 24 vertical 4.5 Hz geophones attached to a steel land streamer to ensure good contact with the granular road surface. Such geophone mounting produces data in a shorter time than using spikes to fix the geophones to the ground surface. All receivers were connected to a 24-channel Geometrics Geode seismograph. The triggering load applied for the MASW test was much smaller than that applied during the FWD test; it was produced by using a 945 g hammer to strike a 2.5-cm-thick-15 cm² aluminum plate used to couple the impact energy from the hammer with the surface layer. Using such a base plate as a coupler mechanism improves conversion of the impact energy of the hammer into seismic wave energy [35]. The phase-velocity and intercept-time scanning (PIS) method [29] was used to generate the dispersion curves by transferring the space–time domain data to the space–frequency domain. Then a hybrid genetic-simulated annealing optimization algorithm (GSA) was employed for the inversion procedure [36]. Poisson's ratios for the surface and subgrade layers were assumed to be 0.3 and 0.4, respectively. The thicknesses of the surface layers were determined from DCP tests, with the subgrade layer thickness assumed to be infinite for a two-layered system. The shear and elastic modulus values for the surface and subgrade layers were then calculated using Eqs. (1) and (2);

$$G = \rho V_s^2 \quad (1)$$

$$E = 2G(1 + \nu) \quad (2)$$

where G is shear modulus (kPa), ρ is the dry density of the surface and the subgrade materials (kg/m³), ν is Poisson's ratio, V_s is shear wave velocity (m/s) from the inversion procedure, and E is elastic modulus (kPa).

3 Data Modeling

The Pearson correlation test was conducted before developing univariate and multivariate models to evaluate the correlations between both dependent and independent factors. The correlation factor shows the strength of a linear relationship between each pair of variables; a value of zero indicates no relationship between two variables, a correlation factor of 1 indicates a perfect direct linear relationship and a correlation factor of -1 indicates a perfect inverse linear relationship. Then, the analysis began with a univariate linear regression. In this study, surface elastic modulus values from MASW (E_{MASW}) and FWD (E_{FWD}) tests are the response variables, while CBR correlated from DCP tests (CBR_{DCP}) and the density (γ), surface layer thickness (h), moisture content (ω), fines content (F), and gravel-to-sand ratio (G/S) are the independent variables or predictors. Linear regression has several key assumptions that need to be validated. Three different forms of the most widely used univariate models proposed to predict the E_{MASW} and E_{FWD} are the simple linear, second-order polynomial, and exponential models. For an independent variable X among several exogenous variables, these three models are expressed, respectively, as follows:

$$E = \beta_0 + \beta_1 X \quad (3)$$

$$E = \beta_0 + \beta_1 X + \beta_2 X^2 \quad (4)$$

$$E = \beta_0 + \beta_1 e^X \quad (5)$$

where E = predicted surface elastic modulus values as a function of X ; X = reported values of independent variables; and β_i = coefficients estimated from the data using the maximum likelihood estimation method (MLE).

Further, two multivariate models were developed for both E_{MASW} and E_{FWD} ; (1) a linear model including all independent factors, and (2) a full factorial model considering all possible combinations of the independent factors. Equations (6) and (7), respectively, show the full linear and factorial models for E as the dependent variable and X_i and X_j as independent variables.

$$E = \beta_0 + \sum_{i=1}^n \beta_i X_i \quad (6)$$

$$E = \beta_0 + \sum_{i=1}^n \beta_i X_i + \sum_{i=1}^n \beta_{n+i} X_i \left(\sum_{j=1}^n X_j \right) \quad (7)$$

In order to use the limited number of data sets efficiently in this study (35 points), a fivefold cross-validation scheme was used for both univariate and multivariate predictive models. In this regard, cross-validation randomly divides the data into

five equal-sized subsets while one subset remains for validation and the other four subsets are used as training sets [37]. The best validation statistics will be selected among all five models as the final model. Residuals were assessed for multivariate models by fitting their results to the actual E_{MASW} and E_{FWD} data to find the best model which has residuals that are unstructured and randomly distributed [38, 39]. Finally, the Akaike information criterion (AIC) and Bayesian information criterion (BIC) methodologies were investigated and compared for optimizing each model and assessing the quality of the models obtained by the cross-validation methodology. These methodologies help to deliberate between the models' complexity and quality and compensate for overfitting [40, 41].

4 Results and Discussion

4.1 Univariate Models

Figure 1 demonstrates the Pearson correlation between the investigated properties. The squares above the diagonal contain the correlation coefficients between the elastic modulus values calculated by MASW (E_{MASW}) or FWD (E_{FWD}), and the CBR_{DCP} , density, thickness, moisture content, fines content, and G/S ratios. The squares below the diagonal contain the corresponding correlation graphs between the aforementioned variables. The results show that correlation between E_{MASW} and E_{FWD} results is not significant ($R^2 = 0.4$), which is expected due to the different procedures, and most importantly the differences in stress/strain levels applied for these two tests [17]. Correlations among the remaining variables were not significant, except for values of E_{FWD} which showed stronger correlation with F compared to the rest of the variables.

The statistical parameters determined through the simple regression analysis of all three univariate models (Eqs. 3–5) to predict the E_{MASW} and E_{FWD} are given in Tables 1 and 2. The statistical values in Table 1 are R^2 and F_{test} , where they, respectively, indicate the proportion of the variance for a dependent variable based on an independent variable, and the “Lack of Fit Test,” while a small F_{test} value indicates a significant lack of fit. Table 1 shows that the polynomial model worked better for univariate models involving CBR, density, thickness, moisture content, and G/S ratio, while the exponential model was the best for fines content as the independent factor for predicting E_{MASW} . However, the polynomial model was the best for predicting E_{FWD} using all independent variables. R^2 values for univariate models showed that all models for all independent variables were not powerful for predicting E_{MASW} , as the maximum R^2 value was 0.1 for the exponential univariate model with fines content as the independent variable (Table 1). The same results were also observed for univariate models to predict E_{FWD} , where the highest R^2 value was 0.29 for the polynomial univariate model with fines content as the independent

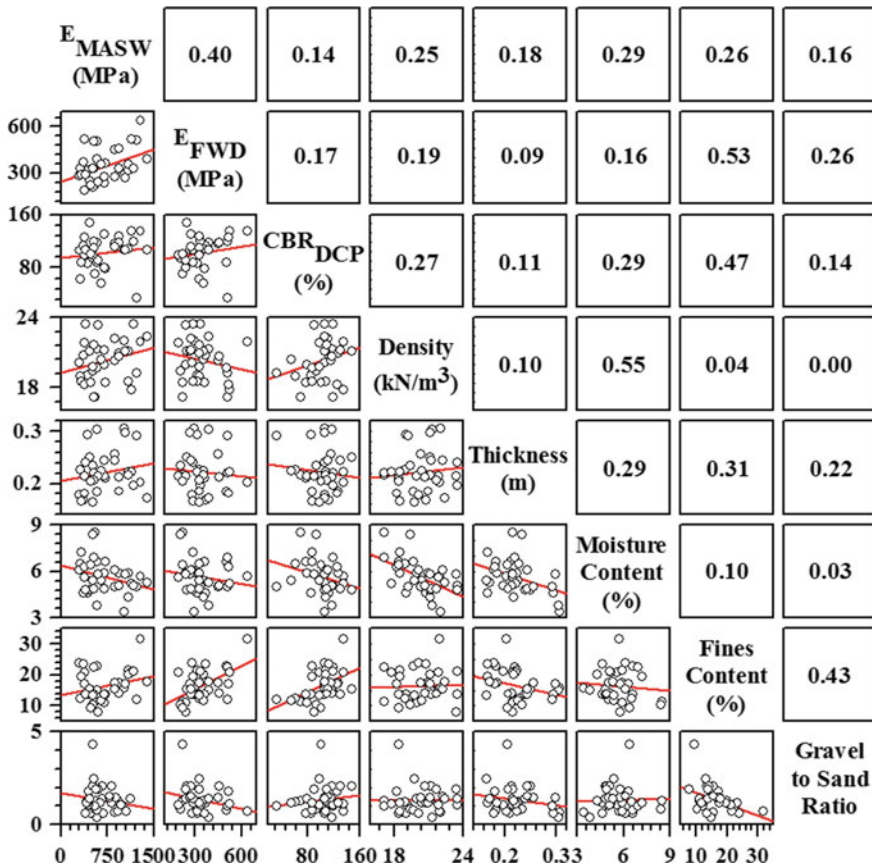


Fig. 1 Pearson correlation results among different variables

variable (Table 2). The maximum R^2 values for CBR_{DCP} , fines content, and gravel-to-sand ratio variables were higher than other independent variables for the predictive univariate models indicating these models were more effective in prediction of FWD surface elastic modulus values. However, density, thickness, and moisture content had higher R^2 values for prediction of MASW surface elastic modulus values by the univariate models.

4.2 Multivariate Models

Two multiple predictive regression models (Eqs. 6 and 7) were developed through linear and full factorial statistical methodologies to determine the most adequate

Table 1 Univariate regression models to estimate E_{MASW} from different factors

Factors	E_{MASW} (MPa)			
	Model	Equations	R^2	F_{test}
CBR _{DCP} (%)	Linear	$547.73 + 1.29CBR$	0.02	0.41
	Polynomial	$387.39 + 2.48CBR + 0.07(CBR - 102.68)^2$	0.09	0.22
	Exponential	$684.62 - 8.54 \times 10^{-63}e^{CBR}$	0.02	0.44
Density (kN/m ³)	Linear	$47.84 - 31.09\gamma$	0.06	0.14
	Polynomial	$43.32 + 31.07\gamma + 1.66(\gamma - 20.33)^2$	0.07	0.34
	Exponential	$663.16 + 7.02 \times 10^{-9}e^\gamma$	0.02	0.43
Thickness (m)	Linear	$467.13 + 956.11h$	0.03	0.30
	Polynomial	$463.56 + 978.21h - 876.92(h - 0.22)^2$	0.03	0.59
	Exponential	$-263.34 + 754.46e^h$	0.03	0.30
Moisture content (%)	Linear	$993.52 - 55.52\omega$	0.08	0.09
	Polynomial	$973.48 - 50.38\omega - 7.74(\omega - 5.65)^2$	0.09	0.23
	Exponential	$706.3 - 0.05e^\omega$	0.05	0.19
Fines content (%)	Linear	$502.47 + 10.74F$	0.07	0.14
	Polynomial	$509.31 + 10.04F + 0.2(F - 16.51)^2$	0.07	0.33
	Exponential	$668.61 + 7.11 \times 10^{-12}e^F$	0.10	0.07
Gravel-to-sand ratio	Linear	$742.69 - 47.49G/S$	0.03	0.35
	Polynomial	$724.34 - 29G/S - 12.32(G/S - 1.33)^2$	0.03	0.62
	Exponential	$695.56 - 2.66 \times e^{G/S}$	0.02	0.38

model for prediction of MASW and FWD elastic modulus values. First, the five-fold cross-validation analyses were carried out on all stepwise regression models and confirmed by AIC and BIC criteria to penalize the complexity and overfitting. Equations (8) and (9) show the linear multivariate predictive regression models for E_{MASW} and E_{FWD} , respectively;

$$E_{MASW} = -284.90 - 0.93CBR + 24.43\gamma + 1424.04h - 12.75\omega + 17.21F + 26.16G/S \tag{8}$$

$$E_{FWD} = 893.04 - 0.37CBR - 23.36\gamma - 94.11h - 34.55\omega + 11.27F - 2.53G/S \tag{9}$$

Table 3 shows the significance of each independent variable in the linear multivariate predictive models to find E_{MASW} and E_{FWD} . ‘‘Std Error’’ is defined as the ‘‘Standard Deviation’’ of the resultant values from mean, which calculates by dividing the root mean square ‘‘RMSE’’ by the square root of the independent values. ‘‘P Value’’

Table 2 Univariate regression models to estimate E_{FWD} from different factors

Factors	E_{FWD} (MPa)			
	Model	Equations	R^2	F_{test}
CBR _{DCP} (%)	Linear	$269.18 + 0.75CBR$	0.03	0.34
	Polynomial	$148.2 + 1.66CBR + 0.05(CBR - 102.68)^2$	0.18	0.04
	Exponential	$349.34 - 4.98 \times 10^{-69}e^{CBR}$	0.02	0.37
Density (kN/m ³)	Linear	$581.22 - 11.55\gamma$	0.03	0.28
	Polynomial	$582.21 - 11.54\gamma - 0.36(\gamma - 20.33)^2$	0.03	0.57
	Exponential	$357.35 - 4.585 \times 10^{-9}e^{\gamma}$	0.03	0.31
Thickness (m)	Linear	$398.76 - 234.97h$	0.01	0.62
	Polynomial	$422.73 - 383.37h + 5887.84(h - 0.22)^2$	0.02	0.75
	Exponential	$572.35 - 180.67e^{ht}$	0.02	0.63
Moisture content (%)	Linear	$436.2 - 15.87\omega$	0.03	0.35
	Polynomial	$401.58 - 6.99\omega - 13.38(\omega - 5.65)^2$	0.08	0.27
	Exponential	$363.15 - 0.03e^{\omega}$	0.08	0.10
Fines content (%)	Linear	$161.27 + 11.22F$	0.28	0.00
	Polynomial	$173.7 + 9.94F + 0.35(F - 16.51)^2$	0.29	0.00
	Exponential	$337.95 + 5.46 \times 10^{-12}e^F$	0.22	0.00
Gravel-to-sand ratio	Linear	$397.95 - 38.82G/S$	0.07	0.13
	Polynomial	$396.06 - 36.92G/S - 1.27(G/S - 1.33)^2$	0.07	0.33
	Exponential	$358.57 - 2.03 \times e^{G/S}$	0.05	0.19

Table 3 Parameter estimates for linear multivariate predictive models for E_{MASW} and E_{FWD}

Term	E_{MASW}		E_{FWD}	
	Std error	P value	Std error	P value
Intercept	911	0.76	400	0.03
Fines content (%)	12	0.15	5	0.04
Density (kN/m ³)	26	0.35	11	0.05
Moisture content (%)	45	0.78	20	0.09
CBR _{DCP}	2	0.65	1	0.68
Thickness (m)	1227	0.26	539	0.86
Gravel-to-sand ratio	70	0.71	31	0.94

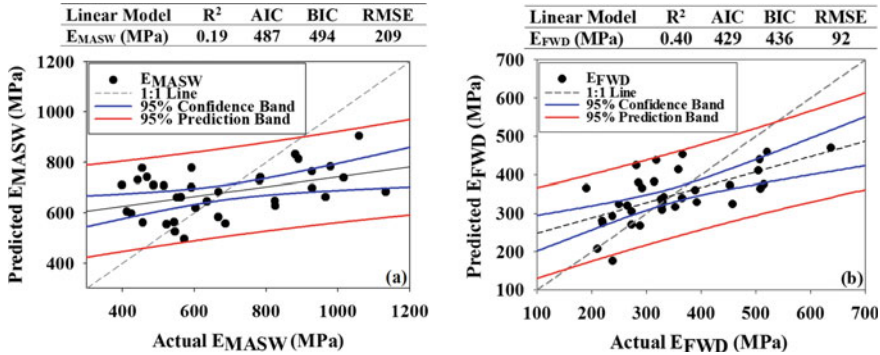


Fig. 2 Actual versus predicted values from linear models for a E_{MASW} and b E_{FWD}

is the probability of obtaining a different value than the actual results in a predictive model. According to the results, the intercept, F , and γ had the most significant contribution for the 95% confidence level in the E_{FWD} predictive model, and the significance of CBR, h , and G/S was the lowest (Table 3). For E_{MASW} linear multivariate predictive model, although none of the independent variables had significant contributions into the model, the contribution of CBR_{DCP}, G/S, intercept, and ω was the lowest.

As shown in Fig. 2, the correlations between actual and predicted values of E_{FWD} ($R^2 = 0.4$) matched better than E_{MASW} ($R^2 = 0.19$) for linear multivariate models. “Confidence” and “Prediction” bands indicate uncertainty of the function and new data points, respectively, in regression results in the statistical analyses. Moreover, lower AIC and BIC values and RMSE for E_{FWD} relative to E_{MASW} linear multivariate models indicate higher quality for the E_{FWD} predictive model.

Table 4 shows the parameter estimates for factorial multivariate predictive models for E_{MASW} and E_{FWD} . Parameters with log worth ($-\log(p \text{ value})$) higher than 0.1 were sorted based on their significance in the models and the parameters. Interaction of $h \times F$, $h \times G/S$, ω^2 , F , ω , intercept, $DCP \times h$, and $\gamma \times \omega$ was the most significant parameters for the E_{MASW} factorial multivariate model. On the other hand, F , $CBR \times \omega$, $CBR \times h$, $\gamma \times F$, $F \times G/S$, $\omega \times F$, $\gamma \times G/S$, and $h \times G/S$ were the most significant parameters with 95% confidence level for the E_{FWD} factorial multivariate model (Table 4).

Figure 3a and b shows that there is a better agreement between the actual and the predicted elastic modulus values for FWD compared to MASW, where the R^2 for factorial multivariate models for E_{FWD} and E_{MASW} was equal to 0.77 and 0.7, respectively. Correlations between the predicted and the actual results for E_{FWD} were still better than E_{MASW} . Moreover, lower AIC and BIC values and root mean square error (RMSE) for E_{FWD} over E_{MASW} factorial multivariate models showed higher quality for the E_{FWD} predictive model. However, comparisons between the results shown in Figs. 2 and 3 prove that factorial multivariate models for both E_{MASW} and E_{FWD} produce significantly better predictions compared to the linear models. Therefore, the

Table 4 Parameter estimates for factorial multivariate predictive models for E_{MASW} and E_{FWD}

E_{MASW}				E_{FWD}			
Term	SE ¹	PV ²	LW ³	Term	SE	PV	LW
$(h - 0.22)(F - 16.51)$	653	<0.01	2.82	F	6	<0.01	2.52
$(h - 0.22)(G/S - 1.33)$	3901	0.01	1.90	$(CBR - 102.68)(\omega - 5.65)$	3	0.01	1.91
$(\omega - 5.65)^2$	67	0.02	1.68	$(CBR - 102.68)(h - 0.22)$	58	0.01	1.91
F	11	0.02	1.65	$(\gamma - 20.33)(F - 16.51)$	5	0.02	1.81
ω	53	0.03	1.52	$(F - 16.51)(G/S - 1.33)$	25	0.02	1.74
Intercept	556	0.04	1.44	$(\omega - 5.65)(F - 16.51)$	14	0.02	1.74
$(CBR - 102.68)(h - 0.22)$	59	0.04	1.39	$(\gamma - 20.33)(G/S - 1.33)$	58	0.04	1.44
$(\gamma - 20.33)(\omega - 5.65)$	58	0.04	1.36	$(h - 0.22)(F - 16.51)$	265	0.04	1.42
$(h - 0.22)^2$	30,080	0.1	1.00	$(G/S - 1.33)^2$	59	0.08	1.09
$(CBR - 102.68)(\gamma - 20.33)$	1	0.12	0.92	$(h - 0.22)(\omega - 5.65)$	929	0.09	1.06
$(\omega - 5.65)(F - 16.51)$	15	0.13	0.89	$(\gamma - 20.33)(\omega - 5.65)$	25	0.09	1.04
$(\gamma - 20.33)^2$	16	0.21	0.69	$(F - 16.51)^2$	2	0.09	1.04
H	1555	0.24	0.63	$(CBR - 102.68)^2$	0	0.17	0.77
$(G/S - 1.33)^2$	103	0.25	0.61	$(\omega - 5.65)^2$	35	0.18	0.73
$(F - 16.51)(G/S - 1.33)$	37	0.29	0.54	$(CBR - 102.68)(G/S - 1.33)$	4	0.21	0.69
$(F - 16.51)^2$	2	0.31	0.51	$(CBR - 102.68)(F - 16.51)$	1	0.31	0.51
$(\gamma - 20.33)(h - 0.22)$	933	0.31	0.51	H	596	0.47	0.33
$(\omega - 5.65)(G/S - 1.33)$	126	0.40	0.40	ωs	25	0.52	0.28
$(CBR - 102.68)(G/S - 1.33)$	6	0.47	0.32	Intercept	269	0.53	0.28
$(CBR - 102.68)^2$	0	0.56	0.25	$(h - 0.22)(G/S - 1.33)$	1578	0.67	0.17
				$(\gamma - 20.33)(h - 0.22)$	497	0.78	0.11

¹Standard error, ²P value, ³Logworth

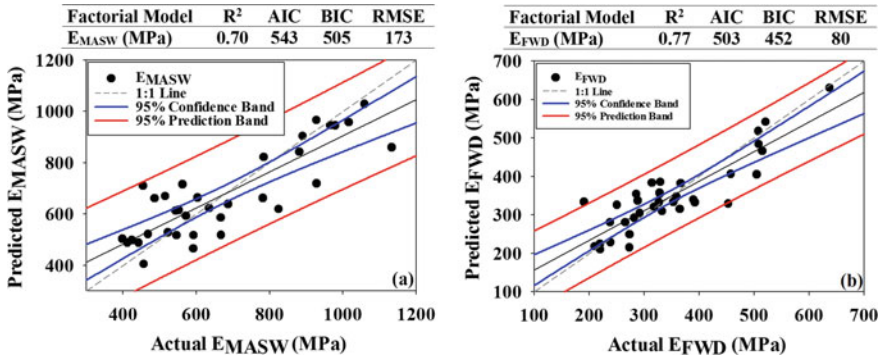


Fig. 3 Actual versus predicted values from factorial models for a E_{MASW} and b E_{FWD}

inclusion of interactions between independent variables in multivariate models helps to increase the correlation between the predicted and actual results of elastic modulus for both MASW and FWD tests and the likelihood of the model. However, this may result in overfitting. Accordingly, AIC and BIC are used to penalize the overfitting in the models [38]. Although the results of the factorial multivariate analysis showed better fitting with higher R^2 values compared to the linear multivariate model, the lower number of variables in the linear multivariate models, as highlighted in Fig. 2, caused lower AIC and BIC values for linear multivariate model.

Figure 4 shows the residual plots of the linear and factorial multivariate models for prediction of both E_{FWD} and E_{MASW} . All the residual plots are similar in terms of being randomly scattered around zero and having no structure and are therefore adequate for statistical predictions. However, lower dispersion was observed for factorial models compared to linear models for both E_{MASW} and E_{FWD} . Moreover, lower RMSE confirms that the equations derived based on factorial multivariate regression were the most adequate model for predicting the E_{FWD} and E_{MASW} . Therefore, the proposed factorial models seemed more adequate for predictions.

5 Conclusions

This study used the results of independent factors including CBR_{DCP} , thickness, and density of the surface layer, moisture content, fines content, and gravel-to-sand ratio to investigate their suitability for the prediction of the granular road surface elastic modulus. The predicted results were compared to the results of field MASW and FWD tests, of which the non-destructive test methods to determine the stiffness of the pavement layers in a timely manner. Fivefold cross-validation was used to develop univariate models, as well as linear and factorial multivariate models. Based on the results reported herein, the following main conclusions can be drawn:

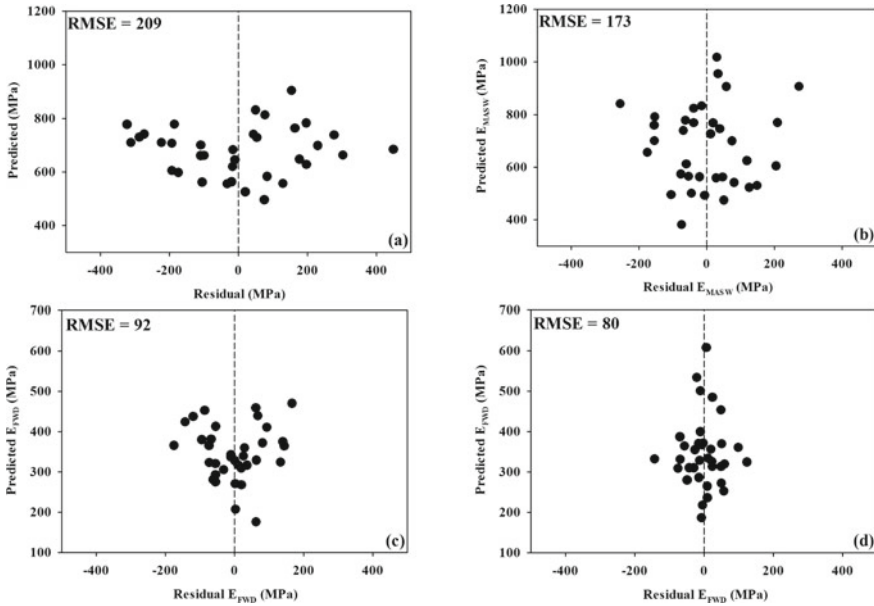


Fig. 4 Residual plots of the proposed models: **a** E_{MASW} linear; **b** E_{MASW} factorial; **c** E_{FWD} linear; and **d** E_{FWD} factorial

- There is a poor correlation between elastic modulus values for FWD and MASW and independent variables. Therefore, univariate models are not suitable to develop predictive models for predicting elastic modulus of the granular surface course.
- Linear multivariate models with inclusion of all independent variables had higher likelihood compared to the univariate models for both E_{MASW} and E_{FWD} .
- Correlations between predicted and actual results for factorial multivariate models with the inclusion of interaction between independent variables were higher than linear multivariate models for both E_{MASW} and E_{FWD} . However, the inclusion of a higher number of factors increased overfitting. This was also confirmed through regression analysis, AIC, and BIC measures.
- It is recommended to use factorial multivariate models over linear multivariate models due to the greater agreement between predicted and actual elastic modulus values for both FWD and MASW. However, further validation and expansion of this study to other elastic modulus constitutive models are suggested for future studies.

References

1. Gopiseti LSP, Cetin B, Forman BA, Durham S, Schwartz CW, Ceylan H (2019) Evaluation of four different climate sources on pavement mechanistic-empirical design and impact of surface shortwave radiation. *Int J Pavement Eng* 1–14
2. Satvati S, Cetin B, Ashlock JC, Ceylan H, Rutherford C (2020) Binding capacity of quarry fines for granular aggregates. In: ASCE geo-congress
3. Wu Y, Ashlock JC, Cetin B, Satvati S, Li C, Ceylan H (2020) Mechanistic performance evaluation of chemically and mechanically stabilized granular roadways. In: *Geo-congress 2020: geotechnical earthquake engineering and special topics*, pp 591–601
4. Mahedi M, Satvati S, Cetin B, Daniels JL (2020) Chemically induced soil water repellency and the Freeze-Thaw durability of soils. *J Cold Reg Eng*
5. Farhangi V, Karakouzian M (2020) Effect of fiber reinforced polymer tubes filled with recycled materials and concrete on structural capacity of pile foundations. *Appl Sci* 10(5):1554
6. Ashtiani RS, Morovatdar A, Licon C, Tirado C, Gonzales J, Rocha S (2019) Characterization and quantification of traffic load spectra in texas overweight corridors and energy sector zones
7. Satvati S, Ashlock JC, Nahvi A, Jahren CT, Cetin B, Ceylan H (2019) A novel performance-based economic analysis approach: case study of iowa low volume roads. In: 12th TRB international conference on low-volume roads
8. Vennapusa PKR, White DJ (2009) Comparison of light weight deflectometer measurements for pavement foundation materials. *Geotech Test J* 32(3):239–251
9. Grasmick JG (2013) Using the light weight deflectometer with radial offset sensors on two-layer systems for construction quality control/quality assurance of reclaimed and stabilized materials
10. Ullidtz P, Askegaard V, Sjølin F (1996) Normal stresses in a granular material under falling weight deflectometer loading. *Transp Res Rec* 1540(1):24–28
11. Gopalakrishnan K, Papadopoulos H (2011) Reliable pavement backcalculation with confidence estimation. *Sci Iran* 18(6):1214–1221
12. Satvati S (2020) Benefit cost analysis of aggregate options for a granular roadway
13. Robertson PK, Campanella RG, Gillespie D, Rice A (1986) Seismic CPT to measure in situ shear wave velocity. *J Geotech Eng* 112(8):791–803
14. Campanella RG, Robertson PK, Gillespie D (1983) Cone penetration testing in deltaic soils. *Can Geotech J* 20(1):23–35
15. Park C, Ivanov J, Miller RD, Xia J, Ryden N (1999) Multichannel analysis of surface waves (MASW) for pavement : feasibility test May 2017
16. Coe P, Mahvelati JT, Asabere S (2016) A case study of multichannel analysis of surface waves (MASW) as a tool to characterize unknown foundations. In: *International conference on deep foundations, seepage control and remediation (41st annual)*, p 9
17. Li C, Ashlock JC, Lin S, Vennapusa PKR (2018) In situ modulus reduction characteristics of stabilized pavement foundations by multichannel analysis of surface waves and falling weight deflectometer tests. *Constr Build Mater* 188:809–819
18. Lin S, Ashlock JC (2014) Multimode rayleigh wave profiling by hybrid surface and borehole methods. *Geophys J Int* 197(2):1184–1195
19. Cetin B, Satvati S, Ashlock JC, Jahren CT (2019) Performance-based evaluation of cost-effective aggregate options for granular roadways. Ames, IA
20. Morovatdar A, Ashtiani R, Licon C, Tirado C (2019) Development of a mechanistic approach to quantify pavement damage using axle load spectra from South Texas overload corridors. In: *Geo-structural aspects of pavements, railways, and airfields conference, (GAP 2019)*
21. Nazarian S (1983) Use of spectral analysis of surface waves method for determination of moduli and thicknesses of pavement systems.pdf. *Transp Res Board* 930:38–45
22. Nazarian S, Stokoe KH (1985) In situ determination of elastic moduli of pavement systems by spectral analysis of surface waves method (practical aspects), Report No. FHWA/TX-86/13 + 368-IF 2, p 190

23. Stokoe (1994) Characterization of geotechnical sites by SASW method.pdf
24. Mazari M, Nazarian S (2017) Mechanistic approach for construction quality management of compacted geomaterials. *Transp Geotech* 13:92–102
25. Puppala AJ (2008) Estimating stiffness of subgrade and unbound materials for pavement design, vol. 382. *Transp Res Board*
26. Tutumluer E (2013) Practices for unbound aggregate pavement layers, no. Project 20-05, Topic 43-03
27. Xiao Y, Tutumluer E, Mishra D (2015) Performance evaluations of unbound aggregate permanent deformation models for various aggregate physical properties. *Transp Res Rec* 2525(1):20–30
28. Satvati S, Cetin B, Ashlock JC (2020) Investigation of the performance of different surface aggregate materials of an unpaved road. In: *ASCE geo-congress*
29. Stokoe KH, Wright SG, Bay JA, Roesset JM (1994) Characterization of geotechnical sites by SASW method. pp 15–25
30. Saltan M, Uz VE, Aktas B (2013) Artificial neural networks-based backcalculation of the structural properties of a typical flexible pavement. *Neural Comput Appl* 23(6):1703–1710
31. Boussinesq J (1885) *Application des potentiels à l'étude de l'équilibre et du mouvement des solides élastiques*. Gauthier-Villars
32. Grasmick J, Voth M, Asce AM, Senseney C, Asce M (2014) Capturing a layer response during the curing of stabilized earthwork using a multiple sensor lightweight deflectometer. *J Mater Civ Eng* 27(6):1–12
33. Odemark N (1949) Investigations as to the elastic properties of soils and design of pavements according to the theory of elasticity
34. Li C, Ashlock JC, White DJ, Vennapusa PKR (2017) Mechanistic-based comparisons of stabilised base and granular surface layers of low-volume roads. *Int J Pavement Eng* 8436:1–13
35. Mereu RF, Uffen RJ, Beck AE (1963) The use of a coupler in the conversion of impact energy into seismic energy. *Geophysics* 28(4):531–546
36. Lin S (2014) Advancements in active surface wave methods modeling, testing, and inversion
37. Krzanowski W (2000) *Principles of multivariate analysis*, vol 23. OUP Oxford
38. Draper NR, Smith H (1998) *Applied regression analysis*, vol 326. Wiley
39. Hjorth JSU (2017) *Computer intensive statistical methods: validation, model selection, and bootstrap*. Routledge
40. Dziak JJ, Coffman DL, Lanza ST, Li R, Jermiin LS (2019) Sensitivity and specificity of information criteria. *bioRxiv*, 449751
41. Amini K, Wang X, Delatte N (2018) Statistical modeling of hydraulic and mechanical properties of pervious concrete using nondestructive tests. *J Mater Civ Eng* 30(6):4018077

Influence of Foundation Layer Properties in a Roller-Compacted Concrete Pavement System Subjected to Heavy Vehicle Loads



Nancy Aguirre, Abbasali Taghavighalesari, Richard Rogers, Cesar Carrasco, and Soheil Nazarian

Abstract The current design methods of concrete pavements assume that the pavement layers will experience stresses/strains that are within their elastic limits. The increase in industrial traffic has led pavement engineers to increase the thickness of the concrete layer to withstand the heavy loads without considering the impact on the foundation layers resulting, in some cases, in premature failure. This highlights the importance of relying on an analysis tool capable of accurately predicting the responses of each pavement layer to ensure that the design limits are not exceeded. Current rigid pavement analysis tools model the supporting layers as a single bed of spring elements (Winkler foundation), which leads to a design process that primarily focuses on the concrete layer and overlooks the advantages or disadvantages of considering specific material properties for each supporting layer. To overcome this limitation, researchers from The University of Texas at El Paso have incorporated a three-dimensional solid foundation model into a finite element analysis tool called rigid pavement analysis system (RPAS). In this study, a comparison between the Winkler and three-dimensional solid foundation models in RPAS has been carried out to evaluate the effects that heavy vehicle loads may have on the responses of roller-compacted concrete (RCC) pavements. The results show that the supporting layer responses are greatly affected by the heavy vehicle loads and ultimately have a significant impact on the overall RCC pavement performance. Additionally, the results show the benefits of using stabilizing materials to optimize the pavement structure by reducing the thickness of the concrete pavement layer and increasing the stabilized foundation layer thickness.

Keywords Concrete pavements · Roller-compacted concrete pavements · Heavy vehicle loads · Elastic limits · Winkler foundation · Finite element analysis · 3D solid foundation

N. Aguirre (✉) · A. Taghavighalesari · C. Carrasco · S. Nazarian
The University of Texas At El Paso, El Paso, TX 79968, USA
e-mail: naguirre@cementx.org

N. Aguirre · R. Rogers
Cement Council of Texas, Hurst, TX 76054, USA

1 Introduction and Background

In the current design procedure of concrete pavements, the contribution of the foundation layers is defined as the strength of the foundation, and it is quantified as the modulus of subgrade reaction or k -value. The calculation of the k -value is an approximated value, and it is defined as the reaction of the subgrade per unit area of deformation typically given in psi/in or pci. When a base layer is included, a composite or equivalent k -value is calculated, which varies in magnitude depending on the material properties and whether the base is treated or untreated. Compared to unstabilized bases, stabilized bases provide a higher degree of support to the pavement layer and, as a consequence, result in higher k -values. In the current design procedure, it is assumed that the concrete layer thickness is not significantly affected by variations of subgrade or composite k -values [1]. However, a study on thin concrete pavements by Cervantes and Roesler [2] determined that when the concrete slab's geometry is optimized, the base and subgrade stiffness (k -value) does play an important role in designing for the slab's thickness. Furthermore, it has been demonstrated that for thinner concrete pavements the accumulation of deformations in the underlying layers is much more critical than previously assumed, which can lead to pumping, erosion, and permanent deformation of concrete pavements [2, 3].

The constant increase in vehicle traffic and heavy axle loads in highways and industrial facilities has led pavement engineers to thicken concrete pavements and, in some cases, to include stabilized base layers as a method to reduce pavement distresses. The use of stabilized base layers offers considerable resistance to erosion and pumping, improves load transfer efficiency, can reduce pavement cracking and improves foundation support (increased k -value) and thereby improves the load carrying capacity of the pavement structure [4–8]. However, while a higher k -value is beneficial in reducing stresses imposed by wheel loads, its effectiveness in doing that decreases with increasing thickness of the concrete layer. For example, for a given slab's thickness and joint spacing in a jointed concrete pavement (JCP) system, increasing the foundation k -value can actually increase the curling and warping slab stresses induced by temperature and moisture gradients, respectively. Depending on the combinations of slab thicknesses and joints spacing, the slab stresses for a higher k -value can be higher than for a lower k -value.

With the increasing use of stabilized base layers in a concrete pavement system, it is important to rely on a tool capable of considering a system approach, in which the pavement is designed as a system, as opposed to the common component approach, to ensure that the appropriate concrete pavement design combination for a particular site and loading conditions is achieved. For this reason, researchers from the University of Texas at El Paso (UTEP) continue to enhance the rigid pavement analysis system (RPAS) [9], an analysis tool for evaluating the responses (stresses, strains, and deformations) of concrete pavement systems under environmental and traffic loadings. The use of a one-parameter model (k -value) limits the accurate analysis of multiple supporting layers in a pavement system. To improve on this model, a three-dimensional solid foundation was incorporated into RPAS. This method uses

the moduli of each supporting layer and allows the extraction of responses at any given depth for each foundation layer.

2 Objectives

The main goal of this study is to utilize the capabilities of RPAS to demonstrate the importance of considering the contribution of all layers (surface layer, unstabilized or stabilized base, subbase and subgrade) in a rigid pavement system under heavy vehicle loads or weak foundation layers. To achieve that goal, an existing roller-compacted concrete (RCC) pavement design that includes a cement-treated base (CTB) and a cement treated subgrade (CTS) layer was modeled in RPAS using two different foundation models, a 3-D solid foundation model and a Winkler model. The capabilities and limitations of each foundation model are presented in this study. With the purpose of demonstrating that the pavement responses are more sensitive to varied foundation properties when a 3D foundation model is implemented, the responses from the RCC model using both foundation models were compared. Different pavement parameters were also analyzed, and the effects that those parameters have on an RCC pavement system were documented. Finally, to show the benefits of utilizing stabilized materials as a technique to optimize concrete pavements, the RCC layer thickness was reduced and the CTB layer was increased so that the assumed concrete elastic limit was not exceeded.

3 Modeling of Concrete Pavements in RPAS

RPAS makes use of the finite element (FE) method and was developed with the purpose of calculating pavement responses due to any arbitrary vehicle loading configuration using different foundation models and their respective parameters and temperature profiles. Additionally, vehicles can have any axle configuration, i.e., axle spacing, tire dimensions, and tire spacing. The concrete layer is modeled using plate elements, and there is no explicit limit on the number of concrete layers that can be modeled in RPAS. The interface between the layers can be considered either bonded or unbonded. Bonded concrete layers are modeled using the Mindlin-laminated plate theory where the shear stresses are transferred through their interface and, as a consequence, no sliding or separation can occur. Unbonded concrete layers are modeled independently from one another and from the foundation so that they can separate and move relative to each other, which will result in shear stresses at the interface due to friction.

The contact between pavement layers is modeled using Bhatti [10] nonlinear contact and friction constraints. The use of this nonlinear model, as opposed to the typical 1D spring connections between contact nodes, allows the proper distribution of the normal and tangential stiffness and tractional forces for nonuniform meshes

and, as a consequence, allows the friction and separation between layers due to slab curling to be more realistically represented. RPAS is capable of considering the uniform temperature change, within the depth of the pavement layer, for jointed slabs and nonlinear thermal change for any number of pavement layers.

Three foundation models are available in RPAS for the modeling the underlying layers: Winkler, Vlasov, and 3D solid foundation models. In the FE method, a one- or two-parameter model is defined as a bed of spring elements with the k -value being equivalent to the normal spring constant, also known as the Winkler model, or when a shear stiffness is also provided, the Vlasov model. To determine the modulus of subgrade reaction (k -value), field tests (plate load test) and correlations with other tests are available. Hoffman and Thompson [11] introduced an alternative approach called AREA method that is based on the field measurements from falling weight deflectometer (FWD) test. The limitation of AREA method in considering a horizontally infinite concrete slab can be compensated by using the deflection basin obtained from FE analysis to calculate the area [12]. This procedure was employed in this study in the determination of k -value for different supporting layer configurations. However, the use of a one-parameter model limits the true analysis of multiple supporting layers. To overcome this limitation, the 3D solid foundation model was developed and incorporated into RPAS. In this model, each foundation layer is discretized using second-order hexahedron elements, which provide much higher accuracy and higher convergence rate. This method, in comparison to the use of modulus of subgrade reaction, makes use of the elastic modulus and Poisson's ratio for each supporting layer simplifying the process of assigning properties when two or more layers are simulated. Furthermore, this method allows the extraction of responses at any given depth for each foundation layer.

To ensure that the responses predicted by the 3D foundation model are an accurate representation of the field performance of concrete pavements, another study focused on the validation of RPAS using the data measured from large-scale and field pavement testing is ongoing. As shown by TaghaviGhalesari et al. [13], the deflections and strains of JCPs calculated using RPAS are consistent with those from the tests within reasonable agreement. The results from the validation study indicate that employing the 3D foundation results in a better modeling of the pavement responses in the field as compared to using Winkler foundation. There was a 9% difference between the deflections obtained from field measurements and the deflections obtained using RPAS, and the corresponding strain responses between RPAS and sensor measurements indicated less than a 20% difference. Given the different methodologies and the assumptions typically made in numerical models and considering experimental errors, the difference between responses indicates a reasonable agreement.

4 Comparison Between Different Foundation Models

RCC pavement is a form of hydraulic cement pavement composed of a stiff mixture of aggregates, cementitious materials, and water. RCC gained popularity in the paving

industry due to its history of low cost, rapid construction, and durable performance. The RCC pavement model developed for this study was based on an RCC pavement design with very weak soils in a coastal area in Texas that is constantly subjected to super heavy vehicle loads. The material properties for the RCC pavement model created in RPAS are shown in Table 1.

According to the idealization of the Winkler model, deformation of the foundation due to an applied load is confined to the loaded region. In contrast to the 3D foundation model used in RPAS, the Winkler model is incapable of considering the foundation deformation beyond the edge of the slab, which can cause a significant effect on edge stresses and deformations. For this reason, an RCC model mimicking an interior load was developed for this study. The model consisted of a 12 by 12 ft RCC slab with a total depth of 72 in. (including pavement layer, base, subbase, and subgrade). It is important to mention that for the purpose of providing an equal comparison between the responses obtained from the two foundation models, only a single tire load at the center of the RCC slab was considered. Table 2 shows the different tire load input parameters used in RPAS that were obtained from the load inputs used for the coastal RCC pavement design in Texas previously mentioned.

The RCC pavement model was evaluated using two different foundation models available in RPAS, the Winkler model, and the 3D solid foundation model. The Winkler model was chosen over the Vlasov model since it is the most commonly used by pavement engineers. When the Winkler model is used in RPAS, the contribution of temperature gradients is considered by a linear distribution of temperature stresses applied throughout the depth of the slab, which in effect results in a constant term that is added to the responses of the model. Moreover, the Winkler model is not

Table 1 Material properties for RCC pavement model

Layer	Young’s modulus, <i>E</i> (ksi)	Poisson’s ratio, <i>v</i>	Thickness (in.)
RCC	5000	0.15	8, 12, 16, and 20
Stabilized base (CTB)	500	0.20	6
Stabilized soil (CTS)	100	0.20	8
Subgrade	10, 5, and 1.3	0.40, 0.45, and 0.45	Total depth of 72 in

Table 2 Load input for RCC pavement model

Load parameter	Load scenario 1	Load scenario 2
Tire load	20 kips	50 kips
Tire pressure	140 psi	140 psi
Contact area	143 in ²	357 in ²
Tire width	10 in	23 in
Tire length	14.3 in	15.5 in

capable of considering moisture conditions. Thus, to better represent the differences between the responses obtain from the Winkler and 3D foundation models, none of the models took into consideration the environmental effects, and the weight of the pavement layers was also neglected.

To determine which foundation model provides a better evaluation of RCC pavement responses, a comparison of the maximum responses using both models was conducted. The RCC layer varied in thickness with increments of 4 in. and the responses were documented for each RCC thickness. For the 3D solid foundation model, each supporting layer was modeled with the corresponding material properties from Table 1 and with a subgrade modulus and Poisson’s ratio of 10 ksi and 0.40, respectively. The corresponding *k*-value was calculated using the AREA method-based procedure described in the previous section and was set to 305 pci. The contact between the concrete and base layers was modeled using the nonlinear contact model available in RPAS. Due to the inability of considering shear interactions between slab and soil elements using the Winkler model, the friction between the two layers was neglected.

Since the Winkler model is limited to capturing the responses for the RCC layer only, the responses for the supporting layers could not be compared. For the case of an interior load, all maximum responses are located underneath the tire load. Figure 1 shows the maximum horizontal (longitudinal and transverse) stresses obtained at the bottom of the RCC pavement layer for each model.

The use of the Winkler foundation model resulted in higher stresses in the RCC layer for a thinner pavement. Although the tensile stresses obtained from both models converge as the RCC layer thickness increases, for an 8-in RCC pavement subjected to the 20-kip load, the Winkler responses were about 15% higher than the responses obtained using the 3D solid foundation model. When the tire load was increased from 20 to 50 kips, the maximum stresses obtained from the Winkler model were about 23% higher than the maximum stress obtained from the 3D solid foundation model. Based on these results, it can be implied that as the applied load increases the percent

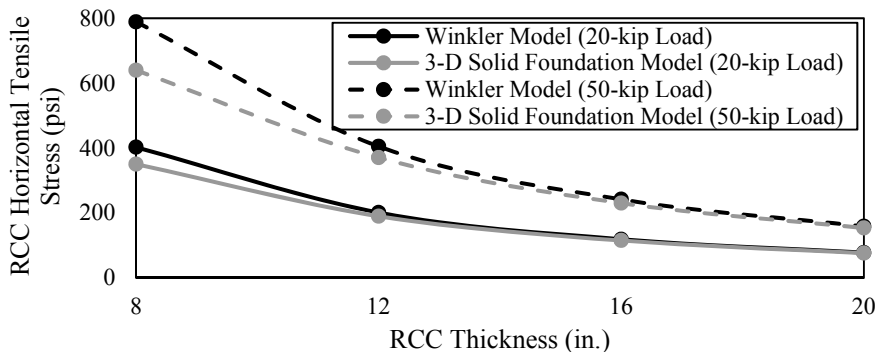


Fig. 1 RCC maximum horizontal stresses at the bottom of RCC layer (with subgrade modulus of 10 ksi)

difference between the two models will also increase. Hence, the Winkler model will continue to overestimate pavement responses, especially for thinner concrete pavements. This observation suggests that using the k -value leads to an inaccurate estimation of the concrete stresses and, consequently, to an over design of concrete pavements.

5 Effects of Varying Different Pavement Parameters in an RCC Pavement System

To determine the effects that different pavement parameters have on RCC pavement systems that are subjected to heavy vehicle loads, the RCC pavement model created in RPAS was analyzed for different foundation material properties using the 3D foundation model described above. For the following analyses, the RCC layer varied in thickness with increments of 4 in. and the responses were documented for each RCC thickness.

5.1 Effects of Different Subgrade Materials

Three different subgrade material properties (see Table 1) were entered into the RCC model, and the responses were compared under two different tire loads. Figure 2 shows the maximum responses (under tire load) at the bottom of the RCC, CTB, and CTS layers and at the top of the subgrade for the different subgrade modulus E with the corresponding Poisson's ratio.

As expected, the results show that a weaker subgrade results in an increase of the horizontal tensile stresses in the RCC, CTB, and CTS layers as well as an increase in the vertical compressive strains in the subgrade. For the 12 in. RCC pavement case subjected to the 20-kip load, the maximum stress for the RCC layer increased by 10.5%, and the maximum stress for the CTB layer increased by 20% when the subgrade modulus decreased from 10 to 1.3 ksi. Similarly, for the 12 in. pavement case subjected to the 50-kip load, the maximum RCC stress increased by about 23% and the CTB maximum stress also increased by 23% when the subgrade modulus decreased from 10 to 1.3 ksi. Very similar increases were observed for the stresses in the CTS layer, and as depicted in Fig. 2d, the vertical strains in the subgrade were increased by over 100% when the subgrade modulus decreased from 10 to 1.3 ksi for both load cases.

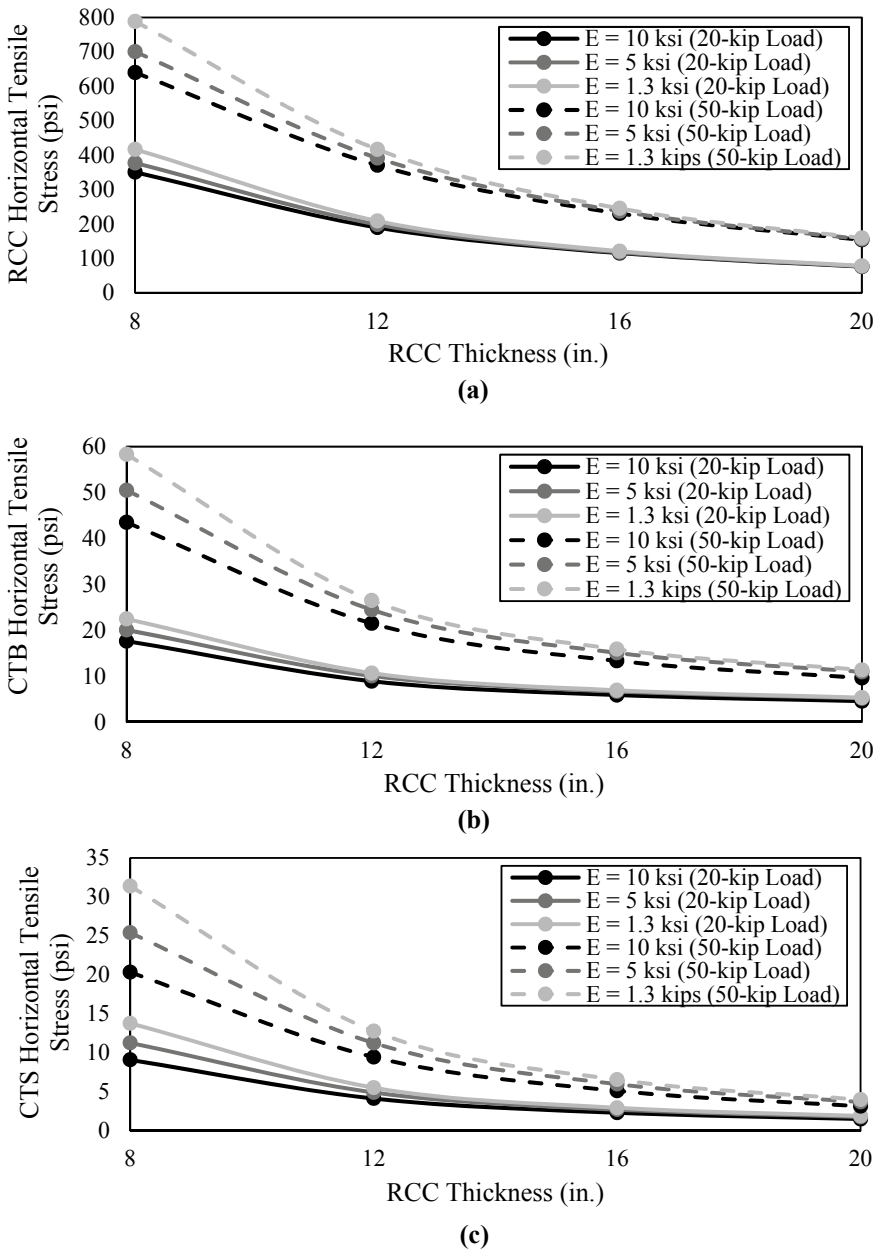


Fig. 2 Comparison of maximum responses from different subgrade materials. **a** Maximum horizontal stresses at the bottom of the RCC layer. **b** Maximum horizontal stresses at the bottom of the CTB layer. **c** Maximum horizontal stresses at the bottom of the CTS layer. **d** Maximum vertical strains at the top of the subgrade

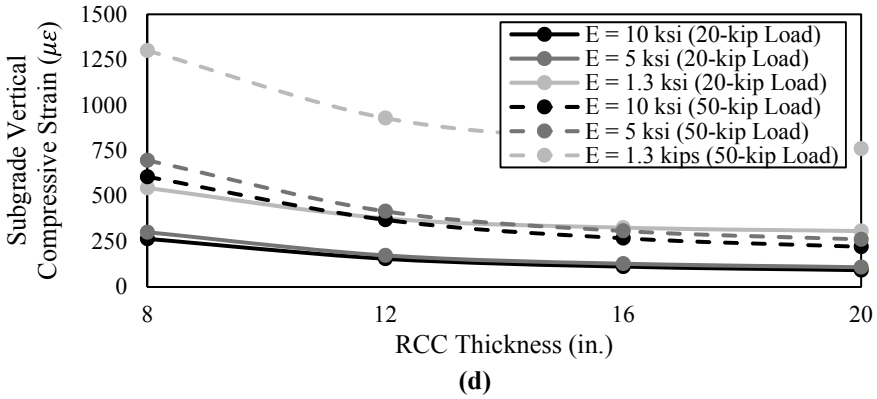


Fig. 2 (continued)

5.2 Effects of Using Different Stabilized Material Properties

To show the benefits of using stiffer base and subbase layers on top of weak soil, the modulus for both the CTB and CTS layers were increased. For simplification purposes, the RCC pavement structure previously shown in Table 1 will be referred as Case I and the RCC pavement structure shown in Table 3 will be referred as Case II. Both cases kept the same material properties for the RCC layer and subgrade as shown in Table 3.

The maximum responses (obtained using the 3D solid foundation model in RPAS for both cases) were documented. Figure 3 shows the critical responses at the bottom of the RCC and CTB layers and at the top of the subgrade for the different tire loads.

The results obtained from using the 3D solid foundation model were able to demonstrate the benefits of including stronger materials in an RCC pavement design so that lower tensile stresses in the RCC layer and lower vertical strains in the subgrade are achieved. As shown in the figure above, the maximum tensile stresses in the RCC layer and the compressive stains on top of the subgrade layer decreased

Table 3 Material properties for RCC pavement model (Case II)

Layer	Young’s modulus, E (ksi)	Poisson’s ratio, ν	Thickness (in.)
RCC	5000	0.15	8, 12, 16 and 20
Stabilized base (CTB)	1000	0.20	6
Stabilized soil (CTS)	300	0.25	8
Subgrade	1.3	0.45	Total depth of 72 in

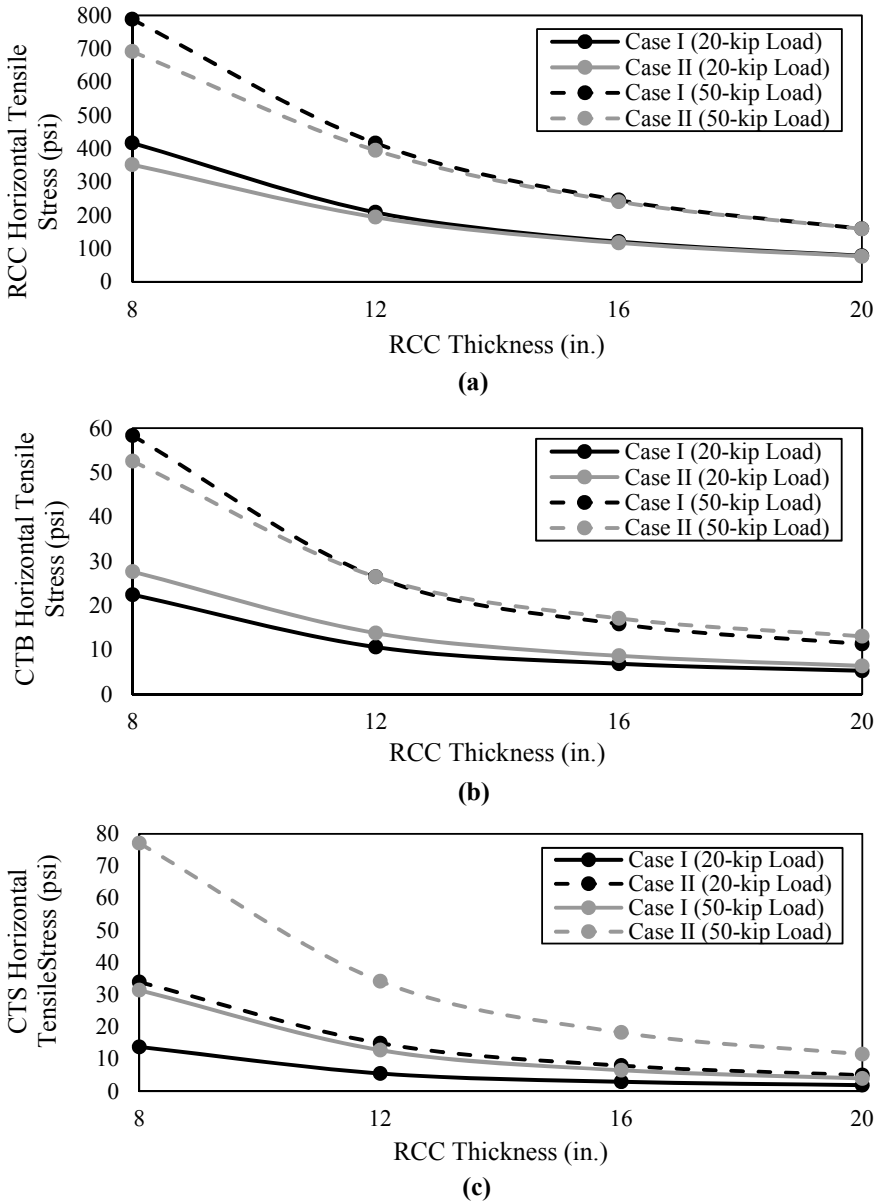


Fig. 3 Comparison of maximum responses from different stabilized materials. **a** Maximum horizontal stresses at the bottom of the RCC layer. **b** Maximum horizontal stresses at the bottom of the CTB layer. **c** Maximum horizontal stresses at the bottom of the CTS layer. **d** Maximum vertical strains at the top of subgrade

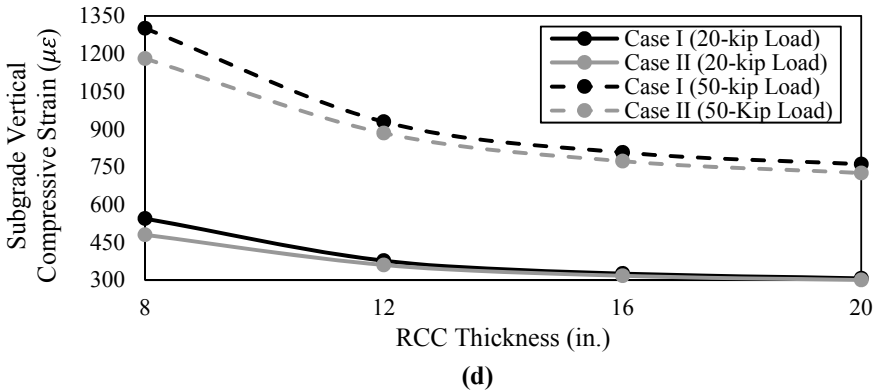


Fig. 3 (continued)

when stiffer base and subbase materials were used for thinner RCC pavements. For example, for the 12 in. RCC pavement case subjected to the 20-kip load, the maximum stress for the RCC layer decreased by 7% and the maximum strains at the top of subgrade decreased by almost 12% when stiffer base and subbase layers were used. When the load was increased to 50 kips, the maximum RCC stress decreased by 5%, and the maximum strains at the top of subgrade decreased by 9% when stiffer base and subbase layers were used. However, the critical stresses in the CTB and CTS layers were higher when the modulus of both layers was increased. Except for the 50-kip load case, where the CTB stresses were lower for an RCC layer with a thickness less than 12 in. and then increased for an RCC thicknesses equal to or greater than 12 in.

6 Demonstrated Benefits of Optimizing the Pavement Layers

Based on the authors’ experience in concrete pavement design, it was assumed that the concrete stresses for a 12 in. RCC pavement should not exceed more than 130 psi. The results previously provided in Fig. 3a show that increasing the modulus for the CTB and CTS layers is not enough to decrease the maximum concrete stresses so that they do not exceed the assumed allowable limit. It can easily be concluded that increasing the RCC layer thickness is an adequate approach to achieve a proper RCC pavement design. In fact, for the RCC pavement structure modeled in RPAS with the material properties shown in Table 3, subjected to a 50-kip load, a 22 in. RCC is required so that the maximum concrete stresses do not exceed the allowable limit of 130 psi. However, the cost of increasing the RCC layer’s thickness versus considering increasing the CTB layer thickness can be much greater.

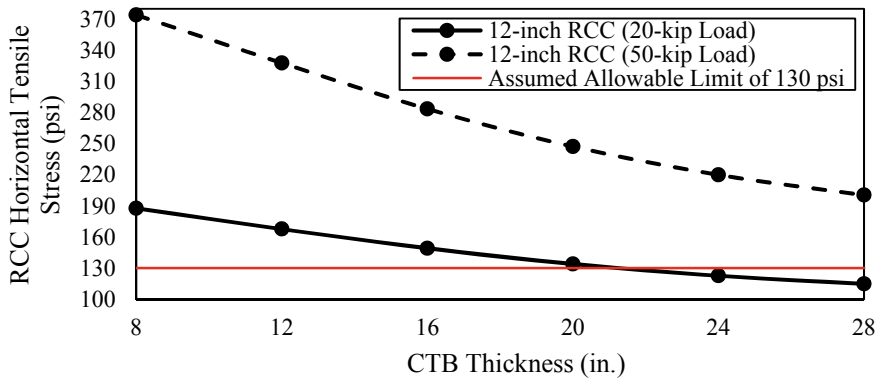


Fig. 4 Comparison of RCC maximum horizontal stresses under tire load with assumed allowable limit of 130 psi at the bottom of RCC layer for varied CTB thicknesses

To demonstrate that the RCC pavement structure can be optimized by increasing the CTB layer thickness, the 12 in. RCC pavement model with the material properties provided in Table 3 was subjected to the 20 and 50-kip load, while the thickness of the CTB layer varied until the stresses in the concrete layer did not exceed the allowable limit of 130 psi. Figure 4 shows the results of that analysis.

Based on the results, it was determined that the 12 in. RCC model that was subjected to the 20-kip load requires a 22 in. CTB so that the stresses in the RCC layer do not exceed the allowable limit of 130 psi. However, for the RCC pavement model subjected to the 50-kip load, it was determined that a CTB layer with a thickness of 28 in. still exceeded the assumed allowable limit of 130 psi with a maximum tensile stress of 200 psi. Realizing that a CTB layer thickness greater than 30 in. might not be reasonable, the RCC layer thickness was increased to 18 in., and it was determined that a 30 in. CTB was required to stay within the assumed RCC allowable limit. The 18 in. RCC pavement model subjected to the 50-kip load produced a maximum stress of 128 psi.

7 Summary and Conclusions

The benefits of being able to consider different pavement parameters using the 3D solid foundation model in RPAS were demonstrated in this study through a comparison with a spring foundation (Winkler model). The Winkler model provided higher concrete stresses and was unable to provide responses for the supporting layers since the model is limited to the assessment of the RCC layer only. On the other hand, the 3D solid foundation model provided lower concrete stresses for thinner RCC pavements and was able to provide an assessment of the actual influence that heavy vehicle loads and different soil material properties have on the critical responses for each pavement layer. To achieve optimum design options that decrease the critical

responses in the pavement and do not exceed the assumed allowable elastic limit, the RCC and CTB layers were varied in thickness and different stabilized material properties were considered. The results indicated that applying a base layer with sufficient thickness and stiffness led to optimum design of the pavement considered in this study with minimal or no change to the RCC thickness depending on the loading conditions. The supporting layers (CTB, CTS, and subgrade) were assumed to stay within their elastic limits if the concrete stress did not exceed the assumed allowable limit of 130 psi. Further investigation on the magnitude of pavement layer's allowable limits is recommended to ensure that the stresses/strains in each layer are not exceeding those limits. A second study varying the CTS layer is also recommended to be developed to determine if the RCC pavement structure can be further optimized for super heavy vehicle loads.

References

1. ACPA (2007) Subgrades and subbases for concrete pavements. Concrete Paving Technology, Skokie, IL
2. Cervantes V, Roesler J (2009) Performance of concrete pavements with optimized slab geometry. Research Report ICT-09-053. Illinois Center for Transportation, Rantoul, IL
3. Taylor PC, Kosmatka SH, Voigt GF (2007) Integrated materials and construction practices for concrete pavement: a state-of-the-practice manual, Report FHWA HIF-07-004
4. Neal BF, Woodstrom JH (1977) Faulting of portland cement concrete pavements. Report FHWA-CA-TL-5167-77-20, Department of Transportation, California
5. Applied Research Associates, Inc. (2004) Guide for mechanistic-empirical design for new and rehabilitated pavement structures. Final Report NCHRP 1-37A, Transportation Research Board, National Research Council, Washington D.C.
6. Selezneva O, Jiang J, Tayabji SD (2000) Preliminary evaluation and analysis of LTPP faulting data. Final Report FHWA-RD-00-076
7. Ruiz JM, Rasmussen RO, Chang GK, Dick JC, Nelson PK, Ferragut TR (2005) Computer-based guidelines for concrete pavements, vol 1. Project Summary, Report FHWA-HRT-04-121 2005
8. Hall K, Crovetti J (2007) Performance of drained and undrained rigid pavements in the LTPP SPS-2 Experiment. TRB 2007 Annual Meeting, Washington D.C.
9. Aguirre N, Taghavi Ghalesari A, Carrasco CJ (2019) A comparison of concrete pavement responses using finite element method with foundation springs and 3-D solid elements. In: International airfield and highway pavements conference, Chicago, IL
10. Bhatti MA (2006) Advanced topics in finite element analysis of structures: with mathematica and MATLAB computations. John Wiley and Sons Inc., New York
11. Hoffman MS, Thompson MR (1981) Mechanistic interpretation of nondestructive pavement testing deflections. Report No. FHWA/IL/UI-190. Illinois Department of Transportation, Springfield, IL
12. Hall KT, Darter MI, Hoerner TE, Khazanovich L (1997) LTPP data analysis. Phase I: validation of guidelines for k-value selection and concrete pavement performance prediction, Report FHWA-RD-96-198. ERES Consultants, Inc., Champaign, IL
13. Taghavi Ghalesari A, Aguirre N, Carrasco CJ, Vrtis M, Garg N (2020). Verification and validation of the response of a 3-D finite element model for the characterization of jointed concrete pavements. In: TRB 99th Annual Meeting, Washington D.C. (Accepted)

***R*-Value and Resilient Modulus Prediction Models Based on Soil Index Properties for Colorado Soils**



Cara Fragomeni  and Ahmadreza Hedayat 

Abstract Resilient modulus (M_r), as an important mechanical property of soil, is used for analysis and design of pavements. M_r can properly describe the stress-dependent elastic modulus of soil materials under traffic loading. In addition to the resilient modulus, *R*-value test is commonly used to measure the strength of subgrade, subbase, and base course materials for use in pavements. Both tests are expensive and time consuming to run, and establishing accurate and reliable correlations between the test results and soil physical properties can save a considerable amount of time and money in testing and analyzing the construction materials properties. An extensive database of systematically conducted resilient modulus and *R*-value tests along with basic soil properties for Colorado soils was established. This paper presents the prediction equations developed through (a) regression analysis of over 2600 *R*-value data points and associated soil basic properties for soil types (A-1-a, A-1-b, A-2-4, A-2-6, A-2-7, A-4, A-6, and A-7-6) and (b) regression analysis of over 200 resilient modulus tests and associated soil basic properties for soil types (A-1-b, A-2-4, A-4, and A-6). It is demonstrated that the proposed models predict the *R*-value and resilient modulus values close to the laboratory measured values for all studied soil types.

Keywords Resilient modulus · *R*-value · Multiple linear regression · Soil basic properties

1 Introduction

The Mechanistic Empirical Pavement Design Guide (MEPGD) requires the resilient modulus of soil and aggregate materials for structural design of the layers. Several studies have shown the drastic influence of M_r on the thickness of the base course and the asphalt layers [1, 2]. A successful implementation of the MEPGD requires a comprehensive and accurate M_r database for the local subgrade soils and base

C. Fragomeni (✉) · A. Hedayat
Colorado School of Mines, 1500 Illinois Street, Golden, CO, USA
e-mail: carafragomeni@mines.edu

coarse materials. Three common approaches used for estimating the resilient modulus include (a) conducting repeated load triaxial tests; (b) back-calculating values from in situ tests such as Dynaflect and falling weight deflectometer (FWD); and (c) correlating values with physical properties of soils. In fact, the AASHTO mechanistic-empirical (M-E) design approach, adopted by many state transportation agencies such as the Colorado Department of Transportation (CDOT), employs a hierarchical approach to design input parameters that allows providing the input values using all the above-listed approaches.

For laboratory measurements of the resilient modulus, the repeated load triaxial test is conducted based on the AASHTO T307: "Determining the Resilient Modulus of Soils and Aggregate Materials." The resilient modulus is defined as the ratio of the repeated deviator stress (cyclic stress in excess of confining pressure) to the recoverable resilient (elastic) strain in a repeated dynamic loading. The resilient modulus value can be determined from the established correlations between laboratory or in situ measurements of the resilient modulus and the soil's physical properties. Many researchers and transportation agencies have studied the relations between the resilient modulus and the soils properties to save time and costs associated with laboratory testing. Examples of research work include but are not limited to [1, 3–10].

Factors that influence the resilient modulus of subgrade soils may include physical condition of the soil, stress level, soil type, loading conditions (i.e., confining stress and deviator stress), amount of fines, clay content, plasticity characteristics, particle size distribution, specific gravity, and organic content. Several studies reported the interrelations between the abovementioned variables and the resilient moduli of fine-grained and coarse-grained (granular) soils. In many cases, including for the Colorado soils that were studied, the behavior and the relations are different for fine- and coarse-grained soils. For example, as the deviator stress increases, the resilient modulus of fine-grained soils decreases while the resilient modulus of coarse-grained soils increases [11]. Also, although sensitive to the confining stress, the resilient modulus is more significantly influenced by the confining stress for coarse-grained soils than the fine-grained soils [12].

In addition to the resilient modulus, *R*-value test is commonly used to measure the strength of subgrade, subbase, and base course materials for use in pavements. The *R*-value is used by many transportation agencies as a quantifying parameter in the evaluation of subgrade and base course for pavement design as well as a criterion for acceptance of aggregates for pavement system. The test is conducted using a device called stabilometer, where the material's resistance to deformation is expressed as a function of the ratio of the transmitted lateral pressure to that of the applied vertical pressure. The test can be performed according to AASHTO T190, ASTM D2844, and Colorado CP-L3101 procedures.

R-values can range from 0 to 100, representing low soil strength to high soil strength. This test is time consuming, requires specific equipment and trained personnel, and is not commonly available at commercial testing facilities. In *R*-value tests, there are four steps that need to be taken: (a) compacting a 4-inch specimen using a kneading compactor, (b) loading the compacted specimen in a steel mold until enough moisture is squeezed out of the specimen to light up five out of six bulbs

on an exudation indicator device and recording the exudation pressure, (c) soaking the specimen for 24 h, and (d) testing the specimen in a stabilometer to measure the R-value. The R-value is defined as follows:

$$R - \text{value} = 100 - \frac{100}{\frac{2.5}{D_2} \left(\frac{P_v}{P_h} - 1 \right) + 1} \tag{1}$$

where P_v and P_h are the vertical and horizontal (lateral) pressures applied/experienced by the soil specimen, respectively, and D_2 is the number of turns of the screw to inject oil into the chamber. The lateral pressure depends on the stiffness of the soil. For example, for the soil with R-value of 100, the soil does not deform under the vertical load. In contrast, R-value of zero indicates that the soil deforms the same amount laterally as vertically, like a liquid.

Reporting of R-value for each soil specimen requires testing at least three specimens at three different moisture contents and exudation pressures. The final R-value is obtained by extrapolating at an exudation pressure of 300 psi. The New Mexico Department of Transportation developed a chart for estimating R-values for soils from different AASHTO classifications based on the plasticity index (PI) values with the reliability of 60% (i.e., 60% chance of having estimated values from the charts being equal or greater than the actual R-values). Since R-value is the indication of the soil strength and stiffness, it cannot be properly represented by the plasticity index of the soil only. Lenke et al.[13] performed R-value tests for 15 collected specimens from different sites and compared the actual R-values against the estimated R-values obtained by the use of the NMDOT R-value chart and reported a best fit line with an R^2 value of 0.5837. The closer the R^2 is to one, the better the regression model is. This average level coefficient of determination confirmed that the plasticity index alone cannot be a good indicator of the R-value for soils.

2 Resilient Modulus Constitutive Models

Several different models have been proposed to correlate the resilient modulus with the stresses and the physical soil properties. The generalized resilient modulus model that was developed through NCHRP project 1–28 A is adopted for this study. This model is widely accepted and applicable to all types of subgrade materials. The resilient modulus model is as follows:

$$\frac{M_r}{P_a} = k_1 \left(\frac{\theta}{P_a} \right)^{k_2} \left(\frac{\tau_{oct}}{P_a} + 1 \right)^{k_3} \tag{2}$$

where τ_{oct} is the octahedral shear stress, and k_1 , k_2 , and k_3 are material model parameters (material constants). In resilient modulus tests on cylindrical specimens, σ_1 is

the major principal stress, σ_3 is the minor principal stress, and σ_2 is the intermediate principal stress, which is the same as the minor principal stress (i.e., $\sigma_2 = \sigma_3$). The bulk stress, $\theta = \sigma_1 + 2\sigma_3$, and the octahedral shear stress is equal to $\tau_{oct} = \sqrt{2}/3(\sigma_1 - \sigma_3)$. The resilient modulus model parameters k_{1-3} will need to be correlated to basic soil properties for each soil group, where M_r is the resilient modulus, and P_a is the atmospheric stress (101.4 kPa). Several studies have developed relationships between the soil properties and the k parameters in Eq. (1) (e.g., [9, 14, 15]). Earlier studies that attempted to find correlations between the k_{1-3} parameters and a wide range of soil types and conditions reported poor correlations but studies that confined the scope of correlations to specific soil types (i.e., fine-grained, plastic coarse-grained soils, non-plastic coarse-grained soils, specific AASHTO soil types) reported good correlations (e.g., [9]). The variability of a given soil type in different regions and states requires developing modified and specific correlations for different states based on statistical analysis of collected statewide soil data.

The resilient modulus is considered as the dependent variable, and the bulk and octahedral shear stresses are the independent variables according to Eq. 1. Statistical analysis was carried out for each soil test to determine the k_{1-3} model parameters from the results of the 15 stress combinations applied during repeated load triaxial test (15 load sequences according to AASHTO T 307).

3 Basics of Regression Analysis Method

A multiple regression analysis to correlate R -value and resilient modulus values as dependent variables with the fundamental soil properties as independent variables was performed. All fundamental soil properties available in established databases were treated as potential independent variables. Numerous combinations of soil properties (independent variables) were used in the regression analysis. The general multiple linear regression model is expressed as follows:

$$R - \text{Value or Resilient Modulus} = A_0 + A_1x_1 + A_2x_2 + \dots + A_kx_k + \varepsilon \quad (3)$$

where A_0 is the intercept of the regression plane, A_i is the regression coefficient, x_i is the independent variable (soil parameter or combination of soil properties), and ε is the random error.

To assess the models, two performance indices of coefficient of determination, R^2 , and root mean square error, RMSE, were considered with the following equations:

$$R^2 = \frac{\sum_{i=1}^N (y - y')^2}{\sum_{i=1}^N (y - \tilde{y})^2} \quad (4)$$

$$\text{RMSE} = \sqrt{\frac{1}{N} \sum_{i=1}^N (y - y')^2} \quad (5)$$

where y and y' are the predicted and measured dependent variables, respectively, \bar{y} is the mean of the y values, and N is the total number of data points or observations. The predictive equation will be excellent if $R^2 = 1$ and $\text{RMSE} = 0$. The adjusted R^2 , a modified version of R^2 , is also evaluated. The adjusted R^2 is adjusted for the number of independent variables in the model and increases only if the new variable improves the model more than would be expected by chance. The model with the highest adjusted R^2 was selected as the best model.

To perform the regressions, MATLAB scripts were written that first sorted the data by the AASHTO soil type, then produced models using different combinations of the independent variables, as available in the databases. Each unique combination of variables was tested, starting with individual variables and adding more and more independent variables until a maximum of 12 variables was explored.

Some linear regressions can suffer from multicollinearity, which means that independent variables are more strongly correlated with each other than with the dependent variable. For example, the liquid limit and plastic limit are the indicators of the plasticity index of a soil. However, if a model includes liquid limit, plastic limit, and plasticity index as independent variables, it will artificially give too much weight to the plasticity index because it is effectively also included in the plastic limit and liquid limit variables. The variance inflation factor (VIF) is commonly used for evaluation of multicollinearity issue. It is suggested that when VIF is greater than 8, some multicollinearity problems may exist. In our study, the VIF was required to be less than 8 for a model to be considered.

4 Data for R-Value Regression Analysis

An extensive database of systematically conducted R -value tests provided by the Colorado Department of Transportation including 2632 sample tests was analyzed for establishing relationships between the R -value and the basic soil properties. Reporting of R -value for each soil specimen requires testing at least three specimens at three different moisture contents and exudation pressures. The final reported R -value is obtained by interpolating at exudation pressure of 300 psi. The range and distribution of R -values for each AASHTO soil group are presented in Fig. 1.

Note that each point in Fig. 1 has an associated exudation pressure (EP) based on the specimen condition, and the pressure is not necessarily 300 psi. Due to the nature of the testing procedure, a higher EP typically produces a greater R -value. The R -value is strongly affected by the change in the moisture content (exudation pressure), especially for cohesive soils. An increase in the moisture content generally reduces the R -value for the cohesive soils. Since the exudation pressure has such a large effect

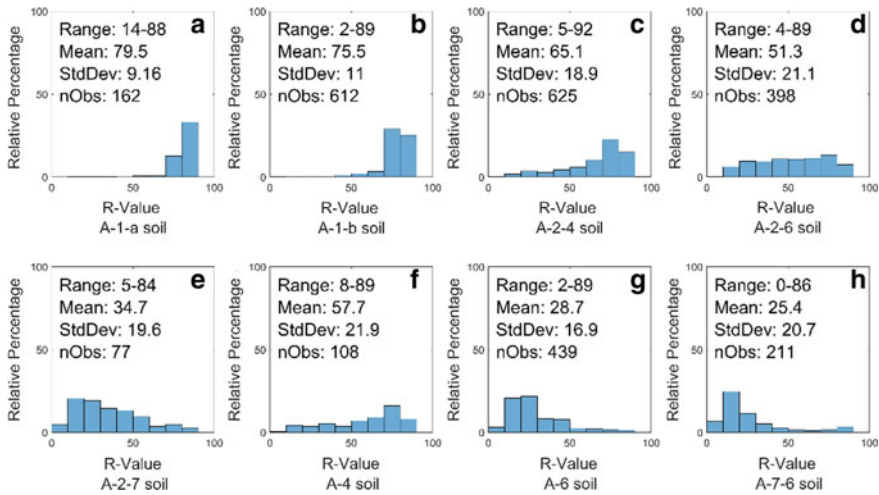


Fig. 1 Histogram and summary statistics of R -values by AASHTO soil group classification (nObs indicates the number of observations (data points) used for regression analysis in each soil type, and StdDev indicates the standard deviation)

on the R -value, it is included in the regression analysis as an independent variable. Table 1 presents the ranges of the soil properties that were used as independent variables in the regression analysis.

The independent variables are as follows: specific gravity (SpG), absorption (Abs), maximum dry density (MDD), optimum moisture content (OM), in situ moisture content (MC), liquid limit (LL), plastic limit (PL), plasticity index (PI), percent passing of #4 sieve ($P_{\#4}$), percent passing of #10 sieve ($P_{\#10}$), percent passing of #40 sieve ($P_{\#40}$), percent passing of #200 sieve ($P_{\#200}$), difference in moisture content ($MC_{diff} = MC - OM$), moisture content differential ratio multiplied by plasticity index ($MCDRPI = (MC_{diff})/OM \times PI$), and exudation pressure (EP).

5 Data for Resilient Modulus Regression Analysis

The values of k coefficients were calculated using the constitutive model presented in Eq. 2. The NCHRP Design Guide (NCHRP 2003, 2004) recommends soil tests with high R^2 for the constitutive model should be used to develop regressions, because these k values are the most accurate ones that produce high-quality M_r models. Once the three k values for each sample were calculated, regression equations were developed using MATLAB for various possible combinations of independent variables. The independent variables used in this regression in addition to the typical properties listed for the R -value regression include percent passing of 2-inch sieve ($P_{2\text{ in}}$), percent passing of 1-inch sieve ($P_{1\text{ in}}$), percent passing of 1/2 inch sieve ($P_{1/2\text{ in}}$),

Table 1 Limits of soil properties values used in R-value regressions

Property (units)	Limits	A-1-a soil	A-1-b soil	A-2-4 soil	A-2-6 soil	A-2-7 soil	A-4 soil	A-6 soil	A-7-6 soil
SpG	Min	2.35	1.92	2.12	2.12	2.35	1.95	1.00	2.25
	Max	2.75	3.13	2.92	2.77	2.63	2.76	2.92	2.68
Abs (%)	Min	0.38	0.38	0.20	0.50	0.58	0.50	0.58	0.55
	Max	8.0	8.8	9.1	7.4	4.6	7.9	5.7	7.0
MDD (pcf)	Min	106	103	100	105	99.7	98.8	93.6	84.9
	Max	139	139	138	140	122	134	131	125
OM (%)	Min	5.88	5.78	5.97	6.03	10.2	7.03	8.36	10.5
	Max	13.9	16.5	19.3	17.5	22.7	19.8	21.6	34.9
MC (%)	Min	5.50	1.66	3.55	2.69	7.83	7.98	7.35	6.09
	Max	29.5	85.3	70.3	15.2	20.9	48.7	23.6	40.2
LL (%)	Min	17	17	17	23	41	14	23	41
	Max	32	32	39	40	87	37	40	76
PL (%)	Min	14	13	9	11	16	11	5	14
	Max	29	29	34	25	28	53	26	29
PI (%)	Min	1	1	1	11	17	1	11	13
	Max	6	6	10	25	71	10	27	49
P#4 (%)	Min	9	37	33	19	57	64	57	66
	Max	100	100	100	100	100	100	100	100
P#10 (%)	Min	7	31	23	17	47	59	51	61
	Max	50	99	100	100	99	100	100	100
P#40 (%)	Min	5	8	6	9	16	49	45	47

(continued)

Table 1 (continued)

Property (units)	Limits		A-1-a soil	A-1-b soil	A-2-4 soil	A-2-6 soil	A-2-7 soil	A-4 soil	A-6 soil	A-7-6 soil
	Max	Min								
$P_{\#200}$ (%)	Max	30	50	100	83	56	100	100	100	100
	Min	0.5	0.7	1.60	3.8	8.3	36	36	36	36
	Max	15	25	35	35	34	100	100	94	99
MC_{dir} (%)	Min	-5.44	-7.57	-8.61	-5.68	-8.81	-5.94	-4.92	-4.92	-14.6
	Max	21.6	77.7	59.3	2.48	6.57	12.7	9.99	9.99	18.2
MCDRPI (%)	Min	-1.21	-2.43	-3.41	-8.22	-13.7	-2.53	-7.93	-7.93	-18.5
	Max	8.87	1.34	3.6	4.04	40.1	6.48	17.6	17.6	47.4
	Min	105	47	74	47	115	99	100	100	113
EP (psi)	Max	808	816	860	808	815	800	882	882	816

Table 2 Range of k coefficients for all specimens used in resilient modulus regressions

AASHTO soil type	Variable	nObs	Mean	Standard deviation	Min	Max
A-1-b	k_1	9	1140.9	450.10	540.03	2030.8
	k_2	9	0.481	0.292	0.105	1.061
	k_3	9	-1.42	1.56	-3.89	0.45
A-2-4	k_1	56	1603.4	894.90	0.68	4914.3
	k_2	56	0.365	0.643	-3.875	0.985
	k_3	56	-2.40	1.33	-4.27	0.89
A-4	k_1	29	1622.1	755.68	501.08	3529.3
	k_2	29	0.312	0.307	-0.356	0.792
	k_3	29	-3.62	0.89	-5.58	-1.48
A-6	k_1	57	1376.5	515.26	533.87	2588.1
	k_2	57	0.184	0.195	-0.264	0.534
	k_3	57	-3.66	0.99	-5.92	-1.19

percent passing of 3/8 inch sieve ($P_{3/8 \text{ in}}$), percent passing of #16 sieve ($P_{\#16}$), percent passing of #50 sieve ($P_{\#50}$), and percent passing of #100 sieve ($P_{\#100}$). The range of the k coefficients for each soil type is presented in Table 2.

The limits of the soil properties were used as independent variables are presented in Table 3.

6 Results of Regression Analysis for R-Value

To evaluate the merit of the possible regressions, the R^2 and adjusted R^2 values were calculated for each regression model. The following regression models were selected as the top ranked ones with the highest adjusted R^2 values to estimate the R -value based on the basic soil properties. To calculate the final R -value for any soil type, the value of 300 psi needs to be assumed for the EP value.

Soil type: A-1-a

$$R\text{-value} = -293 + 134 \text{ SpG} + 4.45 \text{ Abs} - 1.16 \text{ PI} - 1.08 P_{\#200} + 0.0147 \text{ EP} + 3.93 \text{ MC} - 9.85 \text{ MCDRPI} \{ R^2 = 0.954, \text{ Adj. } R^2 = 0.944, \text{ RMSE} = 3.83 \} \tag{6}$$

Soil type: A-1-b

$$R\text{-value} = -12.7 + 0.772 \text{ MDD} - 2.23 \text{ LL} + 2.99 \text{ PL} - 0.633 P_{\#40} - 0.570 P_{\#200}$$

Table 3 Limits of soil properties values used in resilient modulus regressions

AASHTO group	A-1-b soil		A-2-4 soil		A-4 soil		A-6 Soil	
nObs	9		56		29		57	
Limits	Min	Max	Min	Max	Min	Max	Min	Max
Unit weight (pcf)	116.4	136	110.9	136.9	95.5	122	93.9	123.7
MC (%)	6.7	10.5	5.9	14.6	10.1	19.9	11	23.3
MDD (pcf)	122.5	137	111	137.6	100.4	128.4	100.3	130.2
OM (%)	6.7	9	5.5	13.2	9.2	19	9	22.7
$P_{2 \text{ in}}$ (%)	95	95	87	100	100	100	100	100
$P_{1 \text{ in}}$ (%)	90	100	79	100	100	100	100	100
$P_{1/2 \text{ in}}$ (%)	84	100	73	100	92	100	97	99
$P_{3/8 \text{ in}}$ (%)	77	99.7	70	100	85	100	95	100
$P_{\#4}$ (%)	63	96	66	100	76	100	90	100
$P_{\#10}$ (%)	52	74	60	99.8	66	99.9	84	99.5
$P_{\#16}$ (%)	40	60	53	99.4	62	98.6	77	98
$P_{\#50}$ (%)	15	40	33	81	50	92.1	60	88
$P_{\#100}$ (%)	6	32	24	61	43	100	54.2	100
$P_{\#200}$ (%)	2.9	24.9	11.3	35	35.2	82.1	37	83.5
LL (%)	13	23	15	29	20	32	25	41
PI (%)	3	6	1	10	6	10	11	20

$$+ 0.0231EP - 8.89 \text{ MCDRPI} \{R^2 = 0.552, \text{Adj. } R^2 = 0.529, \text{RMSE} = 9.38\} \quad (7)$$

Soil type: A-2-4

$$\begin{aligned} R\text{-value} = & 150 - 28.8\text{SpG} - 3.83\text{OM} + 0.730\text{LL} - 1.233\text{PI} + 0.170P_{\#10} \\ & - 0.999P_{\#200} + 0.0422EP - 7.05\text{MC}_{\text{diff}} \\ & \{R^2 = 0.628, \text{Adj. } R^2 = 0.618, \text{RMSE} = 12.44\} \end{aligned} \quad (8)$$

Soil type: A-2-6

$$\begin{aligned} R\text{-value} = & 179 + 4.16\text{Abs} + 1.52\text{MDD} - 0.469\text{LL} + 2.38\text{PL} + 0.582P_{\#40} \\ & - 1.846P_{\#200} + 0.0616EP - 6.19\text{MC}_{\text{diff}} \\ & \{R^2 = 0.693, \text{Adj. } R^2 = 0.684, \text{RMSE} = 11.83\} \end{aligned} \quad (9)$$

Soil type: A-2-7

$$\begin{aligned}
 R\text{-value} &= -35.9 + 1.15PL + 0.969P_{\#10} - 1.66P_{\#40} + 1.12P_{\#200} \\
 &\quad + 0.0411EP - 2.86MC_{\text{diff}} \\
 &\quad \{R^2 = 0.708, \text{Adj. } R^2 = 0.683, \text{RMSE} = 11.02\}
 \end{aligned}
 \tag{10}$$

Soil type: A-4

$$\begin{aligned}
 R\text{-value} &= -427 - 156\text{SpG} + 4.47\text{MDD} - 1.96\text{LL} + 9.38\text{PL} + 3.32P_{\#10} \\
 &\quad - 1.98P_{\#200} + 0.0281\text{EP} - 23.2\text{MCDRPI} \\
 &\quad \{R^2 = 0.911, \text{Adj. } R^2 = 0.891, \text{RMSE} = 7.13\}
 \end{aligned}
 \tag{11}$$

Soil type: A-6.

$$\begin{aligned}
 R\text{-value} &= 29.7 - 3.51\text{Abs} + 5.01\text{OM} - 0.951\text{PI} + 0.0430\text{EP} - 4.45\text{MC} \\
 &\quad \{R^2 = 0.697, \text{Adj. } R^2 = 0.688, \text{RMSE} = 9.22\}
 \end{aligned}
 \tag{12}$$

Soil type: A-7-6

$$\begin{aligned}
 R\text{-value} &= 0.919 + 5.38\text{Abs} - 0.557\text{LL} + 0.473P_{\#4} + 0.0137\text{EP} - 4.26\text{MC}_{\text{diff}} \\
 &\quad + 0.897\text{MCDRPI} \{R^2 = 0.858, \text{Adj. } R^2 = 0.844, \text{RMSE} = 8.02\}
 \end{aligned}
 \tag{13}$$

The plots of *R*-values predicted by above equations and the laboratory *R*-value are presented in Fig. 2. The diagonal line represents the case where the predicted

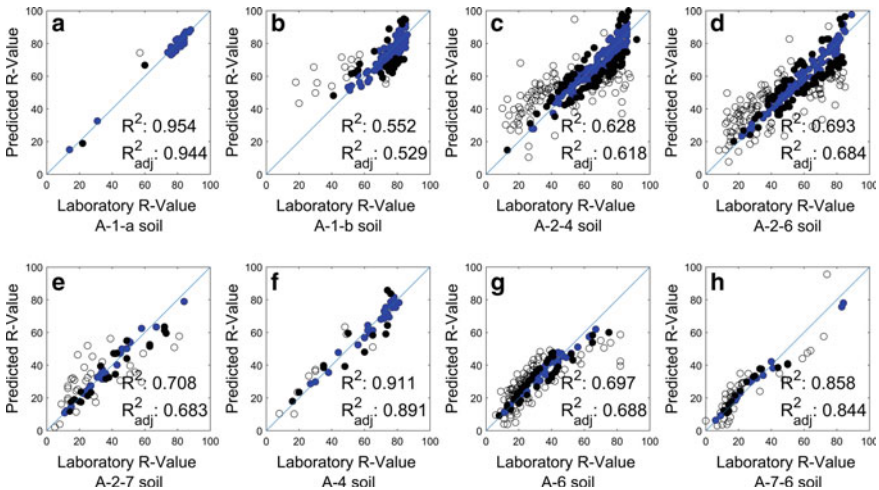


Fig. 2 Predicted versus laboratory measured *R*-values for different soil types

Table 4 Specimens with predicted R -values within ± 10 and $\pm 20\%$ of the laboratory R -value

	A-1-a soil (%)	A-1-b soil (%)	A-2-4 soil (%)	A-2-6 soil (%)	A-2-7 soil (%)	A-4 soil (%)	A-6 soil (%)	A-7-6 soil (%)
$\pm 10\%$	93	68	43	35	29	53	24	22
$\pm 20\%$	98	90	73	64	57	80	48	46

value is equal to the laboratory value. A comparison of the percentage of data points where the predicted is within $\pm 10\%$ or $\pm 20\%$ of the laboratory measured R -value is shown in Table 4. Predicted values that were within $\pm 10\%$ of the laboratory value are shown in blue-filled circles, while those within $\pm 20\%$ of the laboratory value are shown in black-filled circles. All other cases are plotted in hollow circles.

7 Results of Regression Analysis for Resilient Modulus

The resilient modulus model parameters k_1 , k_2 , and k_3 were first determined for all soil tests adopting the resilient modulus model (Eq. 2). These parameters are then considered as dependent variables and were individually correlated to basic soil properties. Various fundamental soil properties were considered as independent variables and used in regression analysis. The multiple linear regression model presented in Eq. 3 was used, and the top model based on R^2 adjusted was identified. The following equations present the top regression models with more than 30 soil test results.

Soil Type: A-1-b; M_r model $\{R^2 = 0.905, R^2_{adj} = 0.903\}$

$$k_1 = 1123 - 33.7P_{1in} + 72.0P_{\#10} - 42.3P_{\#200} \{R^2 = 0.999, \text{Adj. } R^2 = 0.999\} \quad (14)$$

$$k_2 = 0.115 + 0.0833P_{\#100} - 0.0611P_{\#200} - 0.134PI \{R^2 = 0.999, \text{Adj. } R^2 = 0.999\} \quad (15)$$

$$k_3 = 6.28 + 1.11MC - 0.605P_{\#50} + 0.876PI \{R^2 = 0.999, \text{Adj. } R^2 = 0.999\} \quad (16)$$

Soil Type: A-2-4; M_r model $\{R^2 = 0.497, R^2_{adj} = 0.488\}$

$$k_1 = 3218 - 103P_{2in} + 74.3P_{\#4} + 354PI \{R^2 = 0.999, \text{Adj. } R^2 = 0.995\} \quad (17)$$

$$k_2 = 7.16 - 0.0753P_{2in} + 0.0199P_{\#16} - 0.155PI \{R^2 = 0.999, \text{Adj. } R^2 = 0.999\} \quad (18)$$

$$k_3 = 1.40 + 0.0131 P_{2 \text{ in}} - 0.168 P_{\#100} \{R^2 = 0.999, \text{Adj.}R^2 = 0.999\} \quad (19)$$

Soil Type: A-4; M_r model $\{R^2 = 0.608, R^2_{\text{adj}} = 0.595\}$

$$k_1 = 13475 - 91.4 P_{1/2 \text{ in}} - 408 \text{PI} \{R^2 = 0.995, \text{Adj.}R^2 = 0.986\} \quad (20)$$

$$k_2 = 2.62 - 0.00816 P_{1/2 \text{ in}} - 0.216 \text{PI} \{R^2 = 0.985, \text{Adj.}R^2 = 0.954\} \quad (21)$$

$$k_3 = -3.9743 - 0.0866 \text{UW} + 0.133 P_{3/8 \text{ in}} - 0.401 \text{PI} \{R^2 = 0.962, \text{Adj.}R^2 = 0.924\} \quad (22)$$

Soil Type: A-6; M_r model $\{R^2 = 0.730, R^2_{\text{adj}} = 0.721\}$

$$k_1 = -310 + 76.9 P_{3/8 \text{ in}} - 166 \text{LL} \{R^2 = 0.997, \text{Adj.}R^2 = 0.992\} \quad (23)$$

$$k_2 = 3.41 - 0.0245 P_{3/8 \text{ in}} - 0.0278 \text{LL} \{R^2 = 0.972, \text{Adj.}R^2 = 0.915\} \quad (24)$$

$$k_3 = 17.8 - 0.391 \text{MC} - 0.199 P_{\#4} + 0.413 \text{LL} - 0.679 \text{PI} \{R^2 = 0.939, \text{Adj.}R^2 = 0.877\} \quad (25)$$

The plot of M_r predicted using Eqs. (14)-(25) and the laboratory measured M_r is presented in Fig. 3. The diagonal line represents the predicted value being equal to the laboratory value. For A-1-b soil, 40.9 and 86.4% of predicted values were within 10 and 20% of the laboratory measured values, respectively. These percentages were 21.3 and 41.3% for soil type A-2-4; 36.7 and 56.7% for soil type A-4, and 16.7 and 20.0% for soil type A-6. Predicted values that were within $\pm 10\%$ of the laboratory value are shown in blue-filled circles, while those within $\pm 20\%$ of the laboratory value are shown in black-filled circles. All other cases are plotted in hollow circles.

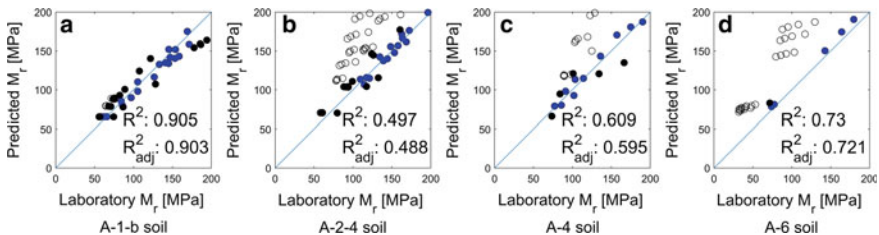


Fig. 3 Predicted versus laboratory M_r values

8 Conclusions

An extensive database of R -value and resilient modulus tests was established for Colorado soils, and multiple linear regression analysis was performed to develop prediction models for estimating the R -value and the resilient modulus based on basic soil properties. The database included over 2600 R -value data points and associated soil basic properties as well as over 200 resilient modulus tests and associated soil basic properties. Prediction models for R -value for AASHTO soil types had the adjusted R^2 values ranging from 0.529 to 0.944. The results showed that 98, 90, 73, 64, 57, 80, 48, and 46% of R -values obtained from the prediction equations for A-1-a, A-1-b, A-2-4, A-2-6, A-2-7, A-4, A-6, and A-7-6, respectively, fell within $\pm 20\%$ of the laboratory R -values. The adjusted R^2 values obtained for the prediction models for k coefficients, using the generalized resilient modulus model that was developed through NCHRP project 1-28A, ranged from 0.488 to 0.903. The prediction models showed that 87, 41, 57, and 20 of resilient modulus values obtained from the prediction equations for A-1-b, A-2-4, A-4, and A-6, respectively, fell within $\pm 20\%$ of the laboratory resilient modulus values. These models have only been evaluated based on the existing database; further research is needed to validate the models using a separate set of R -value and soil property data.

Acknowledgements This research work was funded by the Colorado Department of Transportation with study No. 418.01 and award #430143. This financial support is greatly appreciated. The authors would like to thank the members of the study panel for their support and assistance by providing access to the Colorado Department of Transportation's soil database and written test reports. The authors acknowledge Mr. Jon Grinder's excellent testing and reporting practice. Ground Engineering Consultants willingness in providing an extensive database of resilient modulus tests and associated soil properties is also greatly appreciated. The contents of the paper reflect the views of the authors and do not necessarily reflect the views of the Colorado Department of Transportation.

References

1. Darter MI, Elliot RP, Hall KT (1992) Revision of AASHTO pavement overlay design procedures. Appendix: Documentation of design procedures. National Cooperative Highway Research Program Study Rep. No. 20-7, TRB, National Research Council, Washington, D.C.
2. Nazzal MD, Mohammad LN (2010) Estimation of resilient modulus of subgrade soils for design of pavement structures. *J Mater Civ Eng* 22(7):726-734
3. Chang NY, Chiang HH, Jiang LC (1994) Resilient modulus of granular soils with fines content. Report No. CDOT-DTD-R-95-9, Colorado Department of Transportation, Denver
4. Carmichael III RF, Stuart E (1978) Predicting resilient modulus: a study to determine the mechanical properties of subgrade soils. Transportation Research Record. 1043, TRB, National Research Council, Washington, D.C.
5. Drumm EC, Boateng-Poku Y, Pierce TJ (1990) Estimation of subgrade resilient modulus from standard tests. *J Geotech Eng* 116(5):774-789
6. George KP (2004) Prediction of resilient modulus from soil index properties. Rep. No. FHWA/MS-DOT-RD-04-172, University. of Mississippi, Miss

7. Santha BL (1994) Resilient modulus of subgrade soils: comparison of two constitutive equations. Transportation Research Record. 1462, TRB, National Research Council, Washington, D.C.
8. Malla RB, Joshi S (2007) Resilient modulus prediction models based on analysis of LTPP data for subgrade soils and experimental verification. *J Transp Eng* 133(9):491–504
9. Titi HH, Elias MB, Helwany S (2006) Determination of typical resilient modulus values for selected soils in Wisconsin. Project ID 0092-03-11, Wisconsin Department of Transportation, Madison, p 175
10. Von Quintus H, Killingsworth B (1998) Analysis relating to pavement material characterizations and their effects on pavement performance. Rep. No. FHWA-RD-97-085, FHWA, U.S. DOT, Washington, D.C.
11. Rada G, Witczak MW (1981) Comprehensive evaluation of laboratory resilient moduli results for Granular Material. Transportation Research Record No. 810, Transportation Research Board, pp 23–33
12. Thompson MR, Robnett QL (1979) Resilient properties of subgrade soils. *Trans Eng J ASCE* 105(TE1):71–89
13. Lenke LR, Kias EMC, Jenkins R, Grgich C (2006) Field R-value correlation method development. (Interim Report Phase 1). Rep. No. NM04MSC-02.1, NMDOT Research Bureau, Albuquerque, NM
14. Archilla R, Ooi P, Sandefur K (2007) Estimation of a resilient modulus model for cohesive soils using joint estimation and mixed effects. *J Geotech Geoenviron Eng* 133(8):984–994
15. Shongtao D, Zollars J (2002) Resilient modulus of Minnesota road research project subgrade soil. Transportation Research Record. 1786, TRB, National Research Council, Washington, D.C.

Performance Evaluation of Flexible Pavements with Asphalt-Treated Base Courses



Jun Liu, Jenny Liu, Peng Li, and Stephan Saboundjian

Abstract The base course is an essential component in a flexible pavement which supports the surface course and distributes traffic loads to the subbase and subgrade. Asphalt treatment has been widely used on granular base course material to enhance the material's properties and overcome its deficiencies. However, a comprehensive evaluation on the performance of flexible pavements with different asphalt-treated base materials has not been done yet in the literature. In this study, the AASHTOWare Pavement Mechanistic-Empirical (ME) Design software and Alaska Flexible Pavement Design (AKFPD) program were used to predict the performance of flexible pavements with four different ATBs, i.e., hot asphalt-treated base (HATB), emulsified asphalt-treated base (EATB), and foamed asphalt-treated base (FATB), and reclaimed asphalt-pavement-treated base (RAP-TB), and one control granular base. The International Roughness Index (IRI), rutting, and fatigue cracking of flexible pavements with different base materials were predicted and compared. The structure number (SN) of pavements (with the same pavement structures) with different base materials was calculated and compared. The results indicated that pavements constructed with ATBs or RAP-TB can have similar or better performance than those constructed with granular base.

Keywords Asphalt-treated base · MEPDG · AKFPD · Structure number

J. Liu · J. Liu (✉)

Department of Civil, Architectural and Environmental Engineering, Missouri University of Science and Technology, Rolla, MO 65409, USA

e-mail: jennyliu@mst.edu

J. Liu

e-mail: j14h6@mst.edu

P. Li

School of Highway, Chang'an University, Xi'an, Shanxi 710064, China

e-mail: Lipeng2013@chd.edu.cn

S. Saboundjian

Alaska Department of Transportation and Public Facilities, 5800 E. Tudor Rd, Anchorage, AK 99507, USA

e-mail: steve.saboundjian@alaska.gov

1 Introduction

In many areas of Alaska, clean, durable aggregates normally utilized for base course either require long hauls from outside, or they are difficult to obtain within the project limits. The capacity to stabilize the available lower quality materials for use as base course strengthens pavements, thus extending their lifespans and saving the state money in the long run. Asphalt-treated bases (ATBs) are the most commonly used type of stabilized layers in Alaska because of material availability and relative cost. ATB is composed of asphalt binder and graded granular materials. Depending on the method of mixing the asphalt with the granular material, there are three types of ATBs: hot asphalt-treated base (HATB), emulsified asphalt-treated base (EATB), and foamed asphalt-treated base (FATB).

Studies have been conducted in the past decades to characterize ATBs and evaluate their performances [1–4]. Those studies found that the resilient modulus (M_r) of ATB exhibits a stress-dependent property due to its lower binder content and lower quality granular material. Li et al. [3] indicated that adding asphalt binder in different format greatly affects the mechanical behavior of ATBs. In HATB and EATB, aggregate particles are well coated by asphalt binder, which provides a good bonding strength between particles, and therefore, the M_r s of HATB and EATB have higher resistance to the change of stress state. On the other hand, in FATB, asphalt binder is spread as small droplets between aggregate particles and the bonding between particles is weaker than that of HATB and EATB [3]. However, no much efforts looked into the overall performances of pavements with ATBs. This study systematically investigated the performances of three types of ATBs and mixture of reclaimed asphalt pavement (RAP) and granular base course material (D-1) at 50–50% ratio (RAP-TB).

2 Objective and Scope

The main objective of this study is to evaluate the performance of ATBs used in Alaska. Performances of pavements with ATBs were predicted by using the fatigue cracking transfer function in Alaska Flexible Pavement Design (AKFPD) program adopted by Alaska Department of Transportation and Public Facilities (ADOT&PF). AASHTOWare Pavement Mechanistic–Empirical (ME) Design software was also used to compare the performances of pavements with different ATBs. The structure numbers (SNs) of typical pavements with different ATBs were calculated based on AASHTO 1993 design guide.

Table 1 Gradation of D-1 materials

Sieve designation		% Passing			
Standard (mm)	Alternate	Central region (%)	Reference (%)	D-1 standard	
				Lower (%)	Upper (%)
25	1"	100.0	100.0	100.0	100.0
19	3/4"	99.6	100.0	70.0	100.0
9.5	3/8"	72.6	72.4	50.0	80.0
4.75	#4	50.0	46.7	35.0	65.0
2.36	#8	37.5	31.3	20.0	50.0
0.3	#50	9.9	9.8	8.0	30.0
0.075	#200	2.9	3.2	0.0	6.0

3 Laboratory Experiments

3.1 Materials

The base materials evaluated included HATB, EATB, FATB, and RAP-TB. Granular materials used for base course construction, known as D-1 materials (Table 1), were collected from the central region of Alaska. The asphalt binder used for this study was PG 52-28 asphalt, which is the neat asphalt type used in Alaska. Three binder contents, 2.5%, 3.5%, and 4.5%, by weight of total mixture were introduced to prepare specimens of HATB. The PG 52-28 binder was also used to generate foamed asphalt with the WLB 10 foamed asphalt laboratory system to prepare FATB specimens, and the percentages of foamed asphalt (residual binder) applied to FATB were 1.5%, 2.5%, and 3.5% in this study. The type of emulsified asphalt used in this study to prepare EATB specimens was CSS-1, a cationic emulsion with low viscosity. The percentages of emulsion added were 1.5%, 2.5%, and 3.5% of residual binder. The solid content of emulsified asphalt was 59%, which met the requirement (57%) specified in AASHTO M 208. The RAP was collected from a local source in Fairbanks, Alaska.

3.2 Laboratory Tests

The repetitive triaxial compressive test was used to measure the M_r of the ATBs and RAP-TB at three different temperatures (i.e., -10 , 0 , 20 °C, which were used to represent temperatures of winter, spring, and summer & fall, respectively) using a close-loop testing system according to the standard of AASHTO T307. The detailed M_r testing descriptions can be found in elsewhere [2, 3]. The stress-dependent behavior of M_r of the ATBs and RAP-TB was confirmed. The M_r model in the MEPDG program was calibrated (modified) for the HATB (Eq. 1), EATB (Eq. 2), FATB

(Eq. 3), and RAP-TB (Eq. 4) based on the testing results [5].

$$M_r = e^{1.1548+0.04736F-0.0596T-0.1723P_b} P_a \left(\frac{\theta}{P_a} \right)^{0.2669} \left(\frac{\tau_{\text{oct}}}{P_a} + 1 \right)^{-0.4109} \quad (1)$$

$$M_r = e^{4.1205+0.0025F-0.0567T-0.0048P_b} P_a \left(\frac{\theta}{P_a} \right)^{0.0842} \left(\frac{\tau_{\text{oct}}}{P_a} + 1 \right)^{-0.2236} \quad (2)$$

$$M_r = e^{-2.9060+0.0623F-0.0363T-0.2346P_b} P_a \left(\frac{\theta}{P_a} \right)^{0.0029} \left(\frac{\tau_{\text{oct}}}{P_a} + 1 \right)^{4.285-0.0434F-0.0206T-0.1365P_b} \quad (3)$$

$$M_r = e^{-9.0482+0.1294F-0.2346T} P_a \left(\frac{\theta}{P_a} \right)^{0.00294.5056-0.00406F+0.0586T} \left(\frac{\tau_{\text{oct}}}{P_a} + 1 \right)^{0.1578-0.0099F-0.031T} \quad (4)$$

where M_r is resilient modulus, ksi; θ is bulk stress, $\sigma_1 + \sigma_2 + \sigma_3$, psi; τ_{oct} is deviatoric stress: $1/3[(\sigma_1 - \sigma_2)^2 + (\sigma_1 - \sigma_3)^2 + (\sigma_2 - \sigma_3)^2]^{1/2}$, psi; P_a is atmosphere air pressure, psi; T is temperature, °C, P_b is asphalt content, %; and; F = fractured surface, %.

3.3 AKFPD Analysis

The fatigue life (Eq. 5) and rutting life (Eq. 8) transfer functions in AKFPD manual were employed in this study to predict the fatigue and rutting performance of pavements with different base materials [6]. A typical Alaska pavement structure was used for AKFPD analysis in this study. The pavement consisted of a 5-cm (2 in.) HMA surface layer, 10-cm (4 in.) ATB (HATB, EATB, FATB, or RAP-TB), 60-cm (24 in.) aggregate subbase (with lower quality aggregate), and subgrade. In order to obtain the critical pavement responses (i.e., ε_h) considering the stress-dependent behavior of M_r of the ATBs and RAP-TB, Eqs. 1–4 were implemented into a finite element (FE) program [5]. The layers were assumed to fully bond with each other. The single-axle dual-wheel loads were used as standard loads. Each wheel load equaled to 20 kN (4500 lb) and the spacing between centers of wheels was 0.343 m (13.5in.). The contact area between tire and pavement was simplified as a circular area with the radius of 0.1 m, and the pressure was evenly distributed on this area with the magnitude of 620 kPa (90 psi). More details about the FE model can be found in the reference [5]. The E^* values of asphalt concrete were set as 1500, 750, and 550 ksi for winter, spring, and summer & fall conditions, respectively. The parameter M

relates to HMA volumetric properties. In this study, the air void volume (V_v) was 4%, and the binder volume (V_b) was 12%.

$$N_{Ff} = C \times 0.07958 \times \varepsilon_h^{-3.291} \times (E^*)^{-0.854} \quad (5)$$

$$C = 10^M \quad (6)$$

$$M = 4.84 \times \left(\frac{V_b}{V_v + V_b} - 0.69 \right) \quad (7)$$

where N_{Ff} is fatigue life (number of design load repetitions to fatigue failure); ε_h is maximum horizontal tensile strain at the bottom of asphalt concrete layer, %; E^* is dynamic modulus of the asphalt concrete, psi, V_v is percent air voids volume in total asphalt concrete; V_b is percent binder volume.

3.4 MEPDG Analysis

MEPDG software was used to compare the performance of pavements with different ATBs. All pavements had the same structure, which consisted of a 5-cm (2 in.) HMA surface layer, 10-cm (4 in.) ATB, 60-cm (24 in.) aggregate, and subgrade. The analysis was conducted for a 20-year design period. The initial two-way average annual daily truck traffic was assumed to be 200 vehicles per day with 50% trucks in the design direction and 95% trucks in the design lane. The values for vehicle class distribution, number of axles per truck of each class, and axle configuration were collected from long-term pavement performance (LTPP) database in the analysis. Monthly adjustment factors were set at 1.0. The traffic growth rate was 3% per year. Level III inputs were used for the asphalt concrete mixture layers and subbase layers. Level II inputs were used for the ATBs layer. For ATBs layers, there were two options for analysis. One is treating the ATBs as asphalt concrete base layer, which requires the dynamic modulus (E^*) values of ATBs materials. The other is treating the ATBs as aggregate base. The difference between different ATBs were the MR inputs. In this analysis, since the E^* values are not available, the ATBs were treated as aggregate bases. A summary resilient modulus (SMR), as recommended by NCHRP-28A report [7], was calculated for each ATBs at different temperature conditions and binder contents by considering bulk stress (θ) equal to 30.2 psi and the deviatoric stress (τ_{oct}) equal to 7 psi by using Eqs. 1–4. Table 2 presents a summary of the input parameters used in the MEPDG analysis.

Table 2 MEPDG input parameters of pavement layers

Material	Input level	Input parameter
Asphalt concrete	III	Thickness: 2 in. PG 52-28; Poison ratio: 0.3; Density: 150 pcf
ATB	II	Aggregate gradation SMR; Poison ratio: 0.35; Density: 157 pcf
Aggregate subbase	III	M_R : 18 ksi Poison ratio: 0.35; Density: 157 pcf
Subgrade	III	M_R : 10 ksi Poison ratio: 0.35; Density: 157 pcf

3.5 AASHTO 1993 Design Analysis

The structure numbers (SNs) of typical pavements with different ATBs were calculated based on AASHTO 1993 design guide. According to the AASHTO 1993 Design Guide, the structural number, SN, was a function of layer thickness, layer coefficients, and drainage coefficients, as expressed in Eq. 8. The typical Alaska pavement structure used for AKFPD and MEPDG analysis was employed. For this paper, since the modulus of the asphalt concrete layer was constant (refer to Table 2), the corresponding layer coefficient of the asphalt concrete layer, a_1 , was 0.26 for all cases. Equation 9 gives the empirical equation to determine the layer coefficient of the ATBs. Assuming the drainage coefficient of the ATBs and aggregate subbase, m_2 , to be 1.0 and 0.8, respectively. The layer coefficient of the aggregate subbase layer, a_3 , was 0.11 for all cases.

$$SN = a_1 D_1 + a_2 D_2 m_2 + a_3 D_3 m_3 \quad (8)$$

$$a_2 = 0.249 * \log(SMR) - 0.977 \quad (9)$$

where SN is structural number; a_1 , a_2 , and a_3 are layer coefficients for the asphalt concrete layer, ATBs, and subbase layer, respectively; m_2 and m_3 are drainage coefficients for the ATBs and subbase, respectively; D_1 , D_2 , and D_3 are layer thicknesses for the asphalt concrete layer, ATBs layer, and subbase layer, respectively; and SMR is summary resilient modulus of ATBs, psi.

4 Results and Analysis

4.1 AKFPD Analysis

In this study, the critical pavement responses (i.e., maximum horizontal tensile strain at the bottom of asphalt mixture layer and maximum vertical compressive stress at the top of the base layer) were selected from the a FE analysis [5] and substituted into the fatigue failure model (Eq. 5), corresponding to the condition of fatigue cracking (bottom-up) covering 45% of the wheel path area, to calculate the fatigue life. The fatigue life was calculated for different ATBs at different season conditions (i.e., winter, spring, and summer & fall conditions). According to the AKFPD manual, the climate and traffic distribution of Central Region could be 40%, 10%, and 50% for winter, spring, and summer&fall conditions, respectively. Therefore, an overall fatigue life was calculated for each ATB by considering the climate and traffic distributions as weights. The predicted fatigue lives of pavements with different ATBs are summarized in Fig. 1. It can be seen that the pavements with HATBs showed the highest fatigue lives. The pavements with FATBs showed the lowest fatigue lives. The binder contents covered in this study showed insignificant effects on the predicted fatigue lives of pavements with ATBs. This might be attributed to the change of binder content within this small range did not make significant difference in the resilient modulus of the material.

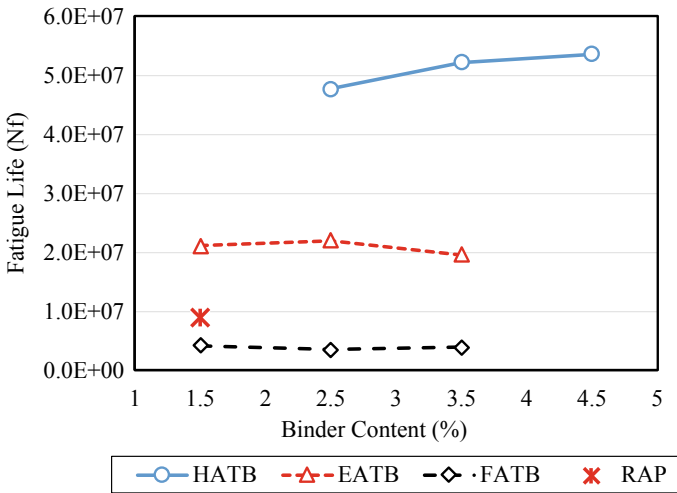


Fig. 1 Predicted fatigue life from AKFPD

4.2 MEPDG Analysis

MEPDG software was used to predict the distress parameters for the pavements with different ATBs. The distress parameters included rutting, alligator fatigue cracking, and IRI. Similar to AKFPD analysis, an overall distress parameter value was calculated for each ATB by considering the climate and traffic distributions as weights. Figure 2 presents the total predicted rut depths after 20 years of service. As shown, the predicted rut depth of pavements with ATBs were lower than that of the one with granular base. The pavement with HATB showed similar rutting performance to the one with EATB. The binder content showed insignificant effect on the rutting performance of pavements with HATB and EATB, while showed notable effect on pavement with FATB. The pavement with RAP-TB showed higher predicted rut depth than the ones with ATBs (except for the FATB with 3.5% binder content) while showed lower predicted rut depth than the one with granular base.

Figure 3 shows fatigue cracking at the end of the analysis period for pavements with different base materials. It is clear that pavements with ATBs showed lower fatigue cracking values than the one with granular materials. The pavements with HATB and ETAB possessed a similar fatigue cracking performance, which is inconsistency to AKFPD analysis. The binder contents covered in this study showed insignificant effects on the predicted fatigue cracking values of pavements with HATB and ETAB. The pavement with RAP-TB showed slightly higher fatigue cracking value than the one with granular base. This is easy to understand that RAP-TB contains stiff asphalt binder which is prone to cracking.

Figure 4 presents the IRI values predicted at the end of the 20-year analysis period. The pavements with ATBs and RAP-TB had a slightly lower IRI value than the one with the granular base. In summary, the results of the MEPDG analysis

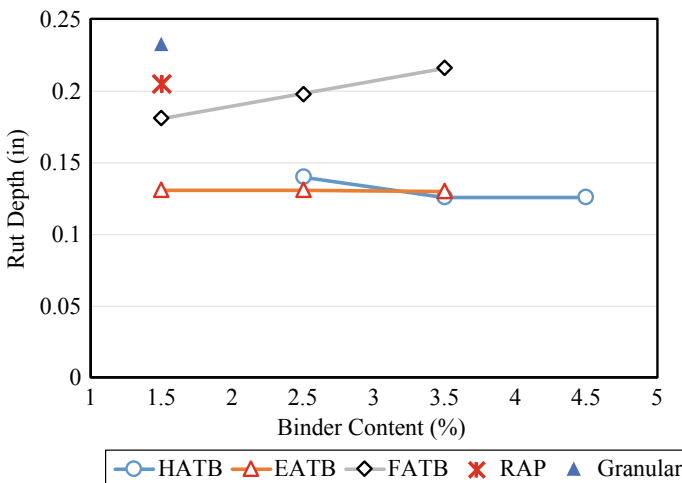


Fig. 2 Rutting results of MEPDG prediction

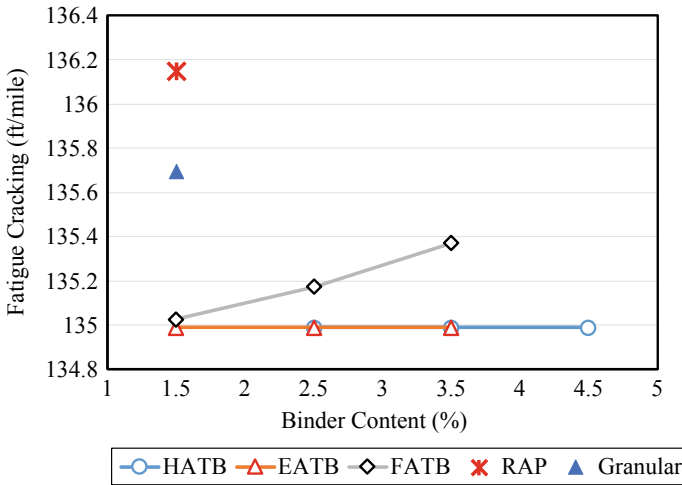


Fig. 3 Fatigue cracking results of MEPDG prediction

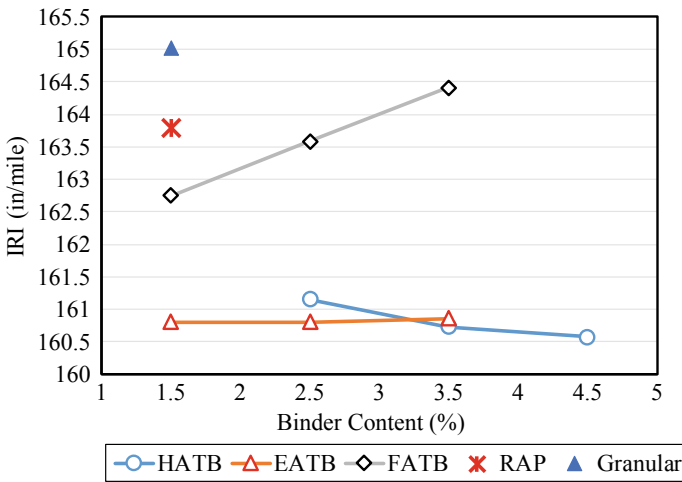


Fig. 4 IRI results of MEPDG prediction

suggest that pavements constructed with ATBs or RAP-TB can have similar or better performance than those constructed with granular base. The commonly used binder contents for HATB, EATB, and FATB are 3.5%, 2.5%, and 2.5%, respectively. By overall comparing the performances of pavements with 3.5% HATB, 2.5% EATB, 2.5% FATB, RAP-TB, and granular base, the pavement with 3.5% HATB showed the best performance, followed by the ones with 2.5% EATB, 2.5% FATB, RAP-TB, and granular base.

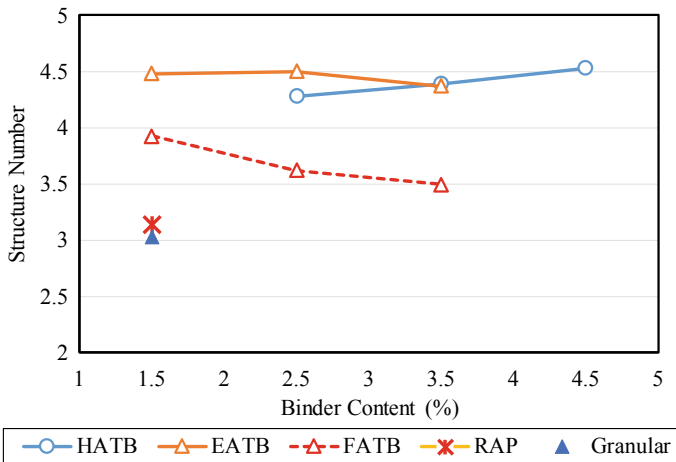


Fig. 5 SN of pavements with different base materials

4.3 AASHTO 1993 Design Analysis

The structure numbers (SNs) of pavements with different ATBs (with the same pavement structures) were calculated (Eq. 8). Figure 5 presents the results. In general, the pavement with higher SN could have better performance [6]. As shown, the pavements with ATBs had higher SN values than the one with granular base. The pavements with HATB and EATB showed similar SN values, and showed higher SN values than the ones with FATB and RAP-TB. The pavement with RAP-TB showed similar SN value as the one with granular base. As indicated by Eq. 8, in this study, the SNs were mainly dependent on the base course layer coefficient (a_2) which is closely related to the M_r of the ATBs. According to Li [5], the HATB generally showed higher M_r values than other types of ATBs [5].

5 Conclusions

In this study, the AKFPD, MEPDG, and AASHTO 1993 design methods were used to predict the performance of flexible pavements with four different base materials, i.e., hot asphalt-treated base (HATB), emulsified asphalt-treated base (EATB), foamed asphalt-treated base (FATB), and reclaimed asphalt-pavement-treated base (RAP-TB), and one control granular base. Based on the results, the following conclusions can be drawn:

- According to the AKFPD analysis results, the pavements with HATBs showed the highest fatigue lives.

- The results of the MEPDG analysis suggested that pavements constructed with ATBs or RAP-TB can have similar or better performance than those constructed with granular base.
- The pavements with ATBs had higher SN values than the one with granular base.
- The effect of binder content on the predicted distress parameters or pavement performance are different for pavements with various ATBs.

References

1. Li P, Liu J (2014) Predictive model for nonlinear resilient modulus of emulsified asphalt treated base. *Pavement materials, structures, and performance*, GSP239, Geo-Shanghai 2014, Shanghai, China, pp 383–394
2. Li P, Liu J, Saboundjian S (2011) Materials and temperature effects on the resilient response of asphalt treated Alaskan base course materials. *J Mater Civ Eng* 23(2):161–168
3. Li P, Zhao S, Liu J (2016) Characterizing stress–strain relationships of asphalt treated base. *ASCE J Mater Civ Eng* 28(8):49
4. Fu P, Harvey JT (2007) Temperature sensitivity of foamed asphalt mix stiffness: field and lab study. *Int J Pavement Eng* 8(2):137–145
5. Li P (2013) Characterization and implementation of stress dependent resilient modulus of asphalt treated base for flexible pavement design. Dissertation (Ph.D.). Fairbanks, AK: University of Alaska Fairbanks. (2013)
6. Huang YH (2004) *Pavement analysis and design*, 2nd edn. Prentice Hall Inc, Englewood Cliffs, N.J.
7. NCHRP (2004) *Guide for mechanistic-empirical design of new and rehabilitated pavement structures*. National cooperative highway research program transportation research board national research Council. <https://doi.org/10.1111/cpf.12185>

Investigation of Instantaneous Shear Failure in Pavement Subgrade Subjected to Superheavy Load Vehicle



Hadi Nabizadeh , Mohamed Nimeri , Elie Y. Hajj ,
Raj V. Siddharthan , and Sherif Elfass 

Abstract The movement of superheavy loads (SHLs) on the US highways is an increasingly common, economic necessity for many important industries, such as chemical, oil, electrical, and defense. They often require specialized trailers and components that are assembled to suit the SHL vehicle's characteristics. The SHL vehicles are often oversized and exceed legal gross vehicle weight, axle, and tire load limits. The overlapping stress distributions in pavement layers under such high tire loads can render a critical condition of instantaneous ultimate (global) shear failure, especially in the subgrade pavement layer. In this paper, a methodology to examine the risk of instantaneous shear failure in a flexible pavement subjected to an SHL vehicle movement is presented. To this end, Meyerhof's general bearing capacity equation is employed since it is a well-established and validated foundation design procedure under static or slow-rate loading conditions. The proposed ultimate failure analysis that considers the influence of pavement layers with distinct stiffness and strength properties, focuses on the failure of subgrade layer as it is generally the weakest layer in a pavement structure. The distributed vertical stress induced by an SHL vehicle on top of the subgrade layer is compared to the bearing capacity of the subgrade layer. In order to demonstrate the developed methodology, the analysis

H. Nabizadeh (✉)

Applied Research Associates, Inc. (ARA), 100 Trade Centre Dr, Suite 200, Champaign, IL, USA
e-mail: hnabizadeh@ara.com

M. Nimeri

King County International Airport, 7277 S Perimeter Road S, Suite 200, Seattle, WA, USA
e-mail: mnimeri@kingcounty.gov

E. Y. Hajj · R. V. Siddharthan · S. Elfass

Department of Civil and Environmental Engineering, University of Nevada, Reno, 1664 N. Virginia St., Reno, NV 89557, USA
e-mail: elieh@unr.edu

R. V. Siddharthan

e-mail: siddhart@unr.edu

S. Elfass

e-mail: elfass@unr.edu

steps and the associated results for an SHL vehicle configuration permitted by the Louisiana Department of Transportation and Development (LaDOTD) are presented.

Keywords Superheavy load · Ultimate shear failure · Bearing capacity · Pavement subgrade

1 Introduction

The movement of superheavy loads (SHLs) on the US highways have become more common over the years for many important industries, such as chemical, oil, electrical, and defense. The SHL vehicles are often oversized and exceed legal gross vehicle weight (GVW), axle, and tire load limits. Therefore, they require special permits to operate on U.S. highways. Such vehicles usually operate under single-trip permits that require pavement structural analysis. Accommodating SHL movements without undue damage to highway infrastructure requires the determination of whether the pavement is structurally adequate to sustain the SHL movement and protect any underground utilities. Such determination involves analyzing the likelihood of instantaneous or rapid load-induced shear failure of the pavement structure [1, 2].

As part of a Federal Highway Administration project, Analysis Procedures for Evaluating Superheavy Load Movement on Flexible Pavements, a comprehensive mechanistic-based analysis approach consisting of several analysis procedures was developed for evaluating SHL movement on flexible pavements. In general, the approach consists of four major components: (a) Ultimate failure analyses; (b) Buried utility risk analysis; (c) Service limit analyses; and (d) Cost allocation analysis. Mitigation strategies may be needed at any stage of the evaluation process when the calculated results fail to meet the respective requirements imposed (e.g., when results indicate a high potential for shear failure of the pavement or damage to buried utilities).

2 Problem Statement

SHL hauling units are much larger in size and weight compared to standard trucks, and they travel at much lower speeds. They often require specialized trailers and components that are assembled to suit the SHL vehicle's characteristics. Although the tires used in the transport are often conventional, the axle and tire configurations used are variable. This means that the spacing between tires and axles is not standard, and the tire imprints can span more than the entire width of a lane. Three examples of permitted SHL vehicles are illustrated in Fig. 1 through Fig. 3. Figures 1 and 2 were SHL vehicles permitted by Louisiana Department of Transportation and

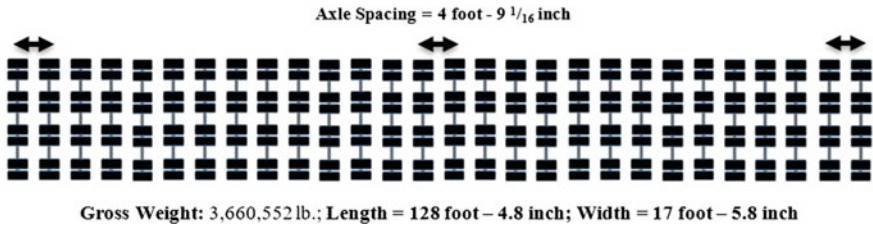


Fig. 1 Example configuration (LA-8 T-14) of a permitted SHL vehicle with continuous axle configuration

Development (LaDOTD), while Fig. 3 was an SHL permitted in Nevada Department of Transportation (NDOT) [3].

As a representative example, the case of a five-line load model is shown in Fig. 4. The elevation plot shows the overlapping of vertical stresses (σ_v) at deeper locations

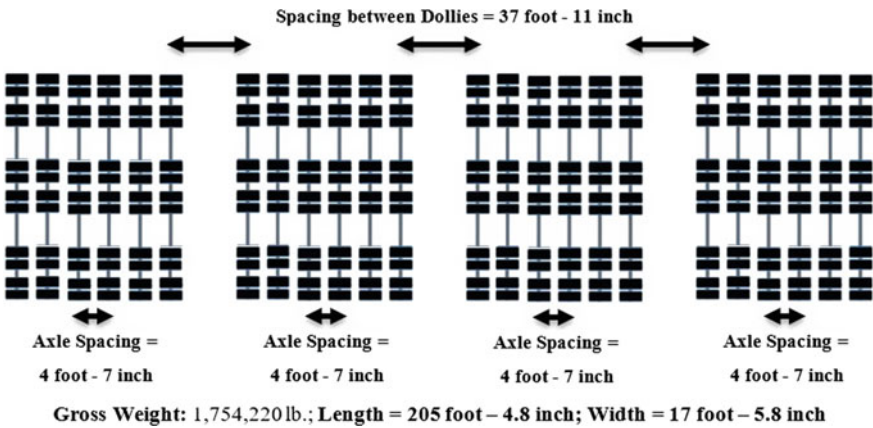


Fig. 2 Example configuration (LA-12 T-16) of a permitted SHL vehicle with fragmented axle configuration

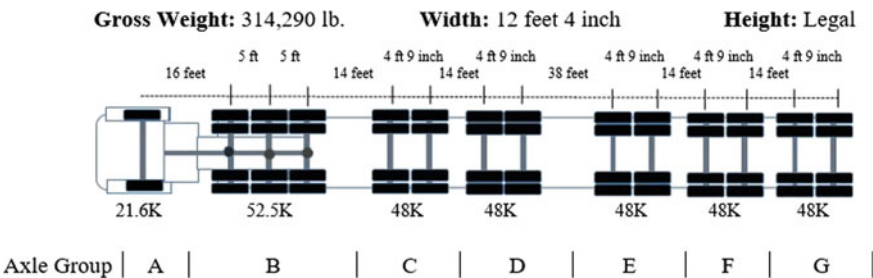


Fig. 3 Example configuration (NV-4 T-10) of a permitted SHL vehicle

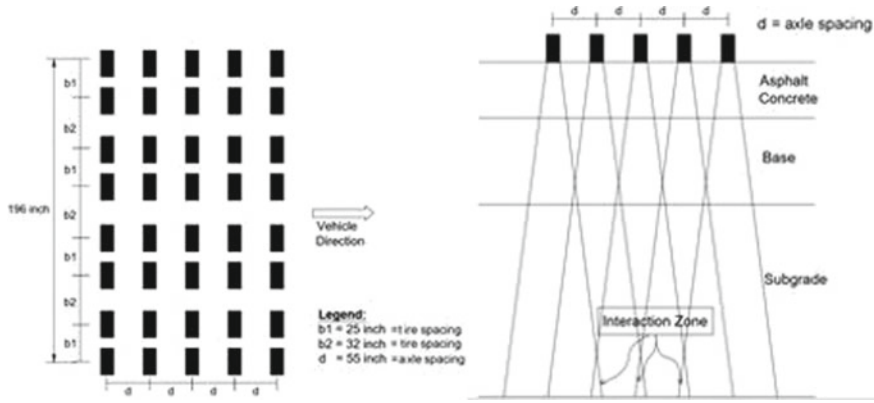


Fig. 4 Five-line model for SHL vehicle simulation; left: plan view; right: elevation view

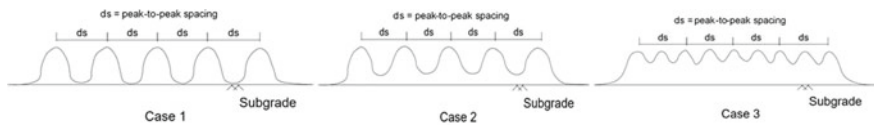


Fig. 5 Vertical stress distribution within pavement

within the pavement. These overlapping stresses, at any interior plane, can fall under one of the three cases shown in Fig. 5. Case 1 represents no overlapping, case 2 shows moderate overlapping, and case 3 shows substantial overlapping of vertical stress. The vertical stress resulting from surface tire loads of the SHL vehicle is expected to overlap beyond a specific depth within the pavement structure. The extent of overlapping is highly affected by the surface-load magnitude and configuration as well as the pavement layer properties and thicknesses.

The vertical stress distribution below the pavement surface under an SHL vehicle represent a critical condition of instantaneous ultimate (global) shear failure, because of the combined effect of heavy tire loads and the overlapping of stress distributions, especially in the deeper zone of the subgrade. It should be noted that the most vulnerable layer for shear failure is likely the subgrade because it is the weakest layer in the pavement structure [1, 2].

3 Ultimate Failure Analysis

In this study, Meyerhof’s general bearing capacity theory was used to investigate the likelihood of instantaneous shear failure in a pavement subgrade subjected to an SHL movement. Meyerhof’s ultimate bearing capacity (q_u) equation is applied to estimate bearing capacity of the subgrade layer. The distributed vertical stress on

top of the subgrade layer induced by an SHL vehicle is then compared against the bearing capacity of the subgrade to identify the possibility of ultimate shear failure in the pavement structure.

3.1 General Bearing Capacity Equation

Terzaghi presented a comprehensive theory for evaluating ultimate bearing capacity (q_u) of shallow strip foundations, using a uniform pressure [4]. Several studies aiming to improve the estimation of q_u followed Terzaghi's work. Meyerhof suggested a generalized bearing capacity equation that accounts for continuous, rectangular, square, and circular foundations and any inclination in the load [5, 6]. Meyerhof's general bearing capacity equation is shown in Eq. 1. In the following sections, the various components of Meyerhof's general bearing capacity equation are described.

$$q_u = cN_c F_{cs} F_{cd} F_{ci} + q'N_q F_{qs} F_{qd} F_{qi} + \frac{1}{2}\gamma B N_\gamma F_{\gamma s} F_{\gamma d} F_{\gamma i} \quad (1)$$

where: c = cohesion; q' = effective stress at the bottom of the foundation level; γ = unit weight of SG soil; B = width of the foundation (or diameter); F_{cs} = shape factor with respect to c ; F_{qs} = shape factor with respect to overburden; $F_{\gamma s}$ = shape factor with respect to unit weight; F_{cd} = depth factor with respect to c ; F_{qd} = depth factor with respect to overburden; $F_{\gamma d}$ = depth factor with respect to unit weight; F_{ci} = load inclination factor with respect to c ; F_{qi} = load inclination factor with respect to overburden; $F_{\gamma i}$ = load inclination factor unit weight; N_c = bearing capacity factor with respect to c ; N_q = bearing capacity factor with respect to overburden; and N_γ = bearing capacity factor with respect to unit weight.

3.2 Application of Meyerhof's Bearing Capacity for SHL Movement

SHL vehicles typically vary in terms of axle and tire configurations (i.e., number of axles, spacing between the axles, number of tires per axle, spacing between the tires, and tire loads). In general, SHL vehicles fall into three categories. In the first category, similar axles (i.e., similar number of tires per axle, spacing between the tires, and tire loads) are evenly distributed along the length of an SHL vehicle. In this category, the spacing between axles is close enough, so that stress distributions from tires on two adjacent axles clearly overlap beyond a specific depth in the pavement (e.g., the top of the subgrade layer). The SHL vehicle permit LA-8 T-14, for example, shows similar axles evenly distributed by 4.6 ft spacing along the length of the SHL vehicle (Fig. 1). In this case, all the axles can be treated as one group, and identifying the average uniform vertical stress (q_{ave}) on top of the subgrade layer can be initiated for

this group. The entire SHL vehicle is, therefore, assumed to be the bearing capacity investigation zone (i.e., loaded area) applying q_{ave} .

In the second category, an SHL vehicle consists of two or more dollies, the gaps between which are relatively large in comparison with the spacing between the axles within the dollies. As shown in Fig. 2, the SHL vehicle in the LA-12 T-16 permit consists of four individual dollies where each dolly has 6 axles and 12 tires per axle and the spacing between the dollies is nearly 38 ft. Each dolly should be considered one group, so there is a total of four groups in this case. The q_{ave} on top of the subgrade layer for one axle group (i.e., one dolly) should be used for investigating the bearing capacity since the four axle groups are identical. In this case, the loaded area is constrained to the length and width of one dolly.

The third category covers general cases with any axle and tire configuration. Figure 3 shows a schematic of an SHL vehicle configuration that encompasses cases with different axles (single, tandem, and tridem axle) with spacings. As such, there are many axle groups in this category, and each group can have an individual q_{ave} on top of the subgrade layer. Therefore, each axle group is assumed to be a bearing capacity investigation zone.

Meyerhof's general capacity equation requires the loaded area to be a fixed shape (e.g., strip, circle, or rectangle) with a uniform pressure distribution. As presented in Eq. 2, q_{ave} can be calculated by taking the integral of the induced vertical stress (σ_v) distribution on top of the subgrade layer and then dividing it by the affected area ($A_{affected}$).

$$q_{ave} = \frac{\int \sigma_v dx dy}{A_{affected}} \quad (2)$$

where: dx = differential of the variable x ; and dy = differential of the variable y .

As a conservative measure, q_{ave} is assumed to cover the entire rectangular area of the axle group. This stress distribution can be considered the most critical possible scenario. It may be noted that a smaller subset of tires or axles within the SHL truck may be assumed to be the bearing capacity investigation zone (i.e., loaded area). However, it is physically impossible, because of the interconnectivity of the axles, to have one part of the vehicle develop a general bearing capacity failure mechanism while the rest does not. The entire axle group, since it is interconnected, will behave as a unit, and therefore, the failure should be undertaken for the entire axle group.

4 Illustration of Ultimate Failure Analysis

The SHL vehicle cases presented in Fig. 1 (namely LA-8 T-14) were selected to present the application of Meyerhof's general bearing capacity for the investigation of instantaneous shear failure under an SHL vehicle movement. The SHL vehicle in this case had 28 line axles and 8 tires per axle with GVW was over 3.6 million lb with a tire load of 16,342 lb. The SHL vehicle consisted of uniformly spaced axles,

the tires were sequentially spaced at 25 and 32 inch. Hence, it is considered as a single axle group.

3D-Move Analysis was the software of choice to compute the stress distributions within the pavement structure. The software calculates pavement responses at selected depths within a pavement structure as a function of axle load configuration, pavement structure, and material properties [7]. 3D-Move Analysis is capable of handling multiple load combinations with loaded areas of virtually any shape. The load-input file can be manually uploaded that allows for simulating any loaded area with nonuniform, normal tire–pavement contact stress distribution, and nonuniform interface shear stresses caused by braking and turning forces [7]. In this study, a uniformly distributed circular load configuration was used with a uniform tire pressure of 120 psi.

The synthetic pavement structure in this study consisted of 9 inches of asphalt concrete (AC) on top of 10 inches of crushed aggregate base and a semi-infinite subgrade layer. The asphalt layer was considered as a linear viscoelastic material, while unbound materials (base and subgrade) were assumed to behave as linear elastic. The viscoelastic properties of the AC layer were characterized using the dynamic modulus (E^*) laboratory data and asphalt binder properties as a function of temperature and frequency. 3D-Move Analysis generates E^* master curves at any reference temperature. Table 1 lists the material properties of each layer, and Tables 2 and 3 show the selected viscoelastic properties of the AC material. The dynamic modulus data are for a dense-graded hot-mix asphalt with a PG64-22 unmodified asphalt binder [3]. For this case example, 10 mph for the SHL vehicle traveling speed and 100°F for the AC layer temperature were assumed.

Table 1 Material properties

Layer type	Material	Thickness (inch)	Unit weight (pci)	Poisson's ratio	Resilient modulus (psi)
AC	Linear viscoelastic	9	0.08	0.40	Variable
CAB	Linear elastic	10	0.06	0.40	30,000
SG	Linear elastic	240	0.06	0.45	5,000

Table 2 Dynamic modulus values for a dense-graded asphalt mixture with PG64-22

Temperature (°F)	Frequency (Hz)					
	0.1	0.5	1	5	10	25
40	693,889	1,012,294	1,163,463	1,530,813	1,690,524	1,898,005
70	141,296	262,736	334,941	554,052	670,382	842,418
100	21,439	45,076	61,705	123,984	164,420	233,925
130	4,025	7,934	10,801	22,592	31,147	47,465

Table 3 Phase angle values for a dense-graded asphalt mixture with PG64-22

Temperature (°F)	Frequency (Hz)					
	0.1	0.5	1	5	10	25
40	22.1	19.0	17.3	15.5	15.9	18.1
70	31.2	29.8	30.1	27.8	27.4	26.3
100	28.5	29.9	31.3	35.0	35.5	36.8
130	23.2	26.8	27.0	33.9	34.1	40.1

An important initial step for determining the load-induced vertical stress (σ_v) distribution in the pavement structure is to simulate the SHL axle and tire configuration in a realistic manner. As such, a segment (or element) of the axle load configurations, referred to as Nucleus, can be regarded representative of the SHL vehicle. Hence, the σ_v distribution (or any other pavement responses) under the entire SHL configuration can be estimated by superimposing the σ_v calculated under the Nucleus, eliminating the need to model the entire SHL [3, 8].

To identify a representative Nucleus, an incremental tire load approach is used. First, a single-tire load is applied at the surface of known pavement-layer thicknesses and properties. The σ_v response is then calculated at the point of interest (i.e., centerline of the tire load at the specific depth). Afterward, the next tire load in travel direction is added, where the σ_v at the point of interest is observed. Additional tire loads are applied one at a time, and the pavement σ_v values at the point of interest are monitored. The tire addition process continues until the last added tire does not influence the point of interest, which means that the load-induced σ_v at the interest point is not affected by adding a new tire in that direction. In a similar fashion, the number of tires in the transverse direction of the Nucleus's configuration can be identified. Detailed discussions about identifying the Nucleus can be found elsewhere [3, 8].

Figure 6 presents the computed σ_v distribution on top of the SG layer under the Nucleus which consists of five axles and six tires per axle. In this case, σ_{ave} equaled 10.5 psi, which was calculated by dividing the volume of stress distribution by the affected area (see Fig. 7).

For the bearing capacity analysis, the shear strength parameters of the subgrade soil (friction angle, ϕ , and cohesion, c) were estimated for a soil with a resilient modulus of 5,000 psi using the following suggested values from other literature: $\phi = 26^\circ$ and $c = 1.5$ psi. Meyerhof's equation was used to estimate the bearing capacity of the subgrade soil. The investigation zone for bearing capacity was the entire SHL vehicle because it had only one axle group. The ultimate bearing capacity (q_u) was calculated as 54.2 psi. The factor of safety (FOS) against the bearing capacity failure was then calculated as the ratio of q_u to q_{ave} , which is equal to 5.1. Since the calculated FOS is significantly greater than 1.0, the likelihood of ultimate shear failure may not be a concern.

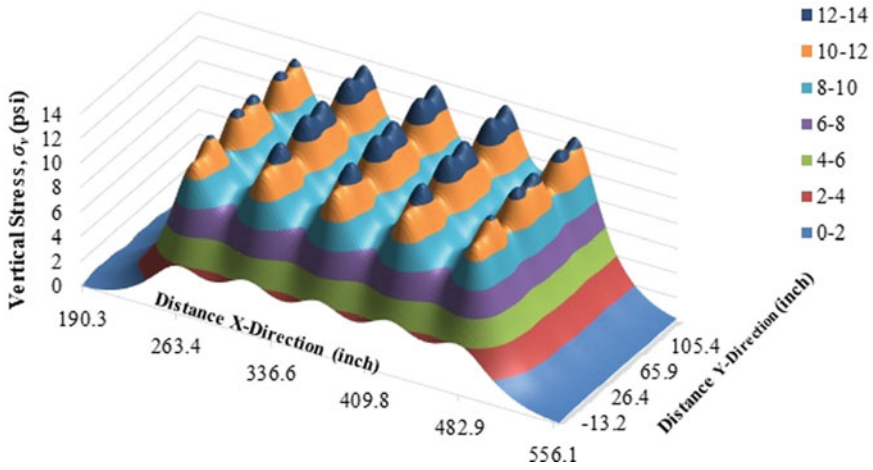


Fig. 6 3D view of vertical stress distribution on top of the subgrade

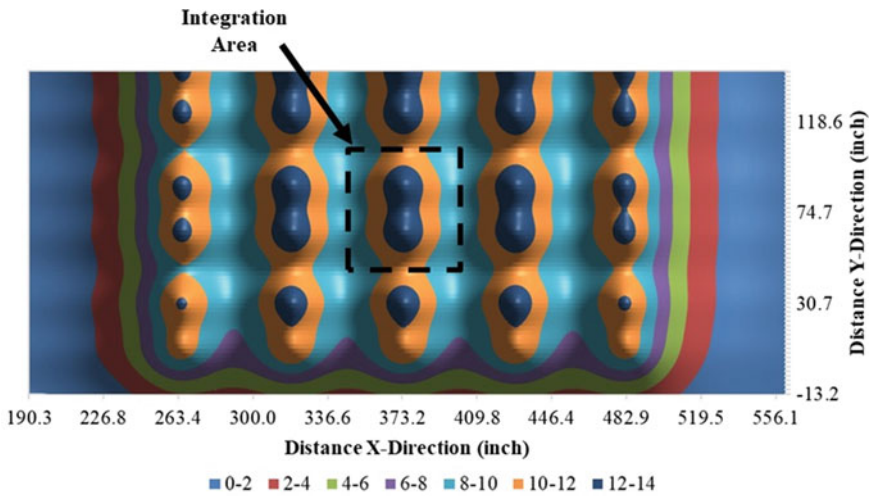


Fig. 7 Integration area for calculating average uniform vertical stress (q_{ave})

5 Summary and Conclusion

Superheavy load (SHL) vehicles are much larger in size and weight than standard vehicles and often require specialized trailers and hauling units. SHL vehicle movements may sometimes approach loads of few million pounds. Such non-standard heavy loading can render a critical condition (i.e., distress mode) of instantaneous ultimate shear failure, localized shear failure, or excessive surface deflections in a pavement surface. To examine the risk of instantaneous shear failure, Meyerhof's

general bearing capacity equation was used. The ultimate failure analysis that focuses on the subgrade layer compares the distributed vertical stress on top of the subgrade layer induced by an SHL vehicle movement to the bearing capacity of the subgrade layer itself.

To model SHL vehicle moves on flexible pavements while considering the non-standard axle and tire configurations, approach to identify element(s) of the SHL configuration that can be regarded as representative of the entire SHL vehicle (referred to as Nucleus) was adopted. The vertical stress distribution (or any other pavement response) under the entire SHL configuration can be estimated by superimposing the stresses calculated under the Nucleus, hence eliminating the need to model the entire SHL.

The analysis steps and the associated results were illustrated using an SHL vehicle configuration permitted by the Louisiana Department of Transportation and Development (LaDOTD). In this case illustration, the factor of safety (FOS) against the bearing capacity failure indicated the adequacy of pavement structure to withstand the general shear failure. Further validation of the numerical modeling of SHL vehicle and subsequent results via actual field measured data and pavement performance under SHL cases are recommended.

References

1. Hajj EY, Siddharthan RV, Nabizadeh H, Elfass S, Nimeri M, Kazemi SF, Batioja-Alvarez D, Piratheepan M (2018) Analysis procedures for evaluating superheavy load movement on flexible pavements, volume I: final report. Report no. FHWA-HRT-18-049. FHWA, U.S. Department of Transportation. Washington, D.C.
2. Nabizadeh H (2017) Development of a comprehensive analysis approach for evaluating superheavy load movement on flexible pavements. University of Nevada, Reno, NV
3. Nimeri M, Nabizadeh H, Hajj EY, Siddharthan RV, Elfass S (2018) Analysis procedures for evaluating superheavy load movement on flexible pavements, volume III: appendix B, superheavy load configurations and nucleus of analysis vehicle. Report no. FHWA-HRT-18-051. FHWA, U.S. Department of Transportation. Washington, D.C.
4. Terzaghi K (1943) Theoretical soil mechanics. Wiley, New York, NY
5. Meyerhof GG (1963) Some recent research on the bearing capacity of foundations. *Can Geotech J* 1(1):16–26
6. Hanna AM, Meyerhof GG (1981) Experimental evaluation of bearing capacity of footings subjected to inclined loads. *Can Geotech J* 18(4):599–603
7. Siddharthan RV, Yao J, Sebaaly PE (1998) Pavement strain from moving dynamic 3D load distribution. *J Transp Eng* 124(6):557–566
8. Nimeri M, Nabizadeh H, Hajj EY, Siddharthan RV, Elfass S (2018) Nucleus approach for pavement analysis under superheavy load. In: Masad E, Bhasin A, Scarpas T, Menapace I, Kumar A (eds) *Advances in materials and pavement prediction, AM3P 2018*. CRC Press, London, pp 527–530

Evaluation of Flexible Pavement Performance Models in Mississippi: A Neural Network Approach



Patrick Duckworth, Hakan Yasarer, and Yacoub Najjar

Abstract One of the main responsibilities of state transportation departments is the construction of new roadways and the maintenance of existing highways. The main concern for transportation agencies is prioritizing the decisions for maintenance and rehabilitation actions. Mississippi Department of Transportation (MDOT) currently utilizes Markov probability matrices, which provides the probability of a pavement section that needs to be rehabilitated. Flexible pavements are affected by various factors such as design parameters, traffic load, climate, and environmental factors. The probability matrices utilized are not based on these factors, which significantly affect the rate of deterioration of the roads and highways. Critical maintenance scheduling is a needed action to limit further problems as the deterioration rate increases over time. To properly assess the condition of the pavement and operate maintenance, prediction models with significant design and condition variables are essential. The rate of deterioration of the pavement and its condition need to be predicted, so that the effectiveness and timing of the maintenance can be estimated. In this study, an artificial neural networks (ANNs) approach was used to develop pavement performance prediction models. The effect of rehabilitation actions were included as part of the inputs. The number of outputs were determined after various trials. The two output model for predicting Performance Condition Rating (PCR) and International Roughness Index (IRI) have found to be the most promising. ANN model successfully characterized the behavior even though the statistical measures are not within a suitable range. Rehabilitation actions were efficiently incorporated in the model and were found to be accurate.

Keywords Artificial neural network · Pavement performance analysis · Performance models · Flexible pavement · Maintenance and rehabilitation

P. Duckworth (✉) · H. Yasarer · Y. Najjar
Civil Engineering Department, University of Mississippi, 106 Carrier Hall University, Oxford,
MS 38677, USA

H. Yasarer
e-mail: hy@olemiss.edu

1 Introduction

One of the problems that state transportation agencies encounter is proper maintenance and rehabilitation of roads and highways to meet the public's needs and safety concerns. The importance of safe roadways cannot be understated. Quality roadways ensure the safe passage of not only passengers, but goods and products. Pavement performance models help agencies foresee how a pavement deteriorates over time due to traffic and environmental conditions. Accordingly, agencies have to plan for when rehabilitation will need to occur to ensure public safety. If needed rehabilitation actions can be determined, budgeting can be planned out and secured.

Predicting Performance Condition Rating (PCR) and International Roughness Index (IRI) accurately is a vital process for state agencies. Pavement condition rating (PCR) is the sum of deduction factors. Every distress type has a dedicated deduction factor. The weights of distresses, severity, and extent is multiplied to find the deduction for each distress type. International roughness index (IRI) summarizes surface deviations for only one-wheel track. A quarter car system is used to travel along the roadway. Whenever roughness is encountered, velocity is generated to the sprung and unsprung masses. The IRI equation takes this into effect for a certain length.

$$\text{PCR} = 100 - \sum_1^n \text{Deduct}_i \quad (1)$$

PCR = Pavement Condition Rating, n = number of observable distresses, and Deduct_i = (weight of distress) (weight of severity) (weight of extent) for distress i .

$$\text{IRI} = \frac{1}{L} \int_0^X |\dot{z}_s - \dot{z}_u| dt \quad (2)$$

IRI = International Roughness Index, L = length in section (m), X = longitudinal distance (m), V = speed of quarter car (m/s), X/V = time it takes the model to run distance X , dt = time increment, \dot{z}_s = vertical speed of the sprung mass, and \dot{z}_u = vertical speed of the unsprung mass.

Each state maintains a data record of road conditions on a regular basis. 784,910 miles of flexible pavements existed in the USA in 2017 [1] making it the most commonly used type of pavement in the USA. Flexible pavement is most widely used for state agencies due to the low construction cost when compared to concrete pavements even though life span of pavement is less than of concrete. However, the need for regular maintenance and rehabilitation of flexible pavement is greater. In most states, prediction models are used to determine pavement's serviceability in order to allocate funds. One of the most commonly used method to develop prediction models is artificial neural networks (ANNs), which is a powerful computational tool that is widely used to model complex relationships between input(s) and output(s). ANNs can learn from history of data. In this study, approximately 13,500 miles of

flexible pavements throughout the state of Mississippi were considered to develop prediction models using ANNs approach. A feed-forward single-layer network with a back-propagation algorithm is utilized for ANN model development. Four models (models 1, 2, 3, and 4) predicting two outputs (i.e., PCR and IRI) were developed.

2 Literature Review

Roughness is an indicator of pavement serviceability and condition. Serviceability is the perception a user has of a roadway. In any given road, drivers will often disagree on the quality of said road. Based on a vehicle's speed and the tolerance of the driver, road quality can be a varying measurement [2]. Road serviceability can be determined by periodic measurements of ride quality. There is a minimum level of acceptability of ride quality a pavement must perform above for its design period. A pavement's condition can be deemed acceptable or unacceptable depending on whom is determining the quality [3].

Attoh-Okine [4] developed an ANN model to predict roughness progression in flexible pavement. Modified structural numbers, incremental traffic loadings, thickness of cracked layer, and incremental variations of rut depth were considered. The effect of environmental and surface distress changes were also studied. Kargah-Ostadi et al. [5] developed an ANN model to provide rehabilitation recommendations based on IRI predictions. Initially, twenty variables were used to predict IRI. After determining significance of the inputs in relation to IRI, eight inputs were found to have the most impact. The R^2 of 0.9578 was observed between the predicted and measured IRI values, which showed that it is feasible to use IRI as the prediction criteria. In most studies regarding pavement roughness, several factors are routinely determined to have the most influence. Those factors include initial roughness, pavement age, traffic, climatic conditions (i.e., average annual precipitation and average annual freezing index), pavement structural properties, subgrade properties (i.e., moisture content and percent passing No. 200 sieve), drainage type and conditions, and maintenance and rehabilitation treatments. The seven factors deemed to have the most significant relationship with IRI including previous IRI, time passed since rehabilitation, time passed since previous IRI, average annual freezing index, overlay thickness, total pre-overlay HMA thickness, and subgrade percent passing sieve No. 200 [5].

Artificial neural network's architecture includes a number of layers, a number of nodes in each layer, and a connection scheme between the nodes [6]. "The idea of ANNs is not to replicate the operation of the biological networks but to make use of what is known about the functionality of the biological networks for solving complex problems. The attractiveness of ANNs comes from the remarkable information processing characteristics of the biological system and their capability of learning from the data" [7]. ANN is an advanced computing system established from several simple, highly interconnected elements that process information through dynamic responses to the external inputs (independent variables). The neural network gains

its knowledge through trained feed-forward propagation. During this process, a set of training data is presented consisting of inputs and outputs (dependent variables). The targeted values are compared to the resulted output. Back propagation then adjusts the connection weights to gradually reduce error between actual and predicted outcomes. Once properly trained, the network provides a functional mapping of any input pattern into the proper output pattern. The validation process involves running a data set the mode has not previously seen [8]. “ANN based models are empirical in nature; however, they can provide accurate solutions for problems and for phenomena that are only understood through experimental data and field observations” [7].

3 Database Description

The database for flexible pavement was collected by the Mississippi Department of Transportation. The database included: roadway section ID, beginning and ending latitudes and longitudes of sections, thickness of pavement layer, section length, pavement condition rating (PCR), the year of construction, and international roughness index (IRI). Database included survey data, which is collected every two years to monitor PCR and IRI. Rehabilitation actions were reported as they were implemented.

The purpose of developing an ANN model was to predict when rehabilitation was needed to occur and how affected the roadway. In order for model to accurately predict how a roadway performed after a rehabilitation, it had to be decided when rehabilitation occurred. Rehabilitation actions provided by the agency were considered. However, some instances where the PCR and IRI values improved without rehabilitation actions were noticed. Through the examination, if PCR increased by more than 2.5 or IRI decreased by more than 0.2, the section was marked as if the rehabilitation occurred. Assumed that 2.5 increase in PCR and 0.2 decrease in IRI were found to be significant by the experts from MDOT. In the database, rehabilitation action was assigned “1” if it occurred, and assigned “0” if it did not.

Datasets prior to 2010 were not included in the model development stage due to the changes in data measurement system, and pavement design and materials after 2008. After removing the datasets prior to 2010, 15,720 datasets remained. 3,970 road sections include even years after 2010 (i.e., 2010, 2012, 2014, 2016, and 2018). In order to train ANN models precisely for generating consecutive year predictions, additional datasets were needed to be created for odd years. Odd year values of PCR and IRI were generated by averaging the values of the year before and after.

Final database had grown to include 31,440 data sets. In order for the model to accurately predict PCR and IRI together, complimentary PCR (i.e., 100-PCR) is proposed to be used for ANN model development because IRI and PCR changes are inversely related to time. For example, if the roadway condition improves, PCR will increase and IRI will decrease. In the same example with the complimentary arrangement, both IRI and 100-PCR will decrease.

A feed-forward ANNs approach with error back-propagation algorithm was deployed using only one layer of hidden nodes. Four different models in total were developed for this study. Initially, one output mode was developed to predict PCR and IRI individually. However, it was found that two output models have better statistical accuracy measures. Only four models predicting two outputs (i.e., PCR and IRI) are presented in this paper.

4 ANN Model Development

The ANN models were developed in five stages. Stage one involved choosing input and output variables. In addition, the datasets are split into training, testing, and validation datasets. Stage two included training and testing the networks and finding the optimum number of hidden nodes and iterations to determine the best performing networks. In stage three, the best three networks from stage 2 were tested with the validation datasets. In the fourth stage, the best three networks from stage 2 were trained on all datasets. Retraining the network on all datasets typically gives a better accuracy measurement [9]. Stage five involved selecting the best network based on the statistical accuracy measures, which are average square error (ASE), mean absolute relative error (MARE), and coefficient of determination (R^2) values. The network with the lowest ASE, lowest MARE, and highest R^2 , respectively, was chosen for each four models (i.e., Models 1, 2, 3, and 4).

The equations for ASE and MARE are shown below:

$$ASE = \frac{\sum_{i=1}^N \sum_{j=1}^n (Y_{ij}^P - Y_{ij}^O)^2}{N.n} \tag{3}$$

$$MARE = \frac{\sum_{i=1}^N \sum_{j=1}^n \left| \frac{Y_{ij}^P - Y_{ij}^O}{Y_{ij}^O} \right|}{N.n} \tag{4}$$

Here, Y_{ij}^P = Predicted output, Y_{ij}^O = Actual output, N = number of dataset, and n = number of outputs.

4.1 Model 1: Predicting PCR and IRI Based on PCR and IRI Rehabilitation

The inputs for this model were beginning and ending longitude and latitude, structural number, length of section, age of section, PCR at 2010, IRI at 2010, time from the year of 2010, PCR rehabilitation, and IRI rehabilitation. As stated previously, if PCR is increased by 2.5 points from the previous year, PCR rehabilitation is

assumed to occur. IRI rehabilitation was assigned if IRI decreased by 0.2 points from the previous year. The outputs were complimentary PCR and IRI for each year. With the PCR and IRI rehabilitation considered individually, 12 input variables are included in the ANN model development, in which the five stages were followed to find the best-performing network. The statistical measures of the best-performing network for Model 1 are given in Table 1 column 1. Of the four models considered in this section, this model's ASE of 0.00438 was found to be the lowest. The R^2 value is; 0.367 in training, 0.345 in testing, 0.352 in validation, and 0.362 in all data. The final network structure of Model 1 is given in Table 1 with the following designations: 12 inputs, 15 hidden nodes, and 2 outputs (i.e., 12-15-2). To evaluate the performance of the two output models, an additional table, highlighting each model and the corresponding output, is generated. The statistical measures for each output of this model as well as the other models are given in Table 2. The predicted outputs versus actual results relationship charts are displayed in Figs. 1, 2, 3, 4, 5, 6,

Table 1 Statistical measures for all models

Predict		PCR and IRI			
Model		1	2	3	4
Structure		12-15-2	11-13-2	11-15-2	11-15-2
Training	MARE	23.82	24.28	25.22	24.76
	R^2	0.367	0.350	0.338	0.353
	ASE	0.00441	0.00456	0.00465	0.00449
Testing	MARE	24.18	24.65	25.55	25.14
	R^2	0.345	0.324	0.318	0.333
	ASE	0.00452	0.00470	0.00473	0.00459
Validation	MARE	24.14	24.52	25.45	25.14
	R^2	0.352	0.335	0.322	0.335
	ASE	0.00437	0.00453	0.00463	0.00451
All data	MARE	23.94	24.23	24.42	24.69
	R^2	0.362	0.351	0.338	0.351
	ASE	0.00438	0.00447	0.00460	0.00445

Table 2 Statistical measures for PCR and IRI outputs

Model		1	2	3	4
PCR	MARE	7.95	8.16	23.17	23.10
	R^2	0.414	0.389	0.369	0.393
	ASE	0.00570	0.00600	0.00620	0.00591
IRI	MARE	26.04	25.70	25.67	26.28
	R^2	0.307	0.314	0.310	0.310
	ASE	0.00300	0.00300	0.00300	0.00298

Fig. 1 Model 1 training accuracy

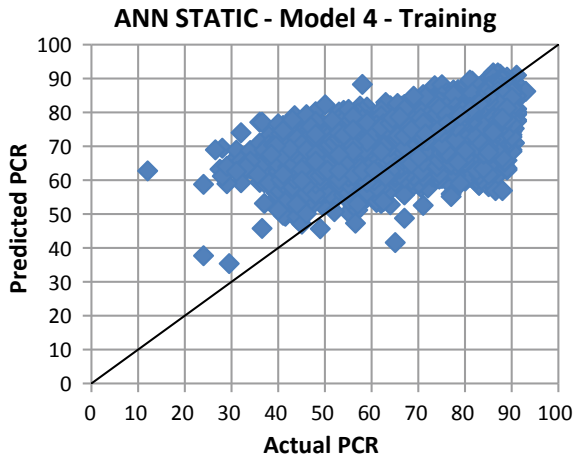
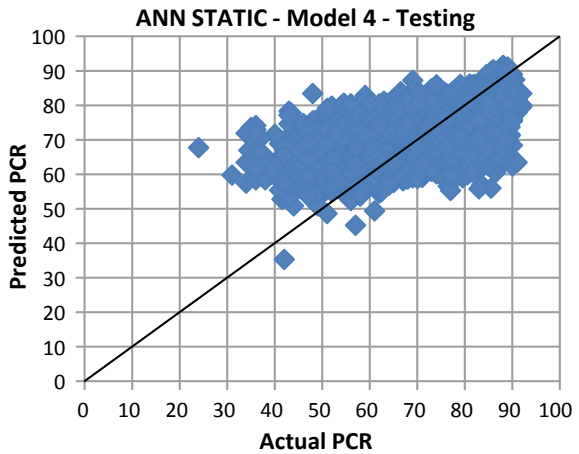


Fig. 2 Model 1 testing accuracy



7, and 8. The graphs show a consistent overestimation of PCR predictions once the actual PCR is lower than 60. Additionally, once the actual IRI value exceeds 2.5, the model routinely underestimates IRI predictions.

4.2 Model 2: PCR and IRI Trial Based on PCR Rehabilitation

In order to analyze the effect of the two rehabilitations, the same inputs and outputs from Model 1 were utilized except IRI rehabilitation which was removed. Rehabilitation of PCR was designated the same way as the Model 1. A total of 11 inputs

Fig. 3 Validation accuracy

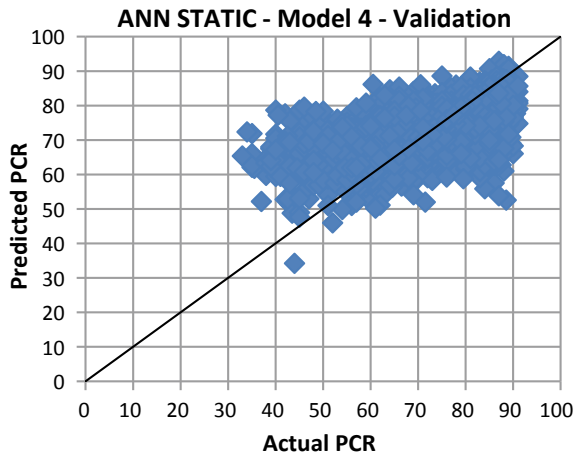
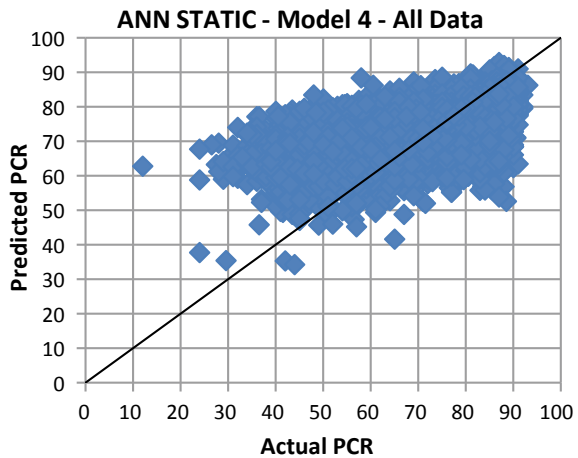


Fig. 4 All data accuracy



were used to predict complementary PCR and IRI. The best-performing network is given in Table 1 column 2. The coefficient of determination was found to be; 0.350 in training, 0.324 in testing, 0.335 in validation, and 0.351 in all data stages. Table 2 shows that Model 2 has a higher R^2 when examining IRI statistics compared to Model 1.

4.3 Model 3: PCR and IRI Based on IRI Rehabilitation

In this model, the same inputs and outputs from Model 2 were utilized except PCR rehabilitation was replaced with IRI rehabilitation and resulted in a total of 11 inputs.

Fig. 5 Training accuracy

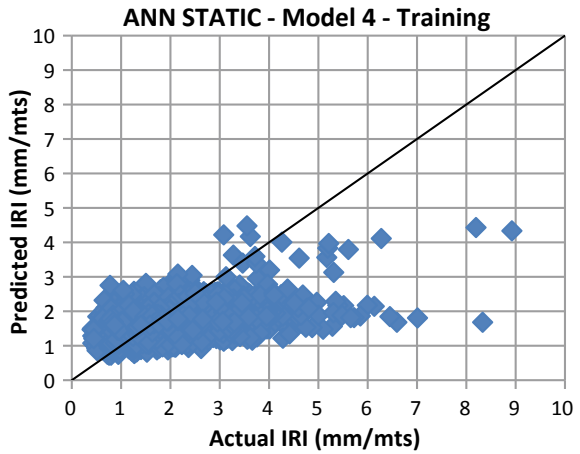
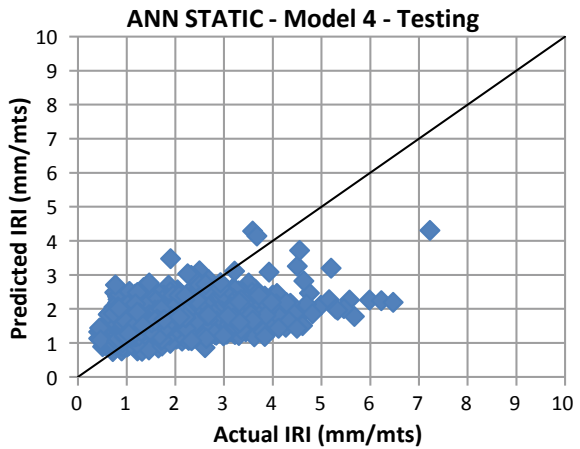


Fig. 6 Testing accuracy



The category of rehabilitation actions is given similarly as the previous models. In Table 1, column 3 presented the best-performing network for Model 3S. The R^2 values have resulted in 0.338, 0.318, 0.322, and 0.338 in training, testing, validation, and all data stages, respectively. In can be observed from Table 2 that IRI statistics of Model 3 are similar to Model 2 while PCR statistics worsened.

Fig. 7 Validation accuracy

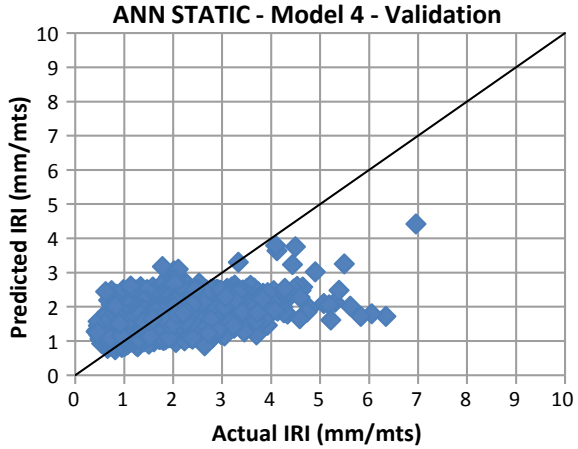
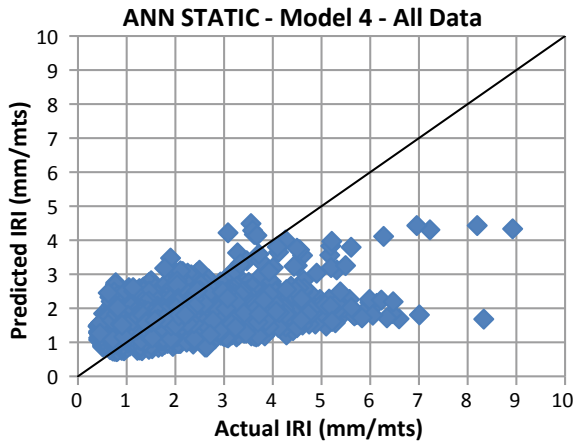


Fig. 8 All data accuracy



4.4 Model 4: PCR and IRI Trial Based on Matching Rehabilitation

In addition to studying the effect of assigned rehabilitation that was completed in previous models (i.e., Models 5S and 6S), different assignment category was considered for this model. If a section was assigned PCR and IRI rehabilitation in the same year, then it was considered a single rehabilitation action for the input. Otherwise, all other unmatched rehabilitations were categorized as “0” even if one category is indicated a rehabilitation. For example, if IRI rehabilitation is “1” and PCR is “1,” the rehabilitation was noted as “1.” If IRI rehabilitation assignment is “0” and PCR one is “1,” the rehabilitation is recorded as “no rehabilitation” which is noted “0” in the input. Therefore, 11 inputs were incorporated into the ANN model development.

The fourth column in Table 1 depicted the optimal network for model 4. The average R^2 value for Model 4 is 0.353 in training, 0.333 in testing, 0.335 in validation, and 0.351 in all data. Statistics given in Table 2 portrays this model as the second-best for both PCR and IRI predictions.

5 Conclusion

Feed-forward neural network approach with the back-propagation algorithm was utilized to develop pavement performance models. Four models were developed to predict PCR and IRI values with different rehabilitation assignments. As can be seen from the results shown in Tables 1 and 2 and Fig. 1 through Fig. 8, statistical accuracy measures of the models are promising. Model 1 was chosen to be the best model among the four models based on the lowest ASE and MARE and the highest R^2 values. When examining all the models, model 1 was the best at predicting PCR and IRI when two rehabilitations were assigned. Even though the statistical measures are not in an acceptable range, these models were able to learn the trend and they can be used for predicting the near future conditions along with the impact of rehabilitation. At the time of modeling, some of the data related to traffic loading and environmental conditions were not available. Thus, the models were not expected to perform up to the standards. Furthermore, flexible pavement is highly affected by traffic loading as well as the environmental conditions. With the addition of more data as well as the additional inputs, the statistical accuracy measures are expected to improve by retraining the ANN models. A previous year's pavement rating is directly correlated to the next year. A model which can use the previous year's rating to predict the current year would be immensely more powerful and capable of correctly predicting pavement performance. In addition, having climatological or traffic data, which is known to directly affect pavement performance, would immensely help these models. Sadly, this information was not available at time of publication.

References

1. U.S. Department of Transportation/Federal Highway Administration (2018) Table HM-12 - highway statistics 2017 - policy: federal highway administration. 23 Aug 2018. www.fhwa.dot.gov/policyinformation/statistics/2017/hm12.cfm
2. Haas R et al (1994) Modern pavement management. Krieger Publishing Company
3. Felker V (2005) Characterizing the roughness of Kansas PCC and superpave pavements. Kansas State University
4. Attoh-Okine NO (1993) Predicting roughness progression in flexible pavements using artificial neural networks. Transportation research board conference proceedings, 30 Nov 1993. trid.trb.org/view.aspx?id=390719
5. Kargah-Ostadi N et al (2010) Network-level pavement roughness prediction model for rehabilitation recommendations. Transp Res Rec: J Transp Res Board 2155(1):124–133. <https://doi.org/10.3141/2155-14>

6. Alsugair AM, Al-Qudrah AA (1998) Artificial neural network approach for pavement maintenance. *J Comput Civil Eng* 12(4)
7. Basheer IA, Hajmeer M (2000) Artificial neural networks: fundamentals, computing, design, and application. *J Microbiol Methods* 43(1):3–31. [https://doi.org/10.1016/s0167-7012\(00\)00201-3](https://doi.org/10.1016/s0167-7012(00)00201-3)
8. Mohamed Jaafar ZFB (2019) Computational modeling and simulations of condition deterioration to enhance asphalt highway pavement design and asset management. University of Mississippi
9. Yasarer H, Najjar Y (2012) Development of void prediction models for Kansas concrete mixes used in PCC pavement. *Procedia Comput Sci* 8:473–478. <https://doi.org/10.1016/j.procs.2012.01.088>

Field Monitoring of Flexible and Rigid Pavement Responses in Thailand



Auckpath Sawangsuriya, Apiniti Jotisankasa,
and Suphawut Malaikrisanachalee

Abstract Characterization of pavement layer properties and responses under traffic loads, local materials, and weather conditions in Thailand is essential for accurate pavement performance prediction, pavement deterioration models development, as well as pavement management system. This study presents the flexible and rigid pavement responses for long-term pavement monitoring in Thailand. Two pavement sites situated near permanent weigh station and weigh-in-motion system on Highway No. 4 in Nakorn Phathom and Rachaburi provinces were instrumented with pressure cells, strain gauges, thermocouples, and moisture sensors. These test sections represented typical pavement structure in Thailand according to the Department of Highways design standard and specification. Field pavement response and environmental data including stress, strain, moisture, temperature from the embedded instrumentation were monitored since late 2017.

Keywords Pavement response · Pavement monitoring · Field instrumentation

1 Introduction

The department of highways (DOHs) in Thailand is responsible for the national highway network of approximately 60,000 km. The impact of increasing overweight truck traffic and climate on highways due to economic growth is a growing concern within the DOH. Current pavement design and rehabilitation procedures are based mainly on the asphalt institute (AI) and the portland cement association (PCA) for flexible and rigid pavements, respectively, which uses limited performance models developed from the AASHTO road test in the late 1950s [1]. In addition to the difference in material, traffic, and environment, the construction and rehabilitation techniques may not be relevant to local Thailand conditions. Characterization of pavement layer properties and responses under traffic loads, local materials, and weather

A. Sawangsuriya (✉)

Department of Highways, Bureau of Road Research and Development, Bangkok 10400, Thailand

A. Jotisankasa · S. Malaikrisanachalee

Faculty of Engineering, Kasetsart University, Bangkok 10900, Thailand

conditions in Thailand is essential for accurate pavement performance prediction, pavement deterioration model, as well as pavement management system.

In 2017, the DOH in cooperation with Kasetsart University built two experimental test sections: A rigid pavement in Nakorn Chaisri district, Nakorn Phathom province and a flexible pavement in Potaram district, Rachaburi province. These sections were chosen to represent typical cross sections for a flexible pavement structure (e.g., asphalt surface, base course, subbase course, and selected material above subgrade) and a rigid pavement structure (e.g., joint reinforced concrete pavement slab, sand cushion, subbase course, and selected material above subgrade) in Thailand. The joints were doweled and sealed. Both sites were situated near permanent weigh station and weigh-in-motion (WIM) system on national highway No. 4.

This paper summarized a comprehensive field instrumentation plan for these two experimental sites in order to monitor load and environmental responses as well as their performance of pavement sections. A discussion of instrumentation, type of sensors, installation procedures, and instrumentation layout is also presented.

2 Background

Pavement instrumentation has been extensively conducted over the past few decades to observe pavement response, behavior, and performance under actual loads [2–10]. It was proven to be critical for analysis and design toward the mechanistic-empirical approach, which allowed transportation agencies to improve their pavement design and performance prediction. It also provided an insight into structural responses of pavement under moving loads at various speeds as opposed to the static load assumption given for the traditional pavement design and analysis.

Pavement instrumentation provided extensive data for analysis of pavement performance and its long-term under seasonal variations due to moisture and temperature, which are increasingly important for Thailand. It also served as an effective tool to measure and validate damage effects from overweight trucks as well as to monitor the long-term performance under local trafficking, climate, materials, construction, maintenance and rehabilitation. In addition, pavement instrumentation offered a mechanistic approach to determine the load equivalency factors (LEFs) based on the country's local permitted loads (e.g., single, tandem and tridem axles) to accurately convert various vehicle load configurations into standard equivalent loads.

3 Description of Field Instrumentation

3.1 Experimental Sites

A comprehensive instrumentation plan was implemented to monitor responses and performance of pavement sections. The rigid pavement section was situated on national highway No. 4 at STA 41 + 750 (South Bound), approximately 100 m from WIM system and 550 m from Nakhon Chaisri Weight Station, Nakhon Phatom province as shown in Fig. 1. The instrumented section had 3.5-m wide and 10-m long as shown in Fig. 2. The pavement structure consisted of 250-mm joint reinforced



Fig. 1 Location of an experimental rigid pavement site



Fig. 2 A field instrumented rigid pavement section

concrete pavement (JRCP) with doweled and sealed joints, 50-mm sand cushion, 100-mm soil-aggregate subbase, and 150-mm selected material over subgrade.

The flexible pavement section was situated on national highway No.4 at STA 88 + 770 (South Bound), approximately 40 m from WIM system and 400 m from Potaram Weight Stations, Ratchaburi province as shown in Fig. 3. The instrumented section had 3.5-m wide and 10-m long as shown in Fig. 4. The pavement structure consisted of 200-mm asphalt surface, 200-mm crushed rock base, 200-mm soil aggregate subbase, 250-mm selected material over subgrade.



Fig. 3 Location of an experimental flexible pavement site

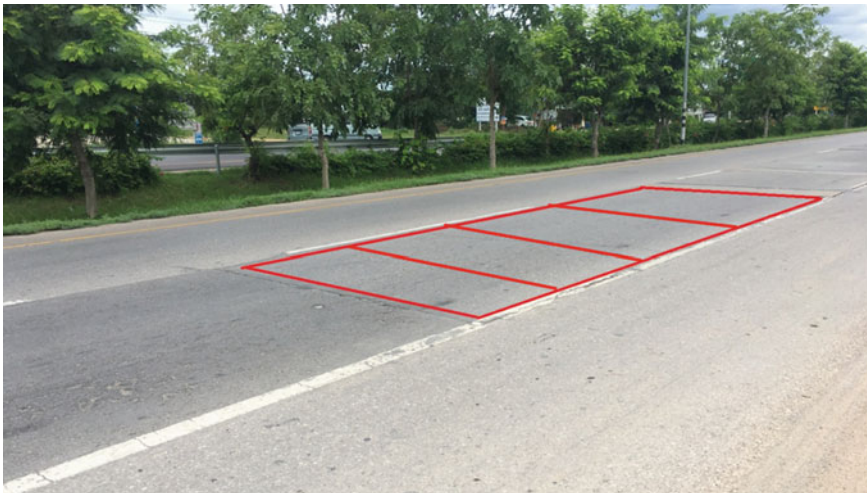


Fig. 4 Field instrumented flexible pavement section

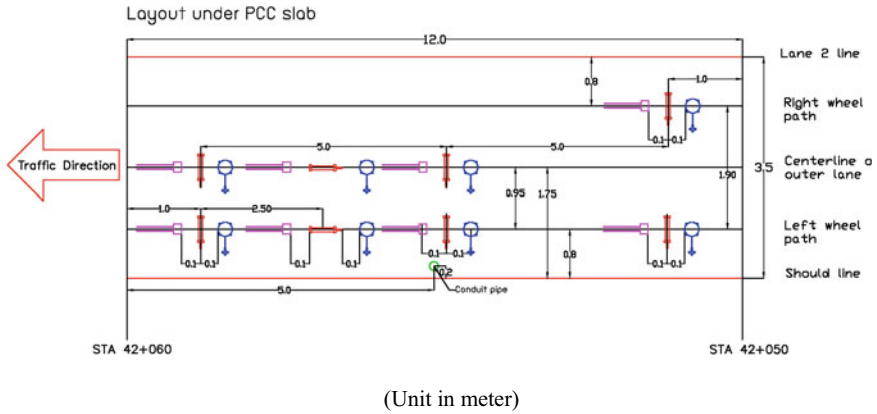


Fig. 5 Installation plan for experimental rigid pavement—bottom of asphalt surface

3.2 Type of Sensors and Instrumentation Layout

A series of sensors were installed in both experimental sites. The field instrumented rigid pavement section consisted of sixteen strain gauges, sixteen pressure cells, sixteen moisture sensors, two observation wells, one data logger, one data processing unit, one AC to DC adaptor, and one UPS. The field instrumented flexible pavement section consisted of eight asphalt strain gauge, sixteen strain gauges, sixteen pressure cells, sixteen moisture sensors, eight thermocouples, two observation wells, one data logger, one data processing unit, one AC to DC adaptor, and one UPS.

The typical layout of instrumentation is illustrated in Figs. 5, 6, 7 and 8. In general, the sensors were installed both along and in between the wheel paths. The asphalt strain gauges, strain gauges, and pressure cells were placed under the surface and base course as well as above the subgrade, while the thermocouples and moisture sensors were embedded within these pavement layers. The 6-m deep observation wells were installed outside the pavement shoulder. Four cross sections of installation layout were considered in order to incorporate various measurement locations and directions with respect to stress-strain responses under the traffic loads.

3.3 Installation Procedures

The installation procedures for field instrumentations consisted of four major parts: (1) the excavation of existing pavement, (2) the placement and compaction of pavement layers, (3) the installation of field instrumentations, and (4) the quality control assessment. The existing pavement was excavated to the subgrade level. Each pavement material was filled and compacted in accordance with the original

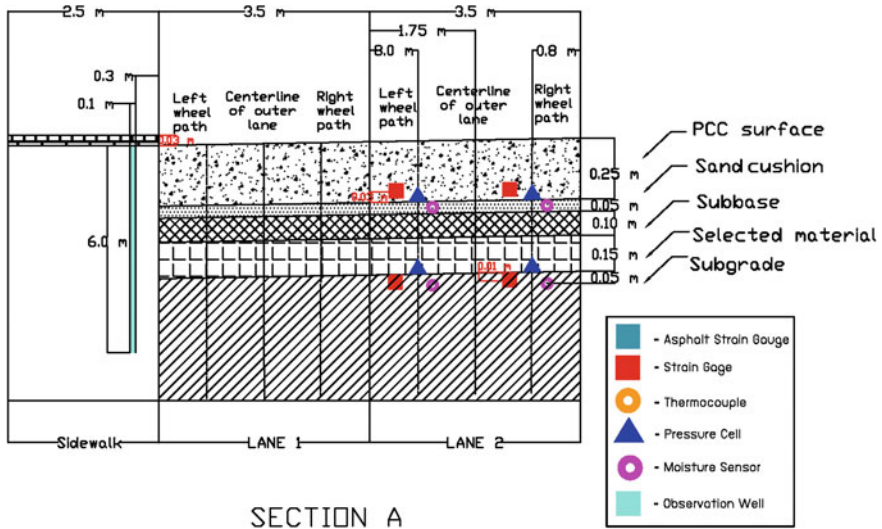


Fig. 6 A cross section of experimental rigid pavement

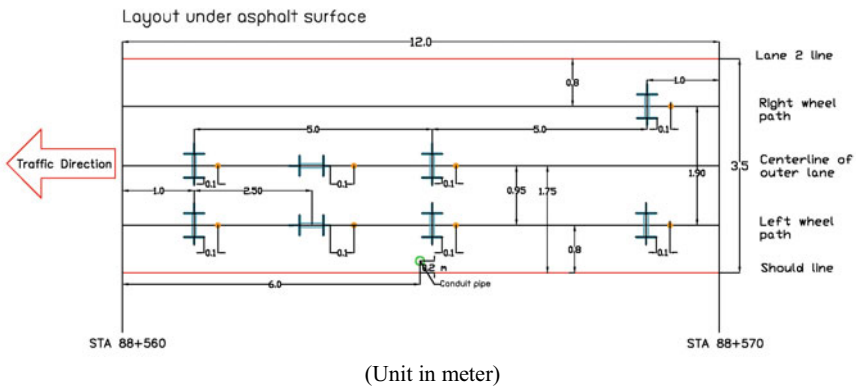


Fig. 7 Installation plan for experimental flexible pavement—bottom of asphalt surface

layer thickness. The construction process also followed the DOH standard and specification. Every instrument was carefully laid down to the specified level and location. The PE pipeline was utilized to protect and shield the cable. The conventional field moisture-density measurements were performed for compaction quality control assessment.

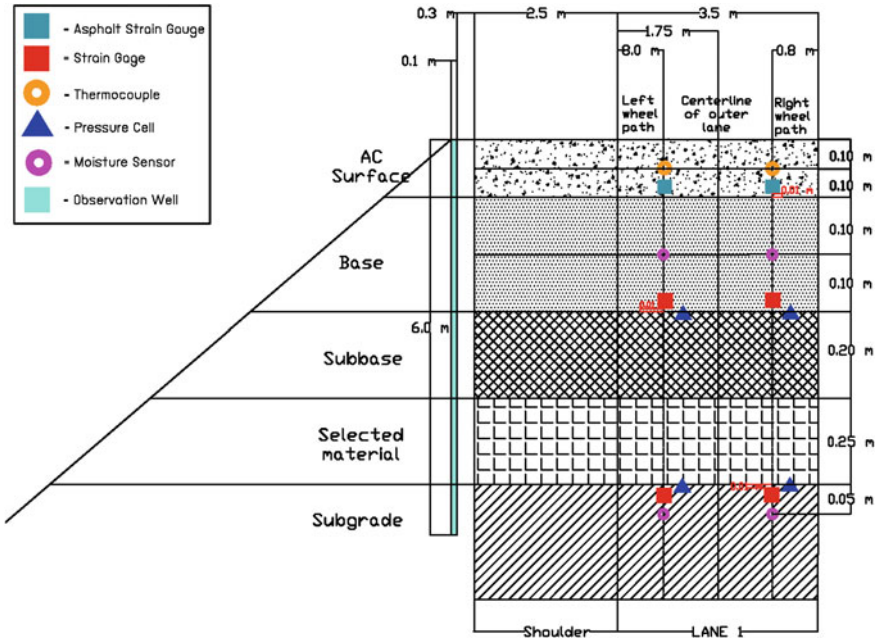


Fig. 8 A cross section of experimental flexible pavement

4 Responses and Performance of Instrumented Pavement Sections

Typical responses of the instrumented section are explained in this section in order to illustrate the key behavior which was observed during the monitoring period. Figure 9 shows the pulses of induced vertical stresses observed in the flexible pavement site above the subbase during passages of several trailer trucks at a speed of about 40 km/hr. The subbase stresses below the right wheel were slightly lower than that below the left wheel (~93%), while that below the center line of lane was only about 2% of the left wheel stress. That the left wheel stress being the largest was expected since the road surface transverse slope was downward to the left. At a greater depth, the stresses on the subgrade showed a somewhat different behavior, indicating that along the center line, the induced stress was of a greater proportion as shown in Fig. 10. This is expected according to the greater projected area of stress distribution with depth.

The stress for rigid pavement along the left wheel is shown in Fig. 11a. The induced stress below the concrete slab ($\sigma_{conc,left}$) was greater than that in the subgrade ($\sigma_{sub,left}$) by about 30%. However, along the center of lane, $\sigma_{conc,center}$ was only 9% of the stress $\sigma_{sub,center}$ at a greater depth. In comparison with the stresses in flexible pavement (Fig. 11b) the proportions between stresses at these depths and locations

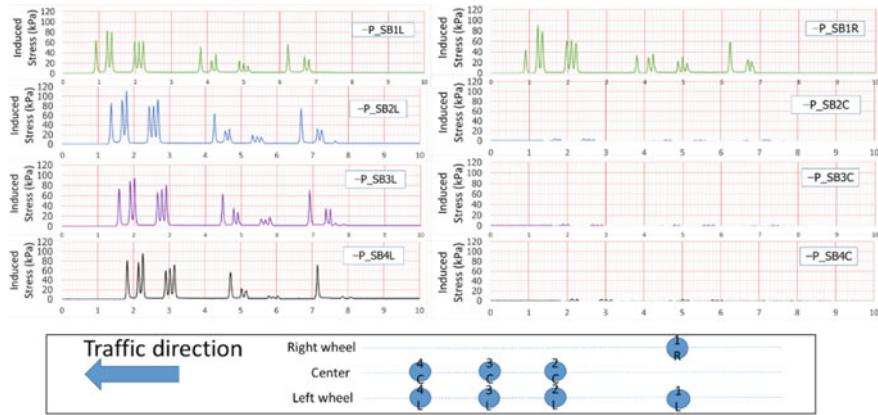


Fig. 9 Typical pulses of induced stresses on the subbase of flexible pavement section (legend code: P = pressure induced by traffic; SB = subbase; 1,2,3,4 = location of sensors; L = left wheel; R = right wheel; C = center)

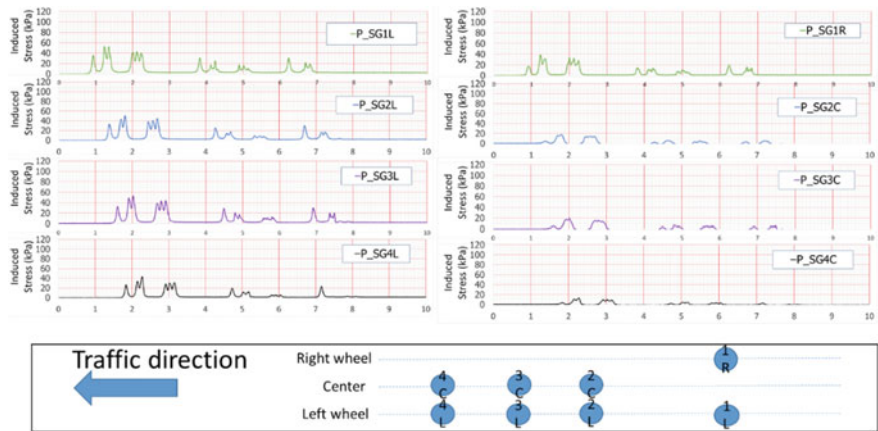


Fig. 10 Typical pulses of induced stresses on the subgrade of flexible pavement section (legend code: P = pressure induced by traffic; SG = subgrade; 1,2,3,4 = location of sensors; L = left wheel; R = right wheel; C = center)

were different, effectively as a result of fundamental difference in the rigidity ratio and thickness.

These average trends of induced stresses at various depths in both rigid and flexible pavement sites were then compared in Fig. 12a based on the full-scale static load test of 9.7-ton truck. The induced stress in the subgrade below rigid pavement was clearly lower than that below the flexible pavement. Figure 12b also shows normalized stress ratio with depth for cases of 6- to 10-ton trucks, which indicates the lower stresses in

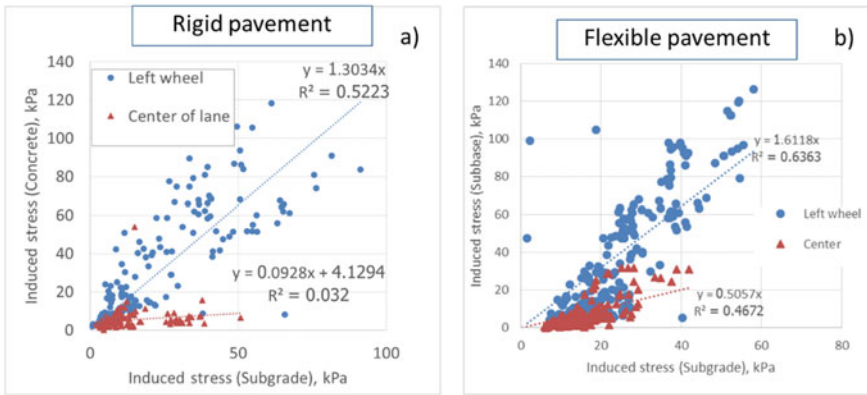


Fig. 11 Correlation between the induced stresses at two different depths along left wheel and center of lane for a) rigid pavement b) flexible pavement

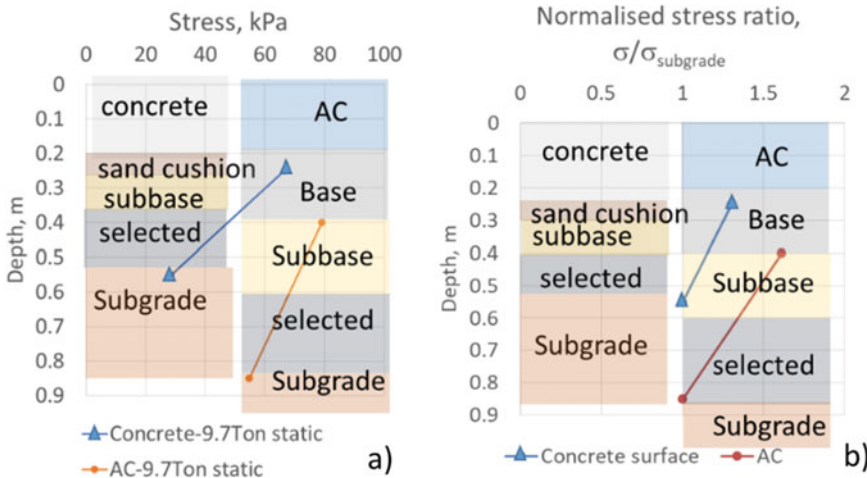


Fig. 12 Distribution of a induced vertical stress with depth and b normalized stress ratio = induced stress/induced stress in the subgrade for both rigid and flexible pavement sites

the rigid pavement than those in the flexible pavement when considering at the same depth.

Figure 13 shows the comparison between the induced stresses under the right and left wheels for both rigid and flexible pavement sites. It can be seen that the stress under right wheel is higher than the left wheel for rigid pavement (by 22% in concrete slab, and by 77% in subgrade). Different behavior was observed in the flexible pavement where the induced stress under left wheel was higher than that that under right wheel. This contrast in behavior could be due to the difference in rigidity

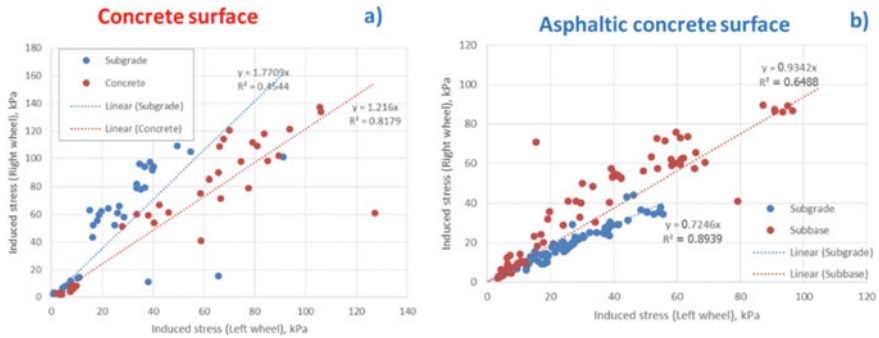


Fig. 13 Comparison between induced stresses in subgrade, concrete, and subbase for **a** rigid and **b** flexible pavement sections

as well as the inclusion effect of the instruments, although the exact explanation is still not available at the moment.

Figure 14 shows the variation of volumetric water content with time for the rigid pavement site. Changes in the moisture content appeared to be more pronounced in the sand cushion layer than in the subgrade, which indicated much lower moisture content. The changes in moisture content also seemed to be in response to the rainfall. This might indicate the moisture infiltrated into the rigid pavement structure from the upper part, rather than from the lower base.

The moisture content behavior of flexible pavement was quite different as shown in Fig. 15. The change in moisture content appeared more noticeable in the subgrade than in the subbase. This could be due to the fact that moisture movement was caused by upward capillary rise rather than downward infiltration. This was expected since the asphalt surface is more effective waterproof than the concrete slab.

Figure 16 shows the temperature variation with time at the flexible pavement site. As expected, the subbase exhibited more fluctuation in the temperature with time than the subgrade. The daily temperature oscillation is approximately sinusoidal and its amplitude decreased with depth. Note that there was not much spatial deviation in temperature within the same layer at the same depth. As for the rigid pavement site (Fig. 17), the temperature variation with time was of a similar trend, showing more fluctuation in the sand cushion layer than in the subgrade.

5 Conclusions

This paper presented some typical behavior of instrumented rigid and flexible pavement test sections situated in Central Thailand. The study investigated the long-term pavement monitoring under regular trafficking. It is noteworthy that the speed effect also plays a major role in the collected data. The influence of speed on the pavement response to dynamic loading can vary significantly depending on the type of

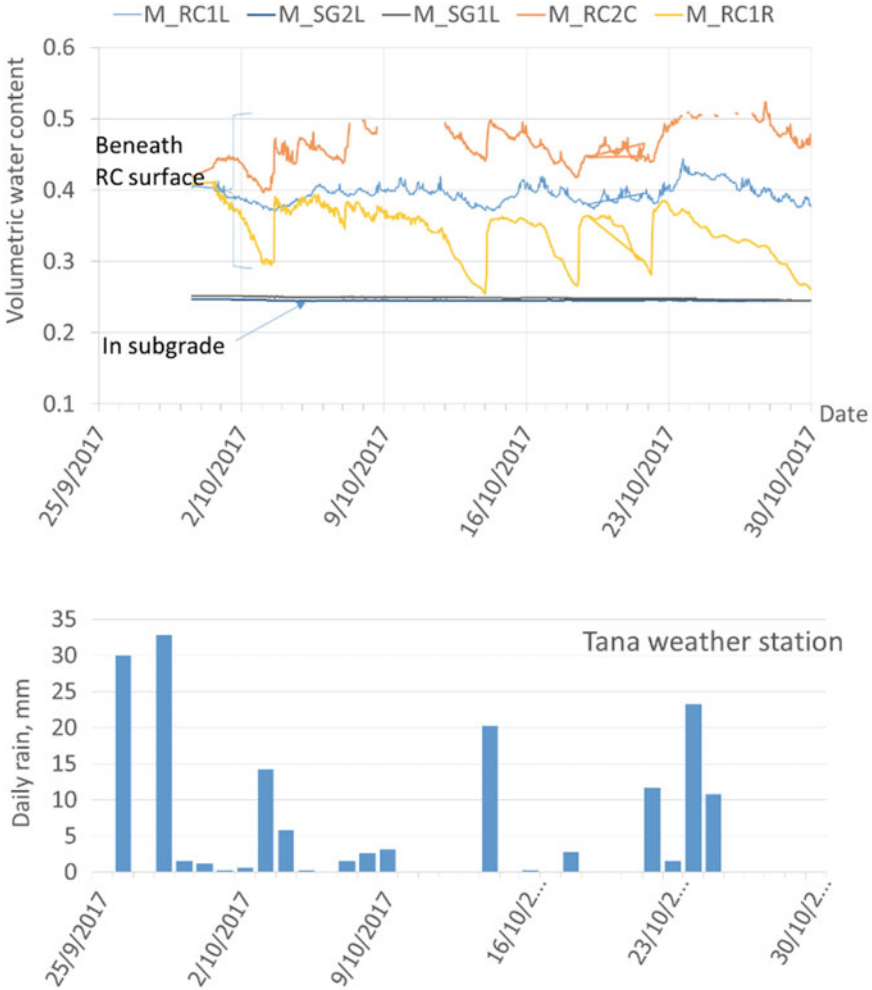


Fig. 14 Variation of volumetric water content with time and daily rainfall at the rigid pavement site (legend code: M = moisture sensor; RC = bottom of reinforced concrete slab; SG = subgrade; 1,2,3,4 = location of sensors; L = left wheel; R = right wheel; C = center)

the pavement system [11]. Results of induced stresses and moisture contents have been shown, which highlighted the contrast behaviors between these two types of pavement structures.

- For flexible pavement, the induced stress above subbase below the wheel was about 60–80% higher than the value of induced stress above subgrade depending on the truck weight. Along the center line, however, the induced stress above the subbase was smaller, being only 30–50% the value of induced stress on subgrade.

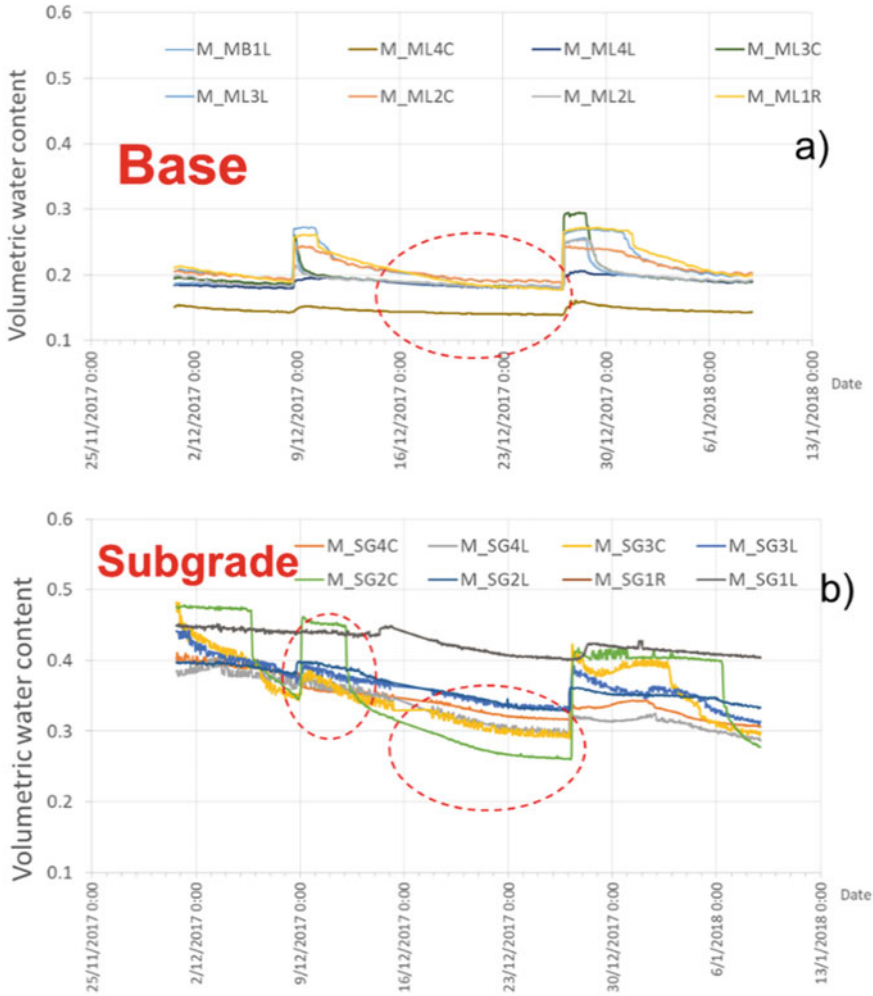


Fig. 15 Variation of volumetric water content with time at the flexible pavement site (legend code: M = moisture sensor; MB = middle of base course; SG = subgrade; 1,2,3,4 = location of sensors; L = left wheel; R = right wheel; C = center)

- At a certain depth, the induced stress in subgrade under the rigid pavement was lower than that under the flexible pavement. In particular, the proportion between right and left wheel stresses appeared to be different depending on the type of pavement, although it needs further study to confirm this.
- The moisture content in the sand cushion layer under the rigid pavement appeared more pronounced and was dependent upon the rainfall condition, than those below the subgrade. However, for the flexible pavement, the moisture content in subgrade was more sensitive than those in the base. This might be probably due to the

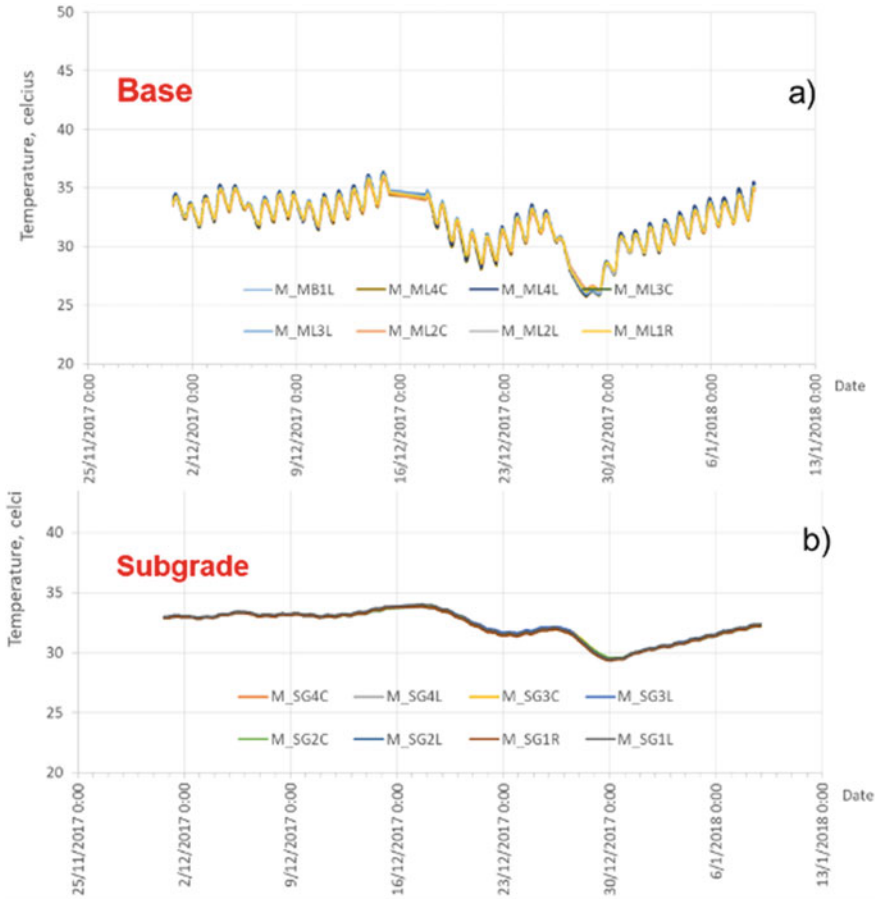


Fig. 16 Variation of temperature with time at the flexible pavement site

moisture movement in the flexible pavement was more susceptible to the capillary rise rather than downward infiltration.

- The daily temperature oscillation within the pavement layers was approximately sinusoidal and its amplitude decreased with depth.

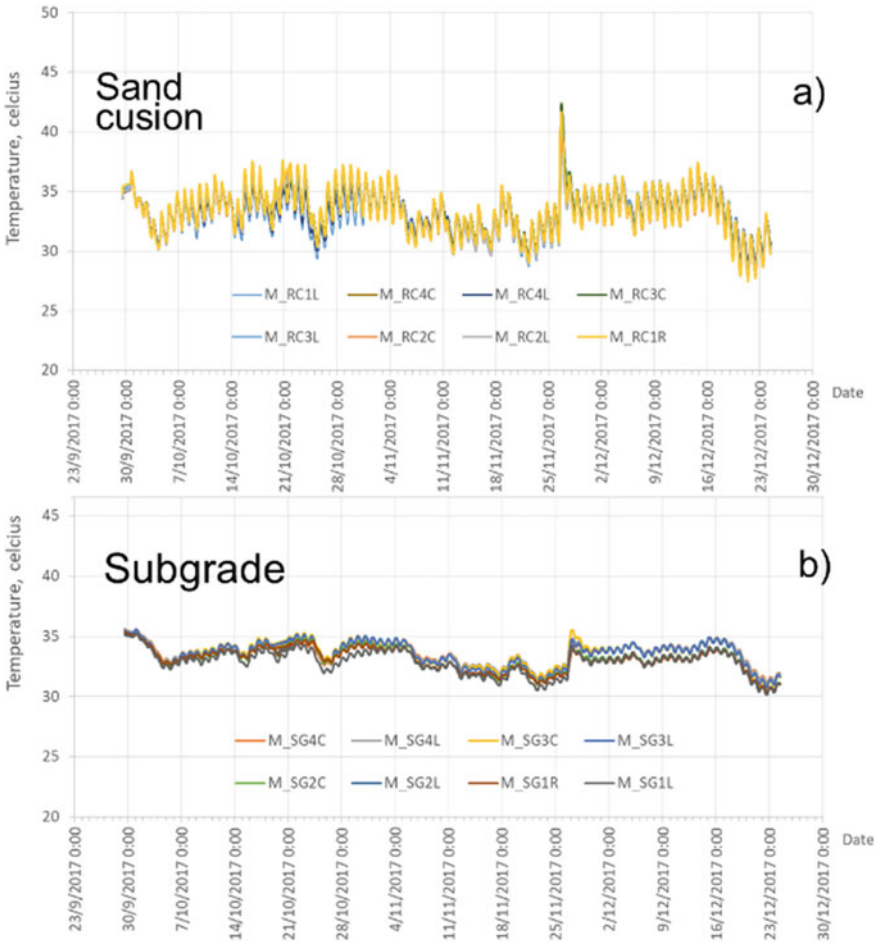


Fig. 17 Variation of temperature with time at the rigid pavement site

References

1. American Association of State Highway and Transportation Officials (1993) Guide for design of pavement structures. AASHTO, Washington, DC
2. Barksdale RD (1971) Compressive stress pulse times in flexible pavements for use in dynamic testing. Highw Res Rec Issue 345:32–44
3. Tabatabaee N, Al-Qadi IL, Sebaaly PE (1992) Field evaluation of pavement instrumentation methods. J Test Eval 20(2):144–151
4. Rada GR, Lopez A Jr, Elkins GE, Richter CA, Henderson B (1994) Long-term pavement performance seasonal monitoring program: instrumentation selection and installation. Transp Res Rec Issue 1432:32–43
5. Okamoto P, Tayabji S (1995) Instrumentation and evaluation of prestressed pavement section in pennsylvania. Transp Res Rec Issue 1505:103–111

6. Chen DH, Bilyeu J, Hugo F (1999) Monitoring pavement response and performance using in-situ instrumentation. *ASTM Spec Tech Publ Issue 1358*:121–134
7. Al-Qadi IL, Loulizi A, Elseifi M, Lahouar S (2004) The virginia smart road: the impact of pavement instrumentation on understanding pavement performance. *Asphalt Paving Technology, AAPT*, pp 427–465
8. Goulias DG, Kim H, Schwartz CW (2011) Evaluation of in situ pavement material properties and behavior through field instrumentation and load testing. *J Trans Eng 137(7)*:466–473
9. Zhao H, Wu C, Wang X, Zheng Y (2014) Pavement condition monitoring system at shanghai pudong international airport. *Geotech Spec Publ (239 GSP)*:283–295
10. Maadani O, Abd El Halim AO, Mostafa N (2015) Instrumentation for monitoring pavement performance in cold regions. *J Cold Regions Eng 29(4)*
11. Mshali MRS, JvdM Steyn W (2020) Incorporating truck speed effect on evaluation and design of flexible pavement systems. *Int J Pavement Res Technol 13*:55–63

Class Discriminatory Information for Unbound Granular Layers Using Statistical Pattern Recognition Techniques



Reza S. Ashtiani

Abstract The directional dependency of unbound granular soils substantially impacts the orthogonal load distribution capacity of pavement structures. Laboratory determination of such anisotropic properties is often overlooked by design engineers due to the time constraints, budgetary issues, and lack of available protocols and equipment. Besides anisotropic behavior, several physical and mechanical factors, such as degree of saturation, particle geometry, gradation, fines content, and the nature of stress paths contribute to the performance of pavement foundations. This study is aimed to explore the potential of nontraditional statistical pattern classification techniques to unravel underlying relations between the aggregate features and the anisotropic behavior of unbound aggregate systems. To achieve this objective, an experimental program was designed to evaluate physical and mechanical characteristics of different aggregate types with distinct lithology and gradations. The permutations of the experiment design were subjected to Variable Dynamic Confining Pressure (VDCP) stress path tests to study the effect of moisture state, fines content, particle geometry and the lithology on the anisotropic behavior of aggregate specimen. The Aggregate Imaging System (AIMS) was also incorporated in the experiment design to characterize the contribution of particle geometry of aggregates to the level of anisotropy of the unbound aggregate systems. 18 features for 68 aggregate specimens were measured/determined and incorporated in a multi-dimensional aggregate feature database for post processing of the experimental data. Subsequently, several statistical pattern recognition techniques were used to extract physically meaningful relations between the features of the aggregate database. The results indicate that Fisher's Linear Discriminant Analysis (LDA) juxtaposed by K-Nearest Neighbor (KNN) algorithms can potentially provide an efficient protocol for classification of the data. Additionally, dimensionality reduction techniques were used to identify the features that best describe the anisotropic behavior of the tested specimens. The results of this study can provide a valuable means for the pavement design industry to potentially reduce the number of features needed to be determined in the laboratory for a refined and cost-effective testing protocol.

R. S. Ashtiani (✉)

Civil Engineering Department, University of Texas at El Paso, El Paso, USA

e-mail: reza@utep.edu

Keywords Unbound granular soils · Statistical pattern recognition · K-Nearest neighbor (KNN) · Fisher's linear discriminant analysis (LDA)

1 Introduction

Unbound granular layers are integral component of the highway pavements and airfield runways. The primary role of base layers is to distribute and reduce the traffic induced stress to a tolerable level for subgrade soils. Additionally, granular layers serve as robust platform to support the surface layers and to maintain adequate ride quality. Several factors such as degree of saturation, particle geometry, gradation, fines content, plasticity of fines present in the mix, and the nature of applied stresses contribute to the performance of the Unbound Aggregate Base (UAB) layers in pavement structures. Several researchers studied the systematic error imposed by the isotropic characterization of the pavement materials [1–5]. The anomalies associated with the isotropic assumptions can potentially manifest itself in overestimation of the structural capacity of the pavement foundations which consequently results in premature failure of pavements. Therefore, the updated design and analysis protocols should depart from isotropic models to more representative cross-anisotropic characterization to mitigate such systematic errors. There are five material properties namely, modulus values in horizontal and vertical directions, (E_x and E_y), shear modulus (G_{xy}) and two Poisson ratios (ν_{xx} , ν_{xy}) required for cross anisotropic characterization of unbound granular layers. Reliable and repeatable estimation of such material properties is a complex and time-consuming process in the laboratory.

There are two distinct sources that contribute to the anisotropic behavior of the granular layers in pavement structures. The geometry of the particles, characterized by aggregate shape, angularity and surface macro-texture is traditionally termed as inherent anisotropy. Additionally, the dynamic nature of the moving traffic loads result in the rotation of the principal planes, and the shear reversal in the unbound granular layers. This load-related component is termed as stress-induced anisotropy. The study of the role of particle geometry on performance dates back to pioneering works of Parkin et al., El-Sohby, and Oda [6–8]. Adu-Osei et al. demonstrated that the level of anisotropy, defined by the ratio of modulus values E_x/E_y , is correlated to particle size distribution, particle geometry, and moisture content at a given level of compaction [9]. Ashtiani et al. proposed a simple procedure to evaluate the level of anisotropy of aggregate systems using easily determinable aggregate properties [2]. The level of anisotropy was then used as an input to evaluate the performance of aggregate bases. Tutumluer & Seyhan studied the influence of multiple stress path on the anisotropic behavior of granular materials [1]. Adu-Osei et al. tested aggregate materials at different stress states and dynamic stress paths using Rapid Triaxial Testing (RaTT) cell, and calculated the anisotropic parameters using System Identification (SID) scheme [9].

Pattern classification can be defined as the study of how machines can observe the environment, learn to distinguish patterns of interest from their background, and

make sound and reasonable decisions about the categories of the patterns [10]. These techniques have been successfully applied in several engineering practices. Geotechnical site characterization [11], detection of crack in pavements [12], prediction of landslides due to rainfalls [13] and travel time prediction on highways [14] are some examples of such applications in geotechnical engineering.

The main objective of current study was to unfold underlying relationships between the parameters characterizing the behavior of pavement foundations subjected to traffic loads using pattern classification techniques. It was also aimed to evaluate important physical information such as aggregate mineralogy, moisture state, particle size distributions as pre-defined classes and to observe which classification results in better groping within the aggregate matrix. For this purpose, a comprehensive experiment design was initially developed to establish a multi-dimensional aggregate feature database. The database consists of features of aggregates mixes, with different lithologies and gradations, tested at different saturation levels. Nonlinear and cross-anisotropic material properties were determined using SID based on the results of variable dynamic confining pressure (VDCP) stress path tests. Particle geometry parameters were characterized using the Aggregate Imaging System (AIMS). Subsequently, Hierarchical Clustering Analysis (HCA) techniques were employed to assess the similarities between the parameters. Moreover, Fisher's Linear Discriminant Analysis (Fisher-LDA) and K Nearest Neighbors (KNN) algorithm were used to classify the data based on predefined criteria. The results of this study identify the aggregate features with similar patterns and thus provide a deeper understanding of the underlying relations and interactions between the features of aggregate database. This information can be useful to eliminate the number of features needed to be measured in the lab for a more cost-effective testing protocol.

2 Statistical Pattern Classification

Several aggregate features influence the anisotropic characteristics of unbound aggregate material. therefore, a high-dimensional aggregate database will be generated after any comprehensive experimental study. Generally, the more information we collect about the features that influence a phenomenon, the better understanding of that phenomenon will be achieved. On the other hand, high-dimensional data bases are difficult to handle since they introduce more complexity into the problem. In such circumstances, dimensionality reduction techniques may be effectively employed to eliminate correlated features. By means of dimensionality reduction, one is able to select the features with highest significance. As described in the following subsections, dimensionality reduction is closely related to classification and clustering techniques.

Clustering is basically organizing groups of objects that share similar characteristics. In other words, the objective of clustering is organizing data into clusters such that there is high intra-cluster and low inter-cluster similarity. The "similarity" may

be expressed in terms of a distance function. Clustering algorithms are generally categorized as supervised and unsupervised approaches. In supervised algorithms, the clustering is done based on pre-defined training patterns, while unsupervised approaches cluster the data only according to intrinsic scatter of the data.

During recent years, classification approaches have had numerous applications in different fields of engineering, medicine, humanities, etc. Pattern recognition techniques have been successfully employed for interpretation of hand-written structured documents, such as architectural drawings [15]. These techniques (for instance, Linear Discriminant Analysis) have been also used for recognition of Chinese complex scripts [16]. Pattern classification has also helped medical practitioners for more accurate diagnosis of problems like human brain tumors [17] and Parkinson [18]. Financial institution can also take advantage of such techniques to manage credit risks and credit scores for businesses and consumers [19]. In this section, some statistical classification approaches which have been used in current study are discussed in more detail. These approaches are utilized for further assessment of the data obtained from the experimental program.

2.1 K Nearest Neighbors

The objective in the K Nearest Neighbors (KNN) algorithm is to predict the classification of a new sample point in a database, where the data points have been already separated into distinct classes [20]. In this algorithm, we start with a data set consisting of data points of known classes. This database may be regarded a training set since it provides information about the objects of the different classes. Then, the classification of the new observation is done based on its similarity to the classes in the database. After deciding on the measure of similarity, we still need to decide which classes from the database are suitable enough to include the new observation. K Nearest Neighbors algorithm suggests solving this problem by taking a certain number (say K) of the nearest points. In binary classification problems, the K would be chosen as an odd number to avoid tied votes. Usually, K is assumed as a positive integer typically smaller than 10. If $K = 1$, the data point is simply assigned to the class of its immediate neighbor.

This algorithm can be summarized as the following:

1. Decide on the value of K (a positive integer).
2. Select the K entries in the database which are closest to the new sample.
3. Find the most common classification of the selected entries (which is the classification of the new sample).

2.2 Hierarchical Clustering Analysis

Hierarchical methods are well-known clustering techniques that produce a sequence of clustering each of which is nested into the next clustering in the sequence. In other words, hierarchical clustering can be thought of as a set of flat clustering methods organized in a tree structure. In these methods, the clusters are developed through recursive partitioning of the data in either top-down or bottom-up fashion. The bottom-up approaches tend to be more accurate but have higher computational cost as well. This higher computational complexity is not necessarily associated with increased conceptual (or algorithmic) complexity since the hierarchical construction of clusters can be organized as a sequence of basic cluster merging or partitioning operations [21].

The similarity criteria used in these algorithms are minimum distance, maximum distance, average distance, and center distance. A bottom-up approach initially assumes each individual sample to represent a cluster of its own. Then, similar clusters are iteratively merged until the desired cluster structure is obtained. On the other hand, a top-down approach puts all samples in a single root cluster initially. Then, the existing clusters are iteratively partitioned into sub-clusters. Hierarchical algorithms are of great interest due to their advantages such as ease of handling different forms of similarity and applicability to various feature types.

2.3 Fisher's Linear Discriminant Analysis

Principal Components Analysis (PCA), the most famous example of dimensionality reduction, searches for directions in the data space which give the best variance of the data projection. Hence, we may obtain a lower dimensional representation of the data by removal of noisy directions. PCA is an unsupervised technique since it does not include label information of the data. The question arises here is “how can we utilize the label information in finding informative projections?”. To resolve this issue, Fisher-LDA suggests minimizing within class scatter matrix (S_W) and, simultaneously, maximize between class scatter matrix (S_B). Mathematically, the best direction vector (\mathbf{w}) can be obtained by maximizing the following objective function [22]:

$$J(\mathbf{w}) = \frac{\mathbf{w}^T S_B \mathbf{w}}{\mathbf{w}^T S_W \mathbf{w}} \quad (1)$$

An important property of the objective function J is that rescaling of the vectors ($\mathbf{w} \rightarrow \alpha \mathbf{w}$) does not affect it. Thus, \mathbf{w} can be always chosen such that the denominator is simply $\mathbf{w}^T S_W \mathbf{w} = 1$, since it is a scalar.

2.4 *K-Means Clustering*

K-means is one of the simplest unsupervised learning algorithms that solve well-known clustering problems. K-means is basically a partitioning method in which the objects are classified as belonging to one of K clusters. The main idea is to define centroids, for each cluster, which may be considered as the cluster representative. In the case of real-valued data, the arithmetic mean of the attribute vectors for all objects within a cluster can be an appropriate representative. Alternative types of centroid may be required in other cases. These centroids should be located carefully since different locations may cause different result. The general rule is to place the centroids far away from each other to end up with a better classification scheme.

The second step is to take each point in the given data set and associate it to the nearest centroid. This will be done for all the data points and then the early grouping is completed. At this point the new centroids need to be recalculated based on the results of the previous step. Now, we go back to the second step and regroup the objects with regard to the new centroids. As a result of this loop, the location of K centroids change step by step, and the algorithm keeps running until no further movement of the centroids is observed.

Although it can be proved that the procedure will always terminate, the K-means algorithm does not necessarily find the best grouping configuration. Also, this algorithm is considerably sensitive to the randomly selected centroids. This effect, however, can be reduced by multiple time running of the algorithm [10].

3 Anisotropic Behavior of Aggregate Layers

The resilient modulus of unbound aggregate material is nonlinear, stress-dependent and anisotropic in nature. The directional dependency of mechanical properties of UAB is either due to the geometry, texture and size distribution of the aggregates or due to the rotation of the applied stresses. This implies that, a system of UAB consisting of single-sized and equi-dimensional aggregates subjected to hydrostatic stresses is most likely to show isotropic behavior. Previous researches have revealed the strong correlation between some physical features such as water content, dry density, aggregate shape and angularity, stress rate, etc. and the resilient behavior of unbound aggregates. Dawson et al. [23], for instance, indicated that the resilient modulus of granular materials significantly decreases at higher levels of saturation [23]. Dry density, or degree of compaction, is another factor which plays a crucial role in the resilient behavior. Generally, the aggregate matrix becomes stronger and stiffer as its dry density increases. The correlation between dry density and resilient modulus, however, is not the same for aggregates systems with different lithology, fine contents and stress state [24]. Aggregate shape is the other factor which profoundly affects the resilient behavior of granular materials. Previous studies have revealed

that crushed aggregates with high angularity and rough texture develop strong interlocking forces and thus have higher resilient modulus compared with the systems composed of rounded and smooth material [2].

Oda and Nakayama proposed the following equation for resilient modulus (MR) to capture its nonlinearity as well as hardening-softening behavior [25]:

$$M_R = k_1 P_a \left(\frac{I}{P_a} \right)^{k_2} \left(\frac{\tau_{oct}}{P_a} + 1 \right)^{k_3} \quad (2)$$

where P_a = atmospheric pressure; I = first stress invariant; τ_{oct} is octahedral shear stress; and k_1, k_2, k_3 are fitting parameters. In the above equation, the term $(I/P_a)^{k_2}$ is known as the hardening component, which captures the stiffening effect when the aggregate matrix is subjected to increasing confinement. On the other hand, $(\tau_{oct}/P_a)^{k_3}$ is referred to as the softening component, which reflects the reduction of stiffness as a result of the cumulative deflection (or damage) induced to the matrix. Anisotropic characterization of the UAB requires the values of the horizontal resilient modulus (E_x) as well as the shear modulus (G_{xy}), which may be represented in the form of Eq. 2 as follows:

$$E_x = k_4 P_a \left(\frac{I}{P_a} \right)^{k_5} \left(\frac{\tau_{oct}}{P_a} + 1 \right)^{k_6} \quad (3)$$

$$G_{xy} = k_7 P_a \left(\frac{I}{P_a} \right)^{k_8} \left(\frac{\tau_{oct}}{P_a} + 1 \right)^{k_9} \quad (4)$$

where, k_4, k_5, k_6, k_7, k_8 and k_9 , are fitting parameters (similar to Eq. 2).

The conventional triaxial test is usually used to determine the shear strength parameters of soils in general geotechnical engineering applications. In pavement engineering applications, however, the cyclic triaxial test is preferred to the traditional triaxial shear test. The stress state experienced by an element of material in the pavement structure due to moving traffic loads consists of pulses of vertical and horizontal stresses accompanied by a double pulse of shear stress. From another perspective, the principal stresses rotate as the wheel load approaches and then departs [26] (Fig. 1). Thus, an extension-compression-extension stress regimen is experienced by the material element as the wheel load passes over. Although the magnitude of the tensile stresses may be very small, the changes in the stresses result in additional anisotropy of material properties in the pavement structure. Hornych et al. pointed out that the aforementioned stress regimen can increase the rate of plastic strains up to three times greater than those measured from repeated plate load tests [27].

An appropriate testing protocol of pavement material must be capable of providing a situation which accurately replicates the stress regime induced by traffic loads. On the other hand, laboratory testing methods must be simple and repeatable so that the practitioners can easily acquire the required material parameters. Using Hollow Cylinder Apparatus (HCA), the stress field rotations observed in the field may be

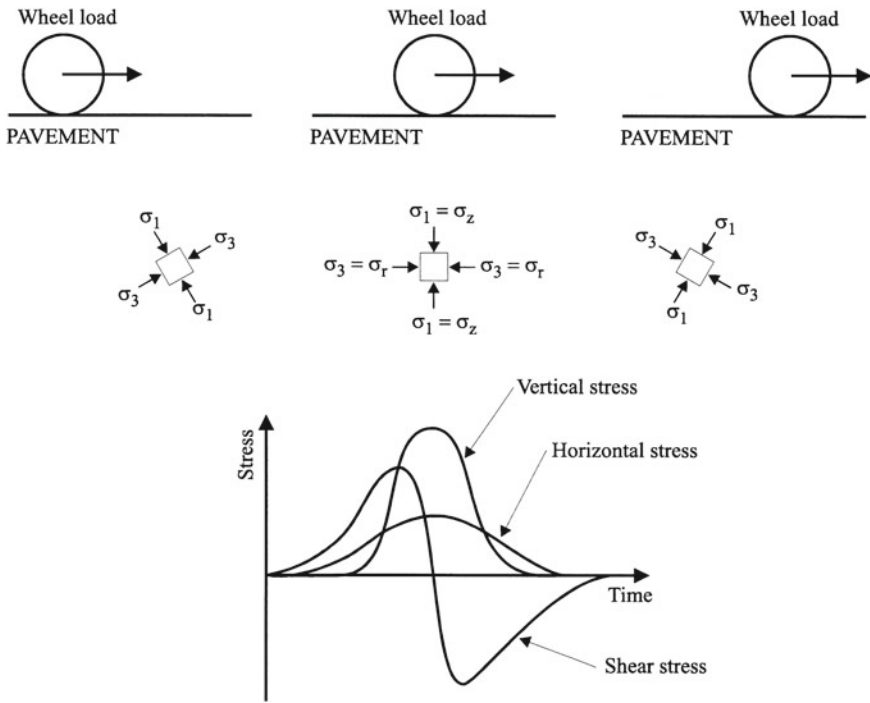


Fig. 1 Stress states developed in the pavement structures due to moving traffic loads [26]

adequately simulated in the laboratory. However, HCA is difficult to be implemented for practical purposes and is usually used for research projects [28]. Adu-Osei developed a laboratory testing protocol for anisotropic characterization of unbound granular material. He applied static stress states followed by small dynamic increments in the principal stresses to obtain three stress regimes namely triaxial compression, triaxial extension and triaxial shear [9]. Using the results of the first two set of tests, he determined the cross-anisotropy parameters of aggregate material through a back-calculation scheme called system identification (SID). A similar testing protocol is adopted in current study for anisotropic characterization of UAB. SID suggests iterative modification of the parameters until a desirable level of accuracy is achieved. This procedure will give four out of five cross-anisotropy parameters namely: E_x , E_y , ν_{xx} and ν_{xy} . On the other hand, the value of G_{xy} may be determined using the results of shear regime test with regard to the concepts of potential strain energy. In current study, a similar testing protocol was adopted for anisotropic characterization of the UAB.

4 Experimental Program

4.1 Material

In order to study the influential factors in the cross anisotropic behavior of UABs, various aggregate mixes with distinct lithologies were incorporated into the experimental program. Different granite, limestone and gravel aggregates with three gradation variants (i.e. coarse, well and fine gradations) were collected from ten sources in Texas, Oklahoma and Minnesota. The materials were tested in three moisture conditions: Optimum Moisture Content (OMC), dry of optimum moisture content (-2% of OMC), and wet of optimum moisture content ($+2\%$ of OMC) to evaluate the effect of moisture state on the mechanical response of the aggregate systems. OMC and maximum dry density of each gradation variant were determined in accordance with ASTM D1557.

As discussed earlier, the aggregate geometry characterized by its shape, angularity, and texture considerably influences the level of anisotropy unbound aggregate systems. This is mainly due to the contribution of the geometry to the interlocking mechanism in particulate media. In this study, aggregate geometry was characterized in terms of particle form, angularity, and texture. Aggregate form refers to flat or elongated shape of the particles, angularity defines the degree of roundness or sharpness of aggregate corners, and texture pertains to small asperities at the surface of particles from which the surface roughness originates [29].

Fifty-six aggregate particles from three aggregate sizes of each source were evaluated using the AIMS device. AIMS uses a simple setup consisted of one camera and two different lighting schemes to capture images of aggregates at different resolutions, from which aggregate geometrical properties are quantified using image analysis techniques (Fig. 2). The system operation is based on two modules. The first module is for the analysis of fine aggregates, smaller than 4.75 mm (#4 sieve), where black and white images are captured. The second module is devoted to the analysis of coarse aggregate, larger than 4.75 mm (#4 sieve), where gray images as well as black and white images are captured. Combining both the coarse and fine aggregate analyses into one system is considered an advantage to reduce the cost of developing the system.

Several two parameter and three parameter distribution functions were fitted to the aggregate geometry data. Based on the best fit analysis of the database, it was observed that the two-parameter Weibull distribution provides a reasonable fit for both particle size distributions and geometrical properties of the aggregates data at a 95% confidence level. The cumulative Weibull distribution function is of the following form:

$$Q(d) = 1 - \left[-\left(\frac{d}{\alpha}\right) \right]^\beta \quad (5)$$

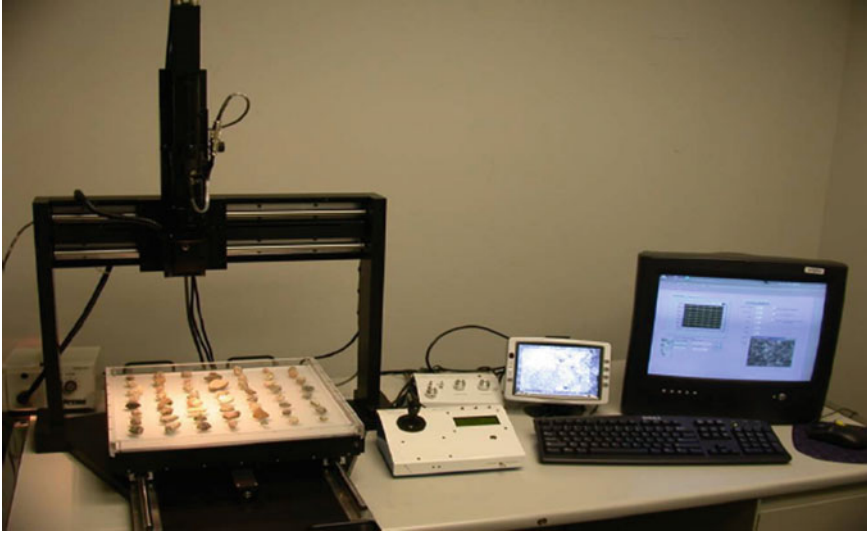


Fig. 2 Aggregate Imaging System (AIMS)

where, d = the aggregate size; α = scale parameter; and β = shape parameter. These distribution parameters, which can be determined through fitting the particle size distribution and aggregate shape properties data to the Weibull distribution function, were later imported to the aggregate feature database.

Methylene blue test (ASTM C832-2003) was adopted to provide a measure of activity of the fine particles in the matrix. Methylene blue is a large polar organic molecule that is adsorbed onto the negatively charged surfaces of clay minerals. The amount of methylene blue adsorbed by a given mass of clay depends on the relative concentration of negatively charged sites on the clay particle surfaces as well as surface area of the clay per unit mass.

4.2 Dynamic Triaxial Testing

A proper testing protocol for evaluation of mechanical response of UAB should be able to capture the extension-compression-extension stress regimens induced by moving traffic loads. Dynamic stress path tests are preferred to the traditional triaxial test protocols which are commonly suitable for simulating the state of the stresses under stationary loads. Particularly, VDCP type stress path tests take advantage of applying dynamic vertical pressure as well as dynamic confinement on the specimen for a more realistic simulation of field conditions. In this study, a customized triaxial setup called Rapid Triaxial Tester (RaTT) was used to perform VDCP stress path tests in accordance with the stress path protocol outlined in ICAR/508 report [30]. The general setup for the stress path test using this apparatus is consisted of RaTT cell mounted

in the Universal Testing Machine (UTM), data acquisition system, and a computer for control and storage of the data. This customized setup supports automated cell movement and multiple displacement measurement with Linear Variable Differential Transducers (LVDT) in both directions.

The specimens tested in triaxial cell were prepared in four different stages namely mixing, moisturizing, compacting, and sealing. The mixing of the material for each aggregate matrix was done manually inside a plastic container according to the intended gradation. Subsequently, the prescribed water content (OMC, wet of optimum, or dry of optimum) was slowly added and thoroughly mixed. This mixture was given sufficient time to assure uniform distribution of the water content. After pouring the mixture into the mold and the compaction process, the specimens were covered with a rubber membrane to prevent moisture loss throughout the test.

5 Results and Discussion

In this study, two general approaches were employed to provide physically meaningful class discriminatory information about cross-anisotropic behavior of aggregate samples by unfolding relationships between the influential features. Supervised clustering analysis was performed on the aggregate database where the aggregate samples were labeled according to their lithology, gradation and volumetric water content as summarized in Table 1. Lithology provides information on the mineralogy and the origin of each aggregate type; gradation represents the particle size distribution; and moisture state is the gravimetric water content of the aggregate blend at the time of testing.

Hierarchical unsupervised clustering techniques were also performed on the aggregates' feature database. Two different proximity measures namely average (or Euclidian) and Mahalanobis distance were employed to find the best interpretable results according to the mechanical behavior of the aggregate systems. The Euclidian distance between all pairs of objects in two clusters (r and s) is defined as:

$$d(r, s) = \frac{1}{n_r \cdot n_s} \sum_{i=1}^{n_r} \sum_{j=1}^{n_s} \text{dist}(x_{ri}, x_{sj}) \tag{6}$$

Table 1 Classification criteria and class labels of the aggregate database

Classification criteria	Class labels		
	Lithology	Limestone (L)	Granite (N)
Gradation	Coarse (1)	Well (2)	Fine (3)
Moisture state	Dry (D)	Optimum (O)	Wet (W)

where, n_r and n_s are the number of samples in the clusters r and s , respectively. On the other hand, the Mahalanobis distance is defined as:

$$\text{dist}(x_{ri}, x_{sj}) = (x_{ri} - x_{sj})D^{-1}(x_{ri} - x_{sj})^T \quad (7)$$

In this equation, the distance between data points is normalized by the covariance matrix D . Thus, this measure is less sensitive to the outliers of the system and usually results in better classification rates.

In another attempt, Fisher's Linear Discriminant Analysis (LDA) accompanied by K Nearest Neighbor (KNN) were used to find class discriminatory information based on the key features. To accomplish this, the Eigenvectors of the fishers' LDA ($S_W^{-1} S_B$) were calculated and the data were projected onto the two components with highest Eigenvalues. Projections Then KNN algorithm was employed to give class rates according to the true class labels.

5.1 Supervised Clustering Analysis

Supervised clustering analysis was performed on the aggregate data based on three classification criteria (lithology, gradation, and moisture state) and the class labels presented in Table 1. In addition, the features that minimize the mean square error function over the data were determined through Sequential Forward Feature Selection (SFFS) algorithm. Classification based on the aggregates' lithology resulted in a 73% classification rate. Moreover, it was observed that angularity parameter, dry density, and k_6 (the exponent of the hardening term for horizontal modulus) are the most significant features in this case. Classification based on gradation resulted in a 62% classification rate. Angularity parameter, k_3 and k_9 (exponents of softening terms for vertical and shear modulus, respectively) were selected by SFFS algorithm as the features that best explain the system's behavior. Finally, classification based on the moisture state resulted in a 52% classification rate and the features selected by SFFS were k_3 (softening exponent of vertical modulus) and k_7 (multiplier in the shear modulus model) in this case.

The best classification rate (73%) was observed when classification was performed based on lithology. This clustering analysis revealed that angularity plays an important role in the anisotropic behavior of aggregate systems. Since the main mechanism of load transfer in particulate media is based on grain interlocks, aggregate systems with more angular particles are less prone to develop plastic deformations when subjected to external loads. In another attempt, shape and scale components of angularity were removed from the database and the classification was performed without these parameters. Accordingly, a dramatic drop in the classification rate was observed (from 73 to 46%) indicating the significance of angularity features.

5.2 Hierarchical Clustering Analysis

Hierarchical unsupervised clustering analyses were performed on the database in order to find physically meaningful patterns among the features of the aggregates. The results of hierarchical clustering of the features based on Euclidian and Mahalanobis proximity measures are depicted in Figs. 3 and 4, respectively.

These two dendograms suggest very similar interpretations. According to Fig. 3, k_1 and k_4 (which are hardening multipliers of the elastic modulus in vertical and horizontal directions, respectively) have the closest patterns in the dataset. This is in line with our prior knowledge about the behavior of aggregate systems. On the other hand, Figs. 3 and 4 show similar patterns for softening parameters (k_3 and k_9) and the water content (w). It is well established in the literature that intrusion of moisture in unbound aggregate systems decreases the orthogonal stiffness and thus accelerates rutting. This reduction of stiffness properties in the unbound matrix is synonymous with increase of the softening parameter in Eq. 1. Hence, the inter-relationship between the softening parameters and water content observed in this analysis is in conformity with the actual behavior of unbound aggregates.

Fig. 3 Hierarchical clustering of aggregates' features using Euclidean distance as the proximity measure

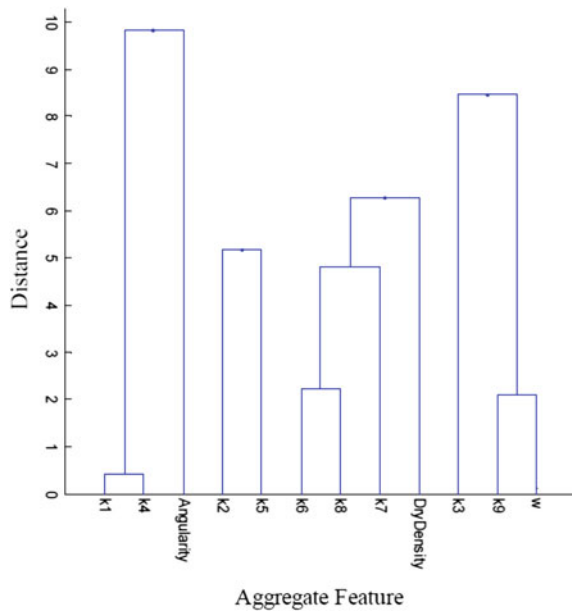
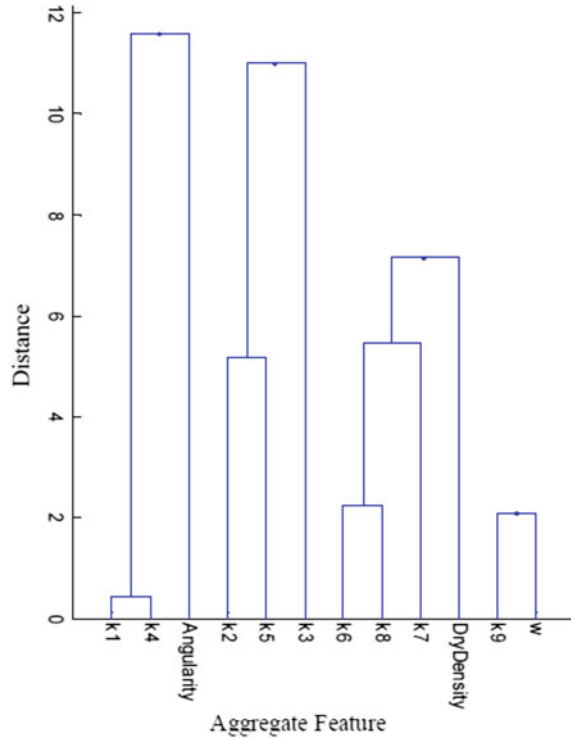


Fig. 4 Hierarchical clustering of aggregates' features using Mahalanobis distance as the proximity measure



5.3 Discriminant Analysis

The aggregates features' database was analyzed via Fisher's LDA to provide class discriminatory information associated with these features. For this purpose, the eigenvalues and eigenvectors of Fisher's criterion ($S_W^{-1}S_B$) were determined initially. Subsequently, the data points were projected onto the principal components with highest eigenvalues. The knee in the resulted plot (Fig. 5) suggests that the first two principal components of Fisher's criterion can reasonably explain the behavior of the system. Furthermore, KNN classifier with different values of K (number of neighbors) was applied to the projected data to determine the performance of the classifier.

The classification rates for both raw data and the projected data after applying KNN classifier are demonstrated in Fig. 6. According to this figure, Fisher's LDA together with KNN classifier is well capable of providing class discriminatory information when the class labels are based on lithology. Moreover, Fig. 6 suggests that this analysis does not provide reliable class discriminatory information when particle size distributions and moisture state are regarded as class labels.

Figure 7 illustrates that Fisher's LDA accompanied by KNN classifier results in meaningful classification of the aggregate data based on lithology. Per this figure,

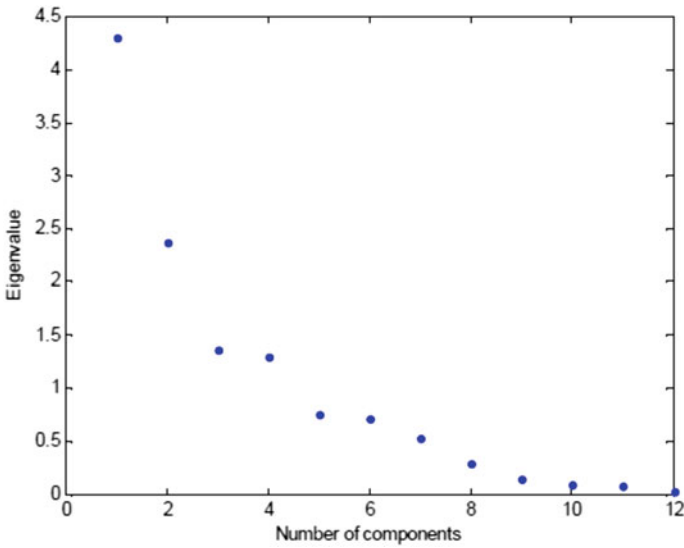


Fig. 5 Eigenvalues of Fishers' criterion ($S_W^{-1} S_B$)

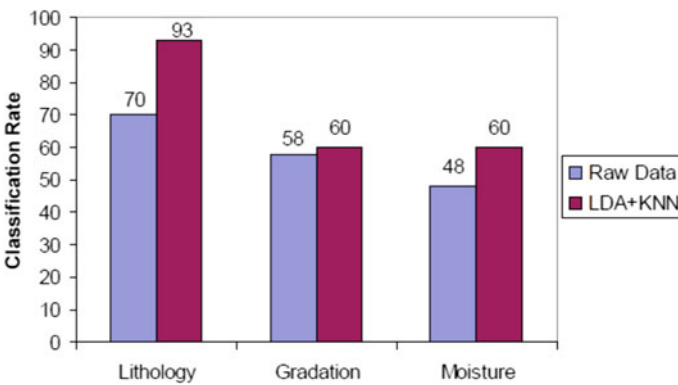


Fig. 6 Performance of the classifier based on different criteria

limestone and gravel aggregates have more condensed projections compared with granite aggregates. This could be attributed to the identification of aggregate types in construction where limestone and gravel have more distinct definitions compared with granite.

Distribution of the data points before inclusion KNN in the analysis is shown in Fig. 8. This plot clearly demonstrates the significance of LDA + KNN method in providing appropriate class discriminatory information of the aggregate data. The results of classification analyses regarding other criteria and the corresponding distributions are shown in Figs. 9, 10, 11 and 12.

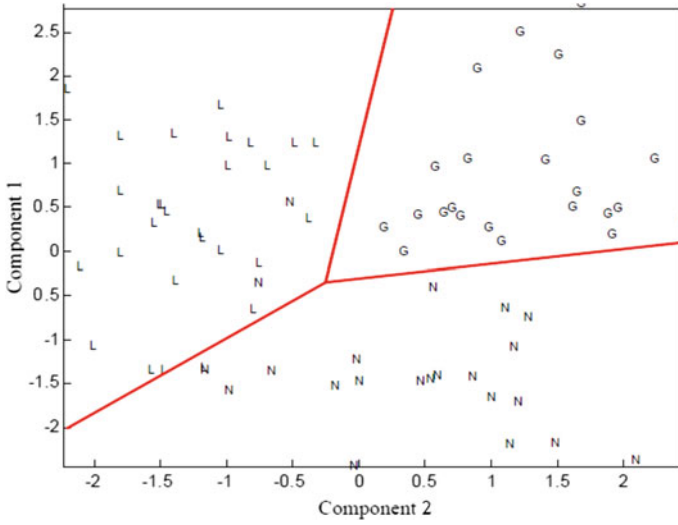


Fig. 7 Classification using LDA + KNN projection based on lithology (L: Limestone, N: Granite and G: Gravel)

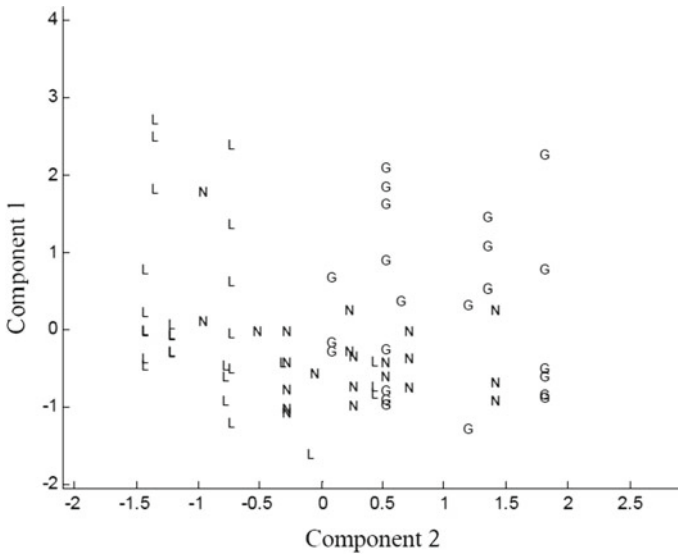


Fig. 8 Classification using LDA projection based on lithology (L: Limestone, N: Granite and G: Gravel)

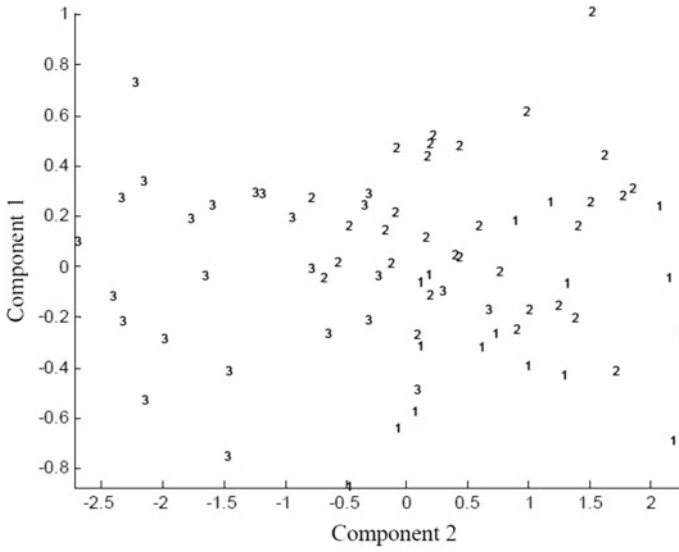


Fig. 9 Classification using LDA + KNN projection based on gradation (1: Coarse, 2: Well and 3: Fine)

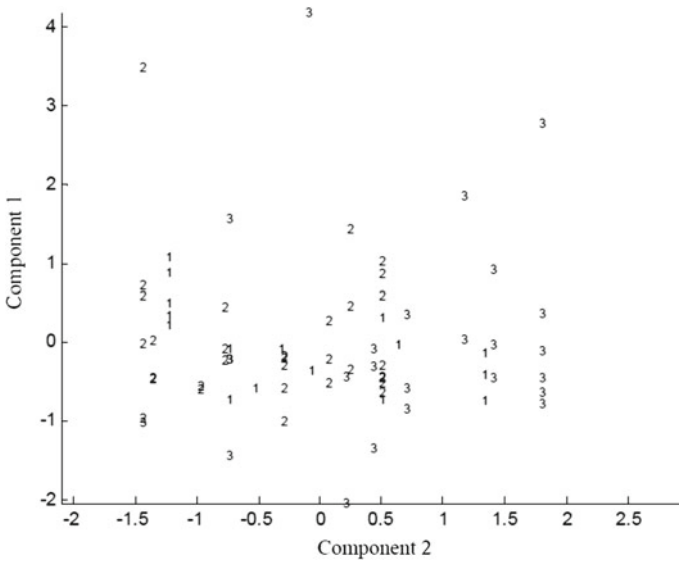


Fig. 10 Classification using LDA projection based on gradation (1: Coarse, 2: Well and 3: Fine)

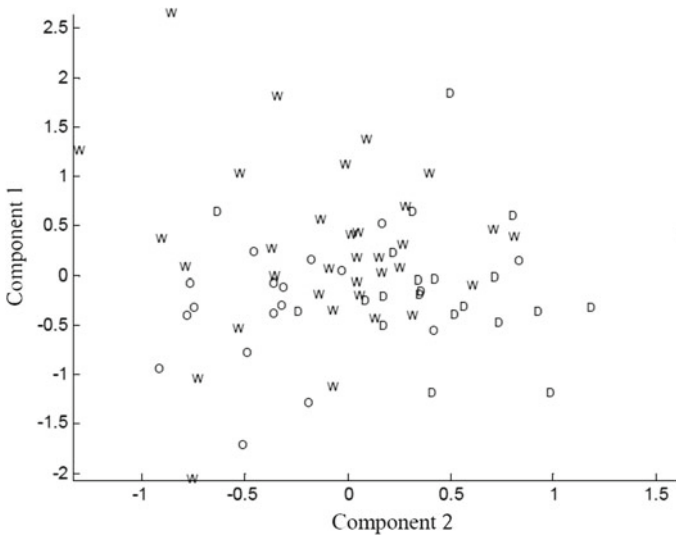


Fig. 11 Classification using LDA + KNN projection based on moisture state (D: Dry, O: Optimum and W: Wet)

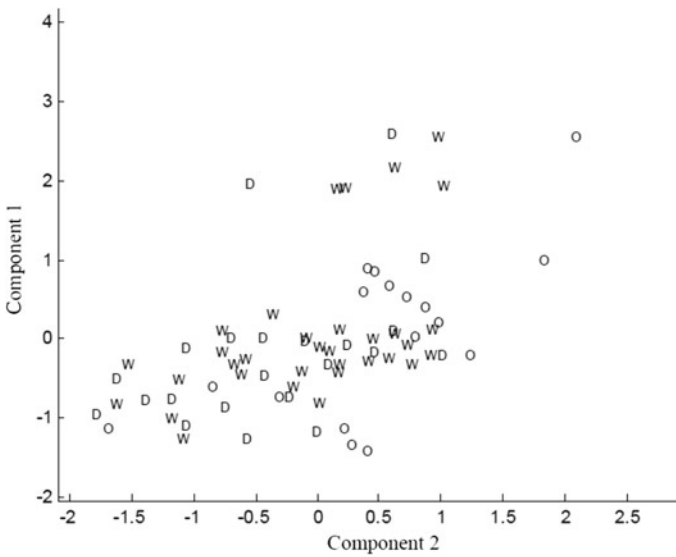


Fig. 12 Classification using LDA projection based on moisture state (D: Dry, O: Optimum and W: Wet)

6 Concluding Remarks

Statistical pattern classification analyses were conducted over aggregate samples characterized by 12 features in this research in order to explain the underlying behavior of anisotropic granular materials. The features were believed to fully characterize the nonlinear, stress sensitive and cross anisotropic behavior of the aggregate systems. Sequential Forward Feature Selection (SFS) and hierarchical unsupervised clustering were used to find the features that best explain the dynamics of the aggregates' behavior and results in highest classification rates. Discriminant analysis of the dataset accompanied by KNN was also employed as another attempt to unfold hidden class discriminatory information of the aggregate matrix. The findings of this research can be useful to eliminate the number of features needed to be determined by laboratory tests for a more cost-effective testing protocol. Furthermore, this information can be used to develop more precise data-driven models such as regression models and artificial neural networks.

A comprehensive experiment design consisted of three aggregate types from ten different sources with three distinct gradations molded at three different moisture states were incorporated into this research effort. The compacted aggregate specimens were subjected to multiple variable dynamic confining pressure stress path tests to determine the parameters associated with anisotropic properties of the material. The cumulative Weibull distribution function was used to quantify the distributions of geometry parameters. Also, the activity of fine particles in the matrix was taken into consideration through Methylene blue test results. General findings of this study can be summarized as follows.

- Sequential Forward Feature Selection (SFFS) revealed that aggregate angularity, is the most important feature in providing class discriminatory information of the aggregate dataset. This fact was in conformity with the behavior of aggregates in the lab.
- Projection of the data onto the Eigenvectors of the LDA with highest Eigenvalues accompanied by KNN classifier was found to provide high classification rate based on lithology of the aggregates.
- Supervised clustering analysis of the aggregate database was performed using three different classification criteria: lithology, gradation and moisture state. Best performance was observed when the clustering is conducted based on lithology (with 73% classification rate). The classification rate based on gradation and moisture state were found to be 62% and 51% respectively. This suggests that characterization of aggregate systems with higher fine content and saturation levels requires other features.
- Hierarchical clustering analysis of the features using Mahalanobis distance and Euclidean distance were found to provide information which is mechanically interpretable. Particularly, hierarchical clustering of the features using average distance categorized softening and hardening components of the constitutive model in different classes.

References

1. Tutumluer E, Seyhan U (1999) Laboratory determination of anisotropic aggregate resilient moduli using an innovative test device. *Transp Res Rec J Transp Res Board* 1687:13–21
2. Ashtiani RS, Little DN, Masad E (2008) Material factors that influence anisotropic behavior of aggregate bases. *Transp Res Rec J Transp Res Board* 2059:20–30
3. Karasahin M, Dawson AR, Holden JT (1993) Applicability of resilient constitutive models of granular material for unbound base layers. TRB, National Research Council, Washington, D.C., pp 98–107
4. Masad S, Little DN, Masad E (2006) Analysis of flexible pavement response and performance using isotropic and anisotropic material properties. *J Transp Eng (ASCE)* 132(4):342–349
5. Wang H, Al-Qadi I (2013) Importance of nonlinear anisotropic modeling of granular base for predicting maximum viscoelastic pavement responses under moving vehicular loading. *J Eng Mech (ASCE)* 139(1):29–38
6. Parkin A, Gerrard C, Willoughby D (1968) Discussion: deformation of sand in shear. *J Soil Mech Found Div* 94(SM 1):336–340
7. El-Sohby M (1969) Deformation of sands under constant stress ratios. Mexico
8. Oda M (1972) Deformation mechanism of sand in triaxial compression tests. *Soils Found* 12(4):45–63
9. Adu-Osei A (2000) Characterization of unbound granular base. Ph.D. dissertation, Texas A&M University, College Station, USA
10. Jain AK (2010) Data clustering: 50 years beyond K-means. *Pattern Recogn Lett* 31:651–666
11. Hegazy YA, Mayne PW (2002) Objective site characterization using clustering of piezocone data. *J Geotech Geoenvironmental Eng (ASCE)* 128(12):986–996
12. Wu L, Mokhtari S, Nazef A, Nam B, Yun H-B (2014) Improvement of crack-detection accuracy using a novel crack defragmentation technique in image-based road assessment. *J Comput Civil Eng (ASCE)* 30(1):04014118
13. de Souza FT, Ebecken NFF (2012) A data based model to predict landslide induced by rainfall in Rio de Janeiro city. *Geotech Geol Eng* 30:85–94
14. Tak S, Kim S, Jang K, Yeo H (2014) Real-time travel time prediction using multi-level k-nearest neighbor algorithm and data fusion method, In: Issa RI, Flood I (eds) *Computing in civil and building engineering (ASCE)* Orlando, USA
15. Ghorbel A, Lemaitre A, Anquetil E, Fleury S, Jamet V (2015) Interactive interpretation of structured documents: application to the recognition of handwritten architectural plans. *Pattern Recogn* 48:2446–2458
16. Gao TF, Liu CL (2008) High accuracy handwritten Chinese character recognition using LDA-based compound distances. *Pattern Recogn* 41(11):3442–3451
17. El-Dahshan ESA, Mohsen HM, Revett K, Salem ABM (2014) Computer-aided diagnosis of human brain tumor through MRI: a survey and a new algorithm. *Expert Syst Appl* 41(11):5526–5545
18. Cho CW, Chao WH, Lin SH, Chen YY (2009) A vision-based analysis system for gait recognition in patients with Parkinson's disease. *Expert Syst Appl* 36(3):7033–7039
19. Šušteršič M, Mramor D, Zupan J (2009) Consumer credit scoring models with limited data. *Expert Syst Appl* 36(3):4736–4744
20. Hastie T, Tibshirani R (1996) Discriminant adaptive nearest neighbor classification. *IEEE Trans Pattern Anal Mach Intell* 18(6):607–616
21. Berkhin P (2006) A survey of clustering data mining techniques. Grouping multidimensional data. In: Kogan J, Nicholas C, Teboulle M (eds) *Berlin Heidelberg, Germany: Springer*, pp 25–71
22. Duda R, Hart P, Stork D (2000) *Pattern classification*. Wiley, New York
23. Dawson AR, Thom NH, Paute JL (1996) Mechanical characteristics of unbound granular materials as a function of condition. Balkema, Rotterdam
24. Hicks RG (1970) Factors influencing the resilient properties of granular material. Ph.D. dissertation, University of California, Berkeley

25. Oda M, Nakayama H (1989) Yield function for soil with anisotropic fabric. *J Eng Mech (ASCE)* 115(1):89–104
26. Lekarp F, Isaacson U, Dawson A (2000) State of the Art. I: resilient response of unbound aggregates. *J Transp Eng ASCE* 126(1):66–75
27. Hornych P, Kazai A, Quibel A (2000) Modeling a full-scale experiment of two flexible pavement structures with unbound granular bases. University of Nottingham, UK, pp 359–367
28. Van Niekerk AA (2002) Mechanical behavior and performance of granular bases and sub-bases in pavements. Ph.D. dissertation, Delft University of Technology, Delft, The Netherlands
29. Kim S, Little DN, Masad E (2005) Simple Methods to estimate inherent and stress-induced anisotropy of aggregate base. *Transp Res Rec J Transp Res Board* 1913:24–31
30. Ashtiani RS, Little DN (2009) Methodology for designing aggregate mixtures for base courses. In: College station: international center for aggregates research (Report No: ICAR/508)

Deformation and Failure Parameters of Cement-Modified Loess: Application to the Calculation of the Safety Factor of a Road Structure



Thomas Lenoir, Thierry Dubreucq, Thibaut Lambert, and Denis Killinger

Abstract Loess is a geological formation with poor geotechnical performances that covers up 10% of the world's land surface area. To upgrade and allow optimal use of this kind of material in civil engineering, it is common to add few percent of hydraulic binders. This technique significantly increases their engineering and mechanical properties and has the advantage of minimizing environmental impact and reducing the cost of infrastructures. However, the real mechanical properties of those materials are seldom estimated and their performances are sharply downgraded during structure design processes. The deformation and failure parameters of six mixtures of cement-modified loess have been determined based on direct tensile stress testing, indirect tensile testing and unconfined compressive stress testing. Results have been used to determine the parameters of the Mohr-Coulomb failure criterion and the parameter of the Hoek-Brown failure criterion. The Hoek-Brown model clearly shows that results from indirect tensile stress measurement must be weighted to describe materials properly. Both models' results were then used to calculate the safety factor of a road structure with cement-modified loess used as subgrade material using reduction techniques. Specifically, for the Hoek-Brown model, a new calculation adapted to structures with tensile stresses is proposed. Results vary by around 8.9 for the Mohr-coulomb model and around 3.2 for the Hoek-Brown model. These shows at the laboratory scale that resource-based economies could be expected if cement-modified loess mechanical parameters were considered in the design of

T. Lenoir (✉)
IFSTTAR, MAST, MIT, 44344 Bouguenais, France
e-mail: thomas.lenoir@univ-eiffel.fr

T. Dubreucq
IFSTTAR, GERS, GMG, 44344 Bouguenais, France
e-mail: thierry.dubreucq@univ-eiffel.fr

T. Lambert
CEREMA, Direction Est, Site de Strasbourg, Strasbourg, France
e-mail: thibaut.lambert@cerema.fr

D. Killinger
HANS G. HAURI KG Mineralstoffwerke, Bötzingen, Germany
e-mail: d.killinger@hauri.de

structures. It also shows that the Hoek-Brown model is a promising tool to study tensile stressed structures made with cement-modified materials.

Keywords Cement-modified loess · Mohr-Coulomb model · Hoek-Brown model · Safety factor · Reduction techniques

1 Introduction

Loess is a detrital sedimentary rock, resulting from the accumulation of silt from wind erosion (deflation) in desert and periglacial regions with poor mechanical properties. To upgrade it for optimal use in civil engineering, it is common to add few percent of hydraulic binders. Adding binder to fine-grained soils like loess significantly increases their engineering and mechanical properties [1, 2]. This process has the advantage of minimizing environmental impact and reducing the cost of the infrastructures [3]. It is used in numerous civil engineering applications [4, 5]. Nevertheless, nowadays, in the field, the mechanical properties are often limited to unconfined compressive strength (R_{UCS}), tangent or secant modulus E and indirect tensile strength (R_{IDT}). Though these measurements are easy to make, they are not enough to fully design structures, and the real mechanical performances of these materials are sharply downgraded during design processes [6] and their uses are limited [7]. For complete design of structures, materials' deformation and failure properties are needed. Cement-modified soils represent the transitional environment between soils and rocks and often have characteristics of both. The most widely used geotechnical model in the field of soil mechanics is the Mohr-Coulomb failure criterion (MC). In the field of rock mechanics, it is the Hoek-Brown criterion [8]. The parameters of these geotechnical models are generally determined through laboratory triaxial tests. However, these types of experiments are rarely suitable outside research laboratories; triaxial tests are interpretable when done on soaked or dried materials, but cement-modified soils are non-saturated materials and are never found dried or soaked in the field. To avoid the use of triaxial testing, unconfined compression (UCS) testing and the direct tensile (DT) testing could be used to determine the geotechnical parameters of the two models [9]. Nevertheless, DT testing is also hard to implement outside research laboratories. From a purely theoretical point of view, indirect diametrical tensile (IDT) testing could replace DT testing [10–12], but it does not consider the occurrence of microcracks in the materials [8]. However, the failure of brittle materials is governed by the presence of microcracks [13]. As UC testing and DT testing are homogenous stress testing, the entire volume of the sample is concerned by the presence of microcracks. In the case of IDT testing, stress distribution is concentrated in the center of the cylindrical sample along its height. Therefore, the volume concerned by the occurrence of microcracks is substantially lower than the DT volume. Thus, a weighting coefficient must be used to compare IDT testing with DT testing.

Based on DT testing, IDT testing and UC testing, the deformation and failure parameters of six mixtures of cement-modified loess were determined. The Mohr-Coulomb and Hoek-Brown models' parameters were calculated. Then, two simulations of a road structure to be implemented on a project site are presented. In this structure, cement-modified loess is used in the foundation layer and in the capping layer. The first simulation was made in accordance with technical guides. In the second simulation, measured mechanical performances were considered in both layers. Based on models' parameters and reduction techniques, safety factors were determined. Specifically, for the Hoek-Brown model, a new calculation adapted to structure with tensile stresses is proposed.

2 Materials and Methods

2.1 Soil

The material studied is a loess from the Alsace plain in France. The sampling was performed with an excavator equipped with a ditch bucket at a depth between 2 and 3 meters. The soil is classified A-4 following the AASHTO Soil Classification System, at the edge between lean clay (CL) and silt (ML) following the USCS Soil Classification System.

2.2 Treatment and Sample Preparation

To prepare samples, three different binders were mixed with the loess in a blender. In each case, 5.5 and 7% by weight of dry matter were added to the soil. These six different configurations of treatment are all in accordance with usual treatments that could be found in the field of earthworks. The three binders came from the German cement manufacturer HAURI. ZIP 35 is a pozzolanic binder HRB 32.5 E made of 55% clinker and 45% natural pozzolans. PHOCAL C15 is also a pozzolanic binder HRB 32.5E. It is made of 47% clinker, 15% lime and 38% natural pozzolans. PHONOS is a hydraulic binder CEMII/B-Q 42.5 N made of 75% clinker and 25% natural pozzolans.

The optimum moisture content (OMC)/normal optimum proctor dry density (OPD) relationships (W_{OPN}/γ_d) of the cement-modified materials (Table 1) were determined. For mechanical experiments, samples were prepared at W_{OPN} and 96% of γ_d . Samples were compacted in a double static mode in one layer in a cylindrical mold. For UCS and DT testing, diameter and height were 10 cm and 20 cm, respectively. For IDT testing, both diameter and height were 10 cm. After preparation, samples were stored in a room with temperature regulated at 20 °C and protected

Table 1 Optimum Proctor dry densities and corresponding moisture contents of the six cement-modified loess

Treatment	ZIP35		PHOCAL C15		PHONOS	
	5.5%	7%	5.5%	7%	5.5%	7%
W_{OPN} (%)	16.5	15.3	17.2	17.3	16.0	15.7
γ_d (T/m ³)	1.80	1.81	1.78	1.76	1.80	1.80

with thin plastic films to keep constant water content. Curing time was 90 days before testing.

2.3 Experiments

All tests were carried out on a Zwick/Roell Z150 press with a crosshead speed of 0.3 mm/min in absolute value. Elastic moduli and Poisson's ratios were determined in compression and in tension with UCS and DT testing. In both cases, two samples were molded. Local vertical displacements were measured with three Micro-Epsilon CS5 capacitive sensors and radial strain perpendicular to the loading was measured with two HBM LY41-20/120 strain gauges. For the calculation five loading/unloading cycles were done. To reduce friction boundary effects, only the strain/stress relationships during unloading were considered and averaged. For UCS testing, loading/unloading cycles varied between 100 N and 500 N and applied load (F in N) was measured with a force sensor TME F522TC (max. load = 100 kN). For DT testing, loading/unloading cycles varied between 100 N and 200 N and applied load (F in N) was measured with a force sensor TME F521TC (max. load = 10 kN). After E and ν measurements, samples were broken to determined maximum loadings and strains in tension and compression. Rupture parameters were also determined using IDT testing [12]. In that case, four samples were molded. Applied load (F in N) was measured with a force sensor TME F521TC (max. load = 10kN). Diametrical displacements perpendicular to the loading were measured with RDP D6 linear variable differential transformers (range ± 0.25 mm).

2.4 Numerical Modeling

Selected structure

The structure under consideration is to be built as part of the beltway construction project in Strasbourg in France. It is a composite pavement that consists of four layers defined as follows: A 6 cm surface course of bituminous materials (medium-grained asphaltic concrete), a 12 cm base layer of bituminous materials (bitumen-bound graded material), a 20 cm subbase layer of cement-modified loess, and a subgrade.

The subgrade is divided in two layers, with a 55 cm capping layer of cement-modified loess and with the natural ground that is loess that has been graded and compacted.

Modeling

All layers of the studied structures (Table 2) are in accordance with the French design of pavement [14] and are assumed to have an elastic behavior (Hooke’s law) as described by the Young moduli and Poisson’s ratios. In the first simulation, the subgrade layers ([4]) are considered as a single layer in the modeling with a modulus of 200 MPa and a Poisson’s ratio of 0.35. In the second simulation, measured mechanical properties of cement-modified loess in the capping layer are considered and thus, two layers ([4a] and ([4b]) are considered for the subgrade. Values of elastic modulus and Poisson’s ratio of the layers ([3]) and ([4a]) (subbase layer and capping layers) depend on the specific mixture of cement-modified loess and will be justified later.

Calculations are done with the software ALIZE-LCPC, which is commonly used in the French design of pavements. ALIZE-LCPC computes the Burmister solution of an elastic multilayered-space under static loading. The reference loading used in the French design of pavements represents a 65 kN axle. It is made of two disk-shaped loads (0.6620 MPa) of 0.25 m in diameter spaced by $d = 0.375$ m applied on the free surface of the pavement structure [15].

Table 2 Properties of the two pavement structure layers. Values of elastic modulus and Poisson’s ratio of layers [3] and [4a], X and Y , depend on the specific mixture of cement-modified loess

Structure 1					
Layer	Thickness (m)	E (MPa)	ν	Bonding conditions	Type
[1]	0.06	7000	0.35	Bonded	Asphalt concrete
[2]	0.12	9000	0.35	Half bonded	Bitumen-bound material
[3]	0.20	X	Y	Bonded	Cement-modified loess
[4]	Infinite	200	0.35		Subgrade
Structure 2					
Layer	Thickness (m)	E (MPa)	ν	Bonding conditions	Type
[1]	0.06	7000	0.35	Bonded	Asphalt concrete
[2]	0.12	9000	0.35	Half bonded	Bitumen-bound material
[3]	0.20	X	Y	Bonded	Cement-modified loess
[4a]	0.55	X	Y	Bonded	Cement-modified loess
[4b]	Infinite	35	0.35		Subgrade

Table 3 Values of E and ν parameters of different mixtures. Standard deviations are given in brackets

Treatment	ZIP35		PHOCAL C15		PHONOS	
	5.5%	7%	5.5%	7%	5.5%	7%
ν_{UCS}	0.13 (0.02)	0.14 (0.03)	0.12 (0.03)	0.14 (0.02)	0.13 (0.02)	0.14 (0.04)
E_{UCS} (MPa)	4346 (89)	5221 (167)	3531 (198)	3810 (122)	4582 (134)	5230 (220)
ν_{DT}	0.12 (0.03)	0.10 (0.03)	0.12 (0.04)	0.12 (0.02)	0.10 (0.02)	0.14 (0.04)
E_{DT} (MPa)	4100 (401)	5061 (546)	3461 (242)	3490 (254)	4097 (523)	5367 (856)

3 Results and Discussion

3.1 Linear Elasticity

Values of E and ν parameters determined with different configurations are summarized in Table 3. Poisson's ratios range between 0.10 and 0.14 with a standard deviation around 0.03 regardless of the testing type and regardless of the type and amount of binder.

Elastic moduli depend on the type and the amount of binder. Cement-modified loess exhibits lower stiffness with the binder PHOCAL C15 that is lime-rich and clinker-poor. Results are close for ZIP 35 and PHONOS. Amounts of pozzolans do not seem to impact E . On the other hand, for each binder, the higher its amount, the higher the material stiffness. With values close to 5000 MPa, these results are also in accordance with previous measurements of elastic moduli at small strain [7, 16, 17].

3.2 Failure Criteria

Failure parameters

Range of R_{UCS} (Table 4) are in accordance with range previously reported for loess treated with cement [18]. Therefore, as elastic moduli, R_{UCS} , R_{DT} and R_{IDT} depend on the type and amount of binder. Surprisingly, direct tensile strength R_{DT} seems not to be correlated with R_{UCS} ($R = 0.21$). The sensibility of direct tensile stress to (micro-)crack occurrence [8] is probably responsible for this lack of correlation. Nevertheless, the R_{DT}/R_{UCS} ratio is 0.09 (0.04), which is similar to the ratio already observed for cement-treated aggregate material [19] and lightly cemented sand [20]. As reported for other cement-stabilized materials [21], unconfined compressive strength R_{UCS} is correlated with R_{IDT} ($R = 0.96$). The R_{IDT}/R_{UCS} ratio = 0.11 (0.01) and the R_{DT}/R_{IDT} ratio = 0.84 (0.30). All observed ratios are similar to values observed in literature and generally imposed for practical applications [7, 19–21].

Regarding the local strain that leads to rupture in compression, $\varepsilon_{rupt,UCS}$ ranges are around 1.5–2 times higher than the range found on cement-mixed gravelly or sandy

Table 4 Maximum stress/strain values for the different treatment and test configurations (unconfined compression $R_{UCS}/\varepsilon_{rupt,UCS}$, direct tension $R_{DT}/\varepsilon_{rupt,DT}$ and indirect tension $R_{IDT}/\varepsilon_{rupt,IDT}$). Standard deviations based on four measurements are given in parentheses; differences based on two measurements are in square brackets

Treatment	ZIP35		PHOCAL C15		PHONOS	
	5.5%	7%	5.5%	7%	5.5%	7%
R_{UCS} (MPa)	3.82 [0.11]	4.86 [0.05]	3.14 [0.01]	3.33 [0.16]	4.40 [0.09]	4.81 [0.15]
$\varepsilon_{rupt,UCS}$ (%)	0.648 [0.001]	0.618 [0.019]	0.695 [0.034]	0.673 [0.035]	0.639 [0.028]	0.640 [0.036]
R_{DT} (MPa)	0.35 [0.09]	0.46 [0.15]	0.16	0.55 [0.00]	0.31 [0.01]	0.35 [0.03]
$\varepsilon_{rupt,DT}$ (%)	0.013 [0.001]	0.016 [0.001]	0.006	0.024 [0.000]	0.012 [0.000]	0.011 [0.001]
R_{IDT} (MPa)	0.39 (0.05)	0.49 (0.02)	0.33 (0.04)	0.39 (0.03)	0.48 (0.07)	0.53 (0.01)
$\varepsilon_{rupt,IDT}$ (%)	0.010 (0.002)	0.014 (0.004)	0.009 (0.003)	0.013 (0.002)	0.011 (0.002)	0.011 (0.000)

soils. The local strains that lead to rupture in traction $\varepsilon_{rupt,DT}$ and $\varepsilon_{rupt,IDT}$ are within the range of results found on lightly cemented sand but five times higher than the values found on soil-cement blocks using highly sandy materials [20, 22].

Mohr-Coulomb criterion

This criterion can be written following the formula: $\tau = C + \sigma \tan(\phi)$, with τ shear stress, σ normal stress, C material apparent cohesion, and ϕ apparent angle of internal friction. The apparent parameters C and ϕ are generally graphically determined in the $\{\sigma, \tau\}$ plane using at least two Mohr's circles. For unconfined compressive measurements with a cylindrical shape, R_{UCS} is the major principal stress, while the minor principal stress is zero. For direct tensile measurements with a cylindrical shape, the major principal stress is zero, while $R_{DT} (< 0)$ is the minor principal stress. For indirect tensile measurements, $R_{IDT} (< 0)$ is the minor principal stress and $-3R_{IDT}$ is the major principal stress [17].

The tangent to the circles represents the envelope of Mohr-Coulomb's failure. In addition, considering the well-used relationship $R_{DT} \approx 0.8 \times R_{IDT}$ measured in Table 4, and knowing the higher repeatability of the indirect tensile test compared with the direct tensile test, parameters C and ϕ were also determined using direct tensile measurements principles with the value of $0.8 \times R_{IDT}$ (Table 5). Cohesions depend on the type and amount of binder. Unlike cohesion, ϕ_{DT} , ϕ_{IDT} and $\phi_{IDT} \times 0.8$ did not exhibit a high dependency to the type and amount of binder. Results were still in the upper range compared with literature results [18, 23]. However, the cohesion and friction angles of cemented materials are known to increase with curing time. Thus, considering that in this study, cement-modified loess performances were measured after 90 days of curing and that materials were unsoaked, the results can be considered as relevant. On the other hand, all results obtained with IDT testing are in accordance with results from literature [10] obtained in similar conditions.

Table 5 Cohesion and internal friction angle values based on UCS testing and DT testing (C_{DT} , ϵ_{DT}) and UCS testing and IDT testing (C_{IDT} , ϵ_{IDT})

Treatment	ZIP35		PHOCAL C15		PHONOS	
	5.5%	7%	5.5%	7%	5.5%	7%
C_{DT} (MPa)	0.58	0.75	0.35	0.68	0.58	0.65
ϕ_{DT} (°)	56	56	65	46	60	60
C_{IDT} (MPa)	0.73	0.92	0.62	0.71	0.89	0.98
ϕ_{IDT} (°)	48	48	47	44	46	46
$C_{IDT \times 0.8}$ (MPa)	0.55	0.69	0.46	0.51	0.65	0.71
$\phi_{IDT \times 0.8}$ (°)	58	58	58	56	57	57

Hoek-Brown criterion The Hoek-Brown criterion is a failure law that is widely used in the field of rock mechanics. For intact rock material, it is expressed as follow [8, 24]:

$$\sigma_1 = \sigma_3 + (m\sigma_c\sigma_3 + \sigma_c^2)^{1/2}$$

Parameters of this law are σ_c , the unconfined compressive strength (R_{UCS}), and σ_1 and σ_3 , which are respectively the major and minor principal stresses (Fig. 1). The constant m depends on rock properties. As with Mohr-Coulomb criterion, for DT measurements $\sigma_3 = R_{DT}$ (<0) and $\sigma_1 = 0$. For IDT, $\sigma_3 = R_{IDT}$ (<0) and $\sigma_1 = -3R_{IDT}$. As previously, m was also determined using direct tensile measurements principles with the value of $0.8 \times R_{IDT}$. Thus, values of m are: $m = ((\sigma_1 - \sigma_3)^2 - \sigma_c^2) / (\sigma_c\sigma_3)$.

Values of m determined with DT testing (m_{DT}), and IDT testing (m_{IDT} and $m_{IDT \times 0.8}$) under different treatment configuration (Table 6) do not seem to depend on type and amount of binder. In the case of DT testing, the values of m_{DT} were on average 12.42 (4.17) and correspond to values generally attributed to lithified argillaceous rocks. This is relevant to describe the cement-modified loess. For IDT testing, in average, $m_{IDT} = 7.61$ (0.56). This range is generally attributed to carbonate rocks with well-developed crystal cleavage [8]. Interestingly, $m_{IDT \times 0.8} = 11.58$ (0.59). These

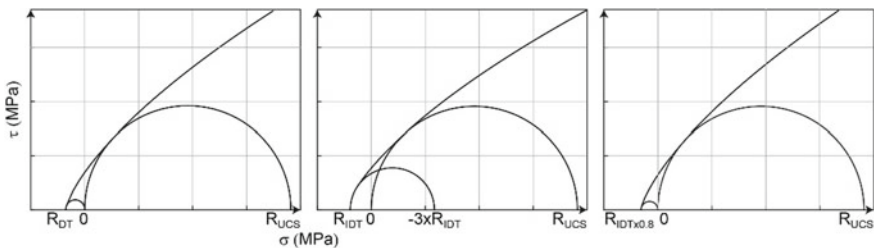


Fig. 1 Principle of the hoek-brown model based on UCS testing and DT testing (left), and UCS testing and IDT testing (middle and right)

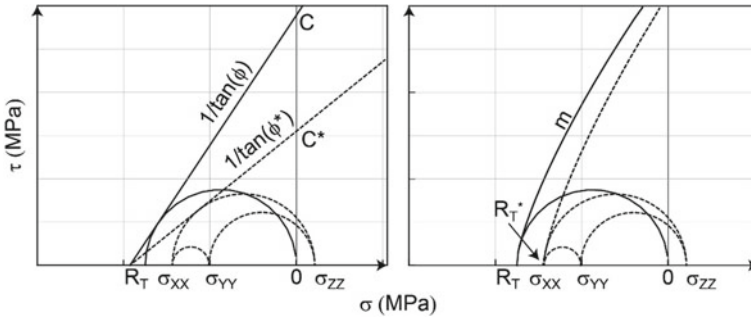


Fig. 2 Principle for safety factor determination in Mohr’s plan. In solid lines, circles deduced from tensile measurements and rupture criteria (left, mohr-coulomb, right, hoek and brown) determined from materials properties. In dotted lines, circles representing serviceability tensor

Safety factors The Hoek-Brown model clearly highlights that results from indirect tensile stress measurements describe a non-relevant material. They cannot be considered without weighting.

Therefore, in the following only results from DT measurements and 0.8*IDT measurements are considered. With the Mohr-Coulomb model, the safety factor can be defined using a Phi-c reduction method [59]. Based on the serviceability tensor, a reduced cohesion c^* and a reduced angle of friction ϕ^* are determined (Fig. 2). Naming c and ϕ the material cohesion and angle of friction, the safety factor F_n is determined following the formula: $F_n = c/c^* = \tan(\phi)/\tan(\phi^*)$.

With the Hoek and Brown model, reduction techniques can also be applied [60]. Generally, those approaches are used to deal with slope stability issues or deep foundation issues. In these issues, confining stresses are positive (compression). Thus, the tensile stress is kept and the compressive strength is reduced following the formula:

$$F_n = R_{UCS} / R_{UCS}^*$$

However, in this issue, only one principal stress is positive (ϕ_{ZZ}), and it is very close to zero compared with the absolute values of the two other principal stresses σ_{XX} and σ_{YY} (Table 7) which are tensile stresses. On the other hand, in the Mohr’s plane, the radius of the serviceability tensor $(\sigma_{ZZ}-\sigma_{YY})/2$ is lower than the tensile circle radius $R_T/2$. It is thus impossible to determine a reduced compressive strength. To adapt this approach to the specific case of pavement layers made with cement-modified soils, it is proposed to keep the compressive stress and based on the serviceability tensor deduce a new value of m , named m_2 that leads to a reduced tensile stress:

$$m_2 = ((\sigma_{ZZ} - \sigma_{XX})^2 - R_{UCS}^2) / (R_{UCS} \sigma_{XX})$$

Table 8 Safety factors. MC refers to Mohr-Coulomb and HB to hoek and brown

	Treatment	ZIP35		PHOCAL C15		PHONOS	
		5.5%	7%	5.5%	7%	5.5%	7%
		Structure 1					
		Structure 2					
MC	R_{DT}	1.87	2.51	/	3.52	1.31	1.10
		8.87	11.36	4.21	11.46	8.63	9.05
	$R_{IDT \times 0.8}$	1.38	1.88	1.18	1.70	2.26	2.01
		8.16	10.20	6.93	7.86	10.07	10.37
HB	R_{DT}	1.22	1.40	0.63	2.08	1.06	1.02
		3.24	4.05	1.56	5.22	2.85	2.99
	$R_{IDT \times 0.8}$	1.08	1.19	1.05	1.18	1.31	1.24
		2.89	3.45	2.57	2.96	3.53	3.62

From this new value, it is possible to determine a reduced tensile strength R_T^* (Fig. 2) which is the solution of the quadratic equation:

$$R_T^{*2} - m_2 R_T^* - R_{UCS}^2 = 0$$

The safety factor is thus expressed as: $F_n = R_T/R_T^*$

For structure 1 (Table 8), if R_{DT} is used, treatments with 5.5% of PHOCAL are not suitable. The absolute value of R_{DT} is lower than the corresponding absolute value of ϕ_{XX} (Tables 4 and 7). Still with R_{DT} , for all other treatments, safety factors are on average 2.06 (0.98) with MC and 1.24 (0.49) with HB. With $R_{IDT \times 0.8}$, all treatments are suitable regardless of the model used with a mean of 1.74 (0.40) with MC and of 1.18 (0.10) with HB. For structure 2, i.e. when mechanical performances of the cement-modified loess are considered in the capping layer, all the treatments are suitable. On average, if R_{DT} is used, $F_n(MC) = 8.93$ (2.63) while it is $F_n(MC) = 8.93$ (1.46) when $R_{IDT \times 0.8}$ is used. With HB, $F_n(HB) = 3.32$ (1.23) with R_{DT} while it is $F_n(HB) = 3.17$ (0.42) with $R_{IDT \times 0.8}$. These results show that current design procedures are relevant when the subgrade mechanical properties are downgraded because factors of safety range between 1 and 2. It also justifies the selected structure after the fact. When the measured mechanical properties are considered in design process, safety factors are greater than two and resource-based economies could be expected in the field.

4 Conclusions

Based on the elastic and failure parameters of cement-modified loess measured with direct tensile stress testing, indirect tensile stress testing and unconfined compressive testing, parameters of the Mohr-Coulomb and Hoek-Brown failure criteria were calculated. The Hoek-Brown model clearly shows that results from indirect tensile

stress measurements must be weighted to describe materials properly. For a classical road structure with some subgrade layers made with cement-modified loess, parameters from both models can be input in numerical modeling. Based on reduction techniques, safety factors adapted to structures with tensile stresses are determined. Results vary around 8.9 for the Mohr-Coulomb model and around 3.2 for the Hoek-Brown model. To generalize these results in the field, rock mass parameters of cement-modified loess must be determined to consider the frequency of discontinuities and how they are distributed but resource-based economies could be expected if cement-modified loess mechanical parameters were considered in the design of structure.


References

1. Bell FG (1996) Lime stabilization of clay minerals and soils. *Eng Geol* 42(4):223–237
2. Chew SH, Kamruzzaman AHM, Lee FH (2004) Physicochemical and engineering behavior of cement treated clays. *J Geotech Geoenviron Eng* 130(7):696–706
3. Nunes MCM, Bridges MG, Dawson AR (1996) Assessment of secondary materials for pavement construction: technical and environmental aspects. *Waste Manage* 16(1):87–96
4. Khay SEE, Neji J, Loulizi A (2010) Compacted sand concrete in pavement construction: an economical and environmental solution. *ACI Mater J* 107(2):195–202
5. Okyay US, Dias D (2010) Use of lime and cement treated soils as pile supported load transfer platform. *Eng Geol* 114(1–2):34–44
6. SETRA-LCPC (2004) Soil treatment with lime and/or hydraulic binders—application to the construction of fills and capping layers—technical guide, SETRA-LCPC Ed. Paris
7. Preteseille M, Lenoir T (2016) Structural test at the laboratory scale for the utilization of stabilized fine-grained soils in the subgrades of high speed rail infrastructures: experimental aspects. *Int J Fatigue* 82:505–513
8. Jaeger JC, Cook NGW, Zimmerman R (2007) *Fundamentals of rock mechanics*, 4th edn. Wiley-Blackwell
9. Wang W, Shen J (2017) Comparison of existing methods and a new tensile strength based model in estimating the Hoek-Brown constant m_i for intact rocks. *Eng Geol* 224:87–96
10. Piratheepan J, Gnanendran T, Arulrajah A (2012) Determination of c and φ from IDT and unconfined compression testing and numerical analysis. *J Mater Civil Eng* 24(9):1153–1163
11. Consoli NC, Da Silva Lopez L, Consoli BS, Festugato L (2014) Mohr-Coulomb failure envelopes of lime-treated soils. *Geotechnique* 64(2):165–170
12. Preteseille M, Lenoir T, Genesseeux E, Hornych P (2014) Structural test at the laboratory scale for the utilization of stabilized fine-grained soils in the subgrades of high speed rail infrastructures: analytical and numerical aspects. *Constr Build Mater* 61:164–171
13. Hoek E, Martin CD (2014) Fracture initiation and propagation in intact rock—a review. *J Rock Mech Geotech Eng* 6(4):287–300
14. SETRA-LCPC (1997) French design manual for pavement structures, SETRA-LCPC Ed., Paris
15. Chupin O, Chabot A, Piau JM, Duhamel D (2010) Influence of sliding interfaces on the response of a layered viscoelastic medium under a moving load. *Int J Solids Struct* 47(25–26):3435–3446
16. Preteseille M, Lenoir T, Hornych P (2013) Sustainable upgrading of fine-grained soils present in the right-of-way of high speed rail projects. *Constr Build Mater* 44:48–53
17. Preteseille M, Lenoir T (2015) Mechanical fatigue behavior in treated/stabilized soils subjected to a uniaxial flexural test. *Int J Fatigue* 77:41–49
18. Zhang C, Jiang G, Su L, Zhou G (2017) Effect of cement on the stabilization of loess. *J Mt Sci* 14(11):2325–2336

19. Xuan DX, Houben LJM, Molenaar AAA, Shui ZH (2012) Mechanical properties of cement-treated aggregate material—a review. *Mater Des* 33:496–502
20. Dass RN, Yen SC, Das BM, Puri VK, Wright MA (1994) Tensile stress-strain characteristics of lightly cemented. *Sand Geotech Test J* 17(3):305–314
21. Babić B (1987) Relationships between mechanical properties of cement stabilized materials. *Mater Struct* 20:455–460
22. Reddy BVV, Gupta A (2005) Characteristics of soil-cement blocks using highly sandy soils. *Mater Struct* 38(6):651–658
23. Harichane K, Ghrici M, Kenai S (2011) Effect of curing time on shear strength of cohesive soils stabilized with combination of lime and natural pozzolana. *Int J Civ Eng* 9(2):90–96
24. Hoek E, Brown ET (1980) Empirical strength criterion for rock masses. *J Geotech Eng-ASCE* 106(GT9):1013–1035

Physical Modeling of the Washboard Effect on Unpaved Roads



Bernardo Caicedo  and Gregoire Aguetant

Abstract Unpaved roads are the predominant type of road in most countries around the world. The construction practices for this type of roads rely on empirical rules. However, sometimes, the emerging transversal ripples produce a phenomenon known as washboard, which affects these roads. The washboard effect appears when a car is rolling on roads made of sand, gravel or mud. It creates waves that are uncomfortable for the driver and can be dangerous due to the possibility of losing contact between the wheel and the road. It starts initially with small ripples that grow bigger and bigger. The amplitude of the ripples in terms of height can reach 20 cm, and the wavelength can be between 30 cm and 1 m. This wavelength is a function of the car's speed, car's weight, car's characteristics (springs, tire pressure, etc.) and climatic conditions. Ripples can move with time, changing its wavelength. It can move in the same direction of the car, or opposite to it. This work presents results from an experimental setup with a rotating machine dragging a wheel arm on sandy soil. Several variables were changed to understand which variable develops or erases the washboard effect and in which rate of growing. The variables that had been studied are the compaction and mass of the wheel arm. These variables were compared at different velocities, in terms of waves' height, waves' wavelength and axial forces of the wheel, to set the critical velocity where washboard can be observed.

Keywords Washboard effect · Wheel road interaction · Unpaved roads

1 Introduction

The washboard effect appears when a car is rolling on an unpaved road made of sand, gravel or mud. It creates waves that are uncomfortable for the driver and can be dangerous due to the possibility of losing contact between the wheel and the road. It

B. Caicedo (✉)
University of Los Andes, Bogotá, Colombia
e-mail: bcaicedo@uniandes.edu.co

G. Aguetant
École Polytechnique Fédérale de Lausanne, Lausanne, Switzerland

is a very tough problem because of its robustness. It starts initially with small ripples that grow bigger and bigger. The amplitude of the ripples in terms of height can reach 20 cm, and the wavelength can be between 30 cm and 1 m. This wavelength is function of the car's speed, car's weight, car's characteristics (springs, tire pressure, etc.) and climate conditions. According to the field observation, the ripples are bigger in the turns, cross section, slopes, where cars are adding stresses on the road. Ripples can move with time, changing its wavelength. It can move in the same direction of the car, or opposite to it [1].

There are three options nowadays to reduce this phenomenon: build concrete or asphalt roads, add additives on the road to raise the material cohesion (like bituminous materials), flat the road, which is the common method, good on a short term. However, it has to be done frequently because the ripples are emerging pretty fast if the road is often used

Studies about the washboard effect are scarce; indeed, there are not more than ten articles on this subject. However, there are similarities with other phenomena like rail train wavy wear and tears, sandy dunes, sandy ripples and ski bumps, which have been deeply studied.

One of the first reported experimental studies about washboard effect was reported in [2]; then, another study showed that there was no need for an initial bump to create washboard [3]. Also, they observed that there is a maximum bump height and that the ripple wavelength is not directly linked to the suspension frequency. More recent research [1, 4] study the formation of washboard waves with a wheel tracked with a uniform velocity. Two different experimental setups were proposed to study the washboard effect: one in Cambridge University (UK) with a rotating table with a sandy bed, in this apparatus the wheel is fixed and only the table is rotating. It is, therefore, easier to instrument the wheel, but the sand is subject to centrifugal forces. The other one, located at the ENS Lyon (France), is composed of circular track with rotating arm dragging a wheel. This last experimental concept was used at the University of Andes in this study, this means that the wheel is turning over the sandy track, and so the track is not subjected to centrifugal forces. It can be a wheel or a slab that is dragged and the arm has no suspension.

Taberlet in [1] proposed to decompose the washboard phenomenon into four modes, shown in Fig. 1, these modes occurs as follows:

- In the first mode, the road is smooth, and all the different little ripples will be erased if a car is rolling at speed lower than v_c .
- In the second mode, increasing the speed after v_c , the washboard effect appears, but the wheel is all the time in contact with the path.

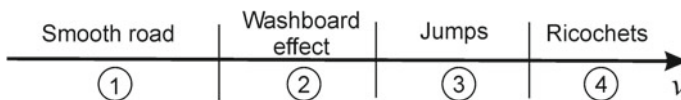


Fig. 1 Organization of the four different states observed in function of the wheel velocity

- In the third mode, increasing the speed after v_2 , the ripples are still growing to a certain height and amplitude, so that the wheel jumps at the summit of the next ripples.
- In the fourth mode, increasing the speed after v_3 , the speed is so high that the instability comes fast, and the wheel jumps from one summit to the next one.

To simplify the experimental model, researches about washboard were carried out in [5] using inclined plates. This study reported in [5] also includes the interaction of two or three inclined plates; the results of this study also show that there was a critical speed where washboard effect could not be seen.

The experimental results reported in [1, 4, 5] allowed observing the following trends regarding the washboard effect:

- The washboard waves come from the repeated path of cars.
- There is a critical speed that distinguishes two phases: smooth road and wavy road.
- The critical speed depends on the mass and velocity.
- The waves are moving on the track, forward in the case of a wheel and forward and backward for a slab.
- Neither tires nor suspensions are necessary to obtain the washboard effect. The ripple wavelength is not simply the speed of the wheel times the bounce frequency of the suspension.
- The size of the wheel (diameter) and the size or the shape of the grains have no influence on the pattern, meaning that the soil can be considered as continuous.
- The washboard effect is not due to segregation, which is confirmed in [6] where it was demonstrated that the material composing the underlying substrate does not need to be granular. Indeed, washboards can be permanently imprinted on viscoplastic fluids or ephemerally generated on viscous fluids.
- Even if an inclined plate replaces the tire, the washboard effect can be seen and the instability presents the same character as if it was with a wheel.
- The washboard effect does not result from internal resonance of the car. This phenomenon is very robust because it can be obtained whatever was the material (sand, rice, coarse or small grain), also adding a spring, with different weights of the wheel, and with a dry or a wet soil, with a non-rotating wheel (meaning that they blocked it) and with a large range of speed. However, there is a critical speed where, if not reached, the road remains flat.
- Experiments carried out with plates shown that the ripple growth rate is directly related to the mass of sand moved as well as the wavelength and the critical speed. However, this relationship works for slow speed, because it is a linear expression, and so it does not show the saturation of the ripples.
- Regarding the effect of friction and/or cohesion, tests were carried out in [5] using mineral oil, which creates a kind of apparent cohesion and decreases the friction. Results show that adding oil lowers the critical speed, but the ripples take time to form.

These research studies have shown the waves' characteristics and how it grows depending on different variables. However, the reason why it starts and it develops is still unknown. The purpose of this work is to develop of an experimental setup with dragging a wheel arm on sandy soil, then to change some variables one by one to understand which variable develops or erases the washboard effect and in which rate of growing. The variables that had been considered here are compaction and different masses added to the wheel arm.

2 Experimental Setup

Figure 2 shows the whole experimental setup, which has four systems:

1. Soil container: it is a double-walled tank having internal and external diameters of 1.19 m and 1.65 m, respectively, and it permits to tests layers of soil of 0.9 m. The tank has two holes at the bottom that permits controlling the position of the water table.
2. Wheel loading system: this system permits us to obtain the repetitive effect of the wheel passing over the soil. The wheel system has 3° of freedom shown in Fig. 2b. The θ_1 degree of freedom permits to obtain the rotation of the wheel

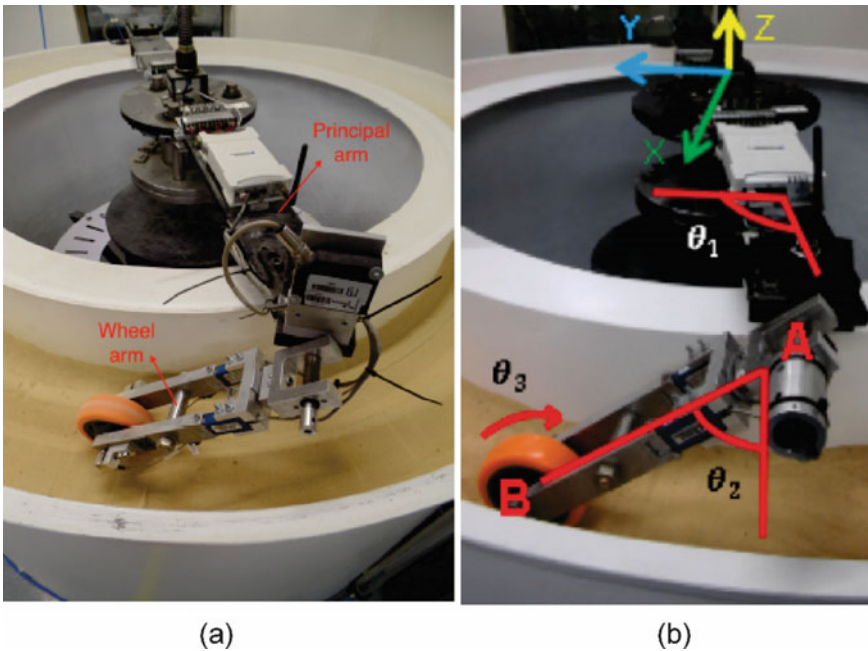


Fig. 2 a General layout of the experimental setup and b degrees of freedom of the wheel system

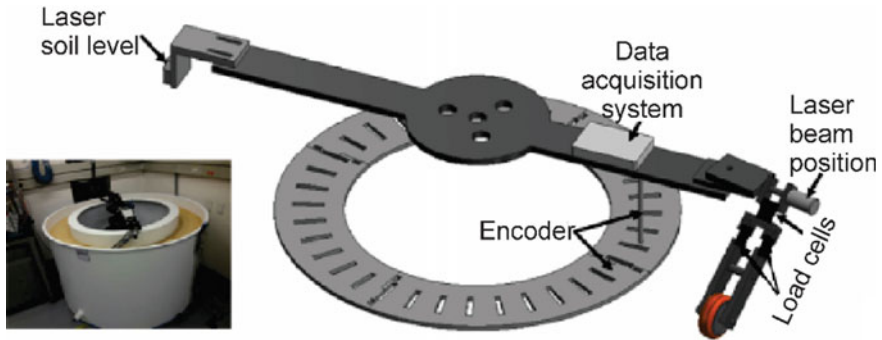


Fig. 3 Main components of the monitoring system

on the soil around the Z-axis. θ_2 permits the rotation of the wheel arm so that it can change its Z-coordinates, and θ_3 permits the wheel to roll on the soil. On this system, there are no springs to simulate car’s shock absorbers.

3. Water-table level system: this system permits to add water in the tank, and to set the water-level wished in a controlled way. A hydraulic circuit permits the water to enter and drain through two points, controlled with two electro-valves and a sensor of water level.
4. Instrumentation and data acquisition system: with those systems, it is possible to measure the forces from the wheel to the soil, the topography of the soil, the wheel position, and the water-level profile.

As shown in Fig. 3, the components of the monitoring system are:

- Encoder: the encoder is a static disk with holes separated 10° , a proximity laser sensor, placed in the principal arm, allows reading the disk with an on-off mode, and permits to compute the angular position of the main arm of the apparatus for each tour.
- Laser sensor for soil profile measurement: the soil profile measurement is the key to observe the evolution of the phenomenon of the waves, especially the wave wavelength and height. This measurement is possible using a laser optoNCDT 1302-100 located in the main arm of the apparatus on the opposite side of the wheel. The sensor is an optic triangulation laser with a measurement range of 100 mm and a resolution of $50 \mu\text{m}$.
- Laser sensor for beam-wheel position: a second laser sensor was installed on the arm of the apparatus to measure the distance between the arm and the beam carrying the wheel. This measurement permits to obtain the angle of the beam for computing the position of the wheel continuously. The laser is an optic triangulation laser, optoNCDT 1302-50, with a measurement range of 50 mm and a resolution of $25 \mu\text{m}$.
- Wheel forces measurement, the system to measure the forces is composed of 4 load cells, 2 of them measure the axial load (i.e., along the direction of the beam

carrying the wheel), and 2 others measure the bending moment in the beam that allows computing the perpendicular force.

- The data acquisition system has a wireless unit NI WLS-9163 working at a sampling frequency of 20 kHz for all the sensors; this frequency permits to measure the dynamic peaks of forces as well as the soil level.

The soil material is composed of one unique layer with 65 cm depth of river sand that had been previously washed. The characterization of the soil is silty sand with a medium to fine grain size. Its specific gravity is 2.66, and its maximum grain size 2.4 mm. The dimensions in millimeters of the fractiles of the grain size distribution are $d_{10} = 0.08$; $d_{30} = 0.18$; $d_{60} = 0.28$. The dry density of the soil in the loose state is $\rho_d = 1493.0 \text{ kg/m}^3$ and 1599.4 kg/m^3 in the compacted state.

3 Results

The critical velocity for which the washboard appears was analyzed regarding two variables: compaction and the mass of the wheel arm.

Figure 4 shows an example of the results regarding the evolution of the soil's profile. This test was carried out at a tangential velocity of 1.59 m/s that corresponds to 5.72 km/h, on a soil in a loose state (dry density $\rho_d = 1493.0 \text{ kg/m}^3$) and without applying additional mass to the wheel arm. The initial lap is not perfectly flat; it has a 1.5 cm maximal height difference along the track, which has a perimeter of 458.7 cm. During testing, the washboard appears after 45 s; then, the ripples grow in amplitude and wavelength, which means that the number of waves decrease with time. Indeed, the final lap is composed of 17 waves, with a mean height amplitude H_{waves} of 2.160 cm and a mean wavelength λ_{waves} of 25.67 cm (the mean wavelength was measured by dividing the travel length by the number of waves). At the velocity of the test, the wheel jumps from one wave to the other when the waves are fully developed. On the other hand, the mean axial peak force measured with the load cells is 80.1 N.

Figure 5 shows the mean height of the waves depending on the tangential velocity. This figure shows a clear relationship between the rotating velocity of the principal arm and the development of the waves. It is clear that when reaching a critical velocity, the development of the waves begins, and after this critical velocity, their height increases as the velocity grows.

The results suggest that the washboard effect appears after a rotating velocity of 4.48 km/h for the two tests when the mass of the swinging arm is $m_0 = 1200 \text{ g}$. Furthermore, it seems that the density of the soil does not have a significant effect on the critical velocity.

Regarding the effect of the mass on the swinging arm, it seems that the critical velocity increases as the mass of the arm grows as shown in Fig. 5 ($v_c = 4.98 \text{ km/h}$ for $m = m_0 + 318 \text{ g}$, and $v_c = 5.21 \text{ km/h}$ for $m = m_0 + 581 \text{ g}$). As well, when

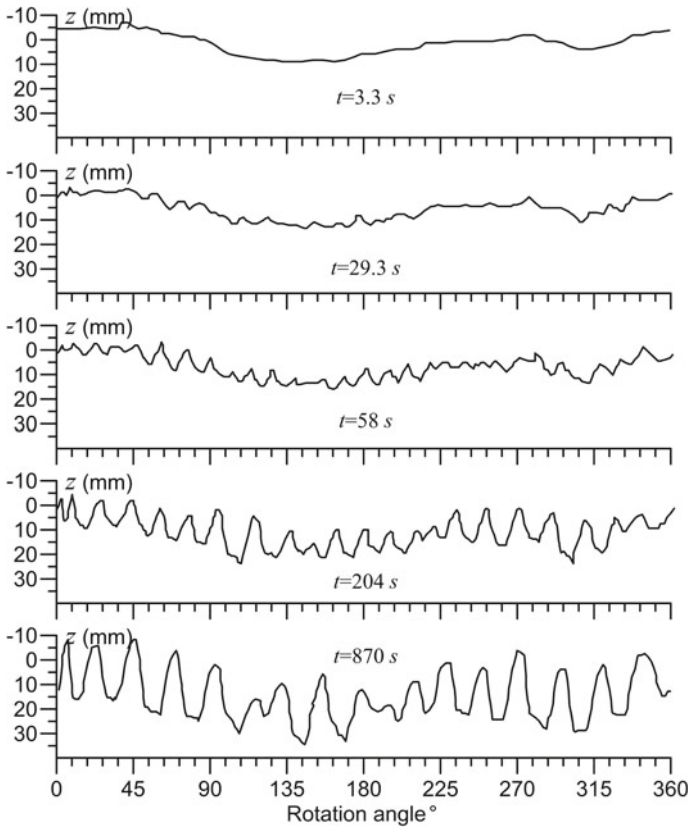


Fig. 4 Evolution of the soil's profile with time

the washboard effect appears, the height of the waves increases when increasing the mass.

Figure 6 shows a strong relationship between the mean axial force depending with the mean height of the wave. Indeed, as the force increases, the mean height of the waves increases as well following a linear relationship. It is important to remark that this linear relationship seems to be unique, regardless of the density of the material and the mass on the swinging arm. However, it is important to note that the axial force measured in the swinging arm differs from what a real quarter car would produce, which certainly better models the truck-road interaction. For this reason, future studies could include a reduced scaled quarter car at the end of the rotating beam.

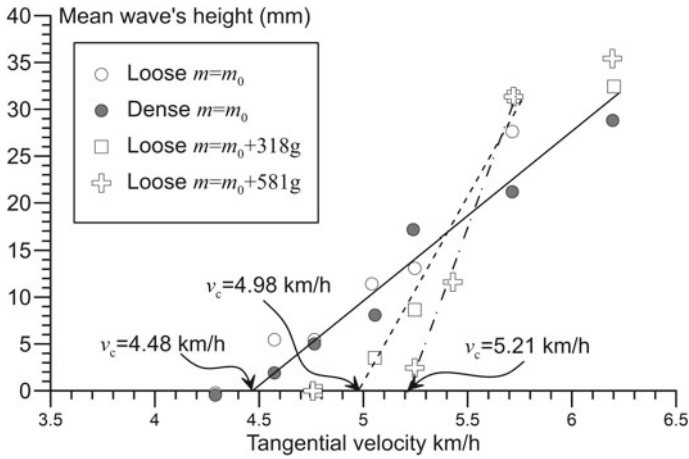


Fig. 5 Mean waves's height depending on the tangential velocity for the different masses and density state of the soil

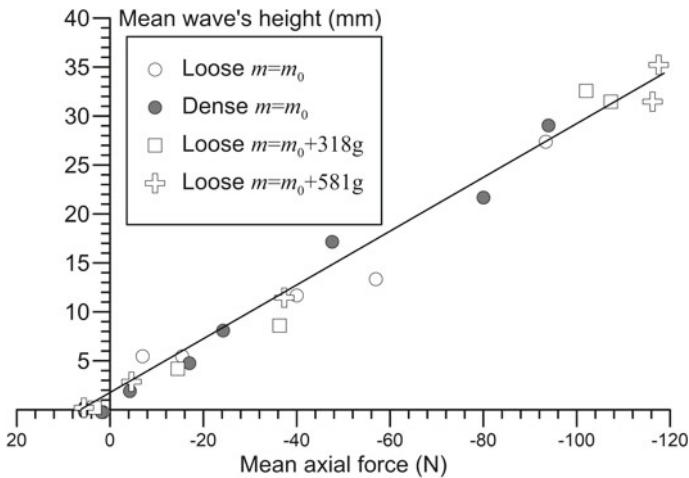


Fig. 6 Relationship between the mean axial force and the mean wave's height for all the tests

4 Conclusions

This work permitted to confirm results highlighted in previous research regarding the washboard and to find new relationships. These new findings could be useful for modeling the phenomenon and for upscaling the results of the test track into a field scale.

The main findings of this work are summarized below:

Washboard waves develop quickly through the sandy track of the experimental machine, and the washboard effect is dependent on the rotating speed, and it can be split into three phases:

- Smooth track, where the soil keeps its shape, and no wave appears, when the speed is slower than the critical velocity.
- Intermediate state, where the soil first appears with waves, but then they decrease both in terms of height and forces.
- Washboard waves, where the waves are increasing and developing until its maximum point.

The mechanism of the “intermediate” phase, where the waves at some point start to decrease, is not well understood. This phenomenon could be related to a phase difference between the axial force peaks with the waves; this phase lag erases the waves.

Regarding the effect of the different variables, it is possible to conclude the following.

- Compaction does not have any influence on washboards, in terms of waves’ characteristics or critical velocity, equal in both cases to 4.5 km/h.
- Mass of the wheel arm has a slight effect on the critical velocity.

Finally, it is important to highlight the strong relationship between the forces and the waves’ height. This result shows that the dynamic force is the key variable to analyze the washboard effect.

References

1. Taberlet N (2012) Washboard road, the dynamics of granular ripples formed by rolling wheels. Phd thesis, ENS Lyon
2. Mather KB (1962) The cause of road corrugations and the instability of surfaces under wheel action. Parts 1&2. Civil Eng & Public Works Review/UK/
3. Furry RB (1973) Simulation of the road-corrugation phenomenon. Highw Res Record 438:54
4. Bitbol AF, Taberlet N, Morris SW, McElwaine JN (2009) Scaling and dynamics of washboard roads. PhD thesis, Cambridge University
5. Percier, B. (2013). Dynamique d’un empilement granulaire: instabilité de tôle ondulée et fluage d’une colonne de grains. Phd thesis, ENS Lyon
6. Hewitt I, Balmfort NJ, McElwaine JN (2011) Granular and fluid washboard. PhD thesis, Cambridge University

Finite Element Analysis of Nonlinear Elastic Behavior of Unbound Aggregate Materials Under Repeated Loading



Haohang Huang , Jiayi Luo , Issam I. A. Qamhia, Erol Tutumluer ,
Jeb S. Tingle, and Carlos R. Gonzalez

Abstract During the analysis and design of flexible pavements, the nonlinear elastic behavior of unbound aggregate layers and subgrade soils is a crucial component for establishing proper material characterization. This paper presents a validation case study regarding the nonlinear elastic behavior of unbound aggregate specimens in repeated load triaxial testing. An advanced triaxial testing framework, the University of Illinois FastCell (UI-FastCell), was selected for this study considering its capability to conduct cycled independent stress from both axial and radial directions. In total, ten unbound aggregate materials were tested in the laboratory under varying repeated loading conditions. A newly developed 2D axisymmetric finite element method (FEM)-based analytical tool was used to simulate the nonlinear elastic behavior based on a secant modulus iteration scheme. A comparison of the resilient stress–strain curves between the experimental and simulation results showed good agreement. Based on the findings of this study, the advanced characterization of material nonlinearity was shown to be both necessary and practical by utilizing FEM-based analytical solutions for flexible pavements.

Keywords Finite element method · Nonlinear elasticity · Aggregates · Numerical analysis · Repeated load triaxial testing

1 Introduction

Modern flexible pavements have enhanced serviceability and performance requirements that demand accurate and efficient pavement structural analysis involving various considerations for stress states, repeated loading, pavement temperature, and moisture conditions. Under the repeated application of moving traffic loads, the

H. Huang · J. Luo · I. I. A. Qamhia · E. Tutumluer (✉)
Department of Civil and Environmental Engineering, University of Illinois at Urbana-Champaign,
205 N Mathews, Urbana, IL 61801, USA
e-mail: tutumlue@illinois.edu

J. S. Tingle · C. R. Gonzalez
U.S. Army Engineer Research and Development Center, 3909 Halls Ferry Rd, Vicksburg, MS
39180, USA

pavement layers are assumed to behave as elastic solids with recoverable deformations and are often characterized using the resilient modulus (M_R) to capture the elastic stiffness. Unbound granular bases, often under the influence of high wheel load stresses, have been shown to accumulate locked-in residual compressive stresses due to compaction and subsequent trafficking and behave differently in the vertical wheel load direction than in the horizontal direction leading to direction-dependent or anisotropic layer moduli [1]. Additionally, the proper characterization of the nonlinear stress-dependent behavior of geomaterials significantly impacts the accuracy of predictions of critical pavement responses [2]. To evaluate the resilient properties as a function of stress states, repeated load triaxial tests are commonly employed for unbound aggregate materials and subgrade soils. Therefore, emphasis should be given in structural pavement analysis to realistic nonlinear material modeling in the base, subbase, and subgrade layers primarily based on repeated load triaxial test results [3, 4].

As compared to traditional numerical analysis approaches such as the layered elastic analysis (LEA), finite element method (FEM) analysis with material nonlinearity module is more suitable and accurate to capture the nonlinearity of pavement layers [5, 6]. Extensive research has been accomplished to improve the performance of the FEM-based numerical simulation approaches. Early work by Dehlen [7] considered the nonlinearity of both modulus and Poisson's ratio with stress level. Thompson and Garg [6] modeled the pavement as an axisymmetric solid with selected resilient response. The GT-PAVE finite element program developed by Tutumluer [1] considered nonlinear material characterization of granular materials and subgrade soils. When properly addressing material nonlinearity, the FEM-based analysis approach can characterize the material behavior and evaluate the critical responses of flexible pavements [8].

2 Methodology

A newly developed 2D axisymmetric FEM analysis tool is used in this study to simulate the nonlinear elastic behavior of unbound materials. The material nonlinearity was characterized by the K - θ model [9], the Uzan model [10], and the Mechanistic-Empirical Pavement Design Guide's (MEPDG) model [11]. A direct secant stiffness approach is implemented as the nonlinear solution scheme. A sequence of repeated loading triaxial tests on different aggregate materials was conducted to validate the accuracy of the FEM analysis results. Additionally, a comprehensive comparison was made for different material nonlinearity models to measure their effectiveness for characterizing the stress-hardening behavior of unbound aggregate materials.

3 FEM Program with Nonlinearity Material Properties

3.1 General FEM Analysis Procedure

The finite element analysis method is an approximation method of continuum problems such that (a) the continuum is discretized into a finite number of parts (elements), the behavior of which is defined by a finite number of parameters, and (b) the solution of the whole system follows the same governing rules as the original continuum problems [12].

The FEM approach develops a numerical solution for the given physical problem, i.e., the pavement structure subjected to traffic loads. First, the model subdivides the pavement structure into an assembly of small elements. Second, the physical problem is generalized into a mathematical model with differential equations governing the model mechanics. Individual elements all conform to the model mechanics; therefore, the solution at each element provides a numerical approximation of the original pavement structure. Since the finite element method technique is a numerical approach, it is necessary to assess the accuracy of the solution. If the target accuracy has not been achieved, the solution parameter (mesh resolution, number of iterations, etc.) should be refined until a convergence is reached under a given criteria [13]. The general FEM analysis procedure is summarized in Fig. 1.

3.2 Selection of FEM Analysis Type

Based on the incremental damage and reliability formulations proposed in the American Association of State Highway Transportation Official's (AASHTO) Mechanistic-Empirical Pavement Design Guide (MEPDG) [11], the analysis efficiency is given priority when selecting an appropriate finite element program for the flexible pavement response modeling. Thus, the model should analyze the problem both accurately and efficiently, with a proper level of sophistication such that increasing the accuracy beyond what the problem demands does not result in a negative impact on the efficiency.

A factor that has major impact on analysis accuracy and efficiency is the analysis type. Kim [14] conducted a research study which concluded that utilizing 2D axisymmetric and 3D analyses techniques for nonlinear solutions did not produce major differences in the predicted pavement responses. It was seen that the time and resource demands for mesh generation, FEM analysis, and post-processing of a 3D analysis are significantly higher than that of a 2D analysis. The 2D axisymmetric method can obtain precise numerical results with a significant reduction in the computation intensity compared with the 3D analysis method. Moreover, the choice between static analysis and dynamic analysis yields different computational analysis times. Dynamic analysis is usually computationally intensive; thus, the practical demand of a dynamic analysis is relatively low in design approaches.

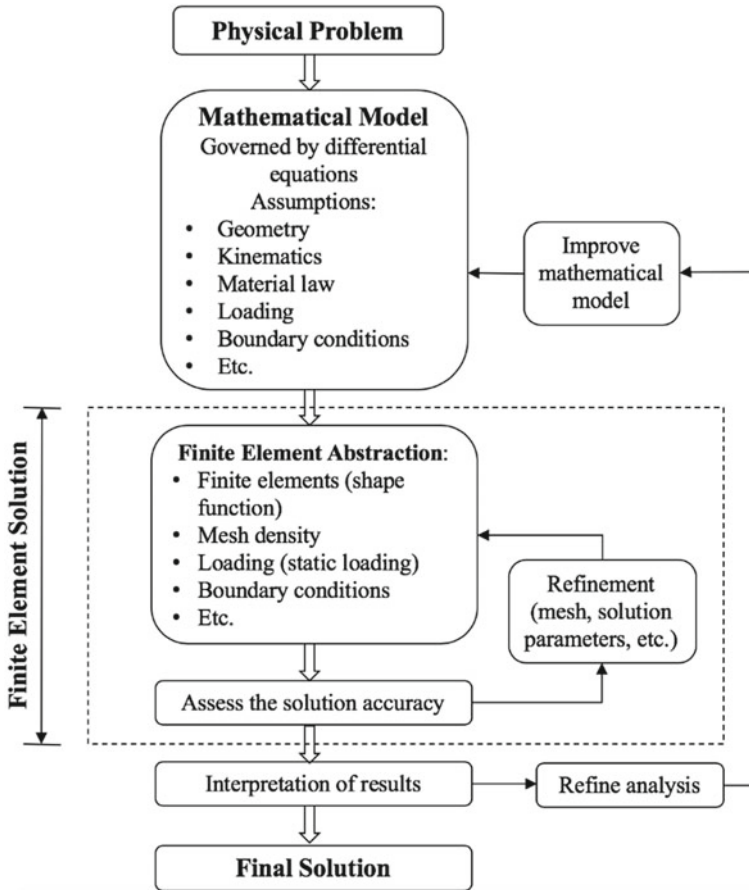


Fig. 1 General FEM analysis procedure

Another major factor that influences the accuracy and efficiency is the mesh design [13]. Fewer mesh elements reduce the computational time yet degrade the solution accuracy. A typically adopted procedure of mesh generation is to minimize the number of elements at boundary locations and use a denser mesh beneath the highly stressed loading areas. Furthermore, high-order elements improved the efficiency while using fewer elements. When nonlinearity is introduced, high-order elements increase the analysis time but provide better accuracy for nonlinear convergence. As such, a trade-off is made between accuracy and efficiency, and an axisymmetric 2D FEM model formulation with high-order quadrilateral element mesh was selected as the candidate for static analysis in this study.

3.3 Analysis Flowchart

An axisymmetric, 2D FEM-based analytical tool was developed with material nonlinearity programmed as a key subroutine. The detailed computation flowchart with the proposed analytical tool is presented in Fig. 2.

First, the pavement section is considered as a 3D cylinder, and then, a slice in 2D axisymmetric space is selected as the analysis domain. Next, during the discretization phase, the analysis domain is divided into a series of second-order quadrilateral elements. Each element consists of eight nodes with four corner nodes and four edge nodes. The corresponding shape function is applied to the element based on the pre-defined element type. After that, the static loading and boundary conditions are applied at associated nodes/elements in the mesh. The shape geometry, loading, and boundary constraint of all elements form a set of differential equations that describes the mechanical problem.

After the formulation of the equations set, the nonlinear models for characterizing material properties for different layers are implemented in an iterative solution scheme. By solving the equations, the nodal displacements for each element are obtained. Accordingly, other element properties including stress, strain, and internal forces can be indirectly calculated following the constitutive equations and shape functions by interpolating and averaging at given locations as shown in Fig. 2.

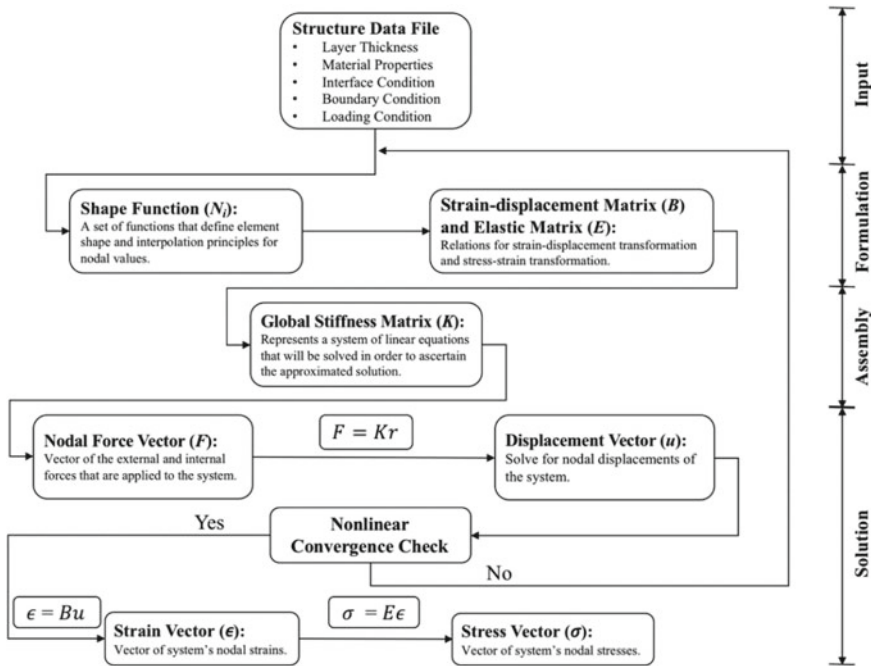


Fig. 2 FEM nonlinear analysis flowchart

3.4 Nonlinear Models and Iterative Solution Scheme

The behaviors of both granular base and subbase materials and subgrade soils are well known to be stress dependent. Such nonlinear layer stiffness trends shall be characterized by a direct secant modulus based on a nonlinear iterative scheme. This characterization method was successfully developed and implemented in the GT-PAVE FEM analysis tool by Tutumluer [1]. Different stress-hardening resilient modulus models for unbound aggregate layers are implemented in the nonlinear analysis module:

The K - θ model [9] was selected as the first model for unbounded aggregate materials with stress-hardening resilient modulus property:

$$M_R = K_1 \theta^{K_2} \quad (1)$$

where

θ bulk stress ($\sigma_1 + 2\sigma_3$) or ($\sigma_1 + \sigma_2 + \sigma_3$) in triaxial conditions;
 K_1, K_2 Material constants obtained from regression analyses of the repeated load triaxial test data

The Uzan model [10] was selected as the second model with stress-hardening resilient modulus property:

$$M_R = K_1 \theta^{K_2} \sigma_d^{K_3} \quad (2)$$

where

θ bulk stress ($\sigma_1 + 2\sigma_3$) or ($\sigma_1 + \sigma_2 + \sigma_3$) in triaxial conditions;
 σ_d deviator stress ($\sigma_1 - \sigma_3$) in triaxial conditions;
 K_1, K_2, K_3 Material constants obtained from regression analyses of the repeated load triaxial test data

The MEPDG model [11] was selected as the third model option with stress-hardening resilient modulus property:

$$M_R = K_1 P a \left(\frac{\theta}{P a} \right)^{K_2} \left(\frac{\tau_{\text{oct}}}{P a} + 1 \right)^{K_3} \quad (3)$$

where

θ bulk stress ($\sigma_1 + 2\sigma_3$) or ($\sigma_1 + \sigma_2 + \sigma_3$) in triaxial conditions;
 τ_{oct} octahedral shear stress $\left(\sqrt{\frac{(\sigma_1 - \sigma_2)^2 + (\sigma_1 - \sigma_3)^2 + (\sigma_2 - \sigma_3)^2}{3}} \right)$;
 $P a$ Atmospheric pressure (14.7 psi or 101.325 kPa);
 K_1, K_2, K_3 Material constants obtained from regression analyses of the repeated load triaxial test data

The direct secant stiffness approach was implemented for the nonlinear analysis of the unbound granular materials. The direct secant method addresses the nonlinear load–displacement behavior by updating the secant stiffness of the material with the proposed resilient modulus characterization models in each iteration until convergence is achieved for the load increment. For every load increment, the previously-calculated secant stiffness is used as the starting value of the analysis. To ensure smooth convergence for each load increment, a damped fixed-point iteration solution scheme was developed as an improved estimate of the resilient modulus for the next iteration in the following form:

$$M_R^j = (1 - \lambda)M_R^{j-1} + \lambda M_{R_{\text{model}}}^j \quad (4)$$

where

- M_R^j actual M_R (resilient modulus) to be used at the end of iteration number j ;
- M_R^{j-1} M_R used at the end of the previous iteration (i.e., iteration $j - 1$);
- $M_{R_{\text{model}}}^j$ M_R computed from the model at the end of iteration number j ;
- λ Damping factor (0–1.0)

The nonlinear iteration scheme is applicable for both internal forces (body force, thermal force, etc.) and external forces (applied surface force). For each load increment, the new values of secant modulus are calculated based on the principal stresses at each integration point of each element. As suggested by Tutumluer [1], the damping factor is selected to be 1.0 for internal forces and 0.3–0.4 for external forces. After satisfying the convergence criteria, the analysis proceeds to the next iteration until all the load increments have been accomplished.

4 Validation Study: UI-FastCell Repeated Load Tests

4.1 Introduction of the University of Illinois FastCell

The repeated load tests presented in this paper were conducted using a state-of-the-art triaxial testing device known as the University of Illinois FastCell (UI-FastCell). In the UI-FastCell, the axial pressure is applied from a pneumatic actuator, whereas the confining pressures are cycled through a hydraulic fluid within a rubber membrane. The driving cylinders on the back of the confining cell include an air–fluid interface, which provides fast application and switching of the dynamic loading in the confinement cell [15].

As for the FastCell loading scheme, the repeated triaxial loading tests were performed at five incremental confining pressure levels. At each confining pressure, the specimen was tested under multi-stage incremental loading conditions (three different deviator stress levels at each confining pressure), following the AASHTO T307 procedure [16]. The test sequence consists of 1000 conditioning load cycles

Table 1 AASHTO T307 resilient modulus test applied stress states using the UI-FastCell

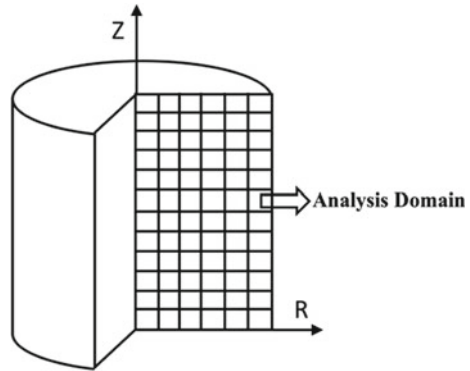
Confining pressure (psi)	Deviator stress (psi)
3	3
	6
	9
5	5
	10
	15
10	10
	20
	30
15	10
	15
	30
20	15
	20
	40

followed by 100 load cycles at each of the 15 incremental stress states. At each stress state, the resilient displacement is measured by LVDTs, and the resilient strain is calculated knowing the specimen geometry. The stress states are shown in Table 1. The haversine load waveform is applied with a load pulse duration of 0.1 s and a rest period of 0.9 s.

4.2 Material Description

Ten different sources of crushed aggregate materials, commonly used for unbound base/subbase applications in the state of North Carolina, were tested and evaluated in this study. These ten materials are referred to as $M_1 - M_{10}$ in the following context. The specimen used in the triaxial tests had the dimensions of 150-mm (6-in.) height, and 150-mm (6-in.) diameter. A simple axisymmetric mesh of the cylindrical test specimen is illustrated in Fig. 3. Note that the UI-FastCell device requires a specimen size with height–depth ratio of 1:1, which is different from the AASHTO procedure [16]. Other than the specimen size, the loading sequence and stress levels strictly follow the AASHTO procedure, as mentioned above. Material preparation and triaxial tests were conducted in the Advanced Transportation Research and Engineering Laboratory (ATREL). Following the triaxial testing, regression analyses were conducted on the raw test data to determine the regression model parameters (K_i) in the $K-\theta$ model, Uzan model, and MEPDG model. These model parameters were then used as inputs to the 2D FEM model as material properties.

Fig. 3 Cylindrical test specimen mesh used in the axisymmetric FEM analysis



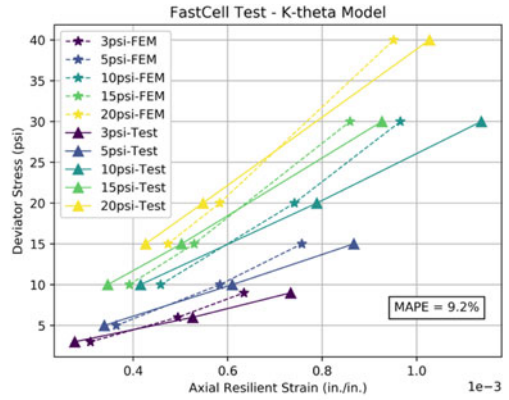
4.3 Comparison Between FEM and Laboratory Test Results

After specifying the corresponding material model and pre-calculating the regression model parameters, the 2D FEM analytical tool was used to model the test specimens under the given loading conditions. As the error analysis metrics, the mean-absolute-percentage-error (MAPE) was used to indicate the standard deviation of the numerical results with respect to laboratory test measurements.

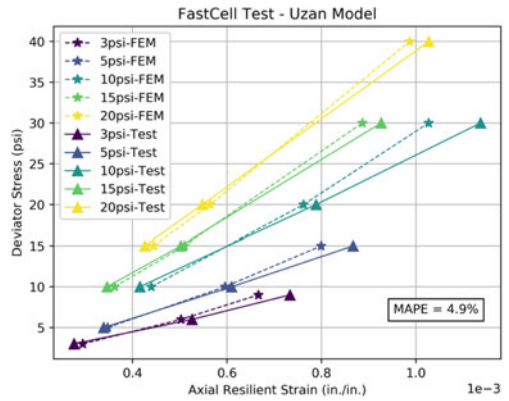
For each material, the FEM results and the laboratory test measurements under incremental loading conditions are plotted in the same figure for comparison (see Fig. 4). For conciseness, only one set of comparison figures for material M_1 (the first tested material) is shown. The results at different stress levels are represented with different colors. FEM results are presented as dashed lines while the laboratory test results are solid lines. Figure 4 indicates that the nonlinear stress-hardening property of unbound aggregate materials can be well predicted by the 2D FEM analytical tool with all three resilient modulus models. Good agreements between the FEM results and laboratory measurements were achieved for all ten materials with analyses conducted using the three resilient modulus models. The results and comparisons are summarized in Table 3. Note that small errors may exist between the resilient modulus from testing and the FEM predictions using the resilient model parameters. This is likely due to the less than 0.99 coefficient of determination or R^2 values obtained for the resilient model parameters from regression analyses of the test data.

The average MAPE value for the three resilient modulus models considering all stress states is 6.42%, which validates the feasibility and accuracy of this nonlinear approach. The Uzan model had the best performance with the lowest average MAPE value (4.87%), followed by the MEPDG model (5.67%) and the $K-\theta$ model (8.73%). This observation suggests that the Uzan and MEPDG models may be used as the best model options for finite element analysis in the proposed scheme to characterize the stress-hardening behavior of aggregate materials under repeated loading.

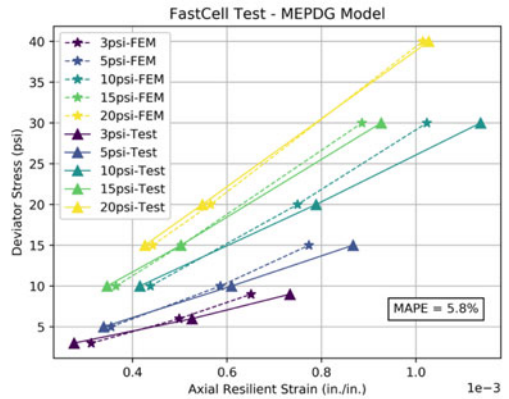
Fig. 4 Comparisons of test measurements and FEM predictions for M_1 material



(a)



(b)



(c)

Table 3 Comparisons of test measurements and FEM predictions

Material	MAPE (%)		
	K - θ model	Uzan model	MEPDG model
M_1	9.2	4.9	5.8
M_2	8.8	5.0	5.6
M_3	6.7	4.7	5.1
M_4	7.5	4.5	5.2
M_5	8.5	4.8	5.8
M_6	10.7	5.0	6.3
M_7	9.5	4.7	5.8
M_8	8.8	4.8	5.8
M_9	9.9	5.4	6.0
M_{10}	7.7	4.9	5.3
Maximum	10.7	5.4	6.3
Minimum	6.7	4.5	5.1
Average	8.73	4.87	5.67

5 Conclusion

A newly developed axisymmetric 2D FEM-based analytical tool with advanced material nonlinearity modules was used to simulate various aggregate materials under repeated loading conditions. A series of laboratory-repeated loading triaxial tests using the UI-FastCell were conducted to validate the accuracy of the FEM results. Good agreement was achieved between the 2D FEM modeling results and the test measurements in terms of the nonlinear elastic behavior of unbound aggregate materials under repeated loading. The 2D FEM-based analytical tool demonstrates its potential to provide an accurate numerical approach for the resilient behavior of aggregates. Further investigation of the different aggregate resilient models indicates that the Uzan and MEPDG models can be used as the recommended model options in FEM analysis considering the stress-hardening behavior of unbound aggregate materials.

Acknowledgements This study was made possible through the financial support provided by The U.S. Army Engineer Research and Development Center (ERDC) of the United States Army Corps of Engineers (USACE). The contents of this paper reflect the views of the authors who are responsible for the facts and the accuracy of the data presented herein. The contents do not necessarily reflect the official views or policies of the ERDC. This paper does not constitute a standard, specification, or regulation.

References

1. Tutumluer E (1995) Predicting behavior of flexible pavements with granular bases. Ph.D. Dissertation, School of Civil and Environmental Engineering, Georgia Institute of Technology, Atlanta, GA
2. Kim M, Tutumluer E, Kwon J (2009) Nonlinear pavement foundation modeling for three-dimensional finite-element analysis of flexible pavements. *Int J Geomech* 9(5):195–208
3. AASHTO T307-99 (2000) Determining the resilient modulus of soils and aggregate materials. In: Standard specifications for transportation materials and methods of sampling and testing, 20th edn. AASHTO, Washington, DC
4. European CEN Std EN 13286-7 (2003) Unbound and hydraulically bound mixtures—Test methods—Part 7: cyclic load triaxial test for unbound mixtures. European Standard, European Committee for Standardization, European Union
5. Saadeh S, Masad E, Little D (2007) Characterization of asphalt mix response under repeated loading using anisotropic nonlinear viscoelastic-viscoplastic model. *J Mater Civ Eng* 19(10):912–924
6. Thompson MR, Garg N (1999) Wheel load interaction: critical airport pavement responses. In: Proceedings of the federal aviation administration airport technology transfer conference, Atlantic City, NJ
7. Dehlen GL (1969) The effect of nonlinear material response on the behavior of pavements subjected to traffic loads. Ph.D. thesis, University of California, Berkeley, Berkeley
8. Huang H, Luo J, Moaveni M, Qamhia II, Tutumluer E, Tingle JS (2019) Advanced analytical tool for flexible pavement design and evaluation. In: International airfield and highway pavements conference 2019: design, construction, condition evaluation, and management of pavements. American Society of Civil Engineers (ASCE), pp 61–71
9. Hicks RG, Monismith CL (1971) Factors influencing the resilient response of granular materials. *Highway Res Rec* 345:15–31
10. Uzan J (1985) Characterization of granular material. *Transp Res Rec* 1022(1):52–59
11. ARA, Inc., ERES Consultants Division (2004) Guide for mechanistic–empirical design of new and rehabilitated pavement structures. Final report, NCHRP Project 1-37A
12. Zienkiewicz OC, Taylor RL, Zhu JZ (2013) The finite element method: its basis and fundamentals. 7th edn. Elsevier
13. Bathe KJ (2006) Finite element procedures. Klaus-Jurgen Bathe
14. Kim M (2007) Three-dimensional finite element analysis of flexible pavements considering nonlinear pavement foundation behavior (vol. 69, no. 02)
15. Tutumluer E, Byun YH, Feng B, Qamhia I, Moaveni M (2018) Impact of quarry gradation and material properties on base course aggregate testing and rutting model calibration. NCDOT project 2015-23, FHWA/NC/2015-23, Illinois center for transportation, July
16. Groeger JL, Rada GR, Lopez A (2003) AASHTO T307—background and discussion resilient modulus testing for pavement components. In: Durham GN, Marr WA, De Groff WL (eds) ASTM STP 1437, ASTM international, West Conshohocken, PA

**Optimized Geomaterial (Including
Hydraulically Bound Materials
and Asphalt Mixtures) Use, Reuse
and Recycling in Road Embankments
and Structural Layers**

Feasibility of Using Selected and Mixed Recycled Aggregates from Construction and Demolition Waste in Unbound Pavement Layers



Castorina S. Vieira , Paulo M. Pereira , and Maria de Lurdes Lopes 

Abstract The proper use of the natural resources is one of the fundamental pillars for the sustainable development required to current society. Construction and demolition (C&D) wastes have been considered as a priority stream because of the large amounts that are generated and their high potential for reuse and recycling. Despite their high potential, reuse and recycling rates vary widely across countries. Recycled C&D materials have been increasingly used as recycled aggregates in pavement base and subbase layers and other road construction applications. However, most of the research studies were carried out on selected recycled aggregates (recycled concrete aggregate, crushed brick or reclaimed asphalt pavement) not always available in quantities for full-scale use. This paper presents the laboratory characterization of two recycled aggregates coming from C&D waste (a non-selected (mixed) recycled aggregate and a selected recycled aggregate) to evaluate whether they meet the technical requirements established in Portuguese specifications, which would enable their application in unpaved rural and forest roads and embankments and capping layers of other transport infrastructures. A series of relevant physical, mechanical and chemical properties are evaluated, and the fulfilment of the requirements is subsequently discussed.

Keywords Recycled aggregates · Unbound pavement layers · Unpaved rural roads

1 Introduction

Minimizing the consumption of non-renewable natural resources for the production of construction materials is considered one of the key aspects to achieve sustainability in the construction sector. The recovery of construction and demolition (C&D) waste as aggregate is an efficient way to achieve this purpose. Adopting and implementing this principle are particularly relevant for an industry that consumes more raw materials than any other economic activity and produces huge amounts of waste.

C. S. Vieira (✉) · P. M. Pereira · M. de L. Lopes
CONSTRUCT, Faculty of Engineering, University of Porto, R. Dr. Roberto Frias, s/n, 4200-465
Porto, Portugal
e-mail: cvieira@fe.up.pt

The use of C&D recycled materials in base and subbase layers of transport infrastructures have been studied by several researchers over the years [1–4]. However, most of these studies were carried out on selected recycled aggregates, i.e. recycled concrete aggregate, crushed brick or reclaimed asphalt pavement. In Mediterranean countries, such as Portugal, Spain or Italy, the most part of produced recycled aggregates are mixed recycled aggregates (comprising not only concrete but significant amounts of masonries). It is therefore of great relevance studying the feasibility of the use of these recycled materials, even if in less demanding applications such as unpaved rural or forest roads.

This paper presents a laboratory study carried out on two coarse recycled aggregates and discusses their suitability for construction of embankments and capping layers of transport infrastructures, including rural and forest roads.

2 Materials and Methods

2.1 Materials

The study was carried out on two coarse recycled aggregates collected at a Portuguese recycling plant (Fig. 1). Based on their constituents, one is referred to as mixed C&D recycled material and the other one as selected C&D recycled material.

The mixed C&D recycled material results from the screening process carried out at the recycling plant, and it is commercialized as a recycled aggregate with gradation 10–30 mm (Fig. 1a). The selected C&D recycled material comes from large concrete components, resulting from a demolition, which after the previous sorting process was inserted into a mobile crusher (Fig. 1b). The constituents of these recycled aggregates will be presented in Sect. 3.



Fig. 1 Visual appearance of the recycled aggregates: **a** mixed C&D recycled material; **b** selected C&D recycled material

Table 1 Laboratory testing methods

Assessed properties	Standard
<i>Geometrical properties</i>	
Particle size distribution	EN 933-1: 2012
Flakiness index	EN 933-3: 2012
Shape index	EN 933-4: 2008
Sand equivalent—Assessment of fines	EN 933-8: 2012
Methylene blue—Assessment of fines	EN 933-9: 2009
Constituents	EN 933-11: 2009
<i>Physical and mechanical properties</i>	
Particle density and water absorption ^a	EN 1097-6: 2013
Resistance to fragmentation (Los Angeles)	EN 1097-2: 2010
Aggregate crushing value	BS 812-110: 1990
<i>Environmental properties</i>	
Water-soluble sulphates	EN 1744-1: 2009
Potential risk of ground contamination (leaching)	EN 12457-4: 2002/EN 16192: 2011
pH value (leaching)	EN 16192:2011

^aFor different particle size fractions

2.2 Laboratory Study

The laboratory study was designed to assess the geometrical, physical, mechanical and environmental properties of the recycled materials, in order to evaluate their suitability as aggregates for construction of rural roads and embankments and capping layers of other transport infrastructures. Table 1 summarizes the assessed properties and the related testing methods.

3 Results and Discussion

3.1 Constituents of the Recycled Material

The constituents of the recycled materials, evaluated by hand sorting of particles, are presented in Fig. 2. The contents of concrete, concrete products, mortar, concrete masonry units, Rc, unbound aggregate, natural stone, hydraulically bound aggregate,

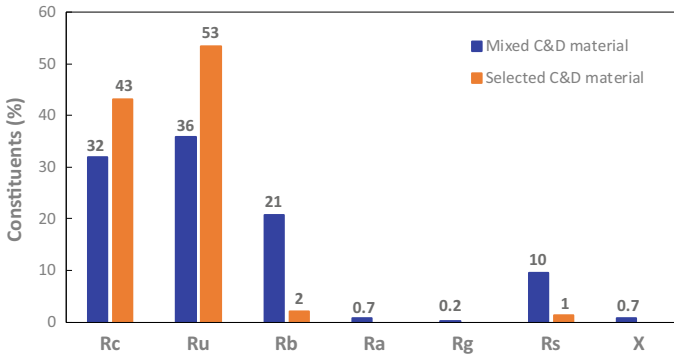


Fig. 2 Constituents of the recycled aggregates

Ru, clay masonry units, calcium silicate masonry units, aerated non-floating concrete, Rb, bituminous materials, Ra, glass, Rg, soils, Rs, and other materials, X, were assessed.

As shown in Fig. 2, the mixed C&D recycled material consists mainly of concrete and mortars, Rc, unbound aggregates, Ru, masonries, Ru and soils, Rs (see also Fig. 1a). The selected C&D recycled material is composed mostly of concrete and mortars, Rc and unbound aggregates, Ru (see also Fig. 1b).

The floating particles content, FL, estimated during the classification test for the constituents was 0.8 and 0.1 cm³/kg for mixed and selected C&D materials, respectively.

3.2 Geometrical Properties

Taking into account the heterogeneity of these recycled materials, the particle size distribution was carried out on three samples. Figure 3 shows the gradation curves of the mixed C&D recycled material (Fig. 3a) and selected C&D recycled material (Fig. 3b).

As mentioned before, the mixed material is commercialized as a recycled aggregate with gradation 10–30 mm. In fact, about 80% of the material (on average) is larger than 10 mm. The mean value of the maximum particle size (D_{max}) is 31.5 mm, and its fine content is around 5%.

The selected C&D recycled material is an aggregate with extensive granulometry (tout-venant), comprising particles from 63 mm (D_{max}) to lower than 0.063 mm (fines content = 3.6%).

Further discussion on the maximum particle size and fines content will be presented in Sect. 4.

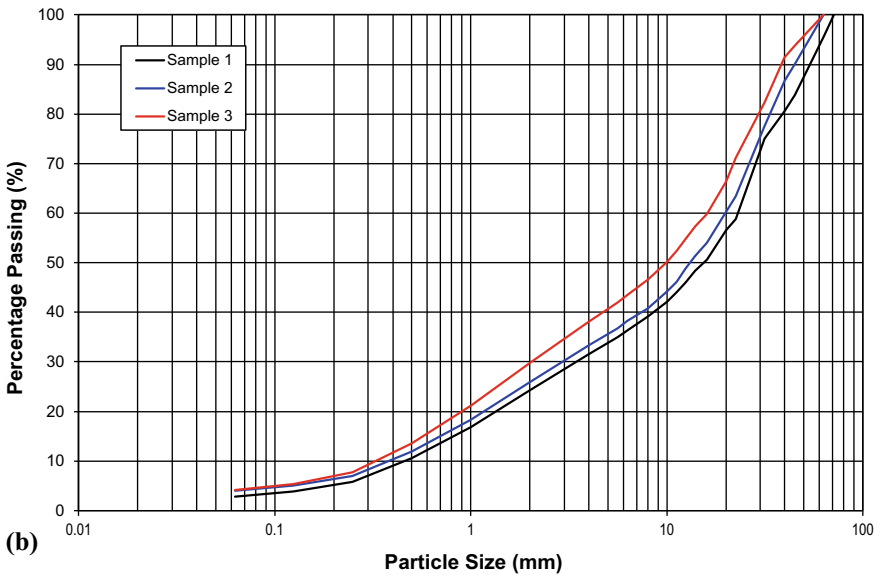
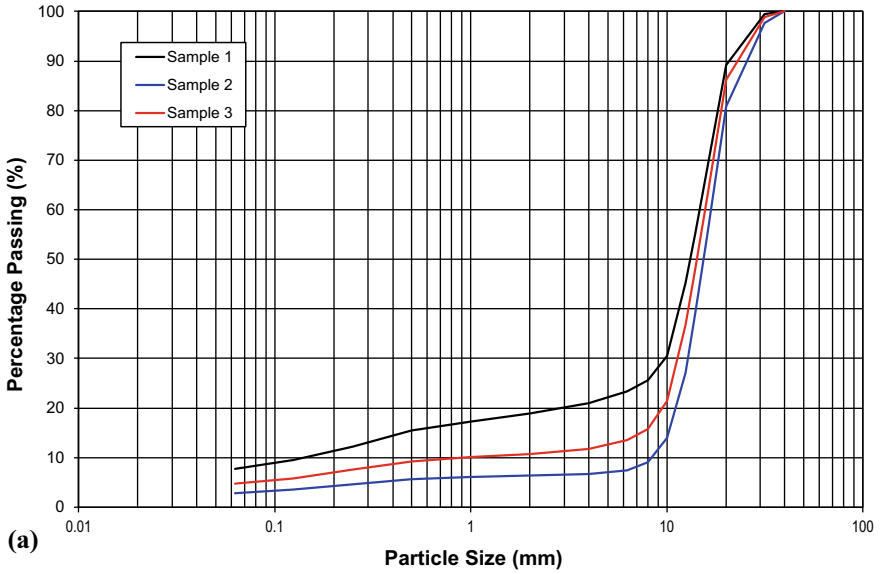
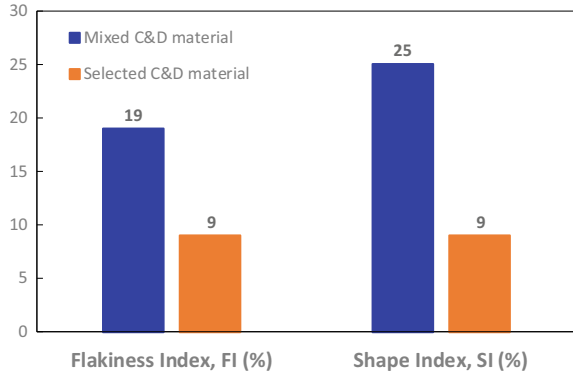


Fig. 3 Particle size distribution of three samples for: **a** mixed C&D recycled material; **b** selected C&D recycled material

Fig. 4 Particle shape characteristics



Although the flakiness and shape indexes play a more relevant role in concrete production and bituminous mixtures, these geometric characteristics were also evaluated for both aggregates (Fig. 4). The mixed C&D material shows higher flakiness and shape indexes, which means that its particles are flakier and longer, than those of the selected C&D recycled material. This evidence can be explained by its content of ceramic materials that are usually thin and long (Figs. 1a and 2).

The presence of flaky and long particles is undesirable in pavement construction, particularly in surface courses, since they may get broken down easily under traffic loads. It is expected lower resistance to rutting in unpaved roads constructed with aggregates exhibiting high flakiness and shape indexes.

The assessment of fines was performed through the sand equivalent and the methylene blue tests performed on the 0/2 mm size fraction. Figure 5 shows the sand equivalent value (SE) and the value of the methylene blue (MB). The values of the parameter $MB_{0/D}$ (stipulated in the Portuguese specifications) are also presented in Fig. 5. $MB_{0/D}$ is the value of MB multiplied by the percentage of material passing the 2 mm sieve.

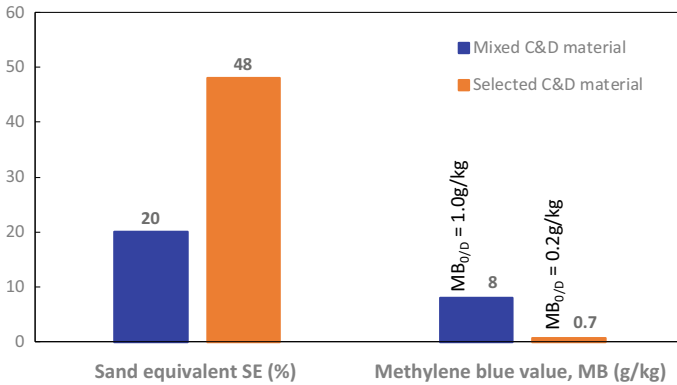


Fig. 5 Results of the assessment of fines

The sand equivalent value refers the relative proportions of sand versus plastic fines and dust. The SE value of the selected C&D recycled material is greater than twice the SE value of the mixed material. These results are in agreement with the grain size distributions shown in Fig. 3. The value of MB for the mixed C&D recycled material is much higher than that of selected material, probably resulting from the disintegration of clay masonries. It is worth noting that the value of MB reflects the amount and characteristics of clay minerals, which can be potentially harmful to the performance of the pavement layers.

The lower cleanliness exhibited by the mixed C&D recycled material (low SE and very high MB), as will be discussed in Sect. 4, may restrict the field of application of this material.

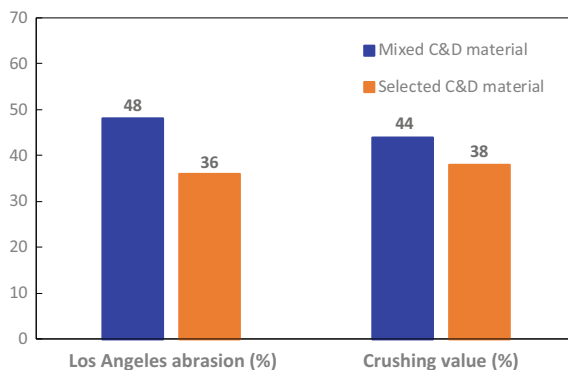
3.3 Physical and Mechanical Properties

Table 2 presents the particles density and water absorption values for different particle size fractions of the recycled materials. The density of particles in the range 4/31.5 mm tends to be slightly higher for the selected C&D material, with the reverse trend for the smaller particles. The values of particle density for these recycled materials are consistent with those typically obtained for natural aggregates.

Table 2 Particles density and water absorption values

Parameters	Mixed C&D material	Selected C&D material
<i>Particle size fraction 31.5/63 mm</i>		
Apparent particle density (Mg/m ³)	–	2.510
Oven-dried particle density (Mg/m ³)	–	2.257
Saturated and surface dried particle density (Mg/m ³)	–	2.357
Water absorption (%)	–	4.5
<i>Particle size fraction 4/31.5 mm</i>		
Apparent particle density (Mg/m ³)	2.573	2.623
Oven-dried particle density (Mg/m ³)	2.205	2.404
Saturated and surface dried particle density (Mg/m ³)	2.348	2.487
Water absorption (%)	6.5	3.5
<i>Particle size fraction 0.063/4 mm</i>		
Apparent particle density (Mg/m ³)	2.693	2.619
Oven-dried particle density (Mg/m ³)	2.506	2.359
Saturated and surface dried particle density (Mg/m ³)	2.575	2.458
Water absorption (%)	2.8	4.2

Fig. 6 Resistance to fragmentation and crushing



Due to the high content of ceramic materials, it was expected that the mixed C&D material would exhibit higher values of the water absorption value than those of the selected C&D material. However, this trend did not occur for particles in the range 0.063/4 mm.

Figure 6 presents the resistance to fragmentation of both aggregates assessed through Los Angeles abrasion and aggregate crushing tests. Possibly due to the high content of clay masonries (Figs. 1a and 2), the mixed C&D material shows lower resistance to fragmentation and crushing, expressed by higher LA abrasion and crushing values, which may compromise its performance. High Los Angeles abrasion values have been identified in the literature [1, 3] as a constraint in mixed C&D recycled aggregates.

3.4 Geo-environmental Behaviour

Table 3 shows the results of the laboratory leaching test carried out on the recycled materials as well as the acceptance criteria for leached maximum concentration for inert landfills stipulated by the European Council Decision 2003/33/EC [5]. It is assumed that if a recycled aggregate fulfils the requirements set for inert landfills, it can be considered as an inert material. As shown in Table 3 only the content of sulphate, SO_4 , and total dissolved solids, TDS, in the eluate of the mixed C&D material exceeded the threshold values. However, it should be mentioned that the above-mentioned European Council Decision [5] states that “if the waste does not meet these values for sulphate, it may still be considered as complying with the acceptance criteria if the leaching does not exceed 6000 mg/kg at $L/S = 10 \text{ l/kg}$...”, which means that the sulphate content found in the eluate is not of concern. The total dissolved solids (TDS) also exceeded the threshold but its evaluation is not compulsory [5], meaning that it will not be a concern either.

High concentrations of TDS and sulphate in mixed C&D wastes have been reported by other authors [6, 7].

Table 3 Results of laboratory leaching test and acceptance criteria for inert landfill

Parameter (mg/kg dry matter)	Mixed C&D recycled material	Selected C&D recycled material	Acceptance criteria—Inert landfill [5]
Arsenic, As	<0.005	<0.005	0.5
Lead, Pb	<0.01	<0.01	0.5
Cadmium, Cd	<0.003	<0.003	0.04
Chromium, Cr	0.18	0.45	0.5
Copper, Cu	0.021	0.037	2
Nickel, Ni	<0.01	<0.01	0.4
Mercury, Hg	<0.002	<0.002	0.01
Zinc, Zn	<0.1	<0.1	4
Barium, Ba	0.088	0.049	20
Molybdenum, Mo	0.014	0.015	0.5
Antimony, Sb	<0.01	<0.01	0.06
Selenium, Se	<0.02	<0.02	0.1
Chloride, Cl	240	51	800
Fluoride, F	5.1	2.3	10
Sulphate, SO ₄	2800	670	1000
Phenol index	<0.05	<0.05	1
Dissolved organic carbon, DOC	21	29	500
Total dissolved solids, TDS	4970	2090	4000

The pH value of the eluates was 10.1 and 10.2 for the mixed and selected C&D materials, respectively. These values are within the expected range. Butera et al. [8] reported values in the range 9–13 from twenty-nine samples of C&D aggregates collected from different recycling facilities. Roque et al. [9] achieved values between 9 and 12 from four distinct coarse C&D aggregates.

The content of water-soluble sulphates, estimated by spectrophotometry, for the mixed and selected C&D recycled materials was 0.12% and 0.05%, respectively.

4 Feasibility Analysis

The Portuguese specifications for recycled materials coming from construction and demolition wastes classify these alternative materials on the basis of their constituents and possible applications. Table 4 presents the material classes for use in rural and

Table 4 Classification of C&D recycled materials based on their constituents

Material Class	Constituents						
	Rc + Ru + Rg (%)	Rg (%)	Ra (%)	Rb (%)	Rb + Rs (%)	X (%)	FL (cm ³ /kg)
<i>Rural and Forest Roads, LNEC E 484 [10]</i>							
CRA	No limit	≤25	No limit	–	No limit	≤1	≤5
CRB	≥20	≤5	≤80	–	≤10	≤1	≤5
CRC	≥50	≤5	≤30	–	≤10	≤1	≤5
<i>Embankments and capping layers of transport infrastructures, LNEC E 474 [11]</i>							
B	≥90	≤10	≤5	–	≤10	≤1	≤5
MB	≤70	≤25	≥30	–	≤70	≤1	≤5
C	No limit	≤25	≤30	–	No limit	≤1	≤5

forest roads (in accordance with Portuguese specification LNEC E 484 [10]) and in embankments and capping layers of other transport infrastructures (LNEC E 474 [11]). Note that the meaning of Rc, Ru, Rg, Ra, Rb, Rs, X and FL was presented in Sect. 3.1.

On the basis of its constituents, the mixed C&D material can be classified as CRA material for use in rural and forest roads and Class C for embankments and capping layers of transport infrastructures (Fig. 2 and Table 4). On the other hand, the selected C&D material can be considered as Class CRA, Class CRB and Class CRC, when used in rural and forest roads or belonging to Class B and Class C for embankments and capping layers of transport infrastructures (Fig. 2 and Table 4).

Table 5 presents the minimum requirements of C&D recycled materials to be used in rural and forest roads set out in the Portuguese specification LNEC E 484 [10]. The C&D recycled materials can be classified in four distinct categories (CR1, CR2, CR3 and CR4) with different applications in rural and forest roads. In embankments for rural and forest roads, the four categories, CR1, CR2, CR3 and CR4, are allowed. CR1 is not suitable for subbases, being permitted materials CR2, CR3 and CR4. Only materials categorized as CR3 and CR4 are suitable for base courses, and just CR4 materials are appropriate for unsealed wearing courses.

The minimum requirements of the recycled materials for embankments and capping layers of transport infrastructures in accordance with Portuguese specification LNEC E 474 [11] are represented in Table 6. For this application, there are two material categories (MAT1 or MAT2). MAT1 materials can be used in embankments of transport infrastructures, while MAT2 can also be applied in capping layers (except for MB class).

For use in rural and forest roads, both the mixed and the selected C&D recycled materials can be included in category CR2 (Table 5), which means that these materials are suitable for application in embankments construction and in subbase layers. If it was not for the high value of D_{max} , the selected C&D recycled material could be

Table 5 Minimum requirements of C&D recycled materials to be used in rural and forest roads in accordance with LNEC E 484 [10]

Compliance requirements		Material category/class			
		CR1	CR2	CR3	CR4
Parameters	Property	CRA, CRB, CRC	CRA, CRB, CRC	CRB, CRC	CRC
Geometry and nature	D_{max}	≤ 180 mm	≤ 80 mm	≤ 40 mm	≤ 40 mm
	Fines content (≤ 0.063 mm)	–	$\leq 12\%$	$\leq 12\%$	$\leq 12\%$
	Assessment of fines ($MB_{0/D}$)	–	≤ 2.0	≤ 2.0	≤ 1.0
Mechanical behaviour	Resistance to fragmentation (LA)	–	$LA \leq 50$	$LA \leq 45$ or $MDE \leq 45$	$LA \leq 40$ or $MDE \leq 40$
	Resistance to wear (MDE)				
Chemical behaviour	Water-soluble sulphates	$\leq 0.7\%$	$\leq 0.7\%$	$\leq 0.7\%$	$\leq 0.7\%$
	Release of dangerous substances	Classification as inert waste for landfill			

Table 6 Minimum requirements of C&D recycled materials to be used in embankments and capping layers of transport infrastructures in accordance with LNEC E 474 [11]

Compliance requirements		Material category/class		
		MAT1	MAT2	
Parameters	Property	B, MB, C	B, C	MB
Geometry and nature	D_{max}	≤ 150 mm	≤ 80 mm	
	Fines content (≤ 0.063 mm)	$\leq 10\%$	$\leq 10\%$	
	Assessment of fines ($MB_{0/D}$)	< 2.0	< 1.0	
Mechanical behaviour	Resistance to fragmentation (LA)	–	$LA \leq 45$ $MDE \leq 45$	–
	Resistance to wear (MDE)			
Chemical behaviour	Water-soluble sulphates	$\leq 0.7\%$	$\leq 0.7\%$	
	Release of dangerous substances	Classification as inert waste for landfill		

considered as CR4, the highest category, which would enable its application in any of the pavement layers of a rural road, including the base course and unsealed wearing course.

For embankments and capping layers of transport infrastructures, the mixed C&D aggregate is a Class C material. Based on the geometrical, physical, mechanical and chemical properties of this aggregate, it can be included in material category MAT1 (Table 6), which means this recycled material can only be used in embankments construction.

As mentioned before, the selected C&D recycled material for use in embankments and capping layers of transport infrastructures belongs to Class B and Class C. Although it was not possible to evaluate the resistance to wear (MDE), due to a technical problem with the laboratory equipment, based on Los Angeles abrasion value (Fig. 6), it is acceptable to admit that MDE is also lower than 45, which means this recycled material can be included in the highest category, MAT2 (Table 6). Being a material of category MAT2, it is enabled its application in embankments construction as well as in capping layers of transport infrastructures.

5 Conclusions

This paper presented a laboratory study carried out on two coarse recycled aggregates and discussed their suitability for construction of embankments and capping layers of transport infrastructures, including rural and forest roads. Based on the recommendations of Portuguese specifications, the mixed C&D aggregate presents suitable characteristics to be used in the construction of embankments, as well as alternative aggregate for the subbase layer of rural and forest roads. This recycled material is not appropriate for capping layers of other transport infrastructures.

The selected C&D recycled material is suitable for application in embankments construction and capping layers of transport infrastructures, but due to its high maximum particle size (D_{max}), it does not meet the requirements for being used in base course and unsealed wearing course of rural and forest roads.

It is worth mentioning that none of these recycled materials raised any environmental concerns.

Acknowledgements This work was financially supported by: Project PTDC/ECI-EGC/30452/2017—POCI-01-0145-FEDER-030452—funded by FEDER funds through COMPETE2020—Programa Operacional Competitividade e Internacionalização (POCI) and by national funds (PIDDAC) through FCT/MCTES; Base Funding—UIDB/04708/2020 of the CONSTRUCT—Instituto de I&D em Estruturas e Construções—funded by national funds through the FCT/MCTES (PIDDAC). The second author would also like to thank Fundação para a Ciência e Tecnologia (FCT) for his research grant: SFRH/BD/147838/2019.

References

1. Vegas I, Ibañez JA, San José JT, Urzelai A (2008) Construction demolition wastes, Waelz slag and MSWI bottom ash: a comparative technical analysis as material for road construction. *Waste Manage* 28(3):565–574
2. Arulrajah A, Disfani MM, Horpibulsuk S, Suksiripattanapong C, Prongmanee N (2014) Physical properties and shear strength responses of recycled construction and demolition materials in unbound pavement base/subbase applications. *Construct Build Mater* 58:245–257
3. Agrela F, Barbudo A, Ramírez A, Ayuso J, Carvajal MD, Jiménez JR (2012) Construction of road sections using mixed recycled aggregates treated with cement in Malaga, Spain. *Resour Conserv Recycl* 58:98–106
4. Cristelo N, Vieira CS, Lopes ML (2016) Geotechnical and geoenvironmental assessment of recycled construction and demolition waste for road embankments. *Procedia Engineering* 143:51–58
5. Council Decision 2003/33/EC (2003) Council decision establishing criteria and procedures for the acceptance of waste at landfills pursuant to Article 16 of and Annex II to Directive 1999/31/EC. Official J Eur Union, pp. L11–27
6. Townsend TG, Jang Y, Thurn G (1999) Simulation of construction and demolition waste leachate. *J Environ Eng* 125(11):1071–1081
7. Barbudo A, Galvín AP, Agrela F, Ayuso J, Jiménez JR (2012) Correlation analysis between sulphate content and leaching of sulphates in recycled aggregates from construction and demolition wastes. *Waste Manage* 32:1229–1235
8. Butera S, Christensen TH, Astrup TF (2014) Composition and leaching of construction and demolition waste: Inorganic elements and organic compounds. *J Hazard Mater* 276:302–311
9. Roque AJ, Martins IM, Freire AC, Neves JM, Antunes ML (2016) Assessment of environmental hazardous of construction and demolition recycled materials (C&DRM) from laboratory and field leaching tests application in road pavement layers. *Procedia Eng* 143:204–211
10. LNEC E484 (2016) Guide for the use of materials resulting from construction and demolition waste in rural and forest roads. In: LNEC (Portuguese Laboratory of Civil Engineering), 8p (in Portuguese)
11. LNEC E474 (2009) Guide for use of recycled materials coming from construction and demolition waste in embankment and capping layers of transport infrastructures. In: LNEC (Portuguese Laboratory of Civil Engineering), 5p (in Portuguese)

Study of Deformation and Failure States of Reinforced Mesh Cushion in the Geosynthetics-Reinforced and Pile-Supported Structure of High-Speed Railway



Tai-Feng Li, Degou Cai, Zhi-Bo Cheng, Qian-Li Zhang, Yin Gao, Colin Basye, Jing-Yu Liu, and Xin-Gang Zhang

Abstract Settlement deformation is a major problem faced by high-speed railways, especially in soft soil subgrade areas. The geosynthetics-reinforced and pile-supported (GRPS) composite foundation is an effective design method to minimize the differential settlement between the piles and supporting soil, which can also influence the overall post-construction settlement of composite foundations. With the advantage of a short construction period and small lateral deformation, etc., the GRPS composite foundation has been widely used in both highway and railway engineering projects. However, there is no unified analysis and evaluation method for the calculation theory of the deformation of reinforced mesh cushion (RMC) in GRPS composite foundation, and the failure mode of the RMC is not adequately researched. In this paper, the deformation and failure states of reinforcement body of high-speed railway GRPS composite foundation in soft soil and the principle of deformation of RMC under different conditions are analyzed and studied with numerical analysis and simulation calculation of single piles. Secondly, through the model test, the load transfer and deformation characteristics of GRPS composite foundations are studied. The load distribution characteristics of pile body and the deformation characteristics of both pile top and bottom piercing are analyzed. The interaction characteristics and deformed failure states of RMC and pile ends are revealed, which indicated the integral deformation shapes of reinforcement body located at both pile tops and pile interval regions. The maximum stress of the reinforcement body is calculated, which is distinguished from the original suspension theory. Finally, the existing reinforcement tensile force calculation equation has been optimized and improved, which can be used for the RMC design in the GRPS composite foundation.

T.-F. Li (✉) · D. Cai · Q.-L. Zhang · J.-Y. Liu · X.-G. Zhang
Railway Engineering Research Institute, China Academy of Railway Sciences Corporation Limited, Beijing 100081, China

Z.-B. Cheng
Institute of Computing Technologies, China Academy of Railway Science Corporation Limited, Beijing 100081, China

Y. Gao · C. Basye
Transportation Technology Center, Inc, Pueblo, CO 81001, USA

Keywords High-speed railway · GRPS composite foundation · Reinforced mesh cushion · Failure states

1 Background

The geosynthetics-reinforced and pile-supported (GRPS) composite foundation has the advantages of short construction period, low lateral deformation, and small post-construction settlement. It has been applied for the first time in the reconstruction project of the Japanese embankment in the early 1970s and has been widely used in highway and railway engineering [1, 2]. In recent years, such technologies have been adopted in passenger dedicated railway lines and high-speed railways under construction and will be built in China. The great progress has been made in theory and engineering practice, but its mechanism research still lags behind engineering practice [3].

The interaction mechanism of GRPS composite foundation is more complicated than that of traditional composite foundation [4]. The existing theories do not study the interaction of pile, soil, reinforced body and subgrade structure deeply enough, and the calculation is based on many assumptions to make the design partial conservative. Moreover, the calculation based on many assumptions makes the design tend to be conservative, and the results only meet specific conditions. When different methods are used, the calculated results are obviously different. There is no unified understanding and necessary analysis and evaluation methods for the calculation theory of the deformation of the reinforced mesh cushion (RMC) of the GRPS composite foundation.

At present, the design of the RMC in the GRPS composite foundation is mainly in two aspects. One is to determine the load of the reinforced body; the second is to determine the tensile strength of the reinforced body. However, there is a lack of understanding on the calculation methods of failure mode and damage form of RMC in the GRPS composite foundation.

Settlement deformation is the main problem faced by high-speed railway subgrade, and the foundation is the main region of settlement deformation, especially in deep soft soil areas. The GRPS composite foundation is a main ground treatment method for high-speed railways in China.

The source of settlement of GRPS composite foundation is multifaceted, such as the compression of RMC, the piercing deformation of pile top, the compression settlement in reinforcement zone, the compression of lower layer, and the piercing deformation of the pile bottom.

In the GRPS composite foundation system, there are many researches on the settlement deformation of the reinforcement zone. There is still no reliable analysis and calculation method for the both top and bottom of the pile. The inherent characteristic of overall settlement has yet to be studied in depth. Moreover, for high-speed railway, there is still a need for fine calculation and high precision control.

Therefore, with the rapid development of high-speed railway all over the world, the proportion of subgrade will inevitably increase. The higher economic and safety requirements make the above problems seriously restrict the development of high-speed railway subgrade engineering projects.

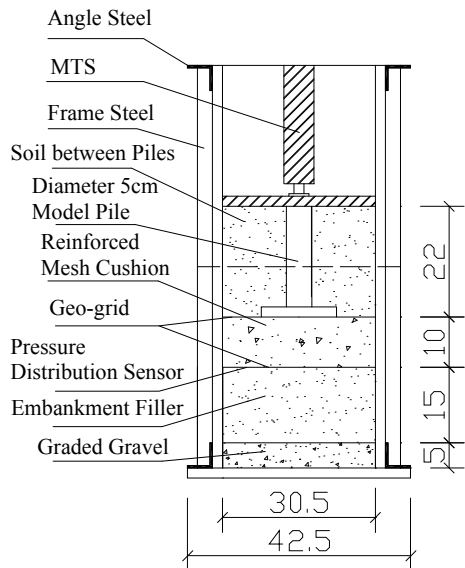
It is very important for controlling the settlement of subgrade to reveal the deformation characteristics of the RMC of the high-speed railway GRPS composite foundation and propose the corresponding RMC design and calculation method.

In this paper, based on the research of interaction behavior between pile, soil and RMC, the stress and strain calculation theory of RMC is analyzed. The design optimization method of RMC of composite foundation pile structure is proposed, which provides guidance for the optimization design of high-speed railway GRPS composite foundation in the future.

2 Experimental Study on Failure State of Reinforced Mesh Cushion

The main purpose of this model test is to study the main factors affecting the deformation of the RMC of the GRPS composite foundation [5] and to analyze the characteristics of the RMC deformation. The effects of pile cap size, reinforced body strength, number of reinforced layers, and thickness of RMC on the deformation of pile foundation under the load of embankment are analyzed [6, 6]. This model test is a single pile model test (Fig. 1). In order to facilitate the test operation and consider the sensor range, the inversed short model pile is used for loading.

Fig. 1 Schematic diagram of model test device (cm)



2.1 Pressure Distribution Situation

The purpose of this test is to study the failure mechanism of the RMC of the GRPS composite foundation under extreme pressure conditions. Therefore, the MTS loading equipment (Fig. 2) is used to apply a large vertical load to the single pile to study the geogrid strain and the pressure distribution in the lower part of the RMC [8, 8]. The model test is made with 10 cm RMC, double-layer geogrid (tensile strength 15 kN/m, Young’s modulus 60 MPa), 50 mm in model pile diameter (no pile cap).

It can be seen from Fig. 3a that the maximum stress occurs at the position of 0.5–0.75 times of the pile diameter from the pile top, not directly at the position where the pile top is located. The pressure on the left side of the pile top was slightly higher than that on the right side at the position within 2 times the pile diameter (may be caused by slight inclination of the pile body), and the vertical pressure was 20–30 kPa higher than that on the central position of the pile top. The specific pressure distribution was shown in Table 1.



Fig. 2 Failure test of reinforced mesh cushion

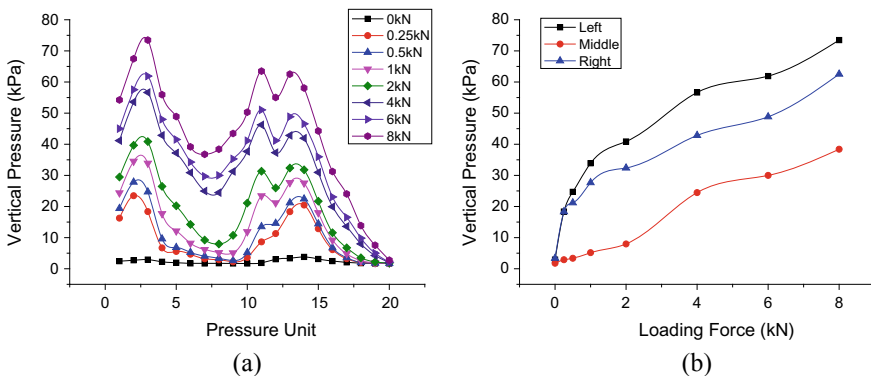
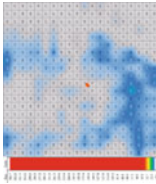

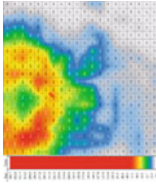
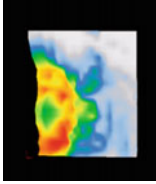
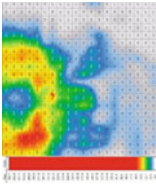
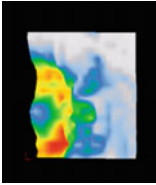
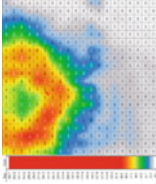
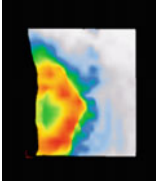


Fig. 3 Pressure distribution of reinforced mesh cushion failure

Table 1 Pressure distribution nephogram of reinforced mesh cushion failure

Load	2 D chart	3 D chart	Load	2 D chart	3 D chart
0 kN			4 kN		
2 kN			8 kN		

Based on the above test results, it can be found that the upper geogrid damage is concentrated at the position of 0.5–0.75 D (diameter) from the edge of the pile top, and the lower-layer geogrid damage is mainly concentrated in the range of 2.5 D on both sides of the pile top, which is consistent with the results considering stress diffusion angle.

Figure 3b shows the maximum strain at the left and right sides of the model pile, and the minimum strain at the center with the vertical load. Under the assumption that the elastic modulus of the geogrid is constant, the force at each part of the geogrid can be derived. In this case, the maximum tensile force appears at 0.5 D from the edge of the pile top.

2.2 Vertical Settlement Situation

Through the previous FEA modeling simulation, it is found that when the geogrid permanent strain is 2%, the vertical stress of the pile top is about 416.75 kPa. Compared with the results measured in this test, it can be found that when the vertical stress is 1kN, the vertical load at the pile top is about 509.3 kPa, with 2% geogrid permanent strain at the same time.

The vertical stress distribution at the center of each depth under different vertical loads can be obtained by numerical treatment of the vertical stress at both pile top and 2 D from the pile top. Figure 4 shows the vertical stress (less than 4 kN) attenuates nearly to zero and loses disturbance to the surrounding soil, when it transmitted to the range 2 D zone.

It can be considered that the upper and lower ends of the pile have a range of 2–2.5 D, and the original subgrade main body and the lower layer can be refinished into the upper local stress concentration zone and the lower local stress concentration zone.

It can be seen from Fig. 4 that when the vertical load applied to the RMC is 1 kN, the permanent strain is about 2%. The overall stress state of the RMC is relatively

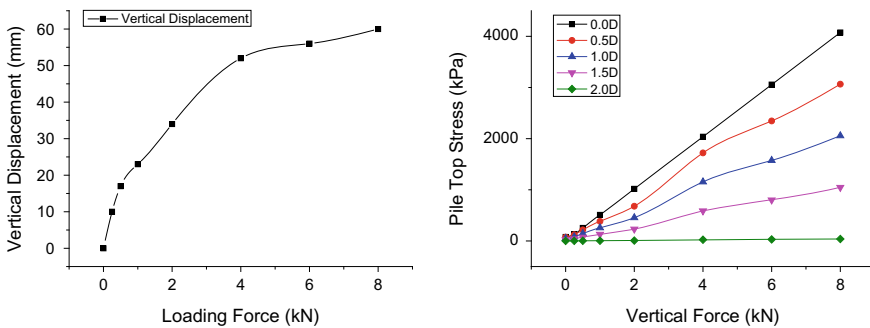


Fig. 4 Vertical stress and displacement change with vertical load

well, which can transmit the load of the upper subgrade stably and effectively, which can exert the comprehensive effect of the GRPS composite foundation effectively.

It is important to note that, when the upper load increases to about 4 kN, the RMC gradually transitions from elastic failure to plastic failure, the settlement curve tends to be gentle, and the RMC gradually reaches the ultimate bearing capacity. The strain is about 3.68%, and the RMC has partially failed, resulting in the gradual instability of the GRPS composite foundation.

In conclusion, considering the uncontrollable natural reasons such as construction technology, site construction environment, temperature, and humidity, it is reasonable to limit the permanent strain of the geogrid to about 2%. It can maximize the effect of GRPS composite foundation, effectively reduce the uneven settlement of subgrade and superstructure, and provide a strong guarantee for the smooth and safety operation of high-speed railway.

2.3 Geogrid Strain Situation

Figure 5 shows the force and strain of the upper and lower geogrid in this model test. According to the difference value, when the geogrid permanent strain is 2%, the vertical load is about 427.45 kPa, which is very close to the previous FEA modeling simulation result (416.75 kPa), which can provide data support for the mutual verification of laboratory test and simulation calculation.

Figure 6 shows the strain distribution of the upper and lower geogrids with the change of vertical stress, which is consistent with the pressure distribution. The maximum strain occurs at the 0.5–0.75 D from the edge of the pile top, and the shape of the geogrid in the failure mode presents an ‘M’ form distribution [10].

Therefore, the existing tensile force calculation equation of geogrid can be simplified. When the geogrid bears a certain vertical load, the strain at 0.5 D from the edge of pile top (upper layer) is about 1.5% larger than the strain at the center of the pile

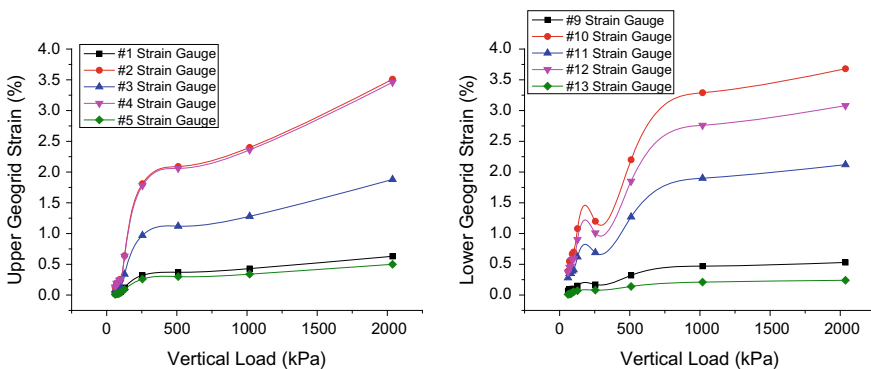


Fig. 5 Upper and lower geogrid strains in RMC failure test

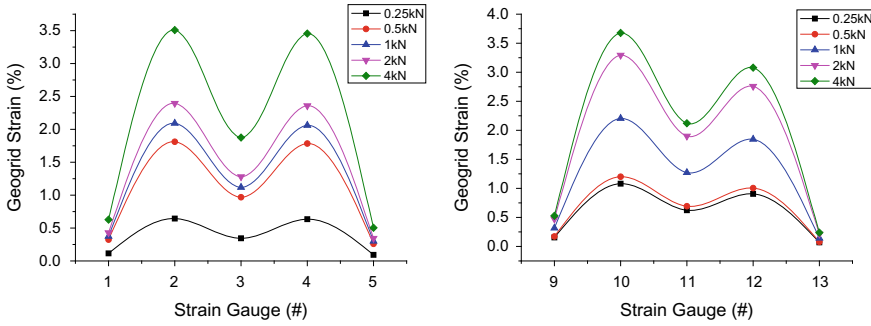


Fig. 6 Geogrid strain distribution in RMC failure test

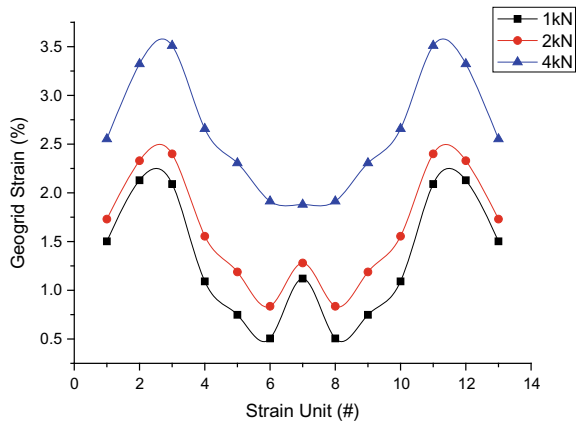
top, which is about 1.0% for the lower layer. When the elastic modulus of the geogrid is constant, the tensile force of the geogrid under the vertical load can be obtained.

2.4 Geogrid Tension Situation

According to the above test data, it can be found that there is a certain relationship between the geogrid strain and the vertical pressure. With data processing, the distribution of the geogrid strain can be further refined and shown in Fig. 7.

The tensile strength of the geogrid used in this test is 15kN/m (60 MPa), and therefore, the tensile force of the geogrid can be calculated. Under the vertical load of 1 kN, 2 kN, and 4 kN, the total geogrid stress at the pile top position is 672 kPa, 768 kPa, and 1128 kPa, respectively, and the total geogrid stress at 0.5 D from the edge of the pile top is 1254 kPa, 1440 kPa, and 2106 kPa, respectively.

Fig. 7 Fitting curve of geogrid strain



Through the simple calculation, the geogrid tensile force at the position of the pile top is 3.36 kN/m, 3.84 kN/m, 5.64 kN/m respectively, and the tensile force at the 0.5 D from the edge of the pile top is 6.27 kN/m, 7.20 kN/m, and 10.53 kN/m, respectively. The existing equation [11] for the calculation of the geogrid tensile force is:

$$T = \frac{w_T(s - a)}{2} \sqrt{1 + \frac{1}{6\varepsilon}} \quad (1)$$

where T is the tensile force of geogrid, a is pile cap diameter, s is pile spacing, and w_T is uniformly distributed load on the geogrid. For this test, take $w_T = 20.6$ kPa, $(s-a) = 0.12$ m, $\varepsilon = 2.09\%$, the tensile force at the position of the pile top can be calculated as 3.70 kN/m, 4.56 kN/m, 6.08 kN/m, respectively, under the vertical load of 1 kN, 2 kN, and 4 kN. Compared with the actual tensile force values of 3.36 kN/m, 3.84 kN/m, and 5.64 kN/m measured in this test, it can be found that the geogrid tensile force calculated by the standard calculation is slightly larger than the actual tensile force at the pile top. There is a highly similar consistency between these two results, which can prove the correctness of this test. However, the existing standard calculation method is relatively ideal, which assume that the deformation of the geogrid is parabolic, without considering the actual strain distribution law of the geogrid.

Therefore, in the calculation of the stress of the RMC geogrid in the future, the maximum tensile force of geogrid (at 0.5–0.75D from the edge of the pile top) should be mainly controlled and checked, so as to control the settlement of the GRPS composite foundation within a reasonable range. According to the data of this test, the existing standard calculation method can be partially modified to calculate the maximum reinforcement tensile force.

$$T_{0.5D} = \eta \times \frac{w_T(s - a)}{2} \sqrt{1 + \frac{1}{6\varepsilon}} \quad (2)$$

where η is the correction coefficient 1.65, which is related to the geogrid strength and vertical stress, and the other physical meanings are the same as above. Considering the general GRPS composite foundation loading situation, the above Eq. 2 can be expanded to:

$$T_{0.5D} = \eta \times \frac{W_T(s - a)}{2a} \sqrt{1 + \frac{1}{6\varepsilon}} \quad (3)$$

where W_T is the vertical stress (kPa) assumed by soil between adjacent two piles.

3 The Maximum Vertical Stress of a Single Pile

By fitting the FEA modeling simulation data, the maximum vertical stress P_v of a single pile can be obtained, and the following equation can be obtained:

$$P_v = 527h^{0.85}d^{0.50}\tan\varphi^{1.94}E_1^{0.35} \quad (4)$$

where h is the thickness of the RMC, d is the pile diameter, φ is the internal friction angle of the cushion material, E_1 is the elastic modulus of the cushion material.

The typical working conditions were taken for verification, in which the geogrid thickness was 0.6 m, the pile diameter was 0.5 m, the internal friction angle of the cushion material was 30° , and the elastic modulus of the cushion material was 100 MPa. The maximum vertical stress of single pile is calculated as 416.8 kPa, which is quite close to the simulation results. Table 2 shows the comparison between equation calculated values and simulation values under ten typical working conditions.

This equation can provide a more accurate calculation of the maximum vertical stress of a single pile in the GRPS composite foundation under normal conditions. The maximum difference error is about 25%, and the result is within an acceptable range. This equation has certain applicability, the thickness of the RMC should be 0.5–0.7 m, and the pile diameter should be 0.35–0.75 m. There is no special requirement for the elastic modulus of cushion material and internal friction angle, the general engineering measured valued can be used.

After considering the influence of geogrid strength, Eq. 4 can be further optimized as follows:

Table 2 Calculation of maximum vertical stress of single pile

Working case	h	d	$\tan\varphi$	E	Calculation result	Simulation result	Percentage difference
No	m	m	–	MPa	kPa	kPa	%
1	0.6	0.375	0.58	100	360.95	478.79	24.61
2	0.6	0.75	0.58	100	510.46	662.16	22.91
3	0.6	0.5	0.36	100	170.29	219.33	22.36
4	0.6	0.5	0.47	100	275.39	285.19	3.44
5	0.6	0.5	0.58	100	416.79	416.75	0.01
6	0.6	0.5	0.70	100	605.99	637.81	4.99
7	0.6	0.5	0.84	100	860.84	1130.58	23.86
8	0.6	0.5	0.58	80	385.48	384.38	0.29
9	0.6	0.5	0.58	120	444.25	441.58	0.61
10	0.6	0.5	0.58	150	480.34	480.50	0.03

Table 3 Geogrid strength correction of maximum vertical stress of single pile

Tensile strength (kN/m)	Geogrid modulus (MPa)	Correction coefficient (β)	Vertical stress (kPa)
15.00	60.00	1.00	420.51
20.00	80.00	1.33	560.68
25.00	100.00	1.67	700.85
30.00	120.00	2.00	841.02
35.00	140.00	2.33	981.19
40.00	160.00	2.67	1121.36

$$Pv = 527h^{0.85}d^{0.50}\tan\varphi^{1.94}E_1^{0.35}\times\beta \quad (5)$$

where β is the strength modification value of geogrid. Taking the above typical working conditions as an example, the maximum vertical stress of a single pile is 416.8 kPa, seen from Table 3 for details.

In the construction design process, the vertical stress required by a single pile can be determined first, and then the parameters of each part of the RMC (cushion thickness, pile diameter, cushion material elastic modulus, internal friction angle, and geogrid strength) can be selected according to this equation to satisfy the vertical stress requirements of a single pile in the GRPS composite foundation.

4 Conclusions

1. For the modeling of the failure state of the geogrid, FEA modeling is carried out. The deformation characteristics of the reinforced body in the failure state are pointed out. The damage of the geogrid mainly occurs at the top of the pile. The failure modes mainly include the piercing failure at the pile top and the shear failure near the edge of the pile top. The strain and tensile force of the geogrid shown an 'M' form distribution.
2. The change of the elastic modulus of the cushion material has little effect on the failure mode of the geogrid. When the thickness of the cushion is small, the geogrid is mainly shear-damaged. When the cushion thickness increases, the geogrid shows piercing damage and shear failure at the pile top.
3. With the increase of either the contact area or the internal friction angle of the cushion material, the main failure mode of the geogrid changed from the piercing damage at the pile top to the shear failure near the edge of the pile top. In the failure mode, the vertical displacement of the geogrid shows a parabolic shape, and as the contact area increases, the parabolic shape gradually becomes gentle.

4. Based on the research achievements in this paper, a combination of both numerical simulation and laboratory testing is used to further systematically study the factors affecting the deformation of the RMC and the failure characteristics of the geogrid. The research results show that it is reasonable to use a geogrid permanent strain of 2% as the basis for judging the failure of the RMC, and the effective settlement can be controlled within a reasonable range. At the same time, the position of the maximum tensile force of the reinforced body is pointed out and a simplified calculation equation is derived.
5. The maximum vertical stress of single pile in the failure state of the grid is further analyzed, and an empirical calculation equation with good engineering applicability is proposed. The equation is further optimized by considering the strength of the reinforced body. The reliability and effectiveness of the equation are verified by laboratory tests.




Acknowledgements This work was funded by the National Natural Science Foundation of China (Grant 41731288, U1834206), the Science and technology research and development plan of China National Railway Group Co., Ltd (Grant 2017G008-J) and the Foundation of China Academy of Railway Sciences Co., Ltd. (Grant 2020YJ048).

References

1. Zhou J, Ye YS, Cai DG (2007) Analysis of calculation method for foreign geosynthetic reinforced pile supported embankments. *China Railway Sci* 28(2):1–6
2. Ohkubo T, Asada S, Karube D (1996) A study on the reinforcing effects of geogrids over laid on pile group for the embankment foundations. *Earth Reinforcement*, 641–646
3. Cai DG, Ye YS, Zhang QL et al (2009) Field test study on the mechanical behaviors of the geosynthetic-reinforced pile-supported embankment and the deformation of the reinforced bedding. *China Railway Sci* 30(5):1–8
4. Low BK, Tang SK, Choa V (1994) Arching in piled embankments. *J Geotech Eng* 120(11):1917–1938
5. Cai DG, Yan HY, Dong L et al (2008) Numerical analysis of composite foundation with different cushion structure. *Railw Eng* 2008(1):48–52
6. Cai DG, Yan HY, Ye YS et al (2011) Model study on arch effect and bedding force of geosynthetics reinforced and pile supported embankment. *J China Railway Soc* 33(11):85–92
7. Cai DG, Yang GT, Ye YS et al (2013) Calculation method for the mechanical force of reinforced bedding in the geosynthetics reinforced and pile supported embankments of high-speed railway. *China Railway Sci* 34(5):1–5
8. Cai DG, Ye YS, Yan HY et al (2010) Numerical analysis on the mechanical properties of geosynthetic reinforced and pile supported embankment. *China Railway Sci* 31(3):1–8
9. Ye YS, Cai DG, Yan HY et al (2009) Model test method of geosynthetic net-reinforced and CFG pile-supported subgrade structure. *Railw Eng* 2009(7):40–43
10. Li TF, Ye YS, Zhang QL et al (2017) Deformation characteristics of reinforced bedding in the geosynthetics reinforced and pile supported structure of high-speed railway. *Railw Eng* 2017(1):40–43
11. Rogbeck Y, Alén C, Franzén G et al (2003) Nordic guidelines for reinforced soils and fills. Nordic Geosynthetic Group of the Nordic Geotechnical Societies, Nordic Industrial Fund

Structural Pavement Rehabilitation with Recycled Materials in a Circular Economy Approach



A. C. Freire , E. Correia, J. Neves , I. Martins, A. J. Roque, M. I. M. Pinto , C. Ferreira, and A. Martins

Abstract The construction sector accounts for about 34% of the total waste produced in the European Union (EU), with the transportation infrastructure sector, namely the road construction, having a huge impact on waste generation. Asphalt pavements stand for more than 80% of EU's road network with about 950 billion tons of asphalt being used. A great investment is made every year in maintenance and rehabilitation (M&R) with a view to maintain the minimum levels of service. Being aware that pavement materials are non-renewable resources, it is urgent to ensure cost-effective M&R solutions that promote the transition to new economic models. The overall increase in the use of recycled materials is a main goal for achieving a

A. C. Freire (✉) · I. Martins · A. J. Roque
Laboratório Nacional de Engenharia Civil, Avenida do Brasil 101, 1700-066 Lisboa, Portugal
e-mail: acfreire@lnec.pt

I. Martins
e-mail: imartins@lnec.pt

A. J. Roque
e-mail: aroque@lnec.pt

E. Correia
Infraestruturas de Portugal, Praça da Portagem, 2809-013 Almada, Setúbal, Portugal
e-mail: eugenia.correia@infraestruturasdeportugal.pt

J. Neves
CERIS, Instituto Superior Técnico, Universidade de Lisboa, Avenida Rovisco Pais 1, 1049-001 Lisboa, Portugal
e-mail: jose.manuel.neves@tecnico.ulisboa.pt

M. I. M. Pinto
Department of Civil Engineering, CEMMPRE, Rua Luís Reis Santos, Pólo II, University of Coimbra, 3030-788 Coimbra, Portugal
e-mail: isabelmp@dec.uc.pt

C. Ferreira
Ouzo Engenharia, Rua Escultor Barata Feyo 140, 2º, Sala 2.11, 4250-076 Porto, Portugal
e-mail: claudia.ferreira@ouzo.pt

A. Martins
Infraestruturas de Portugal, Praça da Portagem, 2809-013 Almada, Setúbal, Portugal
e-mail: anabela.martinsa@infraestruturasdeportugal.pt

better efficiency in the technical, economic and environmental management of pavement materials, by making it possible to preserve natural resources for the generations to come and to reduce waste disposal. This approach aims to promote a circular economy, as opposed to a linear economy, by changing the material consumption pattern. The main objectives of this paper are to analyze and compare approaches regarding the different methodologies proposed for structural pavement rehabilitation with recycled materials, by considering the implementation of recycling processes in M&R activities during the asphalt pavement life cycle. The potential application of rehabilitation methodologies using recycled materials will be assessed in terms of production quantities and costs, in comparison with traditional M&R solutions using primary raw materials.

Keywords Recycled materials · Circular economy · Maintenance and rehabilitation

1 Introduction

A great investment is done every year in pavement maintenance and rehabilitation (M&R) with a view to maintain the minimum levels of service. Being aware of the fact that used pavement materials are non-renewable resources, it is urgent to ensure cost-effective M&R solutions that promote the transition to new sustainable economic models.

Based on a real case study, different structural pavement rehabilitations using on-site recycling technologies will be established and compared. The assessment of the potential application of these optimized rehabilitation geomaterials (including hydraulically bound materials and asphalt mixtures) to recycle in road embankments and structural layers is of major importance.

The main objectives of this paper are to present and analyze the best approaches regarding different methodologies for performing structural pavement rehabilitation using recycled materials. For the purpose, both the implementation of recycling processes in M&R activities during the asphalt pavement life cycle was taken into consideration, by having in mind a circular economy approach. Recommendations for the practical implementation will be presented.

2 Recycling Strategies

Extraction and consumption of natural resources are expected to double by 2060 compared to 2011, according to OECD [1]. Furthermore, there has been a recent decrease in the production of resources around the world, including in G20 countries (UNEP/IRP, [2, 3]). The continuous increase in both the use and the consumption of resources, due to globalization and economic development, is highly responsible for

the increased amount of waste production and consequent environmental impacts. Steffen et al. [4] pointed out that to achieve the *Sustainable Development Goals* in our planet, in such a way that the developed activities are within the safe operating space, it is essential to control the meteoric growth in the consumption of natural resources, to magnify the use of secondary resources, and finally, to move toward an increased use of a service-based economy. These actions will definitely lead to a real and effective transition into a circular economy and society.

The construction sector accounts for about 34% of the total waste produced in the EU, and the transportation infrastructure sector, in particular the road construction, has a huge impact on waste generation. Asphalt pavements stand for more than 80% of EU's road network with about 950 billion tons of asphalt being used. Knowing that governments of many countries dedicate large amounts of money to M&R activities on roads and that pavement materials are non-renewable resources, after the transition to new economic models, an effective resource management must be implemented with a view to contribute to reduce the speed at which natural resources are depleted.

Ambitious resource efficiency and greenhouse gas emission (GHG) abatement policies in the G7 could have significant impacts, namely a 28% reduction in natural resources used globally by 2050, in combination with ambitious global actions on climate change. Furthermore, stabilizing per capita resources used at current levels and reducing GHG by an additional 15% to 20% by 2050, with global emissions in 2050 falling to 63% below 2015 levels, and emissions in G7 countries in 2050 falling to 74% below 2015 levels [4].

The overall increased use of recycled materials is a main goal for achieving a better efficiency in the technical, economic, and environmental management of pavement materials, by making it possible to preserve the natural resources for the generations to come and to reduce waste disposal. This approach is intended to promote a circular economy, as opposed to a linear economy, by changing the material consumption pattern.

Cabrera et al. [5] presented different asphalt pavement recycling techniques, namely the full-depth renovation, the hot in-place recycling, the cold in-place recycling, and the hot recycling, which can be employed to contribute to a circular economy approach:

- The full-depth renovation is performed with a specific binder by an in-situ procedure that consists of grinding up the existing bituminous and granular layers, mixing, and replacing them in the subgrade soil. Sometimes, the application of this technique aims to produce a stabilized base course, which will help correct some road base problems.
- The hot in-place recycling is usually applied to the pavement layer at a depth of up to 3 cm. The top bituminous layer is heated, softened and then scarified. Afterward, an asphalt emulsion or any other recycling agent is added to the mixture, and one of the referred procedures is applied, then new hot mixture is added.
- The cold in-place recycling is also an in-situ rehabilitation technique where the existing pavement is treated to a depth of 5 to 10 cm. The bituminous pavement layers are milled, and the obtained material, reclaimed asphalt pavement (RAP),

is mixed with an asphalt emulsion or an emulsified recycling agent, being then spread and compacted to produce a new pavement layer. Usually, the cold recycled bases require a new bituminous surface layer.

- The hot recycling considers the addition of RAP to new aggregates and to new bitumen and rejuvenator to produce a hot bituminous mixture. While batch type hot mix plants can be used, drum plants are the ones normally employed to produce the recycled bituminous mixtures. The placement and compaction equipment and procedures are the same as those of new hot bituminous mixture constructions. Once removed and processed, the pavement material becomes RAP, which contains valuable asphalt binder and aggregate. Due to the increased demand and the limited aggregate and binder supply, the producers have begun using RAP as a valuable component. Although several factors influence the use of RAP in asphalt pavement, the two primary factors are economic savings and environmental benefits.

Gu et al. [6] report that cold in-place recycling can use up to 100% of RAP. Typically, asphalt overlays on top of the recycled asphalt pavement are used for high traffic volume pavements as they have a significant impact on pavement performance.

Hajj et al. [7] reviewed the performance of both highway and airfield pavements with hot mixed recycled asphalt. They observed that highway pavements with 15–20% recycled asphalt generally have a performance as good as virgin asphalt pavements with similar environmental and loading conditions. Pavements containing 20–50% recycled asphalt, in different projects with roughly the same conditions, showed a similar performance to that of conventional pavements for a period of 6 to 9 years after construction.

Thenoux et al. [8] compared three different pavement rehabilitation alternatives available in Chile, by using an energy consumption methodology. They did not consider some factors also identified by them as very important, such as the impact of road users and the possible need for lateral works (necessary for asphalt overlay). For determining energy consumption, these authors defined a methodology taking into account a number of aspects of a typical road rehabilitation project:

- Identification of the conditions of the existing pavement, including the structural condition of the pavement, traffic prediction, soil support capacity, climate (this data helps design pavement solutions for the rehabilitation alternatives);
- Design of the pavement solutions for the rehabilitation alternatives under study;
- Evaluation of the resources needed for the construction procedure to be used in each rehabilitation alternative, including the amount of materials removed and produced for the construction;
- Consideration of all activities necessary to produce each resource;
- Calculation of the energy consumption for each construction resource. The energy supplies (machinery performance, consumption of diesel, gas, or electricity) are converted to equivalent energy contents and afterward to the energy necessary to produce a volumetric unit of each resource (MJ/m^3);
- Calculation of the total energy consumption (MJ/m^3) for each rehabilitation alternative.

Yang et al. [9] pointed out that the environmental study must associate, not only the processing of the materials but also the removal activity, which gives an automatic credit to recycled materials. When comparing ten asphalt recycled mixtures with those using only primary raw materials, the authors found a clear trend in decreasing energy and global warming potential for higher asphalt binder replacements.

For airfield pavements, a study was conducted on 35–60% recycled asphalt mixtures [7]. The reduced number of cases where this technique was used and the conjugation of several different parameters at once (times of service, climatic conditions, amounts of recycled asphalt and recycling binders) limited significantly the analysis. However, in general, the use of such a high percentage of recycled asphalt provided the pavement with a good resistance to rutting but with a decreased durability in its properties.

The properties of recycled asphalt pavements are highly dependent on the properties of their constituent materials, including aggregate type, quality and size, binder properties, etc. Furthermore, they are affected by the previous maintenance activities on the pavement [7].

In Europe, the Member States follow different approaches regarding the administration of road networks. In some countries, like Greece, where road management revolves around economic factors: The sole basis for pavement construction is the initial cost, which rules out the use of concrete roads and favors asphalt roads (Anastasiou et al. [10]).

In other countries, like UK, the economic and environmental pillars of sustainability support the benefits of M&R over new road construction, and hence, recommendations on the maintenance of long-life flexible pavements have been developed (Merrill [11]).

The European DIRECT-MAT research project emphasized the need to gather information on pavement structure, material properties, and additionally, to perform cost-efficiency and environmental assessments before choosing the best approach for road management (Mollenhauer and Gáspár [12]).

Some case studies also highlight that M&R needs to integrate both the analysis of materials and the techniques used. As an example, the comparison between CO₂ emissions from concrete pavements with a high content of alternative materials and CO₂ emissions from asphalt pavements demonstrated the benefits of the former (OECD [1]). In another research, carried out in Slovenia, comparison of the techniques of cold in-place recycling of pavements to a traditional approach, in which removed materials were replaced by primary raw materials, did not show any difference in GHG between the two methodologies, although it emphasized the relevance of local climate in pavement design when choosing the most adequate rehabilitation technique (Turk et al. [13]).

A life cycle approach has been increasingly used as an alternative methodology to assess the sustainability of materials and procedures linked to pavements since their construction until their effective end of life. Within this framework, life cycle assessment (LCA) of pavements shows that construction and maintenance procedures consume much less energy and emit much lower quantities of GHG when compared to the road traffic component (Chappat and Bilal [14]). Even so, some LCA by

the analysis of different road rehabilitation techniques have identified the factors responsible for the higher energy and GHG demand of plain cement concrete paving materials and procedures, followed by hot mix asphalt paving, the cold in-place recycling being the least energy consuming procedure.

In Portugal, the module strategy evaluation tool (SET) of the pavement performance model, developed for the Portuguese main road concessionaire, enables different M&R multiannual approaches based on minimum quality level and/or minimization of total costs (Ferreira and Picado Santos [15]). However, new challenges, namely in the field of the use of alternative materials, require introducing some changes in M&R methodology for.

3 Methodology

The decision for pavement rehabilitation should be based on a preliminary and adequate assessment of the condition of the existing pavement (visual inspection and prospection, bearing capacity and functional evaluation), complemented by other inventory data related to design, construction and traffic. If the existing pavement requires a structural rehabilitation, desirably, the rehabilitation design should include the use of recycled materials and techniques. For the purposes of this paper, Fig. 1 presents the proposed general flowchart of pavement rehabilitation methodology over the life cycle of the road infrastructure. Before establishing different alternative solutions, further information on existing pavements should be obtained: integrity of asphalt mixtures (visual inspection), bearing capacity (deflectometer tests), and irregularity (profilometer tests). Depending on the identified pavement condition, three different solutions for pavement rehabilitation may be considered:

- Pavement with bearing capacity and asphalt mixtures presenting medium to high degradation—*reinforcement with a new surface course*;
- Pavement with bearing capacity and asphalt mixtures presenting medium to high degradation, as well as transversal and longitudinal irregularity—*reinforcement and regularization of asphalt layers*;
- Pavement without bearing capacity—*reconstruction by total replacement of all layers since the foundation to the surface course*.

For each solution, two main alternatives should be compared:

- Pavement rehabilitation based on the linear economy model by considering the exclusive application of primary raw aggregates;
- Pavement rehabilitation based on the circular economy model by considering the use of recycled materials and innovative techniques.

For the pavement rehabilitation situation based on a circular economy model, the availability of recycled materials and techniques is fundamental (see Fig. 1). However, RAP production is invariably present in each rehabilitation solution for asphalt pavements due to the milling of the top asphalt layers. This means that the

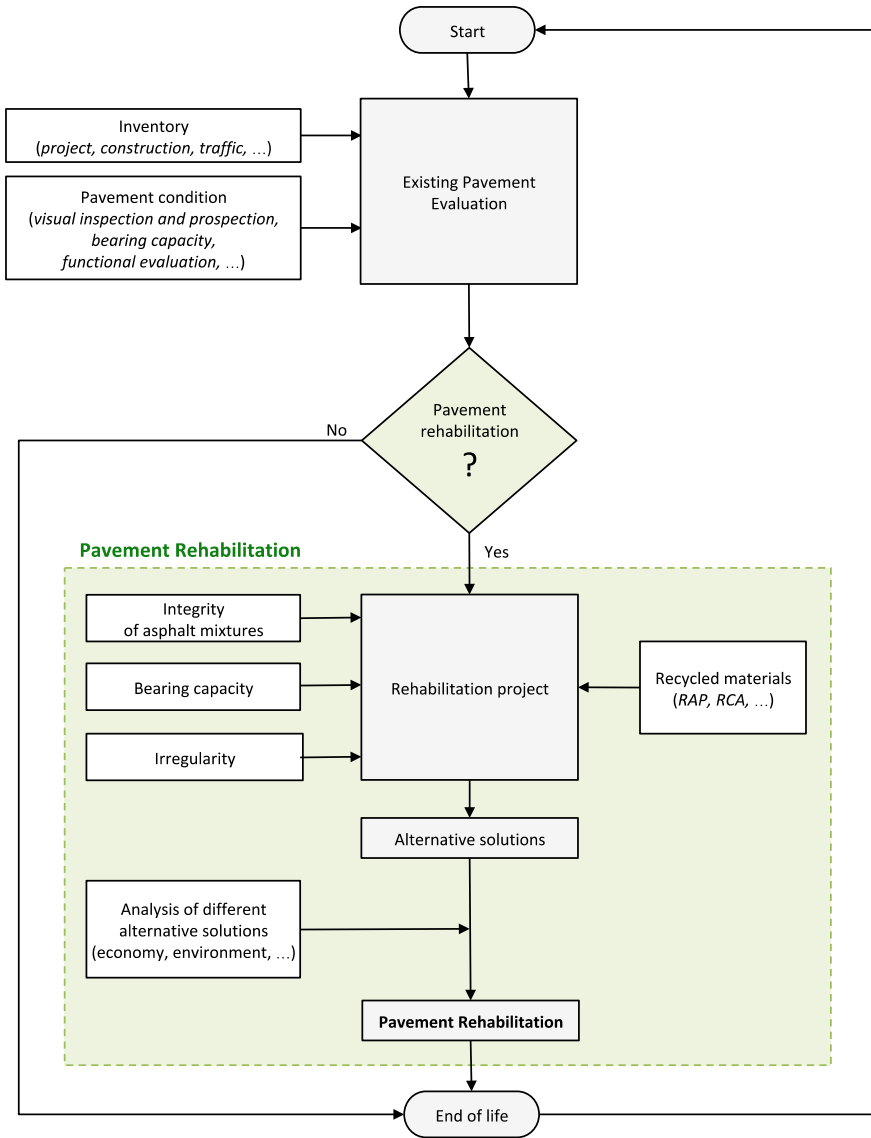


Fig. 1 Flowchart of pavement rehabilitation methodology

pavement under rehabilitation can be considered as a linear quarry of recycled materials with an enormous potential to be used in new asphalt mixtures. If the pavement does not have enough bearing capacity, it will be necessary to carry out its reconstruction by total replacement of all layers since the foundation to the surface course. The new foundation and the unbound granular layers can be recycled and can also incorporate other recycled materials (e.g., RAP and recycled concrete aggregates—RCA).

In order to increase the bearing capacity, both the base and the sub-base layers can be treated with hydraulic binders. In summary, two main strategies can be considered for the structural rehabilitation of pavements, including the one based on a circular economy approach for the use of recycled materials:

- Pavements with bearing capacity: Recycled materials can be used in the production of new asphalt mixtures. Construction and demolition waste (e.g., RAP and RCA) can be used as aggregates in the design of the asphalt mixtures, with the possible incorporation of binder rejuvenators and other additives.
- Pavements without bearing capacity: Recycled materials can be used in the base and sub-base layers, possibly with hydraulically bound mixtures, by the application of cold in-place recycling; the production of new asphalt mixtures may also incorporate several recycled materials.

The analysis of alternative solutions should be entirely supported by common evaluation tools such as life cycle assessment (LCA) and life cycle cost analysis (LCCA). LCA is a procedure to calculate the lifetime environmental impacts of the pavement rehabilitation solution. LCCA is intended to estimate the overall costs of rehabilitation alternatives and to select the most adequate design that ensures the lowest overall cost of ownership, by simultaneously guaranteeing the quality and compliance of the function requirements. However, road administrations have limitations to the implementation of these most complex and powerful tools of analysis. Alternatively, these entities can implement more simplified analysis tools based on economic and environmental criteria. This paper, based on a real case study, describes a simplified analysis by considering technical, economic, and environmental factors to support the decision on the best alternative solution for the pavement rehabilitation.

The main goal of the proposed simplified methodology is to demonstrate that the implementation of pavement rehabilitation techniques using recycled materials, and based on a circular economy approach, is the most advantageous and sustainable strategy and can be considered at design level. Using a simplified analysis, it is possible to overcome the limitation of resources in order to make the best decision.

4 Case Study

The case study to which these two rehabilitation approaches were applied refers to the rehabilitation of a section of the national road EN 4, intersection with E118/near Montijo (km 18 + 750) and intersection with EN10/Pegões (km 44 + 257). According to the National Highway Plan 2000 (PRN2000) [16], this road section belongs to the concession of *Infraestruturas de Portugal, S.A.* (IP) and is part of the Complementary Network of the National Road Network [17], having a total length of 25.5 km.

The pavement section consists of a two lane road (1×2), with a carriageway 7.0 m wide in general and berms with different widths along the section (0.50 m to 1.00 m), being sometimes unpaved. Along the section, there are eight structures (1 viaduct and 7 pontoons).

Table 1 Average annual daily truck traffic (AADTT) classes

Pavement section	2018	2028
km 18 + 662 – km 42 + 172 (zone 1)	T4	T4
km 42 + 172 – km 44 + 257 (zone 2)	T3	T3

Legend T3—500–800 AADTT; T4—300–500 AADTT, [18]

The traffic volume is considered to be not significant, although having a high percentage of heavy vehicles (above 15%). The values of heavy traffic for the commissioning year (2018) and horizon year (2028) are presented in Table 1, according to the AADTT values and the ranges established by *Infraestruturas de Portugal, S.A. (IP)* [18].

According to the available information in CENOR [17], it can be concluded that the pavement is flexible. The results from visual inspection and rotational boreholes performed on the pavement indicate that the latter has undergone many rehabilitations during its design life (namely in 1946, 1956, 1986, 1989, 2002, and 2010), which has led to a high heterogeneity in the pavement structures. The visual inspection and rotational boreholes procedures are defined by *Infraestruturas de Portugal, S.A. (IP)* [19].

From the visual inspection carried out in the characterization phase, it was observed that, in general, the pavement presented degradations resulting from a high level of fatigue. A few sections with reasonable and good behaviors were also identified.

The degradations observed were, among others, crocodile cracking, transverse and longitudinal cracks, ruts and deformations due to tree roots.

From the IRI evaluation done in both directions, and according to CETO [19], the section under rehabilitation was generally classified as “Bad.” After an IRI statistical analysis, by every 500 m extension and by direction, it was concluded that about 80% of the extension could be classified as “Bad.”

The thicknesses of the pavement layers of EN 4 and of the foundation pavement section, obtained from the rotation boreholes and wells performed in the pavement, presented hot bituminous layers at the central lane from 0.05 to 0.20 m, cold bituminous mixture layers with an average thickness of 0.09 m and crushed stone aggregate layers with 0.18–0.30 m, according to CENOR [20].

5 Results and Discussion

In order to evaluate the major impacts of both the linear and the circular economy approaches, in terms of pavement rehabilitation solutions, different pavement structures were considered in the design phase.

For a linear approach regarding pavement rehabilitation design, and after complete evaluation of the pavement conditions, two major solutions were considered:

- For pavement zones with adequate bearing capacity and low to severe degradation, and in some situations with serious transverse and longitudinal irregularities: some milling of existing bituminous layers (0.13 m) and application of new bituminous layers (AC20reg35/50 (0.06 m) + AC20bin35/50 (0.04 m) + AC10surf (0.03 m));
- For pavement zones without bearing capacity: total removal of the damaged layers (bituminous mixtures and granular materials) and full reconstruction of paving structures for the two traffic classes T3 and T4 (ABGE (0.20 m) + AC32base35/50 (0.09 m + 0.10 m) + AC 14bin 35/50 (0.04 m) + AC10surf (0.03 m)) and (ABGE (0.20 m) + AC20base35/50 (0.09 m + 0.09 m) + AC 14bin 35/50 (0.04 m) + AC10surf (0.03 m)), respectively.

On the other hand, for the circular economy approach, i.e., promoting rehabilitation solutions with high percentages of recycled pavement materials, two different solutions were considered:

- For pavement zones with adequate bearing capacity and low to severe degradation, and in some situations with serious transverse and longitudinal irregularities: milling of existing bituminous layers (0.07 m) and application of new bituminous layers (AC20reg35/50/AC20reg 10/20 (0.07 m + 0.07 m) + SMA11surfPMB45/80–65 (0.04 m));
- For pavement zones without bearing capacity: total removal of the damaged layers (bituminous mixtures and granular materials) and full reconstruction of paving structures for the T4 traffic class (in-situ base course recycled with cement (0.30 m) + Bituminous mixture with rubber (0.04 m) and SMA 11surfPMB45-80–65 (0.04 m).

Table 2 shows a comparative analysis of the two M&R solutions, considering both the linear economy and the circular economy approaches. The economic and

Table 2 Evaluation of pavement solutions

Evaluated parameter		Linear economy approach	Circular economy approach
Economic		About 208 k€/km	About 100 k€/km
Environmental	Milling and landfill disposal	174.291 ton	10.067 ton
	New bituminous mixtures	117.807 ton	46.892 ton
	Recycling rate	0%	74%
Techniques	Equipment	Traditional	Specific
	Constructive process	Traditional	Complex
	Construction yield	532 ton/day/team; 2913–5989m ² /day	1626 m ² /day/team
	Healing time	0 days	7 days
	Quality control	Traditional	More demanding

environmental aspects, as well as the application techniques, are also compared. The same table clearly demonstrates the advantages associated with the circular economy approach; as refers to the paving cost, the value for the circular economy is about half of the value for the linear economy approach. Regarding the environmental aspects, a recycling rate of 74% was reached, with a major reduction in landfill disposal.

6 Final Considerations

This document presents a general flowchart of a pavement rehabilitation methodology over the life cycle of the road infrastructure and defines the actions to be performed to promote M&R under a circular economy approach.

A case study regarding the EN4 pavement was presented, which made it possible to perform a comparative evaluation of the major impacts of both the linear and the circular economy approaches in terms of pavement rehabilitation solutions with different pavement structures, considered in the design phase.

The results demonstrate that the implementation of pavement rehabilitation techniques using recycled materials and based on a circular economy approach is the most advantageous and sustainable strategy and can be considered at design level. Using a simplified analysis, it is possible to overcome the limitation in resources toward making the best decision.

References

1. OECD (2018) Global material resources outlook to 2060—Economic drivers and environmental consequences. OECD Publishing, Paris
2. UNEP/IRP (2016) Global material flows and resource productivity. an assessment study of the UNEP international resource panel. In: Schandl H, Fischer-Kowalski M, West J, Giljum S, Dittrich M, Eisenmenger N, Geschke A, Lieber M, Wieland HP, Schaffartzik A, Krausmann F, Gierlinger S, Hosking K, Lenzen M., Tanikawa H, Miatto A, Fishman T (eds) Paris, United Nations Environment Programme
3. UNEP/IRP (2018) Resource efficiency for sustainable development: key messages for the group of 20. United Nations Environment Programme, International Resource Panel
4. Steffen W, Richardson K, Rockström J, C’Vornell SE, Fetzer I, Bennett EM, Biggs R, Carpenter SR, de Vries W, de Wit CA, Folke C, Gerten D, Heinke J, Mace GM, Persson LM, Ramanathan V, Reyers B, Sörlin S (2015) Planetary boundaries: guiding human development on a changing planet. *Science* 347(6223):1259855
5. Cabrera MB, Satomi T, Takahashi H (2017) Study on recycling of waste asphalt blocks containing roadbed materials using new screenless separation equipment with a vibration device. *Int J Pavement Res Technol* 10(3):228–244
6. Gu F, Ma W, West RC, Taylor AJ, Zhang Y (2019) Structural performance and sustainability assessment of cold central-plant and in-place recycled asphalt pavements: a case study. *J Clean Prod* 208:1513–1523
7. Hajj EY, Sebaaly PE, Kandiah P (2008) Use of reclaimed asphalt pavements (RAP) in airfield HMA pavements. AAPT Project No. 05–06, University of Nevada, Reno, USA

8. Thenoux G, González A, Dowling R (2007) Energy consumption comparison for different asphalt pavements rehabilitation techniques used in Chile. *Resour Conserv Recycl* 49:325–339
9. Yang R, Kang S, Ozer H, Al-Qadi IL (2015) Environmental and economic analyses of recycled asphalt concrete mixtures based on material production and potential performance. *Resour Conserv Recycl* 104:141–151
10. Anastasiou EK, Liapis A, Papayianni I (2015) Comparative life cycle assessment of concrete road pavements using industrial by-products as alternative materials. *Resour Conserv Recycl* 101:1–8
11. Merrill D (2005) Guidance on the development, assessment and maintenance of long-life flexible pavements. TRL Report TRL639 prepared for Highways Agency, Quarry Products Association, and Refined Bitumen Association
12. Mollenhauer K, Gáspár L (2012) Synthesis of European knowledge on asphalt recycling: options, best practices and research needs. In: 5th Eurasphalt & Eurobitume Congress, Istanbul, 472
13. Turk J, Mauko PA, Mladenovič A, Cotič Z, Jurjavčič P (2016) Environmental comparison of two alternative road pavement rehabilitation techniques: cold-in-place-recycling versus traditional reconstruction. *J Clean Prod* 121:45–55
14. Chappat M, Bilal J (2003) The environmental road of the future: life cycle analysis, energy consumption & greenhouse gas emissions. Colas Group
15. Ferreira A, Picado Santos L (2008) Contributions to the development of the portuguese road administration's pavement management system. In: 3rd European pavement and asset management conference, Coimbra
16. National Highway Plan 2000 (PRN2000) Ministério do Equipamento, do Planeamento e da Administração do Território. Decreto Lei 222/98 de 17 de Julho (1998). (in Portuguese)
17. CENOR (2016a) EN 4—Interseção com a EN 118 prox. de Montijo (km 18+750) e Interseção com a EN10 (Pegões) (km 44+257) – Projeto de execução. P3 – Pavimentação. Memoria Descritiva e Justificativa, março (in Portuguese).
18. JAE (1995) Manual de Conceção de Pavimentos para a Rede Rodoviária Nacional. Infraestruturas de Portugal, ex-JAE (in Portuguese)
19. CETO (2014) Estradas de Portugal, SA, Caderno de Encargos Tipo Obra (in Portuguese)
20. CENOR (2016b) EN 4—Interseção com a EN118 prox. De Montijo (km 18+750) e Interseção com a EN10 (Pegões) (km 44+257) – Projeto de execução. P21 – Plano de Prevenção e Gestão de Resíduos de Construção e Demolição, março (in Portuguese).

Crushed Rock Geopolymer as a Future Road Construction Material: An Evaluation of Compaction and Strength Characteristics



Peerapong Jitsangiam, Teewara Suwan, Korakod Nusit,
Prinya Chindapasirt, and Sararat Kwunjai

Abstract To be more sustainable in the road construction industry, the rock-based geopolymer concept should be applied with an aim to create a geopolymer-based road structural layer. This research episode concentrated on the primary study of compaction characteristics of crushed rock geopolymer (CR-GP) in conjunction with its unconfined compressive strength (UCS) and micro-observations through XRF and XRD. The new grain size distribution curve, namely practical grading, was produced for use as a prime material in CR-GP. Especially, CR-GP is a mixture of CR practical grading (B) and liquid alkaline activator (L) of Na_2SiO_3 (SS) and NaOH (SH) with a concentration value of five molar. The SS/SH ratio of 0.67 was also used. Test results showed that the compaction curves of CR-GP can be established as the bell curve with a peak point. The modified compaction curve showed higher maximum dry density (MDD) of 2210 kg/m^3 and optimum liquid alkaline activator content (OLC) of 11%. It was found that higher compactive efforts of the modified compaction, higher densification than that of the standard compaction, corresponding to the compaction theory in soil mechanics. CR-GP having practical grading achieved higher UCS up to the minimum requirement of the normal cement-stabilized road base as a benchmark material. Based on the micro-observation of this research, an applicable level of alkaline solution concentration could dissolve silica (Si), alumina (Al), and calcium (Ca) from crushed rock with the practical crushed rock grading

P. Jitsangiam (✉)

Department of Civil Engineering, Faculty of Engineering, Chiang Mai University, Chiang Mai, Thailand

e-mail: peerapong@eng.cmu.ac.th

T. Suwan

Department of Civil Engineering, Chiang Mai University, Chiang Mai, Thailand

K. Nusit

Department of Civil Engineering, Naresuan University, Phitsanulok, Thailand

P. Chindapasirt

Department of Civil Engineering, Khon Kaen University, Khon Kaen, Thailand

S. Kwunjai

Chiang Mai University, Chiang Mai, Thailand

characteristics, leading to an increase in strength up to an appropriate level for the road construction material.

Keywords Compaction characteristics · Compressive strength · Geopolymer · Liquid alkaline activator · Road construction · Crushed rock

1 Introduction

Generally, the cement stabilization technique is widely used to improve the engineering properties of road bases. Cement is used as a prime stabilizer of this technique. As known, even cement can provide a stiff manner of materials, and it also produces a large amount of greenhouse gas to the atmosphere during its production processes. It has been reported that one ton of cement production emits approximately one ton of carbon dioxide (CO_2) to the atmosphere [1]. For this point, cement would not be a sustainable material in the climate change era nowadays. Therefore, an attempt to use alternative construction materials with the green material concept has been widely presented. Since late 1970, a new green material cementing agent synthesized by the alkali activation of alumina (Al_2O_3) and silica (SiO_2)-rich material was produced [2]. For commonly acceptably, geopolymer (GP) was named to represent such a new cementing agent.

GP with an environmentally friendly manner, therefore, has numerously been studied with a main aim to replace cement in construction industry [3]. GP can be synthesized by using wastes or by-product materials, e.g., fly ash and bottom ash [4, 5], which can be classified as the silica- and alumina-rich materials. The strength development of inorganic alumina–silicate polymer can be achieved by the incorporation of alkali activators such as sodium hydroxide and sodium silicate solutions [6]. GP would be an option to provide not only a potentially sustainable manner with much less CO_2 emission than that of conventional cement stabilization but also demonstrate through to use of waste materials as their prime materials. Furthermore, Hardjito et al. [7] found that geopolymer can be produced from both natural and by-product materials from the industry.

In terms of a stabilizing agent for road rehabilitation and construction, many research studies have confirmed that the properties of GP are similar to that of cement [8]. Hoy et al. [9] demonstrated the use of GP synthesized from recycled asphalt pavement (RAP) and fly ash (FA) could be theoretically utilized as a pavement material. The results of GP-stabilized pavement material tests passed the minimum strength requirement of Thailand's road authorities. This FA-based GP with RAP resulted in significant energy saving and a reduction in greenhouse gas emission [10]. GP binders could be used as an alternative to cement for soil base and subbase stabilization [11]. In fact, fly ash from the coal-fired power plant (ASTM C618) [12] was the most popular material for producing GP as a prime material because of its accessibility and being a normal cement-substituted material for concrete production. However, to introduce GP in the road construction industry, the starting material could

be easily obtained and abundantly available. The challenge of using crushed rock, a commonly used road construction material, as a precursor for geopolymer synthesis would be addressed.

This study was to investigate compaction characteristics of geopolymer having crushed rock as parent materials, so-called crushed rock geopolymer (CR-GP). CR-GP is a mixture of crushed rock (B) and liquid alkali activator (L), a solution of sodium silicate (Na_2SiO_3), and sodium hydroxide (NaOH). Test variables for this study were influent factors affecting to compaction ability of CR-GP, which is the energy of compaction and curing temperature conditions. Unconfined compressive strength (UCS) of CR-GP and micro-observations through XRF and XRD were also performed.

Within a series of the CR-GP research project at Chiang Mai University, Thailand, a preliminary study of CR-based geopolymer was carried out. Results showed that the size of CR directly affects the strength of CR-GP. Consequently, a new grain size distribution curve called ideal grading was produced in corresponding to a range of effective sizes of CR. CR-GP having an ideal (reconstituted) grading curve achieved higher compressive strength than the strength requirement of Thailand's road authorities. However, practically, CR with ideal grading characteristics was difficult to obtain. Therefore, a practical grading curve of CR was produced using a regrading process through mixing a various size of CR. CR with practical grading characteristics was used to produce CR-GP in this study.

2 Material and Methodology

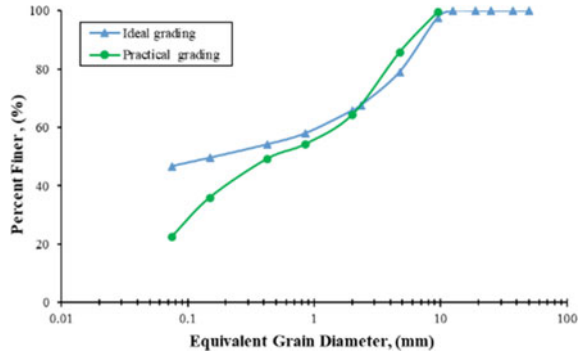
2.1 Materials

CR was sourced from a local quarry located in Chom Thong, Chiang Mai, Thailand. The chemical compositions of CR were obtained based on the technique of X-ray fluorescence (XRF) as shown in Table 1. The liquid alkaline activators were sodium silicate (Na_2SiO_3) composed of Na_2O (8.39%), SiO_2 (20.24%) by mass with a five molar sodium hydroxide (NaOH) solution. The grain size distribution curve of CR relied on the practical grading curve constituted by mixing fine CR (1 mm) (CR1): CR 3/8' (9.50 mm): baghouse dust (CR2) (less 0.075 mm) was 40: 20: 40%. The grading curve of both ideal and practical grading curves shown in Fig. 1.

Table 1 Chemical composition of crushed rock by using XRF analysis

Composition	Al_2O_3	SiO_2	CaO	Fe_2O_3	K_2O
CR 1	1.80	10.85	80.43	4.31	1.196
CR 2	2.34	26.85	78.58	3.38	0.91

Fig. 1 Practical grading curve and ideal grading curve



2.2 Experimental Works

Compaction test. The compaction test was carried out using the standard proctor compaction test in accordance with ASTM method B (ASTM-D689, 2012) and the modified proctor tests in accordance with ASTM method B (ASTM-D1557, 2012). CR-GP compaction tests were performed by using the alkaline solution with the SS/SH ratio of 0.67 instead of water. Once the compaction curves were obtained, the optimum liquid alkaline activator content (OLC) corresponding to the maximum dry density (MDD) could be established.

Unconfined Compression Strength test (UCS). The UCS of the samples was carried out in accordance with ASTM D1633 (ASTM-D1633, 2007). The samples were dismantled from the cylindrical molds, then wrapped within a vinyl sheet cured at room temperature and under 40 °C for 24 h at 7 and 28 days. The maximum load failure was recorded, and UCS was computed using Eq. (1).

$$UCS = \frac{P}{A} \tag{1}$$

where P = maximum load and A = cross-sectional area of the specimen (m^2).

Microstructure analyses. The UCS of the samples before and after testing were investigated the chemical composition by XRD, using sample collected after UCS tests.

3 Mixtures and Testing Procedures

3.1 Mixtures

CR with practical characteristics was prepared to mix with an assigned alkaline solution based on the quartering method to reach a target weight per a test sample. A

Table 2 Mixture of crushed rock-based geopolymer for UCS test

NaOH (m.)	SS/SH ratio	Compaction	MMD (%)	Liquid alkaline content	Curing		Testing
					Temp	Age	
5	0.67	Standard (592.5 kJ/m ³)	100	OLC	Room, 40 °C	7, 28 days	UCS
			95	Dry			
			95	Wet			
		Modified (2693.3 kJ/m ³)	100	OLC			
			95	Dry			
			95	Wet			

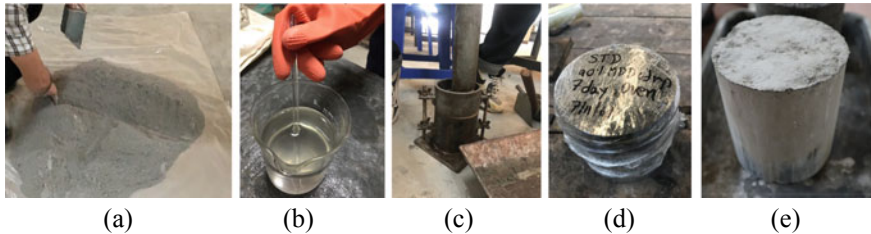


Fig. 2 Specimen preparation **a** CR of practical grading, **b** alkali, **c** compaction of the specimen, **d** wrapped for curing, **e** at the testing age

target CR-GP constituent for the compaction tests was derived from a preliminary test through the GP paste tests. Results demonstrated that the target CR-GP constituent consisted of NaOH with a concentration value of 5 molar, a sodium silicate-per-sodium hydroxide (SS/SH) ratio by weight of 0.67, and alkali liquid-per-crushed rock (L/B) ratio by weight of 0.55. The CR-GP mixture of CR and the target liquid alkali activator were then compacted based on the compaction test procedures. Details of CR-GP mixtures are as shown in Table 2. Figure 2 exhibits UCS sample preparation corresponding to the target MDD assigned.

3.2 Testing Procedures

The maximum MDD of CR-GP mixtures was determined from the compaction curves derived from the compaction tests of the standard compaction and the modified compaction. From this study, an optimum liquid alkali activator content (OLC) which is a liquid alkaline activator content corresponding to MDD was established. UCS test samples were fabricated in corresponding to density conditions at the liquid alkaline activator contents of OLC, less than OLC (dry), and more than OLC (wet). Two curing conditions were employed at room and 40 °C-oven temperatures for 24 h. Figure 3 shows UCS test samples before and after testing.

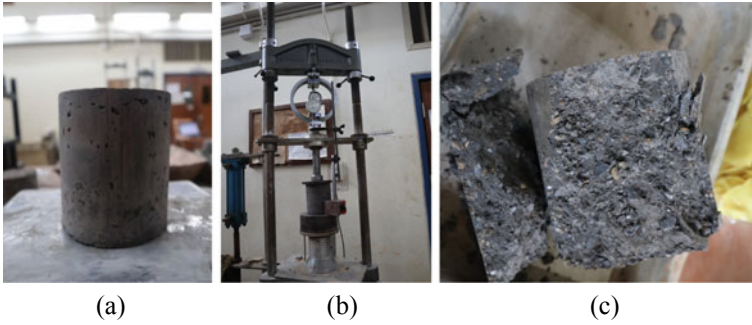


Fig. 3 a CR-GP of practical grading. b UCS testing. c UCS test failure

4 Results and Discussion

4.1 Compaction Test

Figure 4 shows the relationship between dry density and liquid alkaline content (L) and the compaction curves could be well established as bell-like curves. As a result, MDD increases with a higher compaction energy level. An increase in MDD is associated with a decrease in OLC among a comparison of both the standard and modified compaction curves. This finding in agreement with the previous studies [9, 10, 13]. Test results showed that the compaction curves of GR-GP can be established as the bell-like curves with a peak point. CR-GP compaction characteristics demonstrate in line with the compaction theory explained soil mechanics. The compaction test results are as shown in Table 3.

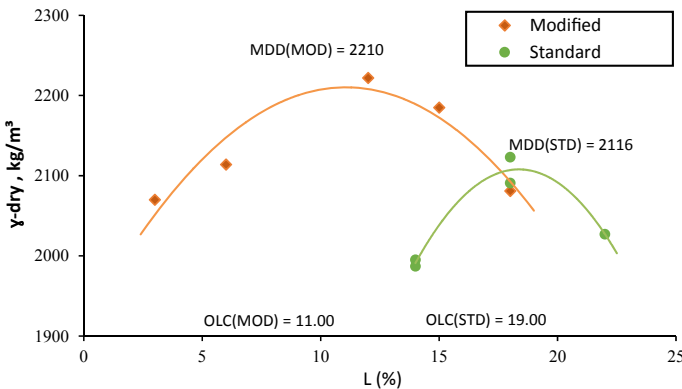


Fig. 4 Compaction curve of practical grading

Table 3 Mixture of crushed rock-based geopolymer for UCS test

Compaction	Percent of MMD	Dry density (kg/m ³)	OLC (%)
Standard (592.5 kJ/m ³)	STD-MDD	2116	19.00
	STD-95%MDD-Dry	2010	14.50
	STD-95%MDD-Wet	2010	11.00
Modified (2693.3 kJ/m ³)	MOD-MDD	2210	4.40
	MOD-95%MDD-Dry	2100	4.40
	MOD-95%MDD-Wet	2100	17.80

4.2 Unconfined Compressive Strength

UCS test results of curing periods of 7 and 28 days are exhibited in Fig. 5. The highest compressive strength was clearly seen at the condition of MDD-MOD. Furthermore, the samples with 40 °C curing for 24 h provide higher strength than that of room temperature curing. This demonstrates curing temperature also influences the strength of CR-GP, which is the same as the conventional GP of previous research works. For example, to achieve better mechanical properties of GP, they increase with an increase in heating energy up to a certain level [13]. The heat curing process is needed to apply to geopolymer around 40–90 °C [14].

When considering two influential factors of curing temperatures and curing periods to UCS values, the 40 °C curing temperature plays a role in providing higher UCS values only for a 7-day curing period and for a 28-day curing period, the 40 °C curing temperature seems not to play any effect to UCS of test samples.

The samples prepared based on the modified compaction also achieved higher UCS values than those of the standard compaction. Figure 6 shows that CR-GP can overcome the strength requirements of road bases of 7 ksc of Thailand’s road authorities.

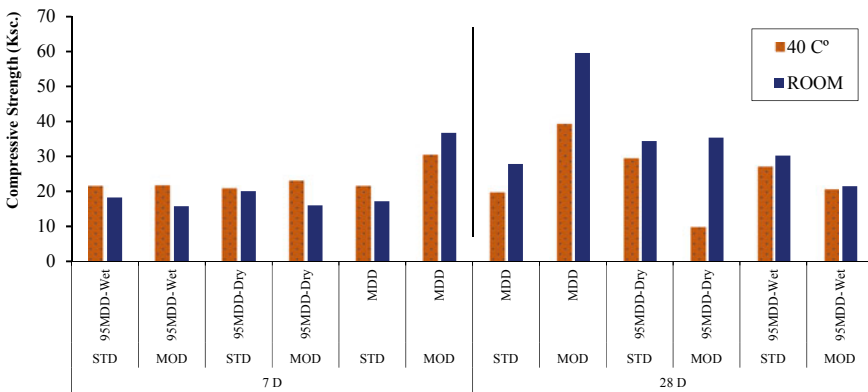


Fig. 5 UCS test of CR-GP for cured at room temperature and 40 °C

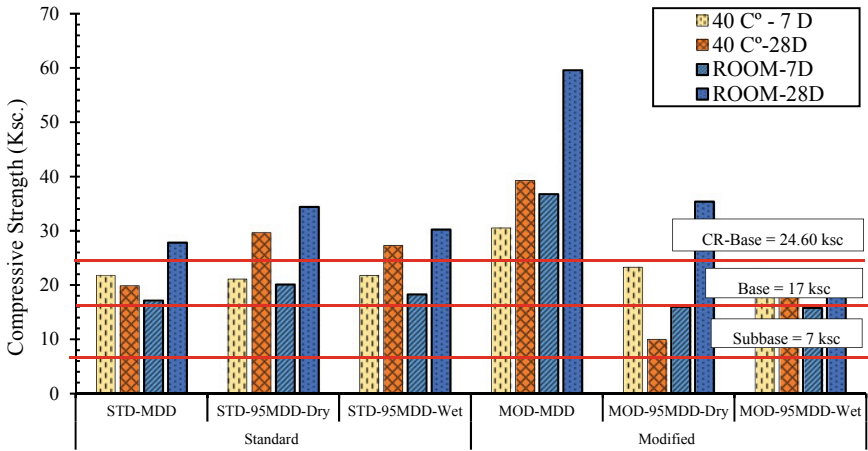


Fig. 6 Practical grading of UCS test at 7 and 28 days

Figure 7 demonstrates the stress–strain characteristics of CR-GP at a 7-day curing condition. It could be noted the stress–strain curves of test samples prepared at the dry condition show higher maximum stresses and lower failure strains with a more brittle manner than those of test samples prepared at the wet side condition. The samples prepared with the wet side has low strength, more strain, failure similar to the cement mixture [15].

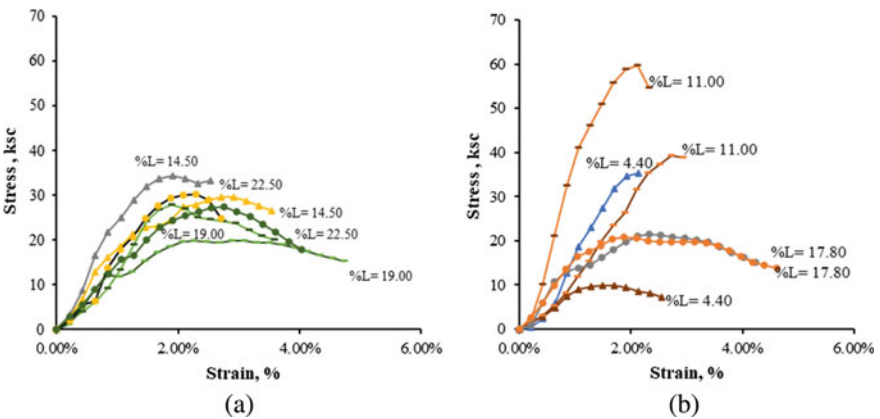


Fig. 7 UCS stress–strain of samples CR-GP by energy a standard, b modified

5 X-Ray Diffraction Analysis

Figure 8 shows the XRD patterns of starting materials (CR1, CR2) and CR-GP at room and 40 °C temperatures. From Fig. 8, the crystalline phases of portlandite (Ca(OH)₂), calcium silicate hydrated (Ca), calcite (C), and portlandite (P) clearly exist. This would imply that high CaO contents in CR1 and CR2 could lead to the formation of C-S-H which is a hardening substance from the hydration reaction like cement and water. This would conform with the concept of the self-cured geopolymer at ambient temperature, of which cement (a high CaO content material) was added to normal GP to form C-S-H in a geopolymeric binder. This would help to improve the harding properties of GP and relatively low temperature, leading to the development of self-cured geopolymer at ambient curing temperature [14]. Zeolite (Na₄(Al₄Si₁₂O₃₂)(H₂O)₁₄) were formed around 13° 2θ.

This study concentrated on a medium NaOH concentration (five molar). For CR as a precursor of this GP, CR contains significantly low alumina and silica contents but rich in calcite; therefore, the geopolymerization would not be dominant. However, with a medium concentration level of NaOH, sodium aluminosilicate hydrate (NASH) and sodium-calcium silicate hydrate (NCSH) compounds could formulate and crystalline CASH phases NASH phases were in forms of zeolitic and geopolymeric [16]. At the same time of building up geopolymer structure via polymerization, crystalline zeolite could also be formed [5]. It could be said that CR-GP would contain with CSH gels and crystalline CASH phases.

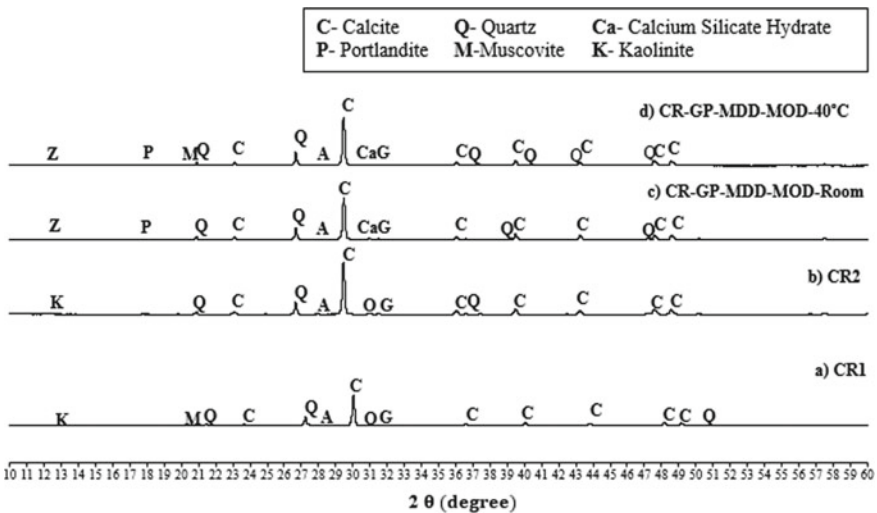


Fig. 8 XRD patterns of CR and CR-GP a

6 Conclusions

Concluding remarks of this study can be summarized as follows:

- 1 The size of crushed rock significantly affects the properties of CR-GP.
- 2 The relatively high curing temperature played a role in higher UCS of CR-GP only for the short term, but not for the long term.
- 3 More compaction energy (the modified compaction) achieved higher UCS values than that of the standard compaction. Moreover, UCS test results of samples prepared at the wet side condition show low peak strength with more failure strain
- 4 CR-GP with practical grading characteristics exhibited higher UCS values than the requirements of Thailand's road authorities for all types of road bases.
- 5 High CaO contents of CR under a target condition of the liquid alkaline solutions of this study could lead to the formation of C-S-H, within a geopolymeric binder, leading to strength gain of CR-GP based on the UCS test results.

Acknowledgements The first author wishes to express gratitude to the Thailand Research Fund (TRF) scheme 'TRF Research Career Development Grant (2016–2018)' for the financial support of this project (RSA5980070). Moreover, the research team of the Civil Engineering Department at Naresuan University, Chiang Mai University, and Khon Kaen University, Thailand, are also gratefully acknowledged for providing overview guidance and valuable inputs into this work.

References

1. Davidovits J (1991) Geopolymers. *J Therm Anal Calorim* 37(8):1633–1656
2. Davidovits J (2013) Geopolymer cement a review. *Institute geopolymer*, 1–11
3. Malhotra VN (2002) Introduction sustainable development and concrete technology. *ACI Concr Int* 24:7–22
4. Chindapasirt P, Chareerat T, Sirivivatnanon V (2007) Workability and strength of coarse high calcium fly ash geopolymer. *Cement Concr Compos* 29(3):224–229
5. Chindapasirt P, Jaturapitakkul C, Rattanasak U (2009) Comparative study on the characteristics of fly ash and bottom ash geopolymers. *Waste Manag* 29(2):539–543
6. Davidovit J (2015) Geopolymer chemistry and applications, *Geopolym. Institute, France*
7. Hardjito D, Wallah SE, Sumajouw DMJ, Ranga BV (2004) Brief review of development of geopolymer concrete/interviewer: G. H. Symposium. American Concrete Institute, USA, Los Vegas
8. Rattanasak U (2018) Geopolymer. *Thailand concrete asso, Thailand*
9. Hoy M, Horpibulsuk S, Rachan R, Arulrajah A (2016) Recycled asphalt pavement—fly ash geopolymers as a sustainable pavement base material: strength and toxic leaching investigations. *Sci Total Environ* 573:19–26
10. Horpibulsuk S, Hoy M, Witchayaphong P, Rachan R, Arulrajah A (2017) Recycled asphalt pavement—fly ash geopolymer as a sustainable stabilized pavement material. *Mater Sci Eng* 273:1–10
11. Deventer VSJ, Provis JL, Duxson P (2012) Technical and commercial progress in the adoption of geopolymer cement. *Miner Eng* 29:89–104

12. ASTM C618-19 (2015) Standard specification for coal fly ash and raw or calcined natural pozzolan for use in concrete. ASTM International, West Conshohocken, PA
13. Sukmak P, Horpibulsuk S, Shen S-L (2013) Strength development in clay-fly ash geopolymer. *Constr Build Mater* 40:566–574
14. Wattanachai P, Suwan T (2017) Strength of geopolymer cement curing at ambient temperature by non-oven curing approaches: an overview. In: *The 4th international conference on manufacturing and industrial technologies, materials science and engineering*, pp 1–6
15. Adhikari S, Khattak JM, Adhikari B (2018) Mechanical characteristics of Soil-RAP-Geopolymer mixtures for road base and subbase layers. *Int J Pavement Eng* 1–14
16. Boonjaeng S, Chindapasirt P, Pimraksa K (2014) Lime-calcined clay materials with alkaline activation: phase development and reaction transition zone. *Appl Clay Sci* 95:357–364s

Considerations for Design of Aggregate Gradation in Pavement Drainage Layers



Shubham A. Kalore, G. L. Sivakumar Babu, and Ratnakar R. Mahajan

Abstract The key to the success of a drainage layer in pavements is the provision of moisture insensitive granular layer that has the optimum gradation to provide adequate drainage and stability. This study investigates the influence of aggregate gradation on drainage in terms of saturated hydraulic conductivity (K_s) and stability in terms of the void ratio. A new semi-analytical approach is presented to predict the K_s of granular soil based on the grain size distribution, porosity, and relative densities. The model is derived for estimating the K_s from the pore size distribution and porosity based on the Hagen–Poiseuille law. Based on the results obtained from published literature and laboratory testing, the model is validated, and model comparison demonstrates that the approach is an improvement over existing empirical and semi-empirical models. Further, simulations are performed for the optimized design of drainage layer aggregate gradations by varying coefficient of uniformity (C_u) and coefficient of curvature (C_c). The results demonstrate that the C_c significantly affects the K_s compared to the void ratio, which specifies a range of C_c for achieving optimum drainage and stability in the pavements drainage layer.

Keywords Hydraulic conductivity · Drainage layer · Aggregate gradation · Coefficient of curvature · Coefficient of uniformity

1 Introduction

The performance of a pavement is significantly influenced by the performance of the pavement subsurface drainage system. The important component of a subsurface

S. A. Kalore (✉) · G. L. Sivakumar Babu
Department of Civil Engineering, Indian Institute of Science, Bangalore 560012, India
e-mail: kalores@iisc.ac.in

G. L. Sivakumar Babu
e-mail: gl@iisc.ac.in

R. R. Mahajan
Maccaferri Environmental Solutions Private Limited, Gurugram 122001, India
e-mail: r.mahajan@maccaferri.com

drainage system is a drainage layer, which drains excess moisture that enters the pavement to side drains within a reasonable time to prevent material deterioration due to a high level of saturation. The key to the success of a drainage layer is the provision of moisture insensitive granular layer that has the optimum gradation to provide adequate drainage and stability.

Aggregate gradation with fines content is the most influencing factor for stability and drainage [1]. Gradations with high fines content have higher density resulting in higher stability but lower K_s , whereas gradation with no fines achieves stability through inter-grain friction, resulting in low density, high K_s , and less frost susceptibility [2]. Numerous studies [3–5] have been conducted on the pavement base course to quantify the stability and drainage considering particularly the amount of fines content.

For pavements drainage layer, the fine content should be minimum to achieve adequate K_s . The only way for an unbound base layer to achieve maximum stability and maximum K_s with minimum fines content is by altering the coarser fractions in an optimal condition. This can be achieved by performing simulations on various grain size distributions (GSD) to evaluate stability and drainage. This study investigates the influence of aggregate gradation on drainage in terms of K_s and stability in terms of the void ratio. To evaluate K_s , this paper introduces a new semi-analytical approach to predict the K_s for a wide range of particle sizes and GSD. The corresponding densities and void ratios are obtained from the comprehensive approach proposed by Aberg [6].

2 Saturated Hydraulic Conductivity Model

Hydraulic conductivity is a measure of the ease with which water flows through the porous media. Measuring hydraulic conductivity of soils using conventional geotechnical laboratory or field-testing methods can be complex and highly variable. Many efforts are being made to find a simple alternative approach to estimate the hydraulic conductivity based on the empirical and physical approaches.

Empirical approaches involve correlating the statistically significant parameters with the measured saturated hydraulic conductivity to achieve minimum prediction error. Freeze and Cherry [7] reported that hydraulic conductivity has a good correlation with the squared indices of some representative grain sizes commonly known as the effective diameter representing the equivalent diameter of a pore channel. Based on this theory, numerous empirical models have been proposed to predict saturated hydraulic conductivity correlating easily measurable properties such as GSD indices, porosity, density, etc. Several empirical equations have been developed, the earliest being Hazen [8] in the year 1892 followed by Karmen-Cozney [9], Breyer [10], Terzaghi [11], etc.

Water flows through the complex void network of soils, which can be assumed as an assembly of cylindrical pores of various diameters. Several studies (Childs and Collis-George [12]; Burdine [13]) exist regarding the derivation of hydraulic

conductivity function by considering the contribution of the conductivity of each group-size pore, which rationally relates the hydraulic conductivity with the pore size distribution. Juang [14] proposed a model to predict K_s by correlating it to pore size distribution of sandy soils which is obtained by extensive laboratory testing. Due to the difficulty in direct measurements of pore size distribution, empirical approaches are preferred.

Jaafar and Likos [15] proposed a model to estimate K_s based on the pore-scale modeling of liquid configurations in idealized unit pores. Indraratna et al. [16] presented a model to estimate K_s by correlating it with inter-grain constrictions size distribution obtained based on Silveira [17] model. Recently, alternative approaches are proposed to estimate K_s such as machine learning is implemented by Araya and Ghezzehei [18], whereas Feng et al. [19] presented a grading entropy approach for gravels.

Numerous models exist in the literature as discussed above for the estimation of K_s . The models are mainly constrained to uniformly graded soil and lack efficiency in estimation for well-graded and gap-graded soils. Additionally, due to the unavailability of the naturally occurring uniformly graded soils for pavement layers, it is crucially important to understand the influence of variation in aggregate gradation on its hydraulic conductivity and stability. Therefore, this paper introduces a semi-analytical approach for predicting the saturated hydraulic conductivity of granular soil based on the GSD, porosity, and relative densities. The applicability of the model is demonstrated for a wide range of granular soils based on the experimental data obtained from the published literature and laboratory tests.

2.1 Model Development

G. Hagen and J.L. Poiseuille proposed an exact solution for the Navier–Stokes equation for steady-state flow through pore channels of circular cross-section. The Hagen–Poiseuille Eq. (1) is derived from the Navier–Stokes equation by considering cylindrical coordinates and assuming the flow is steady, axisymmetric, and fully developed with radial and swirl components as zero [20].

$$\frac{\Delta p}{L} = \frac{32\mu_w}{D^2} v = \frac{32\mu_w}{D^2} \frac{Q}{A} \tag{1}$$

where Δp is the pressure difference along the capillary of length L and diameter D and cross-sectional area A . By definition, substituting for $\Delta p = \gamma_w \cdot \Delta h$, $i = \Delta h / L$, and $A_w = \pi D_w^2 / 4$ re-arrangements yields Eq. (2):

$$Q_k = \frac{\pi}{128} \frac{\gamma_w}{\mu_w} D_k^4 i \tag{2}$$

Equation (2) represents a discharge (Q_k) through a unit pore of diameter D_k with a hydraulic gradient i . The total discharge (Q_t) through the assembly of all m pores is given as Eq. (3).

$$Q_t = \frac{\pi}{128} \frac{\gamma_w}{\mu_w} \left(\sum_{k=1}^m D_k^4 \right) i \tag{3}$$

Comparing Eq. (3) with Darcy’s law ($Q_t = k_s A_t i$), the saturated hydraulic conductivity is given as Eq. (4).

$$k_s = \frac{1}{A_t} \frac{\pi}{128} \frac{\gamma_w}{\mu_w} \left(\sum_{k=1}^m D_k^4 \right) \tag{4}$$

The total cross-sectional area (A_t) is equal to the pore area divided by porosity (n) and can be written as Eq. (5).

$$A_t = \frac{\pi}{4} \left(\sum_{k=1}^m D_k^2 \right) / n \tag{5}$$

Substituting Eq. (5) in Eq. (4) and knowing the pore size distribution, i.e., the probability ($P(D_j)$) for a group of pore diameter (D_j) Eq. (4) can be rewritten as Eq. (6).

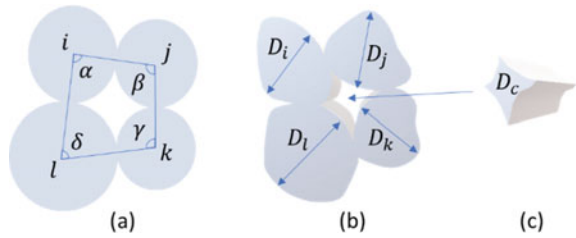
$$k_s = \frac{n}{32} \frac{\gamma_w}{\mu_w} \frac{\left(\sum_{j=1}^z P(D_j) D_j^4 \right)}{\left(\sum_{j=1}^z P(D_j) D_j^2 \right)} \tag{6}$$

where z is the total number of groups of pore diameter. The integral form of Eq. (6) is as follows:

$$k_s = \frac{n}{32} \frac{\gamma_w}{\mu_w} \frac{\int_{D_{\min}}^{D_{\max}} p(D) D^4 dD}{\int_{D_{\min}}^{D_{\max}} p(D) D^2 dD} \tag{7}$$

where $p(D)$ is the pore size density function, D_{\min} and D_{\max} are the minimum and maximum diameters of pores. Equation (7) represents the analytical solution for the estimation of K_s , which depends on the pore size distribution and porosity. The pore size distribution can be obtained by performing extensive laboratory tests such as mercury intrusion technique for fine-grained soil, but estimation for coarse-grained soil is difficult due to sample size restrictions. The practical approach to estimate pore size distribution would be to estimate it based on a mathematical model that

Fig. 1 a Idealized grain configuration and geometry. b Actual grain geometry. c Constriction size pore formed in actual grain geometry



depends on easily measurable variables such as GSD, void ratio, etc. The following section describes the mathematical model to estimate pore size distribution.

Pore Size Distribution Estimation

In soils, the smallest aperture between the inter-grains is known as constriction, and the space connecting these constrictions is known as pores. The GSD obtained using the routine geotechnical procedure (sieve analysis) gives only the single dimension of grain; therefore for mathematical modeling, the only way is to assume grains as spherical, disregarding the other dimensions. Thus, with the reduced complexity, the constriction size distribution can be theoretically obtained from GSD and relative density [17]. Indraratna et al. [16] have shown a good correlation between the mean constriction size obtained using the Silveira [17] model and saturated hydraulic conductivity. In this paper, the constriction size distribution (obtained using the spherical grain theoretical model) is assumed as analogous to pore size distribution due to the non-spherical geometry of grains in reality which leads to almost constant constriction size along a pore in soils as shown in Fig. 1.

The mathematical approach to estimate CSD was introduced by Silveira [21] for the densest state with a combination of three grains configuration. Later, Silveira et al. [17] extended the Silveira [21] for the loosest state with a combination of four grains configuration. Schuler [22] proposed a modified model at any relative density considering the combination of four grains configuration. Based on the critical review of Wang and Dallo [23], in this paper, the improved Silveira model by Schuler [22] is implemented for the estimation of CSD and is discussed in the following section.

The constriction diameter (D_c) for the four-grain configuration can be computed as Eq. (8).

$$D_c = \frac{4S_v}{P_v} \tag{8}$$

where P_v and S_v are the perimeter and area formed among the four particles. The P_v and S_v depend on the internal angles of the quadrilateral formed by joining the centers of the four grains (Fig. 1 a). The internal angle (α_{RD}) at given relative density (RD) is computed as Eq. (9).

$$\alpha_{RD} = \alpha_{Sv_{max}} - \frac{RD}{100} [\alpha_{Sv_{max}} - \alpha_{Sv_{min}}] \tag{9}$$

where $\alpha_{S_{v_{\max}}}$ and $\alpha_{S_{v_{\min}}}$ are the angles that give the maximum and minimum constriction area among the four-grain configuration. The other internal angles β , γ and δ can be represented with respect to α from on the plane geometry's law. The maximum and minimum constriction area is computed in an iterative process by changing the value of α from α_{\min} to α_{\max} . The α_{\min} and α_{\max} are computed as Eqs. (10) and (11), respectively.

$$\alpha_{\min} = 2 \tan^{-1} \left(\sqrt{\frac{D_j D_l}{D_i (D_i + D_j + D_l)}} \right) \tag{10}$$

$$\alpha_{\max} = 2 \tan^{-1} \left(\sqrt{\frac{D_k D_l}{D_i (D_i + D_k + D_l)}} \right) + 2 \tan^{-1} \left(\sqrt{\frac{D_j D_k}{D_i (D_i + D_j + D_k)}} \right) \tag{11}$$

The GSD obtained from the routine geotechnical procedure (sieve-analysis) represents the GSD by mass. Humes [24] suggested that the CSD evaluated from GSD by mass gives higher weights to coarser particles, whereas CSD evaluated from GSD by number gives higher weights to finer particles. Therefore, CSD evaluated from GSD by surface area is the optimal choice. The probabilities of grains of GSD by surface area are obtained by discretizing a GSD by mass into n divisions of grains diameter (D_1, D_2, \dots, D_n) with the corresponding probability of occurrence ($P_{m1}, P_{m2}, \dots, P_{mn}$) is given as Eq. (12).

$$P_i = \frac{P_{mi}}{D_i} \bigg/ \sum_{i=1}^n \frac{P_{mi}}{D_i} \tag{12}$$

The probability of occurrence (P_L) of the constriction size D_{cL} is computed as Eq. (13)

$$P_L = \frac{4!}{r_i! r_j! r_k! r_l!} P_i^{r_i} P_j^{r_j} P_k^{r_k} P_l^{r_l} \tag{13}$$

where $r_i, r_j, r_k,$ and r_l are the number of times that the diameter $D_i, D_j, D_k,$ and D_l appear in the four-grain configuration, respectively. $P_i, P_j, P_k,$ and P_l are the probability of occurrence of diameters $D_i, D_j, D_k,$ and D_l appear, respectively.

2.2 Model Calibration

In this section, the proposed model is evaluated and then calibrated against the experimental datasets to demonstrate its applicability and efficiency in estimating the K_s . A total of 46 datasets are obtained from the recently published literature Feng et al. [19], Indraratna et al. [16], and Indraratna et al. [25]. The soil types and properties

Table 1 Goodness of fit parameters for predicted K_s

Model	R^2	SE
Current model (Eq. 15)	0.963	2.239
Hazen (1982)	0.906	3.576
Kozeny-Carman (1956)	0.943	2.783
Indraratna et al. (2012)	0.913	3.445

are summarized in Table 1. These datasets represent a wide range of grain sizes from sands to gravels. For estimating pore size distribution, the minimum and maximum void ratio for the data obtained from Feng et al. [19] is not provided in the literature; therefore, the corresponding void ratios are obtained from the comprehensive approach proposed by Aberg [6]. The model (Eq. 14) considers the GSD, shape of grain, and degree of compaction.

$$e = 2c \frac{\sum_{i=1}^n \left[\frac{F_i}{D_i} \right] P_i}{\sum_{i=1}^n \left[\frac{P_i}{D_i} \right]} + 2d \tag{14}$$

where F_i is the percentage passing for grain diameter D_i , c is a coefficient that depends on the shape of grains and is equal to 0.75 for sand and gravel, and d is a coefficient that depends on the compaction. d is equal to zero and 0.18 for RD of 1 and 0, respectively.

Comparing the results obtained in Table 1, the coefficient of determination (R^2) between the K_s obtained experimentally and from Eq. (7) is 0.735 and the standard deviation is 6.001. The model can be improved by introducing a lumped correction factor for capturing the effects due to uncontrollable factors such as grain geometry and the assumptions leading to estimate the pore size distribution such as analogous of CSD and pore size distribution, four-grain configuration, etc. Iterative nonlinear regression analysis is performed with different functional forms of correction factor with easily measurable variables such as d_{10} , C_c , C_u , void ratio, etc., to achieve maximum adjusted R^2 and minimum standard deviation. The best fit function is obtained with two variables, i.e., C_c and C_u and two parameters. The parameters are estimated using an nlinfit function in MATLAB using the Levenberg–Marquardt nonlinear least-squares algorithm with 46 datasets (Table 1). The improved model with calibrated correction factor is presented as Eq. (15). Table 1. shows the predicted values of K_s evaluated using Eq. (15). The R^2 between the K_s obtained experimentally and from the improved model (Eq. 15) significantly increased to 0.964 and the standard deviation decreased to 2.238. The comparison of K_s obtained from model (Eq. 7) and improved model (Eq. 15) with experimental data is shown in Fig. 2a, which demonstrates the excellent performance in predicting the K_s for the considered published literature data.

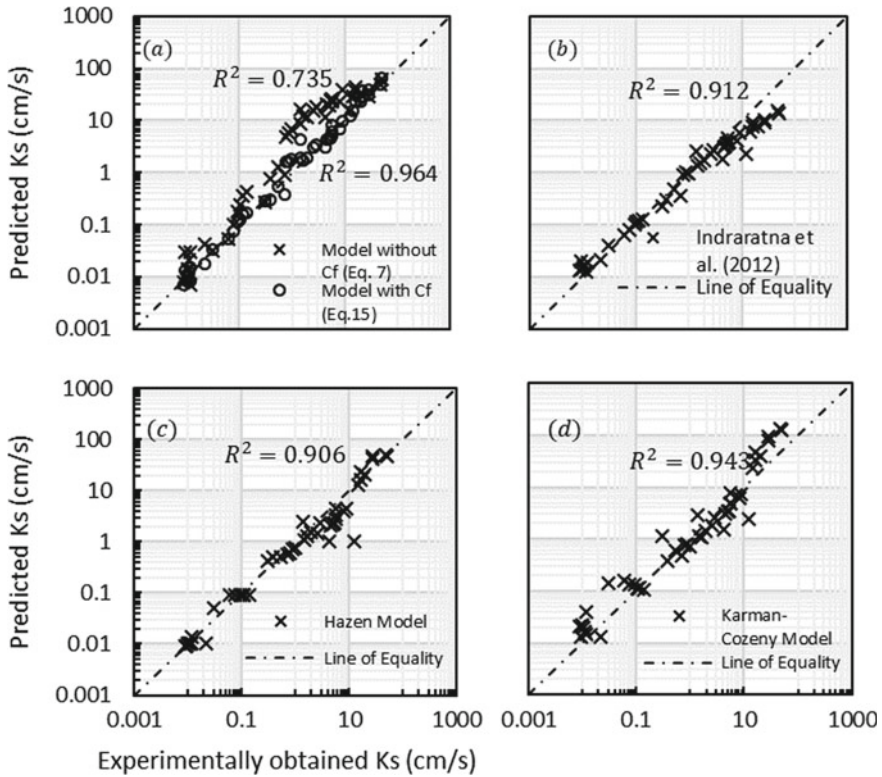


Fig. 2 Comparison of models against experimentally obtained K_s

$$k_s = \frac{1.5}{C_c^{0.386} C_u} \frac{n}{32} \frac{\gamma_w}{\mu_w} \frac{\int_{D_{min}}^{D_{max}} p(D) D^4 dD}{\int_{D_{min}}^{D_{max}} p(D) D^2 dD} \tag{15}$$

2.3 Comparison of Other Published Model Results

In this section, the dataset (Table 1) is used to obtain the results from other widely used published empirical and semi-empirical models for comparison purposes. Figure 2 and Table 2 summarize the goodness of fit of the current model and other widely used models with experimental data.

Table 2 Published literature granular soil properties and results of evaluated K_s

Grad. ID	C_c	C_u	d_{10} (mm)	RD	n	Sat. Hydraulic conductivity K_s (cm/s)		
						Lab. Test	CM* Eq. 7	CM* Eq. 15
Feng et al. [19]								
E1	0.88	1.60	7.02	0.36	0.46	47.66	48.54	48.03
E2	2.05	3.93	2.01	0.28	0.41	8.04	23.56	6.82
E3	2.23	4.40	1.66	0.16	0.42	5.67	23.97	6.00
E4	2.15	4.83	1.49	0.22	0.41	4.99	19.87	4.59
E5	0.99	3.54	0.72	0.62	0.38	0.54	1.27	0.54
E6	0.49	6.15	0.78	0.35	0.39	0.78	4.92	1.58
E7	0.62	7.16	0.88	0.44	0.36	0.98	7.00	1.77
E8	2.45	4.20	2.12	0.19	0.41	8.93	38.65	9.77
E9	1.13	2.00	4.86	0.29	0.43	16.44	43.45	31.15
E10	1.82	5.90	1.22	0.31	0.38	2.55	15.53	3.13
F1	0.90	1.51	6.94	0.15	0.46	50.11	62.63	64.66
F2	3.22	5.20	1.54	0.45	0.37	2.88	18.55	3.41
F3	3.37	6.78	1.15	0.52	0.35	1.63	12.11	1.67
F4	2.61	6.34	1.23	0.49	0.36	1.93	11.84	1.94
F5	1.01	3.75	0.72	0.89	0.34	0.38	0.74	0.30
F6	1.49	4.87	1.58	0.39	0.38	1.41	16.29	4.31
F7	0.97	5.69	1.02	0.20	0.40	4.31	11.25	3.00
F8	0.97	5.69	1.02	0.15	0.44	12.38	15.46	12.38
F9	1.31	2.19	4.07	0.28	0.43	16.37	36.64	22.62
F10	1.81	3.83	2.09	0.22	0.42	5.57	25.99	8.10
G1	3.12	5.20	1.54	0.26	0.40	5.23	24.91	4.64
G2	0.91	1.48	6.89	0.65	0.43	27.79	28.57	30.02
G3	0.97	3.60	0.75	0.81	0.35	0.71	0.91	0.38
G4	1.52	2.37	3.58	0.34	0.42	14.50	28.55	15.34
G5	2.41	5.21	1.44	0.25	0.40	4.53	20.64	4.23
G6	0.64	6.43	0.84	0.40	0.38	0.87	5.81	1.61
G7	1.27	6.00	1.05	0.45	0.37	1.45	8.40	1.91
G8	1.26	1.97	4.57	0.36	0.43	20.08	32.78	22.83
G9	0.91	1.52	6.47	0.43	0.43	27.61	37.05	38.04
G10	3.04	4.54	1.83	0.31	0.40	5.65	23.41	5.04
Indraratna et al. [16]								
G1	0.99	1.53	0.30	0.53	0.42	0.06	0.05	0.05
G2	0.90	2.07	0.30	0.56	0.40	0.08	0.10	0.08
G3	0.86	2.50	0.30	0.47	0.40	0.09	0.18	0.12

(continued)

Table 2 (continued)

Grad. ID	C_c	C_u	d_{10} (mm)	RD	n	Sat. Hydraulic conductivity K_s (cm/s)		
						Lab. Test	CM* Eq. 7	CM* Eq. 15
G4	0.84	3.00	0.30	0.47	0.38	0.10	0.24	0.13
G5	0.76	3.67	0.30	0.44	0.38	0.11	0.36	0.16
G6	0.81	4.17	0.30	0.47	0.38	0.14	0.44	0.17
Indraratna et al. [25]								
1	0.93	1.33	0.12	0.50	0.46	0.01	0.01	0.01
2	0.91	1.43	0.23	0.50	0.46	0.03	0.03	0.03
3	0.94	1.49	0.65	0.50	0.46	0.31	0.27	0.28
8	0.91	1.85	0.10	0.50	0.44	0.01	0.01	0.01
9	0.83	2.20	0.10	0.50	0.43	0.01	0.01	0.01
10	0.83	2.70	0.10	0.50	0.41	0.01	0.02	0.01
11	0.80	3.20	0.10	0.50	0.40	0.01	0.03	0.02
13	0.90	1.74	0.10	0.50	0.44	0.01	0.01	0.01
14	0.85	3.80	0.10	0.50	0.39	0.02	0.04	0.02
15	0.79	3.58	0.10	0.50	0.40	0.01	0.03	0.01

Note CM stands for current model

3 Simulations of Aggregate Gradation

To design pavements drainage layer aggregate gradation with optimal drainage and stability, simulations are performed by altering the coarser fractions. The coarser fractions can be varied by varying the moments of GSD, i.e., C_u (coefficient of uniformity) and C_c (coefficient of curvature). The C_u is defined as the ratio of d_{60} to d_{10} . A value of C_u greater than 4 to 6 classifies the soil as well-graded. C_c is defined as the ratio of squared indices of d_{30} to the product of d_{10} and d_{60} . For soil to be well-graded, C_c should be less than 3 and greater than 1 for both sand and gravel. Considering the GSD as analogous to cumulative distribution function (CDF), the C_u is reflected in terms of standard deviations/variance, i.e., flatter is the GSD curve higher is the standard deviation and wider is the range of particles enclosed under the curve. However, C_c is reflected in terms of skewness of GSD. Skewness is a measure of asymmetry, in which the curve appears distorted or skewed either to the left or to the right. Left skewed GSD will have higher C_c value which infers that larger is the proportion of coarser particles compared to fines, whereas for right-skewed GSD will have lower C_c , larger is the proportion of fines compared to coarser particles. Figure 3a, b shows the physical significance of C_u and C_c with respect to CDF and probability density function (PDF), respectively.

The objectives of simulating such design are to understand the individual influence of C_u and C_c on K_s and to validate the proposed approach to predict K_s . The values of C_u are varied from 4 to 10 and that of C_c from 0.5 to 3.5 for simulation purposes.

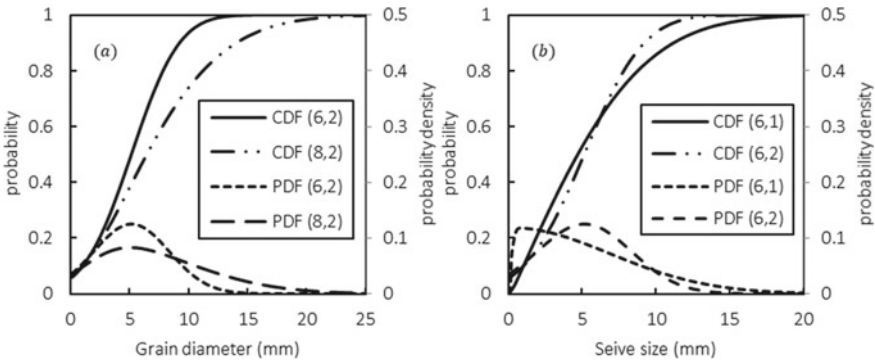


Fig. 3 Variation of variance and skewness with the variation in C_u and C_c

A subset of 9 datasets from the simulation dataset is used for validation of the proposed approach by performing laboratory tests. Constant head permeability test was conducted as per ASTM standard D2434-68. K_s is mainly influenced by the pore size distribution which is reflected in terms of GSD and amount of compaction efforts. To solely consider the effect of GSD shape, the compaction efforts are taken care of by maintaining the relative density as 0.8 for all gradations. The corresponding maximum and minimum void ratios are estimated as per ASTM D4254 and ASTM D4253, respectively. For simplification purposes, the value of d_{10} is kept as constant (equal to 1 mm), and by gradually varying the values of C_u and C_c , the corresponding d_{30} and d_{60} values are calculated. The points on gradation other than d_{10} , d_{30} , and d_{60} are interpolated by joining these points linearly on a semi-log plot as shown in Fig. 4.

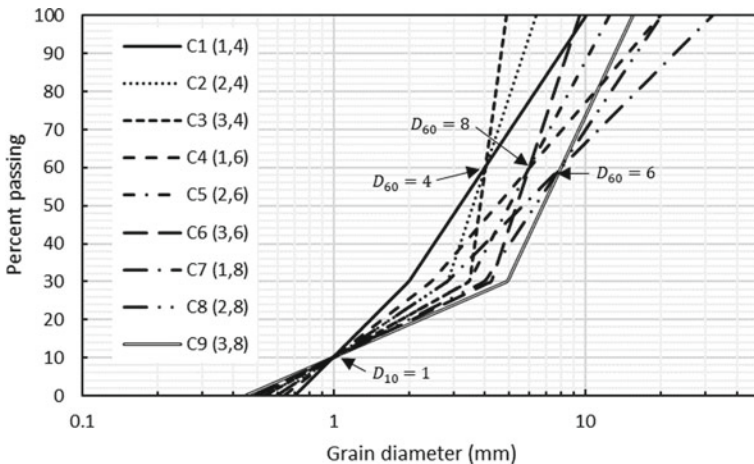


Fig. 4 Examined GSD of 9 samples with constant D_{10} and varying C_u and C_c (Note: The first value in parenthesis is C_u and the second value is C_c)

Table 3 Results of laboratory tests of considered GSDs (Fig. 4) and results of evaluated K_s

ID	C_c	C_u	e_{min}	e	e_{max}	RD	Sat. Hydraulic conductivity K_s (cm/s)		
							Lab. Test	Equation 7	Equation 15
C1	1	4	0.45	0.52	0.81	0.81	0.82	2.24	0.84
C2	1	6	0.38	0.45	0.74	0.81	1.15	4.52	1.13
C3	1	8	0.33	0.40	0.69	0.82	1.49	7.52	1.41
C4	2	4	0.47	0.54	0.83	0.81	0.59	2.15	0.62
C5	2	6	0.38	0.45	0.74	0.80	0.81	4.22	0.81
C6	2	8	0.33	0.40	0.69	0.80	1.10	6.85	0.99
C7	3	4	0.48	0.54	0.84	0.83	0.53	2.12	0.53
C8	3	6	0.39	0.47	0.75	0.79	0.66	4.13	0.68
C9	3	8	0.33	0.41	0.69	0.80	0.82	6.62	0.82

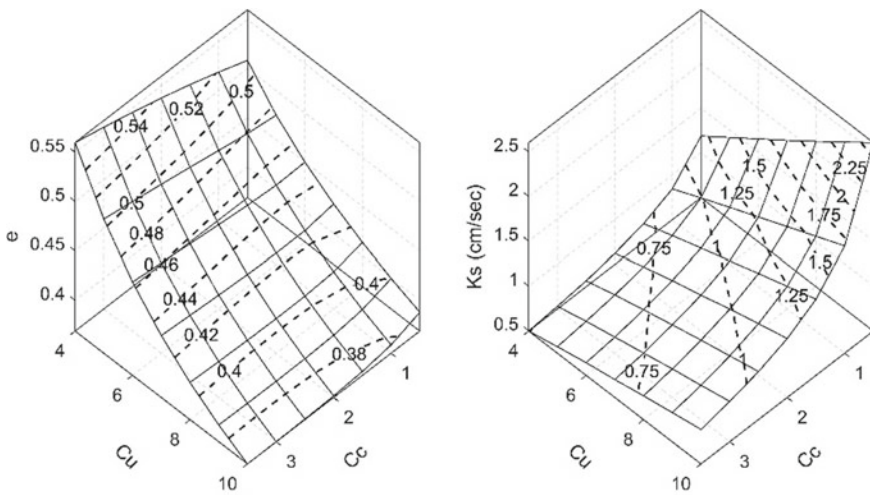


Fig. 5 Influence of C_u and C_c on **a** Void ratio, e and **b** Sat. Hydraulic conductivity, K_s

The results obtained from laboratory tests and the current model are summarized in Table 3. The results obtained from the simulations are shown in Fig. 5.

4 Discussion

Observations from the obtained results are summarized below:

1. A comparison of results (Fig. 2 and Table 2) of the current model against experimentally obtained K_s demonstrates that the approach is an improvement over existing empirical and semi-empirical models.
2. Model validation results summarized in Table 3 give satisfactory results with the experimentally obtained K_s . The predicted void ratios based on Aberg (1992) model are in well-agreement with measured void ratios with the R^2 of 0.986.
3. Fig. 5a shows the influence of C_u and C_c on the void ratio. The variation in the void ratio is more significant with the variation in C_u , whereas for C_c , the variation is trivial. As expected, the increase in C_u with constant d_{10} leads to a wider range of particles, which produces a compact matrix leading to a decrease in void ratio and an increase in density. The effect of variation of the proportion of different coarser particles, i.e., the variation of C_c on a void ratio is trivial as it produces a similar compact matrix.
4. Fig. 5b shows the influence of C_u and C_c on the K_s . Both C_u and C_c significantly affect the K_s value. Hydraulic conductivity depends on the size of the particles (coarse and fines). As C_u increases, the proportion of coarser particles increases that leads to an increase in K_s . However, from Fig. 5b, the rate of increase K_s not only depends upon C_u , but also on the value of C_c . The rate of increase of K_s with an increase in C_u is high at low C_c value compared to high C_c value. For lesser C_c values, the proportion of coarser aggregate is high compared to fine aggregates; whereas, for high C_c values, the proportion of coarser aggregate is less compared to fine aggregates. However, for a constant C_u value, the void ratio remains the same, and the K_s increases rapidly with a decrease in C_c value.
5. From Fig. 5, it is evident that apart from d_{10} , void ratio, and values of C_u , C_c also plays a crucial role in determining K_s of sands and gravels. Therefore, a high C_u and low C_c value would result in a high K_s and low void ratio, i.e., better drainage and stability. The value of d_{10} can be chosen based on the requirement of the degree of drainage, and a value of 1 mm is recommended as it gives K_s values sufficiently higher than 300 m/day for an RD of 0.8. The criteria of 300 m/day are the minimum requirement of the K_s value as per the AASHTO Standards.
6. For pavement drainage layer, the stability is defined in terms of the resilient modulus (M_r). Sun et al. [26] have observed a decrease in M_r with the increase in C_u which specifies an upper bound on C_u for achieving higher stability.
7. To achieve optimum drainage and stability, the recommended C_u range is 6–8, and a value of C_c near 1 is recommended for a pavement drainage layer. The value of d_{10} and RD can be fixed based on the requirement of K_s and M_r . For structures where drainage is trivial, a high value of C_c is recommended, and the value of C_u and d_{10} should be chosen based on the required stability.

5 Conclusions

In this paper, the influence of aggregate gradation on drainage in terms of K_s and stability in terms of the void ratio is studied. A new semi-analytical approach is presented to predict the K_s of granular soil based on the grain size distribution, porosity, and relative densities. The model is derived for estimating the K_s from the pore size distribution and porosity based on the Hagen–Poiseuille law. The pore size distribution is considered analogous to inter-grain constriction size distribution which can be obtained from grain size distribution and relative densities. A correction factor is introduced in the model for capturing the effects due to uncontrollable factors such as grain geometry and the assumptions leading to estimate the pore size distribution. The correction factor is calibrated based on the 46 datasets obtained from published literature. A comparison between predicted and measured soil samples demonstrates that the approach is an improvement over existing empirical and semi-empirical models.

To achieve maximum stability and maximum K_s with minimum fines content, simulations are performed by varying C_u and C_c with constant d_{10} and RD. The results demonstrate that the variation in the void ratio is more significant with the variation in C_u ; whereas, for C_c , the variation is trivial. However, both C_u and C_c significantly affect the K_s value, and C_c plays a crucial role in the design of aggregate gradation of drainage structures. Therefore, based on the simulations results, a C_u range of 6–8 and a value of C_c near 1, for the pavement drainage layer is recommended. The value of d_{10} and RD can be designed based on the requirement of K_s and M_r . However, for structures where drainage is trivial, a high value of C_c is recommended, and the value of C_u should be chosen based on the requirement of stability.

Acknowledgements The work described in this paper is financially supported by Prime Minister's Fellowship Scheme for Doctoral Research, a public-private partnership between Science and Engineering Research Board, Department of Science & Technology, Government of India, and Confederation of Indian Industry with industry partner Maccaferri Environmental Solutions Pvt. Ltd, India.

References

1. Ferguson EG (1972) Repetitive triaxial compression of granular base course material with variable fines content, PhD Dissertation submitted to Department of Civil Engineering, Iowa State University, Ames, Iowa
2. White DJ, Jähren C, Vennapusa P (2004) Determination of the optimum base characteristics for pavements. Iowa: Report No. TR-482, Iowa Department of Transportation
3. Highlands KL, Hoffman LG (1988) Subbase permeability and pavement performance. *Transp Res Rec* 1159:7–20
4. Kolisoja P, Saarenketo T, Peltoniemi H, Vuorimies N (2002) Laboratory testing of suction and deformation properties of base course aggregates. *Transp Res Rec* 1787:83–89

5. Bowders JJ, Blanco AM, Parra JR (2003) Characterization of permeability of pavement bases in missouri department of transportation's system, Report No. RI 01-006/RDT 03-005, Prepared for Missouri Department of Transportation, Research, Development and Technology, MO
6. Åberg B Void ratio of noncohesive soils and similar materials. *J Geotech Eng* 118(9):1315–1333. [https://doi.org/10.1061/\(ASCE\)0733-9410\(1992\)118:9\(1315\)](https://doi.org/10.1061/(ASCE)0733-9410(1992)118:9(1315))
7. Freeze RA, Cherry JA (1979) *Groundwater*. Prentice-Hall, Inc., Englewood Cliffs, N.J.
8. Hazen A (1892) Some physical properties of sands and gravels, with special reference to their use in filtration. In: 24th annual report, massachusetts state board of health. Pub Doc 34:539–556
9. Carman PC (1956) *Flow of gases through porous media*. Butterworths Scientific Publications, London
10. Kresic N (1998) *Quantitative solutions in hydrogeology and groundwater modeling*. CRC Press, Boca Raton, FL
11. Odong J (2007) Evaluation of empirical formulae for determination of hydraulic conductivity based on grain-size analysis. *J Am Sci* 3(3):54–60
12. Childs EC, Collis-George N (1950) The permeability of porous materials. *Proc Roy Soc London A*:201:392–405
13. Burdine NT (1953) Relative permeability calculation size distribution data. *Trans Am Inst Min Metall Pet Eng* 198:71–78
14. Juang CH (1981) Pore size distribution of sandy soils and the prediction of permeability. Joint Highway Research Project Report No. 81–15
15. Jaafar R, Likos WJ (2014) Pore-scale model for estimating saturated and unsaturated hydraulic conductivity from grain size distribution. *J Geotech Geoenviron Eng*. [https://doi.org/10.1061/\(ASCE\)GT.1943-5606.0001031.1-12](https://doi.org/10.1061/(ASCE)GT.1943-5606.0001031.1-12)
16. Indraratna B, Nguyen VT, Rujikiatkamjorn C (2012) Hydraulic conductivity of saturated granular soils determined using a constriction-based technique. *Can Geotech J* 49(5):607–613
17. Silveira A, de Lorena Peixoto T, Nogueira J (1975) On void size distribution of granular materials. In: *Proceedings of 5th pan-am conference on soil mechanics and foundation engineering*, Buenos Aires, Argentina, pp 161–176
18. Araya SN, Ghezzehei TA (2019) Using machine learning for prediction of saturated hydraulic conductivity and its sensitivity to soil structural perturbations. *Water Resour Res* 55:5715–5737
19. Feng S, Vardanega PJ, Ibraim E, Widyatmoko I, Ojum C (2019) Permeability assessment of some granular mixtures. *Géotechnique* 69(7):646–654
20. White FM (1999) *Fluid mechanics*, 4th edn. McGraw Hill, Boston
21. Silveira A (1965) An analysis of the problem of washing through in protective filters. In: *Proceedings of 6th international conference on soil mechanics and foundation engineering*, ICSMFE, Montreal, Canada, vol 2, pp 551–555
22. Schuler U (1996) Scattering of the composition of soils, an aspect for the stability of granular filters. In: Lafleur J, Rollin A (eds) *Geofilters'96*. Montreal: Bitech Publications, pp 21–34
23. Wang Y, Yousif AH, Dallo (2014) On estimation of the constriction size distribution curve for cohesionless soils. *European J Environ Civ Eng* 18(6):683–698
24. Humes C (1996) A new approach to compute the void size distribution curves of protective filters. In: Lafleur J, Rollin A (eds) *Geofilters*. Montreal: Bitech Publications, pp 57–66
25. Indraratna B, Vafai F, Dilema ELG (1996) An experimental study of the filtration of a lateritic clay slurry by sand filters. *Proc ICE Geotech Eng* 119(23):75–83. <https://doi.org/10.1680/igeng.1996.28167>
26. Sun Y, Nimbalkar S, Chen C (2018) Grading and frequency dependence of the resilient modulus of ballast. *Géotechnique Lett*. 8:305–309. <https://doi.org/10.1680/jgele.18.00084>

The Potential of Quartzitic Rock for Use as Coarse Aggregates in Asphaltic Concrete



Thomas D. Arthur, Samuel I. K. Ampadu, and Simon K. Y. Gawu

Abstract Asphaltic concrete material continues to be a much-preferred road surfacing material in Ghana, because of its benefits like lower cost, good resistance to high traffic volume, lower noise, and easy maintenance. The mix is commonly produced using bitumen as a binding agent, crushed rock aggregates, natural sand, and sometimes active fillers such as cement or hydrated lime or limestone. Because crushed aggregates from granite and gneiss have over the years yielded good wearing and binder courses, they have become the default aggregates used for asphaltic concrete production in Ghana. However, these two key rock formations do not cover the whole country, and in some parts of the country, they are unavailable thereby making asphaltic road construction relatively uneconomical in these parts of the country. This study seeks to evaluate the potential of rocks derived from quartzitic rock formation which exists in huge deposits in some parts of the country, for use as crushed aggregates for asphaltic concrete material. This is a comparative laboratory study of the characteristics of asphaltic concrete prepared using granitic and quartzitic rocks. The index properties of aggregates obtained from granitic and quartzitic rocks were determined. Then, a mix design by the Marshall method was carried out on mixes consisting of crushed quartzites as aggregates and AC 20 as binder with different percentages of active fillers of cement, hydrated lime, and limestone ranging from zero to 2.5%. An identical set of mixes consisting of crushed granite was also made. Then the briquettes of the various mix proportions were evaluated for their Marshall properties of stability and flow. The results from the sets of mixes and the index properties are analyzed and discussed.

T. D. Arthur (✉)
ACON House, 33 Royalt Castle Road, Accra, Ghana

S. I. K. Ampadu
Department of Civil Engineering, Kwame Nkrumah University of Science and Technology,
Private Mail Bag, University Post Office, Kumasi, Ghana

S. K. Y. Gawu
Department of Geological Engineering, Kwame Nkrumah University of Science and Technology,
Private Mail Bag, University Post Office, Kumasi, Ghana

Keywords Quartzitic rock · Granite rock · Aggregates · Hot mixed asphalt · Stability · Flow

1 Introduction

1.1 Background

Hot mixed asphalt (HMA) is a pavement construction material consisting of a mixture of aggregates and bitumen mixed at an elevated temperature. In the mixture, aggregates constitute about 90–95% by weight of the total mix and 75–85% of the total volume of the mix [1] and therefore greatly influence the properties of the HMA. Aggregates in HMA may be classified as coarse aggregates, fine aggregates, or mineral filler depending on the particle sizes. Coarse aggregates are those retained on a 4.75 mm sieve while fine aggregates are those passing 4.75 mm but retained on 0.075 mm. The mineral fillers are the portion passing the 0.075 mm sieve. The fine aggregates may be natural or manufactured sand sieved to obtain the desired gradation. The coarse aggregates are usually produced as mechanically crushed rock obtained from a parent rock.

Over the years, in Ghana, granitic and gneiss rocks have been considered the most suitable aggregates for HMA. This preference had meant that contractors working in areas where aggregates of these rock types are not available, within the immediate environs of the project corridor, are compelled to travel very long haulage distances to seek them at the expense of the project budget. However, there are other rock formations with the potential to serve as aggregates for HMA. These have not been seriously considered as an alternative to the granites and the gneiss. One such rock is the quartzites of the Togo Series of rock formation of Ghana which is readily available in areas where large road construction projects are currently ongoing. This problem is worldwide and there is a general trend toward making effective use of available local aggregate resources. The use of limestone aggregates in asphaltic concrete in Poland has been studied in the laboratory and in the Heavy Vehicle Simulator by Sybilski et al. [2] while the suitability of aggregates from volcanic rocks from Turkey for HMA layers have also been investigated in the laboratory by Huseyin et al. [3]

In addition to this the specifications for HMA used in Ghana [4] covers only the inert type filler obtained from crushed aggregates and the active type which may be ordinary Portland cement (OPC) or hydrated lime (HL). However, the emergence of limestone quarries in the country in recent times has seen the substitution of limestone (LS) as an active filler in HMA despite the fact that locally it has not been extensively studied unlike elsewhere where limestone has been used successfully as a filler [5, 6]. There is the need therefore to investigate the influence of the type of filler alongside the aggregate behavior. The objective of the study therefore is to investigate whether the quartzitic rocks of the Togo Series of rock formation of Ghana can be suitably used as coarse aggregates for HMA by investigating its Marshall properties and the influence of various fillers on these properties.

1.2 Geology of Ghana

Figure 1 is the geological map of Ghana which shows among other things that about two-thirds of the land surface area is occupied by Paleoproterozoic Birimian rocks which consist of five evenly spaced volcanic belts trending northeast-southwest and the North–South trending Wa-Lawra belt. In between the metavolcanic belts are intervening metasedimentary basins which also strike NE-SW. The Birimian metasedimentary and metavolcanic rocks have been intruded by basin (Cape Coast) type granitoids and belt (Dixcove) type granitoids, respectively. The basin (Cape Coast) type which is more massive batholiths is predominantly intermediate in composition (generally K-rich) with biotite being the most common mafic mineral and typically display foliation that are often gneissic. The belt (Dixcove) type granitoids, on the other hand, are also generally of an intermediate composition although more mafic and felsic phases are not uncommon and tend to be more Na- rich. Whereas the basin type is usually described as concordant and commonly have migmatitic phases on the margins and display prominent contact metamorphic aureoles, the belt type

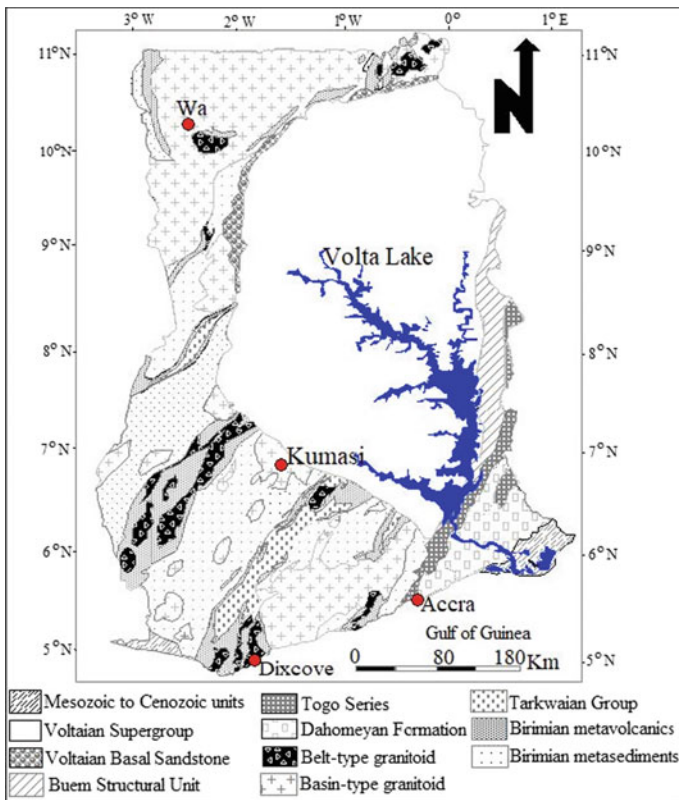


Fig. 1 Geological map of Ghana

is frequently described as discordant intrusives and has hornblende as the usually dominant mafic mineral and, in many cases, the intrusives lack strong foliation. Furthermore, the belt type occurs in quite small plutons to very large batholiths, although not as extensive as the major basin (Cape Coast) type complexes. The basin (Cape Coast) type intrusives are syn-tectonic bodies, whereas the belt (Dixcove) type units were considered to be late tectonic to post-tectonic intrusions.

The Neoproterozoic terranes in Ghana are underlain by the Voltaian basement sediments, Buem and Togo structural units as well as the Dahomeyan formation. However, the highly metamorphosed Togo structural unit is predominantly composed of quartzite, chert, mica schist and phyllite. Structurally, the Togo Units display penetrative structures in the quartzites and mica schists with prominent lineations typified by fold rods. The quartzites in Togo structural unit have well interlocking textures which make them good candidates for aggregates. Quartzite is the most durable of common rocks used for construction, because of its hardness and because of the fact that quartz is not susceptible to chemical weathering. The quartzites of the Togo Series of Ghana come with different colors including violet, gray, ash, pink, and yellow. The predominant mineral in quartzite is quartz.

These quartzites had in the past been used as aggregates for concrete works on a large scale for the construction industry in Accra, and its environs and several large quarries had been set up in these formations. These aggregates being clean, compact, and highly siliceous, had performed well especially in areas where exposure of the works to water had been limited to forestall alkaline silica reaction. However, its use in the past as aggregates for HMA is unclear.

1.3 The Marshall Mix Design Method

Of the different asphalt design methods, perhaps the Marshall [7], the Hveem [8] and the Superpave [9] mix design methods are the most widely used. However, the current trend is toward the use of the Superpave design method which is a performance-based mix design method where for a given traffic level, the optimum amounts of bitumen in a mix is established to satisfy the rut and fatigue cracking resistance [10]. In Ghana, despite the known limitations of the Marshall method including the fact that it is effectively an unconfined test and does not simulate any real pavement performance, it is still the most widely used method for HMA mix design mainly because it requires only simple and inexpensive equipment. The Marshall method is applicable only to HMA using penetration, viscosity or performance grade (PG) bitumen and aggregates having maximum sizes of 25.0 mm. The Marshall method seeks to determine the optimum bitumen content necessary for a particular blend of aggregate materials that meets the desired properties of density, stability, and flow. It uses 102 mm diameter \times 63.5 mm high HMA briquettes compacted by applying either 75 or 50 blows per side with the Marshall compaction hammer, depending on expected traffic level. The briquettes are then used to determine the mix properties for each bitumen content. The density-voids analysis is used to determine the unit

weight, air voids, voids in mineral aggregate (VMA), and percentage voids filled with bitumen (VFB). The Marshall apparatus is used to determine the stability and the flow.

1.3.1 Aggregates

Within the HMA, the aggregates need to be tightly packed together to ensure a continuously dense graded mix. This is achieved by ensuring grading bands that follow the idealized Fuller curve [11] but adjusted to achieve specified volumetric requirement. The mix should have voids in mineral aggregates (VMA), defined as the sum of the percentage air voids and the percentage volumetric bitumen content, sufficiently high to accommodate the volume of bitumen but ensuring adequate air void levels to prevent flushing. In order to ensure bonding with bitumen and also promote particle interlocking resulting in better engineering properties for a mix, the aggregates are expected to be cubical in shape, fractured on at least three faces and durable in strength [12].

The inert mineral filler is usually crushed rock fine materials passing the 0.075 mm sieve and is added to the asphalt mix in situations where the combined aggregate for the mix shows deficiency in fines. The presence of water is known to lead to problems with adhesion in some asphaltic concrete mixes resulting in bitumen-aggregate bonds failure [13] and active fillers such as hydrated lime and ordinary Portland cement may be used to prevent the effects of aggregate stripping with moisture susceptibility aggregates.

1.3.2 Bitumen

In the HMA, the bitumen serves as the binding agent between the coarse and fine aggregates and also the filler materials. Bitumen has thermoplastic properties and its consistencies change with variations in temperature. When heated to very high temperatures, it becomes liquid and is able to coat aggregate particles during asphaltic concrete production process and hardens up as it cools to hold the aggregate particles together. In the viscosity grading system of bitumen, the results of a viscosity test at 60 °C are used to grade the bitumen which is equivalent to the maximum temperature that the pavement is likely to be exposed to during its service life. A second viscosity test at 135 °C approximates to the viscosity of the bitumen during the mixing and laying of the HMA in the field.

2 Materials and Methods

2.1 *The Component of HMA*

The quartzite aggregates were obtained from a quartzite stone breaking pit at Pokuase while the granite aggregates were obtained from Nsokot Stone quarry at Kasoa. The fines were obtained from the quartzite rocks and from the granites for the quartzitic and granitic aggregate mixes, respectively. The filler used in the studies was made up of inert fillers consisting of crushed rock fine materials passing the 0.075 mm sieve. Clean, clay free river sand was sourced from Aveyime Battor in the Volta region of Ghana. The three active fillers of hydrated lime (HL), limestone (LS) and ordinary Portland cement (OPC) were obtained from commercial sources. The bitumen was sourced from Tamcotank, in Switzerland, and it is a viscosity grade bitumen AC.

2.2 *Preparation of HMA Samples*

The general procedure for designing HMA mixes using the Marshall mix design method and testing equipment described in [14] was followed in this study. A series of Marshall mixes were prepared using blends of quartzite aggregates (coarse and fine), quartzite aggregates (coarse only) plus 10% natural sand, granite aggregates (coarse and fine), and granite aggregates (coarse only) plus 10% natural sand. To each blend, active filler consisting of OPC, HL, and LS was added at application rates of 0.0, 1.0, 1.5, 2.0, and 2.5%. Each prepared aggregate and filler mixture was heated to a temperature of 150 °C and then poured into a hot asphalt mixing bowl. Then AC 20 bitumen also heated to 150 °C was added at 0.5% increment, starting from 4.0 to 6.0% and thereafter thoroughly mixed together until all aggregate particles were well-coated with bitumen. Hot samples from each mix were then obtained and placed loose into preheated Marshall compaction molds. A Marshall drop hammer, with its face heated so that it does not cool the mix surface when it strikes it, was then used to compact the mix by applying 75 blows to one face first and another 75 blows to the other face. On completion of the compaction process, the specimens are allowed to cool down sufficiently and then removed from the molds producing 102 mm diameter × 63.5 mm high HMA briquettes. When the test briquettes attain room temperature, their bulk specific gravities were determined in accordance with procedures outlined in [15–17]. The test briquettes were then placed in a water bath, heated to 60 °C and then removed and damp dried after which they were placed in the Marshall apparatus where loads were applied to them at constant rate of 51 mm per minute until failure occurs. The loads at failure were recorded as the Marshall stability value with the amounts of deformation recorded as the flow values. The briquettes are then used to determine the mix properties for each bitumen content following the procedures described in [18]. The density-voids analysis is used to determine the unit weight, air

Table 1 Summary of physical properties and threshold values of coarse aggregates

Parameter	Threshold value	Quartzite	Granite
Los Angeles abrasion (LAA)	30 Max	22	25
Flakiness index (FI)	20 Max	12	16
10% Fines dry (kN)	160 Min	181	185
Wet: Dry ratio (%)	75 Min	86	79
Water absorption (%)	1.0 Max	1.0	0.7

voids, voids in mineral aggregate (VMA), and percentage voids filled with bitumen (VFB).

3 Results and Discussions

3.1 Properties of Materials Used for Asphaltic Concrete

3.1.1 Physical Properties of Aggregates

A summary of the physical characteristics of the quartzite and granite aggregates is shown in Table 1 and compared with the threshold values specified in Ministry of Transport [4]. It is clear that both the quartzitic aggregates and the granite aggregates met the minimum physical properties required. In fact, with a Los Angeles abrasion (LAA) value of 22 compared with 25 for granite, the quartzite had a superior resistance to abrasion and the lower Flakiness index (FI) implies that it also has more favorable aggregate shape for interlocking. Furthermore, it also has a higher resistance against strength deterioration on wetting as shown by a higher wet: dry ratio of the 10% Fines.

Its weakest point appears to be the higher water absorption value than granite aggregates. However, it still falls within the specification. Thus overall, the quartzite appears to have even better physical properties.

3.1.2 Petrographic Properties of Aggregates

The results of petrographic analysis of the quartzite from the Togo Series are shown in Fig. 2, and it shows that the quartz mineral content was 95% and opaque mineral (iron oxide) content was only 5%. The type of granite rock used in this study is the belt (Dixcove) type of granites and its petrographic analysis shown in Fig. 3 reveals the following: Quartz-20%, Potassium feldspar-20%, Plagioclase-40%, Hornblend-5%, Biotite-8%, Muscovite/Sericite < 1%, Sphene < 0.1%, and Opaque minerals < 0.1%.

Fig. 2 Photomicrograph of quartzite



Fig. 3 Crystalline rock texture of dixcove granite: quartz, (Qz), feldspars (Fd), biotite (Bi), and fine muscovite; crossed polars



3.1.3 Properties of Bitumen

The bitumen used sourced from Switzerland is a viscosity grade AC-20 with the characteristics summarized in Table 2.

3.2 Properties of Asphaltic Concrete

Figure 4 shows the design gradation which was used in the HMA. Though the grading is within the specified grading band, it is slightly toward the lower limit for the coarse aggregates and slightly toward the upper limit for the fine aggregates. A summary of the properties of the HMA prepared with coarse and fine aggregates of granite and of quartzites is shown in Table 3 alongside the specification requirements of [4]. The values are without any fillers. It can be seen that the values are all within the specified ranges.

Table 2 Characteristics of the AC 20 viscosity grade bitumen

Parameter	Threshold value	Test results
Penetration at 25 °C, 10 g, 5 s	40 Min	88
Softening point temperature	48–56 (°C)	55
Flash point (Cleveland open cup)	232 °C Min	269
Kinematic viscosity at 135 °C,	210 Cst, Min	338
Absolute viscosity at 60 °C,	1600–2400 P	2212
Specific gravity at 25 °C	1.01–1.06	1.04
<i>Test on residue of thin film oven test</i>		
% Mass change at 163 °C	0.2 Max	0.102
Viscosity at 60 °C	10,000 P, Max	8986

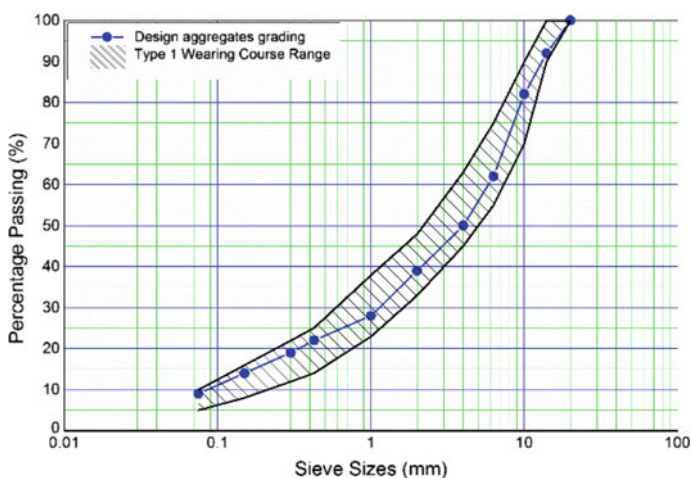


Fig. 4 Design gradation

Table 3 Test results and test requirements for HMA

Asphalt concrete	Type I wearing course	Quartzitic aggregates	Granitic aggregates
Marshal stability (2 × 75 blow) (kN)	9–18	13.8	15.1
Marshal flow value (mm)	2–4	2.6	3.7
Voids in total mix (%)-VIM	3–5	4.06	4.22
Voids fill with binder (%)- VFB	65–75	74.2	72.2

All the mixes fall within the 9–18 kN limit of stability required by [4] and shown in Table 3. Figure 5 shows that without any fillers the stability of HMA composed of granites are 1.3 kN higher than those composed of quartzites. With the addition of OPC and LS, there is insignificant change in stability. However, for HL filler, there is a significant increase in stability of both quartzitic aggregates and granitic aggregates for filler content exceeding 1.5%. Local experience suggests that HMA with stability values higher than 16kN tends to perform poorly since such mixes end up becoming brittle and therefore susceptible to early crack development. Figure 6 shows that when the fine aggregates are replaced with 10% natural sand without fillers the stability of HMA composed of granitic coarse aggregates increases from 15.1 to 16.6 kN while that of the equivalent quartzitic coarse aggregates increases from 13.8 to 15.6 kN. However, when OPC or LS is added as a filler, the stability falls initially until a filler content exceeding 1.0% and 1.5%, respectively.

3.3.2 Flow

Figure 7 shows the variation of the flow with filler content for HMA prepared with the quartzite and granite aggregates, while Fig. 10 shows the equivalent plot when the fine aggregates are replaced with 10% natural sand. Figure 8 shows that without any active filler, the quartzite mixes showed a much smaller flow value of 2.6 mm compared with 3.8 mm for the granite mixes. For granite aggregates, increasing filler content either maintains or slightly reduces the flow. However, there was an overall increase in flow for the quartzitic aggregate mixes especially for filler contents exceeding about 1.5%. Figure 8 shows that when the fine aggregates are replaced with 10% natural sand, without any fillers, there is effectively no difference between the flow of HMA made with quartzite and those made with granite aggregates. The figure also shows that the addition of up to 3.0% active fillers leads to only a slight overall increase in flow with increasing filler content.

Fig. 7 Flow and filler content for aggregates of quartzite and granite

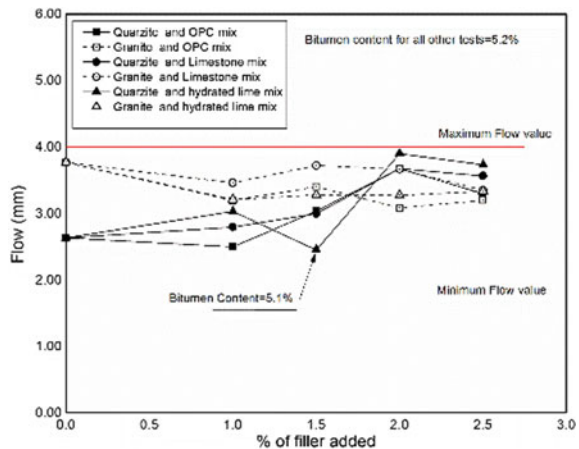
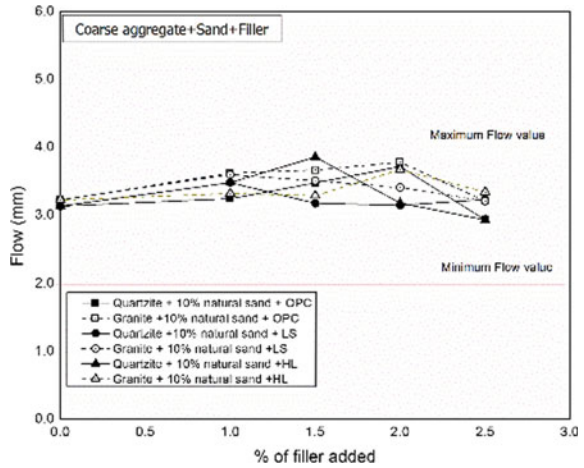


Fig. 8 Flow and filler content for coarse aggregates 10% natural sand



3.3.3 Voids Filled with Binder

The effect of different percentages of the three active fillers on the VFB at their respective optimum bitumen contents is shown in Figs. 9 and 10 for the quartzite and granite aggregates and when the fine aggregates are replaced with 10% natural sand, respectively. Without any fillers, the HMA with quartzite aggregates has a VFB of 74.2% which is 2.0% higher than the VFB of the equivalent HMA of granite aggregates. However, upon addition of the active fillers, the VFB of the quartzite HMA reduces while that of the granite HMA tend to increase slightly.

Fig. 9 Variation of VFB with filler content for granite and quartzite aggregates

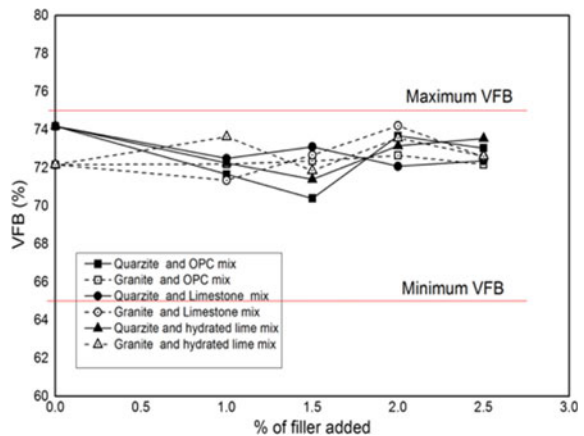
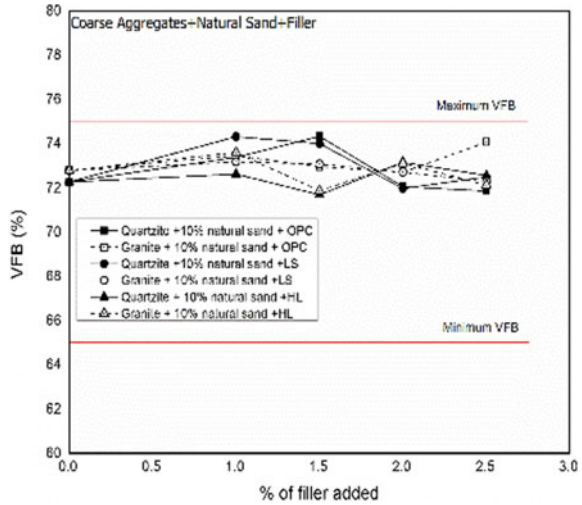


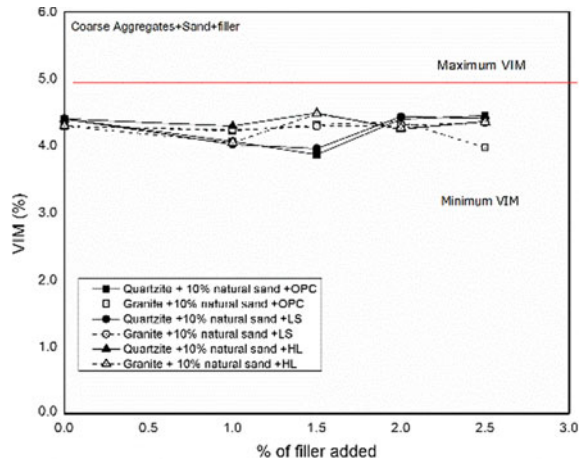
Fig. 10 Variation of VFB with filler content for coarse aggregates of quartzite and granite and fine aggregates of natural sand



3.3.4 Voids in Total Mix

The voids in total mix (VIM) is plotted against the filler content for the quartzite and granite aggregates in Fig. 11. It is clear that HMA made from aggregates of quartzites and granites have similar VIM values and changes only slightly with filler content. The behavior is similar for HMA made from the aggregates but blended with 10% natural sand.

Fig. 11 Variation of VIM with filler content for granite and quartzite aggregates



4 Conclusions and Recommendations

A comparative study of the properties of HMA made from aggregates from quartzites and from granites was conducted to determine whether aggregates from quartzites of the Togo Series of rock formation of Ghana can be used for HMA and the influence of three different fillers. The study concludes that:

1. Whereas the quartzite is composed of 95% quartz with opaque minerals constituting less than 5% the granites has with only 20% quartz with less than 0.1% opaque minerals
2. Aggregates from quartzites like those from granites meet the minimum physical properties specified for aggregates for HMA for Type 1 Wearing Course. In terms of abrasion, flakiness index and resistance to strength loss on wetting the quartzites are superior to the granite aggregates
3. The HMA produced from the quartzite aggregates using the Marshall methods met all the minimum requirements for stability, flow and volumetric requirements of VFB and VMA
4. Without any fillers, HMA composed of granites has slightly higher stability and higher flow than those composed of quartzites.
5. Whereas the addition of OPC and LS as fillers causes insignificant change in stability for both aggregates, increasing HL filler content leads to a significant increase in stability of both aggregates but only a slight increase in flow for quartzitic aggregates for filler content exceeding 1.5%.
6. The values of VIM and VFB for the quartzite aggregates and for the granite aggregates were almost identical and were in the range of 3.9% to 4.5% and 70% to 74%, respectively

The quartzite from the Togo series therefore appears to have very good potential to be used for HMA. But there is the need for further studies into the long-term performance including moisture susceptibility testing.

References

1. Asphalt Institute (1981) Asphalt mix design method, 6th edn
2. Sybilski D, Bankowski W, Krajewski M (2010) High modulus asphalt with limestone aggregates. *Int J Pavement Res Tech* 3(2):96–101
3. Huseyin A, Cahit G, Sedat C (2011) Use of volcanic aggregates in asphalt pavement mixes. *Proc Inst Civ Eng-Trans* 164(2):111–123
4. Ministry of Transport (2007) The standard specification for road and bridge works, Accra Ghana
5. Sady AT, Aqeel RJ (2011) The effect of filler type on the hot mix asphalt behavior
6. Mehari ZB (2007) Effect of different types of filler materials on characteristics of hot-mix-asphalt concrete
7. ASTM D1559 (AASHTO T 245) Standard test method for resistance to plastic flow of bituminous mixtures using marshall apparatus, ASTM Book of Standards Vol 04.03

8. ASTM D1560, Standard test method for resistance to deformation and cohesion of asphalt mixtures by means of Hveem apparatus, ASTM Book of Standards vol 04.03
9. Asphalt Institute (1995) Superpave level 1 mix design asphalt institute superpave series No. 2 (SP2) Lexington KY
10. Bahai HU (1993) Bibliographies for physical properties of asphalt cement, SHRP-A-626. National Research Council, Washington DC
11. Fuller WB, Thompson SE (1907) The laws of proportioning concrete. Trans Am Soc Civil Eng 59:67–172
12. Saad A-Q, and Haider A-S (2005) Effect of aggregate properties on asphalt mixtures stripping and creep behavior
13. Little DN, Jones JR (2003) Chemical and mechanical mechanisms of moisture damage in hot mix asphalt pavements. National Seminar in Moisture Sensitivity, San Diego, CA
14. MS-22: HMA Construction (2nd edn) by Asphalt Institute
15. AASHTO T166, Standard Test method for Bulk specific gravity of compacted HMA using Saturated Surface-Dry Specimens
16. AASHTO T 275, Standard Test method for Bulk specific gravity of compacted Asphalt Mixtures using Paraffin Coated Samples, AASHTO
17. AASHTO T 209 (ASTM D 2041), Standard test method for theoretical maximum specific gravity and density of asphalt mixtures, AASHTO
18. AASHTO T 164, Standard test method for quantitative extraction of asphalt binder from HMA, AASHTO

Introduction of Stone Matrix Asphalt for National Highways in Japan's Cold, Snowy Regions



Shunsuke Tanaka, Kimio Maruyama, and Shuichi Kameyama

Abstract In cold, snowy Hokkaido, Japan, the road traffic environment is severe, particularly in winter. The Hokkaido Regional Development Bureau (HRDB), which administers the national highways in Hokkaido, has started to install porous asphalt to better secure the safety of vehicular traffic. However, the durability of such pavement has become an issue. In addition to the need to maintain vehicular traffic safety, the need to maintain sufficient durability has become important for pavements of national highways in the cold, snowy regions of Japan. We developed an asphalt mixture called high-performance stone matrix asphalt (HP-SMA). To evaluate its durability in a cold, snowy region, we conducted laboratory experiments using methods commonly used in Japan. The experiments clarified that HP-SMA has higher durability than porous asphalt. As the next step, the HP-SMA was installed on a trial basis on a section of a national highway. Through such installation, appropriate methods for installation and quality control were determined. The trial installation clarified that the durability of the HP-SMA depends heavily on the compaction quality. Therefore, in compacting HP-SMA, there are more points to bear in mind than for dense-graded asphalt. The most suitable compaction method for securing the required pavement quality with conventional machinery was determined. The proposed compaction method uses a three-wheel roller, a tandem roller, and a tire roller. To obtain higher durability than that achieved by the proposed method, the use of an oscillatory tandem roller was found to be effective.

Keywords High-performance SMA · Durability · Safety of vehicular traffic

S. Tanaka (✉) · K. Maruyama

Civil Engineering Research Institute for Cold Region, Hiragishi 1-3-1-34, Toyohira-ku, Sapporo 0628602, Japan

e-mail: s-tanaka@ceri.go.jp

K. Maruyama

e-mail: k.maruyama@ceri.go.jp

S. Kameyama

Hokkaido University of Science, Maeda 7-15-4-1, Teine-ku, Sapporo 0068585, Japan

e-mail: kameyama@hus.ac.jp

1 Introduction

Approximately 60% of Japan is cold and snowy. One characteristic of Japan's cold, snowy regions is snowfall of a scale that is rare around the world. These areas are inhabited by about 20% of the population of Japan. The people there lead active lives. In Sapporo, a city of about 2 million people, the annual snowfall exceeds 5 m (see Table 1) [1]. It is rare to find such a large city with such extreme snowfall. In Sapporo, there is a need to secure winter road traffic by maintaining a certain level of road management. National highways in Japan's cold, snowy regions have been paved with porous asphalt (PA) in consideration of the safety of vehicles traveling at high speeds. PA is expected to facilitate safe driving. In winter, PA affords good skid resistance even when the roads are icy. PA effectively mitigates hydroplaning and visibility reductions under rainy conditions [2–4].

However, many problems have been found regarding the durability of PA (Fig. 1). In cold, snowy regions, highway pavements are exposed to the severe conditions of low temperature, repeated freeze–thaw of snowmelt, and abrasion from tire chains and steel snowplow blades [5]. These adverse conditions greatly affect the road surfaces in Japan, where snowfall is extreme.

To solve these problems, we developed high-performance stone matrix asphalt (HP-SMA). The goal was to provide an asphalt mixture that could secure safe traveling, while also excelling in durability.

Table 1 Population and annual snowfall of major cities in the cold, snowy regions of the world

City (country)	Population (million)	Snowfall (m)
Sapporo (JPN)	1.9	5.82
Shenyang (CHN)	7.8	0.49
Montreal (CAN)	1.6	2.15
Vienna (AUT)	1.7	1.72
Munich (GER)	1.3	1.00
St. Petersburg (RUS)	4.6	2.97



Fig. 1 Damaged porous asphalt (PA)

In this study, laboratory experiments were conducted to evaluate the durability of HP-SMA. The experiments clarified that HP-SMA has higher durability than PA. As the next step, the HP-SMA was installed on a trial basis at our winter test track and on a section of national highway administered by the Hokkaido Regional Development Bureau (HRDB). The test track and the national highway are in Hokkaido, a cold, snowy region of Japan. The trial installation clarified the following: (1) the durability of the HP-SMA depends heavily on the compaction quality, and (2) the use of an oscillatory tandem roller produces pavement that excels in durability and resistance to aggregate scattering and is effective in improving the durability of HP-SMA.

2 High-performance SMA

HP-SMA is an asphalt mixture that was developed for cold, snowy regions. It has an excellent surface texture and the high durability of SMA. The uppermost layer has a texture similar to that of PA. The deeper part has a dense structure of aggregates whose voids are filled with a mortar of asphalt and fillers (Fig. 2). Table 2 shows an example of a mix ratio for HP-SMA. Examples of PA (void ratio 17%) and dense-graded asphalt (DGA13F) for cold, snowy regions in Japan, which were compared with the HP-SMA in this study, are also shown in this table. HP-SMA specifications require an asphalt content of around 6.0%. This is to secure the standard surface roughness (mean profile depth [6] ≥ 0.9 mm), which greatly affects driving safety, and to maintain sufficient durability in Japan's cold, snowy environment.

SMA 11S, which is a standard SMA made in Germany and is representative of general SMAs, has an asphalt content of 6.6% or more [7]. HP-SMA has an asphalt content of 5–7%. This shows that HP-SMA may have a slightly lower gravel content than conventional SMAs. The void content is 2.5–3.0% for SMA 11S and 3.0–7.0% for HP-SMA. The road surface texture cannot be compared because SMA 11S has no specified value, although HP-SMA does. However, judging from the specified values for asphalt quantity and void content, the road surface texture of HP-SMA may be coarser.

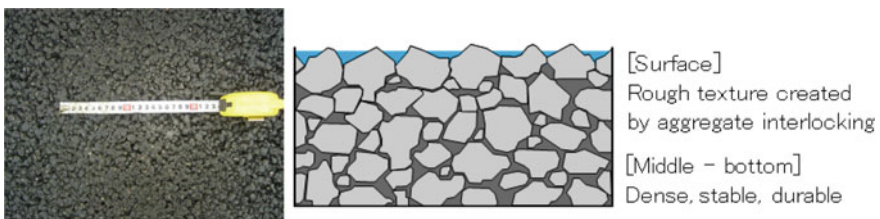


Fig. 2 The surface and cross section of high-performance SMA

Table 2 Mix ratio of HP-SMA

Mix ratio (%)	Asphalt	Stone powder	Screenings	Coarse sand	#7 crushed stone	#6 crushed stone	Cellulose fiber	Total
HP-SMA	Modified asphalt type II (PG70-22) 5.9	10.4	6.1	6.1	8.5	63.0	0.3 (outer percentage)	100.3
DGA13F	Straight asphalt –Non modified–(PG58-22) 5.8	9.4	3.8	35.8	8.5	36.7	–	100
PA (void ratio 17%)	Modified asphalt-type H (PG76-22) 5.1	4.8	–	16.3	–	73.8	–	100

3 Verification of Durability

The coarse surface texture of roads paved using HP-SMA supports safe traveling. A previous study [8] found that HP-SMA is as good as PA and is better than DGA13F with respect to three points, which are related to how the pavement supports travel safety: (1) improving visibility on wet roads by reducing the splashing of water, (2) improving night-time visibility on wet roads by reducing the glare of lights from oncoming vehicles reflecting from the road, and (3) providing sufficient skid resistance on roads with black ice. The present study also clarified that HP-SMA is more durable than PA. In addition to the need to maintain vehicular traffic safety, the need to maintain sufficient durability has become important for HP-SMA in cold, snowy regions. To evaluate the durability of HP-SMA in a cold, snowy region, laboratory experiments were conducted using methods commonly used in Japan.

The durability of HP-SMA and PA is compared here with two indoor tests called the low-temperature Cantabro test and the raveling test. The methods of both tests are specified in “Pavement Performance Evaluation Methods” of the Japan Road Association [9]. The low-temperature Cantabro test is used to assess the aggregate fretting resistance of pavement, and the raveling test is used to assess resistance to raveling. Both tests aim to assess durability in a cold environment by setting the test temperature below 0 °C.

3.1 Low-temperature Cantabro Test

The low-temperature Cantabro test was developed to assess the impact aggregate loss of PA at low temperature. In Japan’s cold, snowy regions, the impact forces of tire chains and the blades of snow graders cause aggregates to separate from the pavement body. The test is used in Japan to assess durability against aggregate fretting for pavements in cold, snowy environments.

First, the test room and the HP-SMA and PA specimens are cured at room temperature. In this study, the temperature was set at −20 °C. Wellcured specimens underwent 300 revolutions in a Los Angeles abrasion testing machine. Then, the low-temperature Cantabro loss was calculated as the percentage of weight loss over the initial weight. The test specimens were the same size, and the same preparation method for the Marshall test was used. The Los Angeles abrasion testing machine and a view of the test specimens before and after the test are shown in Fig. 3. Figure 4 shows the test results. The low-temperature Cantabro loss of HP-SMA is shown to be about half that of PA. This shows that the aggregate fretting resistance of HP-SMA is superior to that of PA. The low-temperature Cantabro loss of PA is specified as less than or equal to 20% for national highways managed by the HRDB. As HP-SMA has been confirmed to have higher aggregate fretting resistance than that of PA, the HRDB decided to put into practice the specified value of low-temperature Cantabro loss in HP-SMA “less than or equal to 16%” (a stricter value than that for PA).

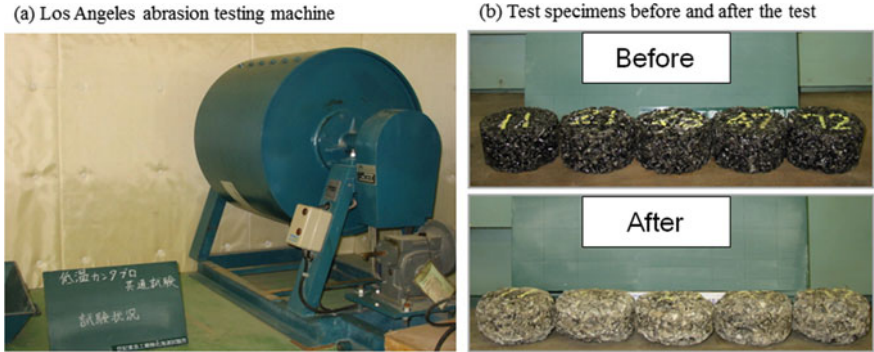
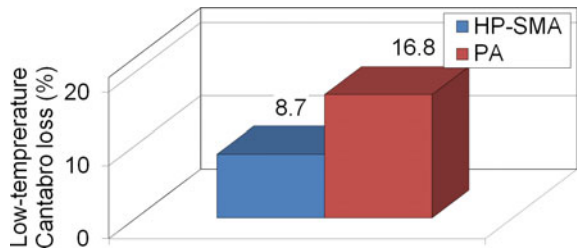


Fig. 3 Los Angeles abrasion testing machine, and the test specimens before and after the test

Fig. 4 Low-temperature Cantabro losses of HP-SNA and PA



3.2 Raveling Test

The test was made using CERI’s unique wheel-tracking test machine (Fig. 5). This test machine has a circular table for specimens and two wheels to which chains are attached. While the table and the wheel rotate, the chain hits the specimen. Then, the area of abrasion on the specimen was measured to assess durability.

The room temperature was kept at the test temperature (−10 °C). The specimen was cured at that temperature. The machine simulates driving at 40 km/h for 10 min. The cross-sectional area of raveling or aggregate fretting on the specimen was measured at three cross sections with a laser displacement sensor. Assessment



Fig. 5 Wheel-tracking test machine and raveled area as determined by raveling test

of the aggregate interlocking capability of the specimen was made for the averaged areas of aggregate loss in the three cross sections.

Figure 5 shows the wheel-tracking test machine and the raveled areas for HP-SMA and PA, as determined by the raveling test. HP-SMA has a smaller raveling area than PA has. HP-SMA has a 150 mm^2 smaller raveling area than PA has at 1000 wheel rotations, and a 250 mm^2 smaller raveling area than PA at 2000 wheel rotations. From these results, the raveling resistance of HP-SMA is considered to be higher than that of PA.

4 Relationship Between Compaction Technique and Product Quality

HP-SMA can be compacted by using compaction machines that are ordinarily used in Japan, including three-wheel rollers, tandem rollers, and tire rollers. For HP-SMA, sufficient compaction at high temperature is necessary, because the optimal temperature for compaction of HP-SMA, in which modified asphalt is used, is higher than that for DGA13F. In cold, snowy regions, it is necessary to investigate and decide the following before construction: The compaction temperature, the combination of compaction machines, and the number of runs of the machine. This is because it may be necessary to conduct work under environmental conditions in which the mixture temperature may quickly decrease. It is very important to clarify the influence of compaction techniques on the quality of HP-SMA, because the pavement has to have both an appropriately coarse texture and sufficient durability.

HP-SMA's ability to support safe traveling lies in its pavement surface texture. To secure durability, it is necessary to secure sufficient compaction. To clarify the relationship between the surface texture and the degree of compaction, the authors experimentally constructed pavement sections in which multiple compaction techniques were used at a winter test track (Fig. 6).

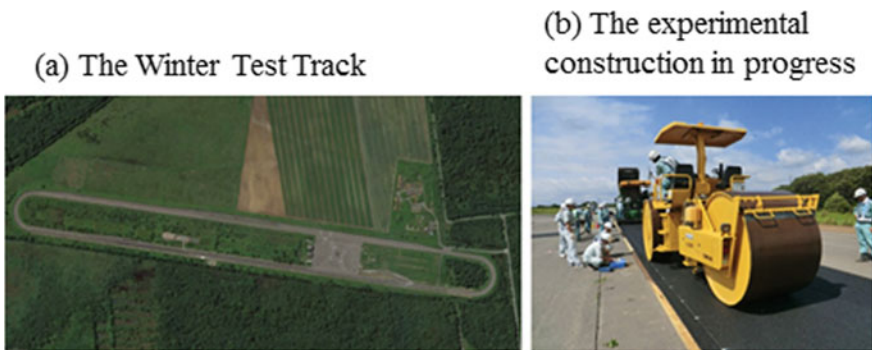


Fig. 6 The winter test track (left) and the experimental construction in progress (right)

4.1 Outline of the Experiment

The experiment was conducted on September 3, 2014. The weather on the day of the experiment was fine, and the day was favorable for pavement construction. All five sections were constructed continuously under strict observance of the target temperature of the mixture. The construction was done to facilitate a comparative examination later. The pavement thickness (the surface layer) was 40 mm. Five patterns of compaction were used: (A) without compaction (spreading only), (B) compaction by 3 runs with a three-wheel roller, (C) roller compaction by 11 runs with a three-wheel roller, (D) breakdown compaction by a three-wheel roller, secondary compaction by a tandem roller, and finishing compaction by a tire roller (the most common pattern of compaction in actual construction), and (E) compaction by an oscillatory tandem roller (Table 3). The three roller compaction machines are shown in Table 4. The measurement items were the mean profile depth (MPD) [6] measured

Table 3 Compaction conditions

Conditions	Breakdown compaction (target temperature: 150–170 °C)	Secondary compaction (target temperature: 120–140 °C)	Finishing compaction (target temperature: 60– 80 °C)
A	Without compaction (spreading only)	–	–
B	3 runs with a three-wheel roller	–	–
C	11 runs with a three-wheel roller	–	–
D	7 runs with a three-wheel roller	7 runs with a tandem roller	3 runs with a tire roller
E	Oscillatory tandem roller 1 run without oscillation	Oscillatory tandem roller 6 runs with oscillation	3 runs with a tire roller

Table 4 Machines used for compaction

Machine			
	Three-wheel roller	Oscillatory tandem roller	Tire roller
Machine weight	9300 kg	6800 kg	12,925 kg
Other	–	Centrifugal force: 105 kN Oscillatory frequency: 51.6 Hz	–

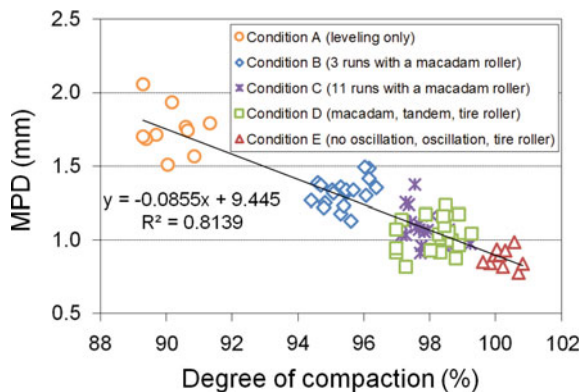
by circular track meter (CTM) [10] and the degree of compaction of the core sampled at the location where the MPD was measured.

4.2 Relationship Between the Road Surface Texture and the Degree of Compaction

The relationship between the road surface texture and the degree of compaction, which was clarified in the experimental construction, is shown in Fig. 7. A close inverse correlation is observed between the MPD and the degree of compaction. If construction is done to achieve great MPD in order to enable pavement to better support traveling safety, it is possible that the degree of compaction will decrease and that the durability of the pavement will also decrease.

Next, the difference in compaction conditions was examined. The quality standard values for pavement compacted under Condition D are 97.0–99.3% for the degree of compaction and 0.86–1.20 mm for the MPD. The HRDB sets the degree of compaction as 96% or higher and the MPD as 0.90 mm or greater (both are the average values for a specified number of points) for the standard values of quality for HP-SMA. The quality of pavement constructed under Condition D roughly satisfies these standard values. Of the conditions tested in this experiment, Condition D is the appropriate compaction condition when examined based on the idea of selecting compaction that is able to achieve an appropriate surface texture and degree of compaction. When the quality of pavement constructed under Condition E, in which an oscillatory tandem roller was used, is examined, there are some values for surface texture that are lower than the standard value of 0.9 mm. However, the degree of compaction of the pavement constructed under Condition E was the highest among all experimentally constructed pavement in this study. Therefore, it is possible to secure high durability by using Condition E. As discussed earlier, damage to PA

Fig. 7 Relationship between the road surface texture and the degree of compaction



under the severe environment of cold, snowy regions was one impetus for the development of HP-SMA. It is necessary to achieve a high degree of compaction in a short period of time when the air temperature is low. To meet such a need, Condition E is thought to be an effective compaction condition under certain construction conditions.

5 Experimental Construction on a National Highway

In 2014, experimental construction of HP-SMA was done on two sections of pavement constructed on a national highway managed by the HRDB. On each of the two completed sections, the density, degree of compaction, and surface texture were measured, and cores sampled from those sections were subjected to the durability performance assessment test. By using the measurements and the test results, the appropriate compaction technique was examined, variations in the quality of actual construction were determined, and points to bear in mind for securing pavement quality were clarified.

5.1 Outline of the Experimental Construction

The sections for the experimental construction are outlined in Table 5. For Section A, compaction was done by using an oscillatory tandem roller. A measurement point was set every 100 m on the 300 m pavement section (i.e., 9 measurement points in total). Compaction using a three-wheel roller was done for Sections B. A measurement point was set every 20 m on the 100 m pavement section (i.e., 15 measurement points in total). The surface texture was measured (MPD measured using CTM) and cores were sampled at each measurement point. The sampled cores were used for measuring the degree of compaction and for the low-temperature Cantabro test.

Table 5 Outline of the experimental construction on the national highway

Section	Spreading (°C)	Breakdown compaction	Secondary compaction	Finishing compaction
A	145–165	Oscillatory tandem roller Compaction: 2 runs (without oscillation) Target temperature: 140–160 °C	Oscillatory tandem roller Compaction: 7 runs (with oscillation) Target temperature: 120–130 °C	Tire roller Compaction: 3 runs Target temperature: 70–90 °C
B	160–180	Three-wheel roller Compaction: 6 runs Target temperature: 155–175 °C	Tandem roller Compaction: 6 runs Target temperature: 120–140 °C	Tire roller Compaction: 4 runs Target temperature: 70–90 °C

5.2 Comparison of Qualities of HP-SMA Constructed by Using Two Different Compaction Techniques

We compared the quality of the HP-SMA on Section A, which was compacted by an oscillatory tandem roller, to the quality of the HP-SMA on Section B, which was compacted by a three-wheel roller. Sections A and B abutted each other. The temperature of the mixture used for the construction was within the target temperature for each section. Therefore, comparison between the qualities of these three sections was appropriate. Table 6 shows the conditions under which Sections A and B were constructed. Figure 8 shows the MPD measured using a CTM, the degree of compaction, and the result of the low-temperature Cantabro test on the sampled cores. The conditions for the low-temperature Cantabro test are shown in Table 7.

Table 6 Effect of variables

Section	Weather	Air temp. (°C)		Avg. wind speed (m/s)	Temp. of the mixture (°C)			Duration of construction (min)
		Highest	Lowest		At start of spreading	At end of compaction	Temp. difference	
A	Fine	22.7	19.9	2.9	159	74	-85	34
B	Fine	18.9	16.5	3.5	155	76	-79	31

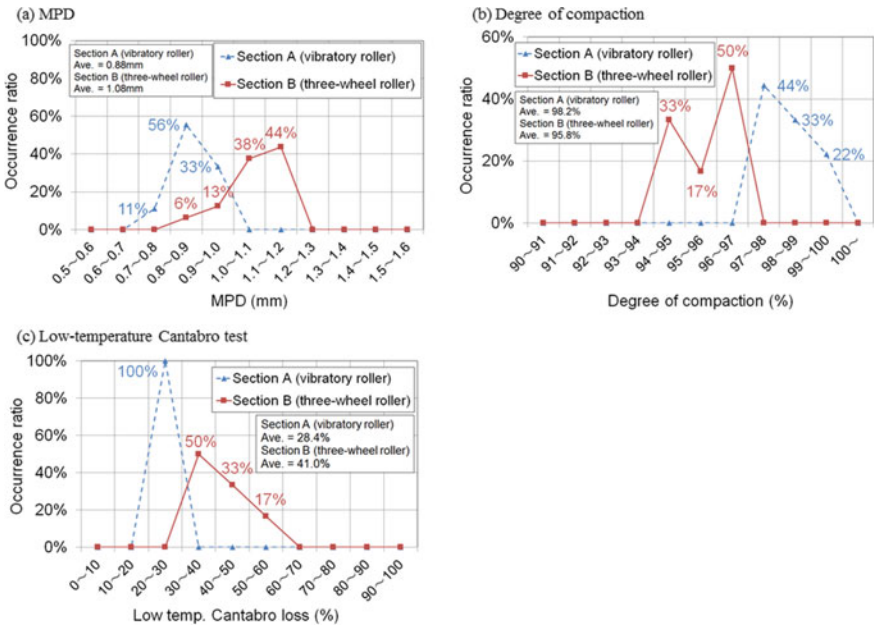


Fig. 8 Survey results

Table 7 Effect of variables

Measurement item	Test temp (°C)	Test technique
Low temp. Cantabro loss	-20	Los Angeles abrasion testing machine revolutions: 300

The average MPD for Section A, where an oscillatory tandem roller was used, is 0.88 mm, and that for Section B, where a three-wheel roller was used, is 1.08 mm. The average MPD for Section B is 0.2 mm greater than that for Section A. In contrast, the average degree of compaction for Section A is at least 2% greater than that for Section B. The average of the low-temperature Cantabro loss for Section A is at least 12% smaller than that for Section B. It is thought that the pavement constructed by using an oscillatory tandem roller is superior in terms of durability and resistance to aggregate scattering. To achieve sufficient compaction, HP-SMA requires temperatures higher than those for ordinary asphalt. Therefore, the oscillatory tandem roller, which uses dynamic loading from oscillation in addition to the weight of the machine, has the ability to achieve a high degree of compaction [11]. The oscillatory tandem roller is thought to be effective in improving the durability of HP-SMA.

6 Conclusions

In conclusion, this study clarified the following.

- The durability of high-performance stone matrix asphalt (HP-SMA) was assessed by indoor tests. HP-SMA was found to be more durable than porous asphalt (PA).
- There is an inverse correlation between the road surface texture (MPD) and the degree of compaction. If construction is done to achieve great MPD in order to enable the pavement to better support traveling safety, it is possible that the degree of compaction will decrease and that the durability of the pavement will also decrease. Therefore, sufficient care should be taken to achieve compaction of appropriate quality.
- The use of an oscillatory tandem roller produced pavement that excels in durability and resistance to aggregate scattering. To achieve sufficient compaction, HP-SMA requires temperatures higher than those for ordinary asphalt. Therefore, it is effective to use an oscillatory tandem roller in some cases in which a high degree of compaction needs to be achieved in a short period of time, including when the air temperature is low.

References

1. Tanaka S, . and Maruyama K (2018) Development of a high-performance SMA suited to the surface course of national highways in Japan's Cold, Snowy Regions. In: 1st international conference on stone matrix asphalt, Atlanta, Georgia
2. Gibbs D, Iwasaki R, Bernhard R, Bledsoe J, Carlson D, Corbisier C, Fults K, Hearne T, McMullen K, Newcomb D, Roberts J, Rochat J, Scofield L, Swanlund M (2005) Quiet pavement systems in europe, federal highway administration, U.S. department of transportation and american association of state highway and transportation officials, FHWA-PL-05-011
3. Isenring T, Koster H, Scazziga I (1990) Experiences with porous asphalt in Switzerland. In: Transportation research record 1265, Transportation Research Board, Washington, D.C., pp 41–53
4. Cahill Associates (1993) Stormwater management systems: porous pavement with underground recharge beds
5. Maruyama K, Miura G, Oyama K, Kimura T (2015) Effect of snow and ice on the road surface on vehicle running resistance and fuel efficiency. In: The 9th international conference on road and airfield pavement technology (ICPT), China
6. ISO 13473-1: 1997. (1997) Characterization of pavement texture by use of surface profiles—Part 1: Determination of Mean Profile Depth, ISO
7. Blazejowski K (2010) Stone matrix asphalt: theory and practice. CRC Press
8. Tanaka S, Abe R, Maruyama K, Takeichi K, Kimura T (2018) Study on the effectiveness of high-performance SMA developed as a measure for improving the winter road surface, 15th International Winter Road Congress. PIARC, Poland
9. Japan Road Association (2008) Pavement performance evaluation method—Separate Volume, Japan, pp 24–37 (in Japanese)
10. ASTM E2157-01 (2001) Standard test method for measuring pavement macrotexture properties using the circular track meter. ASTM International, West Conshohocken, PA
11. Tsubota M, Tamai A (1991) An examination of degree of compaction depending on the difference of compaction machines. *Pavement* 26(10):24–29 (in Japanese)

Effects of Using Recycled Aggregates and Large Stones for Base and Subbase Layers on Modulus Properties of Pavements



Haluk Sinan Coban, Bora Cetin, Halil Ceylan, William Likos, and Tuncer B. Edil

Abstract Recycled concrete aggregate (RCA), recycled asphalt pavement (RAP), and large stones were used to replace natural aggregates to build pavement base and subbase layers in this study. Two RCA materials with different gradations and a mixture of RCA and RAP materials were used to build recycled aggregate base (RAB) layers at the same thickness. Moreover, large stones were used to build large stone subbase (LSSB) layers at two different thicknesses. Two different geogrids (triaxial and biaxial) and one type of geotextile were applied between the thinner LSSB and subgrade layers, whereas no geosynthetics were used in the thicker LSSB layers. Light weight deflectometer (LWD) and falling weight deflectometer (FWD) tests were performed during construction to make a preliminary stiffness evaluation of the built test cells. In addition, the results of the two field tests were compared with each other. Test results showed that the highest moduli were observed in the test cells built with RAB layers in which RCA materials were used. On the other hand, the lowest moduli were observed in test cells built with the thinner LSSB layers. The two field tests yielded similar modulus trends overall.

Keywords Recycled concrete aggregate · Recycled asphalt pavement · Recycled aggregate base · Large stone subbase · Modulus · Stiffness · Geosynthetics

1 Introduction

Every year, more than one billion tons of natural aggregates are produced, and around 75% of the production was utilized in pavement maintenance and construction [1]. Using large amounts of natural aggregates have caused depletion of such aggregates

H. S. Coban · B. Cetin (✉)
Michigan State University, East Lansing, Michigan 48824, USA
e-mail: cetinbor@msu.edu

H. Ceylan
Iowa State University, Ames, IA 50011, USA

W. Likos · T. B. Edil
University of Wisconsin-Madison, Madison, WI 53706, USA

and an increase in their unit price [2]. To increase the pavement sustainability and reduce the use of natural aggregates, recycled concrete aggregate (RCA) and recycled asphalt pavement (RAP) materials have been used in asphalt mixtures and aggregate base layers [3, 4]. In addition, the use of large stones (or unconventionally large aggregates) to replace conventional natural aggregates for subbase layer construction has gained popularity [5, 6].

RCA materials consist of natural aggregates and residual mortar, which is the mortar that remains attached to aggregates after crushing and processing the existing hardened concrete. RAP materials are produced by milling and crushing the existing asphalt layers of pavements and contain natural aggregates and asphalt binder, which is attached to aggregates. There is no specific definition of large stones in the literature; however, they can be defined as highly porous materials that contain a considerable number of particles larger than 25.4 mm. While RCA materials generally exhibit hydrophilic properties due to the presence of residual mortar, RAP materials tend to exhibit hydrophobic properties due to the presence of asphalt binder [4]. The general trend in the literature is that such recycled aggregates show higher stiffness than natural aggregates [4, 7–9]. Due to the size limitations of the existing test equipment, not much information is available for large stones.

In this study, coarse RCA, fine RCA, and RCA + RAP materials were used to build recycled aggregate base (RAB) layers at the same thickness for full-scale test cells. In addition, large crushed granite was used to build large stone subbase (LSSB) layers at two different thicknesses. To investigate the modulus properties of the test cells built with RAB and LSSB layers (before the placement of asphalt layers), a series of light weight deflectometer (LWD) and falling weight deflectometer (FWD) tests, which are non-destructive field tests, were performed and their results were evaluated.

2 Test Cells

Eleven test cells were built on the Minnesota Road Research Project (MnROAD) low volume road (LVR), a pavement research facility owned by the Minnesota DOT (MnDOT) (Fig. 1).

The test cells were divided into two groups: (1) RAB group and (2) LSSB group. The LSSB group consisted of two subgroups: (1) thicker LSSB subgroup and (2) thinner LSSB subgroup. In the RAB group, coarse RCA, fine RCA, and RCA + RAP were used to build 300-mm thick RAB layers in cells 185, 186, and 189, respectively. Crushed limestone was also used to build a 300-mm thick aggregate base layer in cell 189 as a control in the RAB group. Each cell was 61 m long and 7.4 m wide in the RAB group. In the thicker LSSB subgroup, two 460-mm thick LSSB layers were built with large crushed granite in cells 127 and 227 (each cell was 79.2 m long and 7.4 m wide). In the thinner LSSB subgroup, which consisted of cells 328, 428, 528, 628, and 728, all the 230-mm thick LSSB layers were also built with large crushed granite. The LSSB layers of cells 328–628 were built over different geosynthetics

Recycled Aggregate Base (RAB) Group				Large Stone Subbase (LSSB) Group						
				Thicker LSSB		Thinner LSSB				
Cell 185	Cell 186	Cell 188	Cell 189	Cell 127	Cell 227	Cell 328	Cell 428	Cell 528	Cell 628	Cell 728
90 mm Asphalt	90 mm Asphalt	90 mm Asphalt	90 mm Asphalt	90 mm Asphalt	90 mm Asphalt	90 mm Asphalt	90 mm Asphalt	90 mm Asphalt	90 mm Asphalt	90 mm Asphalt
300 mm Coarse RCA Base	300 mm Fine RCA Base	300 mm Crushed Limestone Base	300 mm RCA+RAP Base	150 mm Class 6 Aggregate Base	150 mm Class 6 Aggregate Base	150 mm Class 5Q Aggregate Base	150 mm Class 5Q Aggregate Base	150 mm Class 5Q Aggregate Base	150 mm Class 5Q Aggregate Base	150 mm Class 5Q Aggregate Base
90 mm Sandy Subbase	90 mm Sandy Subbase	90 mm Sandy Subbase	90 mm Sandy Subbase	460 mm LSSB	460 mm LSSB	230 mm LSSB	230 mm LSSB	230 mm LSSB	230 mm LSSB	230 mm LSSB
Sandy Subgrade	Sandy Subgrade	Clayey Subgrade	Clayey Subgrade			TX	TX+GT	BX+GT	BX	
						Clayey Subgrade	Clayey Subgrade	Clayey Subgrade	Clayey Subgrade	Clayey Subgrade
				Clayey Subgrade	Clayey Subgrade					

TX = Triaxial Geogrid
 BX = Biaxial Geogrid
 GT = Nonwoven Geotextile

Fig. 1 Test cells and their compositions (not to scale)

(each test cell was 33.5 m long and 7.4 m wide). A triaxial geogrid (TX) was used alone in cell 328 and in combination with a nonwoven geotextile (GT) in cell 428. In addition, a biaxial geogrid (BX) was used in combination with the GT in cell 528 and alone in cell 628. No geosynthetic was used in cell 728 (this test cell was 39.6 m long and 7.4 m wide).

3 Soils and Aggregates

In total, 10 different soils and aggregates were used to build the test cells shown in Fig. 1. The particle size distributions and the classification of the materials are provided in Fig. 2 and Table 1, respectively. Other material properties, including maximum dry density (MDD), optimum moisture content (OMC), specific gravity (G_s), absorption, asphalt content, and mortar content, are summarized in Table 2.

4 Test Methods

4.1 Light Weight Deflectometer (LWD) Test

LWD tests (ASTM E2583) were performed on the subgrade (for the RAB group) and base layers (for both groups) to determine LWD elastic modulus (E_{LWD}) values. An LWD with a plate diameter of 200 mm, a drop mass of 10 kg, and a drop height of 500 mm was used. The influence depth was between 200 and 300 mm (1–1.5 times

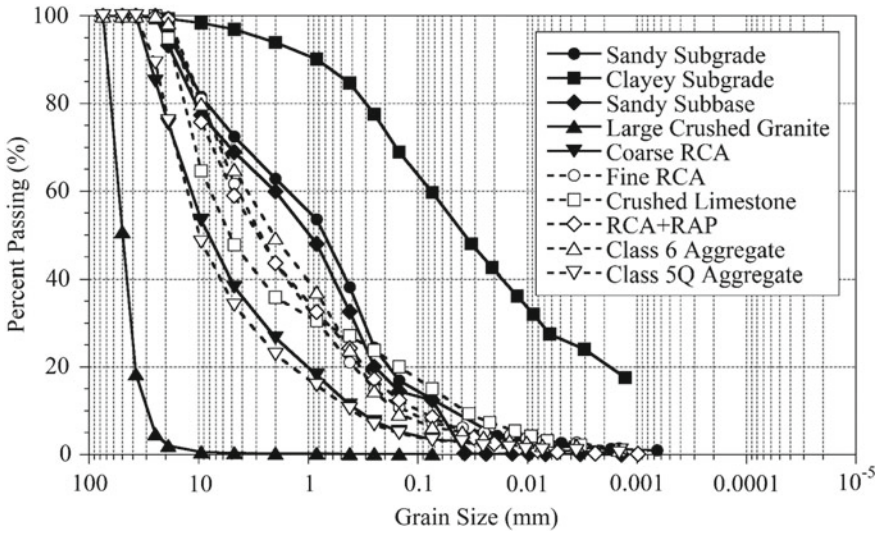


Fig. 2 Particle size distributions of the soils and aggregates used in this study

Table 1 Classifications of the soils and aggregates used in this study

Material	Gravel ¹ (%)	Sand ¹ (%)	Fines ¹ (%)	C _u ¹	C _c ¹	LL ²	PI ²	USCS ³
Sandy subgrade	27.6	59.8	12.6	33.12	1.24	19.9	NP	SM
Clayey subgrade	3.1	37.2	59.7	NA	NA	36.3	12.4	CL
Sandy subbase	31.1	56.5	12.4	30.30	1.10	18.9	NP	SM
Large crushed granite	99.6	0.3	0.1	1.84	1.08	NA	NP	GP
Coarse RCA	61.7	34.9	3.4	34.49	1.75	NA	NP	GW
Fine RCA	38.3	54.6	7.1	33.93	1.12	32.7	NP	SW-SM
Crushed limestone	52.3	32.6	15.1	211.31	1.91	17.9	NP	GM
RCA + RAP	41	50.4	8.6	49.41	0.98	27.4	NP	SP-SM
Class 6 aggregate	35.1	58.6	6.3	23.82	0.60	27.4	NP	SP-SM
Class 5Q aggregate	65.9	30.9	3.2	33.69	2.60	NA	NP	GW

C_u uniformity coefficient; C_c coefficient of curvature; LL liquid limit; PI plasticity index; USCS Unified Soil Classification System; NP non-plastic; NA not available. ¹ASTM C136, D6913, and D7928; ²BS 1377-2 and ASTM D4318; ³ASTM D2487.

Table 2 Other properties of the soils and aggregates used in this study

Material	MDD ¹ (kN/m ³)	OMC ¹ (%)	G _s ²	Absorption ² (%)	Asphalt content ³ (%)	Mortar content ⁴ (%)
Sandy subgrade	21.6	5.6	2.6	1.84	NA	NA
Clayey subgrade	19.6	10	2.68	NA	NA	NA
Sandy subbase	22	5.3	2.62	1.53	NA	NA
Large crushed granite	NA	NA	2.6	0.36	NA	NA
Coarse RCA	20.2	9.5	2.25	6.97	0.1	33.4
Fine RCA	19.1	11.1	2.17	8.65	0.38	29.6
Crushed limestone	22.5	6.3	2.66	1.72	0.35	1.3
RCA + RAP	19.8	10	2.28	4.34	1.58	20.1
Class 6 aggregate	20.2	8.3	2.35	3.86	1.77	25.6
Class 5Q aggregate	20.1	9.6	2.28	6.32	0.28	37.1

MDD maximum dry density; OMC optimum moisture content; G_s specific gravity; NA not available. ¹ASTM D1557 and D4718; ²ASTM C127, C128, and D854; ³AASHTO T 164; ⁴Abbas et al. (2008).

the plate diameter) [10, 11]. For each test, three seating and three measurement drops were performed. Deflections, caused by the measurement drops, were recorded. A force of around 6 kN (190 kPa stress for the 200 mm plate) was applied at each drop. Boussinesq elastic half-space equation (1) was used to determine the E_{LWD} values [12].

$$E_{LWD} = \frac{(1-\nu^2)\sigma_0 r}{d_0} f \quad (1)$$

where E_{LWD} is the LWD elastic modulus (MPa); ν is the Poisson's ratio [0.40 and 0.35 for the subgrade and base layers, respectively]; σ_0 is the applied stress (MPa); r is the radius of the plate (mm); d_0 is the average deflection (mm); and f is the shape factor [$\pi/2$ for tests performed on the clayey subgrade layers and $8/3$ for tests performed on the sandy subgrade and base layers].

4.2 Falling Weight Deflectometer (FWD) Test

FWD tests were performed on the subgrade (for the RAB group) and base layers (for both groups) to determine FWD elastic modulus (E_{FWD}) values. A trailer-mounted FWD with a 450-mm diameter rigid loading plate was used. The influence depth was between 450 and 675 mm (1–1.5 times the plate diameter) [10, 11]. Three different loads, varying between 7.4 and 31kN, were applied to the loading plate. Maximum deflections, measured under the second loading, were normalized for a 22.2-kN loading (140 kPa stress for the 450 mm plate). Similar to the LWD test, Eq. (1) was used to determine the E_{FWD} values [12, 13].

5 Test Results

5.1 Recycled Aggregate Base (RAB) Group

E_{LWD} and E_{FWD} values throughout the test cells are summarized in box plots in Figs. 3 and 4, respectively. For both tests, the subgrade layers exhibited lower E_{LWD} and E_{FWD} values than the aggregate base layers, as expected. E_{LWD} and E_{FWD} values

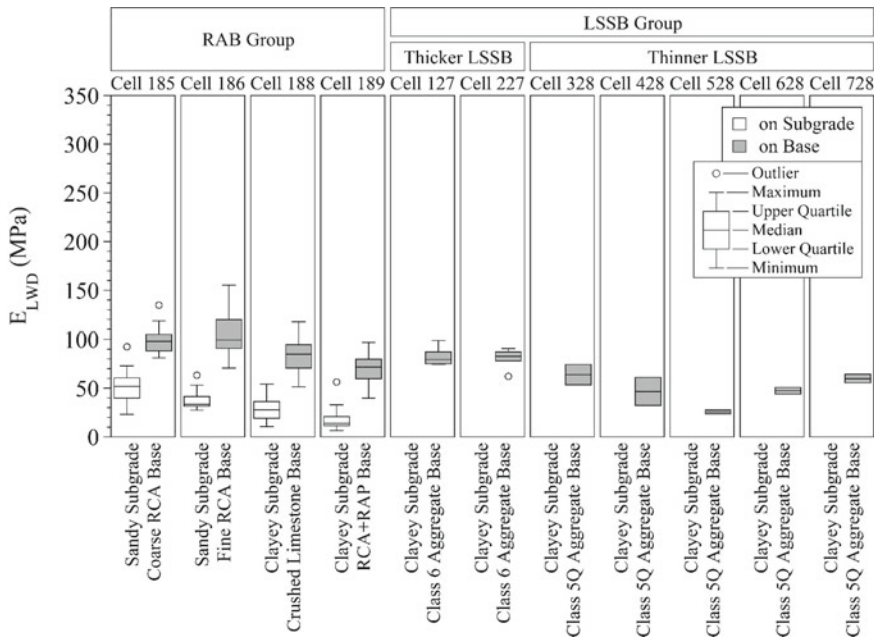


Fig. 3 E_{LWD} values determined by LWD tests

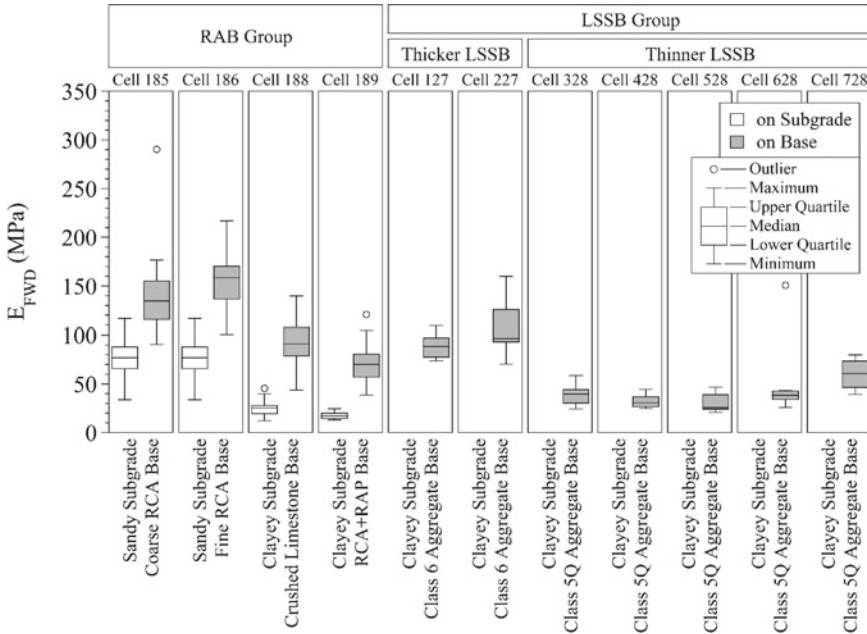


Fig. 4 E_{FWD} values determined by FWD tests

of the sandy subgrade layers (cells 185 and 186) were higher than those of the clayey subgrade layers (cells 188 and 189) (Figs. 3 and 4).

The test cells built with the coarse RCA and fine RCA base layers (cells 185 and 186, respectively) exhibited higher modulus values than the ones built with the crushed limestone and the RCA + RAP base layers (cells 188 and 189, respectively). This result may be due to the cementation of unhydrated cement in coarse RCA and fine RCA. In general, RCA materials tend to have a rougher surface texture due to the residual mortar, and such surface characteristics may improve the particle interlocking [4]. Therefore, this result may also be because of the rougher surface characteristics of coarse RCA and fine RCA compared to crushed limestone and RCA + RAP. In fact, the test cell built with the fine RCA base layer (cell 186) exhibited higher modulus values than the test cell built with the coarse RCA base layer (cell 185). Unhydrated cement can present on the surface of the coarser RCA particles and in the finer RCA particles. Since fine RCA's fines content (7.1%) was higher than that of coarse RCA (3.4%), this result may be because of fine RCA's possible higher unhydrated cement content.

As stated, the test cell built with the RCA + RAP base layer (cell 189) exhibited lower modulus values than those built with coarse RCA and fine RCA base layers (cells 185 and 186, respectively). Due to the presence of hydrophobic RAP material, the absorption of RCA + RAP (4.34%) was lower than coarse RCA (6.97%) and fine RCA (8.65%). Therefore, it may be speculated that the presence of RAP particles

reduced the amount of water that could react with the unhydrated cement in the RCA material's matrix and caused lower modulus values. The test cell built with the crushed limestone base layer (cell 188) exhibited relatively lower modulus values than other test cells in the RAB group (cells 185, 186, and 189), as expected. The general trend is that natural aggregates tend to show lower modulus values than RCA and RAP materials [4, 7–9].

5.2 Large Stone Subbase (LSSB) Group

Overall, the modulus values of the test cells built with the thicker (460 mm) LSSB layers (cells 127 and 227) were somewhat similar to those of the test cell built with the RCA + RAP base layer (cell 188). Although the test cells with the thicker LSSB layers (cells 127 and 227) consisted of similar clayey subgrade and class 6 aggregate base layers, they behaved differently from each other under FWD testing (Fig. 4). This result may be attributed to the instability of the thicker LSSB layers under loading. The literature has shown that test results may fluctuate for layers built with large aggregates due to the presence of large voids and particle reorientation during loading [6, 14].

The test cells built with the thinner (230 mm) LSSB layers (cells 328–728) exhibited lower modulus values than the test cells in the thicker LSSB subgroup (cells 127 and 227). This may be because of the different aggregate base layers in these two subgroups. As shown in Fig. 1, the test cells in the thicker LSSB subgroup (cells 127 and 227) were built with the class 6 aggregate base layers, and the ones in the thinner LSSB subgroup (cells 328–728) were built with the class 5Q aggregate base layers. In fact, the class 5Q aggregate base layers of the test cells in the thinner LSSB subgroup (cells 328–728) could not be compacted effectively (field compaction data is not included in the context of this study) and this was attributed to the instability of the thinner LSSB layers. This instability may be related to the thickness of the thinner LSSB layers. Thinner layers are prone to exhibit lower modulus values because thinner layers cannot distribute the loads as effectively as thicker layers [15]. While the test cells built with thinner LSSB layers (cells 328–728) exhibited different modulus values under LWD testing (Fig. 3), no significant difference was observed between those test cells in terms of modulus values under FWD testing (Fig. 4). Therefore, it was concluded that the use of the geosynthetics (TX, TX + GT, BX + GT, and GT in cells 328, 428, 528, and 628, respectively) did not contribute the modulus values.

6 Conclusions

The objective of this study was to investigate the modulus properties of the test cells built with RAB and LSSB layers. For this purpose, coarse RCA, fine RCA, crushed

limestone, and RCA + RAP materials were used to build four aggregate base layers at the same thickness. In addition, large crushed granite was used to build LSSB layers at two different thicknesses. LWD and FWD tests were performed on the subgrade and aggregate base layers. Field test results showed that the test cells built with the fine RCA and coarse RCA base layers exhibited the highest and the second highest modulus values. The test cell built with the RCA + RAP base layer exhibited higher modulus values than the one built with the crushed limestone. Overall, the test cells built with the thicker LSSB layers performed better than the test cells built with the thinner LSSB layers. In addition, the use of geosynthetics in the test cells built with thinner LSSB layers did not contribute to the modulus values.

References

1. USGS (United States Geologic Survey) (2019) Mineral commodity summaries 2019. U.S. Department of the Interior, U.S. Geological Survey, Reston, VA
2. ACPA (American Concrete Pavement Association) (2019) Why recycle concrete pavements?, <http://1204075.sites.myregisteredsite.com/downloads/TS/EB043P/TS043.1P.pdf>, last accessed 2019/10/2019
3. Westover TM, Labuz JF, Guzina BB (2007) Resilient modulus development of aggregate base and subbase containing recycled bituminous and concrete for 2002 design guide and Mn/Pave Pavement Design. Report No. MN/RC-2007-25, Minnesota Department of Transportation, St. Paul, MN
4. Edil TB, Tinjum JM, Benson CH (2012) Recycled unbound materials. Report No. MN/RC 2012-35, Research Services, Minnesota Department of Transportation, St. Paul, MN
5. Uhlmeier J, Pierce L, Lovejoy J, Gribner M, Mahoney J, Olson G (2003) Design and construction of rock cap roadways: case study in Northeast Washington State. *Transp Res Rec: J Transp Research Board* 1821:39-46
6. Kazmee H, Tutumluer E, Beshears S (2016) Pavement working platforms constructed with large-size unconventional aggregates. *Transp Res Rec: J Transp Res Board* 2578(1):1-11
7. Bennert T, Papp W Jr, Maher A, Gucunski N (2000) Utilization of construction and demolition debris under traffic-type loading in base and subbase applications. *Transp Res Rec: J Transp Res board* 1714:33-39
8. Kuo SS, Mahgoub H, Nazef A (2002) Investigation of recycled concrete made with limestone aggregate for a base course in flexible pavement. *Transp Res Rec: J Transp Res Board* 1787:99-108
9. Abdelrahman M, Alam T, Zollars J (2010) Performance of high recycled asphalt pavement (RAP) content as base layer in flexible pavement. *J Solid Waste Technol Manage* 36(3):131-142
10. Mooney M, Rinehart RV, Facas NW, Musimbi OM (2010) Intelligent soil compaction systems. Report No. NCHRP Report 676. National Cooperative Highway Research Program, Transportation Research Board, Washington, D.C
11. Vennapusa PKR, White DJ, Siekmeier J, Embacher RA (2012) In situ mechanistic characterizations of granular pavement foundation layers. *Int J Pavement Eng* 13(1):52-67
12. Vennapusa PK, White DJ (2009) Comparison of light weight deflectometer measurements for pavement foundation materials. *Geotech Test J* 32(3):1-13
13. Li C, Ashlock JC, White DJ, Vennapusa PKR (2019) Mechanistic-based comparisons of stabilised base and granular surface layers of low-volume roads. *Int J Pavement Eng* 20(1):112-124
14. Kazmee H, Tutumluer E (2015) Evaluation of aggregate subgrade materials used as pavement subgrade/granular subbase. Report No. FHWA-ICT-15-013. Illinois Department of Transportation, Bureau of Materials and Physical Research, Springfield, IL

15. Tanyu BF, Kim WH, Edil TB, Benson CH (2003) Comparison of laboratory resilient modulus with back-calculated elastic moduli from large-scale model experiments and FWD tests on granular materials. In: Resilient modulus testing for pavement components. ASTM International

Analysis of the Applicability of USCS, TRB and MCT Classification Systems to the Tropical Soils of Pernambuco, Brazil, for Use in Road Paving



Roberto Quental Coutinho  and Mayssa Alves da Silva Sousa 

Abstract The purpose of this article is to analyze the applicability of USCS, TRB and MCT soil classification systems in tropical soils for use in road paving. Two soils from the State of Pernambuco (Brazil) were chosen for analysis. The grading composition indicated essentially fine soils, classified as follows: USCS—ML and TRB—A-4 and A-7-6 and CBR \cong 15% and expansion \cong 0%. Considering these results and the Brazilian criteria for acceptance of soils for paving use, it is found that the soils in question would be summarily discarded. On the other hand, the characteristic curves showed soils with high suction values, and the EDS and XRD tests revealed the presence of kaolinite and iron and aluminum hydroxides/oxides, evidencing the lateritic nature of the soils and corroborating with MCT classification findings. The USCS and TRB systems are shown to be important for analyzing the fraction controlling the soil's behavior, since the MCT classification proved helpful to identify the lateritic character of the soils (LA' and LG'—lateritic sandy and clayey soils), based on responses to compaction and total immersion in water, which are the closest conditions to the site reality. Furthermore, it was found that the soils can be used as embankment material and subgrade reinforcement and have potential use in the main layers of paving (base course and sub-base). It was found to be necessary to incorporate more modern parameters, such as resilient modulus and permanent deformation (the next stage in this study), in order to provide a complete classification.

Keywords Tropical soil · Lateritic soil · Classification systems · Road paving

1 Introduction

In Brazil, in general, soil selection criteria for paving are not fully adapted to Brazilian soils, since they are based on standards developed for soils in temperate countries. Normally, the Unified Soil Classification System (USCS) or the Transportation Research Board (TRB) system is used together with California Bearing Ratio (CBR)

R. Q. Coutinho · M. A. da Silva Sousa (✉)
Federal University of Pernambuco, Recife, Brazil

values. Minimum values are considered, so most of the soils are discarded and therefore fewer meet the specifications, generating higher transport costs, which has been a problem for projects and works in the country.

The climate effects are important in this respect, since soils formed in tropical regions have different geological and geotechnical characteristics than those formed in a temperate climate.

Research has indicated the possibility of using fine soils that do not fit traditional classification systems, but present good mechanical performance. These soils can be classified by adopting the miniature, compaction, tropical (MCT) methodology proposed by Nogami and Villibor (see [1–3]).

However, there is the necessity to continue studying the soils typical of the tropical environment, based not only on specific methodologies (namely, MCT) but also on modern analysis such as resilient behavior.

In this regard, a study is being carried out in the Metropolitan Region of Recife (Pernambuco, Brazil) about fine tropical soils for use in road paving, based on the study of 13 local soils. As part of this research, two soils have been chosen for this article, whose deposits could be proposed as borrow areas. In this article, the geotechnical characteristics of the soils will be analyzed in order to critically evaluate the applicability of the classification systems of materials (USCS, TRB and MCT) for use in the pavement layers.

2 Tropical Soils and the Soil Classification Systems

Tropical soils could be intuitively defined as soils occurring in regions with a tropical climate, that is, situated between the Tropics of Cancer and Capricorn. However, from [4], it is said that the term “tropical soils” is not so geographically inclusive as might be implied by the name. From a pedological viewpoint, the term does not traditionally include all soils occurring in tropical environments and excludes low latitude desert soils, as well as some pedogenically young soils (underdeveloped).

From this perspective, this study resolved to adopt by definition the same concept adopted by the Committee on Tropical Soils of the International Society of Soil Mechanics and Foundation Engineering (ISSMFE) (1985 [2]), in which tropical soils “have different properties and behavior than non-tropical soils, due to geological and/or pedological processes typical of tropical wet regions.”

In this context, combining the concepts of pedology and geotechnical engineering, the profiles of these types of soil can then be associated in the Brazilian Soil Classification System (SiBCS) with the Latossolo and Argissolo classes and in accordance with the international soil classification system of the Food and Agriculture Organization of the United Nations (FAO [5]) with the ferralsols, Acrisols and some Alisols and Lixisols. Figure 1 shows a global map with the location of these soil groups, and their predominance is visible precisely in the regions of tropical and subtropical wet climate.

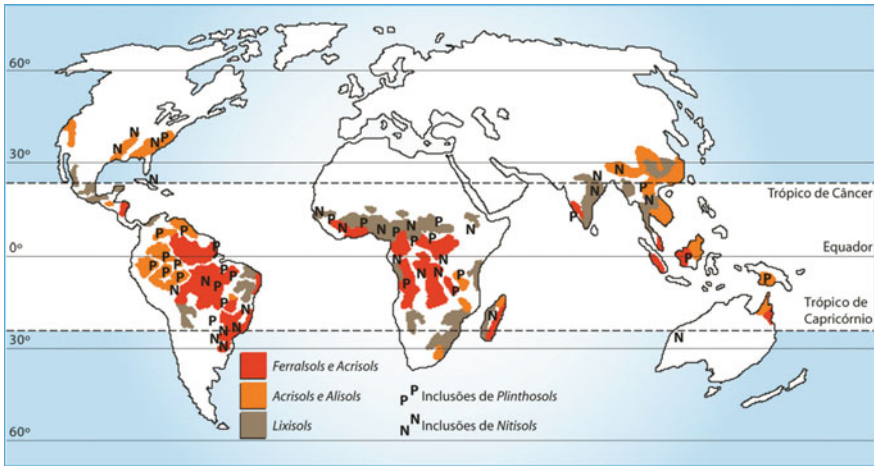


Fig. 1 Global distribution of areas where well-developed soil groups prevail [6]

According to the report by Presa [7], lateritic and saprolitic tropical soils are found almost always in overlapping layers in the same soil profile, but, although presenting similar properties indices, they almost always have quite different engineering properties and behaviors. Saprolitic soils (underdeveloped) are those commonly found below the lateritic soils (more weathered). So, although they belong to the same geotechnical group of traditional classifications (USCS and TRB), the peculiar behavior of tropical soils causes the traditional soil mechanics paradigms to lose their validity.

Therefore, Gidigasú [8] says that the geotechnical characteristics and field performance of most lateritic soils (tropical) are considerably influenced by the genesis, degree of weathering, morphological characteristics, chemical and mineral composition, as well as the environmental conditions, namely their formation process.

2.1 The Unified Soil Classification System—USCS

The USCS is one of the soil classification systems created by the engineer Arthur Casagrande, which is the object of standard D2487 of the American Society for Testing and Materials (ASTM) [9]. The system is considered traditional and, in short, divides soil types in three large groups: coarse, fine and peat.

According to USCS, coarse soils are those with more than 50% of their particles retained on no. 200 sieve, that is, larger than 0.074 mm; thus, they include gravels, gravelly or sandy soils with a small quantity of silt and/or clay and sand. The possible classes are GW, GC, GP, GM, SW, SC, SP and SM.

The fine soils are silts or clays with more than 50% of their material with particles smaller than 0.074 mm. They may have low compressibility (liquid limit—LL < 50) or high compressibility (LL > 50), and the classes of which can be CL, CH, ML, MH, OL and OH. On the other hand, peat includes highly organic and compressible soils, classified as Peat (Pt).

The soil class is identified by joining two letters: The first refers to the soil type and the second to the general characteristics of its behavior, such as, for example, Class GW, the G indicates the soil type (G—gravel), the W indicates that it is a well-graded soil, and Class CL, the C indicates clay and the L a low compressibility soil.

2.2 The Transportation Research Board—TRB Classification

The soil classification system of the Transportation Research Board (TRB) is presented in the document M 145 of the American Association of State Highway and Transportation Officials (AASHTO) and in the standard ASTM D3282 [10].

The classification is based on the division of the soils into two large groups: granular materials (with 35% or less material passing through the no. 200 sieve—75 μm), which are indicated as soils of “excellent to good” behavior and the clayey-silty soils (more than 35% passing through no. 200 sieve), which are indicated as having “fair to poor” behavior as a subgrade layer.

Each division has classes according to the percentage of material passing through no. 10 (2 mm), no. 40 (425 μm) and no. 200 sieves and with the values of the Atterberg limits (liquid limit—LL and plasticity index—PI).

2.3 The MCT Classification for Tropical Soils

In the 1980s, engineers Nogami and Villibor developed in Brazil the MCT classification, specifically for soils in the tropical environment. The classification is made considering the parameters obtained through two tests: 1—mini-MCV compaction (mini of miniature and MCV of moisture condition value) and 2—mass loss by immersion (PMI). The tests use 5 (five) miniature specimens (50 mm in diameter and height also close to this value), consisting of 200 g each and humidity varied (one close to the optimum humidity— W_o , and the others with approximately +2%, -2%, +4% and -4% humidity in relation to W_o).

The mini-MCV compaction test is carried out with the energies by applying increasing strike numbers (n) until there is a difference between the last height reading (A_n) and the fourth previous reading (A_{4n}) less than 2 mm. With the data of this test, two parameters related to the classification are obtained, which is the c^* (slope of the deformation curve) and d^* (dry branch slope of the compaction curve, corresponding to 12 strokes).

The PMI test is performed by immersion in water (for 24 h) of the specimens from the mini-MCV compaction test. Before immersion, 10 mm of soil should be drawn out of each specimen. The masses released during immersion should be weighed after drying in an oven.

The methodology was developed for essentially fine soils (maximum 10% of material retained in no. 10 sieve), which are the reality of a large part of the tropical soils. The vast majority of these soils are considered having “fair to poor” behavior, as a subgrade in the TRB classification, but Brazilian experience has shown high potential of use of such materials for road paving.

The classification divides the soils into two behavioral groups, as follows: the lateritic (L) and non-lateritic (N) soils. This division takes into account the parameter e^* which is calculated considering d^* and PMI, through the following relationship: $e^* = \sqrt[3]{\left(\frac{20}{d^*} + \frac{PMI}{100}\right)}$. As in the other classification methodologies, in this there is a division into sub-groups, being based on the soil behavior with regard to the dominant particle size, and thus, the soil is as follows: clayey (G'), silty (S'), sandy (A') and sand (A).

Figure 8b provides the graph of the aforementioned classification, including location of the classes obtained for the soil in the present study. For clearer understanding of the details of the MCT classification, the recommendation is to consult references [1, 3, 11] and [12].

3 Materials and Methods

This study considers two Brazilian soils collected in two cities in the State of Pernambuco (Brazil), namely 01—Recife (capital) and 02—Araçoiaba (which makes up the metropolitan region). Figure 2 provides a location map of the study points and images indicating characteristics of the soils on site. The UTM coordinates of the collection points were as follows: Zone 25 M, 288,637.84 m E, 9,119,539.26 m S, and 268,843.00 m E, 9,138,709.61 m S, respectively.

The collections were made using a pick and shovel, and the samples were stored in polyethylene (to preserve the humidity) and nylon bags. The collection depths were 1.45 m and 1.80 m, respectively, avoiding organic matter.

The graph in Fig. 3 shows the rainfall variations recorded by the Pernambuco Water and Climate Agency (APAC) in 2018, as well as the monthly averages over the past seven years (2012–2018) and the maximum and minimum average temperatures recorded in Recife by the National Meteorology Institute (INMET) for 2018. The data confirm the tropical environment of the sample collection points due to the heavy rainfall (1000–1500 mm per year [3]) and temperatures (>20 °C [4]).

The tests were carried out in accordance with DNIT standards and, in some cases, those of the Brazilian Association of Technical Standards (ABNT) and ASTM. Table 1 summarizes the tests performed and the standards used as a benchmark.

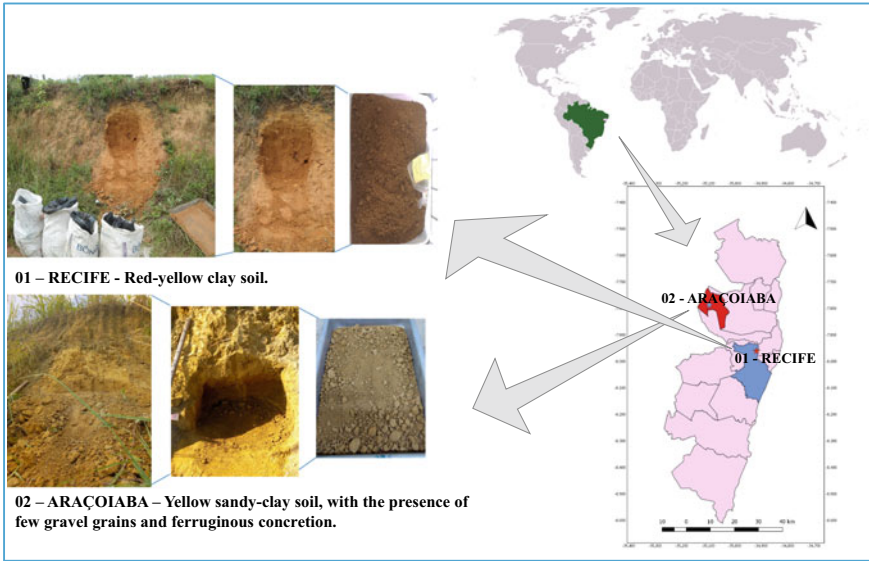


Fig. 2 Map of location and identification of soils

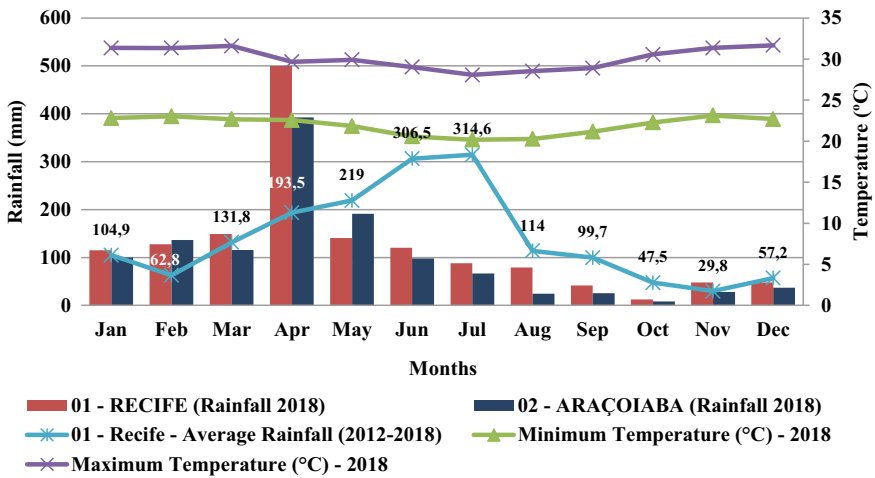


Fig. 3 Rainfall and temperature data in the research region

To carry out the tests, soils were air dried, and the soil clod were broken (carefully). Consistency limit tests were also performed without clod breaking in order to assess the impact of breaking the clods of soil on the results of these parameters, which directly influence the USCS and TRB classifications.

For the test to obtain the characteristics curve using the filter paper method, compacted test samples using intermediary Proctor energy were used. And for the

Table 1 Tests performed and benchmark standards used

Test	Standard
Sample preparation—characterization	DNER-ME 041/94
Hygroscopic moisture	ABNT NBR 6457/16 & DNER-ME 213/94
Crumb test	ABNT NBR 13601/96
Grain density (pycnometer method)	DNER-ME 093/94
Grain-size distribution (screening and sedimentation)	ABNT NBR 7181/16 & DNER-ME 051/94
Liquid limit—LL	ABNT NBR 6459/16
Plastic limit—PL	ABNT NBR 7180/16
Compaction (intermediary Proctor energy)	ABNT NBR 7182/16 & DNIT 164/2013 ME
CBR and expansion	ABNT NBR 9895/16 & DNIT 172/2016-ME
Miniature compaction (classification MCT)	DNER-ME 258/94
Weight loss due to submersion (Class. MCT)	DNER-ME 256/94
Suction (filter paper method—mixed course)	ASTM D5298/16
Dispersive energy spectroscopy (EDS) & X-ray diffraction (XRD)	Specific methodology

EDS and XRD tests, fractions of soils passing through the no. 200 sieve, oven-dried at 105 °C, were used. For the XRD, the Bruker diffractometer, model 2D phaser was used, configured to perform the test considering a scanning strip from 2° to 45°, angular step of 0.05 s and velocity of 2°/min.

4 Results and Discussion

The soils in this study belong to the Barreiras Geological Formation, which consists of sandy to quartz clayey sandy sediments, with fine to coarse grading, yellowish to reddish colors, sometimes with pebbles and/or ferruginous concretions.

In relation to the pedological classes, soil 01 is a red-yellow dystrophic Argissolo (Acrisol [5]) and soil 2 a dystrophic yellow Latossolo (Ferralsol [5]). So, they are very weathered soils, whose sand fraction is predominantly quartz, and in the clay, the kaolinite is overlaid with iron oxides and/or aluminum.

The grading composition of the soils is similar, as can be seen in Fig. 4a. They are essentially fine soils (100% and 97% passing through the no. 10 sieve, respectively) and with a high percentage of clay (>40%).

The density values of the particles were similar, being 2.699 g/cm³ and 2.674 g/cm³, respectively, for soil 01 and soil 02. In the Crumb test, both soils were classified as non-dispersive (Grade 1), since there was no water turbidity.

Figure 4b presents the results of the consistency limit tests performed with previous air-drying (more clod breaking) and without previous drying (no clod

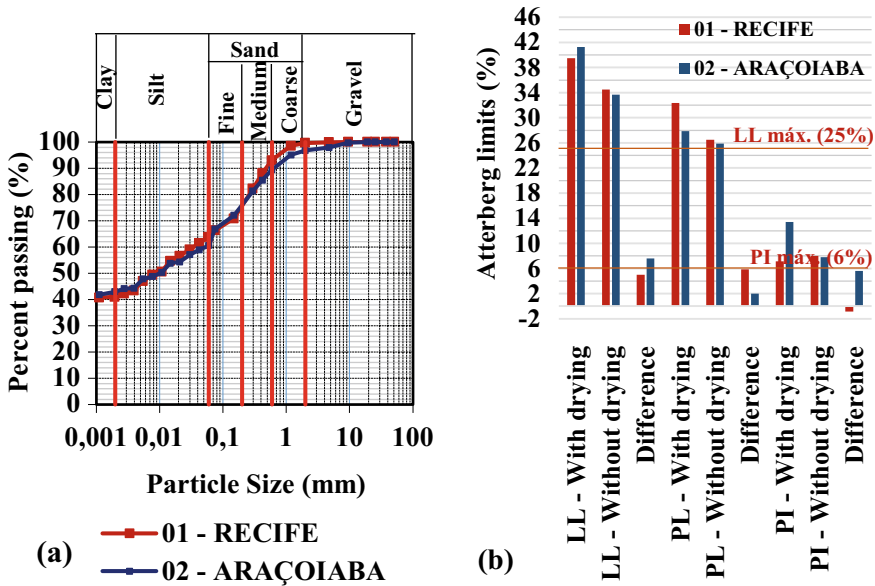


Fig. 4 a Granulometric curves (test with deflocculant and disperser) and b Consistency limits with and without previous drying

breaking). It was found that there was an increase of LL in both samples, when they underwent the drying and clod breaking process. In the PL, the behavior was the same, but further accentuation in sample 01 was noted.

With regard to the PI (difference between LL and PL), in sample 01, the value was similar in both situations, but in sample 02, there was a considerable impact caused by the drying and clod breaking, showing that the soil preparation process, by altering its natural characteristics, causes significant changes in the test results and, consequently, affects the geotechnical classification of the soils. In this regard [13], it is recommended that in lateritic soils the aforementioned tests are performed without previous drying.

On analyzing the results of the Atterberg limits of the soils with a view to deploying in paving, it is found that considering the Brazilian recommendations [14] both soils could not be used as a base layer, since it requires the soils to have LL < 25% and PI < 6%. In Brazil, there is a standard [15] regulating the use of lateritic soils for this layer, accepting LL < 40% and IP < 15%, but restricts the soils from fitting into two grade bands that require a considerable amount of pebbles, in addition to the CBR values.

Figure 5a presents the result of the EDS test, which is able to check the prevailing presence of O, Al, Si and Fe, corroborating the results of the XRD tests (Fig. 5b) which indicated a kaolinite (Al₂Si₂O₅(OH)₄) and quartz (SiO₂) predominance, as well as the presence of iron hydroxides and oxides (hematite—Fe₂O₃, goethite—FeO(OH)) and

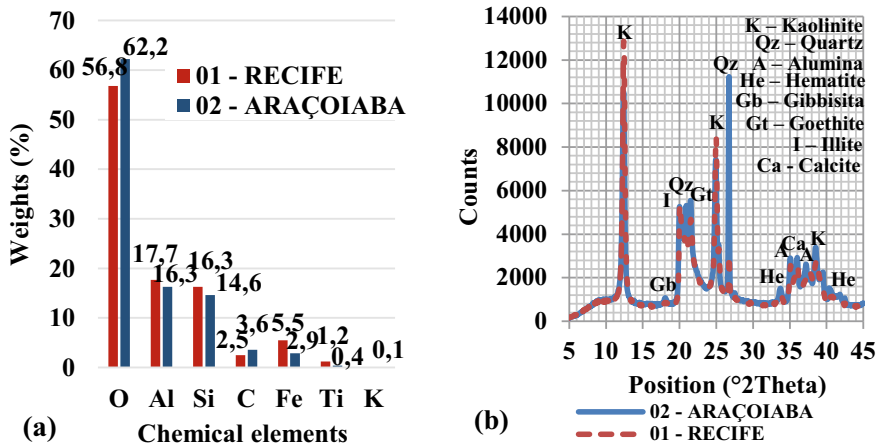


Fig. 5 Results of a EDS and b diffractogram of the soils in the study

aluminum (alumina— Al_2O_3 gibbsite— $Al(OH)_3$), which are elements often found in lateritic soils [5, 6, 8].

Also, by analyzing the diffractogram presented, due to the intensity of the recorded peaks, it can be inferred that the presence of kaolinite is greater in sample 01, unlike the quartz that is shown to be in a higher proportion in sample 02. Such conclusions agree with the result in the EDS test.

Figure 7a presents the soil–water characteristic curves (SWCC) in which there are high air entry values at a suction of about $\cong 6000\text{--}7000$ kPa. The shape of the curve suggests clayey soils, since they have higher air input values than sandy and silty soils and residual points that cannot always be visually identified [16].

In the CBR and expansion tests, analog values were 01—Recife: CBR 15.2% and expansion 0.1%, and 02—Araçoiaba: CBR 15% and expansion 0%. In relation to expansion, according to Brazilian standards, these soils are within the limit values for any pavement layer, but in relation to the bearing capacity, both could only be used for embankment layers and subgrade reinforcement, being discarded its use for nobler layers such as base and sub-base.

However, considering the MCT classification and Brazilian experiments using lateritic fine soils, these soils could be used in the different layers since, considering the resilient modulus (M_r), such solos have produced satisfactory results, sometimes similar to the results obtained from crushed stone ($M_r \cong 400$ MPa), see [17] and [18]. Preliminary tests of the M_r were carried out on the studied soils, and the average values were 436 and 394 MPa, respectively, but these results will be the subject of a future article.

4.1 USCS, TRB and MCT Classification

Concerning the geotechnical classification, considering the Atterberg limits carried out with oven drying and clod breaking (traditional method), both soils were classified as ML (silts with low compressibility) in USCS, and in the TRB, they obtained classes A-4 and A-7-6 for soils 01 and 02, respectively, see Fig. 6.

Class A-4 is where, according to the TRB classification, there is a predominance of silty soils. Although in soil 01 only around 19% of silt was obtained, it is found that there was compatibility between the TRB and USCS classifications, by identifying the same type of behavior in this soil.

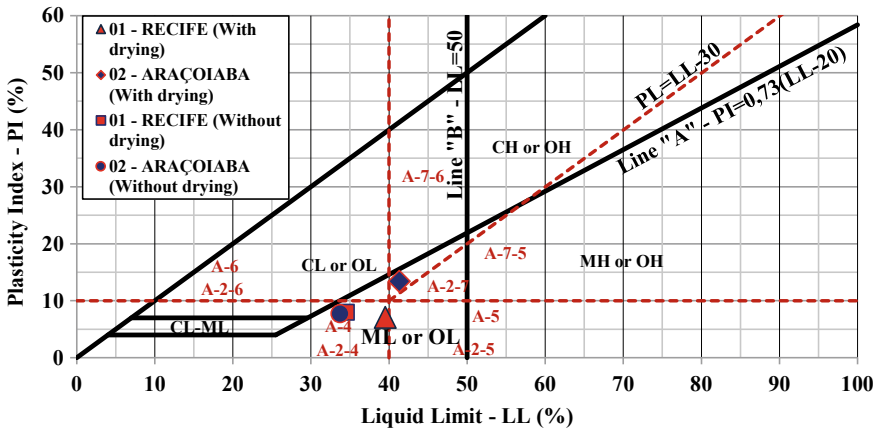


Fig. 6 Plasticity graph indicating USCS and TRB classifications obtained

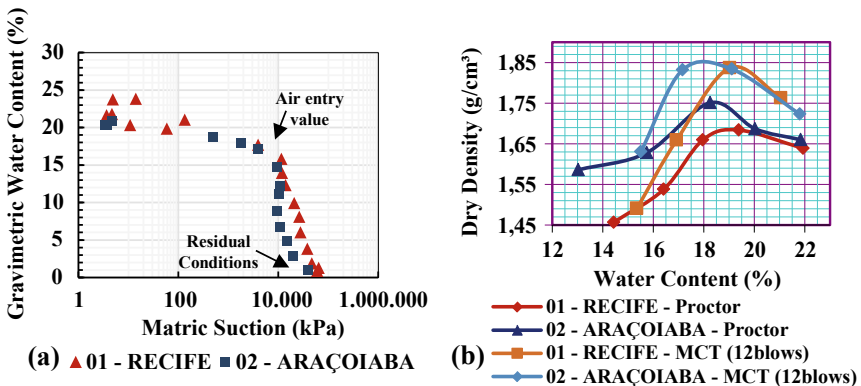


Fig. 7 a Soil–water characteristic curves and b Soil compaction curves (determination d^*)

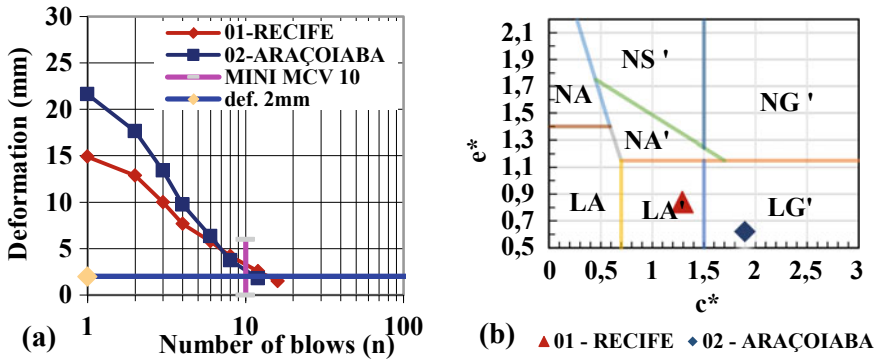


Fig. 8 a Deformability curve—determination c^* and b Classification MCT

On the other hand, in the case of sample 02, the TRB classification resulted in behaviors diverging from the USCS, since the TRB Class A-7-6 refers to predominantly clayey and non-silty soils, but the TRB nevertheless proved compatible with the grading distribution of the soil in question.

After completing the classification with the procedure without pre-drying, there is found to be no alteration in relation to the USCS classification, but in the TRB classification, there is an alteration in the class of soil 02—Araçoiaba to A-4, which would now indicate the same behavior indicated by the USCS.

The soil compaction curves (Intermediary Proctor), presented in Fig. 7b, show similar shapes and value of optimum water content (W_o) (19 and 18.4%), but different dry apparent maximum densities, the largest being in sample 02.

Figure 7b also presents the curves obtained (for 12 blows) in the miniature compaction test, required for the MCT classification. The two soils have similar density and W_o values corresponding to those obtained in the traditional compaction test. The steep angles of the curves (on the dry side) indicate typical behavior of lateritic soils (soil 1 – $d^* = 107.14$ and soil 2 – $d^* = 138.9$).

Using the aforementioned data with the PMI, the MCT classification of the soils (Fig. 8b) was done. The PMI values used to calculate the e^* were soil 1 = 40% and soil 2 = 10%, respectively, considering rules of the classification, but in the optimum water content, both soils remained intact after immersion (PMI=0%).

Figure 8a shows the soil deformability curves, from which (by calculating their slope) the parameter c^* of the MCT classification was obtained (soil 1 – $c^* = 1.29$ and soil 2 – $c^* = 1.9$). This parameter (c^*) reflects the soil's behavior with regard to grading ($c^* > 1.5$ —clayey, $0.7 < c^* < 1.5$ —sandy and $c^* < 0.7$ —sand).

From the results, soil 01 was classified as LA'—lateritic sandy soil (the most class recommended for use in the different pavement layers, in accordance with the methodology [3]), and soil 02 was classified as LG'—lateritic clayey soil (the clayey behavior was also identified by the TRB). By observing the positioning of the MCT classification points in Fig. 8b, it is found that sample 02 had a greater degree of laterization ($e^* = 0.62$) than sample 01 ($e^* = 0.84$).

5 Conclusions

Based on the results, the conclusion is that USCS and TRB classifications have their valid applications when aiming to check the grading fraction dominating the soil's behavior that on occasions does not match with the predominating material. However, in order to use the tropical soils in paving layers, there is a need to complement the classification method to check the real potential for use.

The MCT classification, developed specifically for tropical soils, has proved very useful, since it uses parameters based not only on the grading of the soil, but also on its behavior as compacted soil, when analyzing the variation in the density with the variation in water content, the deformability and material loss due to total immersion in water, which is the reality of the paving layers on site.

The MCT methodology demonstrated that soils with such similar grading and consistency rates can have quite different geotechnical behaviors, indicating that various other factors (genesis, chemical, mineralogical composition and so on) can influence the results.

Moreover, it is suggested that the fine lateritic tropical soils (LA', LG' and LA) have potential to be used in the different pavement layers, including base and sub-base, which according to Brazilian experiments, mentioned in the article, are possible since they can show excellent resilient behavior.

It was found that the premises for the use of the soils require not only classification, but also satisfactory CBR values that often tend to confirm the discarding of the fine lateritic tropical soils. In this context, the implementation of a mechanistic analysis, considering the behavior of the soil with regard to the resilient modulus and permanent deformation (next stage of this study), proves extremely important in providing a complete soil classification/selection system.

Acknowledgments The authors would like to thank the Foundation for Science and Technology of Pernambuco (FACEPE) for financial support (PhD scholarship to the author Mayssa Sousa, grant number IBPG-0126-3.01/18) and encouragement in this research. We would also like to thank the Federal University of Pernambuco (UFPE) for the opportunity of a doctorate, especially the GEGEP group and the Laboratory of Soils and Instrumentation for all the support provided.



References

1. Nogami JS, Villibor DF (1985) Additional considerations about a new geotechnical classification for tropical soils. In: First international conference on geomechanics in tropical lateritic and saprolitic soils (TropicalLS'85). Brasilia, Brazil, pp 165–174
2. Nogami JS, Villibor DF (1995) Pavimentação de Baixo Custo com Solos Lateríticos. Editora Villibor, São Paulo
3. Villibor DF, Nogami JS (2009) Pavimentos econômicos: Tecnologia do uso dos solos finos lateríticos. Arte & Ciência, São Paulo
4. Chesworth W et al (2008) Tropical soils. In: Chesworth W (eds) Encyclopedia of soil science. Springer, Dordrecht. https://doi.org/10.1007/978-1-4020-3995-9_607.

5. FAO (2015) Food and agriculture organization of united nation: world reference base for soil resources 2014, 193 pp. World Soil Resources Reports, Rome
6. Lespsh IF (2010) Formação e conservação dos solos. 2nd ed Oficina de Textos, São Paulo
7. Presa EP (1951–1998) Relatório geral da 7ª seção técnica: solos tropicais, especiais (expansivos, colapsíveis e dispersivos) e pavimentos. In: X Cobramsef Brazilian Soil Mechanics Association (ABMS)
8. Gidigas MD (1976) Laterite soil engineering: pedogenesis and engineering principles. Elsevier, Amsterdam
9. ASTM D2487-17 (2017) Standard practice for classification of soils for engineering purposes (Unified Soil Classification System). ASTM, West Conshohocken
10. ASTM D3282-15 (2015) Standard practice for classification of soils and soil-aggregate mixtures for highway construction purposes. ASTM, West Conshohocken
11. Villibor DF, Alves DML (2017) Classificação de Solos Tropicais de Granulação Fina e Grossa. Revista Pavimentação 43:16–37
12. Departamento Nacional de Estradas de Rodagem. Classificação dos solos tropicais para finalidades rodoviárias utilizando corpos de prova compactados em equipamento miniatura, DNER - CLA 259/96. Rio de Janeiro
13. Ampadu SIK (2017) Laterites and lateritic soil and the potential use of the dynamic cone penetrometer. Int Soc Soil Mech Geotech Eng Issmge
14. Departamento Nacional de Infraestrutura de Transportes (2006) Manual de Pavimentação. 3rd ed. 274p. Rio de Janeiro
15. Departamento Nacional de Infraestrutura de Transportes (2007) Pavimentação—base estabilizada granulometricamente com utilização de solo laterítico, DNIT 098/2007 – ES. Rio de Janeiro
16. Gitirana Jr, Gilson de FN, Fredlund DG (2004) Soil-water characteristic curve equation with independent properties. J Geotech Geoenviron Eng 130(2):209–12. [https://doi.org/10.1061/\(ASCE\)1090-0241\(2004\)130:2\(209\)](https://doi.org/10.1061/(ASCE)1090-0241(2004)130:2(209)).
17. Lima C, de Motta L, da Aragão, F. Guimarães, A.: Mechanical Characterization of Fine-Grained Lateritic Soils for Mechanistic-Empirical Flexible Pavement Design. Journal of Testing and Evaluation, ASTM International, West Conshohocken, PA (2019). <https://doi.org/10.1520/JTE20180890>.
18. Sousa MAS (2016) Análise geotécnica de solos tropicais de ocorrência ao longo da Estrada de Ferro Carajás para uso como camadas de pavimento rodoviário. 222p. Instituto Militar de Engenharia, Rio de Janeiro
19. Departamento Nacional de Estradas de Rodagem (1994) Solos compactados em equipamento miniatura - Mini-MCV, DNER - ME 258/94. Rio de Janeiro

Behavior of Compacted Collapsible Soil After Adding Calcium Chloride



Weijuan Geng , Weiyang Zhou, and Jiankun Liu 

Abstract The collapse behavior of subgrade soil presents stability problems on road construction in collapsible soil region due to its sudden reduction in volume when encountering an increased soil moisture. Compaction is widely accepted as a densifying method for collapsible soil. Recent studies pretreated the loess soils by mixing with chemical agents to obtain an enhanced mechanical behavior. However, studies in stability properties (e.g., under compaction) of chemically modified soils are limited. This study aims to evaluate the behavior of compacted collapsible soils by mixing with chemical agents. This paper presents the first stage results of the study: Behavior of soil treated by calcium chloride (CaCl_2) subjected to compaction. Experiments including liquid/plastic limit, oedometer, unconfined compression and hydraulic conductivity tests were conducted to evaluate the engineering behavior of compacted collapsible soil treated at different CaCl_2 concentrations. Results indicate that soil treated with higher CaCl_2 concentration exhibits an overall enhanced performance in resisting wetting-induced collapse. The addition of CaCl_2 could reduce the modified collapse ratio and show less sensitivity to molding water content. Scanning electron microscopy (SEM) was used to visually capture the size of soil aggregates due to enhanced cementation, which was formed by the dual effect of salt concentration and compaction effort. Unconfined compression strength (UCS) of treated soils generally increases with increasing water content at dry of optimum conditions and decreases as water content increases toward wet of optimum conditions. The preparation method for sampling soil from compaction has an essential influence on the measured soil strength. Hydraulic conductivity decreases with increasing CaCl_2 concentration. Studies on the mechanism of cementation in compacted collapsible soil treated by chemical agents are ongoing.

W. Geng

Department of Civil Engineering, Jiangsu University, Zhenjiang 212013, China

e-mail: geng@ujs.edu.cn

W. Zhou · J. Liu (✉)

School of Civil Engineering, Sun Yat-Sen University, Zhuhai 519082, Guangdong, China

e-mail: liujiank@mail.sysu.edu.cn

W. Zhou

e-mail: zhouwy36@mail2.sysu.edu.cn

Keywords Collapsible soil · Compaction · Chemical treated soil

1 Introduction

Soils with collapse behavior were widely distributed in the region of Lanzhou, China [1]. Previous research studies have been conducted on the collapsible soil properties and the geotechnical behavior due to such soils' extensive distribution and associated engineering problems, i.e., wetting-induced collapse [2–5]. The collapsible soil is identified by the sudden volumetric reduction with an increase in water content due to the breakdown of cementation between soil particles [6]. This characteristic can cause engineering problems when the soil is directly used for construction. Thus, over the years many methods, such as compaction, injection and chemical stabilization, were developed to improve the collapsible soil behavior [7–10]. Among all the available improving methods for collapsible soil, chemical stabilization is a popular choice for industry professionals and researchers.

Although there are various organic chemical agents that have been successfully applied to improve the collapsible soils, they are not widely accepted due to the potential environmental hazard. The organic chemical stabilizers are not considered environment friendly since they would change the pH of soil and contaminate soils and ground water [11]. Thus, traditional methods such as compaction is still widely employed in engineering application with collapsible soils, i.e., improving surface soil in road construction. The density level after compaction would have an effect on the hydraulic and mechanical behaviors of soil. Thus, it is essential to determine the maximum dry density for collapsible soil and its corresponding optimal moisture content. A study was initiated aiming to evaluate the behavior of compacted collapsible soils by mixing with two chemical agents. Two types chemical agents were chosen: Calcium chloride and polymer, aiming to evaluate collapsible soil properties of chemical treated soil and to compare the effectiveness of the two chemical agents.

This paper attempts to present the first stage results of the study: Soil treated by calcium chloride at different concentrations. Engineering properties including liquid/plastic limit, modified collapse ratio, unconfined compression strength and hydraulic conductivity were evaluated with compacted collapsible soil using calcium chloride.

2 Materials and Methods

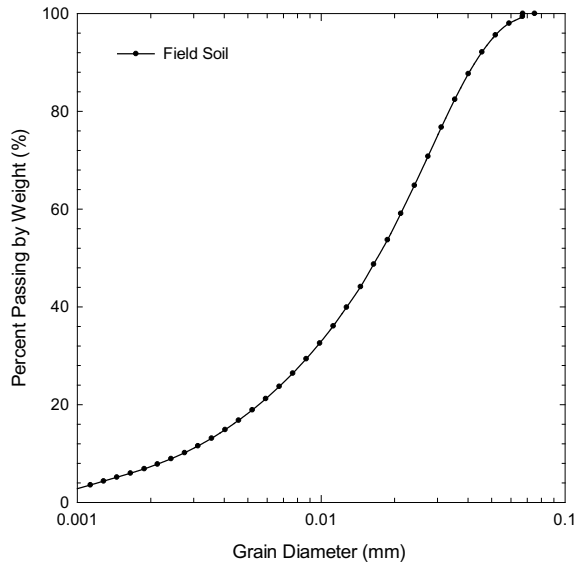
2.1 Soil Properties

Soil used in this study was a nature collapsible soil sampled from Lanzhou, China, where located in the Loess Plateau. The air-dried soil has a unit weight of 12.48 kN/m^3

Table 1 Physical properties of field soil

Property	Water content	Specific gravity	Nature unit weight	Plastic limit	Liquid limit	Plasticity index
Unit	%	—	kN/m ³	%	%	%
Value	11.0	2.68	12.48	14.28	25.21	10.93

Fig. 1 Grain size distribution of collapsible soil sample collected from field



with a water content of 1.92%. The dominant fraction of studied soil is silty loess with a liquid limit of 25.2% and a plastic index of 10.9%. Table 1 summarizes physical and index properties of untreated soil. Particle size analysis was determined using a wet dispersion method by a laser analyzer, and the grain size distribution was given in Fig. 1.

To prepare the treated soil samples, nature soil was air-dried after transported from field to laboratory, and then mixed with deionized water (DI) and calcium chloride (CaCl₂) solutions for tests. CaCl₂ solutions were prepared by dissolving reagent grade dehydrate-calcium chloride (CaCl₂ · 2H₂O) in Type II DI water per ASTM D1193. The solution concentrations were calculated as the ratio between dry mass of solvent to mass of solution at 2, 5 and 10% for this study.

2.2 Fall Cone Test

Plastic and liquid limits of DI and CaCl₂ treated soil were determined by the British Fall Cone test in accordance with the procedure described in BS 1377. The treated

Table 2 Plasticity index of DI water and CaCl₂ treated soil

	DI	2% CaCl ₂	5% CaCl ₂	10% CaCl ₂
Plastic limit (%)	14.3	15.1	10.4	10.2
Liquid limit (%)	25.2	25.5	24.2	20.5
Plasticity Index	10.9	10.4	13.8	10.3

soil was sealed and cured in a plastic bag for 24 h prior to sampling. The surface of samples was leveled-off under fall cone. The depth of penetration was recorded upon the stabilization of releasing cone. Water content was correlated with the penetration depth using the method described in ASTM D2216. Table 2 summarizes the plasticity index of treated soils.

2.3 Compaction

Compaction tests were carried out on soils treated with DI water and CaCl₂ solutions at various concentration. All the soils samples were molded with a drop hammer (2.5 kg) in four lifts with a mold size of 100 mm in diameter and 127 mm in height and each lift is tamped 27 times. The height of drop of the hammer is 30 cm, and the compaction effort was calculated as 797 kN-m/m³. DI water/CaCl₂ solutions were carefully mixed with soil to achieve the desired water content, then sealed for 12 h before initiation of compaction. Dry unit weight was calculated for each specimen. Water content was measured at three points of different depth for each specimen, and average water content was taken within the error of 1%.

2.4 Oedometer Test

Oedometer test was conducted for treated soil at optimum water content. Treated soil samples were extruded and trimmed to fit the oedometer apparatus (61.8 mm in diameter and 20 mm in height) from the compacted soils, while the untreated soil sample was loaded at its nature water content. Compression curve was thus obtained, and a modified collapse ratio is defined as

$$R_c = \frac{H_t}{H_o} \quad (1)$$

where H_t and H_o are the stabilized height of specimens with deionized water or chemical treated and untreated soil under a given vertical stress, respectively. In this study, incremental vertical stresses ranging from 50 to 3200 kPa were employed.

2.5 Unconfined Compression Test

Unconfined compression test was conducted to determine the unconfined compression strength (UCS) of treated soils. All of the UCS samples were obtained from the compaction mold after compaction test. Two methods were employed for sample preparing. For soil treated by DI water, a “directly trimming” method was employed where sample obtained from compaction was directly trimmed to a 39.1 mm in diameter and 80 mm in height specimen. For soils treated by CaCl_2 , a “remolding” method was used. The sample from compaction was cut into small clods in a plastic bag, then remolded into UCS specimen by calculating a precise soil weight at corresponding water content and wet density. UCS tests were conducted immediately after sampling to minimize water evaporation. Soil specimens were loaded to failure at a constant rate of 0.09 mm/minute in a triaxial compression apparatus.

2.6 Hydraulic Conductivity Test

Hydraulic conductivity tests were performed on treated soils employing the falling head method in rigid wall permeameters. Treated soil samples were compacted at optimum water content prior to hydraulic conductivity test. The top surface of the specimen was trimmed and then placed between the end plates of the compaction mold permeameter. The hydraulic gradient was in the range of 20–30, and the permeant liquid was deionized water all tests. Hydraulic conductivity values were taken as the hydraulic conductivity becoming stable and the outflow and inflow ratio exhibited no temporal trend.

2.7 Scanning Electron Microscopy

Scanning electron microscopy (SEM) was conducted on treated soils following compaction. Soil samples were cut into thin specimens (~5 mm × 8 mm) using a razor knife, mounted on holders using carbon tape, and coated with gold using a sputtering system. SEM images of the cut surfaces were obtained using a 15-keV electron beam and backscattered electron detector. Elemental analysis was conducted on untreated soil specimen using integrated energy dispersive spectroscopy (EDS), shown in Fig. 2.

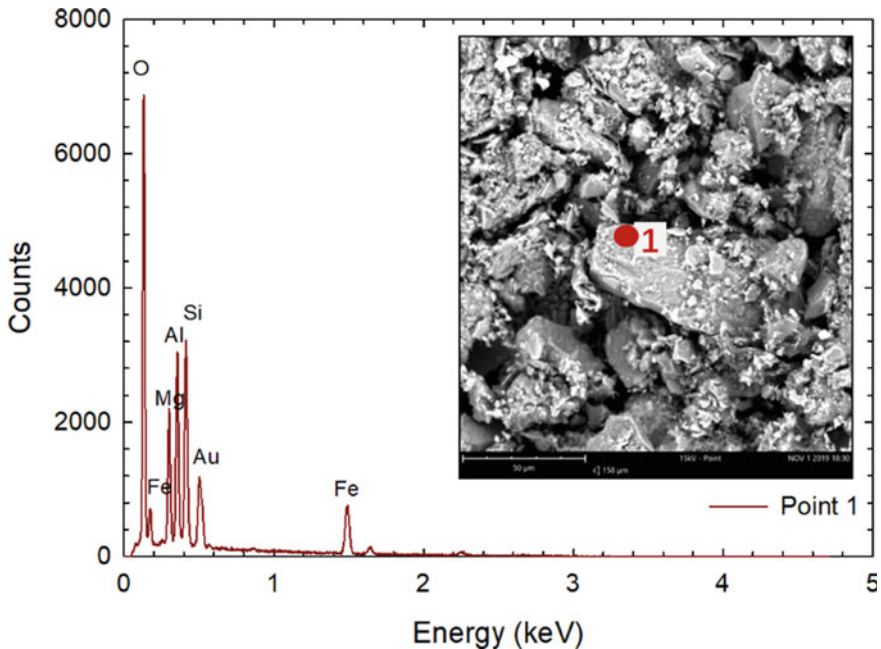


Fig. 2 Scanning electron microscopy (SEM) image of untreated soil using energy dispersive spectroscopy (EDS)

3 Results and Discussion

3.1 Influence of CaCl_2 Concentration on Compaction Curve

Compaction curves are shown in Fig. 3 for soils treated with DI water and CaCl_2 solution at concentration of 2, 5 and 10%. The maximum dry density increased from 1.7 to 1.9 g/cm^3 by increasing CaCl_2 concentration from 0 to 10%, suggesting the presence of larger pore volumes. The optimum water content decreases with an increasing concentration of saline solution. Soil treated by lower CaCl_2 concentration exhibits a compaction curve with a much flatter peak, suggesting less sensitivity to molding water content.

For soils with water contents dry of optimum, soil treated with higher concentration of CaCl_2 could be compacted more effectively than soil with DI water, since a higher dry density was observed. The noticed compaction behavior is hypothesized to be attributed to the enhanced cementation effect caused by CaCl_2 in collapsible soil. Figure 4 shows the SEM images of soil compacted at optimum water content treated with DI water (a) and 10% CaCl_2 (b) at same scale. The aggregates are observed with much larger diameters ($\sim 314 \mu\text{m}$) with 10% CaCl_2 than those with DI water ($\sim 108 \mu\text{m}$), suggesting soil retains as a stronger cluster in CaCl_2 . It suggests that

Fig. 3 Compaction curves for soil treated by deionized water and CaCl₂ at concentration of 2, 5 and 10% by mass

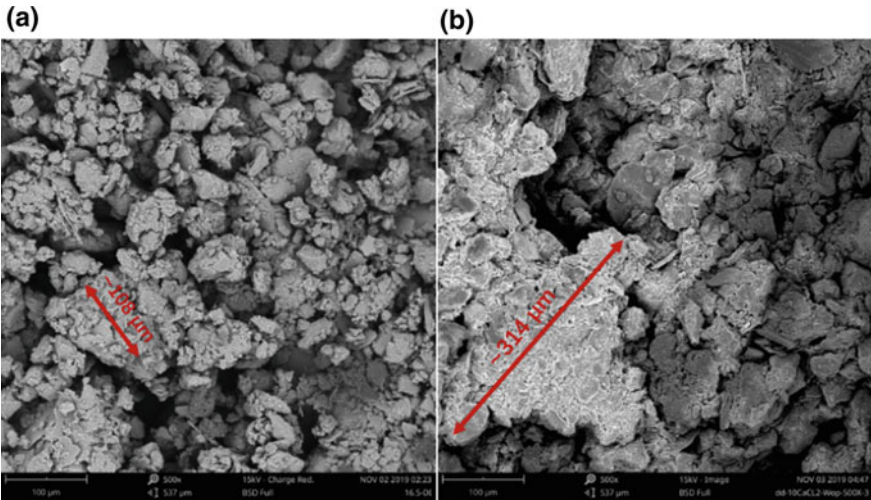
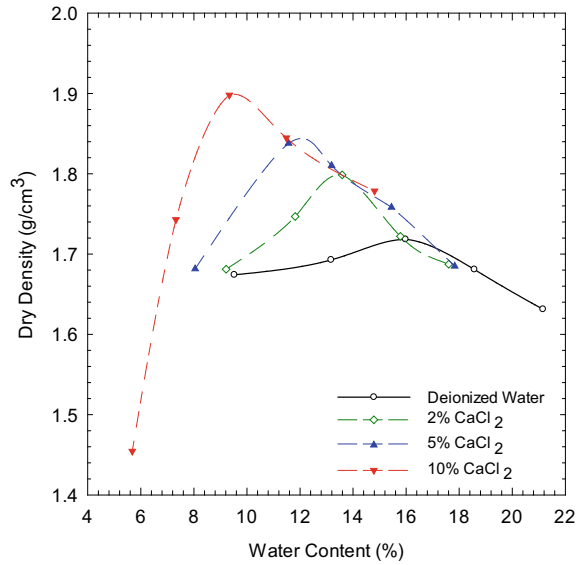


Fig. 4 Scanning electron microscopy (SEM) image of compacted soil at optimum water content treated with **a** DI water; and **b** 10% CaCl₂

the addition of CaCl₂ triggers extra cementation in the collapsible soil. However, Guo [12] suggested that salt dissolution would weaken bonding strength and induce collapse upon wetting. It is hypothesized herein that the salt concentration and compaction effort have dual effect on soil cementation. That is, a strong cementation can only be obtained in condition of an optimized salt concentration with

proper compaction effort. Ongoing study is conducted to develop detailed relation between salt concentration and compaction effort for collapsible soil.

3.2 Compression and Modified Collapse Ratio

A series of oedometer tests were conducted on treated soils at optimum water content to study the compressibility and collapse behavior of CaCl₂ treated soils. Figure 5a shows the compression curves of treated soil at optimum water content. Soils exhibit low compressibility after compaction. Soil sample was obtained immediately after compaction at optimum water content for each CaCl₂ treated soil, thus a higher initial void ratio was corresponding to soil specimen treated by lower CaCl₂ concentration.

Figure 5b presents the modified collapse ratio for treated soils. The modified collapse ratio intends to compare the strains level of soil treated by DI water/CaCl₂ and that of untreated at a certain vertical stress. The steepest change in modified collapse ratio is observed with soil treated at 2% CaCl₂, whereas the modified collapse ratio exhibits a mild change with soil treated at 10% CaCl₂ as increasing the vertical stress. It suggests that soil treated at 10% CaCl₂ is much less sensitive to stress. While there is scatter in the relation, there is a general trend toward increasing modified collapse ratio with increasing vertical stress. A trendline fit through the data set is in the form:

$$R_c = 0.102\sigma^{0.126} \tag{2}$$

where R_c is the modified collapse ratio and σ is the vertical stress (kPa). The relationship could be used to predict the modified collapse ratio for treated soil at certain vertical stress. Future test will conduct on soil treated at a wider range of saline

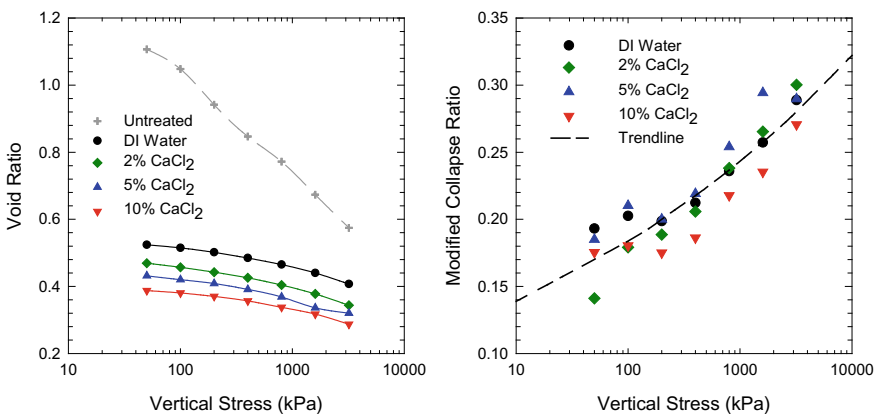


Fig. 5 a Compression curves; and b Modified collapse ratio for treated soil at optimum water content

solution to establish a more systematic relationship between modified collapse ratio and stress under the influence of saline solution.

3.3 Unconfined Compression Strength (UCS)

All UCS samples were obtained and trimmed following the compaction. Figure 6 shows the unconfined compression strength of treated soils after compaction at different water content. Error bar indicates the results obtained from duplicate tests. For treated soil at all concentration, the strength has an increase as increasing water content on the dry of optimum side, indicating a closer packing of soil particles and a stronger cementation within the soils. Then, the strength decreases as water content continues increasing on wet side of optimum. It suggests a changed soil fabric in the presence of “extra” water, since the water/solvent would destroy the chemical bonds of cementation materials thus change the structure of soil packing. In addition, it can be observed that soil treated with DI water has the sharpest decrease in strength with increasing water content. The strength reduction rate decreases as the centration of CaCl₂ increases from 0 to 10%, which could be attribute to the stronger cementation in the soil treated with higher concentration of CaCl₂. The presence of CaCl₂ improves the cementation of soil and results in a relatively low-collapse potential, which fits well with the results suggested by collapse ratio. The enhanced cementation effect could be caused by the formation of calcium carbonate or by the enhanced clay bonding by adding CaCl₂ to soils. Study is ongoing to unveil the underlying mechanism.

Fig. 6 Unconfined compression strength of DI water and CaCl₂ treated soil following compaction

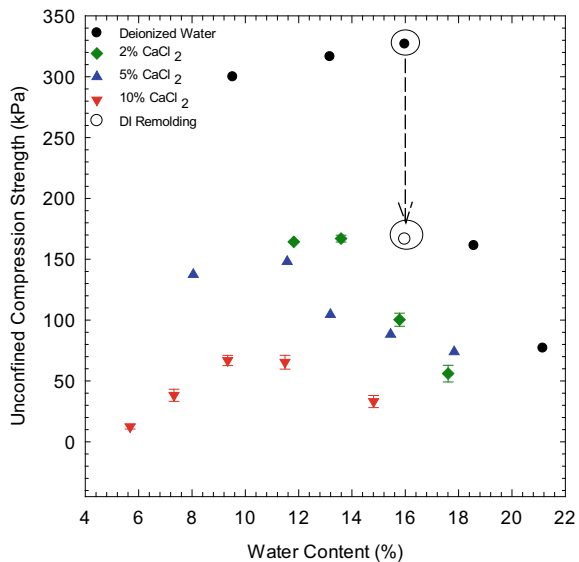
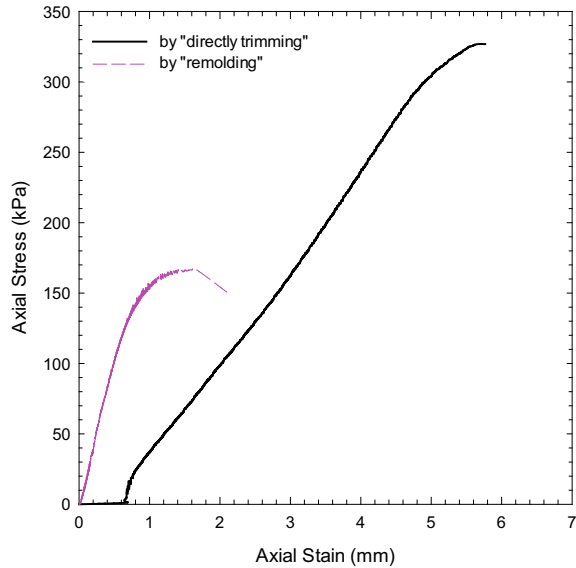


Fig. 7 Influence of sampling on unconfined compression strength with deionized water treated soil at optimum water content

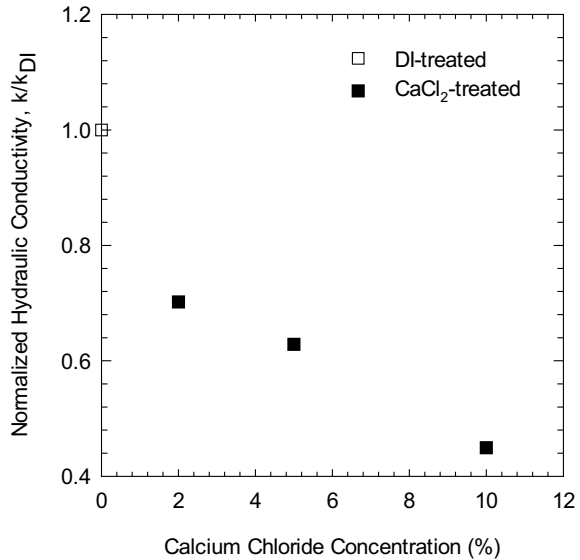


However, it needs to be noted that the strength has an overall decreasing trend with increasing CaCl_2 concentration, which appears an opposite result as expected. This phenomenon could be attributed to the sample preparation method, where the soil was disturbed, while remolding sample from compaction. To compare the two sampling methods, one extra UCS test was conducted with DI water treated soil at optimum water content using “remolding” method for preparing soil specimen. It is observed that the strength reduced by 54% from 362.9 kPa to 166.7 kPa as using different sampling methods. Figure 7 shows the stress–strain relationship of soil treated by DI water at optimum water content with “direct trimming” and “remolding” method. It suggests that soil specimen prepared by “remolding” yield at a much earlier stage than the soil specimen prepared by “directly trimming” method since the intrinsic cementation was broken down. Therefore, the soil fabric was actually re-structured with little cementation once using the “remolding” method for sampling. Future test was suggested to employ the “direct trimming” method rather than the “remolding” method for sampling soil specimen from compaction.

3.4 Hydraulic Conductivity

The relationship between normalized hydraulic conductivity (hydraulic conductivity of CaCl_2 treated soil/hydraulic conductivity of DI treated soil) of soil compacted at optimum water content and calcium chloride concentration is shown in Fig. 8. The hydraulic conductivity of DI treated soil was measured at 1.2×10^{-7} cm/s, which is higher than that of soil treated by CaCl_2 regardless of concentration. The

Fig. 8 Normalized hydraulic conductivity for treated soil compacted at optimum water content



hydraulic conductivity of soil treated with CaCl₂ decreases with increasing CaCl₂ concentration from 2 to 10%. It indicates a more tortuous flow with the soil treated by higher concentration of CaCl₂, suggesting an enhanced cementation effect which bridging the soil particles. The results give evidence to the enhanced cementation in addition of CaCl₂. In the presence of CaCl₂, chemical bonds between soil particles were formed, holding together the silt particle as illustrated in Li et al. [13] by cementation. The cementation blocks water flow path in the soil void thus contributes to a lower hydraulic conductivity. Post pore size analysis will be conducted on soil samples once the tests are terminated.

4 Conclusions and Recommendations

This paper evaluated the behaviors of compacted collapsible soil treated by CaCl₂. A series of laboratory tests including compaction, oedometer, unconfined compression, hydraulic conductivity tests and scanning electron microscopy were employed. The conclusions and recommendations derived from this paper are as follows:

- Soil treated by higher concentration of CaCl₂ exhibited a higher dry density with a lower optimum water content, and the compaction curve suggests it is more sensitive to molding water content. Salt concentration and compaction effort have a dual effect that influences the soil cementation.
- Soil treated at higher concentration of CaCl₂ shows a lower modified collapse ratio compared to soils treated at lower concentration of CaCl₂ and is much less

sensitive to the vertical stress. A link for treated soil is established between modified collapse ratio and vertical stress, where the modified collapse ratio generally increases with increasing stress. Future test program is recommended to conduct on soil treated at a wider range of saline solution to find out a more systematic relationship between modified collapse ratio and stress under the influence of salts.

- Unconfined compression strength of treated soils generally increases with increasing water content on dry of optimum side and decreases as water content continuing increasing on wet of optimum side. The presence of CaCl_2 in collapsible soil improves the cementation of soil by forming calcium carbonate or enhancing the clay bonding.
- Collapsible soil is highly sensitive to disturbance; it should be caution when preparing soil samples. “Direct trimming” method is recommended for sampling the soil from compaction, since “remolding” would change the intrinsic soil fabric and destroy the formed cementation resulting in a much lower measured strength.
- Hydraulic conductivity of treated soil compacted at optimum water content decreases with increasing CaCl_2 concentration, further give evidence in the enhanced cementation caused by CaCl_2 .
- Future research is being conducted with polymer treated collapsible soil in the same testing program to further study the enhanced cementation and its underlying mechanism. Microstructure analysis of soil fabric with chemical treated soil under compaction is ongoing.

References

1. Sun JM (2002) Provenance of loess material and formation of loess deposits on the Chinese Loess Plateau. *Earth Planet Sci Lett* 203:845–859
2. Dijkstra TA, Rogers CDF, Smalley IJ, Derbyshire E, Li YJ, Meng XM (1994) The loess of north-central China: geotechnical properties and their relation to slope stability. *Eng Geol* 36:153–171
3. Dijkstra TA, Smalley IJ, Rogers CDF (1995) Particle packing in loess deposits and the problem of structure collapse and hydroconsolidation. *Eng Geol* 40:49–64
4. Delage P, Cui YJ, Antoine P (2005) Geotechnical problems related with loess deposits in Northern France. In: *Proceedings of international conference on problematic soils*. Eastern Mediterranean University Press, Famagusta, North Cyprus pp 517–540
5. Xu Z, Lin Z, Zhang M (2007) Loess in China and loess landslides. *Chin J Rock Mech Eng* 26:1297–1312
6. Peck RB, Hanson WE, Thornburn TH (1974) *Foundation engineering*, 2nd edn. John Wiley and Sons, New York
7. Jefferson I, Rogers C, Evstatiev D, Karastanev D (2005) Treatment of metastable loess soils: lessons from eastern Europe. In: *Ground improvement—case histories*. Elsevier, pp 723–762
8. Rollins KM, Kim J (2010) Dynamic compaction of collapsible soils based on U.S. case histories. *J Geotech Geoenviron Eng* 136(9):1178–1186
9. Mohamed AM, El Gamal M (2012) Treatment of collapsible soils using sulfur cement. *Int J Geotech Eng* 6(1):65–77

10. Fattah MY, Al-Ani MM, Al-Lamy MTA (2015) Wetting and drying collapse behaviour of collapsible gypseous soils treated by grouting. *Arab J Geosci* 8(4):2035–2049
11. Ayeledeen M, Negm A, El-Sawwaf M, Kitazume M (2017) Enhancing mechanical behaviors of collapsible soil using two biopolymers. *J Rock Mech Geotech Eng* 9:329–339
12. Guo JY (1958) Study on the reasons for collapse. *Hydrogeol Eng Geol* 4:7–11 (in Chinese)
13. Li P, Vanapalli S, Li T (2016) Review of collapse triggering mechanism of collapsible soils due to wetting. *J Rock Mech Geotech Eng* 8:256–274

Evaluation of the Performance of SMC Modified Asphalt Mixtures and Its Environmental Benefits Analysis



Haoyuan Luo , Yanjun Qiu, and Ting Su

Abstract Styrene methyl copolymers (SMC) are researched as one innovative additive in asphalt and have been widely applied in numerous engineering practical issues within only 3 years because of its distinctive construction temperature-reducing property. However, due to a lack of systemic research of its mechanism, mixture property is ignored while seeking lower construction temperature. In this study, Fourier transform infrared (FTIR) is selected to investigate its mechanism, and a series of experiments are designed for asphalt mixture with different amounts of SMC added. The experiments consist of two main parts: One is its practical performance verification, and the other is its environmentally friendly property investigation. Finally, SMC belongs to a kind of amide-containing quaternary ammonium salt surfactant. The experiment results reveal that SMC is efficiency in temperature reduction. It is better than many other warm-mix additives but still far from the cold-mix additive definition, this is because the mixture is irregularly with a lower strength when SMC contents are raised upon to 8%. In this proportion, construction temperature decreases to 85–105 °C, and those main pollution gas (SO₂, NO_x, PM_{2.5}, PM₁₀, benzopyrene.et.al) emission is reduced by 40%.

Keywords Pavement materials · Warm-mix asphalt · Cold-mix asphalt · Styrene methyl copolymers (SMC) modified additive · Construction temperature · Emission reduction · Modification mechanism

H. Luo · Y. Qiu (✉) · T. Su

School of Civil Engineering, Southwest Jiaotong University, Chengdu 610031, China
e-mail: publicqiu@vip.163.com

Key Laboratory of Highway Engineering of Sichuan Province, Southwest Jiaotong University, Chengdu 610031, China

H. Luo

School of Transportation, Southeast University, Nanjing 211189, China

1 Introduction

In a global view, sustainable and lower greenhouse gas emission topics remain its heats for a period, and those related materials were provided general by genera [1, 2]. For asphalt materials in road construction field, fetal disadvantages are frequently addressed as high in situ paving temperature, high energy consumption and cancer-related health problems [3]. Thus, lower mixture temperature and lower temperature paving technology caught more and more researchers' attention. Warm-mix asphalt (WMA) and cold-mix asphalt (CMA), supported by a series of additive, are selected as two alternative ways to solve those problem in hot-mix asphalt [4].

Research toward warm-mix asphalt is firstly raised by Shell and Kolo-Veidekke. These two companies created warm-mix techniques in a co-operation, and the first warm-mix test pavement was built in 1996 [5]. By progressed for approach 30 years, warm-mix additive is matured and widely applied all over the world. Currently, three major technical categories have gradually formed which are organic viscosity reducing type, foaming viscosity reducing type and surfactant type [6]. Modification mechanism and technical characteristics of common warm-mix additive are summarized in Table 1.

Organic and foaming warm-mix additive may damage the performance of asphalt while reducing the construction temperature [13]. Surfactant warm-mix additive is well known of its better performance, but its cost is very too high for small construction projects [14]. For most additives, the temperature reduction range is only 20–40 °C, which are far from a solution to heating problems in asphalt; thus, cold-mix additive is a milestone issue [15]. Besides this, cold-mix asphalt (CMA) is a progress of warm-mix asphalt technology, and it makes asphalt which can be mixed and paved in a room temperature without any heat process. Common types of cold-mix asphalt contain emulsified type, foaming type and solvent type [16]. The technical principle of CMA is similar to foaming warm-mixing asphalt. Water and surfactant are added to make the asphalt turn to liquid at room temperature to satisfy the fluidity required for mixed production. However, due to the mixing of a large amount of water during production, CMA often has the shortcomings of insufficient moisture stability and weak adhesion of asphalt-aggregate interface [4, 17]. As a result, it is difficult to completely replace HMA or WMA as a kind of full-width paving material but only an alternative in pavement repairing and overlaying in a small area [18]. Recently, CMA is developed by several researchers, and Valencia et al. [17] found that polyvinyl acetate emulsion (PVAC-E) can significantly improve the high-temperature stability of emulsified asphalt, and application prospects are wide. Shanbara [19, 20] improved the toughness of cold-mix asphalt mixture at low-temperature by adding fibers. Dulaimi [21, 22] modified cold bituminous emulsion mixture (CBEM) by using new binary blended cementitious filler mixed cementitious filler high calcium ash powder and high aluminosilicate waste. The water sensitivity of the new CBEM mixture has been significantly improved. However, these improvements are limited by the instability of raw material sources and higher costs and have not been used on a large scale.

Table 1 Common warm-mix additive products mechanism and evaluation

Type	Name	Region	Mechanism	Evaluation
Organic [7–8]	Sasobit	South Africa	Main components: saturated long-chain aliphatic compounds (C_nH_{2n+2} , $n \approx 30-50$) Added at asphalt heating step, the long aliphatic hydrocarbon chain of the substance is allowed to rotate and stretch independently; after energy gained gradually, the originally tightly fitting asphaltene molecules are divided; repolymerizing is restrained This results in the viscosity of asphalt are reduced	Temperature reduction capacity is 20–30 °C As one initial warm-mix additive, its characteristics include lower coast, simple technique and stability in high temperature; the disadvantages are its negative impacts on
	Haichuan EC-20	China		
	LeadCap	South Korea		
Foaming [9–10]	Warm-foam	Britain	Main components: surfactants which increase the strength of the vapor bubble surface of water in asphalt. When the product is added into asphalt, water in it is quickly evaporated and transformed to vapor bubbles; at this time, surfactant makes these bubbles stably exist in asphalt without overflowing or breaking. This results in asphalt are expanded by about 8 times in volume, and thereby, the fluidity of asphalt is raised	Temperature reduction capacity is 30–40 °C The price of this product is lower, and viscosity is weakened significantly. Due to the remains of water, interfacial adhesion between asphalt and aggregates is destroyed; this directly impairs the moisture stability and freeze–thaw resistance of asphalt concrete
	Aspha-min	Germany		
	Kolo-Veidekke	Norwegian		
	Double-Barrel Green Aster	US		
	LEAB Royal BAM Group	Netherland		

(continued)

To combine advantages of those both, styrene methyl copolymers (SMC) modified additive is noticed as a kind of possible additive recently. The main component is high-polymer elastomer extracted from wasted rubber and plastic, the amount is as high as 80%, and the rest 20% is auxiliary chemical materials such as diluent as its container [23]. It is claimed that this product is able to produce and compact asphalt

Table 1 (continued)

Type	Name	Region	Mechanism	Evaluation
Surfactant [11–12]	Evotherm [®] DAT	US	<p>Main components: surfactant with both hydrophilic and lipophilic groups</p> <p>The lipophilic group is firmly adsorbed on the asphaltene surface, while the hydrophilic group attracts free water molecules in the asphalt and forms a water film around the asphaltene, which isolates the asphaltene molecules from each other</p> <p>As a result, workability of asphalt is improved</p>	<p>Temperature reduction capacity is 30–40 °C</p> <p>As one patent product, it is expansive. This product not only reduced construction temperature and improved compaction effect but also raised elastic modulus and anti-rut capacity slightly</p>

mixtures at room temperature, and because water is unnecessary during this step to reduce the viscosity, the problem of insufficient asphalt-aggregate interface adhesion is vanished. Therefore, HMA can be replaced in full-width paving. In addition, its main raw materials are waste plastics and rubber from a wide range of sources, so the cost and selling price of the product are lower [24]. Since it was launched in China in 2016, the product has been used in more than a thousand kilometers of road paving projects within only 4 years. Among them, there are many long-distance high-grade pavement full-width paving projects SMC modified asphalt mixture products. The application of SMC modified asphalt mixture products statistic result is listed in Table 2.

However, due to the fierce development of SMC and the lack of summary of material properties and application experience, some practical projects have caused problems as lower mixture strength causes by higher SMC proportion in order to pursue lowering construction temperature. In addition, the research on the modification mechanism of SMC modifiers is also lacking. This paper will focus on SMC promoted asphalt and its function by applying in asphalt concrete. To achieve this, experiments are designed to investigate its paving function, and its mechanism will be observed via Fourier transform infrared (FTIR). Meanwhile, a comparison is operated to analyze the amount diversity of by-products discharged between hot-mix asphalt concrete and SMC modified ones. And those elements in by-products are mainly seven wasted gas which are CO₂, CO, SO₂, NO_x, PM_{2.5}, PM₁₀, benzopyrene (BaP, one of the main components of asphaltic gas, is a highly carcinogen). By doing this, this paper will give a thorough investigation about the property of this new materials including its performance, modifying mechanism and environmentally property.

Table 2 Application statistic result of SMC modified asphalt in China

Year	Location	Road type	Engineering content	Extent (km)
2019	Qingdao Shandong [25]	Urban pavement	Pavement overlay	0.3
2019	Jiayuguan Jiangsu [26]	National highway G30	Pavement overlay	5.2
2019	Urumqi, Xinjiang [27]	National way G312	Pavement maintenance	–
2018	Dingxi, Gansu [28]	National highway G22	Pavement overlay	2.0
2018	Tianshui, Lanzhou [29]	Provincial road	Pavement rebuilding	1.0
2018	Panzhihua, Sichuan	National way G108, G227, G353	Pavement rebuilding	400
2018	Jiuquan, Gansu [28]	Provincial road S202	Pavement overlay project	7.5
2018	Yuncheng, Shanxi [30]	Urban expressway	Pavement overlay project	6.0
2018	Tongzhou, Beijing	Test pavement	Test road paving	1.0
2017	Altay, Xinjiang [31]	Avenue	New pavement building	500
2017	Korla, Xinjiang [31]	National way G218	Pavement repairmen	48
2017	Korla, Xinjiang [31]	National way G218	Test road paving (altitude 3000 + m, temperature 6 °C)	1.0
2017	Liangshan, Sichuan	National way G108	Pavement rebuild	10.0
2017	Liangshan, Sichuan	National way G108	Pavement maintenance	80.0
2016	Urumqi, Xinjiang [31]	Inner pavement in venue	Pavement maintenance	200 m ²

2 Materials and Methods

2.1 Experiment Material

2.1.1 Asphalt

In this study, a 70 pen asphalt produced in Zhonghai, Sichuan, China is selected as matrix asphalt to blend SMC modified asphalt, and its properties are illustrated in Table 3.

The specimen is prepared in a critical condition, because its quality is crucial. During this process, the amount of additive is computation benchmark which is asphalt mass. First, the temperature for matrix asphalt is controlled at 110 °C strictly. Then, based on the percentage of asphalt mass, SMC is directly added into. Finally, SMC modified asphalt is stirred in a high speed for 30 min. The above is the steps

Table 3 Properties of the matrix 70 pen asphalt binder

Properties	Test method	Values
Penetration at 25 °C (dmm)	ASTM D5 [32]	61.2
Softening point (°C)	ASTM D36 [33]	48.1
Ductility at 15 °C, (cm)	ASTM D113 [34]	≠100
Performance grade	AASHTO M320 [35]	70–22
Performance grade at mid-temperature	AASHTO M320 [35]	22

sequence of asphalt specimen preparation of all experiment established in this paper. The specimen is illustrated as Fig. 1 as an example. The surface of 8 wt% SMC (by mass of asphalt) modified asphalt is shown, and it is emulsion state. The basic properties of 8 wt% SMC modified asphalt after evaporation and residue steadied are listed in Table 4.

Fig. 1 Appearance of 8 wt% SMC—modified asphalt

Table 4 Properties of 8 wt% SMC modified asphalt

Properties	Test method	Values
Evaporation mass loss (%)	ASTM D402 [36]	14.3
Residue penetration at 25°C (dmm)	ASTM D5 [32]	248
Residue ductility at 25 °C (cm)	ASTM D113 [34]	71
Flash point (TOC)	ASTM D92 [37]	221

2.1.2 Asphalt Mixture and Its Grading Composition.

According to in-being SMC application instance and previous research, major difference between SMC modified asphalt and traditional hot mix ones is their construction temperature only, and their grades level, paving and manufacture method, are the same. Hence, in this study, the grade is designed base on AC-13 and AC-20, and the models constructed are named as SMC-13 and SMC-20 asphalt concrete. The detail is demonstrated in Table 5, where the aggregate is made of basalt gravel filled with mineral powder.

2.2 Experiment Methods

2.2.1 Experiment Outline

The experiment of this study consists of three steps:

Step 1: The investigation for mechanism and property of SMC modified asphalt by FTIR.

A reasonable construction temperature range reference is offered via tests in volatilization time and viscosity difference. At the same time, the capacity of SMC in reducing construction temperature is inquired thoroughly, what is realized by the observation for the temperature reduction status in an increasing amount range of SMC in modified asphalt.

Step 2: The performance of SMC modified asphalt mixture.

The groups of models are ranged as its SMC addition percentage (0, 4, 6, 8, 10, 12%, by mass of asphalt). For each group, tests are designed to exam its volumetric properties, strength, high-temperature rutting performance, moisture stability and low-temperature crack resistance. All that performance is crucial for pavement usage asphalt concrete, and for all additive including SMC, unwanted influence to them is forbidden because those properties are the criterion for manufacturers.

Step 3: Harmful gas (CO₂, CO, SO₂, NO_x, PM_{2.5}, PM₁₀, BaP) emission comparison between SMC modified asphalt concrete and formal hot-mix asphalt concrete.

One major advantage of SMC is its characteristic in harmful gas emission reduction. Thus, a comparison test is needed between SMC modified asphalt and

Table 5 Gradation of SMC normal temperature modified asphalt mixture

Sieve size (mm)	26.5	19	16	13.2	9.5	4.75	2.36	1.18	0.6	0.3	0.15	0.075
SMC-20	100	98.0	86.4	74.7	53.6	36.7	24.3	18.5	14.7	7.2	6.4	4.8
SMC-13	–	–	100	95.1	76.8	43.2	36.4	28.9	22.4	16.1	11.6	6.8

common asphalt in the amount diversity of harmful gas emission. By this test, its environmentally friendly effect is discovered.

2.2.2 Volumetric Properties

According to ASTM D2726 [38], the bulk density of SMC-13 and SMC-20 mixtures is determined firstly. Then, three volume indexes are calculated in accordance with ASTM D3203 [39]. The air voids (VV) are voids in the mineral aggregate (VMA), and voids filled with asphalt (VFA) were the most commonly used indexes for volumetric properties of the mixtures.

2.2.3 Marshall Stability Test

According to ASTM D6927 [40], two types of mixtures prepared in the laboratory are transformed into standard Marshall specimens. Then, Marshall stability (MS), flow value (FL) indexes and immersion residual stability (IRS) were obtained. According to AASHTO T283 [41], Marshall stability value was tested to obtain the tensile strength ratio (TSR).

2.2.4 Low-Temperature Crack Resistance Test

According to the low-temperature bending test method in Chinese Standard JTG E20-2011 [42], the low-temperature crack resistance is necessary for analyses. Rut specimens were cut into beams, and their size are all $250 \times 30 \times 35$ mm. Before the test, the length (L), width (d) and height (h) of the beam have been accurately measured to the nearest one decimal place. The beams were tested under 50 mm/min loading rate at -10 °C, and the span-deflection curve was recorded. The maximum bending strain ε_B characterizing the low-temperature performance of the asphalt mixture was calculated, as Eq. (1).

$$\varepsilon_B = \frac{6 \times h \times d}{L^2} \quad (1)$$

2.2.5 Fourier Transform Infrared Analysis

. Fourier transform infrared analysis is operated under a resolution of 0.2 cm^{-1} , and the test time is set to 32 s with a range from 4000 to 400 cm^{-1} [43].

2.2.6 Viscosity

The viscosity test of asphalt utilizes the DSR rotary plate viscosity test methods based on previous studies [44]. It relies on the dynamic shear remoter to appreciate the viscosity-temperature curve drawing under continuous temperature scanning of asphalts with different SMC contents.

3 Results and Discussion

3.1 Analysis of SMC Modification Mechanism Based on FTIR

FTIR is considered as one feasible method to identify the mechanism. This method is capable to analyze inner construction of asphalt, mainly molecule and functional group. As the result, functional groups transformation after SMC added will be conspicuous, and this is the key for its mechanism research. The tested material includes SMC, 70# matrix asphalt and SMC modified asphalt. The result is demonstrated below and is illustrated in Fig. 2. The analyses are as follows:

1. There is a characteristic peak belonging to secondary amide bond $\text{R}-\overset{\text{O}}{\parallel}{\text{C}}-\text{NH}-\text{R}$ in SMC. The basic evidence is as follows:
Extensible vibrational peak of N-H bond (secondary amine) at 3278 cm^{-1} ; there is a stretching vibration peak of C=O double bond at the position of 1660 cm^{-1} ,

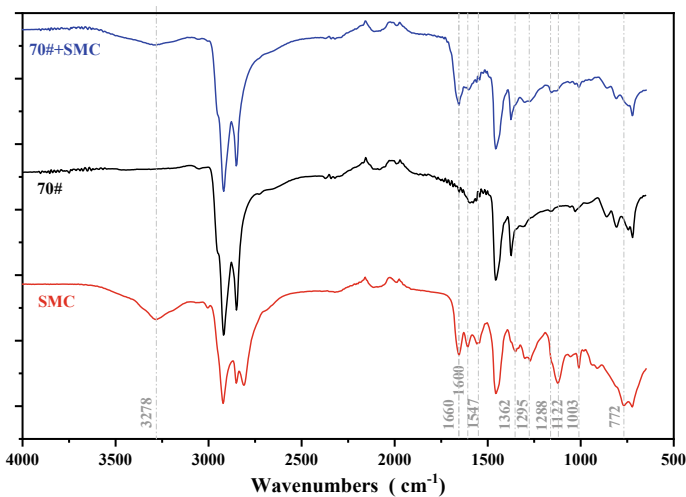


Fig. 2 SMC modification mechanism analysis based on flourier transform infrared

which belongs to the characteristic range of the amide I band; there are coupling vibration peaks of secondary amides $\delta\text{N-H}$ and $\nu\text{C-N}$, and their peak positions are 1547 and 1295 cm^{-1} , respectively, which belong to the characteristic range of amide II band and amide III band [45, 46].

2. There is a characteristic peak belonging to saturated cyclic ether.
The basic evidence is that the double peaks at 1122 and 1003 cm^{-1} belong to the characteristic range of $\nu_{\text{as}}\text{C-O-C}$ and $\nu_{\text{s}}\text{C-O-C}$, respectively [47, 48].
3. The ether ring and secondary amide bond are broken after SMC being added into 70# matrix asphalt.
The basic evidence is as follows: After adding 8% SMC to 70# matrix asphalt, the two coupled vibrational peaks of $\delta\text{N-H}$ and $\nu\text{C-N}$ of the secondary amide bond disappeared; the saturated cyclic ethers $\nu_{\text{as}}\text{C-O-C}$ and $\nu_{\text{s}}\text{C-O-C}$ characteristic peaks vanished [49, 50].
4. There are characteristic peaks of bisphenol A epoxy resin in SMC, and after forming 70#+8% SMC modified asphalt, the characteristic peaks of epoxy resin basically disappear.
The basic evidence is as follows:
5. In the characteristic graph of SMC, the characteristic peaks at 772 and 1003 cm^{-1} prove the existence of terminal epoxy ring.
6. The characteristic peak at 1362 cm^{-1} proves the existence of benzyl ($-\text{C}(\text{CH}_3)-$) bending vibration.
7. The characteristic peak at 1600 cm^{-1} proves that it has the bending vibration of benzene ring $-\text{C}=\text{C}-$.
8. 1288 cm^{-1} is the stretching peak of aliphatic-aromatic ether C-O-C .

The above four points confirm the presence of bisphenol A epoxy resin in SMC, but after adding SMC to the base asphalt to volatilize for 2 h, the characteristic peaks in a. and b. basically disappear, and the characteristic peaks in c. and d. become weaker and combine. In the literature [31], this phenomenon should be caused by the volatilization of bisphenol A epoxy resin as a solvent.

Based on previous research, those three characteristic reactions in result (a)–(c) belong to the basic reaction of the action principle of the amide-containing quaternary ammonium salt surfactant [51]. This surfactant is a cationic surfactant that changes the surface tension of the surface of the solution to provide lubrication [52]. In summary, the essence of SMC is a surfactant, which can reduce the viscosity and the construction temperature by changing the surface tension and surface free energy among asphalt molecules. This is similar with mechanism of some surface-active warm-mix additives.

3.2 Effect of Volatilization Time on the Performance of SMC Asphalt

The key technology of SMC modified asphalt lies on its volatilization. Because the SMC is dissolved in organic container to guarantee the largest engage area between SMC and asphalt during mixture. This container also ensures that SMC is able to distribute evenly. After being added into the container will volatilize automatically, and SMC remains only. Therefore, its volatilization time is crucial, and it is essential to observe this process. The result is gained by comparing the mass of volatilized modified warm-mix asphalt with 8% SMC with its original mass under 25 °C and 60% relative humidity, and the Brookfield viscosity tests are also conducted under the same condition. Finally, two repeatable results will be obtained as a proportion of rudimental mass in asphalt and the Brookfield viscosity index. The change of these two indices is illustrated in Fig. 3 where three significant durations are highlighted under a 0–672 h (28 d) test rotate, including:

Primary duration (0–4 h): Within this duration, the asphalt is steady, its volatilization velocity is slow. The rudimental mass proportion is around 98% by the end, and viscosity change is no more than 10%. This duration is the key for mix and compaction.

Secondary duration (4–100 h): Within this duration, the container volatilizes dramatically and results in asphalt transforms to binder. In this duration, the rudimental mass proportion is 88% at the end of this duration; meanwhile, its viscosity increases by over 100%. Therefore, approximate care process and traffic control are required.

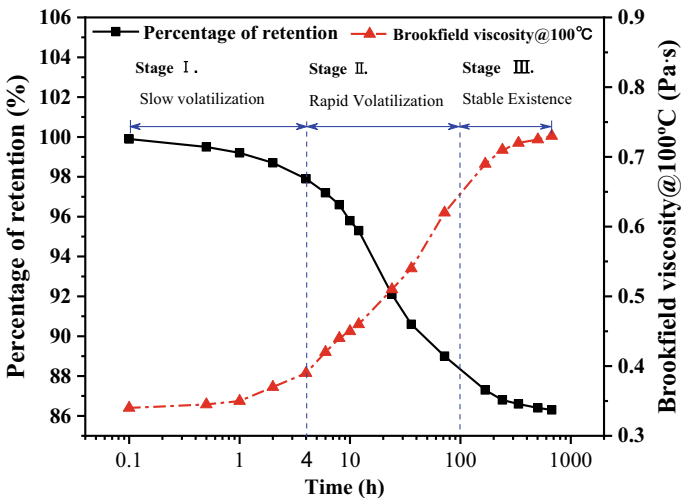


Fig. 3 Change relation of quality residual rate and viscosity of SMC modified asphalt with volatilization time

Final duration (after 100 h): Within this duration, volatilization tends to terminate its rudimental mass proportion which remains around 86% and viscosity changed in little range.

3.3 Determination of Construction Temperature of Different SMC Contents

Temperature is an important element in asphalt mixing for environment reasons, particularly in modified asphalt because it is designed to solve that possible pollution under a high construction temperature. Hence, it is essential to probe the relationship between temperature and materials' performance modified by different SMC contents. According to the standard ASTM D2493 [53], the common method to predict construction temperature of asphalt mixture consists of two steps: First, the viscosity-temperature curve of target asphalt at 135–175 °C is ascertained by Brookfield viscometer. Second, two temperature ranges in this curve which are corresponding to the viscosity ranges 0.17 ± 0.02 Pa s and 0.28 ± 0.03 Pa s are selected as the mixing (θ_M) and compaction (θ_C) temperature range, respectively. The result for six groups of SMC modified asphalt is shown in Table 6, and the construction temperature trend is illustrated in Fig. 4.

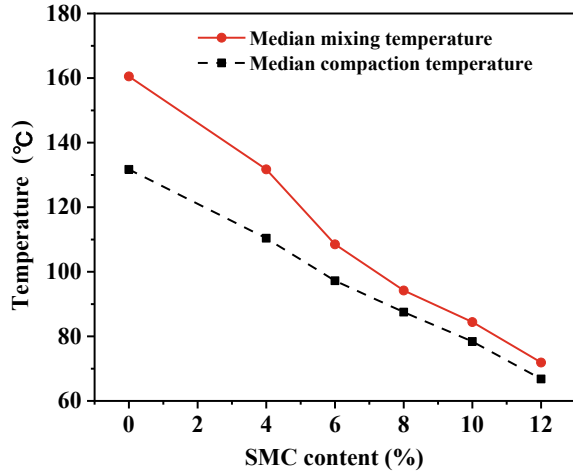
From the line in Fig. 4, the construction temperature of the SMC modified asphalt mixture drops significantly with the increase of the SMC content. When it is 4%, the mixing temperature of the mixture can be effectively reduced by about 30 °C, where the material can be considered as warm-mix asphalt mixture; when the line reaches 8%, the mixing temperature can be reduced to below 100 °C. Nevertheless, lower mixing temperature may result in negative impact on strength. From the line in Fig. 4, when the content of SMC is increased to 12%, then its mixing temperature is decreased to 71.9 °C. Therefore, a key question lies on a balance point seeking between its mixing temperature and the whole material property.

The result of volatilization and viscosity tests shows comparability between SMC and emulsifier or warming agent since there is the same function which is the reduction on viscosity and mixing temperature, whereas the difference is water is not

Table 6 Construction temperature of asphalt mixture under different content of SMC (°C)

w(SMC)(wt%)	θ_M	Median of θ_M	θ_C	Median of θ_C
0	157.2–163.8	160.5	129.2–134.2	131.7
4	129.4–134.2	131.7	107.2–113.6	110.4
6	105.6–110.7	108.5	98.1–101.9	97.2
8	92.1–96.3	94.2	94.1–100.3	87.5
10	84.6–90.2	87.4	75.4–81.4	78.4
12	67.8–76.0	71.9	59.1–71.5	65.3

Fig. 4 Change relation of mixing and compaction temperature of asphalt mixtures with different content of SMC



necessary for SMC modified asphalt, and the final viscosity reduction effect is more significant than those two.

3.4 Effect of SMC Content on the Volumetric and Marshall Properties of Mixtures

As mentioned in Sect. 2.2.1, mixture properties need to be guaranteed while construction temperature is reduced; thus, in this part, an experiment is established in order to prove that its strength is less than the requirement offered by standard. For the strength test of mixture, several groups of Marshall specimens need to be built based on the rules in standards. The main test contains measurement for air voids (VV), the voids in the mineral aggregate (VMA), the void filled with asphalt (VFA), Marshall stability (MS) and flow value (FL). These are applied on four specimens in each group, and the result is recorded as the average one. For two types of grades, results are listed in Table 7. Via comparing the volume index in among different specimens, it can be concluded as:

1. For a determined bitumen-aggregate ratio, as SMC increases from 4 to 12%, decreased trends are observed in VV, VMA, MS and FL, but the value of VFA increases. This can be summed as SMC results in a positive impact in mixture compacting but a negative impact in strength.
2. Specimens with 4% SMC added are irregular because its lower VV value; similar, the strength of specimens with over 12% SMC added is too low to comply with the standard.

As mentioned in Sect. 2.2.1, the key question of SMC is the seeking of a balanced point between its contents and strength. From the result above, for SMC-13, an

Table 7 Volume index of Marshall specimen under different content of SM

Mixture type	Bitumen-aggregate ratio	w _{SMC} (%)	VV (%)	VMA (%)	VFA (%)	MS (kN)	FL (mm)
SMC-13	4.8	0	4.01	15.0	73.3	10.78	3.5
		4	5.11	14.7	65.4	10.34	3.4
		6	4.59	14.4	68.1	10.12	3.2
		8	4.21	14.2	70.4	9.93	3.0
		10	3.87	13.9	72.2	8.65	2.9
		12	3.42	13.7	75.1	7.38	2.7
Requirement of AC-13 in the standard			3–5	≥13	65–75	≥8	2–4
SMC-20	4.2	0	4.37	13.9	68.6	10.23	3.3
		4	5.00	14.9	66.5	9.67	3.2
		6	4.64	14.6	68.2	9.21	3.1
		8	4.35	14.3	69.6	8.81	3.0
		10	3.91	14.1	72.3	7.99	2.8
		12	3.60	13.9	74.1	7.04	2.6
Requirement of SMC-13 in the standard			3–5	≥ 11	55–70	≥ 8	2–4

Note The Standard is the JTG F40-2004 *Technical Specifications for Construction of Highway Asphalt Pavement* of Ministry of Transport of China [54]

approximate proportion of SMC in mixture is from 6 to 10%, and for SMC-20, the proportion is from 6 to 8%.

3.5 Effect of SMC Content on Performance of Mixture

The performance of mixture is mainly indicated by dynamic stability (DS), residual stability (MS_0), freeze–thaw splitting strength ratio (TSR) and low-temperature bending failure strain (ϵ_B). The test results about the relationship between SMC proportion and those elements are listed below in Table 8. The performance of SMC modified asphalt mixture is changed as the proportion of additive increasing.

The detail is demonstrated as below:

For high-temperature stability, the addition of SMC produces a deteriorating effect. When the amount of SMC increases, the dynamic stability of the mixture is decreasing. At the same time, the dynamic stability of coarse-grained SMC-20 is greater than that of medium-grained SMC-13 under the same SMC content. The above phenomenon indicates that SMC deteriorates the high-temperature stability of asphalt binder. With the increase of SMC content, in response to high-temperature wheel load, the mixture relies more and more on the skeleton formed by the aggregate

Table 8 Influence on road performance index of asphalt mixture under different contents of SMC

Mixture type	$w_{SMC}(wt\%)$	$DS(\text{times}\cdot\text{mm}^{-1})$	$MS_0(\%)$	TSR (%)	$\varepsilon_B(\mu\text{m m}^{-1})$
SMC-13	0	1788	89	87	2381
	4	1531	85	81	2484
	6	1479	84	79	2545
	8	1412	83	78	2601
	10	1340	81	76	2 564
	12	1241	77	74	2434
SMC-20	0	2014	87	84	2141
	4	1811	84	80	2257
	6	1764	83	78	2341
	8	1725	82	77	2411
	10	1625	80	75	2186
	12	1511	78	73	1955
Requirement of AC-13/20 in the standard		≥ 1000	≥ 80	≥ 75	≥ 2000

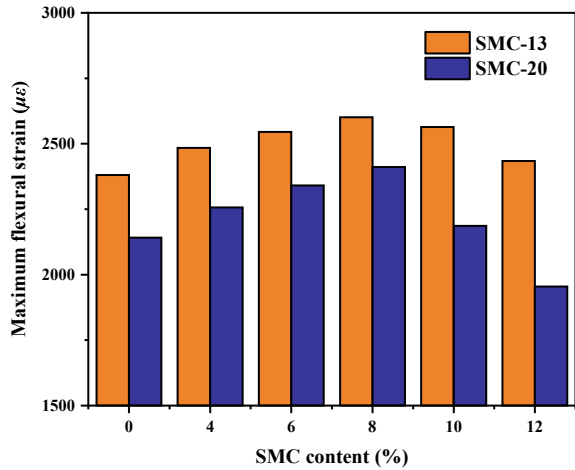
Note The Standard is the JTG F40-2004 *Technical Specifications for Construction of Highway Asphalt PAVement* of Ministry of Transport of China [54]

to resist deformation, which also explains why the dynamic stability of SMC-20 is greater than that of SMC-13 under all the content of SMC.

For moisture stability, the addition of SMC also results in a negative impact. While the increase of SMC content, both MS_0 and TSR are gradually reduced. These two indexes of the mixture at 12% dosage level are even lower than the general requirements of JTG F40-2004 for hot-mix asphalt specifications. What needs to be pointed out is that during the process of increasing the amount of SMC, the asphalt saturation is gradually increased, indicating that the gap between the aggregates is filled with more asphalt, which makes the water less likely to invade the interior of the mixture. However, the moisture stability is still reduced, which may be due to the decrease of the adhesion of asphalt binder to aggregate caused by the addition of SMC.

The addition of SMC can optimize the low-temperature crack resistance performance to a certain extent, and the optimum content of SMC is about 8%. The variation of ε_B with SMC content is shown in Fig. 5. When SMC content increases from 0 to 12%, the ε_B of the two graded mixtures first increased and then decreased rapidly, reaching its peak at around 8%. Compared with the common mixture, the ε_B of SMC-13 and SMC-20 can be increased by about 11% and 15%, respectively, under the condition of 8% SMC added. However, for AC-20, the ε_B of the mixture with 12% SMC content is less than that of the mixture with 0% SMC, indicating that the low-temperature crack resistance of the mixture has begun to deteriorate due

Fig. 5 Relation changes of ϵ_B with different content of SMC



to the excessive addition of SMC. The main purpose of bending test is to investigate flexural-tensile properties, and this performance is determined by the quality of asphalt binder. For SMC-20, due to its grade characteristics, more asphalt binder is needed. Therefore, SMC contributes more in this material for its low-temperature tensile strength.

3.6 Emission Detection in the Production Process of SMC Normal Temperature Modified Asphalt Mixture

In previous research [4, 55], a relationship between construction temperature and CO₂ emission is discovered. The detail result is concluded as the emission decreases by at least 30% with 10 °C temperature reduction. And asphalt gas can be controlled when heating temperature is beneath 140 °C. These effects can promote work environment for operators during mixing asphalt and reduce greenhouse gas emission; briefly, SMC is a type of environmental friendly additive. Based on this, its impacts on emission reduction are necessary to investigate conspicuously. One experiment is designed to achieve this; it compares the gas emission amount, mainly CO₂, CO, SO₂, NO_x, PM_{2.5}, PM₁₀, BaP, in 6 and 8% SMC modified asphalt mix with 70# matrix asphalt mix. In these gas, the first six emissions measured are the main pollutants in air quality assessment, while BaP is the main component of asphalt smoke and has strong carcinogenicity [56].

In this test, temperature requires to be controlled rigorously because as mentioned before that gas emission related to temperature changes. And the temperature range for each mix process refers to Table 6.

The equipment is STD-F02-20 type 20L automatic mix pot. There is only one vent which means that the gas sample gained is reliable and sufficient. During the mixing

Table 9 Seven kinds of waste and the detection methods of them

Test item	Detection method	Standard	Test equipment
CO	Non-spectral infrared analysis	GB/T 18204.2—2014(3.1) [58]	GXH-3011A CO infrared analyzer
CO ₂	Non-spectral infrared analysis	GB/T 18204.2—2014(4.1) [58]	GXH-3010E CO ₂ infrared analyzer
SO ₂	Spectrophotometric Determination of para rosaniline hydrochloride by formaldehyde absorption	HJ 482—2009 [59]	7230G visible spectrophotometer
NO _x	Ndiethylenediamine hydrochloride spectrophotometric method	HJ 479—2009 [60]	7230G visible spectrophotometer
PM ₁₀	Light scattering method	GB/T 18204.2—2014(5.2) [58]	LD-5C(b) laser dust meter
PM _{2.5}	Light scattering method	GB/T 18204.2—2014(6) [58]	LD-5C(b) laser dust meter
BaP	High-performance liquid chromatography method	HJ 956—2018 [61]	HPLC

Note The standards beginning with HJ come from the Ministry of Environmental Protection of China, and those beginning with GB/T come from the Ministry of Health of China

process, emission samples discharged were collected by a QCS-6000 atmospheric sampler for subsequent analysis [57].

To analyze components within collected gas sample, the quantitative analysis of the seven target components was carried out by applying the air component detection method in Table 9. Among them, CO₂ and CO are determined by non-spectral infrared analysis; for SO₂, spectrophotometric determination of para rosaniline hydrochloride by formaldehyde absorption is used; for NO_x, ndiethylenediamine hydrochloride spectrophotometric method is used for determination; PM_{2.5} and PM₁₀ are measured by light scattering method; for BaP, high-performance liquid chromatography (HPLC) method is selected.

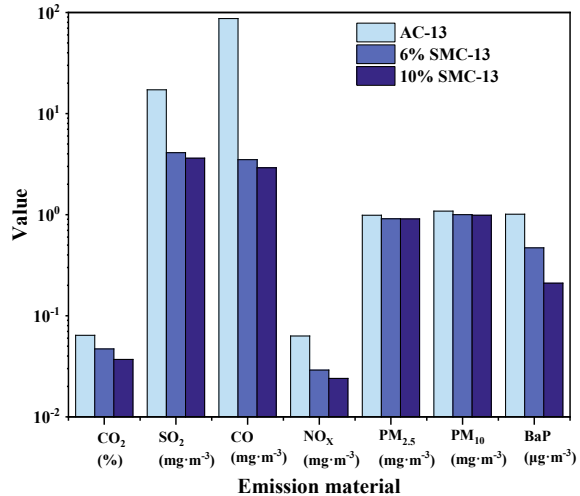
Table 10 details the result of this test, and to be clearer, a comparison is summed as Fig. 6. Based on this, all these seven types of pollution are declined in different degrees including:

1. With the increase of SMC content (i.e., the drop in mixing temperature), the emission of CO₂, CO, SO₂, NO_x and BaP decreased significantly. In another word, SMC contributed greatly to control these five types of wastes. However, there are no optimization effects on emission of PM_{2.5} and PM₁₀.
2. The effects for CO, SO₂ NO_x are various. 6% SMC (mixing temperature is about 105–110 °C) and 10% SMC (mixing temperature is about 90–95 °C) bring similar effects. This is because of the release temperature of those three

Table 10 Result of waste discharge in asphalt mixture mixing

Mixture type	$w_{SMC}(\%)$	θ_M ($^{\circ}C$)	Emission material					BaP ($\mu g m^{-3}$)	
			CO ₂ (%)	SO ₂ ($mg m^{-3}$)	CO ($mg m^{-3}$)	NO _x ($mg m^{-3}$)	PM _{2.5} ($mg m^{-3}$)		PM ₁₀ ($mg m^{-3}$)
AC-13	0	157.2-163.8	0.064	17.20	87.00	0.063	0.988	1.083	1.01
SMC-13	6	105.6-110.7	0.047	4.10	3.50	0.029	0.911	1.001	0.47
SMC-13	10	92.1-96.3	0.037	3.62	2.91	0.024	0.907	0.987	0.21

Fig. 6 Seven kinds of harmful gas emission in different mixtures



components which are at a high-temperature range. Therefore, the emission can be restrained significantly.

- For Benzoapyrene (C₂₀H₁₂, BaP), although the emission has been significantly controlled, its concentration is still several times higher than the carcinogenic concentration. The concentration of non-cancerous BaP in ambient air is about 0.066 ng/m³, the carcinogenic concentration is 12.7 ng/m³, and the strong carcinogenic concentration is 0.12 μg m⁻³ [62, 63]. The data obtained by the emission test showed that when the hot-mix process was used, the BaP concentration exceeded the allowable value by 78 times, and after using the 10% SMC to lower the construction temperature by 65 °C, it still exceeded the allowable value of 16.5 times.

4 Conclusions

The SMC modified asphalt has strong volatility as a kind of warm-mix asphalt. It is proved by the volatile energy test that the optimal construction time after unsealing is within 4 h, and the curing time should be guaranteed to be 100 h (about 4d). By infrared spectroscopy analysis of SMC normal temperature modifier asphalt, it can be inferred that SMC belongs to the amide-containing quaternary ammonium salt surfactant, which can reduce the viscosity and the construction temperature by reducing the surface of the asphaltene molecule and indicating the tension and surface free energy. By infrared spectroscopy analysis of SMC normal temperature modifier asphalt, it can be inferred that SMC belongs to amide-containing quaternary ammonium salt surfactant, which can reduce viscosity and construction temperature by reducing the surface tension and surface free energy of asphaltene molecules.

As the SMC content (0–12%) increases, the corresponding asphalt mixture will become more compact (VV reduction), but it will deteriorate its strength (MS decreases, FL decreases); the high-temperature stability is gradually deteriorated (dynamic stability DS decreases); same trend occurs in moisture stability performance (MS₀ and TSR are continuously reduced); low-temperature crack resistance performance is slightly optimized in the range of 0–8%, but it will rapidly decline after the content exceeds 8% (low-temperature bending damage strain ε_B first increases and then decreases).

For AC-13 and AC-20 gradation, the suitable content of SMC is 6–8% and 6–10%, respectively. Under the above suitable content, the suitable mixing temperature of SMC normal temperature modified asphalt mixture is about 85–105 °C, the suitable compacting temperature is 75–95 °C, and there is a gap to realize room temperature mix and paving.

The emission of CO₂, CO, SO₂, NO_x and Benzoapyrene in an ideal condition was significantly controlled by SMC modifier to effectively reduce the mix temperature of the mixture. The emission reduction ratio of the above emissions is over 40% when the amount of SMC reaches 12%, but the emission reduction effect of PM_{2.5} and PM₁₀ is not conspicuous.

References

1. Zhu S, Ma J, Tang T, Shi Q (2020) A combined modal and route choice behavioral complementarity equilibrium model with users of vehicles and electric bicycles. *Int J Environ Res Publ Health* 17(10)
2. Ma J, Xu M, Meng Q, Cheng L (2020) Ridesharing user equilibrium problem under OD-based surge pricing strategy. *Transp Res Part B: Methodolog* 134:1–24
3. Klinsky L, Kaloush K, Faria V, Bardini V (2018) Performance characteristics of fiber modified hot mix asphalt. *Constr Build Mater* 176:747–752
4. Thives L, Ghisi E (2017) Asphalt mixtures emission and energy consumption: a review. *Renew Sustain Energy Rev* 72:473–484
5. Wen Y, Wang Y, Zhao K, Chong D, Huang W, Hao G, Mo S (2018) The engineering, economic, and environmental performance of terminal blend rubberized asphalt binders with wax-based warm mix additives. *J Clean Prod* 184:985–1001
6. Luo H, Leng H, Ding H, Xu J, Lin H, Ai C, Qiu Y (2020) Low-temperature cracking resistance, fatigue performance and emission reduction of a novel silica gel warm mix asphalt binder. *Constr Build Mater* 231
7. Jamshidi A, Hamzah MO, You Z (2013) Performance of warm mix asphalt containing sasobit®: State-of-the-art. *Constr Build Mater* 38:530–553
8. Hossain Z, Zaman M, Wasiuddin NM, Sneed J, O’Rear EA (2011) Rheological evaluation of warm mix and anti-stripping additives modified performance grade binders. *Road Mater Pavement Des* 12–4:875–895
9. Mohd Hasan MR, You Z, Yang X (2017) A comprehensive review of theory, development, and implementation of warm mix asphalt using foaming techniques. *Constr Build Mater* 152:115–133
10. Bairgi BK, Mannan U, Tarefder R (2019) Influence of foaming on tribological and rheological characteristics of foamed asphalt. *Constr Build Mater* 205:186–195
11. Li K, Guo D (2013) Study on water stability of Evotherm® warm asphalt mixture. *Adv Mater Res* 753:819–822

12. Yu H, Leng Z, Dong Z, Tan Z, Guo F, Yan J (2018) Workability and mechanical property characterization of asphalt rubber mixtures modified with various warm mix asphalt additives. *Constr and Build Mater* 175:392–401
13. Liu K, Zhang K, Wu J, Muhunthan B, Shi X (2018) Evaluation of mechanical performance and modification mechanism of asphalt modified with graphene oxide and warm mix additives. *J Clean Prod* 193:87–96
14. Wu S, Zhang W, Shen S, Li X, Muhunthan B, Mohammad LN (2017) Field-aged asphalt binder performance evaluation for Evotherm warm mix asphalt: comparisons with hot mix asphalt. *Constr Build Mater* 156:574–583
15. Yu H, Leng Z, Zhou Z, Shih K, Xiao F, Gao Z (2017) Optimization of preparation procedure of liquid warm mix additive modified asphalt rubber. *J Clean Prod* 141:336–345
16. Shifa X, Huang Y, Cai S, Li S, Li J (2018) Progress of technologies for cold mix asphalt. *Road Mach Construct Mech* 02:34–36
17. Valencia LE, Alonso E, Manzano A, Pérez J, Contreras ME, Signoret C (2007) Improving the compressive strengths of cold-mix asphalt using asphalt emulsion modified by polyvinyl acetate. *Constr Build Mater* 21(3):583–589
18. Jain S, Singh B (2021) Cold mix asphalt: an overview. *J Cleaner Prod* 280
19. Shanbara HK, Ruddock FM, Atherton W (2017) Improving the mechanical properties of cold mix asphalt mixtures reinforced by natural and synthetic fibers. In: *International conference on highway pavements and airfield technology*
20. Shanbara HK, Ruddock F, Atherton W (2018) A laboratory study of high-performance cold mix asphalt mixtures reinforced with natural and synthetic fibres. *Constr Build Mater* 172:166–175
21. Dulaimi A, Hashim NHK, Ruddock FM (2016) Investigation into the stiffness improvement, microstructure and environmental impact of a novel fast-curing cold bituminous emulsion mixture. In: *Conference: 6th Eurasphalt & Eurobitume Congress*
22. Dulaimi A, Nageim H, Seton L, Ruddock F (2017) A novel cold bituminous emulsion mixture for road pavement using a new cementitious filler. In: *The 3rd BUiD doctoral research conference*
23. Chaoyang X (2018) Research on properties of recycled asphalt mixture with high RAP content and SMC at room temperature. *Southwest Jiaotong University*, pp 8–10
24. Ai C, Li QJ, Qiu Y (2013) Testing and assessing the performance of a new warm mix asphalt with SMC. *J Traff Transp Eng (English Edition)* 2(6):399–405
25. Dong K, Tiao M (2019) Application of SMC normal temperature asphalt mixture in Huangdao area of Qingdao City. *Transp World* 23:154–155
26. Li D, Guo C, Tian Q (2019) Application of 1.5–2.0 cm thin layer overlay of room temperature modified asphalt in preventive maintenance construction of g 30 lianhuo expressway (jia'an section). *Highway Traffic Tech (Appl Tech Edition)* 15(06):129–131
27. Wang Y (2019) Application of SMC normal temperature modified asphalt concrete in highway maintenance engineering. *Value Eng* 38(16):87–90
28. Sun Z (2018) Application of SMC modified asphalt mixture at room temperature in highway maintenance in Qingyang area. *High Traff Tech (Appl Tech Edn)* 12(14):8–10
29. Wang X (2019) Research on application of SMC modified asphalt concrete at room temperature in highway maintenance engineering. *China Standardization* 24:146–147
30. Qu H (2019) Application of SMC modified asphalt at room temperature in highway overlay engineering. *Shanxi Arch* 42(32):166–167
31. Sa R (2017) Research on preparation technology of normal temperature modified asphalt, China University of Petroleum (East China), China University of Petroleum (East China)
32. ASTM-D5/D5M-20 (2020) Standard test method for penetration of bituminous materials, American Society of Testing Materials, Washington D.C.
33. ASTM -D36/D36M (2014) Standard test method for softening point of bitumen (ring-and-ball apparatus). American Society of Testing Materials, Washington D.C.
34. ASTM-D113 (2017) Standard test method for ductility of asphalt materials. American Society of Testing Materials, Washington D.C.

35. AASHTO-M320 (2017) Standard specification for performance-graded asphalt binder, American Association of State Highway, Washington D.C.
36. ASTM-D402/D402M (2014) Standard test method for distillation of cutback asphalt, American Society of Testing Materials, Washington D.C.
37. ASTM-D92 (2018) Standard test method for flash and fire points by cleveland open cup tester, American Society of Testing Materials Washington D.C.
38. ASTM-D2726/D2726M (2019) Standard test method for bulk specific gravity and density of non-absorptive compacted asphalt mixtures, American Society of Testing Materials, Washington D.C.
39. ASTM-D3203/D3203M (2017) Standard test method for percent air voids in compacted asphalt mixtures, American Society of Testing Materials, Washington D.C.
40. ASTM-D6927 (2015) Standard test method for marshall stability and flow of asphalt mixtures, American Society of Testing Materials, Washington D.C.
41. AASHTO-T283 (2018) Standard method of test for resistance of compacted asphalt mixtures to moisture-induced damage, American Association of State Highway, Washington D.C.
42. JTG-E20-2011 (2011) Standard test methods of bitumen and bituminous mixtures for highway engineering, Ministry of Transport of China, Beijing
43. Ding H, Hesp SAM (2020) Variable-temperature Fourier-transform infrared spectroscopy study of wax precipitation and melting in Canadian and Venezuelan asphalt binders, *Constr Build Mater* 264
44. Luo H, Ouyang C, Xu J, Zheng P, Yang E (2019) Rotational plate viscosity test: A new method to measuring the viscosity of SBS—modified asphalt. *J Build Mater* 23(03):724–732
45. Hou X, Lv S, Chen Z, Xiao F (2018) Applications of fourier transform infrared spectroscopy technologies on asphalt materials. *Measure* 121:304–316
46. Zhihui L, Rui Z, Yonghua Z, Qian C, Weijun Q (2019) Discriminating wavenumbers selection of ATR-FTIR spectra for identifying graded asphalt. *J Build Mater* 214: 565–573
47. Sun D, Sun G, Du Y, Zhu X, Lu T, Pang Q, Shi S, Dai Z (2017) Evaluation of optimized bio-asphalt containing high content waste cooking oil residues. *Fuel* 202:529–540
48. Mannan U, Ahmad M, Tarefder R (2017) Influence of moisture conditioning on healing of asphalt binders. *J Build Mater* 146:360–369
49. Yao H, Dai Q, You Z (2015) Fourier transform infrared spectroscopy characterization of aging-related properties of original and nano-modified asphalt binders. *J Build Mater* 101:1078–1087
50. MFAS Araujo, VFC Lins, VMD Pasa (2012) Infrared spectroscopy study of photodegradation of polymer modified asphalt binder. *J Appl Poly Sci* 125(4):3275–3281
51. Miao ZC, Ren JW (2014) Preparation of novel diester gemini quaternary ammonium salt cationic surfactant. *Adv Mater Res* 1004–1005:699–702
52. Muzyczko TM, Shore S, Loboda JA (1968) Fatty amidoamine derivatives_ N, N-dimethyl-N-(3-alkylamidopropyl)amines and their salts. *J Am Oil Chem Soc* 45:720–725
53. ASTM-D2493/D2493M (2016) Standard practice for viscosity-temperature chart for asphalt binders. American Society of Testing and Materials, Washington D.C.
54. JTG-F40-2004 (2004) Technical specifications for construction of highway asphalt pavement Ministry of Transport of China, Beijing
55. Fernandes S, Silva HM, Oliveira JR (2019) Carbon dioxide emissions and heavy metal contamination analysis of stone mastic asphalt mixtures produced with high rates of different waste materials. *J Clean Prod* 226:463–470
56. Yang X, You Z, Perram D, Hand D, Ahmed Z, Wei W, Luo S (2019) Emission analysis of recycled tire rubber modified asphalt in hot and warm mix conditions. *J Hazard Mater* 365:942–951
57. Qiu Y, Luo H, Zhang J, Leng H, Ai C (2020) Comparative of emissions from production and construction of hot mix and warm mix asphalt pavement. *J Chang’an Univ (Natural Science Edition)* 40(01): 30–39
58. GB/T18204.2-2014 (2011) Examination methods for public—Part 2: Chemical pollutants, China National Standardization Management Committee, Beijing

59. HJ-482-2009 (2009) Ambient air—determination of sulfur dioxide—Formaldehyde absorbing—pararosaniline spectrophotometry Ministry of Environmental Protection of the People's Republic of China, Beijing
60. HJ-479-2009 (2009) Ambient air—determination of nitrogen oxides - N - (1 -Naphthyl) diamine dihydrochloride spectrophotometric method Ministry of Environmental Protection of the People's Republic of China, Beijing
61. HJ-956-2018 (2018) Ambient air—determination of benzo[a]pyrene—High performance liquid chromatography method Ministry of Environmental Protection of the People's Republic of China, Beijing
62. Yagishita M, Kageyama S, Ohshima S, Matsumoto M, Aoki Y, Goto S, Nakajima D (2015) Atmospheric concentration and carcinogenic risk of polycyclic aromatic hydrocarbons including benzo[c]fluorene, cyclopenta[c, d]pyrene, and benzo[j]fluoranthene in Japan. *Atmos Environ* 115:263–268
63. Mo S, Wang Y, Xiong F, Ai C (2019) Effects of asphalt source and mixing temperature on the generated asphalt fumes. *J Hazard Mater* 371:342–351
64. Edwards Y, Tasdemir Y, Isacsson U (2005) Influence of commercial waxes on bitumen aging properties. *Energ Fuel* 19:2519–2525
65. Hurley GC, Prowell BD (2006) Evaluation of potential process for use in warm mix asphalt. *J Assoc Asphalt Paving Technol* 75:41–90
66. Zhao Y (2012) Performance of warm-mix asphalt treated by quaternary ammonium salt surfactant. *J Highway Transp Res Dev* 29–8:20–24

Discrete Element Simulation of the Internal Structures of Asphalt Mixtures with High Content of Tire Rubber



Xiaodong Zhou, Siyu Chen, Dongzhao Jin, and Zhanping You

Abstract Increasing rubber content in asphalt mixtures is recognized as a practical approach to consume fast-growing waste tires. The reacted rubber technology using the dry process was developed to address the rubber swelling and poor performance of rubber asphalt mixtures. Although the tire rubber has proved to increase the low-temperature performance, fatigue life, cracking resistance, and rutting resistance of asphalt mixtures, the impacts of high content tire rubber on the mixtures' internal structures have not been revealed. This study is a preliminary research that utilized the laboratory and numerical simulation approach to investigate the strength, skeleton structures, and stress distribution of the tire rubber asphalt mixtures. The discrete element method (DEM) was employed to establish asphalt mixture models with a high content of tire rubber. New modeling procedures were developed to incorporate coarse aggregate shapes and rubber particles. Indirect tensile strength (ITS) values of specimens with rubber content up to 4.5% by mass were tested in laboratory and simulation. The results from DEM simulation had better consistency than the laboratory results. However, the test results showed that as the rubber content increased, the ITS of asphalt mixtures significantly decreased. Besides, the simulation indicates that the ITS decreased linearly as the percentage air void increased. The specimen ITS value decreased by half as the void ratio reached 15%. Furthermore, the internal structures and stress distribution of specimens with different rubber content were analyzed. The gap gradation proved to have a functional capacity of accommodating fine aggregates and rubber particles, all while forming a coarse aggregate skeleton.

Keywords Asphalt mixtures · Reacted and active rubber · Dry process · Indirect tensile strength · Discrete element method · Internal structure

X. Zhou · S. Chen · D. Jin · Z. You (✉)

Department of Civil and Environmental Engineering, Michigan Technological University, Houghton, MI 49931, USA

e-mail: zyou@mtu.edu

1 Introduction

As the number of waste tires keeps increasing rapidly, it has become a major environmental issue in many countries. According to the U.S. Rubber Manufacturer Association (RMA), alone in the United States, 263.4 million tires that weigh 4.46 million tons were generated in 2019 [1]. Incorporating crumb tire rubber into civil engineering applications has been done for several decades. The crumb tire rubber is commonly used as modifiers or fillers in the asphalt mixtures. There are two methods to incorporate crumb tire rubber with asphalt mixtures, the wet process and the dry process.

In the wet process, the crumb rubber is thoroughly mixed and reacted with asphalt binder under high heat for 45 min to one hour [2, 3]. The rubber modifier increased the performance of the asphalt mixture in rutting, fatigue, and cracking [4]. However, several barrels limit the utilization of the wet process. The most direct limit is the wet process cost higher in construction and needs extra equipment. Storage of rubber modified asphalt binder is another major problem because the rubber and asphalt tend to segregate. In addition, only a small amount of rubber can be utilized in wet process. The rubber is commonly no more than 1% of the asphalt mixture by mass.

In the dry process, the crumb rubber is used to partially replace the fine aggregates and fillers in the asphalt mixture [5, 6]. Thus, the dry process needs no extra equipment and can consume a higher amount of crumb rubber. The limitation of the dry process is the added crumb rubber may undermine the performance of asphalt mixture [7]. It was reported that the bond between binder and rubber particles was weaker than bond between binder and aggregates [8]. Another engineering problem of the dry process is that the rubber would have a physical and chemical reaction with the hot binder and significantly swell rubber particles' volume. Therefore, the dry process would decrease the workability of asphalt mixture and increase its percentage air void [9]. To address these problems, reacted rubber was developed [10]. Tire rubber particles are pretreated with asphalt binder to achieve partial swelling. High contents of tire rubber can be directly mixed with aggregates and asphalt binder using this method. The tire rubber was reported to improve the low-temperature performance, rutting resistance, fatigue life, and noise level of ultra-thin asphalt overlay [11]. However, tire rubber is evidently different from other components in asphalt mixtures concerning material stiffness. The high content of tire rubber still has the potential to impacts the strength of asphalt mixtures. Thus, there is a demand to fully investigate the internal-structure and stress distribution of asphalt mixtures with high content of tire rubber.

The discrete element method (DEM) was developed to simulate the mechanical behavior of granular material [12]. It has become a practical approach to investigate the asphalt mixtures [13, 14]. Many works had been carried out to develop asphalt mixture DEM models [15, 16]. The interlock effect between aggregates is recognized as an essential factor that determines the strength, rutting resistance, and fatigue resistance of asphalt mixtures [17–19]. Images taken from sliced specimens and X-ray tomography were used to capture aggregate distribution [20, 21]. However,

obtaining the specimen images is costly work and heavily dependent on laboratory specimens. Thus, researchers used simple irregular shapes [22, 23] or random generated particles [15, 24] as more economical replacements. The disadvantage of this method is evident that the simulation accuracy is impaired without realistic aggregate morphology.

This study aims to propose a new generation procedure for the DEM models, which is free from specimen images and meanwhile using realistic coarse morphologies. In addition, based on the DEM models, this study aims to investigate the impacts of high content of tire rubber on the strength, internal-structure, and force distribution of asphalt mixtures.

2 Materials and Laboratory Tests

2.1 Materials

The PG 58-28 asphalt binder was selected as the base binder. The reacted rubber (as shown in Fig.1) contains 22% asphalt binder, 16% fillers, and 62% tire rubber by mass. Different from the conventional dry process, the rubber has reacted with asphalt binder and partially swelled. The added fillers, majorly contain hydrated lime and silica, were used to enhance the moisture susceptibility. The specific gravity of the reacted rubber is 1.031. The specific gravity of rubber particles after swelling is about 0.72. The grain size of reacted rubber particles ranges from 0.4 to 0.6 mm.

As Chen et al. suggested in a previous study [11], a gap-graded gradation was selected, as given in Table. 1. Six groups (Control, GTR26, GTR34, GTR37, GTR41,

Fig. 1 Reacted rubber particles



Table 1 Aggregate gradation for tire rubber asphalt mixture

Sieve size (mm)	Percent passing
12.5	100.0
9.5	99.6
4.75	57.5
2.36	26.7
1.18	11.0
0.6	5.7
0.3	3.3
0.15	2.3
0.075	1.8

and GTR45) of tire rubber contents were designed and named based on the tire rubber contents by mass of the mixture (0, 2.6, 3.4, 3.7, 4.1, and 4.5%). The detailed material proposition is listed in Table 2. It is worth noting that the density of rubber particles has a pronounced decrease after swelling. Thus, the rubber particles occupied a large percentage of volume in the asphalt mixture even with a small amount of mass content, as given in Table 2.

Table 2 Material proposition of tire rubber, binder, aggregates, and air void in the tire rubber asphalt mixture test groups

		Control	GTR26	GTR34	GTR37	GTR41	GTR45
Percentage by Mass (%)	Tire rubber	0.00	4.10	5.50	6.00	6.60	7.20
	Virgin binder	6.00	6.00	6.00	6.00	4.00	5.00
	Virgin aggregates	94.00	89.90	88.50	88.00	89.40	87.80
	Tire rubber	0.00	2.55	3.41	3.72	4.09	4.46
	Total binder	6.00	6.90	7.21	7.32	5.45	6.58
	Total aggregates	94.00	90.56	89.38	88.96	90.46	88.95
Percentage by Volume ^{*1} (%)	Void ^{*2}	3.40	3.20	3.40	3.90	5.60	4.40
	Tire rubber	0.00	7.83	10.23	11.01	12.10	13.05
	Total binder	13.89	14.86	15.12	15.14	11.27	13.46
	Total aggregates	82.71	74.11	71.25	69.95	71.04	69.09

*1 The volume is calculated based on material specific gravity: Tire rubber (after swelling) 0.72; binder 1.03; coarse aggregates 2.65; fine aggregates 2.71

*2 The percentage air void is measured after the specimens being compacted in the laboratory.

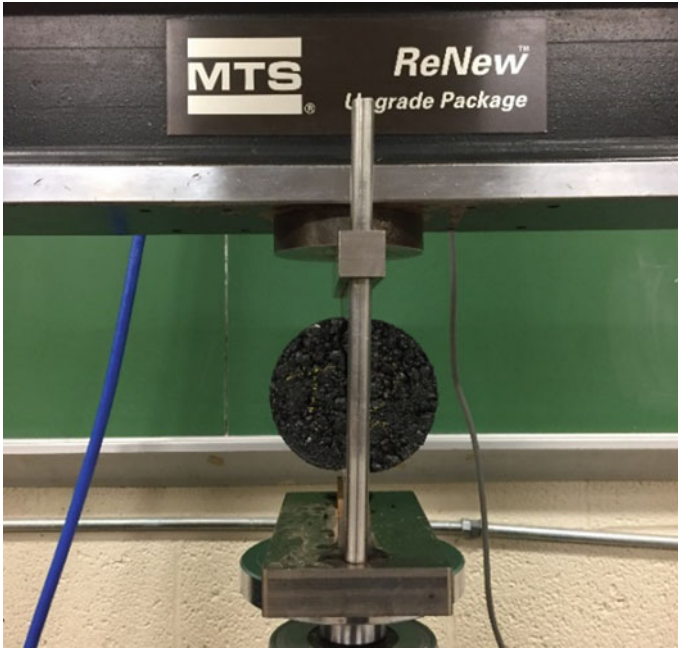


Fig. 2 Indirect tensile strength (ITS) test of tire rubber asphalt mixture

2.2 Indirect Tensile Test

The aggregates were heated for 2 h at 180 °C before being mixed with the reacted rubber at ambient temperature in a buck mixer for 1 min. Then, the asphalt binder, which was heated for 2 h at 180 °C, was added to the mixer and mixed for no less than 1 min until the aggregates were fully covered. The mixed loose mixtures were then placed in the oven for another hour at 180 °C. After heating, the mixtures were compacted via a gyratory compactor for 100 gyration times to obtain a percentage air void of 4.0%. Three samples were tested for each mixture design through an MTS machine, as shown in Fig. 2.

3 DEM Simulations

3.1 Modeling Procedures

The element arrangement of the DEM models has pronounced impacts on the fabric of heterogeneous material. The cubic arrangement, hexagonal arrangement, and random arrangement are the three major element arrangements used in the modeling

of asphalt mixture. In this study, the hexagonal arrangement with the equal-diameter ball was used to model the asphalt mixture specimen. Compared with the cubic ball array arrangement, which was commonly used in previous studies [15, 25, 26], the hexagon array arrangement model can simulate Poisson's effects [27]. The random arrangement has advantages in simulating the randomness in particle sizes, force distribution, and bond-break [28, 29]. However, the random arrangement is sensitive to the packing states, contact coordinate number, and particle gradation. Delicate calibration in respect of material modulus, strength, and boundary conditions is needed when applied to a specific model. The hexagonal arrangement, with all ball elements' position, was strictly controlled and can be applied to more general cases. The modeling procedures are presented as follows:

(1) **Generation of Non-overlap Clumps**

The geometries of clumps were obtained from scanning aggregate with different grain sizes via a 3D scanner. The generation method and grain size determination method of clumps were described in previous studies [16, 30]. The grain sizes of clumps were calculated based on mixture design. All clumps were generated in a 100 mm × 63 mm cylinder container. In this step, each clump was generated with 70% of its designed grain size for the sake of a successful generation. The coarse aggregates of grain size G2 (9.5–12.5 mm), G3 (4.75–12.5 mm), and G4 (2.36–4.75 mm) were generated in turn, as shown in Fig. 3 (1).

(2) **Grain Size Expansion of Clumps**

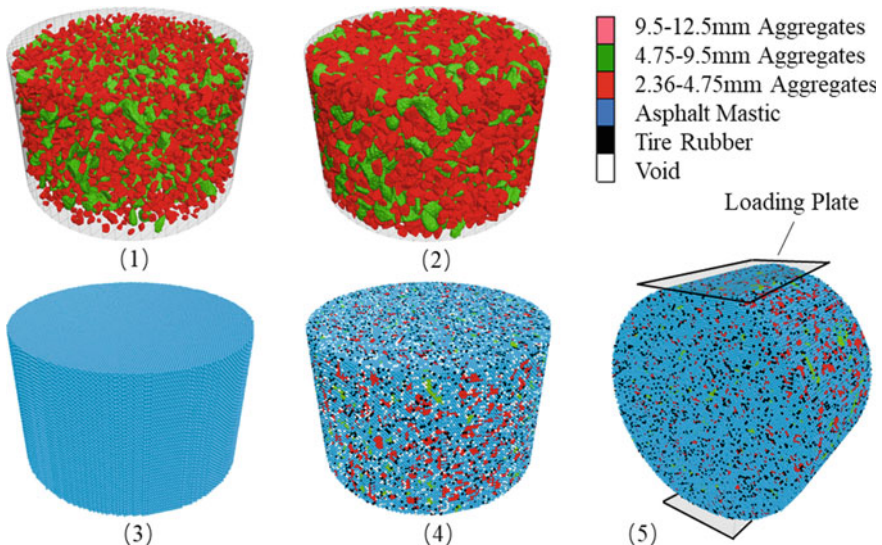


Fig. 3 Modeling procedures of the tire rubber asphalt mixtures: (1) generation of non-overlap clumps; (2) clumps volume expansion; (3) generation of HCP balls; (4) grouping HCP balls based on clump geometry; (5) IDT loading phase

The grain sizes of clumps were expanded until they reach their design values, as shown in Fig. 3 (2). The expansion process contained several iterative steps to avoid considerable overlap occurrences in one single expansion. In the presented case, the grain sizes of clumps were expanded ten times. The expansion ratio of each step was determined as $(1/0.7)^{1/10} \approx 1.03631121$. Between two expansion steps, the model was set to solve the state until the maximum overlap ratio between clumps is less than 0.1%. One can directly find out the overlap ratio by looping the entire clump set. However, this may add an extra computational burden to the host computer. Alternatively, one can estimate the maximum overlap ratio by monitoring the maximum contact force. To limit the movement of clumps and to increase efficiency, a large damp ratio (0.7) was attributed to all clumps.

(3) **Generation of Hexagonal Close-packed (HCP) Balls**

Two kinds of lattices achieve the highest density for equal-diameter ball arrangement. They are called face-centered cubic (FCC) and hexagonal close-packed (HCP). In this study, the hexagonal arrangement was selected. The balls were generated in a cubic space for the sake of ball numbering convenience. Then, the balls outside the cylinder container range were deleted, as shown in Fig. 3 (3).

(4) **Grouping HCP Balls Based on Clump Geometry**

Depending on whether the center position of an HCP ball is within a clump, they were grouped into coarse aggregates or asphalt mastic. In addition, the number of HCP balls that represent rubber particles and voids was calculated according to the mixture design. These two groups of HCP balls were then randomly selected within the mastic. The final grouping results are shown in Fig. 3 (4).

(5) **Installation of Contact Properties**

There are ten categories of contacts between particles in the presented DEM model, as given in Table 3. The contact model parameters were calculated based on material macro-properties [25, 31–33] and adjusted by fitting the laboratory results. The contact-bond model was chosen because it has been verified capable of simulating the fracture behavior of asphalt mixtures. Almost all the aggregates and rubber particles would be covered by asphalt; however, bond strength exists between two direct connected aggregates or rubber. In addition, the linear contact model was set as the default models for all the future contacts (after fracture), and the contact properties will be inherited from the mother particles.

(6) **Loading Phase**

The contact force, particle velocity, and mechanical time were set to zero. Two facets were generated as loading plates and attributed a deformation rate of 50 mm/min (ASTM D6931), as shown in Fig. 3 (5) The displacement of the loading plates was recorded during loading. The loading phase was halted after the forces on the loading plates were below 80% of the maximum forces on the loading plates.

Table 3 Contact model assignment table

Contact type	Contact model name	Normal stiffness (N/m)	Shear stiffness (N/m)	Friction coefficient	Normal bond force (N)	Shearing bond force (N)
Inside Aggregate	Linear parallel-bond model	2.36E+07	9.82E+06	1.07	7.23	14.45
Aggregate-Aggregate	Linear contact model	2.36E+07	9.82E+06	1.07	0.00	0.00
Aggregate-Asphalt Mastic	Contact-bond model	1.16E+07	4.91E+06	0.58	3.00	5.70
Aggregate-Rubber	Contact-bond model	8.64E+03	2.98E+03	0.58	2.66	5.06
Aggregate-Loading Plate	Linear contact model	3.62E+07	–	0	0.00	0.00
Asphalt Mastic-Asphalt Mastic	Contact-bond model	7.70E+06	3.28E+06	0.58	3.33	6.33
Asphalt Mastic-Rubber	Contact-bond model	1.73E+04	5.95E+03	0.58	2.66	5.06
Asphalt Mastic-Loading Plate	Linear contact model	2.02E+07	–	0	0.00	0.00
Rubber-Rubber	Contact-bond model	4.32E+03	1.49E+03	0.58	2.66	5.06
Rubber-Loading Plate	Linear contact model	7.85E+07	–	0	0.00	0.00

3.2 Simulation of Tire Rubber Asphalt Mixtures

In addition to the six test groups (tire rubber content 0, 2.6, 3.4, 3.7, 4.1, and 4.5%) in laboratory, three extral test groups (tire rubber content 1, 2, and 3%) were added to enrich the simulation process. Three replicated specimens were generated and tested for each test group through the above simulation procedures.

Due to the elasticity of rubber particles, the material rebound could happen in the laboratory and construction compaction. Therefore, tire rubber asphalt mixtures with a large percentage air void (3, 5, 7, 9, 11, 13, and 15%) were simulated in the DEM models to investigate the influence of insufficient compaction or material rebound.

4 Test Results and Discussion

4.1 Indirect Tensile Strength (ITS)

The ITS of six groups of laboratory specimens and nine groups of DEM specimens are shown in Fig. 4. For the laboratory tests, the control group which did not contain tire rubber received the highest ITS. The specimens' ITS decreased as the tire rubber content reached 2.6 and 3.4%. However, a reverse trend was observed when the tire rubber content was 3.7 and 4.1%. Then, the ITS decreased again at 4.5%. For the DEM simulation, the ITS values decreased as the tire rubber content increased, except for the 4.5% group, which has a small increment. The standard deviation of the laboratory results ranged from 5.1 to 8.9%, which is significantly higher than the range of 0.4–3.9% from simulation results. The simulation well agreed with the laboratory at the control group, 2.6, and 3.7%. Material differences and insufficient compaction may cause the ITS variation of laboratory specimens at 3.4, 4.1, and 4.5%. The ITS variation of these groups was relatively more extensive, and the measured percentage air void was more significant than the design value due to the elasticity of rubber particles. In general, the DEM simulation results were

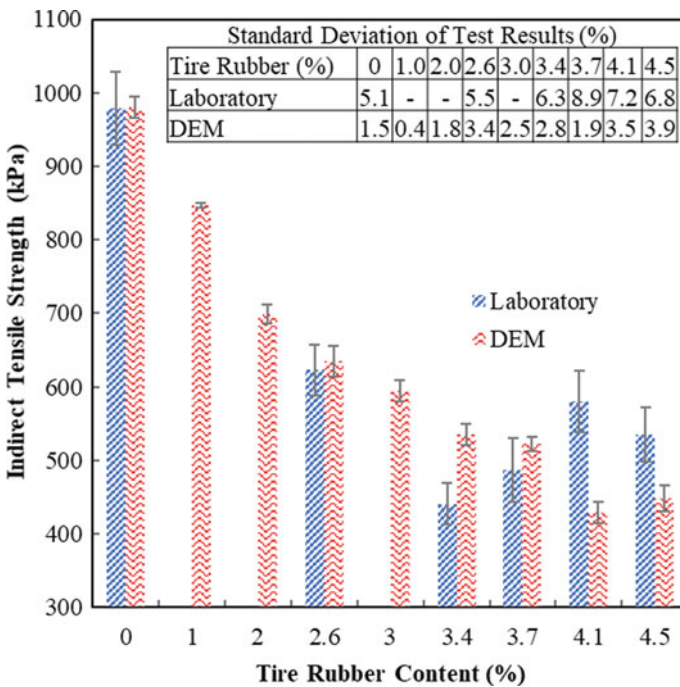


Fig. 4 Indirect tensile strength (ITS) and standard deviation of specimens with different tire rubber contents from laboratory tests and the DEM simulation

more consistent compared with the laboratory results because the material modeling was strictly controlled. The laboratory tests, on the other hand, were affected by many factors, such as material differences, human errors, and compaction efforts. Although differences existed between laboratory and simulation results at high tire rubber contents, they had a fair agreement at low tire rubber contents and shared the same trend that the ITS decreased as the tire rubber content increased.

4.2 Loading Curves of IDT Tests

The reaction force measured on the loading plate from the laboratory and simulation was plotted in Fig. 5. The DEM simulation results agreed with laboratory test results when the tire rubber contents were zero and 2.6%. For the laboratory tests, the two loading curves of the 4.1% group and 4.5% group had a sharper increase before peak value and more rapidly decrease after peak value. This may be caused by the larger percentage air void and more inhomogeneous materials in the specimens with higher tire rubber contents. For the DEM simulation, the measured percentage air void was set to the corresponding models. However, the loading curves kept the same variation tendency, and the peak values are shown to have a declining trend as the tire rubber contents increased.

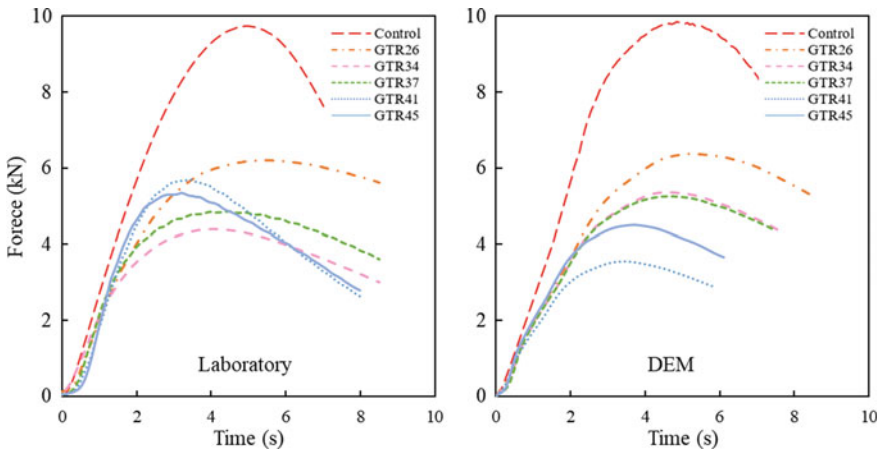
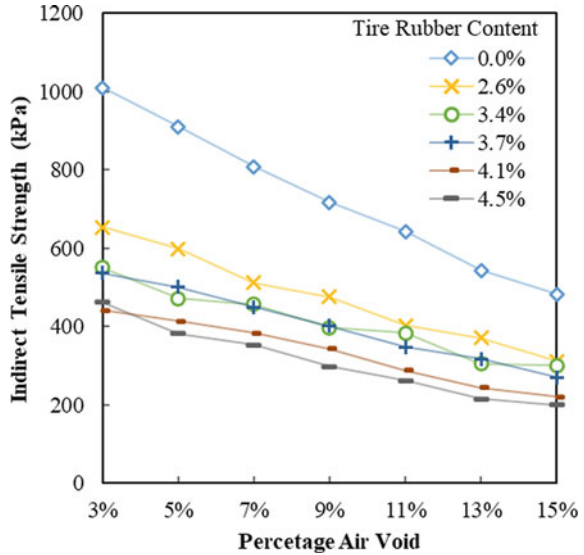


Fig. 5 Loading curves of specimens with different tire rubber contents from laboratory tests and the DEM simulation

Fig. 6 ITS of specimens with different tire rubber contents as a function of percentage air void from the DEM simulation



4.3 Influence of Percentage of Air Void

Previous literature review and test results indicate the percentage of air void has profound impacts on the internal structure of asphalt mixtures. Besides, the high content tire rubber has the potential to decrease the workability of asphalt mixtures during compaction, therefore increase the percentage air void. Percentage air void ranged from 3 to 15% was set to specimens with different tire rubber contents in DEM models. The ITS results are shown in Fig. 6. The ITS values of specimens had linear declining trends as the air void increased for all the tire rubber contents. The ITS values reduced about a half when the percentage air void reached 15%. The results indicate that the percentage air void is critical to the strength of tire rubber asphalt mixtures, due to it is more vulnerable to insufficient compaction.

4.4 Internal Structures of the Tire Rubber Asphalt Mixtures

The gap gradation used in this study was intended to form a skeleton by coarse aggregates and meanwhile accommodate fine aggregates and rubber particles as fillers among the skeleton. Cross sections were taken from the middle part of the specimens, as shown in Fig. 7. For the control group, it can be seen that the coarse aggregates were well connected with each and form a good skeleton. The asphalt mastic was filled in the interspace of the skeleton. As the tire rubber content increased, more rubber particles were positioned between the aggregates. For the GTR26 group, the rubber is filled between the aggregates; however, the coarse aggregates still can

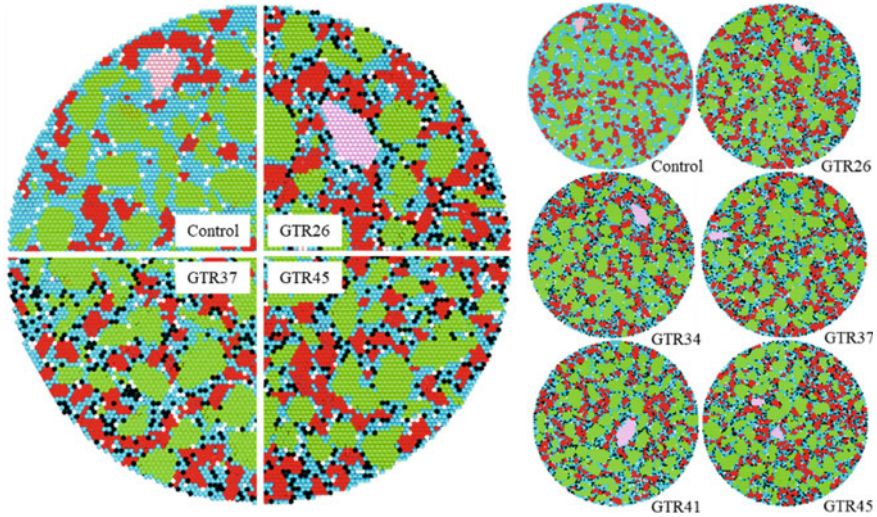


Fig. 7 Cross section slices of specimens with different tire rubber contents

form a clear skeleton structure. For the 4.5% group, a large number of rubber particles surrounded the coarse aggregates. The rubber particles separated the coarse aggregate skeleton. It should be pointed out that the aggregate gradation design for all the specimens was the same. Therefore, the volume of rubber particles was not considered in the mixture design stage. The added rubber particles occupied up to 13.71% volume of the total mixture. For further study, they should be designed to replace part of the fine aggregates, so that the gap gradation mixture can accommodate more rubber particles without affecting its skeleton structures.

4.5 Contact Force Distribution

The contact force distribution when the loading force reached the peak value is shown in Fig. 8. The maximum contact concentrated at the ends of loading plates and emanate to the periphery along the loading direction. For the control group, there is a large amount of force chain in the middle part of the specimen that transfers the external forces. This indicated the coarse aggregate skeleton was strong and effective. As the tire rubber content increases to 3.4%, the force chain in the middle part became weaker. When the tire rubber content was 4.5%, the strong force chains connected the two loading ends disappeared, which indicates the rubber particles separated the coarse aggregate skeleton.

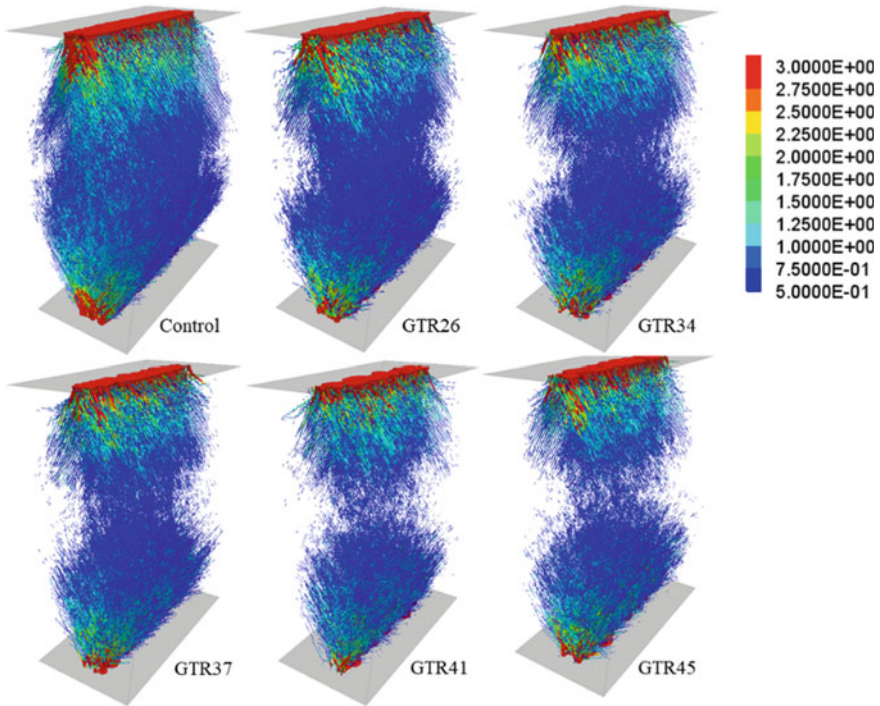


Fig. 8 Contact force distribution in the specimens at peak loading

5 Conclusions

This study investigated the internal structures of the asphalt mixture with high content of reacted rubber through the discrete element simulation and laboratory tests. A new modeling approach was proposed to generate tire rubber asphalt mixture with realistic aggregate shapes that are free of laboratory specimen images. The indirect tensile strength (ITS) values of specimens were tested in laboratory and simulations. The internal structures and stress distribution in DEM models were analyzed. The conclusions are summarized as follows:

- (1) The ITS decreased while the percentage of air void increased as the tire rubber content increased in the laboratory specimens. The ITS and loading curve results from the simulation had the same trends as the laboratory results. The simulation results had a better agreement with low tire rubber contents.
- (2) According to the simulation, the percentage of air void significantly impacts the ITS of asphalt specimens. The ITS decreased linearly as the percentage air void increased. The ITS reduced by half for all the tire rubber content when the percentage air void reached 15%.

- (3) The gap gradation formed a strong coarse aggregate skeleton and accommodated the asphalt mastic and rubber particles as fillers when tire rubber content was lower than 3.4%. The rubber particles interrupted the coarse aggregate skeleton as the tire rubber content overpass 3.4% by mass in the gap gradation mixture design.
- (4) Rubber particles should be used to replace part of the fine aggregates in the mixture design stage. The new mixture design will enhance the gap gradation to accommodate more rubber particles. Thus, a new design method would enable the tire rubber asphalt mixture to consume more waste tire rubber.

References

1. Messenge B Tackling tyre waste. Available from <https://www.ustires.org/system/files/2019%20USTMA%20Scrap%20Tire%20Management%20Summary%20Report.pdf>
2. Heitzman M (1992) Design and construction of asphalt paving materials with crumb rubber modifier. *Transp Res Rec* 1339
3. Heitzman MA (1992) State of the practice-design and construction of asphalt paving materials with crumb rubber modifier
4. Huang B et al (2002) Louisiana experience with crumb rubber-modified hot-mix asphalt pavement. *Transp Res Rec* 1789(1):1–13
5. Cao W (2007) Study on properties of recycled tire rubber modified asphalt mixtures using dry process. *Constr Build Mater* 21(5):1011–1015
6. Hernández-Olivares F et al (2009) Rubber-modified hot-mix asphalt pavement by dry process. *Int J Pavement Eng* 10(4):277–288
7. Arabani M, Tahami SA, Hamed GH (2018) Performance evaluation of dry process crumb rubber-modified asphalt mixtures with nanomaterial. *Road Mater Pavement Des* 19(5):1241–1258
8. Wang H et al (2012) Laboratory evaluation on high temperature viscosity and low temperature stiffness of asphalt binder with high percent scrap tire rubber. *Constr Build Mater* 26(1):583–590
9. Tahami SA et al (2019) The use of high content of fine crumb rubber in asphalt mixes using dry process. *Constr Build Mater* 222:643–653
10. Sousa JB et al (2013) Reacted and activated rubber: elastomeric asphalt extender. *Transp Res Rec* 2371(1):32–40
11. Chen S et al (2019) Use of reacted and activated rubber in ultra-thin hot mixture asphalt overlay for wet-freeze climates. *J Cleaner Prod*
12. Cundall PA, Strack OD (1979) A discrete numerical model for granular assemblies. *Geotechnique* 29(1):47–65
13. You Z, Buttlar WG (2004) Discrete element modeling to predict the modulus of asphalt concrete mixtures. *J Mater Civ Eng* 16(2):140–146
14. Cai W, McDowell GR, Airey GD (2014) Discrete element visco-elastic modelling of a realistic graded asphalt mixture. *Soils Found* 54(1):12–22
15. Liu Y, You Z (2009) Visualization and simulation of asphalt concrete with randomly generated three-dimensional models. *J Comput Civ Eng* 23(6):340–347
16. Liu Y et al (2017) Discrete element modeling of realistic particle shapes in stone-based mixtures through MATLAB-based imaging process. *Constr Build Mater* 143(Supplement C):169–178
17. Dondi G et al (2012) Discrete element modelling of influences of grain shape and angularity on performance of granular mixes for asphalts. *Procedia Soc Behav Sci* 53:399–409
18. Jiang J et al (2017) Effect of the contact structure characteristics on rutting performance in asphalt mixtures using 2D imaging analysis. *Constr Build Mater* 136(Supplement C):426–435

19. Pan T, Tutumluer E, Carpenter SH (2006) Effect of coarse aggregate morphology on permanent deformation behavior of hot mix asphalt. *J Transp Eng* 132(7):580–589
20. Kim H, Buttlar WG (2005) Micromechanical fracture modeling of asphalt mixture using the discrete element method. In: *Advances in pavement engineering*, pp 1–15
21. Peng Y, Sun LJ (2016) Micromechanics-based analysis of the effect of aggregate homogeneity on the uniaxial penetration test of asphalt mixtures. *J Mater Civ Eng* 28(11):04016119
22. Chen J, Pan T, Huang X (2011) Discrete element modeling of asphalt concrete cracking using a user-defined three-dimensional micromechanical approach. *J Wuhan Univ Technol Mater Sci Ed* 26(6):1215–1221
23. Hou S et al (2015) Investigation of micro-mechanical response of asphalt mixtures by a three-dimensional discrete element model. *J Wuhan Univ Technol Mater Sci Ed* 30(2):338–343
24. Ding X et al (2018) Effects by property homogeneity of aggregate skeleton on creep performance of asphalt concrete. *Constr Build Mater* 171:205–213
25. Khattak MJ et al (2015) Imaged-based discrete element modeling of hot mix asphalt mixtures. *Mater Struct* 48(8):2417–2430
26. Zhang D, Ma T, Ding X, Zhang W, Huang X (2018) Effects of internal structure on anisotropic creep behavior of asphalt mixture based on user-defined three-dimensional discrete element method. *J Test Eval* 46(4):20170742
27. Kim H, Wagoner MP, Buttlar WG (2008) Simulation of fracture behavior in asphalt concrete using a heterogeneous cohesive zone discrete element model. *J Mater Civ Eng* 20(8):552–563
28. McDowell GR, Collop AC, Wu JW (2009) A dimensional analysis of scaling viscosity and velocity in DEM of constant strain rate tests on asphalt. *Geomech Geoengin* 4(2):171–174
29. Loreti S, Wu CY (2018) Three-dimensional discrete element modelling of three point bending tests: the effect of surface energy on the tensile strength. *Powder Technol* 337:119–126
30. Liu Y et al (2019) Determining aggregate grain size using discrete-element models of sieve analysis. *19(4):04019014*
31. Liu Y, Dai Q, You Z (2009) Viscoelastic model for discrete element simulation of asphalt mixtures. *J Eng Mech* 135(4):324–333
32. Yang X, Dai Q, You Z, Wang Z (2015) Integrated experimental-numerical approach for estimating asphalt mixture induction healing level through discrete element modeling of a single-edge notched beam test. *J Mater Civ Eng* 27(9):04014259
33. Feng H, Pettinari M, Stang H (2015) Study of normal and shear material properties for viscoelastic model of asphalt mixture by discrete element method. *Constr Build Mater* 98:366–375

Beneficial Use of Dredged Material in Flowable Fill



Pranshoo Solanki, Juan David Lopez, Harshvardhan Jain, and Bhupesh Jain

Abstract US Army Corps of Engineers (USACE) annually dredge 300 million cubic yards nationwide to maintain channels' navigation. Treating this huge amount of dredged material is a major challenge due to the mobilization of potential contaminants causing depreciation in water quality and depletion of valuable land. Rather than treating the dredged material as a waste, investigating alternative ways to recycle and reuse the dredged material is needed. Therefore, the aim of this study was to evaluate the feasibility of utilizing dredged material as a substitute for sand in flowable fill. A total of five mixtures were prepared by using different proportions of dredged material and virgin fine aggregates (sand) in flowable fill. Each mixture was tested for flowability and compressive strength. Both flow consistency and strength results were found within required specification for flowable fill.

Keywords Dredging · Flowable fill · Cement · Recycling

1 Introduction

The depletion of natural sources of aggregates is challenged for all the construction activity, making urgent to find an alternate source of fine and coarse aggregate [1]. The volume of dredged material from water bodies is extremely large because of the activities to maintain the navigation channels or increase storage capacities [2]. A summary of recent studies related to beneficial utilization of dredged material in construction is provided in Table 1. As noticed in Table 1, most of the studies focused on concrete which is one of the most widely used construction material.

P. Solanki (✉)

Construction Management Program, Department of Technology, Illinois State University, Normal, IL 61790, USA

e-mail: psolanki@ilstu.edu

J. D. Lopez

Department of Technology, Illinois State University, Normal, IL 61790, USA

H. Jain · B. Jain

Department of Civil Engineering, Manipal University Jaipur, Jaipur, Rajasthan 303007, India

Table 1 Summary of studies utilizing dredged material in construction

Researcher	Study	Results
Mymrin et al. [3]	Overburden clayey soil (50%), waste from lime production as binder (20%) and dredged material (30%)	Compressive strength of 18.9 MPa after 365 days
Erdogan et al. [4]	Comparison of use of treated and untreated marine dredge material	34.6 MPa compared to 28.9 MPa with 100% of dredged material instead of sand
Wang [5]	Silt from reservoir of South Taiwan	Durability and hardening characteristics of self-consolidated lightweight aggregate concrete made from dredged silt
Zhu [6]	More chloride content of dredged sand instead of use of silica fume in concrete	Reduction in the porosity and ion permeability
Chu et al. [7]	Mix of dredged river material, iron tailing slag and calcium carbide slag with cement in a ratio of 60:40:4:16	Unconfined compressive strength of 2.8 MPa in 7 days
Junakova and Junak [8]	Dredged material from Ruzin replacing 40% cement	20% reduction in 28 days compressive strength and 14% reduction in flexural strength
Lim et al. [9]	Lightweight aggregate prepared with dredged harbor sediment and basic oxygen furnace slag	Less water-soluble chloride and tendency of heavy metal leaching, compressive strength of 23.2 MPa when there is 27% basic oxygen furnace slag
Limeira [1]	Up to 50% Natural sand replaced with dredged marine sand	Compressive strength of 39 MPa after 28 days (10,25% more than control mix), and concrete made from dredged material can be used in marine exposure also up to 30 MPa strength
Dubois et al. [10]	Dredged material from north of France used in base course for pavement	The amount of binder required was comparable with standard mix and also mix passed leaching test requirement
Wang et al. [11]	100% replacement of sand with coral waste sand	Compressive strength reduction by 27% and increasing of chloride diffusion coefficient by 36%, after 28 days
Dang [12]	Material from northern coast of Brittany (France) as a mineral admixture	Addition of 33% dredged material in cement increased its strength by 26% when compared with 33% limestone cement

(continued)

Table 1 (continued)

Researcher	Study	Results
Cheng et al. [13]	Comparison of coral sand concrete with river sand concrete	Coral sand concrete is better in early age strength, sulfate drying-wetting cycle and chloride penetration but river sand concrete had less drying shrinkage, carbonation depths and capillary water absorption
Xiao et al. [14]	Sea sand concrete vs regular concrete	Concrete showed higher early age strength but latter age. The chloride induced corrosion is more in sea sand concrete but very less effect on carbonation
Wang [15]	Micro-coral sand and coral sand in ultra high-performance concrete	Workability increased and reduction in autogenous shrinkage without compromising durability of the concrete. Also, environmental impact is reduced

However, concrete industry is not very excited in using dredged material due to tight concrete design specifications and the presence of contaminants in dredged material. Therefore, the primary objective of this study was to investigate the feasibility of utilizing dredged material as a substitute of natural sand in flowable fill.

A flowable fill is defined by the American Concrete Institute (ACI) [16] as a Controlled Low-Strength Material (CLSM). Flowable fill is self-consolidating and contains cementing material, and it can be used for non-structural application such as backfill. It typically does not require conventional curing, and one could walk on it after 20–35 min. Smith [17] noted several advantages such as readily availability, easy deliverability and reduced equipment cost.

The use of dredged material in flowable fill could reduce the barriers to reusing dredged material more broadly as a sand substitute in concrete mixes. First, flowable fill is non-structural, and the authority to specify mix components generally rests with local governments or contractors. Moreover, the risks from under-performance are small compared to structural or pavement concrete. This will allow local ready-mix plants to gain experience and confidence with dredged material, encouraging its application in other concrete mixes. Second, flowable fill is known for its ability to tolerate contaminated input materials. Third, sand that do not meet requirements for structural or pavement concretes is often acceptable in flowable fill.

2 Methodology and Experimental Design

2.1 Dredged Material and Natural Sand

The dredged material samples were collected in coordination with US Army Corps of Engineers (USACE) from the stockpile near Illinois River close to Glasford, Illinois. It was sitting in two piles with approximate height of forty feet (see Fig. 1). The top of the pile was washed away by rain revealing large quantities of clam shells, but the collection of material was deeper into the pile to make sure not to get washed-out material.

The sand used for this study was from Rowe, Heyworth Pit, and it was naturally collected, not manufactured, because of that we named it “Natural Sand.” The process included dredging the sand out from under water. Some of the fines were removed with US#200 sieve at the source. Most of these fines removed were dirt. Other than this, the sand is kept natural in most part. Figure 2 shows a photographic view of

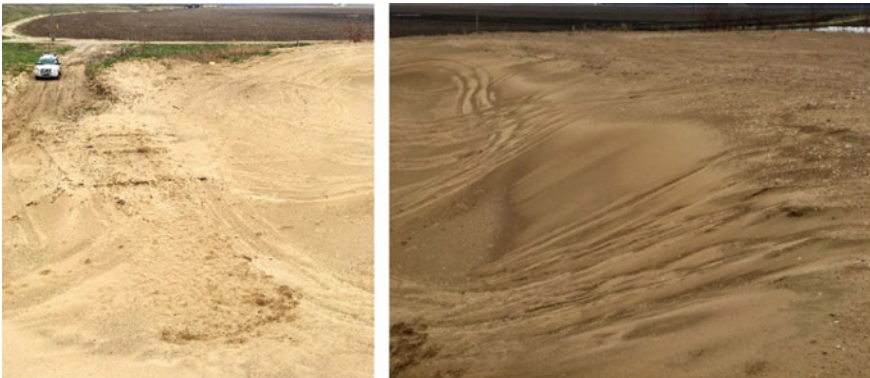
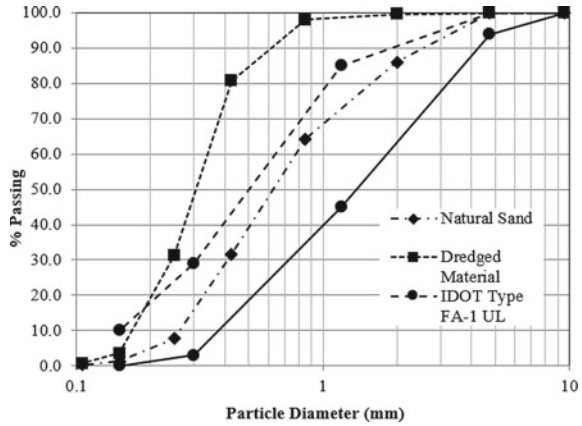


Fig. 1 Dredged material stockpiles



Fig. 2 Left pan shows natural sand, and right pan shows dredged material

Fig. 3 Sieve analysis results



natural sand and dredged material. It is evident from Fig. 2 that natural sand was coarser than dredged material.

Further, sieve analysis was performed on two samples of each material in accordance with ASTM C136 test method. The results were compared to the sieve sizes recommended by the Illinois Department of Transportation (IDOT) [18] for flowable fill fine aggregates, called as FA-1 by IDOT. Sieve analysis test results are presented in Fig. 3. Each data point in Fig. 3 shows an average value of the two tests for each material. It is evident from Fig. 3 that the content of fine particles in the dredged material is more in proportion compared to the natural sand, to the point that gradation is out of the boundaries established by the IDOT for the FA-01 material.

Besides above-mentioned materials, other materials used were Portland cement Type 1, and class C fly ash was collected from Prairie materials, a local ready-mix concrete plant, located in Normal, Illinois.

2.2 Mix Design

A total of five flowable fill mixtures containing different sand, cement, fly ash, dredged material and water were prepared in this study. Table 2 shows the tentative proportions of all flowable fill mixtures that were considered in this study; proportion of each ingredient was selected in accordance with Illinois Department of Transportation [18] specifications for flowable fill Mix#1. The exact amount of water was decided based on the flow consistency of mix in accordance with ACI 229R [16] recommendations; ACI 229R provides a procedure for designing flowable fill mixtures. One control mixture was prepared by mixing only Portland cement, fly ash, fine aggregates (i.e., sand) and water (no dredged material). All remaining four mixtures (three samples in each group) were prepared by substituting 25, 50, 75 and 100% of sand with dredged material by weight.

Table 2 Design of flowable fill mix proportions.

2.3 Specimen Preparation and Testing

All five mixtures were prepared by adding required amount of dry ingredients in a concrete mixer and mixing for 15 min. After preparation of mixtures, the flow consistency of mixtures was evaluated by conducting flow test in accordance with ASTM D 6103 [19] test method. To evaluate the strength of flowable fill mixes, the unconfined compressive strength (UCS) was measured after 28 days of curing.

The strength test was performed using cylindrical specimens of 101.6 mm by 203.2 mm size (4 in. × 8 in.) which were cast and cured following ASTM D 4832 [20] test method. Due to the low strength of flowable fill specimens, the plastic cylindrical molds used for specimen casting were specially fabricated in the laboratory for easy demolding (Fig. 4a). The plastic pipe molds were pre-cut on two opposite sides and then restored to their original shape by sealing them with steel strap and screws as shown in Fig. 4b. Three molds were tied to a plywood board for easy handling and transportation after casting specimens out of each mix (Fig. 4b). The wet flowable fill mix was cast into the molds and finished using a tamping rod. After finishing, the specimens were covered with plastic wrap and cured for four days. On the fourth day, split molds were demolded after removing steel straps, and specimens were placed in plastic storage box at a temperature of approximately 21 °C (69.8 °F) and high humidity environment (>95% relative humidity) until the time of testing (Fig. 4c). Then, specimens were tested for compressive strength after 28 days of curing in accordance with ASTM D 4832 test method.

3 Results and Discussion

Results of all five mixtures tested in this study, including the control mix, are presented in Table 3. Further results are discussed in subsequent sections.

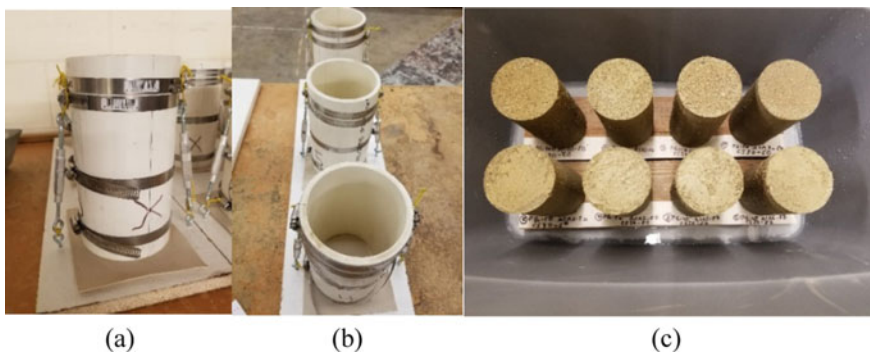


Fig. 4 **a** Specimen mold; **b** three molds tied to a plywood board; and **c** specimens in a box under curing

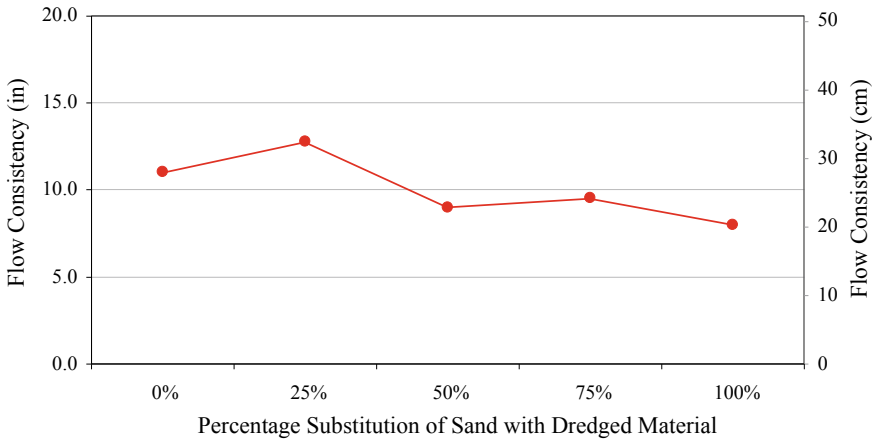


Fig. 5 Variation of flow consistency with percentage substitution of sand with dredged material

Table 3 Summary of results of dredged material specimens

3.1 Flow Consistency

Variation of flow consistency with percent dredged material substitution is graphically presented in Fig. 5. In general, introducing more dredged material shows a decrease in the flow consistency values. Mixtures prepared by using 100% dredged material substitution showed decrease in flow consistency by 3 in. (from 11 in. to 8 in.). This could be attributed to finer size of the dredged material particles. Finer particles provided larger surface area which might have resulted in lower amount of water for lubrication/flow between particles. It is also important to note that all mixtures tested in this study showed a flow consistency of greater than 7 in. (17.8 cm), as required by IDOT [18] specification for flowable fills.

3.2 Compressive Strength

Compressive strength test results are graphically presented in Fig. 6. It is evident from Fig. 6 that compressive strength increases with increase in the percentage substitution of sand with dredged material up to 50% beyond which strength decreased. For example, substitution of sand with 50% dredged material is provided an increase in strength by approximately 83%.

To further understand this behavior, variation of density and moisture content with percentage substitution of sand with dredged material was plotted in Fig. 7. A mixture

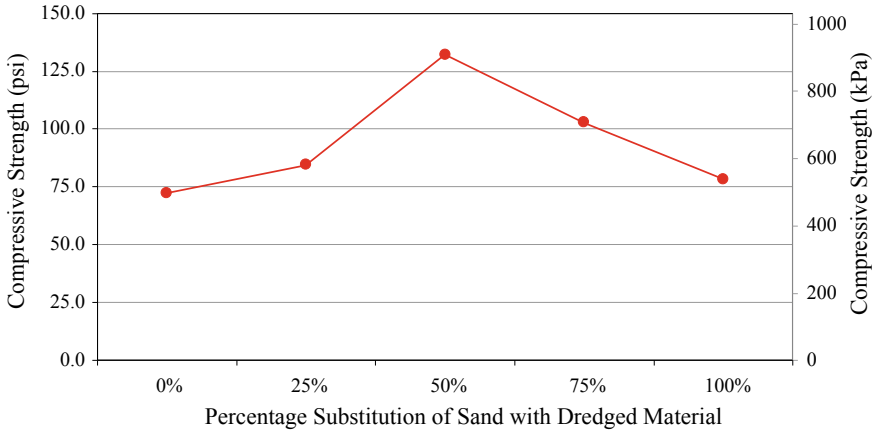


Fig. 6 Variation of compressive strength with percentage substitution of sand with dredged material

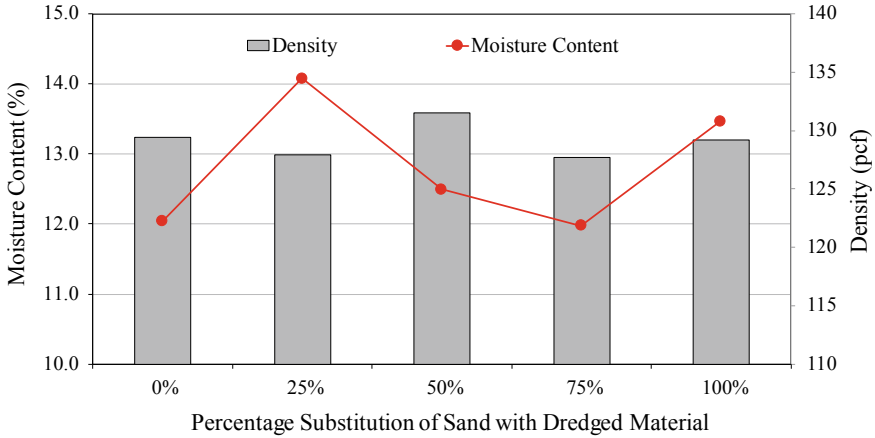


Fig. 7 Variation of moisture content and density with percentage substitution of sand with dredged material

containing 50% sand and 50% dredged material provided densest structure which resulted in highest strength among all the mixtures tested in this study. Further, all specimens tested in this study provided strength within IDOT specifications; IDOT requires a strength value between 30 and 150 psi for flowable fill mixtures [18].

4 Conclusions

Based on the results presented in this study, following conclusions can be drawn:

- (1) Based on flow consistency results, dredged material has the potential to be a suitable substitute of natural sand in flowable fill. Flow consistency was found to decrease with increase in the amount of dredged material in flowable fill. However, all specimens showed flow consistency values of more than 7 in. which is recommended by IDOT.
- (2) Compressive strength was found to improve with amount of dredged material in flowable fill up to 50% beyond which strength starts decreasing. All mixtures tested in this showed strength within IDOT specifications. However, additional study is needed to investigate the influence of source or gradation of dredged material on flow consistency and compressive strength of flowable fill.

Acknowledgements This work was supported by Illinois-Indiana Sea Grant. The material collection assistance provided by Prairie Materials and US Army Corps of Engineers (USACE) is gratefully acknowledged. Also, authors would like to acknowledge graduate students, namely Mobi Singh and Xi Hu for collecting and preparing dredged material specimens.

References

1. Limeira J, Etxeberria M, Agulló L, Molina D (2011) Mechanical and durability properties of concrete made with dredged marine sand. *Constr Build Mater* 25:4165–4174. <https://doi.org/10.1016/j.conbuildmat.2011.04.053>
2. Zhang R, Dong C, Lu Z, Pu H (2019) Strength characteristics of hydraulically dredged mud slurry treated by flocculation-solidification combined method. *Constr Build Mater* 228:116742. <https://doi.org/10.1016/j.conbuildmat.2019.116742>
3. Mymrin V, Pan RCY, Alekseev K, Avanci MA, Stella JC, Scremim CB, Schiavini DN, Pinto LS, Berton R, Weber SL (2019) Overburden soil and marine dredging sludge utilization for production of new composites as highly efficient environmental management. *J Environ Manag* 236:206–213. <https://doi.org/10.1016/j.jenvman.2019.01.065>
4. Ozer-Erdogan P, Basar HM, Erden I, Tolun L (2016) Beneficial use of marine dredged materials as a fine aggregate in ready-mixed concrete: Turkey example. *Constr Build Mater* 124:690–704. <https://doi.org/10.1016/j.conbuildmat.2016.07.144>
5. Wang HY (2009) Durability of self-consolidating lightweight aggregate concrete using dredged silt. *Constr Build Mater* 23:2332–2337. <https://doi.org/10.1016/j.conbuildmat.2008.11.006>
6. Zhu N, Jin F, Kong X, Xu Y, Zhou J, Wang B, Wu H (2018) Interface and anti-corrosion properties of sea-sand concrete with fumed silica. *Constr Build Mater* 188:1085–1091. [https://doi.org/10.1016/j.conbuildmat.08.040.\(2018\)](https://doi.org/10.1016/j.conbuildmat.08.040.(2018))
7. Chu C, Deng Y, Zhou A, Feng Q, Ye H, Zha F (2018) Backfilling performance of mixtures of dredged river sediment and iron tailing slag stabilized by calcium carbide slag in mine goaf. *Constr Build Mater* 189:849–856. <https://doi.org/10.1016/j.conbuildmat.2018.09.049>
8. Junakova N, Junak J (2017) Recycling of reservoir sediment material as a binder in concrete. *Procedia Eng* 180:1292–1297. <https://doi.org/10.1016/j.proeng.2017.04.291>
9. Lim YC, Lin SK, Ju YR, Wu CH, Lin YL, Chen CW, Di Dong C (2019) Reutilization of dredged harbor sediment and steel slag by sintering as lightweight aggregate. *Process Saf Environ Prot* 287–296. <https://doi.org/10.1016/j.psep.2019.04.020>
10. Dubois V, Abriak NE, Zentar R, Ballivy G (2009) The use of marine sediments as a pavement base material. *Waste Manag* 29:774–782. <https://doi.org/10.1016/j.wasman.2008.05.004>

11. Wang Y, Shui Z, Gao X, Huang Y, Yu R, Li X, Yang R (2019) Utilizing coral waste and metakaolin to produce eco-friendly marine mortar: hydration, mechanical properties and durability. *J Clean Prod* 219:763–774. <https://doi.org/10.1016/j.jclepro.2019.02.147>
12. Dang TA, Kamali-Bernard S, Prince WA (2013) Design of new blended cement based on marine dredged sediment. *Constr Build Mater* 41:602–611. <https://doi.org/10.1016/j.conbuildmat.2012.11.088>
13. Cheng S, Shui Z, Sun T, Yu R, Zhang G (2018) Durability and microstructure of coral sand concrete incorporating supplementary cementitious materials. *Constr Build Mater* 171:44–53. <https://doi.org/10.1016/j.conbuildmat.2018.03.082>
14. Xiao J, Qiang C, Nanni A, Zhang K (2017) Use of sea-sand and seawater in concrete construction: current status and future opportunities. *Constr Build Mater* 155:1101–1111. <https://doi.org/10.1016/j.conbuildmat.2017.08.130>
15. Wang X, Yu R, Shui Z, Song Q, Zhang Z (2017) Mix design and characteristics evaluation of an eco-friendly ultra-high performance concrete incorporating recycled coral based materials. *J Clean Prod* 165:70–80. <https://doi.org/10.1016/j.jclepro.2017.07.096>
16. ACI 229R (2013) Report on controlled low-strength materials. American Concrete Institute, Farmington Hills, MI
17. Smith A (1991) Controlled low-strength material, concrete construction
18. IDOT (2016) Standard specification for road and bridge construction. Illinois Department of Transportation, Springfield, Illinois
19. ASTM D 6103/D6103M-17 (2017) Standard test method for flow consistency of controlled low strength material (CLSM). ASTM International, West Conshohocken, PA. www.astm.org
20. ASTM D4832-16e1 (2016) Standard test method for preparation and testing of controlled low strength material (CLSM) test cylinders. ASTM International, West Conshohocken, PA. www.astm.org

Effective Subgrade Remediation by Materials Improved with Blast Furnace Type B Cement



Atsuko Sato, Osamu Hatakeyama, and Naoyuki Kuji

Abstract In cold regions, the road surface sometimes deforms from frost heaving of the subgrade. For this reason, road construction in the cold regions of Japan is done by using non-frost heaving materials for the layers within the frost penetration depth of the subgrade. In Japan, materials generated at road construction sites are reused in order to make effective use of resources. Measures are taken when the materials generated from construction are unsuitable for use as subgrade materials. One method for improving such soil is by adding a solidifier. To use solidified soil, which is a material improved by the addition of a solidifying agent, for the subgrade in cold regions, such soil must have sufficient strength and must not be susceptible to freezing. Quality control of subgrades made with solidified soil is expensive and time consuming. Therefore, a simple method has been called for. To develop such a method, we experimentally solidified some poor-quality soil specimens and investigated their strength and frost heave susceptibility by several types of tests. The tests revealed that a strength much higher than that required for ordinary subgrade is needed to use solidified soils as subgrade materials. It was also found that a method involving impact acceleration can be applied for quality control checks of a subgrade made with solidified soil.

Keywords Effective use · Blast furnace type B cement · Subgrade

1 Introduction

Hokkaido is in northern Japan and is a cold region; therefore, the road surface deformation shown in Fig. 1 may occur when the subgrade undergoes frost heaving. To prevent damage caused by frost heaving, the Hokkaido Regional Development Bureau of the Ministry of Land, Infrastructure, Transport and Tourism (MLIT) specifies that subgrade layers within the frost penetration depth (Fig. 2) be constructed with non-frost heave susceptible materials [1]. In Japan, resources are effectively used in

A. Sato (✉) · O. Hatakeyama · N. Kuji
Civil Engineering Research Institute for Cold Region, Hiragishi 1-3-1-34, Toyohira-ku, Sapporo, Japan
e-mail: atsuko@ceri.go.jp



Fig. 1 Deformation due to frost heave of pavement surface

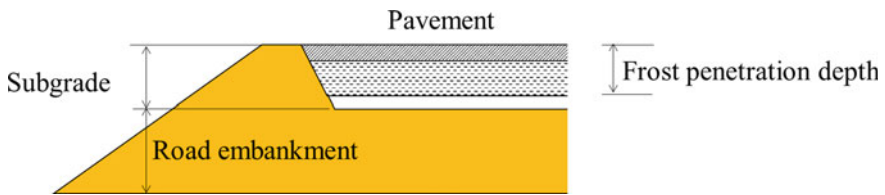


Fig. 2 Cross section of road in cold region

civil engineering works, and surplus soil generated at road construction sites is used as much as possible. If the soil generated in construction is favorable in quality, it is used unmodified for construction. However, in the case of poor-quality soil that is not able to be used without modification, measures are taken. The Hokkaido Regional Development Bureau has been implementing countermeasures, in accordance with the Manual of Measures against Unsuitable Soil in Hokkaido [2] (hereinafter: Unsuitable Soil Manual), when poor soil is generated at construction sites and then is used for road embankments. Of these measures, a method in which soil is solidified by the addition of a solidifier was found to achieve stable improvement and is used for road embankments that do not freeze.

If solidified soil, which is often used for road embankments that do not freeze, is able to be used in the frost heave susceptible layers of the subgrade, the amount of poor-quality soil to be discarded will be reduced, and the costs for disposing of such soil will be eliminated. The land required for such disposal could be utilized for other purposes. Furthermore, if road subgrade construction is able to be done in the same way as that for the road embankments and the same quality control method as that for the embankment is able to be applied to the subgrade, the total construction cost would be considerably reduced. Few studies have examined the frost heave characteristics of solidified soil with the purpose of using such soil as

a material for the subgrade in cold regions [3, 4]. To effectively use material that has been improved by the addition of solidifiers (solidified soil) as material for the subgrade, we examined and clarified the relationship between the strength of the solidified soil and the frost heave characteristics. We also examined the applicability of a quality control technique that relies on impact acceleration [5], which has been used for quality control on embankments constructed with solidified soil, to subgrade constructed with solidified soil. The impact acceleration is measured using a steel weight with a built-in accelerometer, which was dropped in a free-fall condition. This method of measurement is applied at construction sites as a quality control technique by the Hokkaido Regional Development Bureau of the Ministry of Land, Infrastructure, Transport and Tourism.

2 Testing Methods

Three types of soil generated at road construction sites in Hokkaido (soil samples) were tested. The basic physical properties of these three soil samples are shown in Table 1.

The cone index of each soil sample is 300 kN/m² or less. They are soft materials with insufficient strength to support a traveling swamp bulldozer [6]. Each soil sample had a freezing rate of 0.3 mm/h or greater and was a material with high frost heave susceptibility [7]. Both the strength and frost heave susceptibility of these soil samples are those for materials that are unusable for the subgrade without modification. Portland blast furnace slag cement B (hereinafter referred to as solidified) was mixed with these soil samples for wet weight at the mix ratios shown in Table 2, and the design CBR test, impact acceleration test, CBR test after freeze-and-thaw [8],

Table 1 Basic physical properties of the soil samples

Sample No.	1	2	3
Collection site	Kushiro	Engaru	Kikonai
Soil particle density ρ_s (g/cm ³)	2.550	2.638	2.682
Natural water content w_n (%)	60.1	24.5	64.0
Grain size characteristics	2 mm (%)	0.6	43.7
	75–2 mm (%)	41.8	27.6
	–75 m (%)	57.6	28.7
Liquid limit w_L (%)	70.5	43.6	89.9
Plastic limit w_P (%)	45.0	24.7	58.9
AASHTO Soil Classification System	Clayey soils	Silty or clayey gravel and sand	Clayey soils
Cone index q_c (kN/m ²)	Less than 300	170	127
Frost heave rate (mm/h)	0.783	0.803	0.557

Table 2 Formulation (for wet sample)

Sample No	Amount of solidifier (%)
1	6.0, 15.4, 21.4, 27.4
2	2.9, 3.7, 4.4
3	4.3, 5.5, 6.7

unconfined compression test, and frost heave test were conducted. Specimens for the design CBR test on the solidified material for the subgrade are generally prepared by compacting the soft soil using a 4.5 kg rammer and compacting the soil in three layers at 67 blows per layer. However, the soil samples used in the current study were too soft to be prepared in this way. The strength of the soil samples immediately after the addition of solidifier was very low, and compaction using the 4.5 kg rammer resulted in the overcompaction of the samples. We were unable to prepare test specimens in the ordinary preparation procedure. Therefore, we prepared specimens by using a 2.5 kg rammer to reduce the compaction energy. The specimens for the impact acceleration test and CBR test after freeze–thaw were prepared by using the same procedure. The specimens for the unconfined compression test and the frost heave test were prepared by static compaction so as to give the specimens the same density as those for the design CBR test.

The design CBR test is generally conducted after 3-day atmospheric curing and 4-day water curing. We tested specimens prepared under various conditions, including those without any water curing and those with 28-day atmospheric curing.

The CBR test after freeze–thaw was performed only for sample No. 1, from Kushiro. The test items and the specimen preparation conditions are shown in Table 3. Each specimen was cured in a room at a constant 20 °C and at a constant humidity, and each test was conducted after curing for the period shown in Table 4.

Example 3–4: after 3-day atmospheric curing and 4-day water curing.

Table 3 Test items and specimen preparation conditions

Test items	Applicable criteria	Specimen preparation method	Specimen size
Design CBR test	JIS A 1211	15 cm mold, 2.5 kg rammer 3 layers 55 blows compaction	CBR mold Diameter 10 cm
Impact acceleration test	Hokkaido Development Bureau		
CBR test after freezing and thawing	NEXCO112		
Unconfined compression test	JIS A 1216	Practice for making and curing statically compacted stabilized soil specimens (JGS 0812)	Diameter 5 cm Height 10 cm
Frost heaving test	JGS 0172		Diameter 10 cm Height 5 cm

Table 4 Curing period for each test

Sample No.	1	2	3
Design CBR test Impact acceleration test	3-4, 7-0	3-4, 7-0, 24-4, 28-0	3-4, 7-0
CBR test after freezing and thawing	3-4		
Unconfined compression test	3-4, 7-0, 28-0, 220-0	3-4, 7-0, 27-1, 24-4, 28-0	3-4, 7-0
Frost heaving test	3-4, 7-0, 28-0, 220-0	3-4, 27-1, 28-0 27-1, 28-0	3-4

3 Test Results

3.1 The Relationship Between the Amount of Solidifier and the CBR, Unconfined Compressive Strength, and Impact Acceleration

The relationship between the amount of solidifier and the CBR, unconfined compressive strength, and impact acceleration for each specimen with the 3-day atmospheric and 4-day water curing are shown in Figs. 3, 4, and 5. In the range of amounts of solidifier mixed in the soil tested, the CBR, unconfined compressive strength, and impact acceleration increased with increase in the amount of solidifier and had a proportional relationship with the amount of solidifier for each sample.

The relationship between the CBR, which is used as an indication of the target value for subgrade, and the unconfined compressive strength was obtained. As

Fig. 3 Relationship between the amount of solidifier and the CBR

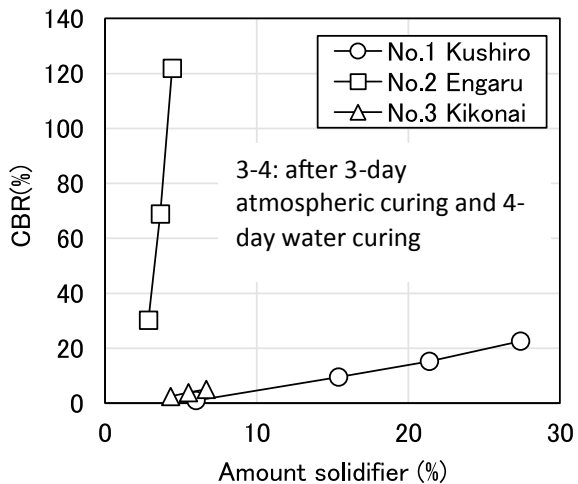


Fig. 4 Relationship between the amount of solidifier and the unconfined compressive strength

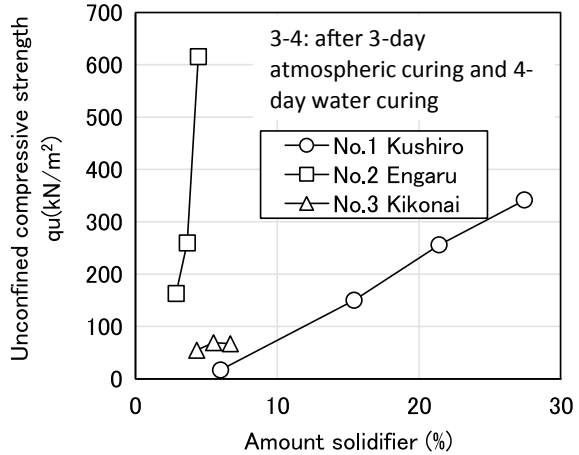
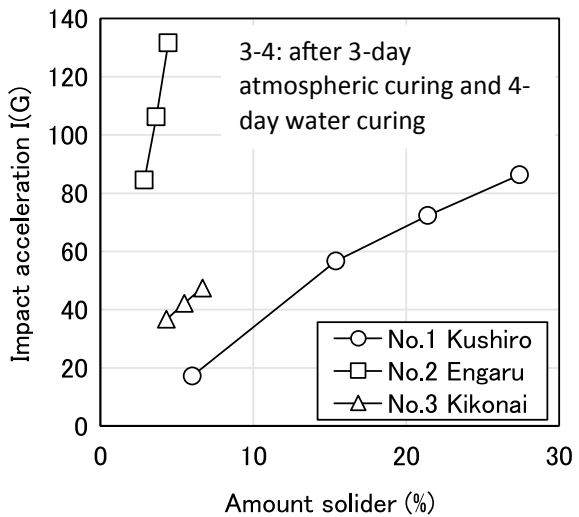


Fig. 5 Relationship between the amount of solidifier and the impact acceleration



an example of the relationship between the CBR and the unconfined compressive strength, the results for the Kushiro sample are shown in Fig. 6. As the unconfined compressive strength increased, the CBR also increased. For the samples cured in the same method, the unconfined compressive strength and the CBR showed a highly correlated, proportional relationship. However, the relationship between the unconfined compressive strength and the CBR tended to differ between the samples cured under different water immersion conditions. A similar trend was seen in the sample from Engaru and that from Kikonai.

An example of the relationship between impact acceleration and CBR for the Kushiro sample is shown in Fig. 7. The relationship between impact acceleration

Fig. 6 Relationship between the unconfined compressive strength and the CBR

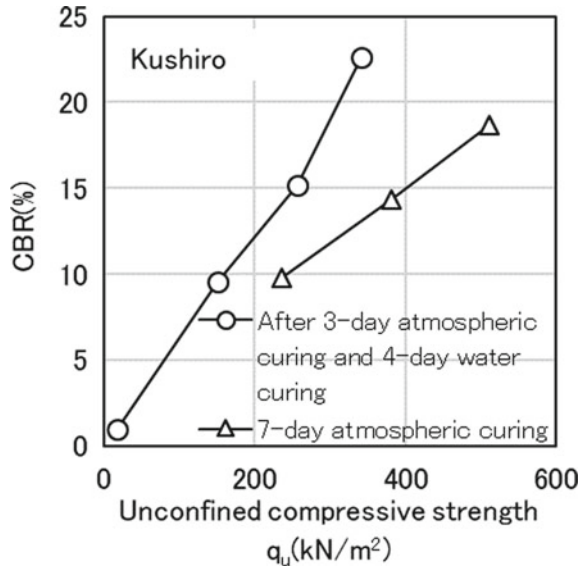
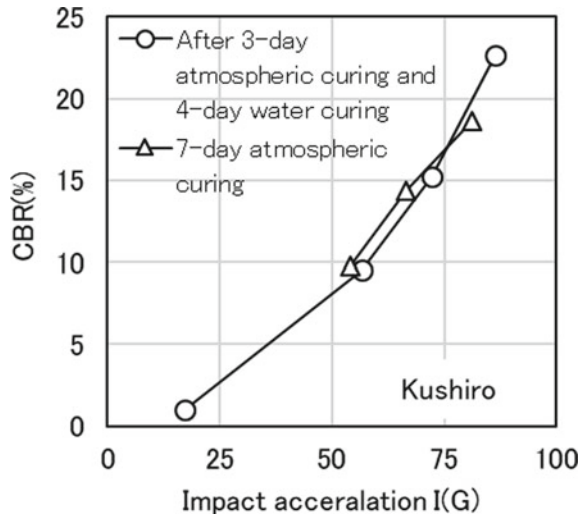


Fig. 7 Relationship between the impact acceleration and CBR



and CBR was the same regardless of the presence or absence of water immersion. The same tendency was observed in Kikonai and Engaru.

Unconfined compressive strength is plotted against CBR in Fig. 8 for all the specimens immersed in water for 4 days after atmospheric curing. Although there is a correlation between the unconfined compressive strength and the CBR for each specimen, it is difficult to find a similar correlation among all specimens. Figure 9 shows the relationship between impact acceleration and CBR for all tests. Impact

Fig. 8 Relationship between the unconfined compressive strength and the CBR (all the specimens)

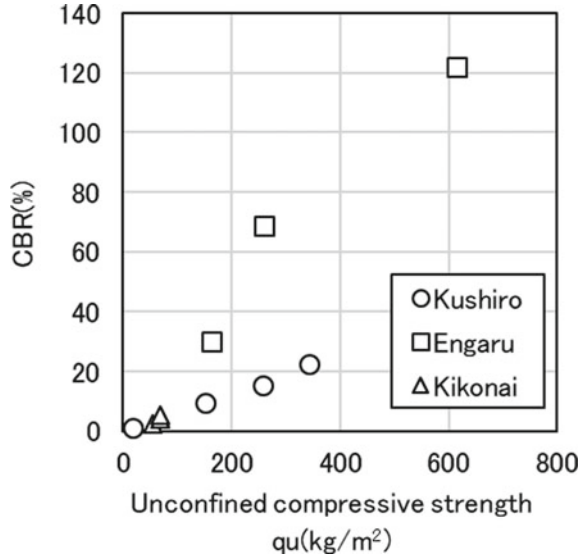
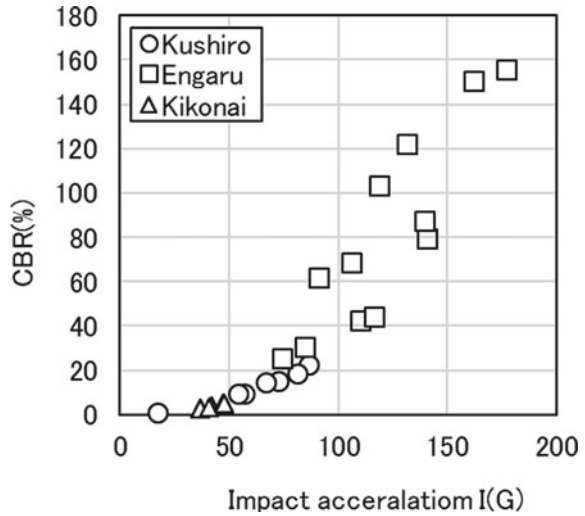


Fig. 9 Relationship between the impact acceleration and CBR (all the specimens)



acceleration and CBR are highly correlated for all specimens. From this, the CBR can be estimated from the impact acceleration. Impact acceleration may be applicable for quality control of the subgrade.

Fig. 10 Effect of the presence or absence of water immersion on each strength (Kushiro)

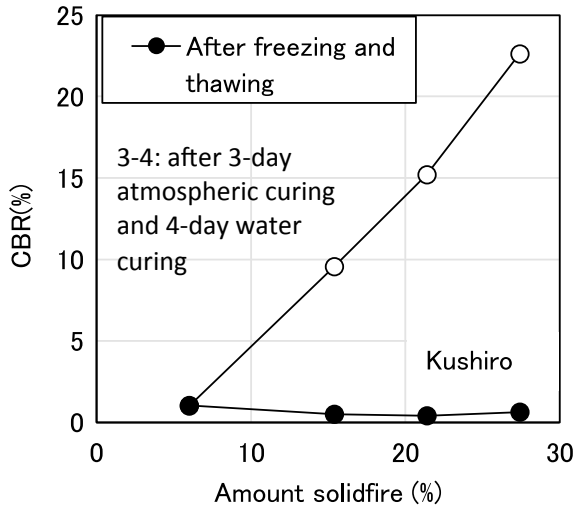


Table 5 Freezing mode

Amount of solidifier (%)	Freezing mode
6.0	5
15.4	4
21.4	4
27.4	4

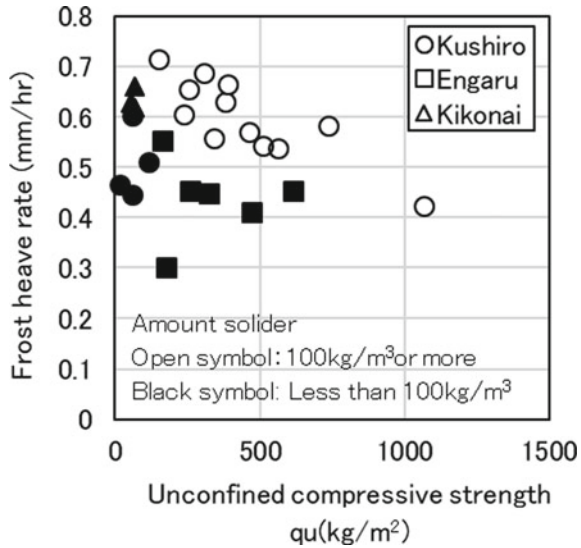
3.2 CBR After Freeze–Thawing

As an example of strength change due to freezing, Fig. 10 shows the amount of solidified material added, the CBR, and the CBR after freezing and thawing for the Kushiro specimen. Table 5 shows the freezing mode. For the Kushiro specimen without freezing, the CBR was about 10% when the amount of solidifier was 15% or more; however, after freeze–thaw, the CBR became very low. The CBR for this specimen was about 1% regardless of the solidifier amount. The freezing mode was 5 (frost column freezing) at 6% of solidifier. For the specimens with other amounts of solidifier, the freezing mode was 4 (frost freezing). Within the scope of this test, none of the samples pass the freezing criteria and none can be used in places that freeze.

3.3 Freezing Property of Solidified Soil

The relationship between the unconfined compressive strength of solidified soil and the freezing rate is shown in Fig. 11. Regardless of the type of soil and the curing

Fig. 11 Relationship between the unconfined compressive strength and the freezing rate



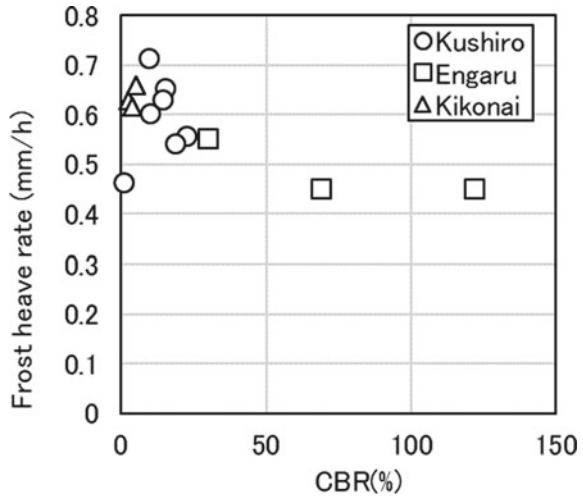
method, the freezing rate is 0.3 mm/h or higher. The Japanese Geotechnical Society specifies that materials with a freezing rate of 0.3 mm/h or higher are highly frost heave susceptible. The tested specimens had freezing rates of 0.3 mm/h or higher; therefore, all were highly frost heave susceptible. The tested soil samples had high frost heave susceptibility, because the freezing rate was 0.4 mm/h or higher even in the sample with an unconfined compressive strength of 1000 kN/m² or higher. Past data [9] showed an example in which the amount of mixed solidifier was about 100 kg/m³ and the freezing rate was 0.2 mm/h or lower, which are different from this data.

The relationship between the CBR of solidified soil and freezing rate is shown in Fig. 12. No correlation between the CBR and the freezing rate was found in the tested range. All these samples were of high frost heave susceptibility with the freezing rate of 0.3 mm/h or higher, even when their CBRs exceeded 100%. Care must be taken when using materials modified with blast furnace class B cement in subgrades in cold regions. It is considered that the physical characteristics of the original soil also affect the frost heave susceptibility of the solidified soil; therefore, we would like to investigate the factors that affect the frost heave susceptibility of solidified soil in the future.

4 Summary

We examined a few solidified soil samples for their CBR, unconfined compressive strength, impact acceleration, and frost heave susceptibility. The following was found.

Fig. 12 Relationship between the CBR of solidified soil and freezing rate



- (1) (1) The CBR, unconfined compressive strength, and impact acceleration increased with increases in solidifier amount. The unconfined compressive strength and CBR of the solidified soil had a highly correlated proportional relationship; however, this relationship varied depending on the origin of the soil.
- (2) A proportional relationship was found between the impact acceleration and CBR regardless of the type of soil and the curing method. From this, the CBR of solidified soil can be estimated based on the impact acceleration; therefore, it is possible to apply impact acceleration as an onsite quality control measure.
- (3) In some cases in which the unconfined compressive strength was improved by the addition of a solidifier and the CBR was sufficiently high as a subgrade material, the solidified soil was not usable for the subgrade because of the high frost heave susceptibility of that soil.

5 Conclusion

In this study, frost heave susceptibility was found in specimens that had relatively high strength. In future studies, we would like to find the strength at which soft soil becomes a non-frost heave susceptible material. We would also like to propose a quality control method that uses the impact acceleration technique for inspecting constructed subgrade.

References

1. Civil Engineering Research Institute for Cold Region (2013) The manual of measures against unsuitable soil in Hokkaido
2. Hokkaido Regional Development Bureau (2019) Road design guidelines
3. Shinichiro K, Mitsuhiko K (2000) Effect of water retention on frost heave characteristics of lime-stabilized soils. *JSCE Proc* (666):261–268
4. Takashi O (2006) Controlling effects of stabilizer and its content on frost heave of stabilized soil. In: *Proceedings of the 50th anniversary symposium of the geotechnical society of Hokkaido*, pp 129–132
5. Hokkaido Development Bureau (2019) Specifications for Road and River Construction Work
6. Japan Road Association (2009) Road construction summary, p 287
7. Japanese Geotechnical Society (2009) “Test method for frost heave measurement” and “Test method for frost susceptibility” in the Japanese Standards and Explanations of Laboratory Tests of Geomaterials, pp 226–258
8. NEXCO (2018) Test method for frost susceptibility of soils
9. Research Committee on Preventive Measures for Frost Heaving in Soils (2009) Geotechnical engineering in cold regions—frost heave of ground and preventive measures. Japanese Geotechnical Society Hokkaido Branch, p 98

Particle Breakage of a Crushed Sandstone–Mudstone Particle Mixture



Zhenfeng Qiu, Shaobo Yang, Junjie Wang, and Ting Cao

Abstract Sandstone–mudstone particle mixture (SMPM) is often used as a main filling material in many agriculture-related and civil engineering works such as in rockfill dams and filling foundations. The SMPM was found crushed seriously since it is mixed with mudstone particles. In this study, the compressive rheological test was conducted to investigate the influence of different vertical stress and mudstone particle content on the particle breakage of SMPM. Research findings suggested that particle breakage of SMPM in the conditions of different pressure and mudstone particle content ranged between 4.24 and 24.34% and rose along with the increase in vertical pressure and mudstone particle content. A power function relation between particle breakage and vertical pressure was proposed. It was found that, with small confining pressure, the particle breakage of SMPM particles calculated by the proposed prediction formula was larger than that of rockfill materials. The particle breakage prediction formulas of rockfill materials underestimated the particle breakage of SMPM during the small confining pressure.

Keywords Soil-sand · Rheological test · Mudstone particles · Particle breakage · Prediction formulas

1 Introduction

Rockfill is composed of particles of different sizes, with randomly distributed contact points between the particles. Since there are often point contacts between particles, they are vulnerable to breakage even with small energy and peripheral pressure applied in the presence of external forces, such as compacting force and shear force

Z. Qiu · S. Yang · T. Cao

Key Laboratory of Hydraulic and Waterway Engineering (Chongqing Jiaotong University),
Ministry of Education, Chongqing 400074, P. R. China
e-mail: qiuzhenfeng3012@126.com

J. Wang (✉)

National Engineering Research Center for Inland Waterway Regulation, Chongqing Jiaotong
University, Chongqing 400074, P. R. China
e-mail: wangjunjiehu@163.com

[1, 2]. The stress–strain relationship, strength, deformation, permeability, and other factors of coarse aggregates are all associated with the breakage degree of particles caused by stress changes [3–5]. Rockfill contraction is the decisive factor influencing the stress of concrete-faced rockfill dam, whereas the plastic volumetric strain of rockfill materials is mainly caused by the breakage of particle edges and corners [6].

Particle breakage has been investigated considerably by researchers, which suggest that particle breakage is in connection with particle size [7, 8], shape [9], strength [10, 11], grading [12], density [13, 14], stress conditions [5, 12], etc. The larger the particle size is and the sharper the edges and corners are, the lower the strength of crushing critical stress is. The larger the confining pressure is, the more vulnerable particles are to breakage and larger will be the quantity of crushed particles.

A study on the factors influencing the particle breakage of coarse aggregates by Fu et al. [15] suggested that particle breakage was associated with stress level, particle strength (parent rock lithology), grading, test method, particle roundness, etc. They investigated that the particle breakage was intensified with confining pressure. Wei et al. [16] also found a similar rule when they investigated the particle breakage of coarse aggregates. They argued that particle breakage increased in the function of power along with the growth of confining pressure. In a study on the particle breakage rule of coarse-grained soil by Cai et al. [17], a relationship between particle breakage and initial fractal dimension using the fractal dimension theory was proposed. They also established the relationship between particle breakage and fractal dimension, confining pressure, density, etc. Zhao et al. [7] studied the particle breakage of coarse-grained soil, which indicated that particle breakage rose with confining pressure. And the contact stress and interlock capacity between particles increased in the presence of high stress.

However, the interspace between sand particles could be fully filled by fine particles while the finer are enough, for which the particle breakage declined due to the increase of contact area and decrease of contact stress that was shared by both fine and coarse particles. To the contrary, the contact stress between coarse particles increased in the soil–sand with fewer fine particles, which resulted in serious breakage of particle corners and edges. Therefore, the particle breakage of the soil–sand with fewer fine particles was smaller than that with more fine particles. Liu et al. [18] revealed the hyperbolic relation between particle breakage and confining pressure when they conducted the particle breakage test to the rockfill materials of the dam for the pumped storage power station located in Yixing, Jiangsu province.

The deformation characteristic of soil–sand has gradually been recognized. Most of the quarries in Southwest China are interbed formations comprising hard and weak rocks, instead of hard rocks only, sandstone, and mudstone interbeds. Therefore, the filler is not made up of a single kind of hard coarse aggregates. For the sake of cost reduction, designers have worked out the designing methods using weak rock materials. For example, mudstone has been mixed in the filler used for various construction projects, such as the expansion project of Chongqing Jiangbei International Airport and the bank slope of Huangqi fitting-out quay in Chongqing. However, the particle breakage rule and crushing mechanism of coarse-grained soil mixed with

mudstone still remain unknown. To this end, compressive rheological test was carried out to study the influence of various factors, including vertical pressure and mudstone particle content, on particle breakage of coarse aggregates with mudstone.

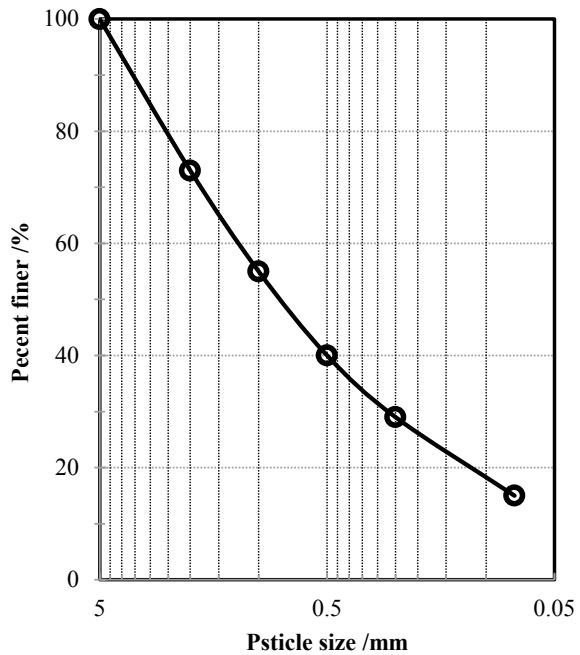
2 Tested Materials and Testing Methods

2.1 Tested Materials

In this study, the sandstone and mudstone particle mixture was used. The sandstone and mudstone blocks were lightly weathered rocks and collected from the Jurassic Shaximiao Formation in Three Gorges Reservoir Region. The uniaxial compression strengths of the blocks were tested in the laboratory, which were 60.0–72.2 MPa for the sandstone and 8.3–25.8 MPa for the mudstone. Large sandstone and mudstone blocks were crushed separately first and then went through the screen test to obtain sandstone and mudstone particle groups whose particle sizes were 5–2 mm, 2–1 mm, 1–0.5 mm, 0.5–0.25 mm, 0.25–0.075 mm, and smaller than 0.075 mm, respectively.

The dry density and moisture content of the sample were 1.83 g/cm³ and 8%, respectively. Particle grading curve of the test material is shown in Fig. 1. And the

Fig. 1 Particle grading curve of the test material



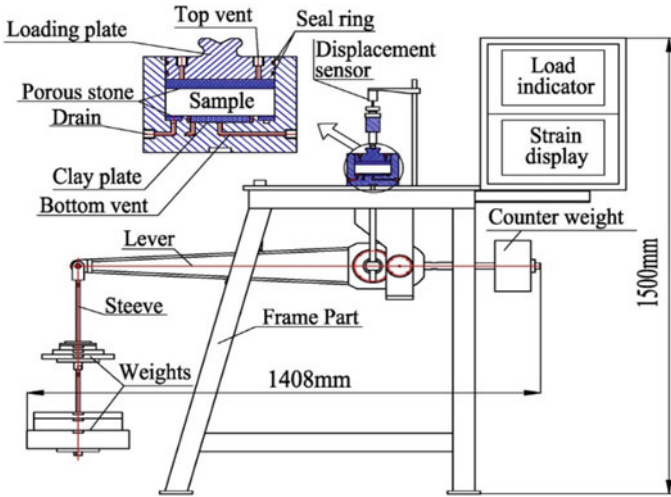


Fig. 2 Test instruments

maximum particle size, mean particle size, nonuniformity coefficient, and curvature coefficient were 5 mm, $d_{50} = 0.83$ mm, 25.56, and 1.16, respectively.

2.2 Compression Tests

As shown in Fig. 2, the rheological test was carried out using an oedometer that consists of the axial loading system, axial deformation sensor, automatic test data acquisition, process system, etc. The axial deformation of the test instrument ranged between 0 and 15 mm. This test instrument presents the advantages of high precision in the deformation while acquiring the loading and deformation data during the test. The accuracy of axial deformation was 0.001 mm. Axial pressure was loaded by means of the lever and weights, with a maximum axial pressure of 2.4 MPa. For the purpose of drainage, an annular porous stone and a round ceramic plate were mounted at the bottom of the instrument, with which the compressive rheological test with consolidation by dewatering could be conducted. Sample size was $\Phi 100 \times H30$ mm.

2.3 Testing Method

A total number of 24 specimens of SMPM with mudstone were prepared and divided into four groups (six samples in each group). Mudstone particle content in the four groups was 20%, 40%, 60%, and 80%, respectively. The compressive rheological

test was conducted to each group at six different vertical pressure levels, namely 100, 200, 400, 800, 1200, and 1600 kPa, respectively.

The test was carried out by the following steps. Firstly, the sandstone and mudstone particles were measured and weighed by the density and grading, and mudstone particle content was mixed evenly with 8% distilled water. Next, the materials were sealed for 24 h for thorough mixing between the materials and water. Secondly, the prepared materials were divided into three equal parts, which were then compacted. Each compacted layer should be roughened to ensure that the materials at the compaction interfaces contacted well with each other. Thirdly, the specimen tube was cleaned up and applied with lubrication oil to the base and inner wall using a banister brush. Specimens were loaded in the tube following the order of specimen, filter paper, porous stone, and pressure cover. Fourthly, 1 kPa pressure was loaded for precompaction; the displacement reading was reset 10 min later. The predetermined axial pressure was loaded by phases (50, 100, 200, 400, 800, and 1200 kPa). It was required that the drain valve be open at the base during solidification. Fifthly, it was considered stable when the deformation rate fell below 0.005 mm/h. The compressive rheological test was conducted for 4.5 days.

The specimens were removed and dried after the test, followed by particle analysis test using the vibrating screen. Each specimen underwent vibration for 20 min. The apertures of the circular vibrating screen were 5 mm, 2 mm, 1 mm, 0.5 mm, 0.25 mm, and 0.075 mm, respectively.

Particles might be crushed during compaction and drying operation. To eliminate the influence of such particle breakage due to compaction on test result, the specimens were compacted first and then dried and screened before the test, thus obtaining the material grading. In this study, this grain grading was considered the initial particle grading.

2.4 Calculating Method for Particle Breakage

Specimens of coarse-grained soil mixed with mudstone after rheological tests were analyzed by particle screening test. The particle grading of different specimens was achieved by particle screening test. The difference between each particle grading was described using the Marsal particle breakage [19], which was calculated by the following equation:

$$B_g = \sum |W_{ki} - W_{kf}| \quad (1)$$

where B_g is the sum of the positive difference between the content of each particle group before and after the test; W_{ki} is the mass percentage of a certain particle group before the test; and W_{kf} is the mass percentage of a certain particle group after the test.

3 Testing Results

Particle grading curves of four groups of samples with different mudstone content before and after the test are shown in Fig. 3a–d. It could be seen that particle grading curves with different vertical pressure differed after the rheological test. The higher the vertical pressure was, the more significant was the particle grading variation. Particle grading variation was associated with mudstone particle content—the larger the mudstone particle content was, the more significantly particle grading before

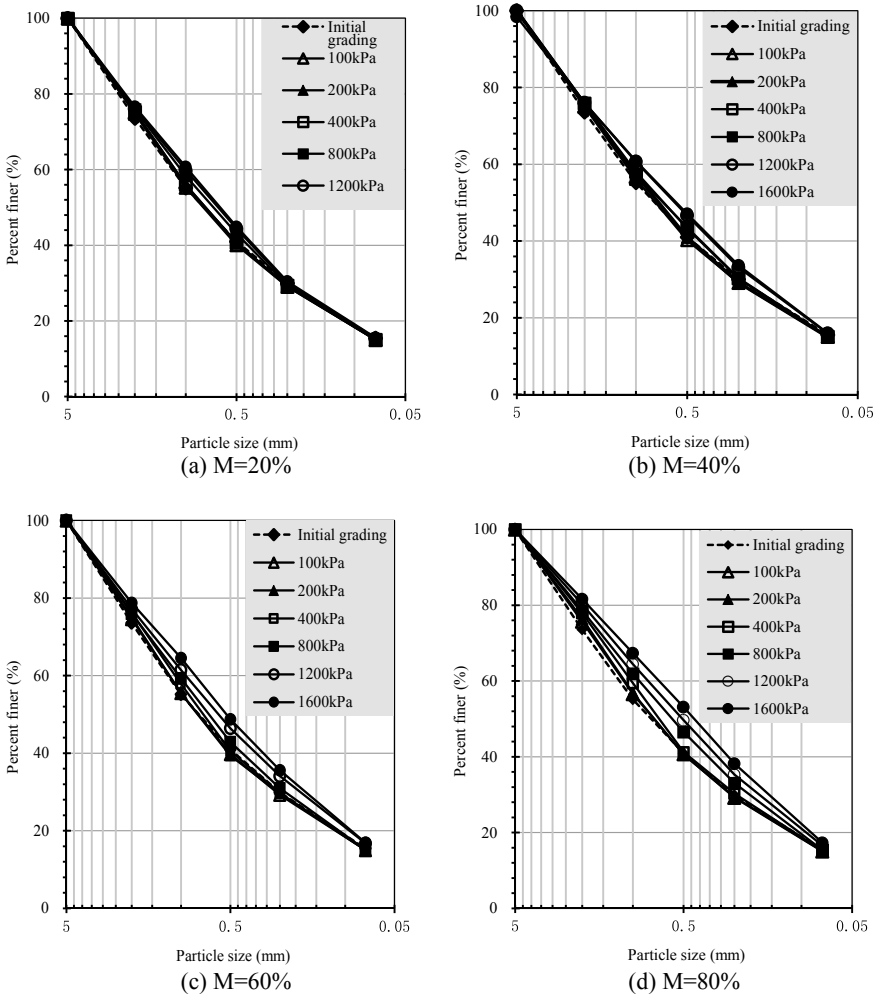
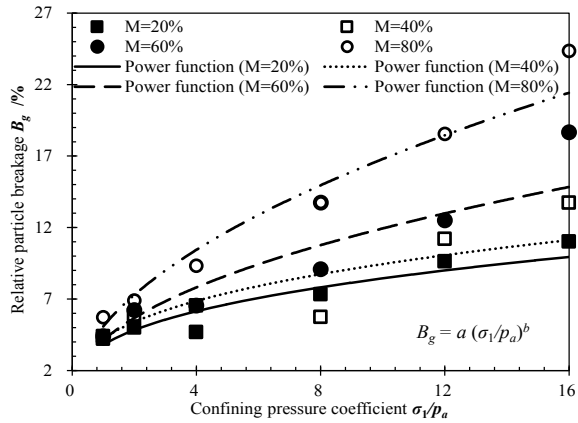


Fig. 3 Particle grading curves before and after the rheological test

Fig. 4 Relationship between particle breakage and axial stress



and after the test differed. Particles of different groups also showed varied particle breakage phenomena.

For example, when the mudstone particle content was 80%, the mass percentage of particles of the 2–5 mm group was 26.4% before the rheological test and dropped by 8.03–18.37% after the test; the mass percentage of particles of the 1–2 mm group was 18.4% before the test and declined by 4.14–14.26% after the test. Changes of the grading curves of coarse-grained soil mixed with mudstone were investigated using particle breakage, as shown in Fig. 4.

The relationship between particle breakage and pressure is shown in Fig. 4. While the vertical pressure ranges from 100 to 1600 kPa, particle breakage was 4.24–9.66%, 4.43–13.75%, 4.40–18.67%, and 5.72–24.34% when mudstone particle content was 20%, 40%, 60%, and 80%, respectively. With rheology, the particle breakage of coarse-grained soil mixed with mudstone increased with vertical pressure. It was in connection with mudstone particle content: The larger the mudstone particle content was, the more serious was the particle breakage. The relationship between relative particle breakage and vertical pressure was fitted using the power function, as shown below:

$$B_g = a(\sigma_1/p_a)^b \tag{2}$$

where σ_1 is vertical stress (kPa); p_a is atmospheric pressure (kPa); and a and b are both fitting parameters.

The relationship between fitting parameters a and b and mudstone particle content is shown in Fig. 5. It could be seen that both a and b declined with the increase of mudstone particle content. As shown in Fig. 5, the relationship between fitting parameters a and b and mudstone particle content M was fitted using the linear relation, with the relation given as follows:

$$a = c_1M + d_1 \quad (R^2 = 0.90) \tag{3}$$

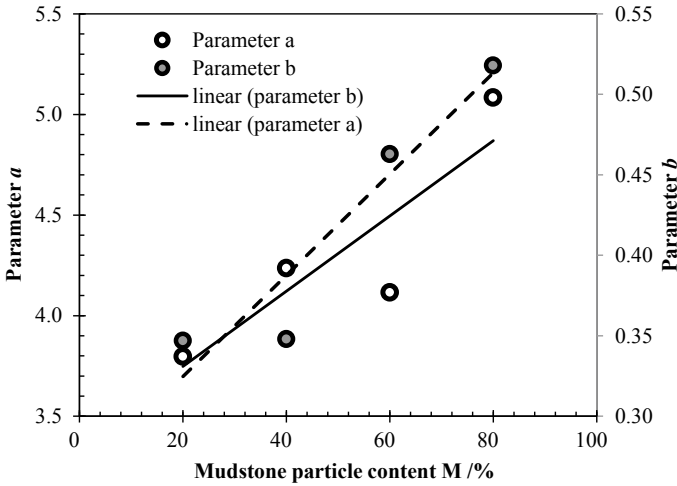


Fig. 5 Relationship between fitting parameters *a* and *b* and mudstone particle content

$$b = c_2M + d_2 \quad (R^2 = 0.79) \tag{4}$$

where *a* and *b* are the fitting parameters of particle breakage and vertical stress by power function; and *c*₁, *d*₁, *c*₂, and *d*₂ are fitting parameters whose values are 0.019, 3.373, 0.003, and 0.262, respectively.

The relationship between particle breakage and mudstone particle content could be obtained by substituting Eqs. 3 and 4 into Eq. 2, as shown below:

$$B_g = (c_1M + d_1)(\sigma_1/p_a)^{c_2M+d_2} \tag{5}$$

where *B_r* is particle breakage rate (%); *M* is mudstone particle content (%); *σ*₁ and *P_a* are vertical pressure and atmospheric pressure (kPa); and *c*₁, *d*₁, *c*₂, and *d*₂ are fitting parameters.

4 Discussions

The test results suggested that the particle breakage of SMPM grew in function of power as vertical pressure increased. The proposed equation was obtained at the vertical stress of 100–1600 kPa. So this empirical formation just can be used in a certain range of vertical stress.

The equation for lateral pressure coefficient developed by Terzaghi signifies the ratio between effective horizontal stress and effective vertical pressure. Thus, lateral pressure could be derived:

$$\sigma_1 = \frac{\sigma_3}{K_0} \quad (6)$$

where σ_3 is confining pressure in the conventional triaxial test and σ_1 is vertical pressure. According to the investigation by Qiu et al. [20], the average lateral pressure coefficient K_0 of SMPM is 0.36. When vertical pressure ranges from 100 to 1600 kPa, confining pressure could be obtained by Eq. 6, which was 36–576 kPa.

The following equation could be derived by substituting Eq. 6 into Eq. 5:

$$B_g = (c_1 M + d_1) \left(\frac{\sigma_3}{p_a K_0} \right)^{c_2 M + d_2} \quad (7)$$

where the parameters are the same as those in Eqs. 5 and 6. The confining pressure of this equation ranges from 36 to 576 kPa. For the soil–sand without mudstone particles, Eq. 7 could be further denoted as:

$$B_g = d_1 \left(\frac{\sigma_3}{p_a K_0} \right)^{d_2} = \frac{d_1}{K_0^{d_2}} (\sigma_3 / p_a)^{d_2} \quad (8)$$

where d_1 and d_2 are the fitting parameters whose values are 3.373 and 0.262, respectively; and K_0 is static lateral pressure coefficient whose value is 0.36. According to Wei [21], the relation between the particle breakage of coarse-grained soil (sandstone materials) and confining pressure was a power function:

$$B_g = m_1 (\sigma_3 / p_a)^{n_1} \quad (9)$$

where m_1 and n_1 are the parameters of soil materials whose values are 0.382 and 0.739, respectively; confining pressure ranges from 300 to 900 kPa.

When conducting the triaxial test to the limestone rockfill of Xibeikou Dam, Liu et al. [18] found the following hyperbolic relation between particle breakage and confining pressure:

$$B_g = \frac{\sigma_3 / p_a}{m_0 + n_0 (\sigma_3 / p_a)} \quad (10)$$

where m_0 and n_0 are test parameters whose values are 0.523 and 0.061 for the rockfill materials of Tianshengqiao Hydropower Station and 0.457 and 0.086 for those of Xibeikou Dam, respectively.

The comparison between the predictions of Eqs. 8–10 is shown in Fig. 6. It could be seen that the particle breakage predicted by the equation developed by Wei [21] was significantly smaller than that of the proposed equation when confining pressure coefficient was within 0 ~ 13.75. And the value predicted by the equation for Xibeikou

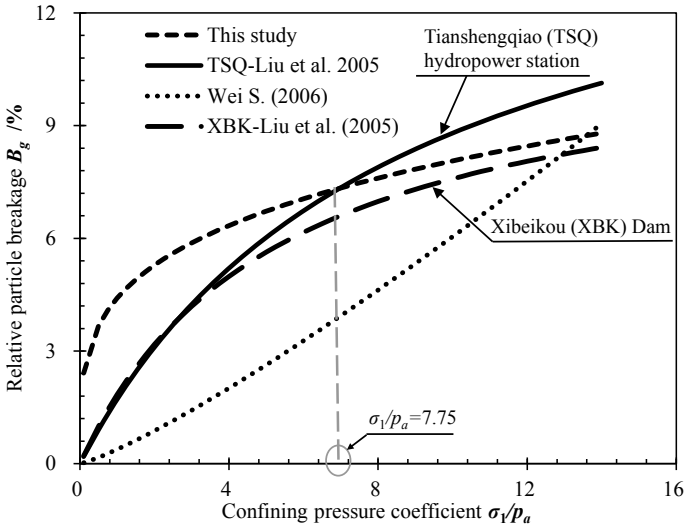


Fig. 6 Comparison between particle breakage predictions

Dam was smaller than that of the proposed equation; the difference between them was narrowed as confining pressure coefficient increased. When confining pressure lied between 0 and 7.75, the value predicted by the equation for Tianshengqiao Hydropower Station was smaller than that of the proposed equation. However, the value predicted by the equation for Tianshengqiao Hydropower Station turned larger than that of the proposed equation when confining pressure was larger than 7.75.

In terms of the prediction of particle breakage of coarse aggregates with mudstone, the equations developed by Liu et al. [18] and Wei [21] both underestimated the particle breakage at lower confining pressure, which might be associated with test materials. The rockfill materials of Xibeikou Dam are calcite dolomite with compressive strength of 130–150 MPa, which was close to the strength of sandstone materials used in this study. In contrast, the rockfill materials of Tianshengqiao are lightly weathered and fresh limestone materials with higher strength than that of the sandstone materials.

5 Conclusion

In this study, the particle breakage of SMPM was investigated by the compressive rheological tests. The particle rheological breakage of SMPM was affected by axial pressure and mudstone particle content. Conclusions are given as follows:

1. Particle breakage is 4.24– 9.66%, 4.43–13.75%, 4.40–18.67%, and 5.72–24.34%, under the vertical stress 100–1600 kPa, when mudstone particle content

- is 20%, 40%, 60%, and 80%, respectively. The particle breakage of SMPM increases with vertical pressure. In addition, a power function relationship was suggested to estimating the particle breakage.
2. The empirical equation proposed in this study degrades into one for particle breakage calculation of SMPM. Comparing with the value predicted by the proposed equation and those by the equations suggested by Liu et al. [18] and Wei [21], it indicates that both of Liu et al. [18] and Wei [21] have underestimated the particle breakage at low confining pressure for coarse-grained soil. The particle breakage predicted by the empirical equation of this study was similar to the value of Xibeikou Dam. During the rise and fall of the water level, the stress level of the dam body may change. This formula cannot be used to estimate the particle breakage of the dam filling material through the stress level accurately. More in-depth research on particle breakage effects by stress level can be carried out in future research.

Acknowledgements The authors gratefully acknowledge financial support from the National Natural Science Foundation of China under Grant No. U1865103, the Chongqing Science and Technology Commission of China under Grant No. cstc2017jcyjA1642, the Technology Innovation and Application Demonstration Project in Chongqing under Grant No. cstc2018jscx-msyb0328, the Chongqing, the Chongqing Municipal Education Commission of China under Grant No. KJ1705123, the China Postdoctoral Science Foundation Funded Project under Grant No. 2019M663890XB, Chongqing Postdoctoral Science Foundation Funded Project, the Key Laboratory of Hydraulic and Waterway Engineering of the Ministry of Education, Chongqing Jiaotong University, Grant No. SLK2017B01, and Postgraduate Research and Innovation (Innovation Fund) Project of Chongqing Jiaotong University, No. 2019S0126, respectively.

References

1. Coop MR, Sorensen KK, Freitas TB, Georgoutsos G (2004) Particle breakage during shearing of a carbonate sand. *Geotechnique* 54(3):157–163
2. Wei S, Zhu JG (2006) Study on wetting breakage of coarse-grained materials in triaxial test. *Chin J Geotech Eng* 25(6):1252–1258
3. Bandini V, Coop MR (2011) The influence of particle breakage on the location of the critical state line of sands. *Soils Found* 51(4):591–600
4. Xiao Y, Liu H, Ding X, Chen Y, Jiang J, Zhang W (2016) Influence of particle breakage on critical state line of rockfill material. *Int J Geomech* 16(1):04015031
5. Ueng TS, Chen TJ (2015) Energy aspects of particle breakage in drained shear of sands. *Géotechnique* 50(1):65–72
6. Yu FW, Su LJ (2016) Particle breakage and the mobilized drained shear strengths of sand. *J Mt Sci* 13(8):1481–1488
7. Zhao XJ, Ling H, Fu H, Han HQ (2013) Effect of grain size composition on particle breakage and mechanical properties of rock-fill materials. *J Water Resour Architect Eng* 11(4):175–202
8. Wang JJ, Zhang HP, Deng DP (2014) Effects of compaction effort on compaction behavior and particle crushing of a crushed sandstone-mudstone particle mixture. *Soil Mech Found Eng* 51(2):67–71
9. Hill PJ (2004) Statistics of multiple particle breakage accounting for particle shape. *Aiche J* 50(5):937–952

10. Hassanlourad M, Salehzadeh H, Shahnazari H (2008) Dilation and particle breakage effects on the shear strength of calcareous sands based on energy aspects. *Cytometry Part A J Int Soc Anal Cytol* 6(2):108–119
11. Indraratna B, Salim W (2002) Modeling of particle breakage of coarse aggregates incorporating strength and dilatancy. 155(4):601–608(8)
12. Wang JJ, Cheng YZ, Zhang HP, Deng DP (2015) Effects of particle size on compaction behavior and particle crushing of crushed sandstone-mudstone particle mixture. *Environ Earth Sci* 73(12):8053–8059
13. Leung CF, Lee FH, Yet NS (1996) The role of particle breakage in pile creep in sand. *Can Geotech J* 33(6):888–898
14. Shahnazari H, Rezvani R (2013) Effective parameters for the particle breakage of calcareous sands: an experimental study. *Eng Geol* 159(9):98–105
15. Fu H, Lin H, Cai ZY (2009) Influencing factors for particle breakage of coarse grained soil. *J Hohai Univ (Natural Sciences)* 37(1):75–79
16. Wei S, Zhu JG, Qian QH, Li F (2009) Particle breakage of coarse-grained materials in triaxial tests. *Chin J Geotech Eng* 31(4):533–538
17. Cai ZY, Li XM, Guan YF, Huang YH (2016) Particle breakage rules of rockfill materials. *Chin J Geotech Eng* 38(5):923–929
18. Liu HL, Qin HY, Gao YF, Zhou YD (2005) Experimental study on particle breakage of rockfill and coarse aggregates. *Rock Soil Mech* 26(4):562–566
19. Marsal RJ (1967) Large scale testing of rockfill materials. *J Soil Mech Found Div* 92(2):27–43
20. Qiu ZF, Wang JJ, Chen YL, Yang Y, Li YS (2020) Effects of periodic saturation on K_0 for a sandstone-mudstone particle mixture. *Marine Georesour Geotechnol* 38(7):867–875. <https://doi.org/10.1080/1064119X.2019.1637486>
21. Wei S (2006) Study on setting deformation behaviour and numerical model of coarse-grained materials. PhD dissertation, Hohai University, P. R. China (in Chinese)

Field Evaluation of Using Slag as Aggregates for Otta Seal Surfacing



Bo Yang , Yang Zhang , Halil Ceylan , and Sunghwan Kim 

Abstract Otta seal surfacing technology is an application of thin bituminous surface treatment (BST) with graded aggregates and emulsified or cutback asphalt binder. Due to the employment of locally available aggregates and ordinary construction equipment, it dramatically reduces road resurfacing costs compared to traditional BSTs such as chip seal. In recent years, Otta seal has been tried for low-volume roads in a few states in the USA. However, most of the Otta seals adopted crushed limestone or river gravels, and recycled materials, such as slag, have never been investigated. To evaluate the performance of using slag for Otta seal, two gravel roads in Louisa County, Iowa were selected to be resurfaced. Slag collected from a steel mill was applied instead of regular road aggregates. To monitor the performance, dust caused by passing traffic was measured, and elastic modulus, skid resistance, and international roughness index (IRI) were tested before and after the Otta seal construction. The results indicate that slag-based Otta seal reduced the surface dust dramatically and maintained an acceptable skid resistance. However, it also presented a high IRI values due to the poor compaction and unsatisfied slag gradation. In addition, the newly constructed surface exhibited excellent appearance, and no distress was found after eight-month service. In summary, the findings from this study showed that recycling slag as an alternative aggregate for Otta seal is quite feasible.

Keywords Otta seal · Dust measurement · Roughness measurement · Elastic modulus

B. Yang · H. Ceylan · S. Kim
Department of Civil, Construction and Environmental Engineering, Iowa State University, Ames, IA 50011, USA
e-mail: ybys1989@iastate.edu

H. Ceylan
e-mail: hceylan@iastate.edu

S. Kim
e-mail: sunghwan@iastate.edu

Y. Zhang (✉)
School of Transportation, Southeast University, Nanjing 211189, China

1 Introduction

Iowa has tens of thousands miles of unpaved secondary roads carrying very low daily traffic volumes, but frequently supporting heavy vehicles. As a result, the local road agencies spend millions of dollars annually to replace the aggregates for unpaved roads. In order to maintain or restore low-volume roads with low costs, diverse technologies have been invented and applied to practice. Among them, most of these technologies focus on improving pavement surface performance, such as chip seal, fog seal, and slurry seal. Comparing to these commonly employed technologies, Otta seal is a relatively new one, especially to pavement engineers and road agencies in the U.S.

Otta seal (first developed and trialed in the Otta valley in Norway) was developed in 1963 by the Norwegian Road Research Laboratory (NRRL) as a low-cost maintenance surface alternative, in light of budgetary constraints, for unpaved gravel roads with low bearing capacity under spring–thaw periods [1]. Consequently, Otta seal has been used in northern Europe, Africa, among others, as an economical and practical alternative to traditional bituminous surface treatments (BSTs). Existing studies [2] have reported Otta seal's lower life cycle costs in comparison with other BSTs. In the USA before 2017, South Dakota (SD) and Minnesota (MN) had been the only two states tried Otta seal on their low-volume roads with granular surface, respectively, since 2008 and 2010. In 2017, a 6.4 km (4 miles) long road section with deteriorated asphaltic cement pavement was resurfaced with Otta seal in Iowa (IA), which was the first well document Otta seal study in the USA [3]. All these U.S. Otta seal projects which built with locally available aggregates showed satisfied performance.

Even though either crushed lime stone or river rock have proven to be a success, there was no attempt before trying to use recycled materials (e.g., slag and recycled asphalt pavement as Otta seal aggregates all over the world). Slag is a material type of material with high stiffness usually from metal production [4]. It has been reported with well performance of employing slag in multiple infrastructure applications. For instance, Roy [4] reported that slag-based cement and concrete provided higher values of mechanical parameters. Slag was reported as a feasible structural fill material in reinforced soil structures [5]. However, feasibility of using slag as Otta seal has never been studied.

The principal objective of this study was to construct Otta seal with slag and evaluate the performance of the slag-based Otta seal. For this objective, international roughness index (IRI) test, dustometer test, lightweight deflectometer (LWD) test, and British pendulum test were conducted at different periods before, during, and after the Otta seal implementation, together with visual inspections to document the Otta seal appearance.

Table 1 Summary of site information

Road name	142nd Ave., Louisa County, Iowa	K Ave., Louisa County, Iowa
Average daily traffic (ADT)	150	200
Primary vehicles (resident vehicle primarily: farm equipment primarily, or both)	Both	Both
Road length	0.8 km (0.5 mile)	1.1 km (0.7 mile)
Road width	8 m (26 ft)	8 m (26 ft)
Surface type of existing road	Gravel Road	Gravel Road
Maintenance history	Grading 3–5%	Grading 3–5%

2 Methodology

2.1 Description of Project Background

As the first Otta seal field application using slag aggregate, site conditions have to be carefully documented. After communicating with the county, the basic information of the two selected sites, 142nd Ave. and K Ave. in Louisa County, IA was gathered and is summarized in Table 1. The two sites are 0.8 km (0.5 mile) and 1.1 km (0.7 mile) long respectively with 150 and 200 average daily traffic. The truck traffic on both roads was low and varied daily. The existing surfaces were both gravel roads.

2.2 Otta Seal Design

Aggregate. Based on the traffic volume and truck traffic, it was recommended to apply dense aggregate gradation for double Otta seal in Louisa County. As shown in Fig. 1, the gradation of the slag alone does not fall into the criteria range for dense aggregate gradation for Otta seal. However, it is not known how the gradation will look like after mixing the slag with the regular aggregate that is going to be used for the Otta seal surfacing. Slag has low fines content, but most regular aggregates have higher fines content than slag, which will help adjust the lower part of the gradation curve. Based upon the gradation of aggregate, the spreading rate of 18.96 kg/m² (50 lbs./yd²) was determined.

Asphalt Binder. MC-3000 cutback asphalt is the original proposed binder type in the Otta seal design in Overby [1]. In Africa and Europe, it has been very widely used for large number of Otta seal projects. The recommended spray rate is 1.81 L/m² (0.40 gal./yd²).

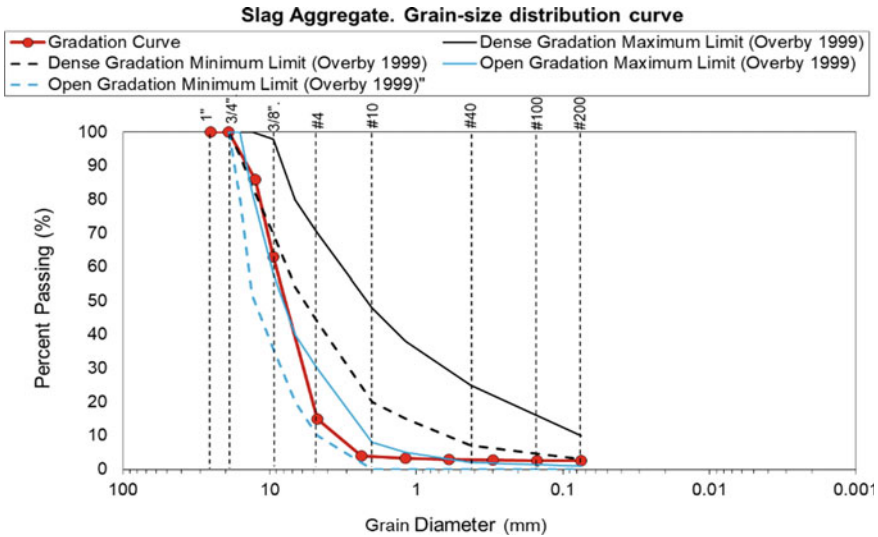


Fig. 1 Slag aggregate gradation comparing to Overby (1999) open and dense gradation limits

2.3 Otta Seal Construction

The Otta seal was implemented on these two roads in Louisa County, IA on July 31, 2018. A month before the Otta seal implementation, the subgrade of the two road sections were stabilized with a commercial chemical stabilizer (Fig. 2a). On the day of the first layer Otta seal construction, the first step was to spray binder (Fig. 2b). A test section of 30.5 m (100 ft) long was recommended to ensure an application rate of 1.81 L/m² (0.40 gal./yd²) that is maintained. Per Overby [1], the required storage temperature was 122–140 °F (50–60 °C), and the required application temperature was 122–185 °F (50–85 °C). The construction can be initiated with the binder spraying if the above requirements were met.

Following binder spraying, the second step was to spread slag aggregates (Fig. 2b). It was required to calibrate the aggregate spreader in accordance with ASTM D5624-13 [6]. It was noted that aggregates were applied at a rate of 18.96 kg/m² (50 lbs./yd²) in steel container and were weighed to confirm the actual aggregate application rate which is 18.96 kg/m² (50 lbs./yd²). The aggregate spreading truck operated at the same speed of binder spraying truck according to recommendations in Overby [1]. Similarly, the construction was continued with the aggregate spreading if the application rate is correct.

The third operation was rolling compaction (Fig. 2c). On the day of construction, a minimum of 15 passes with a pneumatic-tired roller on each direction were recommended, which was total of 30 passes on both directions. For each of the next two days after construction, a total of 30 passes on both directions were suggested. The field engineer may request more passes to ensure that the rolling is sufficient. The



Fig. 2 Otta seal construction sequence in Louisa County, IA using slag

suggested speed to reach the required compaction level is 6.4 km/h (4 mph). The field engineer may ask the operator to maintain that speed or lower it.

The second application of binder and aggregate was 10 weeks after the initial application, and steps 1–3 repeated for successful second layer. The first layer’s surface was swept on the same day that the second layer was constructed. One month post construction of the second layer, the final surface was suggested to be swept of loose aggregate.

To evaluate the performance of Otta seal by using slag aggregate in Louisa County, in-situ tests including international roughness index, dustometer, and lightweight deflectometer were performed before and after the implementation of Otta seal. Visual appearance inspection for these two roads were conducted as well.

3 Results and Discussion

3.1 Appearance Evaluation

Visual inspection is a straightforward method to evaluate the surface condition of roads. Figures 3 and 4 exhibit the appearance images of K Ave. and 142nd Ave. after Otta seal implementation. As shown in these images, both two roads still had a dark color, indicating that slag aggregates were coated and held very well by bitumen. The latest visual inspection was conducted on May 20, 2019. During this field visit, both two roads were concluded to have a very good surface condition because there was no distress and aggregate loss appeared ten months after Otta seal construction.



Fig. 3 Appearance of the slag Otta seal on K Ave. in Louisa County, IA **a** immediately after construction, **b** one month after construction, **c** eight months after construction, and **d** ten months after construction



Fig. 4 Appearance of the slag Otta seal on 142nd Ave. in Louisa County, IA **a** before construction, **b** immediately after construction, **c** one month after construction, and **d** eight months after construction

3.2 International Roughness Index Test

IRI is a worldwide accepted roughness index which obtained from the longitudinal road profiles. In this study, a smartphone-based app named “Roadroid” [7] was used to document the IRI data for two roads after Otta seal construction. Figure 5 shows the IRI of K Ave. and 142nd Ave. one day, one month, and six months after installation of Otta seal, respectively. The results indicate that IRI was increased after implementation of the second Otta seal layer, reflecting the decreased ride quality and driving comfort. However, the IRI changes between one month and six months after Otta seal construction are small, revealing that the increased IRI was caused by the poorer compaction during the second Otta seal construction. In addition to the potential compaction issue, the unsatisfied slag gradation may contribute to the increased IRI.

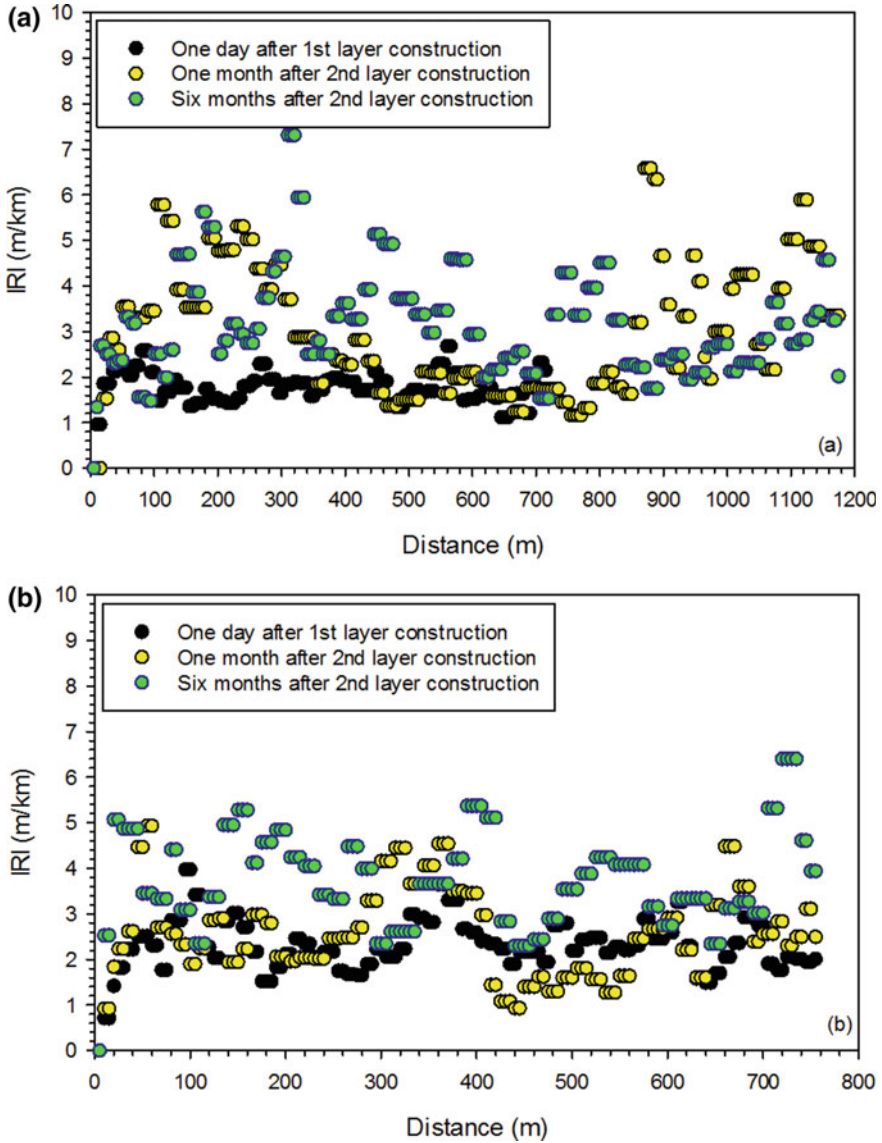


Fig. 5 IRI measurements at different time on a K Ave. and b 142nd Ave

3.3 Dustometer Test

Dust is a common issue for unpaved roads. As a bituminous surface treatment (BST), Otta seal can provide the remarkable benefit with respect to dust control. In this study, a dustometer was used to evaluate the reduction of dust after Otta seal construction.

Figure 6 presents the collected dust in unit length at two treated roads. The results show that K Ave. and 142nd Ave. had the dust of 5.8 g and 7.1 g per kilometer, respectively. Six months after Otta seal construction, both the dust of two roads dramatically decreased to 0.3 g and 0.1 g per kilometer, respectively. Furthermore, between one week and six months after Otta seal construction, the amount of dust did not change significantly, reflecting the consistent dust control resulted from Otta seal.

3.4 Lightweight Deflectometer Test

LWD test is a common test utilized to measure the bearing capacity (deflection) of in-situ subsoils. Generally, various types of BST technologies can construct a protective surface against tire wearing on the existing unpaved roads to extent its lifespan. However, they are not intended to strengthen engineering properties of subgrade. Hence, Otta seal was not expected to improve pavement structures. To evaluate the elastic modulus of subsoil before and after Otta seal implementation, LWD test was performed on both test sections. In this study, both subgrades of K Ave. and 142nd Ave. were stabilized with a liquid proprietary stabilizer named Base One.

Figure 7a, b exhibits the measured elastic modulus for K Ave. and 142nd Ave. in Louisa County, IA, respectively. The results indicate that the elastic modulus of K Ave. increased a lot but 142nd Ave. did not have the similar trend after Otta seal implementation. The increased elastic modulus at K Ave. is due to the soil stabilization prior to the Otta seal construction. Although 142nd Ave. was stabilized as well, the different subgrade conditions and the addition of excessive moisture may mitigate the effects of soil stabilization. The finding indicate that Otta seal did not cause the deficiencies to pavement structures.

3.5 British Pendulum Test

The skid resistance is a significant safety factor to road surface treatment. The British pendulum test was performed in accordance with ASTM E303-93 [8] in this study to measure the surface friction of Otta sealed roads in Louisa County, IA. As shown in Fig. 8, both K Ave. and 142nd Ave. exhibited very high British pendulum numbers (BPN) of 144 and 147, respectively, resulting from the poor compaction and unsatisfied gradation of slag. After eight months, both two roads showed the reductions in BPN values due to the polished aggregates from tire wear but were still acceptable [9]. The results indicate that Otta seal surface can provide a high friction surface.

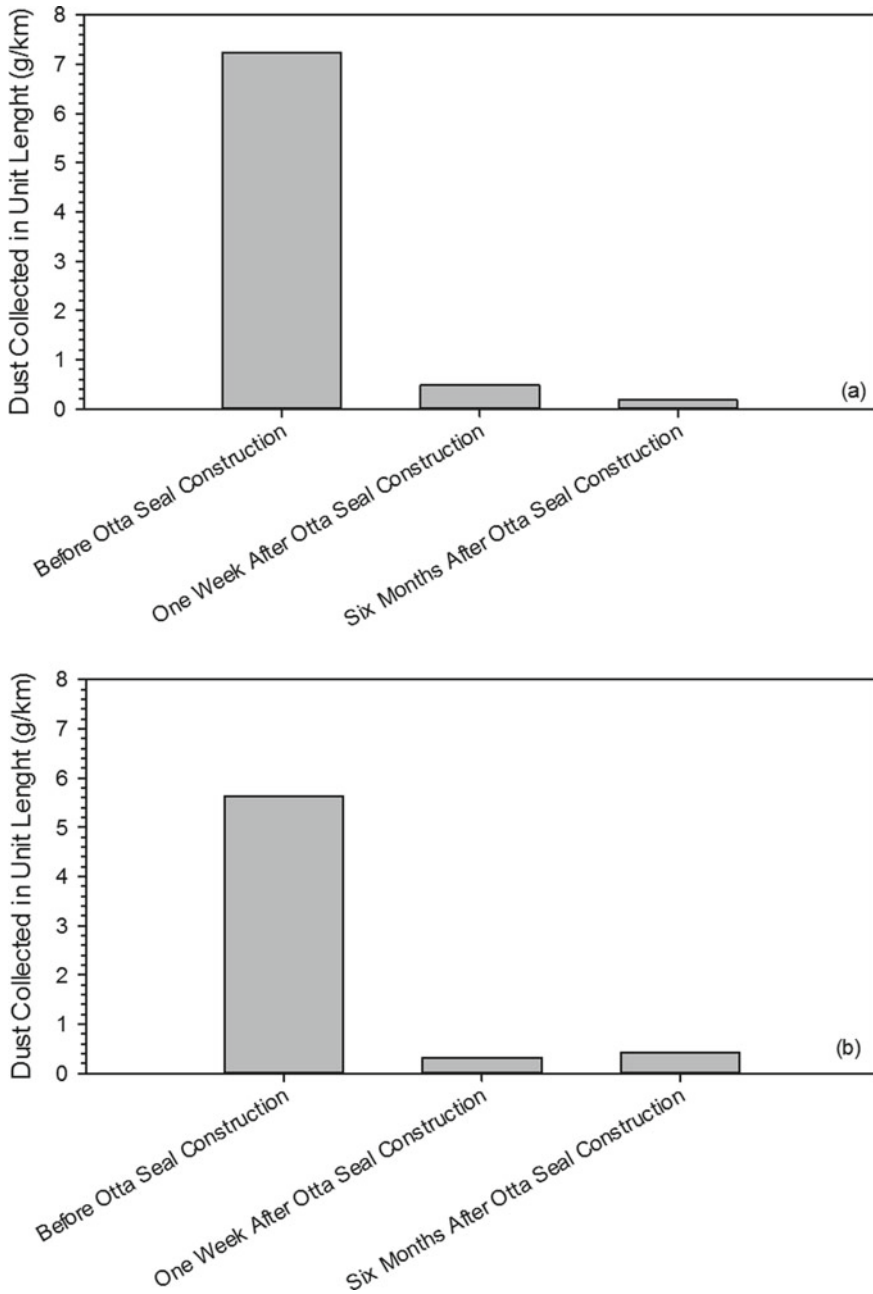


Fig. 6 Dustometer test results at different periods on a K Ave. and b 142nd Ave

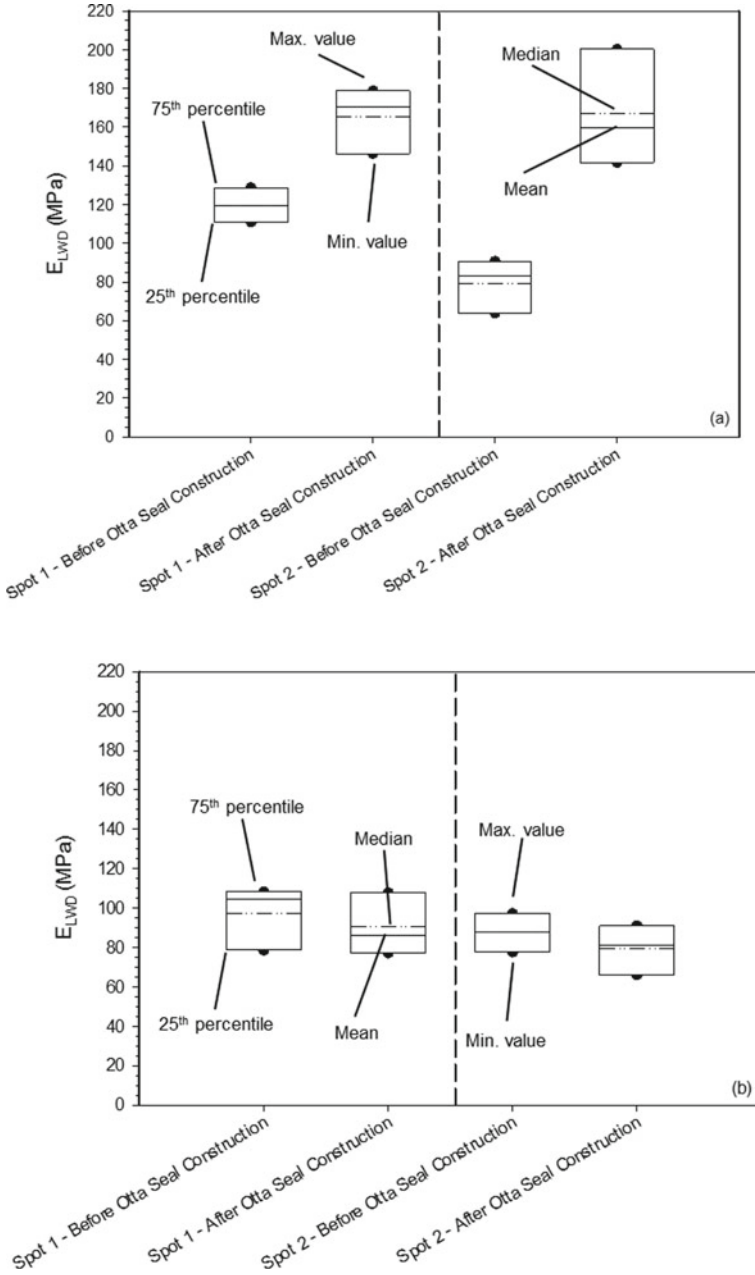


Fig. 7 LWD test results at different periods on a K Ave. and b 142nd Ave

Fig. 8 British pendulum test results on K Ave. and 142nd Ave



4 Conclusions

As a more cost-effective and durable bituminous surface treatment technology, Otta seal has been successfully implemented in many locations by using the local aggregates such as limestone and river gravel. This field study evaluated the performance of K Ave. and 142nd Ave. in Louisa County, IA which constructed Otta seal with local slag as the aggregate. The road appearance, IRI, dust control, and elastic modulus of subgrade were assessed in this study. The key findings are summarized as follows:

- Slag can be utilized in Otta seal surface treatment, even if its gradation does not meet the recommended dense criteria but meet the general gradation requirements. A short test section with 30.5 m (100 ft) prior to construction is recommended to validate the determined spreading rates of bitumen and aggregate are practical.
- Two roads in Louisa County, IA with slag-based Otta seal exhibited the excellent surface condition. There was no distress observed ten months after Otta seal construction and surface friction is still at a high level.
- Compaction is a key to implement Otta seal successfully. Proper compaction can produce a desired surface with lower IRI value. The compaction roller type and the amount compaction passes should be in accordance with the design guide [2].
- Otta seal by using slag has a significant benefit with respect to the reduction of surface dust. The excellent dust control can last over six months after Otta seal construction.
- Otta seal by using slag did not cause the deficiencies for pavement structures. Soil stabilization prior to Otta seal is strongly recommended because it can provide the desired foundation, improving the performance of Otta seal.

Acknowledgements The authors gratefully acknowledge sponsorship for this research study from the Iowa Highway Research Board (IHRB) and the Iowa Department of Transportation (DOT). The authors are also grateful to the Technical Advisory Committee members Paul Assman, Brandon Billings, Lee Bjerke, Scott Cline, Vanessa Goetz, Zach Gunsolley, Brian Keierleber, James D. King, Todd Kinney, Travis Malone, Brian Moore, Patrick Mouw, Tammy Nicholson, Larry Roehl, Joshua Sebern, David Shanahan, Francis Todey, Sarah Tracy, Danny Waid, and Jeff Williams for providing

their invaluable guidance in this study. The findings and opinions in this study are solely those of the authors. Endorsements by the IHRB or Iowa DOT are not implied and should not be assumed.

References

1. Overby C (1999) A guide to the use of Otta seals. Publication No. 93, Norwegian Directorate of Public Roads, Road Technology Department, International division, Oslo, Norway
2. Overby C, Pinard MI (2013) Otta seal surfacing: practical and economic alternative to traditional bituminous surface treatments. *Transp Res Rec J Transp Res Board* 2349:136–144
3. Ceylan H, Kim S, Zhang Y, Nahvi A, Gushgari S, Jahren CT, Gopalakrishnan K, Douglas D, Gransberg, Arabzadeh A (2018) Evaluation of Otta seal surfacing for low-volume roads in Iowa. Final Report, IHRB Project TR-674. Institute for Transportation, Iowa State University
4. Roy DM (1982) Hydration, structure, and properties of blast furnace slag cements, mortars, and concrete. *ACI J Proc* 79(6)
5. Prasad PS, Ramana GV (2016) Feasibility study of copper slag as a structural fill in reinforced soil structures. *Geotext Geomembr* 44(4):623–640
6. ASTM D5624-13 (2013) Standard practice for determining the transverse-aggregate spread rate for surface treatment applications
7. Roadroid. (Software). Available at <https://www.roadroid.com/>. Accessed on 1 May 2018
8. ASTM E303-93 (2013) Standard test method for measuring surface frictional properties using the British pendulum tester
9. Yang B, Zhang Y, Ceylan H, Kim S (2020) Evaluation of bio-based fog seal for low-volume road preservation. *Int J Pavement Res Technol* 1–10

The Key Technology of High-Speed Railway Foamed Lightweight Soil Subgrade



Jianping Yao, Degou Cai, Guanzhi Cheng, Si Li, and Jiao Xie

Abstract The demand for high-speed railways for new line access has gradually increased with the continuous expansion of the scale of China's high-speed railway network. It is necessary to solve the problem of settlement control of the existing station subgrade formation with the increased load of new line access. Foamed lightweight soil is a type of material formed by cement, foaming agent, and water hardened by physical and chemical actions. Featuring high strength and lightweight, it is used to widen the subgrade, which effectively solves the differential settlement and deviation caused by the traditional roadbed filling. Meanwhile, the roadbed treatment technology can be simplified, and the construction period can be shortened. In this paper, strength development mechanism and performance evolution law of foamed lightweight soil in China's high-speed railway, subgrade structure type and design method of foamed lightweight soil subgrade structure in high-speed railway, and application of high-speed railway subgrade widening engineering are introduced. The results show that as a new type of lightweight and high-strength subgrade structure, the foamed lightweight soil subgrade is an effective mean to solve the problem of settlement and deformation control of high-speed railway subgrade widening and also provides a new solution for settlement control of transition sections, soft soil subgrade, steep slope sections, and other sections.

Keywords High-speed railway · Foamed lightweight soil subgrade · Strength mechanism · Structural design · Settlement control

1 Introduction

It is necessary to widen the subgrade of the existing stations to enable the new lines to be connected to the existing high-speed railway network in the process of railway construction. The traditional subgrade filling method is difficult to solve the impact of subgrade widening on the settlement and deviation of existing station subgrade.

J. Yao · D. Cai · G. Cheng (✉) · S. Li (✉) · J. Xie
Railway Engineering Research Institute, China Academy of Railway Sciences Co. Ltd. Limited,
No. 2 Daliushu Road, Haidian District, Beijing, China
e-mail: chengguanzhi@163.com; tktzls@qq.com

© The Author(s), under exclusive license to Springer Nature Switzerland AG 2022
E. Tutumluer et al. (eds.), *Advances in Transportation Geotechnics IV*, Lecture Notes
in Civil Engineering 164, https://doi.org/10.1007/978-3-030-77230-7_37

489

Therefore, a lightweight and high-strength geotechnical material for subgrade filling should be developed. Foamed lightweight soil is a lightweight material which is prepared by turning a foaming agent aqueous solution into foam by physical methods and mixing with cement-based cementitious materials, water, optional component aggregates, mineral admixture, and additive in a certain proportion, which then hardens by physical and chemical actions. High-speed railway foamed lightweight soil subgrade is a new type, lightweight, and high-strength railway subgrade. The foamed lightweight soil prepared on site is poured into high-speed railway subgrade to fill all or part of the roadbed filler, to satisfy the material performance, structural type, stress characteristics, and durability index of high-speed railway. It can be used to solve the settlement and deformation control problems of subgrade widening engineering, transition sections, soft soil foundations, and steep slope sections of high-speed railway [1].

At present, mix ratio [2], pore structure [3], mechanical properties [4], thermal insulation performance [5], and durability [6] of foamed lightweight soil have attracted particular attention from scholars and have achieved considerable results. Cheng [7] studied the effects of different preparation parameters, such as water–binder ratio, wet density, and water-reducing agent, on the work performance and mechanical properties of the foamed lightweight soil. Wang [8, 9] studied the improvement effect of glass fiber and polypropylene fiber on the mechanical properties of foamed lightweight soil. Wang [10] and Yang [11] studied the endurance quality of foamed lightweight soil in different environments. Zhao and Deng [12, 13] studied and applied the treatment project of subgrade widening and soft foundation of high-speed railway. They have made an intensive study on the material properties, improvement methods and engineering applications of the foamed lightweight soil and put forward the possibility of the application of the foamed lightweight soil on the subgrade of high-speed railway, while the research direction is relatively single. To solve this problem, this paper put forward subgrade structure type and design method and analyzes the engineering case of width of foam light soil roadbed of high-speed railway based on the study of strength development mechanism and property evolution law of foam light soil.

2 Strength Development Mechanism and Performance Evolution Law

The foamed lightweight soil is a kind of porous Portland cement, and the physical and mechanical properties depend on the structure after maintenance, including the hole structure and the composition of the hole wall. The foam lightweight clay slurry is a non-equilibrium system whose internal structure changes with time until hardening completion, and the change process can be divided into three stages: (1) initial stage. The foamed lightweight soil is unsteady “gas–liquid–solid” three-phase system when the lightweight soil is pumped to the casting area, and the mechanical stability is

determined by the mechanical strength of foam; (2) reaction stage. With the end of the pouring process, the foamed lightweight soil gradually loses its fluidity under the action of cement hydration and the foamed lightweight soil transforms from the “gas–liquid–solid” three-phase system to the “gas–solid” two-phase system; (3) hardening stage. The state of the two-phase system of “gas–solid” foamed lightweight soil is basically stable in this stage, and the void structure is basically formed, which has a certain compressive strength, and the strength further develops slowly with the slow progress of hydration reaction.

2.1 Testing and Characterization

The flow factor, wet density, and wet density increase rate of the foamed lightweight soil mixture are determined with reference to the contents of Sects. 8.2 and 8.3 of the “Technical Regulations for Cast-in-Situ Foamed Light Soil” (CECS249-2008). During the measurement of the loss of working performance over time, the foamed lightweight soil was stirred in a cement foaming mixer at a rate of 60 r/min to a specific time point, and then samples were taken for measurement according to the above method. The specimens used for the mechanical performance test were prepared according to Sect. 8.1 of CECS249-2008, and the specimens were dried (60 °C) before the mechanical strength test. The compressive strength of the test piece was determined in accordance with the content of Sect. 7.3.3 in the standard “Foam Concrete” (JG/T 266–2011).

2.2 Basic Properties

When the water–binder ratio is 0.5, the wet density influences on foam light soil flow factor is shown in Fig. 1, and the wet density effect on the increase rate is represented in Fig. 2. Figure 1 indicates the value of foam light soil flow increases with the increase of wet density. It can be seen from Fig. 2 that the increase rate of wet density changed from negative to positive with the increase of wet density, and the increase rate of wet density of the mixture within 60 min is within 5%.

Water–binder ratio. The water–binder ratio effects on the flow factor of foamed lightweight soil is shown in Fig. 3, and the influence of water–binder ratio on the increase rate of wet density of foamed lightweight soil is presented in Fig. 4, when the wet density is 500 kg/m³. Figure 3 shows that the value of light foam soil flow increases with the increase of water–binder ratio, and the initial flow factor of the mixture changes little after water–binder ratio exceeds 0.55, which indicates that the value of light foam soil flow is insensitivity to the change of water–binder ratio under the condition of high water–binder ratio. It can be seen from Fig. 4 that the

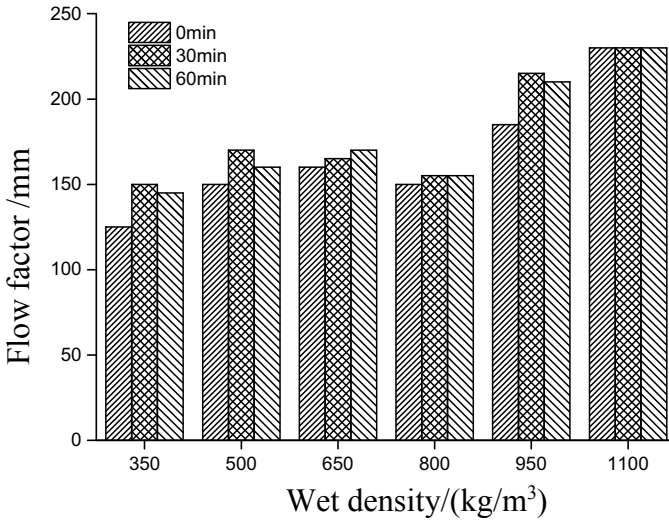


Fig. 1 Wet density influences on the mixture flow factor

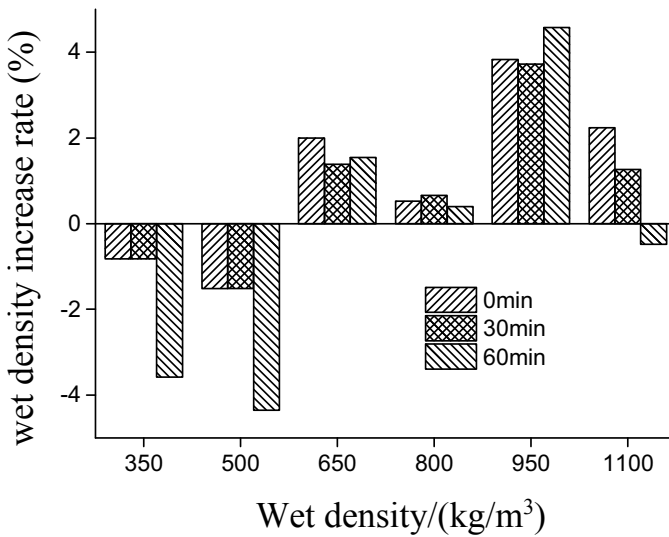


Fig. 2 Wet density influences on the increase rate of wet density of the mixing material

wet density increase rate of foamed lightweight soil fluctuates with the variation of water–binder ratio, while the wet density increase rate is all within $\pm 5\%$ in 60 min.

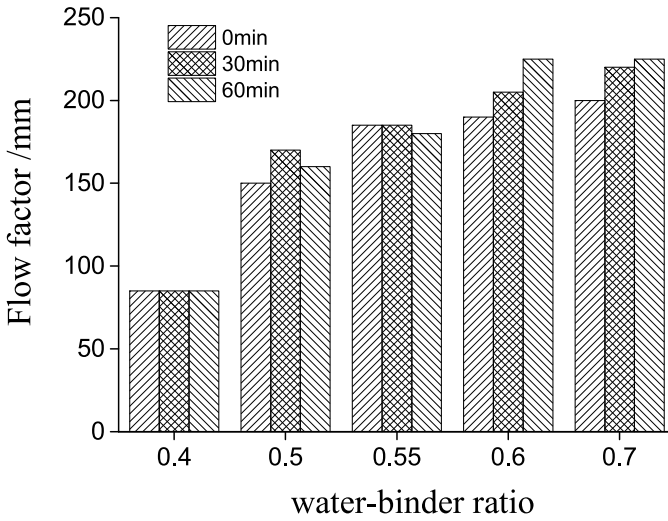


Fig. 3 Water-binder ratio influences on the mixing logistics value of foamed lightweight soil

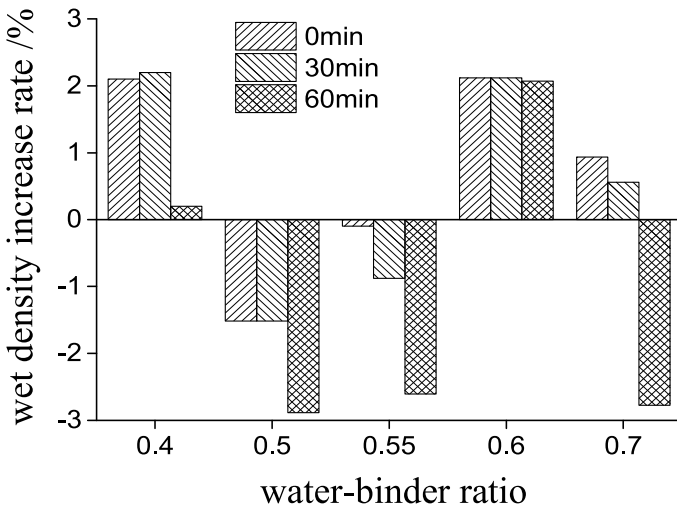


Fig. 4 Water-binder ratio influences on the increase rate of wet density of the mixture

2.3 Statics Performance

Wet density. As illustrated in Fig. 5, the influence of wet density of foamed lightweight soil on the compressive strength of specimens when the water-binder ratio is 0.5. The compressive strength of foamed lightweight soil specimens increases

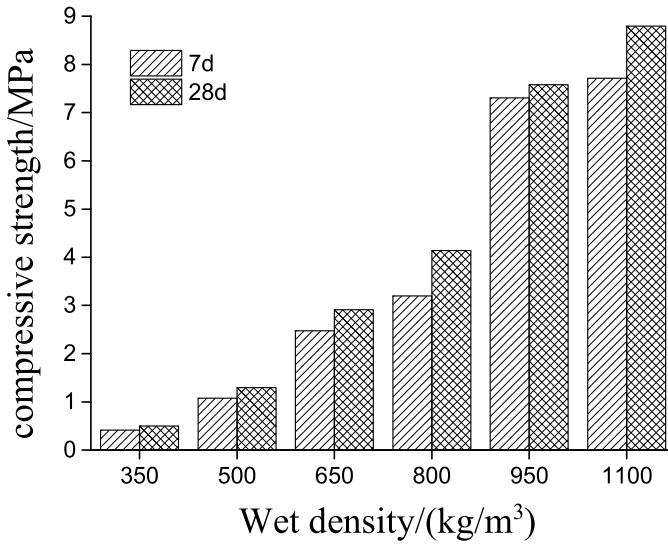


Fig. 5 Wet density effects on compressive strength of specimens

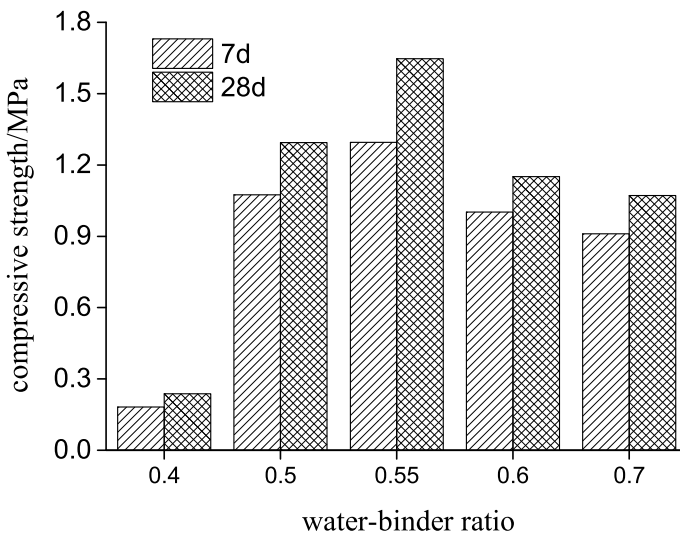


Fig. 6 Water-binder ratio effects on compressive strength of specimens

with the increase of wet density within the wet density range of 350–1100 kg/m³. The compressive strength of specimens had exceeds 1 MPa as the wet density reaches 500 kg/m³.

Water–binder ratio. Figure 6 presents the influence of water–binder ratio on compressive strength of the specimens when wet density is 500 kg/m^3 , which indicates the compressive strength of foamed lightweight soil shows the tendency of increase initially and then decrease with the increase of water–cement ratio. The highest compressive strength of foamed lightweight soil appears at the water–cement ratio of 0.55, which is related to the combined effect of water on the performance and hydration of foamed lightweight soil. When the water gel is relatively low, the workability of foamed lightweight soil is poor and the slurry is easy to occur uneven mixing phenomenon, which leads to the stress concentration point and lower intensity. When the ratio of water–binder is suitable, the performance of foamed lightweight soil is well, and the hydration reaction of cement with the corresponding age is more sufficient, so that the compressive strength is higher. The mixture and workability become worse, the impact on the strength of the test piece exceeds the impact on the cement hydration, making the compressive strength reduces as the water consumption increase continuously.

3 Subgrade Structure Type and Design Method

3.1 Subgrade Structure Type

The subgrade structure type is determined by the requirements from structure application. There are four typical types of foamed lightweight soil subgrade structure, including subgrade widening, transition section, soft soil subgrade, and steep slope section. While designing, the foamed lightweight soil is used to replace part or all of the original filler in the subgrade to reduce subgrade load and the difficulty of foundation treatment. It can solve the problem of subgrade settlement and deviation control effectively. However, the original subgrade design pattern is not changed (Figs. 7, 8, and 9).

3.2 Key Points of Design

The railway subgrade is the foundation of the track, and the main function is to satisfy the laying of the track, bear the load of the track and the train, and provide the necessary conditions for the train operation. The subgrade is subjected to both dynamic and static loads. The foamed lightweight soil subgrade should consider the design shape of embankment, external conditions and loading conditions, refer to similar engineering experience, use the stress compensation (or stress replacement) principle to determine the wet density and compressive strength, so as to check the overall stability of the casting body and subgrade and the settlement deformation of the foundation. In particular, whether the wet density and compressive strength of

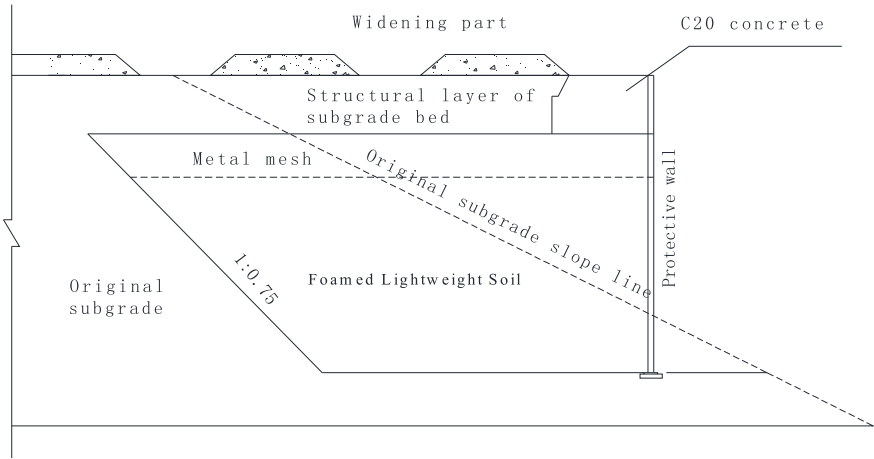


Fig. 7 Structure type of subgrade widening

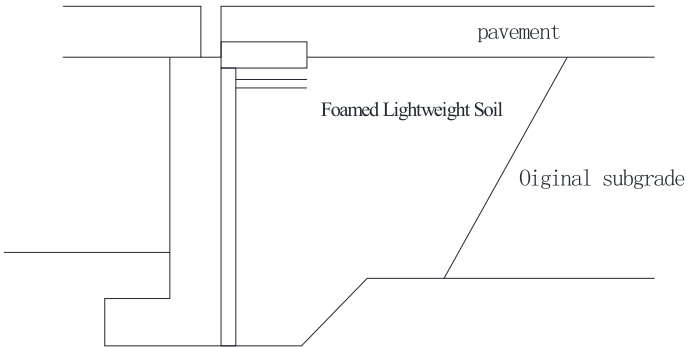


Fig. 8 Structure type of transition section

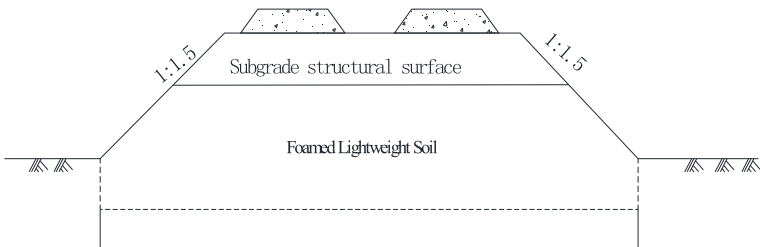


Fig. 9 Soft soil subgrade structure type

each roadbed fill site fulfill the design conditions and material requirements should be considered. The key points of design are: (1) Design the shape of the foamed lightweight soil subgrade, which includes the width and height of the embankment, the slope ratio of the connection between the foam light earth and the conventional filled embankment, and the adjustment steps of the vertical and horizontal slope on the top of the embankment; (2) Determine the bulk density and compressive strength of the foamed lightweight soil and calculate the mixture ratio; (3) Check the self-strength to meet the bearing capacity requirements of various parts of the embankment; (4) Stability check calculation, including foundation stability check and some cases (such as broad road embankment, retaining wall back, and abutment back) anti-sliding and anti-overturning check calculation of foamed lightweight soil embankment; (5) Consider the effects of buoyancy and water absorption on the increase in bulk density when the foamy light soil is below the groundwater level or is flooded; (6) Check foundation settlement to verify whether to fulfill the post-construction settlement requirements.

3.3 Design Parameter

There are two main functions of the surface layer of the subgrade bed, one is to provide a solid foundation for the track structure, and the other is to provide protection for the subgrade. The surface strength of the subgrade bed shall be designed according to the ultimate bearing capacity and meet the requirements of the following formula,

$$r_0 r_f \sigma \leq R / r_R$$

where r_0 is structural importance coefficient, is 1.0; r_f is partial train load coefficient, is 1.3; σ is dynamic stress of surface layer of the subgrade bed, kPa; R is carrying capacity of surface layer of the subgrade bed, kPa; r_R is partial carrying capacity coefficient of surface layer of the subgrade bed, is 2.0.

When the design speed of ballast track is not less than 300 km, and the axle weight of passenger car is 20 T, $R \geq 256.8$ kPa [14]. Considering the long-term service performance of the foamed lightweight soil subgrade, the recommended strength and density of the foam light soil subgrade under freezing–thawing and non-freezing–thawing conditions are listed in Tables 1 and 2, respectively.

4 Application of Subgrade Widening Engineering

It is necessary to widen the subgrade of Xinzhou West Railway Station as the Xiong'an-Xinzhou high-speed railway is connected to the Datong-Xi'an high-speed railway at the Station. In order to avoid the influence of subgrade settlement caused

Table 1 Recommended strength and density of foamed lightweight soil subgrade in non-freezing–thawing environment

Position	Design load		Reduction coefficient		Material strength reduction coefficient	Designed value of strength (MPa)	Proposal density (kg/m ³)
	Design value of static load (kPa)	Design value of dynamic load (kPa)	Dynamic load	Immersion/wet cycle			
Surface layer of subgrade bed	65	100	0.3	0.6	0.5	1.1	≥700
Bottom layer of subgrade bed	110	20	0.6	0.6	0.5	0.45	≥550
Subgrade ontology	130	10	/	0.6	0.5	0.4	≥500

by excessive water, the deviation on existing subgrade caused by lateral pressure, and the cracking risk caused by large-volume cement hydration heat, the subgrade widening design is partition layered pouring by foamed lightweight soil. The cross section of a typical foamed lightweight soil subgrade is drawn in Fig. 10.

The surface layer of foamed lightweight soil subgrade bed is graded aggregate. The bottom layer of the subgrade bed is filled with high-strength foamed lightweight soil which wet density is 700–800 kg/m³ and mixes with 0.4–0.6% of high dispersion alkali resistant glass fiber, $q_{u7d} \geq 0.8$ MPa, $q_{u28} \geq 1.5$ MPa. The subgrade is filled with ordinary foamed lightweight soil which wet density is 550–650 kg/m³, $q_{u7d} \geq 0.6$ MPa, $q_{u28} \geq 1.2$ MPa. High-performance foaming agent is used for foam preparation, which foaming agent dilution ratio is ≥ 50 , prepared foam density is at the range of 40–60 kg/m³, foam standard sedimentation rate is $\leq 1\%$, 1 h bleeding rate is $\leq 60\%$ at 25 °C. As the maximum freezing depth of soil is 1.21 m, the quality loss of ordinary foamed lightweight soil should not be more than 18% after 15 freeze–thaw circulation, and the strength loss of dry and wet soil should not be more than 20% after 15 circulation, and the mass loss of high-strength foamed lightweight soil should not be greater than 2.5% after 25 freeze–thaw cycles. The site construction is shown in Fig. 11.

The successful application of the foamed lightweight soil in the Xiong'an-Xin Zhou high-speed railway connected to the Daxi high railway foundation project significantly reduces the impact of the subgrade on the operation of the existing Daxi high-speed railway line and reduces the subsidence and partiality caused by subgrade widening to the Daxi high-speed railway line effectively and guarantees the long-term safe service of the Daxi high-speed railway line.

Table 2 Recommended strength and density of foamed lightweight soil subgrade in freezing–thawing environment

Position	Design load		Reduction coefficient			Material strength reduction coefficient	Designed value of strength (MPa)	Proposal density (kg/m ³)
	Design value of static load (kPa)	Design value of dynamic load (kPa)	Dynamic load	Immersion/wet cycle	Freeze–thaw cycles			
Surface layer of subgrade bed	65	100	0.3	0.6	0.75	0.5	1.5	≥800
Bottom layer of subgrade bed	110	20	0.6	0.6	0.75	0.5	0.6	≥650
Subgrade ontology	130	10	/	0.6	0.8	0.5	0.5	≥550

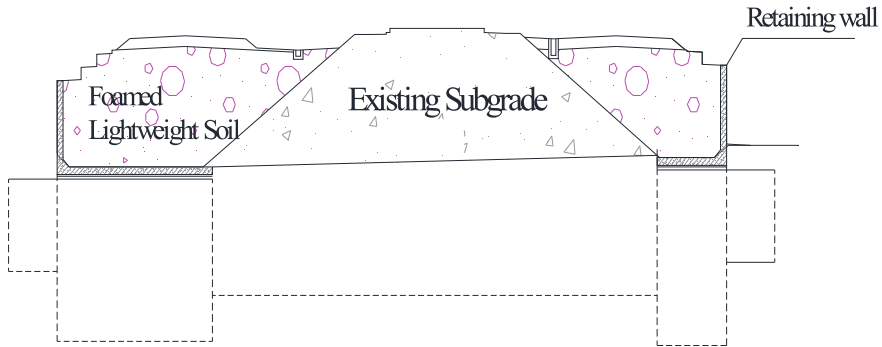


Fig. 10 Schematic diagram of cross section of a typical foamed lightweight soil subgrade



Fig. 11 Site construction picture of foamed lightweight soil subgrade widening

5 Conclusion

As a lightweight and high-strength geotechnical material, foamed lightweight soil can effectively solve the problems of settlement and migration caused by traditional methods in the filling of high-speed railway subgrade. It has important application value on roadbed widths, transition sections, soft soil roadbed, and steep slope sections.

- (1) The value of light foam soil flow increases with the increase of water–binder ratio when the wet density is 500 kg/m^3 . The value of light foam soil flow is insensitive to the change of water–binder ratio under the condition of high water–binder ratio after the water–binder ratio exceeds 0.55, while the wet density increase rate is all within $\pm 5\%$ in 60 min. The strength shows the tendency of increase initially and then decrease with the increase of water–cement ratio. The compressive strength of foamed lightweight soil specimens increase with the increase of wet density within the wet density range of $350\text{--}1100 \text{ kg/m}^3$. The compressive strength of foamed lightweight soil specimen shows the tendency of increase initially and then decreases with the increase of water–cement ratio. The compressive strength of foamed lightweight soil is highest at the water–cement ratio of 0.55.

- (2) The subgrade structure types and design of different sections such as subgrade widening, transition section, soft soil subgrade, and steep slope section are proposed. The recommended density of the surface layer of the subgrade bed, the bottom layer of the subgrade bed, and the basic body of the subgrade in the non-freezing and thawing environment are not less than 700 kg/m^3 , 550 kg/m^3 , and 500 kg/m^3 , respectively. The recommended densities in the freezing and thawing environment are not less than 800 kg/m^3 , 650 kg/m^3 , and 550 kg/m^3 , respectively.
- (3) The case study of Xinzhou west railway station on Xiongxin high-speed railway determines the design scheme which the surface layer of foamed lightweight soil subgrade bed is crushed and filled with graded gravel, the bottom layer of the subgrade bed is filled with high-strength foamed lightweight soil with a wet density of $700\text{--}800 \text{ kg/m}^3$ (mixes with 0.4–0.6% of high dispersion alkali resistant glass fiber) and the subgrade body is filled with ordinary foamed lightweight soil with a wet density of $550\text{--}650 \text{ kg/m}^3$. The case provides reference for other similar projects.

References

1. Li S, Yao JP, Pang S et al (2019) Key control technology for construction of lightweight soil subgrade in high speed railway. *Railway Constr* 59(01):68–71
2. Deng F (2018) Application of foamed lightweight soil in foundation treatment of soft soil road base of hangzhou east railway station. *Railway Stan Des* 3:31–35
3. Ghorbani S et al (2019) Effect of magnetized water on foam stability and compressive strength of foam concrete. *Constr Build Mater* 197:280–290
4. Just A, Middendorf B (2009) Microstructure of high-strength foam concrete. *Mater Charact* 60(7):741–748
5. Li P et al (2005) Preparation and optimization of ultra-light and thermal insulative aerogel foam concrete. *Constr Build Mater* (2005):529–542
6. She W, Chen Y, Zhang Y et al (2013) Characterization and simulation of microstructure and thermal properties of foamed concrete. *Constr Build Mater* 47:1278–1291
7. Tikalsky P, Pospisil J, Macdonald W (2004) A method for assessment of the freeze–thaw resistance of preformed foam cellular concrete. *Cem Concr Res* 34(5):889–893
8. Cheng GZ (2017) Effect of preparation parameters on working performance and mechanical properties of foamed lightweight soil. *Railway Archit* 1:56–60
9. Zhao WH, Su Q, Li T et al (2017) Experimental study on mechanical properties of glass fiber reinforced foam lightweight concrete. *Ind Build* 47(9):110–114
10. Wang WB, Zhao WH, Su Q et al (2017) Experimental study on mechanical properties of polypropylene fiber-reinforced foam lightweight concrete. *Railway Constr* 2:146–150
11. Wang LJ, Ye YS, Zhang QL et al (2017) Experimental study on the flooding performance of foamed lightweight soil. *Railway Constr* 1:103–106
12. Yang WP (2017) Experimental study on durability of lightweight foam soil. *Commun Sci Technol Hunan* 43(2):99–101
13. Zhao XY (2016) Application of bubble lightweight soil in existing high-speed railway roadbed widening project. *Railway Archit* 6:96–98
14. National Railway Administration of the People's Republic of China (2016) Railway subgrade design code. China Railway Publishing House Co. LTD, Beijing, pp 51–52

Field Scale Trial of Fibre-Reinforced Ballast



Geoff Watson , Edgar Ferro , Louis Le Pen , David Milne ,
Tristan Rees White , and William Powrie 

Abstract Rail infrastructure companies spend a substantial proportion of their operating budget on track maintenance and renewal. This could be reduced by extending the life and/or the maintenance interval of ballasted track and minimizing service disruption. A possible means to achieve this is with a fibre-reinforced ballast. Fibre-reinforced ballast is created by randomly introducing fibres to the granular matrix. If appropriately sized, these fibres may be held between grains and develop tensions that increase the effective confining pressure on the assembly. Previous laboratory research has shown that the addition of specific types, quantities and dimensions of fibres can increase the peak strength and reduce settlements of railway ballast. Based on laboratory test results, a field trial has been carried out at a site on a UK mass transit railway. The site was due for trackbed renewal which offered the opportunity to reinforce the replacement ballast with fibres consisting of polyethylene strips 300 mm × 25 mm × 0.5 mm at a concentration of 670 fibres per tonne of a standard ballast gradation. At the trial site, fibre-reinforced ballast was placed along a 48 m length. A further length was renewed with unreinforced ballast as a control. Following the installation, measurements of dynamic track movements as trains pass using a high-speed camera and digital image correlation were carried out on two visits. This paper presents an evaluation of the post-installation monitoring data. Results confirm that the fibre-reinforced ballast performs at least as well as the control section of track.

Keywords Ballast · Fibres · Maintenance

G. Watson (✉) · L. Le Pen · D. Milne · T. R. White · W. Powrie
Infrastructure Research Group, School of Engineering, University of Southampton, Building 178,
Burgess Road, Southampton SO16 7QF, UK
e-mail: g.watson@soton.ac.uk

E. Ferro
Department of Civil Environmental and Mechanical Engineering, University of Trento, via
Mesiano 77, 38123 Trento, Italy

1 Introduction/Background

Rail infrastructure companies spend a substantial proportion of their operating budget (e.g., £4.1 billion or 37% in 2016/2017 in the case of Network Rail, UK; €1.9 billion in 2016 in the case of Rete Ferroviaria Italiana (RFI), Italy [1] and \$27.1 billion in the US in 2015 [2]) on track maintenance and renewal. Conventionally ballasted railway tracks settle differentially along their length leading to a loss of alignment and level that needs to be corrected, usually by mechanical tamping. Tamping is a process whereby a specialized plant vehicle measures and lifts the track to its intended geometry, and then, using vibrating tines, tamps/squeezes ballast into position beneath sleepers (Fig. 1), to support them at their corrected level [3]. However, the accumulation of damage to the trackbed through trafficking and tamping leads to a diminishing return. For example, from placement, a new track could deteriorate geometrically to a point requiring maintenance after 4 years initially. However, the next maintenance interval may be 3.5 years with the return diminishing at each maintenance cycle, so that at some point the trackbed requires more comprehensive treatment such as by ballast cleaning or eventually, complete renewal. If it were possible to increase the intervals between maintenance tamps by even a small amount, this could result in substantial savings and prolong the life of the trackbed.

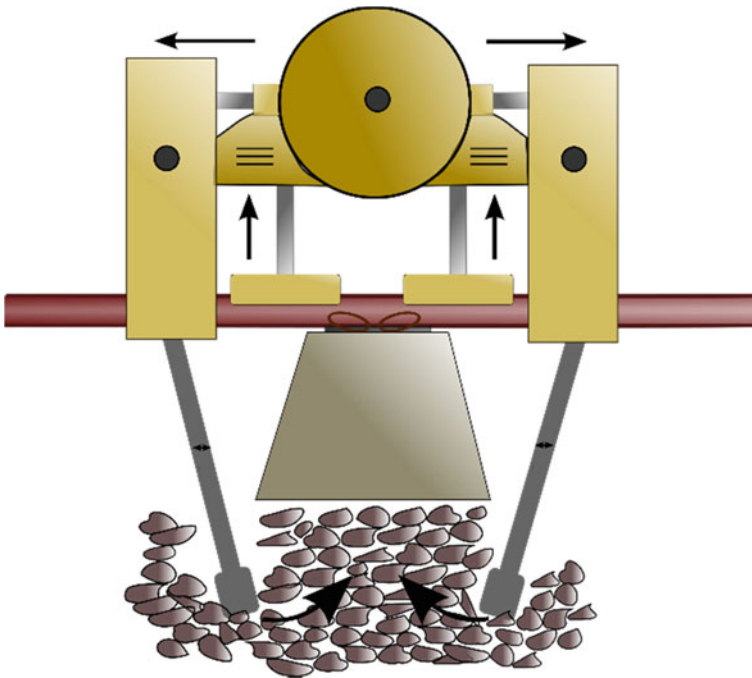


Fig. 1 Schematic showing the tamping mechanism (modified after [2])



Fig. 2 Photographs of the SRTF during preparation (a) and ready for testing (b)

Previous work used triaxial tests to identify scaling relationships for the optimal selection of fibres [3, 4]. Full-size laboratory testing of the most promising fibre dimensions was then carried out using the Southampton Railway Testing Facility (SRTF), shown in Fig. 2. This represents a single sleeper bay on a ballast bed deforming in plane strain, with the sleeper subjected to cyclic loading representative of a 20 tonne train axle [5–7].

The fibres used were formed from strips of polyethylene, 0.5 mm thick, pre-cut to the desired dimensions. These were mixed into the ballast prior to placement into the testing rig.

Figure 3 shows settlement results from the SRTF for the optimal fibre mix and a baseline test for comparison. In these tests, 3 million cycles of a 20 tonne equivalent axle load were applied at 3 Hz. The x-axis shows the number of load cycles on a logarithmic scale and the y-axis shows the permanent settlement of the ballast layer. The baseline test was carried out on standard ballast with a G44¹ sleeper. The optimal fibre dimensions were 300 mm × 25 mm × 0.5 mm at a volume fraction (defined as the ratio of the volume of fibres to the volume of ballast grains) of 0.65%. In practice this meant 670 fibres per tonne of ballast assuming a ballast bulk density of 1600 kg/m³. The addition of fibres to a granular material tends to increase the void ratio and may reduce the stiffness [8–10]. However, owing to the narrow geometry and very small thickness, these fibres do not inhibit the packing of the ballast grains

¹ G44 sleepers are pretensioned, steel reinforced, concrete sleepers (ties). The major dimensions are 2500 mm long and 285 mm wide, with a height of 200 mm at the rail seat. They are a common sleeper used in UK track renewals and are comparable with national counterparts globally.

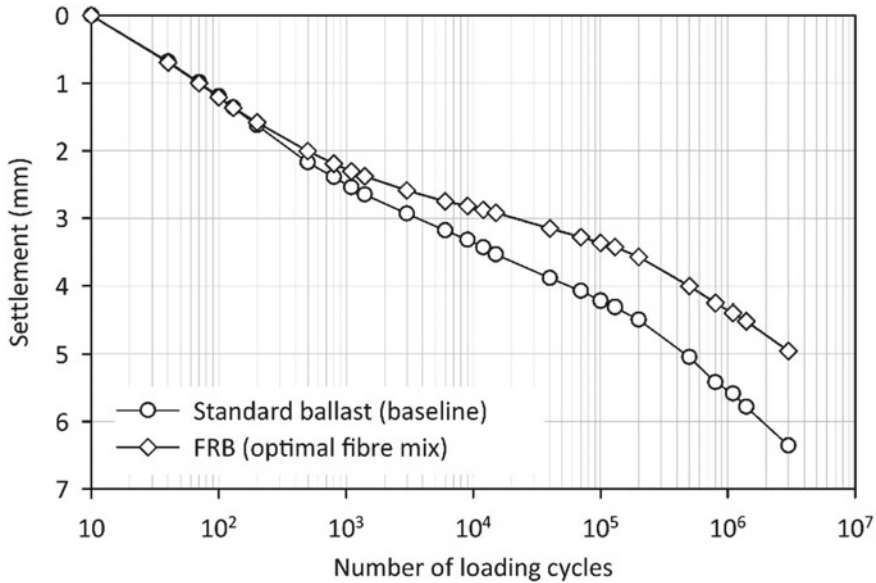


Fig. 3 Full-size laboratory test results for ballast reinforced with optimal fibre mix (polyethylene plastic strips 300 mm × 25 mm × 0.5 mm at 0.6% volume fraction)

and hence are not expected to reduce ballast stiffness, while they have the potential to reduce the permanent settlement [11, 12].

Figure 3 shows that the FRB reduced the settlement from 6.3 to 5.0 mm at 3 million cycles. This is a reduction of ~25%. The relationship between individual settlement tests and along the track differential settlement is unclear and likely to be complex. However, in principle, if the ballast layer is less susceptible to settlement at each sleeper location, then the potential for differential settlement originating from the ballast layer should also reduce. It is in part this lack of a direct link between single sleeper/ballast settlement and differential settlement that necessitates field trials to quantify any potential benefit over the life cycle of a trackbed.

Based on the laboratory testing, a field trial was planned using the fibre dimensions and proportions identified as optimal. This paper presents results from two site monitoring visits carried out within the first 14 months after installation.

2 The Site

A section of a mass transit urban line in North London was selected for the trial, mainly because it was about to be renewed and offered a suitable site with reasonable access. New rails, sleepers and ballast were placed on a 500 m length of one line on the twin track route in May 2017. A section of the renewal formed a 48 m long FRB

trial. This trial length was on an embankment between two underbridges as shown in Fig. 4.

2.1 Ground Conditions

The 48 m trial site is situated on an embankment, between two underbridges. At the south-eastern end of the site, a masonry bridge crosses a road. At the north-western end of the site, there is a bridge that enables pedestrians to cross under the railway. This section of track was originally built in the 1920s. The British Geological Survey (BGS) maps and nearby borehole logs show the embankment to be underlain by stiff brown and grey clays of the London Clay formation. Site investigation records, not in the public domain, show that the embankment is constructed of firm clay.

2.2 Method for Mixing Fibres with Ballast

For the trial, 120 tonnes of ballast were mixed with 80,520 fibres, to give approximately 670 fibres per tonne. The mixing was carried out at a depot (Fig. 5) in stages: (1) suitable proportions of ballast and fibres were placed. (2) The materials were mixed using a crane-mounted grab until the fibres appeared to be well mixed. (3) The mixed batch was moved to the back of the loading bay and the process repeated until complete. The ballast mixture was stored at the depot, and trains were loaded some time later. A thin layer of ballast was placed on top of the FRB after loading into the wagons, so that fibres near the surface would not be blown away in transit.

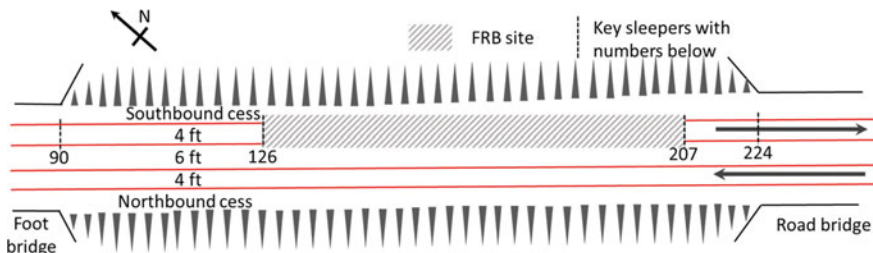


Fig. 4 Site plan including UK rail nomenclature.² The south-eastern end is on the right

² When there are two tracks the term ‘6 ft’ (‘6 foot’) refers to the space between the two lines, 6 ft is not an actual measurement although 6 feet or approximately 1.8 m is the approximate distance between the two adjacent inner rails of the two lines. The term ‘cess’ refers to the area outside of either line. The term ‘4 ft’ (‘4 foot’) refers to the space between the running rails (gauge). The actual gauge is 1,435 mm (4 ft 8½ in).



Fig. 5 Fibres being mixed with ballast at a depot

If the use of FRB were to become commonplace, fibres could be introduced at the quarry to ensure a uniform mix quality and density.

3 Performance Monitoring—Methods

Owing to the low train speeds at the site, (48 km/h or 30 mph) track movement was measured by high-speed filming with digital image correlation (DIC) [13–16].

The equipment used comprised a USB 3 camera (IDS uEye 337) (Fig. 6a) with a data transfer rate of up to 320 MB/s connected to a laptop PC. The camera sensor has a resolution of 2048×2048 pixels and a frame rate of 75 fps (frames per second) at full resolution. By only capturing data from part of the sensor, known as the area of interest (AOI), the frame rate can be increased dramatically (e.g., 300 fps for 640×480 and 1000 fps or more for smaller areas). Typically, data for a single target can be captured at up to 500 fps provided there is sufficient light. To aid the analysis and provide a reference for scaling it is usual (though not necessary) to attach square, textured targets to the sleeper ends (Fig. 6b).

The PC captures the data as an AVI format video file, which is then converted to a series of jpeg images for analysis. Analysis was carried out using a digital image correlation technique [13], in which patterns are matched across frames using normalized cross-correlation. This assumes that the pattern is approximately constant between successive images and that the local textural information is unique.

There are four main causes of noise in the calculated deflections:

- Deflections being too small compared with the size of each pixel
- Ground-borne vibration
- Wind caused by weather and/or the passing of a train
- Heat haze generated by the rails during hot and sunny weather.



Fig. 6 Photographs of the camera setup (a) and targets on sleeper end and rail web (b)

Controlling these potential sources of error is essential if acceptable data are to be obtained, and the difficulty in achieving this tends to increase with train speed. For digital image correlation, the camera position or lens used should be chosen such that the target movement during train passage is sufficient (10–20 pixels).

At this site, the camera was set up in the northbound cess (Fig. 6a) with targets installed on the southbound sleeper ends in the 6 ft (Fig. 6b) as there was insufficient room in the southbound cess owing to the proximity of the cable carriers to the track. The distance between the camera and the track reduced both ground-borne vibration and wind buffeting due to the passage of trains [13, 14] but meant that the line of sight crossed multiple rails. High frequency noise in the data is reduced by low pass Butterworth filtering to give a cleaner signal. The DIC targets used were 50 mm squares on sleeper brackets and 70 mm squares attached to the rail using double-sided tape or glue.

4 Monitoring Visits and Data Gathered

The site was monitored twice, 6 and 14 months after renewal.

All trains were 6 cars, made up of two three-car units each consisting of a driving motor car (DMC-29.4 t), a trailer car (TC-21.5 t) and an uncoupling non-driving motor car (UNMC-27.9 t).

A typical time deflection trace from the high-speed filming with DIC is shown in Fig. 7.

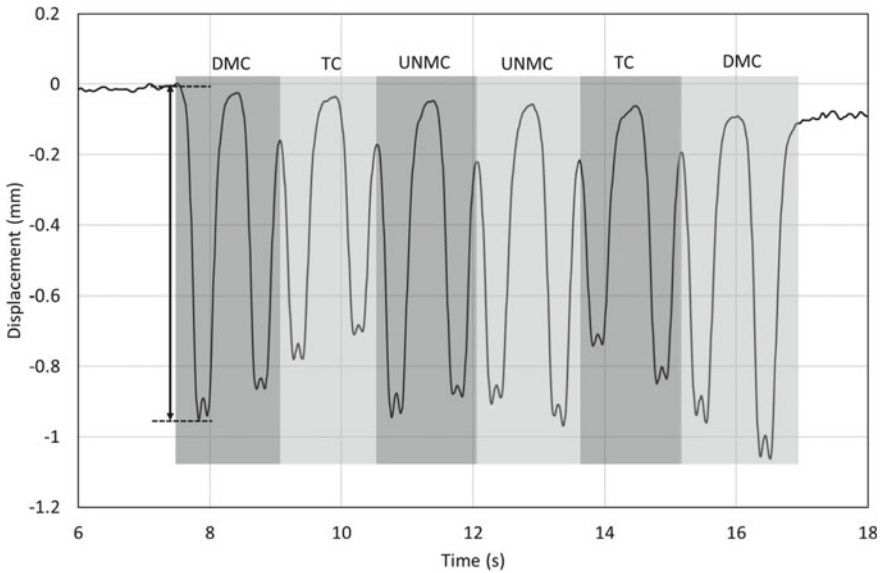


Fig. 7 Typical DIC trace for a 6 car train. This plot is from sleeper 144 and is low pass filtered at 8 Hz with a fourth-order Butterworth filter. A characteristic deflection used in later comparisons is indicated by the arrowed vertical line. Each car is shown by a grey rectangle

5 Results

At each visit (6 and 14 months) a number of trains were monitored (47 and 79, respectively) with the camera moved along the track to capture multiple locations. As each train was of the same type, these data can be combined to create a plot of characteristic sleeper deflection by sleeper location. The characteristic deflection has been taken as the difference between the maximum deflection in the first bogie pass and the lowest point in the trough before initial uplift (as shown in Fig. 7). In each case, data were taken from a plot which had been low pass filtered at 8 Hz using a fourth order Butterworth filter to remove high frequency noise not relevant to the major trackbed motions. Results from the two visits are shown in Fig. 8, and Table 1 shows the statistical data for the FRB and non-FRB sections for each visit. Table 1 shows that the two sections of track produce similar results in terms of the mean, maximum, minimum, standard deviation, and first and third quartiles. This suggests that the performance across the sections is similar and that the performance has remained unchanged between the two visits.

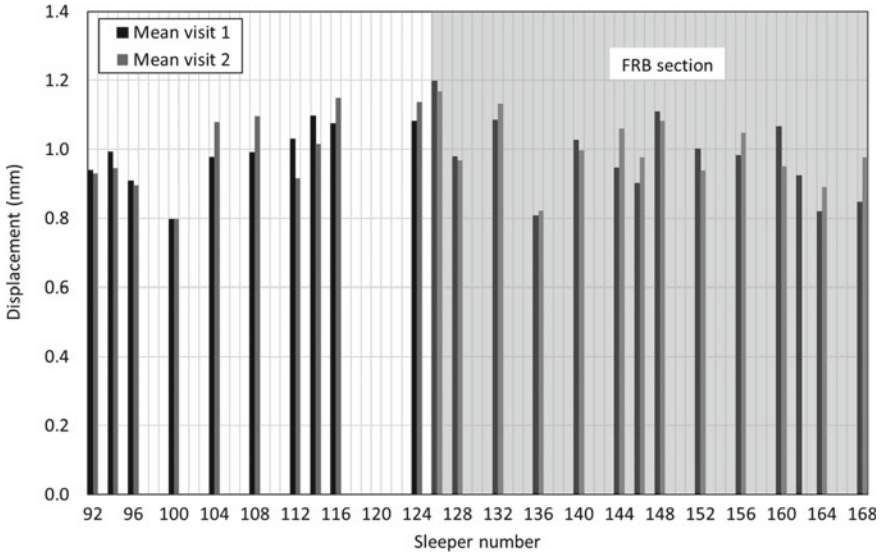


Fig. 8 Displacement data from the DIC measurements in visits 1 and 2. All sleepers in the shaded area are in the FRB test section

Table 1 Analysis of data from both visits by section

Visit	Non-FRB		FRB	
	1	2	1	2
Mean	1.00	0.99	0.98	0.99
Max	1.13	1.15	1.24	1.17
Min	0.80	0.80	0.81	0.82
SD	0.10	0.11	0.12	0.10
1st quartile	0.95	0.92	0.91	0.94
3rd quartile	1.06	1.09	1.06	1.06

6 Discussion

The movements of the sleepers have not changed significantly between the two visits, and the dynamic responses of the sections with and without FRB were very similar on both occasions (Fig. 8). As was expected on the basis of the laboratory tests, the addition of narrow fibres has not affected the stiffness of the ballast bed and is therefore compatible with railway track requirements in terms of its dynamic performance. However, the ability of FRB to reduce the long-term settlement cannot yet be assessed. The small difference in track response between the two visits indicates that, thus far, the sleepers have maintained relatively uniform contact with the trackbed

along the length of the trial site, with negligible adverse effect from differential settlement. Given the recentness of the renewal and the relatively low axle loads (7.35 t maximum unladen weight), this is to be expected. However, as further monitoring visits occur and more data become available, it should be possible to evaluate the longer-term performance of the FRB compared with the classically ballasted track.

It is planned to visit the site again in the near future to repeat the dynamic monitoring and compare the results with other conventional measures of track condition.

Acknowledgements The authors are grateful for the financial support of the Engineering and Physical Sciences Research Council (EPSRC) through the programme grant Track to the Future (EP/M025276/1) and Network Rail through the University Research Partnership in Future Infrastructure Systems. The authors are also grateful for the support of the infrastructure owner, Transport for London (TfL), particularly Stephen Barber, for, enabling the trials to take place.

References

1. Camera dei Deputati: Schema di contratto di programma 2016–2021—parte servizi tra il Ministero delle infrastrutture e dei trasporti e la società Rete ferroviaria italiana Spa (374). url <http://documenti.camera.it/apps/nuovosito/attigoverno/Schedalavori/getTesto.aspx?file=0374.pdf&leg=XVII#pagemode=none> (2017)
2. American Society of Civil Engineers: 2017 Infrastructure report card. url <https://www.infrasctructurereportcard.org/wp-content/uploads/2017/01/Rail-Final.pdf> (2017)
3. Aingaran S, Le Pen L, Zervos A, Powrie W (2018) Modelling the effects of trafficking and tamping on scaled railway ballast in triaxial tests. *Transp Geotech* 15:84–90. <https://doi.org/10.1016/j.trgeo.2018.04.004>
4. Ajayi O, Le Pen L, Zervos A, Powrie W (2016) A behavioural framework for fibre reinforced gravel. *Géotechnique* 67(1):56–68. <https://doi.org/10.1680/jgeot.16.P.023>
5. Ajayi O, Le Pen L, Zervos A, Powrie W (2017) Scaling relationships for strip fibre reinforced aggregates. *Can Geotech J* 54(5):710–719
6. Abadi T, Le Pen L, Zervos A, Powrie W (2016) Improving the performance of railway track through ballast interventions. *Proc Inst Mech Eng Part F J Rail Rapid Transit* 1–17. <https://doi.org/10.1177/0954409716671545>
7. Abadi T, Le Pen L, Zervos A, Powrie W (2019) The effect of sleeper interventions on railway track performance. *J Geotech Geoenviron Eng* 145(4):1–14. [04019009]. [https://doi.org/10.1061/\(ASCE\)GT.1943-5606.0002022](https://doi.org/10.1061/(ASCE)GT.1943-5606.0002022)
8. Dos SS, Consoli NC, Baudet BA (2010) The mechanics of fibre-reinforced sand. *Geotechnique* 60(10):791–799
9. Lirer S, Flora A, Consoli NC (2012) Experimental evidences of the effect of fibres in reinforcing a sandy gravel. *Geotech Geol Eng* 30:75–83
10. Ajayi O, Le Pen L, Zervos A, Powrie W (2014) Effects of random fibre reinforcement on the density of granular materials. In: *International symposium on geomechanics from micro and macro*, Cambridge, UK, pp 1363–1367
11. Ferro E, Ajayi O, Le Pen L, Zervos A, Powrie W (2016) Settlement response of fibre reinforced railway ballast. In: *11th world congress on railway research (WCRR2016)*
12. Ferro E (2018) The mechanical behaviour of fibre reinforced railway ballast. University of Southampton, Doctoral Thesis, p 230

13. Bowness D, Lock AC, Powrie W, Priest JA, Richards DJ (2007) Monitoring the dynamic displacements of railway track. *Proc Inst Mech Eng Part F (Journal of Rail and Rapid Transit)* 221:13–22
14. Le Pen L, Watson GVR, Powrie W, Yeo G, Weston P, Roberts C (2014) The behaviour of railway level crossings: insights through field monitoring. *Transp Geotech Special Issue Rail Geomech*
15. Murray CA, Take WA, Hout NA (2014) Measurement of vertical and longitudinal rail displacements using digital image correlation. *Can Geotech J* 52:141–155
16. Bhandari A, Powrie W, Harkness R (2012) A digital image-based deformation measurement system for triaxial tests. *ASTM Geotech Test J* 35:209–226

Mechanical Performance of Tire-Derived Aggregate Permeable Pavements Under Live Traffic Loads



Ramin Raeesi , Amin Soltani , Russell King, and Mahdi M. Disfani 

Abstract Traditional pavements in urban areas are mainly rigid, impervious surfaces, resulting in augmented surface run off during rainfalls, thereby leading to flash-flooding and pollution of waterways. In comparison, permeable pavements permit percolation of water through surface layers, thus alleviating harmful environmental impacts. This study presents the authors' recent experience in the development of an instrumented large-scale permeable pavement trial site—constructed using a combination of crushed rock (CR) and tire-derived aggregate (TDA), bonded by a polyurethane (PU) binder—located at a car park in South Australia. An area of approximately 400 m² was paved using different TDA-based mix designs—different CR sizes, colors, and shapes, and different PU contents. Moreover, preliminary field performance monitoring results—including surface deflection measurements by the light weight deflectometer test, and strain measurements using optic fiber and strain gauge sensing techniques—are outlined and discussed in detail. The strength and stiffness of the TDA-based blend was found to be dependent on the TDA content, TDA-to-CR size ratio, CR shape, and PU content. The greater the angularity of the CR particles, the more effective the interlocking of the TDA and CR components, and thus the higher the developed strength and stiffness. The amount of strain generated in the permeable surface layer and at its interface with the lower screening layer were both found to decrease with a decrease in TDA content. Preliminary field observations indicate that the TDA-based system can indeed be a viable (and sustainable) solution to effectively mitigate flash-flooding while sustaining low–medium traffic loads.

R. Raeesi · M. M. Disfani (✉)

Department of Infrastructure Engineering, Melbourne School of Engineering, The University of Melbourne, Parkville, VIC 3010, Australia
e-mail: Mahdi.Miri@unimelb.edu.au

A. Soltani

School of Engineering, IT and Physical Sciences, Federation University, Churchill, VIC 3842, Australia

R. King

The City of Mitcham Council, Torrens Park, SA 5062, Australia

Keywords Permeable pavement · Tire-derived aggregate · Field performance monitoring · Lightweight deflectometer · Optic fiber

1 Introduction

Traditional pavements in urban areas are mainly impervious surfaces, which result in augmented surface runoff during rainfalls, thereby leading to flash flooding and pollution of waterways [1, 2]. Consequently, integrated land and storm water management programs—such as water-sensitive urban design (WSUD) in Australia, and sustainable urban drainage systems (SUDS) in Europe—have gained increased attention. A common solution, as suggested by these programs, involves the use of permeable pavement technology, which permits percolation of water through surface layers, thus alleviating harmful environmental impacts associated with traditional impervious pavements. Common permeable pavement technologies include: (i) porous asphalt; (ii) porous concrete; (iii) permeable interlocking pavers; and (iv) grid pavement systems [3]. Though proven effective from a water management perspective, these technologies often suffer from sustainability issues, attributed to their high cost, low bearing capacity, and limited flexibility; as such, they have not gained widespread acceptance among practicing engineers [4]. Accordingly, the development of an alternate permeable paving solution, with emphasis on sustainability, is urgently required.

Recent experimental findings published by the authors indicate that the flexibility provided by the combination of soft tire-derived aggregate (TDA) products and the rigidity of crushed rock (CR) particles, bonded together using polyurethane-based binders, can be effectively utilized to mitigate the settlement induced by natural ground movements while sustaining low–medium traffic loads [4–6]. Moreover, the high porosity of the CR–TDA blend can reduce storm water runoff in flash flooding and potentially improve the quality of water ending in our waterways. In essence, the use of TDA not only serves as a sustainable replacement for quarry materials, but also offers superior drainage, enhanced mechanical performance, long-term resilience (owing to the rubber’s high durability against local environmental conditions), and more importantly, significant cost benefits.

It is well accepted that the loading conditions experienced by pavement systems over time cannot be realistically replicated in the laboratory. Meanwhile, when promoting new pavement technologies, such as the TDA-based permeable pavement system introduced in this study, the need for field strain measurements poses as an inevitable necessity. In such cases, field instrumentation techniques should be implemented to monitor and hence perceive the system’s true potential. Though some experimental studies have been carried out on the TDA-based permeable pavement system, its real-life performance under live traffic loads has not yet been examined.

This study presents the authors’ recent experience in the development of an instrumented large-scale TDA-based permeable pavement trial site constructed at a car park located in South Australia. An area of approximately 400 m², consisting of 24 parking

bays, was paved using different TDA-based mix designs—different CR sizes, colors, and shapes, and different binder contents. Preliminary field performance monitoring results—including surface deflection measurements by the lightweight deflectometer (LWD) test, and strain measurements using optic fiber sensing techniques—will also be outlined and discussed in detail.

2 Materials

2.1 Crushed Rocks

Commercially available dark-gray crushed rock of fine (CRF) and coarse (CRC), shown in Fig. 1, gradations were used as the rigid host material. The particles of CRF were similar in size to medium–coarse sand (particles range between 2 and 5 mm with $D_{50} = 3.80$ mm), whereas CRC was graded into the fine–medium gravel category (particles range between 5 and 7 mm with $D_{50} = 6.01$ mm). The coefficients of uniformity and curvature were, respectively, calculated as 1.61 and 0.89 for CRF, and 1.24 and 0.90 for CRC. As such, CRF and CRC were classified as poorly graded sand (SP) and poorly graded gravel (GP) in accordance with the Unified Soil Classification System (USCS), respectively. Other physical properties included a specific gravity of 2.73 for both CRC and CRF and a bulk density of 1466 kg/m^3 and 1472 kg/m^3 for CRC and CRF, respectively. In addition to the dark-gray rock variants described

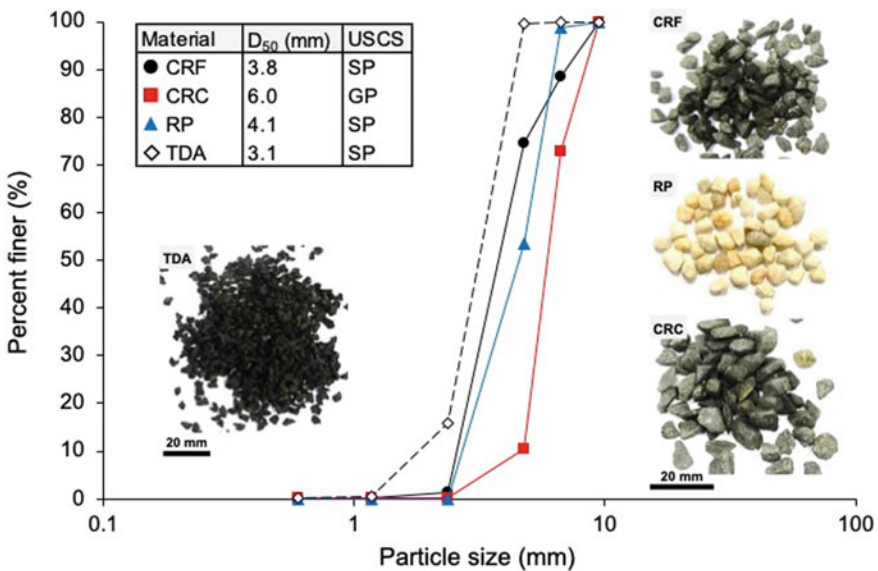


Fig. 1 Particle size distribution of used aggregates

above, an alternate ivory-white river pebble (RP) material (shown in Fig. 1)—with a rather similar gradation to CRF (particles range between 3 and 6 mm with $D_{50} = 4.11$ mm), but a slightly less angular form factor—was also adopted. The use of this alternate material was aimed toward understanding the impact of rock angularity on the mechanical performance of the TDA-based permeable pavement system.

2.2 *Tire-Derived Aggregate*

Commercially available tire-derived aggregate (TDA), shown in Fig. 1, was used as the soft component of the blend to partially replace the rigid host material. Much like CRF and RP, the TDA particles were found to be similar in size to medium-coarse sand (particles range between 2 and 4 mm with $D_{50} = 3.10$ mm). The coefficients of uniformity and curvature were, respectively, obtained as 1.89 and 1.18, such that the TDA material was classified as poorly graded sand (SP) according to the USCS criterion. Other physical attributes included a specific gravity of 1.04 and a bulk density of 503 kg/m^3 ; in comparison with CRF and CRC, the former is lower by more than two-fold.

The soft-to-rigid particle size ratio—commonly defined in terms of the soft-to-rigid D_{50} ratio—was calculated as 0.82, 0.52, and 0.75 for CRF, CRC, and RP, respectively. The particle size ratio controls the permeability of the blend; the closer this ratio to unity, the higher the permeability of the pavement system [4, 7].

2.3 *Polyurethane Binder*

A proprietary polymer agent, chemically referred to as polyurethane (PU), was used as the binder. The PU material is a single component adhesive formed through the combination of polyether polyol and MDI isocyanate. Its basic physical features included a specific gravity (at 22°C) of 1.10 and a dynamic viscosity (at 22°C) of 2800 ± 500 cP. Application prerequisites to ensure maximum workability and hence optimum field performance, as outlined in the manufacturer's literature, include a local temperature of approximately $18\text{--}27^\circ\text{C}$, as well as avoiding, or at least minimizing, direct contact with moisture. The latter offsets PU's performance, as well as its visual appearance, by facilitating the development of an undesirable foam-like material.

3 Field Work

3.1 Site Details

The large-scale TDA-based permeable pavement trial site was constructed at a car park located in St Marys Park, St Marys, South Australia (see Fig. 2a). The car park was planned to be covered by three different pavement technologies (see Fig. 2b): (i) a conventional bitumen-based asphalt system; (ii) a traditional block-paved system; and (iii) the new TDA-based permeable pavement system. The TDA-based system was used to cover a total of 24 parking bays, equivalent to an area of approximately 400 m², thus making this project the largest field trial of its kind.

To accommodate the project’s research agenda, the allocated 400 m²-area was partitioned, using concrete curbs, into six sections (see Fig. 2b), hence allowing for the implementation and monitoring of six different mix designs. Routine in-situ and laboratory tests, carried out on the subgrade soil as per relevant ASTM and Australian (AS) standards, indicated that the subgrade soil can be classified as highly plastic clay (CH). The engineering properties of the clayey subgrade included a California bearing ratio (CBR) of around 3% and a plasticity index (PI) of 54%. The presence of stiff, over-consolidated high plasticity clays also indicated that the subgrade soil may be prone to significant swell–shrink volume changes upon exposure to seasonal fluctuations.

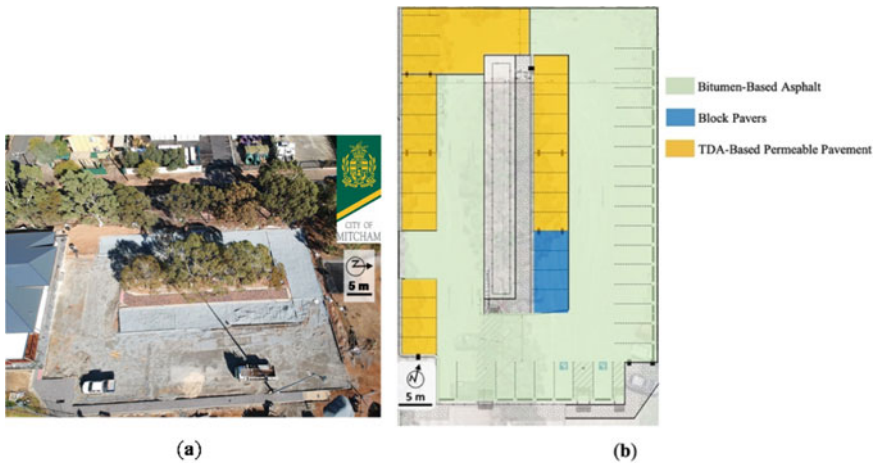


Fig. 2 Site details: **a** Aerial view of the project’s location prior to construction; and **b** Layout of the project illustrating the various implemented pavement technologies

3.2 Mix Designs and Their Preparation

As outlined in Sect. 3.1, a total of six sections, covering 24 parking bays with an approximate area of 400 m², were allocated to this study. Each of the six sections was paved using a relatively unique TDA-based mix design; the various mix designs were selected based on the authors’ previous experimental findings, such that they are able to satisfy the desired degree of permeability while sustaining low–medium traffic loads [4–6]. Figure 3 illustrates a schematic diagram of the various mix designs implemented in each of the six sections. It should be noted that the CR/RP, TDA, and PU contents (all in %), as outlined in Fig. 3, were defined as:

$$\chi_{CR} = \frac{V_{CR}}{V_{CR} + V_{TDA}} \times 100 \tag{1}$$

$$\chi_{TDA} = \frac{V_{TDA}}{V_{CR} + V_{TDA}} \times 100 \tag{2}$$

$$\chi_{PU} = \frac{W_{PU}}{W_{CR} + W_{TDA}} \times 100 \tag{3}$$

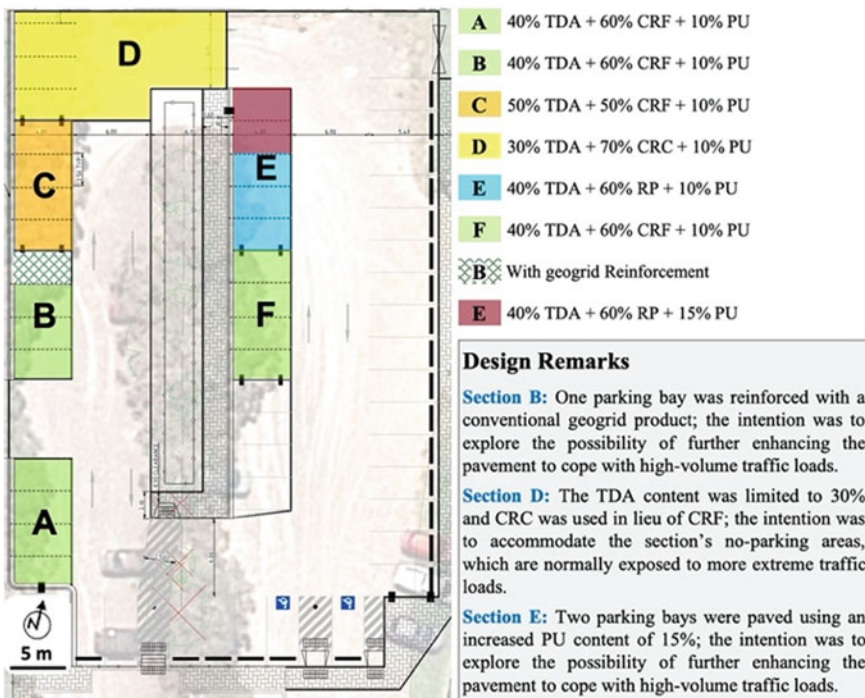


Fig. 3 Layout of the project showing the selected TDA-based mix designs and their properties

where V_{CR} = volume of CR; V_{TDA} = volume of TDA; W_{PU} = weight of PU; W_{CR} = weight of CR; and W_{TDA} = weight of TDA.

The three components, i.e., CR (or RP), TDA, and PU, were mixed on site by an aggregate pan mixer. The CR (or RP) and TDA were first blended in dry form as per the selected mix designs outlined in Fig. 3. Upon gaining visible homogeneity of the ingredients, the required amount of PU (see Fig. 3) was added to the TDA-based blend and allowed to thoroughly mix for 5–10 min, thus ensuring an even distribution of the binder throughout the rigid–soft blend. The prepared pavement blends were then carefully laid in a similar manner to that of laying concrete surfaces.

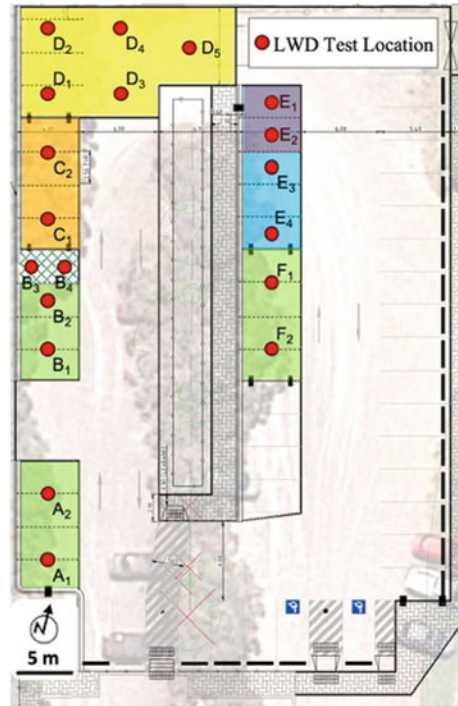
3.3 Field Performance Monitoring

It is well accepted that the loading conditions experienced by pavement systems over time cannot be realistically replicated in the laboratory. Meanwhile, when promoting new pavement technologies, such as the TDA-based permeable pavement, the need for field strain measurements poses as an inevitable necessity. Accordingly, in-situ tests and field instrumentation techniques should be employed to monitor and hence perceive the system's true potential. In this study, optic fiber technology, along with conventional strain gauge systems, were used to assess the system's mechanical performance, namely stress–strain, over time. In addition, in-situ LWD tests were carried out to examine the pavement's response under dynamic loading conditions.

Optic Fiber Sensing. Optic fiber technology was originally developed for long-distance data transmission purposes. As of late, it has gained increased acceptance as a “preferred sensing solution” for many engineering applications, e.g., strain and temperature sensing, owing to its durability and resistance against corrosive chemicals and harsh environmental conditions [8]. More importantly, unlike conventional strain gauge systems, a number of sensors can exist on a single optic fiber. This feature reduces the number of required instruments and hence minimizes the level of disturbance occurring on the structure, allowing for more accurate measurements [8]. In this study, fiber Bragg grating (FBG) sensors were employed; they are categorized as quasi-distributed, reflection-based sensors which follow the physics of Bragg's law. FBGs are created by inscribing systematic (periodic or aperiodic) variation of refractive index into the core of a special type of optic fiber using an intense ultraviolet laser [9]. In its simplest terms, by measuring the shift in wavelength of the reflected light at the Bragg grating point, along with some empirical and theoretical considerations, the incurred strain can be calculated.

Surface Deflection Measurements. Upon completion of the construction stage, each of the six sections, i.e., A–F in Fig. 3, was subjected to regular LWD tests as per ASTM E2583–15 [10]; Fig. 4 illustrates the selected locations for the LWD tests. Testing was carried out using the ZFG LAB 3.0 LWD apparatus. The apparatus consists of a 150 mm base and a loading plate. The built-in 5 kg weight is dropped from a height of 375 mm; upon impact, it produces a force of up to 3.54 kN. The

Fig. 4 Layout of the project showing the selected locations for the LWD tests carried out on the TDA-based surface layer



built-in geophone is employed to measure the pavement's deflection at the center of the load plate. Meanwhile, the applied force, as well as the corresponding surface deflection, is monitored by the equipment software; making use of these data, along with Boussinesq's equation, the in-situ dynamic deformation modulus, denoted as E_D , can be obtained.

3.4 Pavement Design and Instrumentation

Figure 5a illustrates a typical cross section of the selected TDA-based permeable pavement design. The developed design consisted of three main layers: (i) the compacted soil subgrade; (ii) the screening (or reservoir) layer; and (iii) the TDA-based permeable surface layer.

A commercially available geotextile product (EOS of 100 μm) was used for separation between the compacted soil subgrade and the screening layer. The screening layer consisted of uniformly graded gravel (GP as per USCS); it measured 300 mm in depth and the bottom half of it was reinforced with a geocell product (panel depth, sheet thickness, cell length, and cell width of 150, 1.25, 244, and 203 mm, respectively) to further enhance its bearing capacity. The final layer, the TDA-based permeable surface layer, measured 50 mm in depth. A commercially available geocomposite

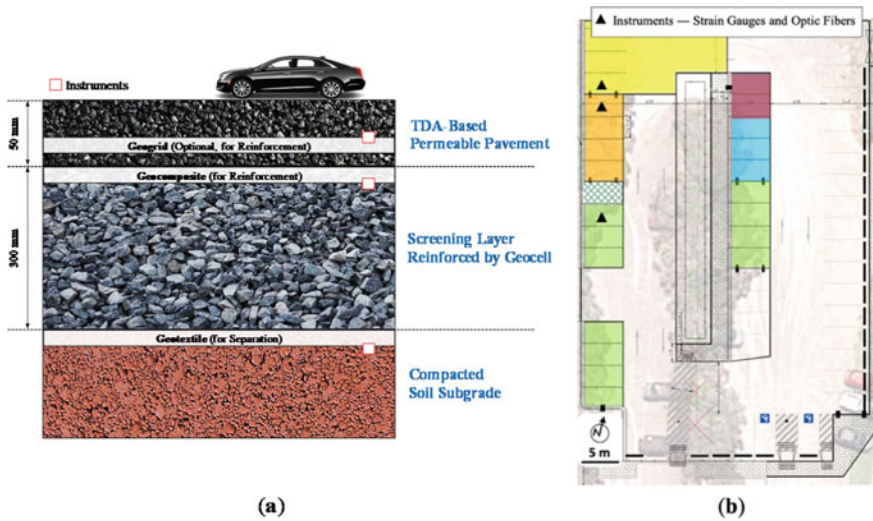


Fig. 5 **a** A typical cross section of the developed TDA-based permeable pavement design; and **b** layout of the project showing the locations of the installed instruments

product—a combination of geotextile and geogrid (biaxial polypropylene, opening of 30 mm)—was also implemented between the screening and permeable surface layers; its main functions were to provide separation between the two layers, and to distribute the stresses on the reservoir layer. As outlined in Fig. 3, the permeable surface layer of one parking bay in Section B was also reinforced with a conventional geogrid product (biaxial polypropylene, opening of 30 mm); the intention was to explore the possibility of further enhancing the permeable surface layer to cope with more demanding traffic loads. Accordingly, the geogrid was placed in the permeable surface layer approximately 15–20 mm above the geocomposite.

As outlined in Fig. 5a, the top two layers of Sections B, C, and D were equipped with optic fibers to monitor the system’s mechanical performance over time. For each section, one optic fiber was placed on top of the screening layer, while another was embedded inside of the permeable surface layer at two-third of the layer’s thickness below ground level (see Fig. 6).

4 Results and Discussion

4.1 Surface Deflection and Dynamic Deformation Modulus

Summary of the LWD test results are provided in Table 1. In general, the greater the TDA content, the lower the E_D value, owing to the TDA’s lower stiffness and higher deformability compared with the rigid CR (or RP) particles. A decrease in

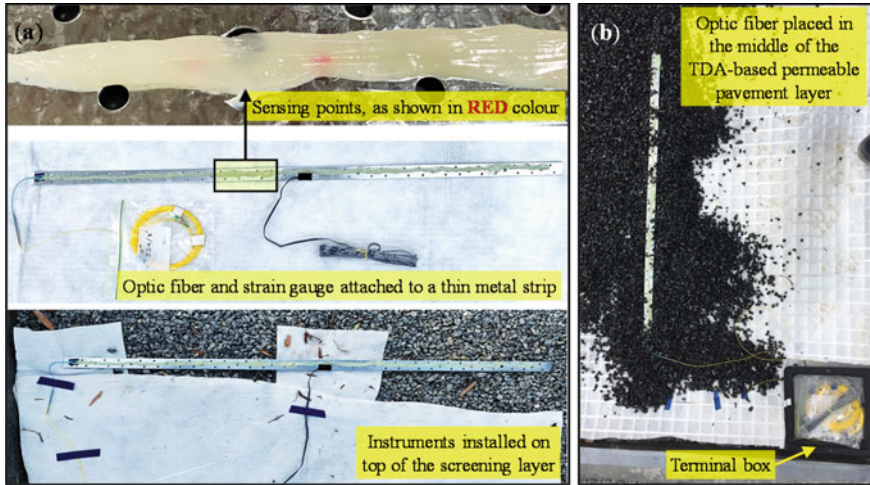


Fig. 6 a Optic fiber and strain gauge (for calibration) placed on top of the screening layer; and b optic fiber embedded inside of the permeable surface layer

Table 1 Summary of the LWD test results

Section	Location ¹	S_D (mm) ²	S_D^m (mm) ³	E_D (MPa)	E_D^m (MPa) ⁴
A	A ₁ (10% PU)	3.163	2.432	7.11	10.18
	A ₂ (10% PU)	1.700		13.24	
B	B ₁ (10% PU)	1.453	1.834	15.49	12.83
	B ₂ (10% PU)	2.215		10.16	
B ⁵	B ₃ (10% PU)	1.445	1.357	15.57	16.66
	B ₄ (10% PU)	1.268		17.74	
C	C ₁ (10% PU)	1.723	2.229	13.06	10.65
	C ₂ (10% PU)	2.735		8.23	
D	D ₁ (10% PU)	0.873	0.854	25.77	26.46
	D ₂ (10% PU)	0.780		28.85	
	D ₃ (10% PU)	0.879		25.60	
	D ₄ (10% PU)	0.941		23.91	
	D ₅ (10% PU)	0.797		28.23	
E	E ₁ (15% PU)	0.920	0.958	24.46	23.54
	E ₂ (15% PU)	0.995		22.61	
E	E ₃ (10% PU)	1.251	1.289	17.99	17.48
	E ₄ (10% PU)	1.327		16.96	
F	F ₁ (10% PU)	1.282	1.230	17.55	18.33
	F ₂ (10% PU)	1.178		19.10	

¹Locations are outlined in Fig. 4; ²Surface deflection; ³Mean surface deflection; ⁴Mean dynamic deformation modulus; and ⁵With geogrid reinforcement

the E_D value signifies an increase in the pavement's ductile character, thus leading to an improved flexibility as a result of the TDA inclusions.

Section E (with 10% PU), which makes use of RP, resulted in slightly lower E_D values compared with similar sections prepared with the more angular CRF variant (e.g., Section F). These trends indicate a rock shape-dependent stress–strain response; it can be hypothesized that the greater the angularity of the rock particles, the more effective the interlocking of the TDA and rock components, and thus the higher the developed strength and stiffness. This interesting aspect, which has not yet been addressed in the research literature, demands further examination under controlled laboratory conditions.

Although Sections A, B, and F were similar in terms of their mix design, the E_D values from Sections A and B were found to be lower than those of Section F; this discrepancy can be attributed to the low experience of the pavers during the installation of Sections A and B, which were both completed prior to Section F. An increase in PU content, in Section E, promoted a significant improvement in the E_D value—the E_D value increased from 17.48 MPa (for 10% PU) to 23.54 MPa (for 15% PU). Interestingly, the use of geogrid reinforcement, in Section B, led to a significant increase in the pavement's dynamic deformation modulus, as the E_D value increased from 12.83 to 16.66 MPa.

4.2 Optic Fiber Measurements

A total of two reflected light spectrum readings were taken for each of the installed optic fibers: (i) without loading; and (ii) with static loading imposed by a full-size SUV. By comparing the two spectrums, the strains were calculated based on the exhibited shift in wavelength of the reflected light at the fiber's Bragg grating points. Moreover, for each of the installed fibers, strain calibration was carried out using a conventional strain gauge (mounted on the same thin metal strip as the fiber) located in close proximity of the fiber's center Bragg grating point (see Fig. 6). The strain gauge reading-to-shift in wavelength ratio (with respect to the center FBG) was then employed to calculate the strain acting on the remainder Bragg grating points.

Figure 7a–c illustrates the strain distribution against distance (from the center of the car tire) for Sections D, B and C (containing 30, 40, and 50% TDA), respectively. An increase in TDA content led to a decrease in the exhibited strain at both layers, i.e., inside of the permeable surface layer, and on top of the screening layer. These trends are in agreement with the LWD test results (see Table 1)—that is, for any given stress level, a decrease in composite stiffness, as is the case with an increase in TDA content (see E_D values in Table 1), should normally produce an increase in the incurred strain.

As expected, for all three sections, the strain acting on top of the screening layer (denoted as ε_B) was consistently lower than that acting inside of the permeable surface layer (denoted as ε_T). Interestingly, reduction in the exhibited peak strain for each section—defined as $\eta = (\varepsilon_T - \varepsilon_B) / \varepsilon_T \times 100$ —increases with increasing

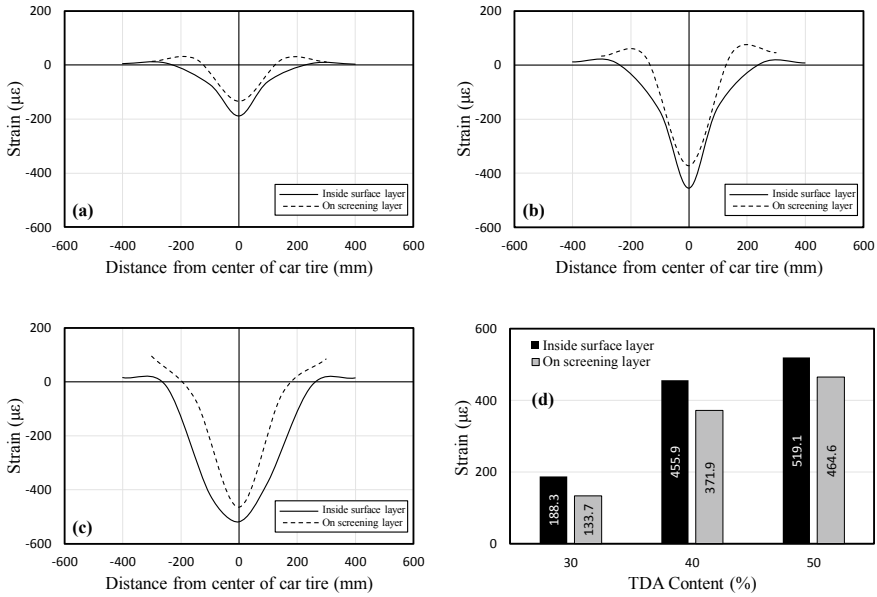


Fig. 7 Strain measurements by optic fibers: **a** Section D (30% TDA); **b** Section B (40% TDA); **c** Section C (50% TDA); and **d** peak strains at various sections

the TDA content and was obtained as 29, 18, and 11% for Sections D, B, and C (containing 30, 40 and 50% TDA), respectively (see Fig. 7d). This behavior can be explained by means of the top layer-to-bottom layer stiffness ratio. The greater this ratio, i.e., decrease in TDA content, the lower the transferred stress to the interface and bottom layer and hence the greater the peak strain reduction or η [11].

5 Concluding Remarks

This study has arrived at the following conclusions:

- The strength and stiffness of the TDA-based blend were found to be dependent on the rock’s shape. It can be hypothesized that the greater the angularity of the rock particles, the more effective the interlocking of the TDA and rock components, and thus the higher the developed strength and stiffness.
- The amount of strain generated in the permeable surface layer and at its interface with the screening layer were both found to decrease with a decrease in TDA content. Interestingly, the difference between the peak strains measured at these two depths was found to increase as the TDA content decreases, which can be attributed to the higher stiffness of the surface layer with lower TDA contents.

- The use of geogrid inside of the TDA-based permeable surface layer, though rather difficult in terms of implementation, can effectively improve the blend's bearing capacity, and thus potentially accommodate more extreme traffic loads. More importantly, geogrid reinforcement can minimize the development and propagation of undesirable tensile cracks. The importance of this design choice will be further examined over time as part of the planned field performance monitoring program.
- The final finish of the TDA-based permeable pavement product, in terms of visual appearance and quality, was found to be highly dependent on the pavers' skills and experience. This, however, was expected, as the product is a relatively new blend which most professional pavers have not yet encountered. As with any newly-developed product, relevant small-scale training courses should be considered to cope with any potential issues in the field.

Acknowledgements This project has been funded by Tyre Stewardship Australia; Research and Development Stream. The authors also acknowledge Melbourne School of Engineering, City of Mitcham (South Australia), and Pacific Urethane for their financial and technical support. The first author gratefully acknowledges The University of Melbourne for making this research possible through the provision of the Melbourne Research Scholarship.

References

1. Shackel B, Beecham S, Pezzaniti D, Myers B (2008) Design of permeable pavements for Australian conditions. In: *ARRB conference, 23rd*, Adelaide, South Australia, Australia
2. Hemachandra P, Disfani MM, Mohammadinia A, Aye L (2018) Field test results on permeable pavements comprising tyre derived aggregates. In: 10th international conference on water sensitive urban design, Perth, Western Australia
3. Eisenberg B, Lindow K, Smith D (2013) ASCE permeable pavements—recommended design guidelines. ASCE
4. Disfani MM, Mohammadinia A, Narsilio GA, Aye L (2018) Performance evaluation of semi-flexible permeable pavements under cyclic loads. *Int J Pavement Eng* 0(0):1–11. <https://doi.org/10.1080/10298436.2018.1475666>
5. Mohammadinia A, Disfani MM, Narsilio GA, Aye L (2018) Mechanical behaviour and load bearing mechanism of high porosity permeable pavements utilizing recycled tire aggregates. *Constr Build Mater* 168:794–804. <https://doi.org/10.1016/j.conbuildmat.2018.02.179>
6. Mohammadinia A, Disfani MM, Narsilio GA, Hemachandra P, Aye L (2017) Application of semi-rigid composite permeable pavements in road network. In: Australian Geomechanics society, Sydney chapter symposium. Sydney, New South Wales, Australia, pp 119–126
7. Lee J, Dodds J, Santamarina J (2007) Behavior of rigid-soft particle mixtures. *J Mater Civ Eng* 19(2):179–184. [https://doi.org/10.1061/\(ASCE\)0899-1561\(2007\)19:2\(179\)](https://doi.org/10.1061/(ASCE)0899-1561(2007)19:2(179))
8. Habel WR, Krebber K (2011) Fiber-optic sensor applications in civil and geotechnical engineering. *Photonic Sens* 1(3):268–280. <https://doi.org/10.1007/s13320-011-0011-x>
9. Zhu H, Shi B, Zhang C (2017) FBG-based monitoring of geohazards: current status and trends. *Sensors* 17(452):1–23. <https://doi.org/10.3390/s17030452>

10. ASTM E2583-15 (2015) Standard test method for measuring deflections with a light weight deflectometer (LWD). ASTM International, United States
11. Burmister DM (1945) The general theory of stresses and displacements in layered soil systems. *AIP J Appl Phys* 16(2):89–94. <https://doi.org/10.1063/1.1707558>

Alternative Materials for the Construction of Landfills and Embankments



Meghana Yeluri, E. C. Nirmala Peter, and Srinivas Allena

Abstract The dynamic increase in the activity of construction industry and lack of availability of suitable in situ soils has paved the way to the use of different stabilization techniques and alternate materials. In the present study, Terrasil and cement are used as admixtures to soils with percentage fines in the range of 15–40% and liquid limit in the range of 25–40%, to study the changes in the stress–strain behavior, stiffness, cohesion (c), angle of shearing resistance (ϕ), and permeability properties of the soils to suit different applications such as foundation soil, clay liners, impermeable barriers in zoned embankments, etc. The percentage fines and liquid limit (which is indirectly a measure of clay content) of the base soil impacted the improvement in the properties of the alternate or treated soils. With Terrasil as admixture, the permeability property of all the soils decreased, and they became impermeable. More reduction in optimum moisture content (OMC) and increase in maximum dry density values are observed in soil with less liquid limit value. A 5–10° improvement in ϕ values, a slight increase in cohesion and stiffness (modulus of elasticity, E) values are observed in soils with more clay content. With Terrasil and cement as admixtures, both c and ϕ increased considerably for soil with higher liquid limit values, indicating a higher impact of clay content on improving these properties than that of the fines percentage.

Keywords Terrasil · Cement · Percentage fines · Liquid limit

M. Yeluri (✉)

Graduate Student, Civil and Environmental Engineering, Cleveland State University, Cleveland, Ohio, USA

e-mail: y.meghana@vikes.csuohio.edu

E. C. Nirmala Peter

Professor, Department of Civil Engineering, JNTUH College of Engineering, Hyderabad 500085, India

S. Allena

Assistant Professor, Civil and Environmental Engineering, Cleveland State University, Cleveland, Ohio, USA

e-mail: s.allena@csuohio.edu

1 Introduction

Soil modified with terrasil have numerous applications that include liners to prevent ground contamination, zoned embankments as clay blankets on the upstream side of water and retaining structures that require impervious materials like clay to curtail flow of contaminated water etc. In all these geotechnical projects, it is not possible to obtain a construction site that will meet the design/construction requirements without replacement or modification of in situ soil. In case of earthen embankments and liner systems, materials have to be acquired and transported from far off places resulting in increased cost of construction.

Different soil stabilization techniques are used to modify the properties of poor quality soils [1] available at the site, to make them meet the desired requirements of design/construction. Chemical additives like Olivine which is capable of binding soil particles, SH-85—a non-traditional stabilizer which is calcium based and contribute to denser soil fabric by filling the pores between the soil particles with a gel formed from the chemical, silicon dioxide nano particles—which increases the hydraulic conductivity and when used in combination with cement increased the strength [2] property of the soils. Bioenzymes—chemical, organic, and liquid concentrated substance has been used to stabilize soil sub-base courses of pavements [3]. Additives like lime, cement, flyash, bitumen and nano materials like zycosil, zycobond, and terrasil have been used for stabilizing the subgrade soils for road construction [4]. These materials have improved the CBR values considerably and helped in cost-effective construction of pavements [4].

The materials used in this study are $c-\phi$ soils, Terrasil, and Ordinary Portland cement. Chemical stabilization is achieved by mixing appropriate percentages of these chemicals. CBR values on Terrasil treated clayey samples increased considerably [1]. Ordinary Portland cement is an actually practical, financially savvy, and fast approach to set up sub-grades for recreation of the runway asphalts. With the pressing need in reducing the costs in acquiring the suitable borrow areas and meeting the design requirements of fast developing construction modes, the commonly used materials are fast depleting, and hence, a search for new materials and improved techniques to process the local / in situ materials has gained great importance. This paper presents the improvement in various properties of soil with only Terrasil as well as Terrasil and cement as admixtures and also the impact of basic properties such as grain size distribution, percentage fines, liquid limit, and plasticity index on the improvement.

2 Materials

To study the improved properties of the given base soil samples, different chemical additives used for conducting the required laboratory tests are Terrasil and cement (added as 3 and 6% to the total weight of the soil sample).

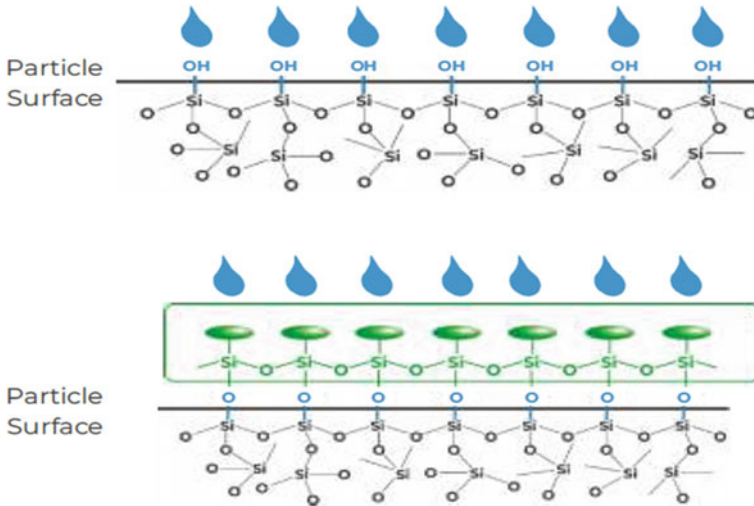


Fig. 1 Chemical reaction of Terrasil

2.1 Terrasil

Terrasil is a commercially available chemical stabilizer which is used in the present investigation. It was bought from Zydex Industries Pvt. Ltd. 61, Gotri-Sevasi Road, Vadodara—3,90,021. Gujarat, India. It is available in concentrated liquid form and is nanotechnology-based 100 percent organo silane, water dissolvable and warmth steady, receptive soil modifier to waterproof soils. The characteristics of Terrasil are that it wipes out narrow ascent and water entrance from top, decreases water permeability. It is a reactive soil modifier that permanently modifies the soil surface, making it hydrophobic. It chemically converts water absorbing hydroxyl groups to water resistant alkyl groups. Terrasil is a non-leachable and safe chemistry and works with all soil types. Chemical action of Terrasil by Zydex Industries Pvt. Ltd. is shown in Fig. 1.

2.2 Cement

In the present study, ordinary portland cement (OPC) with 53 MPa compressive strength at 28 days was used.

3 Methodology

Three locally available soils with percentage fines of 19, 28, and 34 and liquid limit values of 29, 27, and 38 represented as samples S_1 , S_2 , and S_3 , respectively, are taken as the base soils (BS) for alteration with the admixtures. The basic and standard tests including wet sieve analysis, Atterbergs limits, modified compaction tests, direct shear tests, and permeability tests were conducted by constant head methods for all the three base soils. The properties of these base soils are given in Table 1. The alternative materials are prepared by adding only Terrasil (T), Terrasil and 3% cement (T + 3%C), and Terrasil and 6% cement (T + 6%C) as admixtures to the base soils. The properties of the modified or alternate soils are also obtained from modified proctor compaction, permeability, and shear tests. Initially all the soils are treated with Terrasil as given in 3.1, and if cement is to be added as admixture, the oven dried Terrasil treated soil is taken, and the required quantity of cement is added to the soil and compacted by taking OMC. All the tests were conducted on samples prepared at OMC and compacted to almost the maximum densification.

Table 1 Properties of base soils

<i>Soil identification</i>	Sample 1 (S_1)	Sample 2 (S_2)	Sample 3 (S_3)
<i>Grain size distribution</i>			
Gravel (%)	19	6	4
Coarse sand (%)	23	8	11
Medium sand (%)	30	47	34
Fine sand (%)	9	11	17
Silt and clay (%)	19	28	34
<i>Atterberg limits</i>			
Liquid limit (%)	29	27	38
Plastic limit (%)	16	16	19
Plasticity index (%)	13	11	23
IS classification	SC	SC	SC
<i>Modified proctor test</i>			
OMC (%)	7.2	8.1	9
Maximum dry density (kN/m ³)	21.28	20.98	20.20
<i>Permeability test</i>			
Coefficient of permeability, k (cm/s)	8.7*10 ⁻⁶	3.14*10 ⁻⁷	4.2*10 ⁻⁷

Table 2 OMC and MDD values for base soils and soils mixed with Terrasil

Soil identification	% fines	Base soil (BS)		Base soil + Terrasil (BS + T)	
		OMC (%)	MDD (kN/m ³)	OMC (%)	MDD (kN/m ³)
S ₁	19	7.2	21.28	7.2	21.37
S ₂	28	8.1	20.98	6.5	21.18
S ₃	34	9	20.20	8.5	20.98

3.1 Preparation of Soil Treated with Terrasil as Admixture

Terrasil solution is prepared in the proportion of 1 ml of Terrasil in 200 ml of water (1:200). The base soil required for testing is initially immersed in Terrasil solution and allowed to air dry for about 10 days. Before conducting the tests, the samples were oven dried and used for testing. Modified proctor compaction tests are also conducted on Terrasil treated soils, and the OMC and MDD are furnished in Table 2. The OMC values decreased slightly and the MDD values increased with the addition of Terrasil. For all the laboratory tests with Terrasil as admixture, the OMC values given in Table 2 under BS + T are used for the preparation of samples. Same procedure is followed for all the three soils.

3.2 Preparation of Soils Treated with Terrasil and Cement as Admixtures

The alternate materials are prepared by adding the required quantity of cement to the Terrasil treated oven dried soil. The prepared sample is mixed without lumps by adding OMC obtained from modified proctor tests conducted on Terrasil treated soils (given in Table 2 under BS + T) and used for all the other tests. These samples are cured for 14 days (14d) before conducting the tests.

4 Results and Discussion

The test results of base and alternate materials are presented in Tables 2, 3, and 4. Table 2 shows the effect of Terrasil on OMC and maximum dry density (MDD) values. In general, the OMC and MDD values increase with increase in clay content and also with increase in % fines. For S₁ soil, there is no variation in the OMC values but slight increase in MDD is observed for the alternate soil. The alternate soils with S₂ and S₃ as base soils having more % fines yielded considerable increase in the MDD values indicating the impact of % fines is more on the compaction of the

Table 3 Permeability property of base and Terrasil treated soils

Soil identification	Base soil	Base soil + Terrasil
	Coefficient of permeability (cm/s)	Coefficient of permeability (cm/s)
S ₁	8.7*10 ⁻⁶	Impermeable
S ₂	3.14*10 ⁻⁷	Impermeable
S ₃	4.2*10 ⁻⁷	Impermeable

Table 4 c, φ properties of base soils, Terrasil, and cement treated soils

Soil identification	Base soil (untreated soil)		Base soil + Terrasil		Base soil + Terrasil + 3% cement (14 days)		Base Soil + Terrasil + 6% cement(14 days)	
	c (kN/m ²)	φ (°)	c (kN/m ²)	φ (°)	c (kN/m ²)	φ (°)	c (kN/m ²)	φ (°)
S ₁	9.8	39.8	18.6	45.5	51	43.5	87.27	39.3
S ₂	8.8	46	21.6	43.6	98.1	26.6*	112.8	46.5
S ₃	19.6	33.7	28.4	45.7	142.2	47.3	170	51.3

soil. Table 3 presents the permeability properties. All the base soils are rendered to impervious state.

Table 4 furnishes the shear test results for all the base as well as alternate materials. With the addition of Terrasil cohesion values increased in all the soils by 1.5–2.4 times that of the base soils, but with Terrasil and cement as admixtures, the cohesion values increases by almost 3–13 times indicating more improvement in c values for soils with more clay content and more % fines.

The angle of shearing resistance, φ increased by 5–12° in soils as the clay content increases but this increase in φ value is less in soil modified with Terrasil. However, considerable increase in φ value was observed in soil treated with Terrasil and cement as admixtures. However, in soils with less clay content, though the percent fines are more, the variation is almost nil. So it is observed irrespective of the grain size distribution specifically, the amount and distribution of coarse soil content, the factors which are contributing more to the improvement of c and φ are percent fines and clay content.

4.1 Effect of Terrasil on the Permeability of the Soil

The permeability tests on alternate materials show the ability of Terrasil in reducing a permeable soil to impervious condition. Irrespective of the grain size distribution, % fines, and clay content, all the soils have become impermeable.

4.2 Effect of Admixtures on Cohesion Intercept (c) and Angle of Shearing Resistance (Φ)

The properties obtained from direct shear tests for both base soil and alternate materials are presented in Table 4. For S_1 and S_3 soils, both cohesion and angle of shearing resistance increased with the addition of admixtures. However, for sample S_1 with Terrasil and 6% cement and for S_2 with Terrasil and 3% cement as admixtures, the dry densities for the shear tests are found to be less than the MDD values. Hence, the values obtained are less than that of the base soil.

Cohesion intercept (Fig. 2): The improvement in cohesion values is of the order of 1.45–2 times with the addition of Terrasil. With the addition of cement to Terrasil treated soils, the cohesion parameter increased in the range of 5–13 times the base soil value. This indicates that the addition of cement has more impact in increasing the cohesion values of the alternate materials. However, maximum improvement in c values is observed for sample S_2 which is having less liquid limit value/clay content. There is a considerable increase in c values with the addition of cement, but only a slight increase is observed when the % cement content is changed from 3 to 6%.

Angle of shearing resistance (Fig. 3): The improvement in shearing resistance is observed to be in the range of 5–12° with the addition of Terrasil and 3–18° when cement is added to the Terrasil treated soil. No improvement in ϕ values is observed for S_2 . Maximum increase is observed for S_3 which is having more % fines and more clay content/liquid limit values. The difference in % fines for S_2 and S_3 samples is only 6%, but considerable improvement in ϕ values is observed for S_3 . This indicates that the contribution of clay content is more in reacting with the admixtures added in improving the ϕ value irrespective of the coarse soil content and its distribution in the soils.

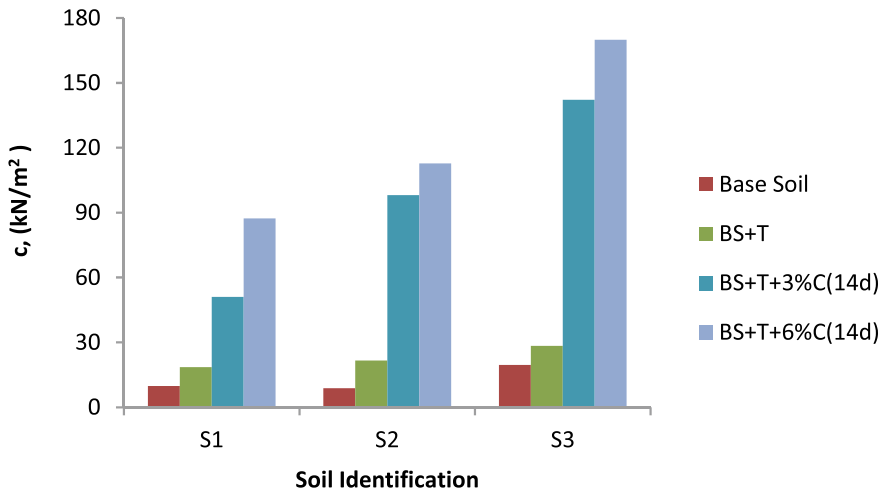


Fig. 2 Effect of admixtures on cohesion intercept of soils

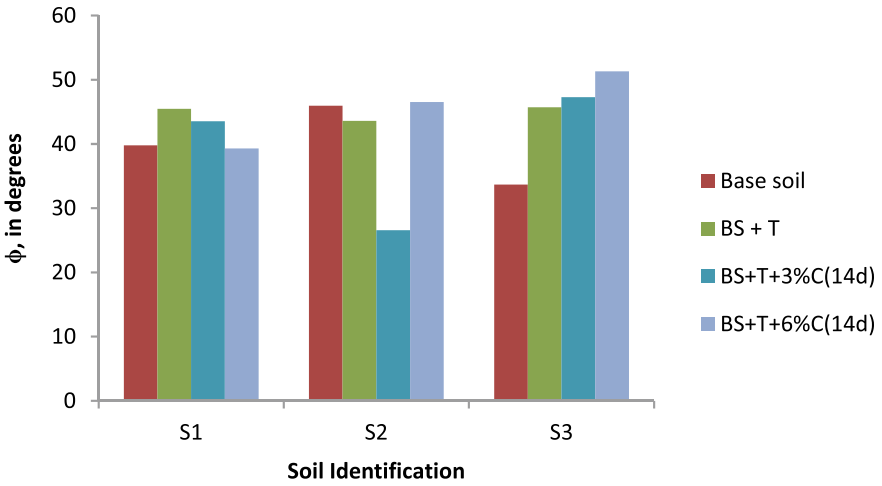


Fig. 3 Effect of admixtures on angle of shearing resistance of soils

Table 5 Stiffness of treated and untreated soils

Soil identification	Type of soil	MDD (kN/m ³)	<i>E</i> (MPa)
S ₁	Base soil	21.28	1.6
	BS + T	21.37	2
	BS + T + 3%C(14d)	21.37	2.4
	BS + T + 6%C(14d)	21.37	2.4
S ₂	Base soil	20.98	1.9
	BS + T	21.18	2
	BS + T + 3%C(14d)	21.18	2.1
	BS + T + 6%C(14d)	21.18	2.3
S ₃	Base soil	20.2	1.9
	BS + T	20.98	3.2
	BS + T + 3%C(14d)	20.98	4.2
	BS + T + 6%C(14d)	20.98	5.1

For S₃, with addition of admixtures, both cohesion intercept and angle of shearing resistance values are increasing. This resulted in considerable increase in stiffness values represented in terms of *E*. The values of *E* are given in Table 5. However in S₂, though there is considerable increase in cohesion intercept values, there is no much

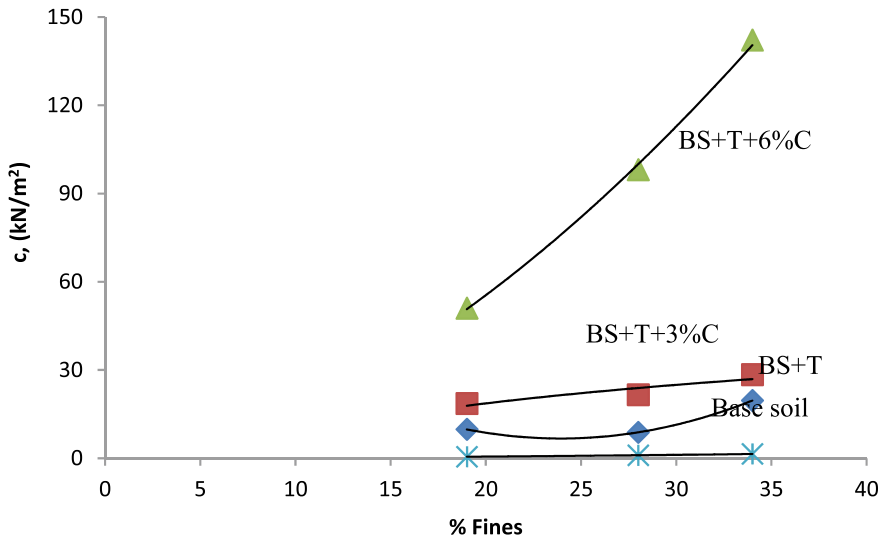


Fig. 4 Stiffness of treated and untreated soils

change in values of angle of shearing resistance, and in S_1 , there is slight increase in cohesion intercept and $5\text{--}8^\circ$ increase in angle of shearing resistance. However, improvement in stiffness is considerably less.

E values are calculated from the secant modulus from the maximum stress values of all the stress-strain curves. A point ($t_{\max}/2$) is taken on the curve, and a tangent is drawn passing through that point and origin. Slope of that tangent is the E value. This can be illustrated in Fig. 4 (Fig. 5).

5 Conclusions

The study on the influence/effect of the admixtures, i.e., only Terrasil and Terrasil plus different percentages of cement yielded the following conclusions.

1. Terrasil increased the densification of all the soils. However, its effectiveness in SC soils with more percentage fines and well-proportioned coarse content.
2. Terrasil rendered imperviousness to all types of soils.
3. Terrasil is more effective in increasing the values of cohesion, c in $c\text{--}\phi$ soils with less clay content. Therefore, for more bonding of the material—soil with less clay content is more suitable. This particular application is suitable for road materials.
4. In $c\text{--}\phi$ soils, soils with more percentage fines, well-proportioned coarse content, and clay content yielded considerable increase in the angle of shearing resistance

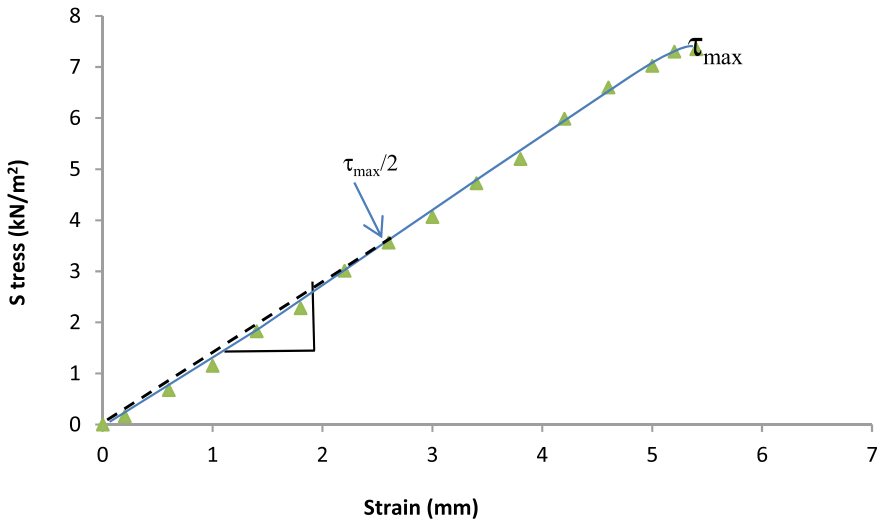


Fig. 5 Stress–strain graph for calculation of stiffness

with the addition of Terrasil. It can be concluded that higher fines percentage and clay content are instrumental in increasing the ϕ value.

5. Soils with more percentage fines have shown considerable increase in cohesion values for a curing period of 14 days.
6. In c - ϕ soils with higher fines percentage, the angle of internal friction (ϕ) slightly increased with increasing the percentage of cement. In soils with less fine percentage, the optimum percent of cement seems to be between 3 and 6%. As a whole, the addition of cement is more effective in soils with more fines.
7. Stiffness of the Terrasil treated soils increased with respect to that of the base soils in soils with higher clay content. The effect on increasing stiffness is more when cement is added to these soils.

References

1. Patel NA, Mishra CB, Pancholi VV (2015) Scientifically Surveying the usage of terrasil chemical for soil stabilization. *Int J Res Adv Technol* 3(6)
2. Bahmani SH, Huat BBK, Asadi A, Farzadnia N (2014) Stabilization of residual soil using SiO₂ nano particles and cement. *Constr Build Mater* 64:350–359
3. Ravi Shankar AU, Rai HK, Mithanathaya R (2009) Bioenzyme stabilized lateritic soil as a highway material. *J Indian Road Congress*

4. Padmavathi V, Peter E, Rao PN (2018) Stabilization of soil using terrasil, zycobond and cement as admixtures. In: Proceedings of the 2nd GeoMEast international congress and exhibition on sustainable civil infrastructures, Egypt – The official international congress of the soil-structure interaction group in Egypt (SSIGE)
5. Adeinola OS, Nnochiri ES (2017) Stabilizing lateritic soil using terrasil solution. SSP J Civ Eng 12(1):19–27

Geotechnical Properties of Modified Railway Sidings Coal Discard



Felix Okonta and Carl Hien Rottcha

Abstract Coal spillage often occurs in railway sidings which are used for the loading and offloading of coals in mining towns. Spilled coal materials are readily exposed to the weather elements and gradually intermixed with soils in the vicinity of the sidings to form coal–soil composite layers. The layer often softens significantly in poor drainage and is also a major source of acid water drainage. Coal–soil composites of 1:1 to 5:1 coal-to-sand ratios were prepared and cured. Another batch of composites was stabilized with 8% cement, compacted and cured. Test results reveal that dry unconfined compression strength and modulus of cured composite were only marginally lower than cement-stabilized composite but were fourfold lower in soaked state. The unconfined compressive strength (UCS) and stiffness of coal–soil composite tend to the cement-stabilized values as coal–soil ratio tends to 5:1. The average coefficient of permeability decreased with cement stabilization. Coal–soil composite backfill and cement-modified composites require proper drainage facilities to provide acceptable pavement service in coal sidings and prevent acid drainage.

Keywords Unconfined compression strength · Permeability coefficient · Coal discard · Soil stabilization · Railway sidings

1 Introduction

Railroad siding is a set of rail tracks branching off the main line. In South Africa, they are managed and operated by Transnet Freight Rail, for the purposes of loading raw materials or products onto rail wagons. As the case in many provinces with active mining operations, a number of sidings are privately owned, operated and maintained near the mining town of Ermelo in Mpumalanga, South Africa. When mined coal materials are being loaded in railway sidings by front-end loaders, excess coal often spilled onto the siding, and after series of heavy traffic loads on the discarded coal, a new pavement layer of soil–coal capping is formed. Thus, the excess coal which is

F. Okonta (✉) · C. H. Rottcha
University of Johannesburg, Auckland Park, Johannesburg 2006, South Africa
e-mail: fnokonta@uj.ac.za

supposed to be removed from the siding on a continuous basis now serves as a pseudo-pavement layer during the dry season in some rail sidings. It was therefore suggested that the discarded coal layer be incorporated into the initial sub-layer design of the loading facility and also to explore methods to improve the geotechnical properties of the coal discard layer especially during the wet season. Initially, the freshly discarded coal is the same as the coal loaded onto the wagons for export; however, over time with exposure to the elements and continuous compression by heavy machinery, the discarded coal undergoes physical and chemical changes. Also the discarded coal which is initially found in close proximity to the rail wagons tended to spread across the entire siding over time. Discarded coal is a major source of hydrocarbon pollutants and acid mine drainage due to the pyrite content. Thus, it poses a great threat to the surrounding environment and underlying groundwater. Mindful of the pollution potential, it is important to investigate the potential application of coal–soil backfill geocomposites in railway siding pavement engineering.

2 Brief Literature

The physical and mechanical properties of the coal from a wide range of sources were investigated and documented [1]. The results reveal uniaxial compressive strength UCS range of 2.42–24 MPa, Young's modulus of 10 GPa, Poisson's ratio of 0.29–0.30, unit weight of 0.25–0.027 MN/m³, cohesion of 55 kPa and friction angle of 37°. Another study [2] observed that the correlation between UCS and point load index for coal can be improved by stabilizing coal with cement and water. Investigation [3] on coal discard conducted in China Xuzhou province was focused on samples that contained slightly weathered sandstone and mudstone that were mixed with granular coal discard mixed with clay and covered with geotextile. Wang-hu (2009) [3] reported coefficient of the permeability of coal reject of 7.43×10^{-2} cm/s, which was dependent on the amount of clay and fly ash present in the coal discard. The coefficient of permeability increased from 10^{-6} to 10^{-3} cm/s with the increase of coarse grain soil content [3]. In addition, the permeability K decreased with the porosity, while the absolute value of non-Darcy's flow coefficient β , which varied between positive and negative values, increased. A study [4] on the engineering properties of Nigerian coal reject and its potential use in engineering construction revealed that coal rejects were suitable for applications in highway backfills, embankments and sub-bases, but not for base course and structural fills, unless improved. The improvement of coal discard was necessary to improve resistance to varying loads imposed by front-end loaders. It was [5] noted that the pH of water contaminated with coal is dependent on the presence of calcareous minerals, such as calcium carbonate (CaCO₃), and the quantity of pyrite (FeS₂) within the coal. Pyrite promotes the formation of acid, whereas calcium carbonate is an acid neutralizer. Series of experiments were carried out on coal shale that consisted mostly of quartz, kaolinite and pyrite that were crushed and placed in vertical columns that were open to the atmosphere [5]. Without the addition of calcite, the leachate from shale typically had pH of 1.5–3.5

and high concentration of sulphate and iron. However, with the addition of calcite, the pH increased from 4.5 to 7, and lower concentrations of sulphate and iron were noted.

3 Test Method

Series of tests were performed on composites on compacted specimens of coal–soil composites and 8% cement-stabilized coal–soil composites.

- X-ray diffraction (XRD) tests were performed on coal and coal discard.
- Particle size analysis tests were performed on the residual soil and coal discard that were sun-dried for 2 days and sieved through 19 mm, 13.2 mm, 4.75 mm, 0.425 mm and 75 μm .
- Specific gravity test was performed on 200 g of coal discard in a pycnometer with de-aired water.
- Compaction properties, i.e., the maximum dry density (MDD) and optimum moisture content (OMC), were determined on coal discard that were subject to 5 layers at 55 blows per layer, to reflect and simulate the heavy axle loads of front loaders.
- UCS tests were conducted on specimens containing mixtures of coal discard and soil that were prepared and compacted at MDD and OMC in $100 \times 100 \times 100\text{mm}$ moulds. Different specimens were tested in the dry and soaked state after overnight drying. Coal discard that were mixed with 8% cement was also prepared at OMC and MDD, demoulded after 24 h. UCS specimens were cured for 28 days even days at temperature of 35 C and humidity of 60%.
- Permeability test (falling head method) was conducted to determine the permeability of the coal discard, coal discard mixed with soil, and coal discard mixed with soil and 8% cement. Specimens were prepared in a mould measuring 102 mm in diameter and 115 mm in height. The density is the same as in the UCS test for the respective mixed samples.

4 Test Method

4.1 Mineralogical Test (X-ray Diffraction)

The mineralogical test indicates that fresh coal contained predominately silicon oxide (SiO_2) copper aluminium sulphate and chlorites $\text{Cu}_6\text{Al}(\text{SO}_4)(\text{OH})_4 \text{Cl}$, benzene (C_6H_6), iron arsenide sulphate (pyrites) $\text{Fe}(\text{S.As})_2$ and aluminium silicate $\text{Al}_2\text{Si}_2\text{O}_5(\text{OH})_4$. The discarded coal contains silicon oxide, SiO_2 , aluminium silicate, $\text{Al}_2\text{Si}_2\text{O}_5(\text{OH})_4$, quinone $\text{C}_6\text{H}_4\text{O}_2$ and calcium phosphate $\text{CaPO}_3(\text{OH})_2$. The quinone was due to oxidation of benzene, and the aluminium silicates were due to the leaching of copper and pyrites in the fresh coal. Silica and aluminium silicates

in discarded coal present good potential for pozzolanic reaction. The silicon oxide indicates the presence of quartz, and the aluminium silicate indicates the presence of clayey material. Calcium phosphate in the coal discard can also enhance pozzolanic reactions.

XRD test was limited to fresh and discarded coal. Subsequent investigations were focused on discarded coals that were sampled from different locations in the siding and coal storage compounds. The samples were dried and mixed and compacted.

4.2 Physical Properties

The particle size distribution curve of the coal discard sampled from different locations, recent discards close to the offloading section [A] and older discard inside the coal yard [B] in the coal sidings was presented in Fig. 1 to evaluate potential variation in particle grading. The grading indicates predominantly sand-size particles with fine sand (0.425 mm) range of 22–53% and coarse sand (4.75 mm) range of 58–94%. The coal discards A and B are well-graded granular coal with particle size distribution that bounds the grading curve of the local residual backfill which is predominantly granular sand. Based on AASHTO backfill classification system, the coal discards are mostly A 2–4 backfill material purely on the bases of the granular size. To determine the Atterberg limits and other properties, the coal discards A and B were mixed at a ratio of 1:1. Table 1 indicates that the mixed coal discard is non-plastic as the plastic limit could not be determined. Both the density from a high compaction effort (5/55 blows) and specific gravity reflected low-density material. The residual backfill soil is a well-graded reddish brown, medium-dense and low-plasticity sandy soil with

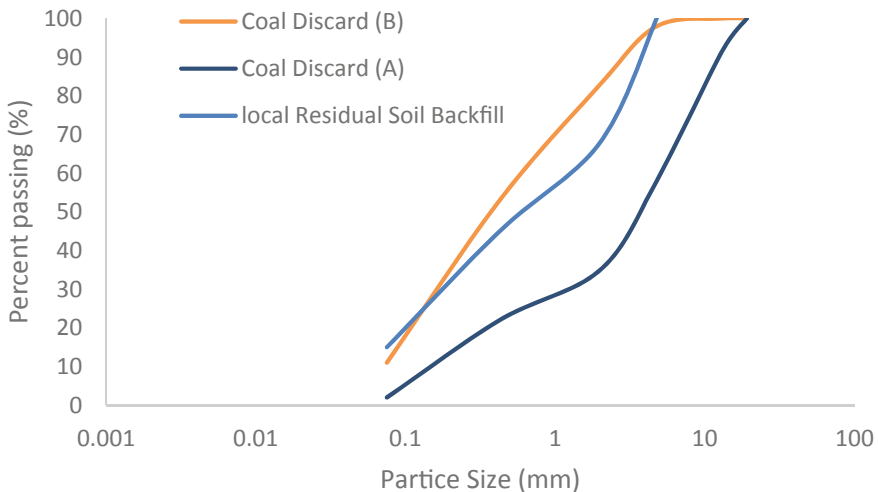


Fig. 1 Grain size distribution coal discard

Table 1 Physical properties of mixed coal discard

Physical properties	Coal discard	Backfill soil
Atterberg limits	Non-plastic	LL 32 Pl 20
Specific gravity	1.16–1.39	2.71–2.73
MDD/OMC 5/55	1262 kgm ⁻³ /14%	1722/16%

Table 2 UCS and Modulus of compacted coal samples

	Strain	Stress (kPa)	Modulus (MPa)
Sample 1	0.0322	879	27.29
Sample 2	0.016	679	42.43
Sample 3	0.0305	820	27.33
Average	0.0262	793	32.35

minimal amount of fines. The Atterberg limits of the soil are liquid limit of 32 and plasticity index of 20.

4.3 Unconfined Compression Strength of Coal Discard

UCS specimens were prepared by compacting 5 layers at 55 blows per layer and then curing the samples for four days at temperature of 35 C and humidity of 60%. After curing, the samples were tested, and the average unconfined compressive strength for all three moulds was 0.793 MPa with an average stiffness of 32.35 MPa (Table 2).

4.4 Unconfined Compression Strength of Coal–soil Composite

A major geotechnical problem of compacted coal discard as a pavement layer at railway sidings is that during the rainy seasons, heavy vehicles and front-end loaders tend to get stuck in the coal discard layer. The UCS of coal–soil composites was presented in Fig. 2 as well as the dry UCS of 8% cement-stabilized coal–soil composites. The result reveals that upon inundation, the coal discard loses the compressive strength. The dry UCS of 8% cement-stabilized composites was lower than the strength of compacted discard for coal–soil ratios of 1:1 to 3: 1, and the difference in strength diminished or converged for coal–soil ratios greater than 4:1.

The soaked and dry UCS of 8% cement-stabilized coal soil composites in relation to coal–soil ratio was presented in Fig. 3. The UCS of both soaked and unsoaked stabilized composites decreased with increase in coal–soil ratio. Figure 3 also revealed an average of fourfold decrease in UCS due to inundation of cement-stabilized composites.

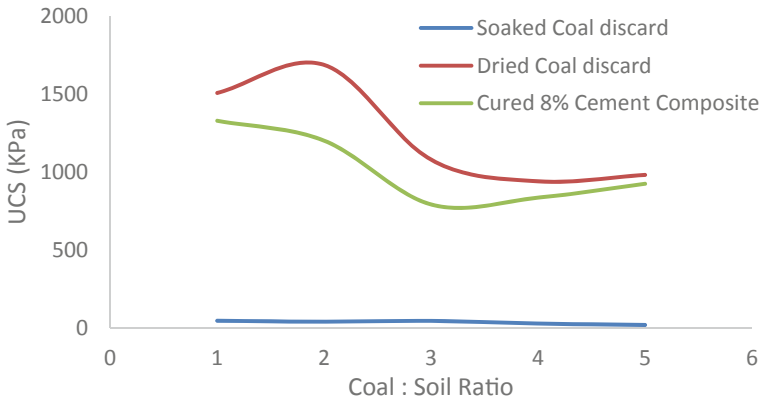


Fig. 2 UCS of dried coal–soil–cement composites in relation to coal–soil ratio

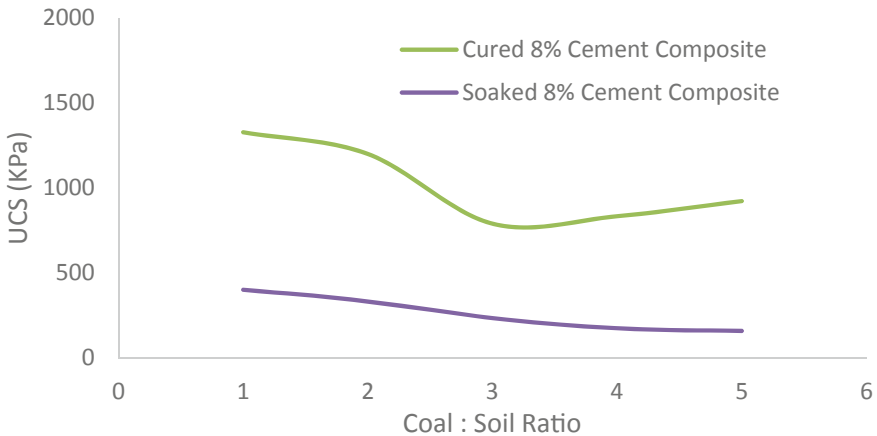


Fig. 3 Soaked and dry UCS of 8% cement-stabilized coal–soil composites in relation to coal–soil ratio

4.5 Modulus of Coal–soil Composites

Figure 4 showed that sample CS1 (1-part coal discard, 1-part soil by mass) exhibited the greatest compressive strength as well as stiffness. With increasing coal discard content, the stiffness decreased stepwise; however, sample C5S showed marginal increase in stiffness. Although the ductility increased with 8% stabilized, the difference in stiffness of both stabilized and unstabilized composites is marginal as coal–soil ratio increased to 4:1. The stiffness of stabilized coal composites decreased by fivefold upon inundation and tended to a constant value for coal–soil ratio greater

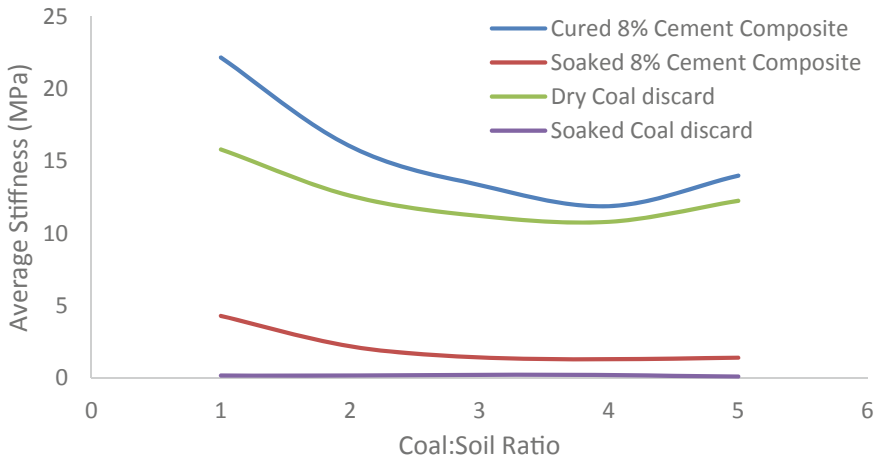


Fig. 4 Modulus of coal–soil cement composites in relation to coal–soil ratio

than 3:1. The significant reduction in stiffness and strength of stabilized composites upon inundation presents a major pavement stability problem in poor drainage environment and in the rainy seasons in sub-tropical regions.

4.6 Permeability of Coal Composites

The result of permeability test conducted on coal discard revealed that the material has a hydraulic conductivity of 2.89×10^{-5} cm/s. Using the Moulton formula (TRH 15,1994), it was found that the hydraulic conductivity of the coal discard was 3.22×10^{-5} cm/s, which is 11% greater than the experimental value. The Moulton formula takes the porosity, particle size and percentage fines into account. The specimens were tested immediately after being prepared at moisture content of 16% and were not allow to dry. Figure 5 shows that the hydraulic conductivity decreased with coal–soil ratio and also with cement stabilization. The composite had a maximum hydraulic conductivity of 2.99×10^{-2} cm/s at a mixed ratio of 2:1 and least hydraulic conductivity of 2.34×10^{-3} cm/s at a mix ratio of 5:1.

When mixed with soil and 8% cement (8% of coal discard and soil mass) at a moisture content of 16%, the coal discard mixture showed a decrease in hydraulic conductivity. The maximum hydraulic conductivity of 1.99×10^{-3} cm/s was exhibited by the 2:1 composites, and further increase in coal–soil ratio resulted in decrease in permeability to a constant value of 1.01×10^{-3} cm/s.

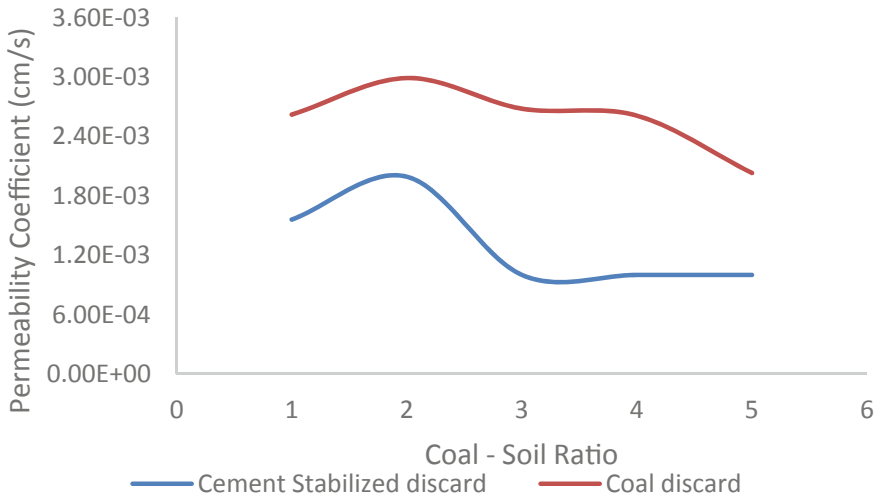


Fig. 5 Effect of coal–soil ratio on permeability coefficient on stabilized and unstabilized coal–soil composites

5 Conclusions

For the coal-to-soil ratios investigated, the addition of 8% cement increased the stiffness of the coal–soil composites at all coal–soil ratios. Also stabilized specimens exhibited significant reduction in strength and stiffness upon inundation. The observed benefit of cement is the improved soaked strength, reduced hydraulic conductivity and increase in pH. TRH4 (1996) recommended that cement-stabilized, soil-modified coal discard can be classified as a cemented natural gravelly soil (code C4). A typical C4 material has a UCS of 0.75 to 1.5 MPa at 100% Mod. AASHTO and maximum PI of 6 after stabilization. For the purposes of designing the pavement layer at a railway siding using coal discard, composites with coal–soil ratio of 1:1 and 2:1 with 8% cement at a moisture content of 16% met the local specification provided that adequate drainage is provided to prevent significant loss in strength.

Acknowledgements Graduate Student Carl Hien Rotcher provided the material and test data. A special thanks goes out to the staff at R & H Railway Consultants, especially D. Bredenkamp, J. Momberg, W. Nederveen and Ms D. Scholtz for funding the project.

References

1. Choochang S (2011) Room-and-pillar method for Petchaboon coal mine. *Int J Coal Geol.* http://www.elsevier.com/wps/find/journaldescription.cws_home/503337/description. Accessed 4 July 2011

2. Jasinge D (2009) Mechanical properties of reconstituted Australian black coal. *J Geotech Geoenviron Eng.* www.ascelibrary.org. Accessed 28 Aug 2011
3. Wang-hua S (2009) Permeability and seepage stability of coal discard and clay mix. In: The 6th international conference on mining science and technology. www.sciencedirect.com. Accessed 4 July 2011
4. Okogbue CO, Ezeajugh CL (1990) The potentials of Nigerian coal-reject as a construction materia. www.sciencedirect.com. Accessed 4 July 2011
5. Cravotta C, Brady K, Rose A, Dondz J (2011) Frequency distribution of the pH of coal-mine drainage in Pennsylvania. U.S. geological survey water-resources investigations report 99–4018A pp 313–324. www.toxics.usgs.gov/./1507_Cravotta.pdf. Accessed 4 July 2011

Fit-for-Purpose Road Recycling? Triaxial Evaluation of Bitumen Stabilized RAP and Secondary Materials



K. J. Jenkins , C. E. Rudman , and N. A. Mazibuko

Abstract Cold recycling technology is widely considered as a sustainable solution for road pavements; however, it is not always effectively implemented. The key to successful recycling is reliable performance evaluation (including durability) of recycled and secondary materials through the identification of the critical parameters, their tests and well defined protocols, a reliable structural design function to estimate their service life, as well as sound specification limits to measure against. This paper uses RAP (Reclaimed Asphalt Pavement) and RCA (Recycled Concrete Aggregate) as two candidates for recycling in road pavements. Triaxial testing is used for performance evaluation and results are measured against reliable specification limits. Both RAP and RCA materials have boundless potential for recycling, provided that their shear properties meet the requirements.

Keywords Cold recycling · RAP or reclaimed asphalt · Triaxial testing · Recycled concrete · Shear strength

1 Awareness of Recycled Materials' Potential

1.1 Background

Cold recycling technology is widely used as a sustainable solution for road pavements. At the onset of implementing this technology, light pavement structures comprising granular or cemented bases were rehabilitated using stabilization with cement or lime, in order to extend the structural life. At the end of the 1980s, the equipment for recycling was significantly improved with a transition from agricultural implements for pulverizing and mixing of the base, to purpose-built recyclers. In the early 1990s, bitumen stabilization began in earnest. It was introduced to provide a flexible recycled layer less prone to cracking.

K. J. Jenkins (✉) · C. E. Rudman · N. A. Mazibuko
Stellenbosch University, Stellenbosch, South Africa
e-mail: kjenkins@sun.ac.za

During the following decades, pavement structures that were carrying heavier loads and higher traffic volumes were identified for rehabilitation using cold recycling. This challenged pavement designers, researchers and practitioners to meet the roads industry needs by addressing:

- Appropriate material characterization: the pavement layers to be recycled and their suitability for bitumen stabilization with foamed bitumen or emulsion [1, 2].
- Reliable test methods, linked to performance: Indicator tests such as the Indirect Tensile Test, is adequate for light pavements, but does not have a sufficiently strong link to performance as a critical parameter for heavily trafficked pavements. Triaxial testing, for example, is a more reliable performance-based test [3, 4].
- Failure mechanisms: Initially design functions for asphalt were adopted and adapted for design of Bitumen Stabilized Materials thus using fatigue as the damage mechanism. Research subsequently revealed that for mixes with 2–2.5% residual bitumen and 1% active filler, permanent deformation is the appropriate damage mechanism [5, 6].

1.2 Updating the BSM Classification

The improvements in bitumen stabilization methodologies and cold recycling technology, in conjunction with the number of successful projects using this method in the twenty-first century, led to treatment of pavements incorporating thick asphalt base layers. Higher percentages of recycled asphalt or RAP encountered in the recycled base, required adjustments to BSM mix design and structural design approach. Research and practice [7, 8], made its contribution to the understanding RAP dominant BSM mixes, both in terms of processing (with an impact crusher) and mix design.

Triaxial testing of recycled and virgin materials stabilized with foamed bitumen or emulsion stems from investigations that date back to the 1990s [3, 9, 10] forms the foundation for performance evaluation of cold recycled mixes. This provides alternative, reliable measures of evaluating non-traditional materials. Subsequently, in excess of 80 BSM mix designs emanating from 2009 to 2019, for global rehabilitation projects were used formed the source of the specification updates [11]. This analysis also enabled separate BSM classifications to be applied, i.e., BSM1 with high shear strength to withstand heavy axle loads or high volumes of traffic and BSM2 with moderate shear strength to withstand standard loads and moderate traffic.

The reuse of recycled concrete aggregate RCA and Recycled Masonry, i.e., secondary materials, received significant attention of researchers in the 1990s [12, 13] for granular and bitumen stabilization applications. The developments of these technologies are discussed below.

2 Specifications for BSMs with RAP and Granular Materials

2.1 Critical Performance Parameters

Shear stress parameters of granular and bitumen stabilized materials, i.e., cohesion (C) and angle of internal friction (ϕ) are strongly linked to their performance in terms of the rate of damage accumulation or plastic strain. The deviator stress ratio can be determined from the ratio of applied shear stress to failure shear stress [12].

Subsequent to the inclusion of triaxial testing into the mix design method for BSMs in 2009, several important initiatives have achieved progress:

- New apparatus has been developed and standardized for the pavement materials testing industry, i.e., vibrating hammer compaction of 150 mm dia. \times 300 mm high specimens for testing and a triaxial testing setup “tube in cylinder” configuration [14]. Protocols have been developed and standardized in South Africa that account for the equipment’s technical specifications and the test procedures.
- Development of a new mechanistic empirical structural design function for BSMs based on a database of laboratory and field tests [15].
- Field performance evaluation of pavement structures incorporating cold recycling of materials [11].

2.2 Structural Design Function

The link between shear properties of the BSM and performance (i.e., the life of this layer) is achieved through analysis using mechanistic empirical design function [15]. This function was developed based on 14 LTPP (Long-Term Pavement Performance) sections and their mix design shear parameters. The friction angle, cohesion and retained cohesion after moisture conditioning, formed the basis of performance classification as provided in Table 1.

The BSM design [6] has four variables that collectively define the rate of permanent deformation correlated to load repetitions. In essence, the variables are linked to reliability, density, moisture sensitivity and the applied deviator shear stress as a ratio of the maximum shear stress to failure of the BSM.

$$\log N = A - 57.286(\text{DSR})^3 + 0.0009159(P_{\text{MDD}} \cdot \text{Ret}C) \quad (1)$$

where

N = Number of axle repetitions to reach a set rut depth

DSR = Deviator Stress Ratio, as a fraction

P_{MDD} = BSM dry density as a percentage of Max Dry Density (%)

$\text{Ret}C$ = Retained Cohesion (%)

Table 1 Performance classification from shear properties

Performance class	Cohesion (kPa)	Friction angle ($^{\circ}$)	Retained cohesion (%)	Traffic class (MESA) BSM @ DSR = 35%*
Very poor	C < 225	<35	<65	<0.5
Poor	C < 250	<38	<75	<1.6
Moderate	C < 265	<40	<85	<12
Good	C > 265	>40	>85	>12

*Note: 1. MESA = Millions of Equivalent 80 kN Standard Axles
 2. BSM life can also be determined with cohesion and friction angle as variables in the ME design function [6] allowing the specification limits to be developed

Table 2 Reliability coefficient

Reliability (%)	A	Rut limit (mm)
95	1.71113	10
90	1.79873	15
80	1.88733	20
50	2.00443	25

A = Reliability Coefficient linked to Road Category (Table 2).

2.3 Mix Design Data Analysis

In total, 82 independent mix designs of BSMs provided the data base for the analysis of the performance properties. The selection of these mixes was based on adherence to standard BSM mixes, i.e., foamed bitumen or emulsion (SS60 or CSS60), 1.8–2.4% bitumen content, 1% or less active filler (cement or lime), measured RAP content (%), compaction to 100% maximum dry density (equivalent of 100% Modified Proctor) and others.

Initially, the entire data set was analyzed as a collective. A skewed distribution with a significant percentage, i.e., greater than 90%, falling into the moderate and good class, is desired as it implies that the materials can carry medium to heavy traffic. Analysis of the entire data set includes frequencies of between 5 and 19% falling into the very poor and poor class (Fig. 1), which is undesirable. So, additional filtering is required.

Research [8] shows the importance of the RAP content on the overall response and damage of the BSM layer. On this basis, it is therefore logical to filter the 82 BSM mixes according to the RAP percentage at a transition point of 50%. In addition, the class of BSM (1 or 2) is also included as a differentiating tool. Figure 2, which includes only the BSM1 mixes with RAP < 50%, provides a significantly improved

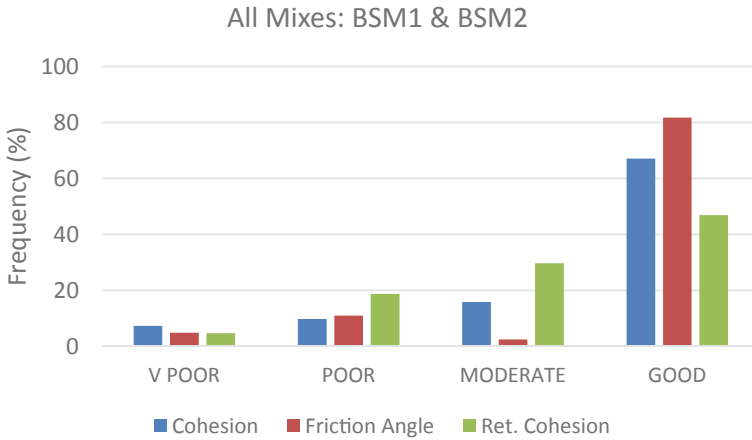


Fig. 1 Frequency of all BSM mixes categorized according to performance class and shear properties of Table 1

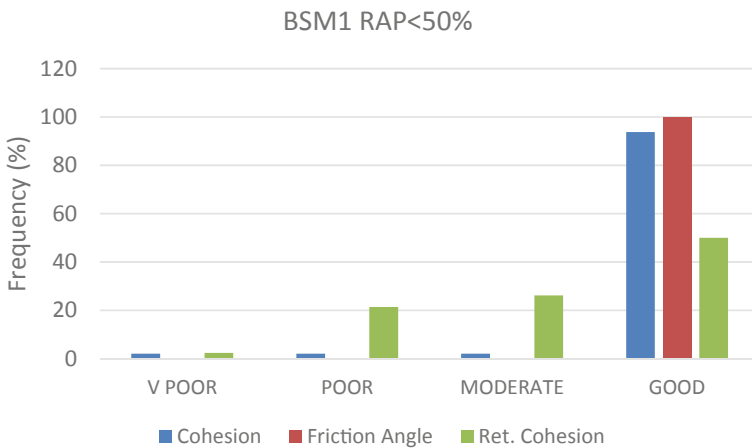


Fig. 2 Frequency of BSM1 mixes with <50% RAP categorized according to performance class and shear properties of Table 1

distribution of mix frequencies. Significantly less mixes fall into the Very Poor and Poor Class.

The BSM1 mixes dominated by RAP, i.e., >50%, also provide an improved distribution of frequencies. Significantly less mixes fall into the very poor and poor class than the analysis of all BSM mixes. Given the shear parameter limits, the retained cohesion in the poor class was the only parameter in the sub-standard performing mixes to show a frequency of significance, see Fig. 3.

For the first time, based on the analysis of shear strength properties for numerous mix designs, BSM technology takes cognisance of the RAP content for material

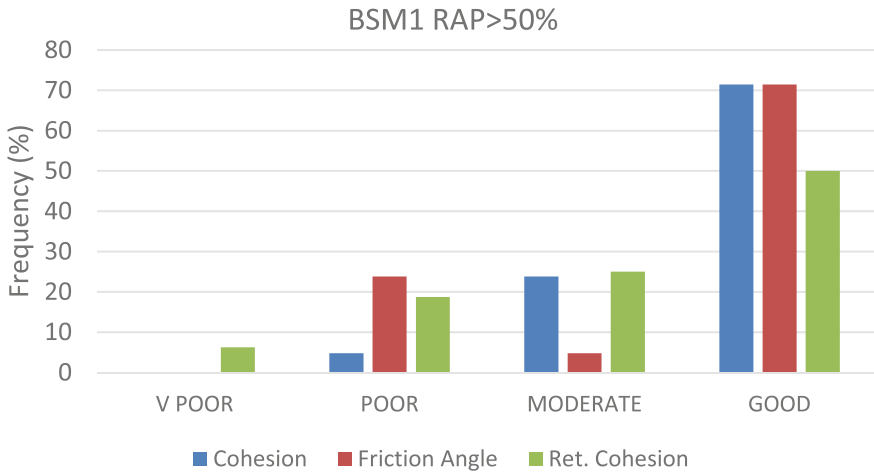


Fig. 3 Frequency of BSM1 mixes with > 50% RAP categorized according to performance class and shear properties of Table 1

classification. Research [4] shows that the addition of high RAP content generally results in an increase in the Cohesion and a slight reduction in the Friction Angle. At the same time, a higher RAP content invariably leads to improved moisture resistance of the BSM. This is captured in an increased Retained Cohesion value measure for triaxial specimens that have been conditioned under water before testing.

Some key findings of this analysis include:

- More than 80% of all the mixes provided match the life of an equivalent BSM1 with <50% RAP, which is known to be a reliable benchmark for medium to heavy traffic, i.e., BSM Classes = Moderate + Good
- Above 85% of BSM1 > 50%RAP mixes match the life of an equivalent BSM1 with <50% RA. The sample in this category includes 21 mixes.
 - 95% of these mixes yield $C > 265$ kPa
 - 76% of these mixes provide $\phi > 38^\circ$
 - The finding supports the perception that with higher RA contents, it is easier to comply with Cohesion limits than friction angle limits.
- Over 76% of BSM2 > 50%RA mixes match the life of an equivalent BSM1 with <50% RA. There sample in this category includes 17 mixes.
 - 65% of these mixes yield $C > 225$ kPa
 - 77% of these mixes provide $\phi > 35^\circ$
 - The BSM2 mixes in this category are unusual. It is apparent that the processing of the RAP to achieve a reliable continuous grading has not occurred, limiting the mix category and performance.

- In excess of 98% of BSM1 < 50%RA mixes match the life of an equivalent BSM1 with <50% RA. There sample in this category includes 48 mixes.
 - 94% of these mixes yield $C > 250$ kPa
 - 100% of these mixes provide $\phi > 40^{\circ}$
 - Compliance with the current Cohesion limits than Friction Angle limits is achieved in a significant percentage of cases.

In addition to the range of BSM shear properties reported here, the Cohesion and Friction Angle limits have been further refined to provide realistic specification limits based on the performance properties of the mixes.

From these findings, the following decisions were necessary:

- Retain BSM1 < 50% RAP limits as they are and not pursued a higher RAP percentage limit, i.e., RAP already has a dominant effect on BSM at 50%.
- Reduce the BSM1 > 50% RAP cohesion limit to 265 kPa and maintain the Friction Angle limit at $> 38^{\circ}$.
- Endorse the approach of using actual C , ϕ and Ret.C values in ME Design of BSMs, provided that the designer is confident that these results will be consistently achieved during construction.

2.4 Shear Property Limits

In summary, the analysis of more than 80 mix designs of Bitumen stabilized materials BSM comprising granular and RAP materials has enabled the refinement of accurate mix compositions and led to reliable specifications, see Table 2. In addition, the measurement of shear parameters has provided a direct link to material performance and the amount of RAP in the mix, for both BSM1 and BSM2 classification (Table 3).

Table 3 BSM Shear property limits for triaxial tests

BSM class	RAP (%)	Triaxial		
		Cohesion (kPa)	Friction angle ($^{\circ}$)	Retained cohesion (%)
BSM1	<50	250	40	75
	50–100	265	38	75
BSM2	<50	200	38	65
	50–100	225	35	75

3 Bitumen Stabilization of Recycled Concrete Aggregate and Masonry

3.1 Challenges of Stabilizing RCA with Bitumen

Recycled concrete aggregate RCA is recognized as a material that is eminently suited to be recycled in new concrete mixes. It can be deduced that RCA is suited for use in a cement stabilized subbase or base layer; however, this results in recycling of the material at a lower level than its original use.

One possible solution for recycling into road pavements is to stabilize RCA with either foamed bitumen or emulsion to create a BSM base. This concept is a research objective that has received focused attention [13]. Guided by the new standard mix design standards for BSMs [10] and [15], the research aimed to extract the maximum performance from RCA. Possible blends with Recycled Masonry RM as well as durability assessments are currently being addressed in further studies.

One of the challenges associated with bitumen stabilization of RCA is the high aggregate porosity after crushing [16]. Recycling of RCA in asphalt mixes becomes unviable due to absorption of up to 1% (or more) bitumen by mass, into the pores of the aggregate. Compared with asphalt, cold recycling with BSMs using RCA has approximately 50% binder content and also includes the presence of moisture at time of mixing, which reduces the bitumen absorption, making the mix more cost-effective [13].

3.2 Analysis of BSM-RCA and Findings

Research of bitumen stabilized RCA requires the consideration of several important variables including the type and age of RCA, its processing and compliance of the gradation in accordance to standardized norms [11]. Once compliant aggregates are available, the mix compositions can be evaluated in two steps, i.e., firstly preliminary evaluation of ITS indirect tensile strength to eliminate undesired variables, followed by triaxial testing for performance evaluations of for the mixes with most potential (Table 4).

The results, for ITS tests on BSM mixes with 2.2% residual bitumen for both foam and emulsion binder types, are reported here. A sensitivity analysis of additional bitumen contents is included elsewhere [13].

The ITS results yield a sufficiently low coefficient of variation (CoV < 15%). The emulsion mixes provide superior values to the foamed bitumen mixes. In addition, the benefits of active filler are visible evident with cement providing the higher moisture resistance than hydrated lime. All six mixes comply with the $ITS_{Dry} > 225$ kPa requirement and $ITS_{Wet} > 125$ kPa limit for BSM1 classification, after 24 h conditioning submerged in water at 25 °C [11]; however, the optimal BSM mixes with 1% cement as active filler were selected for verification using triaxial testing.

Table 4 Experimental matrix for BSM-RCA mixes

Binder type	Bitumen content (%)	Active filler (%)	Test method	Repeats
Foam bitumen	2.2	0	ITS _{dry} , ITS _{wet}	3, 3
Foam bitumen	2.2	1 L	ITS _{dry} , ITS _{wet}	3, 3
Foam bitumen	2.2	1 C	ITS _{dry} , ITS _{wet} , Triaxial	3, 3, 8
Emulsion	2.2	0	ITS _{dry} , ITS _{wet}	3, 3
Emulsion	2.2	1 L	ITS _{dry} , ITS _{wet}	3, 3
Emulsion	2.2	1 C	ITS _{dry} , ITS _{wet} , Triaxial	3, 3, 8

* Active filler AF is either Cement C or Lime L

It should be noted that BSM mixes without active filler have >50% probability of failing to meet the ITS_{wet} limit, however, the RCA in the mix bolsters the moisture resistance of the mixes without active filler. This phenomenon is a function of RCA mixes with free lime that experience self-cementing effects, as shown in separate research [17] (Figs. 4 and 5).

Triaxial testing is undertaken with specially developed equipment for efficient, reliable testing using a standardized confining cylinder and inflatable tube for confining pressure. The test protocol for monotonic triaxial evaluation has been standardized to benchmark results and ensure global repeatability. A total of ten specimens are required to allow for testing at $4 \times \sigma_3$ confining pressures with 2 repeats for each of 8 specimens at optimal conditions. The additional 2 repeats at one confinement for 2 specimens with moisture conditioning were not included in the testing matrix.

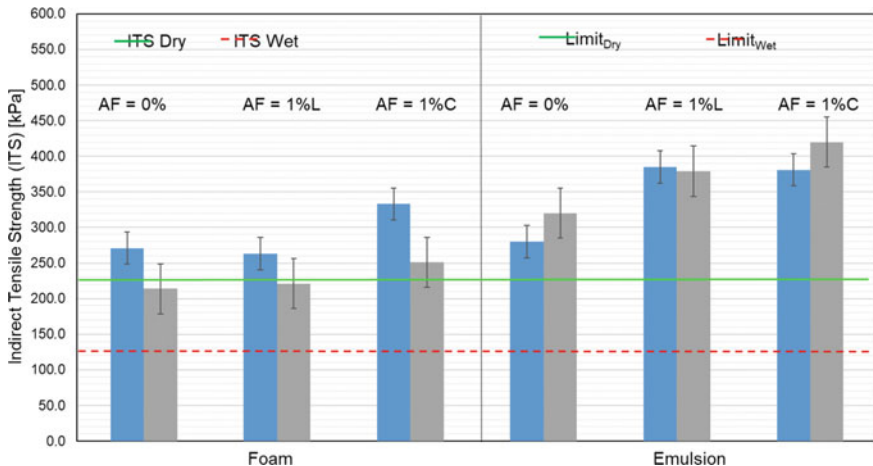


Fig. 4 Influence of active filler AF on BSM-foam and BSM-emulsion with BC = 2.2% (ITS Dry = grey bar and ITS Wet = blue bar)

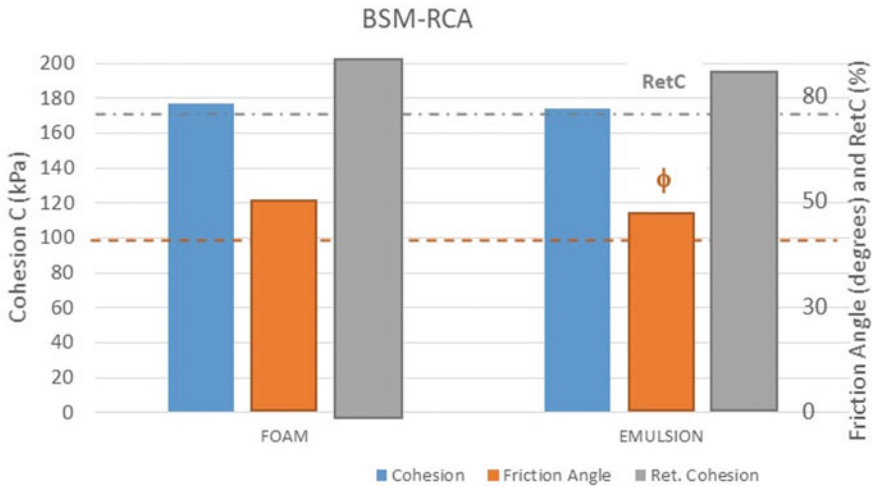


Fig. 5 Measured shear properties of BSM-foam and BSM-emulsion using RCA relative to conventional specification limits (NB: Non-compliance of cohesion limit of $C > 250$ MPa)

Contrary to the ITS results, the triaxial tests show the BSM-foam shear properties to be slightly superior to the BSM-emulsion values. In addition, the friction angle (ϕ) and retained cohesion results far exceed the BSM1 classification for both foam and emulsion. Although the Cohesion values are non-compliant for both binder types, a structural analysis shows that, due to the excessive friction angle and retained cohesion, the combined, measured shear properties could lead to a BSM design life of 20–33 MESAs (Million Equivalent Standard 80 kN Axles). The combined shear properties, therefore, hold significant potential.

4 Conclusions

Several conclusions can be drawn regarding the cold recycling of granular materials and RAP:

- The specifications required for quality assurance of BSM with either foamed bitumen or emulsion binders need to differentiate between low RAP contents (<50%) and high RAP contents (>50%).
- Standardized mix design testing protocols and equipment enables efficient and reliable evaluation of BSMs.
- A new BSM design function for structural performance analysis based on material shear properties enables reliable performance and layer life analyzes with a direct link to mix design data.

Furthermore, conclusions can be drawn regarding cold recycling of RCA materials and their use for bitumen stabilization:

- RCA materials have inherent properties that can provide a first-class classification of BSM material. The absorptivity of RCA materials has a significantly less detrimental influence on bitumen consumption and performance reduction than that of asphalt.
- Cohesion was the only non-compliant shear property for the BSM-RCA mixes, with both foamed bitumen and emulsion. This detracting factor can be addressed with further research exploring the possibilities of blending the RCA with other appropriate secondary or recycled materials.

Recycled materials hold boundless potential for effective application in road pavements. However, in many countries recycled materials are not considered as a substitute for conventional materials in the important load bearing layers of a pavement structure. The key to successful recycling is reliable performance evaluation (including durability) of recycled and secondary materials through the identification of the critical parameters, their tests and well defined protocols, a reliable structural design function to estimate their service life as well as sound specification limits to measure against.

References

1. Jenkins KJ, Collings DC, Johns FM, Hefer AW, Greyling AH, (2019) TG2 removes barriers and elevates the performance of Bitumen Stabilised Materials BSMs. In: 12th conference on asphalt pavements for Southern Africa CAPSA 2019, Sun City, South Africa, pp 668–687. ISBN 978-1-874968-78-8
2. Johns FM, Hefer AW (2019) Revision of the pavement number design system DEMAC and materials classification system. Published by Rubicon Solutions, Johannesburg, South Africa pp 1–35
3. Jenkins KJ, Collings DC, Long FM (main authors) with contributions from Jooste F, Grobler J, Hughes M, Thomson H (2009) Technical Guideline TG2: bitumen stabilised materials: a guideline for the design and construction of bitumen emulsion and foamed bitumen stabilised materials, 2nd edn. Published by Asphalt Academy, Cape Town, South Africa, pp 1–136. ISBN 978-0-7988-5582-2
4. Ebels LJ, Jenkins KJ (2007) Characterisation of bitumen stabilised granular pavement material properties using triaxial testing. In: International conference on advanced characterisation of pavement and soil engineering materials ICACPSEM. Athens, Greece, pp 1–10
5. Jenkins KJ, Collings DC, Jooste FJ (2008) TG2: the design and use of foamed bitumen treated materials. shortcomings and imminent revisions. In: Recycling and stabilisation conference. Auckland, New Zealand, pp 1–16
6. Bierman CR, Jenkins KJ (2019) A design function for bitumen stabilised materials based on laboratory and field evaluation. In: 8th European asphalt technology association EATA conference. Granada, Spain, pp 1–12
7. Collings DC, Jenkins KJ, Souza E (2015) Utilising recycled material stabilised with bitumen to rehabilitate a major highway within stringent time constraints. In: Conference on asphalt pavements for Southern Africa CAPSA 2015. Sun City, South Africa, pp 1–12. ISBN 978-1-874968-69-6

8. Dal Ben M, Jenkins KJ (2015) Durability properties of cold recycling material using bitumen stabilisation incorporating reclaimed asphalt pavement. In: Conference on asphalt pavements for Southern Africa CAPSA 2015. Sun City, South Africa, pp 1–21. ISBN 978-1-874968-69-6
9. Jenkins KJ, Long FM, Ebels LJ (2007) Foamed bitumen mixes = shear performance? *IJPE Int J Pavement Eng* 8(2):85–98
10. Asphalt Academy (2002) Interim Technical Guide TG2: the design and use of foamed bitumen treated materials, 1st edn. Published by Asphalt Academy, Cape Town, South Africa, pp 1–131
11. Jenkins KJ, Collings DC, Johns FM, Hefer AW, (main authors) with contributions from Jooste F (2020) Technical Guideline TG2: bitumen stabilised materials: a guideline for the design and construction of bitumen emulsion and foamed bitumen stabilised materials, 3rd edn. Published by Asphalt Academy, Cape Town, South Africa, pp 1–220
12. Jenkins KJ, Mix design considerations for cold and half-warm bituminous mixes with emphasis on foamed bitumen. doctoral dissertation PhD (Eng). Stellenbosch University, Stellenbosch, South Africa, pp 1–368
13. Mazibuko NMA, Rudman CE, Jenkins KJ (2019) Performance of bitumen stabilised materials using recycled concrete aggregate. In: 12th Conference on asphalt pavements for Southern Africa CAPSA 2019. Sun City, South Africa, pp 1031–1045. ISBN 978-1-874968-78-8
14. Jenkins KJ (2017) Performance of Bitumen Stabilised Materials BSMs—laboratory technology developments and implementation with LCC. In: World conference on pavement and asset management WCPAM 2017. Baveno, Italy, pp 1–10
15. Bierman CR, Jenkins KJ (2019) A design function for bitumen stabilised materials based on laboratory and field evaluation. In 8th European asphalt technology association EATA conference. Granada, Spain, pp 1–15
16. Barisanga F (2014) Material characterization and response modelling of recycled concrete and masonry in pavements. MEng (Research) thesis, Stellenbosch University, Stellenbosch, pp 1–210
17. Rudman CE (2019) Aspects of self-cementation of recycled concrete aggregate when applied in roads. Doctoral dissertation PhD (Eng). Stellenbosch University, Stellenbosch, South Africa, pp 1–339

Sustainability in Transportation Geotechnics

A Mixture of Waste Materials as a Construction Fill in Transportation Infrastructure



Miriam Tawk, Buddhima Indraratna, Cholachat Rujikiatkamjorn, and Ana Heitor

Abstract The reuse of waste materials in engineering projects is a sustainable concept that is being increasingly adopted in civil projects including the transportation infrastructure sector. A mixture of coal wash (CW), a waste produced by the coal mining industry, and rubber crumbs (RC), produced by shredding waste rubber tyres, is a possible alternative to natural quarried rock aggregates that are traditionally used in sublayers of transportation corridors. These materials have different properties than traditional aggregates and their geotechnical behaviour must be investigated before they can be confidently used in transportation infrastructure projects. This study particularly addresses the compaction characteristics of four CWRC mixtures (i.e. 0, 5, 10 and 15% rubber content) with a focus on the energy absorbing nature of rubber. The compaction energy must be increased to compensate for the energy absorbed by rubber and produce a compact packing of particles whilst keeping the breakage levels to a minimum. The strength and deformation properties of the mixture are also addressed through static triaxial tests under three confining pressures to simulate field conditions (i.e. 25, 50 and 75 kPa). The preliminary results showed that the mixture has sufficient strength for transportation sublayers that are not the main load bearing layers such as the subbase layer in roads and the capping/subballast layer in railways. Despite the compressibility of rubber which induces higher settlements, for the loads applied in practice at the level of a subbase or a capping layer, the expected settlements are within the allowable limits.

M. Tawk (✉)

Formerly, School of Civil, Mining and Environmental Engineering and Centre for Geomechanics and Railway Engineering, University of Wollongong, Wollongong, NSW 2522, Australia
e-mail: mst055@uowmail.edu.au

B. Indraratna · C. Rujikiatkamjorn

Transport Research Centre, ARC Industrial Transformation Training Centre for Railroad Technologies (ITTC-Rail), University of Technology Sydney, Ultimo, NSW 2007, Australia
e-mail: buddhima.indraratna@uts.edu.au

C. Rujikiatkamjorn

e-mail: cholachat.rujikiatkamjorn@uts.edu.au

A. Heitor (✉)

School of Civil Engineering, University of Leeds, Leeds LS2 9JT, UK
e-mail: a.heitor@leeds.ac.uk

Keywords Coal wash · Rubber crumbs · Transportation · Sustainability

1 Introduction

The recycling of waste materials in ground engineering projects is becoming more popular in response to the strict environmental legislations associated with both natural quarries and waste landfills. Waste materials such as recycled aggregates from the demolition of existing structures, municipal waste materials such as glass and plastic, and by-products of industrial processes have been proposed by many studies over the past few decades to replace conventional quarried construction materials.

Coal wash (CW), a by-product of the well-established coal mining industry around the world, has been considered in past studies as a potential alternative for natural quarried aggregates [1–5]. For instance, [6] optimized a mixture of CW and steel slag to be used as a port reclamation fill. More recently, [7] proposed a mixture of CW and fly ash as a subbase material for roads. Most of these studies highlighted that coal wash, being weaker than traditional aggregates, is highly degradable and undesirable high-breakage levels were observed. To mitigate the degradation problem of CW, [8] introduced rubber crumbs (RC) into a mixture of CW and steel furnace slag and the mixture was optimized to be used a subballast layer in railways. Rubber crumbs also serve as an energy absorbing component which enhances the damping properties of the mixture [9, 10]. The effect of rubber inclusions on the geotechnical behaviour of traditional aggregates such as gravel and sand was also studied by numerous researchers in the past few years [11–19].

In this study, rubber is mixed with CW to create an energy absorbing layer as a potential construction fill that can be used in transportation sublayers, such as the base/subbase layer in roads or the capping/subballast layer in railways. The compaction characteristics and the strength and deformation properties of four CWRC mixtures with 0, 5, 10 and 15% of added rubber are evaluated. The stress–strain response is studied using monotonic triaxial tests under three low-confining pressures (i.e. 25, 50 and 75 kPa) to mimic field conditions in transportation infrastructure. The effect of rubber on the strength and deformation properties of CWRC mixtures is addressed and these properties are compared with the requirements for the sublayers of transportation corridors.

2 Materials and Testing Programme

CW used in this study was sourced from a colliery near Wollongong (NSW, Australia) and RC were procured from a tyre recycling company in Victoria. CW is a well-graded material with a specific gravity of 2.25, whilst rubber shreds are much lighter having a specific gravity of 1.15. The particle size distribution (PSD) curves of CW and RC are shown in Fig. 1. Four CWRC mixtures were considered in this study

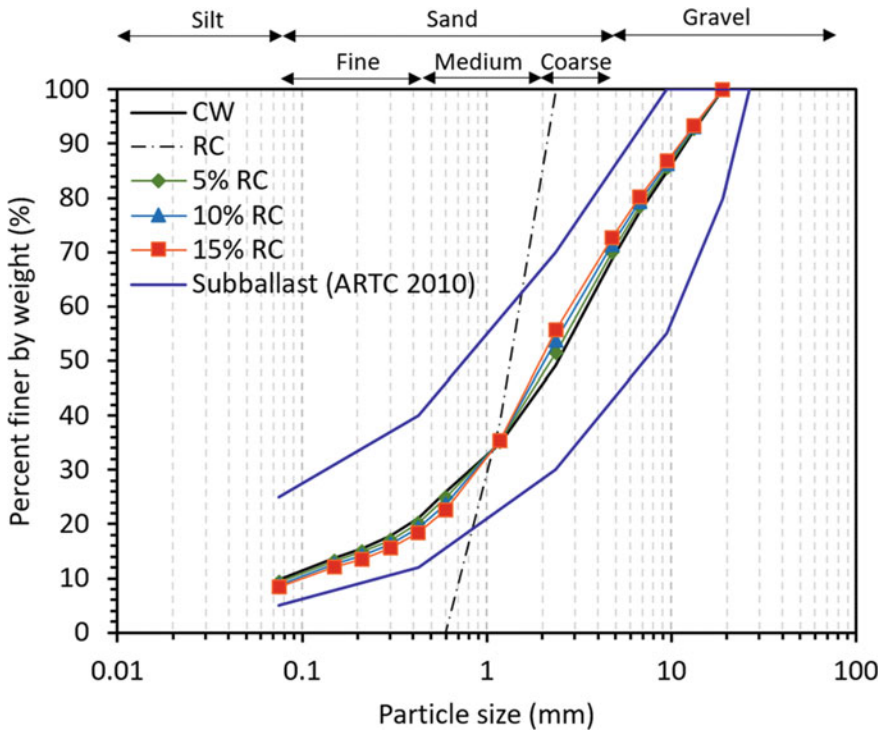


Fig. 1 PSD curves of CW, RC and CWRC mixtures

having 0, 5, 10 and 15% of added rubber which corresponds to 0, 4.76, 9.09% and 13.04% rubber content, respectively, with respect to the total weight of the mixture. A previous study [8] optimized a mixture of CW, SFS and RC as a capping material for railways and found that the optimum rubber content is close to 10%. Therefore, a range between 0 and 15% was selected knowing that more than 15% of rubber would overly reduce the strength of the material, make the blended mix overly compressible, and induce excessive axial settlement. Table 1 shows the physical properties of the CWRC mixtures and Fig. 1 shows that the PSD curves of all mixtures fall within the lower and upper limit for a subballast/capping material [20].

Table 1 Physical properties of CWRC mixtures

Added rubber (%)	Grain size distribution (%)			Specific gravity
	Gravel	Sand	Silt	
0	31.5	58.8	9.7	2.25
5	30.0	60.7	9.2	2.15
10	28.6	62.5	8.8	2.07
15	27.4	64.2	8.4	2.00

Table 2 Details of the compaction tests (modified after [22])

Energy level	Hammer weight (kg)	Layers	Blows/layer	Energy (kJ/m ³)
E ₁	2.7	3	25	596
E ₂	2.7	5	25	993
E ₃	2.7	5	40	1588
E ₄	2.7	5	50	1985
E ₅	4.9	5	25	2703

CW material was sieved using the wet and dry method [21] and each sample was prepared by mixing the exact weight of each size to reach the target PSD curve (Fig. 1). Then, water was added to reach the target moisture content ($\approx 9\text{--}10\%$ for triaxial specimens) and the sample was left in a sealed container for 24 h under constant humidity and temperature for consistent water distribution. Compaction tests were performed at standard Proctor, modified Proctor and three intermediate energy levels (Table 2). Static triaxial tests were performed in three stages. First the specimen (100-mm diameter and 200-mm height) was saturated by increasing the back pressure until a Skempton value greater than 0.97 was achieved. Then, the sample was consolidated at the target effective confining pressure (i.e. 25, 50 and 75 kPa). The shearing stage was then performed at a relatively slow constant strain rate of 0.1 mm/min to ensure fully drained conditions and the test was carried until the maximum strain limit of the equipment was reached, $\approx 20\%$. For the purpose of comparison, all the specimens were compacted to the same initial void ratio by increasing the compaction energy when rubber content increased.

3 Experimental Results

3.1 Compaction

The compaction curves under standard Proctor effort are shown in Fig. 2a. As expected, the dry density of the mixture decreases with increasing rubber content. This is partly due to the lower specific gravity of rubber particles. To eliminate the effect of the difference in unit weight of the components of the mixture and evaluate the effect of the energy absorbing nature of rubber on compaction efficiency, the void ratio is considered a better representation of the compaction efficiency [22].

Figure 2b shows that the void ratio at the optimum moisture content (OMC) increases almost linearly with increasing rubber content and becomes greater than 0.3 (i.e. the maximum acceptable void ratio for a capping layer [20]) when 5% RC are added to the mixture. Therefore, in practice, the compaction energy must be modified to compensate for the energy absorbed by the rubber. The effect of rubber content on the breakage index (BI) was also evaluated by quantifying the shift in the

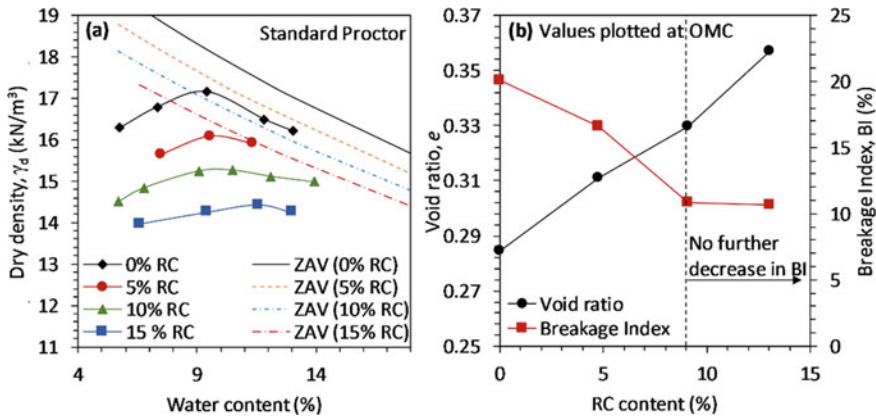


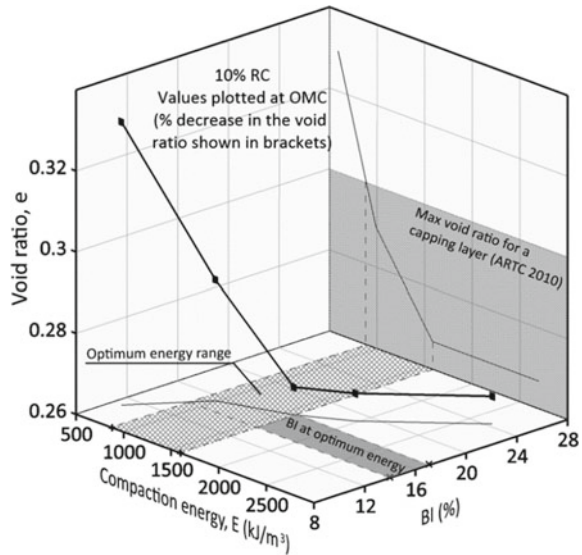
Fig. 2 Compaction of CWRC mixtures at standard Proctor effort (modified after [22])

PSD curve after compaction [23]. Figure 2b shows that the BI decreases significantly when 10% rubber is added to the mixture. However, the change in the BI becomes negligible when more rubber is added. This indicates that for the size of rubber used, the degradation of particles reaches a first minimum at 10% rubber content and might not start to decrease again unless a much higher rubber content is used due to the inevitable breakage of larger particles in the mixture. Based on the above observations, the mixture with 10% of added rubber was compacted at higher energy levels up to modified Proctor to evaluate the effect of rubber on the compaction efficiency at higher energy levels.

Figure 3 shows the change in the void ratio and the BI with increasing energy levels for the CWRC mixture with 10% of added rubber.

The void ratio decreases significantly when the compaction energy increase from E_1 (standard Proctor) to E_3 . After that point, no substantial change in the void ratio is observed when the compaction energy increases to E_4 and E_5 (modified Proctor). This indicates that in the energy range between E_1 and E_3 , the excess energy transferred to the system is employed to compensate for the energy absorbed by rubber particles and to reach a compact rearrangement of particles. The mixture reaches an optimum packing which cannot be enhanced anymore at E_3 and for energies higher than E_3 the extra energy delivered to the system is either dissipated through rubber compression or through the degradation of CW particles. In fact, there is a sharp increase in the BI after E_3 which again shows that the mixture is over compacted and any excess energy would only lead to further breakage. Therefore, in practice the compaction energy must be selected with caution to reach an acceptable void ratio without causing excessive breakage of CW. Figure 3 shows that for just a 34% increase in compaction energy from standard proctor (596 kJ/m³) to 800 kJ/m³, the void ratio of the mixture with 10% rubber content becomes less than 0.3. For instance, if 4 passes are required to compact an incompressible material like CW, a 34% increase in compaction energy is equivalent to 2 more passes which are easily achieved in the field. It is noteworthy

Fig. 3 Void ratio and Breakage Index versus compaction energy (modified after [22])



that for this higher compaction energy, the BI of the CWRC mixture with 10% of added rubber ($\approx 13\%$) is still less than the BI of the mixture with no rubber (i.e. CW) compacted under standard Proctor ($\approx 20\%$).

3.2 Stress–strain Relationship

Figure 4 shows the stress–strain relationship for all CWRC mixtures at three confining pressures (i.e. 25, 50 and 75 kPa). All the mixtures experience a post-peak softening behaviour and the peak deviator stress decreases as rubber is added to the mixture. This is attributed to the lower shear strength of rubber particles. However, even for a low confining pressure of 25 kPa, the strength of the mixture with 15% RC is still higher than 100 kPa, which is the expected load at the level of a subbase layer or capping/subballast layer [8, 24–26]. Moreover, the ductility of the material is significantly improved when rubber is introduced into the mixture. From Fig. 4, it is observed that the post-peak softening modulus decreases when rubber content increases.

Figure 4 also shows that all mixtures reach almost the same critical state at 20% axial strain. This indicates that the inclusion of rubber particles affects the peak stress state only. In a CWRC mixture, three types of contact forces exist: Contact between coal wash particles (CW-CW), contact between coal wash particles and rubber particles (CW-RC) and contact between rubber particles (RC-RC). For the low RC content considered in this study, we may assume that the number of contact points between rubber particles is negligible. At the peak stress state, the number

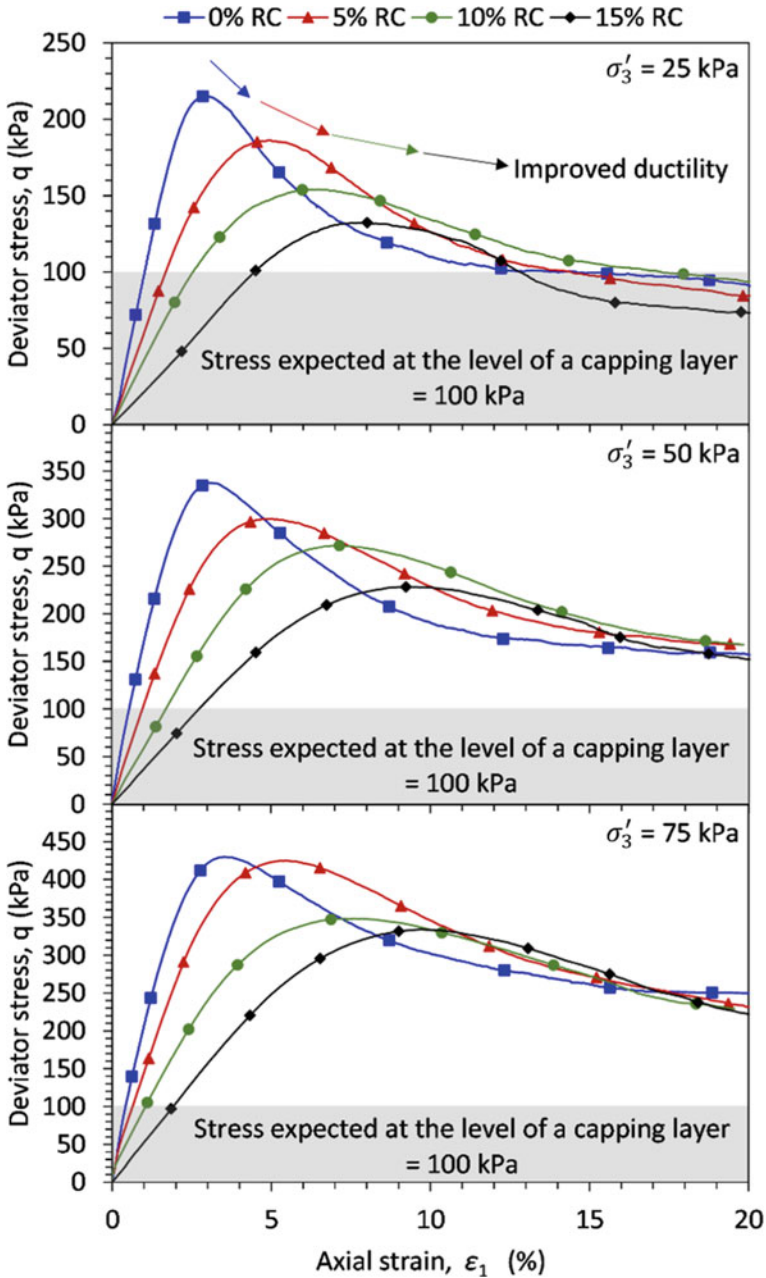


Fig. 4 Stress-strain relationship of CWRC mixtures (modified after [22])

of contact forces between coal wash and rubber crumbs affects the total stress that can be sustained by the mixture. However, at the critical state and when the sample has undergone dilation, the total number of contact points decreases and the number of contact points between rubber particles and CW particles becomes negligible compared to the total number of contact points, thus the behaviour at the critical state is mainly dominated by the frictional resistance between CW particles only. Previous studies also reported a unique critical state for sand-rubber mixtures for a rubber content less than 40% [15].

3.3 Volumetric strain

The effect of rubber inclusion on the maximum compressive volumetric strain is illustrated in Fig. 5. This volumetric strain does not represent the total change in the volume of the mixture, it only represents the change in the volume of voids as it is experimentally determined as:

$$e_v^* = \frac{\Delta V_v}{V_0} = \frac{\Delta V_w}{V_0}$$

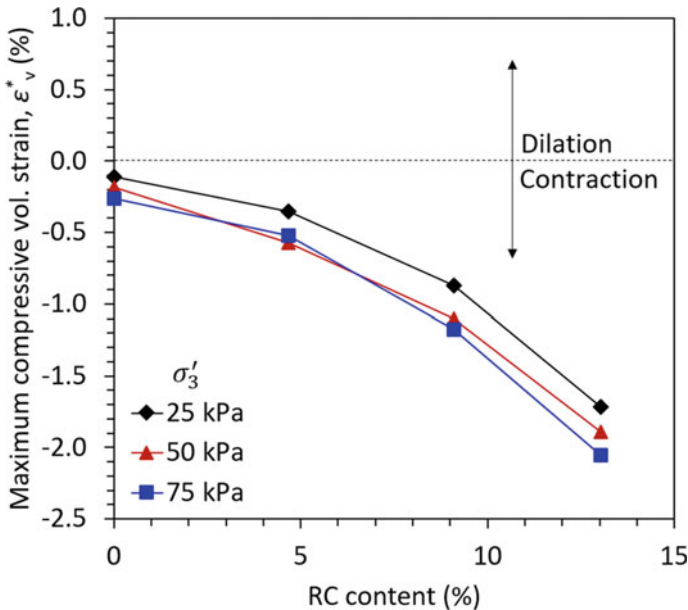


Fig. 5 Effect of rubber inclusion on the maximum compressive volumetric strain

where V_0 is the initial total volume of the sample, V_v is the volume of voids, and V_w is the volume of water within the sample and for saturated conditions, $\Delta V_v = \Delta V_w$. Hence, the compression of rubber particles is not captured. The maximum compressive volumetric strain increases with increasing rubber content indicating a more contractive behaviour as rubber content increases. Rubber particles are highly deformable which facilitates the rearrangement of particles in the compression range. This results in a smaller volume of voids within the sample and hence a higher compressive volumetric strain.

3.4 Strength

Figure 6 shows the relationship between the peak friction angle and the rubber content for all CWRC mixtures. As expected, the peak friction angle decreases with increasing rubber content and this is attributed to the lower shear strength of rubber particles compared to CW. For transportation substructure layers which are not the main bearing layers such as the subballast layer in railways or the subbase layer in roads, a minimum peak friction angle of 45° is considered acceptable. The mixtures with 0, 5 and 10% of added rubber show an acceptable peak friction angle for confining pressures of 25 and 50 kPa. Only when the confining pressure is 75 kPa, the mixture with 10% RC falls below the minimum limit. However, the confining pressure usually encountered at depth of the subbase layer or the capping/subballast

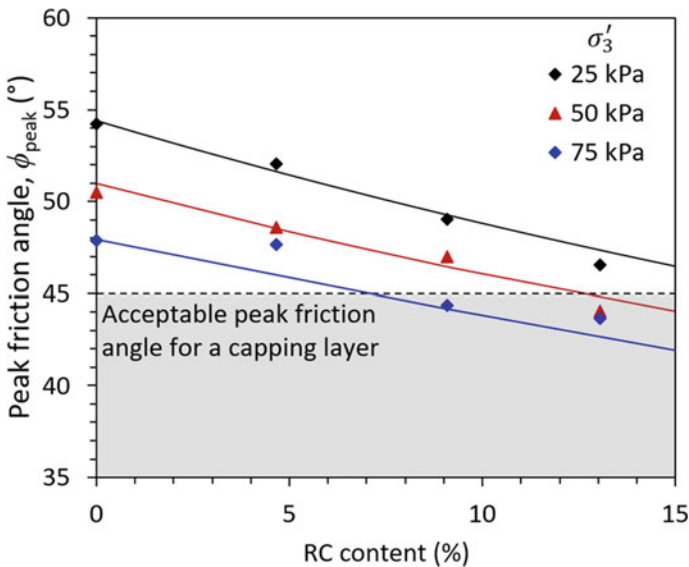


Fig. 6 Peak friction angle of CWRC mixtures (modified after [22])

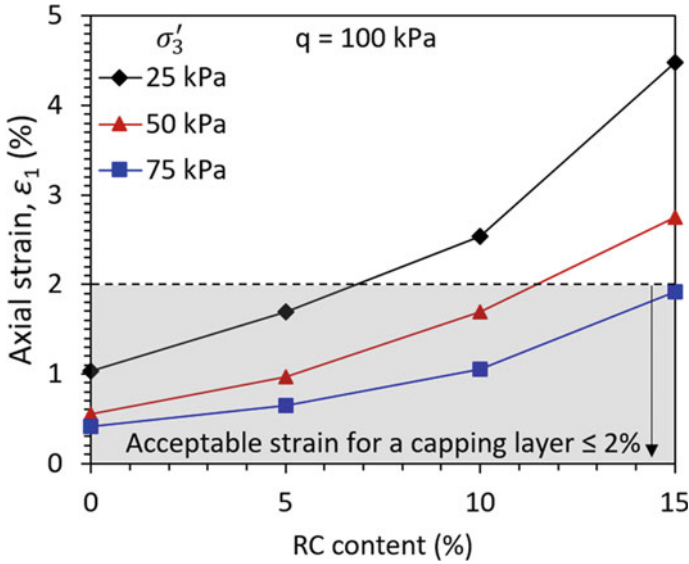


Fig. 7 Axial strain for a deviator stress of 100 kPa

layer is close to 40 kPa [8, 26–28]. Therefore, for these conditions the mixture has an acceptable strength for a rubber content $\leq 10\%$.

3.5 Settlements

Rubber is highly compressible and when added to CW, it induces higher settlements under service loads. The maximum allowable axial strain for a subbase layer in roads or a capping/subballast layer in railways is 2%. Figure 7 shows the axial strain observed for a deviator stress of 100 kPa, which is the representative stress at the top of a subbase material [24–26] and at the level of a capping/subballast layer [8, 29].

The results show that the anticipated axial strain for the mixtures with 0, 5 and 10% of added rubber is below the maximum limit for confining pressures of 50 and 75 kPa and it becomes greater than 2% only when the confining pressure decreases to 25 kPa. The confining pressure expected at the top of a subbase layer or a capping/subballast layer usually ranges between 40 and 50 kPa [8, 26–28]. Therefore, up to 10% of added rubber can be used without inducing unacceptable settlements.

4 Conclusion

A series of compaction and triaxial tests were performed on four mixtures of CW and RC to evaluate its potential reuse as construction fill in transportation sublayers. The following conclusions are made:

- Despite the energy absorbing nature of RC, the mixture can be compacted to an acceptable level by increasing the compaction energy by 34%, i.e. multiplying the number of roller passes by 1.3, which is easily attainable in practice. It is not recommended to significantly increase the compaction energy, as this may only result in excessive breakage of CW without any additional increase in the dry density.
- The ductility of the mixture is significantly improved when rubber is added. This means that the material would not fail abruptly if the encountered loads become greater than the strength of the mixture and excessive immediate settlements can be avoided.
- For 10% of added rubber and for the confining pressures encountered in the field, the strength of the mixture is adequate for sublayers which are not the main bearing layers in transportation infrastructure such as the subbase layer in roads or the capping/subballast layer in railways.
- For the loads expected at the level of a subbase or capping/subballast layer, monotonic triaxial tests showed that the expected settlements are within the acceptable limit of 2%.

Although the properties of the proposed mixture were determined under static conditions, preliminary tests showed promising results and the proposed CWRC matrix could be adequate for a subbase in roads or a capping/subballast layer in railways. However, further testing under cyclic loading must be performed to fully characterize the material so it can be confidently used in transportation infrastructure projects.

Acknowledgements Financial assistance provided by the Australian Research Council (ARC) Linkage Project (LP160100280) is gratefully acknowledged. The assistance provided by industry (RMS, Douglas Partners, South 32, and Tyre Crumbs Australia) in relation to the procurement of material used in this study is gratefully acknowledged. Also, the laboratory assistance provided by Mr. Richard Berndt is appreciated. Some figures in this paper have been modified, whereby the original data has been reproduced with kind permission from Transportation Geotechnics.

References

1. Leventhal A (1996) Coal washery reject as an engineered material. In: National symposium on the use of recycled materials in engineering construction. Institution of Engineers, Australia
2. Indraratna B (1994) Geotechnical characterization of blended coal tailings for construction and rehabilitation work. *Quarterly J Eng Geol* 27(Part 4):353–361

3. Indraratna B, Rujikiatkamjorn C, Chiaro G (2012) Characterization of compacted coal wash as structural fill material. In: *GeoCongress 2012: state of the art and practice in geotechnical engineering*. pp 3826–3834
4. Montgomery DG (1990) Utilisation of coal washery wastes in engineering construction. In: *International coal engineering conference*. Barton, ACT, Australia: Institution of Engineers, Australia
5. Okagbue CO, Ochulor OH (2007) The potential of cement-stabilized coal-reject as a construction material. *Bull Eng Geol Env* 66(2):143–151
6. Chiaro G et al (2015) Optimisation of coal wash-slag blend as a structural fill. In: *Institution of civil engineers: ground improvement*
7. Wang D et al (2019) A mixture of coal wash and fly ash as a pavement substructure material. *Transport Geotech* 21:100265
8. Indraratna B, Qi Y, Heitor A (2018) Evaluating the properties of mixtures of steel furnace slag, coal wash, and rubber crumbs used as subballast. *J Mater Civ Eng* 30(1):04017251
9. Qi Y et al (2018) Effect of rubber crumbs on the cyclic behavior of steel furnace slag and coal wash mixtures. *J Geotech Geoenviron Eng* 144(2):04017107
10. Qi Y, Indraratna B, Vinod JS (2018) Behavior of steel furnace slag coal wash and rubber crumb mixtures with special relevance to stress-dilatancy relation. *J Mater Civ Eng* 30(11):04018276
11. Cho S-D et al (2007) Utilization of waste tires to reduce railroad vibration. *Mater Sci Forum* 544–545:637–640
12. Kim HK, Santamarina JC (2008) Sand–rubber mixtures (large rubber chips). *Can Geotech J* 45(10):1457–1466
13. Lee JH et al (1999) Shredded tires and rubber-sand as lightweight backfill. *J Geotech Geoenviron Eng* 125(2):132–141
14. Nakhaei A et al (2012) Dynamic properties of granular soils mixed with granulated rubber. *Soil Dyn Earthq Eng* 43:124–132
15. Youwai S, Bergado DT (2003) Strength and deformation characteristics of shredded rubber tire-sand mixtures. *Can Geotech J* 40(2):254–264
16. Mashiri MS et al (2015) Shear strength and dilatancy behaviour of sand–tyre chip mixtures. *Soils Found* 55(3):517–528
17. Edil TB, Bosscher PJ (1994) Engineering properties of tire chips and soil mixtures. *Geotech Test J* 17(4):453–464
18. Esmaeili M et al (2016) Experimental study on dynamic properties of railway ballast mixed with tire derived aggregate by modal shaker test. *Adv Mech Eng* 8(5):1–13
19. Zornberg JG, Cabral AR, Viratjandr C (2004) Behaviour of tire shred-sand mixtures. *Can Geotech J* 41(2):227–241
20. Australian Rail Track Corporation (2010) *Engineering (Track & Civil) Standard—Earthworks, Formation and Capping Material*. Australian Rail Track Corporation Limited
21. Standards Australia (2009) *Methods of testing soils for engineering purposes—Soil classification tests—Determination of the particle size distribution of a soil—Standard method of analysis by sieving*. Standards Australia Limited Sydney, Australia
22. Indraratna B et al (2019) Compaction, degradation and deformation characteristics of an energy absorbing matrix. *Transport Geotech* 19:74–83
23. Indraratna B, Lackenby J, Christie D (2005) Effect of confining pressure on the degradation of ballast under cyclic loading. *Géotechnique* 55(4):325–328
24. Bilodeau J-P, Doré G, Schwarz C (2011) Effect of seasonal frost conditions on the permanent strain behaviour of compacted unbound granular materials used as base course. *Int J Pavement Eng* 12(5):507–518
25. Saberian M et al (2018) Permanent deformation behaviour of pavement base and subbase containing recycle concrete aggregate, coarse and fine crumb rubber. *Constr Build Mater* 178:51–58
26. Soliman H, Shalaby A (2015) Permanent deformation behavior of unbound granular base materials with varying moisture and fines content. *Transport Geotech* 4:1–12

27. Saberian M, Li J, Setunge S (2019) Evaluation of permanent deformation of a new pavement base and subbase containing unbound granular materials, crumb rubber and crushed glass. *J Clean Prod* 230:38–45
28. Signes CH et al (2016) An evaluation of the resilient modulus and permanent deformation of unbound mixtures of granular materials and rubber particles from scrap tyres to be used in subballast layers. *Transport Res Proc* 18:384–391
29. Signes CH et al (2016) Analysis of the bearing capacity of unbound granular mixtures with rubber particles from scrap tyres when used as sub-ballast. *Materiales de Construcción* 66(324):e105

Finite Element Simulations of Recycled Asphalt Pavement (RAP) Materials to Be Utilized in Unbound Pavement Layers



Andreas Loizos, Brad Cliatt, and Christina Plati

Abstract The application of recycled asphalt pavement (RAP) materials in a pavement base layer as an unbound material is currently limited despite the potential for usage of lower-quality RAP materials in underlying pavement base layers. An increase in the utilization of these RAP materials can positively impact the long-term sustainability of pavement structures and is a topic that should be investigated more in-depth. These materials have been initially shown to exhibit mechanical characteristics suitable for usage in unbound pavement layers. Based on this, more information is thought to be needed to provide background information concerning the parameterization of the RAP material's mechanical characteristics. In addition, information concerning the most appropriate methodology for the constitutive modeling and simulation of materials containing RAP for pavement design procedures should be investigated. The goal of the current preliminary study is to provide more information on the behavior of RAP material to assist in their increased implementation in unbound pavement layers. The investigation includes an initial characterization of these materials through resilient modulus testing. Based on the results, various constitutive models are investigated in order to provide an analysis and comparison of the results of the variations between models and the potential effects in predicted responses. The goal of the paper is to provide additional research that will aid in the increased adoption of more environmentally friendly pavement construction techniques, leading toward increased sustainability.

Keywords RAP · Sustainability · Constitutive models

A. Loizos (✉)

NTUA Department of Transportation Planning and Engineering, Athens, Greece

e-mail: aloizos@central.ntua.gr

B. Cliatt · C. Plati

NTUA Laboratory of Pavement Engineering, Athens, Greece

e-mail: bcliatt@mail.ntua.gr

C. Plati

e-mail: cplati@central.ntua.gr

1 Introduction

1.1 Problem Statement

The utilization of recycled asphalt pavement (RAP) material in the bound asphalt layers is becoming more commonplace as research and in situ applications have provided evidence of its capabilities when incorporated within the upper bound layers. However, the application of RAP materials within the pavement base layers as an unbound material is more limited despite the potential for usage of lower-quality RAP materials in underlying pavement base layers. An increase in the utilization of these RAP materials will have the potential to positively impact the long-term sustainability of pavement structures and is a topic that should be further investigated. Previous research into these recycled asphalt materials has shown that they have the potential to exhibit the mechanical characteristics that are suitable for usage in underlying unbound pavement layers. Based on this, more information is thought to be needed to in order provide additional background information concerning the parameterization of the RAP material's mechanical characteristics. In addition, information concerning the most appropriate methodologies for the constitutive modeling of the materials containing RAP for pavement design procedures is needed.

1.2 Objectives

The main objective of the current preliminary study is to provide more information on the overall behavior of RAP material to assist in their increased implementation in unbound pavement layers. The current research study is a preliminary investigation that will initially focus on the mechanical characterization of RAP materials in the base layer of flexible asphalt pavement structures through the resilient modulus behavior of the material. Based on the results of this stage of the study, several constitutive models will be investigated to provide an analysis and comparison of the results of the variations between the constitutive models and their potential effect on pavement design processes. The goal of the paper is to provide additional research that will help in the increased adoption of potentially sustainable pavement construction techniques.

2 Theoretical Background

Previous experience has shown that the utilization of RAP material is most often in the upper bound layers of pavement structures. Research and experience, however, have also shown the viability and the potential for these more sustainable materials to be reutilized in the underlying unbound granular base or subbase layers. Potential

environmental and economic benefits for the incorporation of RAP in bound layers are already supported by extensive research and implementation over the years. However, similar information is still more limited for the inclusion of RAP within the unbound layers of a pavement structure. Recent trends indicate both the need and the desire for the implementation of more sustainable technique in regard to pavement design/construction. With this in mind, it is believed that RAP materials should be examined in greater detail to aid in their proper utilization and to gain a more in-depth understanding of their impact within base layers of flexible road pavements in regards the overall pavement structure.

2.1 RAP in Unbound Layers

With virgin aggregate becoming more difficult to source and more costly to implement, the need has arisen to investigate RAP-based materials for implementation within the base layers of pavement structures. The incorporation of RAP can conserve energy, lowers transportation costs required to obtain quality virgin aggregate, and overall preserves valuable resources [1]. Puppala et al. [2] investigated the sustainable reutilization of limestone quarry materials and RAP within pavement base layers and stated that even though the usage of recycled materials as pavement base layer materials has increasingly gained acceptance, comprehensive geotechnical characterization is still required. Alam et al. [3] concluded that RAP has a potential to be utilized at high percentages within pavement base layers. Thakur and Han [4] investigated RAP materials for inclusion in base layers aggregate for highway construction and stated that it was a sustainable solution. Plati and Cliatt [5] in recent research stated that RAP as a material is fully recyclable, and that additional research is vital to increase sustainability.

Multiple research studies over the years have decided upon on the mixing of virgin aggregate with RAP to reach appropriate mechanical properties [6–8]. Despite the existing research, the allowed percentage of RAP in base layers as well as knowledge related to the suitability for utilization in unbound base layers is not currently fully defined and/or researched. Research, for example, is limited, and knowledge is still being developed regarding the strength behavior and characteristics of RAP materials in regards to more traditionally used virgin aggregates within the base course. However, Edil et al. [9] concluded that, in comparison to conventional base layer materials, RAP has an increased modulus. Even more limited information is available concerning the effect of moisture condition on RAP-based materials. Attia and Abdelrahman [6] investigated the effect of moisture content on materials containing 50/100% RAP at OMC, plus/minus 2%. Nourediun and Abdelrahman [10] investigated the effect of moisture percentage above/below OMC on the variables utilized to model the base material modulus containing various RAP percentages. Cliatt et al. [11] concluded that RAP material exhibited modulus values that are equivalent or exceed those of a virgin aggregate utilized for base material at OMC and below. Most other recent research regarding RAP and the resilient modulus is focused on

testing only at optimum moisture conditions. Though there is research in regards to RAP in base layers, the current investigation adds to the current knowledge by combining both a laboratory-based investigation and a computer modeling of this behavior to better understand the effects of material properties on the responses of these materials within flexible pavement structures.

2.2 Constitutive Modeling and Finite Elements (FE)

A multitude of researchers have over the years developed constitutive models to characterize the behavior of unbound granular materials for usage in pavement construction. Upon a review of existing models, the following models were selected for further utilization within the scope of the current investigation due to their wide acceptance and implementation. The $K-\Theta$ model [12] is one of the initially developed and widely recognized constitutive models and still often utilized. Uzan [13] developed a model that incorporated the shear stress effect in the granular material model, to overcome potential issues of the $K-\Theta$ model. Uzan [14] developed/proposed an alteration to the Uzan model by replacing the deviator stress with the octahedral shear stress. The model by introducing a three-dimensional aspect through the octahedral shear stress attempts to more realistically represent actual loading conditions on the unbound material layers.

$$Mr = k_1 P_a \left(\frac{\theta}{P_a} \right)^{k_2} \quad K - \Theta \text{ model} \quad (1)$$

$$Mr = k_1 P_a \left(\frac{\theta}{P_a} \right)^{k_2} \left(\frac{\sigma_d}{P_a} \right)^{k_3} \quad \text{Uzan model} \quad (2)$$

$$Mr = k_1 P_a \left(\frac{\theta}{P_a} \right)^{k_2} \left(\frac{t_{\text{oct}}}{P_a} \right)^{k_3} \quad \text{MEPDG model} \quad (3)$$

where

θ is the first invariant of the tensor stress = bulk stress.

$\theta = \sigma_1 + \sigma_2 + \sigma_3 = \sigma_1 + 2\sigma_3$, or alternatively $(\sigma_1 + 2\sigma_3)$ or $(\sigma_d + 3\sigma_3)$,

σ_d is the deviator stress = $\sigma_d = \sigma_1 - \sigma_3$,

k_1 , k_2 , and k_3 are laboratory determined material constants from regression analysis,

P_a = atmospheric pressure (kPa).

Table 1 Gradation—% passing per material

Sieve (mm)	RAP	VA	50/50
40	100	100	100
31.5	100	97.4	100
16	76.4	80.4	85.2
8	53.5	63.6	65.2
4	42.3	44.7	46.8
2	29.4	31.1	28.6
1	13.5	21.0	14.7
0.5	6.2	14.0	8.2
0.063	0.6	1.4	0.6

Table 2 Material properties

Material	MDD (kg/m ³)	OMC (%)	Classification	Asphalt content (%)
RAP	2078	4.0	GW/A-1-a	4.4
VA	2248	6.2	GW/A-1-a	0.0
50/50	2217	6.0	GW/A-1-a	2.2

3 Materials Tested

3.1 Physical Characteristics

In the current study, three materials were investigated. The first of these materials is a 100% RAP material, the second is a traditional virgin aggregate (VA) material, and the third is a combination of these two materials in a 50/50 percentage ratio by weight (50/50). These materials’ physical characteristics are shown in Tables 1 and 2. Table 1 shows that the gradations for the investigated material are similar for aggregate sizes below 2 mm with an overall distribution of the materials similar overall. In order to produce these mixtures, the materials were partially graded with emphasis on the fine materials as they are known to strongly influence laboratory modulus testing results. Both the maximum dry density (MDD) and the optimum moisture content (OMC) were determined through the modified Proctor test standard—EN 13,286–2 with a type B mold.

3.2 Resilient Modulus

The resilient modulus is defined as: $M_r = \sigma_d / \epsilon_r$ where σ_d is the deviator stress and ϵ_r is the recoverable strain. The materials under investigation were tested according to the AASTHO T-307 (repeated load triaxial test) protocol (material type I) for

determination of their resilient modulus. The materials were all tested at OMC as well as $\pm 2\%$ OMC. The testing protocol consisted of 15 distinct stages of loading. The stages are defined: confining pressures— σ_3 (kPa), axial stresses— σ_{\max} (kPa), cyclic stresses— σ_{cyclic} (kPa), and contact stresses— $0.1\sigma_{\max}$ (kPa). The load is a haversine load with a 0.1 s duration followed by a 0.9 s rest period. Results from the resilient modulus testing formed the basis for the next stages of the investigation.

4 Finite Element Simulation

Based on the results of testing from the laboratory determination of the resilient modulus, a regression analysis was performed for each of the test combinations (material–moisture) to determine the individual regression constants (k_1 , k_2 , and k_3) for each of the constitutive models (K- θ , UZAN, and MEPDG) to be investigated with finite element analysis. The regression analysis, for all cases, was performed for a 95% confidence level.

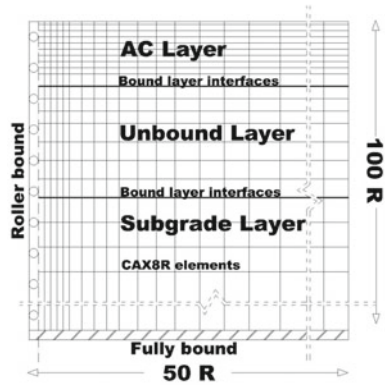
After the determination of regression constants for each case, an FE analysis was then undertaken to investigate the material's predicted responses. For the analysis, the ABAQUS software was utilized for the predicted responses of the pavement materials and pavement structures that are investigated in the current research effort. Before the analysis could begin, individual user MATerial subroutines (UMAT) were coded and verified for each of the constitutive laws (K- Θ , Uzan, and MEPDG) being utilized for modeling of the unbound granular materials of the pavement base layer. For the FE investigation, the critical responses were calculated and exported for further in-depth analysis. These responses included: the predicted vertical deflections u_{22} (μm), the predicted vertical centerline horizontal stress σ_{11} (MPa), the predicted vertical centerline horizontal strain ε_{11} ($\mu\text{m}/\text{m}$), the predicted vertical centerline vertical stress σ_{22} (MPa), and the predicted vertical centerline vertical strain ε_{22} ($\mu\text{m}/\text{m}$).

For the purposes of the finite element analysis, the representative layer moduli of the three layers (asphalt, unbound, and subgrade layers), the Poisson ratios, and other parametrical information were required for the numerical calculations. For these input parameters, previous research on relevant subjects in combination with knowledge of the investigated materials was utilized to determine appropriate input values for analysis purposes (Table 3). For the investigation, a flexible pavement structure was simulated (Fig. 1) to include an asphalt concrete (AC) layer (linear elastic) with variable thicknesses to cover multiple cases, a 30 cm unbound granular base, and a compacted subgrade (linear elastic). The overall FE model dimensions

Table 3 Layer properties

Layer	Thickness (mm)	Modulus (MPa)	Poisson
AC	50,100,200	3000	0.35
Unbound	300	FE simulation	0.35
Subgrade	infinite	80	0.45

Fig. 1 Flexible pavement structure



were chosen in order to eliminate potential boundary effects. Both the AC and the subgrade layers were assumed to behave linearly elastic in order to specifically focus investigation on the base layer effects. For the analysis, a circular wheel load zone was incrementally imposed on the AC surface, and the analysis was based on the modified Newton’s method with secant stiffness.

The various pavement cross sections modeled and the assumptions for the study are shown in Table 3.

5 Finite Element Simulation Results

FE results for each case (model, material, and moisture conditions) were exported for further analysis. Emphasis for the analysis was focused on critical locations in flexible pavement structure. These locations include: (1) surface deflection, (2) strain—bottom of the AC (fatigue), and (3) strain—top of the subgrade (rutting). The following section provides information on each of the investigated critical responses.

Figure 2 and Table 4 show FE-predicted vertical deflection data for the center of the loading for each cross section, model, and moisture condition investigated.

Figure 3 and Table 5 show FE horizontal strains at the bottom of the AC layer.

Shown in Fig. 4 and Table 6 are FE vertical strains at the top of the subgrade layer.

For the predicted vertical deflections u_{22} for all AC layer thicknesses and materials, the $K-\Theta$ model produced the largest predicted vertical deflections. For the 50 mm AC layers, the $K-\Theta$ predicted values were 15–21% higher for RAP, while for the VA, they were 26–47% higher. As the AC layer increased to 200 mm, these same variations were reduced to 0% and 2–4%, respectively. This indicates that as the AC layers increase, the importance of the model utilized is significantly reduced. In regard to the RAP materials predicted, u_{22} deflections versus the VA aggregate materials, as the AC material thickness increased, the variations were greatly reduced. For the 50 mm AC layer, the RAP material predicted deflections were 14, 38, and 25% ($K-\Theta$, Uzan, and MEPDG models, respectively) greater than the VA material. While for the

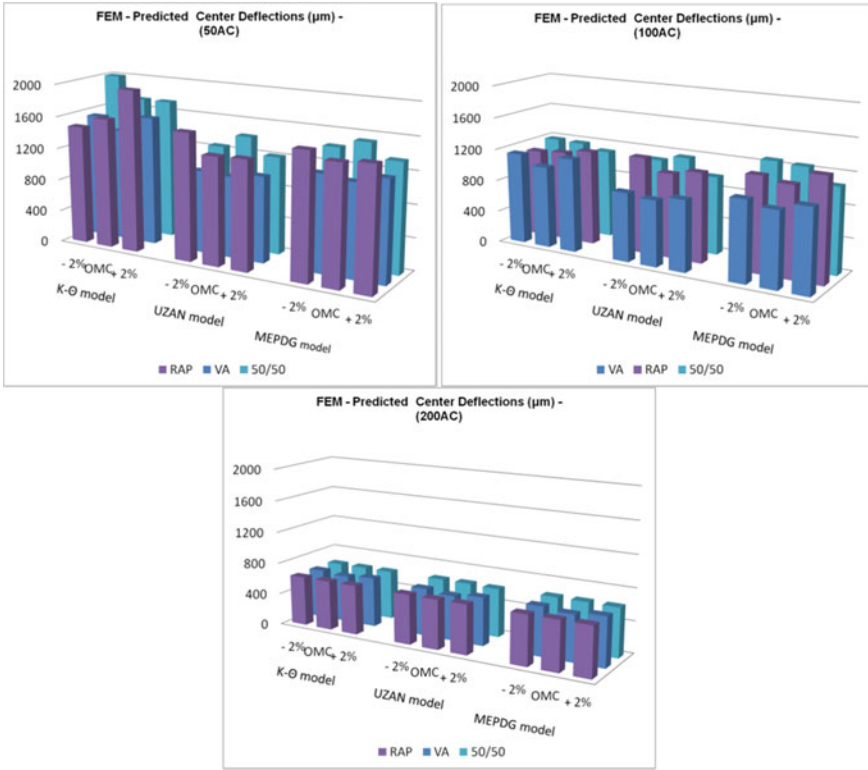


Fig. 2 Predicted vertical deflections u_{22} (μm) for investigated cross sections

Table 4 Predicted vertical deflections u_{22} (μm)—statistics

Material	AC (mm)	Standard deviation			Average deflection		
		$K\Theta$	UZAN	MEPDG	$K\Theta$	UZAN	MEPDG
RAP	50	316	134	46	1719	1417	1496
	100	41	76	80	1138	1124	1199
	200	0	2	0	624	623	624
VA	50	106	29	47	1510	1027	1193
	100	80	31	48	1114	855	987
	200	16	23	22	614	589	605
50/50	50	164	108	88	1830	1293	1431
	100	41	96	2	1155	1078	1196
	200	1	6	3	623	620	622

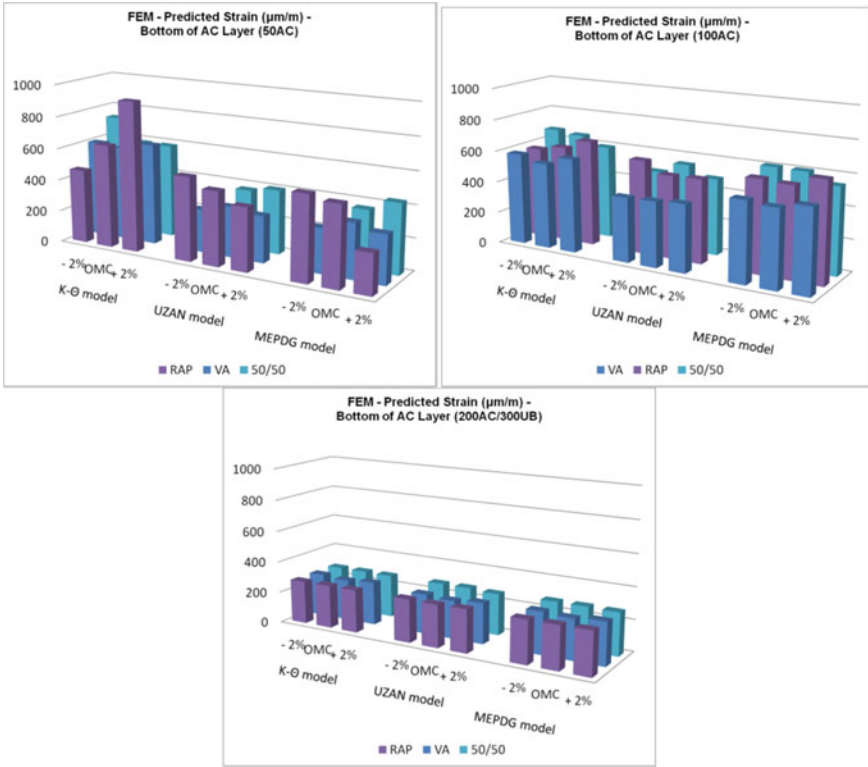


Fig. 3 Predicted horizontal strain ϵ_{11} ($\mu\text{m/m}$) for investigated cross sections

Table 5 Predicted horizontal strain ϵ_{11} ($\mu\text{m/m}$)—Statistics

Material	AC (mm)	Standard deviation			Average deflection		
		$K\Theta$	UZAN	MEPDG	$K\Theta$	UZAN	MEPDG
RAP	50	238	64	152	680	460	425
	100	47	40	32	619	549	595
	200	0	2	0	275	274	274
VA	50	23	23	32	607	292	307
	100	28	9	18	574	415	505
	200	7	8	8	270	252	265
50/50	50	83	81	150	635	342	315
	100	39	39	36	639	505	587
	200	1	5	2	274	272	273

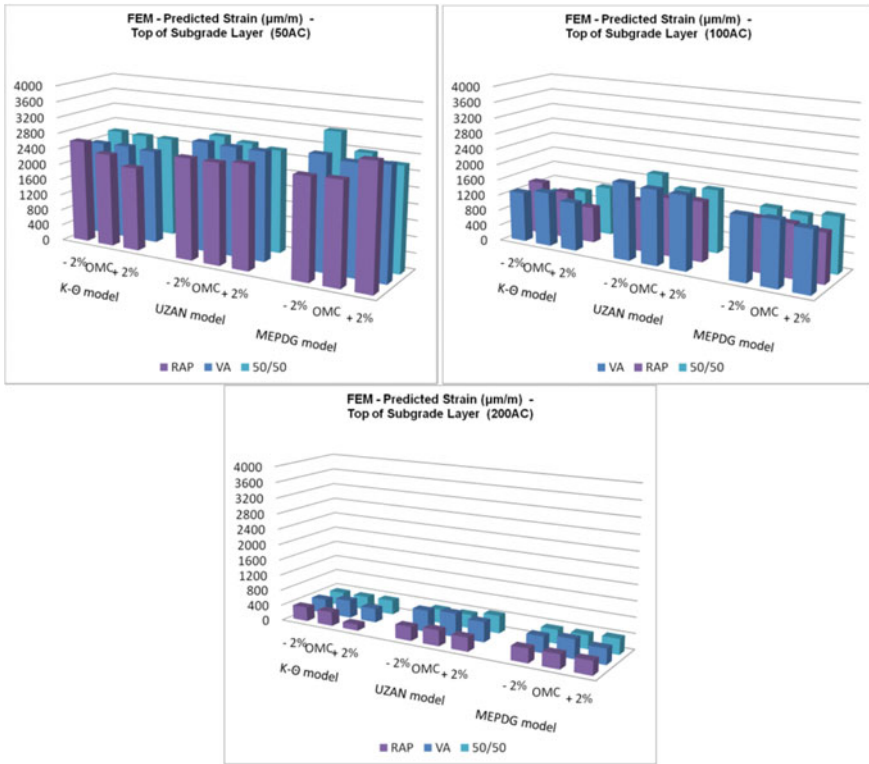


Fig. 4 Predicted vertical strain ϵ_{22} ($\mu\text{m/m}$) for investigated cross sections

Table 6 Predicted vertical strain ϵ_{22} ($\mu\text{m/m}$)—Statistics

Material	AC (mm)	Standard deviation			Average deflection		
		$K\Theta$	UZAN	MEPDG	$K\Theta$	UZAN	MEPDG
RAP	50	241	35	307	2345	2554	2697
	100	230	115	52	1157	1429	1301
	200	116	26	5	291	370	357
VA	50	22	18	43	2388	2749	2794
	100	77	36	45	1293	1895	1588
	200	53	45	46	393	556	430
50/50	50	21	87	315	2542	2684	2881
	100	167	151	44	1062	1639	1371
	200	10	57	24	358	387	366

200 mm AC layer, these variations were reduced to 2, 6, and 3%, respectively. This provides indications that the RAP material has predicted results similar to the VA material within larger AC layer thickness pavements. The 50/50 material produced results similar to the RAP material.

For the predicted horizontal strain ε_{11} , it can be seen that for all AC layer thicknesses and materials that the $K-\Theta$ model produced the largest predicted horizontal strain at the bottom of the AC layer. For the 50 mm AC layers, the $K-\Theta$ predicted values were 48–60% higher for RAP, while for the VA, they were 95–110% higher. As the AC layer increased to 200 mm, these same variations were reduced to 0% and 2–7%, respectively. This indicates that as the AC layers increase, the importance of the model utilized is significantly reduced. In regard to the RAP materials predicted ε_{11} deflections versus the VA aggregate materials, as the AC material thickness increased, the variations were greatly reduced. For the 50 mm AC layer, the RAP material predicted horizontal strains were 12, 58, and 38% ($K-\Theta$, Uzan, and MEPDG models, respectively) greater than the VA material. While for the 200 mm AC layer, these variations were reduced to 2, 8, and 3%, respectively. These provide indication that the RAP material has predicted results similar to the VA material within larger AC layer thickness pavements. The 50/50 material produced results similar to the RAP material.

For the predicted vertical strain ε_{22} , it can be seen that for the 50 mm AC layer thickness and all materials that the MEPDG model produced the largest predicted horizontal strain at the bottom of the AC layer. For the 50 mm AC layers, the MEPDG predicted values were 6–15% higher for RAP, while for the VA, they were 2–17% higher. While as the AC layer was increased to 100 mm, the Uzan model predicted the highest vertical strains. Overall, the $K-\Theta$ model predicted the lowest vertical strains for all materials and AC thickness combinations.

In regard to the moisture conditions investigated, the moisture conditions had the largest influence for the RAP materials at the 50 mm AC layer for all the predicted responses. This provides an indication that moisture conditions for RAP are important in the response of pavements with lower AC layers, while as the AC layers increase to 200 mm, the RAP and the influence of moisture are more similar to the investigated VA material.

6 Discussion

Based on the results of the current investigation, the RAP and 50/50 materials produced significantly larger predicted deformations in respect to the VA materials at the 50 mm AC layer thickness. However, as the thickness of the AC layer increased to 200 mm, the variations between the VA materials in regard to deflections were limited to less than 5% greater. The 50/50 material, in general, had overall the highest predicted deformations for all cross sections and constitutive models with the variations being limited at the 200 mm AC layer pavement section.

For the RAP and 50/50, it appears that overall the RAP material exhibited the largest dependence on the moisture conditions; however, the variations at both OMC + 2% and OMC-2% were, in general, limited to $\pm 15\%$ of the OMC values for the predicted strain ε_{11} . For all investigated materials, as the AC layer increased to 200 mm, the variations with moisture were limited to $\pm 3\%$ in comparison to the OMC predicted values predicted strain ε_{11} , showing that as the AC layer increases, the choice of base materials has less effect overall. The choice of model for the RAP predicted strain ε_{11} had a significant impact of up to 60% variations between the $K-\Theta$ and Uzan model for the 50 mm AC section. However, the choice of model had variations approximately less than 10% for RAP at the 200 mm AC layer. The predicted RAP vertical strains ε_{11} between models did not show a clear variation between the AC thicknesses or the chosen constitutive model. In general, the variations were limited to less than approximately 20%.

In general, for all responses, as the AC layer increased, both the impact of moisture conditions and constitutive model were greatly reduced. This indicates that for lower AC thicknesses, the choice of model and the impact of the moisture conditions are necessary to be considered and justified for all materials including RAP. As can be seen in the investigation, the choice of model/methodology and conditions are important and often overlooked aspects for a FE analysis of pavement structures and their predicted responses. This area still requires further in-depth investigation for RAP-based unbound material to provide more information toward increasing the utilization of these materials toward the goal of increased sustainability.

References

1. Copeland A (2011) Reclaimed asphalt pavement in asphalt mixtures: state of the practice. In: Turner-Fairbank highway research center federal highway administration. Report FHWA-HRT-11-021, Turner-Fairbank Highway Research Center, McLean, VA, USA
2. Puppala A, Sireesh S, Williammee R (2011) Sustainable reuse of limestone quarry fines and RAP in pavement base/subbase layers. *J Mater Civ Eng* 24:418–429
3. Alam TB, Abdelrahman M, Schram S (2010) Laboratory characterization of recycled asphalt pavement as a base layer. *Int J Pavement Eng* 11:123–131
4. Thakur JK, Han J (2015) Recent development of recycled asphalt pavement (RAP) bases treated for roadway applications. *J Transp Infrastruct Geotechnol* 2:68–86
5. Plati C, Cliatt B (2019) A sustainability perspective for unbound reclaimed asphalt pavement (RAP) as a pavement base material. *Sustainability* 11:78
6. Attia M, Abdelrahman M (2011) Effect of state of stress on the resilient modulus of base layer containing reclaimed asphalt pavement. *Road Mater Pavement Des* 12:79–97
7. Kim W, Labuz JF, Dai S (2007) Resilient modulus of base course containing recycled asphalt pavement. *J Transp Res Board* 2005:27–35
8. Dong Q, Huang B (2014) Laboratory evaluation on resilient modulus and rate dependencies of RAP used as unbound base material. *J Mater Civ Eng* 26:379–383
9. Edil TB, Tinjum JM, Benson CH (2012) Recycled unbound materials. MN/RC2012-35, Minnesota Department of Transportation: Saint Paul, MN, USA
10. Noureldin E, Abdelrahman M (2013) Modeling of the resilient modulus for recycled asphalt pavement applications in base course layers. *Transp Res Record* 2371:121–132

11. Cliatt B, Plati C, Loizos A (2016) Investigating resilient modulus interdependence to moisture for reclaimed asphalt pavement aggregates. *Procedia Eng* 143:244–251
12. Hicks RG, Monismith CL (1971) Factors influencing the resilient response of granular materials. *Transp Res Rec* 345:15–31
13. Uzan J (1985) Characterization of granular material. *J Transp Res Board* 1022:52–59
14. Uzan J (1992) Resilient characterization of pavement materials. *Int J Numer Anal Methods Geomech* 16:435–459

Effectiveness of Double-Layer HDPE Geocell System to Reinforce Reclaimed Asphalt Pavement (RAP)-Base Layer



Md. Ashrafuzzaman Khan , Nripojoyoti Biswas , Aritra Banerjee ,
Surya Sarat Chandra Congress , and Anand J. Puppala 

Abstract Geocell has been used for reinforcing foundation soil, stabilizing slopes, construction of retaining walls, and unpaved roads, but limited information is available about the construction of structural/flexible pavement with geocell. It can provide additional confinement for the infill material, which allows the use of recycled material in the base layer. Reclaimed asphalt pavement (RAP) often has adequate stiffness in terms of modulus of resilience, but excessive permanent deformation under repeated loading restricts the use of 100% RAP in the pavement. Though some studies are available regarding the use of geocell with RAP for unpaved roads, there are no established methods or guidelines available for the design and construction of geocell-reinforced structural pavement, especially with multi-layer geocell system. The main objective of this study is to design and construct a pavement section with a double-layer geocell system with RAP and monitor its field performance. A two-lane two-way road in Venus, Texas, which was suffering from cracking and rutting problems, was selected for the construction of the test section using geocell filled with RAP material. Earth pressure cells and shape array sensors were also installed to monitor the performance of the test section. Results obtained from the field show that the use of geocell can reduce the average vertical stress at the bottom of the reinforced base layer by 48%. Performance of the double-layer HDPE geocell system

Md. A. Khan · N. Biswas · S. S. C. Congress · A. J. Puppala (✉)
Texas A&M University, College Station, TX, USA
e-mail: anandp@tamu.edu

Md. A. Khan
e-mail: mak2019@tamu.edu

N. Biswas
e-mail: nripojoyoti.biswas@tamu.edu

S. S. C. Congress
e-mail: congress@tamu.edu

A. Banerjee
University of Delaware, Newark, Delaware, USA
e-mail: aritra@udel.edu

incorporated in the flexible pavement bases with RAP material was found to be satisfactory with no significant deformation or cracking recorded during the first year of monitoring.

Keywords Geocell · RAP · Flexible pavement · Base reinforcement

1 Introduction

High plasticity expansive subgrade is one of the major reasons for pavement failures [1, 2]. Most of the low to medium volume roads, constructed over expansive subgrade, suffer from rutting, longitudinal cracking, shoulder dropping, and other types of depressions which are closely associated with the seasonal movements of subgrade soil [3–8]. Mitigation methods for such problems are available in the literature, which can be grouped into three categories: (1) mechanical/chemical stabilization of base and/or soil, (2) geogrid reinforcement, and moisture control barriers [9]. Several researchers concluded that stabilization increases soil stiffness, reduces swelling, and decreases the permeability of the soil [5, 10, 11]. However, excavating subgrade soil and mixing it with lime may not be a feasible option for highly trafficked areas [4]. Treating with cement may increase the layer stiffness but also increases the brittleness of the layer, which might lead to the block/longitudinal cracking [12]. Planar geosynthetics (i.e., geogrid) can be used in the base layer of the pavement to mitigate the problems associated with pavement rutting and fatigue cracking [13–15]. The planar geosynthetics layer can provide two-dimensional reinforcement, which can enhance the bearing capacity of the pavement layer; however, the excessive permanent deformation of the inferior type base material (i.e., RAP) does not allow the usage of such reinforcement without additional lateral support. Federal highway administration (FHWA) and other state agencies (DOTs) are encouraging the use of recycled material for the construction of pavement [2]. Utilization of recycled material can be a sustainable solution for the rehabilitation of existing road networks, and a special type of three-dimensional (3D) confinement is required to control the permanent deformation of such material [16, 17]. This kind of 3D confinement is commercially known as geocell, which is a honeycomb type structure, made from high-density polyethylene (HDPE) or novel polymeric alloy (NPA). The flexibility and elastic modulus for the NPA geocell are higher at elevated temperature; however, the performance of NPA and HDPE geocell at a lower temperature is almost similar [18]. Several laboratory studies indicated that the inclusion of geocell could significantly control the permanent deformation of the RAP-base layer [19–21]. Strength and stiffness of the geocell-reinforced RAP base (GRRB) layers were also back-calculated from the large-scale repeated load tests conducted by George et al. [22, 23]. The studies showed that the resilient moduli for the GRRB layers were 3–4 times higher than the average modulus obtained from the unreinforced RAP-base layer. Though the laboratory investigation of the GRRB layer showed significant improvement, but very few field studies are documented which hindered the use of

such reinforced layer by the federal or state agencies [24]. Texas DOT (TxDOT) acknowledged the effectiveness of geocell for pavement reinforcement; however, no such use of geocell has been yet documented in the state of Texas [25]. Most of the case studies available on geocell-reinforced paved or unpaved road sections were constructed as a single-layer system [24, 26, 27]. Depending on the traffic and material configurations, thickness of base layer may vary; consequently, geocell of various thicknesses is required. However, the geocells are commercially available with variable heights but proper compaction of the infill materials is very difficult to achieve with higher lift thickness. Instead of a single-thick layer, double-thin layers of equivalent thicknesses may provide better compaction and enhance the performance of the flexible pavement. In this study, a distressed section of a pavement was replaced with double layer of GRRB to mitigate the issues, which are associated with the seasonal movements of the expansive subgrade.

2 Existing Road Section

The test section was constructed in the eastbound lane of a pavement, located in the North Texas region, and the current average annual daily traffic is less than 1500. This road was previously constructed over an untreated expansive subgrade; consequently, it suffered from distresses in the form of rutting, longitudinal cracking, and shoulder dropping. The pavement was rehabilitated by applying overlays; however, the longitudinal cracks reappeared within a year. This is a two-lane, two-way highway having a lane width of 11 ft (3.4 m), and width of the shoulder was 2.25 ft (0.7 m). The existing base layer of the road had a depth of 10 in. (0.25 m), which was revealed during the excavation of the existing road section. The total thickness of the surface layer varied from 2 to 4 in. (5–10 cm) due to the application of overlays over time.

3 The Objective of the Study

One of the main objectives of this construction project was to provide a sustainable solution for the existing pavement, which experienced distresses related to environmental loading. The application of RAP was considered as a sustainable solution, which can significantly reduce the landfill waste and depletion of the natural aggregate [28]. A 10 in. (25 cm) thick reinforced base layer was required for the road section, which is difficult and/or inefficient to construct with a single-layer system, and hence, double-layer geocell system was adopted. The objective of this current study is to evaluate the performance of the newly constructed test section with double-layer GRRBs.

4 Materials

Soil samples were collected from the subgrade level during the initial phase of the project. Subgrade was classified as high plasticity clay (CH) according to the unified soil classification system with a liquid limit of 58% and a plasticity index of 31. Based on ASTM D698, maximum dry density and optimum moisture content of the soil were determined as 14.1 kN/m^3 and 23.5%, respectively. The average swelling potential of 8.5% was determined from the ASTM 4546-method B. Resilient modulus of the soil at different confining pressures was also determined based on AASHTO T307 method. The subgrade modulus of 9 ksi (62 MPa) was used for the pavement analysis. The previous researchers [22] reported that the average resilient modulus for a 4 in. (10 cm) thick GRRB layer is around 43.5 ksi (300 MPa), and the modulus of the unreinforced recycled asphalt pavement was 30 ksi (206 MPa). The height of the geocell used in the current study was also 4 in. (10 cm), which was made from HDPE sheets with a tensile strength of 1370 lb/ft (20 kN/m) and a secant elastic modulus of 48.6 ksi (355 MPa) at 2% strain. According to the data provided by the manufacturer, seam peel strength was 320 lb (1.42 kN), and the nominal expanded cell size was 12.6 in. \times 11.3 in. (32.0 \times 28.7 cm). A nonwoven geotextile was used in between the subgrade and base layer as a separator, meeting the criteria of the TxDOT DMS 6200 type.

5 Pavement Analysis

Most of the state agencies, including TxDOT, follow the linear elastic approach (LEA) for the static analysis of the multi-layered pavement structure. The horizontal strains at the bottom of the surface layer and vertical compressive strains at the top of the subgrade layer are considered for the determination of the fatigue and rutting life of the flexible pavement, respectively. The equivalent composite approach (ECA) considering the vertical strain on top of the subgrade layer has been considered for the pavement analysis in the current study. The ECA can be an effective solution to incorporate the geocells in a two-dimensional framework [29]. Numerous studies can be found where ECA has been adopted to model the geocell [30–33]. In this approach, improved strength and stiffness parameters of the reinforced layer are used, which can be either determined from the laboratory investigation or empirical correlation available in the literature. Results obtained from the ECA are presented in Fig. 1.

George et al. [22] conducted repeated load tests on 4 in. (10 cm) thick single GRRB layer in a laboratory setup to back-calculate the stiffness of the composite layer. The material set used for the laboratory investigation was similar to the material set used for the construction work in the present study. Hence, the equivalent strength and stiffness properties (also shown in Fig. 1) were used for the current pavement analysis with LEA. The rutting life of the flexible pavement was determined with the shell

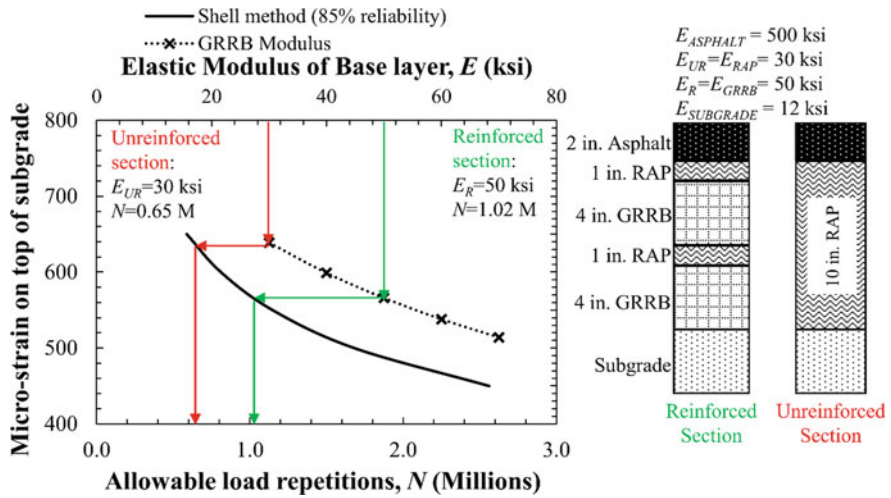


Fig. 1 Pavement analysis based on equivalent composite approach

method with 95% reliability [34]. A uniform circular load of radius 3 in. (7.5 cm) and a magnitude of 100 psi (680 kPa) was applied on the top of the pavement surface to generate the stress–strain profile. However, only the vertical compressive strain, acting on top of the subgrade layer, was used for rutting life analysis. The inclusion of geocell increased the elastic modulus of the base layer from 30 ksi (206 MPa) to 50 ksi (345 MPa), which can increase the pavement rutting life from 0.65 million to 1.02 million load repetitions.

6 Construction of Test Section

The test section was constructed within the eastbound lane, covering a total area of 120 × 15 ft (36.6 × 4.6 m). The existing road section was milled up to a depth of the subgrade level with the help of an RX-600e type cold planar machine. Construction sequence and instrumentation of the test section are discussed in the following sections.

6.1 Construction Sequence

Preparation of Roadbed:

Before the construction of the GRRB layers, a smoother pavement bed surface was achieved with the help of a bobcat with a loader head. A pneumatic-type roller was used to achieve proper compaction.

Placement of Geotextile:

A nonwoven-type geotextile (see Fig. 2a) with a roll width of 15 ft (4.6 m) was used as a separation layer between the subgrade and bottom GRRB layer. Application of geotextile will also prevent the migration of finer particles of subgrade into the base layer and intrusion of base aggregate into the subgrade layer.

Construction of GRRB layers:

The number of geocell panels required for covering the width of the test section was determined by dividing the width of the test Sect. (15 ft or 4.6 m) with the optimum width of the geocell panel after expansion (7.5 ft or 2.3 m). Before the placement of the geocell panel (Fig. 2b) on top of the geotextile, two adjacent geocell panels were tied with each other using commercially available plastic zip ties. Four sets of geocell panels ($2 \times 4 = 8$ panels) were required to construct one single layer of reinforcement, which covered the total area of the test section. After the placement of geocells, RAP materials were dumped (Fig. 2c) with the help of loading trucks. After the placement of the RAP layer, the motor grader was used to scrap and maintain a level surface before compacting the GRRB layer with pneumatic-type roller, shown in Fig. 2d. A cover layer, on top of the geocell, was required to protect the geocell



Fig. 2 Construction sequence: **a** placement of geotextile, **b** placement of first geocell layer, **c** placement of RAP, **d** compaction of GRRB layer, **e** placement of second geocell layer, and **f** final surface layer

from the construction equipment. Consequently, a minimum cover thickness of 1 in. (2.5 cm) was maintained throughout the test section. The second layer of GRRB (Fig. 2e) was constructed following the same technique described above, and the second cover layer was required in between the asphalt and second GRRB layers.

Construction of Top Asphalt Layer

A temporary surface layer with flex base material was used for a week before the application of the final asphalt layer. The test section was opened to traffic during this period, which also helped to compact the base layer. Before the construction of the final layer, i.e., top asphalt layer (Fig. 2f), the top of the base layer was further compacted with a pneumatic roller and coated with a seal coat.

6.2 Instrumentation

Pressure and deformation sensors (Fig. 3) were installed before the placement of the geotextile layer. Shape array accelerometer (SAA) was enclosed in a 2 in. (5 cm) diameter PVC casing, installed during the construction, and placed on top of the subgrade level. Earth pressure cells (EPCs) were also installed on top of the subgrade level to measure the vertical compressive stress under each wheel path. The control Sect. (15 × 1 ft) is located adjacent to the reinforced section, which was constructed before the construction of the reinforced section. The thickness of the unreinforced RAP-base layer was 10 in. (25 cm), and the SAA sensors run across this control section.

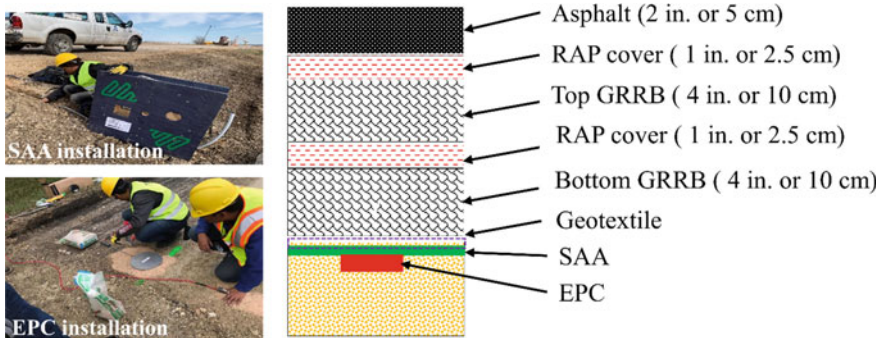


Fig. 3 Instrumentation of the test section

7 Results of Performance Monitoring

The newly constructed test section was opened to traffic from December 15th, 2018, and since then, vertical deformations and vertical stresses data have been collected on a bi-weekly basis. In addition to the sensor data, the performance of the road section was also monitored visually for any depressions or cracking on top of the pavement surface. Stresses and deformation observed from the field are discussed in the following sections.

7.1 Stress Analysis

Vertical stresses obtained from the pavement analyses were compared with the observed stresses from the EPCs installed just under the bottom of the reinforced base layer. The static load of 100 psi (680 kPa) was considered on top of the pavement surface through a 6 in. diameter loading plate to obtain the vertical stresses at various depths based on LEA. The average vertical stress obtained from the EPCs was 3.5 psi (24.1 kPa); however, the average vertical stress obtained from the LEA approach was 6.7 psi (46.2 kPa). The maximum vertical stresses observed in the field were lower compared to the vertical stresses obtained from the theory due to the dynamic nature of loading in the field. The longitudinal strain decreases as the speed of the vehicle increases, which is one of the reasons for getting lower vertical stresses in the field compared to the analytical solution [35]. Comparison of field results with analytical approach shows a 48% reduction in vertical stress; however, field study on geocell-reinforced gravel base layer showed a reduction of 28% in the vertical stress on top of subgrade layer [24]. Experimental results on geocell-reinforced RAP also showed that the inclusion of geocell could increase the stress distribution angle from 19° to 25° [36]. The increase of stress distribution angle indicates the reduction of stresses due to the inclusion of geocell.

7.2 Deformation Analysis

The results obtained from the SAAs provided the actual shape of the sensor array containing x , y , and z coordinates with time. These data were further analyzed to get the deformation values under the right and left wheel path locations, as shown in Fig. 4. Results obtained from the control section were also compared with the reinforced section. The deformation of the subgrade soil also depends on the fluctuation of moisture level. However, moisture sensors were not installed, but rainfall data collected from the nearby weather station were used (shown in Fig. 4) to understand the possible intrusion of moisture into the subgrade soil. Cumulative rainfall data for the two-week period are presented here, which may explain the trend of

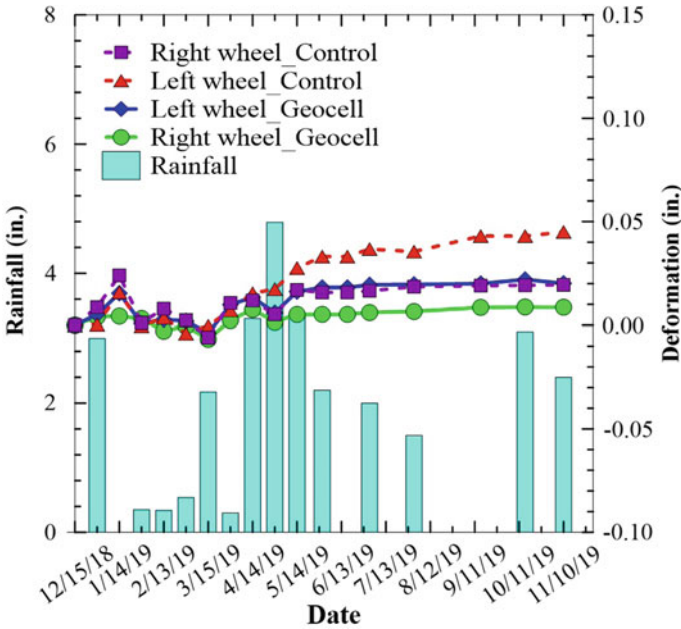


Fig. 4 Subgrade deformation obtained from shape array accelerometer (SAA)

subgrade movement. Positive values of deformation indicate heaving and negative values indicate a settlement. During the months of April and May 2019, a sudden increase in heaving can be attributed to higher rainfall. Average heaving observed after the long wetting period was 0.05 in. (0.11 cm) for the control section, whereas maximum heaving observed under the reinforced section was only 0.03 in. (0.07 cm). The inclusion of geocell can increase the stress distribution angle, which helps to distribute the swelling pressure over a larger area and reduce the subgrade movement [20, 26, 37]. This field study indicates that the average reduction in heaving due to the inclusion of geocell was 36%, which is also supported by the experimental observation by previous researchers, who reported that the inclusion of geocell in the base layer could reduce the heaving of expansive soil by 29% [38].

During the current monitoring period, no surficial cracks or depressions were found on the top surface of the reinforced section; however, the maximum visible depression of 0.5 in. (1.25 cm) was observed on top of the control section. A 10 in. (25 cm) thick unreinforced RAP base layer undergone a large amount of permanent deformation, which was the main reason for the surface depression. In contrast, geocells, within the reinforced section, restrained the lateral movement of the infill material [20, 39], which eventually controlled the vertical permanent deformation of the GRRB layers.

8 Conclusions

In this study, a double-GRRB layer was constructed, and the performance was further evaluated, based on field monitoring. The field results obtained from this initial monitoring period indicated that the inclusion of geocell in the base layer could control the heaving of subgrade and reduce the permanent deformation of the inferior base material. The following conclusions can be drawn from this study.

- Double-layer geocell can be a feasible solution where a thicker base layer is required for highly trafficked roads
- Total time required for rehabilitation work is much less than other types of subgrade stabilization techniques, such as chemical stabilization, and the road section was opened to traffic, immediately after construction
- GRRB has the potential to reduce the vertical stresses on the subgrade layer up to 48%
- GRRB has the potential to reduce the heaving of subgrade soil by 36%

This study only presents the short-term performances of the double-layer GRRB, constructed within a flexible pavement section; however, long-term field studies are required to understand the efficiency of the geocell reinforcement to develop guidelines for future design and construction.

Acknowledgements This research was funded by Texas Department of Transportation (TxDOT)—Fort Worth district (Mr. Richard Williammee, P.E. and Mr. Paul Spraggins, P.E.) and NSF Industry-University Cooperative Research Center (I/UCRC) program funded ‘Center for Integration of Composites into Infrastructure (CICI)’ site at TAMU (NSF PD: Dr. Prakash Balan; Award #2017796). The authors would like to thank their support. The authors also like to express sincere gratitude to the Geo Products, LLC, for providing Envirogrid geocells for the research. The authors would further like to express their sincere gratitude to the TxDOT construction crew, Dr. Sayantan Chakraborty and other members of UTA- SARCI group for their help during the construction phase.

References

1. Puppala AJ, Intharachicagocsombat N, Qasim SR (2004) The effects of using compost as a preventive measure to mitigate shoulder cracking : laboratory and field studies. Arlington
2. Das JT, Banerjee A, Puppala AJ, Chakraborty S (2019) Sustainability and resilience in pavement infrastructure: a unified assessment framework. *Environ Geotech* 1–13. <https://doi.org/10.1680/jenge.19.00035>
3. Banerjee A, Puppala AJ, Hoyos LR, Likos WJ, Patil UD (2019) Resilient modulus of expansive soils at high suction using vapor pressure control. *Geotech Test J* 43:1–17
4. Dessouky SH, Oh J, Ilias M, Lee SI, Park D (2015) Investigation of various pavement repairs in low-volume roads over expansive soil. *J Perform Constr Facil* 29:04014146(1–9). [https://doi.org/10.1061/\(ASCE\)CF.1943-5509.0000623](https://doi.org/10.1061/(ASCE)CF.1943-5509.0000623)
5. Puppala AJ, Musenda C (2000) Effects of fiber reinforcement on strength and volume change in expansive soils. *Transp Res Rec* 1736:134–140. <https://doi.org/10.3141/1736-17>

6. Banerjee A (2017) Response of unsaturated soils under monotonic and dynamic loading over moderate suction states. <https://rc.library.uta.edu/uta-ir/handle/10106/26940>
7. Puppala AJ, Congress SSC, Banerjee A (2019) Research advancements in expansive soil characterization, stabilization and geoinfrastructure monitoring. In: Latha GM (ed) *Frontiers in geotechnical engineering*. Springer, Singapore, pp 15–29
8. Khan MA, Hossain MS, Khan MS, Samir S, Aramoon A(2017) Impact of wet-dry cycles on the shear strength of high plastic clay based on direct shear testing. In: *Geotechnical Special Publication*. American Society of Civil Engineers (ASCE), pp 615–622
9. Zornberg JG, Gupta R (2009) Reinforcement of pavements over expansive clay subgrades. In: *Proceedings 17th International conference soil mechanics geotechnolgy engineering academy practical geotechnolgy engineering*. vol 1. pp 765–768. <https://doi.org/10.3233/978-1-60750-031-5-765>
10. Freeman TJ, Little DN (2002) Maintenance strategies for pavements with chemically stabilized layers
11. Puppala AJ, Hoyos LR, Potturi AK (2011) Resilient moduli response of moderately cement-treated reclaimed asphalt pavement aggregates. *J Mater Civ Eng* 23:990–998. [https://doi.org/10.1061/\(asce\)mt.1943-5533.0000268](https://doi.org/10.1061/(asce)mt.1943-5533.0000268)
12. Chen DH, Hong F, Zhou F (2011) Premature cracking from cement-treated base and treatment to mitigate its effect. *J Perform Constr Facil* 25:113–120. [https://doi.org/10.1061/\(ASCE\)CF.1943-5509.0000140](https://doi.org/10.1061/(ASCE)CF.1943-5509.0000140)
13. Imjai T, Pilakoutas K, Guadagnini M (2019) Performance of geosynthetic-reinforced flexible pavements in full-scale field trials. *Geotext Geomembranes* 47:217–229. <https://doi.org/10.1016/j.geotextmem.2018.12.012>
14. Vennapusa PKR, White DJ, Wayne MH, Kwon J, Galindo A, García L (2018) In situ performance verification of geogrid-stabilized aggregate layer: route-39 El Carbón-Bonito oriental, honduras case study. *Int J Pavement Eng* 8436:1–12. <https://doi.org/10.1080/10298436.2018.1442576>
15. White DJ, Vennapusa PKR (2017) In situ resilient modulus for geogrid-stabilized aggregate layer: a case study using automated plate load testing. *Transp Geotech* 11:120–132. <https://doi.org/10.1016/j.trgeo.2017.06.001>
16. Khan MA, Biswas N, Banerjee A, Puppala AJ (2020) Performance of Geocell-Reinforced Recycled Asphalt Pavement (RAP) bases in flexible pavements built on expansive soils. *Geo-Congress 2020*, American Society of Civil Engineers, Reston, VA, 488–497. <https://doi.org/10.1061/9780784482810.051>
17. Khan MA, Biswas N, Banerjee A, Puppala AJ (2020) Field performance of geocell reinforced recycled asphalt pavement base layer. *Transp Res Rec J Transp Res Board* 2674:69–80. <https://doi.org/10.1177/0361198120908861>
18. Pokharel SK, Han J, Parsons RL, Qian Y, Leshchinsky D, Halahmi I (2009) Experimental study on bearing capacity of geocell-reinforced bases. In: *Bearing capacity of roads, railways and airfields—proceedings of the 8th international conference on the bearing capacity of roads, railways and airfields*. pp 1159–1166
19. Han J, Pokharel SK, Yang X, Manandhar C, Leshchinsky D, Halahmi I, Parsons RL (2011) Performance of geocell-reinforced rap bases over weak subgrade under full-scale moving wheel loads. *J Mater Civ Eng* 23:1525–1534. <https://doi.org/10.1111/vop.12354>
20. Thakur JK, Han J, Parsons RL (2016) Factors influencing deformations of geocell-reinforced recycled asphalt pavement bases under cyclic loading. 29:04016240(1–12). [https://doi.org/10.1061/\(ASCE\)MT.1943-5533.0001760](https://doi.org/10.1061/(ASCE)MT.1943-5533.0001760)
21. Thakur JK, Han J (2015) Recent development of recycled asphalt pavement (rap) bases treated for roadway applications. *Transp Infrastruct Geotechnol* 2:68–86. <https://doi.org/10.1007/s40515-015-0018-7>
22. George AM, Banerjee A, Puppala AJ, Saladhi M (2019) Performance evaluation of geocell-reinforced reclaimed asphalt pavement (RAP) bases in flexible pavements. *Int J Pavement Eng* 1–11. <https://doi.org/10.1080/10298436.2019.1587437>

23. George AM, Banerjee A, Taylor T, Puppala AJ (2019) Large-scale experimental studies to evaluate the resilient modulus of geocell-reinforced reclaimed asphalt pavement bases. In: Geosynthetics conference 2019, Houston, Texas
24. Kief O, Rajagopal K (2019) Three dimensional cellular confinement system contribution to structural pavement reinforcement. In: Geosynthetics India. pp 1–12
25. TxDOT Pavement Manual: Pavement Manual (2019) Austin
26. Kief O, Schary Y, Pokharel SK (2015) High-modulus geocells for sustainable highway infrastructure. *Indian Geotech J* 45:389–400. <https://doi.org/10.1007/s40098-014-0129-z>
27. Rajagopal K, Veeragavan A, Chandramouli S (2012) Studies on geocell reinforced road pavement structures. In: GA 2012-5th Asian regional conference on geosynthetics: geosynthetics for sustainable adaptation to climate change. pp 497–502
28. George AM, Banerjee A, Puppala AJ, Praticò F (2019) An integrated LCA-LCCA framework for the selection of sustainable pavement design. In: Transportation research board, 98th annual meeting. Washington, D.C.
29. Hegde A (2017) Geocell reinforced foundation beds-past findings, present trends and future prospects: a state-of-the-art review. *Constr Build Mater* 154:658–674. <https://doi.org/10.1016/j.conbuildmat.2017.07.230>
30. Hegde A, Sitharam TG (2015) Experimental and analytical studies on soft clay beds reinforced with bamboo cells and geocells. *Int J Geosynth Gr Eng* 1:13. <https://doi.org/10.1007/s40891-015-0015-5>
31. Latha GM, Rajagopal K, Krishnaswamy NR (2001) Measurement of strains in geocells supporting an embankment. *Geosynth Conf 2001*:387–398
32. Mehdipour I, Ghazavi M, Ziaie R (2013) Numerical study on stability analysis of geocell reinforced slopes by considering the bending effect. *Geotext Geomembranes* 37:23–34. <https://doi.org/10.1016/j.geotextmem.2013.01.001>
33. Dash SK, Sireesh S, Sitharam TG (2003) Behaviour of geocell-reinforced sand beds under circular footing. *Proc Inst Civ Eng-Gr Improv* 7:111–115. <https://doi.org/10.1680/grim.2003.7.3.111>
34. Huang YH (2004) *Pavement analysis and design*. Pearson Prentice Hall
35. Al-qadi IL, Wang H (2009) Evaluation of pavement damage due to new tire design. Urbana-Champaign
36. Thakur JK (2013) Geocell-reinforced unpaved and paved roads with recycled asphalt pavement (rap) bases: experimental study and damage model development
37. Pokharel SK (2015) Validation of geocell design for unpaved roads. In: Geosynthetics. Portland, Oregon, pp 711–719
38. Tamim MM (2017) Evaluating the effectiveness of a hybrid geosynthetic reinforcement system to mitigate differential heave on flexible pavement due to expansive subgrades
39. Hegde A, Sitharam TG (2015) Joint strength and wall deformation characteristics of a single-cell geocell subjected to uniaxial compression. *Int J Geomech* 15:04014080. [https://doi.org/10.1061/\(ASCE\)GM.1943-5622.0000433](https://doi.org/10.1061/(ASCE)GM.1943-5622.0000433)

Geotechnical and Geoenvironmental Characterization of Fine-Grained Construction and Demolition Recycled Materials Reinforced with Geogrids



Castorina S. Vieira and Paulo M. Pereira

Abstract Over the last few years, the environmental sustainability has been demanding a progressive increase in the waste recycling in the construction industry. As regards to the use of construction and demolition (C&D) recycled materials in geotechnical works, the valorization is performed mainly in road construction. However, the fine-grained fraction of C&D recycled materials is commonly not considered appropriate for base and sub-base layers of transport infrastructures, being frequently landfilled instead of reused. This paper assesses the feasibility of using fine-grained C&D recycled materials reinforced with geogrids, particularly for their use in unpaved rural roads. The physical, mechanical and environmental characterization of a fine-grained C&D recycled material, as well as its direct shear behaviour is presented and discussed. The characterization of the interfaces between this recycled material and two geogrids is also evaluated through large-scale direct shear. The study focuses mainly on the influence of the moisture content of the recycled C&D material and geogrid type. The results provide evidences of the proper geotechnical and geoenvironmental behaviour of recycled materials and the feasibility of their reinforcement with geogrids.

Keywords Recycled aggregate · Geogrid · Interface shear strength

1 Introduction

The environmental sustainability has been demanding a progressive increase in the waste recycling in all sectors of the economy and in the construction industry in particular. As regards to the use of construction and demolition (C&D) recycled materials, the valorization is performed mainly in road construction and concrete production. However, most of the studies have been carried out with selected recycled aggregates (recycled concrete aggregates, crushed brick and reclaimed asphalt pavement), which do not correspond to the recycled materials frequently available

C. S. Vieira (✉) · P. M. Pereira

CONSTRUCT, Faculty of Engineering, University of Porto, R. Dr. Roberto Frias, s/n, 4200-465 Porto, Portugal

e-mail: cvieira@fe.up.pt

on the market. The study presented herein was carried out with the fine grain fraction (≤ 10 mm) of mixed C&D recycled materials, often considered inappropriate for recycling.

This paper presents a laboratory study comprising the physical, mechanical and environmental characterization of a fine-grained C&D recycled material, as well as the direct shear behaviour of the interfaces between this recycled material and two geogrids.

The interaction mechanism between the geogrid and the filling material has great importance to the suitable behaviour of the reinforced system. Among the laboratory tests for the characterization of this mechanism, the direct shear test is one of the most used, particularly when the sliding in the interface is expected. The effect of soil moisture content on soil/geosynthetic interfaces shear strength has been studied by several authors [1–3]. In general, these studies have revealed that the interface shear strength can reduce at higher moisture contents, especially in soils containing considerable amount of fines. Therefore, the study on the influence of the moisture content of fine-grained mixed C&D recycled materials seems to be pertinent and relevant to assess the feasibility of their use in embankments and sub-base layers of transportation infrastructures.

2 Materials and Methods

2.1 Materials

The laboratory study was carried out using a fine grain construction and demolition (C&D) recycled material collected at a Portuguese recycling plant (Fig. 1). According to its technical sheet, the material results from mixed C&D waste, coming

Fig. 1 Visual appearance of the C&D recycled material (ruler in cms)



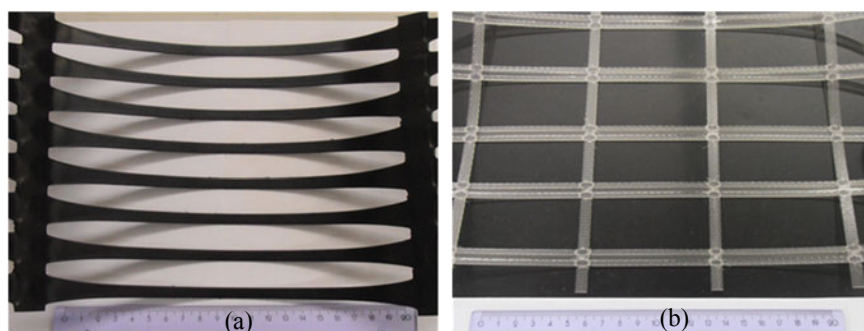


Fig. 2 Geogrids used in the experimental study: **a** High-density polyethylene geogrid (GGR1); **b** Polyester geogrid (GGR2)

Table 1 Main properties of the geogrids used in the experimental study

	GGR1	GGR2
Raw material	HDPE	PET
Mass per unit area (g/m^2)	450	380
Aperture dimensions (mm)	16×219	30×73
Mean value of the tensile strength (kN/m)	60	88
Elongation at maximum load, $\varepsilon_{T_{\max}}$ (%)	10	9
Secant tensile stiffness at 5% strain (kN/m)	718	928
Secant tensile stiffness at $\varepsilon_{T_{\max}}$ (kN/m)	597	907

mainly from maintenance and rehabilitation works of small residential buildings. The constituents of the C&D recycled material will be presented in Sect. 3.

As reinforcement material, two uniaxial geogrids made from different polymers were selected: a high-density polyethylene (HDPE) geogrid, referred to as GGR1 (Fig. 2a) and a geogrid manufactured of extruded polyester (PET) bars with welded rigid junctions, referred to as GGR2 (Fig. 2b). Table 1 summarizes the main properties of the geogrids.

2.2 Laboratory Study

The physical and geotechnical characterization of the C&D recycled material has comprised the determination of the constituents, the grain size distribution, modified Proctor compaction test and large-scale direct shear tests. The geoenvironmental behaviour of the material was evaluated through laboratory leaching tests.

The test procedure depicted in the European Standard EN 933–11 [4] was followed to determine the constituents of the C&D recycled material. It is worth mentioning that only the masses comprised between the sieves 63 and 4 mm were identified.

The particle size distribution of recycled aggregates is commonly determined following the European Standard EN 933–1 [5]. However, as this recycled material has significant fines content, the particle size distribution was determined by sieving and sedimentation following the procedures described in the standard ISO/TS 17,892–4 [6].

Modified Compaction Proctor tests were performed in accordance with the European Standard EN 13,286–2 [7].

The direct shear behaviour of the C&D recycled material and geogrid/C&D recycled material interfaces was analysed through large-scale direct shear tests. The shear box (split into two halves) has dimensions of 300×600 mm in plant and 200 mm in height, being the upper shear box fixed on the horizontal direction, while the lower shear box moves horizontally under a predefined displacement rate. More details on this large-scale direct shear test prototype can be found in [8].

In this laboratory study, a constant displacement rate of 1 mm/min was used and the direct shear tests were performed under normal stresses in the range 25–150 kPa.

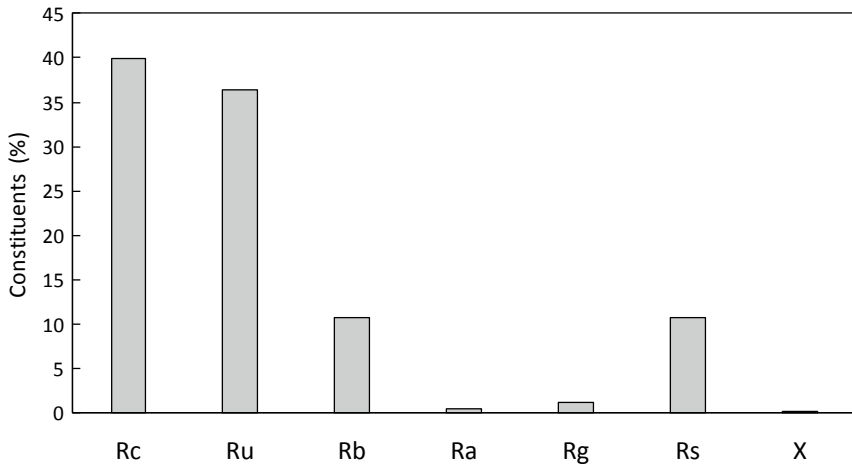
In order to study the influence of the moisture content of C&D recycled material, direct shear tests were carried out on recycled material compacted at its air-dried moisture condition (dry condition) and at the optimum moisture content, w_{opt} . In both conditions, the C&D recycled material was prepared to dry unit weight (γ_d) of 16.1 kN/m^3 (relative density of around 70%—dry condition—and 78% of maximum dry density— w_{opt} condition).

To evaluate the short term release of contaminants, laboratory leaching tests were carried out, at a liquid to solid ratio of 10 l/kg ($L/S = 10$), following the procedures described in the European Standard EN 12,457–4 [9].

3 Results and Discussion

3.1 Constituents of the Recycled Material

Figure 3 presents the constituents of the C&D recycled material. As previously mentioned, it comes from mixed C&D waste submitted to a previous recycling process (removal of impurities such as wood, plastics, foams, ...). The recycled material comprises mainly concrete and mortar, unbound aggregates, masonries and soils. Based on these constituents and according to Portuguese specifications [10, 11], this recycled material, depending on the values of other parameters, may be used in embankments of transport infrastructures and sub-base layers of rural and forest roads.



Rc: concrete, concrete products, mortar, concrete masonry units; Ru: unbound aggregate, natural stone, hydraulically bound aggregate; Rb: clay masonry units, calcium silicate masonry units, aerated non-floating concrete; Ra: bituminous materials, Rg: glass; Rs: soils; X: other materials.

Fig. 3 Composition of the C&D recycled material

3.2 Geotechnical Characterization of the Recycled Material

Particle size distribution of the C&D recycled material, determined by sieving and sedimentation, is illustrated in Fig. 4. According to the technical sheet of the recycled material, its maximum dimension should be lower than 10 mm, and indeed, only 3% of the particles have dimensions higher than 9.5 mm. According to the Unified Soil Classification System (USCS), this C&D recycled material can be classified as silty sand (SM).

The fines content of this C&D recycled material (around 12%) is in the threshold stipulated by LNEC E484 [10] for sub-base layers (12%) and slightly higher than the threshold of 10% determined by LNEC E474 [11] for its application in embankments of transport infrastructures.

Figure 5 presents the results of the Modified Proctor compaction test. The maximum dry unit weight (γ_{dmax}) is 20.7 kN/m³ and the optimum moisture content is around 9.4%. These values are within the range of typical quarry and C&D recycled materials.

The failure envelopes for peak shear stresses achieved on large-scale direct shear tests carried out on C&D recycled material are shown in Fig. 6. Under dry conditions, a peak friction angle of 45.9° and a cohesion of 13 kPa were obtained, while when compacted at optimum moisture content (w_{opt}) and around 80% of γ_{dmax} , the recycled material has exhibited a friction angle of 37.6° and a cohesion of 16.3 kPa. The presence of water has induced the increase of the cohesive component (it is worth

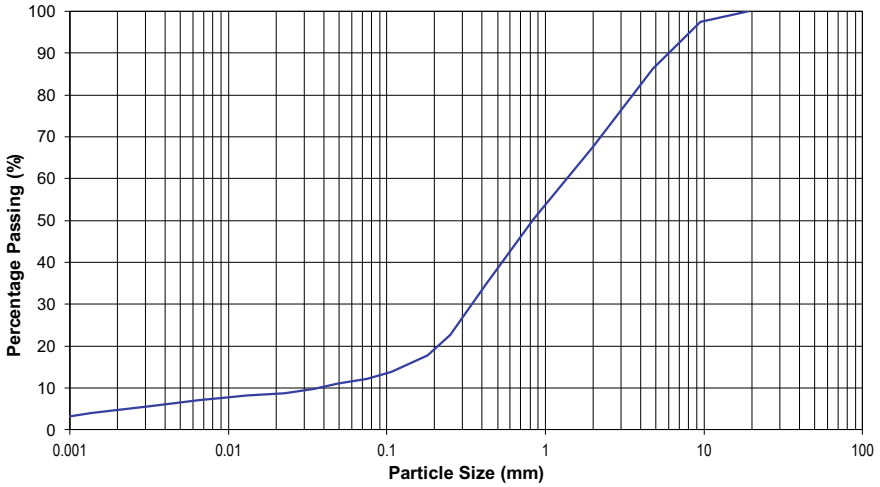


Fig. 4 Particle size distribution of C&D recycled material

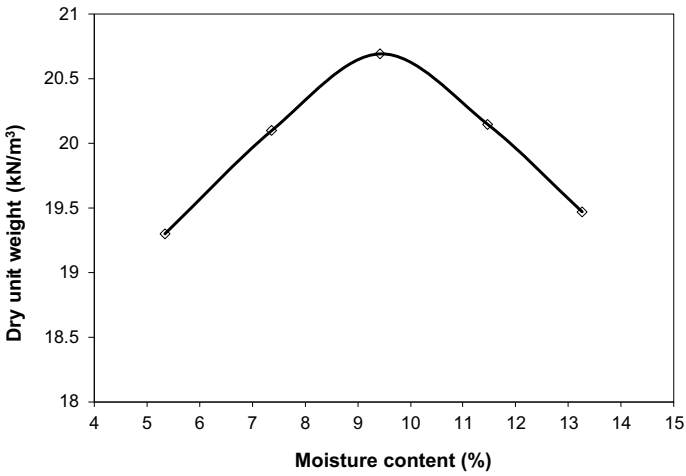


Fig. 5 Modified Proctor compaction test results for the C&D recycled material

noting that this C&D recycled material has around 12% of fine particles) and the decrease of the friction angle.

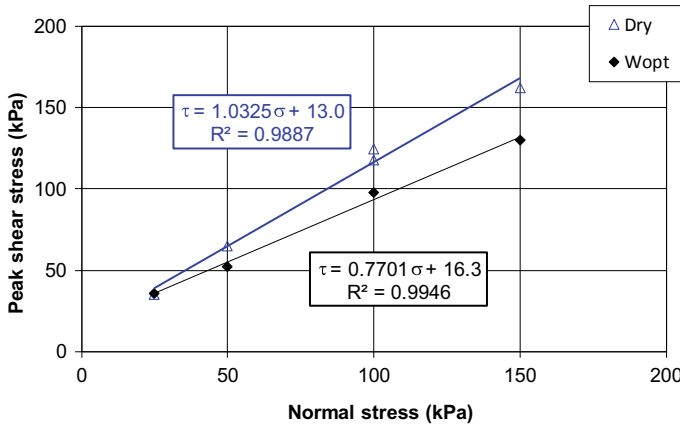


Fig. 6 Failure envelopes for dry and wet C&D recycled material

3.3 Geoenvironmental Behaviour of the Recycled Material

The results of the laboratory leaching tests and the maximum leached concentrations of analysed parameters to allow the deposition of waste in inert landfills, according to the European legislation [12], are presented in Table 2. It should be pointed out that these maximum leached concentrations were used in this study only as mean of classification of C&D recycled material as inert.

Among the metals and other parameters studied, only sulphates (SO₄) and total dissolved solids (TDS) exceeded the maximum concentrations. However, according to [12] “if the waste does not meet these values for sulphate, it may still be considered as complying with the acceptance criteria if the leaching does not exceed 6000 mg/kg at L/S = 10 l/kg”. Furthermore, the evaluation of TDS is not compulsory. In view of this, it is considered that the C&D recycled material can be considered as inert.

3.4 Direct Shear Behaviour of Recycled Material/geogrid Interfaces

In this section, the direct shear behaviour of the interfaces between the geogrids, and the C&D recycled material is presented and discussed.

Influence of the moisture content of the C&D recycled material. Figures 7 and 8 illustrate the evolution of the shear stresses at the interface level with the shear displacement for GGR1 and GGR2, respectively. Regardless the geogrid, the interface shear strength decreases when C&D recycled material is moist and the peak of the shear strength is no longer evident in the curves related to wet material. The maximum shear stresses tend to be achieved for large shear displacements.

Table 2 Results of laboratory leaching test and acceptance criteria for inert landfill

Parameter (mg/kg dry matter)	C&D material	Acceptance criteria for leached concentrations—Inert landfill [12]
Arsenic, As	0.021	0.5
Lead, Pb	< 0.01	0.5
Cadmium, Cd	< 0.003	0.04
Chromium, Cr	0.012	0.5
Copper, Cu	0.10	2
Nickel, Ni	0.011	0.4
Mercury, Hg	< 0.002	0.01
Zinc, Zn	< 0.0.1	4
Barium, Ba	0.11	20
Molybdenum, Mo	0.018	0.5
Antimony, Sb	< 0.01	0.06
Selenium, Se	< 0.02	0.1
Chloride, Cl	300	800
Fluoride, F	6.1	10
Sulphate, SO ₄	3200	1000
Phenol index	< 0.05	1
Dissolved organiccarbon, DOC	220	500
Total dissolved solids, TDS	6580	4000
pH	8.2	–

Bold is used to highlight the values that exceed the threshold

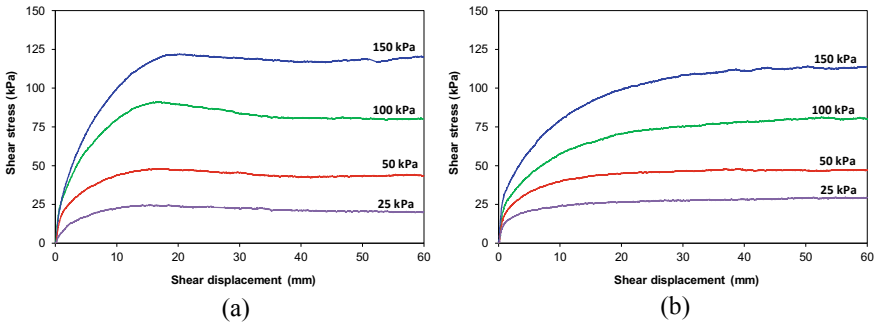


Fig. 7 Direct shear behaviour of interface C&D recycled material/GGR1 under distinct normal stress values: **a** dry C&D recycled material; **b** optimum moisture content

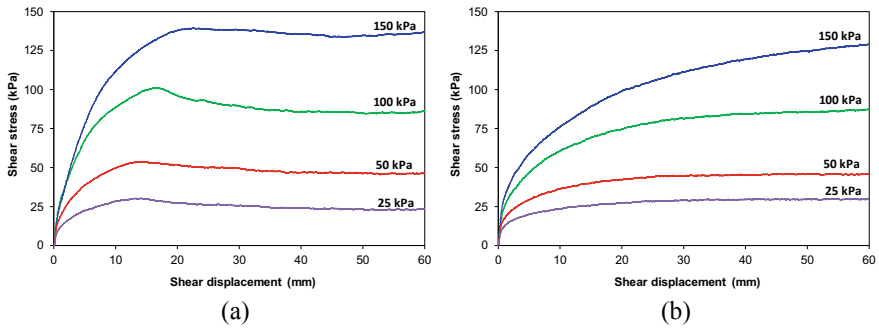


Fig. 8 Direct shear behaviour of interface C&D recycled material/GGR2 under distinct normal stress values: **a** dry C&D recycled material; **b** optimum moisture content

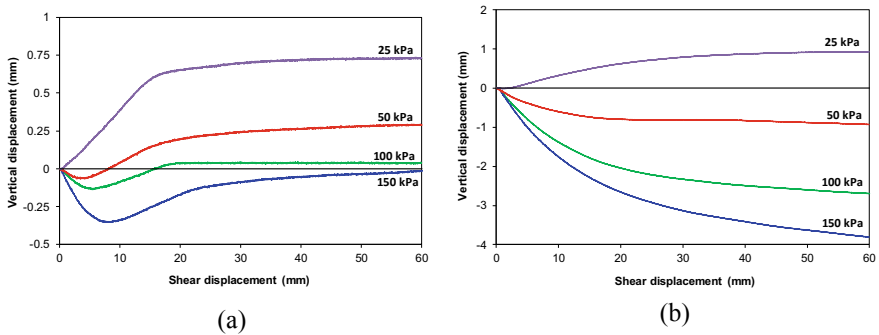


Fig. 9 Vertical displacement of the loading plate during shear—C&D recycled material/GGR2: **a** dry C&D recycled material; **b** optimum moisture content

The dilatant behaviour of the C&D recycled material during interface direct shear tests is presented in Fig. 9 for GGR2 interface. The vertical displacements of the loading plate are in agreement with the shear stress–shear displacement behaviour of the interface (Fig. 8). When C&D material is moist, the interface did not reveal any peak of strength and accordingly, with exception for the lowest confining pressure (25 kPa), the material did not provide evidence of dilatancy (Fig. 9b).

Influence of the geogrid. Figure 10 compares the shear stress–shear displacement recorded in the interfaces with the behaviour of the C&D recycled material for dry (Fig. 10a) and moist (Fig. 10b) conditions under normal stress of 150 kPa. For dry conditions, the inclusion of the geogrid, creating an interface, leads to the decrease of the shear strength. Due to the larger apertures of GGR2 (Fig. 2b), the shear strength of the interface for large displacements is very close to the C&D material strength. The geometric characteristics of GGR1 (narrow apertures and thicker transversal bars)—Fig. 2a—make the interface less efficient.

The direct shear behaviour of GGR2 interface was very similar to that of the C&D recycled material for moist conditions (Fig. 10b). This evidence is consistent with the

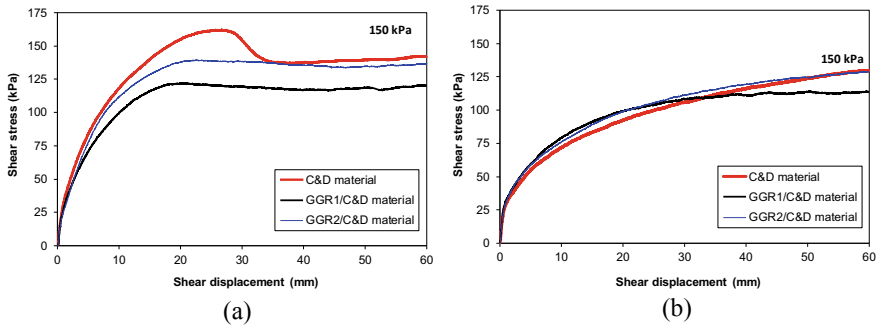


Fig. 10 Influence of the presence of geogrid on the direct shear behaviour: **a** dry C&D recycled material; **b** at optimum moisture content

behaviour of the interface for large displacements under dry conditions (Fig. 10a). GGR1 has also revealed lower shear strength (Fig. 10b).

Direct shear strength parameters. For a better comparison of the interfaces direct shear strength, the failure envelopes for dry and moist conditions are shown in Fig. 11 (GGR1) and Fig. 12 (GGR2). Regardless the geogrid, the interface friction angle decreases when the C&D recycled material is wet. Unlike what was observed for C&D recycled material (Fig. 6), the cohesion has not increase in GGR2 interface when the material became wet.

The interface shear strength is usually defined by a coefficient of interaction, f_g , defined as the ratio of the maximum shear stress achieved in a C&D material/geogrid interface, to the maximum shear stress achieved for C&D material, under the same normal stress. Table 3 presents the range of values of f_g for both interfaces under distinct conditions.

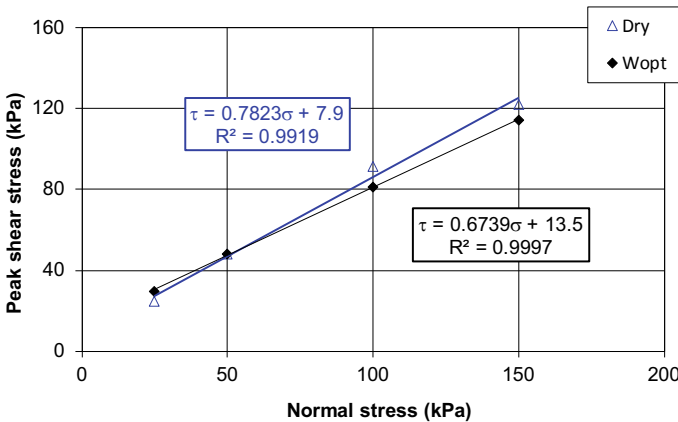


Fig. 11 Failure envelopes for interface C&D recycled material/GGR1

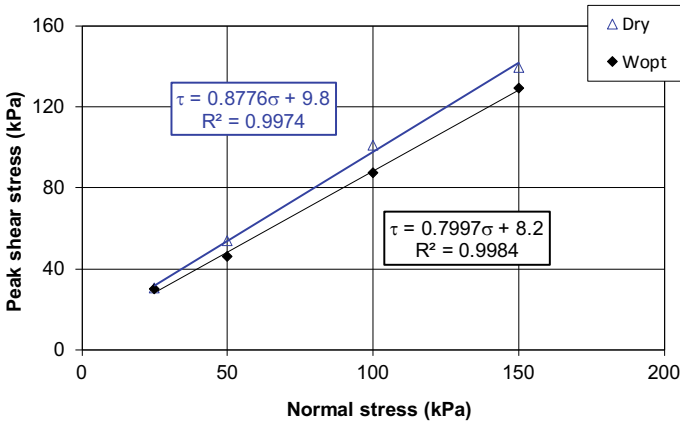


Fig. 12 Failure envelopes for interface C&D recycled material/GGR2

Table 3 Coefficients of interaction for geogrid/C&D recycled material interfaces

	GGR1	GGR2
Dry C&D recycled material	0.71–0.77	0.83–0.87
C&D recycled material at ω_{opt}	0.82–0.91	0.84–0.99

Regardless the condition of the C&D recycled material (dry or at optimum moisture content), the coefficients of interaction for GGR2 interface are higher than those for GGR1 interface. Due to the high values of the shear strength for dry C&D recycled material, the coefficients of interaction for the material compacted at optimum moisture content are higher than those achieved for the dry material for both interfaces.

It is worth mentioning that values presented in Table 3 are within the range of values achieved by other researchers for soils [2, 13].

4 Conclusions

The physical, mechanical and environmental characterization of a fine-grain C&D recycled material was presented and discussed. The characterization of the interfaces between this recycled material and two geogrids was also evaluated through large-scale direct shear.

Based on the results presented in this paper, the following conclusions can be drawn:

- This C&D recycled material, classified as silty sand (SM) according to the Unified Soil Classification System (USCS), has geotechnical properties similar to those of natural soils (under identical conditions).

- Although high concentrations of sulphate and total dissolved solids, the C&D recycled material does not give rise to environmental concerns.
- The shear strength of the C&D recycled material decreased when its moisture content increased from the air-dried condition to the optimum moisture content. Both, the angle of friction and the cohesion have decreased.
- The increase in the moisture content of the C&D recycled material (from dry to optimum moisture content) reduces the interface shear strength, being the reduction more pronounced for GGR2 interface.
- The geogrid GGR2 revealed to be more efficient than geogrid GGR1 with respect to the mobilization of direct shear strength.
- Regardless of the test conditions, the shear strength of C&D recycled material/geogrid interfaces was lower than the internal shear strength of the C&D recycled material. The coefficients of interaction ranged from 0.71 to 0.91 for GGR1 interfaces and from 0.83–0.99 for GGR2 interfaces.

Acknowledgements This work was financially supported by: Project PTDC/ECI-EGC/30452/2017—POCI-01-0145-FEDER-030452—funded by FEDER funds through COMPETE2020—Programa Operacional Competitividade e Internacionalização (POCI) and by national funds (PIDDAC) through FCT/MCTES; Base Funding—UIDB/04708/2020 of the CONSTRUCT—Instituto de I&D em Estruturas e Construções—funded by national funds through the FCT/MCTES (PIDDAC). The second author would also like to thank Fundação para a Ciência e Tecnologia (FCT) for his research grant: SFRH/BD/147838/2019. The authors would like to thank Tensar International and Naeu for providing the geosynthetics used in the study.



References

1. Abu-Farsakh M, Coronel J, Tao M (2007) Effect of soil moisture content and dry density on cohesive soil–geosynthetic interactions using large direct shear tests. *J Mater Civil Eng* 19(7):540–549
2. Ferreira FB, Vieira CS, Lopes ML (2015) Direct shear behaviour of residual soil–geosynthetic interfaces—influence of soil moisture content, soil density and geosynthetic type. *Geosynth Int* 2(3):257–272
3. Hatami K, Esmaili D (2015) Unsaturated soil–woven geotextile interface strength properties from small-scale pullout and interface tests. *Geosynth Int* 22(2):161–172
4. EN 933–11 (2009) Tests for geometrical properties of aggregates—Part 11: classification test for the constituents of coarse recycled aggregate, CEN
5. EN 933–1 (2002) Tests for geometrical properties of aggregates—Part 1: determination of particle size distribution—Sieving method, CEN
6. ISO/TS 17892–4 (2004) Geotechnical investigation and testing—Laboratory testing of soil—Part 4: Determination of particle size distribution, CEN—ISO
7. EN 13286–2 (2010) Unbound and hydraulically bound mixtures. Test methods for laboratory reference density and water content. Proctor compaction, CEN

8. Vieira CS, Lopes ML, Caldeira LM (2013) Sand–geotextile interface characterisation through monotonic and cyclic direct shear tests. *Geosynth Int* 20(1):26–38
9. EN 12457–4 (2002) Characterisation of waste—Leaching—compliance test for leaching of granular waste materials and sludges—Part 4: One stage batch test at liquid to solid ratio of 10l/kg for materials with particle size below 10 mm (without or with size reduction), CEN
10. LNEC E484 (2016) Guide for the use of materials resulting from construction and demolition waste in rural and forest roads. LNEC (Portuguese Laboratory of Civil Engineering), (in Portuguese), pp 8
11. LNEC E474 (2009) Guide for use of recycled materials coming from construction and demolition waste in embankment and capping layers of transport infrastructures. LNEC (Portuguese Laboratory of Civil Engineering), 5p (in Portuguese)
12. Council Decision 2003/33/EC (2003) Council Decision establishing criteria and procedures for the acceptance of waste at landfills pursuant to Article 16 of and Annex II to Directive 1999/31/EC. Official J European Union L11/27
13. Liu C-N, Ho Y-H, Huang J-W (2009) Large scale direct shear tests of soil/PET-yarn geogrid interfaces. *Geotext Geomembr* 27(1):19–30

Strength Assessment of Quarry Dust Treated Soil—Reclaimed Asphalt Pavement (Rap) Mixture



Mildred Cakuru, Rajab Katuntu Tenywa, Samuel Jjuuko,
and Denis Kalumba

Abstract An experimental and quantitative investigation into the properties of laterite soil stabilized with reclaimed asphalt pavement and quarry dust for pavement layers was carried out. Preliminary tests done on the lateritic soil classified it as clayey gravel of intermediate plasticity with sand according to the Unified Soil Classification System. Hence, there is a need to be stabilized for use as pavement layers. The optimal percentage of quarry dust required to stabilize the soil was determined as 30% from the laboratory investigations. The quantity of quarry dust was maintained constant and its combined effect with reclaimed asphalt on the laterite was investigated based on the compaction characteristics, Atterberg limits, particle size distribution, unconfined compressive strength and California bearing ratio tests. The results obtained were analyzed quantitatively and blends containing soil, 30% quarry dust, and 35, 40, 45 and 50% of reclaimed asphalt pavement were found to meet the properties of G30 material suitable for subbase layers according to the General Specifications for Roads and Bridges (2004) of the Ministry of Works, Housing and Communication in Uganda.

Keywords Reclaimed asphalt pavement · Quarry dust · Treated soil

1 Introduction

Over the years, laterite has been effectively used on road construction projects in subgrade, subbase and base applications in Uganda. However, due to the rapid increase in road construction activities in the recent years, in relation to rehabilitation and maintenance [1], laterite has been exhausted. This remains a threat to the construction industry as the resources continue to be depleted. Additionally, the

M. Cakuru · R. K. Tenywa
Ndejje University, 7088 Kampala, Uganda

S. Jjuuko (✉)
Makerere University, 7062 Kampala, Uganda

D. Kalumba
University of Cape Town, Private Bag X3, Rondebosch 7701, South Africa

borrow materials obtained may not meet the required specifications. Hence, there is a need to stabilize the laterite.

Recent trends in general laterite stabilization have evolved innovative techniques of utilizing locally available and industrial waste materials for the modification of this deficient soil. Stabilization using lime and cement has proved to be uneconomical [2]. Furthermore, the use of recycled or secondary materials including quarry dust and recycled asphalt pavement has additional advantages including conservation of natural resources and energy, preservation of the environment and reduction in life-cycle costs [3]. This research investigated the use of quarry dust and recycled asphalt pavement to improve the properties of laterite for use in road subbases (G30 material) in Uganda.

2 Materials and Methods

2.1 *Laterite Soil*

Laterite soil samples were obtained from a borrow pit source along Kitara—Gerenge road. A trial pit was excavated to a depth of 2.0 m, removing the topsoil up to a depth of 0.2 m. The samples were collected from depths ranging between 0.2 and 2.0 m. They were placed in air-tight bags and carefully transported to the laboratory for testing. Laterite was classified as an A-2-7 soil according to the AASHTO classification system with a group index of 3. The Unified Soil Classification System classified laterite as clayey gravel (GC) with sand. The sample consisted of 14% clay, 10% sand and 76% gravel with liquid limit of 49% and plasticity index of 23%.

The material did not meet all the requirements for subbase construction (G30 material) according to the Ministry of Works, Housing and Communication (MoWH&C) General Specifications for National Roads of 2004, (Table 4.1), in reference to Atterberg limits and four-day soaked California bearing ratio (CBR) hence the need to be stabilized.

2.2 *Quarry Dust*

Quarry dust is a byproduct formed in the processing of granite stones into coarse aggregates of different sizes. The quarry dust was obtained from Gayaza quarry site along Gayaza—Kalagi road. From the sieve analysis test, it had 9% fines, 81% sand and 10% gravel particle sizes with a liquid limit of 26% and non-plastic. The grading curve of quarry dust was found to lie within the grading envelopes but tending to the upper limit implying it contained fine particles.

Table 1 Physical and mechanical properties of the soil sample and requirements for subbase course layers of G30 materials

Material properties	Material class G30	
	General requirements	Calcrete or other pedogenic materials
CBR:BS 1377: Part 4		
CBR (%)	Minimum 30 after 4 days soaking	
CBR-swell (%)	Maximum 1.0 measured at BS-Heavy compaction	
Atterberg limits		
Max liquid limit BS 1377: part 2	45	45
Max. plasticity index BS 1377: part 2	16	18
Max. linear shrinkage BS 1377: part 2	8	9
Grading: BS 1377: Part 2		
Particle strength: BS 812: Part 111		
Requirements:	Grading modulus, GM shall be minimum 1.2	

(1) CBR values shall be measured at the specified field density for the layer

(2) Atterberg limits shall be measured according to BS1377: Part 2

2.3 Reclaimed Asphalt Pavement (RAP)

Reclaimed asphalt pavement (RAP) is generally defined as removed pavement materials. RAP material was obtained along the Kampala Northern By-pass where there is on-going expansion works. No proper stock piling of the RAP material was done. It had 6.7% fines, 39.8% sand and 53.5% gravel particle sizes from the sieve analysis test. The grading curve of RAP was lying within the grading envelope. However, it was tending to the upper limit implying presence of more fine particles. The presence of fine particles was attributed to crushing of aggregates as a result of gradual loading impact by traffic (Table 1).

2.4 Sample Preparation

The samples for laboratory testing were prepared in accordance with BS 1377 Part 1: 1990. At the laboratory, a portion of the laterite samples was obtained for natural moisture content determination. Since some tropical soils are sensitive to pre-test drying methods, air-drying was undertaken. Other pre-test sample preparation methods included pulverization, sieving and sub-sampling (coning, quartering and riffing). After air-drying, index properties tests were carried out for classification.

RAP material was obtained in form of chunks/lumps. It was crushed by hand to break it down into smaller particle sizes of approximately 14 mm diameter.

In order to investigate the effect of RAP and quarry dust (QD) on the properties of laterite soil, specimens with specified amounts of RAP, QD and soil were prepared in different mixes. The optimal percentage of quarry dust required to stabilize the soil was determined as 30%. The quantity of quarry dust was maintained constant and its combined effect with RAP on the laterite was investigated in the following mixes: (i) 30%QD + 35%RAP + 35%LATERITE, (ii) 30%QD + 40%RAP + 30%LATERITE, (iii) 30%QD + 45%RAP + 25%LATERITE and (iv) 30%QD + 50%RAP + 20%LATERITE. The mixing was done mechanically on a metal tray. For consistency, soil was mechanically blended before mixing with QD and RAP. Tests of physical properties of the different mixes/blends were conducted.

2.5 Tests

The following tests were carried out on the prepared specimens

- Atterberg limits in accordance with BS 1377: Part 2: 1990
- Sieve analysis test in accordance with BS 1377: Part 2: 1990
- Proctor compaction (BS-Heavy) test in accordance with BS 1377: Part 4: 1990 for natural gravel and BS 1924: Part 2: 1990 for stabilized lateritic gravel
- California bearing ratio (CBR) test in accordance with BS 1377: Part 4: 1990 for natural gravel and BS 1924: Part 2: 1990 for stabilized lateritic gravel
- Unconfined compressive strength (UCS) test in accordance with BS 1377: Part 4: 1990 for natural gravel and BS 1924: Part 2: 1990 for stabilized lateritic gravel

Atterberg Limits Test

The cone penetrometer method was used in this study to determine the liquid limit of the laterite-QD-RAP mixtures. As the moisture content of the soil sample was increased by small amounts, the penetration of the cone was noted and plotted against the respective moisture content. From the same soil sample, a specimen was dried to near its plastic limit by air drying. It was then molded into a ball and rolled between the palms of the hand and glass plate to threads of nearly 3 mm in diameter. The soil was now considered to be at the plastic limit and its moisture content determined.

Sieve Analysis test

A representative sample of about 3 kg was obtained and placed on the metal tray and taken for oven drying at a temperature of 105–110°C for 24 h. The oven dried sample was then soaked for a period of 12 h. The material was washed through the 75 μm test sieve, allowing the material passing through to run as waste. The oven dry sample was then poured onto a stack of test sieves arranged in descending order of sieve sizes including a pan placed at the bottom to receive the finest particles. The stack of sieves was placed on a mechanical sieve shaker for 10 min. The weight of soil retained on each sieve was then recorded and the results were tabulated. A graph

of percentage passing against sieve sizes was plotted on a semi-logarithmic scale resulting into what is called a grading/distribution curve.

Proctor test

The modified compaction test was used. The soil was compacted in five layers of equal thickness, into a metal mold of 105 mm diameter and of one-liter capacity. Each layer received blows from a 4.5 kg mass falling freely through a height of 450 mm, with 27 blows in the one-liter mold. The moisture content of the soil was adjusted, up or down, and the test was repeated to give at least five density values. The dry density of the soil was calculated and plotted versus moisture content.

California Bearing Ratio test

CBR tests were carried out on laterite-QD-RAP mixes. The specimens were prepared at their optimum moisture content. The samples were compacted as to the modified method in the CBR mold. After compaction, they were soaked for four (4) days.

Unconfined Compressive Strength test

UCS tests were conducted on the laterite samples as well as on laterite-QD-RAP blends. Cylindrical specimens used for the experiments were 105 mm diameter and 127 mm height. The samples used for the UCS tests were at their optimum moisture contents. Specified amounts of quarry dust and RAP were added to screened laterite soil and mixed well for homogeneity. The mixture was placed in five layers in a UCS steel mold having an inside diameter of 105 mm and height of 127 mm. All the different soil mixes were compacted as to the modified method (BS 1377: Part4: 1990), trimmed at both ends and wrapped in plastic bags. The UCS tests for the unstabilized and stabilized laterite samples were conducted on all extracted specimens using a strain rate of 1.27 mm/min immediately after mixing. Corrections to the cross-sectional areas were applied prior to calculating the compressive stress on the specimen. Each specimen was loaded until peak stress was obtained.

3 Results and Discussion

3.1 Atterberg Limits

Atterberg limits show the behavior of the soil material with changes in water content. It is a key parameter since variation of weather (rainy to sunny seasons) leads to change in the behavior of soils. They show clearly how the tested material would behave with these changes. Table 2 presents a summary of the Atterberg limit results for various blends. The liquid limit of natural laterite soil was 49%. Addition of quarry dust to laterite soil reduced its liquid limit from 49 to 45, 41 and 36% with 10, 20 and 30% QD, respectively. The plasticity index (PI) obtained for the neat material was 23%. The addition of quarry dust in varying contents, 10, 20 and 30%, led to the decrease in the PI with increasing quantities of quarry dust added, 22, 19 and 16%, respectively. Quarry dust being non-plastic led to further reduction of PI.

Table 2 Atterberg limits for various blends

Sample description	Liquid limit (%)	Plastic limit (%)	Plasticity index (%)	Linear shrinkage (%)
Neat	49	25	23	12
Quarry dust	26	NP	NP	0
10% QD	45	24	22	11
20% QD	41	22	19	9
30% QD	36	21	16	8
30% QD + 35% RAP + 35% LATERITE	30	14	16	8
30% QD + 40% RAP + 30% LATERITE	32	16	16	8
30% QD + 45% RAP + 25% LATERITE	34	18	16	8
30% QD + 50% RAP + 20% LATERITE	30	14	16	8

It was also observed that there was no significant effect on PI with the addition of different percentages of RAP since the fine material in it was bound by bitumen. Linear shrinkage also reduced with increase in percentage of quarry dust since it is closely related to PI. The maximum percentage of 30% for QD was selected since the properties of its blend with laterite soil met the requirements for a G30 material, in terms of liquid limit, plasticity index, linear shrinkage and grading modulus, as stipulated in the General Specifications for Roads and Bridges (2004) for Ministry of Works, Housing and Communication, Uganda.

3.2 Grading Modulus (GM)

The grading modulus of the laterite soil generally augmented with increasing percentage of RAP in the blends as shown in Fig. 1. G30 materials should have a minimum grading modulus of 1.2. The grading modulus was calculated as: $GM = (P_{2.00} + P_{0.425} + P_{0.075} \text{ mm}) / 100$ where P_{2.00} mm, etc., denote the percentage retained on the indicated sieve size.

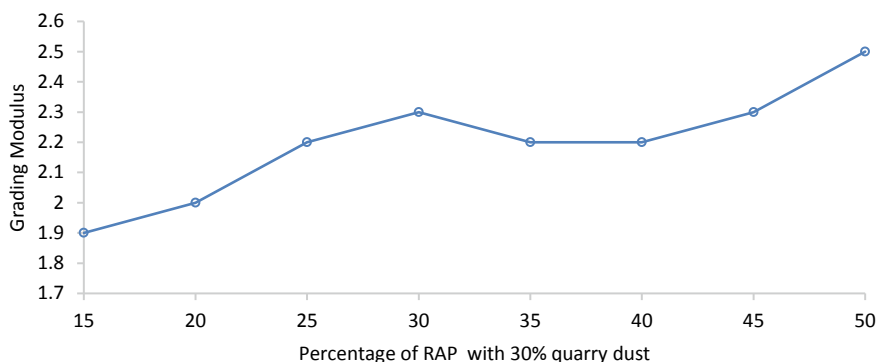


Fig. 1 Grading modulus versus percentage of RAP with 30% quarry dust

3.3 Maximum Dry Density (MDD) and Optimum Moisture Content (OMC)

Table 3 indicates results of MDD and OMC for various blends. From the laboratory test results, it was observed that MDD increased with increasing percentage of RAP with 30% QD up to optimum of 40% RAP and then decreased as shown in Fig. 2. Grading is directly proportional to MDD of the material [4]. The increase in MDD is attributed to the increase in coarser particles of RAP up to the optimum. Beyond the optimum, the larger particle size of RAP lead to a poorly graded material associated with increase in porosity [5]. OMC of the blends decreased with increase in RAP content at 30% QD, Fig. 3. This was due to the decrease in the fines content with increase in the coarse RAP particles that have a low affinity for water. Usually, soils with MDD greater than 2000 kg/m³ and OMC less than 15% are easier to compact and recommended for pavement layers.

Table 3 MDD and OMC for various blends

Material	MDD (kg/m ³)	OMC (%)
Laterite (neat)	1898	12.2
15% RAP + 30% quarry dust + 55% laterite	1921	11.2
20% RAP + 30% quarry dust + 50% laterite	1962	9.9
25% RAP + 30% quarry dust + 45% laterite	1968	9.1
30% RAP + 30% quarry dust + 40% laterite	1974	7.8
35% RAP + 30% quarry dust + 35% laterite	2166	6.6
40% RAP + 30% quarry dust + 30% laterite	2145	6.3
45% RAP + 30% quarry dust + 25% laterite	2115	6.2
50% RAP + 30% quarry dust + 20% laterite	1909	5.2

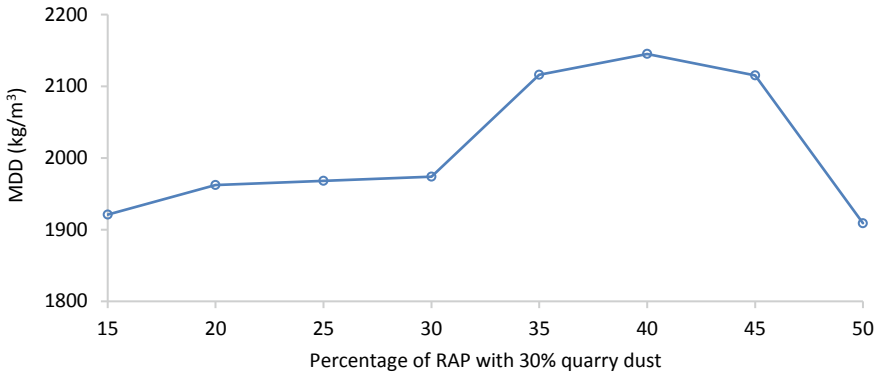


Fig. 2 Maximum dry density versus percentage of RAP with 30% quarry dust

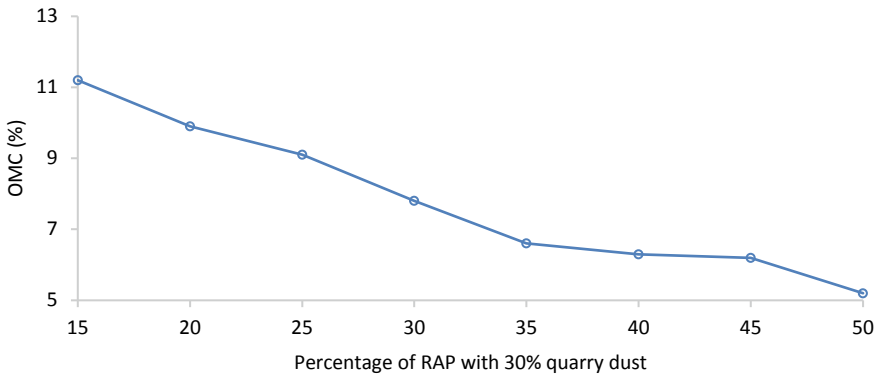


Fig. 3 Optimum moisture content versus percentage of RAP with 30% quarry dust

3.4 California Bearing Ratio (CBR)

The strength evaluation was carried out at the different proportions of RAP with 30% quarry dust added to the soil material. Results indicated that the CBR values obtained from laterite soil were 12, 19 and 29 at 93, 95 and 98% MDD, respectively. The CBR values increased with increase in the percentage of RAP up to the optimum and then decreased, Fig. 4. The general increase in CBR values was a result of increase in the particle densities which is likely to affect the penetration of the plunger. The RAP material is more resistant to crushing under gradually applied loads [6]. The decrease in CBR may be attributed to the decrease in the cohesive material as the non-cohesive RAP material increased leading to a weaker and less dense material (Table 4).

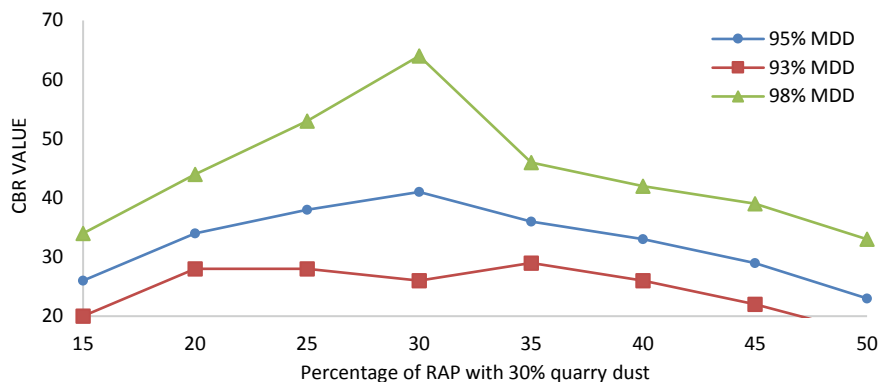


Fig. 4 CBR versus percentage of RAP with 30% quarry dust

Table 4 CBR for various blends

CBR (Soaked)	93% MDD	95% MDD	98% MDD
Laterite (Neat)	12	19	29
15% RAP + 30% quarry dust + 55% laterite	20	26	34
20% RAP + 30% quarry dust + 50% laterite	28	34	44
25% RAP + 30% quarry dust + 45% laterite	28	38	53
30% RAP + 30% quarry dust + 40% laterite	26	41	64
35% RAP + 30% quarry dust + 35% laterite	29	36	46
40% RAP + 30% quarry dust + 30% laterite	26	33	42
45% RAP + 30% quarry dust + 25% laterite	22	29	39
50% RAP + 30% quarry dust + 20% laterite	17	23	33

3.5 Unconfined Compressive Strength (UCS)

As indicated in Fig. 5, UCS generally increased with increasing RAP content up to optimum value of 0.92 MPa at 30% RAP content and then decreased. The increase in UCS was attributed to the increase in density of the compacted blends with increasing RAP content. The RAP material is denser than laterite particles. The decrease in UCS may be attributed to the decrease in the cohesive material as the non-cohesive RAP material increased leading to a weaker and less dense material (Table 5).

4 Conclusions

From the results of the laboratory tests, the following was concluded:

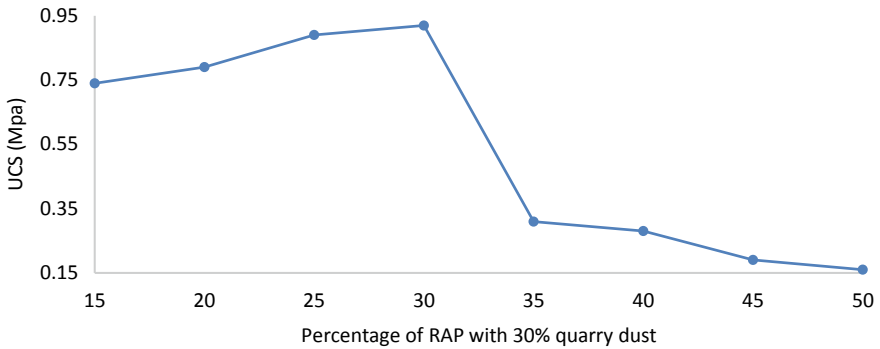


Fig. 5 UCS versus percentage of RAP with 30% quarry dust

Table 5 UCS for various blends

Material	Unconfined compressive strength (MPa)
Laterite (Neat)	0.63
15% RAP + 30% quarry dust + 55% laterite	0.74
20% RAP + 30% quarry dust + 50% laterite	0.79
25% RAP + 30% quarry dust + 45% laterite	0.89
30% RAP + 30% quarry dust + 40% laterite	0.92
35% RAP + 30% quarry dust + 35% laterite	0.31
40% RAP + 30% quarry dust + 30% laterite	0.28
45% RAP + 30% quarry dust + 25% laterite	0.19
50% RAP + 30% quarry dust + 20% laterite	0.16

- Laterite was classified as an A-2-7 soil according to the AASHTO classification system with a group index of 3. The Unified Soil Classification System classified laterite as clayey gravel (GC) with sand.
- The liquid limit, plastic limit, linear shrinkage and plasticity index of laterite decreased with increasing percentages of quarry dust and RAP materials.
- MDD of laterite increased with increasing percentage of RAP with 30% QD up to optimum of 40% RAP and then decreased. OMC of the blends decreased with increase in RAP content at 30% QD.

- The CBR values increased with increase in the percentage of RAP up to the optimum of 30% and then decreased.
- A mixture containing between 15 and 50% of reclaimed asphalt pavement, and 30% quarry dust of the lateritic soil, is recommended for road subbase construction. It resulted into values of CBR greater than 30 at 98% compaction. Thus, met all the requirements for subbase construction according to the Ministry of Works, Housing and Communication (MoWH&C) General Specifications for National Roads of 2004.

References

1. Uganda National Roads Authority: Ongoing Projects (2013) http://www.unra.go.ug/index.php?option=com_content&view=category&id=43&Itemid=66. Last Accessed 23 May 2013
2. Eze-Uzomaka OJ, Agbo D (2010) Suitability of quarry dust as improvement to cement stabilized-laterite for road bases. *Electron J Geotech Eng* 15:1053–1066
3. Saride S, Puppala AJ, William R (2010) Assessing recycled/secondary materials as pavement bases. *Proc ICE-Ground Improvem* 163(1):3–12
4. Adeyemi GO, Afolagboye LO (2013) Mechanical stabilization of a migmatite gneiss-derived lateritic soil from Southwestern Nigeria. *Electron J Geotech Eng* 18:1847–1858
5. Suebsuk J, Suksan A, Horpibulsuk S (2014) Strength assessment of cement treated soil-reclaimed asphalt pavement (RAP) mixture. *Int J Geomate* 6(2):878–884
6. Tugume B, Owani I, Jjuuko S, Kalumba D (2019) Performance of lateritic soils stabilized with both crushed rock aggregates and carbon black as a pavement base layer. In: *The international congress on environmental geotechnics 2018*, Springer, Singapore, pp 382–388
7. Ministry of Works, Housing and Communications (2004) *General Specifications for Road and Bridge Works, Series 3000; Earthworks and Pavement Layers of Gravel or Crushed Stone*
8. British Standard Institution (1990) BS 1377, *Methods of tests for soils*, British Standard Institution, London, UK
9. British Standard Institution (1990) BS 1924, *Methods of tests for stabilized soils*, British Standard Institution, London, UK

Reuse of Waste HDPE Bottle-Derived Geocells for Stabilization of Hilly Roadway Slopes



Punit Bhanwar, Sunil Ahirwar, and Trudeep Dave

Abstract Construction of transportation infrastructure in the hilly region is inevitable due to the scarcity of suitable land. Moreover, construction in hilly terrain is challenging due to reduced bearing area, slope failures, excessive lateral deformation, and high differential settlement. Conventional techniques such as gravity retaining walls, reinforced slopes, soil nailing, and gabion walls employed to deal with these issues, usually lack the sustainability approach. A novel and sustainable approach of providing geocellular retention system for the stabilization of hilly roadway slopes is presented here. In this experimental model study, geocellular retention system in a form of a gravity wall was built by zip-tying waste HDPE intravenous fluid bottles-derived geocells with an aspect ratio of 0.85. Stone quarry dust compacted at optimum moisture content was used as infill and backfill material for these geocell-based retention systems. Load-controlled tests were performed in a model test tank to monitor failure load, settlement of slopes and lateral deformations of geocell stabilized and unstabilized slopes at various facing angles. The peak load-carrying capacity of the geocell stabilized slopes was found to be 24, 17.14, and 15.01% relatively more than corresponding unstabilized slopes for facing angles 90°, 80°, and 70°, respectively. Further, peak settlements were observed to be relatively reduced by 17.42, 15.58, and 15.65% along with lateral deformations also relatively reduced by 17.89, 14.73, and 13.93% for geocell stabilized slopes over unstabilized slopes with respective facing angles.

Keywords HDPE geocell · Stone quarry dust · Model studies · Lateral deformation · Settlement

P. Bhanwar (✉) · T. Dave
Institute of Infrastructure Technology Research and Management, Ahmedabad, India
e-mail: punit.bhanwar.18pc@iitram.ac.in

S. Ahirwar
Shri Govindram Sekseria Institute of Technology and Science, Indore, India

1 Introduction

With increasing demand for suitable and space in the development of transportation infrastructure all over the world, a need to explore new construction techniques for sites considered unsuitable for construction has arisen. Replacement of weak soil by some strong soil or improvement of engineering properties of weak soil by different ground improvement techniques is generally used in such a situation [21]. If such soil cannot be removed or is uneconomical to remove, then various ground improvement techniques are employed. Among such techniques, soil reinforcement [9] has gained considerable popularity in recent times due to benefits like ease of construction, overall economy, and less time consumption. Reinforcing soil using geosynthetics has been increasingly employed in geotechnical and environmental engineering for the last four decades [4]. A three-dimensional geosynthetic called geocell is a reinforced composite that totally encapsulates weak soil material and provides all-round confinement due to its three-dimensional structure [2]. This effect produces higher stiffness, improves shear strength, and reduces lateral spreading when compared to an unreinforced soil. Eventually, this led to their extensive application in a wide array of construction applications like earth retention, slope erosion control, channel protection, and ground stabilization [5, 8, 13, 18, 19].

An externally stabilized retention system that can use the force of gravity to retain or support soil mass is termed as gravity geocellular wall [15]. The said structure can be formed by vertical stacking of geocell planar sections (geocell mattress) which are resisted by large frictional forces between inherent infill layers [7]. Such composite structure behaving as a monolithic gravity mass is flexible enough to adapt with variable soil conditions and lateral forces can be used as a self-contained gravity retaining wall [3, 6]. Additionally, it also offers desirable aesthetics, environmental benefits, and construction ease in locations that are difficult to access.

1.1 HDPE Intravenous Fluid Bottles—Geocell Material

HDPE intravenous fluid bottles are non-infectious bio-medical plastic waste which is generated by healthcare establishments and laboratories. A research study conducted for twenty-two developing nations by WHO with researchers revealed that a large proportion of healthcare facilities, ranging from 18 to 64%, do not employ proper waste disposal methods for these bio-medical waste [17, 20, 22]. To estimate the approximate quantum of rejected HDPE intravenous fluid bottles, a localized survey was done in twenty healthcare facilities located in Indore (M.P.), India. It was revealed that about 300 to 400 bottles per institution per day are nearly generated. Reuse of these HDPE bottles for geoenvironmental applications can provide a sustainable solution. In the present study, an attempt is made to assess the capability of HDPE intravenous fluid bottles to function as geocell in modeled geocellular retention system (GRS).

1.2 Stone Quarry Dust—Backfill and Infill Material

The stone quarry dust is a byproduct produced at stone mining sites, which majorly contains a large amount of silicates and alumina-silicates. It is grayish or brownish in color with very fine aggregate particles, like silty sand. According to a report [11], it is estimated that there are over 12,000 stone crushing units in India, which nearly produce waste stone quarry dust in the magnitude of 25–30 million metric tons per annum. Though it is durable, strong, and can be easily compressed into tight spaces, at the same time, it is a non-biodegradable material. This poses numerous environmental problems, like if dumped on land, then it can reduce the rate of rainwater percolating and deteriorate the soil fertility. Similarly, if dumped in rivers, seas, or streams, it tends to contaminate the water and marine environment as well. In the past, studies have been already carried out for reuse of stone dust in the production of bricks, mortar, tiles, and cement concrete as aggregate and filler material [14]. The current study explores the reuse of stone quarry dust as an infill and backfill material in the proposed GRS.

2 Material Overview

The stone quarry dust used in the present study was collected in air-dried condition from Umbra Mining Corporation, Rewti range MR-10 Indore, Madhya Pradesh. The geotechnical properties so found in the laboratory of stone quarry dust are mentioned (Table 1).

Similarly, waste and rejected HDPE intravenous fluid bottles were collected from medical institutions like hospitals, dispensaries, and pharmaceutical shops. Their

Table 1 Geotechnical properties of stone quarry dust

Properties ^a [10]	Stone quarry dust
Specific gravity	2.76
D_{10} (mm)	0.15
D_{60} (mm)	1.6
D_{30} (mm)	0.6
Liquid limit (%)	25
Plastic limit (%)	NP
Maximum dry density (kN/m^3)	18.73
Optimum moisture content (%)	12
Angle of internal friction (Φ)	29°

^aGeotechnical properties in order of stated values, conforming to IS 2720 [Specific Gravity (Part 3 Section 2 1980), Grain Size Analysis (Part 4 1985), Liquid Limit and Plastic Limit (Part 5 1985), Modified Proctor Test (Part 8 1983), Direct Shear Test (Part 13 1986)]



Fig. 1 Geocells cut from waste HDPE bottles

tensile strength was estimated from a tension test [1] and was found to be 21 kN/m. These bottles were then cut in a manner so as to form cylindrical geocells having a diameter as 70 mm and height as 60 mm. This ensured that the aspect ratio, i.e., height of geocell to the diameter of geocell was maintained less than one, as recommended by a past study [12]. Finally, the HDPE geocells were joined together by locally available nylon-based zip ties (Fig. 1).

3 Experimental Program

Based on principles of similitude [16], model test tank dimensions were derived. The scale factor of (1/5) was adopted to simulate a prototype roadway slope of height 2.1 m as a model slope with a height of 0.42 m. In order to accommodate and test such a model, a tank of dimension 1.17 m (length) \times 0.72 m (high) \times 0.72 m (wide) was fabricated. Figures 2 and 3 represent schematics of tests conducted on unstabilized and geocell stabilized slopes, respectively, (Table 2).

4 Test Setup and Procedure

4.1 Construction and Testing of Unstabilized Slopes

Firstly, a 120 mm thick compacted stone quarry dust was laid at bottom of the tank to act as a foundation layer. The internal walls of the tank were applied with a thin uniform coating of grease to minimize supporting effect from the friction of tank walls. The unstabilized slope sections as per the experimental program were constructed with different facing angles by compacting moist stone quarry dust in

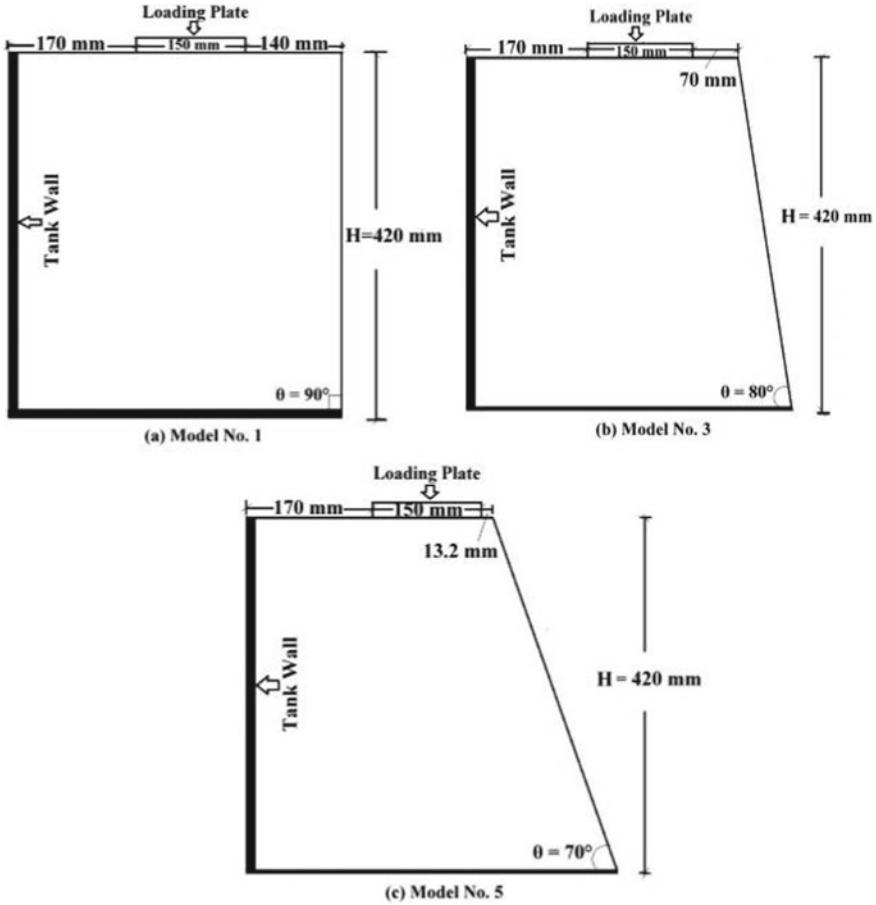
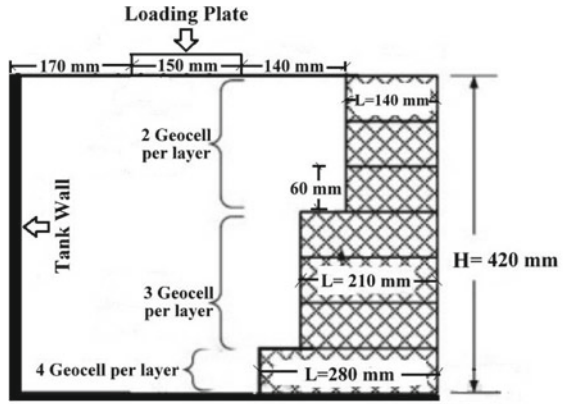


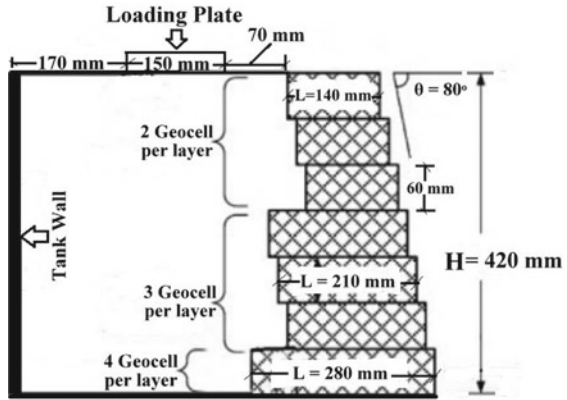
Fig. 2 Test schematics of a model 1 URS 90, b model 3 URS 80, and c model 5 URS 70

layers to the maximum dry density at optimum moisture content. Appropriate care was taken to ensure uniform compaction throughout the section by conducting several trials. After construction of an unstabilized slope, it was allowed to dry for 24 h, and then, testing was commenced. The top surface was leveled before placing a load plate having dimensions 150 × 720 × 10 mm. A load cell was fitted between the piston of jack and loading plate to know instantaneous load while applying pressure on the plate. Lateral deformation was measured by means of six linear variable differential transducers (LVDTs) while two dial gages were rested on pressure plates to determine vertical deformation. Figure 4 illustrates the experimental setup employed in the present study. For each load increment, lateral deformation and settlement of the slopes were measured till failure condition was achieved. When the measured surcharge load is decreasing with the increasing lateral deformation of the slope, it is assumed that failure condition has reached.

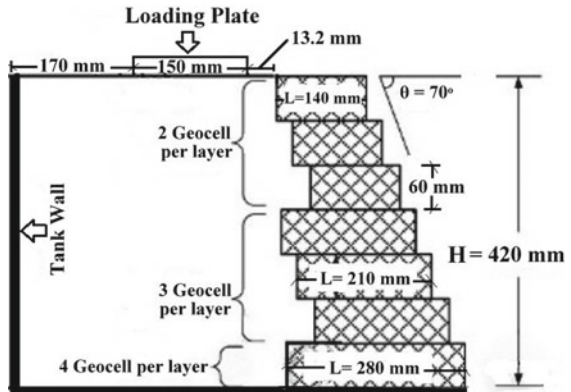
Fig. 3 Test schematics of **a** model 2 GRS 90, **b** model 4 GRS 80, and **c** model 6 GRS 70



(a) Model No. 2



(b) Model No. 4



(c) Model No. 6

Table 2 Scheme of experimentation

Model no.	Slopes	Facing angle	Designation
1	Unstabilized	90°	URS 90
2	Geocell stabilized		GRS 90
3	Unstabilized	80°	URS 80
4	Geocell stabilized		GRS 80
5	Unstabilized	70°	URS 70
6	Geocell stabilized		GRS 70

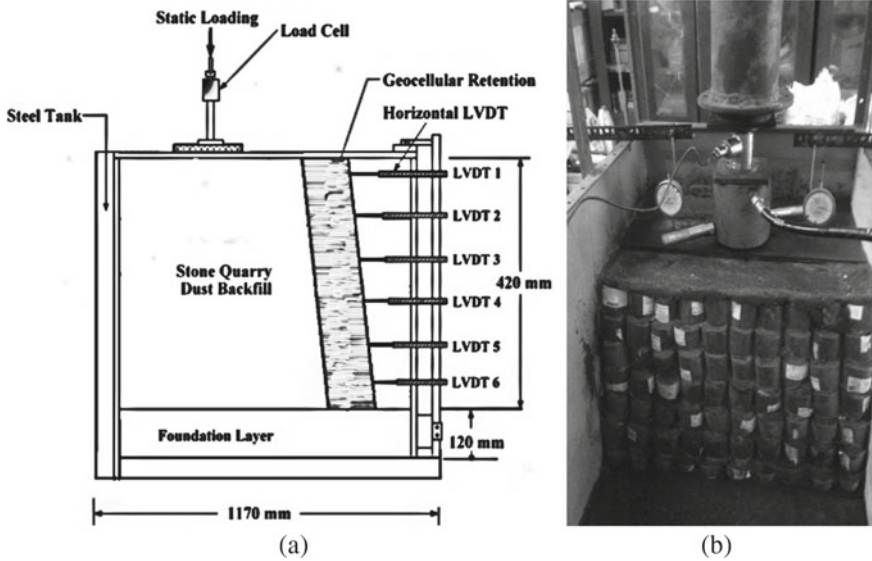


Fig. 4 Experimental setup **a** schematic diagram and **b** pictorial view

4.2 Construction and Testing of Geocell Stabilized Slopes

Initially, the foundation layer of compacted stone quarry dust having 120 mm thickness was laid at bottom of tank. The total height of slope was then divided into seven equal layers with each layer having a thickness equal to 60 mm. Quantity of dry stone quarry dust (W_f) required for each layer was calculated as $W_f = \gamma_d \times V$, where γ_d is maximum dry density of stone quarry dust and 'V' is the volume of each layer. The quantity of water added was (W_w) = ($W_f \times w$), where 'w' is OMC of stone quarry dust. Stone quarry dust and water required for each layer were mixed in a homogeneous mixture by hand in big-size trays. After placing the first layer of geocells on top of the foundation layer, the first layer of moist stone quarry dust was poured into the test tank with help of large size scoops. Appropriate care was taken to ensure

Table 3 Surcharge pressure at failure condition different slope angle

Slope	Failure surcharge pressure		
	90°	80°	70°
URS	46.29 kPa	64.81 kPa	74.07 kPa
GRS	57.40 kPa	75.92 kPa	85.19 kPa
Percentage improvement	24%	17.14%	15.01%

that moist stone quarry dust was spread evenly which was then compacted by standard proctor hammer with a definite number of blows.¹ After compaction, the second layer of geocells was laid, and the procedure was repeated until full geocellular section retained the entire slope (Fig. 4b). Load-controlled testing on these slopes for measurement of lateral deformations and settlements was similarly conducted as mentioned in Sect. 4.1.

5 Results and Discussion

The experimental findings from model tests on unstabilized and geocell stabilized slopes are presented and discussed in Sects. 5.1, 5.2, and 5.3. The parameters which remained constant during a series of tests include the height of slope, number of geocells used, and loading distance. Parameters like surcharge pressure at failure condition, lateral deformation, and slope settlements were monitored for all six models. In order to satisfy similitude requirements [16], surcharge pressures at failure condition, lateral deformations, and slope settlements of GRS 90, GRS 80, and GRS 70 were accordingly scaled down by factor of 1/5.

5.1 Effect of GRS on Surcharge Pressure at Failure Condition

Observed loads corresponding to the failure condition were obtained from load cell placed between the loading plate and loading jack. These loads were then divided by area of loading plate to calculate surcharge pressure at failure condition as mentioned in Sect. 4.1. These are given in Table 3.

The improvements in surcharge carrying capacity can be attributed to additional resistance provided by GRS due to the action of its self-weight. The self-weight of GRS tries to provide lateral confinement to slopes, thereby requiring more surcharge pressure for failure to occur. The near-vertical slope (GRS 90) stabilized by geocell

¹ Number blows were established during compaction of several trial models with predefined moisture content until variation was found to be negligible.

exhibited maximum improvement of 24% as compared to other slopes, i.e., GRS 80 and GRS 70.

5.2 Effect of GRS on Lateral Deformation of Slopes

For this purpose, normalized height of slope, i.e., Y/H where ‘ Y ’ = height of LVDT from foundation layer; ‘ H ’ = height of slope and normalized lateral deformations, i.e., δ/H % where ‘ δ ’ = lateral deformation has been compared. The maximum deformation occurred in the top layer, and it decreased as we progressed down to the base of slope indicating failure of GRS in a tilting mode (Figs. 5 and 6). The maximum normalized lateral deformation for URS 90 was found to be 1.31% while for GRS 90 at the same surcharge pressure of 46.29 kPa, it was found to be 1.076% which means 17.89% reduction in lateral deformation has occurred. On comparing URS 90, URS 80, and URS 70 with GRS 90, GRS 80, and GRS 70, respectively, (see Fig. 7), it can be clearly concluded that all geocell stabilized slopes undergone relatively less lateral deformation than unstabilized slopes. Following a similar comparison for URS 80 and URS 70 with GRS 80 and GRS 70, respectively, manifested, 14.73 and 13.93% reduction in peak lateral deformations at the top layer. This can be attributed to geocellular system capable enough to absorb lateral forces and resist it by tensioned membrane effect and interlayer friction generated on the application of surcharge pressure. The ability of GRS to reduce lateral deformation of slopes with a decrease in slope angle also reduces as seen in Fig. 7. This can be explained considering fact that steeper slopes lacking geometrical stability in lateral direction tend to rely more

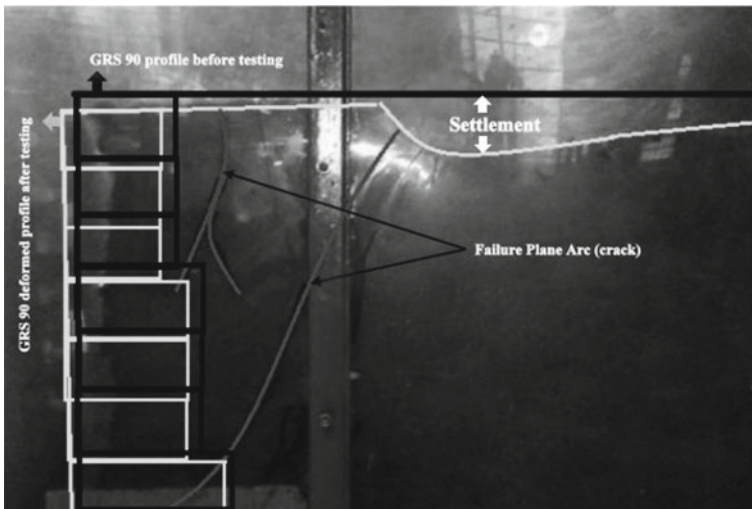


Fig. 5 Visualization of GRS 90 pre- and post-failure condition

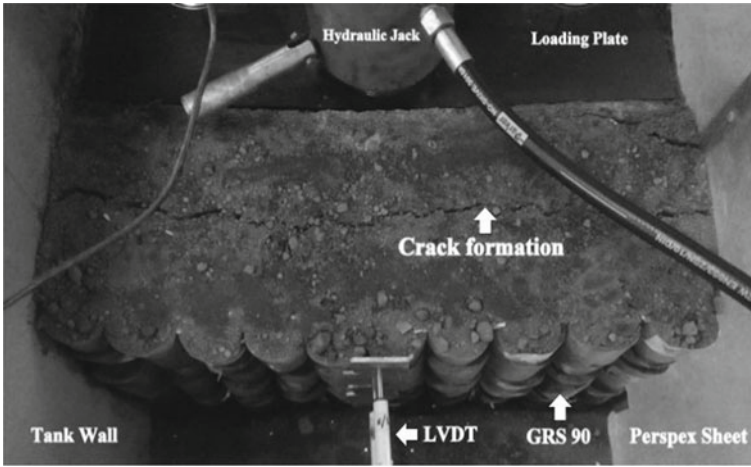


Fig. 6 Top view of GRS 90 post-failure condition

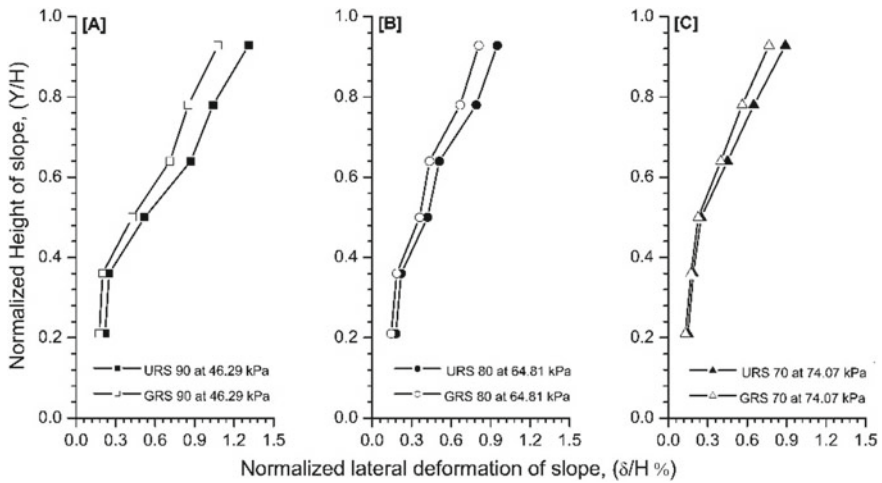


Fig. 7 Comparative analysis between $(\delta/H) \%$ and (Y/H) for a $\theta = 90^\circ$, b $\theta = 80^\circ$, and c $\theta = 70^\circ$

on external support, as opposed to flatter slopes which are relatively more stable. Thus, near-vertical slopes are most benefitted with the GRS.

The effect of GRS on lateral deformation characteristics of model slopes was monitored and analyzed graphically as below.

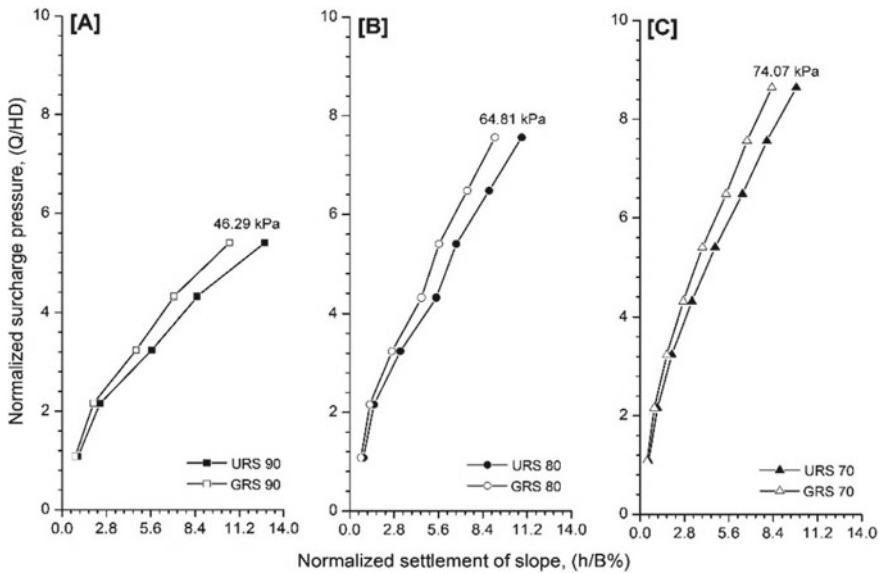


Fig. 8 Comparative analysis between (Q/HD) and $(h/B \%)$ for **a** $\theta = 90^\circ$, **b** $\theta = 80^\circ$, and **c** $\theta = 70^\circ$

5.3 Effect of GRS on Slope Settlement

To understand the effect of GRS on settlement behavior, the relationship between normalized surcharge pressure, i.e., Q/HD where H = height of the slope and D = compacted density of slope and normalized settlement of slope $(h/B) \%$ was plotted. Here, ‘h’ is the settlement of the slope, and ‘B’ is the width of load plate. The settlement curve steepens with a decrease in slope angle (see Fig. 8a–c). This indicates that settlement varies directly with slope angle and slopes accordingly need to be stabilized. On comparing settlements of URS 90, URS 80, and URS 70 with GRS 90, GRS 80, and GRS 70, respectively, (see Fig. 8), it can be clearly drawn out that geocell stabilized slopes relatively undergone less settlement.

The maximum normalized settlement for URS 90 was found to be 12.8% while for GRS 90, it was found to be 10.57% which means that 17.42% reduction in settlement values has occurred. A similar trend of reduction in settlement values for GRS 80 and GRS 70, i.e., 15.58 and 15.65%, respectively, was observed. Hence, GRS proved to be relatively more effective for $\theta = 90^\circ$. The reductions in settlement values can be attributed to geocells which resist mobilization of soil mass and arrest propagation of soil slip failure arc (see Figs. 5 and 6).

6 Summary and Conclusions

A series of model tests on unstabilized and geocell stabilized slopes were performed, to examine the behavior in terms of surcharge carrying capacity, lateral deformations, and slope settlement. Stone quarry dust was used as infill and backfill material, and locally available waste HDPE intravenous bottles were used to prepare geocells for the proposed geocellular retention system (GRS). Total six model slopes, i.e., three unstabilized and three geocell stabilized were built and tested for evaluating performance improvements. Following are the major conclusions drawn out from the present study:

1. For all six models, normalized lateral deformation of slopes (δ/H) % increased with increasing surcharge pressure (Q) until failure occurred. The (δ/H) % increased with increasing normalized height of slope (Y/H), indicating that the maximum lateral deformation of slope occurred at the crest (top) layers. This substantiates that failure mainly occurred in tilting mode.
2. The reduction in normalized lateral deformation (δ/H) % for the geocell stabilized slopes (GRS 90, GRS 80, and GRS 70) was about 17.89, 14.73, and 13.93%, respectively, relative to corresponding unstabilized slopes (URS 90, URS 80, and URS 70).
3. The reduction in normalized settlement (h/B) % for the geocell stabilized slopes was found to be 17.42, 15.58, and 15.65% respective to unstabilized slopes.
4. The peak surcharge carrying capacity of geocell stabilized slopes was found to be improved by 24, 17.14, and 15.01%, respectively, over corresponding unstabilized slopes.
5. Slope with 90° facing angle was most benefitted with the provision of GRS as maximum relative improvement in load-carrying capacity, lateral deformation, and settlement was observed.

The above results obtained for the present study are promising and preliminary support the proposed idea of stabilizing roadway slopes in hilly regions using waste HDPE intravenous fluid bottle-derived geocells. However, more detailed investigations on different loading and geometric conditions can be further explored.

Author Contribution The authors confirm contribution to the paper as follows: data collection and analysis: First Author; compilation and comparison of results: Second Author; analysis and interpretation of results: Third Author; draft manuscript preparation: First Author and Third Author. All authors have reviewed the results and approved the final version of the manuscript.

References

1. ASTM D4595–09 (2009) Standard test method for tensile properties of geotextiles by wide width strip method, Annual Book, ASTM Standards, ASTM Intl., W. Conshohocken, PA
2. Bathurst R, Karpurapu R (1993) Large scale tri-axial compression testing of geocell reinforced granular soils. Geotech Test J 16(3):296–303

3. Bathurst R, Nernheim A (1998) Influence of reinforcement stiffness and compaction on the performance of four geo-synthetic-reinforced soil walls. *Geo-synthetics International* 16(1):43–49
4. Boushehrian J (2011) Modeling of the cyclic behavior of shallow foundations resting on geomesh and grid-anchor reinforced sand. *Geotextiles and Geo-membranes* 29(3):242–248. <https://doi.org/10.1016/j.geotextmem.2010.11.008>
5. Bush D, Jenner C, Bassett R (1990) The design and construction of geocell foundation mattress supporting embankments over soft ground. *Geotext Geomembr* 9(1):83–98
6. Carter G, Dixon J (1995) Oriented polymer grid reinforcement. *Constr Build Mater* 9(6):389–401
7. Chen R, Chiu Y (2008) Model tests of geocell retaining structures. *Geo-textile and Geo-membrane* 26(1):56–70
8. Dash S, Krishnaswamy N, Rajagopal K (2001) Bearing capacity of strip footings supported on geocell-reinforced sand. *Geotext Geomembr* 19(4):235–256
9. Dash S, Rajagopal K, Krishnaswamy N (2004) Performance of different geosynthetic materials in sand foundations. *Geosynth Int* 11(1):35–42
10. Indian Standard 2720 (1985) Specification for Testing of Soil, Specific Gravity (Part 3 Section 2 1980); Grain Size Analysis (Part 4 1985); Liquid and Plastic Limits (Part 5 1985); Modified Proctor Test (Part 8 1983); Direct Shear Test (Part 13 1986), Bur. of Indian Stds., New Delhi
11. Ipsita S, Malik J, Arora N (2016) Material consumption patterns in India—a baseline study of the automotive and construction sector. *Deutsche Gesellschaft für Internationale Zusammenarbeit (GIZ) GmbH, Bonn and Eschborn, New Delhi*
12. Jayamohan J (2016) Influence of properties of Infill material on behavior of geocells. In: Indian geotechnical conference, IIT Madras, Chennai, India
13. Koerner R, Soong T (2001) Geo-synthetic reinforced segmental retaining walls. *Geotextiles and Geo-membranes* 19:359–386
14. Lakhani R, Rajesh K, Tomar P (2014) Utilization of stone waste in the development of value-added products—a state of the art review. *J Eng Sci Technol Rev* 7(3):180–187
15. O'Rourke Jones T (1990) Overview of earth retention systems: 1970–1990. In: Lambe PC, Hansen LA (eds) *Design and performance of earth retaining structures*, ASCE Geotechnical Special Publication No. 25, Amer. Society of Civil Engineers, pp 22–51
16. Pinto M, Cousens T (1999) Modelling a geotextile-reinforced, brick-faced soil retaining wall. *Geosynthetics Int* 6(5):417–447
17. Radha K, Kalaivani K, Lavanya R (2009) A case study of biomedical waste management in hospitals. *Global J Health Sci* 1:82–88
18. Rajagopal K, Krishnaswamy N, Madhavi Latha G (1999) Behavior of sand confined with single and multiple geocells. *Geo-textile and Geo-membrane* 17:171–181
19. Rea C, Mitchell K (1978) Sand reinforcement using paper grid cells. In: *Proceedings symposium on earth reinforcement ASCE annual convention, Pittsburgh, PA*, pp 644–663
20. Singh A, Agarwal A (2014) Evaluation of bio-medical waste management practices in a tertiary care hospital of Rohilkhand region in Uttar Pradesh, India. *Int J Med Sci Public Health* 3(10):1187
21. Tafreshi S, Dawson R (2012) A comparison of static and cyclic loading responses of foundations on geocell-reinforced sand. *Geo-textiles Geo-membranes* 32:55–68. <https://doi.org/10.1016/j.geotextmem.2011.12.003>
22. *The World Health Report (2005) make every mother and child count*, WHO Press, ISBN 924 156290 0 (NLM Classification: WA 540.1) ISSN 1020–3311 World Health Organization, 20 Avenue Appia, 1211 Geneva 27, Switzerland

Physico-Chemical and Mechanical Characterization of Ferrochrome Slag Aggregates for Utilization as a Road Material



Narala Gangadhara Reddy  and B. Hanumantha Rao

Abstract Scarcity of quality conventional materials and jeopardized environment are the prime factors that have been compelling toward the progression of alternate materials to sustain the ever-increasing infrastructure development. The use of locally available industrial wastes as a substitute for natural construction materials can alleviate the demand for such natural materials consumption. In this paper, efforts are made to characterize ferrochrome slag aggregates (FeCr) for assessing its suitability as a replacement to natural aggregates and propose relevant applications linking with characteristics. Mechanical and geoenvironmental properties are established using conventional testing methods as well as advanced macro-level characterization techniques in order to assess the environmental soundness of ferrochrome aggregates. The results in compliance with the relevant road standards demonstrate that the ferrochrome aggregates possess superior properties, rendering them as useful resource materials. Overall, the results highlight that ferrochrome aggregates are environmentally safe to be used as an alternative to natural aggregates, in particular, in road applications.

Keywords Ferrochrome aggregates · Waste utilization · Sustainability · Strength and testing of materials

1 Introduction

Infrastructure projects consume a wide variety of materials. Of late, the use of conventional natural materials became exhaustive, prompting not only increasing the impact on the environment but also causing depletion of quality resource materials [1–3]. In order to overcome these negative aspects, there is a need to imbibe waste or by-product or locally available materials as an alternative to conventional materials

N. G. Reddy (✉) · B. H. Rao (✉)
School of Infrastructure, IIT Bhubaneswar, Arugul, Jatni, Odisha 752050, India
e-mail: gn11@iitbbs.ac.in

B. H. Rao
e-mail: bhrao@iitbbs.ac.in

to keep maintaining the face of sustainable infrastructure development. In India, the vast network of existing industries spread across the length and the breadth and many more to set up in the near future is certainly going to generate millions of tons of a variety of wastes and by-products [1]. Consequently, it is inevitable to minimize their physical presence by appropriately consuming in civil engineering applications and infrastructure projects [2, 4].

Among many industrial wastes types, ferrochrome slag is one of the wastes. The ferrochrome is extracted during the smelting process called sub-merged arc furnace at an elevated temperature of around 1200 °C [5, 6]. After the extraction of FeCr from the ore, hot molten is air-cooled under ambient condition. Over time, the molten slag forms different sizes and shape of aggregates. For the generation of ferrochrome of one metric ton, chromite ore of 2.5–2.6 metric ton is consumed. It is evident that the production of waste slag is more than that of FeCr. The air-cooled slag transforms into aggregates of different size and shape depending upon prevailing cooling process [7, 8].

Across the globe, India is one of the major nations of producing FeCr, just after South Africa and Kazakhstan. Globally, FeCr by-product generation is estimated to be around 12 to 16 million tons per year [6, 9]. The majority of FeCr by-product is not utilized in a systematic way and is currently being stored in impoundments or dumped indiscriminately or filled in low-lying areas without providing an appropriate liner system [9]. Storage of FeCr slag without any precautions occupies not only huge land but also causes environmental problems, such as leaching of hazardous elements like Cr (VI) that prompts to contamination of soil and groundwater [5, 7, 10, 11].

Limited efforts [5, 6, 10] are devoted to comprehend the use of fine and coarse FeCr waste as chief source material for making of concrete in combination with other materials. Yilmaz and Karaşahin [11] used FeCr slag as a road base material after stabilizing with a cement content of 2–10%. Yilmaz and Karasahin [12] assessed the suitability of FeCr slag as a granular base material for flexible pavements and reported better mechanical properties exhibited slag amended material. In similar lines, Niemela and Kauppi [13] have reported that the FeCr slags having glassy and crystalline structure are chemically stable. In similarity, Das [14] reported that the mineralogical composition of FeCr slag is amorphous glassy phase with composition of spinels, forsterite, and olivine, belonging to the family of Fe, Mg, Cr, Al, silicates, and mineral metal alloy components [8]. As such, the above studies demonstrate that the properties of FeCr aggregates are superior to naturally available materials.

Panda et al. [5] reported that FeCr aggregates possess harmful metals like chromium as CrO_2 and are likely get released as hazardous chromium into the ecosystem and thus restrict its use and pose storage-related hazards. Even though the material has desirable properties, its use is constrained due to leaching of chromium. Chromium exists mainly in oxidation state of hexavalent and trivalent form (i.e., Cr (VI) and Cr (III)). As such, Cr (III) is less leachable and has the least detrimental effect. However, Cr (VI) has a high mobility and toxic in nature under most of the environmental circumstances. As per Yilmaz and Karaşahin [11] based on the leaching tests, it is only the Cr present as a major heavy element in FeCr aggregates, but its concentration is reported well within the limits of USEPA. Niemela and

Kauppi [13] performed leaching studies on FeCr slag collected from Finland and observed that the metal leachates are satisfying limits set by various environmental protection agencies.

Available literature shows very limited studies on the use of FeCr aggregates as an alternate material, but limited available data on basic properties suggests that FeCr aggregates could emerge as an alternative to natural aggregates [15]. In the present study, attempts are made to assess the FeCr slag aggregates as an alternative material for natural aggregates and their suitability in roads and other civil engineering applications. The scope of the work is to characterize FeCr aggregates for physical, engineering, chemical, and leachability properties, the analysis of which greatly aids in postulating potential application schemes. In addition, efforts have also been devoted to comparing these properties with that of natural aggregates and standard code provisions.

2 Materials and Methods

2.1 Materials

FeCr slag aggregates used in the present study are collected from Nava Bharat Ferro Alloy Plant of Dhenkanal, Odisha, India. FeCr aggregates are collected from the aggregate's storage area and are produced by the air-cooled process.

2.2 Tests for Physical and Strength Properties

Granular material used for pavements should be strong enough to resist crushing under heavy loads; therefore, the aggregate crushing test is performed in accordance with IS: 2386 (Part-4) [16]. Due to the movements of traffic, road stones will be subjected to wearing; therefore, Los Angeles Abrasion (LAA) test is conducted to test the hardness or resistance to abrasion of the coarse aggregates [16]. When the aggregates are subjected to repeated impact or pounding action, they break into smaller pieces, and thus, the aggregate should be strong enough to resist impact. Aggregate impact test as per IS: 2386 (Part-4) [16] is conducted to measure the resistance of aggregate to impact. Soundness test as per IS:2386 [17] using crystalline magnesium sulfate ($MgSO_4 \cdot 7H_2O$) is conducted to study the resistance of aggregates to weathering action (durability) for five cycles. Shape tests carried out as per IS:2386 (Part-1) [18] to check the presence of flaky and elongated aggregates which is one of the desired values in the properties of aggregate. Specific gravity and water absorption tests are conducted as per IS 2386 (Part-3) [19] to measure the strength or quality of aggregates and to study the water absorption of the aggregates, which reveals their porous nature, respectively. Aggregates should well adhere to the bitumen when they

are being coated with the bitumen. To verify this, stripping test as per IS: 6241–2003 [20] is conducted in the presence of water for its suitability as a resource material in the bituminous pavement. California bearing ratio (CBR) value is used as the basis for the design of sub-base or base layers; hence, the test is carried out as per ASTM D1883 [21] specifications.

2.3 Chemical, Mineralogical, and Leaching Studies

To understand the micro-properties of FeCr slag aggregates, morphological and mineralogical analysis are carried out to decipher some of the macro-properties. The morphological studies are carried out with the help of scanning electron microscope, SEM, (Device: FEI Quanta 250) on the powdered samples. Further, percentage of elemental compositions of a sample is determined using energy-dispersive X-ray spectroscopy, EDX, which is fitted to SEM instrument. X-ray diffraction (XRD) analysis is conducted on a powder sample with the help of Bruker D8 Advance XRD instrument using a copper target.

pH values of FeCr slag aggregates are measured with the help of a benchtop Systronic 335 digital pH meter (India make), corresponding to liquid to solid ratio (L/S) of 2.5, as per the IS 2720 (Part—26) [22]. Besides, electric conductivity is also measured at the same L/S ratio. Toxicity characteristic leaching procedure (TCLP) test is carried out as per the USEPA 1311 [23]. For this purpose, the sample is crushed, and passing sieve opening size of < 2 mm is used. For leaching purpose, extraction fluid is prepared by mixing 5.7 ml of concentrated glacial acetic acid, and 64.3 ml of 1 N NaOH to one liter distilled water, and to this, FeCr slag sample is added. The mixer is agitated for a period of 18 h and then filtered through 0.2 μm filter paper. Additionally, batch leaching experiments have been carried out as per ASTM D 3987 [24] by adopting to water shake extraction procedure at a liquid to solid (L/S) ratio of 10, 20, and 50. Then, all the leachate (both TCLP and water shake extraction) samples are analyzed for determining the concentrations of metal elements such as Cu, Cd, Co, Zn, As, Cr, Hg, Ag, and Pb with the help of an atomic absorption spectroscopy (AAS) analyzer (iCE 3000 series, Thermo Fisher Scientific, US).

3 Results

3.1 Physical and Strength Properties of FeCr Aggregates

Figure 1 shows the gradation curve of FeCr aggregates, and the value of C_u and C_c is calculated from Fig. 1 as 1.64 and 1.02, respectively. The particle size characteristics show that FeCr aggregates contain little to nil fines. Based on the unified soil classification system (USCS), FeCr slag aggregates can be classified as poorly graded gravel

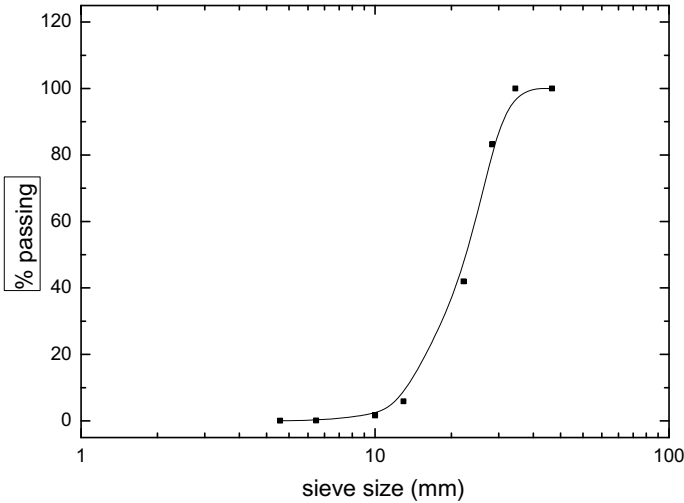


Fig. 1 Gradation curve of FeCr aggregates used in the study

(GP), and as per ASSHTO soil classification, it falls under the group category of A-1. Table 1 presents the summary of test results obtained from a series of experimental investigations, along with the relevant test method followed for testing purpose.

3.2 *Chemical, Morphological, and Mineralogical Properties of FeCr Aggregates*

Figure 2 shows the images of FeCr slag aggregates recorded using SEM. It is obvious from the images that particles are irregular in shape and sizes. EDS analysis conducted on the same material revealed the presence of Mg, Al, Si, and Fe as major elements with glass matrix. Other elements found in the aggregates are as follows: Cr, K, and Ca, apart from a few other minor elements, whereas the chemical analysis shows a high percentage of SiO_2 (41.55) and Al_2O_3 (21.82) followed by MgO (10.52), Cr_2O_3 (9.12), TiO_2 (4.57), CaO (4.14), K_2O (4.04), and a small percentage of Fe_2O_3 (1.65). Figure 3 shows the diffraction pattern of FeCr aggregates obtained by XRD analysis. From the interpretations of diffractograms, Quartz (SiO_4), Forsterite (Mg_2SiO_4), Spinel (MgAl_2O_4), and Oviline are identified as dominant mineral components. The other chemical analysis includes pH and electrical conductivity, which are measured as 8.24 and 179 $\mu\text{s}/\text{cm}$. From the batch leaching analysis (TCLP and water shake extraction) tests, total metal concentrations (Cu, Cd, Co, Zn, As, Cr, Hg, Ag, and Pb) are determined, and the results obtained are summarized in Table 2.

Table 1 Physical and strength properties of FeCr slag and natural aggregates

Type of test	FeCr slag aggregates	Natural aggregates [5, 6]	Standard MoRTH/ASSHTO specifications	Test method
Crushing test	20%	17.66–25.10%	< 40%	IS:2386 (part 4)-1963
Los Angeles abrasion test	15.4%	14–25.81%	< 40%	IS:2386 (part 5)-1963
Aggregate impact test	17.1%	13.87–23.2%	< 30%	IS:2386 (part 4)-1963
Soundness test (magnesium sulfate)	1.2%	2–10%	< 18%	IS:2386 (part 5)-1963
Combined flakiness and elongation	28.5%	10–25%	< 30%	IS:2386 (part 1)-1963
California bearing ratio (CBR)	92%	80–140%	> 25–30 for granular sub-base > 70–80% for granular base material	ASTM D1883-07
Specific gravity	3.15	2.72 – 2.93	2.5 or greater	IS:2386 (part 3)-1963
Water absorption test	0.5%	0.32–1.67	< 2.0%	IS:2386 (part 3)-1963
Stripping	1.5%	2–10%	< 5%	IS: 6241–1971
pH	8.24	6–9	> 2 and < 12.5 (RCRA for corrosivity)	IS 2720 - (Part - 26) - 1987
Electric conductivity	179 μ s/cm	NA	NA	

⁵Panda et al. [5]; ⁹Acharya and Patro [6]

4 Discussion

4.1 Physical and Strength Properties of FeCr Aggregates

As per the MoRTH and IDOT guidelines for selection of granular materials for a base course, FeCr aggregates are found not meeting the set criterion because of their classification under poorly graded gravel (GP) category. However, researchers worked on other recycled aggregates such as construction and demolition (C&D) waste believe that crusher openings sizes of FeCr aggregates can be adjusted to get the desired size so that the modified aggregates meet the criteria set by the above standards without affecting its strength and performance criteria [25]. It is also worth

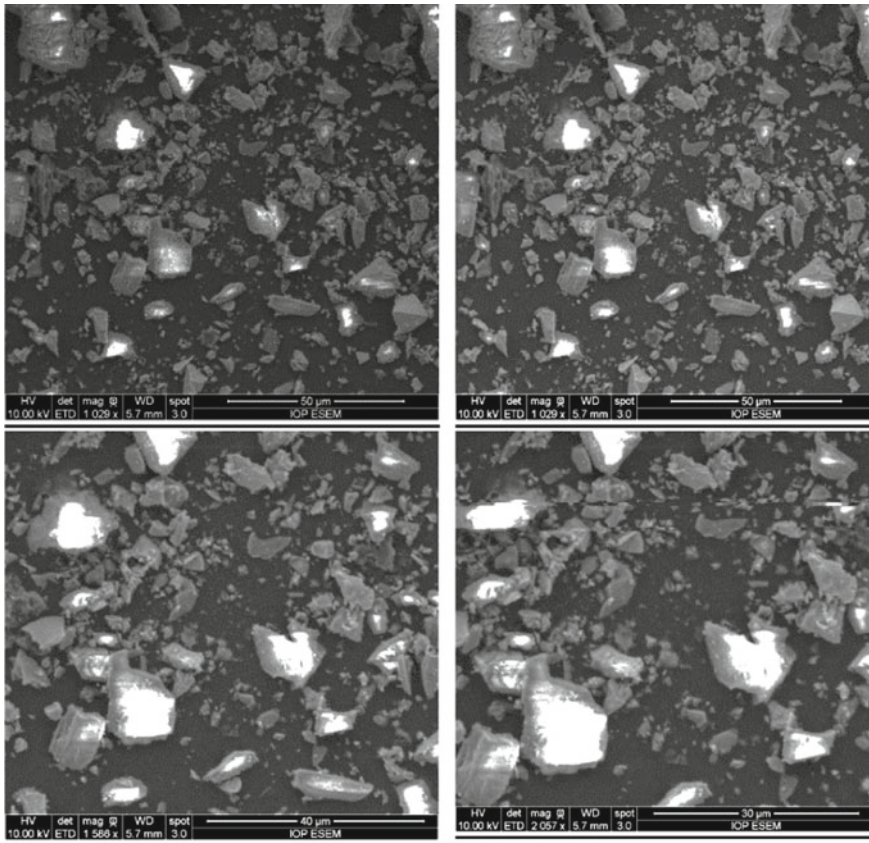


Fig. 2 Photomicrographs of ferrochrome aggregates recorded by SEM at different magnification factors

mentioning here that as per ASSHTO soil classification (A–1), FeCr aggregates fall under the category of excellent to good rating as subgrade material.

The crushing strength of FeCr used in the study is found to be 20.06%. Incidentally, the results of Panda et al. [5], who reported crushing strength in the range from 17.6% to 25.1%, well corroborate with the present values. It is interesting to note that the values of crushing strength are quite lesser than permissible limits stipulated for natural aggregates. The abrasion value is measured as 15.38%, which found to match extremely well with FeCr slag aggregates belonging to other sources that are 19.2% and 18.58% by Panda et al. [5] and Sahu et al. [9]. The measured values of abrasion are well below those normally reported for natural aggregates, confirming that FeCr slag aggregates are resistant to abrasion or even better than the natural aggregates. Ferrochrome slag aggregates can be used in granular layers, as these aggregates are derived from the waste, as these materials are freely available and are economical as compared to those of natural aggregates [9]. FeCr slag when air-cooled results

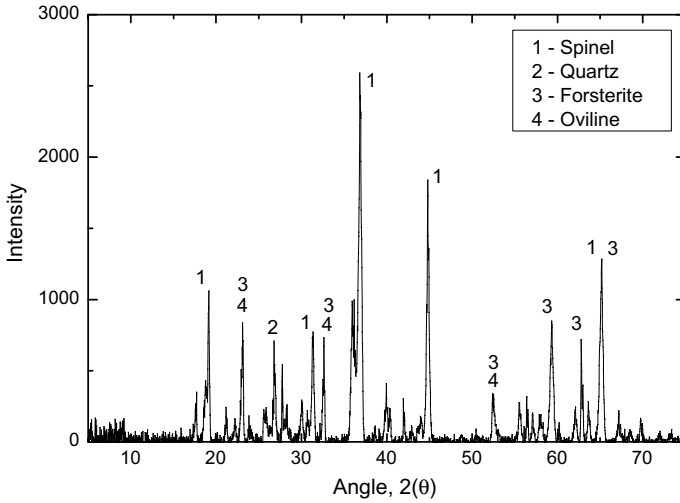


Fig. 3 XRD patterns of ferrochrome slag aggregates

Table 2 Results of TCLP and shake extraction with water of FeCr slag aggregates

Analyte	Concentration based on TCLP		Shake extraction with water (ASTM D3987)		
	Result of FeCr Aggregates (ppm)	Limits (ppm)	L/S-10 (ppm)	L/S-20 (ppm)	L/S-50 (ppm)
Chromium (Cr)	2.3209	5	0.1880	0.2818	0.4690
Arsenic (As)	0.1051	5	0.0033	0.0046	0.0054
Mercury (Hg)	0.0106	0.2	0.002	0.0038	0.0052
Copper (Cu)	BDL	–	BDL	BDL	BDL
Cobalt (Co)	0.2562	–	0.2576	0.1533	0.2394
Silver (Ag)	0.0207	5	0.0061	0.0083	0.0151
Lead (Pb)	1.4739	5	0.8127	0.9402	2.7644
Cadmium (Cd)	0.0526	1	0.117	0.1594	0.1456
Zinc (Zn)	0.592	5	0.0289	0.1739	0.6928

BDL = Below detection limit.

in densely structured and stable crystalline material, the process of which beneficial in terms of imparting better mechanical properties alike that of natural aggregates materials [5]. On the other hand, surface features of aggregates are characterized for rough and porous nature, which are similar to natural aggregates and advantageous as these offer good adhesion and abrasion resistance [12, 26]. These characteristics also bear a practical relevance when selected for the granular layer in pavements. The Los Angeles abrasion (LAA) value is determined as 15.4% for FeCr, which is less as compared with C&D waste materials for which it is in the range of 21–36% [27]. Thus, it can be highlighted that FeCr is superior to C&D waste material. It can also be noted that LAA value is well below the maximum value specified by FHWA [28] guidelines, indicating that the FeCr aggregates are durable.

Aggregate impact value (AIV) of aggregates is found to be 17.1%, and it is much lesser than that of natural aggregates (refer to Table 1). Soundness test (1.2%) shows that FeCr slag aggregates are durable and are resistant to weathering phenomenon. Water absorption value of FeCr slag aggregates is lower than that of natural aggregate, which is due to less porous of FeCr aggregates. The specific gravity is measured as 3.15, which is slightly higher than the natural aggregates, indicating that the aggregates will exhibit better strength than the natural aggregates [5, 9, 12]. The bitumen stripping test conducted on FeCr aggregates shows a value of 1.5%, which is well below the specified stripping limit of < 5%.

Based on the interpretation of obtained results and discussion made herein, it is easy to understand that FeCr aggregates meet the physical and strength requirements specified by different standards, denoting that these aggregates are acceptable to be used in bituminous road construction effectively.

California Bearing Ratio

CBR value is generally determined to evaluate the potential of FeCr aggregates to use as a resource material in sub-base and base courses. The observed CBR value of FeCr is 92%, which is higher than the minimum value prescribed for sub-base and base material (i.e., 30 and 80%) by all the standard codes such as IRC, AASHTO, and FHWA [29–31]. IRC 37–2018 [32] suggests a minimum CBR of 20% and 30% for traffic up to 2 Msa (million standard axles) and exceeding 2 Msa, respectively, for a granular material to be used as a sub-base material in flexible pavement. IRC: SP 20–2001 [31] considers a CBR of at least 15% for rural roads (less than 450 commercial vehicles per day). For granular materials, standards proposed a wide range of grading. However, liquid limit and plasticity index of materials passing through 425 μm sieve shall not be more than 25 and 6%, respectively, [30–32].

Recently, more emphasis is given to resilient modulus for assessing the seasonal variation and moisture movement of a material. Despite the inability of CBR for simulating the traffic load and varying stress state, a simple relation is suggested by IRC 37–2012 (which is lower than other international standards) as given below:

$$M_R(\text{MPa}) = 17.6 * (\text{CBR})^{0.64} \quad (1)$$

From the above equation, M_R value of FeCr aggregate is calculated as 317 MPa, which is well within the range advocated by AASHTO [30] for spring-thaw or winter-frozen conditions (i.e., 137–344 MPa). Based on the above observations, it is prudent to conclude that FeCr aggregates are the ideal material to select in sub-base or base courses of flexible pavements and rural roads. However, extensive studies are necessary for the estimation of M_R values for proper design with real-time stress state.

4.2 Chemical, Mineralogical, and Morphological Properties

XRD analysis shows that Forsterite, Spinel, Quartz, and Oviline are chief mineral components in the slag aggregates. All these mineral phases are mainly constituted with Si, Mg, and Al elements. Studies of Panda et al. [5], Kumar et al. [8], and Mahamaya and Das [33] reported similar mineralogical compositions of FeCr slag aggregates of other sources. However, a few researchers reported hematite as a major mineral component which might be due to the source and method of processing. Mg is a major chemical element after Si and Al in the aggregates. Many researchers [34, 35] used MgO or MgCl₂ as a sustainable and as an alternative cementitious material for stabilization of soils. Kilau and Shah [36] have reported the presence of MgO in the slag prevents the dissolution of chromium under acid medium, and hence, there is less scope for the release of Cr(VI) into the leachate. Therefore, it can be concluded that MgO (about 10%) content in FeCr aggregates can be advantageous [34, 35]. The studies of Petrounias et al. [37] are worth mentioned here that the natural aggregates that had quartz, as a primary mineral shows better physico-mechanical properties for construction purpose.

Higher electrical conductivity (179 $\mu\text{s}/\text{cm}$) value shows the occurrence of the high amount of dissolved oxides such as magnesium, iron, and aluminum oxides. The measured pH of the FeCr slag is found to be 8.24, which is slightly alkaline. But, IRC: SP 20 [31] guidelines clearly say that waste material having pH less than 8.5 can be used as an alternative to that of natural materials for construction purposes. Moreover, RCRA guidelines [38] also clearly show that FeCr is a non-corrosive. Thus, it could be concluded that FeCr slag aggregates can be used as resource material in civil engineering applications.

4.3 Leaching Characteristics of FeCr Slag Aggregates

Batch leaching analysis (TCLP and water shake extraction) for various metals present in the FeCr aggregates was carried out as per guidelines laid in the USEPA 1311 and ASTM D3897. Table 2 shows the total metal concentrations measured for FeCr slag. The selection of elements measured is made based on the literature (Cu, Cd, Co, Zn, As, Cr, Hg, Ag, and Pb). From Table 2, it is seen that a few metal concentrations are

minimal and, in fact, below the detection levels. Among others, the concentrations of Cr and Zn are significantly high. Incidentally, the concentration levels of almost all the elements are well below the limits of USEPA. Similar results were reported by Yilmaz and Karasahin [12], however, as a function of pH and after treating the aggregates with seawater. The lesser concentrations reveal that FeCr aggregates are chemically very stable [13, 26].

Nevertheless, studies of Panda et al. [5] report that residual chromium in the ferrochrome slag mostly remained in immobilized form as Cr(III), which is highly stable and least toxic. The high stability is attributed to spinel mineral phases such as chromite or magnesium alumino-silicates. Lind et al. [10] investigated the environmental implication of FeCr slag in road construction projects subject to extreme conditions of biological activity and acid rain. The study showed a relatively lesser extent of chromium (VI) leaching from slag into aqueous nitric acid solution (one of the acid rain components). As the FeCr is rich with Fe–Mg–Cr–Al-spinels, forsterite, Mg–Al–Si makes the FeCr aggregates which are chemically very stable. However, this depends on the source and extraction of ferroalloys [9].

5 Concluding Remarks

In the present study, extensive characterization studies including geotechnical, geochemical, and geoenvironmental have been conducted on ferrochrome slag aggregates in order to comprehend its behavior. The outcomes of the study are presented as follows:

1. The various strength results portray a fact that FeCr aggregates have the potential to be considered as a construction material, especially in road applications, as they are meeting the technical acceptability proposed for the natural aggregates to be used for highways.
2. A significantly low stripping value vis-à-vis with the permissible limit as per FHWA and IRC guidelines demonstrate that FeCr aggregates are suitable in lower courses such as sub-base in flexible pavements as well as surface dressing material.
3. It has been noticed from the leaching studies that among many elements, only chromium concentration is high at 2.32 ppm, which is still within the permissible limit set by RCRA. Thus, proving that FeCr aggregates are environmental friendly and will not create remarkable ecological contamination.
4. Evidently, the physico-chemico-mechanical behavior of FeCr aggregates is found to resemble that of natural aggregates, proving that they can be used as a partial replacement to natural aggregates in making concrete.

References

1. Rajesh S, Rao BH, Sreedeeep S, Arnepalli DN (2015) Environmental geotechnology: an Indian perspective. *Environ Geotech* 2(6):336–348
2. Reddy NG, Rao BH, Reddy KR (2018) Biopolymer amendment for mitigating dispersive characteristics of red mud waste. *Geotech Lett* 8(3):201–207
3. Rao BH, Nongmaithem RS, Basuc D, Reddy NG (2020) Application of biopolymers for improving the strength characteristics of red mud waste. *Environ Geotech* 1–20
4. Reddy NG, Rao BH (2018) Characterization of settled particles of the red mud waste exposed to different aqueous environmental conditions. *Indian Geotech J* 48(3):405–419
5. Panda CR, Mishra KK, Panda KC, Nayak BD, Nayak BB (2013) Environmental and technical assessment of ferrochrome slag as concrete aggregate material. *Construct Build Mater Constr Build Mater* 49:262–271
6. Acharya PK, Patro SK (2016) Utilization of ferrochrome wastes such as ferrochrome ash and ferrochrome slag in concrete manufacturing. *Waste Manage Res* 34(8):764–774
7. Al-Jabri K, Shoukry H, Khalil IS, Nasir S, Hassan HF (2018) Reuse of waste ferrochrome slag in the production of mortar with improved thermal and mechanical performance. *J Mater Civil Eng* 30(8), 04018152:10
8. Mahamaya M, Das SK (2018) Characterization of ferrochrome slag as a controlled low-strength structural fill material. *Int J Geotech Eng* 1–10
9. Sahu N, Biswas A, Kapure GU (2016) A short review on utilization of ferrochromium slag. *Miner Process Extr Metall Rev* 37(4):211–219
10. Lind BB, Fallman AM, Larsson LB (2001) Environmental impacts of ferrochrome slag in road construction. *Waste Manage* 21:255–264
11. Yilmaz A, Karasahin M (2013) Compressive strength of cement-bound base layers containing ferrochromium slag. *Turk J Eng Environ Sci* 37:247–258
12. Yilmaz A, Karasahin M (2010) Mechanical properties of ferrochromium slag in granular layers of flexible pavements. *Mater Struct* 43:309–317
13. Niemela P, Kauppi M (2007) Production characteristics and use of ferrochromium slags. *Innovation in Ferro Alloy Industry, INFACON XI, New Delhi, India*, pp 171–179
14. Das BB (2014) Characterization of ferrochrome slag as an embankment and pavement material. *Master of Technology (Research), NIT Rourkela, India*
15. Sathwik S, Sanjith RJ, Sudhakar GN (2016) Development of high strength concrete using ferrochrome slag aggregate as replacement to coarse aggregate. *American J Eng Res (AJER)* 5:83–87
16. IS: 2366 (Part 4) (2002) Methods of test for aggregates for concrete, Part IV—Mechanical properties. Bureau of Indian Standards, New Delhi, India
17. IS: 2366 (Part 5) (2002) Methods of test for aggregates for concrete. Part V- Soundness. Bureau of Indian Standards, New Delhi, India
18. IS: 2366 (Part 1) (2002) Methods of test for aggregates for concrete. Part I—Particle size and shape. Bureau of Indian Standards, New Delhi, India
19. IS: 2366 (Part 3) (2002) Methods of test for aggregates for concrete. Part III- Specific gravity, density, voids, absorption and bulking. Bureau of Indian Standards, New Delhi, India
20. IS: 6241(2003) Determination of stripping value of aggregates standard. Bureau of Indian Standards, New Delhi, India
21. ASTM D1883 (2007) Standard test method for CBR (California Bearing Ratio) of laboratory-compacted soils. ASTM International, West Conshohocken, PA, USA
22. IS 2720–26 (2002) Method of test for soils, Part 26: Determination of pH value. Bureau of Indian Standards, New Delhi, India
23. USEPA 1311 (1992) Toxicity characteristic leaching procedure, United States Environmental Protection Agency, Washington, DC
24. ASTM D 3987 (2012) Standard practice for shake extraction of solid waste with water. ASTM International, West Conshohocken, PA, USA

25. Kolay PK, Akentuna M (2014) Characterization and utilization of recycled concrete aggregate from Illinois as a construction material. In: *Geo-Congress 2014: geo-characterization and modeling for sustainability*, GSP 234, ASCE, pp 3561–3570
26. Zelic J (2005) Properties of concrete pavement prepared with ferrochromium slag as concrete aggregate. *Cem Concr Res* 35:2340–2349
27. Arulrajah A, Piratheepan J, Disfani MM, Bo MW (2013) Geotechnical and geoenvironmental properties of recycled construction and demolition materials in pavement subbase applications. *J Mater Civ Eng* 25(8):1077–1088
28. Yilmaz M, Kok BV (2009) Effect of ferrochromium slag with neat and polymer modified binders in hot bituminous mix. *Indian J Eng Mater Sci* 16:310–318
29. FHWA (1998) User guidelines for waste and by-product materials in pavement construction, FHWA-RD-97-148, U.S. Dept. of Transportation, Washington, DC
30. AASHTO (1993) Design of pavement structures. American Association of State Highway and Transportation Officials, Washington, DC
31. IRC SP 20 (2001) Rural roads manual. Indian Road Congress, New Delhi, India
32. IRC 37 (2018) Guidelines for design of flexible pavements. Indian Road Congress, New Delhi, India
33. Kumar PH, Srivastava A, Kumar V, Majhi MR, Singh VK (2014) Implementation of industrial waste ferrochrome slag in conventional and low cement castables: effect of micro silica addition. *J Asian Ceramic Soc* 2:169–175
34. Cai G, Liu S (2017) Compaction and mechanical characteristics and stabilization mechanism of carbonated reactive MgO-stabilized silt. *KSCE J Civ Eng* 21(7):2641–2654
35. Yi YL, Liska M, Unluer C, Al-Tabbaa A (2013) Carbonating magnesia for soil stabilization. *Canadian Geotech J* 50(8):899–905
36. Kilau HW, Shah ID (1983) Chromium-bearing waste slag: evaluation of leachability when exposed to simulated acid precipitation. In: *Hazardous and industrial waste management and testing: 3rd symposium*, Philadelphia
37. Petrounias P, Giannakopoulou PP, Rogkala A, Stamatis PM, Lampropoulou P, Tsikouras B, Hatzipanagiotou K (2018) The effect of petrographic characteristics and physico-mechanical properties of aggregates on the quality of concrete. *Minerals* 8:577
38. RCRA (2001) Characteristics of hazardous waste, Resource Conservation and Recovery Act (RCRA) (40 CFR 261.22)

Durability of Stabilized Quarry By-Products in Base and Subbase Applications



Issam I. A. Qamhia, Erol Tutumluer, Hasan Ozer, Heather Shoup, and Andrew Stolba

Abstract This paper presents findings from a research project conducted at the Illinois Center for Transportation (ICT) to study durability aspects of chemically stabilized Quarry By-product (QB) materials. The studied applications include chemically stabilized QB fines or blends of QB with coarse-recycled aggregates in base and subbase layers. The material combinations studied were evaluated with Accelerated Pavement Testing (APT) by constructing and loading full-scale pavement test sections utilizing stabilized QB mixes in base and subbase layers. All evaluated QB pavement applications showed satisfactory pavement performance trends, i.e., low subgrade stress levels and low surface rutting accumulation compared to a conventional pavement section used as control. QB samples were extracted from seven field sections constructed using cement and Class C fly ash stabilizers for different material combinations and were subjected to freeze–thaw and wet-dry cycles in a controlled laboratory environment. Prior to conducting the durability study, the field-extracted samples were exposed to multiple cycles of freezing/thawing and wetting/drying over the course of three years. Samples were evaluated by AASHTO T 135 and AASHTO T 136 for wet-dry and freeze–thaw durability tests, respectively. The results of durability testing indicated that cement-stabilized QB materials benefited from the long-term curing in the field, while fly ash-stabilized QB materials were less durable after exposure to multiple freeze–thaw and wet-dry cycles in the field. Field samples compacted at or near their maximum dry densities consistently showed better performance trends for durability. Further, samples made with dolomitic QB fines benefited from having higher magnesium oxide content and exhibited better durability performance than those of limestone QB materials having higher calcium oxide content. This was linked to more cementation observed in the dolomitic fines after being exposed to freeze–thaw cycles over three winters in the field.

I. I. A. Qamhia · E. Tutumluer (✉)
University of Illinois At Urbana-Champaign, 205 N Mathews Ave, Urbana, IL 61801, USA
e-mail: tutumlue@illinois.edu

H. Ozer
Arizona State University, 660 S College Ave, Tempe, AZ 85281, USA

H. Shoup · A. Stolba
Illinois Department of Transportation, 126 E. Ash St, Springfield, IL 62764, USA

Keywords Quarry by-product · Quarry fines · Durability · Freeze–thaw · Wet-dry · Chemical stabilization · Aggregates · Recycled materials · Sustainability

1 Introduction

1.1 Background

The Illinois Department of Transportation (IDOT) and the Illinois Center for Transportation (ICT) have been working in collaboration since 2012 to carefully select and evaluate sustainable applications of Quarry By-product (QB) materials in pavements. These QB fines are defined as sand-sized particles, i.e., passing the No. 4 sieve size or finer than 4.75 mm with a small silt and clay fraction, that accumulate at the aggregate production sites due to operations such as blasting, crushing, screening, and washing. The annual QB production was found to exceed 861,825 tons (950,000 short tons) in Illinois; according to a questionnaire responded to by owners of 20 largest crushed stone quarries in Illinois [1]. Such large quantities of excess QB accumulating at quarry sites not only to pose financial challenges to stakeholders but also interfere with quarry operations. Hence, to develop sustainable QB applications, ICT conducted two major studies and evaluated both in the laboratory and in the field expected performance trends of QB fines in unbound and chemically stabilized pavement base and subbase layers [1, 2].

In the first project, the ICT R27-125, a laboratory study was conducted to characterize the engineering properties of QB fines produced from different crushing stages. QB materials were collected from four quarries in Illinois [1, 3]. Index tests were conducted for determining grain size distribution, morphological shape properties, and mineralogy for each sample and crushing stage. Further, Unconfined Compressive Strength (UCS) tests were conducted for the virgin QB fines and for QB stabilized with 2% Type I Portland cement or 10% Class C fly ash. The study concluded that QB collected from different sources and crushing stages had different index properties such as gradation, shape, texture and angularity, and mineralogy. Virgin QB samples had a very low compressive strength (less than 76 kPa or 11 psi), while the UCS of the stabilized QB samples was 10–30 times higher, showing a significant improvement in strength properties.

In the second project, the field performance trends of some of the QB sources considered in the previous study were investigated. Sixteen different full-scale pavement test sections were constructed. Out of these sixteen sections, eight studied unbound applications for QB in construction platforms as aggregate subgrade improvements for flexible pavements. The other eight sections comprised a control section and seven flexible pavement sections with a stabilized QB base or subbase. Chemically stabilized QB sections had either 3% cement or 10% Class C fly ash as the chemical stabilizer. Both QB and blends of QB with recycled coarse aggregates in a 7:3 blending ratio were studied. The typical rutting performance trends of the test sections were evaluated with accelerated pavement testing (APT), Falling

weight deflectometer (FWD) tests, dynamic cone penetrometer (DCP) profiling, and trenching. APT and forensic analyses results concluded that sections with stabilized QB showed improved rutting performances over the control section. Cement-stabilized QB sections, particularly those with QB blended with course recycled aggregates, accumulated lower surface rutting and significantly lower FWD deflections than fly ash-stabilized QB sections. The full suite of performance results can be found elsewhere [2, 4, 5].

One limitation of the field study was that the durability aspects of the evaluated QB applications were not fully investigated during the APT study. Durability aspects were indirectly studied since the constructed test sections were exposed to wet-dry weather conditions and to freeze–thaw cycles over three harsh IL winters [6, 7]. To perform a more systematic study in a controlled environment, samples were collected from the field sections and evaluated for wet-dry and freeze–thaw durability by AASHTO T 135 ‘Standard Method of Test for Wetting and Drying Test of Compacted Soil–Cement Mixtures’ and AASHTO T 136 ‘Standard Method of Test for Freezing and Thawing Tests of Compacted Soil–Cement Mixtures’ laboratory test procedures, respectively. This paper discusses the results and recommendations of this systematic durability study that utilized field samples with known performance trends.

1.2 Past Research Findings on QB Durability

To this end, only few past studies can be found in the literature that were focused on evaluating the durability of chemically stabilized QB fines under wet-dry and freeze–thaw conditions. Most of the previous work reported on the durability of QB or quarry dust in concrete applications as a sustainable replacement of sand or fine aggregates [8–10]. A study by Ilangovana et al. [8] reported that the durability of concrete specimens prepared with QB fines replacing natural sand was 10% higher than that with natural sand. Galetakis and Soutana [9] summarized several studies that concluded the chemical durability of concrete with QB which was higher than that of conventional concrete. Similar conclusions were made by Li et al. [10] for the freeze–thaw durability of concrete with limestone QB fines. Further, Amadi [11] reported a significant enhancement in the wet-dry durability of subgrade soils modified with QB and cement kiln dust. Similarly, Onyejekwe and Ghataora [12] found that QB materials stabilized with cement and a polymeric additive benefited from improved wet-dry durability when evaluated by immersion tests.

For the durability of QB as a base/subbase material, Eze-Uzomaka and Agbo [13] investigated the use of cement-stabilized laterite with quarry fines used as an additive for base course applications. The study defined a durability failure by means of a 20% loss in UCS after durability testing. In accordance, only cement contents exceeding 8% could result in a loss of UCS not exceeding 20%, and all samples stabilized with lower cement contents failed to meet the durability requirements [13]. Gurbuz [14] investigated the use of quarry fines to stabilize subgrade soils for subbase applications in pavements and concluded that subgrade soils stabilized with

marble QB fines could have satisfactory durability under freeze–thaw cycles. The samples prepared with marble QB fines exceeding 10% by weight in composition had a cumulative soil–cement loss of 5% or lower after 12 cycles of freeze–thaw testing [14]. Zhang et al. [15] concluded that stabilized quarry fines could have sufficient durability and strength requirements for use as structural layers in high-volume pavement applications, provided that they are well designed and sufficiently compacted to a proper relative density.

2 Evaluated Quarry By-Product Applications

2.1 Overview of Evaluated QB Applications

In total, seven bound applications of cement- or fly ash-stabilized aggregate QB mixtures were evaluated for durability by wet-dry and freeze–thaw laboratory testing. These applications are summarized in Table 1, where the sample names follow the nomenclature used to label the test sections. Note that QB2 and QB3 refer to fines obtained from two different sources to evaluate the effect of chemical composition on performance and durability. The test sections from which the durability samples were extracted and were constructed in the summer of 2015 and trafficked until summer 2018. The durability samples were extracted and tested in the spring of 2019. Thus, these samples were exposed to several seasonal weather effects in the field for approximately 43 months prior to conducting the durability testing, including several harsh winters and wet summers, i.e., a multitude of wet-dry and freeze–thaw cycles.

Table 1 Descriptions of durability samples extracted from field test sections

Sample name	Field application	Description
C2S1	Base material	A blend of 70% QB2 and 30% FRAP ⁺ , stabilized with 3% cement
C2S2	Base material	A blend of 70% QB2 and 30% FRCA ⁺⁺ , stabilized with 3% cement
C2S3	Base material	A blend of 70% QB2 and 30% FRAP, stabilized with 10% Class C fly ash
C2S4	Base material	QB2 stabilized with 3% cement
C3S1	Base material	QB3 stabilized with 3% cement
C3S2	Subbase material	QB2 stabilized with 3% cement
C3S3	Subbase material	QB2 stabilized with 10% Class C fly ash

+ FRAP = Fractionated Reclaimed Asphalt Pavements.

++ FRCA = Fractionated Recycled Concrete Aggregates.

2.2 Characterizations of Studied Materials

The grain size distributions of the four aggregate material blends, i.e., QB2, QB2 with FRAP, QB2 with FRCA, and QB3, which were used to prepare the seven studied mixes, are shown in Fig. 1a. Both QB2 and QB3 are relatively well-graded and have similar gradations and fines contents ranging between 12 and 13% fines passing the No. 200 (0.075 mm) sieve. The maximum dry densities (MDD) and optimum moisture contents (OMC) for all seven material combinations were determined from laboratory testing using the standard Proctor compaction effort as per ASTM D698 and were presented in Fig. 1b.

Table 2 presents the chemical composition of QB2 and QB3 materials determined by X-Ray diffraction (XRD) test. The values shown represent the average chemical compositions for QB fines collected from three crushing stages (primary, secondary, and tertiary). On average, QB2 has significantly higher magnesium oxide (MgO) content, i.e., higher percentage of dolomitic fines, than QB3. On the other hand, QB3 is primarily calcium oxide (CaO) in composition and comprises mostly limestone fines. By having higher MgO content, QB2 is expected to exhibit longer durations for chemical reactions and associated strength gain.

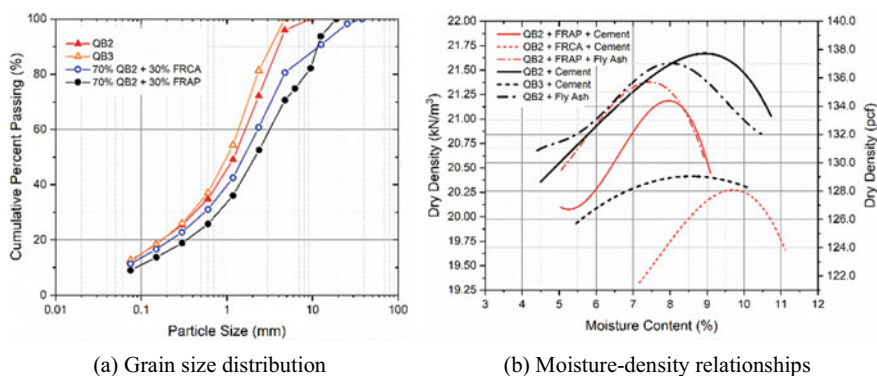


Fig. 1 Gradation curves and moisture-density relationships for the material combinations used in the durability study

Table 2 Chemical composition of QB2 and QB3 determined using XRF

QB material	Composition by weight (%)					
	CaO	MgO	SiO ₂	Al ₂ O ₃	Fe ₂ O ₃	K ₂ O
QB2 dolomite	51.2	34.8	10.7	1.2	0.9	0.6
QB3 limestone	67.2	10.2	17.4	2.9	1.0	0.7

2.3 Preparation of Durability Samples

Following the trenching of the pavement test sections after APT testing, it was realized that the stabilized QB materials could only be recovered as intact slab pieces that were large enough to extract laboratory samples for durability testing (see Fig. 2a). Ideally, durability testing samples required by AASHTO T 136 and AASHTO T 135 standard test procedures are cylindrical specimens with dimensions conforming to the size of the standard Proctor mold. Several attempts to extract intact cylindrical cores of the stabilized base/subbase layers by conventional and dry coring methods were not successful. Ultimately, large blocks (slabs) of intact stabilized QB base/subbase sections were extracted with a mini excavator.

Following the extraction and storage of intact blocks of field samples, the samples were cut into cuboid prisms using a large saw-cutting equipment normally used for cutting hard rocks (Fig. 2b). A dry saw-cutting procedure was adopted to ensure that samples did not disintegrate due to the presence of water. The samples were shaped into prisms with a square cross section having a 71 mm (2.8 in.) side length and a 122 mm (4.6 in.) height (i.e., $L = W = 71$ mm and $H = 122$ mm). In spite of much attention paid, the actual cut sizes were slightly different depending on the slab weight being cut and the wobbling action of the saw blade. Durability samples produced by saw-cutting are shown in Fig. 2c. Samples extracted from sections with blends of QB with recycled coarse aggregates generally had a rougher surface finish.

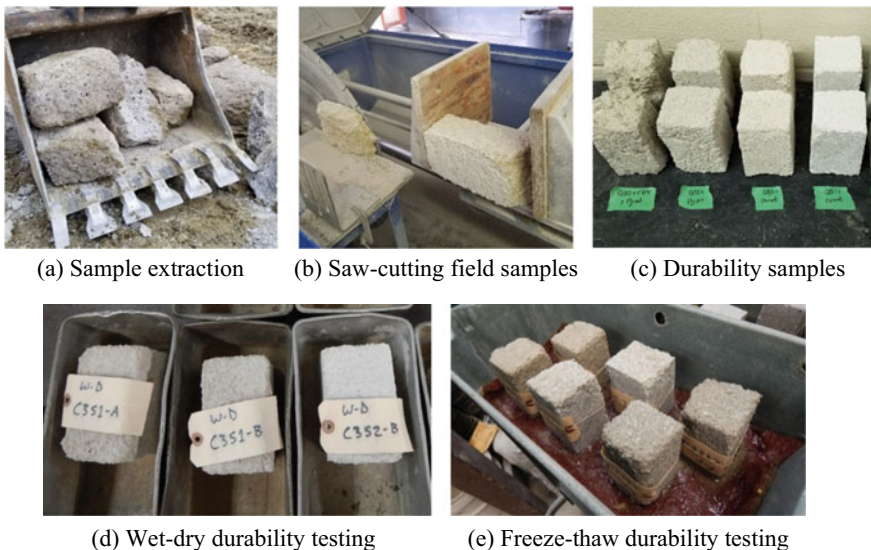


Fig. 2 Extraction, preparation, and durability testing of samples collected from the field

Table 3 Dry density and relative compaction characteristics of the durability samples

Sample name	Sample no.	MDD kN/m ³ (pcf)	Wet-dry durability samples		Freeze–thaw durability samples	
			As-received dry density kN/m ³ (pcf)	RD (%)	As-received dry density kN/m ³ (pcf)	RD (%)
C2S1	# A	21.2 (135.0)	18.6 (118.1)	87.5	18.5 (117.9)	87.4
	# B		18.1 (115.2)	85.3	19.1 (121.4)	89.9
C2S2	# A	20.2 (128.6)	18.7 (119.0)	92.5	18.3 (116.8)	90.8
	# B		19.5 (124.2)	96.6	20.0 (127.2)	99.0
C2S3	# A	21.4 (136.2)	17.6 (111.8)	82.1	17.9 (113.8)	83.5
	# B		18.1 (115.0)	84.4	17.9 (114.0)	83.7
C2S4	# A	21.6 (137.5)	20.7 (131.8)	95.9	20.6 (131.4)	95.6
	# B		20.8 (132.4)	96.3	20.8 (132.2)	96.1
C3S1	# A	20.4 (129.9)	17.6 (111.9)	86.1	17.0 (108.4)	83.5
	# B		17.4 (111.1)	85.5	17.0 (108.5)	83.5
C3S2	# A	21.6 (137.5)	20.6 (131.1)	95.3	20.8 (132.2)	96.1
	# B		20.9 (133.4)	97.0	20.0 (127.5)	92.7
C3S3	# A	21.3 (135.6)	19.2 (122.3)	90.2	19.5 (124.1)	91.5
	# B		19.5 (124.3)	91.7	19.4 (123.5)	91.1

The as-received dry densities and the percentages of the relative densities (RD) of all field-extracted samples are presented in Table 3. The dry densities were calculated based on the as-received density and as-received moisture content of each sample. Table 3 lists low relative densities of some of the extracted samples compared to the maximum dry densities determined from the laboratory compaction tests using standard Proctor compactive effort. Specifically, samples extracted from C2S1 with cement-stabilized QB2/FRAP mixes, C2S3 with fly ash-stabilized QB2/FRAP mixes, C3S1 with cement-stabilized QB3, and C3S3 with fly ash-stabilized QB2 had the lowest field dry densities and relative densities. These low densities could result in rather poor wet-dry and freeze–thaw durability trends when compared to those of the same material combinations compacted at higher relative densities.

3 Durability Testing

3.1 Procedure for Durability Testing

Testing of wet-dry durability samples was conducted in accordance to the AASHTO T 135 standard. After each wet-dry cycle, measurements were taken for moisture

change, volume change, and soil–cement loss by a brushing technique. The standard method ‘B,’ i.e., using soil material passing the 19.0-mm ($\frac{3}{4}$ -in.) sieve, in the AASHTO T 135 specification was used. The testing procedure involved wetting the samples for five hours at room temperature, i.e., 21 ± 2 °C (70 ± 3 °F), followed by oven-drying for 42 h at a temperature of 71 ± 3 °C (160 ± 5 °F). The weight of sample was recorded after each step. The testing procedure involved brushing all areas with two firm strokes using a wire scratch brush and applying a brushing force of approximately 13 N (3 lbf). The wetting and drying steps were repeated for a total of 12 cycles for each tested specimen. Wet-dry durability samples are shown in Fig. 2d.

Testing of freeze–thaw durability samples was conducted according to the AASHTO T 136 standard. Similarly, this procedure involves using the same brushing method. The standard method ‘B’ was also used for freeze–thaw durability testing. The samples were placed in a freezing cabinet for 24 h at a temperature of -23 °C (-10 °F), followed by thawing in a moist room for 23 h at 100% relative humidity and a temperature of 23 ± 2 °C (73.5 ± 3.5 °F). Both freezing and thawing were done in air, i.e., samples were not submerged. The samples were brushed and tested in the exact same manner as the wet-dry samples. After 12 cycles of testing, the samples were dried to a constant weight at a temperature of 110 ± 5 °C (230 ± 9 °F). The freeze–thaw durability samples are shown in Fig. 2e.

3.2 Durability Testing Results

Figure 3 summarizes the results of the wet-dry durability testing for the field-extracted specimens. All samples survived the 12 cycles. Samples with cement-stabilized QB2 or QB2 blended with FRAP/FRCA had significantly low soil–cement loss and slow rates of deterioration. All samples with QB2 and cement had less than 2% average soil–cement loss after 12 cycles of wet-dry durability. All cement-stabilized QB materials or QB blends with FRAP/FRCA passed the IDOT requirement with less than 10% soil–cement loss after 10 cycles of wetting and drying. On the other hand, C2S3 and C3S3 samples with fly ash-stabilized QB2/FRAP and fly ash-stabilized QB2, respectively, had significantly higher soil–cement losses and rates of deterioration. Cement proved to be superior to Class C fly ash for long-term durability. Field samples with fly ash had a relatively high soil–cement loss averaging between 17.6 and 18.6%, which is significantly higher than what is permitted by IDOT design criteria [16].

Shown also in Fig. 3 are the UCS results of the 76-mm (3-in.) cubes extracted and saw cut from the field test sections. The minimum, average, and maximum UCS values are reported, and the best fit linear correlation between the average UCS and the average soil–cement loss of all QB2 samples (i.e., all material combinations excluding C3S1) are shown. Note that the average UCS and wet-dry durability results are well correlated (coefficient of determination, $R^2 = 0.852$), which can be further investigated as a quick and convenient check for durability. On the other hand, the

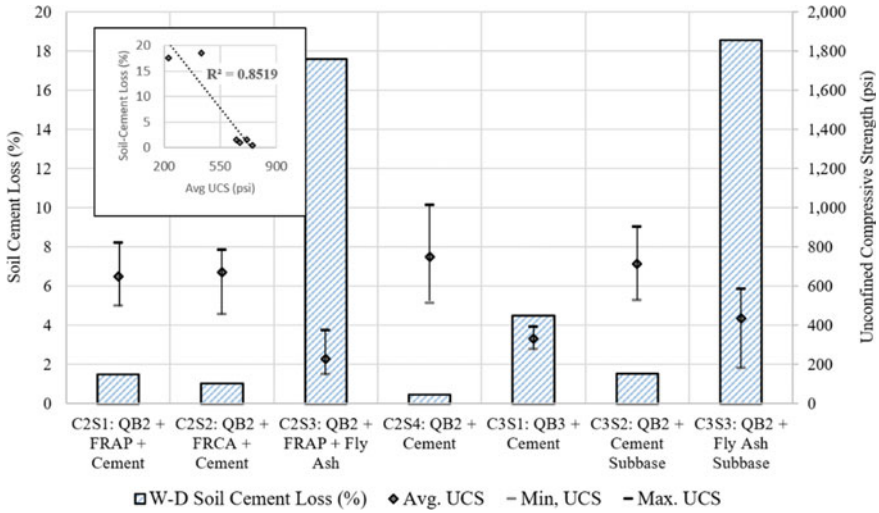


Fig. 3 Wet-dry durability and unconfined compressive strength results for field samples

results comparing the UCS and durability of cylinders molded in the laboratory and tested with the same procedures for these materials were inconclusive, i.e., no clear correlation could be established [6, 7].

Figure 4 summarizes the results of the freeze–thaw durability testing for the field-extracted specimens. All cement-stabilized samples with QB2 or blends of QB2 with coarse-recycled aggregates (FRAP or FRCA) survived the 12 cycles of testing and

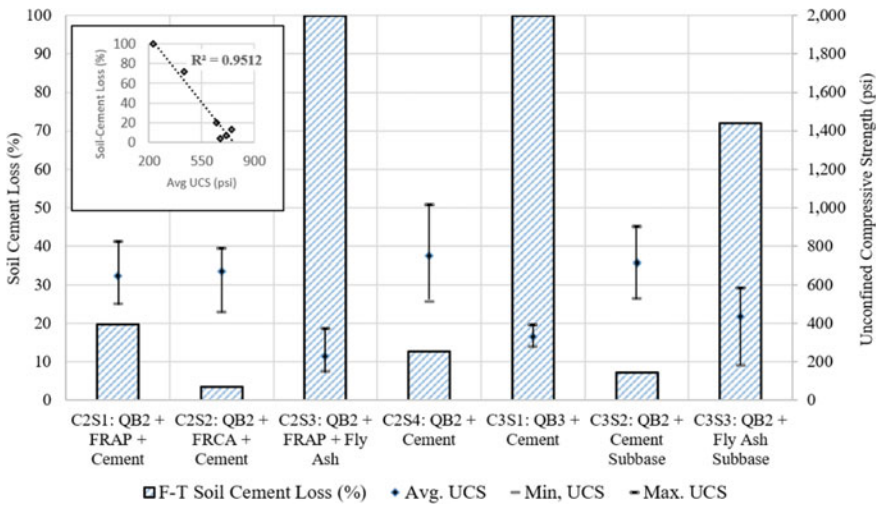


Fig. 4 Freeze–thaw durability and unconfined compressive strength results for field samples

accumulated significantly lower soil–cement losses than the QB2 samples stabilized with fly ash and the cement-stabilized QB3 samples. The low density, in addition to the chemical composition of the QB3 material, may explain the poor long-term performance of C3S1. Further investigations on the effects of density and chemical composition on the durability of QB mixes can be revealing. Similar to the wet-dry durability results, the average UCS and freeze–thaw durability trends are highly correlated (coefficient of determination, $R^2 = 0.951$) for QB2 samples.

Figure 5a and b presents the results for the cement-stabilized QB2 and QB3 samples tested for wet-dry and freeze–thaw durability, respectively. Soil–cement loss is plotted against the number of wet-dry/freeze–thaw cycles to study the effect of mineralogy and chemical composition on the rate of deterioration and the total soil–cement loss with number of cycles. Note that samples with QB2 have higher dolomitic fines content, while QB3 is mostly limestone fines. As shown in Fig. 5a, samples with QB2 had less than 2% soil–cement loss after 12 cycles of wet-dry durability. On the other hand, samples with QB3 had significantly higher soil–cement loss of 4–5% after 12 wet-dry cycles and a higher magnitude and rate of soil–cement loss at any cycle. Knowing that both QB materials had similar gradations and fines contents (see Fig. 1a) and the same cement content of 3%, it is a clear indication that the mineralogy /chemical composition of QB influences wet-dry durability. Note also that samples with QB3 had lower relative densities compared to those of QB2 (see Table 3), which could have also contributed to the lower durability trends.

Similarly, for freeze–thaw durability tests shown in Fig. 5b, samples with QB2 (dolomite) survived the 12 cycles of testing and accumulated significantly lower soil–cement losses than samples with QB3 (limestone). Note that samples with QB3 had a higher rate and magnitude of soil cement loss at any cycle and completely disintegrated after 7–8 cycles. The soil–cement loss values reported for these samples in Figs. 4 and 5 were determined by extrapolating the results to 12 cycles using a third-order polynomial fit. The type of QB also has a clear effect on the freeze–thaw

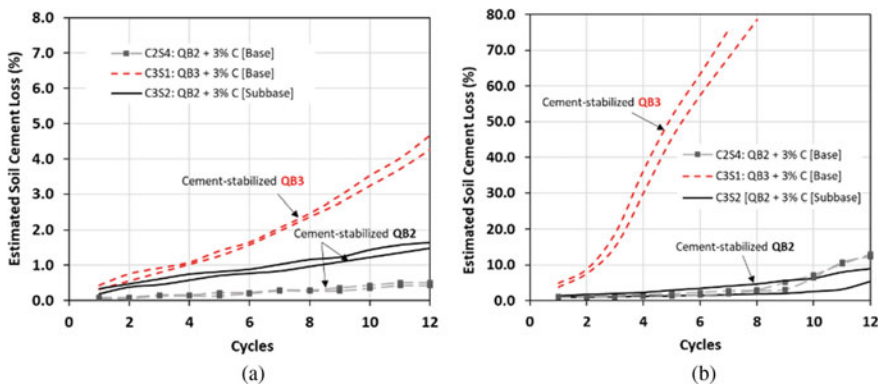


Fig. 5 Estimated soil–cement loss vs. number of cycles for **a** wet-dry durability and **b** freeze–thaw durability testing of cement-stabilized QB2 samples

durability, where dolomitic samples with higher MgO content can benefit from more long-term chemical reactions and associated strength gain.

4 Summary and Conclusions

This paper presented results from a study which focused on the freeze–thaw and wet-dry durability behavior of chemically stabilized Quarry By-product (QB) foundation layer applications in flexible pavements. These base and subbase applications involved 3% cement–or 10% fly ash–stabilized QB materials and QB blends with recycled coarse aggregates. The QB applications studied for durability were previously evaluated for field performance trends through accelerated pavement testing (APT), which provided a unique opportunity to collect field samples with known performance trends. In total, 28 samples were tested. Field samples were collected and saw-cut into prisms having the dimensions of an inscribed cuboid in the standard Proctor mold. Freeze–thaw and wet-dry durability tests were conducted as per AASHTO T 136 and T 135, respectively.

Considering the investigation of durability aspects, the following findings, conclusive remarks, and recommendations can be offered:

- Wet-dry durability tests resulted in lower percentages of soil–cement loss compared to the harsh freeze–thaw durability tests. All wet-dry durability samples survived the 12 cycles of wetting and drying. For freeze–thaw durability testing by the AASHTO T 136 standard, some samples, particularly ones stabilized with fly ash, completely disintegrated before completing 12 cycles.
- Chemical composition of the QB material was found to have a significant effect on the durability of chemically stabilized QB fines, particularly when long-term durability is considered. The QB2 material with more dolomitic fines had more long-term strength gain and better durability than QB3 with limestone fines.
- The durability performance trends and unconfined compressive strength properties of QB2 samples were found to be highly correlated. Samples with higher strength were more durable, especially when freeze–thaw durability was considered.
- The stabilizer selection had a significant effect on the durability of QB applications. Compared to cement’s performance, Class C fly ash was not as effective and may not be recommended for stabilized QB applications due to lower durability despite satisfactory field performance.
- The lower density of the cement-stabilized QB3 samples extracted from the field test section also contributed to the poorer durability performance of this material.

Acknowledgements This publication is based on the results of ICT-R27-SP38 Durability Aspects of Stabilized Quarry By-product Pavement Applications [7]. ICT-R27-SP38 was conducted in cooperation with the Illinois Center for Transportation; the Illinois Department of Transportation, Office

of Program Development; and the US Department of Transportation, Federal Highway Administration. The authors would like to acknowledge the members of IDOT Technical Review Panel for their useful advice at different stages of this research. Special thanks go to Kurt Schmuck, Kyle Hanselman, and Mohammed Altowayti from IDOT Central Bureau of Materials for their help with freeze–thaw and wet-dry durability testing. Thanks are also extended to Greg Renshaw, Marc Killion, Jamar Brown, and all the ICT students for their help at the Advanced Transportation Research and Engineering Laboratory (ATREL). The contents of this paper reflect the views of the authors who are responsible for the facts and the accuracy of the data presented. This paper does not constitute a standard, specification, or regulation.

References

1. Tutumluer E, Ozer H, Hou W, Mwumvaneza V (2015) Sustainable aggregates production: green applications for aggregate by-products. Final Report FHWA-ICT-15–012. Illinois Center for Transportation/Illinois Department of Transportation, Rantoul
2. Qamhia I, Tutumluer E, Ozer H (2018) Field performance evaluation of sustainable aggregate by-product applications. Final Report FHWA-ICT-18–016. Illinois Center for Transportation/Illinois Department of Transportation, Rantoul
3. Mwumvaneza V, Hou W, Tutumluer E, Al-Qadi I, Beshears S (2015) Characterization and stabilization of quarry byproducts for sustainable pavement applications. *Transport Res Record: J Transport Res Board* 2509:1–9
4. Qamhia I, Tutumluer E, Ozer H, Shoup H, Beshears S, Trepanier J (2019) Evaluation of chemically stabilized quarry byproduct applications in base and subbase layers through accelerated pavement testing. *Transport Res Record: J Transport Res Board* 2673(3):259–270
5. Qamhia I (2019) Sustainable pavement applications utilizing quarry by-products and recycled / nontraditional aggregate materials. Doctoral Dissertation, University of Illinois at Urbana-Champaign
6. Qamhia I, Tutumluer E, Ozer H, Boler H, Shoup H, Stolba A (2020) Durability aspects of chemically stabilized quarry by-product applications in pavement base and subbase. *Transport Res Record: J Transport Res Board* 2674(6):339–350
7. Qamhia I, Tutumluer E, Ozer H, Boler H (2019) Durability aspects of stabilized quarry by-product pavement base and subbase applications. Final Report FHWA-ICT-19–012. Illinois Center for Transportation/Illinois Department of Transportation, Rantoul
8. Ilangovana R, Mahendrana N, Nagamanib K (2008) Strength and durability properties of concrete containing quarry rock dust as fine aggregate. *ARPN J Eng Appl Sci* 3(5):20–26
9. Galetakis M, Soultana A (2016) A review on the utilization of quarry and ornamental stone industry fine by-products in the construction sector. *Constr Build Mater* 102:769–781. <https://doi.org/10.1016/j.conbuildmat.2015.10.204>
10. Li B, Zhou M, Fang Y, Song P, Ke G (2011) Self-compacting concrete-filled steel tubes prepared from manufactured sand with a high content of limestone fines. *J Wuhan Univer Technol-Mater Sci Ed* 26(2):325–328
11. Amadi AA (2014) Enhancing durability of quarry fines modified black cotton soil subgrade with cement kiln dust stabilization. *Transport Geotech* 1(1):55–61. <https://doi.org/10.1016/j.trgeo.2014.02.002>
12. Onyejekwe S, Ghataora GS (2015) Stabilization of quarry fines using a polymeric additive and Portland cement. *J Mater Civil Eng* 28(1). [https://doi.org/10.1061/\(ASCE\)MT.1943-5533.0001324](https://doi.org/10.1061/(ASCE)MT.1943-5533.0001324)
13. Eze-Uzomaka OJ, Agbo D (2010) Suitability of quarry dust as improvement to cement stabilized-laterite for road bases. *Electron J Geotech Eng* 15:1053–1066

14. Gurbuz A (2015) Marble powder to stabilize clayey soils in sub-bases for road construction. *Road Mater Pavement Design* 16(2):481–492. <https://doi.org/10.1080/14680629.2015.1020845>
15. Zhang Y, Tantu LK, Borén M (2019) Assessment for sustainable use of quarry fines as pavement construction materials: part II—Stabilization and characterization of quarry fine materials. *Mater J* 12(15):2450. <https://doi.org/10.3390/ma1215245>
16. Illinois Department of Transportation (IDOT) (2016) Standard specifications for road and bridge construction. Springfield, IL

Stabilization and Reinforcement of Geomaterials and Its Implications in Pavement and Rail Track Design

Prediction of Durability, Resilient Modulus and Resistance Value of Cement Kiln Dust-Stabilized Expansive Clay for Flexible Pavement Application Using Artificial Neural Networks



Anigilaje B. Salahudeen , Mehdi Jalili , Danial R. Eidgahee , Kennedy C. Onyelowe , and Mohsen K. Kabiri 

Abstract Artificial neural networks (ANNs) can be used in soil stabilization aspect of geotechnical engineering. As such, this study aimed at applying the ANNs as a soft computing approach to predict the durability, resistance value and resilient modulus of Nigerian expansive clay also called black cotton soil. A soft computing approach using multilayer perceptrons (MLPs) artificial neural networks (ANNs) that are trained with the feed forward backpropagation algorithm was used in this study for the simulation of some strength properties of cement kiln dust-stabilized expansive clay. For each of the three ANN model development, eight input for one output data set were used. The mean squared error (MSE) and *R*-value were used as yardstick and criterions for acceptability of performance. In the neural network development, NN 8-17-1, NN 8-24-1 and NN 8-18-1, respectively, for durability, resilient modulus and resistance value that gave the lowest MSE value and the highest combined *R*-value were used in the hidden layer of the networks architecture which performed satisfactorily except for resistance value. For the normalized data set used in training, testing and validating the neural network, the performance of the simulated network was satisfactory having *R*-values of 0.8388, 0.8433 and 0.7572

A. B. Salahudeen (✉)

Department of Civil Engineering, University of Jos, Jos, Nigeria
e-mail: bunyamins@unijos.edu.ng

M. Jalili

Department of Civil Engineering, Islamic Azad University, Semnan Branch, Semnan, Iran
e-mail: m.jalili@semnaniau.ac.ir

D. R. Eidgahee

Department of Civil Engineering, Faculty of Civil Engineering, Semnan University, Semnan, Iran
e-mail: d.rezazade@semnan.ac.ir

K. C. Onyelowe

Department of Civil Engineering, Michael Okpara University of Agriculture, Umudike, Nigeria
e-mail: konyelowe@mouau.edu.ng

M. K. Kabiri

Department of Civil Engineering, Science and Research Branch, Islamic Azad University, Tehran, Iran
e-mail: mohsen.kabiri@srbiau.ac.ir

for the durability, resilient modulus and resistance value, respectively. The values by durability and resilient modulus met the minimum criteria of 0.8 conventionally recommended for strong correlation condition. A strong correlation was observed between the experimental values as obtained by laboratory test procedures and the predicted values using ANN.

Keywords Artificial neural networks · Cement kiln dust · Durability · Expansive clay · Flexible pavement · Resilient modulus · Resistance value

1 Introduction

California bearing ratio and unconfined compressive strength tests on soft soils are strength characteristics that are used for the determination of long-term performance and behavior of stabilized soils through loss of strength in moisture environment [1]. Durability, which is the ability to retain stability and integrity over years of exposure to adverse environment is one of the most important aspects of additive-based stabilized soil layers in pavement design [2]. The ability of a pavement layer to maintain desired properties over the life of a pavement is an important consideration. Variations in climatic conditions have been recognized as a major factor affecting pavement performance [3]. Cement kiln dust (CKD) was used in this study to stabilize expansive clay. The physical and chemical properties of CKD can vary from plant-to-plant, depending on the raw materials used and type of collection process in the plant [4].

The resistance value (resistance to loss in strength under adverse field conditions) is an engineering property used to characterize materials in construction environments, especially in pavement construction. It measures the materials resistance to loss in strength when immersed in water. In most cases, foundation materials subjected to vertical loading suffer lateral deformation and the ability to withstand this form of failure is known as resistance value [5, 6]. The resistance value is determined in this study through the resistance to loss in strength of the soil specimen. Resilient modulus is used to characterize pavement materials under loading conditions that will not result in failure of the pavement system. Resilient modulus is a measure of elastic modulus of a material at a given stress and is expressed as the ratio of applied deviator stress to recoverable strain. AASHTO [7] pavement design guide requires the use of resilient modulus to represent the material strength of pavement layers. Therefore, an accurate measurement of resilient modulus is needed to ensure the efficiency and accuracy of the pavement design.

Artificial neural network (ANN) is an imitation of the human brain. An artificial thinking machine is really beyond the capacity of the most advanced supercomputers [8]. In recent times, artificial neural networks (ANNs) have been applied to many geotechnical engineering applications. Shahin et al. [9] have used back-propagation neural networks to predict the settlement of shallow foundations on cohesionless soils. The results indicated that ANNs are a promising method for

predicting settlement of shallow foundations. Kolay et al. [10] made use of ANN in predicting the compressibility characteristics of soft soil settlement in Sarawak, Malaysia. Benali et al. [11] used ANNs for principal component analysis and prediction of the pile capacity based on SPT results. ANNs were used by Salahudeen et al. [12] to predict the optimum moisture content and maximum dry density of Nigerian black cotton soil. All these literature are source of hope for the beneficial use of ANNs in geotechnical applications.

Expansive clay is in the group of problem soils encountered by geotechnical engineers. The expansive clays, also known as black cotton soils or black clays, are confined to the semi-arid regions of tropical and temperate climatic zones and are abundant where the annual evaporation exceeds the precipitation [13, 14]. The absence of quartz in the clay mineralogy enhances the formation of fine-grained soil material, which is impermeable and waterlogged. The mineralogy of this soil is dominated by the presence of montmorillonite which is characterized by large volume change from wet to dry seasons and vice versa. Deposits of black clay occupy an estimated area of $104 \times 10^3 \text{ km}^2$ in north-east region of Nigeria. Cracks measuring 70 mm wide and over 1 m deep have been observed and may extend up to 3 m or more in case of high deposit [15].

Durability and resistance value are usually determined from unconfined compressive strength (UCS) test. The resilient modulus of soil is typically determined using the repeated load triaxial test. However, these tests require a well-trained personnel and expensive laboratory equipment. In addition, they are considered to be relatively time consuming [16]. Alternatively, these parameters can be predicted accurately using artificial neural networks (ANN) simulations since they are related to several index properties of soil, such as the particle size, Atterberg's limits and compaction characteristics. This study aimed at using index soil properties to develop an optimized neural network for durability, resilient modulus and resistance value (resistance to loss in strength) using artificial neural networks (ANNs).

2 Materials and Methods

2.1 Materials

The expansive clay soil used for this study was obtained from Dadinkowa, Gombe State, Nigeria. The cement kiln dust (CKD) was obtained from Sokoto Cement Factory, Sokoto, the capital of Sokoto State, Nigeria.

2.2 Methods

Laboratory Tests. Laboratory tests were performed on the natural soil samples in accordance with BS 1377 [17] and on the cement kiln dust-treated expansive clay in accordance with BS 1924 [18]. The tests conducted include particle size distribution, specific gravity, linear shrinkage, Atterberg's limits, compaction characteristics test to determine the OMC and MDD, California bearing ratio and unconfined compressive strength (UCS) test. All tests were first carried out on the natural soil then on the CKD-treated soils in steps of 0, 2, 4, 6, 8 and 10% CKD content by dry weight of the soil. Standard laboratory procedures were used in this study with three compactive energies of British Standard Light (BSL), West African Standard (WAS) and the British Standard heavy (BSH) energies. This assisted in generating the huge database needed for the ANN simulation. The three target parameters were obtained from Eq. 1–3.

$$\text{Durability (kPa)} = \text{UCS}(7 \text{ days cured} + 7 \text{ days soaked}) \quad (1)$$

$$\text{Resilient Modulus (MPa)} = 1500 \times \text{soaked CBR} \quad (2)$$

$$\text{Resistance Value(\%)} = \frac{\text{UCS}(7 \text{ days cured} + 7 \text{ days soaked})}{\text{UCS}(14 \text{ days cured})} \times 100 \quad (3)$$

Artificial Neural Networks Model Development. The types of neural networks used in this study are multilayer perceptrons (MLPs) that are trained with the feed forward backpropagation algorithm. The input from each processing element in the previous layer is multiplied by an adjustable connection weight. This combined input then passes through a nonlinear transfer function (TANSIG function for layer one and PURELIN function for layer two) to produce the output of the processing element. The neurons use the following transfer or activation function:

$$X = \sum_{i=1}^n x_i w_i \quad Y = \begin{cases} +1, & \text{if } X \geq \theta \\ -1, & \text{if } X < \theta \end{cases} \quad (4)$$

The output of one processing element provides the input to the next processing elements. In this study, eight input and three outputs were used separately for the ANN model development. The input data are specific gravity (SG), linear shrinkage (LS), uniformity coefficient (C_u) coefficient of gradation (C_c), liquid limit (LL), plastic limit (PL), optimum moisture content (OMC) and maximum dry density (MDD). The outputs (targets) data are durability, resilient modulus and resistance value (resistance to loss in strength). The multilayer perceptron architecture of networks used for the ANN model development is shown in Fig. 1.

Data Division and Processing in Artificial Neural Network. In developing the ANN model, the available data were randomly divided into three sets: a training set

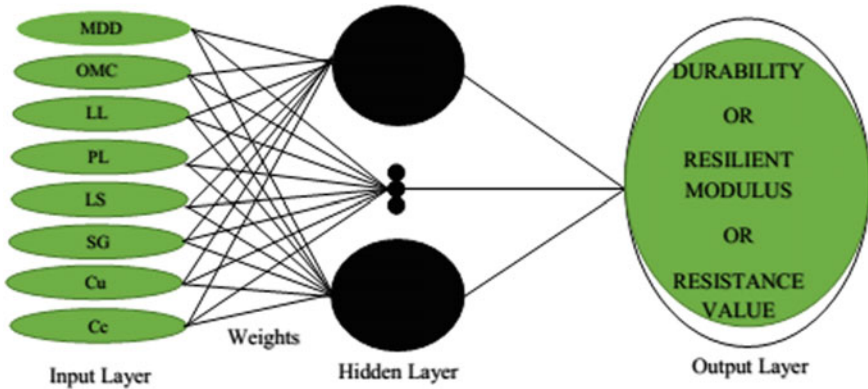


Fig. 1 Multilayer perceptron architecture of ANN network

(70%) for model calibration, a testing set (15%) and an independent validation set (15%) for model verification. Once available data are divided into their subsets, the input and output variables were pre-processed, and in this step, the variables were normalized between -1.0 and 1.0 .

Model Performance Evaluation. The performance of the developed ANNs model was evaluated to ensure that the model has the ability to generalize its performance within the limits set by the training data rather than been peculiar to the input–output relationships contained in the training data. In the literature, the common measures often used are statistical measures which include the correlation coefficient (R), the mean absolute error (MAE) and the root mean square error (RMSE). The formulas used for these measures are:

$$R = \frac{\sum_{i=1}^N (O_i - \bar{O})(P_i - \bar{P})}{\sqrt{\sum_{i=1}^N (O_i - \bar{O})^2 \sum_{i=1}^N (P_i - \bar{P})^2}} \tag{5}$$

$$RMSE = \sqrt{\frac{\sum_{i=1}^N (O_i - P_i)^2}{N}} \tag{6}$$

$$MAE = \frac{1}{N} \sum_{i=1}^N |O_i - P_i| \tag{7}$$

where N is the number of data points used for the model development; O_i and P_i are the observed and predicted outputs, respectively, and \bar{O} and \bar{P} are the mean of observed and predicted outputs, respectively.

3 Results and Discussions

3.1 Data Processing for ANN

In ANN prediction modeling, the efficiency of input data and their ability to accurately predict the output (target) is largely dependent on the relationship between the input and the output. In this study, eight input geotechnical soil parameters that have direct effects on the outputs were considered. In order to give a detailed insight of the general data used for the study, a frequency bar chart was used to present the research data of a total of 72 set as shown in Figs. 2, 3, 4, 5, 6, 7, 8, 9, 10, 11 and 12.

Fig. 2 Frequency of SG

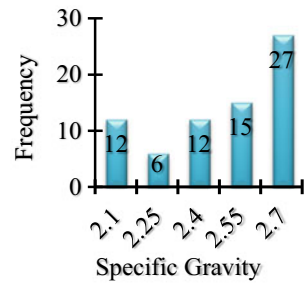


Fig. 3 Frequency of LS

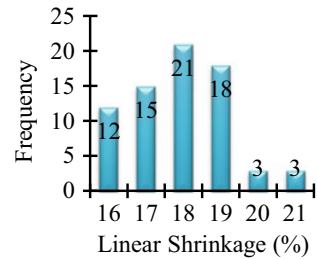


Fig. 4 Frequency of C_u

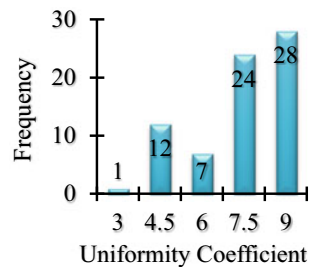


Fig. 5 Frequency of C_c

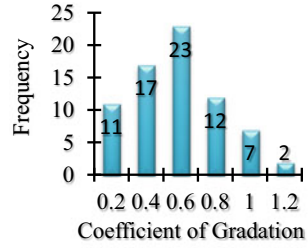


Fig. 6 Frequency of LL

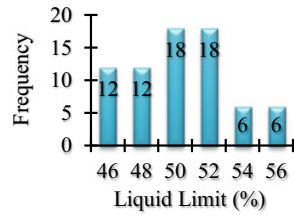


Fig. 7 Frequency of PL

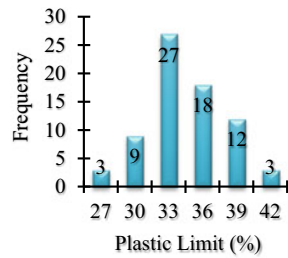
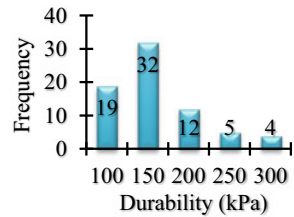


Fig. 8 Frequency of durability



3.2 The Optimized Network

In this study, NN 8-n-1 network architecture was used for the network optimization. The first digit of the component is the number of input nodes, n is the number of hidden nodes (number of neurons) and the third digit is the number of output nodes.

Fig. 9 Frequency of OMC

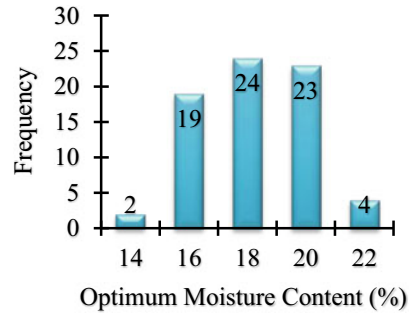


Fig. 10 Frequency of MDD

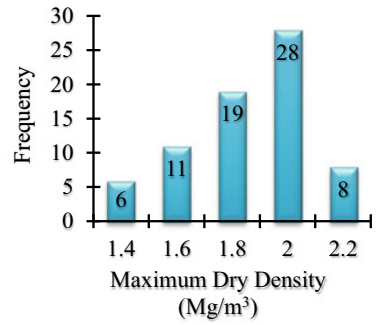


Fig. 11 Frequency of resilient modulus

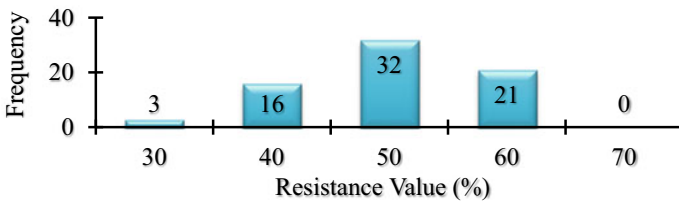
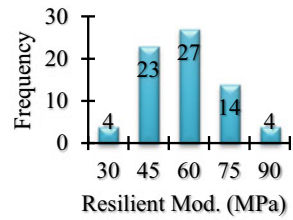


Fig. 12 Frequency of resistance value

These NN 8-n-1 network architectures are shown in Figs. 1, 2 and 3. In this study, 21 different number of hidden nodes (NN 8-5-1 to NN 825-1) were tried in order to determine the best performing n -number. The mean squared error (MSE) and R -value were used as yardstick and criterions in this regard. The choice of 5–25 neurons was based on recommendations in the literature [10, 12, 19, 20] in which it was concluded that the use of neuron number below or above certain limit could cause insufficient or saturation of the network which results to lesser quality simulated results due to undesirable feedbacks to the network. Therefore, $n = 17$, $n = 24$ and $n = 18$ neurons, respectively, for durability, resilient modulus and resistance value that yielded low MSE values and the highest R -value on the average were used in the hidden layers of the three sets of target predicted. Eidgahee et al. [20] stated that the best measure for the performance of the ANN developed models should be based on the lowest MSE values and the highest R -values. However, other researchers like Naderpour et al. [19] used only MSE values as criterion. It was observed, however, in this study, that the best criteria for reliable choice of the neuron numbers to yield better results is the combined (all) R -value that has a reasonably low MSE value and not necessarily the lowest.

3.3 ANN Model Development Results

The regression values for model performance evaluation showing the k (slope), R -values, mean absolute error (MAE), mean squared error (MSE) and the root mean squared error (RMSE) are presented in Table 1. It is obvious from these statistical results that the models developed in this study performed satisfactorily having high R -values and low error values except for that of resistance value which yielded a

Table 1 Parameters and regression values for model performance evaluations

Parameters	Durability	Resilient modulus	Resistance value
Number of neurons	17	24	18
k	0.7013	0.7067	0.404
MSE (ANN)	0.026279	0.011704	0.089317
R -training	0.9908	0.9291	0.954
R -validation	0.8529	0.9032	0.5934
R -testing	0.6359	0.6403	0.2652
R -all data	0.8388	0.8433	0.7572
MAE	0.065	0.081	0.106
MSE (statistical)	0.012583	0.014466	0.023682
RMSE	0.112	0.12	0.154

poor performance. The statistical parameters give acceptable results that confirmed the best generalization of the developed models for durability and resilient modulus.

The variation of experimental and ANN predicted UCS values are shown in Figs. 13, 14 and 15. The performance of the simulated networks for durability and resilient modulus were satisfactory having k values of 0.7013 and 0.7067, respectively. k is the slope of the regression line through the origin in the plot of the experimental values to the predicted values. It was reported by Golbraikh and Tropsha [21] and Alavi et al. [22] that the value of k should be close to unity as a criterion for excellent performance. The poor performance of the simulated networks for resistance value may be due to the fact that it depends on two different UCS tests—7 days curing and 7 days soaking on one hand and then 14 days curing of a different sample on the other hand. This is not the case in durability and resilient modulus which depend on a single UCS and CBR tests, respectively.

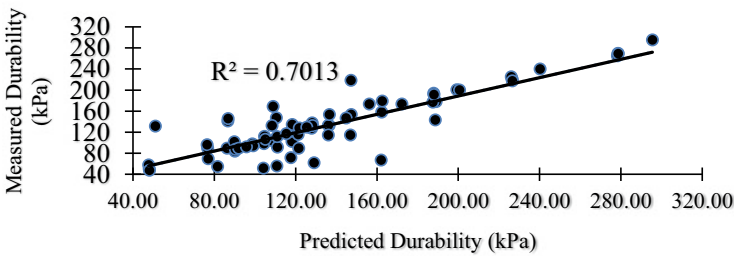


Fig. 13 Variation of experimental and ANN predicted durability

Fig. 14 Variation of experimental and ANN predicted resilient modulus

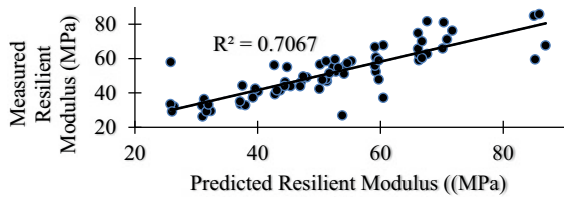
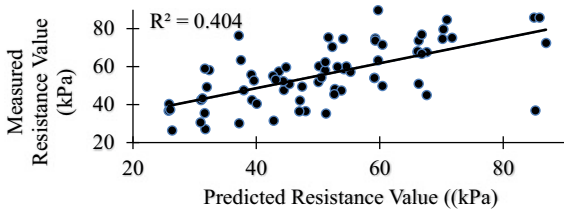


Fig. 15 Variation of experimental and ANN predicted resistance value



3.4 Model Validation

The coefficient of correlation (R -value) is a measure used to evaluate the relative correlation and the goodness-of-fit between the predicted and the observed data. Salahudeen et al. [2] suggested that a strong correlation exist between any two set of variables if the R -value is greater than 0.8. However, Kolay et al. [10] are of the opinion that the use of R -value alone can be misleading arguing that higher values of R may not necessarily indicate better model performance due to the tendency of the model to deviate toward higher or lower values in a wide range data set.

The RMSE on the other hand is another measure of error in which large errors are given greater concern than smaller errors. However, Salahudeen et al. [12] argued that in contrast to the RMSE, MAE eliminates the emphasis given to larger errors and that both RMSE and MAE are desirable when the evaluated output data are continuous. Consequently, the combined the use of R , RMSE and MAE in this study was found to yield a sufficient assessment of ANN model performance and allows comparison of the accuracy of generalization of the predicted ANN model performance. This combination is also sufficient to reveal any significant differences among the predicted and experimental data sets.

The conditions of model validity in this study are stated in Table 2. Based on the results of different NN 8-17-1, NN 8-24-1 and NN 8-18-1 networks used in this study, it was observed that the errors are at their best performance when they are less than 0.01 but still yield good and acceptable performance when greater than 0.1 in a value range of 0–1.

Table 2 Conditions of model validity

Target	Statistical parameter	Condition	Obtained value	Remarks
Durability	R	>0.8	0.8388	Satisfactory
	k	Should be close to 1	0.7013	Good
	MSE	Should be close to 0	0.012583	Satisfactory
	MAE	Should be close to 0	0.065	Satisfactory
	RMSE	Should be close to 0	0.112	Good
Resilient modulus	R	>0.8	0.8433	Satisfactory
	k	Should be close to 1	0.7067	Good
	MSE	Should be close to 0	0.014466	Satisfactory
	MAE	Should be close to 0	0.081	Satisfactory
	RMSE	Should be close to 0	0.12	Good
Resistance value	R	>0.8	0.7572	Poor
	k	Should be close to 1	0.404	Poor
	MSE	Should be close to 0	0.023682	Good
	MAE	Should be close to 0	0.106	Poor
	RMSE	Should be close to 0	0.154	Good

Based on the suggestion of Naderpour et al. [19], argument of Salahudeen et al. [12], conclusions of Shahin [9] and observations in this study, it is obvious from Table 2 that the developed models in this study for durability and resilient modulus performed satisfactorily and have good generalization potential. The achieved high R -values and low values of errors are highly desirable in ANN simulation as they indicate acceptable results. A strong correlation was observed between the experimental values as obtained by laboratory tests and the predicted values using ANN. Eidgahee et al. [20] reported that strong correlation exists between the experimental and predicted values if the R -value is greater than 0.8 and the MSE values are at minimum. The results obtained for durability and resilient modulus in this study can therefore be concluded to be satisfactory and yielded good simulation results.

4 Conclusion

Artificial neural networks (ANNs) were used in this study to develop predictive optimized models for durability, resilient modulus and resistance value of cement kiln dust-treated expansive clay. Based on the results of the developed ANN models, the following conclusions were made:

1. The multilayer perceptrons (MLPs) ANN used for the simulation of durability and resilient modulus of CKD-treated expansive clay that are trained with the feed forward backpropagation algorithm performed satisfactorily.
2. The mean absolute error (MAE), root mean square error (RMSE) and R -value were used as yardstick and criteria. In the neural network development, NN 8-17-1 and NN 8-24-1, respectively, for durability and resilient modulus that gave the low MSE values and the highest R -values were used in the hidden layer of the networks architecture which performed satisfactorily.
3. For the normalized data used in training, testing and validating the neural network, the performance of the simulated networks for durability and resilient modulus was very good having R -values of 0.8388 and 0.8433 for durability and resilient modulus, respectively. These values met the minimum criteria of 0.8 conventionally recommended for strong correlation condition.
4. The obtained simulation results for durability and resilient modulus are satisfactory and a strong correlation was observed between the experimental values as obtained by laboratory tests and the predicted values using ANN. The simulation results of resistance value performed poorly and yielded unacceptable result generally.

References

1. Salahudeen AB, Eberemu OA, Osinubi KJ (2014) Assessment of cement kiln dust-treated expansive soil for the construction of flexible pavements. *Geotech Geol Eng* 32(4):923–931
2. Salahudeen AB, Sadeeq JA (2019) California bearing ratio prediction of modified black clay using artificial neural networks. In: Book of proceedings, West Africa Built Environment Research (WABER) conference, Accra, Ghana, pp 268–281. <https://doi.org/10.33796/wabercconference2019.19>
3. Zhipeng S (2012) Durability performance of cementitiously stabilized layers. An unpublished MSc thesis, Department of Civil and Environmental Engineering, University of Wisconsin-Madison, USA
4. Rahman MK, Rehman S, Al-Amoudi SB (2011) Literature review on cement kiln dust usage in soil and waste stab and experimental investigation. *IJRRAS* 7:77–78
5. Onyelowe KC, Onyelowe FDA, Duc BV, Salahudeen AB, Eberemu AO, Osinubi KJ (2020) Critical state desiccation induced shrinkage of biomass treated compacted soil as pavement foundation, *Építőanyag. J Silicate Based Compos Mater* 72(2):40–47. <https://doi.org/10.14382/epitoanyag-jsbcm.2020.7>
6. Onyelowe KC, Duc BV, Salahudeen AB (2019) Recycling and reuse of solid wastes; a hub for ecofriendly, ecoefficient and sustainable soil, concrete, wastewater and pavement reengineering. *Int J Low-Carbon Technol* 14(3):440–451. <https://doi.org/10.1093/ijlct/ctz028>
7. American Association of State Highway and Transportation Officials (1993) AASHTO Guide for Design of Pavement Structures, Washington, D.C.
8. Harsh K, Bharath N, Siddesh CS, Kuldeep S (2016) An introduction to artificial neural network. *Int J Adv Res Innov Ideas Edu* 1(5):27–30
9. Shahin MA, Maier HR, Jaksa MB (2002) Predicting settlement of shallow foundations using Neural Networks. *J Geotech Geoenviron Eng ASCE* 128(9):785–793
10. Kolay PK, Rosmina AB, Ling NW (2008) Settlement prediction of tropical soft soil by Artificial Neural Network (ANN). In: The 12th international conference of international association for computer methods and advances in geomechanics, pp 1843–1848
11. Benali A, Nechnech A, Ammar BD (2013) Principal component analysis and Neural Networks for predicting the pile capacity using SPT. *Int Eng Technol* 5(1):87–99
12. Salahudeen AB, Ijimdiya TS, Eberemu AO, Osinubi KJ (2018) Artificial neural networks prediction of compaction characteristics of black cotton soil stabilized with cement kiln dust. *J Soft Comput Civil Eng* 2(3):53–74
13. Warren KW, Kirby TM (2004) Expansive clay soil: a widespread and costly geohazard. *Geoinstitute of the american society civil engineers, Jan, Geostrata*, pp 24–28
14. Salahudeen AB, Ochebo J (2015) Effect of bagasse ash on some engineering properties of lateritic soil. *Jordan J Civil Eng* 9(4):468–476
15. Salahudeen AB, Eberemu AO, Osinubi KJ (2019) Microanalysis and compactive efforts study of black cotton soil treated with cement kiln dust. *Fed Univ. Oye-Ekiti J Eng Technol* 4(1):1–7
16. Zumrawi MME, Awad M (2017) Estimation of subgrade resilient modulus from soil index properties. *Int J Geol Environ Eng* 11(9):856–862
17. BS 1377 (1990) Methods of testing soil for civil engineering purposes. British Standards Institute, London
18. BS 1924 (1990) Methods of tests for stabilized soils. British Standards Institute, London
19. Naderpour H, Kheyroddin A, Ghodrati-Amiri, G (2010) Prediction of FRP-confined compressive strength of concrete using artificial neural networks. *Compos Struct* 92:2817–2829
20. Eidgahee DR, Haddad A, Naderpour H (2018) Evaluation of shear strength parameters of granulated waste rubber using artificial neural networks and group method of data handling. *Scientia Iranica, Int J Sci Technol* 25(1):1–14
21. Golbraikh A, Tropsha A (2002) Beware of q^2 . *J Mol Graph Model* 20(4):269–276
22. Alavi AH, Ameri M, Gandomi AH, Mirzahosseini MR (2011) Formulation of flow number of asphalt mixes using a hybrid computational method. *Constr Build Mater* 25(3):1338–1355

Seepage Behavior Within Embankment Constructed of Mixed Soil with Steel Slag



Katsuyuki Kawai , Kaito Arinishi, Satsuki Kataoka, and Koji Nakashima

Abstract Steel slag is a lower cost solidification material than cement, and its use on geotechnical engineering sites is increasing. However, steel slag is an industrial waste containing a lot of calcium. Since most earth structures are exposed to natural weather conditions, it is a concern that chemical material may leach from the earth structure due to external water head fluctuation. Methods of constructing and maintaining embankment containing chemical materials without leaching are required for the effective use of steel slag. In this study, an embankment model test using steel slag mixed soil was conducted, and rainfall infiltration behavior and alkaline component leachate from the embankment were monitored. Moreover, electric prospecting was concurrently conducted. Consequently, it was found that rainfall infiltration behavior strongly depends on the rainfall pattern, which subsequently influences alkaline leaching. This behavior shows good agreement with results obtained from rainfall infiltration simulation.

Keywords Embankment model test · Steel slag · Unsaturated seepage

1 Introduction

A lot of waste soil is generated during earthmoving construction. Since construction waste soil can cause environmental problems and is costly to dispose of, it is necessary to reuse it as material for earthmoving construction sites. However, when construction waste soil consists of a high-fine fraction and exhibits high-water content, it cannot be used for constructing an earth structure as is. Cement is one solidification material used to improve waste soil. It can generate bonding forces between soil particles; change grain size gradation; and improve consistency, shear strength, compressibility, and other characteristics of low-quality soil. Steel slag is a lower cost solidification

K. Kawai (✉) · K. Arinishi · K. Nakashima
Kindai University, 3-4-1 Kowakae Higashi, Osaka, Japan
e-mail: kkawai@civileng.kindai.ac.jp

S. Kataoka
Kobe University, 1-1 Rokkoudai-cho Nada-ku, Kobe, Japan

material than cement, and its effects have been studied [1–4]. It has been increasingly used in civil engineering in Japan for uses including road subgrade material and asphalt concrete aggregate [5–8]. Steel slag is generated during the process of steel manufacturing and is often an industrial waste. If steel slag could be applied to earthworks as a solidification material, the volume of both construction waste soil and steel slag could be reduced. Steel slag contains alkaline components. Earth structures, such as road and railway embankment, are exposed to natural weather conditions and show fluctuation in internal soil moisture distribution due to rainfall and evapotranspiration. When road embankment is constructed with a mixture of construction waste soil and steel slag, careful attention to leachate is required. This study aims to evaluate the effective use of steel slag as a solidification material for low-quality soil by using an embankment model constructed with a mixture of construction waste soil and steel slag. Seepage behavior within the embankment and alkaline leachate are also monitored.

2 Embankment Model Test

Figure 1 shows a schematic view of the embankment model constructed with a mixture of construction waste soil and steel slag. Construction waste soil used for this study is a typical soil categorized as Kobe Group that exhibits a high slaking

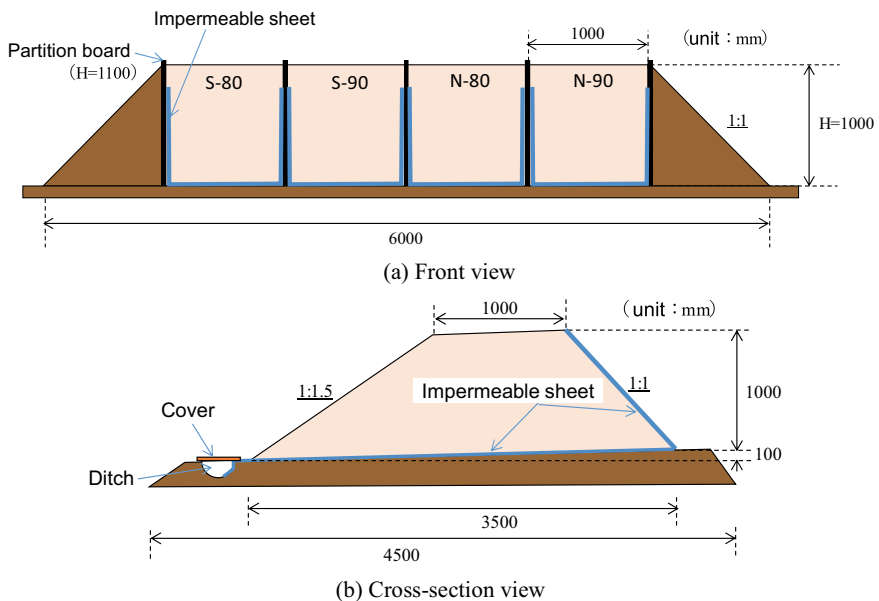


Fig. 1 Embankment model constructed with a mixture of construction waste soil and steel slag

property. Two kinds of steel slag were employed and mixed at a volumetric ratio of 1:3 to the construction waste soil. Figure 2 shows the particle grading curves of construction waste soil and steel slag mixed soils. These show that particle gradation can be improved by steel slag and that there is no difference in particle gradation between the two steel slag mixed soils. Table 1 summarizes the properties of steel slag mixed soils. Each steel slag mixed soil was soaked in distilled water until a steady-state pH value of the initial condition was obtained. Figure 3 shows compaction curves of the steel slag mixed soils. Figure 4 shows changes in unconfined strength with curing days. These figures demonstrate that unconfined strength increases with curing time and reaches its maximum value after one month. The embankment model

Fig. 2 Particle grading curves

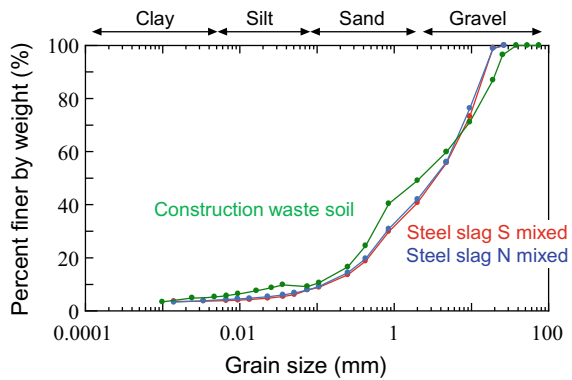


Table 1 Steel slag mixed soil properties

	Steel slag S mixed	Steel slag N mixed
Particle density	2.878(g/cm ³)	2.890(g/cm ³)
Initial pH	12.4	12.2

Fig. 3 Compaction curves

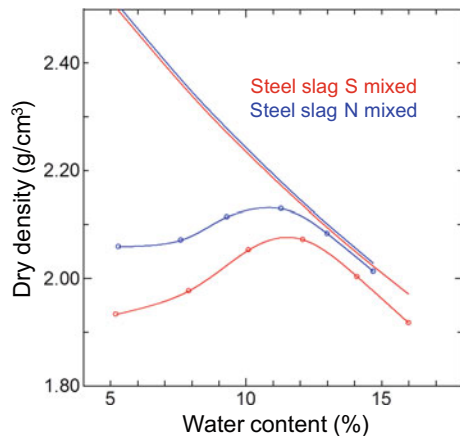
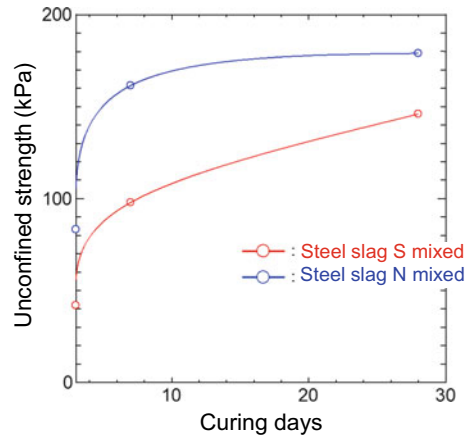


Fig. 4 Changes in unconfined strength



was partitioned with boards and an impermeable sheet and compacted at 80 and 90% degrees of compaction in each steel slag mixed soil. The steel slag embankment models were labeled S-80, S-90, N-80, and N-90. The lab-permeability tests were conducted on steel slag B mixed soil. The measured permeability was 1.91×10^{-4} and 4.18×10^{-6} (m/sec) for N-80 and N-90, respectively. Lower permeability was obtained with a greater degree of compaction. The embankment was 1000 mm high with a 1000 mm crown width. Asymmetrical slopes of 1:15 and 1:1 were utilized, and steep slopes were covered with an impermeable sheet to collect and measure the pH of leached water from the embankment in a ditch at the mild slope toe. Because the embankments were exposed to natural weather conditions, such as rainfall and evaporation, the seepage behavior of infiltrated rainwater was monitored by soil moisture meters and tensiometers. ECH₂O EC-5 soil moisture meters, manufactured by Decagon Devices Inc., were used. Two kinds of tensiometers were used: A DIK-3046 with an 8ch data logger and an i-Tensiometer (both manufactured by Daiki Soil and Moisture). The i-Tensiometer is a codeless type with a built-in data logger, which offers improved battery consumption suitable for long term monitoring. Figure 5 summarizes the monitoring positions. Tensiometers were set at depths of 15 and 25 cm from the slope surface. The shallower area exhibited a more drastic fluctuation of suction, and i-Tensiometers were set here. The numbers shown in Fig. 5b indicate the channel number of the soil moisture meters.

Electric prospecting was also conducted. Electric prospecting is a type of geophysical prospecting that allows determination of the electric resistibility distribution in embankment cross sections. The apparent electric resistibility can be calculated by attenuation from the potential difference between transmission electrodes (C_m , C_n) to the potential difference between receiving electrodes (P_m , P_n) (shown in Fig. 6). Here, apparent electric resistibility denotes the average electric resistibility along the path from transmission electrodes to receiving electrodes. The distribution of true electric resistibility can be obtained by back analysis, considering the form of the ground. There are several methods to select these four electrodes, and measurable

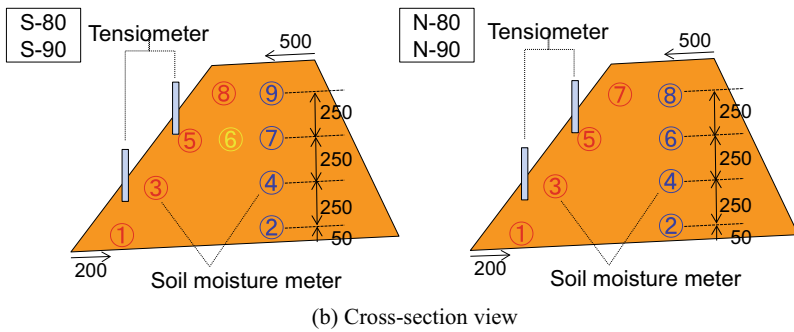
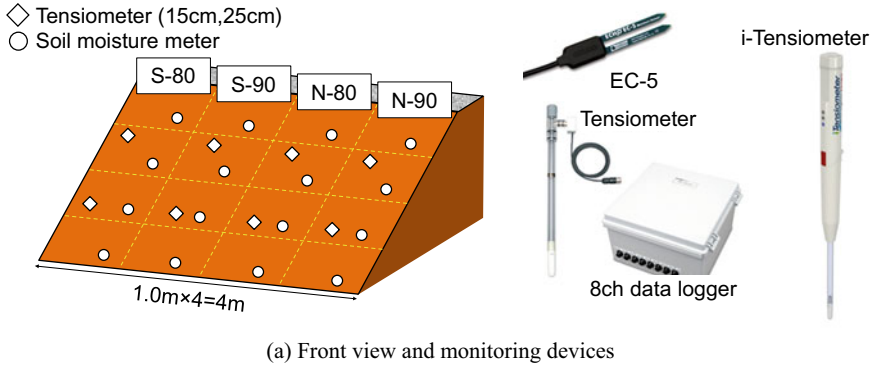


Fig. 5 Monitoring positions

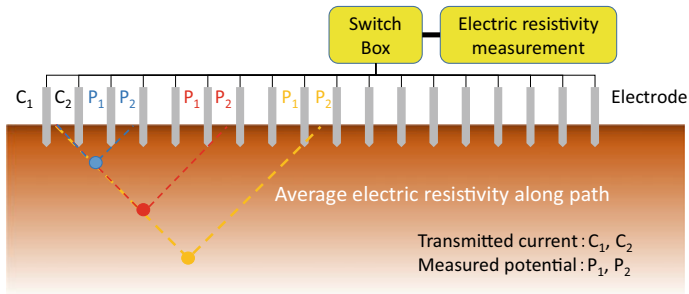


Fig. 6 Electric prospecting

depth and resolution are dependent on the electrode array method. In this study, the electrodes were aligned 10 cm apart from each other on the embankment, and a dipole-dipole array method was adopted.

3 Test Results and Discussions

Figure 7 shows soil moisture changes for S-80 and S-90 in January. January is winter in Japan, and there are hardly any rainy days. Therefore, soil moisture tends to decrease on the whole without rain. The soil moisture meters at the bottom of the embankment, i.e., channels 1 and 2, showed higher values than the other soil moisture meters. The more densely compacted embankment, namely S-90, was expected to have higher soil water retentivity, judging from the comparison of the average degree of saturation between Fig. 7a and b. The infiltrated rainwater drains from the slope toe. Therefore, a decrease in soil moisture at channel 1, around the slope toe, occurred earlier than that at channel 2, around the bottom of the embankment. Moreover, soil moisture around the slope surface, namely channels 1, 3, 5, and 8, showed a drastic increase due to rainfall on January 31st, while other soil moisture measurements hardly changed. Rainwater was found unable to infiltrate deeper after a long term of no rainfall. Figure 8 shows the changes in water pressure measured by tensiometers. Suction, namely negative water pressure, in the middle of the slope in the upper position increased without rainfall. Electric prospecting was conducted on January 14th, shown by the solid lines in Figs. 7 and 8. Figure 9 shows the distribution of electrical resistibility obtained from the electric prospecting. The lower electrical resistibility, expressed by a bluer color, can be regarded as signifying higher soil moisture. Areas of higher soil moisture appeared around the slope toes, and this distribution is identified as being due to the drainage process.

Figure 10 shows the changes in soil moisture in April. During this period, there were some rainy days. Periodic weather changes like this are typical in Japan's early spring. The change in channel 5 showed that the soil moisture around the slope surface

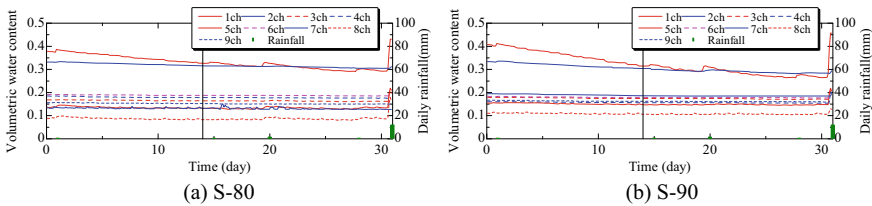


Fig. 7 Changes in soil moisture (January 2019)

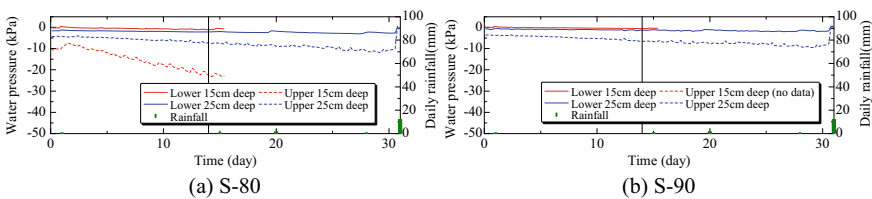


Fig. 8 Changes in water pressure (January 2019)

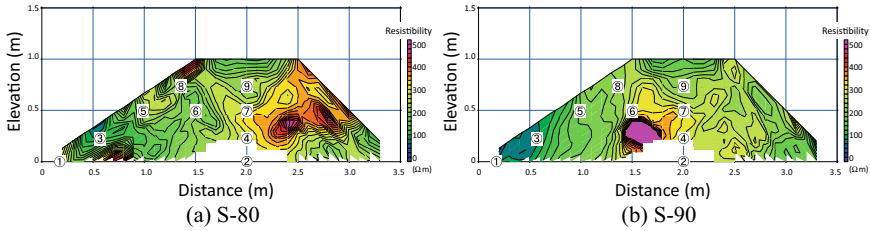


Fig. 9 Distribution of electrical resistivity (January 14th, 2019)

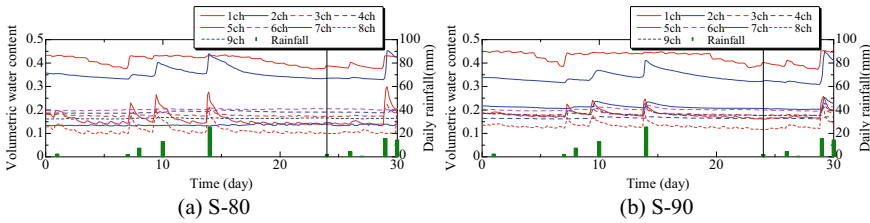


Fig. 10 Changes in soil moisture (April 2019)

drastically increased under rainfall and gradually decreased after rainfall. From this, we can say that rainwater can easily infiltrate, but is difficult to drain. Therefore, soil moisture at the bottom of the embankment, namely channel 2, increased with the next rainfall, before the soil moisture had recovered from the prior rainfall. This indicates that infiltrated rainwater reaches the bottom of the embankment and raises the phreatic surface. This tendency was more obvious in the more densely compacted embankment, S-90. Figure 11 shows changes in water pressure. Suction dissipated under each rainfall, even in the middle of the slope (Fig. 11a). Electric prospecting was conducted on April 24th. It rained for a few hours shortly before the electric prospecting. Figure 12 shows the distribution of electrical resistivity. A higher soil moisture distribution was found on the whole in Fig. 12, compared to Fig. 9. Particularly around the slope surface and crown, soil moisture was relatively high. Major differences between the winter and the spring-based results are attributed to rainfall patterns. There are periodical rainfall events in the spring, while there are hardly any rainfall events in the winter. It takes several days for infiltrated rainwater to drain,

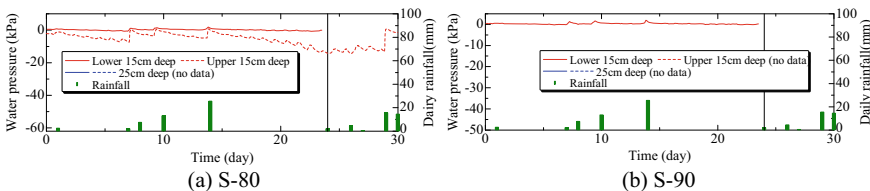


Fig. 11 Changes in water pressure (April 2019)

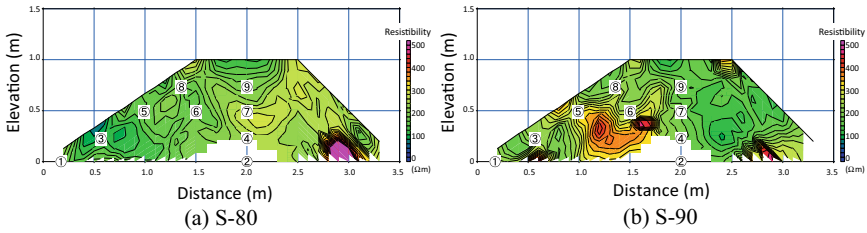


Fig. 12 Distribution of electrical resistivity (April 24th, 2019)

even on small embankments like in the scale of this study. Periodic rainfall maintains embankments at high-moisture contents. On the other hand, a drying process is observable in the winter under no rainfall.

Figure 13 shows the measured pH of leachate water from the embankment after a certain level of rainfall. Red and blue lines in the figure indicate the initial pH of each embankment material. A gradually decreasing trend, though not entirely clear, is suggested with time under little rainfall. However, high pH is observed after a large amount of rainfall. This behavior is attributed to the origin of leachate water within the embankment.

Rainfall infiltration simulation was conducted to explain the seepage behavior of infiltrated rainwater and the leachate behavior of alkaline components in the framework of unsaturated soil mechanics. The soil/water/air/soluble material coupled finite element analysis code, DACSAR-MP_ad [9], was used for simulation. This analysis code can express the deformation of an earth structure, seepage behavior of groundwater, and transfer of soluble material simultaneously. Rainfall infiltration into embankment constructed with soil containing a small amount of soluble material was simulated. Detailed simulation conditions and results are described in another paper [10], but typical simulation results are introduced here. Figures 14 and 15 indicate distribution changes in the degree of saturation and relative concentration under 10 h rainfall with 5 mm/h rainfall intensity. The average permeability of

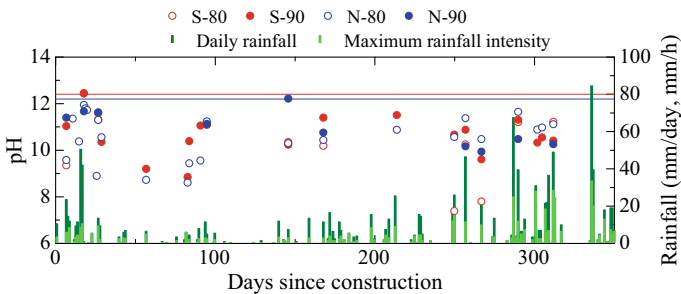


Fig. 13 Measured pH of water leached from the embankment

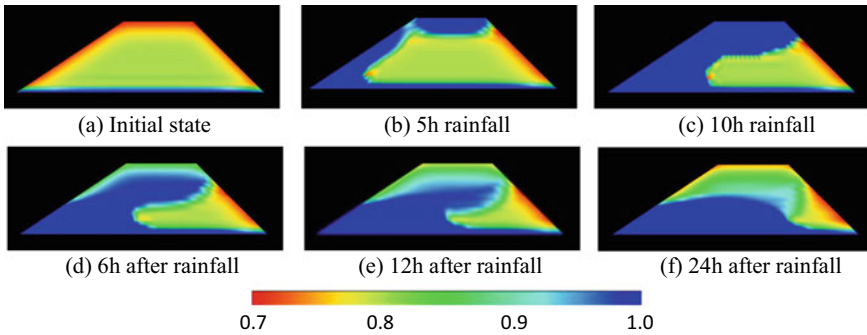


Fig. 14 Degree of saturation distribution obtained from the rainfall infiltration simulation

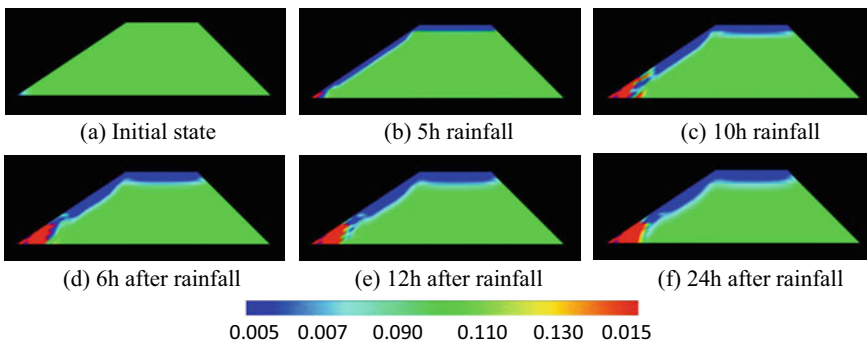


Fig. 15 Relative concentration distribution obtained from the rainfall infiltration simulation

N-80 and N-90 was adopted in this simulation. Two types of seepage flow of infiltrated rainwater were determined. Rainwater infiltrating through the crown flowed downward vertically due to elevation head difference. On the other hand, rainwater infiltrating through the slope surface tended to flow toward the slope toe parallel to the slope, and not downward vertically. This is because unsaturated permeability depends on the degree of saturation. Infiltrated rainwater increases soil moisture around the slope surface and indicates an increase in permeability at this location. Consequently, a relatively higher permeability area was generated around the slope surface, and infiltrated rainwater flowed toward the slope toe parallel to the slope. This tendency depends on both rainfall intensity and the permeability of embankment material. Flow toward the slope toe parallel to the slope was more obvious under stronger rainfall intensity and lower permeability. Therefore, a relatively low soil moisture area was left beneath the slope shoulder (shown in Fig. 14b). Consecutive rainfall causes the expansion of the high soil moisture area toward the bottom of the embankment (Fig. 14c). Infiltrated rainwater is redistributed, even after rainfall (shown in Fig. 14d and e), and finally reaches the bottom to form the phreatic surface (Fig. 14f). The distribution of electric resistibility shown in Figs. 9 and 12 can be

regarded as the redistribution process of infiltrated rainwater after rainfall. Soluble material is advected by groundwater flow. Both infiltrated rainwater flowing around the slope surface and that forming the phreatic surface are finally drained from the slope toe. Therefore, soluble material transfers from the active flow area to the slope toe (shown in Fig. 15). Leaching of alkaline components after rainfall, as shown in Fig. 13, is explainable by this. However, detailed identification of embankment material properties and further simulations are required to predict alkaline leachate behavior.

4 Conclusions

In this study, the embankment model test was conducted to effectively reuse steel slag as a solidification material for earthmoving construction. Seepage behavior of infiltrated rainwater and the pH of leached water were measured, while electric prospecting was also conducted on the embankment model. Consequently, the following conclusions were obtained.

- (1) Rainfall infiltration occurs easily, while drainage of infiltrated rainwater is difficult.
- (2) Infiltrated rainwater tends to flow around the slope surface, as unsaturated permeability is greater in soil with a higher degree of saturation. Consequently, the seepage flow of infiltrated rainwater is categorized into two types: (1) flow around the slope surface parallel to the slope and (2) vertical downward flow. For the former, rainwater drains early, and for the latter, rainwater drains after forming the phreatic surface at the bottom of the embankment.
- (3) The distribution of electric resistibility obtained by electric prospecting can be explained by rainfall infiltration simulations.
- (4) Alkaline components were leached after rainfall. Since alkaline components are advected by groundwater flow, it is important to investigate seepage flow. However, it is difficult to predict leachate behavior, and further investigation based on both monitoring and simulation is required.

References

1. Malasavage NE, Jagupilla S, Grubb DG, Wazne M, Coon WP (2012) Geotechnical performance of dredged material-steel slag fines blends: laboratory and field evaluation. *J Geotech Geoenviron Eng* 138(8):981–991
2. Manso JM, Ortega-López V, Polanco JA, Setién J (2013) The use of ladle furnace slag in soil stabilization. *Constr Build Mater* 40:126–134
3. Akinwumi I (2014) Soil modification by the application of steel slag. *Periodica Polytech Civil Eng* 58(4):371–377
4. Goodarzi AR, Satimi M (2015) Stabilization treatment of a dispersive clayey soil using granulated blast furnace slag and basic oxygen furnace slag. *Appl Clay Sci* 108:61–69

5. Hirai S, Mizutani T, Kikuchi Y, Kawabata Y (2012) Study on the effect of mixing condition on mechanical properties of mixture of dredged soil and steel slag. *Rep Port Airport Res Inst* 51(3):77–106 (in Japanese)
6. Honda H, Hayashi M, Tanishiki K, Tsuchida T, Kameyama T, Ko C, Sugihara H, Kumagai T (2014) The restoration method of the artificial tidal flat using dredged soil and converter slag. *J JSCE B3* 70(2):744–749 (in Japanese)
7. Kiso E, Tsuji M, Ito K, Nakagawa M, Gomyo M, Nagatome K (2008) Method of dredged soil improvement by mixing with converter steel-making slag. *J Ocean Eng* 24:327–332 (in Japanese)
8. Matsuda H, Ishikura R, Wada M, Kitayama N, Beak W, Tani N (2012) Aging effect on the physical and mechanical properties of granulated blast furnace slag as lightweight banking. *Jpn Geotech J* 7(1):33–349 (in Japanese)
9. Nomura S, Kawai K, Iizuka A, Tachibana S, Kanazawa S (2012) Mathematical model of soil/water air coupled problem for unsaturated soils considering mass transfer within pore-water. In: *Proceedings of 5th Asia-Pacific conference on unsaturated soils*. pp 287–292
10. Kawai K, Arinishi K, Kataoka S, Nakashima K (2020) Rainfall infiltration simulation on embankment containing soluble material. In: *Proceedings of 4th European conference on unsaturated soils* (in press)

The Water-Repellent Ability of Road Pavement Material Stabilized with Synthetic and Natural Polymers



Korakod Nusit, Peerapong Jitsangiam, and Prinya Chindaprasirt

Abstract Polymer-stabilized soil continues to be the widely used treatment technique for the road pavement materials. Based on the previous research, the uses of polymer in soil stabilization generally focused on strength and stiffness improvements. Nevertheless, the performance of pavement material is greatly influenced by the moisture ingress, temperature fluctuation, and climate change. In this research, the waterproof ability of soil stabilized with synthetic rubber and natural rubber was investigated. The natural rubber (NR) is one of the natural polymers, which is readily available in Thailand. The styrene butadiene rubber (SBR) is chosen to represent the synthetic rubber in this research. In addition, the performances of soil modified with styrene acrylic (SA) were also evaluated. The SBR and SA are popularly employed as the concrete superplasticizer; they are commonly used to improve the bond of cement paste and waterproof ability of structural concrete. In this research, the optimum dosages of SA, SBR, and NR were determined during the mix design phase. The strength and capillary rise tests of the stabilized soil were conducted and characterized. The images taken from scanning electron microscope were used to evaluate the micro-structural interaction of polymer-stabilized soils. Test results indicate that the synthetic polymers, SA, and SBR, can be used to enhance the strength performance of soil. However, the waterproof abilities of the synthetic polymer-stabilized soils and the compacted soil without stabilizing agent are similar. The NR-stabilized soil showed the poorest performances among the studied materials in this research. On the other hand, the highest 7-day strength and lowest capillary rise values were observed from the cement-stabilized specimen.

Keywords Polymer-stabilized soil · Quarry by-product · Natural rubber · Styrene butadiene rubber · Styrene acrylic

K. Nusit (✉)

Department of Civil Engineering, Naresuan University, Phitsanulok, Thailand

e-mail: korakodn@nu.ac.th

P. Jitsangiam

Department of Civil Engineering, Chiang Mai University, Chiang Mai, Thailand

P. Chindaprasirt

Department of Civil Engineering, Khon Kaen University, Khon Kaen, Thailand

1 Introduction and Background

The road network in Thailand shows signs of fast deterioration due to the extreme weather and the effects of climate change. Literature review indicates that all pavement layers (materials) are susceptible to moisture damages over time and increases in traffic [1, 2]. The previous research strongly suggests that potential climate change would have the effects on pavement infrastructure [3–7]. Accordingly, to minimize these potential impacts, the innovative pavement material is urgently required. Currently, there is no pavement material that effectively resists the damages from moisture ingress [8]. In order to prevent the moisture effects caused by extreme weather, an innovative pavement base material with hydrophobic property is required. Tillman et al. [9] discovered the ‘hydrophobic’ behaviors of some geotechnical materials. The authors established the term ‘subcritical water repellency’ to differentiate the studied soils from highly water-repellent (hydrophobic) soils. The hydrophobic soil is defined as the soils which water infiltration and retention are completely restricted [9].

Polymer additives also increase the degree of water repellent of treated soils [10]. Polymers are large molecules which consist of long hydrocarbon chains. They are easily modified which leads to the endless products of polymer. This highlights the ideal of polymer-stabilized pavement base with hydrophobic behaviors. Natural rubber (NR) is the natural polymer and used extensively in producing many products. The processed NR normally has high resilient and waterproof ability. In Thailand, the soil mixed with NR is employed in many applications, e.g., use as the impermeable wall of agricultural pond, and employ as pavement materials. A so-called natural rubber modified soil cement has been introduced and researched by Thai government for a couple years [11]. However, other additives, such as synthetic polymers and surfactants, are normally added into the NR modified soil cement to enhance its performances. Styrene acrylic (SA) and styrene butadiene rubber (SBR) copolymers are commonly used as the concrete superplasticizers. The SA and SBR are added into the concrete mixture to increase the workability and reduce the air voids of concrete. Since the applications of NR, SA, and SBR to the pavement materials are still limited and doubtful; therefore, this project aims to characterize and examine the performances of polymer-stabilized pavement material and its hydrophobic property. The optimum dosages of polymers were determined by the modified Proctor tests. Then, the strength of polymer-stabilized soil was examined by the unconfined compressive strength (UCS) test. Finally, the capillary rise tests were conducted to characterize the hydrophobic behaviors of the stabilized soils.

2 Materials and Mix Design

2.1 Parent Material

The quarry by-product soil from the local quarry in Sukhothai province, Thailand, was used as parent material in this research. The X-ray diffraction (XRD) test result indicates that the selected parent material is classified as limestone. Figure 1 illustrates the particle size distribution (PSD) curve of the parent material while the engineering properties of the selected soil are summarized in Table 1. Figure 2 presents

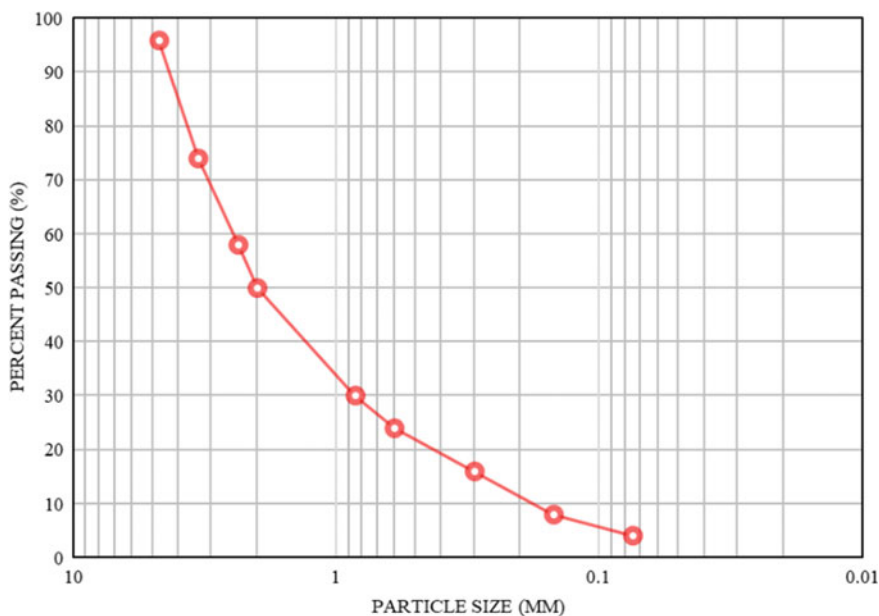


Fig. 1 Gradation of the parent material

Table 1 Engineering properties of the parent material

Geotechnical properties	Test standards	
Liquid limit (%)	ASTM D4318	20
Plastic limit (%)	ASTM D4318	24
Plastic index (%)	ASTM D4318	4
California bearing ratio (%)	ASTM D1883	6
USCS group	ASTM D2487	SW
Maximum dry density (g/cm ³)	ASTM D1557	2.20
Optimum moisture content (%)	ASTM D1557	8.00
UCS (MPa)	ASTM D1633	0.14

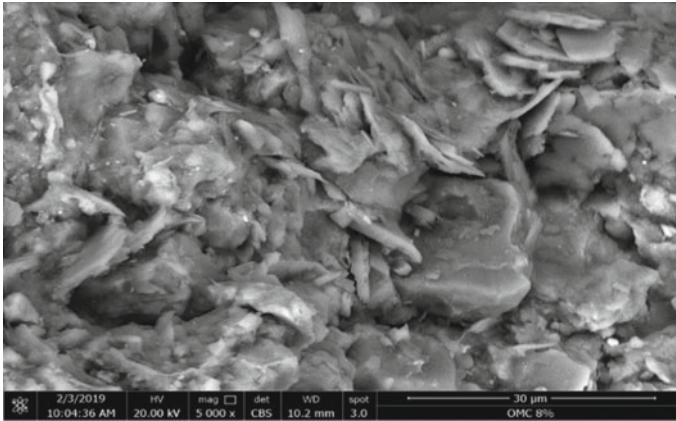


Fig. 2 Image of compacted parent material taken by SEM

Table 2 Polymers used in this research

	Form	Type	pH	Total solid (%)	Ionic nature
NR	Concentrated latex (high ammonia)	–	10	60	Anionic
SA	Liquid polymer	Dispersible	7–9	54–56	Anionic
SBR	Liquid polymer	Dispersible	8.5–11	45–47	Anionic

the soil texture image after it has been compacted at the optimum condition. The image was taken by the scanning electron microscope (SEM) at the magnitude of $\times 5000$.

2.2 Polymers

The important information of polymers used in this research is summarized in Table 2.

2.3 Mix Design of Polymer-Stabilized Soils

The appropriate dosages of polymers used as the stabilizing agent were determined by the modified Proctor test according to ASTM D558. Table 3 summarizes the mixture proportion at the optimum condition or densest state (at maximum dry density (MDD) or optimum moisture content (OMC)) of each polymer-stabilized soil characterized in this research.

Table 3 Mix proportion of polymer-stabilized soils

Type of polymer-stabilized soil	Soil (g.)	Cement (%)	Liquid (%)		
			Water	Polymer	Surfactant
NR-stabilized soil	3000	2	2.0	4.0	2.0
SA-stabilized soil	3000	–	2.5	2.5	–
SBR-stabilized soil	3000	–	3.0	3.0	–

It can be seen from Table 3 that all types of polymer were mixed with water prior to adding them into the parent soils. According to the design guideline, the NR-stabilized soil required few quantities of cement to increase the material bonding [11]; therefore, two percent of cement was employed in this research. Moreover, the surfactant is mandatory ingredient for NR modified soil cement. The concentrated NR will not be well distributed in the soil matrix without the dispersive agents such as surfactant. The non-ionic surfactant used in this research is Nonylphenol Ethoxylate 9 mol (NP-9). Figure 3 illustrates the moisture-density relationship curves obtained from the modified Proctor test.

The moisture-density relationship curves of parent material (quarry by-product) and cement-stabilized soil were also demonstrated in Fig. 3. The synthetic polymer-stabilized soils (SA and SBR) required less amount of compacted moisture than the other to achieve the maximum dry density. However, the natural polymer-stabilized soil (NR) displayed the lowest MDD values among the soil group presented in Fig. 3.

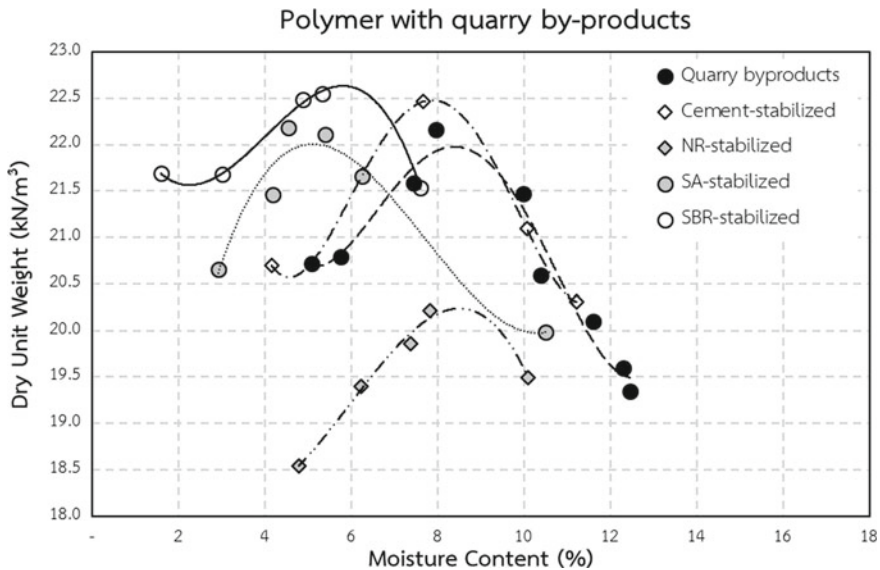


Fig. 3 Water-density relationship curves from modified proctor test

3 Laboratory Testing

3.1 Unconfined Compressive Strength Test

The UCS test in this research was conducted based on ASTM D1633 [12]. After the specimens were prepared in the Proctor mold, they were placed in two different environments for 7 days for curing purpose. The specimens contain cement binder were situated in the controlled humidity and temperature chamber for 7 days prior to the UCS test. This group composes of the cement-stabilized soil and NR-stabilized soil. On the other hand, the SA-stabilized and SBR-stabilized specimens were left in the open-air environment for 7 days before test. Figures 4 and 5 present the UCS test results of compacted soil, polymer-stabilized soils and cement-stabilized soil determined from this research. The UCSs of polymer-stabilized soils at different moisture contents are shown in Fig. 4, while Fig. 5 illustrates the UCS test results at various dry density values.

It can be seen from Figs. 4 and 5 that the strengths of both natural and synthetic polymer-stabilized soils are strongly depended on the compacted moisture content and dry density. The synthetic polymers, SA and SBR, can be successfully used to enhance the strength of quarry by-product soils. Test results show that the strength value of synthetic polymer-stabilized soils developed higher than that required for the cement-stabilized subbase layer (0.7 MPa specified by the Department of Highway

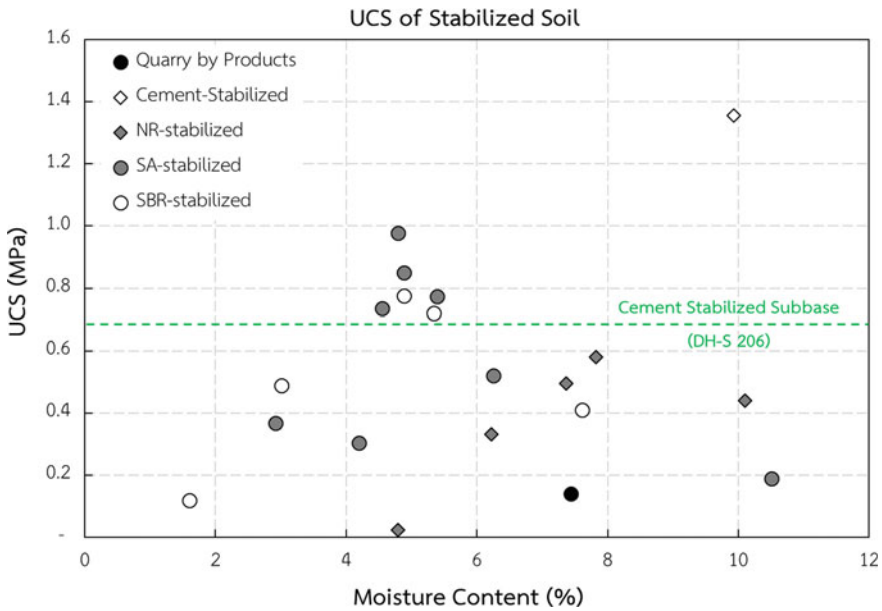


Fig. 4 UCS of polymer-stabilized soils at different moisture contents

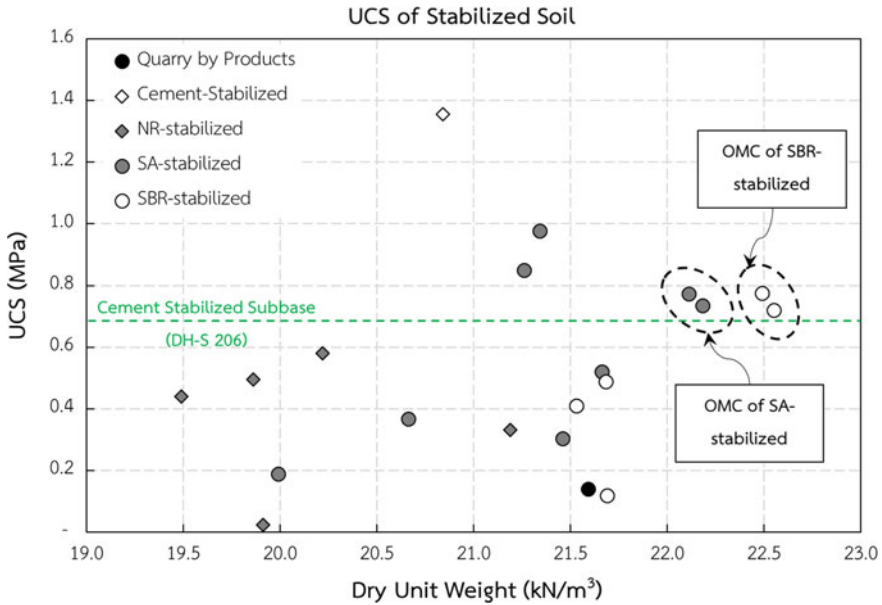


Fig. 5 UCS of polymer-stabilized soil at different dry densities

[11]). To employ the materials as pavement subbase, the other performance tests are also required by the Department of Highway [11], i.e., resilient modulus test, fatigue test, indirect tensile strength test, and permeability test. However, the highest strength of SA-stabilized soil was not observed at the densest state of material (optimum condition) as illustrated by Fig. 5. The previous research reports that the compacted moisture equivalents to OMC is needed to obtain the maximum strength of cement-stabilized soil [13]. For the compacted soil without stabilizing agent, its strength development behavior with respected to various moisture content is complicated. The pore space, pore connection, and degree of saturation of the compacted soil usually play the important roles in strength development behaviors. These parameters may cause the variations in strength of polymer-stabilized soil. The effects of these parameters to the strength of polymer-stabilized soil are, therefore, required to be further investigated in future research.

The SEM images of 7-day polymer-stabilized soils are displayed in Fig. 6. Figure 6a and b illustrate the SBR-stabilized soil image at $\times 5000$ magnitude and SA-stabilized soil image at $\times 2000$ magnitude, respectively. The NR-stabilized soil image at $\times 5000$ magnitude is presented in Fig. 6c, while Fig. 6d shows the NR-stabilized soil image at $\times 120$ magnitude.

The dried synthetic polymer seems to blend with parent material much better than those observed from the dried NR polymer. Figure 6a and b show that the synthetic polymers are well distributed in the soil matrix, while NR polymer formed the rubber lumps and stayed apart from the soil particles (Fig. 6c and d). The separation between

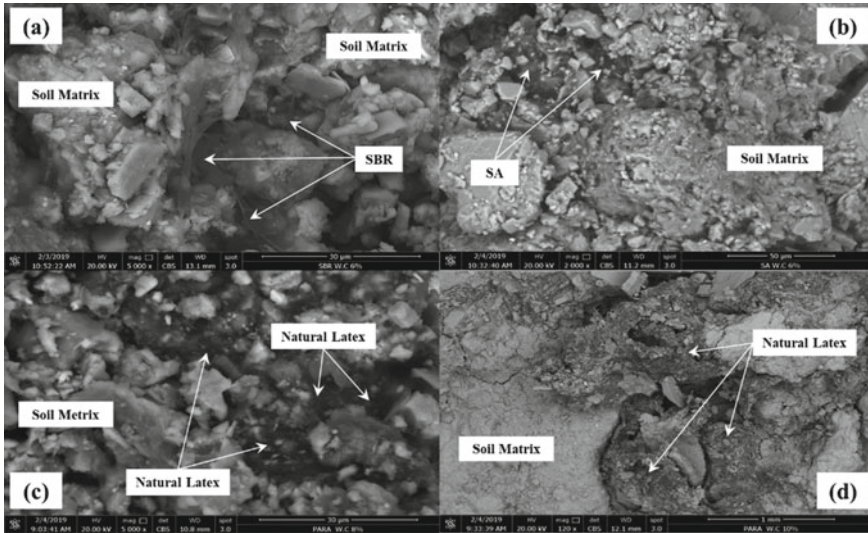


Fig. 6 SEM images of polymer-stabilized soils

NR polymer and the soil matrix may be the cause of strength reduction observed from the NR-stabilized soil (see Fig. 4). Moreover, the inhomogeneity also reduces the relative density (D_r) of the compacted soil, which made the NR-stabilized soil lighter than those measured from the other compacted specimens in this research (see Fig. 5).

Figure 6b shows that dried SA polymers wrapped around the small particles of soil and glued them to the large particles. On the other hand, dried SBR polymers created the web-like linkages and held the soil particles together as illustrated in Fig. 6a. The formations of these synthetic polymers in the soil matrix led to the increase in strength of the polymer-stabilized soils.

3.2 *Hydrophobic Property of Polymer-Stabilized Soils*

The capillary rise test was performed to evaluate the water repellence of polymer-stabilized soil in this research. The capillary rise test was conducted according to AS 1141.53 [14].

Based on the test standard, the dried cylindrical specimen is placed into the tray that filled with water to a depth of 10 mm (see Fig. 7). The height of water rises from the specimen base after 72 h shall be reported as the capillary height (h) value. However, in this research, the capillary heights at different time steps were also recorded and reported. The test standard recommends leaving the specimen in the water tray for 72 h prior to the final measurement. The capillary heights of specimens in this research, therefore, were measured up to 2 h since the compacted soil specimen was completely disintegrated by the absorbed water. Accordingly, the capillary rise

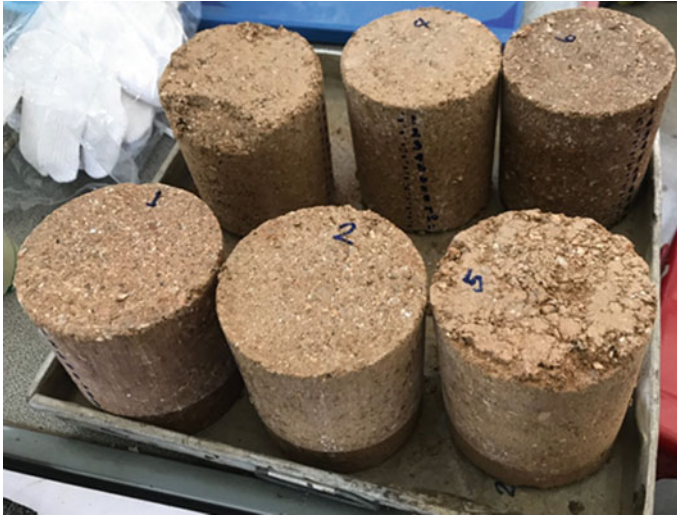


Fig. 7 Capillary rise tests

(CR) and water absorption (*A*) of each specimen at 2 h were used for the analysis. The capillary rise (CR) and water absorption (*A*) of test specimens can be determined from Eqs. (1) and (2), respectively [15].

$$CR = \frac{h}{H} \times 100 \tag{1}$$

$$A = \frac{m_{dmp} - m_{dry}}{m_d} \times 100 \tag{2}$$

In which, *h* is the capillary height at different time steps, *H* is the height of specimen, *m_{dry}* is the mass of oven-dried specimen at 50 °C (before capillary rise test), *m_d* is the mass of oven-dried specimen at 105 °C (after capillary rise test), and *m_{dmp}* is the mass of specimen after placed in the water tray for 2 h.

Table 4 summarizes the test results after 2 h in this research. Figure 8 demonstrates the capillary heights at various time steps of specimens cured for 7 days prior to the

Table 4 Capillary rise test results after 2 h

Test No.	Specimens	CR (%)	A (%)
1	Compacted soil	77.3	7.4
2	Cement-stabilized soil	54.6	13.3
3	NR-stabilized soil	100.0	12.3
4	SA-stabilized soil	58.2	11.1
5	SBR-stabilized soil	86.4	10.8

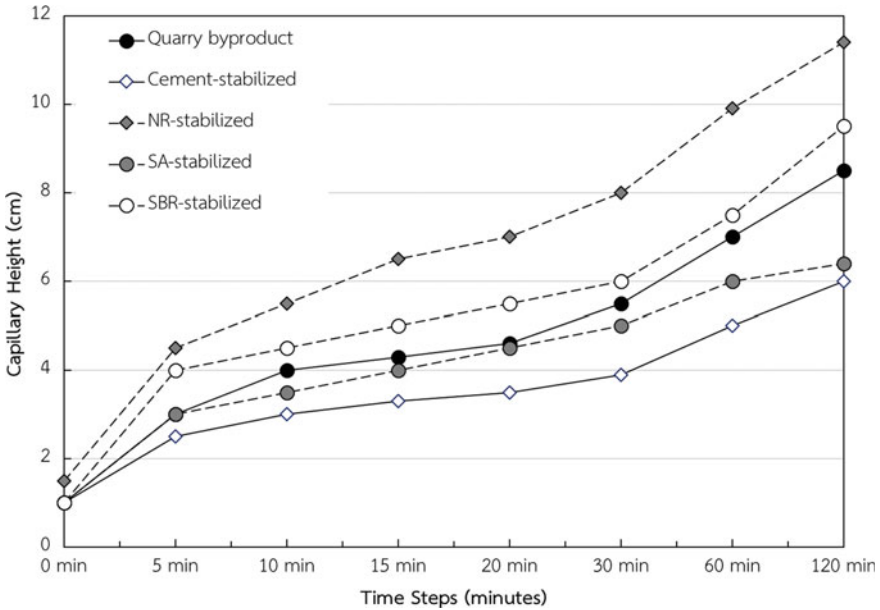


Fig. 8 Capillary heights of test specimens at different time steps

tests. The capillary heights of cement-stabilized soil and compacted soil are also shown in Fig. 8.

Figure 8 shows that the capillary height of NR-stabilized soil developed faster than the other, while capillary height of cement-stabilized soil expanded slowest among the test specimens. The height of water reached the top of NR-stabilized specimen (11 cm) after it left in the water tray for about 2 h. This finding confirms the test results in the previous section that NR-stabilized soil is the most porous media compared to the other compacted materials. The SA-stabilized soil and SBR-stabilize soil exhibited similar capillary rise behaviors with the compacted parent material.

The water absorption reported in Table 4 indicates the amount of water consumed by each specimen after the capillary rise tests were completed. The similar values of water absorption (*A*) were observed from the cement-stabilized and polymer-stabilized soil, although, the capillary height of each specimen rose to a different level at the same time step. The ongoing hydration process of cement-stabilized material might be the cause of high percentage of water absorption with low level of capillary rise. However, the real cause of this behavior should be examined in future research.

4 Conclusions and Recommendations

The strength performance and hydrophobic behavior of natural and synthetic polymer-stabilized soil were characterized in this research. The natural rubber (NR) represents the natural polymer, while the synthetic polymers used in this research are styrene acrylic (SA) and styrene butadiene rubber (SBR). The strength performance of the selected parent material can be enhanced by SA and SBR. However, other performance tests are required by the specification, this includes resilient modulus test, indirect tensile strength test, fatigue test, and permeability test. The synthetic polymers, therefore, can be used to increase the strength of quarry by-product material in this research. The hydrophobic properties of synthetic polymer-stabilized soils are analogous to the compacted soil without stabilizing agent.

To develop the innovative pavement material with hydrophobic property, other types of polymer should be studied. The mixing method, form of polymer additive, and dosage of polymer used in future research shall be varied to gain more understandings on the responses of polymer-stabilised pavement material.

Acknowledgements The authors wish to express their gratitude to the Thailand Research Fund (TRF) scheme ‘TRF Research Grant for New Scholar (2019-2020)’ for the financial support in this project (MRG6280053). Special thanks are extended to the Dr. Nanticha Kalapat for the testing facilities and relevant information to this research. Moreover, the research team of the Civil Engineering Department at Naresuan University, Chiang Mai University and Khon Kaen University, Thailand are also gratefully acknowledged for providing overview guidance and valuable inputs into this work.




References

1. Meyer M, Amekudzi A, O’Har JP (2010) Transportation asset management systems and climate change. *Transp Res Rec* 2160:12–20
2. Meyer M, Weigel B (2011) Climate change and transportation engineering: preparing for a sustainable future. *J Transp Eng* 137(6):393–403
3. Austroads (2004) Impact of climate change on road infrastructure. AP-R243, Austroads, Sydney, NSW
4. Austroads (2004) Pavement design—a guide to the structural design of road pavement (2nd revision). Austroads, Sydney, NSW
5. Austroads. Impact of climate change on road performance: updating climate information for Australia. AP-R358/10, Austroads, Sydney, NSW
6. Mills BN, Tighe SL, Andrey J, Parm S, Huen K (2007) The road well-traveled: implications of climate change for pavement infrastructure in Southern Canada. Final technical report, University of Waterloo, Canada
7. U.S. Climate Change Science Program (2008) Impacts of climate change and variability on transportation system and infrastructure: gulf coast study, phase I. Department of Transportation, Washington, D.C.
8. Jitsangiam P, Nikraz H (2013) Characteristics and performance of cement modified-base course material in Western Australia. *J Mater Civ Eng* 26(9):04014056. [https://doi.org/10.1061/\(ASCE\)MT.1943-5533.0000930](https://doi.org/10.1061/(ASCE)MT.1943-5533.0000930)

9. Tillman R, Scotter D, Wallis M, Clothier B (1989) Water repellency and its measurement by using intrinsic sorptivity. *Aust J Soil Res* 27(4):637–644
10. Raucuh AF, Katz LE, Lijstrand HM (1993) An analysis of the mechanisms and efficacy of three liquid chemical soil stabilizers, vol 1. Texas Department of Transportation, Texas
11. Department of Highway (2017) Specification of natural rubber modified soil cement base course (in Thai). Bureau of materials, analysis and inspection, Department of Highway, Bangkok, Thailand
12. ASTM (2000) Standard test methods for compressive strength of molded soil-cement cylinders. ASTM D1633, ASTM International, West Conshohocken, PA
13. Nusit K, Jitsangiam P, Kodikara J, Bui HH, Leung GLM (2016) Advanced characteristics of cement-treated materials with respect to strength performance and damage evolution. *J Mater Civ Eng* 29(4):04016255
14. Standard Australia (1996) Methods for sampling and testing aggregates Absorption, swell and capillary rise of compacted materials. AS 1143.53, Standard Australia, Sydney NSW

Behavior of Polymer-Reinforced Granular Mixtures for Railway Sub-Ballasts



Eivy Alvarez , Xiaobin Chen , and Francisco Grajales-Saavedra 

Abstract The use of ballasted track in railway construction remains one of the most common techniques internationally, and for such systems, the sub-ballast plays an important role as it provides a solid support and should ensure the functionality of the ballast. However, a common problem with track substructures is that materials slowly deteriorate and break apart due to traffic loading. This causes changes in the geometrical arrangement of particles and clogging of the ballast bed by fine particles thus increasing the cost of routine maintenance needed to restore track alignment. This paper describes the results of an experimental program intended to measure the physical and mechanical properties of polymer-reinforced granular mixtures intended for railway sub-ballast. The main objective is to determine improvements of material behavior when compared to non-reinforced sub-ballast. Polymer-based composite structures have advantages over other materials, especially from the economical, technological and environmental perspectives. For this, investigation several samples of gravel-sand mixtures were prepared using different volumetric ratios of polymer fiber which ranged from 0 to 15%. Samples were tested through large-scale consolidated drained triaxial testing (CDTx). Measured parameters include stress ratios, volumetric ratios, void ratio and rate of dilation. These parameters are important to infer material behavior when used in a larger-scale engineering application. The contribution resulting from this experiment comprises a better knowledge of the physical and mechanical behavior of polymer-reinforced granular mixtures and its applicability to railway ballasts.

E. Alvarez (✉) · X. Chen (✉)

The School of Civil Engineering, Central South University, 22 S. Shaoshan Rd., Changsha, Hunan province, China

e-mail: alvarez_eivy@csu.edu.cn

X. Chen

e-mail: chen_xiaobin@csu.edu.cn

F. Grajales-Saavedra (✉)

School of Civil Engineering, Universidad Tecnologica de Panama, Campus Victor Levi Sasso, Bldg No. 1, Panama, Panama Province, Republic of Panama

e-mail: francisco.grajales@utp.ac.pa

Keywords Railway · Polymer-reinforced granular mixtures · Volumetric fiber ratio · Consolidated drained triaxial test (CDTx)

1 Introduction

The sub-ballast is the granular layer composed by gravel and sand which is placed between the ballast and the subgrade. This granular layer is needed to maintain the integrity of the ballast and the subgrade and to ensure a better performance of the ballasted track system. In addition, it contributes distributing the loads applied to the ballast, reducing stress on the subgrade and providing protection against frost actions, and it also has a critical role in drainage, as it keeps water away from the subgrade, prevents penetration and mixing of the subgrade and ballast layers and prevents subgrade attrition by ballast [1]. However, due to the constant traffic loads and environment loads, many of these properties degrade over time, shortening the lifespan of the sub-ballast material. Ballasted track systems are usually economical; however, the associated costs of such systems could increase when performing constant maintenance [2]. Although these problems are well documented, there has been very little innovation on this topic. The need to find new alternatives and materials to reinforce and stop the accelerated deterioration of the sub-ballast layer is increasingly evident, in terms of intervals between maintenance interventions, tamping and overall life cycle.

The increased environmental awareness on recent decades also calls for the search of environmentally friendly alternatives, imposing challenges, even in the railway field, of advancing in research related to the advantages provided by different material mixtures such as polymer-reinforced soils. Synthetic rubbers are polymers which are synthesized from petroleum byproducts. Its elasticity, toughness and flexibility is well suited for manufacturing products used in transportation, consumer products, industrial products and also in the medical sector [3]. In this particular experiment nitrile butadiene rubber (NBR), generally abbreviated to nitrile rubber, was used, which is a synthetic rubber copolymer of acrylonitrile (ACN) and butadiene. NBR has resistance to abrasion and is considered highly resistant to oil, fuel and other chemicals. Furthermore, it is more resistant to heat aging than natural rubber and other materials, allowing nitrile to not harden and lose its damping capacity so quickly [4, 5]. Because of its compatibility with most environments and relatively low cost when compared to other rubber materials, it is one of the most commonly used types of rubber [4].

Polymer-based composite mixtures present advantages over other materials, especially the superior mechanical properties [6]. The potential uses for polymers are vast and this is also the case within the railway industry. The mechanical and thermal properties of fiber-reinforced composites structures are influenced by the amount of fiber used in the mixture [6], for this reason, several samples of gravel-sand mixture were prepared with varying ratios of polymer-reinforcement fibers, which ranged from 0 to 15%. These samples were subjected to a series of consolidated drained triaxial

test (CDT_x). The assessment of ballast performance is an important aspect of track design and performance evaluation. The strength of track foundation materials is what prevents failure or excessive deformation of track foundations under various types of loadings. For this experiment, monotonic and cyclic loading protocols were used. Monotonic loading allows analysis of the progressive failure of the sub-ballast specimens. On the other hand, cyclic loading is intended to assess the performance of sub-ballast specimens under realistic conditions, considering dynamic loading.

2 Methodology

2.1 Materials

For this experiment, crushed gravel and sand were used, as shown in Fig. 1, with $D_{50} = 9$ mm. Both materials were obtained from a quarry and correspond to typical materials used in railway sub-ballast. The corresponding gradation curve is presented



Fig. 1 Sub-ballast material from quarry

Fig. 2 Gradation of sub-ballast

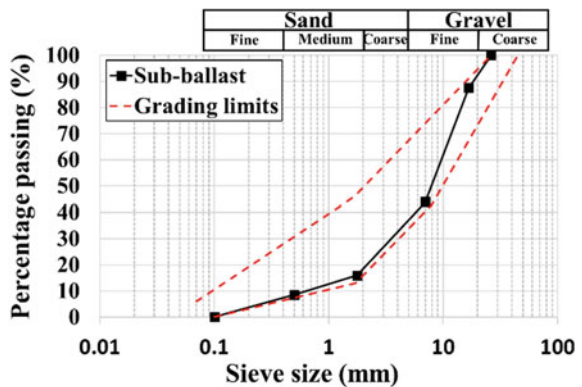


Table 1 Basic properties of nitrile rubber

Property	Value
Hardness, shore A	20–95
Tensile failure stress, ultimate	200–3000 psi
Elongation after fracture in %	600% Maximum
Range temperature usage	from – 40 to 121 °C (–40–250 °F)
Module in 100%	1–7 MPa

in Fig. 2 and was developed using the used the grading limits recommended by the Chinese Standard TB/T 2897 (1998) [7].

At the same time, varying ratios of nitrile rubber fibers were used. The texture of the fiber surface was relatively smooth; thus, soil-polymer roughness was neglected on calculations. The basic properties of nitrile rubber are summarized in Table 1 [5, 8].

2.2 Test Criteria

There is no well-defined criterion to assess the mechanical behavior of fiber-reinforced granular materials, because the fiber volume can be considered as part of the volume of solids or part of the volume of voids [9]. However, in this paper, a three phase system was adopted consisting of voids, fibers and grains treated separately, as proposed by Ajayi et al. [10], where:

Total Volume (V_T): volume of solids (V_s) + volume of voids (V_v) + volume of fibers (V_f):

$$V_T = V_s + V_v + V_f \quad (1)$$

Void ratio (e): the ratio of the volume of voids (V_v) to the volume of solids (V_s):

$$e = \frac{V_v}{V_s} \quad (2)$$

Volumetric fiber ratio (V_{fr}): the ratio of volume of fibers (V_f) to volume of solids (V_s):

$$V_{fr} = \frac{V_f}{V_s} \quad (3)$$

2.3 Sample Preparation

Several pieces of polymer fiber were cut by hand. This study aimed to assess the physical and mechanical properties of the polymer-reinforced samples. The effect of the dimension of individual pieces was not assessed. Instead the dimension of the polymer fiber pieces was adopted according to fiber dimensions proposed by Ferro et al. [10], where fiber length, and the fiber width, are quantified relative to the mean grain size of the scaled sub-ballast D_{50} , as follow (see Fig. 3):

$$\text{Length} = 7.5D_{50} \quad (4)$$

$$\text{Width} = 1.5D_{50} \quad (5)$$

Different sizes of granular material were carefully screened using standard sieves. Then, the different samples were prepared including ratios of polymer-reinforcement fibers using percentages of 0, 5, 10 and 15%, and mixed together in a plastic container until obtaining a homogeneous and reasonably random mixture. The basic geometric properties of the polymer fiber are shown in Table 2.

Samples were compacted to a relative compaction of 90%. Maximum dry density for each volumetric fiber ratio mixture was determined using a BZYS-4212 surface vibrating compaction apparatus (i.e., vibrating hammer), which conforms to British Standard BS1377 among others [11]. The vibrating hammer was set to apply a load of 60 kN with a frequency of 47–50 Hz and a surface static pressure of 18 kPa. The



Fig. 3 Polymer fiber material

Table 2 Basic geometrical properties of nitrile rubber

Dimension	Value
Fiber length	67.5 mm
Fiber width	13.5 mm
Fiber thickness	5 mm
Specific gravity (G_s)	1.30

Fig. 4 Triaxial test apparatus used in the experiment



obtained maximum dry density was used together with each sample's weight and the triaxial cell diameter to estimate the compaction effort to be applied in order to ensure 90% relative compaction. Triaxial samples were compacted using a 10 kg manual tamper. While for both monotonic and cyclic consolidated drained triaxial test (CDTx), a large-scale cylindrical triaxial apparatus was used, as shown in Fig. 4.

2.4 Test Procedure

Conventional monotonic and cyclic consolidated drained triaxial test (CDTx) was conducted on eight sub-ballast specimens: four for monotonic triaxial test and four for cyclic triaxial test. Each of this groups had one unreinforced and three-reinforced sub-ballast material with volumetric fiber ratios (V_{fr}) of 5, 10 and 15%, respectively, under a confining stress of 50 kPa. The testing matrix is summarized in Table 3.

Each mixed unreinforced and reinforced sample is placed inside the rubber membrane and in a cylindrical mold of 300 mm in diameter and 600 mm in height. The specimens were compacted into five layers of 120 mm thickness each, with a compacting hammer, until obtaining a relative compaction of 90% referred to the maximum dry density, described above. After compaction, a top cover is added.

Table 3 Testing matrix

Effective confining pressure (kPa)	Type of load applicant	0% of V_{fr} (A)	5% of V_{fr} (B)	10% of V_{fr} (C)	15% of V_{fr} (D)
50 (A)	Monotonic	AA	BA	CA	DA
50 (B)	Cyclic	AB	BB	CB	DB

Pressure transducers and LVDTs are connected to the digital panel board and a data logger supported by a host computer. All the load, pressure and displacement measurements are recorded by a data logger. The cylindrical sample is placed inside the triaxial cell and the cell is filled with water through the base plate with the pressure in the water being controlled by a pressure unit. The applied confining pressures were increased in several steps. Corrections for filter paper and rubber membrane were not considered. The cyclic triaxial cell is overall constructed in the same way as the static triaxial cell, but with the ability to apply any kind of load sequence to the test sample. The cyclic vertical load was applied by a dynamic actuator at a frequency of 1 Hz.

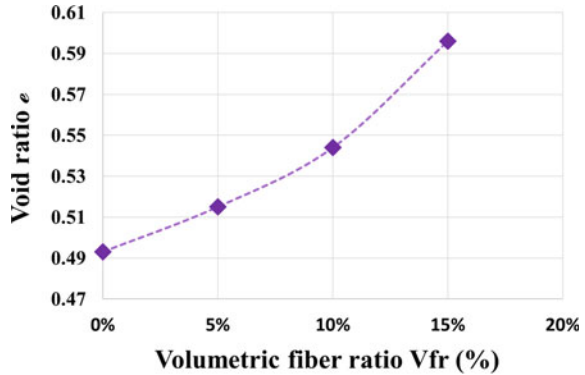
3 Test Result and Analysis

As volumetric fiber ratio (V_{fr}) increased, the void ratios (e) in the samples also gradually increased, as indicated in Table 4 and Fig. 5. The void ratio refers to the degree of accommodation achieved by soil particles, which often leaves empty spaces between them. It is a phenomenon that was discussed before by Ajayi et al. [12], who indicated that the behavior of the relationship between the volume of fiber, solid and voids is not fully understood, but is notable that the addition of volume of fiber (V_f) to a granular material brings about changes in the volume of solids (V_s) and volume of voids (V_v) within a given constant total volume (V_T). The study of this behavior is important to understand the interaction between the particles and the fiber.

Table 4 Relation between void ratio e and volumetric fiber ratio V_{fr}

Volumetric fiber ratio V_{fr} (%)	Void ratio at e
0	0.493
5	0.515
10	0.544
15	0.596

Fig. 5 Relation between void ratio e and volumetric fiber ratio V_{fr} of unreinforced and reinforced sub-ballast samples



3.1 Monotonic Triaxial Test

Monotonic consolidated drained triaxial test (CDT_x) was carried out on four samples at a confining pressure of 50 kPa with different volumetric fiber ratios of 0, 5, 10 and 15%. The effect on the stress–strain behavior of unreinforced and reinforced sub-ballast samples is shown in Figs. 6 and 7. Strength and dilatancy are two important factors that determine the behavior of a material and are associated with failure conditions. For these reasons, these two aspects are studied in this paper.

Figure 6 depicts the measured stress ratio q/p versus axial strain ϵ_1 of unreinforced and reinforced sub-ballast samples. The unreinforced sample showed a typical behavior of a granular material: The deviatoric stress initially increases with increasing axial strain until it reaches the peak strength. However, the reinforced

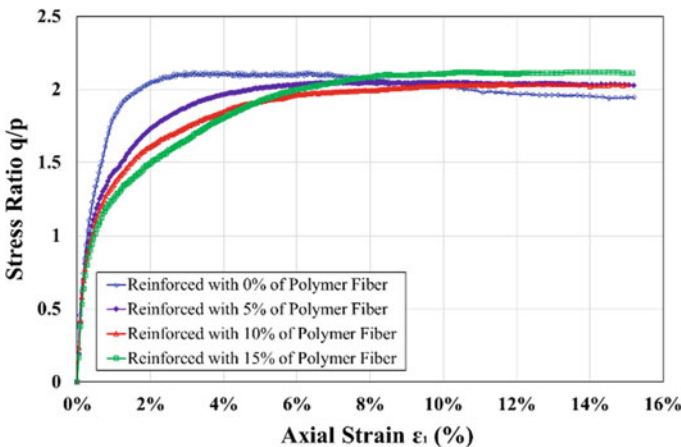


Fig. 6 Relation between the stress ratio q/p and the axial strain ϵ_1 of unreinforced and reinforced sub-ballast samples

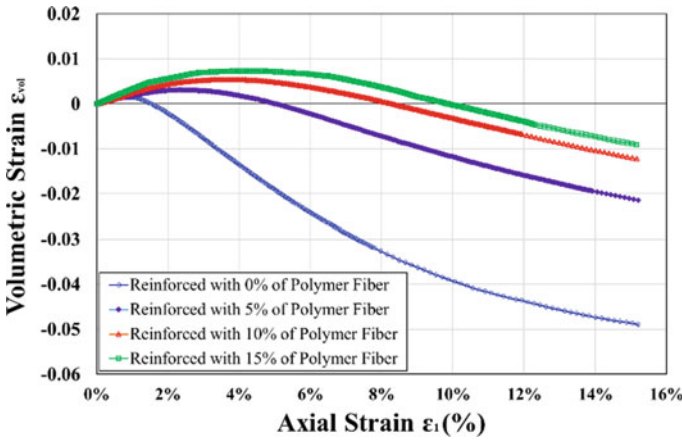


Fig. 7 Relation between volumetric Strain ϵ_{vol} and axial strain ϵ_1 of unreinforced and reinforced sub-ballast samples

samples exhibited quite different behavior, reaching the peak strength at a greater axial strain. As the content of polymer fibers in the sample increased, the peak strength was reached at a higher axial strain, being the sample with 15% of polymer fiber the one that showed a higher displacement in this case, very close to 15% of the axial strain. This axial strain displacement behavior due to the influence of the polymer fiber in the sample was also previously observed by Ajayi et al. in ballast samples [12].

The volumetric strain ϵ_{vol} was also measured for the unreinforced and reinforced sub-ballast samples, as presented in Fig. 7. It is observed that the initial volumetric strain is compressive and becomes dilative with increasing axial strain. However, there is a significant difference between the dilation rate of the unreinforced and reinforced sub-ballast. Dilatancy or dilation may be described as the change in volume that is associated with shear distortion of an element in the material [13]. As the content of polymer fibers was increased, the reinforced samples showed a compressive (less dilation rate) as strain increased, being the sample with 15% of polymer fiber the one with the least dilation.

The influence of polymer fiber on the dilation rate of the material could be appreciated through the relationship between stress ratio q/p versus dilatation d , as shown in Fig. 8, where the variation of the dilatation during the application of the stress is observed. The relation between dilatation d and axial strain ϵ_1 and their variation with different volumetric ratios can be observed in Fig. 9. Dilatation d is defined as:

$$d = -\left(\frac{\delta\epsilon_{vol}}{\delta\epsilon_\gamma}\right) \tag{6}$$

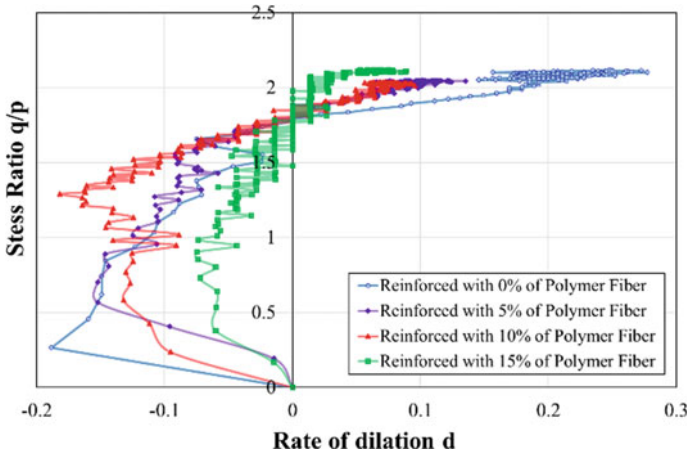


Fig. 8 Relationship between stress ratio q/p versus rate of dilation d

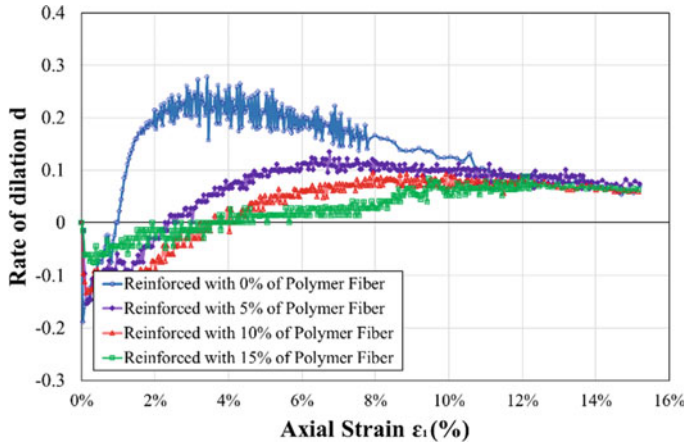


Fig. 9 Relationship between rate of dilation d and axial strain ϵ_1 of unreinforced and reinforced sub-ballast samples

where $\delta\epsilon_{vol}$ correspond to the volumetric strain increment and $\delta\epsilon_\gamma$ the triaxial shear strain increment.

Similar to Fig. 6, in Fig. 9, it is observed that as the content of polymer fiber in the sample increases, and the point of reaching the peak of dilatation translates to greater axial strain, being the sample with 15% of polymer fiber which demonstrated a higher displacement, so the reinforcement with polymers improve the ability of the sub-ballast material to dilate before failure, which shows that the polymer-reinforced material has considerable advantages over the unreinforced material in both the elastic as plastic ranges.

Table 5 Relation between dilation ψ and volumetric fiber ratio V_{fr}

Volumetric fiber ratio V_{fr} (%)	Dilation ψ
0	16°
5	6°
10	5°
15	4°

The dilation is also characterized by the dilatancy angle ψ . The dilatancy angle ψ represents the ratio of plastic volume change over plastic shear strain, as shown in Eq. 7; although this definition is only accurate in the case of simple shear, when is testing a particular material, the dilatancy angle is found to be constant near and at peak strength, according to Vermeer and de Borst [13]:

$$\psi = \arcsin \left[\frac{\delta \varepsilon_v^P}{-2\delta \varepsilon_1^P + \delta \varepsilon_v^P} \right] \tag{7}$$

Using Eq. 7, an approximately value of the dilatancy angle ψ around the peak strength is calculated, as shown in Table 5, where it is observed that exist a really large difference in the dilation angle ψ with the increase in polymer fiber.

3.2 Cyclic Triaxial Test

Cyclic consolidated drained triaxial tests (CDTx) were carried out in a large-scale cylindrical triaxial apparatus, as shown in Fig. 4, on four samples with a confining pressure of 50 kPa, with different volumetric fiber ratios of 0, 5, 10 and 15%. The cyclic vertical load was applied at a frequency of 1 Hz.

The cyclic test is very convenient for railroad applications, as it allows one to simulate the passage of a train wheel in the sub-ballast material. For a better representation of the behavior of the material during the relative motion of the granular particles, all the graphs were plotted from 100 to 10,000 cycles because during the first stage of the cyclic loading application (i.e., generally before 100 cycle), the axial and volumetric strain underwent a slow increment and a very small change due to the re-arrangement of the particles. A similar observation of this particle re-arrangement during cyclical loading has been reported by Brown et al. (1974), Lackenby et al. and Xuecheng et al. [14–16]. Furthermore, the number of cycles was represented on a logarithmic scale.

Figure 10 shows the relationship between axial strain (both total and permanent) and the number of load cycles N , for both unreinforced and reinforced samples. This curve is composed by two lines, the solid line that reflects the total deformation and the dashed line that reflects the permanent deformation. The loading and unloading during the cyclical test produced different displacement for each cycle, with a maximum and minimum peak. For this experiment, the maximum peak was

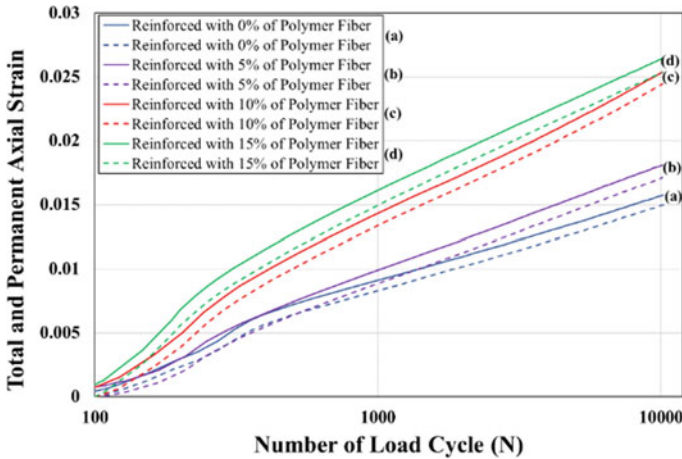


Fig. 10 Relationship between the total and permanent axial strain and the number of load cycle with different volumetric fiber ratio V_{fr} of **a** reinforced with 0% of polymer fiber, **b** reinforced with 5% of polymer fiber, **c** reinforced with 10% of polymer fiber and **d** reinforced with 15% of polymer fiber

considered to represent the total displacement and the minimum peak represents the permanent displacement. The difference between the two lines represents the elastic deformation. Permanent axial strain is useful to analyze the effect of cumulative settlement over a period of time of the sub-ballast track due to the moving traffic loads of the trains [14]. Figure 9 shows that the elastic deformation is affected by the polymer fiber content: as the polymer fiber content increases, the elastic deformation also increases. Therefore, it has an effect on the elastic modulus.

It is also observed that the content of polymer fiber produces an increment of the permanent axial strain, which translates into more settlements when compared to the unreinforced sample. However, to have a definitive conclusion in this regard, it is necessary to analyze the effect of the size of the polymer fiber on the void ratio and settlement of the sub-ballast material. Both parameters (fiber size and void ratio) can seriously affect its performance. This notion is coherent with studies developed by Ferro (2016), which showed the potential of polymer-reinforced fiber to reduce the track permanent settlement depending on the size used in the material [12]. According to Ferro, it is believed that the effect of increased permanent settlement is related to the inhibits of the packing of the particles. However, as mentioned above, the effect of the polymer fiber dimension in the sample was not studied and will be considered in future stages of this research.

4 Concluding Remarks

The physical and mechanical behavior of a nitrile rubber-reinforced sub-ballast has been investigated through monotonic and cyclic drained triaxial compression tests. This work provides a basis for understanding the mechanics of particle–fiber interaction processes.

Many of the results observed in this experiment during the monotonic triaxial test are similar to previous research by Ajayi et al. [9, 12]. The behavior of the polymer fiber-reinforced ballast and sub-ballast material is very similar in relation to the decrease of void ratio, mobilization of strength at large strain and reduction of dilation rate, reducing the volume expansion in shear deformation; in this experiment, the sample with a content of 15% of polymer fiber showed a better performance in all the mentioned aspects. Therefore, the introduction of polymer fiber to the sub-ballast material improves several of its properties. This investigation comprised volumetric fiber ratios ranging from 0 through 15%; however, more experiments could be performed to determine the optimal ratio of polymer fiber required to obtain the best mechanical behavior.

The increment of nitrile rubber in granular materials subjected to cyclic loads can represent an increase in axial strain, but also an improvement in plastic behavior, producing a more ductile material behavior. The dimensions of the fibers proposed by Ferro [10] in Eqs. 4 and 5, correspond to studies based on the effect of fiber width on track response for constant volumetric fiber content (V_{fr}) and fiber length when applying cyclic loads, demonstrating the influence of the fiber size to reduce the permanent settlement of the material [10]; however, it seems that the composition and dimensions of the sub-ballast material considerably affect the use of the aforementioned formulas, so these dimensions were not effective in ensuring less material settlement. Currently, no studies have been conducted to determine the influence of fiber size on the sub-ballast, so further studies should be developed to determine the effect of polymer fiber size on the void ratio and settlement of the sub-ballast material under the action of dynamic load. Results from cyclic tests show a better understanding of the behavior of the polymer-reinforced sub-ballast by simulating the moving load condition of trains.

In addition to the results obtained in this research, there is still more to be investigated regarding the reinforcement of the sub-ballast with polymer fibers, since many other tests can be performed to observe other properties and behavior of the polymer-reinforced sub-ballast and the benefits of using this material. More research will be done in this direction to help improve understanding on this subject.

References

1. Chandra S, Agarwal MM (2007) Railway engineering. Oxford University Press, New Delhi, Oxford

2. Li D, Hyslip JP, Sussmann TR, Chrismer SM (2015) *Railway geotechnics*, 1st edn. CRC Press, Boca Raton
3. The Importance of Synthetic Rubber in Today's World. <https://www.sperryrice.com/post/the-importance-of-synthetic-rubber-in-todays-world>. Last accessed 21 July 2020
4. Is Nitrile Butadiene Rubber a Sustainable Product. <https://monmouthrubber.com/is-nitrile-butadiene-rubber-a-sustainable-product/>. Last accessed 21 July 2020
5. Nitrile Rubber Products. <https://www.timcorubber.com/rubber-materials/nitrile-rubber/>. Last accessed 31 Aug 2020
6. Taşdemir M, Akalin M, Koçak D, Usta I, Merdan N (2010) Investigation of properties of polymer/textile fiber composites. *Int J Polym Mater* 59:200–214
7. [TB/T 2897-1998] Railway gravel track bed ballast. <http://www.doc88.com/p-7068077244668.html>. Last accessed 31 Aug 2020
8. Young Modulus for Rubber Technical Events. <https://www.chevalier-cleret.com/event/young-modulus-for-rubber.html>. Last accessed 22 July 2020
9. Ajayi O, Le Pen L, Zervos A, Powrie W (2017) A behavioural framework for fibre-reinforced gravel. *Géotechnique* 67:56–68
10. Ferro E, Ajayi O, Le Pen L, Zervos A, Powrie W (2016) Settlement response of fibre reinforced railway ballast
11. BZYS-4212 Road Surface Vibrating Compaction Test Instruments. https://www.ecplaza.net/products/bzys-4212-road-surface-vibrating-compaction_4155946. Last accessed 31 Aug 2020
12. Ajayi O, Le Pen L, Zervos A, Powrie W (2014) Effects of random fibre reinforcement on the density of granular materials. *Geomechanics from Micro to Macro*, pp 1363–1367
13. Vermeer PA (1998) Non-associated plasticity for soils, concrete and rock. In: Herrmann HJ, Hovi JP, Luding S (eds) *Physics of dry granular media*. Springer, Netherlands, Dordrecht, pp 163–196
14. Bian X, Jiang J, Jin W, Sun D, Li W, Li X (2016) Cyclic and postcyclic triaxial testing of ballast and subballast. *J Mater Civ Eng* 28:04016032
15. Lackenby J, Indraratna B, McDowell G, Christie D (2007) Effect of confining pressure on ballast degradation and deformation under cyclic triaxial loading. *Faculty of Engineering—Papers 57*
16. Brown SF (1974) Repeated load testing of a granular material

Construction and Monitoring of the Short-Term Strength Development of a Cement-Stabilized Lateritic Pavement Layer Under Tropical Climatic Conditions



Samuel I. K. Ampadu, Thomas D. Arthur, Priscilla Ackah, and Fred Boadu

Abstract Cement-stabilized lateritic soil is increasingly being adopted as the stiff cement-treated foundation layer in inverted base pavement layers for heavily trafficked roads. However, the mixing of cement and lateritic soil in the field without specialized equipment poses various challenges. In one such project, a cement-stabilized lateritic soil was specified as the foundation layer in an inverted pavement structure for a road construction project in Accra. This paper describes the mix design, the characteristics of the cement-treated lateritic soil and the results of the field trials and monitoring of the strength of the 200 mm thick cement-stabilized subbase layer over a 28-day period under tropical climatic conditions. A sample of lateritic soil was characterized, and the mix design using ordinary Portland cement as a binder was undertaken. Based on the mix design, the cement-stabilized layer was constructed first at a trial location to confirm the mixing procedures. Then, a 20 m long section on the permanent works was delineated for monitoring. The dynamic cone penetrometer test was performed on designated sections immediately after placement and after 3, 14 and 28 days to monitor the strength development. The uniformity of the mix in terms of the dynamic cone penetration test results is discussed. The changes in the unconfined compressive strength derived from the dynamic cone penetration index with pavement layer age under tropical climatic conditions is also analyzed, discussed and compared with laboratory prepared samples.

Keywords Lateritic soil · Subbase · Cement stabilization · Mix design · Dynamic cone penetration · Unconfined compressive strength

S. I. K. Ampadu (✉)

Department of Civil Engineering, Kwame Nkrumah University of Science and Technology, Private Mail Bag, University Post Office, Kumasi, Ghana
e-mail: sikampadu@yahoo.co.uk

T. D. Arthur · P. Ackah

ACON House, 33 Royalt Castle Road, Accra, Ghana

F. Boadu

Department of Civil and Environmental Engineering, Pratt School of Engineering, Duke University, Durham NC 27708, USA
e-mail: boadu@duke.edu

1 Introduction

Conventional flexible pavement sections rely on the base and subbase layers to bear and spread traffic loads. With increasing traffic, such pavement structures call for increasingly thicker asphaltic concrete layers at the top which in most countries being the most expensive layer leads to non-economical pavement sections. An inverted base pavement, on the other hand, is a pavement structure that consists of an unbound aggregate base confined by a stiff cement-treated foundation layer and a thin asphalt cover [1–3]. Figure 1 illustrates an inverted pavement structure for a road pavement with a design traffic of 90×10^6 equivalent standard axle loads (ESAL) constructed in the city of Accra. The crushed rock base (CRB) which constitutes the unbound aggregate layer is sandwiched between the 100 mm thick hot-mixed asphaltic (HMA) concrete layer and the cement-stabilized subbase (CSSB) layer.

In the tropics, laterites and lateritic soils abound and extensive laboratory studies reported in [4, 5] have shown that they can be successfully stabilized with cement. However, the tropical climatic conditions under which laterites and lateritic soils are formed also create an aggregated fabric referred to as “ped” that requires vigorous mixing in order to completely destroy them as explained in [6, 7] to ensure uniform mixing with stabilizing agents. Whereas in laboratory trials uniform mixing can easily be achieved, under field conditions, it is not feasible to dry and break up the ped structure for mixing with stabilizing agents. For cement, this is compounded by the need to quickly mix and lay the mixture before it sets. In the absence of specialty soil mixing equipment, the mixing of lateritic soil and cement using conventional construction equipment becomes a construction challenge that requires careful attention. This paper describes the procedures that were followed using conventional construction

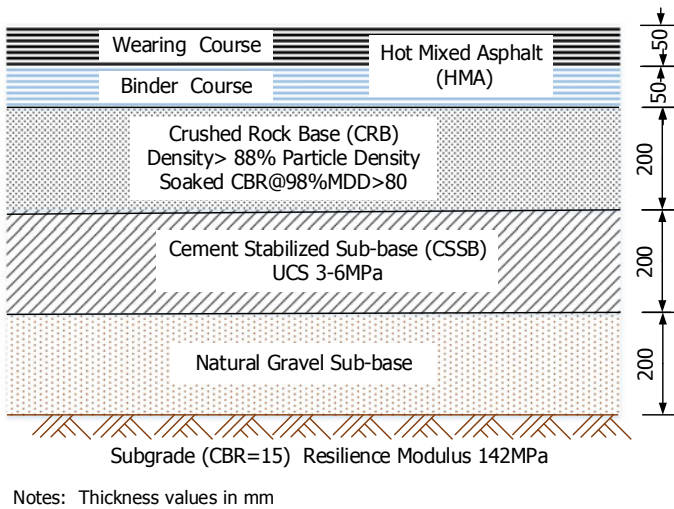


Fig. 1 Structure of inverted pavement used in study

equipment for the in situ mixing of the lateritic soil and the cement binder in order to obtain as uniform a mix as possible for the CSSB in the above project. It also discusses the results of the pavement strength evolution over time measured using the dynamic cone penetration testing under the tropical climatic condition of high temperature and variable humidity.

2 Methodology

2.1 Characterizing the Lateritic Soil Used for the CSSB

Samples of a stockpiled lateritic soil intended to be used for the construction of the CSSB were delivered to the laboratory in sacks for testing. The material was spread out indoors to dry. The index properties of the sample were then determined. The wet sieving method was used for the grading analysis in accordance with the relevant portions of the ASTM standard [8], while the liquid limit was determined using the cone penetration method as detailed in Part 2 Clause 4.3 of the BS standard [9]. The compaction characteristics of the lateritic soil were also obtained using the modified Proctor standard [10]. The strength of the lateritic soil and its dependence on the level of compaction were determined using the CBR test on samples soaked for four days. Samples of the lateritic soil were also taken for the methylene blue test using the spot method according to the procedures described in [11].

2.2 Laboratory Mix Design

The cement used for the stabilization was a Type I Portland cement known locally as “Dangote 42.5R” obtained from the open market. The laboratory mix design of the soil–cement mixture was carried out in accordance with procedures described in [12]. Based on the grading curve of the lateritic soil, the preliminary starting cement content required was determined to be 3%. From this, the cement contents of 1, 3 and 5% were used for this investigation. Each percentage by weight of the cement was hand mixed thoroughly with the air-dried lateritic soil to obtain a uniform mix. The compaction characteristics of each mix was determined using the Modified Proctor standard to obtain the maximum dry density (MDD) and corresponding optimum moisture content (OMC). Samples of the mix were then prepared at the OMC for each of the three cement contents, demoulded and cured in a box for 7 days in the temperature-controlled room. After the 7 days, the samples were subjected to the unconfined compressive strength (UCS) test according to the procedures detailed in [13].

2.3 Field Trials in the Contractor's Yard

Preparation of Subgrade Surface and Mixing of Soil–Cement

Field trials were conducted on a 50×13 m area in front of the Contractor's yard to confirm the mix and the laying procedures. The surface of the subgrade was set out with metal reference stakes at 10 m intervals on the subgrade to indicate the width and thickness of the CSSB layer. The stakes also acted as a guide for the equipment operators during the construction of the subgrade. The subgrade surface was pre-wetted by light sprinkling of water.

Based on the MDD of 2396 kg/m^3 of the CSSB and the 5% cement content, the weight of dry lateritic soil was computed as 2282 kg/m^3 from which the weight of cement of 114.1 kg was also computed. The weight of lateritic soil in a payloader bucket was determined together with its volume. By measurements carried out in the field, the soil–cement mixture was batched in volumes of 20 m^3 and the mix proportions were determined to be equivalent to 7 payloader bucket-loads of lateritic soil and 30 bags of 50 kg cement. Figure 2 shows the batching of lateritic soil and cement. The in situ water content of the lateritic soil was 6.6%, and therefore, no additional water was considered necessary. The soil–cement mixture was prepared by thoroughly mixing the measured volumes of well-mixed soil material with the cement using a payloader and an excavator until a mix with a uniform color and texture was obtained. The batch volume of 20 m^3 was prepared in turns during the construction of the trial layer and the mixing time for preparing each batch was



Fig. 2 Batching of lateritic soil and cement in the yard

recorded. The soil–cement mixture was then hauled in tipper trucks to the trial layer section recording the haul time. Protective covers were used to prevent evaporation losses.

Laying of Cement–Soil Mixture and quality control monitoring

At the construction front, the mixture was tipped into the paver which was used to spread the soil–cement mix for one lane at a time to a depth of 250 mm, which was 25% thicker than the desired final compacted layer. After spreading of the soil–cement mix by the paver to the required grade and cross-section, the CSSB layer was compacted with a 25 ton vibratory-steel wheel roller. The moisture content of the soil–cement mix after shaping and compaction was measured to be between 3.5 and 6.3%. After the laying, shaping, compaction and finishing of the cement-stabilized subbase layer, the treated layer was kept damp for the next 7 days using an 0.1 mm thick moisture retaining cover to retain the moisture and permit the cement to hydrate as shown in Fig. 3.

As part of the process of quality control of the mixing and placement procedures, samples of the field-prepared cement–soil mixture were compacted in the field laboratory in a split-type CBR mold to the mix design density, demolded, cured for 7 days and subjected to the UCS test. On the pavement surface, the levels of the top of the pavement were determined before and after compaction. After the compaction,



Fig. 3 Curing of laid CSSB in the yard

the level of compaction achieved was measured at ten different locations using the sand replacement method as described in [14]. The DCP test was also performed at selected locations after 7 days of curing in accordance with procedures outlined in [15] using a standard cone with a diameter of 20 mm (with 60° apex angle) driven by an 8 kg hammer freely falling through a height of 575 mm.

2.4 Testing in the Permanent Works

A section of the permanent works was used to confirm the CSSB layer uniformity and to monitor the strength development of the CSSB pavement layer over a 28-day period. A 20 m long section on the dual carriageway from km 10 + 650 to 10 + 670 was demarcated into 4 m long × 2.67 m wide subsections to create a network of 5 × 3 columns and rows as shown in Fig. 4. Each column was further subdivided into 1 m long subsections and designated 0, 3, 14 and 28 days, each corresponding to the age of the pavement layer at which testing was to be done. The procedures developed at the trial section in the yard were then employed to construct the CSSB layer except that for practical reasons the moisture retaining cover was dispensed with. Immediately after completion of the compaction, the DCP test was conducted in the area designated 0 in columns 1, 2, 3, 4 and 5 and in rows corresponding to A, B and C. At the beginning of each day, the surface of the pavement was watered to keep it damp. After 3 days, 14 days and finally after 28 days of laying the pavement, the DCP test was performed in the appropriate section of the study section. This arrangement ensured that the location disturbed by the DCP test was not reused

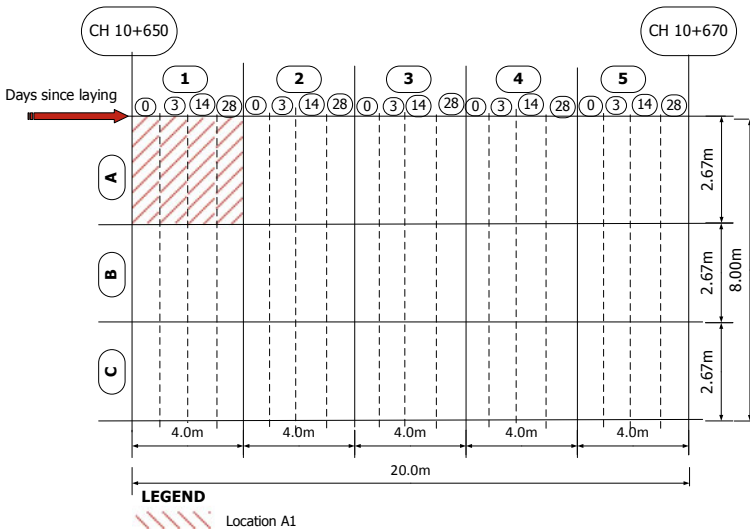


Fig. 4 Layout of study section on permanent works



Fig. 5 Quality control testing on permanent works

in subsequent tests. Figure 5 shows the sand replacement test and the DCP test in progress on the study section.

3 Results and Discussion

3.1 Characteristics of Lateritic Soil

The characteristics of the lateritic soil are summarized in Table 1. The grading curve is shown in Fig. 6, while Fig. 7 shows the variation of the soaked CBR with the level of compaction. Based on the index properties, the lateritic soil may be described as A-2–6 in the AASHTO classification system. The large increase in the soaked CBR of the

Table 1 Summary of index properties of treated and untreated lateritic soil

Sample ID	LL	PI	MBV ^a	FC ^b (%)	OMC (%)	MDD (kg/m ³)
Air-dried lateritic soil	26	11	0.086	23.2	5.66	2.285
CSSB	NP	NP	NA	6.0	6.70	2.396

^aMethylene blue value, ^bFC = fines content, i.e., percentage passing sieve No. 200

Fig. 6 Grading curves for natural and treated soil

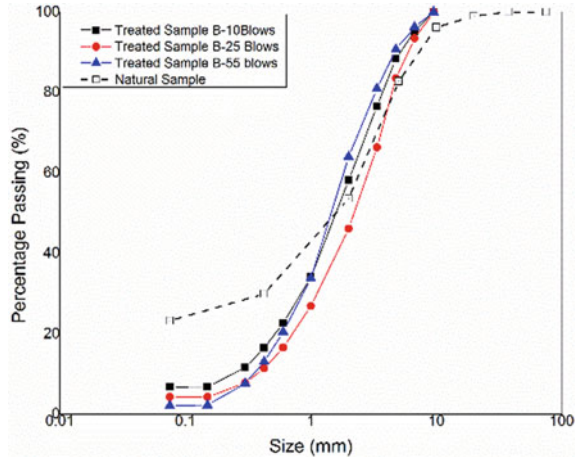
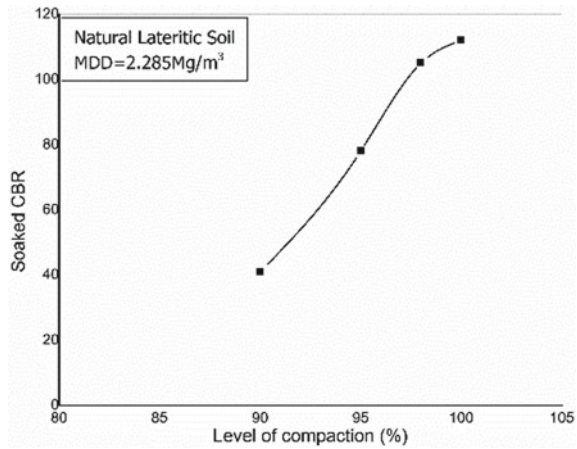


Fig. 7 Variation of soaked CBR of untreated lateritic soil with level of compaction



lateritic soil from 43 at 90% level of compaction to 112 at 100% level of compaction demonstrates that like most lateritic soils with high fines contents the soaked CBR is highly sensitive to the level of compaction. On the other hand, as demonstrated in [7] high compactive efforts are known to tend to lead to particle breakage during compaction leading to generation of fines. The methylene blue value of 0.086 was far below the specified threshold value of two indicating very low organic content.

3.2 Properties of Cement-Stabilized Lateritic Soil

The index properties of the lateritic soil mixed with 5% cement (CSSB) are also summarized in Table 1 side by side the untreated soil. The table shows the non-plastic

tendency of cement mixtures. Also, the grading curve shows that despite a 5.5 increase in compactive effort (10 blows to 55 blows of 4.5 kg rammer), the grading curves remained within a narrow band. This suggests that cement stabilization makes the soil more resistant to crushing and generation of fines during compaction. Figure 8 shows the compaction characteristics of the cement-stabilized soil alongside the untreated soil, while Fig. 9 summarizes the variation of the MDD and OMC with cement content. It can be seen that cement stabilization increased both the OMC and MDD values, but these values level off with negligible increase from 3 to 5% cement content.

Figure 10 shows the variation in UCS after 7 days with cement content, and it can be seen that the UCS increases linearly from 1.02 to 4.30 MPa as the cement content

Fig. 8 Compaction characteristics of natural and cement-treated lateritic soil

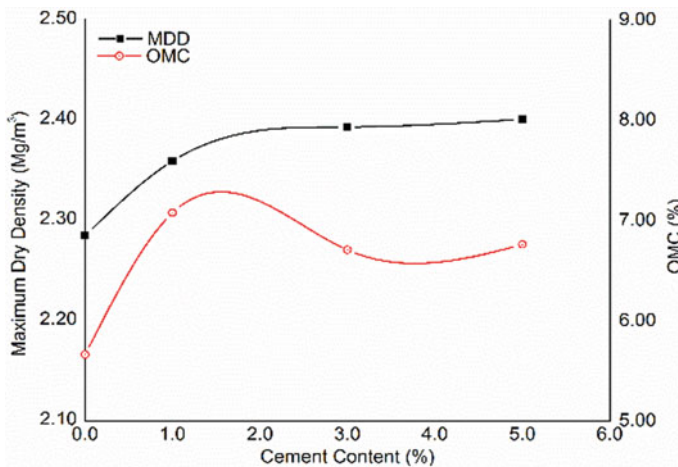
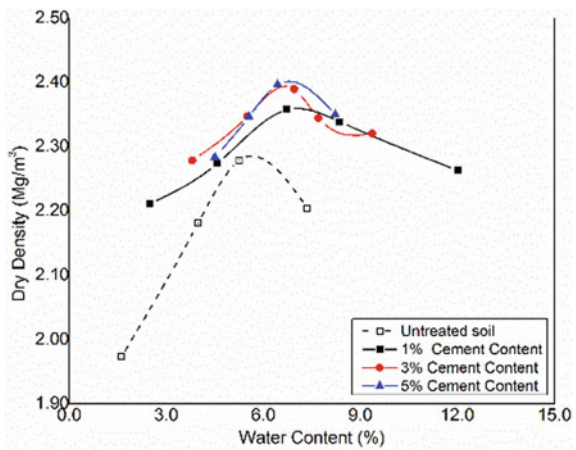


Fig. 9 Maximum dry density-cement content relationship for lateritic soil

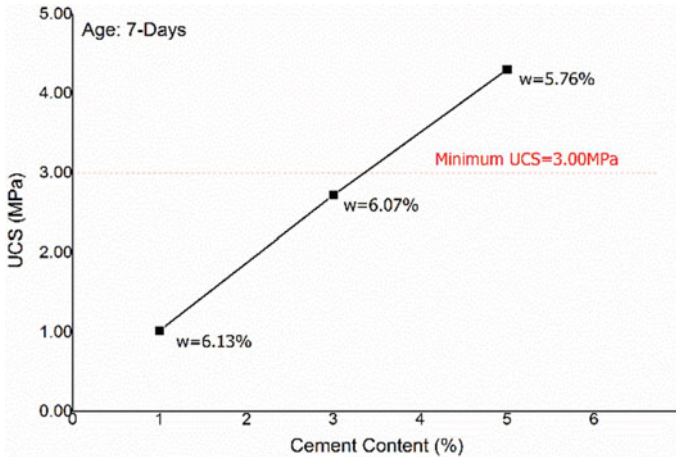


Fig. 10 Relationship between laboratory UCS and cement content

increases from 1 to 5%. The minimum strength requirement of 3.0 MPa is therefore achieved at 5% cement content. A study reported in [4] and corroborated in [5] has shown that most lateritic soils require a minimum cement content of 4% to meet the wet-dry durability requirement. The 5% cement content, therefore, apart from satisfying the minimum strength may also be deemed to have satisfied the durability requirement.

3.3 *In Situ Properties of Test Trials*

Cement being a hydraulic binder commences hydration as soon as water is added hence the need to complete the processes as fast as possible. It has been recommended by [16] that the compaction be completed within two hours of mixing in order to prevent the mix from setting prior to compaction. The elapsed time of the activities recorded during the trials at the yard showed that the batching and mixing required 25 min while the placement, compaction and finishing took another 30 min. Thus, the processes were completed within 60 min well ahead of the setting of the mix. The loose thickness measured at 15 different locations during the trials in the yard varied between 252 and 287 mm which was compacted to a thickness varying between 199 and 229 mm with an average value of 213 mm thus giving an average compaction factor of 1.254. The levels of compaction achieved by four passes of the 25 ton steel vibratory roller measured at ten different locations varied between 97.9 and 99.4% of the MDD. The trials at the yard established that the procedure ensures that the subbase thickness of 200 mm is achieved.

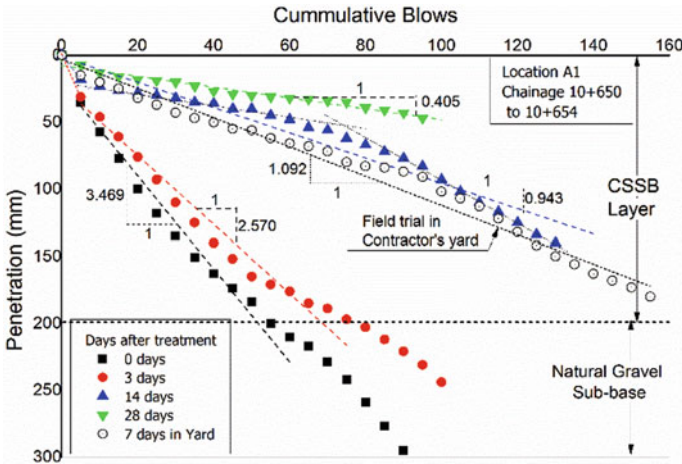


Fig. 11 Variation of DCP penetration–cumulative blows with age at A1

3.4 Construction Monitoring Testing

Figure 11 shows the cumulative blows–penetration plot at location A1 (see Fig. 2) for the CSSB immediately after placement and after 3, 14 and 28 days. The plot for one trial at the yard is also superimposed. This plot is typical of all the other points investigated. In DCP test results, a linear cumulative blows–penetration plot indicates a material of uniform properties and the gradient of the plot is the dynamic cone penetration index (DPI). This parameter has been correlated with various pavement design parameters such as the CBR, the dry density and also the resilient modulus. In the figure, the lines of best fit to each plot for the relevant portions considered are also superimposed. The values of the DPI for the different locations and for the different ages of the pavement layer are summarized in Table 2.

Uniformity of CSSB layer as Laid

The uniformity of the CSSB as laid is assessed using the DPI values at zero age. The details of the cumulative blows–penetration curve near the beginning of the plot for the zero days show that the top 20–40 mm appear to have been loosened perhaps due to activities on the pavement surface and the moistening of the layer as evidenced by the relatively larger DPI. The DPI values of the CSSB were computed down to the depth where there was an obvious change in DPI which was taken to be the thickness of the CSSB layer. At a few locations, this was shallower than the 200 mm thickness. The mean DPI value for the zero age and the relative standard deviation values (RSD) defined as the standard deviation divided by the mean expressed in percentage are also shown in Table 2. The RSD value may be used as an indicator of the uniformity of CSSB layer over the 20 m long section. The results show that immediately after placement, the RSD value obtained from 14 locations over the 20 m study section

Table 2 In-situ DPI values at different locations for various pavement ages

Location	DPI values (mm/blow)			
	0 days	3 days	14 days	28 days
A1	3.469	2.571	0.944	0.405
A2	3.501	1.574	0.372	0.332
A3	2.948	NA	0.633	0.356
A4	2.702	NA	0.397	NA
A5	3.439	NA	NA	NA
B1	3.145	1.722	1.093	NA
B2	3.611	2.256	0.719	NA
B3	3.438	NA	0.459	NA
B4	3.385	NA	0.243	NA
B5	2.638	NA	NA	NA
C1	5.173	2.615	1.930	NA
C2	4.843	1.844	0.448	NA
C3	5.027	NA	0.439	NA
C4	3.217	NA	0.853	NA
Mean	3.610	2.097	0.743	0.364
Standard Dev	0.818	0.446	0.483	–
RSD (%)	22.65	21.29	65.02	–

was about 23%. An RSD value of 10% has been suggested by [17] as the limit of acceptability of repeatability of laboratory test results. No such guidance was found for field test results, but since a much higher variability is expected of field data, an RSD value of the order of 20% (double the laboratory results) which was obtained in this study was considered reasonable. Thus, it may be concluded that the procedures adopted for the mixing and placement of the CSSB gave fairly uniform pavement layers.

Short-term Strength Development.

The air temperature during the period of construction of the CSSB ranged from 22 to 32 °C while the humidity varied between 57 and 100%. After placement, as the pavement aged and the material became stronger, it was not possible to penetrate the full depth of the CSSB. As shown in Fig. 11, the 14 days and 28 days measurements penetrated only 140 mm and 45 mm, respectively. For these cases, the DPI values were obtained as the line of best fit for the total depth penetrated. A detailed analysis of the cumulative blows–penetration curves for the 14 days, for example, shows that the DPI values are higher for the first 50 mm and reduces for subsequent depths suggesting higher strength at the top. This indicates that the hydration of the cement–soil mixture is faster at the top, indicating that deeper layers may not have received sufficient water for the hydration to proceed at the same rate as at the top. The trial at

the Contractor’s yard for the 7-day strength that was superimposed indicates a DPI value of 1.092.

It can also be seen that the cumulative blows–penetration curve for the 3 days has similar characteristics as the case for zero-days suggesting minimal hydration effect and therefore minimal increase in strength from the as-laid value. The similar RSD values for the 3 days as the zero days also support this observation. It must be noted that data was available for only one location for 28 days as it was not possible to penetrate the layer. The RSD value that truly reflects the 28-day strength of the study section could therefore not be computed. The very high value of RSD of 65% for the 14-day strength indicating nonuniformity across different locations in the section may be attributed to the difficulty of ensuring hydration under the prevailing conditions.

There are several correlations reported in the literature [18, 19] between the DPI and the UCS. In this paper, Eq. 1 which was developed by [19] was used to convert the DPI values shown in Table 2 to UCS.

$$\text{Log(UCS)}=[0.29 - 0.809\text{Log(DPI)}]\text{MPa} \tag{1}$$

Figure 12 shows the variation with age of the UCS computed using Eq. 1 for the CSSB layer in the permanent works. The mean values for each age are also shown, and the line of best fit shows effectively a linear relationship between UCS and age for the permanent works. The average 7-day UCS on the permanent works is predicted to be 1.62 MPa which is slightly lower than the 1.82 MPa measured in the Contractor’s yard. The UCS values obtained from testing in situ-mixed laboratory-cured CSSB samples from the Contractor’s yard after 7 days are also superimposed, and they give an average value of 2.56 MPa. The significant difference between the in situ-cured and

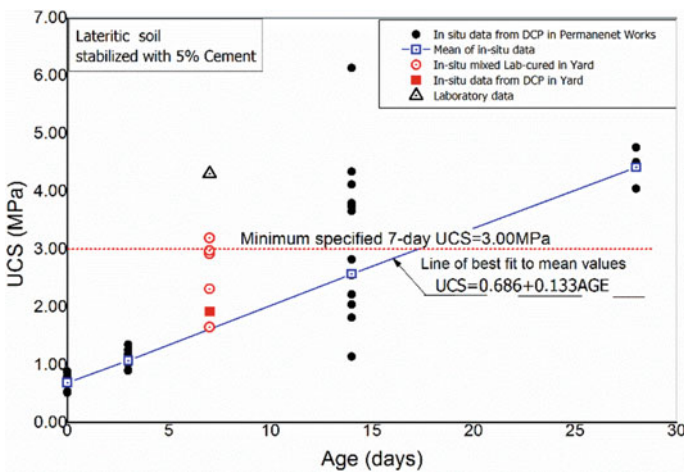


Fig. 12 Variation of UCS with age

laboratory-cured UCS values indicates the important influence of controlled curing conditions. Both of these values, however, are lower than the minimum specified value of 3.0 MPa and indicate a slower strength development in situ. These results suggest that it would take 17 days for the strength on the permanent works to reach the project specified levels. Given that in inverted pavements, the CSSB is used as a solid foundation for the compaction of the CRB, the implication is that the CSSB should not be opened to construction traffic for the compaction of the CRB until sufficient time has elapsed for the CSSB to develop the minimum required strength.

4 Conclusions

Based on the results of laboratory mix design of cement-stabilized lateritic soil and field trials together with data from the permanent works, the following conclusions and recommendations may be made concerning the mixing, laying and monitoring of cement stabilization of lateritic soils in a tropical environment using conventional equipment:

- 1 The procedures adopted for the mixing and placement of the cement-stabilized lateritic subbase layer using conventional construction equipment gave fairly uniform 200 mm thick CSSB layer.
- 2 The 7-day in situ strength of the CSSB is only about 57% of the project specified value and indicates that the curing condition consisting of intermittent watering under the particular tropical conditions on site gave a much slower strength development than project specification. This implies that the CSSB should not be opened to traffic for the compaction of the CRB until 17 days have elapsed.

References

1. Barksdale RD (1984) Performance of crushed-stone base courses. *Transp Res Rec* 954:78–87
2. Tutumluer E, Barksdale RD (1995) Inverted flexible pavement response and performance. *Transp Res Rec* 1482:102–110
3. Titi H, Rasouljan M, Martinez M, Becnel B, Keel G (2003) Long-term performance of stone interlayer pavement. *J Trans Eng* 129(2):118–126
4. Lyon Associates and BRRI (1971) Laterites and lateritic soils and other problem soils of Africa—an engineering study, AIDS/cds-2164
5. Moh ZC, Chin YP, Ng SC (1970) Cement stabilization of lateritic soils. In: *Proceedings of Asian conference of soil mechanics and foundation engineering*, pp 42–46
6. Millard RS (1962) Road Building in the tropics. *J Applied Chem Lond.* 12:342–357
7. Ampadu SIK (2019) The Unique Properties of laterites and lateritic soils and their influence in construction, course on unsaturated soils. In: *XVII African regional conference on soil mechanics and geotechnical engineering*, Cape Town, South Africa 7–9 Oct
8. ASTM D422, Standard test method for particle-size analysis of soils, annual book of ASTM standards, vol 04–08

9. BS 1377 (1990) Methods of test for soils for civil engineering purposes. United Kingdom, British Standards Institution
10. ASTM D 1557-91, Test method for laboratory compaction characteristics of soil using modified effort. In: Annual book of ASTM standards, vol 04-08
11. Topal T (1996) The use of methylene blue adsorption test to assess the clay content of the Cappadocian Tuff. In: 8th international conference on deterioration and con. of stone, Berlin, vol 2, pp 791-79
12. TLT-501 (02) Mix design method for soil-cement mixtures which is based on the portland cement association method of design
13. ASTM D1633-02, Standard test method for compressive strength of molded soil-cement cylinders. In: Annual book of ASTM standards, vol 04-08
14. ASTM D 1556-01, Standard test method for density and unit weight of soil in place by the sand-cone method. In: Annual book of ASTM standards, vol 4.08
15. ASTM D6951-18, Standard test method for use of the dynamic cone penetrometer in shallow pavement applications. In: Annual book of ASTM standards, vol 4.08
16. West G (1959) A laboratory investigation into the effect of elapsed time after mixing on the compaction and strength of soil-cement. *Geotechnique* 9(1):22-28
17. Cuelho E, Mokwa R, Obert K (2007). Comparative analysis of coarse surfacing aggregate using micro-deval, L.A. abrasion and sulfate soundness tests. Montana. http://www.mdt.mt.gov/research/projects/mat/coarse_aggregate.shtml
18. Patel MA, Patel HS (2012) Experimental study to correlate the test results of PBT, UCS, and CBR with DCP on various soils in soaked condition. *Int J Eng* 6(5):244-261
19. McElvaney J, Djatnika J (1991) Strength evaluation of lime-stabilized pavement foundation using the dynamic cone penetrometer. *Austral Rd Res* 21:40-52

Experimental Study on Mass Stabilization of Soft Soil Foundation Based on MgO-CO₂ Carbonation Technology



Song-yu Liu , Guang-hua Cai , Guang-yin Du , Liang Wang , Jia-fu Chen, Chuan Qin, and Jing Ruan

Abstract Mucky soft soil with weak properties was usually improved by the chemical stabilization owing to the high cost of the situ replacement, and the main chemical binder used was Portland cement (PC). However, with the needs of environmental protection, energy conservation and emissions reduction, the research of low-carbon and high-efficiency soft soil treatment technology will be the development trend of modern engineering construction. The combined binder of reactive magnesia (MgO) and carbon dioxide (CO₂) was regarded as a new curing agent instead of traditional PC, and the mass carbonation technology as an innovative idea was put forward to reinforce soft soil. In this view, the field mass stabilization was carried out and the single-point test was analyzed. Research results show that the temperature from the carbonation reaction is higher than that from the hydration reaction, and the temperature, strength and carbonation degree of the upper foundation soils increase significantly compared with the lower foundation soils, while the water content and pH value of the upper foundation soils are less than those of the lower foundation soils; the smaller the distance from the CO₂ gas supply is, the higher the carbonation temperature, resilience modulus, penetration resistance, strength and carbonation degree are; the pipe-cover mass carbonation–stabilization technology can realize the carbonation and reinforcement of the on-site weak soils, but it should be noted that the CO₂ should be injected at the bottom. The maximum ventilation radius should be 60 cm and the distance between the CO₂ pipes should be less than 1.2 m in practical application. The bearing capacities of all regions are above 200 kPa, and the resilient moduli are about 20 MPa. The experimental research of mass stabilization based on

S. Liu · G. Du · L. Wang · C. Qin

Institute of Geotechnical Engineering, Southeast University, Nanjing 211189, China

e-mail: liusy@seu.edu.cn

G. Du

e-mail: guangyin@seu.edu.cn

G. Cai (✉)

College of Civil Engineering, Nanjing Forestry University, Nanjing 210037, China

e-mail: ghcai@njfu.edu.cn

J. Chen · J. Ruan

Jiangsu Traffic Engineering Construction Bureau, Nanjing 210004, China

MgO-CO₂ carbonation technology has groundbreaking scientific significance and application prospects in the emission reduction and sustainable development of civil engineering.

Keywords Magnesium oxide · CO₂ carbonation · Mass stabilization · Mucky soil · Strength

1 Introduction

With the rapid development of national infrastructure construction, many engineering projects such as large highways have to be built on the soft soil, especially the eastern coastal areas along the Yangtze River. It is difficult to directly construct on soft soil due to its weak properties such as high water content, large void ratio, low strength, high compressibility, and the soft soil has to be improved to meet the needs of bearing capacity [1]. The commonly used improvement technologies include the physical reinforcement, chemical reinforcement and biological methods. Physical reinforcement methods include vacuum preloading, compaction and soil replacement. They are simple but need a long processing cycle, are of high economic cost and have limited treatment effect. Biological curing method is a current research hotspot, but it is difficult to be applied in the engineering practice owing to the strict living conditions and high cost of microbes/bacteria as well as long processing period, and its treatment effect needs to be further verified. Chemical solidification technology is widely utilized in various fields of soft soil foundation reinforcement, significantly improving the physical and mechanical properties of soft soil as well as the foundation bearing capacity through a series of chemical reactions between curing binders and soil. In addition, the chemical stabilization has some significant advantages such as simple construction operation, strong applicability and low cost [1, 2]. For the chemical stabilization, the quicklime and Portland cement (PC) are the most common binders in the area of soft soil treatment because of the ion-exchange reaction and pozzolanic reaction between the binder and soil [2]. However, there exist some defects for these binders as follows: (a) serious resource and energy consumption (1 t CaO/1.8 t CaCO₃, high calcining temperature > 1450 °C), (b) serious CO₂ emissions (0.75–0.85 t CO₂/ t PC), dust and other toxic gases and (c) long curing time reaching the requirements of the engineering environment [2, 3]. Therefore, it is necessary to look for a kind of low-carbon, environmental and innovative binder to replace traditional PC.

Reactive MgO can be used in the stabilization of soft soil through the admixture of a certain amount of industrial by-products (such as GGBS, slag). It can be also realized the rapid improvement through the CO₂ carbonation in the soil treatment application. When admixed with soft soil, MgO would take hydration to form Mg(OH)₂, decreasing the water content. Then, Ca(OH)₂ and Mg(OH)₂ can also take ion-exchange and pozzolanic reactions with Si and Al ions to form hydrated magnesium silicate (MSH) and magnesium aluminate (MAH) [2, 4, 5]. Because Mg²⁺

ion has a weaker ion-exchange ability than Ca^{2+} , $\text{Mg}(\text{OH})_2$ has a lower alkaline and solubility as well as slower reaction than $\text{Ca}(\text{OH})_2$. Despite of weak cementation ability of $\text{Mg}(\text{OH})_2$ compared to cement hydration products of CSH, $\text{Mg}(\text{OH})_2$ could easily take carbonation reaction with CO_2 gas in a short period, producing the hydrated magnesium carbonates with high cementing strength [4]. In previous researches, the reactive MgO-treated soils could finish the CO_2 carbonation in 3–6 h, and their strength was higher than that of 28d PC-treated soils with the same dosage, reducing 90% of construction period, 65% of energy consumption and 77% of CO_2 emissions [2, 3]. Moreover, the mechanical, resistivity and microstructural properties of carbonated MgO-admixed silt were investigated and the prediction models of strength and resistivity were proposed respectively, and it was concluded that the strength of MgO-carbonated soil has a good linear relationship with its electrical resistivity [4–6]. Other investigations have been conducted on the influence of MgO activity on the strength properties of carbonated MgO-stabilized clay, the effects of MgO activity index and soil type on mechanical characteristics of carbonated soils. In addition, in view of the MgO- CO_2 carbonation/stabilization method in the application of soft ground, Liu and Cai have applied many invention patents including the carbonating mixing-pile construction, mass carbonation methods. On the basis of mass carbonation method, CAI verified the feasibility of this method in the improvement of soft ground through the indoor model tests [7].

Existing research mainly focused on the indoor model test, revealing the influence of MgO activity and carbonation condition on the physical and mechanical properties and microscopic mechanism, but the pilot-scale field trial has not been carried out based on this new treatment technology. The aim of this paper was to put forward the specific operation technology and to preliminarily study the influence of initial conditions on the treatment effectiveness.

2 Filed Introduction and Test Overview

2.1 Filed Introduction

The field site was located at a Ramp Road (K4 + 500) along the Yichang (Yixing to Changxing) Highway located in Yixing City, Jiangsu Province, China, as shown in Fig. 1. The test site was a low ditch with the area of $\sim 480 \text{ m}^2$, the water depth of 0.8 m and the average mud depth of 1.0 m. After draining water and cleaning weeds, the initial water content was about 85%. Where after, the ditch was excavated to continuously reduce the water content near liquid limit. The mud soil was sampled to measure the physical and chemical compositions, and the test results were shown in Tables 1 and 2. The Atterberg limits and classifications of mud soil were determined according to ASTM D4318 (ASTM 2010) and ASTM D2487 (ASTM 2011), respectively, and the soil was classified as a low plasticity clay. The specific gravity of soil was determined based on ASTM D854 (ASTM 2010), and the soil pH was



Fig. 1 Research overview diagram

Table 1 Physical and chemical properties of experimental materials

Property	Liquid limit /%	Plastic limit /%	Plasticity index	Specific gravity	pH value	Grain size distribution (%)		
						Clay	Silt	Sand
Values	46	20	26	2.70	7.4	15.6	83.3	1.1

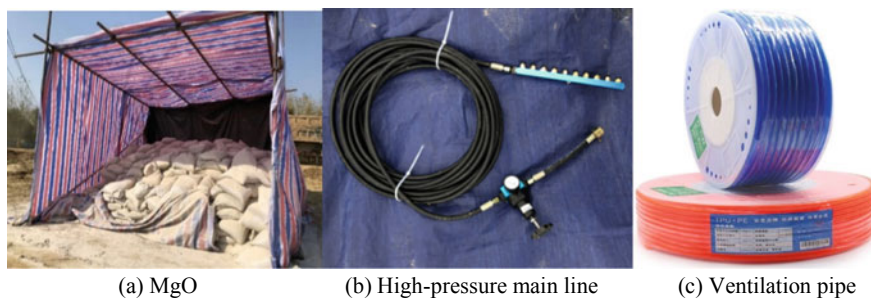
Table 2 Chemical compositions of experimental materials

Oxides	SiO ₂	Al ₂ O ₃	Fe ₂ O ₃	K ₂ O	CaO	MgO	TiO ₂	SO ₃	LOI
Soil	69.79	17.84	5.34	2.05	1.11	1.04	1.00	–	4.8
MgO	5.58	0.42	0.22	0.01	2.46	81.33	–	0.1	9.88

measured by portable D-54 pH meter according to ASTM D4972 (ASTM 2007). In order to facilitate the mechanical construction, it was necessary to perform the preliminary treatment for the site. Field experiment was conducted in the cold winter (middle of January), and the highest temperature was 4–6 °C during the day.

2.2 Materials

The MgO used in this field study was purchased from Dashiqiao, Liaoning, China, and it was obtained from industrial calcination (Fig. 2a). Its activity content was 43% based on the weight change during the hydration reaction, its activity value was 152 s, and its specific surface area was 7.2 m²/g as per the ASAP 2020 Physisorption Analyzer. The content of curing binder was selected as 10% according to the common content of curing agent used in the chemical stabilization. The total amount of MgO was estimated according to the earth volume, water content and density of mucky soil. The CO₂ gas with a concentration of 99.9% was supplied by Yixing Shenniu Special Gases Co. Ltd. The CO₂ gas used was transported in the field site according to 30 kg/bottle and nine bottle for one group, and each group was shared by a vent valve. Ventilation apparatus was consisted of high-pressure pipes, barometer, vent



(a) MgO

(b) High-pressure main line

(c) Ventilation pipe

Fig. 2 Main materials

valves and diverter, and one high-pressure pipe can shunt for 20 branch pipes ($\Phi 8$ + PE hose) which were connected the 20 PVC perforated pipes, respectively. Test materials are shown in Fig. 2.

2.3 Construction Equipment

Field test mixing machinery was used by Southeast University and Nanjing Stirring Pile Special Technology Co. LTD. The construction system used in the study site were mainly consisted of two parts: (a) a power mixer attachment for an excavator, which injected the binder at the point of mixing; and (b) a pressure feeder made up of feed tank and storage tank (its capacity of 1.0 t), which moved the binder from the container, through a powder spraying pipe (or hose), to the middle of the mixing drums of the power mixer (See Fig. 3). The attachments used for the binder feeder



(a) Mixing machine

(b) Storage tank

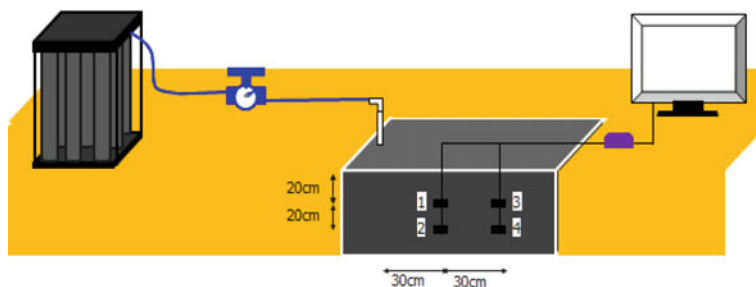
Fig. 3 Mixing equipment

also included the alternator and the air compressor. The power mixer attachment for an excavator was mainly consisted of the supporting arm, power converter, agitator arm (its length of ~3.0 m) and two-directional mixing head (its diameter of 1.2 m). It was worth noting that the supporting arm and agitator arm could usually be worked vertically or at a certain angle. Before mixing, the workers firstly added MgO powder into the mouth of feeding tank, and then, the air pressure compressor was open to pump MgO into spraying tank, and finally, the MgO powder was ejected from the powder spraying mouth at the bottom through the powder spraying pipe.

2.4 Test Plan

Before mixing, the single-point test was conducted to determine the breather pipe spacing and ventilation pressure. A pit of $1\text{ m} \times 1\text{ m} \times 0.6\text{ m}$ was dig, and the MgO powder was evenly mixed according the MgO content of about 10%, water content of ~45% and soil density of 1.7 g/cm^3 [8]. A perforated PVC pipe was inserted into the edge of the test area, and the temperature sensors were placed into the four locations of 30 and 60 cm distance from PVC pipe as well as 20 and 40 cm depth. Moreover, the two sensors at the distance of 30 cm were, respectively, named as #1 and #2 for the upper and bottom layers, and other two sensors at the distance of 60 cm were, respectively, named as #3 and #4 for the upper and bottom layers (Fig. 4). DATATAKER acquisition apparatus was used to collect and record the temperature. The plastic film was covered on the layer surface to avoid the gas leakage. According to previous research, the carbonation efficiency of MgO-treated soils increased with the increasing CO_2 pressure within a certain pressure range, but the too high CO_2 pressure would cause large cracks and the gas waste. Therefore, the CO_2 valve was open and the CO_2 pressure was slowly increased to 500 kPa. The ventilation time was about 3 h.

Light dynamic penetration was adopted to evaluate the bearing capacity of soft foundation before and after processing. The light dynamic penetration instrument was mainly consisted of drop hammer (its weight of 10 kg), penetration rod (outer diameter of 25 mm) and cone head (the cone bottom area of 12.6 cm^2 and cone angle of 60°). During the test process, the penetration depth of cone head was measured when the falling distance of hammer was 50 cm, and the penetration index (N_{10}) was recorded when the penetration depth of the cone tip was 30 cm.



(a) Schematic diagram



(b) Field drawing

Fig. 4 Test arrangement diagram

3 Filed Treatment Effect and Discussion

3.1 Temperature

The temperature of MgO-admixed site was recorded during the CO₂ ventilation, and the monitoring temperature at different positions was shown in Fig. 5. As can be seen from Fig. 5, the monitored temperature of the site (>10 °C) was much higher than the ambient temperature (4 ~ 6 °C), which was attributed to the heat accumulation at the treatment area during the hydration and carbonization exothermic reactions of MgO. Through the temperature comparison of different locations (#1 and #2, #3 and #4), the results can be found that the temperature curves and changes basically were the same trend, indicating that there was little difference for the carbonation effect in the vertical direction at the same ventilation distance and the reaction intensity was relatively uniform. The horizontal comparison showed that the temperature of #1 and #2 decreased abnormally in the early stage of ventilation, which may be due to the gasification cooling of the CO₂ released from the high-pressure tank at the close location of the ventilation pipe. Moreover, it can be also found from Fig. 5 that the sharp carbonation reaction was taken at the first one hour's ventilation, and thereafter, there was no significant fluctuate for temperature curves especially for the

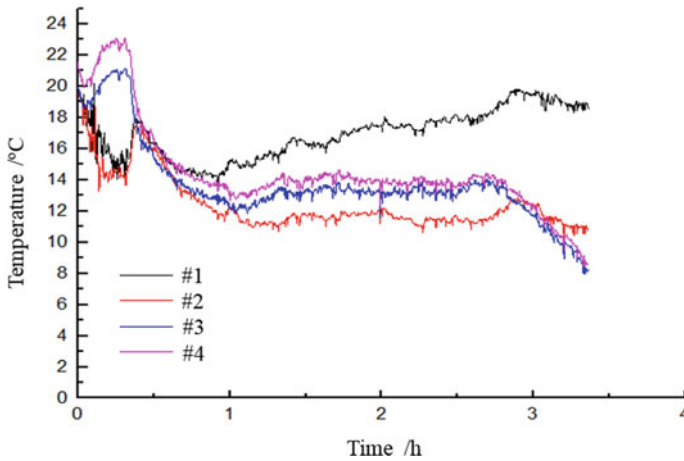


Fig. 5 Changes of temperature with ventilation time at different locations

#1 sensor. The results could be explained by the fact that there was enough hydration time for MgO and the first ventilation facilitated the hydration of MgO; and the long continuous ventilation would cause the CO₂ leakage.

3.2 Dynamic Penetration Results

The dynamic penetration blows were, respectively, three and four for the raw soil and the MgO-admixed soil when the penetration depth was 30 cm. According to *In-situ Test Regulation for Railway Engineering* (TB 10018–2018), the bearing capacity of the ground foundation could be transformed by the following formula:

$$R = 8 * N_{10} - 20 \quad (1)$$

where R is the bearing capacity (kPa), N_{10} is the penetration blows for the falling depth of 30 cm [8, 9].

According to the above calculation formula, the bearing capacity of soft soil foundation could be calculated as 4 and 12 kPa, respectively, before and after admixing MgO. When the MgO-admixed soil was subjected to CO₂ carbonation, the penetration blows of foundation at different distances of 20, 40 and 60 cm from the ventilation pipe were 25, 23 and 17, respectively, and the corresponding bearing capacity were 180, 164 and 116 kPa. The higher bearing capacity above 100 kPa met the bearing requirements of the shallow subgrade of the expressway. Considering the carbonization efficiency of a large area treatment and the strength difference inside and outside of 60 cm distance, the optimal ventilation spacing was recommended to be 60 cm. For the large area treatment, the PVC pipe spacing can be chosen to

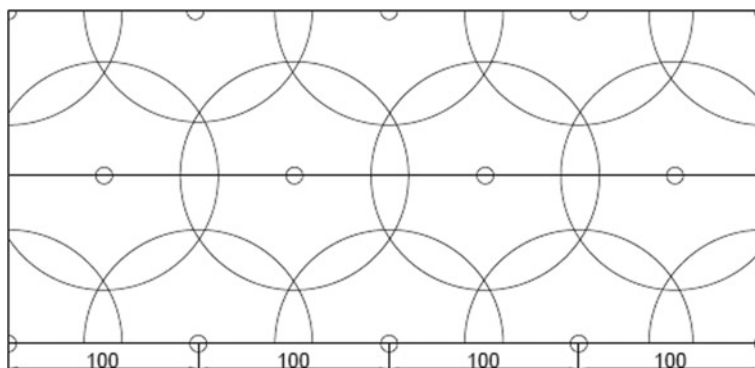


Fig. 6 Schematic diagram of ventilation spacing. *Note:* small circle represents the gas injection point and the large circle represents the carbonization range

be 1–1.2 m, and each carbonization area was overlapped with each other to form a carbonation mass (see Fig. 6).

The preliminary construction technology and parameters can be determined. However, there are still some shortcomings in the field tests on the MgO mass carbonization of soft foundation, including the uniformity of curing agent, the optimization of curing agent and the construction process, which need to be further improved in the subsequent engineering application. In the future study, the relationship between the treatment effect and influence factors should be comprehensively discussed combining with other physical and mechanical tests and indoor microscopic analysis.

4 Conclusion

This paper briefly summarizes the principle and current situation of MgO-CO₂ carbonization technology as well as the field construction of MgO mass carbonization. The corresponding results are preliminarily determined including the appropriate range of ventilation radius and gas pressure of MgO mass carbonization. The maximum ventilation radius is suggested as 60 cm, and the spacing of gas branch pipe should be 1–1.2 m. The output pressure of the gas tank is about 500 kPa. The total ventilation time is 3–6 h, and the intermittent ventilation is recommended as half an hour stoppage for every one hour's ventilation to ensure full utilization of CO₂. After several hours' ventilation carbonization and 1 day maintenance, the soft foundation can meet the bearing requirement of highway subgrade.

Acknowledgements This work is financially supported by the National Natural Science Foundation of China (41902286, 41972269), Open Fund for State Key Laboratory of Geotechnical

Mechanics and Engineering (Z019026), Natural Science Foundation of the Jiangsu Higher Education Institutions of China (18KJB560012) and Youth Science and Technology Innovation Fund of Nanjing Forestry University (CX2018005, GXL2018028).

References

1. Liu SY, Qian GC, Zhang DW (2006) The principle and application of dry jet mixing composite foundation. China Architecture and Building Press, Beijing
2. YI YL (2013) Sustainable novel deep mixing methods and theory
3. YI Y (2013) Carbonating magnesia for soil stabilization. *Can Geotech J* 50(8):899–905
4. Guanghua CAI (2017) Influence of initial water content on strength and electrical resistivity of MgO-carbonated silt. *China J Highw Trans* 30(11):18–26
5. Gh CAI (2015) Physical properties, electrical resistivity and strength characteristics of carbonated silty soil admixed with reactive magnesia. *Can Geotech J* 52(11):1699–1713
6. Gh CAI (2015) Strength and deformation characteristics of carbonated reactive magnesia treated silt soil. *J Cent S Univ* 22(5):1859–1868
7. Liu SY (2017) Model tests on carbonated reactive MgO mixing piles. *Chin J Geotech Eng* 39(S2):136–139
8. Chuan QIN (2019) Process model and application studies on soft foundation overall carbonated and stabilized by reactive magnesia
9. Industrial standards of the People's Republic of China (2018) Code for In-situ Testing of Railway Engineering Geology

Analytical Solution for Plane Strain Consolidation of Soft Soil Stabilised by Stone Columns



Sam Doan, Behzad Fatahi, Hadi Khabbaz, and Haleh Rasekh

Abstract This paper presents an analytical solution for free strain consolidation of a stone column-stabilised soft soil under instantly applied loading and two-dimensional plane strain conditions. Both horizontal and vertical flows of water were integrated into the mathematical model of the problem, while the total vertical stresses induced by the external load were assumed to distribute uniformly within each column and soil region. By utilising the separation of variables method, an exact series solution was obtained to predict the variation of excess pore water pressure and settlement with time for any point in the model. The achieved solution can capture the drain resistance effect due to the inclusion of permeability and size of the stone column in the mathematical model. A worked example investigating the dissipation of excess pore water pressure was conducted to exhibit the capabilities of the obtained analytical solution. The correctness of the solution was verified against a finite element modelling with good agreements. Besides, a parametric study to inspect the influence of consolidation parameters of soil on performance objectives (e.g. average degree of consolidation and average differential settlement) was also reported in this study. The results from the parametric analysis show that an increase in permeability of soil sped up considerably the consolidation and differential settlement. Furthermore, an increase in soil stiffness accelerated the consolidation and reduced the average differential settlement between stone column and soft soil significantly. Eventually, the proposed analytical solution is also feasible to predict the consolidation of soft soil with the inclusion of prefabricated vertical drains or pervious columns by adopting appropriate consolidation parameters and stress concentration ratio.

S. Doan (✉) · B. Fatahi · H. Khabbaz · H. Rasekh
School of Civil and Environmental Engineering, University of Technology Sydney (UTS), City
Campus Broadway NSW 2007, PO Box 123, Sydney, Australia
e-mail: huusam.doan@student.uts.edu.au

B. Fatahi
e-mail: behzad.fatahi@uts.edu.au

H. Khabbaz
e-mail: hadi.khabbaz@uts.edu.au

H. Rasekh
e-mail: haleh.rasekh@uts.edu.au

Keywords Consolidation · Stone column · Free strain · Analytical solution · Plane strain

1 Introduction

Stone columns are widely utilised to improve soft soil beneath structures such as highway embankment, seaport or airport. As reported by many researchers [1–3], stone columns not only speed up the consolidation of soft soil due to their high permeability but also reduce the compressibility of the composite soil foundation because of their extremely greater stiffness compared with the soft soil.

Over the last decades, there have been numerous studies on ground improvement techniques using stone columns. Amongst those, the consolidation problem is one of the topics which has attracted the attention of many researchers. Therefore, various studies have been conducted to investigate the consolidation behaviour of the stone column-stabilised soft soil considering many influencing factors such as smear zone, drain resistance, time- and depth-dependent loading, simultaneous vertical and horizontal flows, viscoelastic and nonlinear properties of soil foundations. Analytical methods play an integral part since they are capable of providing insight into the problem via performing sensitivity analysis and parametric study, which may be more inconvenient via numerical modelling. However, most available analytical studies on the consolidation of stone column-supported soft soil composite ground adopt the equal strain assumption, which is unable to predict the differential settlement between the column and soft soil. Recently, Doan and Fatahi [4] developed an analytical solution for axisymmetric and free strain consolidation of soft ground reinforced by stone columns accounting for space-dependent total stress and drain resistance effects. In spite of that, there is a lack of the analytical solution for plane strain consolidation of the aforementioned composite ground considering the differential settlement condition (i.e. free strain assumption) in the existing literature. Obviously, the behaviour of a permeable column-improved soft soil can be more accurately analysed under three-dimensional (3D) or axisymmetric conditions resembling the actual column–soil foundation in real practice than under the two-dimensional (2D) equivalent plane strain consideration. As reported in various studies [5–7], however, the equivalent plane strain model of the composite pervious column–soil foundation can provide acceptable predictions for the foundation settlement and excess pore water pressure dissipation, particularly at the regions close to the centre of embankment.

The aim of this paper is to provide an analytical solution to investigate the free strain consolidation of a stone column-reinforced soft soil subjected to an instantly applied uniform loading under plane strain condition. A general solution to predict the excess pore water pressure dissipation and thus the consolidation settlement at any point in the model was achieved applying the method of separation of variables. To validate the capabilities of the obtained analytical solution, a worked example was conducted to examine the excess pore water pressure dissipation in the stone column and soft soil. The accuracy of the proposed solution was also verified against a finite

element simulation. Besides, a parametric analysis was performed to investigate the effect of permeability and stiffness of soft soil on the average degree of consolidation for each region of the model and the differential settlement between the two regions.

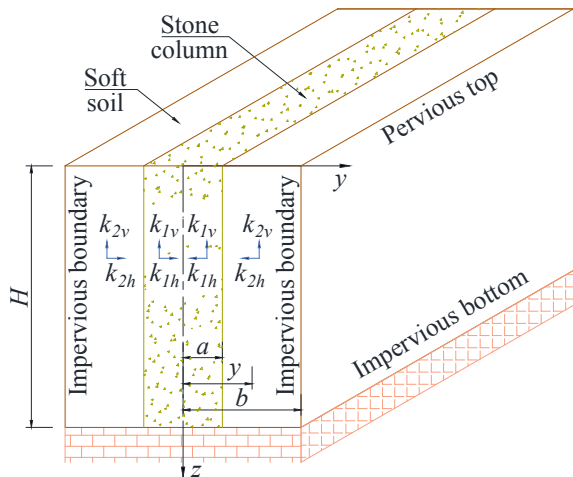
2 Problem Description

Similar to the consolidation of soil with the inclusion of vertical drains, stone columns are commonly installed into soft ground in a square or triangular pattern in real practice [8, 9]. To develop an equivalent plane strain model, several models from available studies [10–13] can be applied in which the equivalent geometries or material properties (e.g. permeability and stiffness) of stone column and surrounding soil are obtainable by matching the analytical solution for consolidation between plane strain and axisymmetric models. It should be emphasised that the main objective of this study is to derive the analytical solution for plane strain consolidation model while the equivalent conversion factors relating to the geometry or material property of the model are assumed to be obtained using the available studies.

Figure 1 illustrates a typical plane strain consolidation model with a stone column region of width $2a$ enclosed by the soft soil region extended to width $2b$. The soil stratum has a thickness H underlain by a stiff layer, and the column is entirely penetrated along the soil depth. The exterior boundaries and bottom base are impervious, while the upper surface of the model is considered to be freely draining. To derive the solution in this study, the following assumptions have been made:

- The column and soil regions are homogeneous.
- The foundation is completely saturated in which soil solid and water are incompressible with the assumption of Darcy’s law for the water flow.

Fig. 1 Model of the problem



- The free strain assumption is adopted; the column and soil solely deform vertically.
- The permeability and compressibility of the column and soil are assumed to be constant under surcharge loading.

It is also assumed that the external load is applied instantaneously and remained unchanged during the consolidation period, which induces time-independent total stress applied in each region of the model. Then, referring to the studies by other researchers [4, 14] and considering the symmetry of the problem, the equations for consolidation of the plane strain model can be expressed by

$$c_{1h} \frac{\partial^2 u_1(y, z, t)}{\partial y^2} + c_{1v} \frac{\partial^2 u_1(y, z, t)}{\partial z^2} = \frac{\partial u_1(y, z, t)}{\partial t} \quad (0 \leq y \leq a) \quad (1a)$$

$$c_{2h} \frac{\partial^2 u_2(y, z, t)}{\partial y^2} + c_{2v} \frac{\partial^2 u_2(y, z, t)}{\partial z^2} = \frac{\partial u_2(y, z, t)}{\partial t} \quad (a \leq y \leq b) \quad (1b)$$

where u_1 and u_2 are the excess pore water pressures at any points in the stone column and soft soil, respectively; y and z are Cartesian coordinates as displayed in Fig. 1; t is the time; $c_{1h} = (k_{1h}M_1)/\gamma_w$ and $c_{1v} = (k_{1v}M_1)/\gamma_w$ are the horizontal and vertical consolidation coefficients of the stone column, respectively; $c_{2h} = (k_{2h}M_2)/\gamma_w$ and $c_{2v} = (k_{2v}M_2)/\gamma_w$ are the horizontal and vertical consolidation coefficients of the soft soil, respectively; k_{1h} , k_{1v} and M_1 are the horizontal and vertical permeability coefficients and constrained modulus of the stone column, respectively; similarly, k_{2h} , k_{2v} and M_2 are the horizontal and vertical permeability coefficients and constrained modulus of the soft soil, respectively; γ_w is the unit weight of water (10 kN/m^3).

Pertaining to Fig. 1, the conditions of no horizontal flows at the centre line and outside boundary of the model can be represented by Eqs. (2a) and (2d), respectively; whereas, the continuities of excess pore water pressure and flow rate at the column–soil interface can be described by Eqs. (2b) and (2c), respectively.

$$\partial u_1 / \partial y = 0 \text{ at } y = 0 \quad (2a)$$

$$u_1 = u_2 \text{ at } y = a \quad (2b)$$

$$k_{1h} \partial u_1 / \partial y = k_{2h} \partial u_2 / \partial y \text{ at } y = a \quad (2c)$$

$$\partial u_2 / \partial y = 0 \text{ at } y = b \quad (2d)$$

The top surface of the composite ground is considered as fully permeable, while the bottom one rests on an impermeable rigid stratum (see Fig. 1). Then, the following conditions can be included in these two boundaries as follows:

$$u_1 = u_2 = 0 \text{ at } z = 0 \quad (3a)$$

$$\partial u_1 / \partial z = \partial u_2 / \partial z = 0 \text{ at } z = H \tag{3b}$$

It is worth noting that the total stresses in the composite foundation are supposed to be carried completely by the excess pore water pressures immediately after loading due to the second assumption. Assuming the total stresses in the stone column and soft soil regions caused by the external load distribute uniformly in each region, the initial conditions for excess pore water pressure can be expressed by

$$u_1(t = 0) = \sigma_1 \quad (0 \leq y \leq a) \tag{4a}$$

$$u_2(t = 0) = \sigma_2 \quad (a \leq y \leq b) \tag{4b}$$

where σ_1 and σ_2 are the total vertical stresses in the column and soil, respectively.

3 Analytical Solution

The set of Eqs. (1)–(4) describe the plane strain consolidation problem in which the governing equations and boundary conditions are homogeneous, while the initial conditions are nonhomogeneous.

According to the studies by Aviles-Ramos et al. [15] and Doan and Fatahi [4], the method of separation of variables can be applied and the solution for the excess pore water pressure at any point in the model is defined as follows:

$$u_i(y, z, t) = u_i^{(i)}(y, z, t) + u_i^{(ii)}(y, z, t) \quad (y_i \leq y \leq y_{i+1}) \quad (i = 1, 2) \tag{5}$$

In which the subscript $i = 1, 2$ denotes the stone column and soft soil regions, respectively; $y_1 = 0, y_2 = a, y_3 = b$; $u_i^{(i)}$ and $u_i^{(ii)}$ are determined as follows:

$$u_i^{(i)}(y, z, t) = \sum_{m=1}^{\infty} \sum_{n=1}^{\infty} C_{mn}^{(i)} Z_m(z) Y_{imn}^{(i)}(y) e^{-\beta_{mn}^{(i)2} t} \quad (y_i \leq y \leq y_{i+1}) \tag{6a}$$

$$u_i^{(ii)}(y, z, t) = \sum_{m=1}^{\infty} \sum_{n=1}^{F(m)} C_{mn}^{(ii)} Z_m(z) Y_{imn}^{(ii)}(y) e^{-\beta_{mn}^{(ii)2} t} \quad (y_i \leq y \leq y_{i+1}) \tag{6b}$$

where m and n are integer index corresponding to z - and y -directions, respectively; $Z_m(z)$ are the eigenfunctions with respect to z -direction and $Z_m(z)$ defined by

$$Z_m(z) = \sin \lambda_m z \tag{7}$$

The term λ_m are the eigenvalues corresponding to $Z_m(z)$ and determined as follows:

$$\lambda_m = (2m - 1)\pi/(2H) \quad \text{for } m = 1, 2, 3, \dots \tag{8}$$

Considering Eq. (6a), the terms $Y_{1mn}^{(i)}(y)$ are the eigenfunctions with respect to y -direction, which are defined, respectively, for the stone column and soft soil regions by substituting the subscript $i = 1, 2$ as follows:

$$Y_{1mn}^{(i)}(y) = A_{1mn}^{(i)} \cos(v_{1mn}^{(i)}y) + B_{1mn}^{(i)} \sin(v_{1mn}^{(i)}y) \tag{9a}$$

$$Y_{2mn}^{(i)}(y) = A_{2mn}^{(i)} \cos(v_{2mn}^{(i)}y) + B_{2mn}^{(i)} \sin(v_{2mn}^{(i)}y) \tag{9b}$$

where $A_{1mn}^{(i)}$, $B_{1mn}^{(i)}$, $A_{2mn}^{(i)}$ and $B_{2mn}^{(i)}$ are the constants to be determined; $v_{1mn}^{(i)}$ and $v_{2mn}^{(i)}$ are the eigenvalues corresponding to $Y_{1mn}^{(i)}(y)$ and $Y_{2mn}^{(i)}(y)$, respectively. The relationships between the eigenvalues pair $(v_{1mn}^{(i)}, v_{2mn}^{(i)})$ and the term $\beta_{mn}^{(i)}$ in Eq. (6a) are given by the following equations:

$$v_{1mn}^{(i)} = \sqrt{\beta_{mn}^{(i)2}/c_{1h} - \kappa_1^2 \lambda_m^2} \quad \text{where } \beta_{mn}^{(i)2}/c_{1h} - \kappa_1^2 \lambda_m^2 \geq 0 \tag{10a}$$

$$v_{2mn}^{(i)} = \sqrt{\beta_{mn}^{(i)2}/c_{2h} - \kappa_2^2 \lambda_m^2} \quad \text{where } \beta_{mn}^{(i)2}/c_{2h} - \kappa_2^2 \lambda_m^2 \geq 0 \tag{10b}$$

$$\kappa_1 = \sqrt{c_{1v}/c_{1h}} = \sqrt{k_{1v}/k_{1h}} \quad \text{and} \quad \kappa_2 = \sqrt{c_{2v}/c_{2h}} = \sqrt{k_{2v}/k_{2h}} \tag{11}$$

It is worth mentioning that the conditions $c_{1h} > c_{2h}$ and $c_{1v} > c_{2v}$ hold true because the stone column possesses larger permeability and constrained modulus than the soft soil. Then, the following condition for $\beta_{mn}^{(i)}$ values can be derived on the basis of the concurrent satisfaction of the inequalities provided in Eqs. (10a) and (10b):

$$\beta_{mn}^{(i)} \geq \max\{\kappa_1 \lambda_m \sqrt{c_{1h}}, \kappa_2 \lambda_m \sqrt{c_{2h}}\} = \kappa_1 \lambda_m \sqrt{c_{1h}} = \lambda_m \sqrt{c_{1v}} \tag{12}$$

For a specified value of m , the subscript n implies an infinite number of different eigenvalues $\beta_{mn}^{(i)}$ and consequent pairs $(v_{1mn}^{(i)}, v_{2mn}^{(i)})$. The eigenfunctions $Y_{1mn}^{(i)}(y)$ and $Y_{2mn}^{(i)}(y)$ are completely disclosed only when the corresponding constants and the eigenvalues pair $(v_{1mn}^{(i)}, v_{2mn}^{(i)})$ are achieved by taking advantage of the boundary conditions in y -direction.

Imposing the boundary condition presented in Eq. (2a) on the solution reported in Eq. (6a) and noting that the subscript $i = 1$ for the stone column region yield $B_{1mn}^{(i)} = 0$. It should also be noted that the incorporation of the boundary conditions described by Eqs. (2b), (2c) and (2d) into the solution in Eq. (6a) with the subscript $i = 1, 2$ would lead to a matrix equation in which the constants $A_{1mn}^{(i)}$, $A_{2mn}^{(i)}$ and $B_{2mn}^{(i)}$ can be determined in terms of any non-vanishing one [16]. By assigning $A_{1mn}^{(i)} = 1$ for simplicity, therefore, the following matrix equation for the determination of $A_{2mn}^{(i)}$

and $B_{2mn}^{(i)}$ is obtained:

$$\Omega^{(i)} K^{(i)} = 0 \tag{13}$$

$$\text{where } \Omega^{(i)} = \begin{bmatrix} \cos(v_{1mn}^{(i)} a) & -\cos(v_{2mn}^{(i)} a) & -\sin(v_{2mn}^{(i)} a) \\ -N_k v_{1mn}^{(i)} \sin(v_{1mn}^{(i)} a) & v_{2mn}^{(i)} \sin(v_{2mn}^{(i)} a) & -v_{2mn}^{(i)} \cos(v_{2mn}^{(i)} a) \\ 0 & -v_{2mn}^{(i)} \sin(v_{2mn}^{(i)} b) & v_{2mn}^{(i)} \cos(v_{2mn}^{(i)} b) \end{bmatrix} \tag{14a}$$

$$K^{(i)} = \{ 1, A_{2mn}^{(i)}, B_{2mn}^{(i)} \} \tag{14b}$$

where $N_k = k_{1h}/k_{2h}$ is the horizontal permeability ratio between stone column and soft soil. Substituting $v_{1mn}^{(i)}$ and $v_{2mn}^{(i)}$ from Eqs. (10a) and (10b) into Eq. (14a), the matrix $\Omega^{(i)}$ with respect to $\beta_{mn}^{(i)}$ is attained. Then, the transcendental equation to determine the eigenvalues $\beta_{mn}^{(i)}$ can be derived by the demand that Eq. (13) has a non-trivial solution (i.e. $\det \Omega^{(i)} = 0$). Once $\beta_{mn}^{(i)}$ have been achieved, $v_{1mn}^{(i)}$ and $v_{2mn}^{(i)}$ can be calculated by Eqs. (10a) and (10b), respectively.

Pertaining to Eq. (6b), similar to the eigen functions $Y_{imn}^{(i)}(y)$, the eigen functions $Y_{imn}^{(ii)}(y)$ corresponding to the stone column and soft soil regions are defined as follows:

$$Y_{1mn}^{(ii)}(y) = A_{1mn}^{(ii)} \cosh(v_{1mn}^{(ii)} y) + B_{1mn}^{(ii)} \sinh(v_{1mn}^{(ii)} y) \tag{15a}$$

$$Y_{2mn}^{(ii)}(y) = A_{2mn}^{(ii)} \cos(v_{2mn}^{(ii)} y) + B_{2mn}^{(ii)} \sin(v_{2mn}^{(ii)} y) \tag{15b}$$

where $A_{1mn}^{(ii)}$, $B_{1mn}^{(ii)}$, $A_{2mn}^{(ii)}$ and $B_{2mn}^{(ii)}$ are the constants to be determined; $v_{1mn}^{(ii)}$ and $v_{2mn}^{(ii)}$ are the eigenvalues corresponding to $Y_{1mn}^{(ii)}(y)$ and $Y_{2mn}^{(ii)}(y)$, respectively. The relationships between the eigenvalues pair ($v_{1mn}^{(ii)}$, $v_{2mn}^{(ii)}$) and the term $\beta_{mn}^{(ii)}$ in Eq. (6b) are given by the following equations:

$$v_{1mn}^{(ii)} = \sqrt{\kappa_1^2 \lambda_m^2 - \beta_{mn}^{(ii)2} / c_{1h}} \text{ where } \kappa_1^2 \lambda_m^2 - \beta_{mn}^{(ii)2} / c_{1h} > 0 \tag{16a}$$

$$v_{2mn}^{(ii)} = \sqrt{\beta_{mn}^{(ii)2} / c_{2h} - \kappa_2^2 \lambda_m^2} \text{ where } \beta_{mn}^{(ii)2} / c_{2h} - \kappa_2^2 \lambda_m^2 \geq 0 \tag{16b}$$

To fulfil the two inequalities provided in Eqs. (16a) and (16b) simultaneously, the $\beta_{mn}^{(ii)}$ values must satisfy the following:

$$\lambda_m \sqrt{c_{2v}} \leq \beta_{mn}^{(ii)} < \lambda_m \sqrt{c_{1v}} \tag{17}$$

where the condition $c_{1v} > c_{2v}$ and Eq. (11) have been utilised to derive the condition for the $\beta_{mn}^{(ii)}$ values. For a given value of m in this case, there is a finite number of eigenvalues $\beta_{mn}^{(ii)}$, which is denoted by $F(m)$ as a function of m . Thus, the index n of the second summation in Eq. (6b) adopts a finite value of the upper limit $F(m)$.

Conducting the derivation analogous to the case of the eigenvalues pair $(v_{1mn}^{(i)}, v_{2mn}^{(i)})$, while $B_{1mn}^{(ii)} = 0$ due to the boundary condition given by Eq. (2a) and $A_{1mn}^{(ii)} = 1$ for the sake of simplicity, the matrix equation to determine the constants $A_{2mn}^{(ii)}$ and $B_{2mn}^{(ii)}$ can be derived as follows:

$$\Omega^{(ii)} K^{(ii)} = 0 \tag{18}$$

$$\text{where } \Omega^{(ii)} = \begin{bmatrix} \cosh(v_{1mn}^{(ii)} a) & -\cos(v_{2mn}^{(ii)} a) & -\sin(v_{2mn}^{(ii)} a) \\ N_k v_{1mn}^{(ii)} \sinh(v_{1mn}^{(ii)} a) & v_{2mn}^{(ii)} \sin(v_{2mn}^{(ii)} a) & -v_{2mn}^{(ii)} \cos(v_{2mn}^{(ii)} a) \\ 0 & -v_{2mn}^{(ii)} \sin(v_{2mn}^{(ii)} b) & v_{2mn}^{(ii)} \cos(v_{2mn}^{(ii)} b) \end{bmatrix} \tag{19a}$$

$$K^{(ii)} = \{1, A_{2mn}^{(ii)}, B_{2mn}^{(ii)}\} \tag{19b}$$

The matrix $\Omega^{(ii)}$ with respect to $\beta_{mn}^{(ii)}$ can be obtained by substituting $v_{1mn}^{(ii)}$ and $v_{2mn}^{(ii)}$ provided in Eqs. (16a) and (16b) into Eq. (19a). Then, the eigenvalues $\beta_{mn}^{(ii)}$ are determined by the requirement $\det \Omega^{(ii)} = 0$, and $v_{1mn}^{(ii)}$ and $v_{2mn}^{(ii)}$ are calculated by Eqs. (16a) and (16b), respectively.

To finalise the solutions in Eqs. (6a) and (6b), the initial conditions in Eqs. (4a) and (4b) are applied for which the coefficients $C_{mn}^{(i)}$ and $C_{mn}^{(ii)}$ are obtainable by taking the orthogonal expansion technique as presented in the study by Doan and Fatahi [4]:

$$C_{mn}^{(*)} = \frac{1}{N_{mn}^{(*)}} \sum_{i=1}^2 \frac{k_{ih}}{c_{ih}} \int_{z=0}^H \int_{y=y_i}^{y_{i+1}} Z_m(z) Y_{imn}^{(*)}(y) \sigma_i \, dy \, dz \tag{20}$$

and

$$N_{mn}^{(*)} = \sum_{i=1}^2 \frac{k_{ih}}{c_{ih}} \int_{z=0}^H \int_{y=y_i}^{y_{i+1}} [Z_m(z) Y_{imn}^{(*)}(y)]^2 \, dy \, dz \tag{21}$$

where the new superscript (*) has been used to denote the superscript (i) or (ii) in order to avoid repeating expressions which have the same formulation.

Once the solutions in Eqs. (6a) and (6b) have been disclosed, the excess pore water pressure at any point in the model is captured using Eq. (5).

By taking average in y - and z -directions, the average excess pore water pressure for stone column \bar{u}_1 and for soft soil \bar{u}_2 is achieved as follows:

$$\bar{u}_1(t) = \left[\int_{z=0}^H \int_{y=0}^a u_1 \, dydz \right] / [aH] \text{ and } \bar{u}_2(t) = \left[\int_{z=0}^H \int_{y=a}^b u_2 \, dydz \right] / [(b-a)H] \quad (22)$$

The average surface settlements of stone column $\bar{S}_1(t)$ and of soft soil $\bar{S}_2(t)$ at time t due to the dissipation of excess pore water pressure are obtainable via the following equation:

$$\bar{S}_1(t) = [\sigma_1 - \bar{u}_1(t)]H/M_1 \text{ and } \bar{S}_2(t) = [\sigma_2 - \bar{u}_2(t)]H/M_2 \quad (23)$$

The average degree of consolidation of the stone column \bar{U}_1 and of the soft soil \bar{U}_2 based on the average surface settlement can be derived as follows:

$$\bar{U}_1(t) = \frac{\bar{S}_1(t)}{\bar{S}_1(\infty)} = \frac{\sigma_1 - \bar{u}_1(t)}{\sigma_1} \text{ and } \bar{U}_2(t) = \frac{\bar{S}_2(t)}{\bar{S}_2(\infty)} = \frac{\sigma_2 - \bar{u}_2(t)}{\sigma_2} \quad (24)$$

where $\bar{S}_1(\infty)$ and $\bar{S}_2(\infty)$ are the final average surface settlements of stone column and of soft soil when time t approaches infinity, respectively.

It is obvious that once the average excess pore water pressures \bar{u}_1 and \bar{u}_2 and the total vertical stresses σ_1 and σ_2 have been determined, the average surface settlement and the average degree of consolidation are completely captured by Eqs. (23) and (24), respectively.

4 Validation of the Proposed Analytical Solution

To validate the capabilities of the proposed analytical solution, this section provides a numerical example in conjunction with a parametric study to investigate the effect of consolidation parameters (e.g. permeability and modulus) on the consolidation behaviour of the composite ground subjected to an instantly applied loading $q = 100$ kPa.

Referring to [12], for simplicity, the geometric parameters and material properties of the equivalent plane strain consolidation model in this example after converting from the axisymmetric configuration were adopted in a typical range as follows:

$$H = 5 \text{ m}, \quad a = 0.4 \text{ m}, \quad b = 1.2 \text{ m}$$

$$k_{1h} = 4 \times 10^{-5} \text{ m/s}, \quad k_{1v} = k_{1h}, \quad E_1 = 30 \times 10^3 \text{ kPa}, \quad \nu_{p1} = 0.33$$

$$k_{2h} = 4 \times 10^{-10} \text{ m/s}, k_{2v} = 0.5 k_{2h}, E_2 = 1.5 \times 10^3 \text{ kPa}, \nu_{P2} = 0.33$$

where E_1 and E_2 are Young’s modulus of the stone column and soft soil, respectively; ν_{P1} ν_{P2} are Poisson’s ratio of the stone column and soft soil, respectively.

The validation was conducted by inspecting the excess pore water pressure dissipation in the model. Besides, the performance objectives were evaluated via the average degree of consolidation for the stone column \bar{U}_1 and for the soft soil \bar{U}_2 along with the average differential settlement $\Delta\bar{S}$ between the two regions. The average differential settlement $\Delta\bar{S}$ was calculated as the difference in average surface settlement between the column and soil regions determined by Eq. (23).

In connection to Eq. (5), the change of excess pore water pressure against each variable y, z or t can be captured by keeping the remaining variables unchanged.

Figure 2 illustrates the isochrones of excess pore water pressure at various time t along the y -direction of the model. It is observed that the isochrones complied with the zero flow conditions as in Eqs. (2a) and (2d) and column–soil interface conditions expressed by Eqs. (2b) and (2c) where excess pore water pressures distributed almost uniform along the column width and attained the maximum values at the exterior boundary $y = b$. The nonzero values of excess pore water pressure in the stone column region illustrate the drain resistance presence for a specified hydraulic conductivity (permeability) of the column. The excess pore water pressure within the stone column dissipated extremely quickly and reduced to almost 7 kPa at time $t = 2 \times 10^2$ s meanwhile that within most of the soft soil stayed almost same as the initial value.

Figure 3 depicts the excess pore water pressure dissipation at points with depth $z = 0.25H, z = 0.5H$ and $z = 0.75H$ and $y = 0.5a$ (in stone column region)

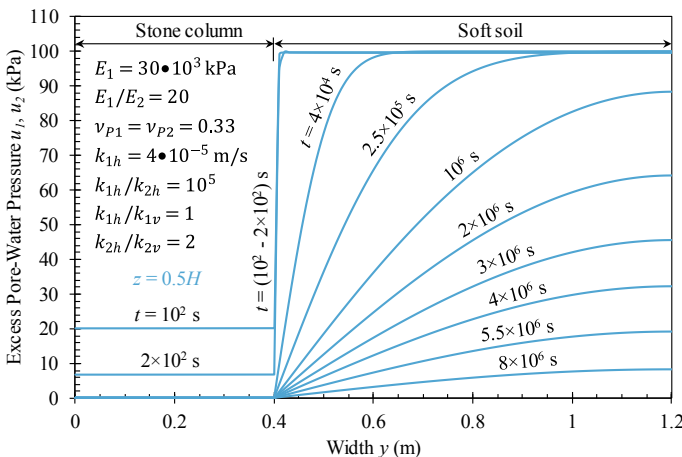


Fig. 2 Excess pore water pressure isochrones against width at depth $z = 0.5H$ for the stone column and soft soil regions

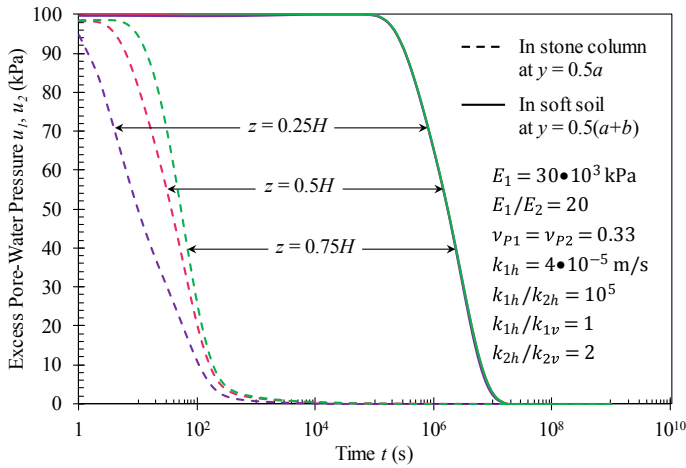


Fig. 3 Dissipation of excess pore water pressure against time at different points in the stone column and soft soil regions

and $y = 0.5(a + b)$ (in soft soil region). As expected, the dissipation of excess pore water pressure for the deeper point of investigation was slower due to the longer upward drainage path to the surface drainage boundary, particularly in the column. Regardless of the difference in depth of the investigation points in the soil, there was almost no discrepancy in the rate of excess pore pressure dissipation among these points. The reason is attributable to the dominance of horizontal flow in the soil together with the extremely faster dissipation rate of excess pore pressure in the column than in soft soil.

Figure 4 presents the verification on average degree of consolidation achieved from the proposed analytical solution and the finite element simulation employing the software PLAXIS 2D [17]. Due to the symmetry of external loading and geometry against z -axis, the numerical model was simulated as a half of the problem model shown in Fig. 1 utilising the plane strain configuration feature and 15-node triangular elements. The stiffness and permeability of stone column and soft soil in the numerical model were identical to those in the analytical model. As observed, the analytical predictions agree well with the results obtained from the finite element simulation.

Referring to the parametric analysis by Doan and Fatahi [4], the investigation parameters in this study including the horizontal permeability coefficient and modulus of soft soil were varied independently in a typical range, while the remaining parameters of the model remained unchanged and the same as the initial values in the defined example. Also for the sake of cross-reference and generality, the investigation factors were examined using normalised parameters k_{1h}/k_{2h} and E_1/E_2 .

Figure 5a exhibits a significant change of consolidation rate with the permeability ratio k_{1h}/k_{2h} , particularly in the soft soil region. The process of consolidation completed earlier when the ratio k_{1h}/k_{2h} became smaller. It should be noted that the

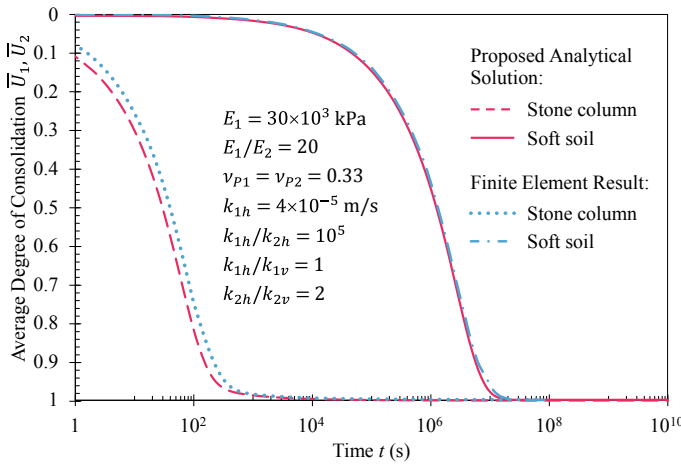


Fig. 4 Comparison in average degree of consolidation obtained from proposed analytical solution and finite element result

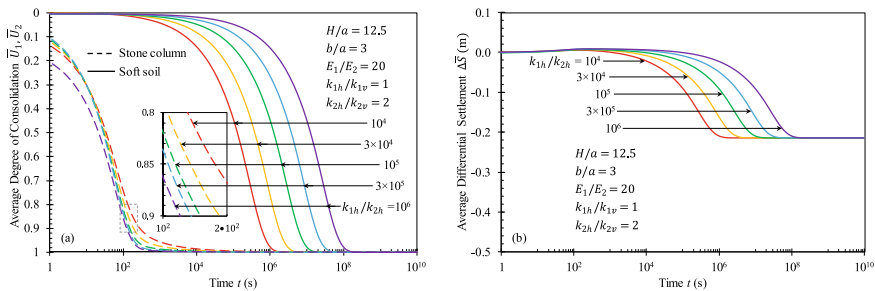


Fig. 5 Effect of permeability ratio k_{1h}/k_{2h} on **a** average degree of consolidation of stone column and of soft soil, and **b** average differential settlement between stone column and soft soil

consolidation of the model was primarily controlled by the horizontal flow from soft soil to stone column and the upward flow to the top drainage boundary in the stone column. A decline in k_{1h}/k_{2h} ratio (i.e. an increase in the horizontal permeability of soft soil) sped up the horizontal flow in soft soil, which accelerated the consolidation of soil considerably but decelerated the consolidation of column. Figure 5b shows the average differential settlement variation with time for different permeability ratio. As observed, the $\Delta \bar{S}$ change patterns were analogous to \bar{U}_2 change patterns in the soil region (see Fig. 5a), where the average differential settlement was accelerated to attain the highest value earlier, corresponding to the decrease of k_{1h}/k_{2h} ratio. The analogy may be elucidated in connection to Eqs. (23) and (24) in which $\bar{S}_2(\infty)$ is much greater than $\bar{S}_1(\infty)$ due to the significantly smaller stiffness of the soft soil compared to the stone column. As a result, the $\Delta \bar{S}$ calculations are mainly governed by \bar{U}_2 regardless of the changes of \bar{U}_1 and \bar{U}_2 during the process of consolidation.

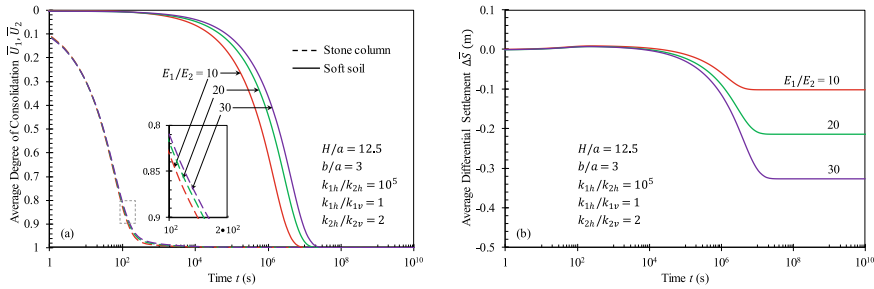


Fig. 6 Effect of modulus ratio E_1/E_2 on **a** average degree of consolidation of stone column and of soft soil and **b** average differential settlement between stone column and soft soil

Figure 6a indicates that a decline of the modulus ratio E_1/E_2 (i.e. an increase in the modulus of soft soil) sped up the consolidation significantly. Furthermore, the acceleration became more remarkable gradually when the smaller modulus ratio E_1/E_2 was adopted. Indeed, the greater the soil stiffness, the faster the transfer process of excess pore pressure onto the effective stress in the soil, which accelerated the consolidation of the composite ground. It is worth noting that the decrease in E_1/E_2 ratio not only increased the consolidation rate but also reduced the average differential settlement dramatically (Fig. 6b), particularly during the later stages of consolidation. The changes in $\Delta \bar{S}$ predictions against consolidation time were principally regulated by the product of \bar{U}_2 and $\bar{S}_2(\infty)$ in which an increase in the soil stiffness diminished $\bar{S}_2(\infty)$ and accompanying $\Delta \bar{S}$ substantially.

5 Conclusions

This paper introduces an analytical solution to the consolidation of a stone column-reinforced soft soil adopting free strain condition for the column and soil under plane strain configuration and instantaneous loading. A mathematical model was developed incorporating simultaneous horizontal and vertical flows in the stone column and soft soil with an orthotropic permeability for each region. Then, an analytical solution in terms of exact double series was derived employing the method of separation of variables and orthogonal expansion technique. The obtained analytical solution is capable of predicting the change of excess pore water pressure and thus settlement against time at any point in the model. Consequently, the differential settlement between stone column and soft soil regions is readily captured during the consolidation process. The capabilities of the proposed solution were validated via an example investigating the excess pore water pressure dissipation in the model, incorporated with the parametric study examining the influence of consolidation parameters of soft soil on performance objectives. The accuracy of the proposed solution was verified against a finite element modelling, which shows good agreements. The achieved analytical solution is also applicable to the consolidation of soft ground improved

by prefabricated vertical drains (PVDs) or permeable columns (e.g. sand column and soil–cement mixing column) in which the consolidation parameters of PVDs and columns may be assigned appropriately. Additionally, a corresponding stress concentration ratio defined as $n_{scr} = \sigma_1/\sigma_2$ should also be adopted along with the equilibrium condition of total vertical stresses over the composite ground area to determine σ_1 and σ_2 . For example, $n_{scr} = 1$ should be adopted for PVDs or sand column-assisted ground to simulate a uniform distribution of vertical stresses on the ground surface due to the slight difference in stiffness between PVDs or sand column and surrounding soil, while $n_{scr} = 2 - 6$ could be assigned to the stone column-improved soft ground supporting a specific flexible embankment [18]. The consolidation behaviour of pervious column-supported soft soil can be analysed via the equivalent plane strain model with acceptable predictions, particularly for the vicinity of embankment centre and when the column spacing in a given direction is small (e.g. continuous column row or column wall), which highly satisfies the symmetry and plane strain conditions of the mathematical model. Therefore, the proposed analytical solution in this study can be utilised as a simple tool to predict the consolidation of the composite ground as well as verify the complex numerical modelling. For further research, the unsaturation and creep effects of soil [19, 20] can be included.

References

1. Castro J, Karstunen M, Sivasithamparam N (2014) Influence of stone column installation on settlement reduction. *Comput Geotech* 59:87–97
2. Zhao L-S, Zhou W-H, Yuen K-V (2017) A simplified axisymmetric model for column supported embankment systems. *Comput Geotech* 92:96–107
3. Basack S, Siahaan F, Indraratna B, Rujikiatkamjorn C (2018) Stone column-stabilized soft-soil performance influenced by clogging and lateral deformation: laboratory and numerical evaluation. *Int J Geomech* 18:04018058
4. Doan S, Fatahi B (2020) Analytical solution for free strain consolidation of stone column-reinforced soft ground considering spatial variation of total stress and drain resistance. *Comput Geotech* 118:103291
5. Chai J-C, Shrestha S, Hino T, Ding W-Q, Kamo Y, Carter J (2015) 2D and 3D analyses of an embankment on clay improved by soil–cement columns. *Comput Geotech* 68:28–37
6. Indraratna B, Ngo NT, Rujikiatkamjorn C, Sloan SW (2015) Coupled discrete element–finite difference method for analysing the load–deformation behaviour of a single stone column in soft soil. *Comput Geotech* 63:267–278
7. Jamsawang P, Phongphinitana E, Voottipruex P, Bergado DT, Jongpradist P (2018) Comparative performances of two-and three-dimensional analyses of soil–cement mixing columns under an embankment load. *Marine Georesour Geotechnol* 1–18
8. Das AK, Deb K (2017) Response of cylindrical storage tank foundation resting on tensionless stone column-improved soil. *Int J Geomech* 17:04016035
9. Sexton BG, Sivakumar V, McCabe BA (2017) Creep improvement factors for vibro-replacement design. *Proc Inst Civil Eng-Ground Improvement* 170:35–56
10. Hird C, Pyrah I, Russel D (1992) Finite element modelling of vertical drains beneath embankments on soft ground. *Geotechnique* 42:499–511
11. Indraratna B, Redana I (1997) Plane-strain modeling of smear effects associated with vertical drains. *J Geotech Geoenviron Eng* 123:474–478

12. Tan SA, Tjahyono S, Oo K (2008) Simplified plane-strain modeling of stone-column reinforced ground. *J Geotech Geoenviron Eng* 134:185–194
13. Parsa-Pajouh A, Fatahi B, Khabbaz H (2015) Experimental and numerical investigations to evaluate two-dimensional modeling of vertical drain-assisted preloading. *Int J Geomech* 16:B4015003
14. Barron RA (1948) Consolidation of fine-grained soils by drain wells. *Trans Am Soc Civil Eng* 113:718–742
15. Aviles-Ramos C, Haji-Sheikh A, Beck J (1998) Exact solution of heat conduction in composite materials and application to inverse problems. *J Heat Transf* 120:592–599
16. Hahn DW, Özişik MN (2012) *Heat conduction*, 3rd edn. Wiley, Hoboken
17. PLAXIS BV. PLAXIS 2D, version 2017—two-dimensional finite element program, The Netherlands
18. Mitchell JK (1981) Soil improvement—state-of-the-art report. In: *Proceedings of 11th international conference on SMFE1981*, pp 509–565
19. Ho L, Fatahi B (2015) One-dimensional consolidation analysis of unsaturated soils subjected to time-dependent loading. *Int J Geomech* 16:04015052
20. Le TM, Fatahi B, Khabbaz H, Sun W (2017) Numerical optimization applying trust-region reflective least squares algorithm with constraints to optimize the non-linear creep parameters of soft soil. *Appl Math Modelling* 41:236–256

Impact of Lime Stabilization on Swelling and Soil Water Retention Behavior of Expansive Subgrade



Asmaa Al-Taie , Mahdi M. Disfani , Robert Evans , Arul Arulrajah , and Ehsan Yaghoubi 

Abstract The impact of lime-stabilized expansive subgrade based on swelling behavior and the soil water retention curve (SWRC) is investigated in this study. The soil selected for this research was a Quaternary age basaltic residual clay located in Victoria, Australia. The basaltic expansive clay forms subgrade layers of a major portion of Victoria's transport infrastructure including local roads, state highways, and national freeways. The selected clay was stabilized using different percentages of lime including 2%, 3%, 4%, 6%, and 8%, and the physical properties of expansive and lime-stabilized specimens were evaluated. The optimum lime content was measured based on a swelling reduction for samples prepared at optimum moisture content to investigate the SWRCs. The yield surfaces were generated for both expansive and lime-stabilized subgrades by establishing compaction curves. To determine the SWRC under the yield surface, Hyprop and WP4C depoint potentiometer were utilized. The swelling potential was obtained at various conditions including initial water contents and net stresses to describe the swelling behavior of expansive and stabilized clay utilizing the SWRC. The results suggest that despite the samples were stabilized with lime at optimum lime content, the serious swelling potential was observed when the stabilized samples prepared at high suction levels were wetted under constant low net stresses.

Keywords Swelling behavior · Lime stabilization · Expansive clay · SWRC

A. Al-Taie (✉) · E. Yaghoubi
Victoria University, Melbourne, Australia
e-mail: Asmaa.Al-Taie@vu.edu.au

M. M. Disfani
The University of Melbourne, Melbourne, Australia

R. Evans · A. Arulrajah
Swinburne University of Technology, Melbourne, Australia

1 Introduction

Expansive subgrades are common and widespread around the world and are known for their ability to shrink, swell, and collapse as a result of drying or wetting [1]. Several research has been achieved to investigate empirical correlations to estimate swelling using the basic laboratory tests including Atterberg limits and liquidity index [2–4]. However, these studies were not consistent in interpreting the behavior of swelling mainly because different subgrades demonstrate very distinct volume change even if they have similar Atterberg limits. Fredlund [5] pointed out that the swelling behavior of unsaturated subgrades could be better interpreting by considering the soil water retention curve (SWRC) which represents the relationship between suction and water content at constant temperature and stress [6–10]. On the SWRC, the air entry value of the soil represents the matric suction value that must be exceeded before air recedes into the soil pores [11]. However, the residual water content represents the water content where a great suction variation is needed to eliminate further water from the soil [12]. Thus, the soil–water retention curve consists of three zones, namely boundary, transition, and residual zones [8, 13]. The suction value which separates the boundary zone from the transition zone is the air entry value. Kodikara [14] referred that most studies worked on identifying the suction vs. water content values were carried out on pressures less than the compaction stress. Hence, all outcomes provided from the experimental laboratory tests are limited to being under the yield surface [13, 15–17]. Kodikara [14] suggested a new framework to interpret the volumetric behavior of compacted unsaturated subgrades. This framework incorporates void ratio, net stress, and moisture ratio (i.e. the product of the specific gravity and water content) as state variables. This framework adopted a static compaction test to generate a yield surface.

The current study investigates the impact of lime-stabilized expansive subgrades based on swelling behavior and the SWRC by adopting Kodikara's framework. The expansive subgrade was stabilized with lime at optimum lime content (OLC) based on swelling reduction. The experimental laboratory tests studied the relationship between suction and water content under the yield surface to explain the swelling behavior for both subgrades. This study, for the first time, uses the Kodikara's framework to investigate whether a considerable swelling potential can be measured if an expansive subgrade is prepared at the dry side of the optimum moisture content and stabilized with lime at the OLC.

2 Methodology and Results

Laboratory experimental tests were carried out to achieve the goal of this study. First, standard proctor compaction and one-dimensional swell tests were performed to obtain the OLC according to swelling reduction. Second, the yield surfaces for both expansive and lime-stabilized subgrades were established by conducting static

Table 1 Geotechnical properties of the selected subgrade [19]

Characteristics	Values
Specific gravity (Gs)	2.71
Sand (4.75 to 0.075 mm)	4%
Silt + clay (finer than 0.075 mm)	96%
Liquid limit	73.7%
Plastic limit	23.2%
Plasticity index	50.5%
Linear shrinkage	20.3%
Soil classification	CH

compaction tests. Next, Hyprop and WP4C depoint potentiometer were utilized to obtain the SWRC under yield surfaces under various stresses. Finally, the swelling potential was obtained at various initial water contents and net stresses.

2.1 Material

The expansive subgrade chosen in this research was a Quaternary age basaltic residual subgrade located in Western Victoria, Australia [18]. This soil was collected from the depth of 2 m below ground. The geotechnical properties of this soil are shown in Table 1 [19].

2.2 Determination of the Optimum Lime Content (OLC)

To measure optimum moisture content and maximum dry density for the selected subgrade, the standard proctor compaction procedure was conducted based on ASTM-D698 [20]. For the lime-stabilized subgrade, the compaction approach described by Ciancio et al. [21] was considered. Distilled water was added to the mixture of the dry expansive subgrade and lime. This mixture was then left for one hour, and the compaction test was then conducted. The same approach was followed for different water contents.

One-dimensional swell tests [22] were also carried out on the expansive and lime-stabilized samples prepared at 2%, 3%, 4%, 6%, and 8% lime contents. The samples were prepared at optimum moisture content and maximum dry density. The lime-stabilized samples were left for curing for one, seven, and 28 days. The temperature was controlled to be about 20 ± 2 °C, and the relative humidity was about 95% during curing. The samples were installed in an oedometer frame, and all samples were inundated under a pressure of 25 kPa to compensate for the field stress conditions from which the sample had been collected. The optimum moisture content

Table 2 Optimum moisture content, maximum dry density, and swelling values of expansive and lime-stabilized subgrades

Lime (%)	OMC (%)	MDD (g/cm ³)	Swelling values after curing (%)			
			0	1	7	28
0	25	1.52	6.3	–	–	–
2	26	1.51		3.3	2.70	2.50
3	26.5	1.50		2.4	1.87	1.68
4	26.9	1.49		0.4	0	0
6	27.8	1.48		0	0	0
8	28.5	1.47		0	0	0

and maximum dry density of the expansive and lime-stabilized samples are shown in Table 2. This table shows that a serious reduction in swelling values happened for the samples stabilized with 2% lime content, and this reduction was negligible with the addition of 4% lime. Therefore, the OLC for this subgrade was measured to be 4%.

2.3 Generation of the Yield Surface

The yield surfaces for the expansive and lime-stabilized samples were generated by conducting static compaction tests. The samples were compressed statically with water contents ranging from 0 to 50%. The static compaction ranged from 2 to 4000 kPa. The stress of 2 kPa was, in fact, the stress due to the loading cap weight.

For the expansive subgrade, various amounts of water were added to the mixture of dry samples and lime. The mixtures were left for seven days to allow thorough permeation of the water throughout the mixtures. The samples were then compacted statically into the mold with a sealed bottom. The rate of stress was managed such that to assure that excess air pressure does not increase during loading. For samples prepared at the dry side of the LOO, as the air is easy to release under high-stress rates, it can be supposed that excess air pressure does not increase during loading. Once the water content of samples reached the LOO, the rate of stress was decreased to build the drained paths averting excess air pressure to increase. The stress rates, applied to compact expansive samples prepared at the dry and wet sides of the LOO, are presented in Table 3. Finally, the void ratios were measured. Consequently, the yield surface for the expansive subgrade was established as presented in Fig. 1a.

The same strategy was followed to establish the surface for the lime-stabilized samples except that the stress rate was increased when the water contents reached the LOO, as shown in Table 3. This was due to the fact that the stabilization process initiated once the water was added [19]. The yield surface for the 4% lime-stabilized subgrades is presented in Fig. 1b.

Table 3 Stress rates applied to compact expansive and lime-stabilized samples

Soil type	Compaction stress (kPa)	Stress rate (kPa/min)	
		Dry side of LOO	Wet side of LOO
Expansive	≤1000	20	0.5
	>1000	100	1.5
Lime stabilized	≤1000	20	4
	>1000	100	8

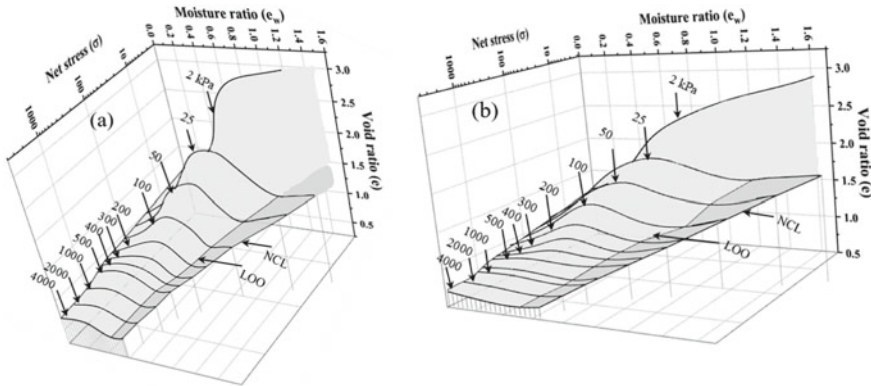


Fig. 1 Yield surfaces for the expansive and lime-stabilized subgrades

2.4 Explanation of Swelling Behavior Using the SWRC

Experimental Procedure for measuring Suction Contours under the Yield Surface

To identify the relationship between suction and water content under the yield surface, at least six identical samples with a particular moisture ratio (e_w) were compacted to the target stress (σ). The samples were next unloaded to the target operational stress and next wetted with various calculated amounts of water under that operational stress. After wetting, the matric suction values were measured by using the Hyprop (for matric suction ranging from 0 to 1.5 MPa) or WP4C depoint potentiometer device (for total suction ranging from 1.5 MPa to 60 MPa) [23–26], and consequently, the SWRC was measured. It is necessary to mention that all the lime-stabilized samples tested in this study followed the same procedure that was applied to the expansive samples except that the stabilized samples were cured for seven days before wetting under the target operational stress. The void ratios were also calculated when the volume change could be neglected. Therefore, the relationship between void ratio and matric suction was measured. As a result, the suction contours under the yield surface were plotted. As the samples were taken out of the setup and

the suction values were then measured, it was necessary to measure the unloading–reloading slope for the expansive and lime-stabilized subgrades at various water contents.

Unloading–Reloading Slope

A set of laboratory experimental tests was performed to present the unloading–reloading behavior of unsaturated expansive as well as lime-stabilized subgrades at water contents varying from 0 to 22%. The average values of the unloading–reloading slope, for the expansive samples, over this range of water contents varied between 0.006 and 0.045. For the lime-stabilized samples, the slope varied between 0.016 and 0.028. As these values were very small for all samples tested, it could be considered as zero. Therefore, it can be considered that the change in void ratio during unloading the samples to the target operational stress is negligible.

Suction Contours under the Yield Surface

Three groups of samples, shown in Fig. 2, were provided based on the initial water content (i.e. $\omega = 0\%$, 10%, and 20%). The first group included at least six identical samples prepared at the water content of zero. The samples were compressed to the stress of 1000 kPa and next unloaded to 2 kPa. Each sample was wetted with various water contents starting from 0% to the saturation under 2 kPa stress. The matric suction values were obtained once the change in volume could be neglected. As a result, the SWRCs for expansive and lime-stabilized samples are shown in Fig. 2a, b ($\omega L U 0 1000 2$). It is important to mention that as the change in void ratio during unloading the samples to the target operational stress (unloading–reloading slope) was negligible, it was applicable to take out the samples from the setup and the suction values were then measured under the net stress of zero. The same approach was followed to measure the SWRC for the other groups except that the samples were prepared at water contents 10% ($e_w = 0.271$) for the second group and 20% ($e_w = 0.542$) for the third group. Besides, the samples were wetted from water content starting from 10 to 20% for the second and third groups, respectively, to saturation as shown in Fig. 2a, b ($\omega L U 10 1000 2$ and $\omega L U 20 1000 2$). To involve a wide range of the SWRCs, the same approach was followed with the change that the samples were wetted under the stresses of 25 kPa and 100 kPa, as presented in Fig. 2.

To identify the behavior of expansive and lime-stabilized subgrades in terms of matric suction and void ratio, a set of experimental tests including $\omega L U 0 1000 2$, $\omega L U 0 1000 25$, and $\omega L U 0 1000 100$ were analyzed as an example. As the volume change was recorded, it is straightforward to measure the void ratio. Consequently, the behaviors of both subgrades in terms of void ratio and matric suction at particular stress were obtained, as shown in Fig. 3. Thus, for each sample, by recognizing the void ratio, matric suction, and moisture ratio, the suction contours under the yield surface at stresses of 2, 25, and 100 kPa within $e-e_w$ - $\log(\sigma)$ space can be obtained. Figures 4 and 5 present the suction contours under the yield surface at stresses of 2 and 100 kPa, as examples, for both the expansive and lime-stabilized samples.

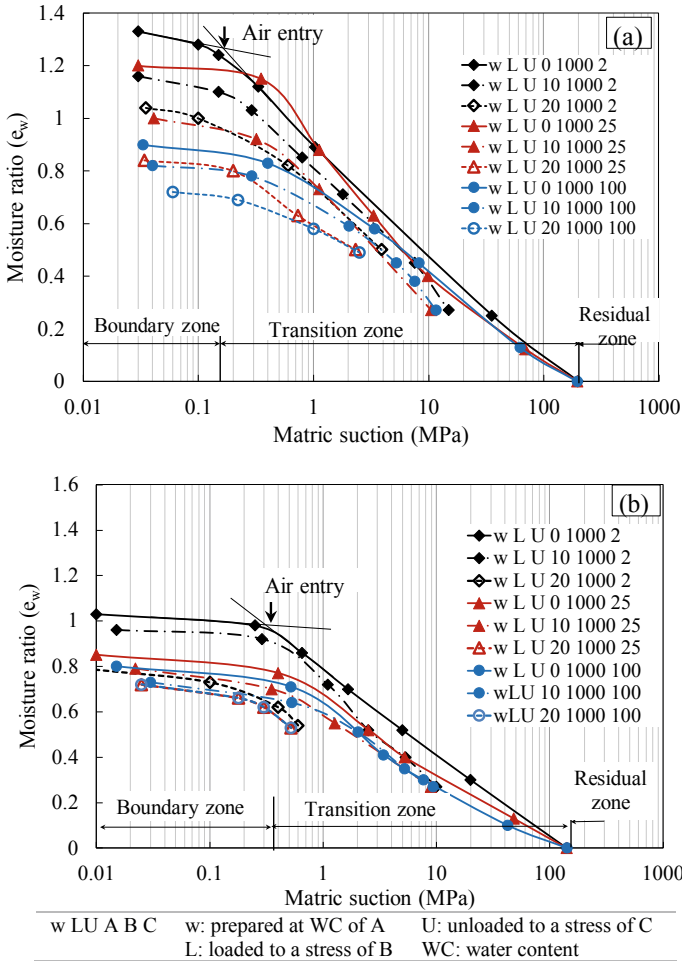


Fig. 2 SWRC under the surface, **a** expansive and **b** lime-stabilized subgrade

Fig. 3 Behavior of expansive and lime-stabilized subgrades in terms of void ratio and suction

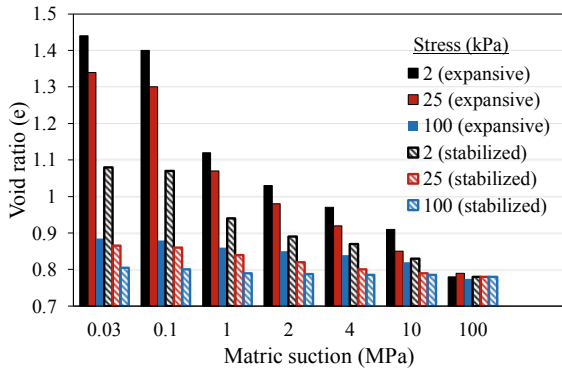


Fig. 4 Suction contours under the yield surface for expansive subgrade

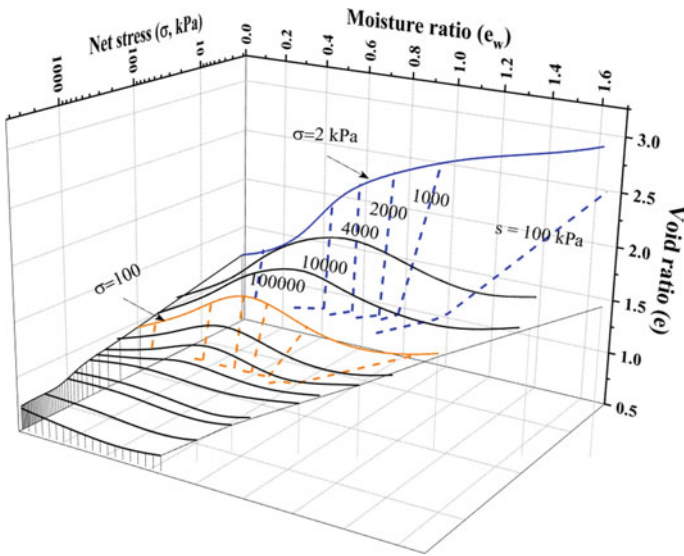
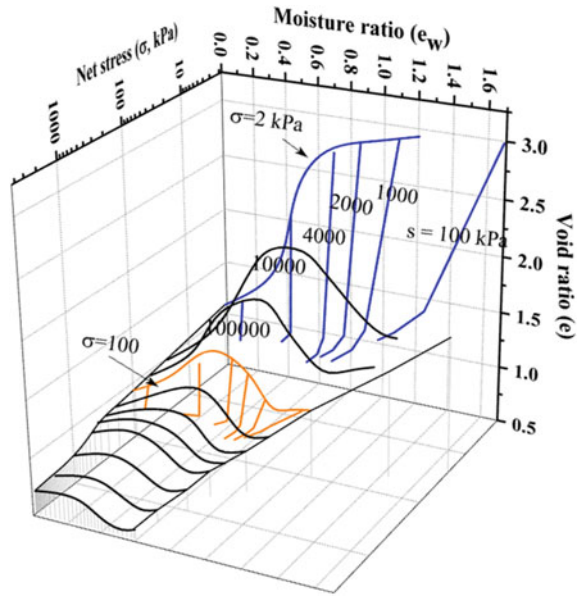


Fig. 5 Suction contours under the yield surface for lime-stabilized subgrade

Table 4 Impact of the matric suction variation on swelling

Set	Operational stress (kPa)	Water content (%)	Expansive subgrade		Lime-stabilized subgrade	
			Matric suction (MPa)	Swelling (%)	Suction (MPa)	Swelling (%)
1	2	0	190	30.0	140	15.0
		10	15	20.1	10	11.3
		20	3.9	17.6	0.4	2.7
2	25	0	181	20.0	140.8	7.5
		10	10.5	10.8	8.9	6.0
		20	2.3	8.2	0.3	1.5
3	100	0	193.1	7.3	142.3	3.3
		10	116	3.5	9.3	2.9
		20	2.5	1.5	0.4	0.5

Swelling Measurements

To study the variation of swelling behavior vs. matric suction, two identical samples prepared at a particular water content were compacted to target stress. The samples were then unloaded to stress lower than the target stress and thereafter wetted to saturation.

The outcomes of three sets of one-dimensional laboratory tests that relied on operational stresses ranged from 2 to 100 kPa are shown in Table 4. Each set involved three groups that relied on water contents ranged from 0 to 20%. Each group involved two identical samples for the expansive subgrade and two for the lime-stabilized subgrade.

For example, all samples in group 1 of set 1 were prepared at zero water content and compacted to the stress of 1000 kPa and next unloaded to 2 kPa. One sample was utilized to obtain the matric suction; however, another sample was saturated, and the final swelling value was recorded. The matric suction and swelling values for the expansive samples were 190 MPa and 30%, respectively, while these values were 140 MPa and 15%, respectively, for the lime-stabilized samples as shown in Table 4. The same approach was followed for group 2 and group 3 except that the samples were prepared at water contents of 10% and 20%, respectively, as presented in Table 4. The same steps were repeated to produce set 2 and set 3 except that the stress of 2 kPa was replaced by 25 and 100 kPa.

3 Discussion

The SWRCs under the surfaces were presented in Fig. 2. It was obvious that the boundary zone of the expansive subgrade began with a moisture ratio greater than

that of the lime-stabilized subgrade. This was due to the fact that the space under the yield surface represents the swelling behavior of samples after adding water. After saturation, the swelling path either remained under the surface or reached the yield surface depending on the slope of the state path [14]. The slope of the path of the expansive subgrade was greater than that of the lime-stabilized subgrade. Hence, it was anticipated that the lime-stabilized samples arrived at the saturation condition at a water content less than of the expansive samples, and therefore, the air entry values for expansive samples were lower than that of stabilized samples as demonstrated in Fig. 2.

Figure 3 showed that the change in the void for lime-stabilized samples decreased and became negligible as samples wetted under stresses >25 kPa. The reason for this behavior attributed to the fact that the samples were stabilized at the optimum lime content, and this lime content was measured based on the swell reduction for samples surcharged under 25 kPa.

Table 4 showed that at particular stress, the swelling potential raised as the suction raised (immediately after unloading). Besides, as the operational stress increased, the swelling values reduced. A noticeable swelling was also observed when the lime-stabilized samples were prepared at suctions ≥ 9 MPa, compacted to 1000 kPa and subsequently wetted at stresses ≤ 25 kPa. To investigate those findings, two similar samples were prepared at the matric suction of 9 MPa and compacted to 1000 kPa. The first sample was unloaded to 25 kPa, subsequently wetted to saturation. The sample was left to swell, and the value of swelling was recorded. The same approach was followed for the second sample except that the sample was left to cure for seven days and then saturated. It was recognized that the disparity in swelling values was negligible. This action can be imputed to the reaction between lime and soil after adding water. Once the water was added to the mixture, the hydrated lime took apart to calcium and hydroxide ions and hence the stabilization process including the cation exchange and flocculation initiated. That implies sufficient water has to be supplied to initiate the stabilization process. Therefore, insufficient water would not impact the stabilization process over the curing. As the optimum lime content was measured for samples prepared at the OMC, enough water was existed to initiate the stabilization process.

4 Conclusions

Experimental laboratory tests were carried out to investigate the impact of lime-stabilized expansive subgrades, based on swelling behavior and the SWRC. The expansive subgrade was stabilized with lime at the optimum lime content (OLC), and then the yield surfaces were established for both expansive and lime-stabilized subgrades. The SWRCs were measured under the surface. The swelling potential was investigated under various moisture ratios and stresses. The outcome of this study showed that a noticeable swelling occurred when the lime-stabilized samples prepared at suction ≥ 9 MPa were compacted to 1000 kPa and subsequently wetted

at stresses ≤ 25 kPa. The stress of 25 kPa represents the surcharge that was applied to find the OLC. Therefore, the condition of ≤ 25 kPa can be replaced by the surcharge provided to measure the OLC.

References

1. Haeri SM, Khosravi A, Garakani AA, Ghazizadeh S (2016) Effect of soil structure and disturbance on hydromechanical behavior of collapsible Loessial soils. *Int J Geomech* 17(1):04016021
2. Richards B, Peter P, Martin R (1984) The determination of volume change properties in expansive soils. In: Fifth international conference on expansive soils 1984: preprints of papers. Institution of Engineers, Australia
3. Der Merwe V (1964) DH the prediction of heave from the plasticity index and percentage clay fraction. *Trans SA Ins Civ Eng* (6)
4. Gomez-Gutierrez I, Bryson L, Hopkins T (2011) Correlations between geotechnical properties and the swell behavior of compacted shales. In: *Geo-frontiers, advances in geotechnical engineering*, pp 4119–4128
5. Fredlund D (2000) The implementation of unsaturated soil mechanics into geotechnical engineering practice. National Research Council of Canada
6. Fredlund DG, Vu HQ (2003) Numerical modelling of swelling and shrinking soils around slabs-on-ground. In: *Proceeding, post-tensioning institute annual technical conference*, Huntington Beach, CA, USA
7. Jones EW, Koh YH, Tiver BJ, Wong MA (2009) Modelling the behaviour of unsaturated, saline clay for geotechnical design. University of Adelaide, Australia, School of Civil Environment and Mining Engineering
8. Fredlund DG (2006) Unsaturated soil mechanics in engineering practice. *J Geotech Geoenviron Eng* 132(3):286–321
9. Iyer K, Jayanth S, Gurnani S, Singh D (2012) Influence of initial water content and specimen thickness on the SWCC of fine-grained soils. *Int J Geomech* 13(6):894–899
10. Krishnapillai SH, Ravichandran N (2012) New soil-water characteristic curve and its performance in the finite-element simulation of unsaturated soils. *Int J Geomech* 12(3):209–219
11. Pasha AY, Khoshghalb A, Khalili N (2015) Pitfalls in interpretation of gravimetric water content-based soil-water characteristic curve for deformable porous media. *Int J Geomech* 16(6):D4015004
12. Fredlund DG, Xing A (1994) Equations for the soil-water characteristic curve. *Canadian Geotech J* 31(4):521–532
13. Colmenares Montanez JE (2002) Suction and volume changes of compacted sand-bentonite mixtures. Imperial College London (University of London)
14. Kodikara J (2012) New framework for volumetric constitutive behaviour of compacted unsaturated soils. *Canadian Geotech J* 49(11):1227–1243. <https://doi.org/10.1139/t2012-084>
15. Dineen K, Colmenares J, Ridley A, Burland J (1999) Suction and volume changes of a bentonite-enriched sand. *Proc Inst Civil Eng-Geotech Eng* 137(4):197–201
16. Romero Morales E (1999) Characterisation and thermo-hydro-mechanical behaviour of unsaturated Boom clay: an experimental study
17. Chinkulkijniwat A, Horpibulsuk S, Yubonchit S, Rakkob T, Goodary R, Arulrajah A (2015) Laboratory approach for faster determination of the loading-collapse yield curve of compacted soils. *J Mater Civil Eng* 28(3):04015148
18. McAndrew J, Marsden MAH (1973) *Regional guide to victorian geology*, Edition. School of Geology, University of Melbourne: Parkville, Victoria 3052, Australia

19. Al-Taie A, Disfani M, Evans R, Arulrajah A (2019) Collapse and swell of lime stabilized expansive clays in void ratio-moisture ratio-net stress space. *Int J Geomech* 19(9):04019105. [https://doi.org/10.1061/\(ASCE\)GM.1943-5622.0001488](https://doi.org/10.1061/(ASCE)GM.1943-5622.0001488)
20. ASTM-D698 (2000) Standard test methods for laboratory compaction characteristics of soil using standard effort (12,400 ft-lbf/ft³). West Conshohocken, ASTM International
21. Ciancio D, Beckett CTS, Carraro JAH (2014) Optimum lime content identification for lime-stabilised rammed earth. *Constr Build Mater* 53:59–65
22. ASTM-D4546 (2014) Standard test method for one-dimensional swell or collapse of soils. West Conshohocken, ASTM International
23. UMS: HYPROP Laboratory evaporation method for the determination of pF-curves and unsaturated conductivity. http://www.ums-muc.de/en/products/soil_laboratory/hyprop.html. Last accessed 2013/08/29
24. Murray EJ, Sivakumar V (2010) *Unsaturated soils: a fundamental interpretation of soil behaviour*. Wiley, Hoboken
25. Decagon: WP4C dewpoint Potentiometer. <http://www.decagon.com/products/environmental-instruments/water-potential-instruments/wp4c-dewpoint-potentiometer/>. Last accessed 2012/05/24
26. ASTM-D6836 (2016) Standard test methods for determination of the soil water characteristic curve for desorption using hanging column, pressure extractor, chilled mirror hygrometer, or centrifuge. West Conshohocken, ASTM International

Evaluation of Strength and Microstructural Characteristics of Weak Lateritic Soil Stabilized with Calcined Clay and Iron Slag Dust



H. A. Quadri, O. S. Abiola, S. O. Odunfa, and J. O. Azeez

Abstract As the trend in research moves towards using locally available materials to formulate binders in flexible pavement construction, this research evaluated strength and microstructural characteristics of subgrade stabilized with calcined clay (CC) and iron slag dust (ISD). Subgrade (S) was modified with different variations (4, 8, 12, 16 and 20%) of calcium carbide waste (CCW) by weight and the blends were subjected to Atterberg limit test to determine blend with least plasticity index (PI). S + 8% CCW was found to give optimum PI reduction (14.8–8.7%). Subgrade was consequently stabilized with blends of 8% CCW and different variations of CC and ISD (3, 6, 9, 12, 15 and 18%) by weight. The blends were subjected to compaction, soaked California bearing ratio (CBR) and unconfined compressive strength (UCS) tests. The specimens for strength tests were cured for 0, 3, 7, 28, 56 and 90 days. Blends with optimum CBR and UCS values at 7 days of curing were subjected to scanning electron microscopy (SEM) testing. Results showed that stabilization of subgrade with variations of ISD and CC reduced MDD (1.82–1.43 Mg/m³) and (1.82–1.54 Mg/m³), respectively; OMC (23.7–8.9%) and (23.7–17.9%), respectively. It increased soaked CBR (0–551.7%) and (0–418.2%), respectively, and UCS (201.59–3096.27 kPa) and (201.59–5660.84 kPa), respectively, for all curing days. Micrograph of subgrade showed a discontinuous structure with voids visible while micrographs of stabilized subgrade showed reticulated structures with voids filled with CC and ISD additives which were responsible for their improved strength values.

Keywords Weak subgrade soil · Iron slag dust · Calcium carbide waste · Micrographs

H. A. Quadri · O. S. Abiola (✉) · S. O. Odunfa
Department of Civil Engineering, Federal University of Agriculture, Abeokuta, Ogun State,
Nigeria
e-mail: abiolaos@funaab.edu.ng

J. O. Azeez
Department of Soil Science and Land Management, Federal University of Agriculture, Abeokuta,
Ogun State, Nigeria

1 Introduction

Premature pavement failures characterize most roads in Nigeria, and the prevalence had been adduced to majorly weak subgrade soils dotting nooks and crannies of the country [1–4]. A good number of pozzolanic and lime based materials (fly ash, rice husk ash, steel slag, palm kernel shell ash, bagasse ash, millet husk ash, cement kiln dust, calcium carbide waste) had been used to improve engineering properties of weak subgrade soils and were found to be effective owing to formation of cementitious compounds (calcium silicate hydrate and calcium aluminate hydrate) from hydration and pozzolanic reactions [2–9]. When cementitious additives are mixed or blended with expansive soils with loose grains, the inter-granular spaces or voids would be filled or covered with hydration reaction products, that is, calcium silicate hydrate (CSH) and calcium aluminate hydrate (CAH) [10–14].

Solanki and Zaman [14] worked on the microstructural and mineralogical characterization of clay stabilized using calcium based stabilizers and reported that, there were significant changes in the microstructure of raw soil when mixed with Cement Kiln Dust (CKD) cured for 28 days. The improved modulus of elasticity exhibited by CKD-stabilized soil specimens after curing was attributed to the aforementioned reaction products.

Indiramma and Sudharani [15] worked on Scanning electron microscope (SEM) analysis of Fly Ash, Quarry Dust stabilized soil and observed that the micrograph of raw soil showed a dispersed fabric in natural state with structure of the soil consisting of a flaky-like particles. It was explained that soils with flaky shapes are likely to have low strength. The micrograph of Fly ash stabilized soil showed smooth surfaces with voids in soils occupied by Fly ash while the micrograph of Quarry dust stabilized soil showed rough surfaces with sharp edges with voids occupied by Quarry dust. They concluded that Quarry dust stabilized soil had more voids when compared with Fly ash stabilized soil and resulted in high strength to soil-Quarry dust mixes.

Many research studies on the geotechnical characteristics and stabilization of clay with Calcium Carbide Waste (CCW) and steel slag are been reported in the literature however, information on stabilization of weak subgrade materials with CCW and Calcined Clay (CC) is scarce. So it is necessary to investigate the geotechnical properties of weak subgrade and CCW-CC and Iron steel dust (ISD) through a series of laboratory tests. This research work evaluated the strength and microstructural characteristics of weak subgrade soil sourced at a section along Ota-Idiroko road, Ogun State, Nigeria stabilized with Calcined clay and iron slag dust.

2 Materials and Methods

Subgrade material (S) was sourced from a section along Ota-Idiroko road at a coordinate of Latitude $6^{\circ} 40' 53.082''$ N and Longitude $3^{\circ} 9' 11.172''$ E while Calcium

carbide waste and raw clay were sourced from automobile workshops and Owode-Ketu in Ogun State respectively. They were air dried, ground to fineness and sieved through 425 μm sieve after the raw clay had been calcined in a Kiln for 2 h at a temperature of 700 °C. Iron slag dust (ISD) was sourced from Federated Steel Company, Ota. These materials were subjected to specific gravity, particle size distribution and X-ray fluorescence tests to determine their properties. Firstly, subgrade was modified with CCW by weight in the following percentage replacements (0, 4, 8, 12, 16 and 20%) and the resulting blends were subjected to Atterberg limit in order to classify subgrade according to AASHTO and Unified systems of soil classification [16] and to determine the blend with the optimum plasticity index reduction which was tagged optimum subgrade lime blend (OSLB). Consequently, the blend of S + 8% CCW exhibited the optimum plasticity index reduction (14.8 to 8.7%). The OSLB (S + 8% CCW) was thereafter blended by weight with calcined clay (CC) and iron slag dust (ISD) in the following percentage replacements (3, 6, 9, 12, 15 and 18%) respectively in order to activate the pozzolanic potentials of CC and ISD for strength enhancement. The blends were subjected to Compaction, California bearing ratio (CBR) (soaked) and Unconfined compressive strength (UCS) tests according to BS 1377 (1990) [17, 18]. However, the specimens for strength test were moist cured for 0, 3, 7, 28, 56 and 90 days respectively. The microstructural characteristics of blends which exhibited 7 days optimum soaked CBR and UCS values were determined using scanning electron microscopy (SEM) test.

3 Results and Discussion

3.1 Physical and Index Properties

The Subgrade material as reflected in Table 1 was classified as A-7-5 (fair to poor subgrade) and ML or OL (inorganic silts and very fine sands, rock flour, silty or clayey fine sands with slight plasticity) according to AASHTO classification and ASTM D2487 (Unified soil classification system) respectively owing to its liquid limit (LL), plasticity index (PI) and percentage passing sieve No. 200 of 46%, 14.8% and 64.21% respectively.

The least and most dense materials are calcium carbide waste (CCW) (1.81) and iron slag dust (ISD) (3.3) with subgrade and calcined clay (CC) having equal weight (2.5) following their specific gravity results. Subgrade was found to be acidic with a pH value of 5.8 and CCW, CC and ISD were found to be alkaline with pH values of 13.5, 8.9 and 10 respectively.

Table 1 Physical and index properties (Subgrade, CCW, CC and ISD)^a

Property	Subgrade	CCW	CC	ISD
Plastic limit (%)	31.2	–	–	–
Liquid limit (%)	46	–	–	–
Plasticity Index (%)	14.8	–	–	–
Clay content (<0.002 mm) (%)	53.3	2.975	1.7225	6.75
Silt content (0.002–0.06 mm) (%)	7.91	2.975	1.7225	6.75
Sand content (0.06–2.0 mm) (%)	35.54	96.75	98.003	98.125
Percentage passing sieve No. 200 (%)	61.21	–	–	–
AASHTO Classification	A-7-5	–	–	–
USCS classification	ML or OL	–	–	–
pH	5.8	13.5	8.9	10.0
Specific gravity	2.5	1.81	2.5	3.3
Colour	Reddish brown	White	Darkish brown	Black

^aAuthor

3.2 Oxide Composition of Materials

The subgrade and calcined clay (CC) were found to be pozzolanic materials and they belong to Class F as according to ASTM: C618-08 [19] standard. The standard as shown in Table 2. However, from Table 2, the calcium carbide waste (CCW) contains 93.74% mass fraction of clinker or quick lime (CaO) which makes it a potent binding materials/binder with tendency to undergoing hydration reaction. The subgrade material can be classified as a laterite and not a lateritic or non-lateritic material owing to its silica sesquioxide ratio of 1.11 as revealed by XRF results (Table 2) according to Martin and Doyne [20, 21] and Winterkorn and Chandrasekharan [22]. According to them, a material with a silica sesquioxide ratio of less than 1.33 is

Table 2 Oxide composition of materials

Oxides	Percentage oxide contents		
	CCW	CC	ISD
SiO ₂	0.83	58.86	23.93
Al ₂ O ₃	0.71	16.23	6.57
Fe ₂ O ₃	0.20	10.11	37.46
CaO	93.74	3.25	12.9
MgO	0	0	0
SO ₃	0.7	7.81	5.29
Na ₂ O	0	0	0
K ₂ O	0	0.35	0.45
LOI	1.04	2.20	1.60

laterite, between 1.33 and 2 is lateritic material and above 2 is non-lateritic material.

$$\begin{aligned}
 \text{Silica Sesquioxide ratio } \left(\frac{S}{R} \right) \text{ of subgrade} &= \frac{\text{SiO}_2}{\text{Al}_2\text{O}_3 + \text{Fe}_2\text{O}_3} \\
 &= \frac{49.57}{28.86 + 15.58} \\
 &= 1.11 < 1.33 \tag{1}
 \end{aligned}$$

Therefore, the subgrade material is classified as laterite.

3.3 Compaction Characteristics

From Table 3, the addition of CC at different variations (3, 6, 9, 12, 15 and 18%) to blend of 8% CCW-Subgrade (OSLB) reduced its maximum dry density (MDD) from 1.6 to 1.54 Mg/m³ except for 3% CC (1.66 Mg/m³) where a slight increment was observed. However, all blends inclusive of OSLB reduced MDD of subgrade across board from 1.82 to 1.54 Mg/m³ with optimum reduction obtained at 18% CC. The addition of additives which led to reduction of MDD of Subgrade for all the percentages considered might be attributed to the superiority of specific gravity of OSLB-CC (1.81 + 2.5) as against specific gravity of Subgrade (2.5) [23–26].

Also in Table 3, the addition of ISD at different variations (3, 6, 9, 12, 15 and 18%) to blend of 8% CCW-Subgrade (OSLB) reduced the MDD from 1.66 to 1.52 Mg/m³ (between 3 to 6% ISD) with least reduction experienced at 6% ISD (1.52 Mg/m³) and

Table 3 Compaction characteristics

Material	MDD (Mg/m ³)	OMC (%)
Subgrade (0%)	1.82	23.7
S + 8% CCW (OSLB)	1.60	17.2
OSLB + 3% CC	1.66	20.3
OSLB + 6% CC	1.59	21.9
OSLB + 9% CC	1.59	19.4
OSLB + 12% CC	1.59	18.1
OSLB + 15% CC	1.59	19.1
OSLB + 18% CC	1.54	17.9
OSLB + 3% ISD	1.43	9.0
OSLB + 6% ISD	1.52	8.9
OSLB + 9% ISD	1.68	14.5
OSLB + 12% ISD	1.70	18.1
OSLB + 15% ISD	1.76	17.4
OSLB + 18% ISD	1.75	20.3

subsequently increased it to 1.76 Mg/m³ (between 9 to 18% ISD) with optimum at 15% ISD. The increment could be attributed to the specific gravity of ISD (3.3) while the reduction experienced with these additives could be as a result of the fact that ISD and CCW are fine materials and these additives changed the granular structure of the subgrade thus making the soil particles to float in CCW-ISD matrix thereby reducing the MDD [23, 24, 25].

From Table 3, the addition of CC at different variations (3, 6, 9, 12, 15 and 18%) to blend of 8% CCW-Subgrade (OSLB) increased its optimum moisture content (OMC) from 17.2 to 21.9%. However, all blends inclusive of OSLB reduced OMC from 17.2 to 14.5% (between 3 and 9% ISD) with least at 9% ISD (14.5%) and subsequently increased to 20.3% (between 12 and 18% ISD) with optimum at 18% ISD (Table 3).

The addition of additives that led to reduction of OMC of Subgrade for all cases considered could be attributed to insufficiency of moisture in the mixtures, resulting in self-desiccation and consequently lower hydration [26, 27]. When no movement of water to and from the paste formed from blend of lime and pozzolanic material is permitted, the water is used up by hydration reaction until little is left to saturate the soil surfaces leading to decrease in relative humidity with the paste.

3.4 California Bearing Ratio

The soaked CBR results of OSLB-CC and OSLB-ISD blends (3, 6, 9, 12, 15 and 18%) ranged from 0 to 418.2% and 0 to 551.7% for the curing periods (0, 3, 7, 28, 56 and 90 days) respectively as captured in Fig. 1. The CBR value of the increases with increase in curing periods owing to formation of cementitious compounds (CSH and CAH) from continuous growth of hydration reactions with age [10, 11, 12, 14].

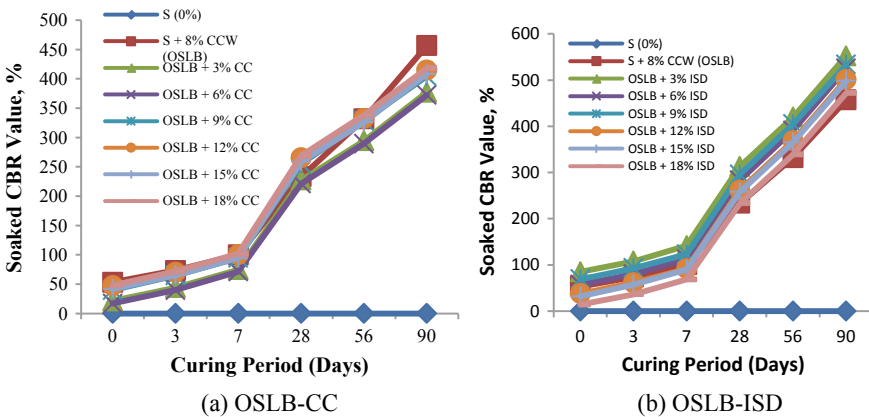


Fig. 1 Soaked CBR results of OSLB-CC and OSLB-ISD blends at varying curing periods

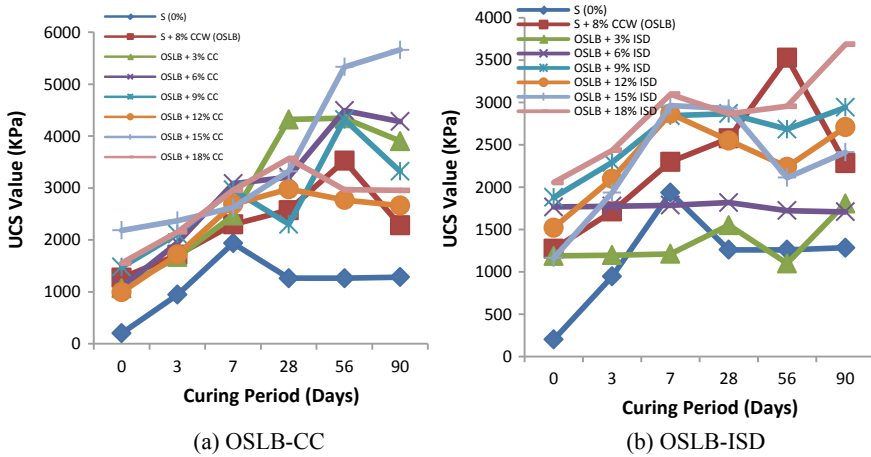


Fig. 2 Results of UCS for OSLB-CC and OSLB-ISD blends for different curing periods

3.5 Unconfined Compressive Strength

Figure 2 shows the UCS results of OSLB-CC and OSLB-ISD blends (3, 6, 9, 12, 15 and 18%) which ranged from 201.59 to 5660.84 kPa and 3684.49 kPa for varying curing periods (0, 3, 7, 28, 56 and 90 days) with the blends of S (0%) at 0 day moist curing and OSLB + 15% CC, OSLB + 18% ISD at 90 days moist curing exhibiting the least and highest UCS values respectively. The UCS value of subgrade increased with increase in curing periods and OSLB-C/OSLB-ISD blends owing to formation of cementitious compounds (CSH and CAH) from continuous hydration reactions with age [10–12, 14]. This trend of results could be attributed to a number of factors such as type and quantity of lime added, curing temperature and grain size of soil to be treated and compactive effort from compactor among others [28, 29]. According to them, higher temperature (20–50 °C) and fineness of composite materials accelerate the formation of cementitious compounds through pozzolanic or hydration reaction when lime is blended with pozzolanic material in the presence of water resulting in rapid soil strength development. The inconsistency in the pattern of hydration reaction with curing periods could be added to fluctuation in curing temperature and non-uniformity in grain sizes of natural subgrade and inconsistency in compactive effort from compactor.

3.6 Microstructural Characteristics

Figure 3 shows the SEM micrograph and EDS of compacted subgrade soil sample at a high magnification (12,000 times). It is clear that the subgrade sample has a discontinuous structure where the voids are more visible (in the form of loose grain

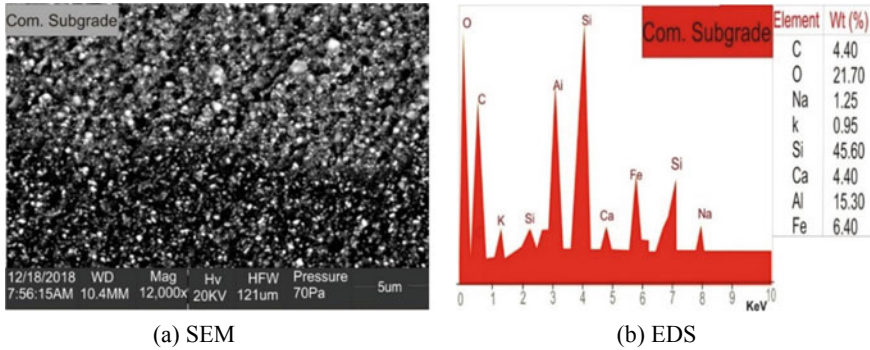


Fig. 3 SEM and EDS result of compacted subgrade (S)

crystals or sands) because of the absence of cementitious binder(s) (CCW-ISD and CCW-CC). Even though the subgrade material possesses some hydration products such as silicon (Si), aluminum (Al) minerals and a little amount of calcium (Ca) which makes it have pozzolanic tendency when compacted together in the presence of water. This is not in agreement with observations of [14] where a raw clay material was described as a discontinuous structure where voids were so visible because of the absence of hydration products (C–S–H and C–A–H) as a result of absence of calcium (Ca) mineral in the clay material. The micrograph shows an open structure or an open type of microstructure with round-like shape particles. According to [10], in an open soil structure, particles are likely to fall into the voids when the soil fabric is destroyed by some destabilizing action such as loading. He added that the existence of the open voids points towards microstructural instability and this could be added to its low bearing capacity (0.0%) and low compressive strength (1934 kPa) and high plasticity (14.8%) when compared with the treated or stabilized subgrade materials. The EDS results as revealed by Fig. 5b showed majority of silicon (Si), oxygen (O), and Aluminum (Al) minerals and trace amounts of potassium (K), iron (Fe), calcium (Ca) and carbon (C) which is similar to observations reported by [14].

Figure 4 shows the SEM micrograph and EDS of OSLB-ISD as per UCS {OSLB (S + 8% CCW) + 18% ISD}. The microstructure of {OSLB (S + 8% CCW) + 18% ISD} is clearly denser and compact as compared to microstructure of the compacted subgrade. Another prominent feature of the microstructure of {OSLB (S + 8% CCW) + 18% ISD} blend was the presence of flower-like or rose-like crystals. The presence of rose-like crystals in OSLB-ISD stabilized soil is consistent with the observations reported by [14, 30, 31]. The micrograph shows a flocculated or agglomerated structure with voids filled by admixtures (8% CCW + 18% ISD) (less voids) when compared with untreated or unstabilized subgrade resulting in decrease in OMC (23.7 to 20.3%), MDD (1.82–1.75 Mg/m³) and increment in bearing capacity (0.0–68.6%) and UCS (1934–3096 kPa). This conforms to the reports [10–12, 15]. The EDS results showed the presence of Ca, Si, Al, Fe, C, O, K and Na minerals with distinct peaks of Si and Al, indicating presence of calcium aluminate silicate

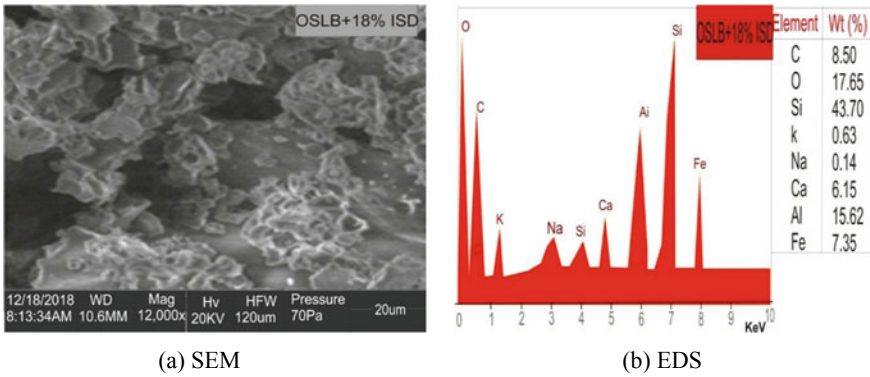


Fig. 4 SEM and EDS result of OSLB (S + 8% CCW) + 18% ISD (OSLISDB according to UCS)

hydrates (C–A–S–H)-like crystals, main cementing products responsible for strength gain [14]. However, when compared with natural subgrade (0%), the addition of S + 8% CCW + 18% ISD in the presence of water reduced silicon (Si) from 45.6 to 43.70% and increased Calcium (Ca) and Aluminum (Al) from 4.40 to 6.15% and 15.30 to 15.62% respectively as result of hydration reaction that took place.

Figure 5 shows the SEM micrograph and EDS of OSLB-ISD as per CBR {OSLB (S + 8% CCW) + 3% ISD}. The microstructure of {OSLB (S + 8% CCW) + 3% ISD} is clearly denser and compact as compared to microstructure of the compacted subgrade. Another prominent feature of the microstructure of {OSLB (S + 8% CCW) + 3% ISD} blend was the presence of plate-like crystals. The presence of plate-like crystals in OSLB-ISD stabilized soil is consistent with the observations reported by [13, 14, 30, 31]. The micrograph shows a flocculated or agglomerated structure with voids filled by admixtures (8% CCW + 3% ISD) (less voids) when compared with untreated or unstabilized subgrade which causes the OMC (23.7–9.0%), MDD (1.82–1.43 Mg/m³) to decrease and increase the bearing capacity (0.0–141.5%).

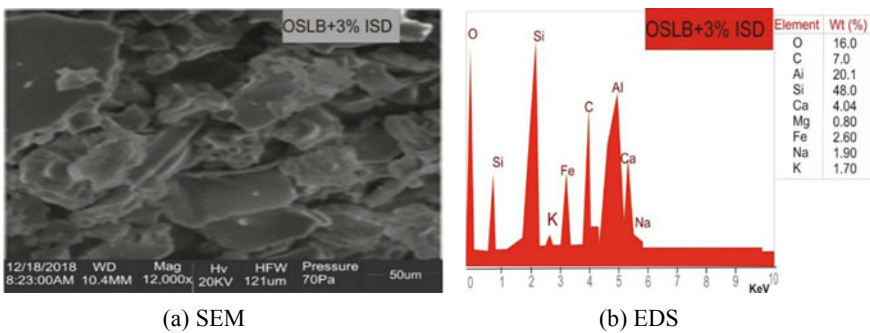


Fig. 5 SEM and EDS results of OSLB (S + 8% CCW) + 3% ISD (OSLISDB according to CBR)

The EDS results showed the presence of Ca, Si, Al, Fe, C, O, K, Mg and Na minerals with distinct peaks of Si and Al, indicating presence of calcium silicate hydrate and calcium aluminate silicate hydrates (C–A–S–H)-like crystals, main cementing products responsible for strength gain [14]. However when compared with natural subgrade (0%), the addition of S + 8% CCW + 3% ISD in the presence of water increased silicon (Si) and Aluminium (Al) from 45.6 to 48.0% and 15.30 to 20.1% respectively and reduced Calcium (Ca) from 4.40 to 4.04% as result of hydration reaction.

Figure 6 shows the SEM micrograph and EDS of OSLB-CC as per CBR {OSLB (S + 8% CCW) + 18% CC}. The microstructure is clearly denser and compact as compared to microstructure of the compacted to microstructure of compacted subgrade. Another prominent feature of the microstructure of {OSLB (S + 8% CCW) + 18% CC} blend was the presence of flower-like crystals. The presence of flower-like crystals in OSLB-CC stabilized soil is tandem with the observations reported. The micrograph shows a flocculated or agglomerated structure with voids filled by admixtures (8% CCW + 18% CC) (less voids) when compared with untreated or unstabilized subgrade resulting in decrease in OMC (23.7 to 17.9%), MDD (1.82 to 1.54 Mg/m³) and increase in bearing capacity (0.0 to 115.9%) and UCS (1934 to 2953 kPa). The EDS results revealed the presence of Ca, Si, Al, Fe, C, O, K and Na minerals with distinct peaks of Si and Al, indicating presence of calcium aluminate silicate hydrates (C–A–S–H)-like crystals, main cementing products responsible for strength gain [14]. However when compared with natural subgrade (0%), the addition of S + 8% CCW + 18% CC in the presence of water reduced silicon (Si) and Aluminium (Al) from 45.6 to 45.10% and 15.30 to 15.10% respectively and increased Calcium (Ca) from 4.40 to 7.15% as result of hydration reaction.

Figure 7 shows the SEM micrograph and EDS of OSLB-CC as per UCS {OSLB (S + 8% CCW) + 6% CC}. The microstructure of {OSLB (S + 8% CCW) + 6% CC} is clearly denser and compact as compared to microstructure of the compacted subgrade. Another prominent feature of the microstructure of {OSLB (S + 8% CCW)

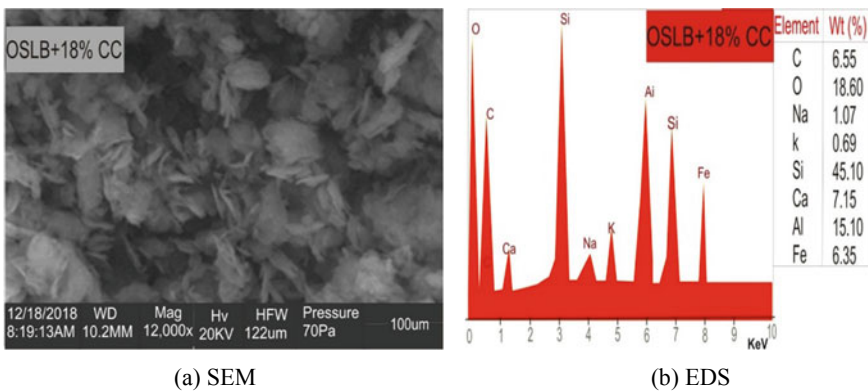


Fig. 6 SEM and EDS of OSLB-CC (S + 8% CCW) + 18% CC from CBR

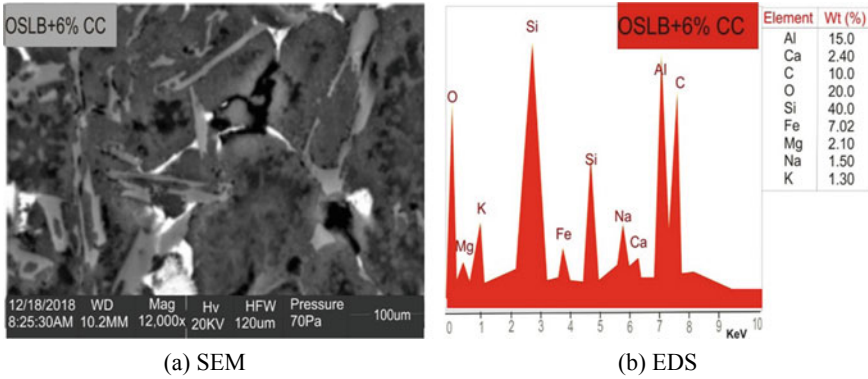


Fig. 7 SEM and EDS result of OSLB (S + CCW) + 6% CC (OSLCCB) according to UCS

+ 6% CC} blend was the presence of poorly defined irregular shaped crystals. The presence of irregular shaped crystals in OSLB/CC stabilized soil is consistent with the observations reported in the published works. The micrograph shows a flocculated or agglomerated structure with voids filled by admixtures (8% CCW + 6% CC) (less voids) when compared with untreated or unstabilized subgrade resulting in decrease in OMC (23.7 to 21.9%), MDD (1.82 to 1.59 Mg/m³) and increase in bearing capacity (0.0 to 98.4%) and UCS (1934 to 3084 kPa). The EDS results showed the presence of Ca, Si, Al, Fe, C, O, K and Na minerals were prominent with distinct peaks of Si and Al, indicating presence of calcium aluminate silicate hydrates (C–A–S–H)-like crystals, main cementing products responsible for strength gain. However when compared with natural subgrade (0%), the addition of S + 8% CCW + 6% CC in the presence of water reduced Silicon (Si), Aluminium (Al) and Calcium (Ca) from 45.6 to 40.0%, 15.30 to 15.0% and 4.40 to 2.40% respectively as result of hydration reaction.

Generally, all blends except S (0%) can be used as sub-base materials for lime-treated heavily trafficked roads in terms of CBR obtained as specified while most of the blends possess a minimum and maximum 7 days moist curing unconfined compressive strengths of 750 and 1500 kPa for base course. According to Chukwudebelu et al. [32] 225,000 metric tons of CCW are generated from the automobile workshop annually and end up in the landfill. Environmental issues have been raised as relating to disposal and this research work will encourage the utilization of this waste. Durability study of the weak subgrade stabilized with calcium carbide waste is on-going. Research on incorporating natural fibres with CCW in stabilizing weak subgrade is hereby recommended for future work.

4 Conclusions

The following conclusions could be drawn from this research work;

Subgrade was classified as A-7-5 and ML or OL soil with silica sesquioxide ratio of less than 1.33 (1.11). The optimum percentage of subgrade-Calcium Carbide Waste stabilization was achieved at 8%

The modification of S-CCW-CC/S-CCW-ISD for soaked CBR/UCS increased in strength for all curing periods

The micrographs of subgrade showed a discontinuous structure which was responsible for its low bearing capacity while for optimum stabilized subgrade materials showed different shapes with voids filled with formation of cementitious compounds which increased the bearing capacity of the stabilized soil

Subgrade was stabilized with different percentage of calcium carbide waste with optimum being at 8% tagged as optimum subgrade lime blend.

References

1. Oduola RO (2010) Engineering potentials of industrial waste materials in low cost and durable flexible pavement construction in Nigeria. In: Conference Proceedings and Annual General Meetings, Nigerian Institution of Civil Engineers (NICE)
2. Salahudeen AB, Eberemu AO, Osinubi KJ (2014) Assessment of cement Kiln Dust-treated expansive soil for the construction of flexible pavements. *Geotech Geol Eng* 32(4)
3. Abiola OS, Madoti OI, Oduyebo TG, Quadri HA (2016) Assessment of subgrade soil stabilized with Calcium Carbide waste, Cement Kiln Dust, and Steel Slag. *LAUTECH J Eng Technol* 10(2):42–47
4. Quadri HA, Abiola OS, Odufa SO, Azeez JO (2019) Application and strength development of subgrade material stabilized with Calcium Carbide waste in flexible pavement construction. *Adeleke Univ J Eng Technol (AUJET)* 2(2):55–65
5. Horpibulsuk S, Phetchuay C, Chinkulkijniwat A, Cholaphatsorn A (2013) Strength development in silty clay stabilized with calcium carbide residue and fly ash. *Soils Foundation* 53(4):477–486
6. Kampala A, Horpibulsuk S (2013) Engineering properties of silty clay stabilized with calcium carbide residue. *J Mater Civil Eng*
7. Eberemu AO, Isah G, Gadzama EW (2013) Compressibility characteristics of compacted black cotton soil treated with Bagasse Ash. *J Civil Eng* 8(1): 26–44 (Publication of Nigerian Institution of Civil Engineers)
8. Akinwumi II (2012) Utilization of steel slag for stabilization of a lateritic soil, Ota, Nigeria. Unpublished M.Eng Thesis, Covenant University, Nigeria
9. Zhang Y, Likos WJ, Soleimanbeigi A, Chen J, Edil TB (2016) Geotechnical properties of aged municipal solid waste incineration fly ash. In: *Proceedings Geo-Chicago 2016 GSP* 272, 42–51
10. Wijeyesekera DC, Ho MH, Bai X, Bakar I (2016) Strength and stiffness development in soft soils: a FFESEM aided soil microstructure viewpoint. In: *IOP Conference Series: Materials Science and Engineering* 136
11. Horpibulsuk S (2012) Strength and microstructure of cement stabilized clay. *Scanning Electron Microscopy, Viacheslav Kazmiruk, Intech. Open.* <https://doi.org/10.5772/35225>
12. Boriana T (2016) Scanning Electron Microscopy (SEM) investigation of stabilized loess soil. *Geosciences*

13. Peethamparan S, Olek J, Diamond S (2008) Physicochemical behavior of Cement Kiln Dust-treated Kaolinite clay. *Transp Res Rec J Transp Res Board* 2059:80–88
14. Solanki P, Zaman M (2012) Microstructural and mineralogical characterization of clay stabilized using calcium-based stabilizers. Dr. ViacheslarKazmiruk (Ed.), ISBN: 978-953-51-0092-8, In Tech
15. Indiramma P, Sudharani C (2018) Scanning electron microscope analysis of fly ash, quarry dust stabilized soil. In: Frikha W, Varaksin S, Viana da Fonseca A (eds) *Soil testing, soil stability and ground improvement. GeoMEast 2017. Sustainable Civil Infrastructures*. Springer, Cham
16. ASTM (2017) Standard practice for classification of soils for engineering purposes (unified soil classification system). ASTM Standard D2487, American Society for Testing and Materials, West Conshohocken
17. BS 1377 Methods of test for soils for Civil Engineering purposes. *British Standard Institute*, London, UK (1990). ASTM C618 Standard Specification for Coal Fly Ash and Raw or Calcined Natural Pozzolan for use in Concrete. *ASTM International*, West Conshohocken, PA, USA, (2008)
18. ASTM D1883–14 (2014) Standard test method for California bearing ratio (CBR) of laboratory compacted soils. West Conshohocken, PA: ASTM International
19. ASTM C618 Standard Specification for Coal Fly Ash and Raw or Calcined Natural Pozzolan for use in Concrete. ASTM International, West Conshohocken, PA, USA, (2008)
20. Martin FJ, Doyne HC (1927) Laterite and Lateritic Soils in Sierra Leone. 1 *J Agric Sci* 17:530–546
21. Martin FJ, Doyne HC (1930) Laterite and Lateritic Soils in Sierra Leone. 2 *J Agric Sci* 20:135–143
22. Winterkorn FH, Chandrasekharan EC (1951) Laterites and their stabilization, highway. *Res Board Wash Bull* 44:10–29
23. Ahmed (1995) Characterization and stabilization of Eastern Saudi marls. MSc Thesis, Department of Civil Engineering, King Fahd University of Petroleum and Minerals, Dhahran, Saudi Arabia
24. Abdullah GMS (2009) Stabilization of Eastern Saudi Soils using heavy fuel oil fly ash and Cement kiln dust. MSc Thesis, Department of Civil Engineering, King Fahd University of Petroleum and Minerals, Dhahran, Saudi Arabia
25. Al-Homidy AA (2013) Improvement of Eastern Saudi Soil utilizing indigenous Industrial by-product. PhD Thesis, Department of Civil Engineering, King Fahd University of Petroleum and Minerals, Dhahra, Saudi Arabia
26. Al-Homidy AA, Abd El Aal AK (2017) Improvement of geotechnical properties of Sabbkha soil utilizing Cement Kiln Dust. *J Rock Mech Geotech Eng* 9(4):749–760
27. Osinubi KJ (1998) Influence of compaction delay on the properties of Cement Stabilized Lateritic Soil. *J Eng Res* 6(1):13–25
28. Al-Mukhtar M, Lasledj A, Alcover J (2010) Behaviour and mineralogy changes in lime-treated expansive soil at 500C. *Appl Clay Sci* 50(2):199–203
29. Garzon E, Cano M, O’Kelly BC, Sanchez-Soto PJ (2016) Effect of Lime on stabilization of phyllite clays. *Appl Clay Sci*
30. Moon DH, Grubb DG, Reilly TL (2009) Stabilization/Solidification of Selenium-impacted soils using Portland Cement and Cement Kiln Dust. *J Hazardous Mater* 68:944–951
31. Chaunsali P, Peethamparan S (2011) Evolution of strength microstructure and mineralogical composition of a CKD-GGBFS binder. *Cem Concr Res* 41:197–208
32. Chukwudebelu JA, Igwe CC, Taiwo OE, Tojola OB (2013) Recovery of pure slaked lime from carbide sludge: Case study of Lagos State, Nigeria. *Afr J Environ Sci Technol* 7(6):490–495

A Case Study on the Efficacy of Cement Treated Base/subbase



Ashish Gharpure, Prashant Navalakha, and Asita Dalvi 

Abstract The phenomenal growth in construction activity and scarcity of conventional construction materials has led to the emergence of new supplies, techniques, and machinery in the field. The revised Indian Road Congress (IRC) 37-2018 guidelines recommend the use of Commercial Chemical Stabilizers (CCSs) for the stabilization of flexible pavements. Cement treated base/subbase (CTB/CTSB) is a general term that applies to an intimate mixture of native soils with measured amounts of ordinary portland cement (OPC) and water that hardens after compaction and curing to form a strong, durable, frost resistant paving material. The main advantage of CTB/CTSB is that it provides a stiffer and stronger base than an unbound granular base. Moreover, a wide variety of in situ soils can be used; this eliminates the need to haul inexpensive select granular aggregates. This paper presents a case study on the efficacy of CCS in powder and liquid form which has been used to improve pavement performance at 7 locations in and around Nashik, Maharashtra, India. These CCS fill the voids between the soil particles to form a flexible and impermeable bond. A comprehensive program comprising of preliminary site survey, pavement design using IITPAVE, and experimental investigation on in situ soil with and without CCS and field performance studies have been formulated. The proposed design mix employed is 4% cement as a source of CaO and 750 ml/cum of CCS in liquid form and 9.8% cement and 0.2% CCS in powder form. The compressive strength and durability aspects are evaluated to ascertain the efficacy of the CCS. Based on the outcome of laboratory investigation, actual construction work is executed on site, field performance tests such as rapid moisture meter, dynamic cone penetrometer; sand replacement, etc. are carried out to ensure quality on site. Based on the study conducted it is concluded that the existing poor conditions and the problems in the pavement stretch have been eliminated and the cement loss is well within acceptance criteria. Improved pavement performance can thus be achieved by using commercial chemical stabilizers (CCSs). However, it is recommended to conduct rigorous laboratory testing to optimize the suitable proportion for pavement stabilization.

A. Gharpure · P. Navalakha · A. Dalvi (✉)
GENSTRU Consultants Pvt. Ltd., Pune, India

Keywords Flexible pavement · Cement treated base and subbase (CTB/CTSB) · Commercial Chemical Stabilizer (CCS) · CBR · Durability · Wetting and drying

1 Introduction

Road connectivity is the key to the socio-economic growth of the country. The development of new roads, enhancement of existing roads is a part of the infrastructure boom in India as well as in Maharashtra. An increasing emphasis has been thus placed on the use of stabilized pavement materials in recent years. The revised Indian Road Congress (IRC) 37-2018, guidelines recommend the use of cementitious/chemically stabilized subbases and bases for flexible pavements, [1]. Through the use of stabilizing agents, low-quality materials can be economically upgraded to the extent that these may be effectively utilized in the pavement structure. Stabilized pavement materials are generally incorporated into the pavement structure as base courses and subbases, [2, 3]. In recent years various commercial chemical stabilizers (CCSs), have been introduced for the stabilization of pavement layers which are mixed with cement to enhance the strength and durability characteristics of the soil–cement mix, [4]. Cement treated base/sub base (CTB/CTSB) is a general term that applies to an intimate mixture of native soils with measured amounts of Ordinary Portland Cement (OPC) and water that hardens after compaction and curing to form a strong, durable, frost resistant paving material. Its advantages of great strength and durability combine with low first cost to make it the outstanding value in its field. A thin bituminous surface is usually placed on the soil–cement to complete the pavement. During soil cement stabilization, the followings are contributing factors (a) Type of soil (b) Quantity of cement (c) Quantity of water (d) Mixing, compaction, and curing (e) Admixtures. This paper discusses a case study illustrating the efficacy of cement/chemical stabilizers (CCS) in pavement stabilization applications. The stabilization of pavement layers is a fairly straightforward operation and with sound construction techniques the properties of materials can be improved significantly by the addition of relatively small quantity of stabilizing agent, [5].

With the initiatives of government authorities to adapt to recent trends in technology and advancement in road construction works, a few selective stretches were identified to explore the efficacy of using CCS for Major District Roads (MDR) in Nashik at 7 different locations. The primary objective to adapt to stabilized pavements is, the huge cost incurred due to recurring maintenance and minimal traffic disruption. Since, the soil is a non-linear material; it is a standard practice to verify the efficacy and integrity of any additive to be blended with residual soil. Thus, this paper is a compilation of such exploratory pavement stabilization work carried out in the Nashik region for rebuilding and reconstruction purpose.

1.1 Advantages of CCS for Stabilization of Flexible Pavements

- It provides a stiffer and stronger base than an unbound granular base. A stiffer base delays the onset of surface distress, such as fatigue cracking, and extends pavement life by reducing deflections due to traffic loads, which results in lower strains in the asphalt surface, [6].
- CTB thicknesses are less than those required for granular bases carrying the same traffic because the loads are distributed over a large area. The strong uniform support provided by CTB results in reduced stresses applied to the subgrade.
- A thinner cement stabilized section can reduce subgrade stresses more than a thicker layer of untreated aggregate base. Subgrade failures, potholes, and road roughness are thus reduced.
- CTB's slab-like characteristics and beam strength are unmatched by granular bases that can fail when the interlock is lost.
- A wide variety of in situ soils and manufactured aggregates can be used for CTB. This eliminates the need to haul in expensive select granular aggregates.
- Rutting is reduced in a CTB pavement. Loads from channelized traffic will displace unbound granular material beneath flexible surface pavements.
- Moisture intrusion can destroy unstabilized pavement bases, but not when cement is used to bind the base. CTB pavements form a moisture-resistant base that keeps water out and maintains higher levels of strength, even when saturated, thus reducing the potential for pumping of subgrade soils.
- CTB provides a durable, long-lasting base in all types of climates. As an engineered material it is designed to resist damage caused by cycles of wetting and drying and freezing and thawing [7].

2 Methodology

The soil sample used in this study was collected from 7 locations in and around Nashik district located in the northwest of Maharashtra state, 180 km from Mumbai. The soils of the district are the weathering products of Basalt and have various shades from gray to black, red, and pink color. The soils occurring in the district are classified in the categories namely lateritic black soil, reddish-brown soil, coarse shallow reddish-black soil, medium-light brownish-black soil. In general, the soils are very fertile and suitable for growing cereal and pulses. The black soil contains high alumina and carbonates of calcium and magnesium with variable amounts of potash, low nitrogen, and phosphorus. The 7 locations in this work have been referred to as Location-1 to Location-7. Mix in place stabilization technique has been adopted on the field.

2.1 Materials

In present work, the top crust material constituted majorly coarse-grained fraction and road filling material. The subgrade soil at all locations is a fine-grained fraction majorly clayey in nature. Around 50–60 kg, sample from each location was collected.

The soil samples as received were oven-dried for 24 h at 105–110 °C. The top crust material was then crushed manually to about 20 mm size. The crushed top crust material was then mixed in proportion with subgrade soil to arrive at raw soil mix. The proportion was kept the same for all locations. The physical and engineering properties of the soil sample have been then determined in the laboratory as elaborated in the subsequent section. The dosage of cement and additive has been decided based on compaction properties.

To verify the long term performance of soil–cement stabilization, durability tests have been performed as per Indian Standard (IS) 4332(IV), [8]. For this, 4 nos. of 1000 cc molds for each of soil type were cast and cured for around 31 days. Overall one test requires 7 days moist chamber, 12 cycles for 48 h. Wetting and drying (5 h) submergence, 42 h oven at 70 °C), thus 7 days + 12 × 2 days = 31 days for complete testing of 1 soil sample.

2.2 Design Mix with Only Cement (OPC)

A typical mix design methodology has been adopted at all locations. Two types of CCS, one in liquid form and other in powder form have been used in the present investigation. Furthermore, to better understand the effect of stabilizer experimental investigation has been carried out by verifying the effect of adding only cement to raw soil.

The sample design for only OPC treated raw soil is as below;

- Take 1.8 kg of oven-dried dry soil
- Dry additive cement @ 4% of the dry weight of soil = 72 gm of cement
- MDD is 2.03 gm/cc, the volume of the 1.8 kg of soil = 890 Cubic centimeter
- OMC is 11.6% Qty of potable water = 210 ml

Casting UCS molds

1. Thoroughly mix oven-dried 1.80 kg of soil + 72 gm of OPC
2. Now mix 210 ml of water to soil–cement of 1.81 Kgs
3. From this design mix, compact 190 gm in the mold of 38-mm diameter & 76-mm height or any mold size as given in codal guidelines
4. Cast 09 specimens from a total mix of 1.81 Kgs
5. From second day onward, start curing specimen 3–4 times a day, every day, until 28 days

6. Test a set of 3 specimens, after 7, 14, and 28 days, respectively, for UCS of soil + OPC.

2.3 *Design Mix with CCS*

As stated earlier the efficacy of CCS, powder and a liquid stabilizer have been verified in the present investigation. Oven-dried raw soil + 4% of dry additive, i.e., cement + liquid CCS in proportion to 750 ml/cum of soil to be treated + potable water required to achieve OMC are blended. Alternatively, Oven-dried raw soil + 9.8% of dry additive, i.e., cement + 0.2% powder CCS + potable water required to achieve OMC are mixed.

The sample design for liquid stabilizer + cement treated raw soil is as below;

- Take 1.8 kg of oven-dried dry soil
- Dry additive cement @ 4% of the dry weight of soil = 72 gm of cement
- MDD is 2.03 gm/cc, the volume of the 1.8 kg of soil = 890 Cubic centimeter
- Liquid stabilizer in proportion of 750 ml / cum, for 0.00089 cum = 0.67 ml or say 1 ml (Standard dose recommended by the manufacturer)
- OMC is 11.6% Qty of potable water = 210 ml

Casting UCS molds

1. Mix 1 ml of liquid stabilizer in 210 ml of potable water
2. Thoroughly mix oven-dried 1.80 kg of soil + 72 gm of OPC
3. Now mix 211 ml of (1 ml stabilizer + 210 ml water) solution, with soil + cement mix of 1.81 Kgs
4. From this design mix, compact 190 gm in the mold of 38-mm diameter and 76-mm height
5. Cast 09 specimens from a total mix of 1.81 kg
6. From second day onward, start curing specimen 3–4 times a day, every day, until 28 days
7. Test a set of 3 specimens, after 7, 14 and 28 days, respectively, for UCS of soil + OPC + CCS

By adopting a similar methodology, the CBR test is also performed and molds with volume 1000 cc are as well cast for durability test as outlined in IS 4332(IV). A similar procedure is adopted for powdered additive. The summary of laboratory results and subsequent interpretations is discussed in the next section. Further, field investigation has been carried out during and post-execution of work and the field performance has been briefed in the next section.

3 Results and Interpretation

A wide range of soil particles from fine-grained to coarse-grained have been covered in this exploratory work. The key results and interpretations are summarized in this section. The soil type varied from fine-grained (CH-Clay with high plasticity) to coarse-grained (well-graded Gravel), covering a broad spectrum of soil type. This facilitated to understand the integrity of stabilizer with each of the soil type and its efficacy in improving soil properties. The performance of CCS (liquid and powder stabilizer) has been categorized as CCS- A and CCS-B such that;

[CCS-A] Liquid Stabilizer: Raw soil + 4% of dry additive, i.e., OPC + CCS in liquid form in proportion to 750 ml/cum of soil to be treated + potable water required to achieve OMC.

[CCS-B] Powder Stabilizer: Raw soil + 9.8% of dry additive, i.e., OPC + 0.2% CCS in powder form + potable water required to achieve OMC.

3.1 Laboratory Investigation

Table 1 summarizes the properties of soil investigated such as Index properties, Compaction properties, and Engineering properties and the respective category of CCS adopted. The key parameters required to assess the pavement stabilization aspect are particularly investigated based on Indian Standard (IS) 2720.

As listed in Table 1, OMC is higher for fine-grained soil than for coarse-grained soil. The soaked CBR and UCS of the coarser fraction are higher than that for fine-grained soil. The CCS-A has been used for locations 1 to 5 and the CCS-B has been used for locations 6 and 7. To analyze the effect of OPC by blending with raw soil, the cement is added proportionately and the compressive strength after 7 days curing has been determined and summarized in Table 2.

From Table 2, it is evident that strength improves by adding cement to soil, however, no significant improvement is observed which fulfills the codal provisions that the CTB/CTSB material shall have a minimum unconfined compressive strength (UCS) of 4.5–7 MPa as per IRC:SP:89 in 7/28 days. This implies that cement may not

Table 1 Summary of soil properties

Location	1	2	3	4	5	6	7
CCS Category	A	A	A	A	A	B	B
Soil Type	CH	CH	SC	GC	GP	GW	GW
Optimum Moisture Content, OMC (%)	12	12	17	10	10	10	10
Maximum Dry Density, MDD (g/cc)	2.03	2.00	2.00	2.09	2.21	2.37	2.33
California Bearing Ratio, CBR-soaked (%)	2.30	5.50	8.55	2.80	22	19	19
Unconfined Compressive Strength, UCS (MPa)	0.21	0.46	0.24	0.36	1.50	1.24	1.23

Table 2 Summary of soil properties by blending with ONLY OPC

Location	5	6	7
CCS category	A	B	B
Soil type	GP	GW	GW
Unconfined Compressive Strength, UCS (MPa) after 7 days curing period	1.96	2.94	2.68
Unconfined Compressive Strength, UCS (MPa) after 28 days curing period	2.08	3.16	3.18

necessarily bind well with soil and thus there is need to mix CCS to further improve strength properties. A bar chart comparing UCS of raw soil, UCS of raw soil + OPC (7 days curing) and UCS of raw soil + OPC + CCS (7 days curing) is illustrated in Fig. 1.

From Fig. 1, it can be observed that by the addition of CCS (liquid or powder stabilizer) the compressive strength significantly increases suggesting its efficacy from strength perspective. The performance of additives in liquid or powder form with engineering properties is summarized in Table 3.

It is observed that with the addition of additive in liquid or powder form (CCS-A), the compressive strength (UCS) gains by over four times as compared to raw soil. Most importantly, the UCS at 7 days curing satisfies the criteria as per code provisions. It is noted that with CCS-B (powder stabilizer), the compressive strength fulfills code provisions at 7 days curing whereas liquid stabilizer fulfills code provisions at 28 days curing. The soaked CBR is also observed to increase substantially with additives or treated soil as depicted in Fig. 2.

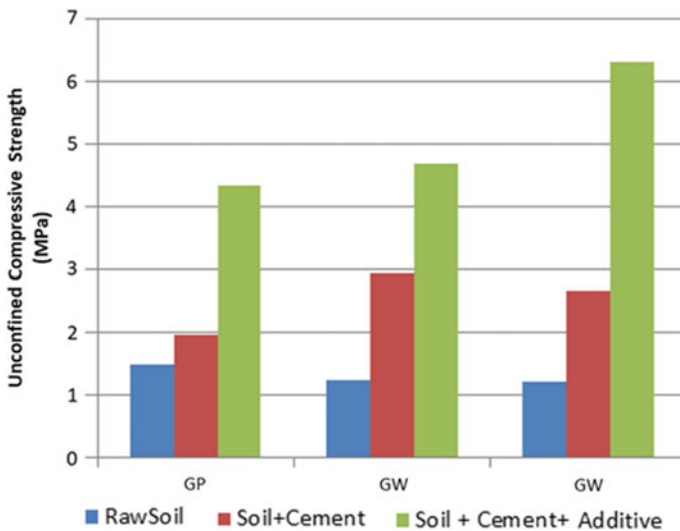


Fig. 1 Efficacy of cement/chemical stabilizer based on the strength

Table 3 Summary of soil properties by blending Stabilizers

Location	1	2	3	4	5	6	7
CCS category	A	A	A	A	A	B	B
Soil Type	CH	CH	SC	GC	GP	GW	GW
California Bearing Ratio, CBR-soaked (%)	36.21	49.84	61.14	80.90	95	77	76
Unconfined Compressive Strength, UCS (MPa) after 7 days curing period	2.12	2.93	3.56	2.75	4.34	5.69	8.87
Unconfined Compressive Strength, UCS (MPa) after 28 days curing period	4.58	4.96	10.86	4.73	5.70	4.70	6.32

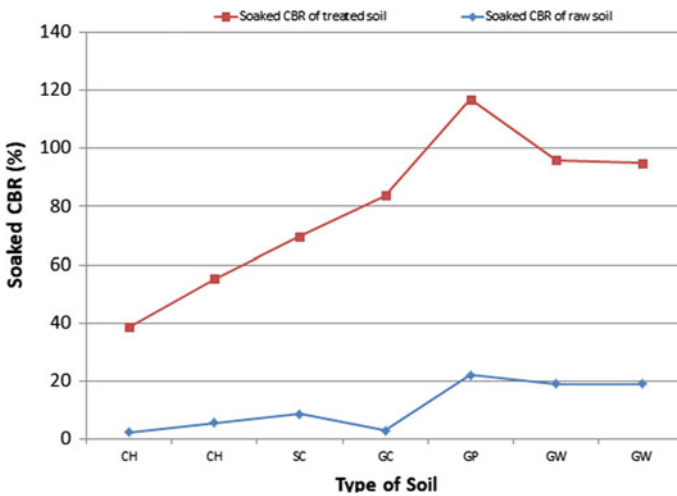


Fig. 2 Comparison of soaked CBR for treated and untreated soil

As shown in Fig. 2, the soaked CBR of treated soil is much higher than that for raw soil, this may be attributed to the fact of gain in strength with curing over 96 h. It is also noted that the soaked CBR of treated soil is higher than that of unsoaked CBR of treated soil which is again attributed to the curing period.

The most crucial aspect of soil–cement stabilization is its long term performance which is gauged by performing durability test as per IS 4332 (IV).

As could be seen from Table 4, the maximum percentage weight loss is within permissible limits (Maximum allowable weight loss (%) is 14% for GW as per IRC-SP89: II). Coarser fractions in general are indicative of better performance over finer fraction, it is thus advised to carry our further research in this regard. The summary of field investigation during and post-execution is discussed in the preceding section.

Table 4 Summary of durability test

Location	6	7
Stabilizer category	B	B
Soil Type	GW	GW
Maximum % weight loss	6	7
Average soil–cement loss (%)	13	14
Maximum volume change (%)	2.60	2.12

3.2 Field Investigation

To monitor the performance of CCS/pavement stabilizer, a detailed quality assurance plan has been prepared to confirm that designed soil properties are achieved as obtained from laboratory results. The interval of testing is decided based on the stretch of stabilized pavement and was marked in a manner such that the entire stretch in the longitudinal and lateral direction is covered. The depth of reclamation is 300 mm at all 07 locations. Rapid moisture meter has been used to gauge field moisture content whereas the in situ dry density is evaluated based on the sand replacement method. The CBR is evaluated by performing a Dynamic Cone Penetrometer (DCP) along the stretch using the following equation, [9].

$$CBR = 2.465 - 1.12 * \log_{10}(N) \tag{1}$$

where, N = Number of blows, mm from DCP.

Moreover, molds were cast during execution and cured for 7, 14, and 28 days to determine unconfined compressive strength. The UCS was observed to be 4.5 MPa at 7 days curing at all locations where CCS-B (powder stabilizer) is used and 28 days at all locations where CCS-A (liquid stabilizer) is used. The summary of the laboratory investigation is tabulated in Table 5.

Table 5 Summary of field investigation

Location	In situ dry density (kN/m ³)	Field moisture content (%)	Maximum dry density (kN/m ³)	Optimum moisture content (%)	% Compaction	Soaked CBR in the lab	In situ CBR based on DCP
1	1.98	2	2.03	12	97.53	36.21	172
2	1.96	3	2.00	12	98.00	49.84	121
3	1.95	3	2.00	17	97.50	61.14	100
4	1.96	4	2.01	10	97.51	80.90	167
5	2.18	2	2.21	10	98.64	95.00	120
6	2.32	3	2.37	10	97.89	77.00	146
7	2.28	4	2.33	10	97.85	76.00	130

The results in Table 5 further reveal that soaked laboratory CBR value is lower than the DCP based soaked in situ CBR value. This is attributed to the higher confinement pressure in the field.

4 Summary and Conclusions

The primary objective to adapt to CCS for flexible pavement stabilization is the huge cost incurred due to recurring maintenance and minimal traffic disruption. Since, the soil is a non-linear material; it is a standard practice to verify the efficacy and integrity of any additive to be blended with residual soil. Thus, this paper is a compilation of such exploratory pavement stabilization work carried out in the Nashik region for rebuilding and reconstruction works. Cement treated base/sub base (CTB/CTSB) is a general term that applies to an intimate mixture of native soils with measured amounts of ordinary portland cement (OPC) and water that hardens after compaction and curing to form a strong, durable, frost resistant paving material. A comprehensive experimental investigation on in situ soil with and without a stabilizer has been carried out. The proposed design mix employed is 4% cement as a source of CaO and 750 ml/cum of stabilizer in liquid form and 9.8% cement and 0.2% stabilizer in powder form. The compressive strength and durability aspects are evaluated to ascertain the efficacy of the stabilizer, [10, 11]. Based on the outcome of laboratory and field investigation, it is concluded that the existing poor conditions and the problems in the pavement stretch have been eliminated and the cement loss is well within acceptance criteria. However, it is recommended to conduct rigorous laboratory testing to optimize the suitable proportion for the proposed pavement stabilization. Improved pavement performance can thus be achieved by using commercial chemical stabilizers (CCS).

References

1. Indian Road Congress, IRC:37 (2018) Guidelines for the design of flexible pavements, The Indian Roads Congress, New Delhi
2. Prasad S (2016) Feasibility study on cement treated base and sub base layers of service roads—a case study on Khed Sinnar NH 50 project
3. Bagui SK (2012) Pavement design for rural low volume roads using cement treatment base, published in Jordan. *J Civil Eng* 6(3)
4. Special Publication, Indian Road Congress, IRC: SP-89: II (2018) Guidelines for the design of stabilized pavements
5. South Africa: Department of Transport (1986) (Technical Recommendations for Highways, TRH13): Cementitious Stabilizers in Road Construction
6. Al-Jumaili MA (2018) Study of cement treated base aggregate properties for pavement structure. *Int J Inf Res Rev*
7. Sarkar PP, Zachariah JP, Debnath P, Saha M, Das A, Kumar P (2018) A study on cement treated base using crushed bricks as aggregate. Seminar on Ground Improvement Techniques

8. Indian Standard (IS) 4332-4 (1968) Methods of test for stabilized soils, Part 4: Wetting and drying, and freezing and thawing tests for compacted soil-cement mixtures
9. Gill, Jha KS, Choudhary JN, AK (2010) CBR value estimation using dynamic cone penetrometer, Indian Geotechnical Conference
10. ASTM-D 6951-3 (2003) Standard test method for use of the dynamic cone penetrometer in shallow pavement applications
11. Hossain MS, Nair H, Ozyildirim HC (2017) Determination of mechanical properties for cement treated aggregate base, Final Report VTRC 17-R21

Comparative Evaluation of Lime and Biopolymer Amended Expansive Soil



G. Landlin, B. Sharmila, and S. Bhuvaneshwari

Abstract The rapid development and infrastructural growth have led to a boom in the construction industry. The space crunch and less availability of suitable sites have led to the utilization of unsuitable sites, after the necessary alteration, to be used for construction activities. The problematic soils (expansive soils, soft clays) pose a great threat to the construction activities. The foundation options available when an unsuitable soil without sufficient bearing capacity is encountered are to go for the expensive pile foundation or any other kind of structural alterations. This indirectly leads to a larger consumption of construction materials and in turn leads to higher greenhouse gas emissions. Nevertheless, the choice of stabilization with alkaline additives (cement, lime, fly ash) has been used for decades with large success rates; however, these additives used in large quantities tend to alter the nature of the ground water as well as affects the biodiversity in the soil and reduces the soil-carbon ratio as well. Thus, this study proposes the usage of an eco-friendly non-traditional additive and checks its suitability for the soil stabilization. Lignosulphonate (LS), a lignin-based product derived as a waste from the paper industry, is to be used as an additive for stabilizing the expansive soils. Its suitability is substantiated with respect to index properties, engineering properties, microstructural changes, and durability aspects. The main objective of the present study is to carry out a comparative study between lime and LS treated soil. The durability of the treated soils is evaluated through strength tests and chemical analysis after cycles of wetting and drying. The results would significantly give a measure of the long-term stability of the LS and lime treated soil.

Keywords Expansive soil · Biopolymer · Lignosulphonate · Durability · Wetting–drying

G. Landlin · B. Sharmila · S. Bhuvaneshwari (✉)
SRMIST, KTR, Kanchipuram 603203, India
e-mail: bhuanes1@srmist.edu.in

© The Author(s), under exclusive license to Springer Nature Switzerland AG 2022
E. Tutumluer et al. (eds.), *Advances in Transportation Geotechnics IV*, Lecture Notes
in Civil Engineering 164, https://doi.org/10.1007/978-3-030-77230-7_62

807

1 Introduction

The rapid pace of industrialization and urbanization causes a great threat on the availability of suitable land for construction activities. At certain locations, the construction activities get delayed or obstructed due to the presence of unsuitable problematic soils. The problematic soils could be either expansive in nature or highly compressible. Soils which are highly expansive, due to the presence of montmorillonite mineral shrinks in summer and alternatively becomes wet and slushy in monsoon; exerting very high swell pressure on the structures constructed on them.

The commonly adopted method when such problematic soils are encountered is bypassing the structural load to a deeper level through pile foundations, which are often very expensive. Use of under reamed pile foundations, mat foundations, cohesive non-swelling (CNS) layer technique and chemical alteration are the most sought-after techniques [1]. However, chemical alteration techniques have been widely practiced and alkaline stabilizers such as the cement, lime, flyash, and industrial by-products (cement bypass dust, copper slag, slag cement, and granulated blast furnace slag (GBFS)) are predominantly used. However, the usage of these additives poses severe long-term environmental threat and affects the biodiversity of the sub-soil strata. The additives increase the pH of the soil environment which in turn causes corrosion of the buried pipelines and sometimes lead to excessive cracking due to brittle behavior [2–4]. Additionally, the performance under traffic loading or impact loading is also questionable [5]. Furthermore, the production of these additives increases the emission of greenhouse gases and also consumes 2% of the global energy in their production [6, 7].

In the recent past, considerable research is focused on the utilization of non-traditional stabilizers which are “environmentally sustainable.” The additives could be a by-product of bio-based energy and paper industry (like natural polymers, lignin-based stabilizers). These non-traditional stabilizers are primarily non-toxic, non-corrosive and can be an effective alternative for alkaline stabilizers [8]. Related reduction in the carbon emissions, increase in soil organic carbon (SOC) can have a direct impact on the global climatic change [9].

Lignin a by-product of timber industry is a kind of organic polymer compound. It's vast global production and low value as an industrial additive has made it a waste material [10–12]. Approximately, 50 million tons of lignin-based by-products are collected from the paper manufacturing industry per year [13]. On account of this, they can cause a serious environmental stockpile and disposal issue. In order to understand the behavior of eco-friendly additive amended soil, biopolymer-based lignosulphonate, a lignin derivative is adopted in this study.

1.1 Lignosulphonate for Soil Stabilization

Many studies have been carried in the past to assess the applicability of lignosulphonate (LS) for soil treatment. The primary interaction mechanism of lignosulphonate with soil aggregate is that of dispersion and cementation as reported by Gow and Davidson [14]. The water-soluble and hygroscopic nature of the polymer attributes to the cementation effects in LS amended soil. Extensive work was carried out on the friable loess of Iowa by the Iowa state university [14, 15]. Demiral and Davidson, used Ca-Lignosulphonate from spent liquor from the paper mills [15]. The usage was initially confined to dust palliation and was later extended to soil stabilization. Efforts were also made to reduce the solubility of lignosulphonate by using polyvalent secondary additives which assists in the formation of insoluble lignosulphonate compounds [15]. Sinha et al. established that lignin is more effective for granular or soil aggregate mixtures and effectively retard moisture adsorption [16].

The durability of expansive soil treated with lignosulphonate (LS) under cycles of freezing and thawing were also investigated, measuring the percent volume change, moisture content variation and mass loss. The LS stabilized soil showed a significant improvement with respect to percent mass loss. The stabilization mechanism of expansive soil with LS is more physically involved by changing the crystallographic properties of soil rather than any significant chemical reaction [17]. LS forms a thin film around particles of the clay which increases the surface area and also involves the ion exchange reaction. FTIR tests confirm that the reaction between the soil and LS is by ion exchange and there is a decrease in the double layer of the clay lattice [18, 19].

The lime reactivity with soil is influenced by the soil origin and geology, soil pH, SSA and charge density, Zeta Potential, CEC, soil acidity, and many other factors [20]. However, the reactivity depends on the optimum consumption of lime for any particular soil based on the pH value [21]. Lime reacts with different clay minerals in two phases: the short-term cation exchange and flocculation reactions followed by the long-term pozzolanic reaction [22]. Thus, the behavior of lime treated soil has been well established over the past decades compared to lignosulphonate amendment [23].

The subgrade soil is susceptible to moisture fluctuations and water logging. The stiffness, strength, and overall durability of the stabilized subgrade material is necessary for efficient pavement functioning. Thus, it becomes essential to understand the performance of the stabilized material under cycles of wetting–drying which simulates the moisture fluctuations in the field. The objective of the present study is to assess the improvement in the properties of expansive soil using lime and lignosulphonate. The improvement is assessed through strength tests and microstructural changes. Further, the durability of the soil additive composite is assessed through strength tests post wetting and drying cycles. This study helps to assess the behavior of lignosulphonate, a non-traditional stabilizer in comparison with lime treatment under varying seasonal conditions and identify the suitability of lignosulphonate amendment for soil stabilization in comparison to lime treatment.

2 Materials and Methods

2.1 Materials

Soil. The soil used is highly expansive in nature, collected from Siruseri, an industrial area near Kancheepuram district (12.85°N, 80.20°E), Tamil Nadu, India. The soil samples were air-dried, pulverized, and sieved through 1 mm sieve for further experimental investigation. All the laboratory classification tests were carried out as per IS 2720 procedures [24]. Based on the plasticity characteristics, the soil is classified as Inorganic clay of high plasticity as per IS 1498 [25]. Based on the values of free swell index (FSI) and swell potential, the soil is classified as highly expansive category [26–28]. The index and engineering properties of untreated soil have been evaluated and tabulated in Table 1. The two stabilizers chosen to study the improvement of the properties of soil are calcium lignosulphonate (LS) and lime (Ca(OH)₂).

Lignosulphonate and Lime. Calcium lignosulphonate (LS) is an amorphous material derived from lignin. A by-product from paper industry, light-yellow brown powder that is soluble in water. Calcium hydroxide (Ca(OH)₂) is produced when quick lime is slaked with water. Both additives were procured commercially from the local market.

Table 1 Index and engineering properties of soil

Property	Values
Specific gravity	2.68
Liquid limit	64.08%
Plastic limit	27.8%
Plasticity index	36.28%
Shrinkage limit	10.37%
Clay fraction	64%
Silt fraction	27%
Sand fraction	9%
Gravel fraction	0%
Differential free swell%	111%
Maximum dry density	15.86 kN/m ³
Optimum moisture content	22.86%
Swell potential	17.6%
Soil classification: Based on plasticity Based on expansivity	CH Highly expansive

2.2 Methodology

The index, engineering, and microstructural properties are evaluated for virgin soil and soil treated with LS and lime. The optimum content of LS was determined from the Atterberg's limits of soil treated with 0.5, 1.5, 3.0% of LS by weight. The optimum content of LS was found out to be 1.5% by weight proportions. Lime treatment of the soil is initiated with the determination of ICL value [21] for the soil which is taken as the optimum content of lime. The optimum lime content is determined as 4% by weight of soil. The compaction test was performed using the mini compaction apparatus suggested by Sridharan and Sivapulliah for both treated and untreated soil to establish the dry density-moisture content relationship [29]. The unconfined compressive strength (UCC) tests were carried out as per IS 2720 (Part 41) [30]. Samples were prepared by static compaction at 95% of maximum dry unit weight and corresponding water content and tested at a strain rate of 1.5 mm/min for different curing periods.

The durability studies were carried out in the laboratory to study the changes in the strength characteristics of the treated samples with respect to cycles of wetting and drying simulating the field conditions. The UCC samples prepared with the respective density and moisture content, cured for 3 days prior to subjecting the samples to alternate cycles of wetting and drying. The compacted samples were first wrapped in filter paper and absorptive cloths, arranged in sand bed and soaked for a period of 2 days and dried at an elevated temperature of 60 °C for a period of 3 days to simulate wetting and drying behavior, respectively (Fig. 1). The period of wetting and drying were selected based on the preliminary weight observation of the samples under soaked and dry conditions. The samples were tested for the

Fig. 1 Arrangement for the cyclic wetting and drying process in sand bath and wrapping of the samples with adsorptive cloth



strength at the intermittent cycles of 1, 3, and 5. The chemical characteristics of the treated soil after cycles of wetting and drying were evaluated through pH and electrical conductivity (EC) measurements. The dried samples, post UCC tests were crushed and about 5 g of the samples were soaked in 100 ml of water, to bring a solid: liquid ratio of 1:20 [3]. After thorough shaking and resting for 24 h., the supernatant solution was tested for pH and EC values. These measurements represent the quantity of ions that would have leached out from the soil when there is water logging. It gives a measure of ion movement in the pore fluid of the treated soil composites.

3 Results and Discussion

3.1 Basic Characteristics of Treated Soil

The behavior of the expansive soil was compared for LS and lime treatment. The free swell index (FSI) of the virgin soil is 111%, however, for lime and LS treated soil, FSI reduced to 84% and 66%, respectively (Fig. 2). The considerable decrease in the values could be attributed to the particle orientation and decrease in the double layer due to cation exchange reactions. The compaction characteristics of the soil and LS amended soil depicted an analogous behavior with similar values of maximum dry density and optimum moisture content. However, for lime treated soils, the maximum dry density reduces from 15.86 to 14.57 kN/m³ and the optimum moisture content increases to 29% from 25% (Fig. 3). The increased OMC for lime treated soil can be attributed to the initial short-term flocculation reaction, which is in a way more beneficial in the field applications as it can help in less control on water content for the compaction sites.

Fig. 2 Free swell index of untreated and treated soil

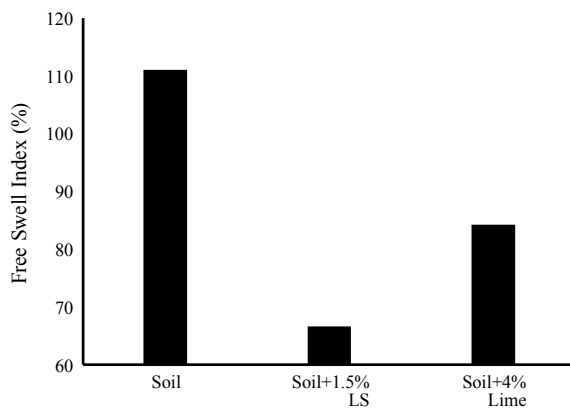
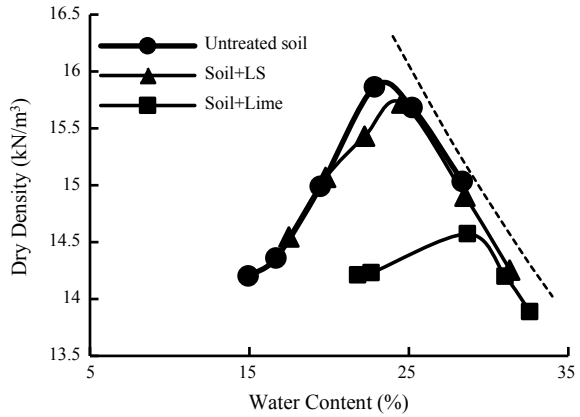


Fig. 3 Compaction characteristics of untreated and treated soil



3.2 Strength Variation of Treated Soil

Unconfined Compression Strength. The UCC strength was determined for both LS and lime amended samples. The strength test was conducted for the additives amended soil at different curing periods (0, 3, 28 days), to observe the variation in strength of the soil samples. 1.5% of LS and 4% of lime were the dosages adopted from the strength tests. The LS treated samples depicted two times increase in strength compared to untreated samples for 3 days curing period (Fig. 4). The 28 days cured samples depicted a strength increase from 220 to 480 kPa, and the failure strain

Fig. 4 UCC strength of 1.5% LS treated soil at various curing periods

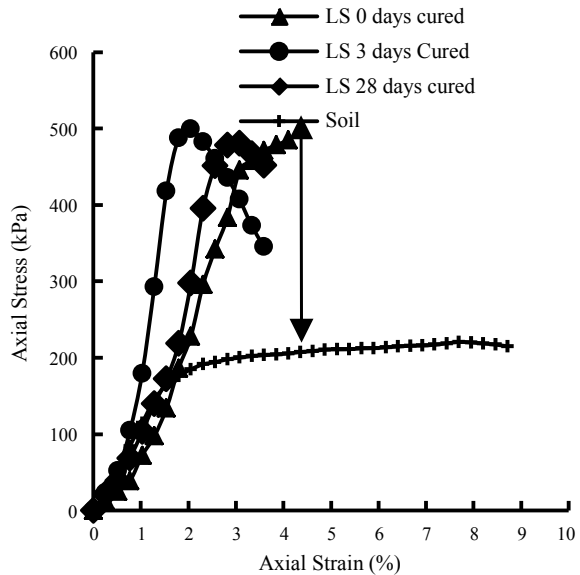
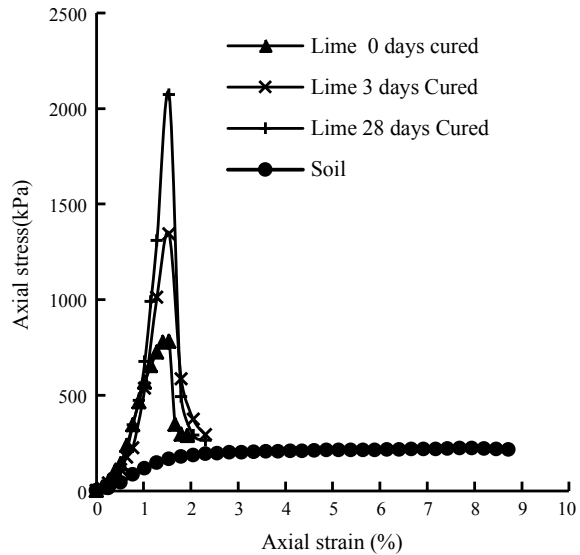


Fig. 5 Unconfined compression strength of 4% Lime treated soil at various curing periods



increased to 3.07%. The LS treatment increased the ductility of the soil sample along with increase in shear strength. The lime treated samples showed a relatively brittle behavior compared to soil. As the curing period was increased from 3 to 28 days, the strength and brittleness of the sample also increases as could be observed from Fig. 5. The higher peak strength was observed at lower strain levels. The increase in strength is attributed to the formation of cementitious compounds—calcium aluminate hydrate and calcium silicate hydrate, with respect to higher curing periods. The peak strength observed for lime treated sample increases from 780 to 2072 kPa through 0 to 28 days curing period. Basically, the LS amendment imparts particle aggregation, the calcium ions provided by LS gets adsorbed onto the surface of the clay minerals causing decrease in double layer. The composite material becomes more ductile [31]. Nevertheless, this conclusion requires more experimental evidence based on higher curing period and increased percentage of LS.

3.3 Durability Studies on Treated Samples—Wet and Dry Cycles

Unconfined Compressive Strength. Durability studies on additives amended soil composites were carried out on 3 days cured samples. After 1, 3, and 5 cycles of wetting and drying cycles, the samples were tested in the earlier stage of the wetting path, respectively. The soil samples and LS treated samples were very fragile and had to be tested very carefully. However, the lime treated samples were intact even after 5 cycles of wetting and drying. At the end of cycle 1, the untreated soil sample

showed nearly 94% decrease from its strength at 220 kPa (Fig. 6). Similar behavior was exhibited by LS treated samples, indicating a decrease of 95% from its strength of 499 kPa and further decrease in the subsequent cycles (Fig. 6). The same decrease was observed after 5 cycles of wetting and drying as well (Fig. 7). However, for lime treated samples, the UCC strength reduced to 970 kPa from 1343 kPa in the first cycle, a near 27% decrease; however, in the subsequent cycles, there was a strength increase to 1222 and 1395 kPa (Fig. 6). The time frame between wet-dry cycles leads to further development of cementitious compounds causing an increase in the strength of the lime treated sample.

The wet-dry cycles depict the moisture fluctuations in the in situ conditions. Parallel conditions simulated in the laboratory reveals that lime treated samples are more stable compared to the LS treated soil samples. The degradability is faster

Fig. 6 Variation in peak strength with cycles of wetting and drying

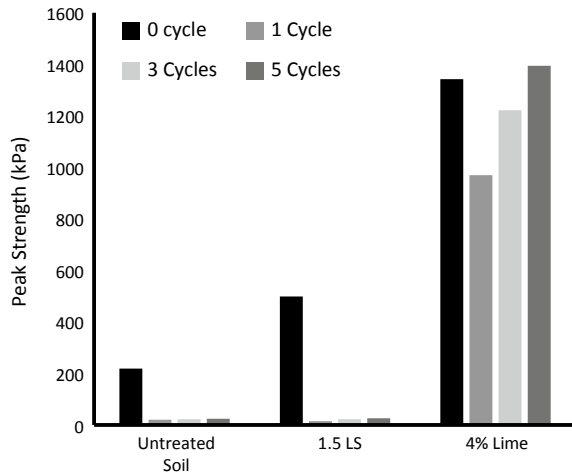
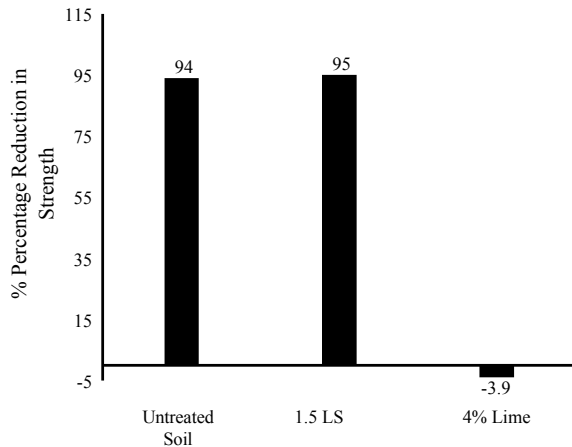


Fig. 7 Percentage reduction in strength after 5 cycles



and occurs at the very first cycle for the LS amended soil and virgin soil. The 5 cycles of wetting and drying took around 3 to 4 weeks to get completed, which is approximately equal to the 28 days' time period, usually adopted for curing. The strength of the lime treated samples tested at 28 days curing period is compared with the 3 days cured samples (initial state before wet-dry cycles), and also with samples after 5 cycles of wetting and drying. Figure 8 reveals that the strength of the samples decreased with wet-dry cycles and also exhibited higher failure strains. Extreme moisture fluctuations had considerable effect on the development of the cementitious compounds—CAH, CASH which progressed unabated in the 28 day cured samples. Simultaneously, the formation of the cementitious products also attributed to the lesser deterioration of the lime treated samples making it more resistant to moisture fluctuations compared to the LS amended samples.

Effect on Chemical properties. The chemical properties of the treated soil were evaluated in terms of pH and electrical conductivity (EC). The supernatant solution of the soil: water suspension was used for the pH and EC determination. The higher pH values represent alkalinity and indicate higher reactivity of the additive-soil mix and leaching of calcium ions into the solution.

From Fig. 9a, it could be observed that the solution obtained from the lime treated soil for '0' cycle indicates a pH of 11; however, in the subsequent cycles, the pH value approaches a constant value of 10.56, indicating a comparatively lesser leaching of the calcium ions. Nevertheless, for the untreated and LS treated samples, the pH remains in neutral range of 7–8 in all the cases, indicating a neutral behavior of LS amended soil. The EC values also show a stable trend for lime treated soil with the value of 500 $\mu\text{S}/\text{cm}$ after cycles of wetting and drying (Fig. 9b). For LS amended soil, with increase in the cycles of wetting/drying, the EC value decreases from 1200 $\mu\text{S}/\text{cm}$ and reaches a stable value of around 450 $\mu\text{S}/\text{cm}$ indicating lesser free ions in the solution, signifying a reduction in leaching of ions with wet-dry cycles.

The EC values of the medium could also be related to the dielectric constant of the medium. The increased EC indicates a decrease in dielectric constant and gives an indication of the particle orientation and double layer spacing [4, 32]. The treated

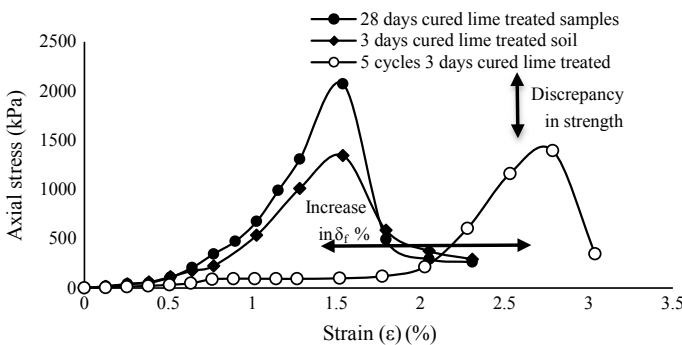


Fig. 8 Variation in UCC strength for lime treated soil samples under different conditions

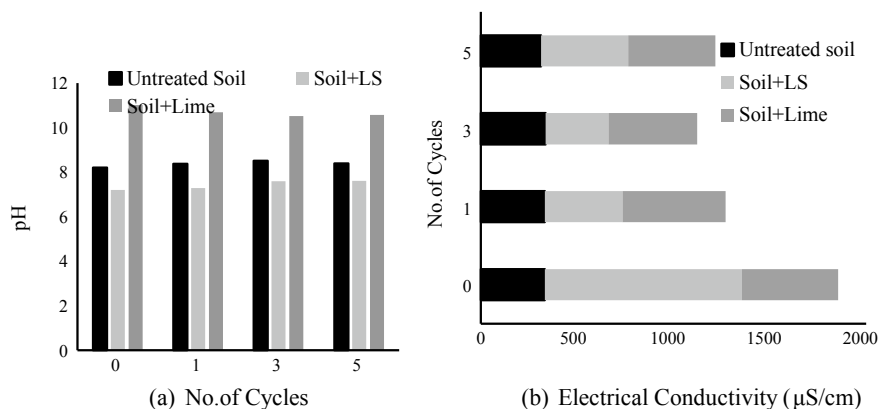


Fig. 9 a Effect of wet/dry cycles on pH of samples. b Effect of wet/dry cycles on electrical conductivity of samples

samples at '0' cycle is characterized by increased EC, lesser dielectric constant, and decreased double layer and particle aggregation, but as cycles of wet-dry increases, the orientation shifts toward particle dispersion, as water intrudes into the samples and reaches a stable orientation at higher cycles.

3.4 Microstructural Aspects-XRD Analysis

The X-ray diffraction intensities are greatly influenced by the chemical and structural composition of the soil minerals, mineral interstratification, crystallite sizes, and 'd' spacing [33, 34]. The treated and the virgin samples after wet and dry cycles were analyzed using the MALVERN PANANALYTICAL High resolution XRD. The samples were scanned in 2θ range of 5° – 70° with a step value of 0.04° . A $\text{Cu-K}\alpha$ with $\lambda = 1.54 \text{ \AA}$ was adopted for the study. The XRD patterns are plotted for the different cycles and analyzed for formation of new peaks, peak broadening, and crystallite size changes, which could be a precursor of the stabilization mechanism. Figures 10 and 11 depict the XRD patterns of the lime and LS treated samples at '0' cycles and after 5 cycles of wetting and drying. The samples are designated as SLS—Soil + LS, SL—Soil + Lime. The crystallite sizes of the clay mineral were determined from XRD data using the Scherrer equation [31].

$$L = \lambda k / \beta \cos \theta \quad (1)$$

where L is the mean crystallite dimension in Angstroms; k = Scherrer constant (0.9 in this study); λ = wavelength of the X-radiation [$\lambda = 1.540538 \text{ \AA}$]; and β = width of a peak at half height expressed in 2θ . The mean crystallite size was measured from the full width half maximum (FWHM) of XRD peaks. The crystallite size reductions

Fig. 10 XRD patterns of untreated and additive amended soil before wet/dry cycles

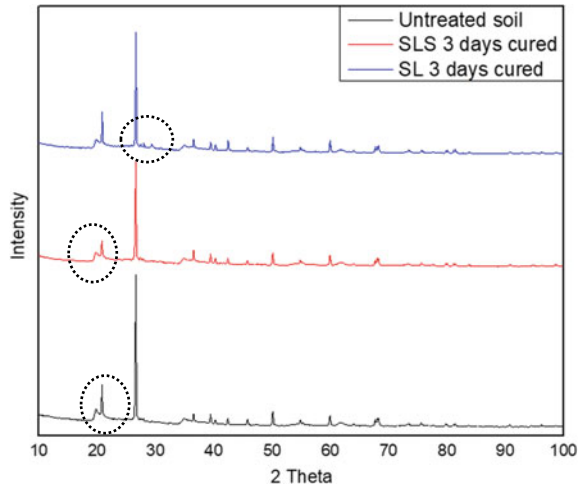
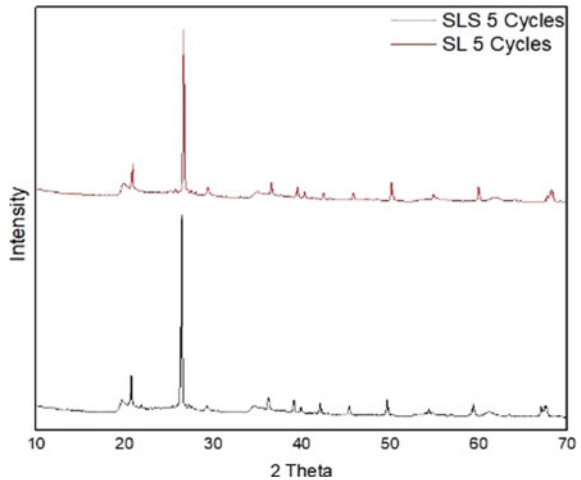


Fig. 11 XRD patterns of LS and lime treated samples after wet/dry cycles



indicate a decrease of surface negative charges and that some chemical interactions have taken place at the microstructural level apart from the surface adsorption of LS to the clay minerals [31]. The treated samples indicate a reduction in the peak intensity and also amorphous humps in the case of lime treated samples (Fig. 10). Table 2 represents the basal orientation of some of the prominent minerals, and crystallite size for the treated samples. The crystallite size of illite and montmorillonite shows a decrease compared to other minerals like kaolinite and quartz and there is also decrease in intensity. But with cycles of wetting and drying, the crystallite size increases indicating that water has imbibed into the mineral lattice, specifically for illite and montmorillonite mineral for both LS and lime treated soil.

Table 2 XRD results of treated and untreated soil with wet-dry cycles

Mineral	Untreated soil				Lime treated			
	2 Theta	Crystallite size	2 Theta	Crystallite size	Crystallite size after 5 cycles	2 Theta	Crystallite size	Crystallite size after 5 cycles
Kaolinite	19.89	7.61	19.76	7.58	7.89	19.89	7.83	7.77
Quartz	26.62	45.33	26.62	44.18	49.66	26.67	47.76	43.12
Illite	45.79	31.26	45.75	22.37	37.36	45.79	26.99	33.89
Quartz	50.10	32.88	50.10	36.74	37.61	50.14	38.49	35.69
Montmorillonite	54.83	22.53	54.83	18.39	26.27	54.88	22.21	24.07
Kaolinite	59.92	29.18	59.92	30.30	44.43	59.96	50.98	32.45
Quartz	68.26	16.44	68.09	18.31	18.97	68.31	25.51	24.28

4 Summary and Conclusion

The present work was carried out to understand the behavior of expansive soil when amended with lime and lignosulphonate which acts as an ionic stabilizer. The key idea in adding lignin-based polymer is to explore its effectiveness as an alternative to alkaline stabilizers. The change in the engineering properties and durability of the additive amended soil was evaluated. Lime depicted a very high increase in the unconfined compressive strength. Lignosulphonate treated soil also depicted an increase in strength compared to the untreated soil. However, when the samples were subjected to cycles of wetting and drying, there was complete degradation in strength of LS treated soil compared to lime treated soil indicating an absence of cementitious compounds. The wet-dry cycles hindered the formation of cementitious compounds in the case of lime treated soil as well. However, there was only 27% decrease observed in the peak strength after 5 cycles. The behavior of the treated soil is further substantiated with chemical analysis and microstructural changes. XRD results also reveal that both the additives alter the soil mineralogy at the microstructural level. However, lime amended soil is stable and more desirable under situations of moisture fluctuations compared to lignosulphonate. Nevertheless, the lignin-based additive requires an additional accelerating agent or binding agents to enhance its stabilization mechanism and form long-term durable composites.

Acknowledgements This work was financially supported by Science and Engineering Research Board-Department of Science and Technology (SERB-DST), Government of India, India, under File No. ECR/2017/002711/ES. The authors would like to thank SRMIST for the usage of the X-Ray Diffraction Facility at the Nanotechnology Research Centre SRMIST.

References

1. Katti RK (1979) Search for solutions to problems in black cotton soils. *Indian Geotech J* 9:1–80
2. Rao SM, Thyagaraj T (2003) Lime slurry stabilization of an expansive soil. *Proc Inst Civil Eng Geotechn Eng* 156(3): 139–146
3. Bhuvaneshwari S, Robinson RG, Gandhi SR (2013) *Indian Geotech J*. <https://doi.org/10.1007/s40098-013-0081-3>
4. Kamruzzamam AH, Chew SH, Lee FH (2009) Structuration and destructure behavior of cement-treated Singapore Marine Clay. *J Geotech Geoenvironmental Eng* 135(4)
5. Lefebvre GZ, Rochelle PL (1974) The analysis of two slope failures in cemented champlain clays. *Can Geotech J* 11(1):89–108. <https://doi.org/10.1139/T74-007>
6. Boynton RS (1980) *Chemistry and technology of lime and limestone*, 2nd edn. Wiley, New York
7. Albino V, Dangelico RM, Natalicchio A, Yazen DM (2011) Alternative energy sources in cement manufacturing: a systematic review of the body of knowledge. Network for Business Sustainability, University of Western Ontario, Ontario, Canada
8. Desmet J, Gabriels W, Dierickx D (1985) Effect of soil conditioners on the permeability and stability of soils. *J Sci Food Agric* 36(4):242–248
9. Chan, Y (2008) Increasing soil organic carbon of agricultural land. *PrimeFacts NSW* 735:1–5

10. Wei JH, Song YR (2001) Recent advances in study of lignin biosynthesis and manipulation. *J Integr Plant Biol* 43(8):771–779
11. Stewart D (2008) Lignin as a base material for materials applications: chemistry, application and economics. *Ind Crops Prod* 27(2):202–207
12. Zhang T, Ca G, Liu S, Puppala AJ (2016) Engineering properties and microstructural characteristics of foundation silt stabilized by lignin-based industrial byproduct. *KSCE J Civil Eng Korean Soc Civil Eng*. <https://doi.org/10.1007/s12205016-1325-4>, 1–12
13. Cai G, Zhang T, Liu S, Li J, Jie D (2016) Stabilization mechanism and effect evaluation of stabilized silt with lignin based on laboratory data. *Mar Georesour Geotechnol* 34(4):331–340
14. Gow AJ, Davidson DT, Sheeler JB (1961) Relative effects of chlorides, lignosulfonates and molasses on properties of a soil-aggregate mix. *Highway Res Board Bull* 282:66–83
15. Demirel T, Davidson DT (1960) Stabilization of a calcareous loess with calcium lignosulfonate and aluminum sulfate. Soil stabilization with chemicals, Joint Publication Iowa Engineering Experiment Station Bulletin 193/Iowa Highway Research Board Bulletin 22, D. T. Davidson and Associates (eds), Ames, IA, pp 206–221
16. Sinha SP, Davidson DT, Hoover JM (1957) Lignins as stabilizing agents for northeastern Iowa loess. *Iowa Acad Sci Proc* 64:314–347
17. Alazigha D, Indraratna B, Vinod JS, Ezeajugh L, Emeka L (2016) The swelling behaviour of lignosulfonate-treated expansive soil. *Proc Inst Civil Eng Ground Improvement* 169 (3):182–193
18. Tingle JS, Newman JK, Larson SL, Weiss CA, Rushing JF (2007) Stabilization mechanisms of nontraditional additives. *J Transp Res Board* 1989, 2: 59–67
19. Indraratna B, Muhamud MAA, Vinod JS (2012) Chemical and mineralogical behaviour of lignosulfonate treated soils. *GeoCongress, ASCE* 1146–1155
20. Cherian C, Arnepalli DN (2015) A critical appraisal of the role of clay mineralogy in lime stabilization. *Int J Geosynth Ground Eng* 1:8
21. Eades JL, Grim RE. Quick test to determine lime requirements for lime stabilization
22. Al-Mukhtar M, Lasledj A, Alcover JF (2014) Lime consumption of different clayey soils. *Appl Clay Sci*
23. Wild S, Arabi M, Leng-Ward G (1986) Soil-Lime reaction and microstructural development at elevated temperatures. *Clay Miner* 21:279–292
24. IS 2720 (1989) Compendium of Indian standards on soil engineering. Bureau of Indian Standards, New Delhi
25. Classification and identification of soils for general engineering purpose, IS: 1498, 1970
26. Methods of Tests for Soil, Part XL, Determination of Free Swell Index of soils, IS: 2720, 1977
27. Methods of Tests for Soil, Part XLI, Determination of Swelling Pressure of soils, IS: 2720, 1977
28. Sridharan A (2000) Classification procedures for Expansive soils. *Proc Instn Civ Engrs Geotech Engn* 143:235–240
29. Sridharan A, Sivapullaiah PV (2005) Mini compaction test apparatus for fine grained soils. *J Test Eval ASTM* 28:240–246
30. Methods of Tests for Soil, Part X, *Determination of Unconfined Compression Strength*, IS: 2720, 1991
31. Vinod JS, Indraratna B, Mahamud MAA (2010) Stabilisation of an erodible soil using a chemical admixture. *Proc ICE Ground Improvement* 163(1): 43–51
32. Kaya, Fang (1997) Identification of contaminated soils by dielectric constant and electrical conductivity. *J Environ Eng* 123(2), Feb 1997
33. Drits V, Srodon J, Eberl DD (1997) XRD measurement of mean crystallite thickness of illite and illite/smectite: mean crystallite thickness of illite and illite/smectite: reappraisal of the Kubler index and the Scherrer equation. *Clays Clay Minerals* 45(3):461–475
34. Singh, Agarwal. Qualitative soil mineral analysis by EDXRF, XRD and AAS probes. *Radiation Phys Chem* 18(12): 1796–1803

Evaluation of Penetration Index of Untreated and Treated Soil Using Dynamic Cone Penetrometer



V. S. N. Pavan Kumar Pratapa 

Abstract Small-scale dynamic cone penetrometer is a rapid and less expensive tool extensively used for assessment of strength of soil layers to a limited depth of highway and airfield pavements. Penetrometer consists of a cone of 20 mm diameter with 60° apex angle driven into the soil by a hammer of weight 8 kg falling freely through a height of 575 mm, and tests are conducted by compacting soil in calibration cylinders of two different sizes. Tests are conducted on untreated, cement or lime treated clay of high compressibility and clayey sand mixed with 5–30% moisture content and compaction energy per unit volume of layer ranged from 0.5 to 6 kg/cm². Penetration index of untreated and treated clay of high compressibility is varied from 5 to 42 mm/blow, and unconfined compressive strength is ranged from 101 to 233 kPa. Unconfined compressive strength, California bearing ratio and penetration index are presented in charts for different moisture content and degree of compaction. The average penetration index decreased with increase of lime or cement content and increase of curing period.

Keywords Dynamic cone penetration test · Penetration index · California bearing ratio

1 Introduction

Highways are subjected to repeated traffic loading at different intensities. Pavement layers shall carry these loads without causing distress and rutting of pavement. Design, strengthening and construction of new pavements and overlays require a thorough evaluation of subgrade by quantifying the in situ density by sand cone method or nuclear density gauge [1]. The other field devices used in highway projects are rapid moisture metre to measure the in situ moisture content, dynamic cone penetrometer to delineate the pavement layers, falling weight deflectometer to measure the structural capacity and Benkelman beam to measure the deflection of pavement. For laboratory investigation high quality, undisturbed soil samples are needed to predict the

V. S. N. P. K. Pratapa (✉)

Vardhaman College of Engineering, Hyderabad 501218, India

California bearing ratio and resilient modulus. It is difficult to get truly undisturbed sand samples, and there is a necessity of using probes, tubes, cones, and projectiles to drive into subgrade for identification of sand layers.

Penetration resistance from the above devices was correlated with denseness, consistency or degree of wetness of soil, shear strength, stiffness of soil layers, deformation characteristics, stress history, consolidation characteristics, permeability and pore pressure of clay soil [2]. Charts were developed to predict the bearing capacity and settlement of shallow foundations and deep foundations using standard penetration test and static cone penetration test [3–6]. Disturbance in soil structure due to driving of intrusion and subsequent changes in stresses and strains influences the predictions of penetration tests.

Pavement layers along an existing highway were explored using a portable and lightweight dynamic cone penetrometer and is an effective and quick method [7]. Strength of new highway and airfield pavements was evaluated rapidly by small-scale dynamic cone penetrometer and is used to estimate the bearing capacity of shallow foundations [8, 9]. This method of exploration does not need a borehole, and depth of exploration is limited.

Dynamic cone penetration test (DCPT) is conducted in the field on local soils, and the results of the test are given by different terms such as penetration rate, DCP number, DCP index and blow number [10, 11]. Several researchers correlated the dynamic cone penetration values with CBR [12, 13], pavement thickness [14] and unconfined compressive strength [15]. California bearing ratio was correlated with dynamic modulus and resilient modulus of soil [16].

Sand samples were compacted in a calibration cylinder in the laboratory, and cone penetration tests were conducted on the compacted surface of soil. Results of the DCPT were correlated with the in situ California bearing ratio. Dynamic cone penetration tests were conducted on lateritic soil stabilized with quarry dust, influence of different percentages of dust, degree of compaction, and water content on penetration index were quantified [17]. Correlations were developed between penetration index and unconfined compressive strength of lime and cement treated soil with different percentage of stabilizer and curing periods [18].

Dynamic cone penetration test was conducted in the laboratory in a calibration cylinder filled with different types of soil compacted to different dry densities and developed correlations between penetration resistance and soil properties. Horizontal stress and angle of internal friction of sand were observed to influence the penetration resistance in sand [19]. Results of these investigations do not follow the field predictions due to the boundaries of calibration container and stress state of soil. As the chamber diameter to the cone diameter ratio increases, the effect of boundary becomes negligible and penetration resistance approaches field value. A semi-analytical procedure based on the spherical cavity expansion of soils was used to convert the penetration resistance measured in the calibration cylinder to equivalent field values [20]. A three dimensional model based on discrete element method was developed to quantify the cone tip resistance in sand at different densities and stress history [21]. Effect of particle shape and their crushing on the tip resistance

of cone was predicted based on crushing and non-crushing models in the discrete element method [22].

2 Field Dynamic Cone Penetration Test and Results

The equipment to conduct dynamic cone penetration test was developed in South Africa, and the design of equipment has undergone several modifications. The apex angle of cone changed from 30 to 60°. Diameter of cone varied from 20 to 38 mm and weight of hammer varied from 8 to 10 kg. The drop of hammer ranged from 0.46 to 0.575 m. In the present study, dynamic cone penetrometer is fabricated to consist of two shafts that can be threaded to each other. The upper shaft is attached to the lower shaft through an anvil. A hammer of 8 kg falls freely through a height of 575 mm along the upper shaft (Fig. 1). Lower shaft is threaded to a replaceable cone with 60° apex angle. Diameter of the cone is 20 mm, and height is 47 mm. Diameter of the upper and lower shafts is 16 mm. Due to free fall of hammer on the anvil, an energy of 45 J is transferred to the lower shaft, and cone penetrates into the soil. A reference mark is made at the top of bottom shaft, and penetration is measured with a steel ruler resting on the level rigid surface. Penetration per blow is recorded in mm as the difference between the reference mark and the rigid surface before and after the blow. Two persons are required to conduct the cone penetration test.

Penetration index, PI is the penetration per blow determined as.

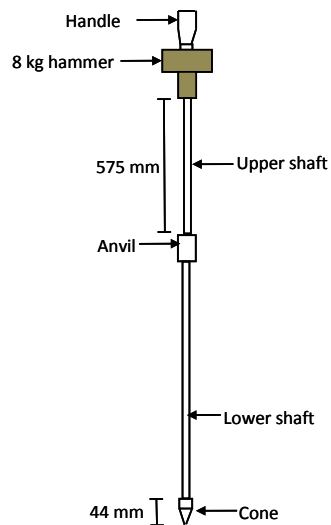


Fig. 1 Cone penetrometer

$$PI = \frac{P_{i+1} - P_i}{(i + 1) - i} \quad (1)$$

P_{i+1} and P_i are the penetration of cone for $i + 1$ and i blows, respectively. Penetration index, PI indicates the slope of penetration vs number of blows curve. Average dynamic cone penetration index of a layer is obtained from the following equation [23]

$$PI_a = \frac{\sum_1^N PI}{N} \quad (2)$$

where N is the total number of penetration index, PI recorded in a pavement layer.

The present work is conducted near Hyderabad, and the major type of soil is red sandy soil formed from weathering of granite. In situ dynamic cone penetration test is conducted on State Highway no. 19, near Ibrahimpatnam, Hyderabad. An excavation is made at the edge of pavement, and the thickness of different pavement layers is recorded. The thickness of BC and DBM layers is about 150 mm, followed by 200 mm thick crushed aggregate base layer mixed with rock dust. Thickness of granular base course is 200 mm and is a free draining layer, a combination of red sandy soil and aggregate. 500 mm thick, subgrade layer of red sandy soil (S-1) follows this.

An undisturbed sample of subgrade is collected using Shelby tube sampler, and a bulk sample is collected for laboratory investigation, and the results of test are mentioned in Table 1. Cone is driven on the surface of undisturbed subgrade soil, and the number of blows for penetration of 300 mm is recorded. The average penetration index, PI_a is recorded as 10 mm/blow, and field moisture content is 11%. The field moisture content is slightly higher than the laboratory optimum moisture content due to watering of adjacent paddy field in the site. The field dry density of subgrade soil is determined by sand cone method and is 1.8 g/cc, and the degree of compaction (ratio of field dry density to the maximum dry density) is 98%. The minimum dry density of subgrade soil is 1.75 g/cc as per the specification of road and bridge works [24]. The minimum degree of compaction for subgrade soil is 97%, and it satisfies the requirement. Soil sample is compacted in the laboratory to the field moisture content and dry density, and the unsoaked California bearing ratio is determined as 22%. The obtained CBR value is compared with the CBR value predicted from TRL [25] as mentioned below.

$$\text{Log}_{10}(\text{CBR}) = 2.48 - 1.057 \text{Log}_{10}(\text{DCPI}) \quad (3)$$

The above equation over predicts CBR value by 120% compared with the laboratory CBR value of red sandy soil in the present study.

DCP test is also conducted in the bed of Ibrahimpatnam Lake, Hyderabad. The Ibrahimpatnam lake and overflowing weir arrangement were built 500 years back. Due to drought condition, the lake is presently dry and has a surface deposit of black clay of high compressibility (S-2). The gradation, Atterberg limits, expansive nature

Table 1 Properties of soil

Soil property	S—1	S—2
% of gravel	3	0
% of sand	72	12
% of silt	13	39
% of clay	12	49
Liquid limit	27%	51%
Plastic limit	12%	26%
Optimum moisture content	10%	24%
Maximum dry density (g/cc)	1.84	1.55
Specific gravity	2.65	2.70
Free swell index	20%	40%
Classification	Clayey sand (SC)	Clay of high compressibility (CH)
Average field moisture content	11%	22%
Average field dry density (g/cc)	1.80	1.52
Average penetration index (mm/blow)	10	20
Unsoaked California bearing ratio	22%	10%

and maximum dry density are presented in Table 1. Results of the test on clay of high compressibility indicate that the material is unsuitable as a subgrade for highway project. Field moisture content is varied from 18% at the surface of deposit to 26% at a depth of 60 cm below the surface. The average field dry density is 1.52 g/cc, and the average penetration index is about 20 mm/blow. Larger penetration index for clay of high compressibility is due to larger void ratio and high moisture content of soil. The laboratory unsoaked CBR for clay of high compressibility is 10%. This laboratory value is low compared to the CBR obtained from Eq. 3.

3 Laboratory Dynamic Cone Penetration Test

DCP test is conducted in two different sizes of calibration cylinders in the laboratory on remoulded samples of red sandy soil and black clay soil collected from field (Fig. 2).

First cylinder referred as small is the standard CBR cylinder of diameter 15 cm, and height is 17.5 cm. Second cylinder is a large cylinder fabricated to a diameter of

Fig. 2 Calibration cylinders



22 cm, and height is 44 cm. Diameter of cylinder to the diameter of cone is 7.5 and 11, respectively, for smaller and larger moulds.

Clay of high compressibility (CH) is mixed with 20, 25, and 30% moisture content, w and clayey sand (SC) with 5, 8, and 15% moisture contents. Soil is compacted to different dry densities with a rammer of weight 2.6 kg falling freely through a height of 31 cm and subjected to different blows on each layer. The compaction energy per unit volume of layer, E is obtained as the product of weight of rammer, drop of rammer and number of blows to the volume of a soil layer varied from 0.52 to 5.68 kg/cm^2 . Cone penetration test is conducted on the compacted surface of soil in the calibration cylinder, and the penetration of cone per each blow is recorded in Fig. 3 for a compaction energy per unit volume of layer, $E = 1.05 \text{ kg/cm}^2$.

Cone penetrates by a depth of 170 mm in the calibration cylinder by giving two and seven blows in clayey sand for a moisture content, $w = 15$ and 5%, respectively. (Fig. 3). Number of blows of cone penetration increased from 4 to 11 in clay of high compressibility with decrease of moisture content from 30 to 20%. Increase of moisture content decreases the base and frictional resistance along the cone and

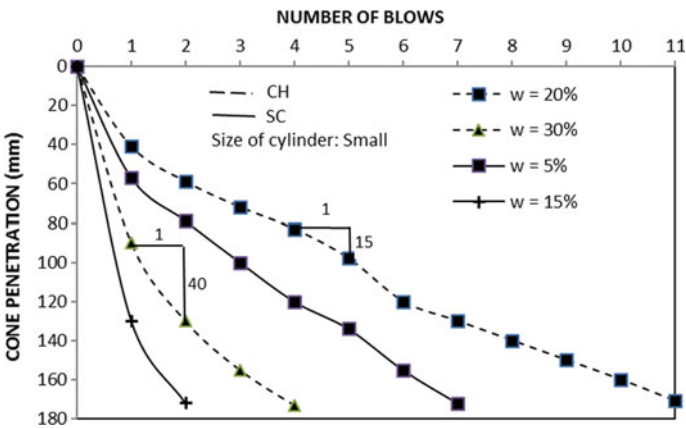


Fig. 3 Variation of penetration in mm with number of blows, $E = 1.05 \text{ kg/cm}^2$

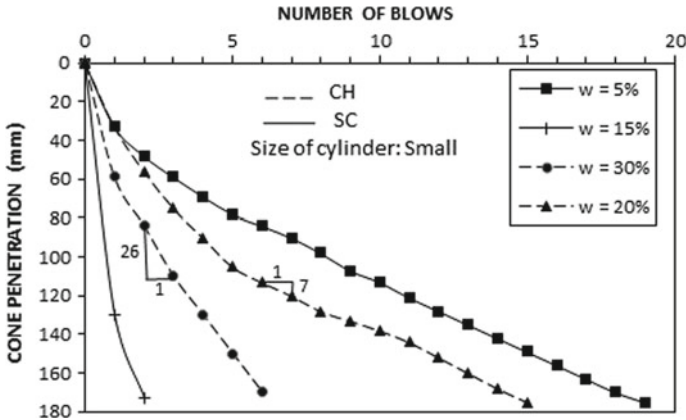


Fig. 4 Variation of penetration in mm with number of blows, $E = 2.63 \text{ kg/cm}^2$

increases penetration index. Figure 4 presents the variation of cone penetration in mm with number of blows for a larger soil compaction energy per unit volume of layer, $E = 2.63 \text{ kg/cm}^2$. Cone penetrates by 175 mm in clayey sand by giving 2 and 19 blows for a moisture content of 15% and 5%, respectively (Fig. 4). Cone penetrates by 175 mm in clay of high compressibility by giving 6 and 15 blows for a moisture content of 30% and 20%, respectively, for a compaction energy per unit volume of layer, $E = 2.63 \text{ kg/cm}^2$.

Figure 3 and Fig. 4 indicate that the penetration of cone is large for first blow. In the subsequent blows, larger and full area of cone rests on the soil and results in development of friction between cone and soil. Penetration index, PI is larger at the surface of the mould and decreases with depth of penetration of cone due to increase of confinement of soil with depth. Diameter of the cone is 20 mm and is larger than the diameter of shaft, 16 mm. There is no friction between lower shaft of DCP apparatus and soil during penetration test and cone is subjected to base resistance during the test.

Average penetration index, PI_a decreased from 127 to 42 mm per blow with increase of compaction energy per unit volume of layer, E from 0.5 to 4.2 kg/cm^2 in clayey sand at a moisture content of 15% (Fig. 5). Increase of compaction energy per unit volume of layer, E increased the density of soil and cone base resistance. Average cone penetration index, PI_a in clay of high compressibility decreased from 112 to 32 mm/blow with increase of compaction energy per unit volume of layer, E from 0.5 to 4.2 kg/cm^2 at a moisture content of 30%.

Unconfined compressive strength of clay of high compressibility (CH) increased from 70 to 290 kPa and from 66 to 85 kPa with increase of degree of compaction of soil (ratio of test density of sample to the maximum dry density) from 80 to 100% for a moisture content of 20% and 30%, respectively (Fig. 6). The consistency of clay based on unconfined compressive strength of soil is marked in Fig. 6. Average

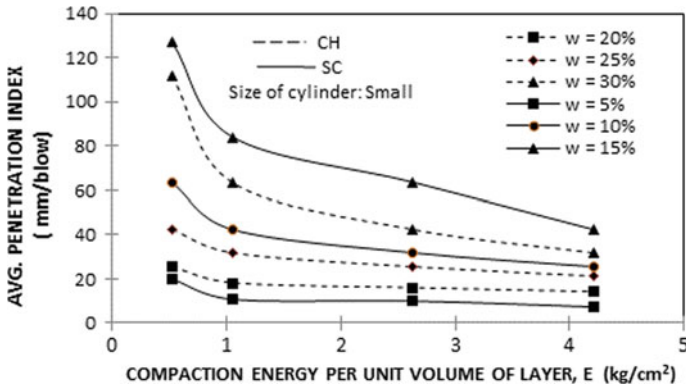


Fig. 5 Variation of average penetration index with compaction energy—effect of moisture content

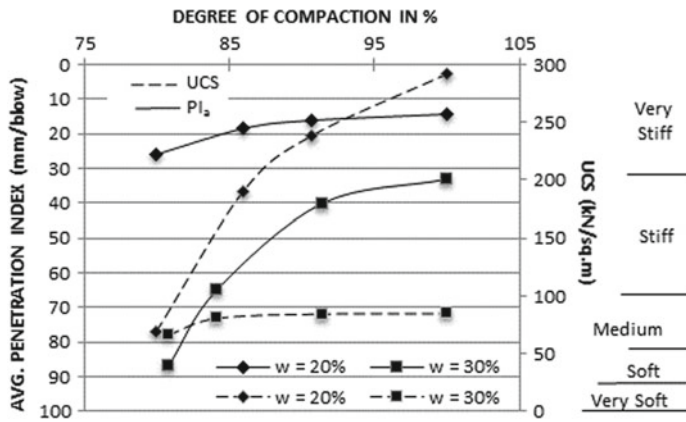


Fig. 6 Variation of PI_a and UCS with degree of compaction of soil—effect of moisture content

penetration index, PI_a decreased from 26 mm/blow to 14 mm/blow with an increase of degree of compaction from 80 to 100% at a moisture content of 20%.

Unconfined compressive strength of soil can be predicted from Fig. 6 by predicting the average penetration index, PI_a , moisture content and degree of compaction of soil in field. Bearing capacity of foundation can be evaluated from the predicted unconfined compressive strength of clay soil.

California bearing ratio of clayey sand increased from 7 to 16% with increase of degree of compaction of soil from 75 to 90% for a moisture content, $w = 8\%$ (Fig. 7). Average cone penetration index, PI_a decreased from 32 to 16 mm/blow with increase of degree of compaction of soil from 75 to 90% for a moisture content of 8%.

California bearing ratio can be predicted from Fig. 7 based on the average penetration index, degree of compaction and field moisture content. Thicknesses of pavement

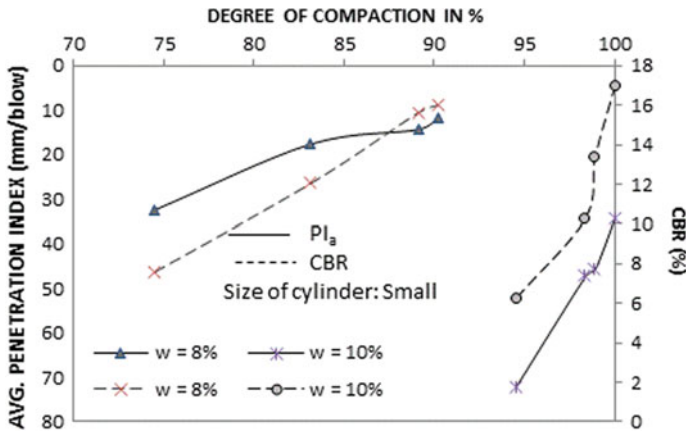


Fig. 7 Variation of PI_a and CBR with degree of compaction for clayey sand—effect of moisture content

layers can be quantified based on the predicted California bearing ratio and intensity of traffic along the highway.

4 Testing of Lime and Cement Treated Soil

Clay of high compressibility (CH) collected from the Ibrahimpatnam lake is mixed with 4, 8 and 12% lime and added with 24% of water content (optimum moisture content of untreated soil) and mixed thoroughly. Lime mixed samples are cured for one hour, one day, three days and seven days by storing in a plastic bag. Lime treated soil samples are compacted in the small mould to a compaction energy per unit volume of layer, $E = 2.63 \text{ kg/cm}^2$.

Dynamic cone penetration tests and unconfined compression tests are conducted on the lime treated soil samples. Three blows are required for penetration of cone by 127 mm in untreated soil (Fig. 8). Number of blows for penetration of cone is 5, 8 and 10 for soil sample treated with 4, 8 and 12% lime and cured for one day. Number of blows for penetration of cone by 127 mm is 8, 15 and 20 for 4, 8 and 12% lime for a curing period of seven days. Variation of unconfined compressive strength of soil and average penetration index, PI_a are presented in Table 2 and Table 3 for different percentages of addition of lime and curing periods. Unconfined compressive strength of untreated soil is 100 kPa and increased to a maximum of 233.2 kPa for 4% lime and seven days of curing period. It is a common observation that lime treatment involves pozzolanic reaction and cation exchange.

This leads to formation of calcium silicate hydrates and calcium aluminate hydrate. These compounds form matrix and improve the strength of lime-stabilized soil [26].

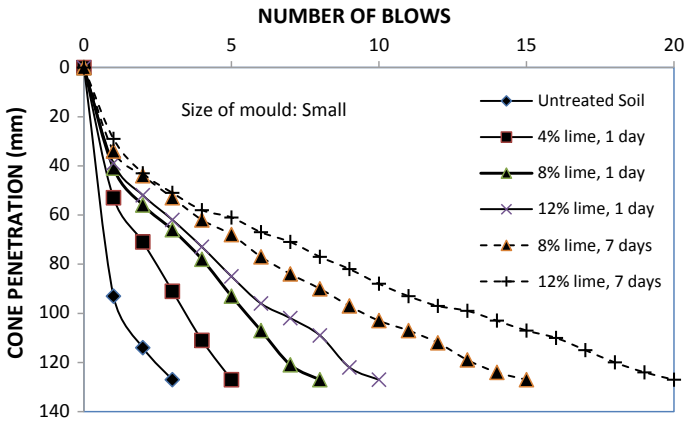


Fig. 8 Variation of cone penetration with hammer blows—effect of lime dosage and curing period

Table 2 Unconfined compressive strength in kN/m^2 of CH soil treated with different percentages of lime and curing period

Curing period	0% lime	4% lime	8% lime	12% lime
1 h	100.78	166.40	171.09	182.81
1 day	100.78	176.95	194.53	164.06
3 days	100.78	175.78	171.09	159.53
7 days	100.78	233.20	133.59	135.93

Table 3 Average penetration index (mm/blow) of CH soil treated with different percentages of lime and curing period, size of mould: small, $E = 2.63 \text{ kg/cm}^2$

Curing period	0% lime	4% lime	8% lime	12% lime
1 day	42.33	25.40	15.88	12.70
3 day	42.33	15.88	9.77	6.35
14 days	42.33	14.11	6.68	5.29
28 days	42.33	9.07	6.05	4.88

The average penetration index, PI_a of untreated soil is 42 mm/blow (Table 3). Average penetration index decreased from 25 to 9 mm/blow with increase of curing period from one hour to 28 days at 4% lime content. Average penetration index decreased from 13 to 5 mm/blow with increase of curing period from one hour to 28 days for 12% lime content.

Clay of high compressibility is mixed with 1, 3, 5 and 10% cement, added with 24% of water content (optimum moisture content of untreated soil) and mixed thoroughly. Cement mixed samples are stored in a plastic bag and cured for 1, 3, 7, 14 and 28 days. Cement treated soil samples are compacted in a large mould to a compaction

Table 4 Average penetration index (mm/blow) of clay of high compressibility treated with different percentages of cement and curing period, size of mould: large, $E = 5.68 \text{ kg/cm}^2$

Curing period (days)	0% cement	1% cement	3% cement	5% cement	10% cement
1	13.33	11.58	7.59	7.33	6.77
3	13.33	12.22	8.30	6.11	7.86
7	13.33	8.30	6.77	7.42	6.98
14	13.33	5.18	7.72	8.00	8.30
28	13.33	4.44	6.38	8.30	8.80

energy per unit volume of layer, $E = 5.68 \text{ kg/cm}^2$. Results of the penetration test are presented in Table 4. The increase of cement content and curing period decreased the average penetration index for cement content up to 3%. Variation of average penetration index with curing period is not consistent for larger cement contents of 5 and 10%.

5 Summary and conclusions

Dynamic cone penetration test, unconfined compression test, and California bearing test are conducted on clay of high compressibility and clayey sand collected from a field investigation of a highway project. Charts are developed between UCS, CBR and penetration index for different moisture contents and degree of compaction. Soil samples are compacted in two sizes of calibration cylinder at moisture content varying from 5 to 30% and compaction energy per unit volume of layer ranged from 0.52 to 5.68 kg/cm^2 . The number of blows for penetration of cone through calibration cylinder increased with decrease of moisture content and increase of compaction energy per unit volume of layer due to improved base resistance of cone.

Charts are developed to predict the consistency and unconfined compressive strength of clay of high compressibility from average penetration index depending on moisture content and degree of compaction of soil. Charts are developed to quantify the California bearing ratio of red sandy soil from average penetration index, moisture content of soil and degree of compaction.

Average penetration index is 42 and 6 mm/blow in untreated clay of high compressibility and clay treated with 12% lime after seven days of curing period. Unconfined compressive strength of untreated clay of high compressibility is 100 kPa and is increased to a maximum value of 233 kPa after addition of 4% lime and seven days of curing period.

Average penetration index is 13.33 mm/blow and 7 mm/blow for untreated clay of high compressibility and 10% cement treated clay. Lime and cement treatment of clay of high compressibility decreases the moisture content of soil and plastic nature of clay and decreases the penetration index with increase of their dosage and curing period.

References

1. Ashan AN (2014) Pavement performance monitoring using dynamic cone penetrometer and geogauge during construction. University of Texas, December (2014)
2. Thomas D (1965) Static penetration tests in london clay. *Géotechnique* 15(2):174–179
3. IS 6403- (1981) Code of practice for determination of bearing capacity of shallow foundations
4. IS 8009 (Part 1) - (1976) Code of practice for calculation of settlements of shallow foundations
5. IS 2911 (Part 1/sec 1) – (1979) Code of practice for design and construction of pile foundations
6. IS 8009 (Part II) – (1980) Code of practice for calculation of settlements of deep foundations
7. Amadi AA, Sadiku S, Abdullahi M, Danyaya HA (2018) Case study of construction quality control monitoring and strength evaluation of a lateritic pavement using the dynamic cone penetrometer. *Int J Pavement Res Technol*
8. ASTM D6951–03 (2003) Standard test method for use of the dynamic cone penetrometer in shallow pavement applications. ASTM International, West Conshohocken, PA
9. Ampadu S, Arthur T (2006) The dynamic cone penetrometer in compaction verification on a model road pavement. *Geotech Test J* 29(1):70–79
10. Kley EG (1975) The use of the dynamic cone penetrometer (DCP). Transvaal Roads Department, Report L2/74, South Africa
11. Harison JA (1987) Correlation between california bearing ratio and dynamic cone penetrometer strength measurement of soils. *Proc Institution Civil Eng Part 2* 83:833–844
12. Lee C, Kim KS, Woo W, Lee W (2014) Soil stiffness gauge (SSG) and dynamic cone penetrometer (DCP) tests for estimating engineering properties of weathered sandy soils in Korea. *Eng Geol* 169:91–99
13. Gabr MA, Hopkins K, Coonse J, Hearne T (2000) DCP criteria for performance evaluation of pavement layers. *J Perform Constr Facil* 14(4):141–148
14. Livneh M (1987) Validation of correlations between a number of penetration tests and in situ California bearing ratio tests. *Transportation Research Record* 1219, National Research Council, Washington, D.C., pp 56–67
15. Patel MA, Patel HS, Dadhich G (2013) Prediction of subgrade strength parameters from dynamic cone penetrometer index, modified liquid limit and moisture content. *Procedia – Soc Behavioral Sciences* 104:245–254
16. Sun X, Han J, Crippen L, Corey R (2017) Back-calculation of resilient modulus and prediction of permanent deformation for fine-grained subgrade under cyclic loading. *J Mater Civil Eng* 29(5)
17. Ampadu SIK, Fiadjoe GJY (2015) The influence of water content on the dynamic cone penetration index of a lateritic soil stabilized with various percentages of a quarry by-product. *Transp Geotech* 5:68–85
18. Enayatpour S, Puppala AJ, Vasudevan H (2006) Dynamic cone penetrometer to evaluate unconfined compressive strength of stabilized soils. In: *Site and geomaterial characterization - proceedings of the geoshanghai conference*, 149th edn. pp 285–292
19. Houlsby GT, Hitchman R (1988) Calibration chamber tests of a cone penetrometer in sand. *Géotechnique* 38(1):39–44
20. Pournaghiazar M, Russell AR, Khalili N (2012) Linking cone penetration resistances measured in calibration chambers and the field. *Géotech Letters* 2(2):29–35
21. Butlanska J, Arroyo M, Gens A (2012) Virtual calibration chamber CPT on Ticino sand. In: *2nd International symposium on cone penetration testing, CPT' 10*, Huntington Beach, California, pp 217–224
22. Falagush O, McDowell GR, Yu HS (2015) Discrete element modeling of cone penetration tests incorporating particle shape and crushing. *Int J Geomech* 15(6):14
23. Edil TB, Benson CH (2005) Investigation of the DCP and SSG as alternative methods to determine subgrade stability. SPR#0092-01-05. Dept. of Civil and Environmental Engineering, University of Wisconsin-Madison
24. Specifications for Road and bridge works (2013) Ministry of road and transport & highways, 5th edn. pp 66

25. Transport Research Laboratory 1993 A guide to the structural design of bitumen-surfaced roads in tropical and sub-tropical countries. TRL, Crowthorne, (Overseas Road Note 31)
26. Kumar PVSNP (2005) Studies on Quick lime treated black cotton soils. Indian geotechnical conference - 2005, Ahmedabad, 227–230

Fundamental Study on Combination of Paper Sludge Ash and Cement for Dredged Clay Soil Stabilization



Nguyen Binh Phan, Kimitoshi Hayano, and Yoshitoshi Mochizuki

Abstract Paper sludge ash, a cinder generated from the incineration process of paper sludge, has high potential if used as complement to cement in stabilizing dredged clayey soil due to its ability of absorbing and retaining water. In this study, paper sludge ash-based improving material (PS ash) was used as water absorbing material to reduce the water content of clay, resulting in a reduction of the ratio of free water in clay to cement by weight and therefore increase the strength of stabilized clay, called hybrid-treated clay. A series of unconfined compression tests was conducted on both cement-treated clay specimens and hybrid-treated clay specimens to evaluate the strength development of stabilized soil and the effect of combination of PS ash and cement in stabilizing dredged clay soil on the strength characteristics. A new parameter, unabsorbed water/cement ratio, W^*/C , which is the ratio by weight of the water content that is not absorbed by PS ash to cement content, was used to assess the strength development of both hybrid-treated clay and cement-treated clay. Experimental results showed that the strength of both types of stabilized clay is governed by the parameter W^*/C . The combination of cement and PS ash gave a treatment effect comparable to that of cement and is even better for high-water content clay. Fundamental results showed that the use of hybrid-treated clay in transportation engineering has high potential for the construction of transportation systems in harbors or reclamation of offshore airports.

Keywords Paper sludge ash · Water-cement ratio · Soil stabilization

N. B. Phan (✉)

Graduate School of Urban Innovation, Yokohama National University, Yokohama 240-8501, Japan

K. Hayano

Faculty of Urban Innovation, Yokohama National University, Yokohama 240-8501, Japan

e-mail: hayano-kimitoshi-hg@ynu.ac.jp

Y. Mochizuki

Sustainable Eco Corp, Yokohama 235-0033, Japan

e-mail: nsgym855@ybb.ne.jp

1 Introduction

The utilization of dredging material for construction has been increasingly demanded for economic and environmental purposes. In general, the dredged soils with low strength and high-water content are stabilized by mixing with additives such as cement by which the mechanical properties, strength and compressibility are enhanced as the result of chemical solidification. However, this method issues include high cost, environment or unexpected engineering properties. In order to promote the cost reduction, improving the engineering properties of cement-treated soil as well as reducing environmental impact, many studies have been conducted on the use of sustainable alternative stabilizing agents and/or complements for soil stabilization, such as adding fly ash, sewage sludge ash [1, 2] and so on.

Paper sludge ash, a cinder that is generated from the incineration process of paper sludge, is such an alternative sustainable material for dredging soil stabilization. The surface of paper sludge ash particle has a porous structure with many complex and irregular voids; therefore, paper sludge ash can absorb and retain excess water into its voids. Due to its ability of absorbing and retaining water, paper sludge ash can improve stability of soft soils by mixing with them [3–6]. Meanwhile, cement improves the soil by cement hydration hardening and pozzolanic reaction hardening [7, 8]. Therefore, it suggests that by combining the stabilizing advantages of paper sludge ash and cement instead of using them separately, the better improvement efficiency can be achieved.

This paper deals with a fundamental experimental study to show the effectiveness of using a combination of paper sludge ash and cement for dredged clay stabilization. A series of unconfined compression test (UCT) was conducted on both cement-treated clay and paper sludge ash–cement-treated clay (hybrid-treated clay) to access and compare the improvement effects achieved on cement-treated clay and hybrid-treated clay.

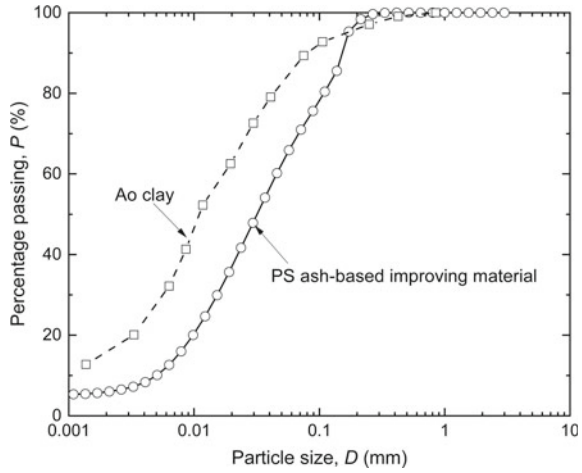
2 Materials and Specimen Preparation Method

2.1 Materials

The clay used in this study is Ao clay, which is categorized into CL (clay (low liquid limit)) according to the unified soil classification system, with following physical properties: Specific density, $\rho_s = 2.716 \text{ g/cm}^3$; Liquid limit, $W_L = 40.7\%$; Plastic limit, $W_P = 23.7\%$; Plastic index, $I_P = 17.0$. Distilled water was used to mix with dry Ao clay to form clay slurry with the selected water content of 81.4% ($W = 2W_L$).

The ordinary Portland cement, which satisfies JIS (Japanese Industrial Standard), and paper sludge ash-based improving material, hereinafter referred as PS ash, were used to stabilize the clay. The specific of Portland cement, G_s , is 3.15 g/cm^3 , and the compressive strength after 3 and 7 days was 12.4 and 19.3 MPa, respectively. The

Fig. 1 Particle size distribution of Ao clay and PS ash-based improving material



PS ash, with G_s of 2.603 g/cm^3 , used in this study is a commercial product in Japan. The particle size distributions of Ao clay and PS ash are shown in Fig. 1.

2.2 Mixture Design Selections

At high value of clay-water/cement ratio, W/C , the compressive strength of cement-treated clay increases as the decrease of W/C [9]. This behavior is similar to that in concrete technology in which the compressive strength of concrete increases as the decrease of ratio of water content and cement content of the mix [10]. However, the range of the validity of water/cement ratio rule is limited as shown in Fig. 2. At very low value of water/cement ratio, the trend of the curve is changed when

Fig. 2 The relation between strength and water/cement ratio of concrete. (Source "Properties of concrete" by A.M. Neville, p. 270 [11])

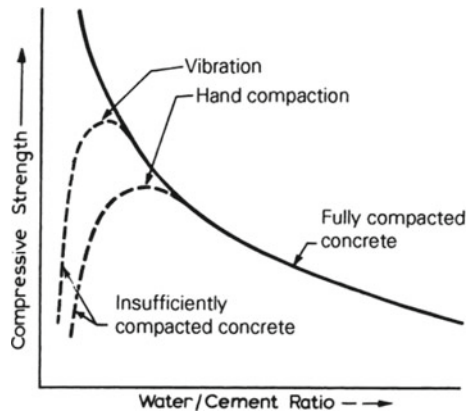


Table 1 Mixing cases of cement-treated clay

Case No	A1	A2	A3	A4	A5	A6	A7
$m_{\text{dry clay}}$	1						
m_{water}	0.814						
m_{cement}	3.256	2.713	2.326	1.628	1.357	1.252	1.163
W/C	0.25	0.3	0.35	0.5	0.6	0.65	0.7
Case No	A8	A9	A10	A11	A12	A13	A14
$m_{\text{dry clay}}$	1						
m_{water}	0.814						
m_{cement}	1.018	0.857	0.74	0.678	0.543	0.407	0.271
W/C	0.8	0.95	1.1	1.2	1.5	2	3

full compaction is no longer possible. The means of compaction available regulate the actual position of the point of departure. It is expected that same performance will happen in case of cement-treated clay. Therefore, different mixture ratios were selected to achieve various values of W/C in both cases of cement-treated clay and hybrid-treated clay.

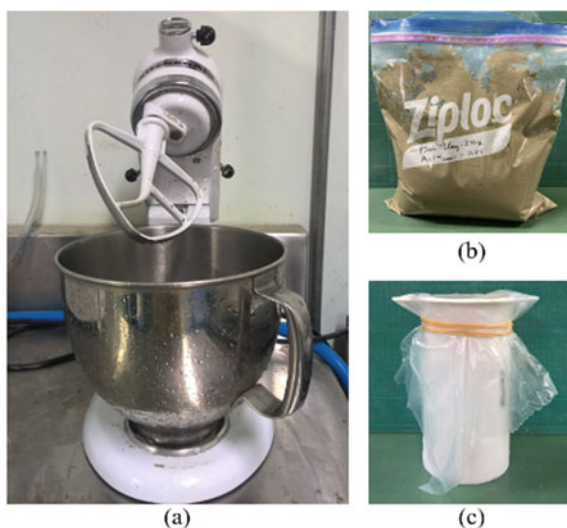
In total, 14 mixing cases of cement-treated clay were conducted with the value of W/C ranged from 0.25 to 3.0. The effects of PS ash were assessed by experimental results of 13 mixing cases of hybrid-treated clay. These 13 cases were divided into five groups with the total amount of stabilizing agents being 1.5, 1.25, 1.0, 0.75 and 0.5 times of amount of dry clay by weight. For hybrid-treated clay, the ratio by weight of PS ash to cement, PS/C , was used to determine the amount of PS ash and cement of each mixing case. Details of material composition for the cases of cement-treated clay and hybrid-treated clay are presented in Table 1 and 2 in terms of mass proportions.

2.3 Specimen Preparation Method

For both cases of cement-treated clay and hybrid-treated clay, specimens were made by using mixing machine shown in Fig. 3a and then cured in plastic circular molds of 50-mm diameter and 100-mm height shown in Fig. 3c. Dry Ao clay was first mixed with distilled water to be a homogenous slurry. Then, based on the soil treatment type, different stabilizers were added into the slurry. To prepare the cement-treated clay specimens, cement was mixed with clay slurry for 10 min. The mixing time was required to ensure the homogenous condition of mixture. After mixing, the cement-treated clay was transferred into the plastic molds in layers of 30 g. Each layer was compacted by dropping the mold 20 times from the height of 2 cm. Specimens then were covered by plastic sheets and cured for 3 days in room temperature (20 ± 1 °C).

Table 2 Mixing cases of hybrid-treated clay

Case No	B1	B2	B3	B4	B5	B6	B7
$m_{\text{dry clay}}$	1						
m_{water}	0.814						
$m_{\text{PS ash}} + m_{\text{cement}}$	1.5			1.25		1.0	
$m_{\text{PS ash}}$	0.25	0.5	0.711	0.114	0.417	0.091	0.231
m_{cement}	1.25	1	0.789	1.136	0.833	0.909	0.769
PS/C	0.2	0.5	0.9	0.1	0.5	0.1	0.3
W/C	0.65	0.81	1.03	0.72	0.98	0.9	1.06
Case No	B8	B9	B10	B11	B12	B13	
$m_{\text{dry clay}}$	1						
m_{water}	0.814						
$m_{\text{PS ash}} + m_{\text{cement}}$	0.75			0.5			
$m_{\text{PS ash}}$	0.068	0.173	0.333	0.25	0.333	0.375	
m_{cement}	0.682	0.577	0.417	0.25	0.167	0.125	
PS/C	0.1	0.3	0.8	1	2	3	
W/C	1.19	1.41	1.95	3.26	4.88	6.51	

Fig. 3 Mixing machine (a), curing condition of clay-PS ash mixture (b), and UCT specimen (c)

As indicated in Mochizuki [12], the time required to represent 100% absorption is different for various types of PS ash. Moreover, Kawai et al. [13] found that excess water in muds is not only simultaneously fixed by water absorption or retention of PS particles but also some amounts are fixed by the hydrated compound, ettringite, during curing.

Therefore, in order to access the effect of water absorbing performance of PS ash for the hybrid-treated clay, two mixing methods were performed, including: *Method 1—Mixing cement and PS ash simultaneously with clay slurry*; and, *Method 2—Adding cement one day after mixing PS ash with clay slurry*. For the *Method 2*, mixture of PS ash and clay slurry was cured in zip-lock plastic bag for 24 h in room temperature ($20 \pm 1 \text{ }^\circ\text{C}$) as shown in Fig. 3(b). The methods of compaction and curing of hybrid-treated clay specimens were same with that of cement-treated clay. In both methods, curing time of 3 days was counted after adding cement.

3 Experiment Results and Discussions

3.1 Influence of W/C to Strength Development of Cement-Treated Clay

Figure 4 summarizes the relationship between unconfined compressive strength, q_u , and W/C of cement-treated clay. The results in the figure show that the effect of W/C on strength developments of cement-treated clay and concrete are alike (see Fig. 2). With the decreases of W/C, the increases of unconfined compressive strength of stabilized clay are observed. At the W/C of 1.2 or more, the value of q_u increases gradually with the decrease in W/C. Then, the unconfined compressive strength increases significantly when W/C decreases from 1.2 to 0.5. However, the trend

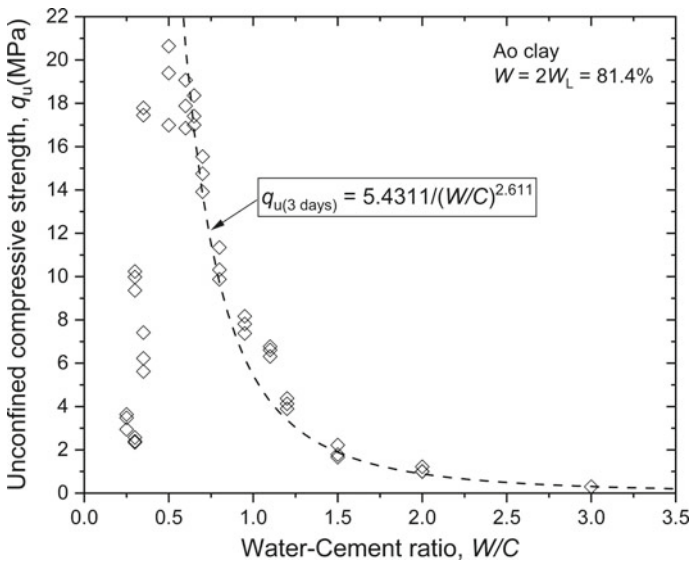


Fig. 4 Relationship between q_u and W/C of cement-treated clay

ceases to follow at the low W/C . The compressive strength of cement-treated clay drops dramatically when the W/C is less than 0.5. It suggests that due to the lack of water, it is difficult to mix the clay and cement thoroughly; therefore, in some cases, cement cannot completely react with water and give lower unconfined compressive strength. These large scattering indicate that without fully compaction, the optimum W/C for stabilizing clay by cement is about 0.5–0.6.

From the figure, a unique relationship between q_u and W/C at W/C of 0.5 and greater is obtained as follows:

$$q_u = \frac{A}{(W/C)^B} \dots (\text{MPa}) \tag{1}$$

where q_u is the unconfined compressive strength at a specific age, W/C is the water/cement ratio by weight, and A and B are empirical constants. Here, $A = 5.4311$ and $B = 2.611$ are obtained.

3.2 Influence of W/C to Strength Development of Hybrid-Treated Clay

Figure 5 summarizes the relationship between q_u and W/C of hybrid-treated clay and compares it to the same relationship of cement-treated clay represented by a

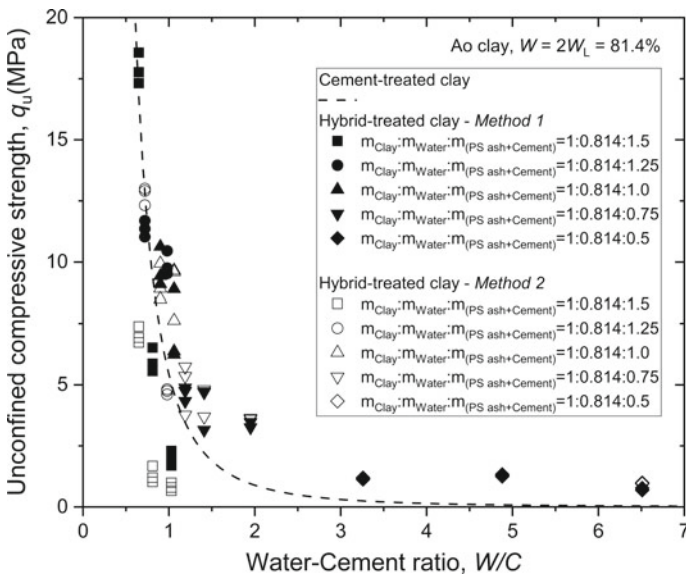


Fig. 5 Relationship between q_u and W/C of hybrid-treated clay

dotted line in the figure. Experimental results of hybrid-treated clay do not seem to follow the relationship between q_u and W/C of cement-treated clay. The fact may suggest that PS ash has absorbed clay-water, so that the actual amount of clay-water reacting with cement is reduced. Therefore, to accurately assess the effect of PS ash in stabilizing clay, the water absorbing performance of PS ash should be considered to determine actual value of W/C .

Experiment results in the figure also indicate that there are differences in improvement effect between the two mixing methods. For example, q_u produced by *Method 2* is higher than that of specimens produced by *Method 1* at high W/C . Instead, the unconfined compressive strength produced by *Method 2* become lower than that of specimens produced by *Method 1* at low W/C , because due to the lack of water, cement cannot completely react with water.

3.3 Influence of Water Absorbing Performance of PS Ash to q_u of Hybrid-Treated Clay

The water absorbing performance of PS ash, W_{ab} , can be identified as the ratio by weight of clay-water absorbed by PS ash to the dry PS ash. Based on that the parameter W/C should be replaced by W^*/C , which is the ratio by weight of clay-water that is not absorbed by PS ash to the cement by weight. Without PS ash, W^*/C is equal to W/C so that W^*/C can also be used in case of cement-treated clay.

Few reports on water absorbing performance of PS ash has been conducted. As indicated in Mochizuki [12], W_{ab} at initial is 80% and be almost double after 24 h. Kawai et al. [13] reported that total amount of water absorbed and retained by PS ash is about 74.3% on the average. As the amount of water absorbed by PS ash increases with time, it proposes that the relationship between q_u and W^*/C of hybrid-treated clay should be evaluated both in terms of water absorbing performance of PS ash in instant, $W_{ab-instant}$, and in curing, $W_{ab-curing}$. Based on the previous studies mentioned above, the values of $W_{ab-instant}$ and $W_{ab-curing}$ in this study were selected as 60% and 90%, respectively, and gave reasonable results as shown later. Table 3 shows the

Table 3 W^*/C of mixing cases of hybrid-treated clay

Case No	B1	B2	B3	B4	B5	B6	B7
W/C	0.65	0.81	1.03	0.72	0.98	0.9	1.06
W^*/C (instant)	0.53	0.51	0.49	0.66	0.68	0.84	0.88
W^*/C (curing)	0.47	0.36	0.22	0.63	0.53	0.81	0.79
Case No	B8	B9	B10	B11	B12	B13	
W/C	1.19	1.41	1.95	3.26	4.88	6.51	
W^*/C (instant)	1.13	1.23	1.47	2.66	3.68	4.71	
W^*/C (curing)	1.1	1.14	1.23	2.36	3.08	3.81	

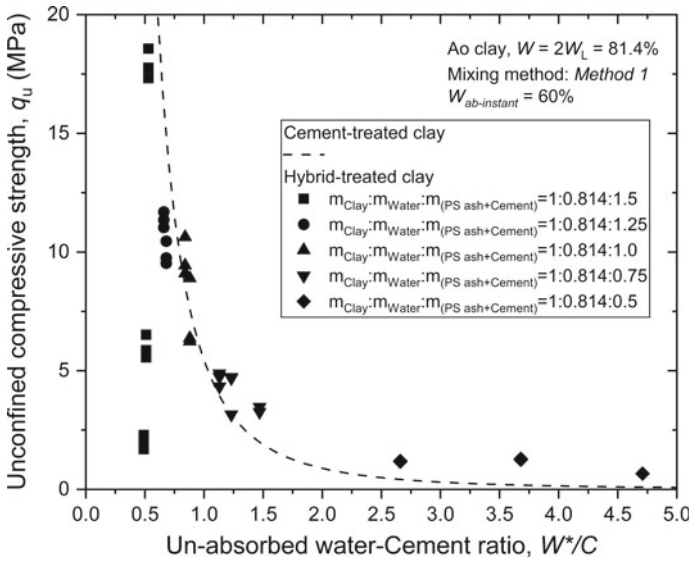


Fig. 6 Relationship between q_u and W^*/C of hybrid-treated clay: *Method 1*—Mixing cement and PS ash simultaneously with clay slurry

W^*/C of mixing cases of hybrid-treated clay corresponding to selected $W_{ab-instant}$ and $W_{ab-curing}$.

Figure 6 and 7, respectively, shows the relationships between q_u and W^*/C of hybrid-treated clay produced by *Method 1* and *Method 2*, corresponding to selected $W_{ab-instant}$ and $W_{ab-curing}$, and compare them to the same relationship of cement-treated clay. The relationships between q_u and W^*/C of hybrid-treated clay become similar to that of the cement-treated clay as in Fig. 4, compared to the results shown in Fig. 5. As same as those of the cement-treated clay, the optimum compressive strengths of hybrid-treated clay in both two mixing methods can be achieved at around W^*/C of 0.53.

Figure 8 summarizes all experiment results of hybrid-treated clay. It can be obtained that there is no difference between *Method 1* and *Method 2*. The fact suggests that it is important to consider the change of the absorption performance of PS ash with time when W^*/C is evaluated.

Based on the results in the figure, the relationship between q_u and W^*/C at W^*/C of 0.53 and greater of both two methods can be expressed as one formula. The relationships of hybrid-treated clay at W^*/C of 0.53 and greater can be expressed in the same form of Eq. 1 as follows:

$$q_u = \frac{E}{(W^*/C)^F} \dots (\text{MPa}) \tag{2}$$

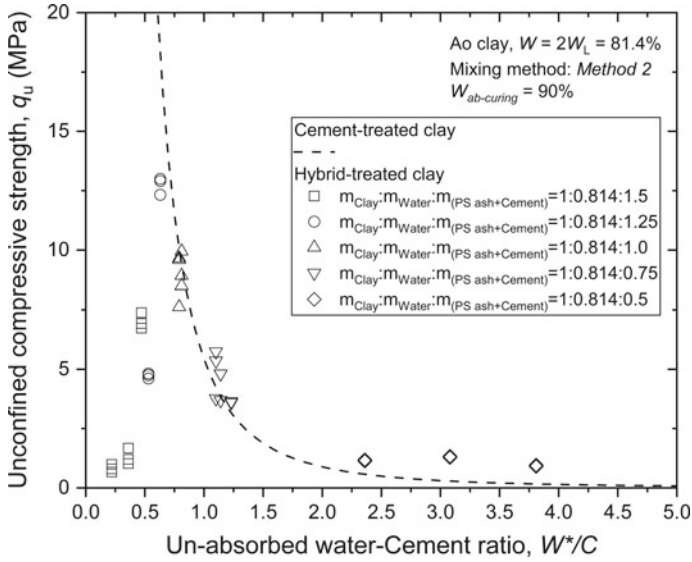


Fig. 7 Relationship between q_u and W^*/C of hybrid-treated clay: *Method 2*—Adding cement one day after mixing PS ash with clay slurry

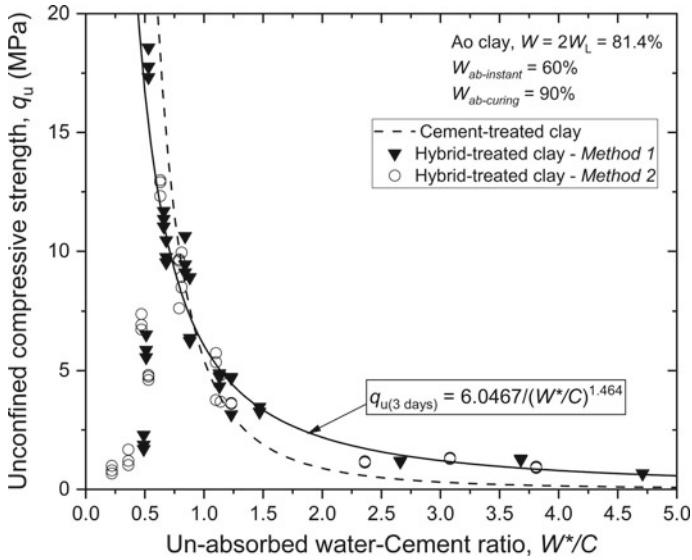


Fig. 8 Relationship between q_u and W^*/C of hybrid-treated clay

where q_u is the unconfined compressive strength of hybrid-treated clay at a specific age, W^*/C is the ratio by weight of clay-water that is not absorbed by PS ash to the cement content, and E and F are empirical constants. Here, $E = 6.0467$ and $F = 1.464$ are obtained.

Figure 8 also shows that effect of combining PS ash and cement in soil stabilization is different for variation of W^*/C . At low W^*/C , q_u of hybrid-treated clay is lower than q_u of cement-treated clay. The trend gradually reverses with the increase in W^*/C . At high W^*/C , q_u of hybrid-treated clay becomes higher than q_u of cement-treated clay. This phenomenon can be explained by the contribution of PS ash in stabilizing clay. As the chemical composition of PS ash is similar to cement [13], PS ash can stabilize clay with bond strength generated by hydrated reaction, though PS ash is not as active as cement so that its improvement effect is inferior to cement. Hence, it suggests that the unconfined compressive strength of hybrid-treated clay may be the sum of bond strength of both cement and PS ash. Besides, PS ash may continue absorbing clay-water during curing time, further reduce W^*/C , resulting in increasing bond strength given by cement.

At high W^*/C , the ratio by weight of initial clay-water to stabilizing agents of hybrid-treated clay is high and thus cement particles in hybrid-treated clay can completely react with water as cement particles in cement-treated clay. Along with further reduction of W^*/C during curing time, and the bond strength contributed by PS ash, q_u of hybrid-treated clay becomes higher than q_u of cement-treated clay. On the other hand, at low W^*/C , ratio by weight of initial clay-water to stabilizing agents is low, resulting in difficulty in thoroughly mixing and achieving satisfying compaction effects. Moreover, the hydration hardening rate and pozzolanic reaction hardening rate of cement are much faster than water absorbing rate of PS ash; and therefore, PS ash cannot generate further reduction of W^*/C . Consequently, the bond strength contributed by cement in hybrid-treated clay is lower than that in cement-treated clay. And so, the q_u of hybrid-treated clay becomes lower than q_u of cement-treated clay at low W^*/C .

4 Conclusions

The experimental framework in this study aims to evaluate the possibility of combining PS ash and cement for dredged clay soil stabilization. A series of unconfined compressive tests was conducted on both cement-treated clay specimens and hybrid-treated clay specimens to evaluate the strength development as well as the effect of combination of PS ash and cement on the strength characteristics in stabilizing dredged clay soil. From the results, several conclusions can be made as follows.

1. The experimental results of cement-treated clay show that the effect of W/C on strength developments of cement-treated clay and concrete are alike. With the

decreases of W/C , the increases of unconfined compressive strength of cement-treated clay are observed. However, the trend ceases to follow at the low W/C . The unconfined compressive strength of cement-treated clay drops dramatically when the W/C is less than 0.5. It suggests that due to the lack of water, it was difficult to mix the clay and cement thoroughly; therefore, in some cases, cement cannot completely react with water and give lower unconfined compressive strength.

2. Experimental results of hybrid-treated clay do not seem to follow the relationship between q_u and W/C of cement-treated clay. The fact suggests that PS ash has absorbed clay-water, so that the actual amount of clay-water reacting with cement has been reduced. Therefore, to accurately assess the effect of PS ash in stabilizing clay, the water absorbing performance of PS ash should be considered to determine actual value of W/C .
3. The parameter W^*/C , which is the ratio by weight of clay-water that is not absorbed by PS ash to the cement, is newly proposed. Without PS ash, W^*/C is equal to W/C so that W^*/C can also be used in case of cement-treated clay. Then, it is found that strength development of both cement-treated clay and hybrid-treated clay is similar and governed by W^*/C . The increase in W^*/C , the decrease in unconfined compressive strength is observed not only for the cement-treated clay but also for the hybrid-treated clay. Without fully compaction, the optimum strength of both cement-treated clay and hybrid-treated clay can be achieved at around the W^*/C of 0.53.
4. It is also found that it is important to consider the change of the absorption performance of PS ash with time when W^*/C is evaluated. For example, *Method 2—Adding cement one day after mixing PS ash with clay slurry* generates lower W^*/C than *Method 1—Mixing cement and PS ash simultaneously with clay slurry* when W/C is the same. Therefore, the unconfined compressive strength of specimens produced by *Method 2* is higher than that of specimens produced by *Method 1* at high W/C . Instead, the unconfined compressive strength of specimens produced by *Method 2* become lower than that of specimens produced by *Method 1* at low W/C , because due to the lack of water, cement cannot completely react with water.
5. A slight difference in q_u of cement-treated clay and hybrid-treated clay was observed corresponding to the changes of W^*/C . The reason is that PS ash may continue to absorb water during the curing time, resulting in further reduction of W^*/C . At high W^*/C , in both hybrid-treated clay and cement-treated clay, cement can completely react with clay-water. However, due to the reduction of W^*/C during curing time, bond strength given by cement in hybrid-treated clay is higher than that in cement-treated clay. Along with the bond strength contributed by PS ash, q_u of hybrid-treated clay becomes higher than q_u of cement-treated clay at high W^*/C . On the other hand, at low W^*/C , due to the lack of water, cement cannot completely react with clay-water in hybrid-treated clay as in cement-treated clay. The lack of water also prevents PS ash from generating much further reduction of W^*/C to enhance the cement bond strength. And so,

q_u of hybrid-treated clay is lower than q_u of cement-treated clay at low W^*/C . However, further studies will be required to confirm the mechanism.

Acknowledgements Authors would like to thank Dr. Yamauchi, H. for the useful discussions.

References

1. Lo SR, Wardani SPR (2002) Strength and dilatancy of a silt stabilized by a cement and fly ash mixture. *Can Geotech J* 39(1):77–89
2. Chen L, Lin DF (2009) Stabilization treatment of soft subgrade soil by sewage sludge ash and cement. *J Hazard Mater* 162(1):321–327
3. Mochizuki Y, Yoshino H, Saito E, Ogata T (2003) Effects of soil improvement due to mixing with paper sludge ash. *Proceeding of China-Japan Geotechnical Symposium*, pp 1–8
4. Shigematsu H, Demura Y, Fujiwa Y (2012) Stabilization of poor soil by paper mill sludge mixing. *J JSCE (C:Geotechnics)* 66(4):695–705 (in Japanese)
5. Elias N (2015) Strength development of soft soil stabilized with waste paper sludge. *Int j Adv Technol Eng Sci* 3(1):141–149
6. Mochizuki Y, Yoshino H, Saito E, Ogata T (2004) Soil improvement due to mixing with paper sludge ash. In: 1st International conference on sustainable construction: waste management. Singapore
7. Chew SH, Kamruzzaman HM, Lee FH (2004) Physicochemical and engineering behaviour of cement treated clays. *J Geotech Geoenvironmental Eng, ASCE* 130(7):696–706
8. Zhu W, Zhang CL, Chiu CF (2007) Soil-water transfer mechanism for solidified dredged materials. *J Geotech Geoenvironmental Eng, ASCE* 133(5):588–598
9. Miura N, Horpibulsuk S, Nagaraj TS (2001) Engineering behavior of cement stabilized clay at high water content. *J JSCE (Soils and Foundations)* 41(5):33–45
10. Abrams DA (1918) Design of concrete mixture. *Bulletin 1 - Structural Materials Research Laboratory*. Lewis Institute, Chicago
11. Neville AM (2000) *Properties of concrete*, 4th edn. Prentice Hall, Upper Saddle River
12. Mochizuki Y (2016) Study on subjects and applicability for mud improvement due to mixing with paper sludge ash. *Japan Geotech Soc Spec Publ* 4(5):105–108
13. Kawai S, Hayano K, Yamauchi H (2018) Fundamental study on curing effect and its factor on the strength deformation characteristics of PS ash-based improved soil. *J JSCE (C: Geotechnics)* 74(3):306–317 (in Japanese)

Shrinkage Curve of Treated Sulfate-Bearing Soils with GGBS



Hussein Al-Dakheeli , Amir Javid , Mengting Chen , and Rifat Bulut 

Abstract Stabilizing sulfate-bearing subgrade soils by lime and cement has widely been known to cause a significant heave in those soils. One of the potential alternative stabilizers is slag cement, or commonly referred to as ground granulated blast-furnace slag (GGBS). Drought causes a volumetric shrinkage and substantial desiccation cracking in clay subgrade soils, which leads to tremendous distress in pavement layers. However, the literature review reveals that the desiccated shrinkage of GGBS-stabilized soils has been paid a little attention. This paper presents experimental results for a sulfate-rich compacted soil treated with GGBS in the laboratory. The experiments involve subjecting treated and untreated soil specimens to wetting until reaching the maximum swelling before being air-dried beyond the shrinkage limit. The soil shrinkage curve (SSC) is employed in this paper to interpret the shrinkage of treated soil. The SSC of the treated soil is compared with that of the untreated native soil to impart the performance of GGBS on mitigating each shrinkage zone of SSC. In general, the results demonstrated the high effectiveness of GGBS in alleviating the swelling-shrinkage behavior of the sulfate-rich soil. Stabilizing the soil by GGBS has diminished all shrinkage zones of SSC, but no considerable effect was observed on the shrinkage limit.

Keywords Slag cement · Sulfate · Shrinkage curve

1 Introduction

Stabilizing sulfate-rich subgrade soils by calcium-based additives, lime, Portland cement, and class C fly ash causes deleterious expansions. This is due to the formation of ettringite minerals which can expand double times in volume and, thus, cause adverse effects on pavement layers [1]. Based on the literature review, slag cement has been found to be a potential alternative for the stabilization of sulfate-bearing

H. Al-Dakheeli · A. Javid · M. Chen · R. Bulut (✉)

School of Civil and Environmental Engineering, Oklahoma State University, Stillwater, OK 74078, USA

e-mail: rifat.bulut@okstate.edu

subgrade soils (e.g., Harris et al. [2]). Slag cement, also referred to as ground granulated blast-furnace slag (GGBS), is a pozzolan that has high silica content such that it has much less potential to create ettringite and damaging expansions (e.g., Little et al. [3]).

Desiccation shrinkage of subgrade soils results in differential settlement and cracking within the edge moisture variation distance [4, 5]. The formed cracks in subgrade may propagate to upper pavement layers [6–8]. In spite of its high importance, the literature review indicates that the shrinkage of GGBS-stabilized soils has been rarely evaluated. In a recent study by Osinubi and Eberemu [9], the treatment with GGBS manifested no noticeable effect on the soil shrinkage behavior, even after subjecting the soil to wetting–drying cycles. Therefore, it is still needed for more evaluation on whether and how the GGBS mitigates the soil shrinkage behavior.

In this paper, experimental results of shrinkage and swelling are presented for a sulfate-bearing soil stabilized by two dosages of GGBS, i.e., 3 and 5%. The soil shrinkage curve was utilized to understand the effect of GGBS on each shrinkage zone. The effect of GGBS on the soil shrinkage curve provides with an insight into how the GGBS changes the soil pore size distribution.

2 Materials

Sulfate-bearing soil was collected from a site known previously for its high sulfate content in Blaine County, State Highway 33, Oklahoma. The soil was collected from 0.8 feet down to 3.5 feet in depth. The collected soil samples were cleaned from plant residues and then air-dried in the laboratory. After completely air-dried, the soils were broken into smaller pieces and then grinded to obtain smaller particles as possible. The dried grinded soils were then used for preparing specimens for the laboratory tests. The soluble sulfate content of the native soils was determined following the procedure outlined in the Oklahoma Department of Transportation (ODOT) OHD L-49: Method of test for determining soluble sulfate content in soil (Table 1). The basic geotechnical properties of the native soils, i.e., grain size distribution, the optimum water content, maximum dry density, liquid limit, and plastic limit were obtained following the corresponding ASTM standards D6913, D7928, D698, and D4318 (Table 1). The GGBS used to stabilize the soil was obtained from Skyway Cement Company, Chicago, Illinois. The chemical composition of GGBS was identified by

Table 1 Sulfate content and the basic geotechnical properties of the soils

Parameter	Sulfate content (ppm)	MDD* (g/cm ³)	OMC** (%)	Clay (%)	LL (%)	PL (%)	PI (%)
Value	27,000	1.84	13.5	23.2	31.0	17.0	14.0

*MDD: maximum dry density; **OMC: optimum moisture content

analyzing powder samples in the X-ray fluorescence spectrometry as listed in Table 2.

3 Testing Program

Test Method A in the ASTM D4546-14 standard was followed to conduct one-directional free swelling tests (FST). The FST was conducted on reconstituted soils treated with slag cement and compacted inside a stainless steel ring with 6.40 cm in diameter and 2.54 cm in height. Among different slag contents mixed with the soil for preliminary swelling tests, it was found that 3 and 5% slag were enough to effectively reduce the swelling behavior. The mixture of soil and GGBS was compacted at the optimum water content in three layers. Each layer received 25 blows using a wooden rod with a rubber cap (diameter = 2.54 cm) to reach a close dry density to the maximum dry density of the soil obtained from the standard proctor compaction test. The compacted specimen with the ring (Fig. 1) was weighed and sealed by plastic wrap and aluminum foil and then stored in an ice chest for curing in a room of constant humidity (70%) and 22 ± 1 °C in temperature. The soil specimens for FST were cured for 7 days. After curing, the one-directional FST, as shown in Fig. 1, was carried out under a pressure of 1 kPa as recommended by ASTM D4546-14. The soil specimens totally ceased swelling after around 7 days. Thereafter, the specimens were stored for 24 h for moisture equilibrium before conducting the shrinkage test.

Since the specimens were freely swollen in one direction in the consolidometer rings, only the shrinkage in one direction was measured. The one-directional shrinkage was measured by a dial gauge set on a porous stone placed on the top of the specimen as shown in Fig. 2. The whole setup was rested on a balance to capture a continuous reading of the specimen's weight, while the soil specimen was air-dried in the laboratory at temperature and relative humidity equal to 22 ± 1 °C and 45%, respectively. All the soil specimens were dried until reaching close to less than 4% of the initial moisture content to obtain the shrinkage curve of the soil.

4 Results

Figure 3 depicts the results of free swelling tests. Three replicate tests for each slag content were carried out. Soil expansion behavior has been substantially mitigated after the treatment with GGBS. The results of subsequent shrinkage tests are illustrated in Fig. 4. Similar to the swelling results, the shrinkage of treated soils came far less than that of untreated soils. The shrinkage results are further discussed in the following section.

Table 2 Chemical composition of GGBS

Material	SiO ₂ (%)	Al ₂ O ₃ (%)	SO ₃ (%)	CaO (%)	Fe ₂ O ₃ (%)	K ₂ O (%)	TiO ₂ (%)	MnO (%)	MgO (%)
Skyway slag cement	34.63	6.72	2.40	45.25	0.54	0.49	0.84	0.72	8.26

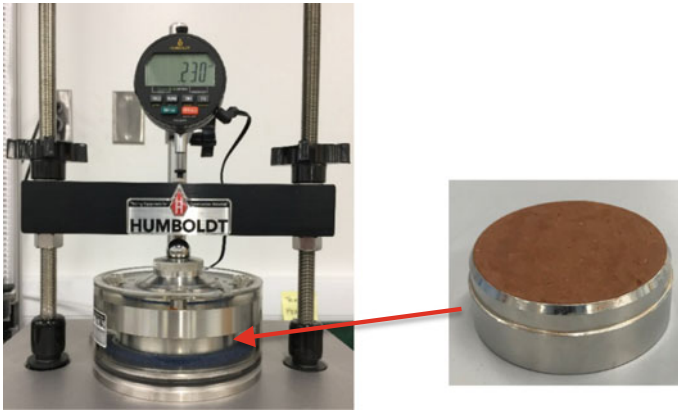


Fig. 1 Setup and specimen of the free swelling test

Fig. 2 Schematic drawing for the one-directional shrinkage test

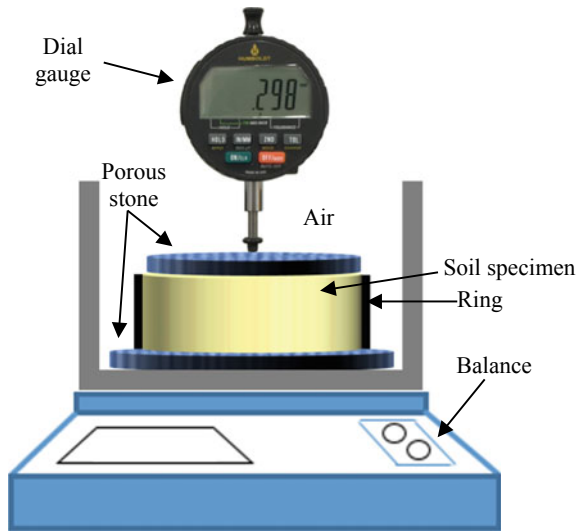
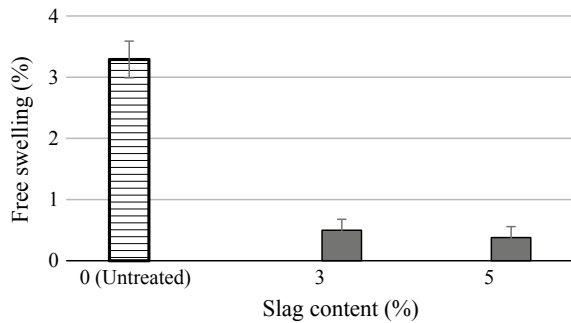


Fig. 3 Results of FSTs, slag content versus free swelling percent



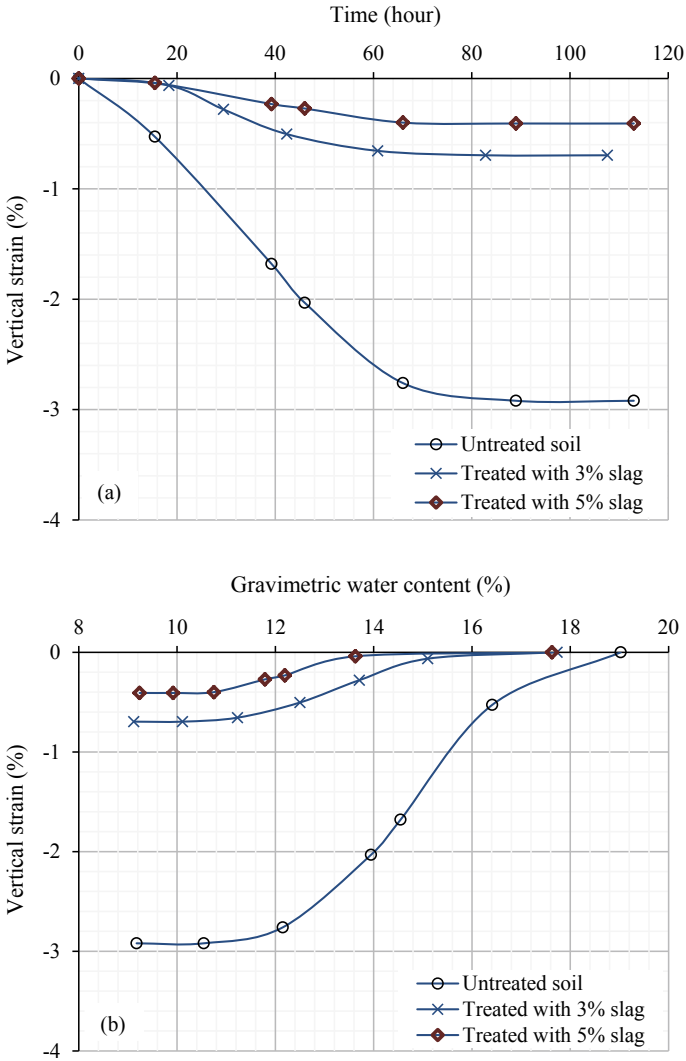


Fig. 4 Shrinkage results, a time versus vertical shrinkage, and b water content versus vertical shrinkage

4.1 Shrinkage Curve

To impart more insight into the shrinkage results, the obtained results in Fig. 4 can be compared with the typical shrinkage curve displayed in Fig. 5. Typical shrinkage curve of aggregated soils can be divided into four major zones. Aggregated soils have dual porosity with two distinct pore sizes, inter-aggregate being relatively large in size, and intra-aggregate being smaller [10]. The structural shrinkage (Fig. 5) occurs

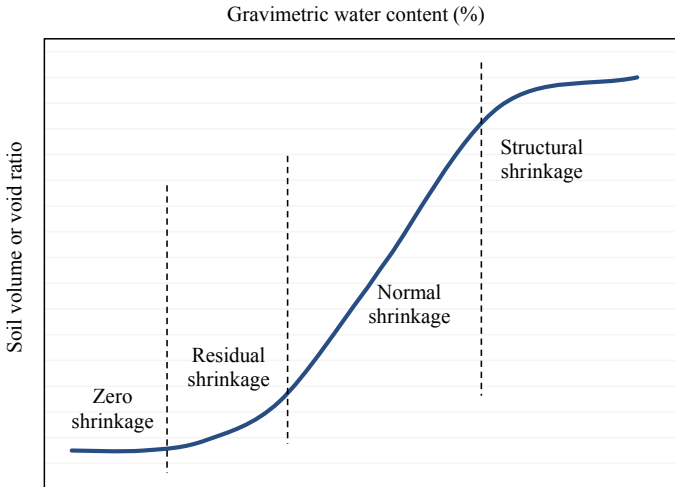


Fig. 5 Typical shrinkage curve of aggregated soils (e.g., Cornelis et al. [11])

mainly due to the removal of water from the inter-aggregate pores, whereas the normal shrinkage primarily results from the shrinkage in the intra-aggregate pores [11, 12].

Comparing the shrinkage results (Fig. 4b) with the typical shrinkage curve shown in Fig. 5 reveals that as the GGBS dosage increases, the moisture range of structural shrinkage becomes wider than that of the normal shrinkage. Analogous shrinkage results have also been reported by Dash and Hussain [13] for lime-treated soils. The extension of structural shrinkage moisture range over that of the normal shrinkage most likely alludes to a change in the pore size distribution by increasing the inter-aggregates' size or quantity in the overall soil. The latter may be attributed to the flocculation-agglomeration of the clay particles through cementation as a result of the chemical treatments. Generally, the stabilization by GGBS has significantly alleviated the shrinkage behavior in all shrinkage zones as summarized in Table 3. Nevertheless, a close observation of Fig. 4b indicates no considerable effect of GGBS on the shrinkage limit, such that treated and untreated soils have ceased the shrinkage at a similar water content, close to 11%.

Table 3 Summary for shrinkage results

Soil	Shrinkage (%)			
	Structural	Normal	Residual	Total
Untreated blaine	0.6	2.0	0.3	2.9
Treated with 3% slag	0.1	0.5	0.2	0.8
Treated with 5% slag	0.1	0.3	0.0	0.4

5 Conclusions

In this paper, a compacted high sulfate soil was stabilized by 3% and 5% GGBS and subjected to swelling and subsequent shrinkage. The following conclusions are drawn from the experimental results:

- The GGBS has substantially enhanced the soil against expansion–contraction behavior. While 3% slag has generated significant improvement, the increase of GGBS dosage from 3 to 5% only added a little more improvement.
- Shrinkage curve of treated soils exhibited similar shape to that of untreated soils with all shrinkage zones including structural, normal, and residual shrinkage. However, the addition of GGBS has reduced the shrinkage in all zones.
- The water content range of structural shrinkage zone was noticeably greater for treated soils than that of untreated soils. This implies that the addition of GGBS has increased the inter-aggregate pores' size or quantity, since the structural shrinkage occurs mainly due to the removal of water from the inter-aggregate pores, the relatively large pores.
- The latter point was ascribed to the flocculation-agglomeration of the clay particles through cementation as a result of the chemical treatment.
- Despite of the remarkable decrease in shrinkage magnitude, the addition of GGBS appeared to have no considerable effect on the shrinkage limit.

The observations described above are applicable to the soil, and slag cement investigated in this study. Therefore, it is recommended for future studies to consider soils with higher plasticity. The swelling-shrinkage of high plastic soils may be more affected by the increase of slag dosage.

Acknowledgements The authors thank and acknowledge the fund provided by the Oklahoma Department of Transportation (ODOT) for this research. The ODOT engineers Scott Garland, Christopher Clarke, and Amanda Warren have helped us in identifying the soil sampling sites and provided significant help with the soil sampling in the field. The help provided is highly appreciated. We also thank the Nebraska Nanoscale Facility (NNF) for providing the XRF test for slag cement.

References

1. Bredenkamp S, Lytton R (1995) Reduction of sulfate swell in expansive clay subgrades in the Dallas district. Texas Transportation Institute, Research Report 3921–1, Texas, United States
2. Harris P, Holdt J, Sebesta S, Scullion T (2006) Recommendations for stabilization of high-sulfate soils in Texas. Texas Department of Transportation (TxDOT), Research Report No. FHWA/TX-06/0-4240–3, Texas, United States
3. Little DN, Herbert B, Kunagalli SN (2005) Ettringite formation in lime-treated soils: establishing thermodynamic foundations for engineering practice. *J Transp Res Board* 1936(1):51–59
4. El-Garhy BM, Wray WK (2004) Method for calculating the edge moisture variation distance. *J geotechn geoenvironmental eng* 130(9):945–955

5. Puppala AJ, Manosuthkij T, Nazarian S, Hoyos LR (2011) Threshold moisture content and matric suction potentials in expansive clays prior to initiation of cracking in pavements. *Can Geotech J* 48(4):519–531
6. Lytton RL, Aubeny CP, Bulut R (2005) Design procedure for pavements on expansive soils. Texas Transportation Institute, Research Report No. FHWA/TX-05/0–4518–1, vol 1. Texas, United States
7. Bulut R, Chen LZ, Mantri S, Amer O, Tian Y, Zaman M (2014) Drying shrinkage problems in high PI subgrade soils. Oklahoma Department of Transportation, SP&R Item Number 2236, Oklahoma, United States
8. Nevels JB, Clarke CR, Chen L, Bulut R (2016) A site assessment of pavement cracking in a drought environment: a case history. In: Delage P, Cui Y, Ghabezloo S, Pereira J, Tang A (eds) 3rd European conference on unsaturated soils, E-UNSAT 2016, vol 9. Article No. 20004. EDP Sciences
9. Osinubi KJ, Eberemu AO (2010) Desiccation induced shrinkage of compacted lateritic soil treated with blast furnace slag. *Geotech Geol Eng* 28(5):537–547
10. Sun H, Mašín D, Najser J, Neděla V, Navrátilová E (2019) Bentonite microstructure and saturation evolution in wetting–drying cycles evaluated using ESEM. *MIP WRC meas Géotech* 69(8):1–14
11. Cornelis WM, Corluy J, Medina H, Diaz J, Hartmann R, Van Meirvenne M, Ruiz ME (2006) Measuring and modelling the soil shrinkage characteristic curve. *Geoderma* 137(1):179–191
12. Al-Dakheeli H, Bulut R (2019) Interrelationship between elastic deformation and soil-water characteristic curve of expansive soils. *J Geotech Geoenvironmental Eng* 145(4):04019005
13. Dash SK, Hussain M (2015) Influence of lime on shrinkage behavior of soils. *J Mater Civ Eng* 27(12):04015041

A Study on Electrokinetic Dewatering of Saturated Soil



Abhishek A. Sutar and Veerabhadrapa M. Rotte

Abstract Differential settlements of foundation rested on saturated soil may lead to a disaster if not appropriately studied. Conventional dewatering techniques are time-consuming and have some limitations. Electrokinetic dewatering is one of the effective methods used to remove water from saturated clay having low permeability. The present study deals with a series of laboratory experiments performed on saturated clay to study the influence of (i) spacing of electrodes, (ii) configuration of electrodes, (iii) number of cathodes and anodes, and (iv) pH of soil on the performance of electrokinetic dewatering. A custom-designed wooden watertight box with internal dimensions of 40 cm length, 40 cm breadth, and 30 cm height was used for experiments. Hollow circular stainless steel tubes with 1.9 cm diameter, 25 cm length having perforations were used as electrodes. Water collected at the cathode was removed and measured manually. The results confirm that increasing the spacing between the anode and cathode causes more area under the influence of electric field, which increases dewatering efficiency. One-dimensional configuration is better than rectangular and hexagonal configurations. Dewatering increases with an increase in number of cathodes. A decrease in pH of soil results in less dewatering competence. This study will be beneficial for ground improvement projects carried out in marshy lands, coastal roads, etc., for improving subgrade soil.

Keywords Electrokinetic dewatering · Direct current · Stainless steel electrodes · Configuration

A. A. Sutar · V. M. Rotte (✉)
Civil Engineering Department, Institute of Infrastructure Technology Research And Management,
Ahmedabad 380026, India
e-mail: vmrotte@iitram.ac.in

A. A. Sutar
e-mail: abhishek.sutar.18pc@iitram.ac.in

1 Introduction

A significant problem in the construction of roads and highways is compaction/consolidation of saturated subbase or subsoil possessing low permeability as well as inadequate bearing capacity. In some of the cases, water table in the soil is very high such that the saturated soil does not meet the required specifications and needs improvement. Stabilization of such soils can be carried out by preloading, prefabricated vertical drains (PVD), and chemical stabilization using cement, fly ash, lime, and admixtures. In some of the cases, vacuum stabilization is also preferred. Electrokinetic stabilization is one of the best alternatives for dewatering soils with low permeability. A direct current is applied to the soil through electrodes causing movement of pore water from the positive to negative electrode. When no extra water or solution is added into the system, then it is known as anode closed-cathode open system. Net consolidation will be equal to the volume of water drained. The rate of drainage of water (q_e) is given by Eq. 1 [1].

$$q_e = k_e \cdot i_e \cdot A \quad (1)$$

where k_e = electro-osmotic permeability, $i_e = dV/dl$, is the electric field intensity or voltage gradient, $A = c/s$ area of the specimen.

Electrokinetic stabilization of soil includes basic phenomena like electro-osmosis, electrophoresis, electrolysis, and electro-migration, which are responsible for the flow of water [2]. Electro-osmosis is a movement of water from anode to the cathode. Electrophoresis is a movement of charged particles. Electrolysis is the decomposition of pore water at electrodes, which occurs due to redox reactions. Electro-migration is the movement of ions causing movement of salts during the electrokinetic process. Reuss [3] is the first researcher who observed electro-osmosis by application of direct current to a mixture of clay and water. Quincke [4] studied the electrical flow and streaming potential. This method was successfully tested by Casegrande [5] on the field. Electrokinetic stabilization is the best method for weak clayey soils which have low hydraulic conductivity and require strengthening [6]. Electrokinetic consolidation is affected by soil type, zeta potential, pH, temperature, water content, soil salinity, electrical resistivity and conductivity, type of electrodes, etc. [7, 8] Several laboratory studies reported the significance of electrokinetic stabilization for the improvement of varieties of saturated soils.

Studies related to electrode material were carried out by comparing inert and reactive electrodes. The impact of copper electrodes was the largest for the improvement of geotechnical properties of soil than inert electrodes, and it is a potential technique for the improvement of expansive soil [9]. The effect of electrode configuration on electro-osmotic consolidation was studied by comparing four main configurations, and results were studied in terms of surface settlements. The study confirmed that hexagonal configuration to be the best one [10]. Electro-osmotic strengthening of silts based on selected electrodes, namely iron, copper, and aluminum, were studied based on drainage, water content, and effective potential. It was observed that iron is

preferable electrode material for electro-osmosis [11]. The combination of electro-osmotic consolidation and chemical stabilization was investigated by using lime and cement columns for soft organic clay, which revealed significant results [12].

Electrokinetic experiments on fine-grained dredged sediments indicated that the improvement in the soil was due to a change in microstructure rather than a decrease in the void ratio of soil [13]. A study related to electrokinetic sedimentation reported that the final void ratio of sediment after electrokinetic sedimentation was related to the initial void ratio. The efficiency of electrokinetic consolidation was observed to improve by allowing gravitational sedimentation before the application of the electric field [14]. It was noted that the addition of polymers enhances the rate of dewatering [15]. The electrokinetic dewatering of dredged mud using stainless steel electrodes and application of surcharge was studied. Electrokinetic sedimentation of the dredged mud was observed to accelerate up to 20 times faster than self-weight sedimentation [16]. Electrokinetic stabilization depends mainly on the pH of the soil, and some reactions take place depending upon freely available ions [17]. It was observed that the electro-osmosis process causes a change in the mineral composition of soil because of cation exchange and pozzolanic reaction resulting from high pH. Jeyakanthan et al. [18] presented a design of an electro-osmotic tri-axial testing apparatus suitable for electro-osmotic treatment of high plasticity black clay. It could also measure electro-osmotic permeability, generated pore-water pressure, and a testing procedure responsible for the improvement of soil properties. Rotte et al. [19] studied the factors affecting the efficiency of electrokinetic dewatering of saturated soil. It was observed that an increase in voltage and pH increases the efficiency of electrokinetic dewatering. However, the effect of the spacing of electrodes needs a more elaborate study.

Very few studies have been reported the effect of pH of the soil, configuration of electrodes, and number of electrodes on the performance of electrokinetic dewatering of saturated soil. The main objective of this study is to study the effectiveness of electrokinetic dewatering technique for saturated soil. In this paper, the influence of various parameters on the efficacy of electrokinetic dewatering and enhancement of dewatering volume were studied. The various parameters considered for the present study were spacing of electrodes, a configuration of electrodes, numbers of cathode and anode, and pH of soil.

2 Materials Used in the Present Study

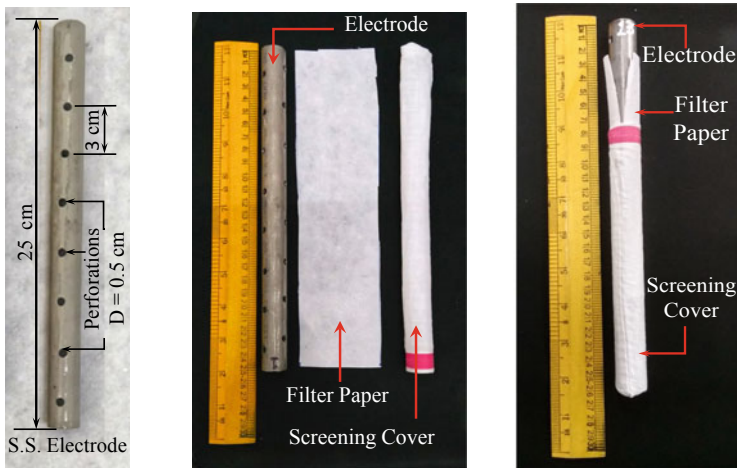
2.1 Soil

In order to accelerate the results, silty soil was selected for the present study. It was borrowed from the Lunawada area of East Gujarat as this soil is present in the region. The soil was tested in a laboratory for finding out different properties as per Indian Standard Codes. The specific gravity of soil was 2.6 with pH 7.5, and it was

classified as silty sand (SM) as per Indian Standard Classification System (ISC). The liquid limit of the soil was 33.5% and found to be non-plastic. Maximum dry density and optimum moisture content were calculated as 17.55 kN/m³ and 15.6%, respectively. Soil sample was dried in an oven for 24 h. After breaking clay lumps by wooden hammer, soil passing through IS sieve size 4.75 mm was collected and used to perform experiments. Moisture content of soil for all the experiments was kept equal to 1.25 times its liquid limit by adding distilled water, and it was appropriately mixed and filled in the box.

2.2 Electrodes

The metal electrodes were used to provide potential differences. Based on the study by Malekzadeh et al. [16], stainless steel electrodes were selected. Stainless steel pipes, having an internal diameter of 1.9 cm, were cut to make electrodes of length 25 cm. The hollow electrodes themselves were used for the collection of water from the surroundings. In view of this, holes of 5 mm diameter were drilled in a staggered pattern on the surface of electrodes keeping 3 cm center to center spacing (Fig. 1a). The total numbers of holes on each electrode were 24 and kept constant for each electrode. The total surface area of an electrode was 70.88 cm², and effective surface area was 66.17 cm². Filter paper and cotton cloth as a screening cover was wrapped around the electrodes along the length and at the bottom to prevent movement of soil particles into drainage pipe (Fig. 1b–c).



a) Electrode with perforations b) Screening cover & filter c) Electrode with screening cover

Fig. 1 Details of electrode with screening arrangements

3 Experimental Test Setup, Procedure, and Program

The dimensions of a box used for the electrokinetic dewatering test were decided based on the study reported by Fourie et al. [20]. The box was made up of a wooden sheet of 15 mm thickness with internal dimensions of 40 cm in length, 40 cm in width, and 30 cm in depth. It was provided with two handles for ease in carrying and handling. A detailed picture of the box is shown in Fig. 2a. Water tightness of the box was achieved by applying waterproofing gel on inner surfaces and at the vertical as well as horizontal joints of the box. Water was filled in the box and kept for 24 h to check any leakages. A syringe of 50 ml capacity and connected with a flexible tube was used to collect the water manually from the bottom of the electrodes (Fig. 2b). The length of the flexible tube was kept sufficient to reach the bottom of the electrode to suck all the water collected in the electrode through perforations.

As per calculations, soil and distilled water were appropriately mixed by using a rotary mixer. The mix was poured in the box in increments of 5 cm thickness up to 25 cm. In each increment of soil pouring, a layer was properly leveled. Electrodes were inserted up to a depth of 23 cm in soil from top, and 2 cm length of the electrode was kept above soil to facilitate connections of wiring. A perspective view of a final setup with all arrangements is shown in Fig. 3a. The whole box was kept in a carton box. The carton box was lined by thermocol sheets from all inner sides to prevent any moisture loss from the setup and to minimize the effect of temperature on the setup (Fig. 3b). DC supply is required to perform electrokinetic dewatering of saturated soil. All anodes were connected in series to a positive source of DC supply. Cathode was connected to a negative source of DC supply. The required voltage was set, and the supply was started. With these arrangements of electrodes, water was observed

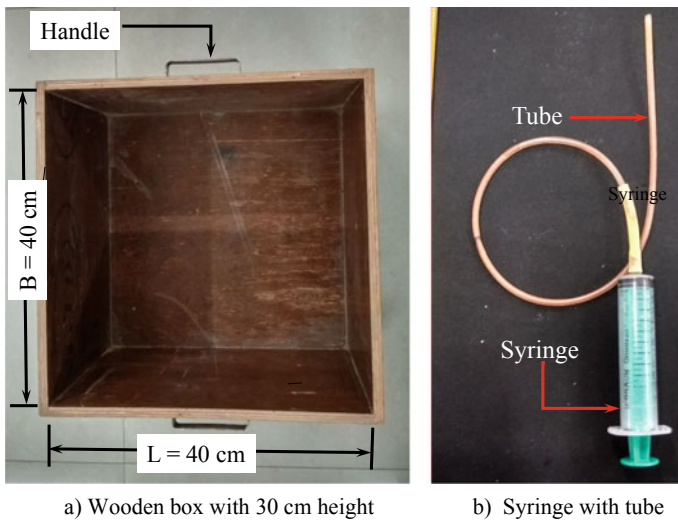


Fig. 2 Details of test box and syringe

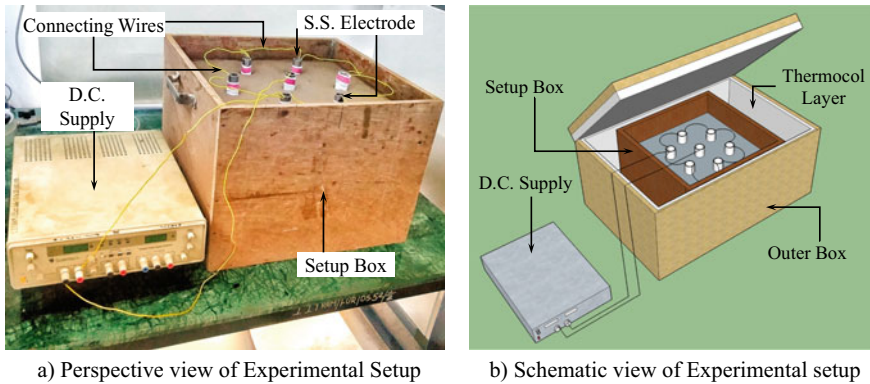


Fig. 3 Developed electrokinetic dewatering setup

to flow from anode to cathode. Water was collected in the hollow space of cathode through perforations provided on the surface of the cathode. Water collected at the cathode was sucked out by syringe (Fig. 2b) manually at each hour, and it continued for 48 h.

The experiments were performed to study the effect of; (i) spacing between electrodes, (ii) configuration of electrodes, (iii) effect of numbers of cathode and anode, and (iv) pH of soil. All the tests were continued up to 48 h. The test program with all details is shown in Table 1. Each test is specified with test legend to identify easily.

4 Results and Discussion

4.1 Effect of Spacing of Electrodes (Series—A)

Electrokinetic dewatering experiments were carried out by varying the center to center spacing between cathode and anodes as 5 cm (EKS-1), 10 cm (EKS-2), 12.5 cm (EKS-3), and 15 cm (EKS-4). One cathode was placed at the center, and six anodes were placed surrounding the cathode to form a hexagonal pattern. A potential difference of 5 V was maintained for all experiments in this series A. Figure 4 shows variation in cumulative water collected at the cathode for various time intervals. It can be clearly seen that as time increases, the cumulative water collection at cathode increases. However, the rate of dewatering decreases with time. It was noticed that with an increase in center to center spacing between cathode and anode, dewatering volume also increases. It may be due to an increase in spacing, an area under the influence of electric field increases, which causes more water to flow from anode to cathode.

Table 1 Test program of the present study

Series	Parametric study	Test legends	Parameters varied	Parameters kept constant
A	Effect of spacing of electrodes	EKS-1, EKS-2, EKS-3 and EKS-4	c/c spacing = 5 cm, 10 cm, 12.5 cm and 15 cm	Voltage = 5 V, pH = 7.5, hexagonal configuration, one anode and six cathodes
B	Effect of electrode configuration	EKS 3, EKS-5 and EKS-6	Configuration = Hexagonal, rectangular and one-dimensional	Voltage = 5 V, pH = 7.5, c/c spacing = 12.5 cm,
C	Effect of numbers of cathode and anode	EKS-3 and EKS-7	Six anodes and one cathode and one anode and six cathodes	Voltage = 5 V, pH = 7.5, c/c spacing = 12.5 cm, hexagonal configuration
D	Effect of pH of soil	EKS-3,EKS-8 and EKS-9	pH of soil = 7.5, 5, and 10	Voltage = 5 V, c/c spacing = 12.5 cm, hexagonal configuration, one anode and six cathodes

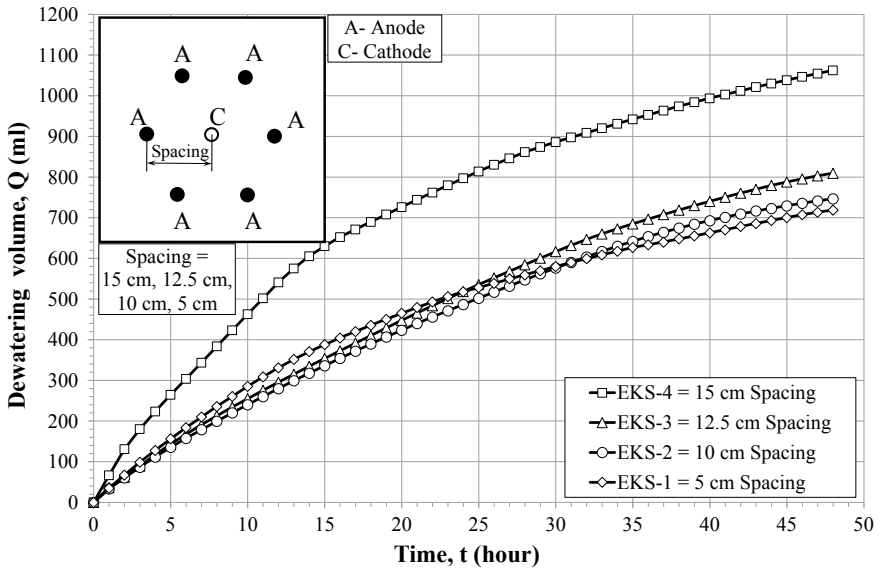


Fig. 4 Variation in dewatering volume with time for different spacing of electrodes

4.2 Effect of Electrode Configuration (Series—B)

Various experiments were performed to study the effect of the configuration of electrodes on electrokinetic dewatering. Three different configurations were considered: (1) Hexagonal configuration (EKS-3) that consisted of one centrally located cathode surrounded by six anodes [7]. (2) Rectangular configuration (EKS-5) in which centrally located cathode was surrounded by two rows of anodes on either side. (3) One-dimensional configuration (EKS-6) had three anodes and three cathodes. Center to center spacing between anodes and cathode was kept as 12.5 cm in all the configurations. In addition to this, for all the three configurations, the area under the influence was kept constant as 405.75 cm². A potential difference of 5 V was applied for all experiments in this series. The graph of cumulative water collected at cathode versus time has been drawn as shown in Fig. 5. In one-dimensional configuration, it was observed that more volume of water was collected at the cathode as compared to hexagonal and rectangular configurations. In one-dimensional configuration, one anode was shared by one cathode, which means the acidic area in the soil was less. For other configurations, the acidic area in the soil was on the higher side, which reduced the flow of water toward the cathode.

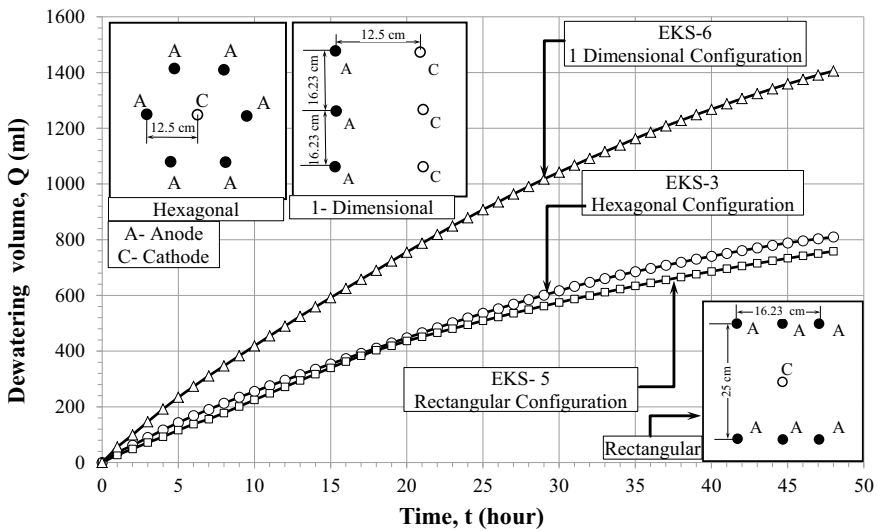


Fig. 5 Variation in dewatering volume with time for different electrode configurations

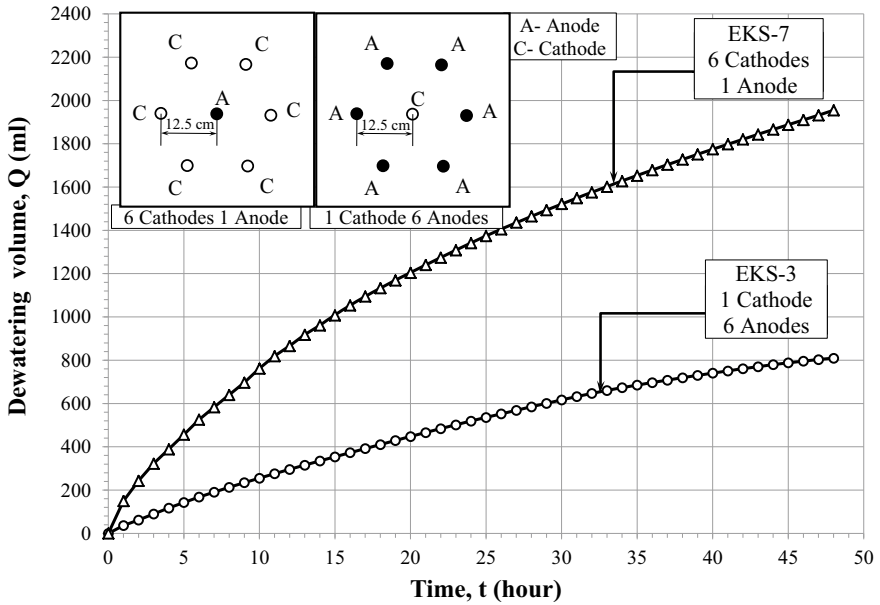


Fig. 6 Variation in dewatering volume with time for different combinations of cathode and anode

4.3 Effect of Numbers of Cathode and Anode (Series—C)

Two experiments (EKS-3 and EKS-7) were carried out to study the effect of numbers of cathode and anode on the efficiency of electrokinetic dewatering. In this series, hexagonal configuration of electrodes was maintained. Experiment EKS-3 consisted of six anodes and one centrally located cathode. However, EKS-7 was provided with one centrally located anode surrounded by six cathodes. A potential difference of 5 V was applied for both experiments in this series. Figure 6 depicts the variation in the amount of dewatering with respect to time for both the experiments (EKS-3 and EKS-7). It can be observed that experiment EKS-7 (six cathodes and one anode) performance superior to experiment EKS-3 (one cathode and six anode). It is because when numbers of anodes are more, they imply high acidic areas near themselves during the treatment that results in reducing the flow of water toward the cathode. It also can be confirmed from series-B, as explained earlier.

4.4 Effect of pH of Soil (Series—D)

To study the effect of pH of soil, tests were performed by varying pH of the soil as 5 (EKS-8), 7.5 (EKS-3), and 10 (EKS-9) and grouped as series-D. The pH of the soil was measured by the pH meter, which was found to be 7.5. The pH of soil

was altered by adding NaOH pellets to make it alkaline and adding sulphuric acid to make it acidic. Firstly, trials were made on soil samples of 30 g to change its pH. Based on the calculations, NaOH pellets or H₂SO₄ solution was added to the whole soil for changing its pH. After adding a derived quantity of acid and base, the soil was kept overnight to get it with an equilibrium of pH value. Electrodes were arranged with one centrally located cathode and six anodes in hexagonal pattern. A potential difference of 5 V was applied. It was observed that soil with acidic (pH = 5, EKS-8) nature showed very less volume of water got collected at the cathode. As the pH of soil increases from 5 to 7.5 and 10, the amount of drained water increases (Fig. 7). The pH of soil is directly related to the hydraulic conductivity of soil. Thus, the soil with more alkalinity allows more volume of water to be drained out. During electrokinetic dewatering, corrosion of anodes takes place due to electrolysis that results in weight loss of anodes. To this effect, weight of anodes before and after each test was measured. The amount of corrosion of anodes was calculated in terms of average percentage weight loss of anodes. For pH of the soil equal to 5, 7.5, and 10, the percentage weight loss (corrosion) of anodes was observed to 9%, 4.75%, and 2.32%, respectively. This confirms that saturated soil with high acidity increases corrosion of anodes and reduces electrokinetic dewatering efficiency.

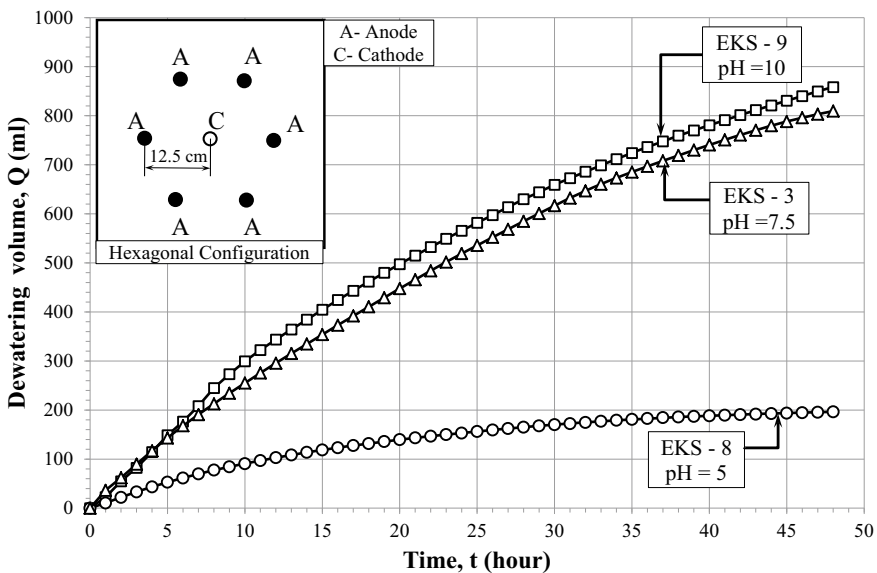


Fig. 7 Variation in dewatering volume with time for different pH of soil

4.5 Water Content Profile

Due to electrokinetic dewatering, water flows from anode to cathode, and it is collected at the cathode. It indicates that there is variation in water content around anode, cathode, and in between them. Because of this, it becomes essential to find out the variation in actual water content at different points on the surface of soil to get water content profiles. For this, the soil was divided into grids of 5 cm × 5 cm, and soil samples were collected from 81 points of grid for water content determination (Fig. 8).

To see the water content profile around anodes, cathode, and at various points, contour maps of water content are drawn for each test by using Surfer-16 software [21]. The contour map of water content for test EKS-8 is shown in Fig. 9. In this, dark gray color shows less water content and white color indicates maximum water content. It can be clearly seen that, as the water flows from anode to cathode, the areas near anode show water content of 37.5%. However, water content near the cathode

Fig. 8 Grids for water content determination

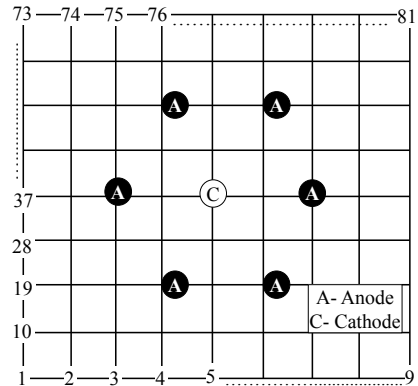
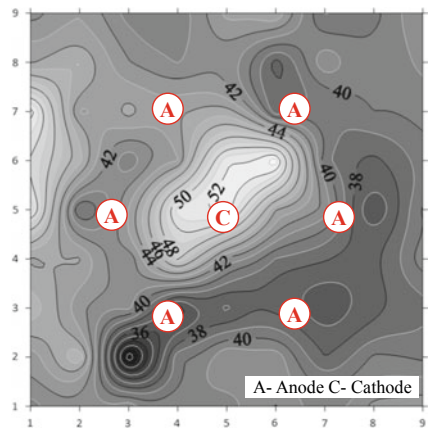


Fig. 9 Contour map of water content (EKS-8)



was calculated as 51.25%. In addition, water content was noticed to reduce only from an effective area between anode and cathode. The area outside of the electric field, which is near to sides of the box, did not experience much reduction in water content. As water is not totally removed at cathode, it shows maximum water content in the middle portion of the box.

5 Conclusions

Different series of experiments were performed to study the influence of various parameters on the performance of electrokinetic dewatering. Based on the results obtained from experiments, the following conclusions can be drawn.

1. The amount of water collected at the cathode was observed to increase with an increase in spacing of electrodes for constant potential difference, pH, and electrode configuration. It may be that an increase in spacing of electrodes that increases the area under the influence of an electric field causes more water to flow from anode to cathode.
2. For identical voltage and pH of the soil, the amount of water collected at the cathode was on the higher side for one-dimensional configuration when it was compared to hexagonal and rectangular configurations. In one-dimensional configuration, one cathode is installed for each anode, causing less acidic area that results in more efficient flow toward the cathode.
3. It was observed for a high number of anodes, the area of soil around the anodes becomes acidic due to electro-osmosis that reduces the flow of water toward the cathode.
4. It was found that the amount of drained water increases with an increase in soil's pH. It was due to an increase in alkalinity, i.e., increase of the pH of soil, which maximizes the flow of water. Alkalinity of soil reduces the corrosion of anodes that results in improving the efficiency of electrokinetic dewatering.

References

1. Mitchell JK (1993) Fundamentals of soil behavior. Wiley, New York
2. Acar YB, Alshawabkeh AN (1993) Principles of electrokinetic remediation. *Environ Sci Technol* 27(13)
3. Reuss F (1809) Sur un nouvel effet de l'électricité galvanique. *Mém de la Société Impériale des Naturalistes de Moscou* 2:327–336
4. Quinke G (1861) Ueber die Fortführung materieller Theilchen durch strömende Electricität. *Ann der phys* 113:513–598
5. Casagrande L (1949) Electro-osmosis in soils. *Geotechnique* 1(3):159–177
6. Azhar ATS, Azim MAM, Syakeera NN, Jefferson IF, Rogers CDF (2017) Application of electrokinetic stabilization (EKS) Method for soft soil. In: Komastu T (ed) IOP conference

- series: materials science and engineering, vol 226, international research and innovation summit (IRIS). Melaka, Malaysia
7. Malekzadeh M, Lovisa J, Sivakugan N (2016) An overview of electrokinetic consolidation of soils. *Geotech Geol Eng* 34(3):759–776
 8. Malekzadeh M (2016) Electrokinetic dewatering and consolidation of dredged marine sediments. Ph.D. Thesis James Cook University, Australia
 9. Wu HL, Hu LM, Wen Q (2015) Electro-osmotic enhancement of bentonite with reactive and inert electrodes. *Appl Clay Sci* 111:76–82
 10. Wu H, Hu LM (2014) Effects of electrode configuration on electro-osmotic consolidation. In: Bouazza A, Brown B, Yuen S (eds) 7th International congress on environmental geotechnics 11–1. Engineers Australia, Melbourne, Australia
 11. Zhou J, Tao YL, Xun CJ, Gong XN, Hu PC (2015) Electro-osmotic strengthening of silts based on selected electrode materials. *Soils Found* 55(5):1171–1180
 12. Kaniraj SR, Yee JHS (2011) Electro-osmotic consolidation experiments on an organic soil. *J Geotech Geol Eng* 29(4):505–518
 13. Flora A, Gargano S, Lirer S, Mele L (2016) Effect of electro-kinetic consolidation on fine grained dredged sediments. In: Gottardi G, Tonni L (eds) VIth Italian Conference of Researchers in Geotechnical Engineering - Geotechnical Engineering in Multidisciplinary Research: from Micro scale to Regional Scale, CNRIG2016 *Procedia Engineering*, vol 158. Elsevier. Bologna, Italy, pp 3–8
 14. Shang JQ (1997) Electrokinetic sedimentation: a theoretical and experimental study. *Can Geotech J* 34:305–314
 15. Reddy KR, Khodadoust AP (2006) Electro-osmotic dewatering of dredged sediments: bench-scale investigation. *Environ Manage* 78(2):200–208
 16. Malekzadeh M, Sivakugan N (2017) Double drain electrokinetic stabilization of dredged mud using stainless steel electrodes and application of surcharge. *KSCE J Civ Eng* 21(7):2615–2621
 17. Asavadorndej P, Glawe U (2005) Electrokinetic strengthening of soft clay using the anode depolarization method. *Article Bull Eng Geol Environ* 64(3):237–245
 18. Jeyakanthan V, Gnanendran CT, Lo CR (2011) Laboratory assessment of electro-osmotic stabilization of soft clay. *Can Geotech J* 48(12):1788–1802
 19. Rotte VM, Sutar AA, Patel A, Patel A (2021) Effect of various parameters on electrokinetic dewatering of saturated clay. In: Proceedings of Indian geotechnical conference (Paper accepted), 19 – 21 Dec 2019, NIT Surat, India
 20. Fourie AB, Jones CJFP (2010) Improved estimates of power consumption during dewatering of mine tailings using electrokinetic geosynthetics (EKGs). *Geotext Geomembr* 28(2):181–190
 21. Surfer, GOLDEN SOFTWARE (A trial version) (2016) Contouring, gridding and 3D surface mapping, USA

Evaluation of Mineral Formation in Sulfate Bearing Soil Stabilized with Slag Cement Using XRD



Mengting Chen , Hussein Al-Dakheeli , Jim Puckette ,
and Rifat Bulut 

Abstract In recent years, several studies have been conducted on the stabilization of sulfate bearing soils treated with ground granulated blast furnace slag (GGBFS), as a partial substitution for calcium-based stabilizers (mainly cement and lime). The treatment of sulfate bearing soils using only slag cement has not been evaluated. In this research, the effectiveness of treatment of sulfate bearing soil with slag cement alone was evaluated through investigating the mineral formation and the rate of hydration of slag cement by XRD analysis. The prepared sulfate bearing subgrade soil specimens (containing 5030 ppm sulfate content) treated with the 3, 5, and 7% of slag cement were investigated after moist curing for 7 and 28 days. The XRD analysis results indicate that there was no mineral formation in the specimens cured for 7 days. However, after curing for 28 days, both the formation of ettringite and calcite minerals have been observed. Gypsum, the soluble sulfate source in native soil samples, was not detected in the samples treated with 7% slag cement stabilized soil. The results indicate that curing period and percentage of slag cement contributed to the ettringite formation in the slag cement treated sulfate bearing soil.

Keywords Mineral formation · Slag cement · Sulfate bearing soil · XRD

1 Introduction

Calcium-based stabilizers (mainly lime and cement) have been utilized to stabilize subgrade soils for several decades now for increasing the strength, reducing the plastic index, aggregating the soil particles, and so forth [1, 2]. However, the soil will expand after the addition of the lime in the presence of soluble sulfate. The high content of calcium in lime releases the aluminum in the soil-lime mixture. The available calcium

M. Chen · H. Al-Dakheeli · R. Bulut (✉)

School of Civil and Environmental Engineering, Oklahoma State University, Stillwater, Oklahoma 74078, USA

e-mail: rifat.bulut@okstate.edu

J. Puckette

Boone Pickens School of Geology, Oklahoma State University, Stillwater, Oklahoma 74078, USA

and aluminum interact with the sulfate in the solution, producing a swelling mineral, ettringite [3]. This phenomenon is referred to as sulfate-induced heave in geotechnical engineering practice [4]. To solve this problem, the applications of different types of stabilizers to treat the sulfate bearing soils have been introduced. The partial substitution of lime with slag cement can reduce the swell of sulfate-containing soil based on reducing the amount of calcium oxide (CaO) in the chemical stabilizer [5].

Slag cement is a by-product of the steel or iron manufacturing process, and thus, it is also named as “Steel Slag” or “Iron Slag” in the literature as well. Slag cement is a hydraulic cement after granulated blast furnace slag (GGBS) is ground to suitable fineness. In the construction industry, the slag cement is used to replace a portion of Portland cement to enhance the strength and durability and provide protection against sulfate attack [5]. Researchers in geotechnical engineering substitute partially the lime with slag cement to reduce the sulfate-induced heave. Wild et al. [6] stabilized sulfate bearing clay soils by partial substitution of lime with slag cement. The swelling associated with ettringite formation was decreased with the addition of slag cement. Harris used different stabilizers including acid, emulsion, enzyme, polymer, lignosulfonate, slag cement, and fly ash to treat soil with more than 20,000 ppm concentration soluble sulfate in Texas and found the minimum swell was the soil treated by 5% slag cement mixed with 1% lime. The addition of 6% lime into sulfate bearing soil resulted in nearly 40% swell, while the use of 5% slag cement + 1% lime suppressed the swell to 8% [7]. Celik and Nalbantoglu [8] evaluated the effect of slag cement on expansive properties of lime treated sulfate holding soils in North Cyprus. In the presence of 6% slag, the swell potential of the lime-treated soil with 10,000 ppm sulfate concentration decreased from 8 to 1%, whereas the lime-treated soil with 5000 ppm sulfate concentration showed no swelling.

The treatment of sulfate bearing soil using only slag cement has not been reported in the literature. Since it is an industry by-product, slag cement is more affordable than lime and cement. The utilization of the slag cement can reduce the construction costs if no expansion issue arises when enhancing the strength of the soil with slag cement. Therefore, it is necessary to determine whether the slag cement can mitigate the swelling of the sulfate-containing soils. To achieve this goal, the investigation of the ettringite formation is important. Also, whether slag cement, like lime and cement, would induce ettringite production. This study focuses on resolving this question and uses X-ray diffraction (XRD) analysis to evaluate the production of ettringite in the sulfate bearing soil treated by 3, 5, and 7% slag cement.

2 Methods

Initially, the soluble sulfate content of the native soils from Oklahoma is determined following the Oklahoma Department of Transportation (ODOT) OHD L-49: *Method of test for determining soluble sulfate content in soil* [9]. The basic geotechnical properties of the native soils, i.e., grain size distribution, Atterberg limits, the optimum

Table 1 Details of specimens for XRD test

Slag cement content (%)	Curing period (d)	Specimen label
3	7	S3_7d
	28	S3_28d
5	7	S5_7d
	28	S5_28d
7	7	S7_7d
	28	S7_28d

water content, and maximum dry density are measured following the ASTM standards. The mineral composition of native soils and that of slag cement treated soil is obtained by X-ray diffraction (XRD) analysis. The chemical composition of slag cement is investigated using X-ray fluorescence (XRF) analysis.

2.1 Test Sample Preparation

The native soil after passing sieve No. 40 (0.425 mm), and mixing it well, was divided into three parts. Each part of the soil was mixed separately with 3, 5, and 7% by weight of dry slag cement, mixing the dry particles thoroughly, adding water above the soil's liquid limit value. To ensure adequate water to complete the chemical reactions, the water content (above the value of liquid limit) of the mixture was brought to 30%. After stirring the mixtures thoroughly, the slurry state specimens were put into plastic cups, and the cups were sealed in plastic bags to avoid any moisture loss. All the sealed specimens were placed in an ice chest for curing 7 days at room temperature (22 °C). The sample preparation procedure described above was followed for the specimens cured for 28 days as well. After the curing period, specimens were removed from the ice chest and sealed bags for air drying at the room temperature and crushed into fine powder and thoroughly mixed before the XRD analysis. The details of the testing program for XRD are shown in Table 1.

2.2 X-ray diffraction

X-ray diffraction is still the primary method used today for identifying minerals in fine-grained soils because different minerals have unique spacings of interatomic planes (i.e., d -spacings) [10, 11]. The XRD results provide the position of diffraction peak (i.e., 2θ angles). The d -spacings within the crystal lattice can be calculated from 2θ angles, allowing for mineral identification. The value of d -spacings correspond to the 2θ angle can be calculated according to Bragg's law,

$$l\lambda = 2d \sin \theta \quad (1)$$

where the value of l would be any whole number.

When $l = 1$, the reflection is referred to as the first-order reflection, $l = 2$ corresponds to second order reflection, and so on. When identifying minerals, all series of reflections should be considered in case some of the reflection beams are interfered [10]. In fact, the second order reflection and next order reflection might not be shown in the diagram because of the limitation of the range of 2θ angles. Therefore, the value of 2θ angles or the d -spacings from the first-order reflection (i.e., $l = 1$) should be prioritized to identify the mineral [10].

For this study, the XRD analysis was performed in the Oklahoma State University Microscopy Laboratory, Stillwater, Oklahoma. The X-ray diffractometer is Bruker D8 Advance (Cu Ka radiation with 1.5406 Å of wavelength) run at 40 kV/40 mA with Lynxeye detector. The identification analysis was performed based on the Joint Committee on Powder Diffraction Standards, and American Society for Testing Materials-*Mineral Powder Diffraction File: Search Manual* (JCPDS) [12]. The data were utilized to identify the minerals in this study are displayed in Table 2, and the identification procedure is summarized as follows [12]:

1. Calculated d -spacings correspond to the 2θ provided by the XRD diagram.
2. Used the calculated value of d -spacings to locate the mineral in the JCPDS file to achieve the preliminary identification.
3. The second order reflection and third order reflection were considered to achieve the final identification.

Table 2 Mineral name, d -spacings, chemical formula, and variation provided by the JCPDS standard manual file for identification minerals in the soils tested in this study [12]

Mineral name	Chemical formula	File No.	d -spacings(Å)	Variation
Albite	NaAlSi ₃ O ₈	9-466	6.39	± 0.10
Augite	Ca(Mg,Al,Fe)Si ₂ O ₆	24-202	2.99	± 0.01
Calcite	CaCO ₃	5-586	2.10	± 0.01
Ettingite	Ca ₆ Al ₂ (SO ₄) ₃ (OH) ₁₂ ·26H ₂ O	9-414	5.61	± 0.05
Gypsum	CaSO ₄ ·SO ₄	6-46	7.56	± 0.10
Halloysite	Al ₂ Si ₂ O ₅ (OH) ₄	9-453	4.42	± 0.03
Illite	K(Al,Mg) ₃ Si ₃ Al ₁₀ (OH) ₂	9-343	10.0	± 0.10
Kaolinite	Al ₂ Si ₂ O ₅ (OH) ₄	14-164	7.17	± 0.10
Quartz	SiO ₂	5-490	3.34	± 0.03

3 Material

3.1 Soil

Native soil was sampled in Woodward, Oklahoma, close to US Highway 412. After drying the sample in room temperature and removing the plant residues, the soil was crushed into smaller size for sample preparation and laboratory testing. The processed soil was tested for soluble sulfate concentration following the OHD L-49 method [9]. Engineering properties of the soil were investigated following the corresponding ASTM standard test methods [13–15]. The mineral components in the soil were obtained by X-ray diffraction (XRD) analysis. The information on soluble sulfate concentration, physical soil properties are listed in Table 3, whereas mineral compounds are listed in Table 4.

The soluble sulfate concentration is 5030 ppm, which is high enough to achieve the level for triggering sulfate-induced heave [16]. According to the investigation of engineering properties of the native soil, the soil was classified as ML. Five non-clay minerals were identified in the native soil, and the clay minerals, kaolinite, illite, and halloysite were detected after XRD analysis. Gypsum, a soluble sulfate mineral, was found in the native soil samples.

Table 3 Soluble sulfate concentration, engineering property of the native soil

Soluble sulfate concentration (ppm)	5030
$\leq 2 \mu\text{m}$ (%)	27.0
Liquid limit (%)	26.0
Plastic limit (%)	NP
Plastic index	NP
AASHTO class	A-4(0)
USCS class	ML
Maximum dry density (MDD) (g/cm ³)	1.88
Optimum moisture content (%)	12.0

Table 4 Mineral compounds of the native soil investigated by XRD analysis

Mineral	Chemical formula
Albite	$\text{NaAlSi}_3\text{O}_8$
Augite	$\text{Ca}(\text{Mg}, \text{Al}, \text{Fe})\text{Si}_2\text{O}_6$
Gypsum	$\text{CaSO}_4 \cdot \text{SO}_4$
Halloysite	$\text{Al}_2\text{Si}_2\text{O}_5(\text{OH})_4$
Illite	$\text{K}(\text{Al}, \text{Mg})_3\text{Si}_3\text{Al}_{10}(\text{OH})_2$
Kaolinite	$\text{Al}_2\text{Si}_2\text{O}_5(\text{OH})_4$
Quartz	SiO_2

Table 5 Chemical composition for slag cement investigated by XRF analysis

Oxide composition	%
CaO	43.08
SiO ₂	39.02
Al ₂ O ₃	8.62
SO ₃	3.32
MgO	3.15
TiO ₂	1.07
K ₂ O	0.64
MnO	0.61
Fe ₂ O ₃	0.49

3.2 Slag Cement

The slag cement used in this study is supplied by the local branch of of Skyway Cement Company in Tulsa, Oklahoma. The chemical composition of the slag cement was determined using X-ray fluorescence (XRF) analysis as depicted in Table 5.

4 Results

The XRD test results for the specimens cured for 7 days present that there are no changes in the XRD pattern diagram (shown in Fig. 1) as compared to the XRD diagram obtained for the native soil. However, after the specimens are cured for 28 days, changes in the XRD diagram are observed as depicted in Fig. 2. This indicates that the longer curing period promoted the mineral formation from the samples of the slag cement and sulfate bearing soil mixtures. In other words, the slag cement hydration had not taken place within the 7 days of the curing period. For the specimens cured for 28 days, the formation of ettringite was detected, indicating that the reactions between the calcium, alumina, silica, and sulfate require longer curing time for ettringite precipitation. The production of calcite was also detected in the specimens cured for 28 days with 5 and 7% slag cement contents. The formation of calcite was probably due to the exposure of the mixtures to air in the laboratory. After curing for 28 days, gypsum was detected in the specimens treated with 3 and 5% slag cement, whereas there was no gypsum in the specimen stabilized with 7% slag cement. This probably means the higher percentage (7%) of slag cement depleted all the soluble sulfate in the specimen during hydration.

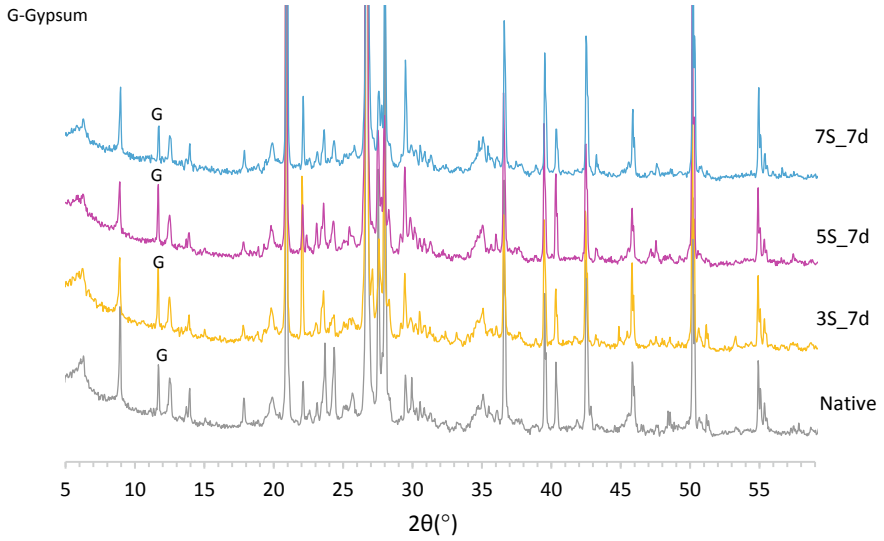


Fig. 1 XRD diagram for native soil and specimens mixed with 3, 5, and 7% of slag cement after curing 7 days

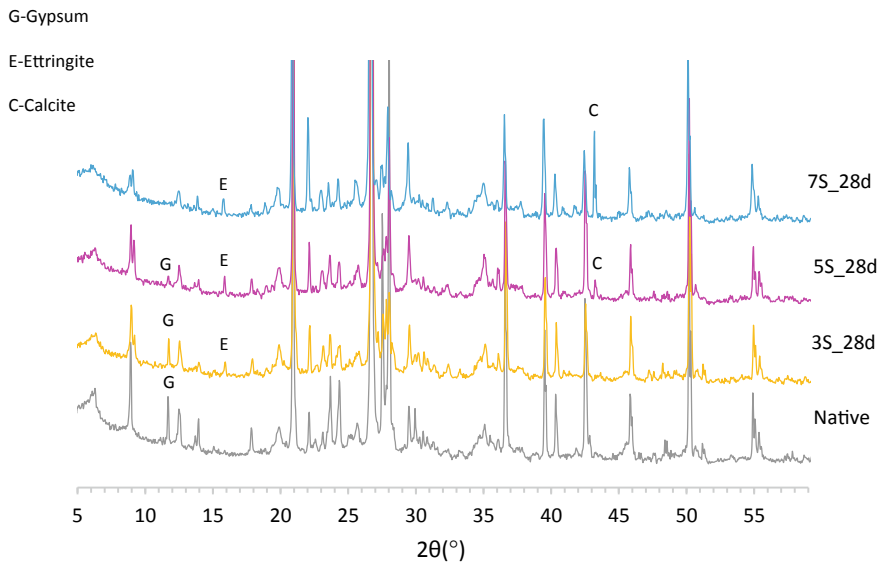


Fig. 2 XRD diagram for native soil and specimens mixed with 3, 5, and 7% of slag cement after curing 28 days

5 Discussions

The result from the XRD analysis for mineral identification in the sulfate bearing soil stabilized with slag cement demonstrates that the ettringite mineral has formed, and the rate of slag cement hydration was slow. The increase in the amount of slag cement also promoted ettringite formation. Those observations are attributed to the following reasons:

1. The ettringite is generated during the reaction between sulfate and alumina in the presence of calcium [3]. The calcium, alumina supplied by hydrated slag cement and dissolved clay minerals, kaolinite and halloysite, reacted with the gypsum to produce the ettringite.
2. Unlike in lime, the proportion of CaO in slag cement is smaller resulting in the lower concentration of $\text{Ca}(\text{OH})_2$ generated by the reaction between CaO and water. Afterward, lesser amounts of OH^- ion are released during the ionization process of $\text{Ca}(\text{OH})_2$. A high concentration of OH^- ion is commonly known as an activator in the process of slag cement stabilization to break the bond between Ca – O and Al – O. Thus, in this study, the concentration of OH^- ion was insufficient to improve the rate hydration of slag cement.
3. The OH^- ion also can release the Al^{3+} from slag cement and clay minerals to produce the $\text{Al}(\text{OH})_4^-$ molecule which combined with the OH^- ion and dissolved gypsum to induce ettringite formation [17]. The increase in percentage of slag cement raised the concentration of OH^- ion, causing more gypsum to dissolve to form ettringite. In this study, when percentage of slag cement increased to 7%, all the gypsum was dissolved and utilized in the ettringite formation (shown in Fig. 2). Thus, the percentage of slag cement also plays an important effect on the ettringite formation.

6 Conclusions

The main points of this study in the investigation of mineral formation in the soils treated by slag cement through XRD analysis are summarized as follows:

1. The formation of ettringite and calcite has occurred from dissolution of gypsum when stabilizing sulfate bearing soil with slag cement.
2. The rate of slag cement hydration is slow.
3. The percentage of slag cement is important in the formation of minerals.

7 Recommendations

The relation between the amount of ettringite formed in sulfate bearing soil stabilized with slag cement and the amount of soil swelling was not investigated in this study.

Therefore, a quantitative analysis of ettringite formation using XRD analysis and the volume change of slag cement treated sulfate bearing soil should be investigated in further studies.

Acknowledgements The authors would like to thank the Oklahoma Department of Transportation (ODOT) for funding this study and the Skyway Cement Company for providing the slag cement.

References

1. Diamond S, Kinter EB (1965) Mechanisms of soil-lime stabilization. Highway Res Rec 92:83–102
2. Thompson MR (1966) Lime reactivity of Illinois soils. J Soil Mech Found Div 92(5):67–92
3. Rajasekaran G (2005) Sulphate attack and ettringite formation in the lime and cement stabilized marine clays. Ocean Eng 32(8–9):1133–1159
4. Adams AG et al (2008) Sulfate induced heave in Oklahoma soils due to lime stabilization. Geotechnical Special Publication
5. Higgins D (2005) Soil stabilisation with ground granulated blastfurnace slag, pp 1–15
6. Wild S et al (1999) Suppression of swelling associated with ettringite formation in lime stabilized sulphate bearing clay soils by partial substitution of lime with ground granulated blastfurnace slag (GGBS). Eng Geol 51(4):257–277
7. Harris P et al (2006) Recommendations for stabilization of high-sulfate soils in Texas, in Transportation Research Record, pp 71–79
8. Celik E, Nalbantoglu Z (2013) Effects of ground granulated blastfurnace slag (GGBS) on the swelling properties of lime-stabilized sulfate-bearing soils. Eng Geol 163:20–25
9. DOT O (2005) OHD L-49: method of test for determining soluble sulfate content in soil
10. Moore DM, Reynolds RC (1989) X-ray diffraction and the identification and analysis of clay minerals, vol 322. Oxford University Press, Oxford
11. Mitchell JK, Soga K (2005) Fundamentals of soil behavior, vol 3. John Wiley & Sons Hoboken, NJ
12. Joint Committee on Powder Diffraction Standards, a.A.S.f.T.M. (1980) Mineral powder diffraction file search manual: chemical name, Hanawalt, Fink, Mineral Name. JCPDS
13. Standard Test Method for Particle-Size Distribution (Gradation) of Fine-Grained Soils Using the Sedimentation (Hydrometer) Analysis
14. Standard Test Methods for Laboratory Compaction Characteristics of Soil Using Standard Effort (12 400 ft-lbf/ft³ (600 kN-m/m³))
15. Standard Test Methods for Liquid Limit, Plastic Limit, and Plasticity Index of Soils
16. Petry TM, Little DN (1992) Update on sulfate-induced heave in treated clays: problematic sulfate levels. Transp Res Rec 1362:51–55
17. Hunter D (1988) Lime-induced heave in sulfate-bearing clay soils. J Geotech Eng 114(2):150–167

CBR Characteristics of Kaolin-Simulated Clay Type Subgrade Stabilised with Cement, Lime, Poly-Fibre and Ionic Compounds mix



Chee-Ming Chan, Abdul Rashid Ahmad Nasri, Poi-Cheong Tan, and Danny Ng

Abstract Soil chemical stabilisation is an effective soil improvement method involving the blending of hydraulic binder with an existing soft soil to enhance the geotechnical properties for improved mechanical performance. Arguably time- and cost-saving as well as less labour-intensive with minimum skill requirement, it is a favourable solution to the construction of rural and farm roads in often economically challenged and resources deprived regions, especially for sites overlying soft grounds like clay deposits. The present study explores the feasibility of stabilising clay type subgrade with a proprietary hydraulic binder admixed with fibrillated polypropylene fibres. The binder—0.9% fibre mix was blended with the base clay of kaolin at optimum water content, in dosages of 0, 1.5 and 4.0% per dry weight of the soil. Soaked and unsoaked CBR tests were carried out on the stabilised specimens at intervals of 3, 7, 14 and 28 days in duplicates to attain the targeted minimum CBR value of 5% stipulated by Malaysian Public Works Department. Stabilisation dosage of 1.5% was found to be inadequate under soaked conditions even with prolonged curing up to 28 days. It was only at 4% dosage that the 3-day old soaked specimen could meet the minimum requirement. 1.5% dosage treatment for the unsoaked specimens recorded CBR values of 12.1–25.0% after curing for up to a week, while a fortnight curing with the 4% dosage specimen raised the CBR value to >30. Overall, the soaked specimens attained about half the strength of the unsoaked ones, with 14 days observed to be the threshold before the strength increment rate plateaued. In summary, the binder-fibre mix could effectively strengthen the clay soil with higher dosages offsetting the curing time, though subject to dry or soaked curing conditions.

Keywords CBR · Clay soil subgrade · Hydraulic binder · Polypropylene fibre

C.-M. Chan (✉) · A. R. A. Nasri

Faculty of Engineering Technology, Universiti Tun Hussein Onn Malaysia, Johor, Malaysia

e-mail: chan@uthm.edu.my

P.-C. Tan · D. Ng

MTS Fibromat (M) S/B, Selangor, Malaysia

1 Background

1.1 Introduction

General roads function as a land-based communication medium for people to connect with each other, hence play an important role in supporting various socio-economic activities of a country [1]. Rural roads in particular are essential to reach plantation and sub-urban areas. High traffic volume and load exceeding the intended design could lead to damages of the infrastructure.

Primarily of the flexible pavement category, i.e. a layered structure consisting of several layers in the order of subgrade, sub-base course, base course, binder course and wearing course [2], the design of rural roads takes into account parameters like wheel load, traffic intensity, climatic conditions, subgrade strength and terrain conditions [3]. Note that subgrade functions as the foundation supporting layer, where volume stability of a pavement is highly dependent upon. As the sub-urban is often under-developed due to poor soil conditions, among other reasons, laying of these roads face the inevitable challenge of subgrade material with low engineering qualities, including low strength and bearing capacity as well as high and non-uniform compressibility behaviour.

In order to ensure stability of the rural road lain on these poorly soils, pre-treatment such as chemical stabilisation is required. Tan [4] reviewed past literature and summarised that chemical stabilisation methods could bring about improvement of soil strength, mitigation of total and differential settlements, shortening of construction period and reduction of construction costs. Essentially, the method eliminates the necessity to remove and replace existing material on site, but effectively reusing it via prior improvement techniques, rendering the stabilisation approach more economically and environmentally viable to a significant extent.

The present work explored stabilisation of simulated clay type subgrade using a proprietary hydraulic binder admixed with a small quantity of polypropylene fibres (0.9%) for structural reinforcement. Indeed, the industry partnership project aimed to identify the application potential of the stabiliser in clay type subgrade, as it has, thus, far been successfully applied in granular material treatment. Adhering to current field practice of 4% stabiliser addition to recycled road base materials, which is mainly a sandy crusher-run mixture, kaolin clay powder (simulating clay type subgrade material) was premixed with the stabiliser at 0, 1.5 and 4.0% per dry weight of the soil, compacted at the optimum water content of the clay-stabiliser mix. Left to cure for up to a month in soaked and unsoaked conditions, CBR test was then performed on the samples at interval ages of 3, 7, 14 and 28 days to gauge the strength development pattern.

1.2 Technical Literature

Poor Subgrade Soils. Soils comprise of an array of particles of different shapes, sizes and quantities. Grain size analysis divides the soil into two main size groups, i.e. coarse-grained and fine-grained soil. Coarse-grained soils include sand, rock, cobbles, gravel and boulder, while fine-grained soils refer to clay and silt. Engineering soil classification systems are used to classify soils into groups and subgroups based on common engineering properties. The Unified Soil Classification System (USCS) and American Association of State Highway and Transportation Official (AASHTO) classification system are among the most widely used, apart from the respective nation-based codes. The soil examined in the present work is clay of the fine-grained family, which poses severe problems in terms of rural road construction and performance due to their poor engineering properties. Pavement damages like premature distresses, potholes and shoulder slippage are among the disruptions to the safety and performance of roads [5].

A fine-grained soil can exist in different states, depending on the amount of water in the soil system. Due the susceptibility of fine-grained soils to water in its composition, Atterberg limit tests on the soil's plasticity are essential to the classification process. With water added to a dry soil, each particle is encapsulated in a film of adsorbed water. Thickness of the water film around the particles would increase with increased addition of water, to an extent where the particles are able to slide past each other more smoothly. Outwardly, this would manifest as the soil lump transforming into a crumbly malleable form, or being 'plastic'. Continuous addition of water would push the soil particles apart from each other as excess water in the system flocculates the solids, turning the soil into a flowable form, or 'being liquid'. The former water content at which the soil begins to demonstrate plastic behaviour is termed 'plastic limit', and the water content at the latter state where the soil starts to become flowable is the 'liquid limit'. Derivation of the indices, i.e. liquidity and plasticity, is calculated from these Atterberg limits for classification of a fine-grained soil sample.

In simple terms, stabilisation would change the water content of a soil to fall within the relevant Atterberg limits, so as to be stronger and stiffer in a permanent or temporary manner. This is achieved by reduced water content in the soil (becoming less liquid and more plastic) and induced cementation (chemical reactions) binding the soil particles together.

Stabilisation. Stabilisation would enhance the engineering performance the existing ground, i.e. subgrade, by blending chemical additives in situ. The positive stabilisation outcomes encompass the following: improvement of strength, workability, stiffness, swelling characteristics and bearing capacity of the originally poorly soil [6]. It follows that stabilisation serves two purposes in road building, namely to provide a safe, comfortable and durable surface for the motorists and to reduce excessive stress on the underlying soil by providing a stronger load-bearing subgrade [7].

A wide variety of binding agents is available in the market for road construction, for example, Portland cement, lime, recycled ashes, furnace cement mixtures and other chemical substances such as sodium and calcium chloride. In addition, agricultural and industrial by-products or wastes have been reportedly used in stabilisation works, such as jute, rice husk, palm fibre, nylon fibre, aluminium or iron residues, fly ash and coal [4]. These additives serve as reinforcement elements for better bondage of the soil particles post-treatment. One example is the discrete polypropylene fibres which has been proven expedient for internal reinforcement of concrete [8], elevating the material's engineering performance with increased post-cracking integrity and toughness as well as reduced plastic shrinkage and substance cracking.

Apparently the stabilisation technique has the advantage of improving the subgrade load-bearing capacity at relatively lower consumption of time, labour and costs and simultaneously minimising waste generation by reusing in situ soils instead of the conventional remove-and-replace approach normally adopted for such problematic soils encountered on site. Besides the global 'green construction', awareness and movement have driven the revival of various, otherwise, discarded materials from the agricultural and industrial sectors as mentioned above. These 'wastes', incorporated in the soil stabilisers, would make further augmentation of the sustainability values of the products and technique, as most of the additives can be sourced locally.

2 Materials and Methods

2.1 Kaolin

Pure kaolin powder was adopted in the present study to simulate clay type subgrade soil. The Kaolin (FM-C) powder (Fig. 1) used was manufactured by Kaolin (Malaysia) S/B. It was an odourless white powder, widely used in the paper, ceramic and cosmetic industries. Mainly comprising of the clay mineral kaolinite, i.e. hydrous aluminosilicate, $\text{Al}_2\text{O}_3 (\text{SiO}_2)_2 (\text{H}_2\text{O})_2$, kaolin is insoluble in water but darkens

Fig. 1 Kaolin in dry powder form



Fig. 2 Stabiliser: binder and fibres



slightly and produces an earthy odour when mixed with water. The kaolin had very low water content, <2% and pH ranging between 3–5. Chemical composition-wise, the clay powder contained mainly aluminium (Al_2O_3) 30–36% and silica (SiO_2) 49–55% with loss on ignition (organic matter content) at 1025 °C 8–12%.

2.2 Stabiliser: Binder + Fibres

The proprietary binder, a mixture of cement, lime, poly-fibre and ionic compounds were reddish pink in colour (Fig. 1). Polypropylene fibre, an abundantly available polymer at low costs is known to have good resistance against most chemical attacks. The high melting point of polypropylene, i.e. 165 °C indicates that the fibre can withstand working temperature of 100 °C for short periods without detriment to fibre properties [7]. A small quantity of the 18.4 mm long fibres was premixed with the binder to form the stabiliser. Note that the fibres were admixed in its original net-like or fibrillated form (Fig. 2), but the mixing process is known to largely break the fabric down into individual filaments. The fibres were also reported to be expedient for plastic shrinkage and non-structural temperature shrinkage control in concrete and properties believed to be similarly beneficial for road building materials.

2.3 Preparation of CBR Samples

The stabiliser was admixed with the kaolin powder at 1.5, 2.5 and 4.0% per dry mass of the clay. The predetermined dosages were governed by two factors: (1) current practice of the proprietor based on field experience, i.e. no more than 4% and (2) past literature of similar binding agents used in clay soils. The samples were labelled accordingly, e.g. 4.0B3d represents 4% stabiliser at 3 days curing.

The theoretical mixing water content was identified via standard compaction test for each mixture. However, the actual mixing water content was an additional 2% to the optimum water content (w_{opt}) determined from the tests. This was to cater

Table 1 Standard compaction test results

Specimen	Optimum moisture content, w_{opt} (%)	Maximum dry density, ρ_{dmax} (g/cm ³)
0B	24	1.45
1.5B	24	1.45
2.5B	24	1.42
4.0B	26	1.34

for water evaporation under the sunlight as commonly encountered on site, as well as to ensure the stabiliser had sufficient moisture for full reaction. Table 1 shows the compaction test results, where the small stabiliser dosages apparently had little effect on both w_{opt} and ρ_{dmax} , except for 4.0 S which recorded slightly higher w_{opt} but lower ρ_d .

The kaolin, stabiliser and water mixture were mixed in a mechanical mixer: at low speed for the first 2 min followed by rapid mixing for the following 13 min. The prolonged mixing was to prevent non-uniform distribution of the binder and fibres, especially. The well-mixed composite material was next transferred to the CBR mould.

2.4 CBR Test

The California bearing ratio (CBR) test is essentially a penetration test for evaluating the strength for pavement component layers. The results are usually correlated with the respective thickness of the component layers established empirically in standard references.

Referring to British Standard 1924: 1990 (Part 2), the material was introduced into the CBR mould to form samples measuring 150 mm in diameter and 115 mm in height, where a 10 mm base plate and 50 mm collar were placed at the bottom and top of the mould, respectively. Note that a perforated base plate was adopted for the soaked samples. Compaction of the material was carried out with 27 blows of a 4.5 kg drop hammer (fall height 300 mm) in 5 layers. Depending on whether the curing condition was soaked (S) or unsoaked (US), surcharge weights amounting to 2.5 kPa were placed over the compacted sample in the water bath for the latter during curing. This was to prevent swelling of the sample due to water infiltration. Note that curing of all samples were carried out at average room temperature of 25 °C. During the test, a 50 mm diameter plunger was pushed through the sample at 1.25 mm per minute penetration rate, and the resultant force was recorded. By dividing the corresponding load with the standard force at a certain penetration depth in Table 2, the CBR value was obtained and reported in percentage format. The value at 2.5 mm penetration depth was reported as the adopted CBR value.

Table 2 Standard force—penetration relationship for compacted stones of CBR = 100%

Penetration (mm)	Standard force, P _{std} (kN)
2.0	11.5
2.5	13.2
4.0	17.6
5.0	20.0
6.0	22.2
8.0	26.3
10.0	31.8

3 Results: Analysis and Discussion

3.1 CBR Test Plots

Figure 3 shows the calculated CBR values plotted against the penetration depth up to 10.0 mm (see Table 2) for all soaked and unsoaked samples. For convenience of the readers, the ensuing discourse refers to the 28-day CBR value at 2.5 mm penetration as the ultimate load resistance of the sample unless otherwise mentioned. In general, all stabilised samples registered a sharp rise upon loading followed by quick decline beyond 2.5 mm penetration. The load resistance was considered to be levelled out by 10 mm penetration for all cases, as depicted in the plots. From Fig. 3, a couple of obvious observations can be made.

Firstly, the soaked curing conditions simulating runoff infiltration and water retention in the subgrade made significant negative impact on the efficacy of the stabiliser’s strengthening effect. This is especially detrimental for samples with 1.5% stabiliser addition, which produced four times less strength compared to the unsoaked counterparts, with limited improvement over time too as noted from the closely spaced plots of S1.5B. The pronounced lack of strength gain in S1.5B in spite of prolonged curing indicates obliteration of the stabilising effect by the excess water.

Secondly, 4% stabiliser addition resulted in marked improvement of the material’s load resistance, even in soaked curing conditions. This is evident in the comparison between US4.0B and S4.0B at 28 days which showed barely 10% difference in strength. Also, 4% stabiliser was found to be adequate to overcome the negative effect of excess water intrusion during soaked curing, though with a lower strength gain rate compared to the unsoaked samples. Nonetheless at the same curing age, US1.5B showed about 20% less strength than US4.0B, suggesting the possibility of reducing the stabiliser dosage if the initial water content of the compacted material can be kept low.

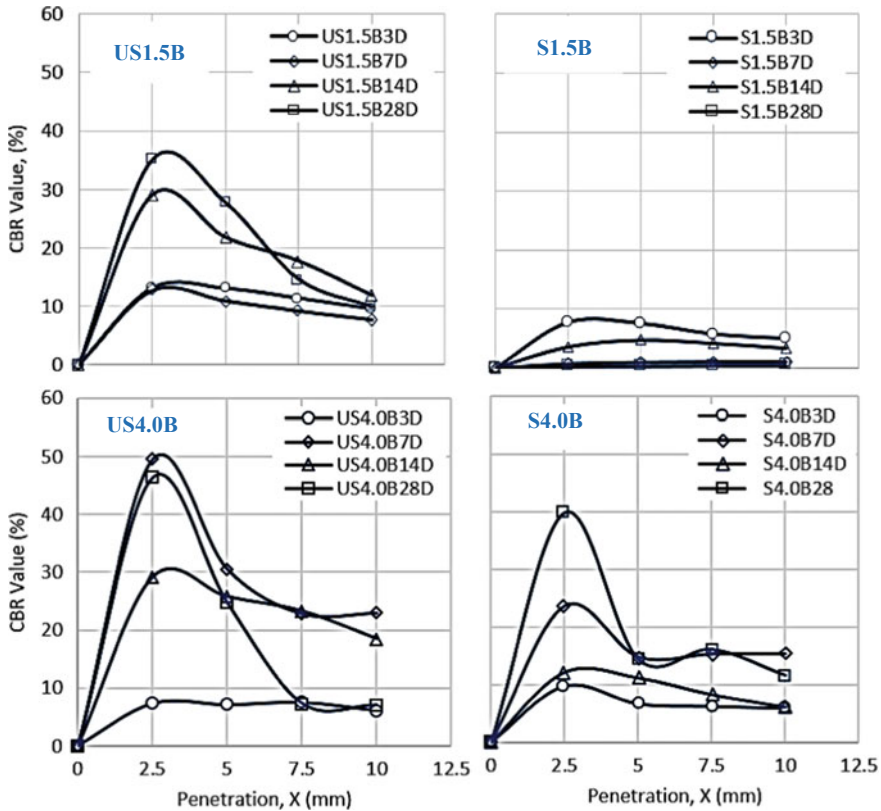


Fig. 3 CBR—penetration relationship for soaked and unsoaked samples

3.2 Strength Development Over Time

The force (P) is plotted against the CBR values in Fig. 4. While the relationship is understandably linear as per the equation, i.e. $CBR (\%) = (P/P_{std}) \times 100\%$, these plots give an overview of the strength development over the 28-day curing period. For 1.5B, samples subjected to soaking underwent negligible strength improvement as mentioned in 3.2. The truncated plot in S1.5B verified the limited strength gain. For the same binder dosage in samples left to cure dry (US1.5B), P increased up to almost 5 kN within 28 days, where a week appeared to be the threshold period for marked strength improvement to take place. For S4.0B, this interval was also noted at 7-day lapse, with subsequent 3.3 times strength improvement between the 7-day and 28-day old samples. Under unsoaked conditions, 4% stabiliser addition to the clay showed gradual strength gain over time but 14 days seemed adequate for almost 70% of P_{28d} to be attained. These charts could be useful as a quick guide to the strength improvement pattern of the stabilised material where time is an important factor for field evaluation of the targeted strength achievement.

3.3 Stabilised Depth Variability

The CBR test samples were prepared in compacted layers and assumed to be uniform and homogeneous throughout the depth. This may not necessarily be true, especially for samples that underwent more significant improvement. The CBR values corresponding to 2.5, 5.0, 7.5 and 10.0 mm penetration depths for all samples are grouped according to the stabiliser dosage and plotted in Fig. 5. These plots are useful for analysis of strength improvement behaviour of the stabilised soil in conjunction with Fig. 3 and Sect. 3.2.

In general, the highest CBR values were recorded at 2.5 mm, followed by the other depths in ascending order, i.e. lower strength for greater depths. Interestingly, CBR value for all the 1.5B samples seemed to dip within the first week, except for US2.5 mm which underwent gradual strength increase within the period and more robust strength gain later on. This continuous strength gain can be observed up to 5.0 mm depth only, beyond which a decrease in CBR value was recorded. Similar observations can be made for the US4.0 samples, though sample US5.0 mm showed almost constant strength after 2 weeks curing.

Also, it is apparent that excessive moisture obliterated the compaction effect where strength was rather uniform for all depths for the soaked 1.5B samples. In the case of 4.0B, soaking retarded strength gain from 7 days onwards, as depicted by the

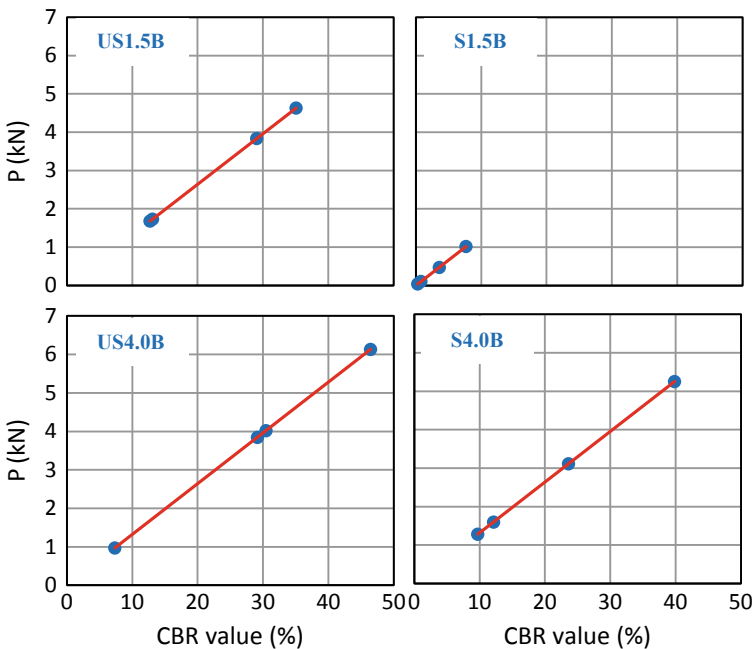


Fig. 4 Penetration force (P)—CBR value correlation over 28 days curing

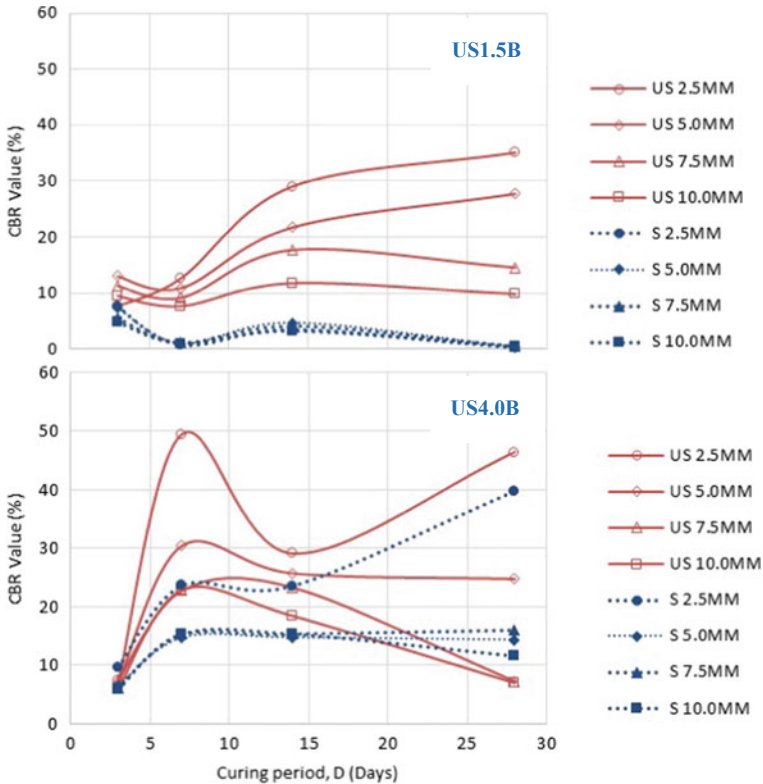


Fig. 5 CBR—curing time plots for samples treated with 1.5 and 4.0% stabiliser

plateaus in the plots. Exception was found in sample S4.0B2.5 mm which plateaued from day 7 to 14, followed by a sharp rise to 40% CBR value 2 weeks later. For the unsoaked samples 4.0B samples, strength improvement was dramatic initially up to a week before a severe drop took place in the second week. This is especially evident at 2.5 mm penetration depth, but the strength clearly picked up again in the final 2 weeks of curing.

4 Conclusions

In accordance with the Malaysian Public Works Department manual ATJ 5/85 (2013) [2], the minimum strength requirement for subgrade is a 5% CBR for supporting design traffic volumes ranging from <10 to >30 ESAL × 10⁶, where ESAL is the equivalent standard axel load, taken as 80 kN in Malaysian practice (see Sect. 2.2 in ATJ 5/85 [2]). Overall S1.5B samples failed to qualify as acceptable subgrade, with CBR < 5%. Other samples fulfilled the criterion. However, Sect. 2.4 in the same

manual cautions that for design traffic $> 10 \text{ ESAL} \times 10^6$, minimum subgrade strength corresponding to CBR value of 12% is recommended. From the present work, it is shown that only the unsoaked samples of treated kaolin meet this requirement. Indeed US1.5 could meet the minimum 12% CBR value in 3 days too. In conclusion, the proprietary stabiliser could potentially produce clay type subgrade of good strength provided excess moisture is kept out, while the composite material matures with time. This could be verified with further experiments on soil samples retrieved from site, followed by in situ pilot study with appropriate instrumentation for the improved performance monitoring.

Acknowledgements The project is made possible via collaboration with MTS Fibromat (M) S/B, who provided research materials and funds for the study. Technical support and assistance by the laboratories at UTHM are duly acknowledged too.

References

1. Khan AJ, Ahmed SS, Hossain N, Islam MS (2016) Prediction of soaked CBR using index properties, dry density and unsoaked cbr of lean clay. *Malays J Civil Eng* 28(2):270–283
2. Jabatan Kerja Raya Malaysia (2013) Public Works Department of Malaysia. ATJ 5/85 (Pindaan / Amendment 2013) Manual for the Structural Design of Flexible Pavement
3. Yashas SR, Harish SN, Muralidhara HR (2016) Effect of California bearing ratio on the properties of soil. *Am J Eng Res (AJER)* 5(2):28–37
4. Tan KL (2017) Chemical stabilization of clay soil as road base for rural road. Universiti Tun Hussein Onn Malaysia: Bachelor's Degree Final Year Project: Thesis
5. Prabhakar K, Reddy KR (2016) Strength characteristics of coir fibers and fly ash on soil. *Int J Eng Sci Comp* 6(10):2961–2969
6. Gupta D, Kumar A (2016) Strength characterization of cement stabilized and fiber reinforced clay-pond ash mixes. *Int J Geosynthetics Ground Eng* 2(4):32
7. Kanalli SA, Palankar R, Kumar B, Kumar P (2014) Comparative study of polymer fibre reinforced concrete with conventional concrete pavement. *Int J Res Eng Technol* 3(1):139–143
8. Parasor SJ (2017) Application of polypropylene fibre as a reinforced concrete. *Int J Eng Res Mech Civil Eng* 2(11):38–41

Influence of Moisture Content on Strength of Stabilised Drilling Slurry



Mingwei Feng, Juan Wang, Shu Liu, and Yunfeng Hu

Abstract Waste drilling slurry from cast-in-place pile construction, after dewatering and stabilisation processes, could be reused as pavement foundation materials. One of the most important factors that influence the strength of the stabilised drilling slurry is the moisture content of the dewatered drilling slurry before stabilisation, which, however, is difficult to control in engineering practice. In this paper, dewatered drilling slurry from a construction site was prepared at different moisture contents and treated with various contents of cement. Through a series of unconfined compressive strength tests and CBR tests, it was found there was a linear relationship between cement content and material strength at any specific moisture content. A contour plot was also developed, which can be used to guide the stabilisation of the dewatered drilling slurry at various moisture contents to achieve a target strength. This was then applied to the treatment of the drilling slurry in an on-site plant and the results match prediction.

Keywords Dewatered drilling slurry · Moisture content · Stabilisation · Unconfined compressive strength

1 Introduction

In the construction of cast-in-place pile foundations, slurry plays an important role in protecting the bored hole, but the treatment of excess slurry has always been a problem that plagues the project construction. The conventional treatment methods are to transport the waste slurry to mud pit in rural area with a tank truck or to simply dispose it offshore, which are outdated and cause many environmental and social problems. This issue is especially severe in the eastern coastal area of China,

M. Feng · J. Wang (✉) · S. Liu
Ningbo Nottingham New Materials Institute, University of Nottingham Ningbo China, 199
Taikang East Road, Ningbo 315100, China
e-mail: juan.wang@nottingham.edu.cn

Y. Hu
Ningbo Transportation Engineering Construction Group Co., Ltd., 32-2 Yinfeng Road, Ningbo
315000, China

where soft soil is widely distributed and pile foundations were commonly used in the construction of building, bridges and so on. Recently, there has been an increasing interest in reusing the waste slurry as raw materials for civil engineering construction [1], because of the global encouragement of sustainable development and the needs of alternative reliable cost-effective materials that are more available locally. In pavement engineering projects, the waste drilling slurry from bridge construction, after treatment, could be used as pavement foundation materials.

In order to meet the requirements of pavement construction, soils with a very high moisture content must be treated. One of the most effective approaches is to use a dewatering-stabilisation technique. The dewatering process involves the separation of a substantial amount of water from solids using a dewatering system, leading to a dewatered soil (or called 'soil cake') with a relatively low moisture content. For fine-grained slurry or sludge, filter press facility, when combined with the usage of additives, can easily produce soil cakes with a moisture content of less than 30% [2]. The stabilisation process requires a certain amount of stabilisers, such as cement or lime, to be added and well mixed with the dewatered soil, so that the properties of the stabilised soils can satisfy the requirements of road construction. This approach has been proved very useful in the treatment of dredged sludge and sewage sludge for pavement construction [2, 3]. For drilling wastes, Shon et al. [4] investigated the basic characterisation and the performance evaluation of drilling wastes modified by sand and cement and evaluated their applicability as base course materials in pavement construction. They found that the modified drilling waste at its optimum moisture content (OMC), when modified with 3% cement, could satisfy the strength requirements of Class M base course materials.

Despite of those meaningful efforts, little attention was placed on the influence of the moisture content on the material property of the dewatered slurry. The waste drilling slurry, after the dewatering process, is usually stockpiled in the field, and therefore, its moisture content is subject to on-site weather condition. And the time gap between the dewatering and the stabilisation processes could range from several hours to several months, depending on construction progress. Although soils at their OMC are preferred in pavement constructions (e.g. [4–6]), this could lead to high costs from extra labour and land use. This work aims to evaluate the possibility of using the stabilised dewatered drilling slurry as subgrade and fill materials for a pavement. In pursuit of a cost-effective treatment strategy, focus will be placed on the influence of the moisture content on the strength of the stabilised dewatered slurry.

2 Methodology

2.1 Materials

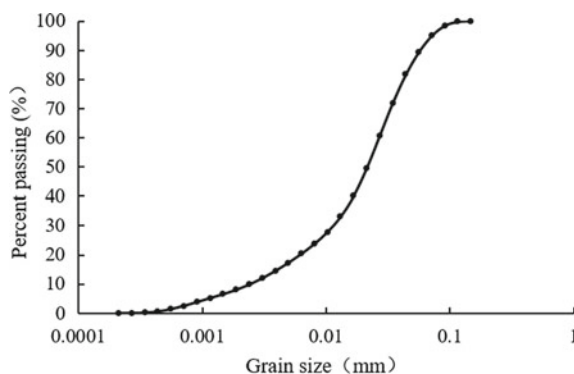
Waste drilling slurry used in the present study was taken from an expressway construction site in Ningbo, China. The slurry was pre-treated by a plate and frame

Table 1 Characteristics of the dewatered soil

Liquid limit %	Plastic limit %	Plastic index	OMC %	Maximum dry density kg/m ³
29.7	19.6	10.1	19.5	1.72

Table 2 Chemical components of the dewatered soil

SiO ₂	Al ₂ O ₃	Fe ₂ O ₃	CaO	K ₂ O	MgO	P ₂ O ₅
73.02%	11.28%	4.29%	3.07%	2.65%	1.85%	0.54%

Fig. 1 Gradation curve of the dewatered soil

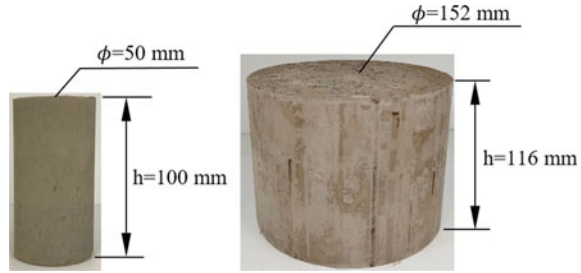
filter press dewatering system, and the obtained soil cakes (dewatered soil) have a moisture content of around 26%. The physical characteristics of the soil cakes are shown in Table 1. Table 2 exhibits the main chemical components of the oven-dried soil which were determined by Epsilon 4 Benchtop X Ray Fluorescence (XRF) analyser. Figure 1 shows the gradation curve obtained by better size 2000 laser particle size analyser. As can be seen, 6.9 and 84.3% of the grains can be classified as clay and silt, respectively, according to the British standard BS1377:2-1990 [7].

2.2 Test Plan and Test Procedure

In the present study, a series of unconfined compressive strength (UCS) tests were conducted to investigate the effects of moisture content and stabiliser (cement in the present study) content. A few California bearing ratio (CBR) tests were also performed, so that the results could be directly compared with the requirements in pavement foundation designs, though CBR is less used for characterising cement-treated soils.

Soil cakes from the construction site were crushed into smaller assemblies. Samples with different moisture contents were prepared by air-drying and/or adding water to the dewatered soils. The soils were then sealed in bags and allowed to rest

Fig. 2 UCS and CBR specimens (h is the height, ϕ is the diameter)



for more than 48 h. The prepared soils were mixed with cement by an electronic mixer and then compacted into moulds layer by layer within 30 min. Dimensions of the UCS and CBR specimens are shown in Fig. 2. Once prepared, the specimens were sealed and placed into a curing chamber with a constant temperature of 20 °C and a humidity of 95% for 7 days. The UCS tests were carried out by using MTS Universal Tester Model E45 following BS1377-1:1990 [8]. The CBR tests were conducted following BS1377-4:1990 [9].

A series of tests were carried out in this study, as shown in Table 3. The group name reflects the moisture and cement contents of the specimen. For instant, CE2-W18 represents that 2% cement was mixed with the dewatered soil with a moisture content of 18%. Note that the cement and moisture contents are by weight of the dry soil. There were at least four parallel tests for each UCS test group, and two parallel tests for each CBR test group.

3 Results and Discussion

3.1 Unconfined Compressive Strength

In total, 23 groups of tests were carried out and the averaged UCS and CBR values were obtained. Figure 3 demonstrates that, for any given moisture content, there exists a proportional relationship between the 7-day UCS and the cement content. The moisture content has a significant effect on the UCS. The largest UCS can be found when the moisture content is decreased to 18%. This is because this moisture content is close to the OMC (19.5%), and the compacted sample is in a very dense condition. During the preparation of test samples, the change of moisture content mainly came from the quick reaction between cement and water, the effect of which was limited due to time and temperature controls thus was not considered in this study. Figure 4 shows the results of CE2-W26 considering different curing periods (7, 14 and 28 days). The UCS is raised with the increasing curing period, by 17 and 52%, respectively.

Failure modes of the specimens are also closely associated with the moisture content and the cement content. The dewatered soil behaves plastically when the

Table 3 Test plan and results

Test type	Test group number	Group name	Cement content (%)	Moisture content (%)	UCS (MPa) /CBR (%)
UCS	1	CE0-W18	0	18	0.274
	2	CE2-W18	2	18	0.669
	3	CE4-W18	4	18	1.053
	4	CE6-W18	6	18	1.355
	5	CE0-W22	0	22	0.104
	6	CE2-W22	2	22	0.368
	7	CE4-W22	4	22	0.565
	8	CE6-W22	6	22	0.833
	9	CE0-W26	0	26	0.078
	10	CE2-W26	2	26	0.343
	11	CE5.04-W26	5.04	26	0.475
	12	CE7.56-W26	7.56	26	0.654
	13	CE0-W30	0	30	0.018
	14	CE1-W30	1	30	0.107
	15	CE2-W30	2	30	0.164
	16	CE4-W30	4	30	0.227
	17	CE6-W30	6	30	0.347
	18	CE8-W30	8	30	0.615
	19	CE2-W26-T14	2	26	0.403
	20	CE2-W26-T28	2	26	0.522
CBR	1	CE2-W22	2	22	13.55
	2	CE2-W26	2	26	11.7
	3	CE2-W30	2	30	9.25

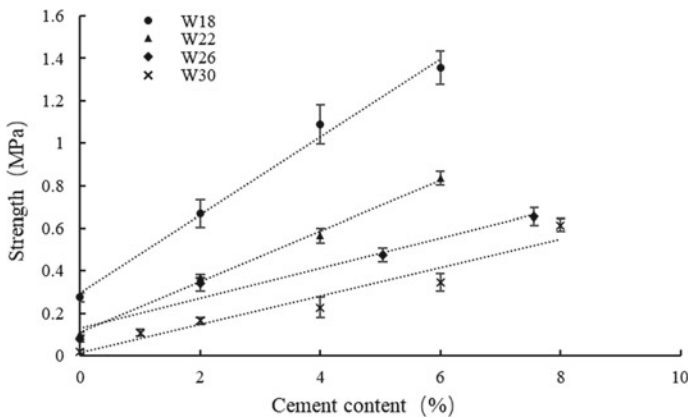


Fig. 3 Effects of cement content on the 7-day UCS

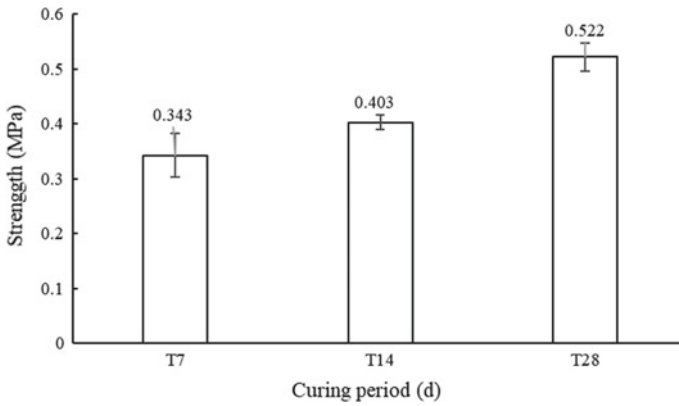


Fig. 4 Effect of curing period on the UCS of CE2-W26

moisture content is relatively high. For instance, when the moisture content is 22%, Fig. 5a demonstrates a shear failure mode with a large plastic deformation, in which the specimen bulges laterally into a ‘barrel shape’ at the beginning and generates a shear plane afterwards. When the moisture content is decreased to 18%, a number of vertical cracks generate during the compression process (Fig. 5b), and the specimen fails in a semi-plastic mode instead, which is consistent with previous studies [10, 11]. Undoubtedly, the stabilised soil could fail in a brittle mode if enough cement was added. In this study, since the cement content is relatively small compared to the corresponding moisture content, a semi-plastic failure mode is observed for the stabilised specimens, as shown in Fig. 5c. Although both CE0-W18 and CE6-W18 failed in the same mode, the CE0-W18 behaves more like a plastic material, as there is no obvious peak in the stress–strain response curve (Fig. 6). Figure 6 also shows

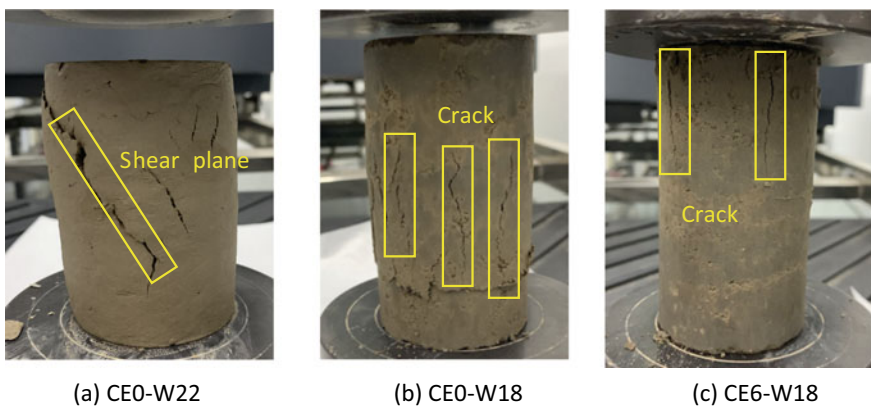


Fig. 5 Failure modes. a CE0-W22. b CE0-W18. c CE6-W18

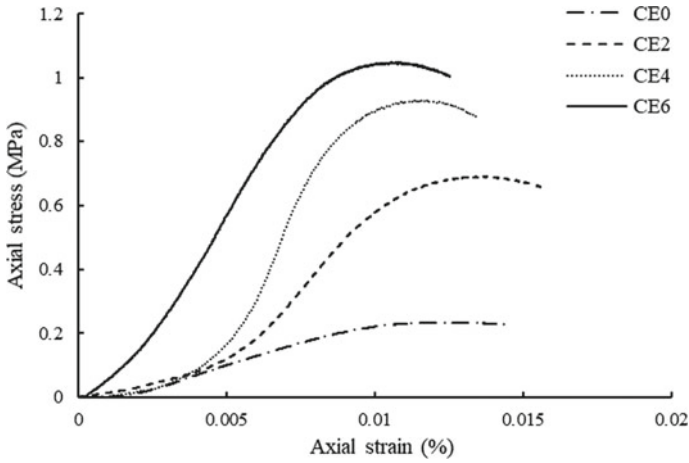
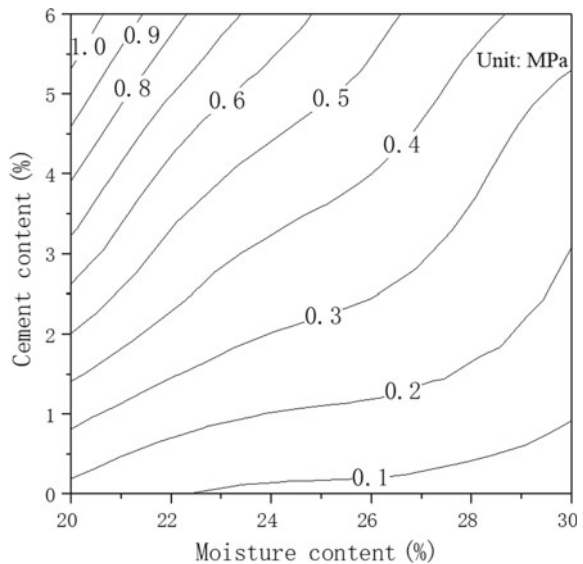


Fig. 6 Stress–strain relationship for samples with a moisture content of 18%

that as the cement content increases, the axial strain at the peak point becomes smaller and the stiffness tends to be higher.

Based on the data above, a contour plot (Fig. 7) was developed, which shows the variation of UCS within practical ranges of moisture and cement contents in this study. As can be seen, the cement content has a more pronounced influence on the UCS when the moisture content approaches the OMC. Despite of that, various combinations of cement and moisture contents could be chosen to achieve a specific

Fig. 7 Contour of UCS



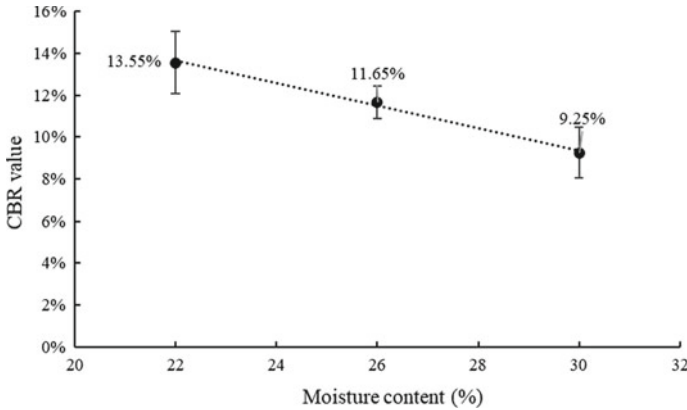


Fig. 8 CBR after 7-day curing (cement content 2%)

strength. In practice, once the moisture content is obtained before the stabilisation process, the required cement content can be efficiently determined in order to achieve a target 7-day UCS. In this work, the stabilised soils will be used as subgrade and embankment fill materials for an expressway, so the target UCS was set as 0.4 MPa.

3.2 California Bearing Ratio

In pavement designs, a minimum CBR is usually required as an index of the subgrade soil strength. In China, the CBR at the top of a pavement foundation should be no less than 8% for expressways [12]. In this study, the influence of the moisture content on the CBR was also studied at the wet side of the OMC. Figure 8 exhibits that the CBR decreases with the increasing moisture content, from 13.55 to 9.25%, in correspondence with the reduction of UCS from 0.37 MPa to 0.16 MPa. It should be noted that compared to non-stabilised soils, CBR values for chemically stabilised soils have less meaning as a measure of strength [13]. Nevertheless, it is still often used in the evaluation of the performance of stabilised soils for comparison purpose [3].

4 Comparison with Plant-Treated Slurry

The slurry treatment plant on-site (Fig. 9) includes a dewatering system and a stabilisation system. The waste drilling slurry was first dewatered and then stockpiled in the field. The stabilisation system mainly includes a crushing set and a mixing set. A moisture content of between 20 and 22% was obtained for soils before the stabilisation process. The cement content designed was 2.5% in order to achieve a target UCS



Fig. 9 Slurry treatment plant in Ningbo. **a** Dewatering facility. **b** Soil cakes. **c** Soil before stabilisation. **d** Stabilisation system

of 0.4 MPa. Additional 1% cement was added considering uncertainties in the stabilisation process. UCS and CBR tests were then conducted on the plant-mixed soil samples. It was found that the averaged UCS was 0.52 Mpa with a standard deviation of 0.094. This value exceeds the target UCS. Also, it matches the lower boundary of the range (0.52 Mpa ~ 0.73 Mpa) obtained from the contour plot considering a cement content of 3.5%, probably because the quality of mixing on-site was not as good as that in laboratory. In addition, the averaged CBR values of the stabilised soil were 22.03 and 25.17% under standard curing and outdoor conditions, respectively.

5 Conclusions

This paper investigated the influences of moisture content and cement content on the strength of the stabilised dewatered slurry. It was found that there was a linear relationship between the cement content and the UCS strength at any given moisture content. The UCS and CBR values decrease with rising moisture content at the wet side of the OMC. A contour plot was further developed which can guide the selection of the stabilisation strategy considering in situ moisture content. This was then used to determine the cement content for the treatment of the waste drilling slurry in an on-site plant. And the results agree with the prediction.

Furthermore, it can be concluded from this research that during pavement construction, stabilised soils can be prepared at a moisture content higher than OMC by adding a relatively high content of stabiliser to reach a target strength. Nevertheless, when selecting the stabilisation strategy for a specific project, one should also consider the other properties (e.g. shrinkage) of the stabilised soil as well as the overall cost.

Acknowledgement Financial support from Ningbo S&T Innovation 2025 Major Special Programme (grant number 2019B10048) is gratefully acknowledged.

References

1. Page PW, Greaves C, Lawson R, Hayes S, Boyle F (2003) Options for the recycling of drilling cuttings. In: SPE/EPA/DOE exploration and production environmental conference, Paper SPE 80583, Soc Petrol Eng, San Antonio, Texas, USA
2. Zhang J, Dai X, Zou W, Xu S, Li Z (2015) Experiments on pavement performance of solidified sediment modified with cement. *J Zhejiang Univ (Eng Sci)* 49(11):2165–2171
3. Lêda C, José F, Manoel G (2014) Potential uses of sewage sludge in highway construction. *J Mater Civ Eng* 26(9):04014051
4. Shon C, Estakhri C, Lee D, Zhang D (2016) Evaluating feasibility of modified drilling waste materials in flexible base course construction. *Constr Build Mater* 116:79–86
5. Abu-Farsakh M, Coronel J, Tao M (2007) Effect of soil moisture content and dry density on cohesive soil-geosynthetic interactions using large direct shear tests. *J Mater Civ Eng* 19(7):540–549
6. Muntohar A (2005) The influence of molding water content and lime content on the strength of stabilized soil with lime and rice husk ash. *Civil Eng Dimension* 7(1):1–5
7. BS 1377–2 (1990) Methods of test for soils for civil engineering purposes—classification tests, BSI Group, London, UK
8. BS 1377–1 (1990) Methods of test for soils for civil engineering purposes—general requirements and sample preparation, BSI Group, London, UK
9. BS 1377–4 (1990) Methods of test for soils for civil engineering purposes—compaction-related Tests, BSI Group, London, UK
10. Vallejo LE (1988) The brittle and ductile behavior of clay samples containing a crack under mixed mode loading. *Theoret Appl Fract Mech* 10(1):73–78
11. Venkatramaiah C (1995) *Geotechnical engineering*, 3rd edn. New age international, New Delhi
12. JTGD30–2015 (2015) Specifications for design of highway subgrades, China Communications Press, Beijing, China
13. Nicholson PG, Vinai K, Clint FF (1994) Lime and fly ash admixture improvement of tropical Hawaiian soils. *Transp Res Rec* 1440:71–77

Compaction and CBR Behaviour of Cement-Stabilised Sand–Black Cotton Soil Mixtures



Charles M. O. Nwaiwu, Baba Benjamin, and Obinna U. Ubani

Abstract Black cotton soil admixed with 0–50% sand was subjected to laboratory tests to determine the index properties, as well as compaction, and CBR behaviour when stabilised with ordinary Portland cement in the range of 0–10%. The results show that by adding sand to black cotton soil, the free swell and plasticity properties reduced with increasing sand content. Three compaction energies were employed, namely BS Light, West African Standard, and BS Heavy. The maximum dry unit weight of the soil mixture increased with sand and cement contents, and the highest value of 21.6 kN/m³ was obtained at 40% sand and 8% cement contents using the BS Heavy compaction energy. The optimum moisture content reduced appreciably on the addition of cement and sand, decreasing from 27.4 to 10.4% on addition of 30% sand and 6% cement using the BS Heavy compaction energy. The soil mixture of 30% sand and 6% cement gave the lowest optimum moisture content for all the compaction energies. Using the BS Light compaction energy, the unsoaked CBR increased from 17 to 56% at 8% cement and 40% sand contents, while for BS Heavy compaction energy, unsoaked CBR increased from 23.5 to 60% at 6% cement and 40% sand contents. At 40–50% sand content alone, the unsoaked CBR of the soil increased to 52.5%. This shows that black cotton soils can be improved upon using sand and cement to meet the requirements for subgrade, sub-base, and base material for highway construction in Nigeria. The analysis of variance shows that at 95% confidence level, sand content, cement content, and compaction energy positively affected maximum dry unit weight of black cotton soils (p -value < 0.05). On the other hand, the effect of compaction energy on optimum moisture content was found

C. M. O. Nwaiwu (✉)

Geotechnical and Geoenvironmental Engineering, Department of Civil Engineering, Nnamdi Azikiwe University, Awka PMB 5025, Anambra, Nigeria
e-mail: cmo.nwaiwu@unizik.edu.ng

B. Benjamin

Department of Civil Engineering, Federal Polytechnic, Oko PMB 021, Anambra, Nigeria

O. U. Ubani

Department of Civil Engineering, Nnamdi Azikiwe University, Awka PMB 5025, Anambra, Nigeria
e-mail: ou.ubani@unizik.edu.ng

not to be statistically significant at 5% level of significance. Compaction energy was found to influence the unsoaked CBR value more than cement and sand contents.

Keywords Sand–black cotton soil mixture · Portland cement · Compaction · CBR

1 Introduction

Black cotton soils are problematic soils that are characterised by high swelling potential, high shrinkage, and high compressibility values. They occur predominantly in north-eastern Nigeria, stretching over an area of about 104,000 km², and pose major challenges to civil engineering works especially in highway construction [1]. The spread of black cotton soils in the area is usually so extensive such that it is difficult to bypass them peradventure there is need for road construction. These soils have been encountered in Nigeria, Cameroon, Ghana, and India. As identified by [2], the poor performance of black cotton soils as highway construction material is mainly due to their behaviour under different moisture conditions. Under dry conditions, they appear firm and hard, but upon wetting, they undergo high swelling. Black cotton soils are formed from the weathering of shaley and clayey sediments and basaltic rocks under conditions of poor drainage and alternating wet and dry climatic conditions [1, 3, 4]. The clay mineral present in the soils is predominantly montmorillonite with high swelling potential [5–7].

The application of ordinary Portland cement for soil stabilisation has been extensively studied in geotechnical engineering, and it is preferred due to the early strength gain it offers when compared with other admixtures [8–10]. Generically, mixing cement with water initiates chemical reaction called hydration, through which a hard cement paste is formed. When the pore water from soil encounters the cement, the hydration reaction of cement compounds (C₃S) and (C₂S) occurs rapidly [11]. Cement particles bind the adjacent cement grains together during hardening, and form a hardened skeleton matrix, which encloses unaltered soil particles. On the other hand, coarse-grained granular materials such as sand and quarry dust can also be used to improve the geotechnical properties of soft clays due to their high angle of internal friction [12].

Akanbi and Job [13] studied the suitability of black cotton soils stabilised with quarry dust and ordinary Portland cement as road bases and foundation materials. [14, 15] studied the improvisation of black cotton soils using quarry dust only, while [16] studied the effect of lime addition on quarry dust-stabilised black cotton soil. The effects of sand and cement admixture on the geotechnical properties of black cotton soil for the purpose of highway construction have been studied by [17–19]. Shreyas [20] studied the effect of admixtures (sand, cement, and fly ash) on black cotton soil. The objective of this study was to assess the contributions of sand, cement, and compaction energy to the improvement in compaction and strength properties of black cotton soils.

2 Materials and Methods

The soil sample used in this study was collected from the outskirts of New Marte (longitude 13°27'N and latitude 13° 50'E) Local Government Area in Borno state, Nigeria. The sand used in the study was Bama Ridge sand. Bama Ridge is a prominent geological feature in north-eastern Nigeria which passes through Bama, Maiduguri, and Magumeri up to Nguru and Gashua before flattening out beneath the sand dunes of Niger plain [21].

The soil samples were prepared in accordance with BS 1377-1:1990 [22]. The black cotton soil sample was later replaced with 10, 20, 30, 40, and 50% of Bama Ridge sand, and 2, 4, 6, 8, and 10% of ordinary Portland cement by weight, in order to study the changes in the engineering properties of the black cotton soil. The samples were subjected to moisture content tests, specific gravity test, sieve analysis test (hydrometer method), free swell test, Atterberg limit test, compaction test, and California bearing ratio (CBR) test in the laboratory. Sieve analysis and Atterberg limit tests were carried out in accordance with BS 1377-2:1990 [23], while compaction tests were carried out in accordance with BS 1377-4:1990 [24]. The compaction tests were carried out with three different compaction energies of BS Light compaction energy (BSL), BS Heavy compaction energy (BSH), and West African Standard (WAS) compaction energy. The WAS compaction was carried out using the method described in [25]. CBR test was carried out according to the procedure described in ASTM D1883-16 [26].

3 Results and Discussion

The properties of the black cotton soil before modification are given in Table 1.

From Table 1, the liquid limit of the black cotton soil was found to be 58.5%, and the plasticity index was found to be 28.50%. This is against the maximum liquid limit of 35% and plasticity index of 12% recommended by Nigeria's highway design standard/specification [27]. Bama Ridge sand was observed to be poorly graded, consisting of about 97.6% sand, and classified under A-3 based on AASHTO classification. The free swell has a value of 4.0%, and the specific gravity was found to be 2.63.

3.1 Effect of Sand on Index Properties

On addition of sand from 0–50% to the black cotton soil, the consistency limits improved as shown in Fig. 1. The liquid limit reduced almost linearly with increase in sand content, dropping from 58.5 to 43.0% at 50% sand content, while the plastic limit also improved. A remarkable improvement was also obtained with the plasticity

Table 1 Geotechnical properties of the unimproved black cotton soil

Property	Quantity
Sand content (%)	22.10
Silt content (%)	30.85
Clay content (%)	47.05
Sample (%) passing sieve No 200 (75 μm)	61.00
Liquid limit (%)	58.50
Plastic limit (%)	30.00
Plasticity index (%)	28.50
Linear shrinkage (%)	10.71
Specific gravity	2.57
Maximum dry unit weight (kN/m ³)—BSL	13.5
Maximum dry unit weight (kN/m ³)—WAS	14.00
Maximum dry unit weight (kN/m ³)—BSH	17.4
Optimum moisture content (%)—BSL	24.6
Optimum moisture content (%)—WAS	28.0
Optimum moisture content (%)—BSH	27.4
CBR (%)—BSL	17.0
CBR (%)—BSH	23.50
Free swell	46.8%
AASHTO classification	A-7-5
Colour	Grey black

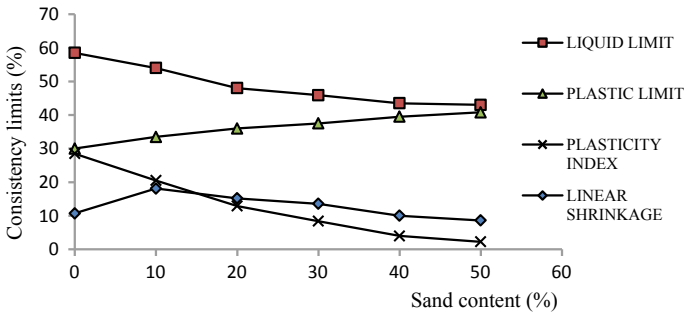


Fig. 1 Variation of consistency limits of black cotton soil with sand content

index which also reduced almost linearly from 28.5 at 0% sand content to 2.24% at 50% sand content. Linear shrinkage of the sample increased when the sand content was increased to 30% and dropped at 50%. Generally, a good improvement in the consistency limits was observed. This behaviour is consistent with what was obtained when quarry dust was added to soft clays in the works of [28, 29].

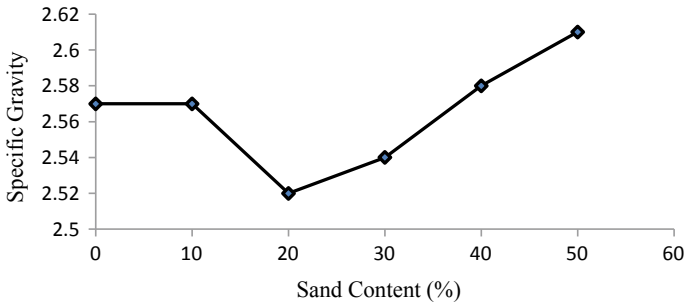


Fig. 2 Variation of specific gravity with sand content

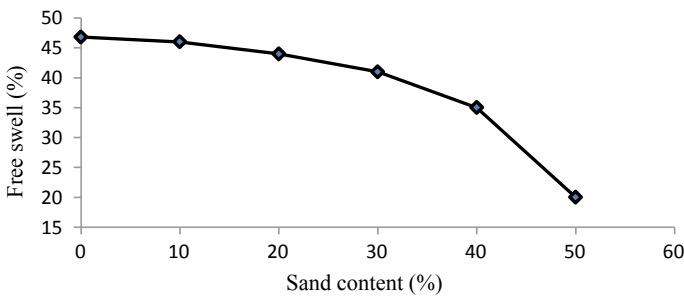


Fig. 3 Variation of free swell with sand content

The variation of specific gravity with sand content is shown in Fig. 2. A drop in the value of specific gravity was observed at 20% sand content, and the value began to increase linearly with further addition of sand, with the highest value observed at 50% sand content. An improvement in the free swell of the soil was also observed with increase in sand content. At 50% sand content, the free swell reduced to 20% from 46.8 at 0% sand content as shown in Fig. 3.

3.2 Effect of Sand and Cement Content on Maximum Dry Unit Weight

On addition of cement to the sand–black cotton soil mixtures, the maximum dry unit weight was found to improve. The variation of maximum dry unit weight with sand and cement contents for BSL and BSH compaction energies is shown in Figs. 4 and 5, respectively. At all compactive efforts, the lowest value of maximum dry unit weight was observed at 10% sand content and 0% cement content. At BSL compaction energy, the highest value of maximum dry unit weight (20.4 kN/m³) was observed at 10% sand and 4% cement contents. However, across all the compaction energies

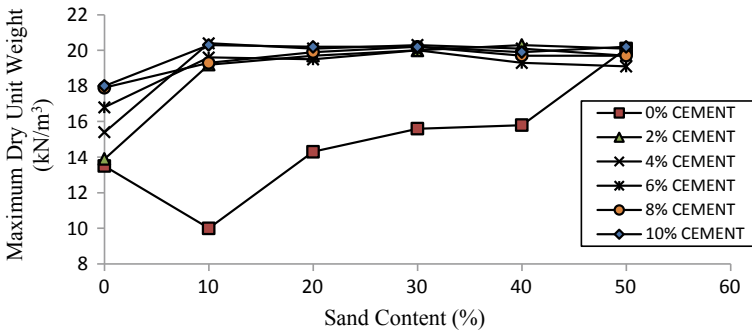


Fig. 4 Variation of maximum dry unit weight with sand and cement contents at BSL light compaction energy ($C_E = 605.89 \text{ kNm/m}^3$)

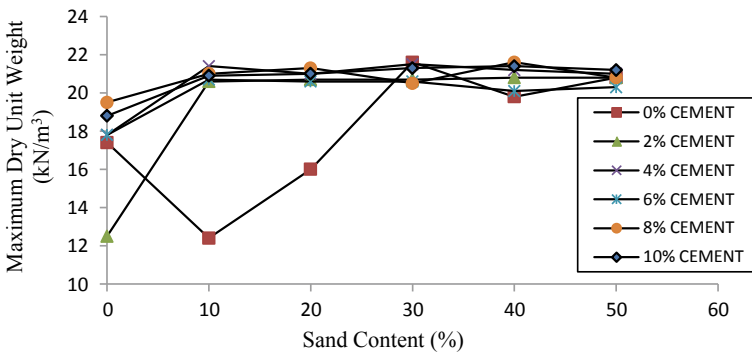


Fig. 5 Variation of maximum dry unit weight with sand and cement contents at BSH compaction energy ($C_E = 2723.52 \text{ kNm/m}^3$)

employed (BS Heavy, West African Standard, and BS Light), the highest value of maximum dry unit weight (21.6 kN/m^3) was obtained at 40% sand and 8% cement contents using the BS Heavy compaction energy.

From ANOVA at 5% level of significance ($p < 0.05$), the effects of sand content, cement content, and compaction energy on maximum dry unit weight were statistically significant (see Tables 2 and 3).

3.3 Effect of Sand and Cement Contents on Optimum Moisture Content

For BSL compaction energy, the optimum moisture content showed a downward trend at low cement contents (<2%), but increment was observed at higher cement contents (see Fig. 6). At WAS compaction energy, the optimum moisture content

Table 2 ANOVA table for maximum dry unit weight and varying cement content

	CC (%)		DOF	Calculated <i>F</i> -value	<i>p</i> -value	Critical <i>F</i> -value
MDUW	0	Sand content	5	30.399	9.71E-06	3.325
		Compaction energy	2	14.030	0.00125	4.102
MDUW	2	Sand content	5	35.808	4.54E-06	3.325
		Compaction energy	2	1.0071	0.39948	4.10282*
MDUW	4	Sand content	5	95.7503	4.1E-08	3.3258
		Compaction energy	2	28.0972	7.87E-05	4.10282
MDUW	6	Sand content	5	226.690	5.94E-10	3.32583
		Compaction energy	2	83.0263	5.91E-07	4.1028
MDUW	8	Sand content	5	15.2533	0.000211	3.32583
		Compaction energy	2	27.2297	8.99E-05	4.1028
MDUW	10	Sand content	5	85.8367	6.98E-08	3.32583
		Compaction energy	2	43.0612	1.22E-05	4.1028

*Not statistically significant at $p = 0.05$; MDUW—Maximum dry unit weight; CC—Cement content

reduced with sand content at 0% cement. However on addition of cement, an upward trend was observed in the sample. The same behaviour observed at BSL compaction energy was observed at BSH compaction energy, where optimum moisture content reduced with sand content at low cement content (0–2%), but increased with further addition of cement (see Fig. 7). This same behaviour of optimum moisture content at higher cement content was observed by [30] when quarry dust and cement were used to stabilise soft white clays.

From ANOVA as shown in Tables 4 and 5, it was observed that the effect of compaction energy on optimum moisture content was not statistically significant ($p > 0.05$) in sand–cement stabilisation of black cotton soils. However, the effects of sand content and cement content on optimum moisture content were found to be statistically significant at 5% level.

3.4 Effect of Sand and Cement Contents on CBR

The variation of unsoaked CBR with sand and cement contents at BSL and BSH compaction energies is shown in Figs. 8 and 9, respectively. At BSL compaction energy, the maximum CBR value was obtained at 8% cement content and 40% sand

Table 3 ANOVA table for maximum dry unit weight and varying sand content

	SC (%)		DOF	Calculated <i>F</i> -value	<i>p</i> -value	Critical <i>F</i> -value
MDUW	0	Cement content	5	8.2285	0.002569	3.325
		Compaction energy	2	14.030	0.015698	4.1028
MDUW	10	Cement content	5	353.2784	5.59E-11	3.3258
		Compaction energy	2	24.0562	0.000151	4.10282
MDUW	20	Cement content	5	397.6966	3.66E-11	3.3258
		Compaction energy	2	55.2786	3.93E-06	4.1028
MDUW	30	Cement content	5	2.00169	0.16392	3.3258*
		Compaction energy	2	3.47844	0.071329	4.1028*
MDUW	40	Cement content	5	9.8489	0.00128	3.3258
		Compaction energy	2	11.07236	0.002914	4.1028
MDUW	50	Cement content	5	12.5601	0.000478	3.3258
		Compaction energy	2	50.82707	5.76E-06	4.1028

*Not statistically significant at $p = 0.05$; MDUW—Maximum dry unit weight; SC—Sand content

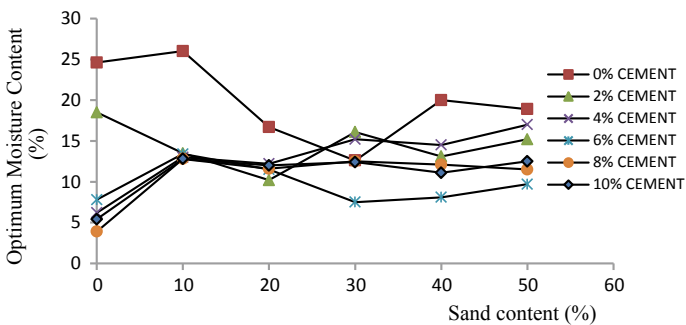


Fig. 6 Variation of optimum moisture content with sand and cement contents at BSL compaction energy ($C_E = 605.89 \text{ kNm/m}^3$)

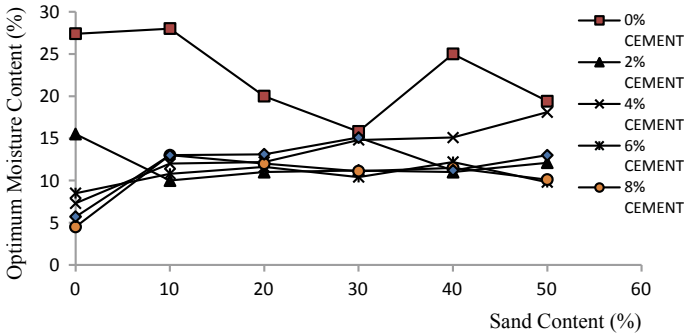


Fig. 7 Variation of maximum dry unit weight with sand and cement contents at BSH compaction energy ($C_E = 2726.51 \text{ kNm/m}^3$)

Table 4 ANOVA table for optimum moisture content and varying cement contents

	CC (%)		DOF	Calculated <i>F</i> -value	<i>p</i> -value	Critical <i>F</i> -value
OMC	0	Sand content	5	20.125	6.29E-05	3.3258
		Compaction energy	2	3.7325	0.06154	4.1028*
OMC	2	Sand content	5	0.6730	0.65337	3.3258*
		Compaction energy	2	2.1695	0.164965	4.1028*
OMC	4	Sand content	5	61.916	3.38E-07	3.3258
		Compaction energy	2	0.3884	0.68790	4.1028*
OMC	6	Sand content	5	3.9649	0.030455	3.3258
		Compaction energy	2	2.1052	0.17257	4.1028*
OMC	8	Sand content	5	92.348	4.89E-08	3.3258
		Compaction energy	2	1.0130	0.397536	4.1028*
OMC	10	Sand content	5	59.700	4.01E-07	3.3258
		Compaction energy	2	2.6597	0.11817	4.1028*

*Not statistically significant at $p = 0.05$; OMC—Optimum moisture content; CC—Cement content

content with a value of 56%. For BSH compaction energy, the maximum unsoaked CBR value of 60.5% was obtained at 50% sand content and 10% cement content. Averagely, higher CBR values were observed at BS Heavy compaction efforts.

At dosages $\leq 2\%$, the effect of cement content on CBR was found to be statistically significant. At dosages $>2\%$, the effect of cement content on CBR was no longer statistically significant at 95% confidence level (see Table 6). Similarly, the effects of sand content were found to be statistically insignificant to CBR at replacement $\leq 20\%$ (see Table 7). However, the effect of compaction energy on CBR was statistically significant at 95% confidence level.

Table 5 ANOVA table for optimum moisture content and varying sand contents

	SC (%)		DOF	Calculated <i>F</i> -value	<i>p</i> -value	Critical <i>F</i> -value
OMC	0	Cement content	5	24.452	2.64E-05	3.3258
		Compaction energy	2	0.44964	0.650146	4.1028*
OMC	10	Cement content	5	28.0759	1.41E-05	3.3258
		Compaction energy	2	0.4759	0.63469	4.1028*
OMC	20	Cement content	5	45.2252	1.51E-06	3.3258
		Compaction energy	2	2.272057	0.153661	4.1028*
OMC	30	Cement content	5	3.44269	0.045512	3.3258
		Compaction energy	2	0.16255	0.85217	4.1028*
OMC	40	Cement content	5	25.0461	2.36E-05	3.3258
		Compaction energy	2	1.55135	0.2589	4.1028*
OMC	50	Cement content	5	27.2901	1.59E-05	3.3258
		Compaction energy	2	0.8019	0.4753	4.1028*

*Not statistically significant at $p = 0.05$; OMC—Optimum moisture content; SC—Sand content

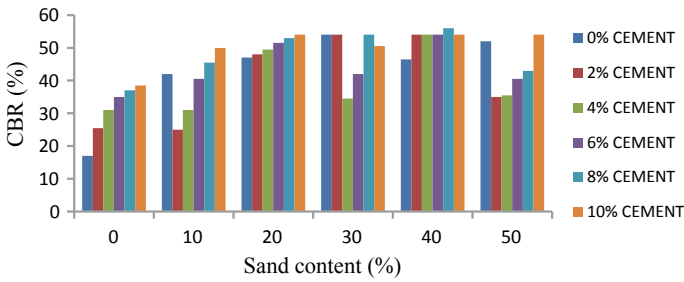


Fig. 8 Variation of CBR with sand and cement contents at BSL compaction energy ($C_E = 605.89 \text{ kNm/m}^3$)

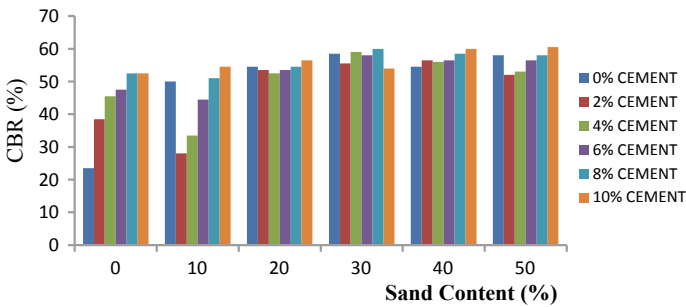


Fig. 9 Variation of CBR with sand and cement contents at BSH compaction energy ($C_E = 2726.51 \text{ kNm/m}^3$)

Table 6 ANOVA table for CBR and varying cement content

	CC (%)		DOF	Calculated F -value	p -value	Critical F -value
CBR	0	Sand content	5	380.022	1.91E-06	5.05032
		Compaction energy	1	145.8	6.88E-05	6.60789
CBR	2	Sand content	5	14.41909	0.00542	5.05032
		Compaction energy	1	7.35294	0.04219	6.60789
CBR	4	Sand content	5	3.059191	0.12259	5.05032*
		Compaction energy	1	7.529412	0.0406	6.60789
CBR	6	Sand content	5	2.68998	0.15069	5.05032*
		Compaction energy	1	10.34242	0.023571	6.60789
CBR	8	Sand content	5	2.65747	0.153548	5.05032*
		Compaction energy	1	9.412811	0.02784	6.60789
CBR	10	Sand content	5	4.532417	0.061372	5.05032*
		Compaction energy	1	13.4479	0.014486	6.60789

*Not statistically significant at $p = 0.05$

Table 7 ANOVA table for CBR and varying sand content

	SC (%)		DOF	Calculated F -value	p -value	Critical F -value
CBR	0	Cement content	5	35.64935	0.000649	5.050329
		Compaction energy	1	93.76623	0.000199	6.607891
CBR	10	Cement content	5	99.99366	5.24E-05	5.050329
		Compaction energy	1	31.97674	0.002403	6.607891
CBR	20	Cement content	5	2.53658	0.165001	5.050329*
		Compaction energy	1	14.7561	0.012107	6.607891
CBR	30	Cement content	5	0.772465	0.60807	5.050329*
		Compaction energy	1	6.64633	0.051748	6.607891*
CBR	40	Cement content	5	3.833107	0.083308	5.050329*
		Compaction energy	1	14.98643	0.011746	6.607891
CBR	50	Cement content	5	4.418743	0.064343	5.050329*
		Compaction energy	1	36.08541	0.001836	6.607891

*Not statistically significant at $p = 0.05$

3.5 Practical Relevance of the Study

Compaction and CBR characteristics of black cotton soil stabilised with a combination of sand and cement have been studied. Although a variety of admixtures have been used to stabilise black cotton soils, previous studies that involved the use of a combination of sand and cement [e.g. 17; 20; 31] have not considered a wide range

of both cement and sand contents. However, the present study showed that a combination of 40% sand and 8% cement gave the highest maximum dry unit weight which can be used to stabilise black cotton soil.

Values of unsoaked CBR were measured and presented in this study. When a combination of 40% sand and 8% cement was used for stabilisation, the CBR value of 56% was obtained for BSL compaction. Unsoaked CBR is appropriate for the semi-arid environment, where the black cotton soil occurs, considering long periods of dry season during which road pavement construction is feasible. Soaked CBR values become relevant when there are possibilities of leakages from drains and water pipes, or when it is possible for water to infiltrate into pavement layers. However, good construction practice will possibly prevent water infiltration. It has also been considered that laboratory-determined soaked CBR has poor reproducibility [32]. Accuracy of results from laboratory-soaked CBR tests is considered to be affected by incomplete moisture conditioning and the number of days of soaking, among other factors [33].

4 Conclusion

From the study of compaction and CBR characteristics of cement-stabilised sand–black cotton soil mixtures, the following conclusions were reached:

- In their natural states, black cotton soils are unsuitable for construction works due to their poor geotechnical properties.
- Addition of Bama Ridge sand to black cotton soil can improve the index properties and free swell of black cotton soils.
- Addition of cement to sand–black cotton soil mixtures can improve the maximum dry unit weight of black cotton soils. The effects of cement content, sand content, and compaction energy on maximum dry unit weight were found to be statistically significant at 95% confidence level.
- The effects of sand and cement contents on variation of optimum moisture content were found to be statistically significant at 95% confidence level, but compaction energy was not.
- Unsoaked CBR values of black cotton soils can be improved by addition of cement and sand. The effect of compaction energy on CBR was found to be statistically significant at 95% confidence level regardless of the cement or sand content.

References

1. Ola SA (1983) The geotechnical properties of black cotton soils of North-Eastern Nigeria. In: Ola SA (ed) Tropical soils of Nigeria in engineering practice, Balkema Rotterdam pp 160–178

2. Bolarinwa A, Ola SA (2016) A review of major problem soils in Nigeria. *FUOYE J Eng Technol* 1(1):20–25
3. Osinubi KJ, Oyelakin MA, Eberemu OA (2011) Improvement of black cotton soils with ordinary Portland cement—Locust bean waste ash blend. *Electron J Geotech Eng* 16:619–627
4. Ijimdiya TS, Ashimiyu AL, Abubakar DK (2012) Stabilisation of black cotton soil using groundnut shell ash. *Electron J Geotech Eng* 17:3645–3652
5. Fologbade O, George M (2011) Groundnut shell ash stabilization of black cotton soil. *Electron J Geotech Eng* 15:415–428
6. Alhassan HM, Olaniyi LF (2013) Effect of ‘ionic soil stabilizer 2500’ on the properties of black cotton soil. *Br J Appl Sci Technol* 3(3):406–416
7. Gidigasu SSR, Gawu SKY (2013) The mode of formation, nature, and geotechnical characteristics of black cotton soils. *Stand Sci Res Essays* 1(14):377–439
8. Pasupuleti RKT, Suresh K, Uday KV (2015) Effect of curing time on behaviour and engineering properties of cement treated soils. *Int Innov Res Sci Eng Technol* 4(6):4649–4657
9. Naveena PC, Mamatha KH, Dinesh SV (2013) Prediction of strength development in stabilised sandy clay at high water content. *Int J Geol* 7(1):9–23
10. Athanasopoulou A (2016) The role of curing period on the engineering characteristics of cement stabilised soil. *Rom J Trans Infrastruct* 5(1)
11. Saaed KA, Kassin KA, Nur H (2014) Physicochemical characterisation of cement treated kaolin clay. *Gradevinar* 66(6):513–521
12. Soosan TG, Jose BT, Abraham BM (2001) Use of quarry dust in embankment and highway construction. In: *Proceedings of Indian geotechnical conference, Indore India*, pp 274–277
13. Akanbi DO, Job FO (2014) Suitability of black cotton soil stabilised with cement and quarry dust for road bases and foundations. *Electron J Geotech Eng* 19:6305–6313
14. Visalakshi KV, Sridevi K, Shivanarayana C, Prasad DSV (2018) A study on strength properties of soil treated with quarry dust. *Int J Eng Sci Invention* 7(7):59–63
15. Chansoria A, Yadav RK (2016) Effect of quarry dust on engineering properties of black cotton soil. *Int J Innov Res Sci Technol* 2(11):715–718
16. Mudgal A, Sarkar R, Sahu AK (2014) Effect of lime and stone dust in the geotechnical properties of black cotton soil. *Int J GEOMATE* 7(2):1033–1039
17. Ramteke NB, Saxena A, Arora TR (2014) Stabilisation of black cotton soil with sand and cement as a subgrade for pavement. *Int J Eng Sci Res Technol* 3(6):688–692
18. Babu VR, Niveditha K, Babu BR (2016) Stabilisation of black cotton soil with sand and cement as subgrade pavement. *Int J Civil Eng Technol* 7(2):341–351
19. Likhitha H, Raghavendra HN, Rakesh KP, Shrihari UP (2018) Stabilisation of subgrade black cotton soil using cement and M-Sand. *Int J Eng Sci Res* 5(1):40–48
20. Shreyas K (2017) Stabilisation of black cotton soil by admixtures. *Int J Adv Res Sci Eng* 6(8):1145–1162
21. Kundiri AM, Muhammed AS, Muhammed IS (2016) An investigation of geotechnical properties of Bama Ridge soil as a suitable subgrade material in road construction. In: *Proceedings to faculty of engineering seminar series, vol 7. University of Maiduguri*, pp 31–35
22. BS 1377–1 (1990) Methods of test for soils for civil engineering purposes—Part 1: general requirements and sample preparation. British Standards Institution
23. BS 1377–2 (1990) Methods of test for soils for civil engineering purposes—Part 2: classification tests. British Standards Institution
24. BS 1377–4 (1990) Methods of test for soils for civil engineering purposes—Part 4: compaction-related Tests. British Standards Institution
25. Nwaiwu CMO, Msheila S, Durkwa J (2012) Compactive effort influence on properties of quarry dust black cotton soil mixtures. *Int J Geotech Eng* 6(1):91–101
26. ASTM D1883–16 (2016) Standard test method for California Bearing Ratio (CBR) of laboratory compacted soils. ASTM International, Conshohocken, PA
27. Federal Ministry of Works and Housing (FMWH) (1997) Specifications for roads and bridges. Federal Ministry of Works and Housing, Nigeria

28. Kumar AU, Biradar KB (2014) Soft Subgrade stabilisation with quarry dust—an industrial waste. *Int J Res Eng Technol* 3(8)
29. Indiramma P, Sudharani C (2016) Use of quarry dust for stabilisation of expansive soils. *Int J Innov Res Sci Eng Technol* 5(1):1151–1157
30. Arinze EE, Agunwamba JC, Mama BO (2018) Geotechnical characteristics of cement quarry-dust stabilised white clays as a sub-base of rural roads. *Electron J Geotech Eng* 23(2):523–535
31. Ali MS, Amir S, Ahmed MA, Ahmed MI, Chouka S (2019) Stabilization of subgrade soil using sand, cement and terrasil chemical as an additive. *Int Res J Eng Technol* 6(5):6758–6771
32. Rallings R (2014) The CBR test—a case for change. *Aust Geomech* 49(1)
33. De Silva VW (2015) Some aspects of pavement design on cohesive and non-cohesive subgrades. In: *International conference on geotechnical engineering, Columbo, 2015, ISSGME*, pp 593–596

Improving Mechanical Properties of Two Mexican Soils by Utilizing Calcium Oxide



Natalia Perez, Paul Garnica, Francisco Javier Castañeda,
and Mario Enrique Peña

Abstract The stabilization with lime has been widely studied all over the world; however, in Mexico, few papers have addressed the improvement in resilient modulus and permanent deformation (Perez et al. in Evaluación del óxido de calcio (estabilizador) como estabilizador de suelo. Publicación técnica No. 560. Instituto Mexicano del Transporte [1]). In this paper, the authors show the results of two soils that do not meet Mexican specifications (for embankment, subgrade and subbase). Specimens were tested under different conditions (specimens stored at different periods, specimens dried and specimens wetted). The results show that unconfined compression strength, resilient modulus and permanent deformation are improved when mixing the soils with calcium oxide.

Keywords Stabilization · Calcium oxide · Permanent deformation · Resilient modulus · Unconfined compression strength

1 Introduction

The use of quarry materials is a common practice in the construction of roads. This has caused a significant degradation to the environment. Likewise, it is also common that during the construction of these structures, several materials that do not meet project specifications are discarded. In past times, the disposal of such materials was so common that it was not a problem. However, currently, the care for the environment is the key to survival of humanity.

Several countries are already taking action on the matter and materials that were previously discarded are now being utilized in the construction of new structures. For example, fine-grained soils with plastic characteristics are the least desirable in road construction because of their volume change when they are subjected to changes in

N. Perez (✉) · P. Garnica
Mexican Transportation Institute, Queretaro, Mexico
e-mail: nperez@imt.mx

F. J. Castañeda · M. E. Peña
Grupo CALIDRA, Ciudad de México, CDMX, Mexico

Table 1 Characteristics of tested soils

Properties and classification	Soil from Monterrey	Soil from Guadalajara
USCS classification	SW	MH
Liquid limit (%)	34	64
Plasticity index (%)	16	34
Gs	***	2.4
Passing no. 200 (%)	4.31	63.7
Sand (%)	61.9	36.3
Clay (<2 micron)	***	16.0

water content. However, one of the techniques that has proven to be very effective in improving the properties of such soils is the addition of lime. This product, used since Roman times, remains as one of the most popular products to improve properties of materials that do not meet specifications.

Since 2007, the Mexican Transportation Institute is validating the behavior of additives with a protocol established for these products. In this paper, the authors present the verification of calcium oxide as an additive to improve mechanical properties of soils. The results shown in this paper are the result of the project IE-12/17 [2].

2 Materials

In this research, two soils were utilized. One soil was sampled in Guadalajara and another in Monterrey, both in Mexico. Table 1 summarizes the properties of each of the soils.

With such characteristics, the MH soil does not meet embankment or subgrade characteristics. The SW meets with gradation for subbase, but does not meet specifications of plasticity.

Regarding calcium oxide, this was a quicklime granulated and with 90% of CaO.

3 Lime Demand

To obtain the percentages of calcium oxide to be added to each soil, the pH test was carried out in accordance with ASTM D6276-99a (2006). The percentages of calcium oxide obtained were 5% and 4% for Monterrey and Guadalajara soils.

4 Compaction Characteristics

Proctor standard and modified tests were carried out for Guadalajara and Monterrey soils, respectively. Figures 1 and 2 show compaction curves of soil with and without calcium oxide.

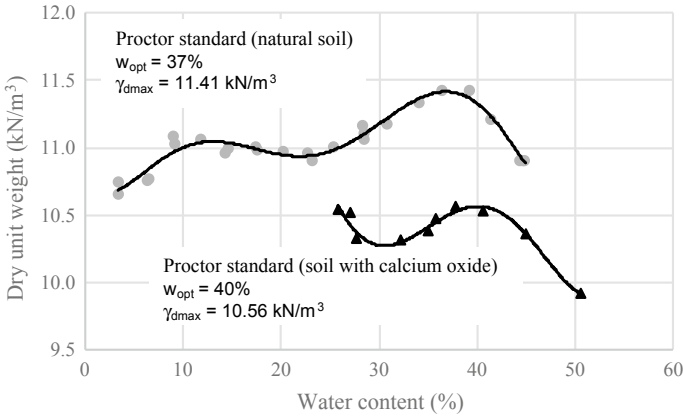


Fig. 1 Compaction curves for Guadalajara soil (evaluated with ASTM D698-12)

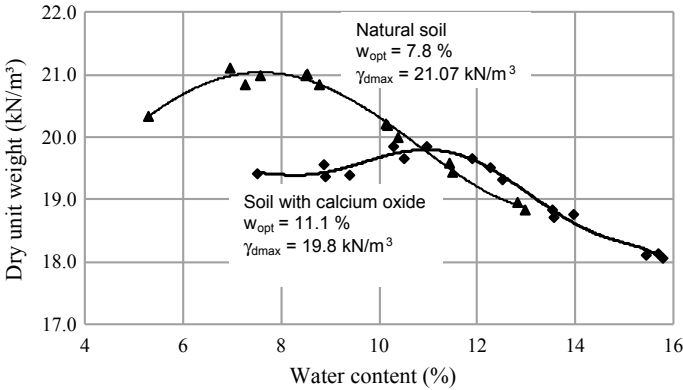


Fig. 2 Compaction curves for Monterrey soil (evaluated with ASTM D1557-12)

5 Laboratory Procedures to Evaluate Mechanical Properties

5.1 Specimen Compaction for Monterrey Soil

To prepare the specimens, the following procedure was followed:

- The soil was mixed with lime followed by the addition of compaction water (Fig. 3). The mix was stored during 24 h before compaction.
- For natural soil, compaction water was added, mixed and stored during 24 h.
- After the storage period, the soil was compacted in a mold of 15 cm diameter and 300 mm height (without collar). A mechanical compactor was used. The soil was compacted in six layers. In each layer, 160 drops were applied with a mass of 4.5 kg and 45.7 cm of drop height for natural soil (Fig. 4a).



Fig. 3 Addition of calcium oxide and mixing procedure

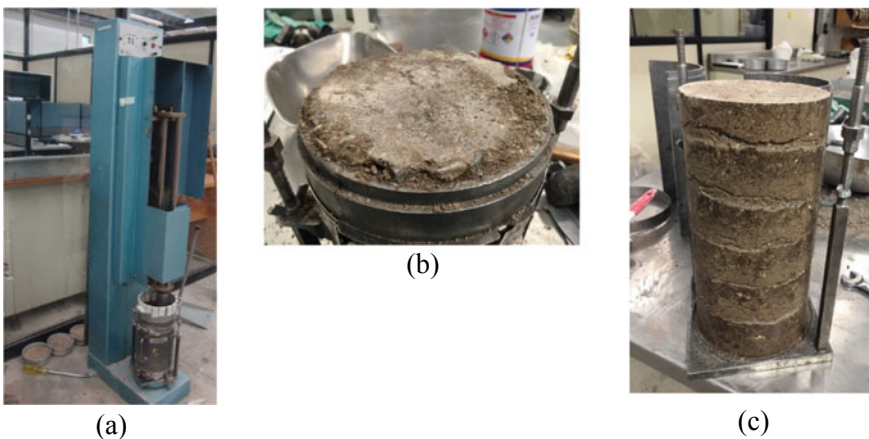


Fig. 4 Sample compaction



Fig. 5 Sample compaction for Guadalajara soil

- After compaction of the last layer, the sample was trimmed to obtain a uniform surface (Fig. 4b–c).
- Samples were tested after one of the following conditions: after compaction, after 7, 14 or 28 days of storage; after 7, 14 or 28 days of drying and 14 days of storage; after 7, 14 or 28 days of storage and 14 days of wetting through capillarity.

5.2 Specimen Compaction for Guadalajara Soil

The procedure for this soil is essentially the same (Fig. 5), except that in this case, the specimen is compacted in a mold of 71 mm diameter and 144 mm height (Fig. 5b).

In this case, the sample was compacted in eight layers; in each layers, 14 drops were applied with a hammer of 1 kg mass and 30.5 cm drop height (Fig. 5a).

The specimens of this soil were tested after the conditions that were already listed for Monterrey soil.

5.3 Procedure for Unconfined Compression Test

Unconfined compression tests were carried out by following the procedure ASTM D 2166. According to this procedure, the sample is placed in the loading machine, and a load is applied at a rate of 0.5–2%/min. In this research, the rate was 1.2%/min. The test was finished when the maximum load was observed; at the end of the test, the specimen was disintegrated to obtain samples to determine the final water content.



Fig. 6 Resilient modulus testing equipment

5.4 Resilient Modulus Test

Figure 6 shows the triaxial test equipment utilized in this research. The resilient modulus tests were conducted in accordance with the NCHRP 1-28A test protocol. According to this protocol, the resilient modulus test for subgrade soils consists of applying a cyclic-haversine-shaped load for a duration of 0.2 s and a rest period of 0.8 s. During the test, 16 sequences with different states of stress were applied.

For the case of granular material (soil from Monterrey), the load is applied during 0.1 s followed by a rest period of 0.9 s. In this case, 30 sequences were applied for base/subgrade materials.

5.5 Permanent Deformation Test

There is not a standard to perform permanent deformation tests. Thus, in this research, for the case of fine-grained soil, the test was carried out by applying 20,000 load cycles. The load was applied during 0.2 s followed by a rest period of 0.8 s. The stress state for this test was a deviator stress of 97 kPa and a confining pressure of 14 kPa. For granular material, the same number of cycles was applied; the deviator stress and confining pressure were 496.8 kPa and 14 kPa.

6 Test Results

6.1 Unconfined Compression

When evaluating an additive, it is common to carry out unconfined compression tests on cylindrical specimens. In this case, unconfined compression test was carried out on specimens that were stored, dried, or stored and wetted.

The results indicate that the unconfined compression of natural soil of Guadalajara (Fig. 7) seems to increase slightly with storage time. However, for the same condition, soil with calcium oxide increases the strength with storage time. In fact, for 28 days of storage, the strength of stabilized soil is twice to that of natural soil.

For natural soil that is allowed to dry, the strength increases with drying time; for stabilized soil, the strength remains almost constant regardless of drying time. When natural soil is exposed to water, the strength is lost almost completely.

In the case of Monterrey soil (Fig. 8), soil strength is almost not affected with storage time, but for stabilized soil, the strength increases for the same condition. In the case of the soil that is dried, it seems that the natural soil has greater strength than the stabilized soil probably due to soil suction generated. The condition of wetting shows that natural soil loses most of its strength, while the strength of the stabilized soil is little affected by wetting.

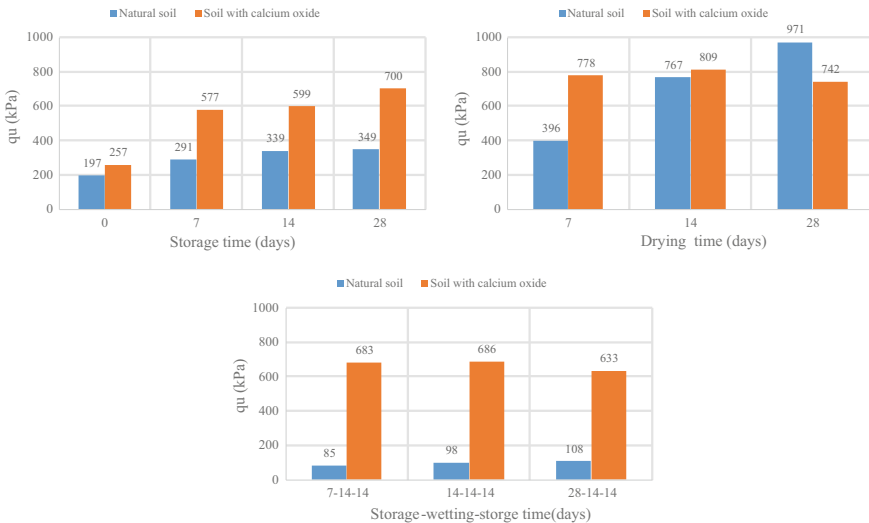


Fig. 7 Unconfined compression results for Guadalajara soil

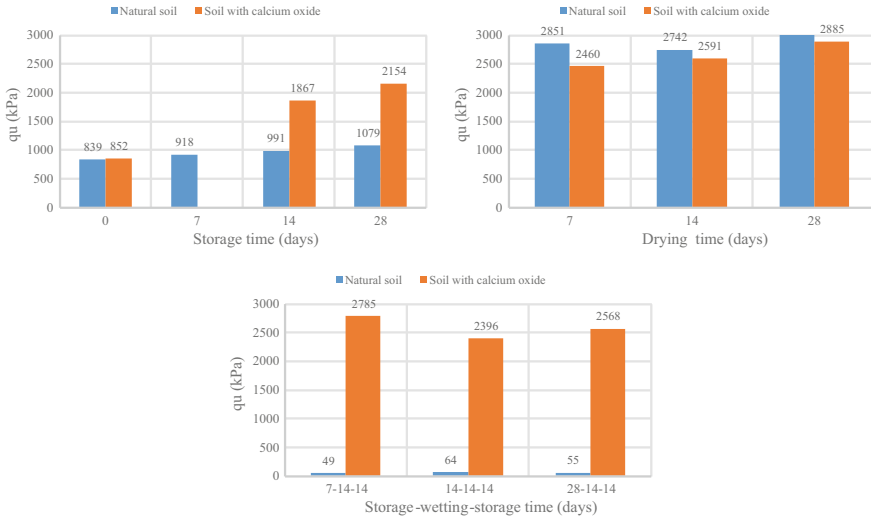


Fig. 8 Unconfined compression results for Monterrey soil

6.2 Resilient Modulus

With respect to resilient modulus of Guadalajara soil, natural soil slightly increases its modulus as storage time increases; when the soil dries, resilient modulus is also increased; however, for 14 and 28 days of drying, the values of this parameter are similar. When the soil absorbs water, the stiffness is lowered such that the resilient modulus goes down to approximately 25 MPa, regardless of the wetting time.

On the other hand, in the case of the soil stabilized with calcium oxide, just after the material is compacted, it already shows resilient modulus values superior to those of natural soil. Similarly, the storage time causes the resilient modulus to increase; however, the resilient modulus values obtained for 14 and 28 days show very little difference. Finally, when the soil is dried, the resilient modulus is in the range of 100 and 250 MPa regardless of the drying time. Furthermore, as it was already shown with results of unconfined compression strength, when the soil is stabilized with calcium oxide and the soil absorbs water, the resilient modulus values are not affected, since they show values between 100 and 250 MPa (Fig. 9).

In the case of Monterrey soil, the natural condition shows that there is not an increment of resilient modulus with storage time, and it seems that this parameter achieves an average value of 500 MPa regardless of the storage time. The soil stabilized with calcium oxide also has an average value of 500 MPa if the specimens are tested immediately after compaction, but if the specimens with calcium oxide are stored for 7, 14 or 28 days, the resilient modulus is similar but increases as bulk stress increases. For this soil, apparently longer storage times do not provide larger resilient modulus values. For specimens that were dried, in both cases, that is to say, soil with and without calcium oxide, the resilient modulus values are similar. The

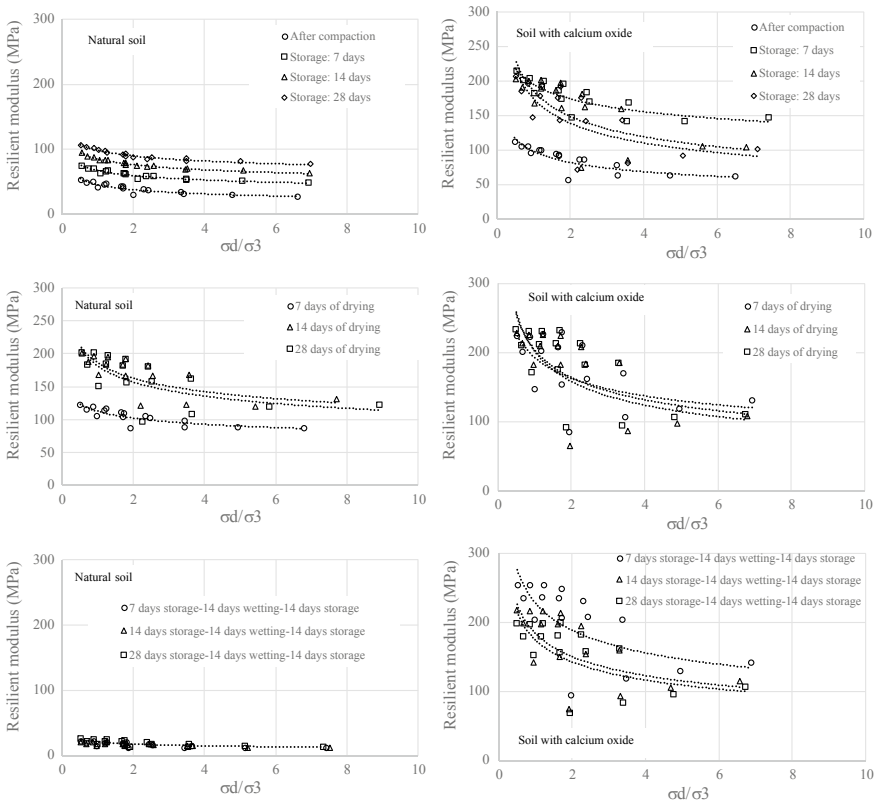


Fig. 9 Resilient modulus of Guadalajara soil with and without calcium oxide

condition that does make a difference is that of wetting. In this case, again, the soil that has calcium oxide does not lose its stiffness. Natural soil loses almost all its strength, and the resilient modulus goes down to values between 50 and 100 Mpa (Fig. 10).

6.3 Permanent Deformation Results

For the soils tested in the research, the permanent deformation tests results presented in Figs. 11 and 12. According to these results, the addition of calcium oxide does make a difference in permanent deformation behavior when the soil is only stored or dried. In addition, the stabilized soil is less susceptible to the effect of water. That is, while natural soils show large permanent deformation when they increase their water contents, the stabilized soils with calcium oxide show permanent deformations very close to zero. These results show clearly the advantage of adding calcium oxide to

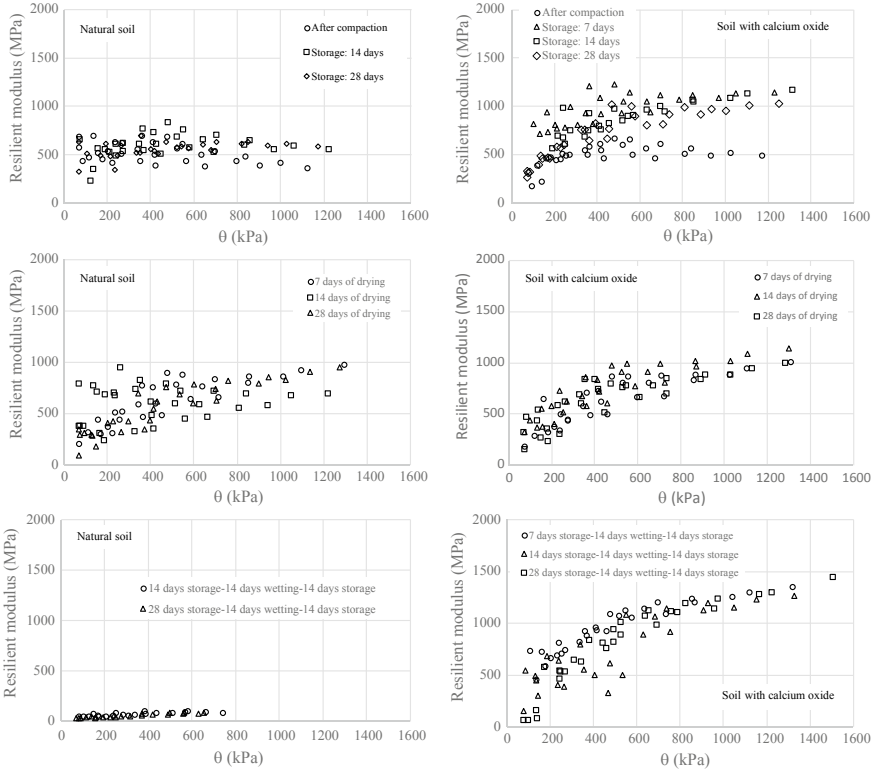


Fig. 10 Resilient modulus of Monterrey soil with and without calcium oxide

the soils. It may be an additional cost in the initial project, but in the future, this may be reflected in lower maintenance costs.

7 Conclusions

The results shown in this paper indicate that if calcium oxide is mixed with soils that do not meet specifications, the mechanical properties are improved. For both studied soils, the unconfined compressive strength and the resilient modulus are larger for stabilized soils (for the drying and storage condition). The condition that clearly discloses the behavior of the stabilized soil is when the soil becomes wetted. Under this condition, natural soils lose most of their strength, reflected in less unconfined compressive strength, less modulus of resilience and larger permanent deformation. On the other hand, soils stabilized with calcium oxide are less affected by water, since the strength and the resilient modulus are maintained at relatively high values, while the permanent deformation is maintained at values close to zero.

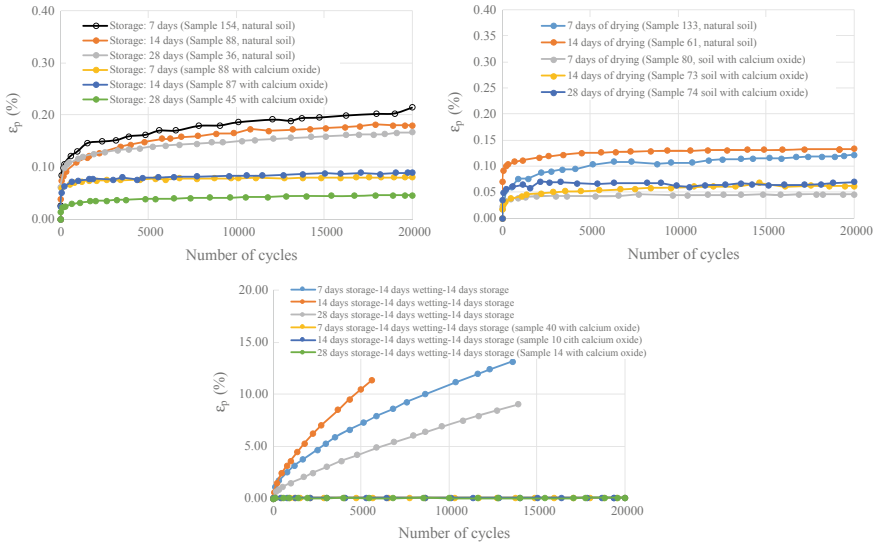


Fig. 11 Permanent deformation results of Guadalajara soil with and without calcium oxide

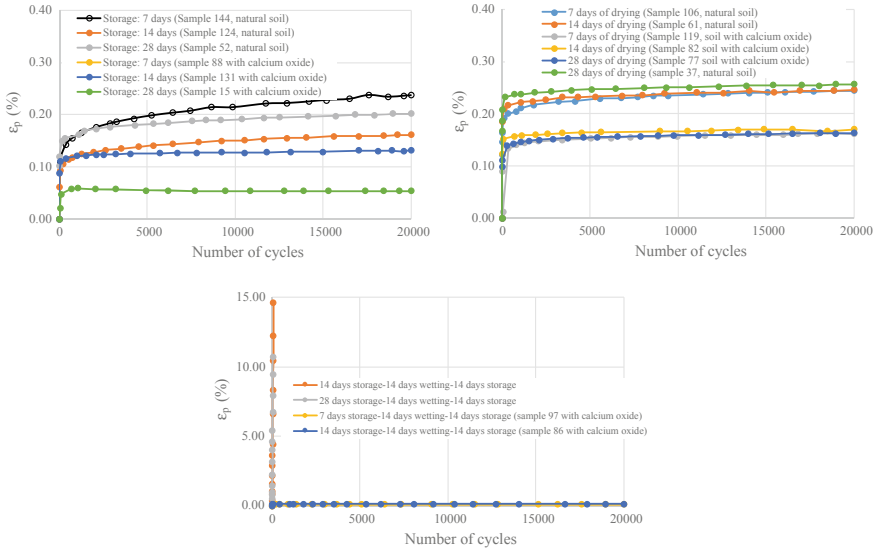


Fig. 12 Permanent deformation results of Monterrey soil with and without calcium oxide

References

1. Pérez N, Pérez A, Garnica P (2019) Evaluación del óxido de calico (estabilical) como estabilizador de suelo. Publicación técnica No. 560. Instituto Mexicano del Transporte. 2019
2. Reporte de Proyecto IE-12/17 Evaluación de las propiedades mecánicas de suelos tratados con estabilical. Agosto 2018. Instituto Mexicano del Transporte

Harbor Geotechnics

Particle Breakage Observed in Both Transitional and Non-transitional Carbonate Sands



Chenxi Tong , Sheng Zhang, and Daichao Sheng

Abstract Particle breakage of carbonate sands is widely encountered during the construction of harbor facilities. In this study, a series of one-dimensional compression tests on carbonate sands with different initial particle size distributions (PSDs) and initial void ratios were completed at high vertical stress (32 MPa), to investigate the influence of PSD and void ratio on the compression behavior of carbonate sands and the corresponding breakage properties. The PSDs used in this study were prepared by fractal distribution with two different fractal dimensions, i.e., 0.5 and 2.0. The results show that samples with fractal dimension of 0.5, where the initial PSDs are poorly graded, have a unique normal compression line (NCL), implying the occurrence of non-transitional behavior. However, when the PSD of samples tend to be better graded with fractal dimension of 2.0, non-convergent compression paths are likely to occur, which means a transitional behavior is identified. Particle breakage is observed after compression tests on samples with two different initial PSDs. It can, therefore, be concluded that particle breakage may have happened in both transitional and non-transitional behavior soils.

Keywords Particle breakage · Carbonate sands · Compressibility

1 Introduction

Particle breakage of carbonate sands has gained significant attention, largely due to the increasing number of offshore structures, harbor facilities and their widespread distribution [1, 2]. Particle breakage will change the particle size distribution (PSD), which will greatly affect the mechanical and deformational behavior of carbonate sands. Particle breakage is strongly affected by many factors including the initial PSD,

C. Tong (✉) · S. Zhang
School of Civil Engineering, Central South University, Changsha 410075, China
e-mail: cxtong@csu.edu.cn

D. Sheng
School of Civil and Environmental Engineering, University of Technology Sydney, Broadway,
Sydney, NSW 2007, Australia

initial void ratio. For example, a well-graded sample will suffer less particle breakage and different breakage pattern compared with the poorly graded one [3, 4]. This is mainly attributed to the different packing efficiency of the well-distributed samples and the higher coordination number for larger particles (i.e., larger particles may have been surrounded by more particles), which results in a low breakage probability within the sample [5–7].

The effect of PSD on the packing characteristics and compressive behavior of carbonate sand is rarely studied. Altuhafi and Coop [6] reported that a well-graded carbonate sand had a lower compression index, and it was more difficult to determine the normal compression line (NCL). When the sample is fractal graded with a fractal dimension D larger than 2.57 (see Eq. (1)), which was thought to be the ultimate PSD for a uniformly graded carbonate sand during ring shearing, a transitional behavior with non-convergent compression paths was observed during 1D compression at a high vertical stress up to 30 Mpa. As expected, no detectable particle breakage was found for such samples with transitional behavior after high stress compression.

In this study, we report the 1D compression test results at high vertical stress (32 Mpa) on carbonate sand with two different initial fractal-graded PSDs and various initial void ratios. A more compressive investigation on the effect of PSD and void ratio on the compression behavior of carbonate sand in terms of the compression index, the tangent-constrained modulus and the particle breakage is also presented with both qualitative and quantitative approaches.

2 Material Tested and Procedures

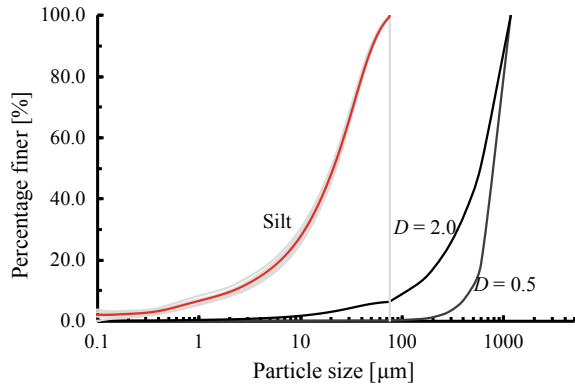
2.1 Material Tested

The carbonate sand tested in this paper was commercially available with almost pure calcium mineral composition with the largest particle size of 1.18 mm. The specific gravity of carbonate sand was measured to be 2.80 by using an automated gas pycnometer (Micromeritics Autopyc II 1340 with accuracy of 0.05%). The original material was sieved carefully to separate into different particle sizes before preparing different initial PSDs that are fractal graded according to the expression:

$$F(d) = \left(\frac{d}{d_{\max}} \right)^{3-D} \quad (1)$$

where $F(d)$ is the mass percentage finer than particle size d , d_{\max} is the maximum particle size, and D is the fractal dimension. In this study, two different values of D (i.e., $D = 0.5, 2.0$) are adopted by mixing particles from each size fraction in a target proportion. It should be noted that Eq. (1) is developed based on fractal theory, which could be used as a typical representation of PSD. The minimum particle size

Fig. 1 Initial PSDs of the tested carbonate sand in semi-log plot



of sample is $0.1 \mu\text{m}$, and the distribution of the silt fraction as shown in the red line in Fig. 1 was determined using the micromeritics X-Ray particle size system (Sedigraph 5120). Since it is difficult and even impossible to separate the silt fraction into different size intervals, an average grading for the silt fraction was adopted for calculating the overall PSD of the sample as shown in the black lines in Fig. 1.

2.2 1D Compression Test

The constant rate of strain (CRS) one-dimensional compression tests was carried out with sample diameter of 60 mm. Samples with a range of initial densities and PSDs were tested dry to a high vertical stress of 32 MPa. The tests were carried out at the displacement rate of 1 mm/min with the sample height of 20 mm for consistency with previous work [1]. Samples were prepared by 10 mm/layer, and the under compaction method proposed by Ladd [8] was adopted to obtain a homogeneous of PSD and a uniform density over the entire range of the sample height. The measured displacement was corrected for apparatus compliance for three different sample heights.

The initial void ratio was calculated by measuring the initial dry weight (readability of 0.01 g) and initial sample height (at least three height measurements with difference less than 0.1 mm). The final void ratio could be calculated from the initial void ratio and the vertical displacement recorded during the loading process as shown in final void ratio 1 in Table 1 or could be measured from the final sample height as shown in final void ratio 2 in Table 1. The difference of ± 0.02 in the final void ratio was acceptable as suggested by Shipton and Coop [9]. Details of the 1D compression tests are summarized in Table 1.

Table 1 Summary of 1D compression tests reported in this study

Test number	Initial void ratio [-]	Final void ratio 1 [†] [-]	Final void ratio 2 [‡] [-]
FG0.5_1 [§]	1.148	0.545	0.546
FG0.5_2	1.099	0.529	0.533
FG0.5_3	1.056	0.528	0.528
FG0.5_4	0.955	0.532	0.531
FG0.5_5	0.907	0.526	0.529
FG2.0_1	0.975	0.504	0.484
FG2.0_2	0.925	0.490	0.481
FG2.0_3	0.862	0.469	0.455
FG2.0_4	0.756	0.462	0.463
FG2.0_5	0.664	0.440	0.435

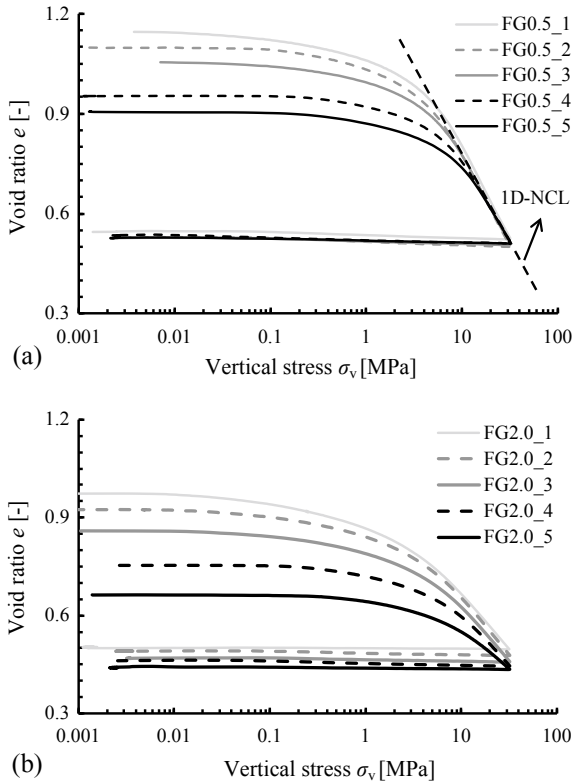
Note § FG0.5_1 the first number means the initial fractal dimension is 0.5, the second number means the different initial void ratio; † means the final void ratio is calculated from initial void ratio and vertical displacement measured by LVDT; ‡ means the final void ratio is calculated from final measurement of sample height

3 Test Results

Compression curves of the two carbonate sands with various initial void ratio are presented in Fig. 2. It is clear from Fig. 2a that the sample with a narrow-graded PSD (i.e., $D = 0.5$) tends to have a unique one-dimensional normal compression line (1D-NCL) in the e -log (σ_v) space. The slope of the NCL, i.e., the compressibility index ($C_c = (-\Delta e)/\Delta \log(\sigma_v)$, where e is the void ratio and σ_v is the effective vertical stress) is calculated to be approximately equal to 0.51. Figure 2b shows little convergence of compression paths for a wider-graded carbonate sand with $D = 2.0$. The difference of void ratio at vertical stress of 32 MPa is three times of the estimated accuracy of the void ratio of 0.02, which indicates that a transitional behavior is observed.

Another obvious evidence to prove the non-transitional and transitional behavior of the samples with two different initial PSDs is presented in Fig. 3, where the relation between the tangent-constrained modulus M ($= \Delta\sigma_v/\Delta\varepsilon_v$, where ε_v is the vertical strain) and the vertical stress is shown. As summarized by Mesri and Vardhanabhuti [10], there are three main shapes of e -log (σ_v) curve of granular soils during compression, i.e., type A, type B and type C. In type A compression curve, M first increases, then decreases and finally increases with increasing vertical stress. In type B compression curve, M first increases, then almost keeps constant (see the red lines in Fig. 3a) and finally increases with increasing vertical stress. In type C compression curve, M always increases with an increase in vertical stress throughout the compression stage. As shown in Fig. 3a, a type B compression curve for the dense sample and a type C compression curve for the loose sample are observed for the sample with $D = 0.5$. All the M for different initial void ratio at high vertical stress

Fig. 2 1D compression of carbonate sand with different initial PSDs: **a** $D = 0.5$, **b** $D = 2.0$



approach to almost the same value, indicating all the compression curves, will eventually be coincident at high vertical stresses for the narrow-graded sample as seen from Fig. 2b. For a wider-graded sample with $D = 2.0$, only type C compression curve is observed with all the range of initial void ratio. The values of M for all the compression curves (except for the densest sample) tend to be identical, which means the compression lines will be parallel at even larger stress level. As we can see from Fig. 2b, the densest sample yields at very large vertical stress, and the linear part of compression curve in the e - $\log(\sigma_v)$ space is still not obvious. In that case, the linear part will be eventually parallel with other compression lines if the vertical stress is large enough. Considering the fact that the other four compression curves have been parallel already at the given stress level, it is still convincing that the behavior of sample with $D = 2.0$ is clearly transitional. As compared with Fig. 3a, b, a decrease in M can be observed as the initial PSD becomes more uniform.

Post-test samples were sieved using standard sieving apparatus to obtain the evolution of PSD due to particle breakage. The PSDs before and after tests are shown in Fig. 4. It is interesting noting that the PSDs are more or less straight lines in the double logarithmic plot, which means the PSD after test is also fractal graded. To quantify particle breakage, the modified Hardin's breakage index B_r , proposed by Einav [11]

Fig. 3 Tangent-constrained modulus of carbonate sand with different initial PSDs: **a** $D = 0.5$, **b** $D = 2.0$

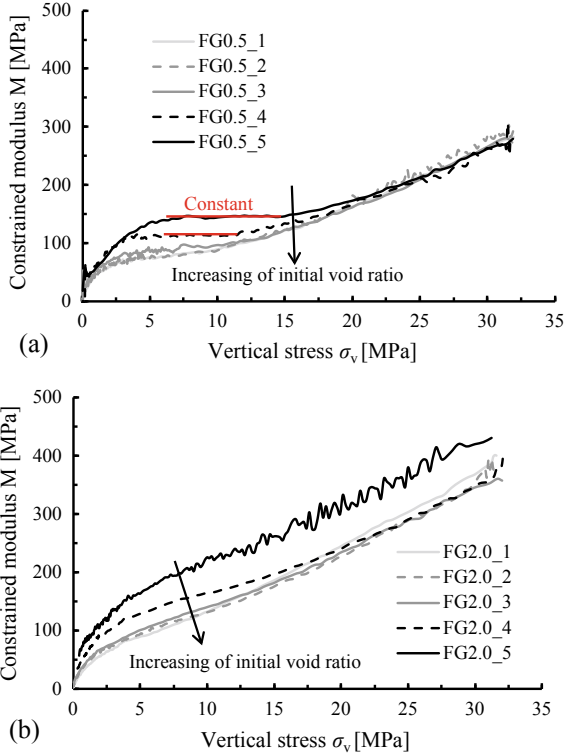
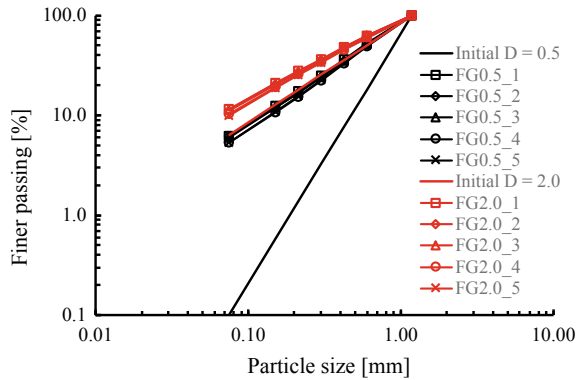
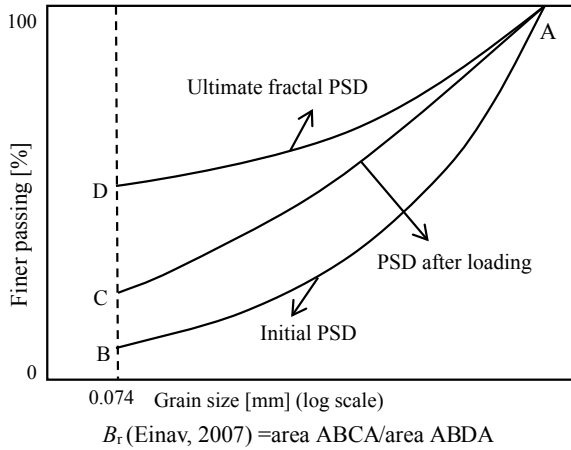


Fig. 4 PSDs of the two soils before and after test



is widely used as it considers the ultimate fractal grading at extreme conditions, and it is defined in Fig. 5. Inspired by the observation that PSDs after test are fractal graded, a new breakage index is defined as

Fig. 5 Definition of modified Hardin's breakage index B_r [11]



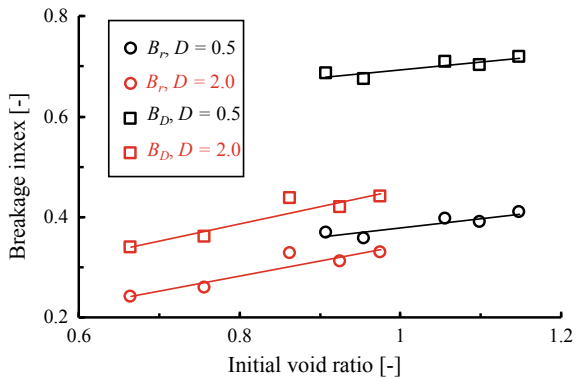
$$B_D = \frac{D - D_{\text{initial}}}{D_{\text{ultimate}} - D_{\text{initial}}} \tag{2}$$

where

- D is the fractal dimension after test, and
- D_{initial} and D_{ultimate} are the fractal dimensional at initial and ultimate state, respectively
- D_{ultimate} is adopted 2.6 for carbonate sand as reported by others [2, 12].

Figure 6 shows the values of B_r and B_D for the two samples with different PSDs and initial void ratios. In general, a denser sample will suffer less particle breakage in terms of both breakage indices B_r and B_D , which is in accordance with previous findings [6, 13]. It seems that the effect of initial PSD on particle breakage is not obvious when using B_r , which is different from what is commonly accepted that initially, the PSD plays a significant role on particle breakage. In that case, using B_D

Fig. 6 Values of B_r and B_D for the two soils with different initial PSD after test



as breakage index will highlight the importance of initial PSD. Overall, significant particle breakage is observed for the narrow-graded and wide-graded carbonate sand with non-transitional and transitional behavior when using both the breakage indices B_r and B_D .

4 Conclusion

Particle breakage of carbonate sand will affect the performance of harbor facilities. This study presents 1D compression tests on carbonate sand with two different initial fractal-graded PSDs. The narrow-graded one shows a non-transitional behavior with unique 1D-NCL. A type *B* compression curve for the dense sample and a type *C* compression curve for the loose sample are observed for the narrow-graded sample. The wide-graded sample, however, shows typical feature of transitional behavior with non-convergent paths in compression. The compression curve is always type *C* compression curve. Significant particle breakage can be observed in both transitional and non-transitional carbonate sands. Particle breakage is significantly influenced by both initial PSD and initial void ratios when using the proposed breakage index B_D , while it seems that particle breakage is not obviously affected by initial PSD when Einav's breakage index B_r is adopted for analysis.

Acknowledgements This research was supported by the National Natural Science Foundation of China (Grant No. 52008402).

References

1. Tong CX, Burton GJ, Pineda J, Zhang S, Sheng D (2020) Particle breakage of uniformly graded carbonate sands in dry/wet condition subjected to compression/shear tests. *Acta Geotech* 15:2379–2394
2. Coop MR, Sorensen KK, Freitas TB, Georgoutsos G (2004) Particle breakage during shearing of a carbonate sand. *Géotechnique* 54(3):157–164
3. Nakata AFL, Hyde M, Hyodo H, Murata (1999): A probabilistic approach to sand particle crushing in the triaxial test. *Géotechnique* 49(5):567–583
4. Nakata Y, Hyodo M, Hyde AF, Kato Y, Murata H (2001) Microscopic particle crushing of sand subjected to high pressure one-dimensional compression. *Soils found* 41(1):69–82
5. McDowell GR, Bolton MD (1998) On the micromechanics of crushable aggregates. *Géotechnique* 48(5):667–679
6. Altuhafi FN, Coop MR (2011) Changes to particle characteristics associated with the compression of sands. *Géotechnique* 61(6):459–471
7. Tong CX, Zhang KF, Zhang S, Sheng D (2019) A stochastic particle breakage model for granular soils subjected to one-dimensional compression with emphasis on the evolution of coordination number. *Comput Geotech* 112:72–80
8. Ladd RS (1978) Preparing test specimens using undercompaction. *Geotech Test J* 1(1):16–23
9. Shipton B, Coop MR (2012) On the compression behaviour of reconstituted soils. *Soils Found* 52(4):668–681

10. Mesri G, Vardhanabhuti B (2009) Compression of granular materials. *Can Geotech J* 46(4):369–392
11. Einav I (2007) Breakage mechanics—part I: theory. *J Mech Phys Solids* 55(6):1274–1297
12. Xiao Y, Liu H, Xiao P, Xiang J (2016) Fractal crushing of carbonate sands under impact loading. *Géotech Letters* 6(3):199–204
13. Xiao Y, Liu H, Chen Q, Ma Q, Xiang Y, Zheng Y (2017) Particle breakage and deformation of carbonate sands with wide range of densities during compression loading process. *Acta Geotech* 12(5):1177–1184

Investigation of Interaction of Piles at New Cargo Sea Transportation Route and LRT Projects with Problematic Soils of Kazakhstan



Askar Zhussupbekov , Victor Kaliakin, Der-Wen Chang , and Abdulla Omarov 

Abstract Two transportation megaprojects in Kazakhstan are considered. The first of these is the cargo offloading facility (COF) that was built on the northeastern shore of the Caspian Sea as part of the New Cargo Sea Transportation Route. The second project is the Light Railway Transport (LRT) public transportation system that was built in the capital city of Nur-Sultan. Due to problematic foundation soils, both of these larger projects employed piled foundations. This paper discusses the field investigations that were performed to quantify the performance of piles driven in the aforementioned soils so as to determine the pile bearing capacities using analytical interpretation techniques.

Keywords Precast concrete joint piles · Bored piles · Integrity testing

1 Introduction

Two notable transportation projects were recently completed in Kazakhstan. The first of these projects is the cargo offloading facility (COF) that was built on the northeastern shore of the Caspian Sea as part of the New Cargo Sea Transportation Route. The second project is the Light Railway Transport (LRT) public transportation system that was built in the capital city of Nur-Sultan. Due to problematic foundation soils, both of these larger projects employed piled foundations. This paper discusses the investigations that were performed to investigate the performance of piles driven in the aforementioned soils, as well as bearing capacities determined using analytical interpretation techniques. Due to space limitations, emphasis is placed on the piles driven at the COF.

A. Zhussupbekov (✉) · A. Omarov
L. N.Gumilyov Eurasian National University, Nur-Sultan City, Kazakhstan

V. Kaliakin
University of Delaware, Newark, DE 19716, USA

D.-W. Chang
Tamkang University, Tamsui, Taiwan



Fig. 1 Overview of the Prorva marine channel

2 Overview of the Cargo Offloading Facility

The COF is part of the future growth project that was undertaken to expand access to the large oil fields of Western Kazakhstan [1–3]. In 2017, a new transportation route was constructed from the northeast part of the Caspian Sea to Tengiz, thus creating channel access to new facilities in the port of Prorva (Fig. 1). The COF is one such facility; it is designed to facilitate the loading of various types of marine vessels [1, 2]. Consequently, the COF is expected to become a future transportation hub between Russia, China and Europe [4]. The construction of the COF was a rather unique undertaking in Kazakhstan.

3 Geological Aspects of Cargo Offloading Facility Soils

The facilities such as the COF are confined to the New Caspian accumulative marine terrace surface. Genetically, they correspond to the period of time passing the Caspian Sea New Caspian ingression. Hypsometrically, the east boundary of terrace is determined by an absolute elevation of -22.0 m; the west boundary of the terrace hypsometrically corresponds to absolute elevation of -26.0 m [1]. The steeply sloping and, more rarely, ridge steeply sloping forms of relief are peculiar to the terrace surface. Absolute surface elevations within the investigated area possess values from -25.65 m up to -25.84 m (Fig. 2). The surface of the terrace is exposed to flooding by Caspian Sea piled-up waters at 2% available 3.0 m high surge wave and 2% available Caspian Sea background level equal to -26.1 m. There is a tendency for

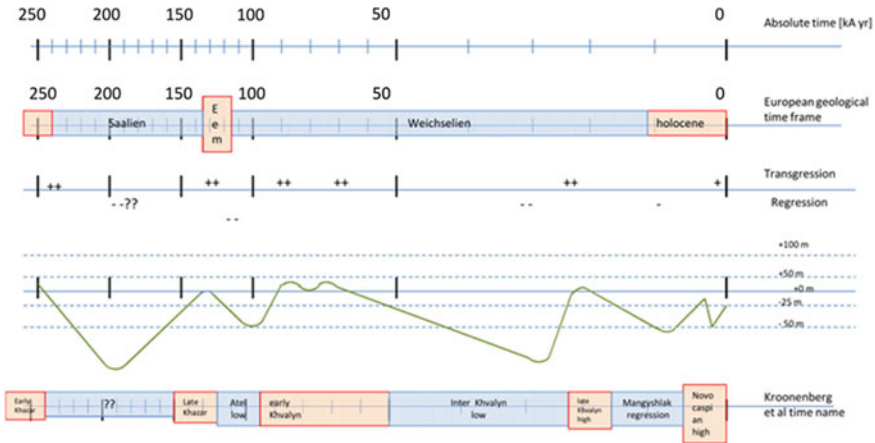


Fig. 2 Overview of the development of the Caspian basin

the terrace surface to rise in the southeast. The geological aspects of the area in question are closely related to its geological evolution and are determined by two stratigraphic sequences of un lithified clastic sediments of marine origin, forming a geological section to a depth of 30 m below the surface [1].

The first sequence of the New Caspian (Holocene un lithified clastic sediments of marine origin—mQ4nk) developed as a sedimentary cover both on land and in the marine part of the designed route. The seabed surface within the route is covered by a thin layer of ooze with sand and shells (GE-2) or by fine clayey sand (GE-3). Lower down the section, there are fine- and medium-sized sands (GE-8) with inter-beds of soft-tight plastic clays and loams (GE-7). The sediments are water saturated and saline; salinization is quite intense with addition of carbonates and gypsum. Their color is mainly gray with hues variations [1].

The second sequence, Khvalyn (upper Pleistocene un lithified clastic sediments of marine origin—mQ3 hv), constitutes the lower part of the section studied by boreholes. The Khvalyn sediments are represented by soft-tight plastic loams (GE-9) and semi-solid (GE-10) with alternation of fine and powder-like sands (GE-8). The sediments are quite saline; salinization is intense with addition of carbonates and gypsum. The sediments swell easily [1].

Soils building up a geological environment at a depth down to 10 m from ground surface is salinized with a high salinity level; at natural salinity levels, they contain increased amounts of carbonates, gypsum and insignificant amount of organic matter (humus). Loamy silt relates to a slightly saturated clayey soil group; it possesses thixotropic properties. Light silty clay possesses a low degree of swelling. The groundwater relates to a weak brine group in an upgraded version. The water-soil environment possesses a medium degree of aggressivity in reference to W8 graded concrete. The soils also possess high aggressivity to low allowed and carbon steel.

Eleven engineering geological elements (units) are identified based on the geological setting and borehole logs. These elements are ordered top-down, which means that unit EGE-1 is located at the top and EGE-11 at the bottom of the soil column; the units EGE-2 to EGE-10 are then situated in between these layers.

4 Installation and Testing of Precast Concrete Joint Piles

The need to ensure high bearing capacity in the complex geological conditions of Western Kazakhstan requires the use of economically and ecologically robust foundation [1–6]. Traditionally, piled foundations have been used. The effectiveness of piles largely depends on the accuracy of determining the bearing capacity of the pile and the design load that it can safely support. Design standards for piles commonly determine the bearing capacity by an analytical method using generalized design tables and charts, or from static or dynamic field test data obtained from a loaded pile.

Design calculations indicated that precast concrete joint piles (PCJPs) would be the most optimal foundation elements for the COF. The main advantages of PCJPs are high productivity in manufacturing, economic efficiency, ease in transportation to the site, quick connection between pile segments, reduced fuel consumption during installation, and relatively low maintenance. More importantly, perhaps, it is the ability to produce piles having the required length so as to provide the bearing capacity specified by structural engineers for the problematic soils of Western Kazakhstan.

Since PCJPs had not previously been used in Kazakhstan, their application for the first time warranted a rather comprehensive field study program [1–5]. It was thus decided to perform such tests at pilot sites. These sites, referred to as construction sites “A” and “B,” are shown schematically in Fig. 3.

The PCJPs considered in the present study had a square cross section measuring 400 mm on a side and consisted of two segments. The length of the lower segment was 16.0 m; the upper segment length was either 11.5 m (actual application) or 9.5 m (for tests at the construction sites A and B). Pin-jointed connections were used to join consecutive lengths of the piles.

Leader boreholes were made to facilitate the installation of the PCJPs. The drilling of such boreholes, and the subsequent removal of soil from the boreholes, was realized using fully hydraulic, self-erecting Soilmec CM-70 and Bauer-28 drill rigs. Once a borehole was drilled, the pile segments were installed using Junttan PM-25HD or PM-25LC driving rigs with HHK-7A or HHK-9A hydraulic hammers [1–5].

Figure 4 shows the testing platform used in performing a typical static compression load test (SCLT). The so-called reference frame consists of two H-beams, each having a depth of 20 cm and a length of 5.3 m. These two beams served as a reference for the displacement sensors; they were regularly checked with an optical level instrument to detect any movements that might affect the displacement readings. The load was applied to the piles by a hydraulic jack that was supported by a main (reaction) beam in the manner shown in Fig. 4.

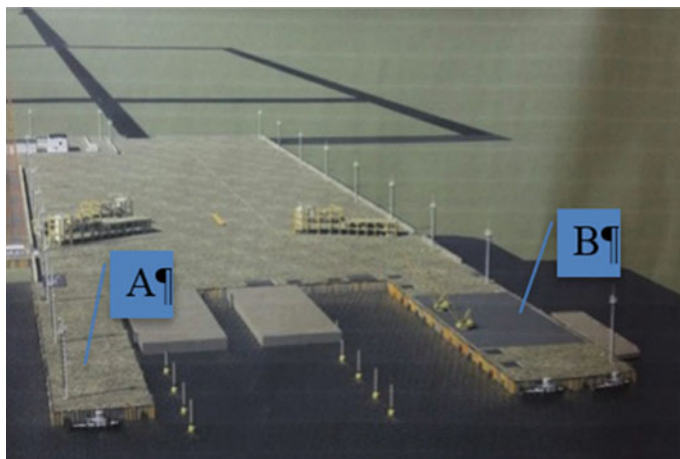


Fig. 3 Cargo offloading facility: construction sites Prorva A and B

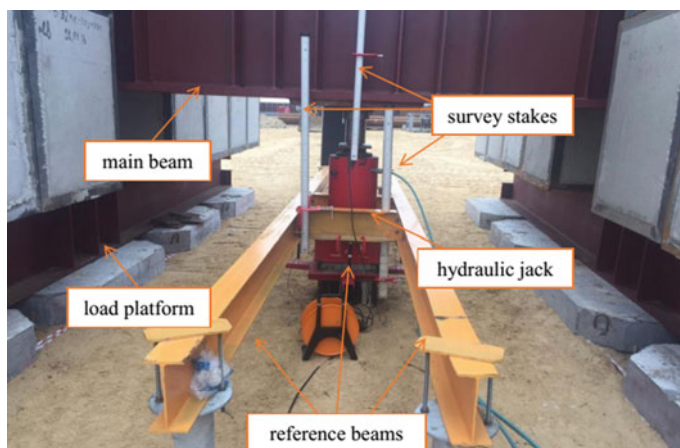


Fig. 4 Testing platform for typical static compression load test [1]

Three SCLTs (denoted by A_1 , A_2 and A_3), with a with maximum load of 3278 kN, were performed at construction site A. Figure 5a shows the load-settlement curves obtained from these tests. Four SCLTs (denoted by B_1 , B_2 , B_3 and B_4), with a maximum load of 1638 kN, were performed at construction site B. Figure 5b shows the load-settlement curves obtained from these tests [1, 2].

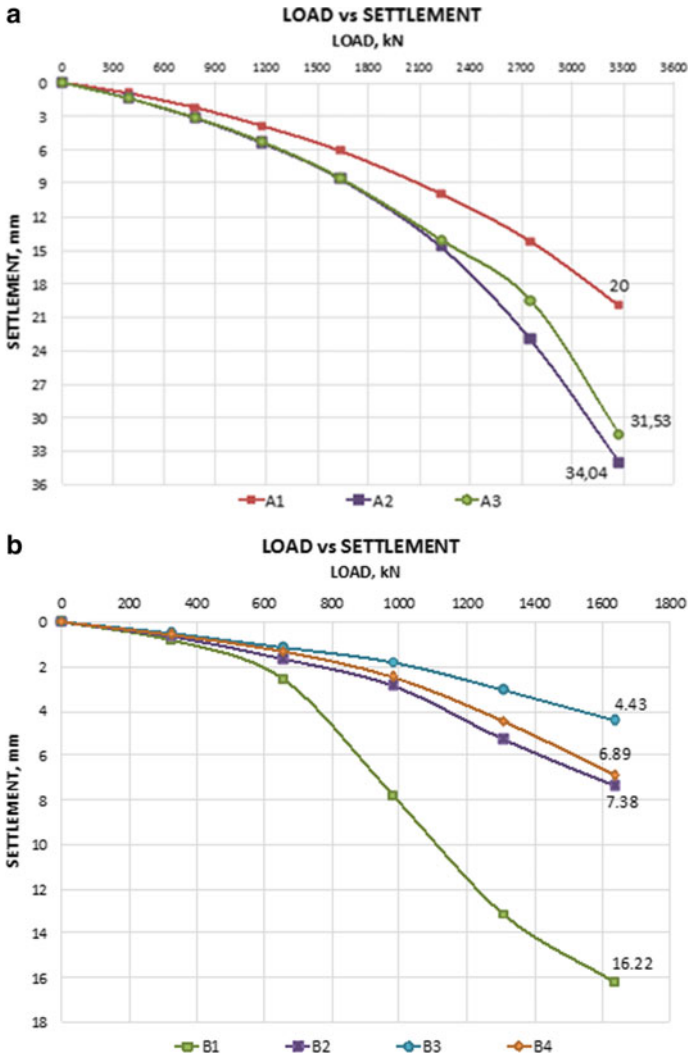


Fig. 5 Static compression load test results at construction sites, a A and b B [1]

5 Bearing Capacity Determined Using Interpretation Methods

Through load-settlement curves such as those shown in Fig. 5, the results of SCLTs allow for an evaluation of the degree of pile settlement resulting from a load applied over a given time to the pile. Various interpretation methods can be used to analyze the results of SCLTs [5–8].

In the present study, the Davisson, Chin and Fuller and Hoy methods [1, 5–8] were investigated in order to estimate the bearing capacity of PCJPs tested in the SCLTs performed at construction sites *A* and *B*.

Figure 6 shows the manner in which the bearing capacity of PCJP A_1 (i.e., PCJP number 1 at construction site *A*) is determined using the Davisson method. In this method, the bearing capacity is determined using an offset or “Davisson limit,” consisting of a line parallel to the initial tangent to the load-settlement curve. This method was suggested in conjunction with the wave equation analysis of driven piles and has gained widespread use over time [1, 2]. The Davisson limit (offset) is defined as a limiting load corresponding to the movement exceeding the elastic compression of a pile by an offset of 3.8 mm, plus a factor equal to the pile diameter (in mm) divided by 120. In the case of a 400 mm square PCJP, the radius of a circle circumscribing the square is $400\sqrt{2} = 566$ mm. Dividing this equivalent diameter by 120 and adding the resulting quotient to 3.8 mm gives an offset of 8.52 mm. Applying this offset in the manner shown in Fig. 6 gives a pile capacity of 2,873 kN [1, 2].

In the Chin method [1, 6, 7], each recorded settlement value is divided by its corresponding load value. The resulting value is plotted against the settlement, and a trend line is drawn on the plot as shown in Fig. 7.

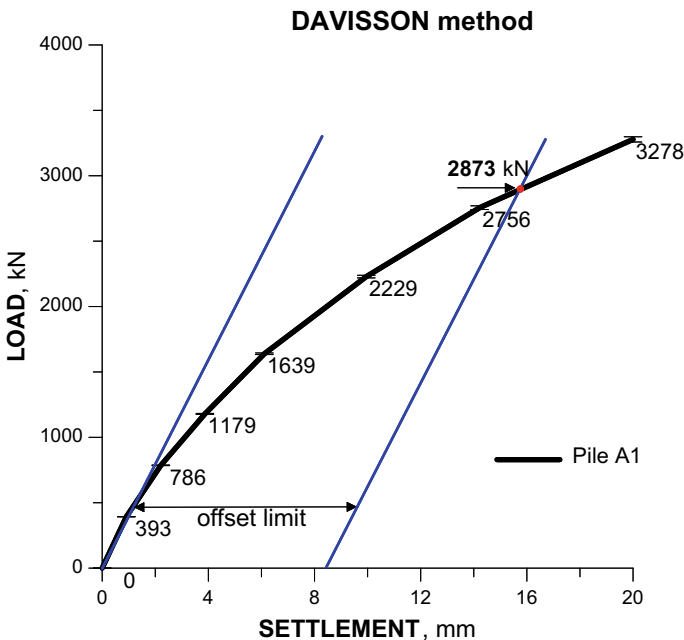


Fig. 6 Bearing capacity of PCJP A_1 computed using the Davisson method [1, 2]

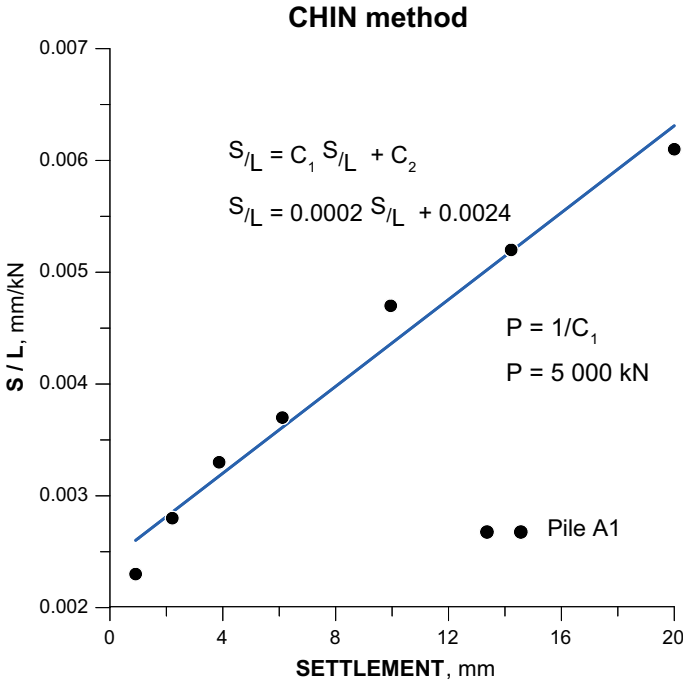


Fig. 7 Bearing capacity of PCJP A₁ computed using the Chin method [1, 2]

In the approach proposed by Fuller and Hoy [1, 2], the pile capacity is equal to the test load at which the inverse slope of the load-settlement curve is equal to 0.14 mm/kN. Figure 8 shown this approach, as applied to PCJP A₁ [1, 2].

Table 1 summarizes the bearing capacities of PCJPs tested at construction sites A and B computed using the Davisson, Chin and Fuller and Hoy methods. Also, listed in this table are the results of dynamic load tests performed on the PCJPs at the same sites. As evident from the results of Table 1, there is rather significant differences in the bearing capacity values obtained using the three aforementioned interpretation methods.

6 Overview of the LRT Project

Although employing a different type of pile than at the COF, the LRT public transportation system in the city of Nur-Sultan is also required an investigation of the interaction between piles and the surrounding problematic soil.

The first phase of the LRT construction project begins at Nazarbaev International Airport and ends 22.4 km later at the newly constructed “Nurly zhol” railway station. The LRT project includes 18 stations. This public transportation system runs

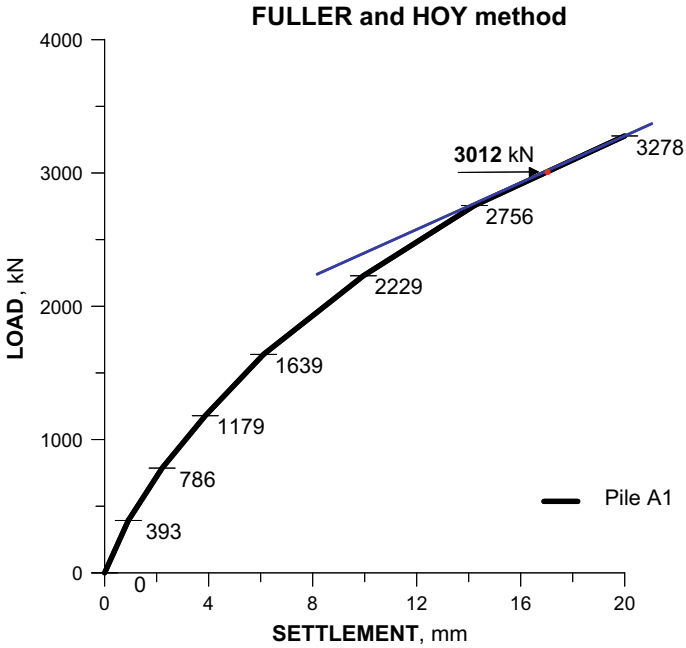


Fig. 8 Bearing capacity of PCJP A₁ computed using the Fuller and Hoy method [1, 2]

Table 1 PCJP capacities as a result of static compression load tests [1, 2]

<i>PCJP capacities obtained by interpretation methods (kN)</i>							
Methods	A ₁	A ₂	A ₃	B ₁	B ₂	B ₃	B ₄
Davisson	2873	2400	2609	1223	–	–	–
Chin	5000	5000	5000	2000	2500	3333	2500
Fuller and Hoy	3012	3025	3028	1070	1325	1295	1326
<i>Results of bearing capacity by pile dynamic tests (PDA) (kN)</i>							
Capacity	2202	1768	2497	2518	2203	2502	1722

completely above ground [8–13]. The track is supported by columns. The foundation for such columns consists of four bored, cast-in-place concrete piles. The diameter of the piles is approximately 1000 mm, and the lengths of the piles range from 8 to 30 m.

7 Field Pile Integrity Tests

The piles used in the LRT project are shorter than those used in the COF. The biggest issue related to the former is the detection of defects in the piles used in conjunction with the column supports. To check for the presence of such defects, ultrasonic integrity tests were performed using a cross-hole analyzer.

Of particular interest to the present discussion are the ultrasonic integrity tests that were performed on piles LRT -114-7 (Pile-1) and LRT -YCR13 (Pile-2). Both of these piles were 1.2 m in diameter; the concrete strength was B40 [9-14]. When installing these test piles, 42 mm diameter steel access tubes were included in the reinforcement cages in order to allow for the cross-hole tests to be performed. Ultrasonic measurements were made between the access tubes, with a vertical resolution of 5 cm. Figure 9 shows the equipment used in performing such integrity tests, as well as the results of a typical integrity test [9-14].

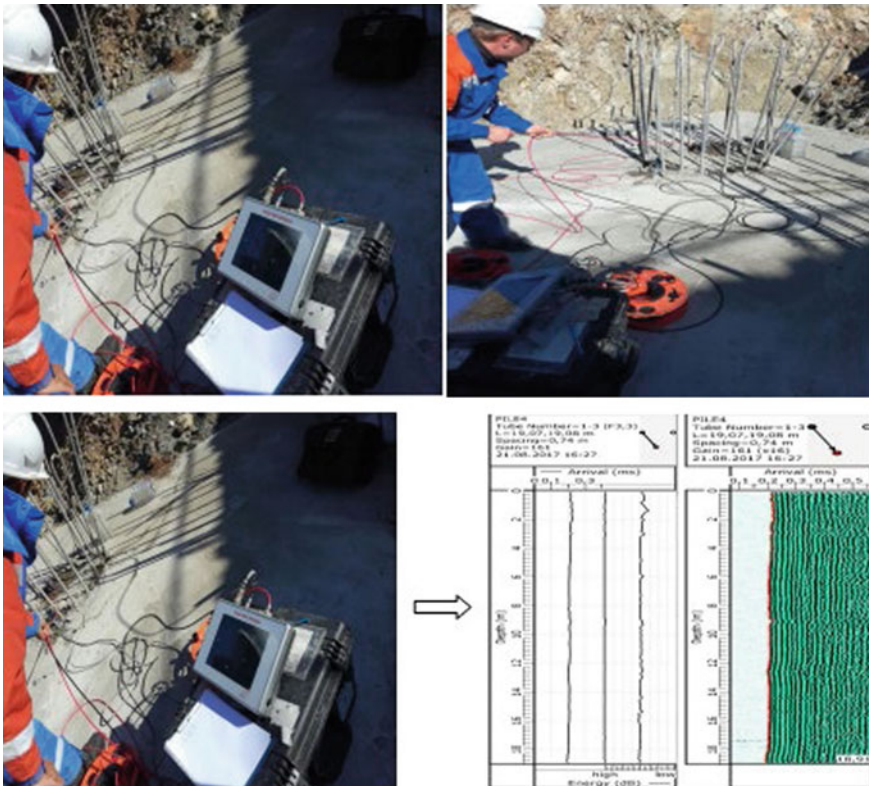


Fig. 9 Field pile integrity test performed at the site of a column support for the LRT project in Nur-Sultan city

Figure 9 shows the results of the ultrasonic integrity tests. Deviations from the concrete continuity or homogeneity are manifested by changes in speed or energy absorption of the transmitted waves. These appear as red lines in Fig. 10 [9–14].

8 Conclusions

The bearing capacities of precast concrete joint piles (PCJPs) under ultimate and working loads in the cargo offloading facility (COF) Project in West Kazakhstan were examined using interpretation methods applied to field test results.

The ultimate capacities of PCJPs at construction site A are reported as 2000–2500 kN, while the yield capacities of the PCJPs under working load at construction site B were 1000–1500 kN. The ultimate capacities of these piles at construction site B are reported as 2000–3000 kN. The factor of safety of the allowable capacity can be satisfied according to the local designing specifications.

At ultimate load, it is found that the Chin interpretation method gave the highest bearing capacity values for both sites A and B.

Results of cross-hole analyzer testing presented have been used to successfully detect defects, the presence of low-quality concrete (i.e., strength lower than the design strength) and poor construction practices. The soil conditions at the construction site also affect the results of ultrasonic testing. The cross-hole sonic logging method is most accurate and highest quality test for field observation of deep pile foundations.

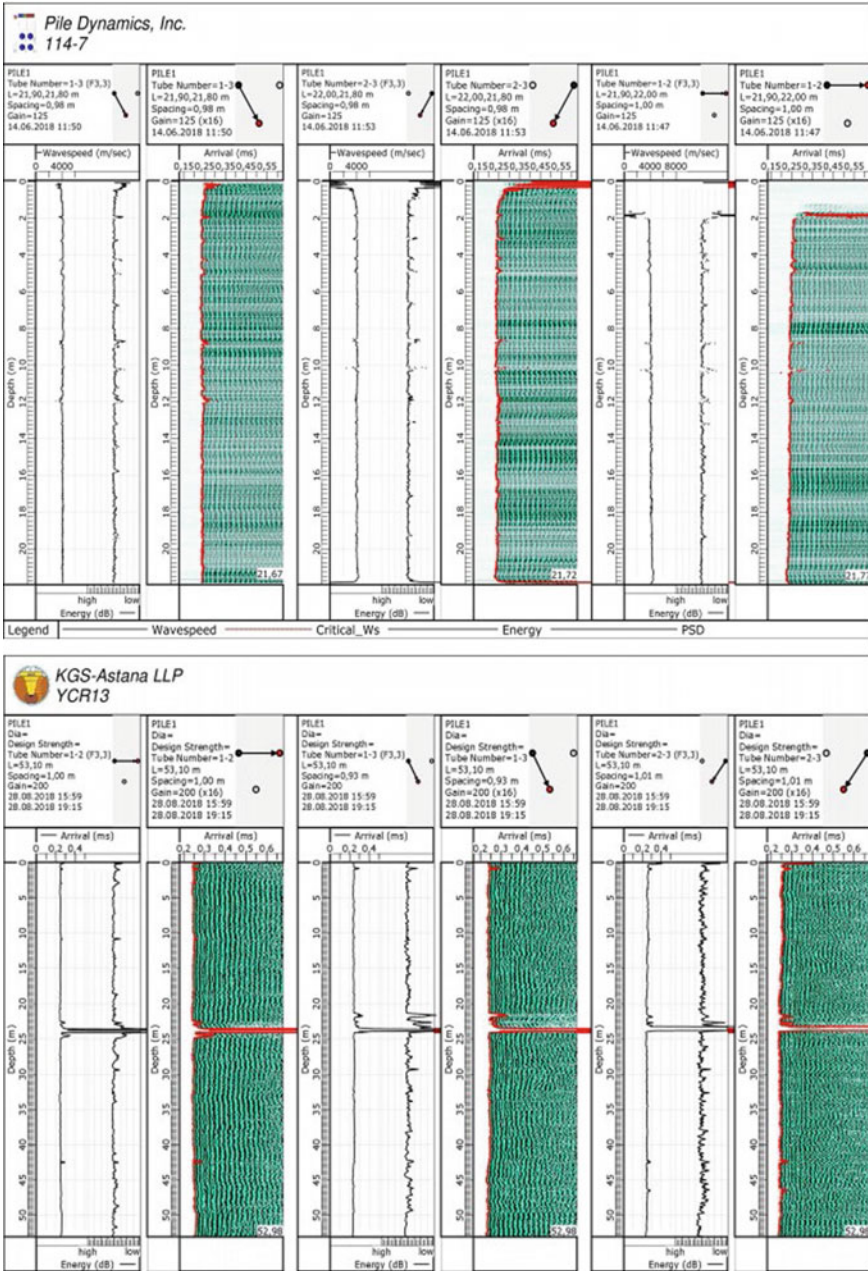


Fig. 10 Results of integrity tests for pile-1 and pile-2 at a LCT site

References

1. Borgekova KB (2020) Analysis of interaction of precast concrete joint piles with soil. Thesis for the degree of doctor of philosophy (Ph.D.), 6D072900—Civil Engineering, Nur-Sultan. Kazakhstan, p 125
2. Zhussupbekov A, Chang D-W, Utepov Y, Borgekova K, Omarov A (2019) Estimating the driven pile capacities for COF project in west Kazakhstan. *Soil Mech Found Eng* 56(20):251–256
3. Zhussupbekov A, Morev I, Omarov A, Borgekova K, Zhukenova G (2018) Geotechnical considerations of piling testing in problematical soils of West Kazakhstan. *Int J GEOMATE* 15(47):111–117
4. Zhussupbekov A, Omarov A, Shakirova N, Abdrakhmanova B, Razueva D (2019) The experience of piling tests on Astana Lrt construction site. In: *The 16th Asian regional conference on soil mechanics and geotechnical engineering (16ARC 2019)*
5. Zhussupbekov A, Omarov A (2016) Modern advances in the field geotechnical testing investigations of pile foundations. In: *Proceedings of the 15th international scientific conference ‘underground urbanisation as a prerequisite for sustainable development. Procedia Eng* 165:88–95
6. Zhussupbekov AZH, Lukpanov RE, Omarov AR (2016) Experience in applying pile static testing methods at the expo 2017 construction site. *J Soil Mech Found Eng* 53(4):251–256
7. Fellenius BH (1980) The analysis of results from routine pile load tests. *Ground Eng Lond* 13(6):19–31
8. Fellenius BH (2001) What capacity value to choose from the results a static loading test. We have determined the capacity, then what? *Deep Foundation Institute. Fulcrum Winter*. pp 19–26
9. Zhussupbekov A, Omarov A, Zhukenova G, Tanyrbergenova G (2017) Pile foundations of mega projects: new railway station and LRT in problematical soil ground of Astana. In: *Proceedings of the international scientific conference transportation geotechnics and geocology. Procedia Eng* 189:511–518
10. ASTM D1143. Standard test methods for deep foundations under static axial compressive load
11. TB 10005–2010 (2010) Code for durability design on concrete structure of railway
12. Zhussupbekov A, Iwasaki Y, Omarov A (2018) The experience different of piling testing on problematical soil ground of Astana, Kazakhstan. *Int J Comput Civ Struct Eng* 14(4):158–171
13. ASTM D6760—08 (2008) Standard test method for integrity testing of concrete deep foundations by ultrasonic crosshole testing. *ASTM International, West Conshohocken*
14. Johnson A (2014) Book recommendations on piling (EA-Pfähle (2013)), Germany

Analysis and Design of a Special Port Pavement for Heavy Steel Coils



Nicolas Echeverri Pinto

Abstract With the current advances in new materials and engineering materials, it has become a common practice that traditional pavements structures made from concrete and asphalt are no longer the most technical and economic structures to guarantee the right balance for the port industry. Ports are industrial facilities with a high demand for strong pavement structures because they are subject to high static and dynamic loads. A pilot project was run in the port facilities of Aguadulce in the town of Buenaventura-Colombia to understand the mechanics and the load transfer to the pavement structure. The test aims to gain a better understanding of the mechanical behavior of a pavement structure made from a granular base, soil–cement and rigid plastic cells filled with concrete. Although the plastic cells have been already used in mining facilities and rural roads, it has never been used in ports under heavy loads, so a pilot structure was built and instrumented with strain gages and pressure cells at the interface of the different materials to measure the horizontal and vertical stresses and strains. Results were compared with axisymmetric and plane strain numerical models, in which pavement layers are modeled with advanced constitutive models like the hardening soil small strain model. A good agreement has been found between the instrumentation results and the numerical model, showing that most of the load is concentrated in the first centimeters, and that plastic cells have a remarkable effect in concrete flexural strength.

Keywords Pavements · Ports · Heavy loads · Dynamic loads · Instrumentation · Numerical modeling

1 Introduction

After the successful construction of the first steelyard in the so-called Patio Sur in the port installation at the Aguadulce peninsula in Buenaventura, more storage space was needed to attend the demand of steel that is growing. However, the port installation

N. Echeverri Pinto (✉)
Risiko Engineering and Risk Management SAS, Calle 114 # 56-45, Bogota, Colombia
e-mail: n.echeverri@risiko.co

has more available storage space in the so-called Patio Norte. The ground surface is not suitable for steel storage, because its surface comprises coarse granular materials very sensitive to water, so with rainwater material loses its strength and stiffness properties that combined with the heavy transit of forklifts, trucks and steel coils, produces unevenness terrain and small holes (see Fig. 1). The above issues were a significant concern of the clients of steel because it reduces the effectiveness of the operation, resulting in additional operating costs. For this reason, investors in steel infrastructure agreed to explore a low-cost alternative. Four alternatives were identified that accurately match the load and surface requirements for the steelyard: A rigid pavement comprising granular soils and typical concrete for pavements structures; granular layer reinforced with geogrid and asphalt layers at the surface; granular materials reinforce with geogrids and at the top of the structure, block pavement made from high-strength concrete.

The final cost of the three pavement alternatives was between 100 USD /m² and 225 USD /m², representing a high initial investment, that did not meet the financial requirements of the project. Therefore, an additional effort was made to identify different and alternative materials that could meet the load requirements. The research ended when rigid plastic cells made from recycled polypropylene with a measured compressive strength of 18 MPa were found.

These plastic geocells are very cheap, reduce carbon emissions and do not need highly specialized equipment to be installed, provide a smooth surface for drivers, and can be filled with almost any material that fits into the cells (see Fig. 2).

Some essential questions arise when trying to define the number and thickness of the different layers that composed the new structure made with a rigid plastic cell structure. Some typical questions were as follows: “Is the behavior rigid or flexible?” “Is the behavior of the plastic cells like concrete blocks?” “What kind of fill material is the most adequate for the heavy loads of the steel coils?” Also, it is presumed

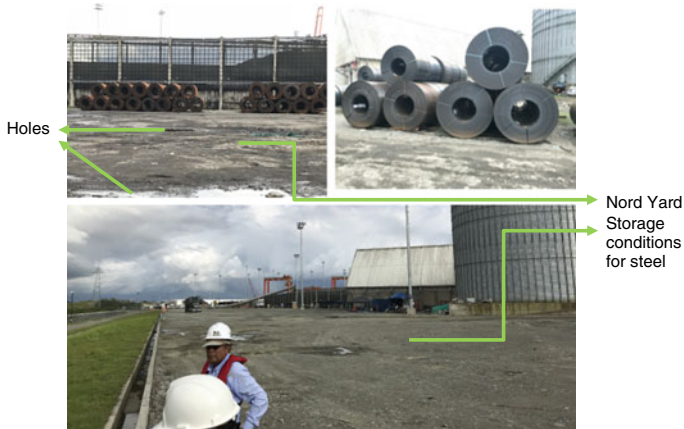


Fig. 1 Current surface conditions for steel storage in Patio Norte

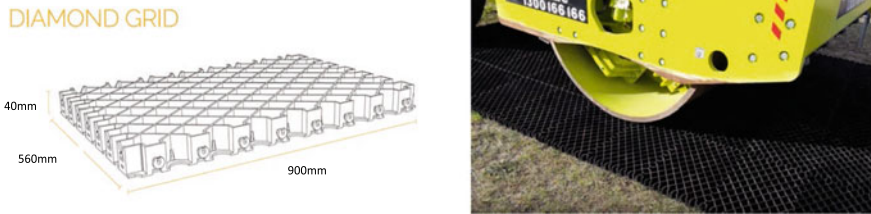


Fig. 2 Typical polypropylene plastic cells. Images Taken From Catalogs of the Product and Published on YouTube

that the mix between concrete and rigid plastic cells reduces carbon emissions. This statement should be tested.

To correctly answer these questions, a pilot pavement test scale 1:1, instrumented with strain gages, and pressure cells were constructed.

Analysis of the pavement structure was evaluated from different perspectives: Numerical models were done to compare and validate the stresses and strains obtained with the results from the instrumentation. Carbon emissions during the construction were evaluated by calculating the global warming potential (GWP) of the structure based on the life cycle inventory (LCI) database from EcoInvent. And the Boussinesq's theory was used to calculate the increment of stresses with depth for three different load cases. Boussinesq's theory was also used to compare and validate the results of the different numerical models.

2 Pavement Structure Geotechnical Engineering and Carbon Emissions

Usually, pavement structures have their specific design methods based on multiple tests and simplify models that result in design charts [1]. Mechanistic-empirical methods have arisen to overcome the empiricism behind this traditional method, like the NCHRP 1-37A report [2]. Although significant advances have been made, these modern methodologies are specific for traffic on roads and highways. The heaviest vehicle that circulates over these roads and highways is a 14 m length truck with a total weight of 520 kN with a typical circulation speed between 60 and 80 km/hr.

Port pavements are, by far, less studied, and design methodologies remain in the traditional semi-empirical methods. One of the most rigorous and best-documented design guides is the ones published by Knapton [3]. Although this guide has many vital recommendations for typical port pavements and considers in the analysis the turns and brakes of heavy equipment like reach stackers, forklifts and cranes, it does not include any recommendations for general cargo elements like steel, big bags among others. It also does not give any recommendations for a different cargo that is not included in the manuals. Therefore, engineering companies usually need to make

their analysis based on experiences and performance of past structures, reducing the possibility of combining different materials that could lead to more economical and suitable pavement designs.

Despite the excellent performance of the designs, there are few studies with field instrumentation that can confirm the performance of the pavement's design. This review points out that pavement and engineering pavement need a solid and consistent background to be used, to answer correctly a more general type of solution that includes different types of cargo and materials.

Considering the nature of pavements, soil mechanics and geotechnical engineering provide one of the most suitable backgrounds to solve pavement problems.

Analysis and design of any structure involve determining actions on the structure and resistance of the materials that composed the structure. In geotechnical engineering, actions are usually lateral loads, vertical loads and earth pressures, and resistance of the materials is based on the shear strength of earth material. Usually, resistance is calculated based on the Mohr–Coulomb criteria.

Like any other geotechnical structure, pavements are made with earth materials and are constructed into or over the ground, so it is expected that the same principles of geotechnical engineering apply. In this sense, pavement structures are like thick footings that distribute the concentrated loads of columns properly into the ground to avoid a bearing capacity failure or excessive settlements. From this point of view, a pavement structure is like an infinite footing laid over the ground, with heavy static and dynamic loads.

As for any footing, it must have enough strength to avoid failure of structural elements, and the settlements of the structure must meet the serviceability requirements. There are many similarities between footings and pavements, and significant differences because pavements should be made without the use of steel reinforcement in concrete because of the cost and are made of different layers that have significant variations in this stiffness. The system to analyze all the aspects of the system (pavement structure) is modeled using finite elements with the program Plaxis. V8.6.

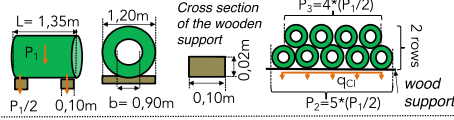
2.1 Simulation and Numerical Analysis

To adequately capture the most critical aspects of the mechanical behavior of the layers that composed the pavement structure and to analyze the pavement structure, three different numerical analyses were used. Two of them are plane strain type, and the third is an axisymmetric type. The first two models are made to study two load cases present in port pavements: The first load case considers the point load that is directly applied from steel elements when they are placed over wooden boards of 0.10 cm width. This load case produces high pressures that in the specific case of steel coils with an average weight of $P = 177$ kN, can reach 1.3 MPa of direct pressure (see Fig. 3 case I).

And as mention above, pavement structure produces in the soil similar effects as a footing or a plate. The structure as a whole can redistribute the point load of

Case I: Maximum Load applied by the Steel coils

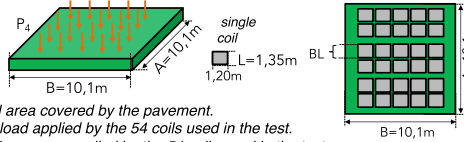
P_1 = Average weight of a single coil.
 A_{cp} = Contact area of the coils in a row.
 BL = Block of coils: configuration 9 coils organized in 2 rows. 5 in the first row and 4 in the second row.
 q_{CI} = Total pressure applied by a block of coils.



Case I: Calculations

$P_1 = 17,7t = 177kN$ $A_{cp} = 0,10m \cdot 1,20m \cdot 5 = 0,60m^2$ $P_2 = 5 \cdot \frac{P_1}{2}$ $P_3 = 4 \cdot \frac{P_1}{2}$ $q_{CI} = \left(\frac{P_2 + P_3}{A_{cp}} \right) = \frac{796,5kN}{0,60m^2} = 1327 kPa = 1,3 MPa$

Case II: Redistribution of the load from the coils due to the pavement structure



A_{CII} = Total area covered by the pavement.
 P_4 = Total load applied by the 54 coils used in the test.
 q_{CII} = Total pressure applied by the 54 coils used in the test.

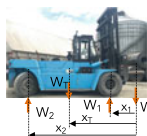
Case II: Calculations

$P_4 = (9) \cdot P_1 \cdot 6 = 9 \cdot 177kN \cdot 6 = 9558kN$
 $A_{CII} = B \cdot A = 10,1m \cdot 10,1m = 102,0m^2$
 $q_{CII} = \left(\frac{P_4}{A_{CII}} \right) = \frac{9558kN}{102,0m^2} = 93,7 kPa$

Fig. 3 Load cases: number I and II in port pavements

the coils, causing that less pressure could reach deeper layers in the ground. This differential aspect with typical road pavements is critical because port pavements need to be analyzed as plate foundations that could have excessive settlements if enough additional stresses reach soft normally consolidated layers (see Fig. 3 case II). Depending on the size of the load applied on the surface of the pavement structure, the load will reach different pavement layers, causing different kind of damages. For example, the high contact pressure of steel coils generates small holes (load case I), which are five centimeters deep, while many coils placed on a large area can produce excessive settlements (20–30 cm) because of stress increment in deep soil layers (load case II). The increment of stress respect to deep can be easily calculated using Boussinesq’s theory (see Fig. 4). The turns, break and accelerations of the forklift also cause small holes, like the ones that are present in the Nord Yard (see Fig. 1). The different kind of damages depends strongly on the increments of stresses experienced by the pavement structure and the soil: The higher the load in a small area, the less deep the damage (see Fig. 4).

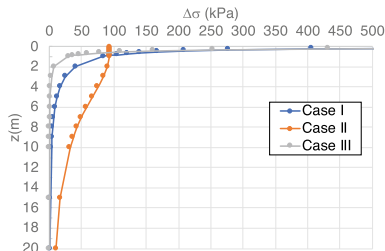
Case III: Dynamic load applied by the Forklift



W_1 = Load on front wheel in (kg)
 W_2 = Load on rear wheel in (kg)
 W_c = Average weight of the coil (kg)
 W_T = Self weight of the truck (kg)
 M = Number of wheels on front axle
 f_d = dynamic factor
 x_i = distances in the Forklift (m)

$A_1 = \left(\frac{-x_2}{x_1 - x_2} \right)$ $A_2 = \left(\frac{-x_1}{x_2 - x_1} \right)$ $B_1 = \left(\frac{W_T(x_T - x_2)}{x_1 - x_2} \right)$ $B_2 = \left(\frac{W_T(x_T - x_1)}{x_2 - x_1} \right)$
 $W_1 = f_d \left(\frac{A_1 \cdot W_c + B_1}{M} \right)$ $W_2 = f_d \left(\frac{A_2 \cdot W_c + B_2}{2} \right)$

Comparison between the load cases and its influence in the soil



Forklift Data:

$x_1 = 2,26m$ $A_1 = 1,57$ $W_1 = 13.531 kg$ $M = 4$
 $x_2 = 6,26m$ $A_2 = -0,57$ $W_2 = 3.500 kg$ $f_d = 25\%$
 $x_T = 4,26m$ $B_1 = 15.600 kg$ $W_T = 31.200 kg$
 $B_2 = 15.600 kg$ $W_c = 17.700 kg$

Contact area of a single tyre:

Tyre pressure (PLL) = 880kPa
 $r = 0,70 \cdot \sqrt{\left(\frac{W_1}{PLL \cdot \pi} \right)} = 0,15m$

Fig. 4 Load case number III

2.2 Geotechnical Parameters

The “Patio Norte” yard was built with fill material coming from the excavation during construction. Because of the fine nature of the material, which is silty clay, it was stabilized with lime. With the purpose of accelerating the expected settlements for consolidation, wick drains were installed. After two years of operation in which different types of cargo were placed over the surface of the yard and according to Boussinesq’s theory, most of the load was concentrated on the first layers of the soil profile (see Fig. 4). Therefore, the over consolidation ratio (OCR) for the first meter varies between 5 and 12, with an average OCR of 8. The mentioned fact is crucial because it defines the initial state of stress of the surface in which the pavement structure will be built.

During the construction, a plate load test was done in several locations at the Patio Norte. Based on the general equation of bearing capacity, Lang [4] combined with the approximate displacement formula, Mayne [5] with a nonlinear variation of the stiffness depending on the level of the applied stress, according to Mayne [6], it was possible to back-calculate (simulate) the plate load test results, which gives strength and stiffness parameters for the subgrade of the pavement structure (see Fig. 5).

Above the subgrade, it is usual to put a granular base layer, which represents a transition between subgrade and bond materials. This transition is best represented by an intermediate stiffness between the two adjacent layers. Typical material strength parameters are considered to calculate its properties, based on the fact, that its properties like grain size distribution have strict limits; also the level of compaction and CBR is defined by the Colombian standard “INVIAS art. 330.” However, the cohesion “c” of this layer is greater than zero (0), and its condition of non-saturated material highly influences it. For the sake of determining the value of the additional strength, the Mohr–Coulomb criteria were modified according to Krahn [7], in which additional strength is given for the suction component (see Fig. 5).

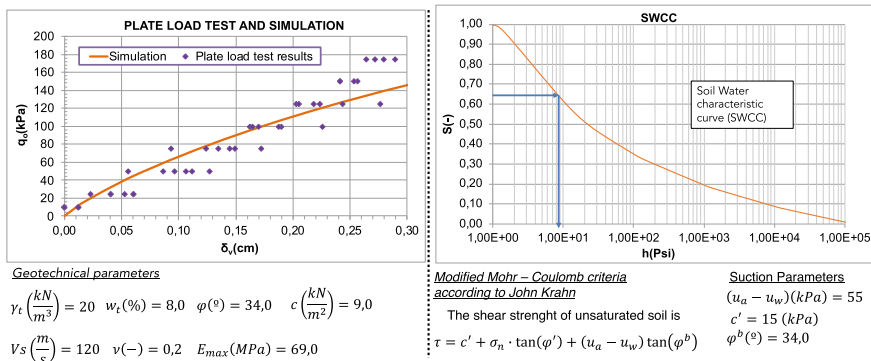


Fig. 5 Plate load test done in Patio Norte and simulation using the bearing capacity theory combined with nonlinear stiffness variation (left). Suction parameters (right)

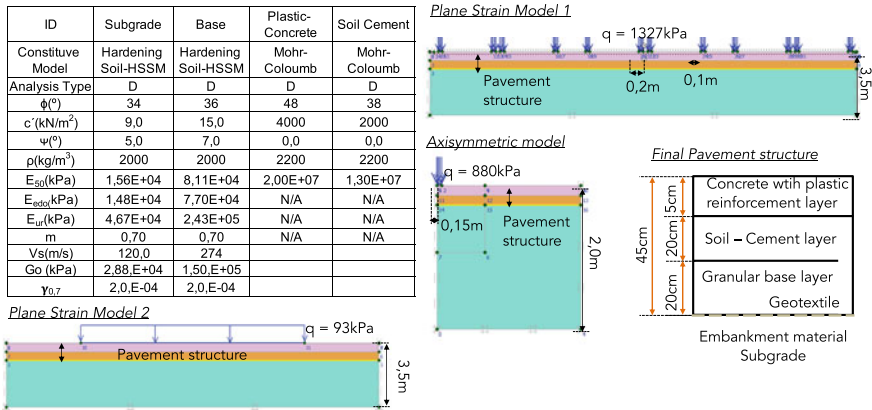


Fig. 6 Final thickness of the pavement structure, numerical parameters for the numerical models and geometric characteristics of the three different numerical simulations

The suggested procedure is given by Barry [8] to calculate the soil–water characteristic curve of the soil was followed. Considering that saturation of the soil will be around 65%, matric suction of the soil (h) will be around 9 PSI, which gives an additional shear resistance of 15 kPa. This value is represented in the numerical model as cohesion (see Fig. 6).

For the soil–cement base layer, a typical dosage of 5% was used. Grain size distribution was done according to the Colombian Standard 350 of INVIAS. To find the Mohr–Coulomb strength parameters, soil–cement was modeled as a rock material using the Hoek–Brown criteria. The shear strength was transformed into Mohr–Coulomb using the equations given by Hoek [9]. The same procedure was done for the plastic cells filled with concrete. Concrete strength specification was set to $f'c = 34$ MPa, to ensure that no failure will occur due to compression or tensile stresses at the bottom of the layer. The data sheet of the plastic cells specifies that compression resistance is around 18 MPa, so no additional considerations were taken to model the mechanical behavior of the plastic cells, waiting to test the response of the plastic cells filled with concrete.

The above parameters were used with three numerical models to identify the proper thickness of each layer. The hardening soil small strains to simulate the granular base layer and the subgrade, the Mohr–Coulomb constitutive model to simulate the behavior of the soil–cement layer and the plastic-concrete layer considering that plastic-concrete and soil–cement layers will fail, because of excessive tensile stress at the bottom of each layer and both the granular base and the subgrade will fail, for excessive vertical deformation.

These failure limitations follow the recommendations made by Reyes [10] for mechanistic pavement designs.

After calculating three numerical models, where the thickness of the layers changed, the final thickness of each layer was defined. With these results, the pilot pavement structure was built.

Plane strain models with steel coils represent the static load in which the maximum resistance calculated in the plastic-concrete base was limited to $MOR = 4.7$ MPa, which corresponds to the maximum tensile stress, that concrete with a compression resistance of $f'c = 34$ MPa can sustain in tension, according to the correlation given by the standard ACI 363. The same procedure was done to limit the tensile resistance of the soil-cement layer, which for concrete of $f'c = 5.5$ MPa is $MOR = 1.92$ MPa.

Numerical simulations give that the maximum tensile stress calculated at the bottom of the plastic-concrete layer is as follows: $\sigma_x = 4.3$ MPa, while in the cement, soil-cement layer is as follows: $\sigma_x = 1.7$ MPa. In the case of the granular base, numerical models (plane strain and axisymmetric) give a vertical deformation of: $\varepsilon_y = 0.18\%$ for static loads and $\varepsilon_y = 0.022\%$ for dynamic loads, while numerical models give values for vertical deformation of: $\varepsilon_y = 0.9\%$ for the subgrade in the case of static loads and $\varepsilon_y = 0.041\%$ in the dynamic load case.

2.3 Carbon Emissions

Previously, it was mention that the use of rigid plastic cells reduces carbon emissions. To properly determine if this is the case for the pavement structure proposed, the construction of the pavement structure with plastic cells was compared with a conventional pavement structure used in port pavements in Colombia with similar subgrade conditions.

Conventional port pavement in Colombia is made of 20 cm thick rigid concrete plate resting over a soil-cement base of 20 cm thick, which is located over a subgrade with an elastic modulus at low deformation of $E_{max} \geq 69$ MPa.

The environmental comparison of the two structures was made based on a simplified life cycle assessment (LCA) of both pavement structures during the construction phase; the operation was not taken into account because it is the same for both pavements. Typical and most common impacts covered by LCA based on midpoint impacts include climate change, stratospheric ozone depletion, acidification, eutrophication among others [11], and the comparison of the two structures is based on its primary environmental impact represented by climate change. To accurately quantify climate change, the global warming potential indicator over 100 years published by the intergovernmental panel on climate change (IPCC) (GWP_{100}) was used. Both pavements were compared based on an area of $100m^2$ with its respective thickness located in the port of Aguadulce in Buenaventura, Colombia.

Using the Internet-based solution LCA calculator, which includes the Ecoinvent database, which is a leading database of life cycle inventory (LCI) used in LCA analysis, the GWP value of the two pavements was calculated [12].

Results of the LCA calculator show that conventional port pavements structure produces a GWP_{100} of 19,000 kg of CO_2 , while the new pavement solution based on rigid plastic cells produces a GWP_{100} of 16,000 kg of CO_2 . This result represents 3000 kg fewer emissions, confirming that the use of recycled polypropylene has a positive impact on reducing CO_2 emissions.

3 Pavement test and Comparison Between Numerical and Theoretical Results

Based on the numerical results, a square area of 100 m² was used to build the pavement structure. The thickness of the layers was built according to the calculated ones given in the numerical models (see Fig. 6). A total number of 16 strain gages were installed at the bottom of the plastic-concrete layer, and two pressure cells were installed at the bottom of the soil–cement layer and the bottom of the granular base layer, directly over the geotextile that separates the granular base and the subgrade (see Fig. 7).

After the construction phase, 14 days were needed to ensure that concrete resistance reached the desired value of $f'c = 34$ MPa for the concrete of the plastic-concrete layer and $f'c = 5.5$ MPa for the soil–cement layer. At 14 days, laboratory compression test results give $f'c = 34.2$ MPa, for plastic-concrete layer and $f'c = 5.7$ MPa for the soil–cement layer.

During the construction of the pavement, a modified proctor test, CBR tests and a density field test were taken to guarantee quality of the construction and consistency with the parameters used in the numerical analysis.

16 days after the completion of the construction of the pavement structure and shortly after a ship arrives at the port with heavy steel coils, the load test was carried out.

During the test, two rows of steel coils were placed at distances varying 10–65 cm according to the numerical simulations and according to typical port operations (see Fig. 7).

From the first coil, until the last one, the data acquisition was continuous to capture all the impacts of the stresses applied over the pavement structure. Three hours [3] after the first coil was placed, the 100 m² was covered with steel coils. A total number of 54 coils were placed, with a total applied weight of 9.248 kN, for an average applied stress of 93 kPa (see Fig. 7).

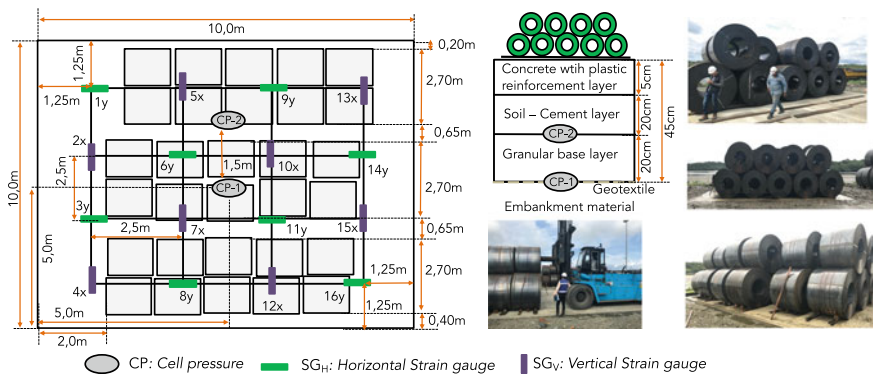


Fig. 7 Layout of the instrumentation and load stages

Results of the strain gauges measurements show that the plastic-concrete layer can sustain tensile stresses because no tension cracks were observed during the test, which is also consistent with the result obtained with the numerical model, where tensile stress at the top is around $\sigma_x = 3.0$ MPa, which is less than the rupture modulus of the concrete of $MOR = 4.7$ MPa. Nevertheless, the numerical simulation was unable to simulate the maximum strain of $\epsilon_x = 0.09\%$, which means that tensile stress could be higher. Numerical tools applied in this analysis are unable to capture the detachment between the soil–cement layer and the plastic-concrete layer (see Fig. 9). Measurements of the vertical displacements between the confinement beam and the plastic-concrete layer reach 1.0 cm. If the tensile stress were above the MOR and the plastic contributes with an additional capacity against tensile stress, it is not possible to determine that with the instruments and measurements made. Laboratory experiments in a more controlled environment are needed to determine the exact interaction between the plastic and the concrete.

Nevertheless, a good agreement between the numerical simulation and the results of the strain measurements from strain gauges was found (see Figs. 8 and 9). It means that the initial hypothesis of the state of stress and the determination of suction parameters, as well as the hypothesis that the soil–cement layer and plastic-concrete layer, can be modeled as rocks, based on the Hoek–Brown criteria works well. This result was also confirmed, with the data recorded from the forklift, where numerical simulations of the axisymmetric model give a value of $-75 \mu\epsilon$, while the instrumentation shows $-86 \mu\epsilon$ (see Fig. 8).

After analyzing the results of the pressure cell, it was observed that the vertical stresses calculated of $\sigma_{yNM} = 750$ kPa corresponded reasonably well with the result

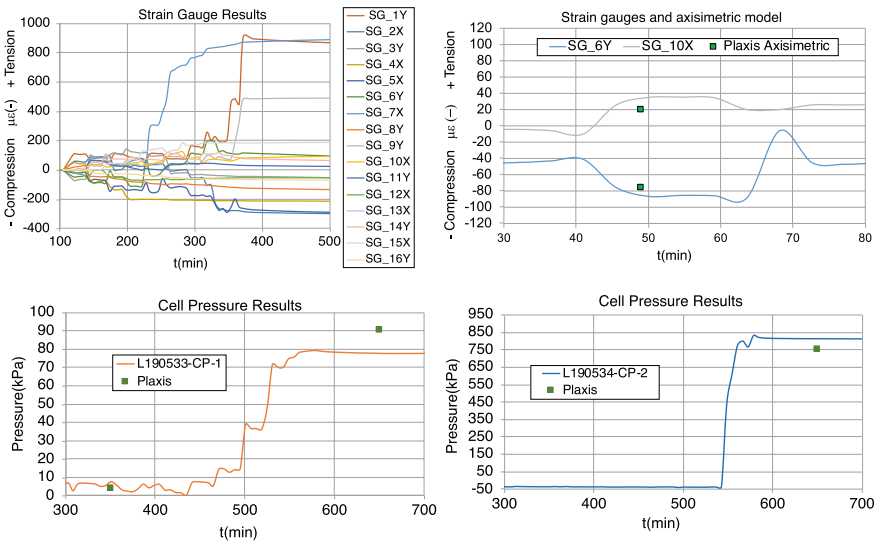


Fig. 8 Strain Gage and pressure cell results from the pavement test and comparison with the results of the numerical simulation

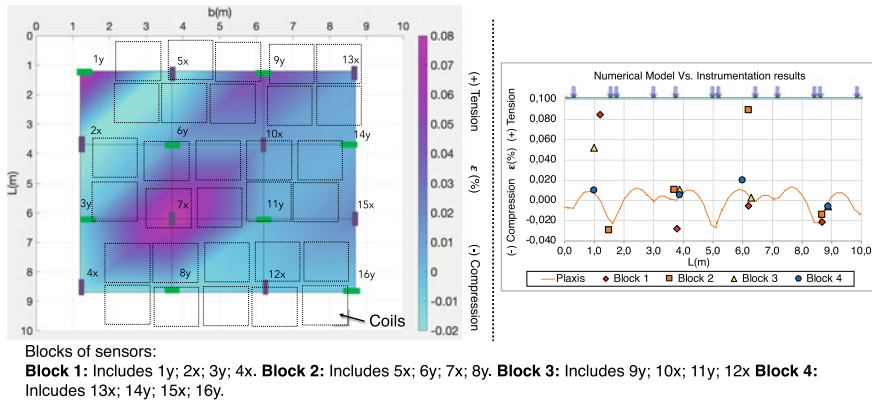


Fig. 9 Results of the instrumentation, its location in the pavement structure and comparison between the numerical model and instrumentation results of the strain gauges. Position of the coils was not perfectly aligned

of the pressure cell, where the measured value reached $\sigma_{yT} = 800$ kPa. Interestingly to notice is the fact that the soil–cement layer acts as the primary load re-distributor because cell pressure at the top of the subgrade measures a value of 80 kPa. This result is possible to be reproduced if the applied load is wholly distributed over the entire area (see Fig. 6 plane strain model 2). Taking this redistribution into account, vertical pressure computed in the numerical simulation of $\sigma_{yNM} = 90$ kPa was near to the measured value of $\sigma_{yT} = 80$ kPa (see Fig. 8). This result is consistent with the initial hypothesis where it was mentioned that pavement layers also act as “plates or footings” for load distribution. A similar result was also obtained based on Boussinesq’s theory (see Fig. 4).

Forklifts, compared to the steel coils, apply less load to the subgrade and the soil–cement layer. For this case, only $\sigma_{yNM} = 11$ kPa was computed while measured values were between $6 \text{ kPa} < \sigma_{yT} < 8 \text{ kPa}$. For the cell pressure CP-2, negative values are not related to real load measurements, because the measure values are almost the same as calibration values of the cell pressure. Although a value of $\sigma_{yNM} = 10$ kPa, was calculated, cell pressure, CP-2 did not notice this minor change because of the lack of reaction of the base layer. It is also possible that during the test base layer got additional compaction, and during this process, CP-2 did not find enough reaction to sense the small load increment.

4 Conclusions

Measurements of pavement structure were consistent with the values calculated with the numerical models. Since numerical models were built using the principles of geotechnical engineering, it means that pavement structures could be also be analyzed

according to laws of soil mechanics. Traditionally, pavements have not been analyzed using all the modern principles of geotechnical engineering because when pavements began to be built in the world, soil mechanics was making its first steps mainly in foundation engineering. Nowadays, with the modern concepts of critical state soil mechanics, partially saturated soil mechanics, pavement structures can be analyzed and model using advanced constitutive models that are more frequently used in geotechnical engineering practice.

From the results of the pavement test and numerical models, it was possible to understand the different aspects that need to be considered, analyzing port pavements. The major difference of road pavement concerning port pavements is the combination of static and dynamic cycles of load, the speed of transit of the vehicles and the amount of pressure applied at the top of the structure. The fatigue analysis of the pavement structure is not analyzed in detail because the test in the port would require a limitation of the operation, and at the moment, this is not possible. Results from the numerical model indicate that the applied stress is more-less 70% of the maximum allowed stress for the pavement materials, which initially shows that the pavement port can sustain the fatigue stresses that will be applied. However, this first study is the first step to go into more detail about the fatigue behavior of port pavement structures and to understand better the mechanical behavior of the plastic reinforcement in the concrete. As an initial hypothesis, the plastic reinforcement does not need to have joints, and apparently, plastic turns concrete into a more flexible and elastic material, favoring its fatigue behavior.

Finally, the author of this study wants to extend its gratitude to the companies involved, which supported the study.

References

1. Huang YH (2004) Pavement analysis and design, 2nd edn. Prentice-Hall, Upper Saddle River
2. ERES Consultants Divison (2004) Guide for mechanistic-empirical design. National Cooperative Highway Research Program, Champaign
3. Knapton J (2008) The Structural design of heavy-duty pavements for ports and other industries. Interpave, Leicester
4. Lang HJ, Bodenmechanik, Grundbau (ed) et al (2007) Springer, Berlin 1; 7 Springer, Zürich
5. Mayne PW, Poulos HG (1999) Approximate displacement influence factors for shallow elastic foundations. *J Geotech Geoenviron Eng* 453–460
6. Mayne PW (2006) In-Situ test calibrations for evaluating soil parameters. In: Characterisation and engineering properties of natural soils, pp 1–56
7. Krahn J (2004) Stability modeling with SLOPE/W. GEO-SLOPE/W International, Ltda., Alberta
8. Barry CR, Schwartz C, Boudreau R (2006) Geotechnical aspects of pavements. Federal Highway Administration (FHWA), Washington
9. Hoek E, Carranza C, Brent C (2002) Hoek—Brown failure criterion—2002 edn. RocLab, Toronto
10. Reyes L, Fredy A, de Pavimentos DR (2003) Bogota: Centro Editorial Javeriano (CEJA)
11. Hauschild, Michael Z, Rosenbaum, Ralph K, Olsen SI (2018) Life cycle assessment theory and practice, sl. Springer. ISBN 978-3-319-56475-3

12. Industrial Design Consultancy (2020) LCA calculator the sustainable design tool (Online). Industrial Design Consultancy. [Cited: 07 5, 2020.] <https://www.lcacalculator.com>

A Study on Suction Properties, Subgrade Modulus and Compressibility of Marine Soil Subgrade for Flexible Pavements



Ram Wanare , Pritam Sinha, and Kannan K. R. Iyer 

Abstract One of the important parameters that governs suitability of soil subgrade for flexible pavements is subgrade modulus and it depends on many factors such as type of loading and its magnitude, soil type and its engineering properties, flexural stiffness of the pavement structure and relative stiffness of the soil subgrade and pavement structure. The strength and stiffness of soil affects its relative stiffness with pavement structure and depends on various factors such as water content, soil type, degree of compaction and soil suction. For most soils, soil suction is mainly due to matric suction. However, for marine soils, soil suction is due to the presence of osmotic suction in addition to matric suction. The evaluation of the influence of both matric and osmotic suction on engineering properties of marine soil would be quite useful to understand its performance as soil subgrade for pavement. In this regard, the present work attempts to understand the relationship between subgrade modulus, suction and compressibility characteristics of marine soil. Experimental studies have been carried out to evaluate the subgrade modulus from California bearing ratio (CBR) tests; matric, total and osmotic suction from filter paper tests; and consolidation and compression characteristics for marine soil from oedometer tests at different degree of compaction. It has been observed that subgrade modulus has good correlation with matric suction in unsoaked condition, however for soaked specimen, the correlation is not conclusive and further studies are envisaged. The study suggests that exhaustive studies on evaluation of variation of soil suction at different water content and degree of compaction for different marine soils can serve as a good tool for understanding the behaviour of soil subgrade for coastal region pavement design.

Keywords Marine soil subgrade · Flexible pavement · Matric suction · Osmotic suction · Subgrade modulus

R. Wanare · P. Sinha · K. K. R. Iyer (✉)

Department of Civil Engineering, Institute of Infrastructure, Technology, Research And Management, Near Khokhra Circle, Maninagar (East), Ahmedabad 380026, India
e-mail: kannaniyer@iitram.ac.in

1 Introduction

Infrastructure development is very important for the development of any country and roadways form a critical part of its infrastructure. Construction of roads/pavements in coastal/marine region requires dealing with challenging soil subgrade conditions such as high-water content, higher compressibility and lower strength. Behaviour of flexible pavement mainly depends on the water content and stiffness of the subgrade soil [1]. The stiffness of the marine soil affects its strength and compressibility and varies as a function of water content [2]. This variation can be quantified through understanding of the energy with which water is held within the soil (viz., soil suction). At lower water content, water is held at very high energy in soil due to high-surface tension and the presence of hydration forces, indicating higher soil suction [3]. Suction reduces with saturation of the soil [4]. Hence, soil suction is an important parameter for understanding the behaviour of embankment and compacted soil subgrade for roadway construction. During compaction of subgrade, the complete removal of air from the residual macro- and micro- voids is not possible. Hence, the soil is partially saturated, and suction is induced the soil [5]. Reduction of soil suction due to inundation or percolation of water in soil subgrade and associated saturation of residual voids and soil particle-air interface would result in lower strength, higher total and differential settlement and distress/damage to the supported pavement structure [6].

Soil suction can be classified mainly as matric suction, ψ_m osmotic suction, ψ_o and total suction, ψ_t [5]. Matric suction in soil is mainly due to the capillary action and hydration forces at the soil particle surface and it reduces with increase in water content of soil during rainy season or due to fluctuation of ground water table [7]. Osmotic suction is due to the presence of salts in soil and also decreases with increase in water content [8]. Sum of matric and osmotic suction constitutes the total suction [9–11].

The factors affecting suction are type of soil, degree of compaction of soil and its microstructure, amount of salt in soil matrix and pore water and soil water content [12]. In most soils, total suction is governed by matric suction. However, in marine soils, due to the presence of salts, the total suction is governed by both matric and osmotic suction. The influence of matric suction on soil subgrade behaviour has been studied by earlier researchers [13–15]. Studies by Sawangsuriya et al. [15] suggested that small strain shear modulus for soil increases with increase in the matric suction and decreases with increase in the volumetric water content. It has been also observed that the initial compaction water content has significant effect on the above stated relationships. Cary and Zapata [14] have reported that the variation in matric suction in unsaturated soils and development of pore water pressure in saturated soils, affects the variation in resilient modulus due to seasonal soil moisture changes. The study recommended the consideration of soil matric suction as an independent stress state variable for obtaining resilient modulus for non-cemented materials. Kim et al. [13] suggested that the mechanical response of soil subgrade depends on matric suction. The study proposed a test procedure for estimation of matric suction for compacted

subgrade soils. It was also noted by the researchers that matric suction was different for soils compacted on dry side of optimum moisture content (OMC) as compared to OMC, whereas matric suction values were close to zero for soils compacted on 2% or more on wet side of OMC.

Other studies [16–18] have indicated that California bearing ratio (CBR), soil compaction characteristics and matric suction are function of soil water content. The study also presented the relationship between CBR value and matric suction above 15,000 kPa. Method to quantify the behaviour of unsaturated soil based on suction characteristics have been developed, and the approach for identifying the suitable material for the road construction has been recommended [19]. Bo et al. [2] reported that the stiffness of the marine soil affects its strength and compressibility and varies as function of its water content. An earlier study has also reported the application of CBR for unstabilized and stabilized marine soil for flexible pavements [20].

The study of literature reveals that limited studies have been carried out on suction characteristics of marine soil and its influence on soil subgrade properties. Further, few studies have attempted to establish the relationship between soil suction and engineering properties of soil subgrade such as compressibility and subgrade modulus, and such studies for marine soils are rare. Hence, this study attempts to quantify matric, osmotic and total suction for marine soil for different states of compaction and to understand the relationship between soil suction, compressibility parameters (obtained from consolidation and compression tests) and soil subgrade modulus (expressed in terms of California bearing ratio). The experimental methodology, results and discussion is elaborated in the following sections.

2 Experimental Investigations

Soil collected for the present study from coastal region in Bhavnagar district, Gujarat state, India is of marine origin, and has been designated as soil S1. The characterization of collected soil was carried out as per ASTM guidelines. The particle size distribution characteristics [21, 22], specific gravity, G [23], liquid limit, w_l ; plastic limit, w_p and shrinkage limit, w_{sl} [24, 25]; maximum dry density, MDD and optimum moisture content, OMC [26]; were obtained and the results are presented in Table 1.

Table 1 Properties of marine soil for experimental study

Soil property	Value	Soil property	Value
G	2.66	w_p (%)	36
Clay (%)	32	w_{sl} (%)	23
Silt (%)	67.5	OMC (%)	23.50
Sand (%)	0.5	MDD (g/cc)	1.435
Soil classification	MH	EC (mS/cm)	7.19
w_l (%)	69		

The electrical conductivity (EC) of the pore solution in soil (obtained by centrifugation method followed by filtering of the supernatant) corresponding to liquid-to-solid ratio (L/S) equal to 5 was measured by employing an EC probe attached to a digital water quality analyser (Auto Ranging Conductivity Metre, Make: Equip-Tronics, India) and the results are presented in Table 1.

The consolidation, compression, CBR and suction measurement tests have been conducted on the soil specimens prepared at three different states of compaction; (a) at $\gamma_d = 1.435$ g/cc and $w = 23.5\%$ viz., MDD and OMC, (b) at $\gamma_d = 1.38$ g/cc and $w = 18.5\%$ viz., dry side of OMC (D-OMC) and, (c) at $\gamma_d = 1.38$ g/cc and $w = 32.44\%$ viz., wet side of OMC (W-OMC). The CBR and suction measurement tests have been conducted for both unsoaked and soaked conditions and the results have been compared with compression and consolidation test results, respectively. The specimen for consolidation, compression and suction measurement by using filter paper have been extracted from the standard compaction test sample at required state of compaction by using standard method for extracting the undisturbed specimens. The total and matric suction of soil specimen have been measured by employing the filter paper method as per guidelines given by [27]. Typical soil specimen for measurement of total and matric suction is shown in Fig. 1. Soil samples have been prepared at three different states of compaction as explained above. The dimensions of soil specimen were 60-mm diameter and 20-mm height, which was same as the specimen utilized for compression and consolidation test.

Matric suction (ψ_m) is measured by the contact method, wherein the Whatman ashless No. 42 filter paper covered by ordinary filter paper on both sides is placed between two cylindrical soil specimens of same soil sample prepared at a given state of compaction. For total suction (ψ_t) measurement, the non-contact method is employed, wherein a small plastic ring of about 5-mm height is placed at top of the upper soil specimen and the Whatman ash less No. 42 filter paper is placed on it as per the guidelines given in literature [27]. The prepared specimen was placed in an



Fig. 1 Placement of filter paper for measurement of matric and total suction. **a** Contact filter paper for measurement of matric suction ψ_m . **b** Non-contact filter paper for measurement of total suction, ψ_t

Table 2 Equations used for obtaining total and matric suction by filter paper method

Suction type	Filter paper water content (w)	Equation	References
Matric suction (ψ_m)	<47%	$\log(\psi_m) = 4.945 - 0.0673(w)$	[3]
	$\geq 47\%$	$\log(\psi_m) = 2.909 - 0.0229(w)$	
Total suction (ψ_t)	<45.3%	$\log(\psi_t) = 5.327 - 0.0779(w)$	[27]
	$\geq 45.3\%$	$\log(\psi_t) = 2.412 - 0.0135(w)$	

air-tight bottle, sealed properly and placed in a desiccator for two weeks’ time [28]. For soaked specimen, saturation has been ensured by placing the soil specimen with rings (used for extraction of undisturbed soil specimen from standard compaction test) in water, covered by filter paper and porous stones at top and bottom sides and applying a surcharge pressure of approximately 5 kPa on top for about 96 h. This was to prevent any disintegration of soil specimen during soaking and to closely replicate the soaking process in the CBR and consolidation tests. The weight of the filter paper is taken after two weeks of equilibration period with soil, and the water content of filter paper is obtained by oven drying the filter paper at $105 \text{ }^\circ\text{C} \pm 5 \text{ }^\circ\text{C}$ for 10 h duration [28]. ψ_t and ψ_m have been obtained from calibration curves recommended by [3] and [27], respectively, (refer Table 2) and the results are presented in Tables 3 and 4. The osmotic suction (ψ_o) has been obtained as difference between ψ_t and ψ_m at a given value of soil specimen water content.

One-dimensional consolidation test as per ASTM guidelines [29] have been performed at three states of compaction (D-OMC, OMC and W-OMC). In addition

Table 3 Soil suction values from filter paper test for unsoaked specimens of soil S_1 at different states of compaction

Compaction state	w_{nfc}^a (%)	ψ_t (kPa)	w_{cf}^a (%)	ψ_m (kPa)	ψ_o (kPa)
D-OMC	10.96	29,758	16.12	7249	22,509
OMC	12.24	23,632	22.58	2664	20,968
W-OMC	13.46	18,994	43.87	98	18,896

* w_{nfc} —water content of non-contact filter paper; w_{cf} —water content of contact filter paper
 The corresponding water content of unsoaked soil specimen (w) was 18.50%, 23.50% and 32.44%, respectively, for dry of OMC (D-OMC), OMC and wet of OMC (W-OMC).

Table 4 Soil suction values from filter paper test for soaked specimens of soil S_1 at different states of compaction

Compaction state ^a	w_{ncf} (%)	ψ_t (kPa)	w_{cf} (%)	ψ_m (kPa)	ψ_o (kPa)
D-OMC	17.50	9204.00	101.67	0.010	9203.99
OMC	17.36	9439.00	73.80	0.950	9438.05
W-OMC	17.08	9919.00	63.48	4.710	9914.29

^aThe corresponding water content of soil specimen (w) after soaking were 45.5%, 38.46% and 37.18%, respectively, for dry of OMC (D-OMC), OMC and wet of OMC (W-OMC)

to that to determine compression characteristics of soil specimen in unsoaked condition, compression tests have been conducted using oedometer cell in the absence of saturation water to ensure the unsaturated state of soil specimen. The results of compression and consolidation tests are presented in Table 5. CBR specimens have been prepared at the different compaction states in CBR test mould of size 150 mm × 173 mm. The CBR test has been performed as per ASTM recommendations, [30] and the results are summarized in Table 6.

Table 5 Compression index (C_C) and Recompression index (C_R) from compression and consolidation tests on specimens of soil S_1 at different states of compaction

Compaction state	Compression test		Consolidation test	
	C_C	C_R	C_C	C_R
D-OMC	0.110	0.010	0.293	0.040
OMC	0.108	0.012	0.260	0.041
W-OMC	0.149	0.020	0.294	0.051

Table 6 California bearing ratio (CBR) for unsoaked and soaked specimens of soil S_1 at different states of compaction

Compaction state	Unsoaked		Soaked	
	CBR value	k^a	CBR value	k^a
		kN/m ³		kN/m ³
D-OMC	12.10	58,361	1.82	13,572
OMC	9.10	51,574	3.43	29,859
W-OMC	6.17	43,431	3.54	30,674

^aObtained as per recommendations of ACI 360R-11 [31]

3 Results and Discussion

The results obtained from suction measurement (total suction, ψ_t matric suction, ψ_m and computed values of osmotic suction, ψ_o), California bearing ratio tests (CBR values and computed values of subgrade modulus, k), consolidation and compression tests (compression index, C_C and recompression index, C_R) are plotted with respect to specimen water content in Figs. 2, 3 and 4. Tables 3 and 4 show the values of ψ_t , ψ_m , and ψ_o for different states of compaction for both soaked and unsoaked conditions. It can be observed from Fig. 2 and Tables 3 and 4 that ψ_o is higher for both soaked and unsoaked specimens. This reiterates the presence of salts due to marine origin of soil S_1 as confirmed by higher value of EC (Table 1). For unsoaked specimen, both ψ_o and ψ_m and hence ψ_t reduce with increase in compaction water content. Further, soaking of soil specimen, results in reduction in ψ_m and ψ_o , with ψ_m converging toward zero, and ψ_o mainly contributing toward ψ_t . From Fig. 3, it can be concluded that CBR and k values are inversely proportional to specimen water content with maximum values at D-OMC (dry side of OMC). This clearly indicates the role of soil suction (ψ)

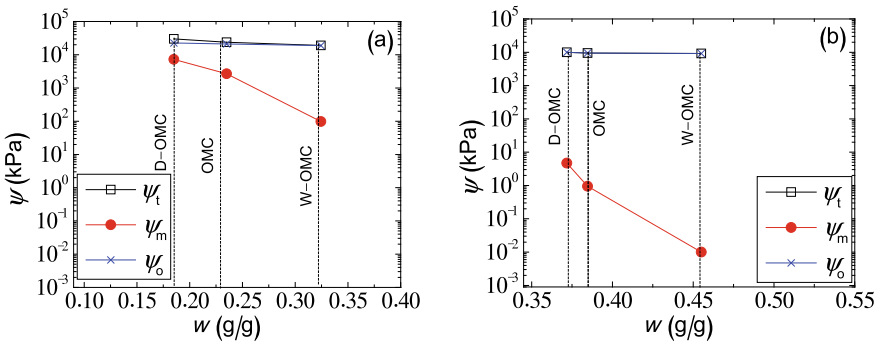


Fig. 2 Suction versus water content for, **a** unsoaked, and **b** soaked conditions

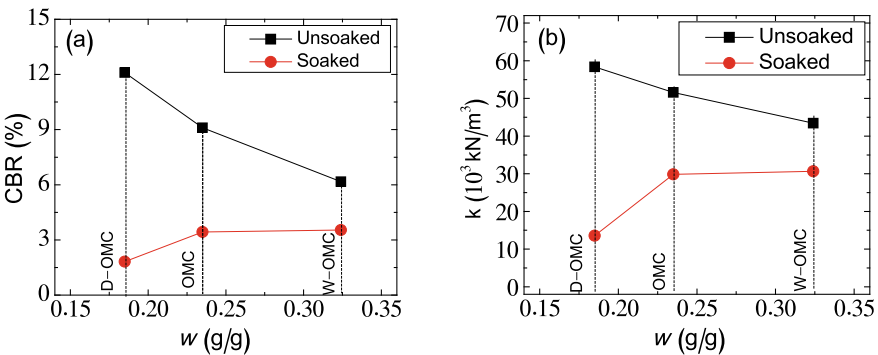


Fig. 3 **a** CBR versus water content, **b** Subgrade modulus versus water content

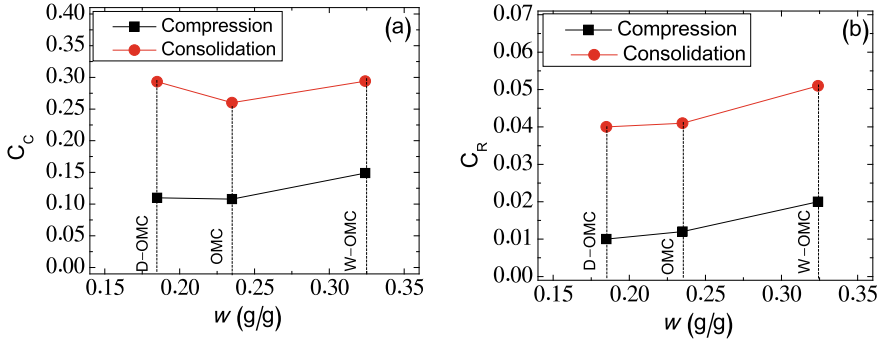


Fig. 4 a Compression index versus water content, b Recompression index versus water content

resulting in higher values of k at lower compaction water content (w), even though the state of compaction is more dense at OMC as compared to D-OMC. Further, for soaked specimens the CBR and k values are lower for D-OMC as compared to OMC and W-OMC. It was observed during the study that the specimen water content after soaking was maximum for specimen compacted at D-OMC, which indicates higher affinity of relatively dry soil for saturation under inundated condition and associated degradation/weakening of soil structure during soaking. Further, it was also opined that the specimen compacted at D-OMC are expected to have more connected and relatively larger voids as compared to specimen compacted at OMC and W-OMC [32], which justifies the above observation.

From Fig. 4, it can be noted that for unsoaked specimen, higher increase in both C_c and C_r with increase in specimen water content is evident between OMC and W-OMC as compared to that between D-OMC and OMC. For soaked specimen, the values of C_c are higher for D-OMC and W-OMC as compared to OMC. Hence it appears that both ψ and voids ratio (which depends on the overall soil microstructure) play an important role in affecting the compressibility characteristics of marine soil S_1 . Further the difference of C_c and C_r between compression (unsoaked) and consolidation tests (soaked) is almost constant for all three initial state of soil compaction (D-OMC, OMC and W-OMC). This difference can be attributed to ψ inherent in the soil for unsoaked specimens which results in pseudo-binding of soil particles; which is subsequently lost due to saturation during soaking. This indicates that the total settlement of soil during consolidation process can be expressed as a function of the compression of soil under sustained loading in unsaturated condition and corresponding reduction in suction, ψ , during saturation. However; further studies are required to get more insight on this hypothesis.

The relationship between ψ and k obtained from the study is plotted in Fig. 5. It can be seen from the figure that ψ_m is directly proportional to k . The variation in k with ψ_o is not very evident. From Fig. 5b, for soaked condition, it can be observed that the reduction in k with reduction in ψ_m is more prominent, when the saturation specimen water content increases (refer Table 4). This indicates that the role of ψ_m is more significant on k in soaked condition (inundated condition of soil) as

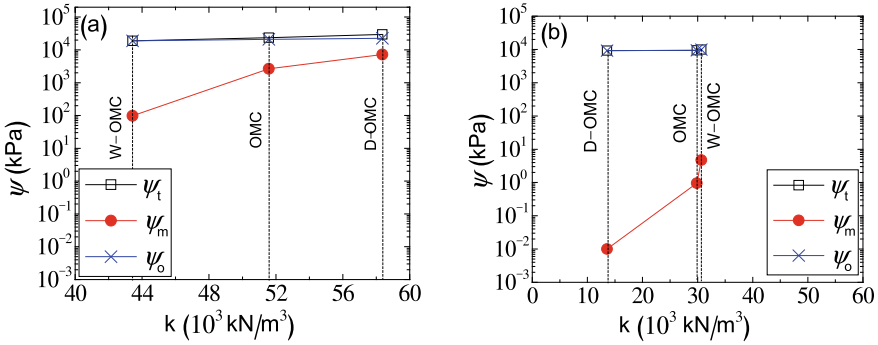


Fig. 5 Comparison of suction and subgrade modulus for, **a** unsoaked condition and, **b** soaked condition

compared to unsoaked condition. This may be attributed to possible alteration in the soil microstructure during soaked condition, resulting in reduction in the soil stiffness and hence k of soil. This aspect can be confirmed by performing microstructural studies on soaked and unsoaked soil specimen at different states of compaction.

Figure 6 depicts the relationship between ψ and C_c for both unsoaked (compression tests) and soaked specimen (consolidation test). It can be seen that the relationship is not conclusive. However, for unsoaked specimen, at D-OMC, both C_c values and ψ values are higher as compared to OMC. The probable reason is that at D-OMC, the ψ values are higher, but the voids ratio is also higher as compared to OMC, which increases the possibility of collapse of larger pores to more dense state during compression test. At OMC, the voids ratio is minimum which reduces the possibility of further collapse of pores to smaller sizes. Further, at W-OMC, the increase in C_c can be attributed to loss of resistance to loading due to loss of suction at higher compaction water content. Hence, it may be opined that both suction and soil microstructure (viz., size of pores, their connectivity and the distribution of different

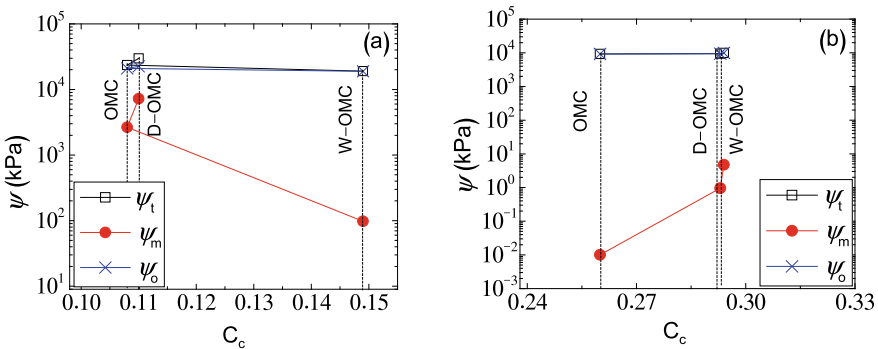


Fig. 6 Comparison of suction and compression index for, **a** unsoaked condition, and **b** soaked condition

sizes of pores) play an important role in controlling the compression characteristics of soil.

C_R appears to vary inversely with both ψ_m and ψ_o for unsoaked specimens, however, the relationship is not conclusive for soaked specimens, as depicted in Fig. 7. The values of C_C and C_R are noted to vary inversely with k for unsoaked specimen (refer Fig. 8), which indicates the role of ψ_m on increasing k and reducing C_C and C_R . However, for soaked condition, the relationship is not well established. This could be attributed to some difference in final water content of specimen after soaking, for specimens prepared for CBR and consolidation test.

Further, Fig. 9 has been plotted to depict the relationship between the soil specimen water content with filter paper water content (contact and non-contact filter paper water content). It has been observed that the soil specimen water content (w_s) correlates well with both contact (w_{cf}) and non-contact filter paper water content (w_{ncf}). However, it is opined that such relationship would depend on other factors

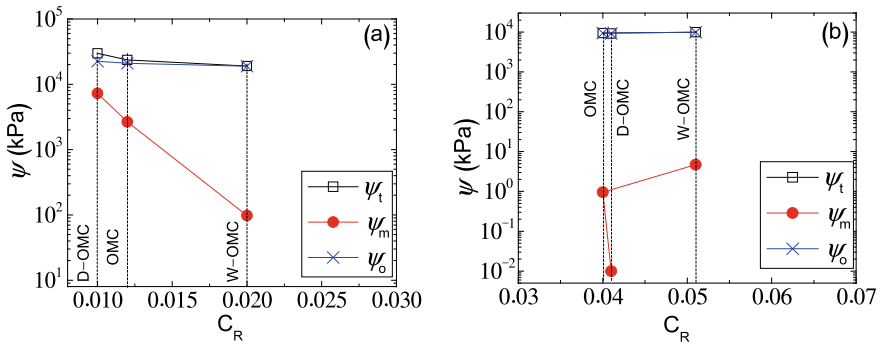


Fig. 7 Comparison of suction and Recompression index for, a unsoaked condition and, b soaked condition

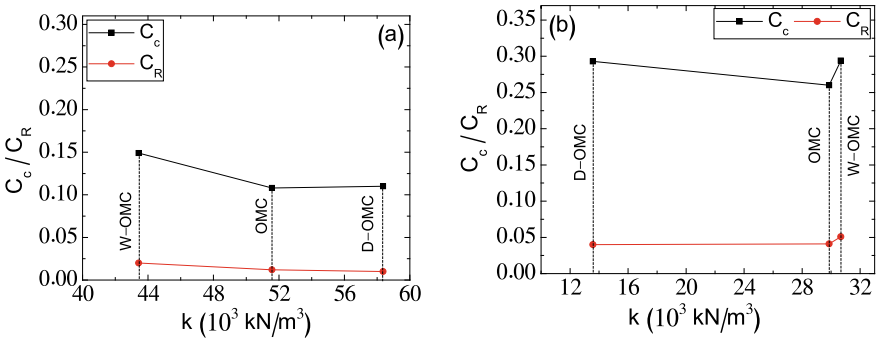
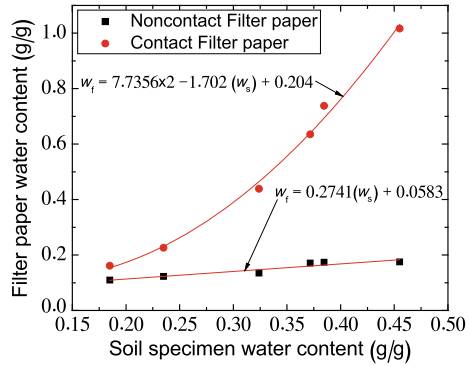


Fig. 8 Comparison of Compression index/recompression index with subgrade modulus for, a unsoaked condition and, b soaked condition

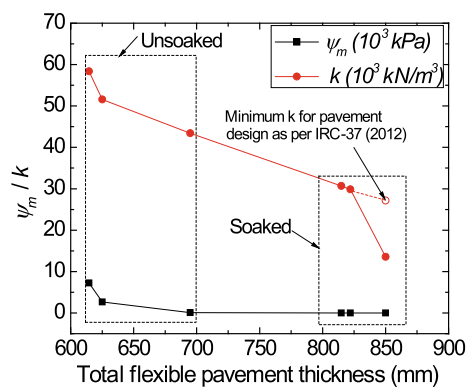
Fig. 9 Comparison of Filter paper water content and soil specimen water content



which are beyond scope of this study and needs to be investigated further for different marine soils at different states of compaction, for generalization of the relationship.

The study indicates that ψ_m shows significant effect on k for unsoaked specimens and also affects compressibility parameters. However, the role of ψ_o is not clearly evident. It is opined that the role of ψ_o is more significant on the rate of wetting or drying of soil and its water holding behaviour, as compared to the strength and stiffness of soil. Further, based on the observed values of k in the study, an attempt has been made to evaluate the total thickness of flexible pavement based on recommendations given in IRC 37 [33] and to study its correlation with ψ_m and k for a typical high -traffic condition (150 msa) as depicted in Fig. 10. As stated earlier, ψ_m affects the pavement thickness for unsoaked condition (fully drained condition in field), as it correlates well with k . However, for soaked condition, understanding the role of ψ_m on flexible pavement design needs more detailed study focussed at low range of suction.

Fig. 10 Comparison of estimated flexible pavement thickness with ψ_m and k



4 Conclusions

The suction, subgrade modulus and compressibility characteristics of marine soil have been established in the study, and their relationship has been studied. Based on the present study, it can be concluded that matric suction influences the subgrade modulus and hence the flexible pavement thickness in unsaturated state (well drained condition). However, for inundated condition, the role of matric suction on variation of subgrade modulus could not be concluded. The relationship between compression index and recompression index with soil suction and subgrade modulus depends on both soil suction and the microstructural features. The study also observed good correlation between filter paper water content and soil specimen water content.

Acknowledgements The authors extend their sincere thanks towards their University; Institute of Infrastructure Technology Research and Management (IITRAM), Ahmedabad, India for extending all the support and providing resources for performing the study. The authors wish to thank Ms. Parishi Dalal (Research Scholar) and Mr. Mustafa Lotia (Former post-graduate student), Ms. Mahi Patil (Research Scholar) at IITRAM for their help in conducting the experimental studies. The authors also acknowledge support from Dr. Yogesh Shah for his support in understanding and interpreting the recommendations of IRC-37 for flexible pavement thickness evaluation. The authors also wish to thank Dr. Jaidevi Jeyaraman for facilitating performance of some experiments at Advanced Environmental Laboratory, IITRAM. The authors also wish to acknowledge Dr. Saurav Das, Dr. Mahuya Bandyopadhyay, Ms. Divya Jadav and Ms. Boni Halder (Chemistry laboratory, IITRAM) for their help for extraction of pore solution by centrifugation method and measurement of electrical conductivity for the soil samples considered in the study.

References

1. Salour F, Erlingsson S (2013) The influence of groundwater level on the structural behaviour of a pavement structure using FWD. The 9th international conference on the bearing capacity of roads, railways, and airfields (BCRRA). ISBN 978-82-3210285-3
2. Bo MW, Choa V, Chu J, Arulrajah A, Horpibulsuk S (2016) Laboratory investigation on the compressibility of Singapore marine clays. *J Marine Georesour Geotechnol* 35(6)
3. Leong EC, He L, Rahardjo H (2002) Factors affecting the filter paper method for total and matric suction measurements. *Geotech Testing J GTJODJ* 25(3):321–332
4. Ridley AM (2015) Soil suction—what it is and how to successfully measure it. In: *Proceedings of the 9th symposium on field measurements in geomechanics*, Australian Centre for Geomechanics, Perth, pp 27–46. https://doi.org/10.36487/ACG_rep/1508_0.2_Ridley
5. Fredlund DG, Rahardjo H (1993) *Soil mechanics for unsaturated soils*. Wiley, New York
6. Zainorabidin A, Agustina DH (2018) Effect of moisture content of cohesive subgrade soil. In: 4th international conference on rehabilitation and maintenance in civil engineering (ICRMCE) MATEC web of conferences 195, 03010
7. Ahmedad A, Hossain S, Alam MJ, Bin, Khan MS (2017) Moisture and matric suction behavior in unsaturated subgrade through field instrumentation and numerical modeling. In: 2nd Pan American conference on unsaturated soils (PanAm-UNSAT 2017)
8. Miller DJ, Nelson JD (2006) Osmotic suction in unsaturated soil mechanics, unsaturated soils. In: 4th international conference on unsaturated soils, April 2–6, Carefree, Arizona, United States. [https://doi.org/10.1061/40802\(189\)114](https://doi.org/10.1061/40802(189)114)

9. Krahn J, Fredlund DG (1972) On total, matric and osmotic suction. *Soil Sci* 114(5):339–348
10. Walker PJ (1997) Measurement of total suction and matric suction in pavement materials at Dandenong ALF site. *Road Trans Res* 6(4):48–58
11. Pufahl DE, Lytton RL (1991) Temperature and suction profiles beneath highway pavements: computed and measured. *Trans Res Record* (1307):268–276
12. Sreedeeep S, Singh DN (2006) Methodology for determination of osmotic suction of soils. *J Geotech Geol Eng* 24(5):1469–1479. Springer. <https://doi.org/10.1007/s10706-005-1882-7>
13. Kim H, Ganju E, Tang D, Prezzi M, Salgado R (2015) Matric suction measurements of compacted subgrade soils. *J Road Mater Pavement Design* 16(2). Taylor and Francis. doi: <https://doi.org/10.1080/14680629.2014.1000945>
14. Cary CE, Zapata CE (2011) Resilient modulus for unsaturated unbound materials. *Road Mater Pavement Design* 12(3):615–638
15. Sawangsuriya A, Edil TB, Bosscher PJ (2009) Modulus-suction-moisture relationship for compacted soils in post compaction state. *J Geotech Geoenviron Eng* 135(10). ASCE. doi: 1943-5606.0000108
16. Innocent S, Ampadu K (2007) A laboratory investigation into the effect of water content on the CBR of a subgrade soil. In: *Experimental unsaturated soil mechanics*. ISSN 0930-8989. ISBN 978-3-540-69872-2. Springer, Berlin, pp 137–144
17. Purwana YM, Nikraz H (2013) The correlation between the CBR and shear strength in unsaturated soil conditions. *Int J Trans Eng* 1(3)
18. Leal FJS (2002) Interpretation of CBR-test results under the shear strength concept of unsaturated soil mechanics. In: *3rd international conference on unsaturated soils*, 10–13 Mar, Recife, Brazil
19. Toll D (1988) *The behaviour of unsaturated compacted naturally occurring Gravel.*, Ph.D. thesis, Imperial College of Science and Technology, University of London, UK
20. Venkateswarlu D, Kumar MA, Raju GVRP, Prasad DSV (2014) A study on the lime-cement stabilized marine clay. *Asian J Microbiol Biotech Environ Sci* 16(2):439–444
21. ASTM D6913M-17 (2017) Standard test methods for particle-size distribution (gradation) of soils using sieve analysis. In: *Annual book of ASTM standards*. ASTM International, West Conshohocken, PA
22. ASTM D7928-17 (2017) Standard test method for particle-size distribution (gradation) of fine-grained soils using the sedimentation (hydrometer) analysis. In: *Annual book of ASTM standards*. ASTM International, West Conshohocken, PA
23. ASTM D854-14 (2014) Standard test methods for specific gravity of soil solids by water pycnometer. In: *Annual book of ASTM standards*. ASTM International, West Conshohocken, PA
24. ASTM D4318-17 (2017) Standard test methods for liquid limit, plastic limit, and plasticity index of soils. In: *Annual book of ASTM standards*. ASTM International, West Conshohocken, PA
25. ASTM D427-04 (2004) Test method for shrinkage factors of soils by the mercury method. In: *Annual book of ASTM standards*. ASTM International, West Conshohocken, PA
26. ASTM D 698-12 (2012) Standard test methods for laboratory compaction characteristics of soil using standard effort. In: *Annual book of ASTM standards*. ASTM International, West Conshohocken, PA
27. ASTM D5298–16: Standard Test Method for Measurement of Soil Potential (Suction) Using Filter Paper, *Annual Book of ASTM Standards*, ASTM International, West Conshohocken, PA (2016).
28. Bulut R, Lytton RL, Wray WK (2001) Suction measurements by filter paper. In: Vipulanandan C, Addison MB, Hasen M (eds) *Expansive clay soils and vegetative influence on shallow foundations*. ASCE Geotechnical Special Publication No. 115. ASCE, Reston, Virginia, pp 243–261
29. ASTM D2435-11 (2011) Standard test methods for one-dimensional consolidation properties of soils using incremental loading, *annual book of ASTM standards*. ASTM International, West Conshohocken, PA

30. ASTM D 1883-07 (2007) Standard test method for CBR (California Bearing Ratio) of laboratory-compacted soils, annual book of ASTM standards. ASTM International, West Conshohocken, PA
31. ACI 360R-06 (2006) Design of slabs on grade. American Concrete Institute, Michigan, United States
32. Tarantino A (2011) Unsaturated soils: compacted versus reconstituted states. In: Alonso and Gens (eds) Unsaturated Soils. Taylor & Francis Group, London. ISBN 978-0-415-60428-4
33. IRC: 37-2012 (2012) Guidelines for the design of flexible pavements. Indian Road Congress, New Delhi, India